Fuling Bian
Yichun Xie
Xiaohui Cui
Yixin Zeng (Eds.)

Communications in Computer and Information Science 398

Geo-Informatics in Resource Management and Sustainable Ecosystem

International Symposium, GRMSE 2013
Wuhan, China, November 2013
Proceedings, Part I

Part 1

Springer

Communications in Computer and Information Science 398

Editorial Board

Simone Diniz Junqueira Barbosa
Pontifical Catholic University of Rio de Janeiro (PUC-Rio), Rio de Janeiro, Brazil

Phoebe Chen
La Trobe University, Melbourne, Australia

Alfredo Cuzzocrea
ICAR-CNR and University of Calabria, Italy

Xiaoyong Du
Renmin University of China, Beijing, China

Joaquim Filipe
Polytechnic Institute of Setúbal, Portugal

Orhun Kara
TÜBİTAK BİLGEM and Middle East Technical University, Turkey

Igor Kotenko
St. Petersburg Institute for Informatics and Automation of the Russian Academy of Sciences, Russia

Krishna M. Sivalingam
Indian Institute of Technology Madras, India

Dominik Ślęzak
University of Warsaw and Infobright, Poland

Takashi Washio
Osaka University, Japan

Xiaokang Yang
Shanghai Jiao Tong University, China

Fuling Bian Yichun Xie Xiaohui Cui
Yixin Zeng (Eds.)

Geo-Informatics in Resource Management and Sustainable Ecosystem

International Symposium, GRMSE 2013
Wuhan, China, November 8-10, 2013
Proceedings, Part I

Springer

Volume Editors

Fuling Bian
Xiaohui Cui
Yixin Zeng
Wuhan University
No. 37 Luoyu Road, Wuhan, Hubei 430079, China
E-mail: {flbian, xcui, yixinzeng}@whu.edu.cn

Yichun Xie
Michigan University, Institute for Geospatial Research and Education
125 King Hall, Ypsilanti, MI 48197, USA
E-mail: yxie@emich.edu

ISSN 1865-0929 e-ISSN 1865-0937
ISBN 978-3-642-45024-2 e-ISBN 978-3-642-45025-9
DOI 10.1007/978-3-642-45025-9
Springer Heidelberg New York Dordrecht London

Library of Congress Control Number: 2013952958

CR Subject Classification (1998): C.3, C.4, G.1.6, H.2.8, H.3.1-4, I.4, I.5

© Springer-Verlag Berlin Heidelberg 2013
This work is subject to copyright. All rights are reserved by the Publisher, whether the whole or part of the material is concerned, specifically the rights of translation, reprinting, reuse of illustrations, recitation, broadcasting, reproduction on microfilms or in any other physical way, and transmission or information storage and retrieval, electronic adaptation, computer software, or by similar or dissimilar methodology now known or hereafter developed. Exempted from this legal reservation are brief excerpts in connection with reviews or scholarly analysis or material supplied specifically for the purpose of being entered and executed on a computer system, for exclusive use by the purchaser of the work. Duplication of this publication or parts thereof is permitted only under the provisions of the Copyright Law of the Publisher's location, in ist current version, and permission for use must always be obtained from Springer. Permissions for use may be obtained through RightsLink at the Copyright Clearance Center. Violations are liable to prosecution under the respective Copyright Law.
The use of general descriptive names, registered names, trademarks, service marks, etc. in this publication does not imply, even in the absence of a specific statement, that such names are exempt from the relevant protective laws and regulations and therefore free for general use.
While the advice and information in this book are believed to be true and accurate at the date of publication, neither the authors nor the editors nor the publisher can accept any legal responsibility for any errors or omissions that may be made. The publisher makes no warranty, express or implied, with respect to the material contained herein.

Typesetting: Camera-ready by author, data conversion by Scientific Publishing Services, Chennai, India

Printed on acid-free paper

Springer is part of Springer Science+Business Media (www.springer.com)

Preface

The 2013 International Conference on Geo-Informatics in Resource Management and Sustainable Ecosystem (GRMSE 2013) was held in Wuhan, China, during November 8–10, 2013. GRMSE 2013 aimed to bring together researchers, engineers, and students working in the areas of geo-informatics in resource management and sustainable ecosystem. GRMSE 2013 featured a unique mix of topics including smart city, spatial data acquisition, processing and management, modeling and analysis, and recent applications in the context of building healthier ecology and resource management.

We received 522 submissions from various parts of the world. The Technical Program Committee worked very hard to have all papers reviewed before the review deadline. The final technical program consisted of 136 papers. There were four keynote speeches, 5 invited sessions. All the keynote speakers are internationally recognized leading experts in their research fields, who have demonstrated outstanding proficiency and have achieved distinction in their profession. The proceedings are published as two volumes in Springer's *Communications in Computer and Information Science* (CCIS) series. Some excellent papers were selected and recommended to the *International Journal of Computational Science and Engineering, Sensors & Transducers Journal* and *International Journal of Embedded Systems*. We would like to mention that, due to the limitation of the conference venue capacity, we were not able to include many fine papers in the technical program.

We would like to express our sincere gratitude to all the members of Technical Program Committee and organizers for their enthusiasm, time, and expertise. Our deep thanks also go to many volunteers and staff for the long hours and hard work they generously gave to GRMSE 2013. We are very grateful to Wuhan University and Eastern Michigan University for their support in making GRMSE 2013 possible. The generous support from the Joint International Center for Resource, Environment Management and Digital Technologies (JIC-REDT), International School of Software, Wuhan University, is greatly appreciated. Finally, we would like to thank all the authors, speakers, and participants of this conference for their contributions to GRMSE 2013, and we also look forward to welcoming you to Michigan in 2014.

Fuling Bian

Organization

International Conference on Geo-Informatics in Resource Management and Sustainable Ecosystem (GRMSE 2013)
November 8–10, 2013 Wuhan, Hubei, China http://www.ggers.org

GRMSE 2013 Committee

Honarary Chair

Michael Batty	Bartlett Professor and Chair of the Centre for Advanced Spatial Analysis (CASA) at University College London, UK
Deren Li	Academician of Chinese Academy of Sciences and Chinese Academy of Engineering, Wuhan University, China

Steering Chair

Fuling Bian	Wuhan University, China

General Chair

Wenzhong Shi	The Hong Kong Polytechnic University, Hong Kong, SAR China
Xiaohui Cui	Wuhan University, China

Executive Chair

Guobin Zhu	Wuhan University, China
Yixin Zeng	Wuhan University, China

Technical Program Chair

YiChun Xie	Eastern Michigan University, USA

Technical Program Chair on Ecological Remote Sensing

Zongyao Sha	Wuhan University, China

Technical Program Chair on Geospatial Information

Richard Sambrook	Eastern Michigan University, USA
Yangge Tian	Wuhan University, China

Technical Program Chair on GIS

Qingwen Xiong	Polytechnic Institute of New York University, USA

Technical Program Committee

YiChun Xie	Eastern Michigan University, USA
Zongyao Sha	Wuhan University, China
George Christakos	San Diego State University, USA
Ping Fang	Tongji University, China
Kuishuang Feng	University of Maryland, USA
Nanshan Zheng	China University of Mining and Technology, China
Changsheng Cai	Central South University, China
Zhenhong Li	University of Glasgow, UK
Yuqi Bai	Tsinghua University, China
Sabine Baumann	Technische Universität München, Germany
Qinghui Huang	Tongji University, China
David Forrest	University of Glasgow, UK
Arie Croitoru	George Mason University, USA
James Cheng	Manchester Metropolitan University, UK
Paul Torrens	University of Maryland, USA
Stephan Mäs	Technische Universität Dresden, Germany
Gina Cavan	Manchester Metropolitan University, UK
Jan Dempewolf	University of Maryland, USA
Bor-Wen Tsai	National Taiwan University, Taiwan
Yu Liu	Peking University, China
Xiaojun Yang	Florida State University, USA
Yan Liu	The University of Queensland, Australia
Jinling Wang	University of New South Wales, Australia
Xiaolei Li	Wuhan University, China
Pariwate Varnakovida	Prince of Songkla University, Thailand
Manfred F. Buchroithner	Technische Universität Dresden, Germany
Anthony Stefanidis	George Mason University, USA
Chaowei Yang	George Mason University, USA
Xiaoxiang Zhu	Technische Universität München, Germany
Matt Rice	George Mason University, USA
Jianjun Bai	Shaanxi Normal University, China
Yongmei Lu	Texas State University, USA
Alberta Albertella	Technische Universität München, Germany
F. Benjamin Zhan	Texas State University, USA
Huamin Wang	Wuhan University, China
Edwin Chow	Texas State University, USA
Lin Liu	University of Cincinnati, USA
Shuqiang Huang	Jinan University, China
Weihua Dong	Beijing Normal University, China
Shuang Li	Wuhan University, China
Mengxue Li	University of Maryland, USA
Wenwen Li	Arizona State University, USA

André Skupin	San Diego State University, USA
Yun Zhang	Wuhan University, China
Alan Murray	Arizona State University, USA
Mike Worboys	The University of Maine, USA
Mu Zhang	Wuhan University, China
Amirhossein Sajadi	Case Western Reserve University, USA

Table of Contents – Part I

Session 1: Smart City in Resource Management and Sustainable Ecosystem

Session 2: Spatial Data Acquisition through RS and GIS in Resource Management and Sustainable Ecosystem

Session 3: Ecological and Environmental Data Processing and Management

Errata

Table of Contents – Part II

Session 4: Advanced Geospatial Model and Analysis for Understanding Ecological and Environmental Process

Session 5: Applications of Geo-Informatics in Resource Management and Sustainable Ecosystem

Mer-Gesh: A New Data Fusion Framework to Estimate Dynamic Road Travel Time

Shudi Zhang*, Bowen Du, and Nianbing Du

Beihang University, Haidian District,
Beijing 100191, P.R. China
zhang_sd@nlsde.buaa.edu.cn

Abstract. The development of a smart city [1] is going to play a leading role in advanced city construction. Therefore, progressively more sensors with heterogeneous features are being, and will be, deployed in such a city, together with an Intelligent Transportation System (ITS). Data fusion is a necessary and sufficient technology for achieving these aims. In this study, we propose a novel data fusion framework (titled **Mer-Gesh**) that Merges multiple data sources in a similar manner to transmission Gears meshing in a uniform spatio-temporal context.

Keywords: Smart City, Data Fusion, Traffic State Perception.

1 Introduction

With rapid growth of population and urbanization, the number of vehicles on the road has risen steeply and urban transportation systems are overcrowded. Realtime travel times play an increasingly important role to observe the performance of street segments in complex urban road networks [2]. However, we also face great challenges when dealing with large arrays of modern traffic sensors because existing systems have to work with a sensor network that: 1) is deployed with uneven density; 2) is heterogeneous; 3) provides noisy data; 4) reports with nonuniform resolutions and frequencies.

The research reported in this paper is a step towards urban computing which improves the performance of smart cities by understanding urban dynamics.

A novel data fusion framework, called **Mer-Gesh** normalizes incomplete multi-sensor properties in a uniform spatio-temporal context and new types of sensors can be added into the model. The framework allows each data source to play a role based on its specific features.

To better understand real-time traffic states, a novel fusion method is proposed to estimate the traffic state based on a citywide traffic scene. In this model, each piece of

* Corresponding author.

F. Bian et al. (Eds.): GRMSE 2013, Part I, CCIS 398, pp. 1–15, 2013.
© Springer-Verlag Berlin Heidelberg 2013

data from sensors is assigned a role that is weighted during every cycle of the fusion process in terms of its level of uncertainty.

Taxi trajectory data, bus trajectory data, fixed sensor data, artificial observation reports and ground truth data are being involved in our research and we have achieved satisfactory results on observing the state of urban traffic.

2 Related Work

The topic of multi-sensor data fusion models has been discussed extensively. Progressively more types of sensors (e.g., loop detectors, probe vehicles, cameras, and cell phones) are employed to detect traffic information. In Chius work [3], a Dynamic Traffic Assignment (DTA) model was proposed to systematically fuse surveillance data from multiple sources and multiple observations over a network. DTA systems have been incorporated in several Traffic Management Centers (TMCs) and can support both planning and real-time applications. DynaMIT [4] is one of the DTA applications which has been implemented and tested in TMCs. It provides a flexible methodology that can be used for the fusion of available data sources. Based on this work, Vaze V et al. [5] formulated the problem of online calibration of the speed-density relationship as a flexible state-space model and presented applicable solutions.

The neural network approach serves as a tool to drive classifiers, estimators and a fusion framework of classifiers and estimators in many applications [7, 8]. In 1995, several studies used neural networks to fuse data for the purpose of detecting traffic information [9, 10]. Cheu et al. [10] used data from probe vehicles and inductive loop detectors to establish an arterial speed estimation model, which was effectively simulated. El Faouzi [11] investigated the use of evidence theory to present a classifier and distance based approach for the fusion of probe vehicle reports and measurements from loop detectors. Kong et al. [6] introduced a fusion model based on evidence theory and inspired by the federated Kalman filter; this model performed well with improved accuracy. Furthermore, Eisenman et al. [12] also proposed a Kalman filter-based approach to numerically evaluate the values of point sensors for real-time network traffic estimation using simulation.

Zhou and Mahmassani [13] developed a non-linear ordinary least-squares estimation model to combine and fuse Automotive Vehicle Identification (AVI) counts, link counts and historical demand information, and solved it as an optimization problem. Wang and Papageorgiou [14] presented a general approach to real-time estimation of the complete traffic state on a freeway. They used a stochastic macroscopic traffic flow model in a state-space formulation. A smart city can be constructed in a sustainable and intelligent way by using ubiquitous sensors [1]. However, the key issue is to fuse the data from these sensors. Unfortunately, to the best of our knowledge, there has been little research on this.

3 Methodology

A transmission gear group is formed by mounting gears on a frame so that the teeth of the gears engage. Gear teeth are designed to ensure the pitch circles of engaging gears roll on each other without slipping; this provides a smooth transmission of rotation from one gear to the next [15]. The variability in traffic sensors creates an important diversity characteristic in information fusion: under conditions of different time slices and different links, real-time data would be collected by different types and quantities of sensors. Features of the above two different concepts have a common point that they both aim at meshing process with gears or data sources, but don't care about concrete gears of sources themselves. Therefore, inspired by this discovery, the traffic data fusion framework we propose in this study is similar to a transmission gear structure; we call it **Mer**ges multiple data sources like transmission **Ge**ars me**sh**ing (**Mer-Gesh**) (Fig.1). It can dynamically adjust the fusion structure based on the diversity of information characteristic mentioned before, just like transmission gears in a motor vehicle. Then we can measure the error of the data sets under the same dimensions without considering where they come from.

The traffic data fusion framework of **Mer-Gesh** is a multi-tier architecture with an emergency brake. In this framework, data units from sensors are assembled and flow up to their own data sources. Then we measure consistencies between each two of them to evaluate their correlation degree, measure each data sources effectiveness including sample confidence measurements, sample fluctuation range measurements and spatio-temporal correlation measurements before they flow to the next fusion level. What's more, variation measurement is conducted to evaluate if estimation result of each data source obey historical law. In particular, the emergency brake is a

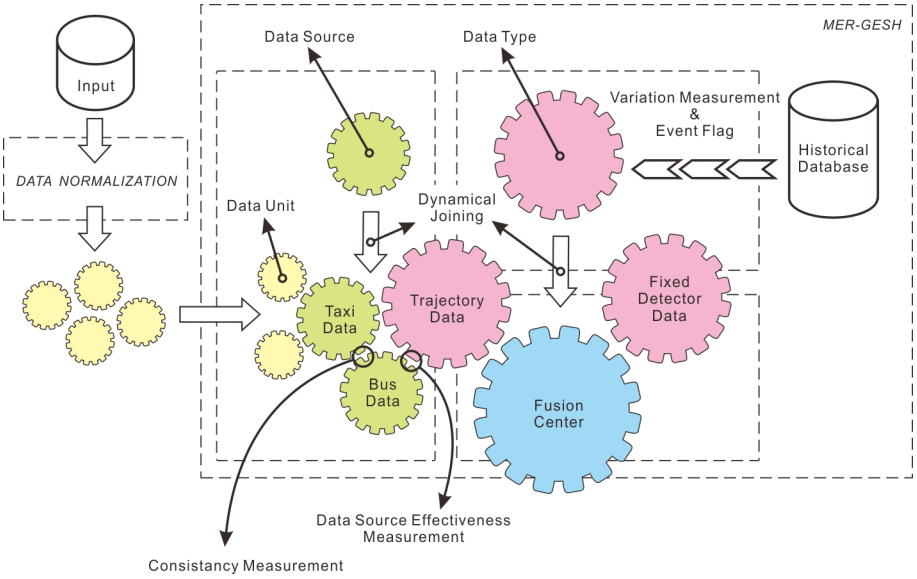

Fig. 1. Data fusion system overview

major element of this framework, which makes use of appropriate data, such as accident or traffic control information to judge if there are traffic emergencies occurred on road sections. An event flag is settled in the framework as an identifier. These emergency data cannot be detected by sensors directly but can be obtained from artificial reports. They provide more traffic details to help the system complete data source estimation process with some targeted adjustment.

At the end of **Mer-Gesh**, fusion center will estimate dynamic road travel time with all data sources based on a weight matrix consisting of each sources measurement results as a weight vector.

3.1 Sample Confidence Measurement

Different types of sources have different confidence levels, which reflect the reliability of the data source. In general, a narrow confidence interval length means more reliable results are obtainable from a data source. To evaluate their reliability, we use the lengths of the confidence intervals under the same confidence level to describe this aspect of data source.

Fixed Detector Sample Confidence Measurement

Suppose there are $m_{(k,l)}$ pieces of sample data collected by fixed detectors in time slice k on link l. $v_1^k, v_2^k, ..., v_m^k$ represent the velocity values of each sample. Assume the data we collect obey normal distribution:

$$V_{(k,l)} \sim N_R\left(\mu_{(k,l)}, \sigma^2_{(k,l)}\right), \tag{1}$$

where $V_{(k,l)}$ is the distribution of velocity in time slice k on link l. Supposing the population distribution is

$$S_{(k,l)} \sim N_R\left(\mu_{(k,l)}, \sigma^2_{(k,l)}\right), \tag{2}$$

We can then obtain the following result beyond the interval estimation:

$$\frac{V_{(k,l)} - \mu_{(k,l)}}{\sigma_{(k,l)} / \sqrt{m_{(k,l)}}} \sim N_R(0,1), \tag{3}$$

which means $\dfrac{V_{(k,l)} - \mu_{(k,l)}}{\sigma_{(k,l)} / \sqrt{m_{(k,l)}}}$ follows a normal distribution which does not rely on any unknown parameter. According to the definition of the upper confidence limit, the length of the confidence interval of the confidence level is:

$$L_{LDD}(k,l) = 2\frac{\sigma_{(k,l)}}{\sqrt{m_{(k,l)}}} z_{\alpha/2}, \tag{4}$$

Moving Detector Data Confidence Measurement

Compared with the methods of population sampling at a fixed road section with a fixed detector, detecting the traffic state by moving detectors reflects population from small samples. Therefore, from existing criteria of data quality, more samples acquired from the road surfaces, results in more accurate traffic conditions. LI [16] reports a threshold value ψ, below which the calculation results obey a t-distribution; while above ψ a normal distribution is followed. Based on statistical theory, ψ is assumed to be 30. In this study, we treat the distribution of a moving car as t-distribution at all times because the size of the trajectory data can barely reach 30 in the short time interval according to long-term statistics.

Using interval estimation theory, we can obtain the length of the confidence interval:

$$L_{FCD} = 2\frac{t_{\alpha/2,n_{(k,l)}-1}\sigma_{(k,l)}}{\sqrt{n_{(k,l)}}}, \tag{5}$$

The confidence level indicates the probability that ground truth data will appear in the confidence interval. In our framework, we calculated the weight of the confidence measurement of the moving detector data source s in time slice k and link l as:

$$\omega_s^{Conf}(k,l) = \frac{L_{Min}}{L_s}, \tag{6}$$

where L_{Min} represents the minimum confidence interval length for all data sources.

3.2 Sample Fluctuation Range Measurement

In an ideal situation, we can obtain the actual traffic state by sampling all the vehicles that have been observed. However, taking the actual situation into consideration, we can only take moving detector data samples from the population. So in this study, the sample fluctuation range is being used as a scale of stability for which the sample data can perfectly reflect the traffic state.

Suppose there are n data sources and the velocity parameter observation function is:

$$Y = Hx + e, \tag{7}$$

where x is the estimated value, Y is an n-dimensional vector, e is an n-dimensional noise vector and H is a known n-dimensional vector, $H = \begin{bmatrix} 1 & 1 & \cdots & 1 \end{bmatrix}^T$. We use the least square estimation to design a minimized sum of errors squared

$$Jw(\hat{x}) = (Y - H\hat{x})^T W (Y - H\hat{x}), \tag{8}$$

where W is a positive definite diagonal weighted matrix, in order to ensure $\partial Jw(\hat{x})/\partial\hat{x} = -H^T(W+W^T)(Y-H\hat{x}) = 0$, we can obtain the sample fluctuation range measurement weight of data source s in time slice k and link l is:

$$\omega_s^{Flu}(k,l) = \omega_s = \frac{1}{\sigma_s^2}, \tag{9}$$

3.3 Spatio-temporal Correlation Measurements

There are two sides reflected by data correlation: one is spatial correlation and the other is temporal correlation. The former means correlation between the traffic state of a target road section and its neighbors. The latter refers to the correlation between the current data point of a road section and a known data point collected on the same site at the same daily time interval but from a different day (as close in time as possible).

Temporal Correlation Measurement

Towards the time slice k, link l, we take velocity parameter values v_s^t and v_{res}^t of ϕ time slices ($k-\phi$ to $k-1$) from the data source s and fusion result database s_{res}^t, to calculate the Pearson correlation coefficient:

$$\omega_s^{Tem}(k,l) = \frac{\sum_{t=k-\phi}^{k-1}\left(v_{res}^t - \overline{v}_{res}\right)\left(v_s^t - \overline{v}_s\right)}{\sqrt{\sum_{t=k-\phi}^{k-1}\left(v_{res}^t - \overline{v}_{res}\right)^2}\sqrt{\sum_{t=k-\phi}^{k-1}\left(v_s^t - \overline{v}_s\right)^2}}, \tag{10}$$

in which $\overline{v}_s$ and $\overline{v}_{res}$ are the separate average velocities from the data source s and the final fusion result in these t time slices.

Spatial Correlation Measurement

Towards time slice k, link l, we select γ levels of cascade links of link l, and these links should be the same road grade to link l. Supposing there are n links, we take the velocity parameter values v_s^t and v_{res}^t of $n+1$ links (link l and n cascade links) from data source s and fusion result database s_{res}^t, to calculate the Pearson correlation coefficient:

$$\omega_s^{Spa}(k,l)=\frac{\sum_{L=1}^{n}\left(v_{res}^{L}-\overline{v}_{res}\right)\left(v_s^{L}-\overline{v}_s\right)}{\sqrt{\sum_{L=1}^{n}\left(v_{res}^{L}-\overline{v}_{res}\right)^2}\sqrt{\sum_{L=1}^{n}\left(v_s^{L}-\overline{v}_s\right)^2}}, \tag{11}$$

in which $\overline{v}_s$ and $\overline{v}_{res}$ are the separate average velocities from the data source and the final fusion result in these links.

3.4 Variation Degree Measurement

Traffic emergency situations are a distinguishing feature of traffic environments. When an emergency occurs on a road section, there will be an obvious difference between the current estimation result and the historical data. However, it is really an existing picture of the road network, such as the traffic state under extreme weather conditions.

Consider data source s, time slice k and link l, we define the variation degree $Var_s(k,l)$ as:

$$Var_s(k,l)=\left|\frac{\mu_s(k,l)-\mu_s^h(k,l)}{\mu_s^h(k,l)}\right|, \tag{12}$$

in which $\mu_s(k,l)$ and $\mu_s^h(k,l)$ represent the velocity parameters of the current time slice and the same period in history. The weight of the degree of variation can then be calculated as:

$$\omega_s^{Var}(k,l)=1-Var_s(k,l), \tag{13}$$

When the value of the degree of variation exceeds a specific threshold, we assume that an emergency has occurred on the target link. In this case, all processes related to historical data are abandoned. On the contrary, the smaller the degree of variation, the more stable the data source.

3.5 Event Detection

Event information, such as traffic controls or traffic accidents in a road network, is similar to an emergency brake in a transmission gears system. In different types of traffic events, the real-time traffic state will not increase in a regular manner. So an event flag parameter is set to reflect whether an event has occurred on the road. This flag can be changed by the degree of variation.

Supposing there are N data sources. The event state is accessed based on the degrees of variation of these data sources:

$$\tau = \begin{cases} 1 & \dfrac{\sum_{s=1}^{N} Chg_s(k,l)}{N} > \theta, \\ 0 & else \end{cases} \tag{14}$$

We divide events into two parts on the basis of the capacity capability of the road's traffic for a normal event and an influential event. The former indicates that even if some event has occurred on the road, it still has the capacity for vehicles. In this situation, we change the flag to $\tau = 0$. The latter indicates that the road has temporarily lost its ability to transport. In this situation, we change the event state to $\tau = 1$. According to τ value, we obtain the event flag:

$$Ent(k,l) = \tau, \tag{15}$$

It is a special index for evaluating the data sources' event state. It has a fixed value irrespective of any one of the data sources, but applies to all of them. Its value can be set to 0 or 1, representing whether there is an emergency event that has occurred on the target link.

3.6 Data Source Consistency Measurement

Because the values of output gathering from multiple data sources in the same time interval and link have redundancy and have some relativity to each other, we can measure the degree of support between each two data sources based on calculating the distance between their parameter values. The data source with a higher degree of support is treated as the more credible source and is given higher weighting in the subsequent fusion process.

In consistency measurement, we assume that if the parameter value of data source s is very different to that of other data sources, it means the observation data from source s has a low degree of support, even when totally separated from each other. Otherwise, the observation data from source s has a high degree of support and its reliability increases.

We define the distance between a data source s and other data sources as:

$$d_s = \sum_{i=1}^{N} |v_i - v_s|, \tag{16}$$

in which $\sum_{i=1}^{N} |v_i - v_s|$ represents the sum of the distances between s and other data sources.

For each data source, we calculate the degree of support by: $r_s = \frac{d_s}{\sum_{i=1}^{N} d_i}$. We can then get the consistency measurement weighting of data source s in time slice k, link l as:

$$\omega_s^{Cons}(k,l) = 1 - r_s, \tag{17}$$

Finally, we have got the weight matrix $Mat(k,l)$.

3.7 Data Fusion

Definition. *Incomplete multi-source fusion issue*: A multiple data source traffic fusion issue is defined as $U = (S, A, \Omega, f)$, where $S = \{s_i, i = 1, 2, ..., N\}$ is a non-empty finite set of data sources participating in the fusion process, $A = \{a_j, j = 1, 2, ..., M\}$ is the set of estimation indexes, $\omega_{s_i}^{a_j}$ represents the weighting value of index a_j of data source s_i, and we can obtain the set $f : U \times A \to \Omega$, $f(s_i, a_j) \in \Omega$, $\Omega = \left\{\omega_{s_i}^{a_j}, i \in 1, 2, ..., N, j \in 1, 2, ...M\right\}$. The abnormal operation state of detectors and the random mobility of moving location detectors, make index values dynamically random, uncertain and partially vacant. In this study, we define this type of transportation data fusion issue based on data with these features as an incomplete multi-source fusion issue.

We combine the sample confidence, sample fluctuation range, spatio-temporal correlation as a feature description matrix:

$$D(k,l) = \begin{pmatrix} \omega_1^{Conf}(k,l) & \omega_1^{Flu}(k,l) & \omega_1^{Tem}(k,l) & \omega_1^{Spa}(k,l) \\ \omega_2^{Conf}(k,l) & \omega_2^{Flu}(k,l) & \omega_2^{Tem}(k,l) & \omega_2^{Spa}(k,l) \\ \vdots & \vdots & \vdots & \vdots \\ \omega_N^{Conf}(k,l) & \omega_N^{Flu}(k,l) & \omega_N^{Tem}(k,l) & \omega_N^{Spa}(k,l) \end{pmatrix}, \tag{18}$$

To evaluate a data source's effectiveness we use the degree of variation measurement diagonal matrix:

$$I(k,l) = diag\left(\omega_1^{Var}(k,l), \omega_2^{Var}(k,l), ..., \omega_N^{Var}(k,l)\right), \tag{19}$$

To reflect the influence from an event, the event flag $Ent(k,l) = \tau$ is used to represent whether there has been an emergency and we use the data source consistency measurement diagonal matrix:

$$H(k,l) = diag\left(\omega_1^{Cons}(k,l), \omega_2^{Cons}(k,l), ..., \omega_N^{Cons}(k,l)\right), \quad (20)$$

to comprehensively evaluate the data source by inter-comparison.

From the feature description matrix D, the variation degree measurement diagonal matrix I, event flag Ent and data source consistency measurement diagonal matrix H, the first order fusion method is defined as:

$$P(k,l) = \left(D^T I^{1-Ent} H\right)^T W, \quad (21)$$

The resulting vector P of the formula represents the reliability of each data source in the data fusion process. $W = \left(w_{Conf}, w_{Flu}, w_{Tem}, w_{Spa}\right)^T$ is the vector of description index weights, in which w_j is the weighting value of the corresponding index a_j in a Spatio-Temporal Context framework. These values reflect the importance of indexes in the description matrix D in participating in the fusion process.

Finally, treating P as weight vector of all data sources, we can get fusion result by easily using weighted average method.

4 Evaluation

In this section, the advantages of the proposed approach are discussed by comparison of data fusion techniques and the accuracy of estimation between single and multiple sources.

The Beijing road network is composed of more than 120,000 road sections and more than 5,000,000 vehicles running on it every day. These road sections are grouped into four datasets: high ways, express roads, national roads and others. Among these, express roads and national roads are typical of the city and the latter are also main roads of the city but with traffic lights. In this paper, three road sections (Fig.2) as three different scenes (Fig.3) are used to represent situation of express road, main road and ideal experimental environment.

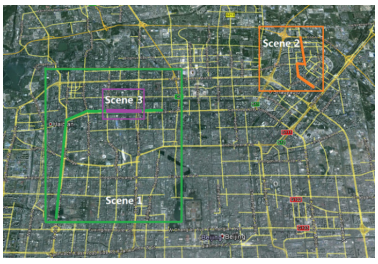

Fig. 2. Road sections in the test bed

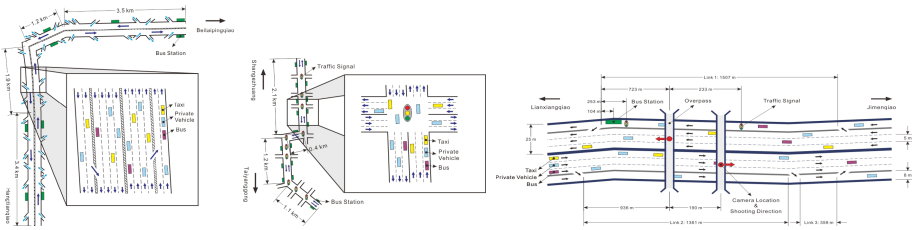

Fig. 3. Illustration of 3 Scenes

4.1 Comparison of Estimation Result between Single and Multiple Sources

Fig.4 shows the velocity estimation results calculated from each type of data source and the fusion method we proposed. Each figure has been divided into two parts: the upper shows the estimation result of each data source in line with the link order (Scenes 1, 2) or time slice order (Scene 3), and the bottom shows the absolute error of the estimation result of these data sources compared with ground truth data. These figures illustrate that the taxi data usually performed better than bus data because there were more taxis on the road reflecting real-time traffic conditions. However, when the road was congested the bus data may generate more accurate results because they have a shorter sampling interval. It shows that nearly all fusion methods in the 3 scenes obtained a significant improvement in accuracy over a single data source. This is of course the most desirable result, where multiple sensors are combined to achieve accuracy greater than when used individually.

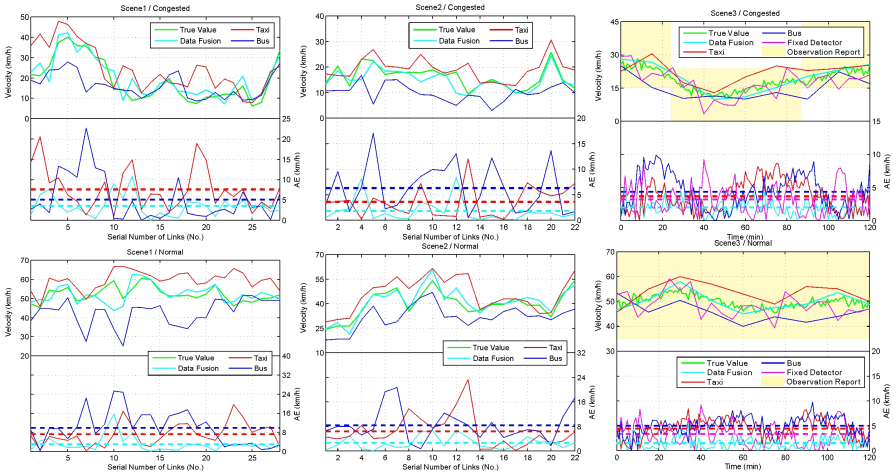

Fig. 4. Error comparisons for different data sources

An interesting outcome is that floating vehicle estimates become more accurate as the probe vehicle sample size increases. Even with uncertain sample sizes, floating cars are usually more accurate than loop detectors. Additionally, their error curves appear sensitive to traffic conditions. All of the data fusion techniques can be trained using a sample set of field collected data. This suggests that a real-time data fusion based traffic monitoring system is entirely feasible.

While single source estimation data have a large error compared with ground truth data, our fusion method based on these data sources showed a much better output result. Which means that ATMS or ATIS based real-time data fusion is entirely necessary and feasible.

4.2 Comparison of Data Fusion Techniques

To prove our method is an improvement on previous methods, we selected *Simple Average* and *Artificial Neural Network* to be typical data fusion methods to perform experiments to compare with our method. At the same time, to ensure the effectiveness and fairness of the final results, the same dataset was used in the comparison experiments below, including data used for module training and traffic state estimation.

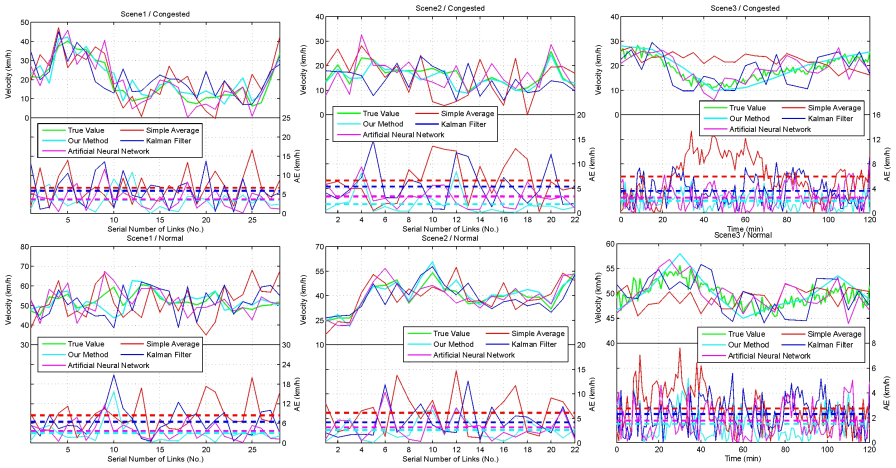

Fig. 5. Error comparison of mainstream approaches

Fig.5 shows the velocity estimation results calculated using different types of data fusion methods and the true value. They show the velocity variation in the same time sequences. All 6 comparisons illustrate that the *Simple Average* fusion method is the traditional midpoint technique by a considerable amount (180 days), but does not have much more improvement from a single data source when compared to other methods used for comparison. In addition, sometimes its estimation results have a

greater RMSE compared with results from the same data source, as shown in Scene 3/Normal in Fig.5. This is because there are big gaps between sensors coming from multiple sources even for single data sources. To go further, road section travel time is not only about sensor outputs, but also about the spatio-temporal context that these sensors locate.

Artificial Neural Network performed much better than the midpoint average in all three scenes. Furthermore, the results gathered are the best among the methods we chose to do comparison experiments with. It is easily seen that this method can do better for a problem with an uncertain size of data. We can easily see in Scene 1 and Scene 3, Fig.5 that its fusion result perfectly avoids some abnormal value collected from a single source. However, when two or more data sources contain outliers, its accuracy may suddenly drop as shown in Scene 2, Fig.5, which means that *Artificial Neural Network* perform irregularly and inconsistently for some time periods. In addition, it needs a mass of historical data to train the model.

It is undeniable that our method has a stronger performance compared with the others we mentioned, and this can be seen in Table 1. When traffic becomes congested, our model can recognize a complex situation by means of the effective data cleaning and weighting module and returns satisfactory results. Compared with estimation results gathered from a single source with any of the methods, fusion techniques with more data sources can always achieve more reliable outputs.

Table 1. AE (km/h) of estimation techniques

Method/Source		Traffic State		
		Congested (8:00 – 9:00)	Normal (12:00–13:00)	Free Flow (21:00–22:00)
Scene 1	Taxi	7.60	7.28	4.73
	Bus	5.10	9.93	6.95
	Simple Average	6.74	8.46	5.37
	ANN	3.72	3.68	3.91
	Our Method	3.52	3.08	2.75
Scene 2	Taxi	3.59	6.36	5.16
	Bus	6.31	8.37	7.15
	Simple Average	6.63	6.16	5.70
	ANN	3.39	3.17	2.59
	Our Method	1.78	2.64	2.62
Scene 3	Taxi	3.69	4.44	3.15
	Bus	4.38	5.02	4.72
	Fixed Detector	3.25	3.23	2.98
	Simple Average	5.88	2.73	2.64
	ANN	2.50	1.78	1.45
	Our Method	2.00	1.52	1.55

5 Conclusions

Data fusion is an efficient method to integrate the heterogeneous data to provide more reliable information. But from the current literature, state-of-the-art techniques seem promising in this particular context. These problems can be overcome by the encouraging results of an operational widespread data fusion system finally being deployed in the transportation field. These problems include the accuracy necessary for effective applications, the dynamic and real time aspects of the traffic and data quality, and the real time dimension.

To systematically fuse data from multiple sources and multiple observations over a network, this research has initially investigated several multi-sensor data fusion based techniques for traffic speed estimation. Two contributions are provided: a novel gear framework which has the ability to add new types of sensors in a dynamic way and a novel fusion model with dynamic properties, which can fuse data collected from different sensors at different location and with different features. The key advantage of the method is its ability to accept any types of sensors deployed anywhere in the network, and output results at any time interval.

We tested the fusion techniques on a wide diversity of links with various features and sensor configurations, which would lead to new insights. Very encouraging results were obtained for travel time estimation using fusion data from different sensors such as taxi trajectories, bus trajectories, fixed detectors, cameras and events. It was shown that the combination of multiple data sources can result in more reliable travel time. By these means, from the experimental results, we have proved that we are able to establish a more comprehensive and accurate estimation of urban road traffic states and their reliability is able to satisfy the requirements of practical applications in a developing smart city, such as Beijing.

References

1. Hancke, G.P., de Carvalho e Silva, B., Hancke Jr., G.P.: The Role of Advanced Sensing in Smart Cities. Sensors 13, 393–425 (2013)
2. Fabritiis, C.D., Ragona, R., Valenti, G.: Traffic estimation and prediction based on real time floating car data. In: Proceedings of the 1lth International IEEE Conference on Intelligent Transportation Systems, pp. 197–203 (2008)
3. Chiu, Y.C., Bottom, J., Mahut, M., et al.: Dynamic traffic assignment: A primer. Transportation Research E-Circular, E-C153 (2011)
4. Milkovits, M., Huang, E., Antoniou, C., et al.: DynaMIT 2.0: The next generation real-time dynamic traffic assignment system. Institute of Electrical and Electronics Engineers (2010)
5. Vaze, V., Antoniou, C., Wen, Y., et al.: Calibration of dynamic traffic assignment models with point-to-point traffic surveillance. Transportation Research Record: Journal of the Transportation Research Board 2090(-1), 1–9 (2009)
6. Kong, Q., Chen, Y., Liu, Y.: A fusion-based system for road-network traffic state surveillance: a case study of Shanghai. IEEE Intelligent Transportation Systems Magazine 1(1), 37–42 (2009a)

7. Han, J., Kember, J.: Data Mining Concepts and Techniques. Morgan Kaufmann Publishers, USA (2000)
8. Hashem, S.: Optimal linear combinations of neural networks. Neural Networks 10, 599–614 (1997)
9. Ivan, J.N., Schofer, J.L., Coppelman, F.S., Massone, L.L.E.: Real-time data fusion for arterial street incident detection using neural networks. Transportation Research Record 1497, 27–35 (1995)
10. Cheu, R.L., Lee, D., Xie, C.: An arterial speed estimation model fusing data from stationary and mobile sensors. In: 2001 IEEE Intelligent Transportation Systems Conference Proceedings, Oakland, CA, pp. 573–578 (2001)
11. El Faouzi, N., Lefevre, E.: Classifiers and distance-based evidential fusion for road travel time estimation. In: Proceedings of SPIE, vol. 6242, pp. 92–107 (2006)
12. Eisenman, S.M., Fei, X., Zhou, X.S., Mahmassani, H.S.: Number and location of sensors for real-time network traffic estimation and prediction: A sensitivity analysis. Transportation Research Record: Journal of the Transportation Research Board No. 1964, 253–260 (2006)
13. Zhou, X., Mahmassani, H.S.: Dynamic OD demand estimation using automatic vehicle identification data. IEEE Trans. Intelligent Transportation Systems 7(1), 105–114 (2005)
14. Wang, Y., Papageorgiou, M., Messmer, A., et al.: An adaptive freeway traffic state estimator. Automatica 45(1), 10–24 (2009)
15. Uicker, J.J., Pennock, G.R., Shigley, J.E.: Theory of Machines and Mechanisms. Oxford University Press, New York (2003)
16. Qiang, L.I.: Arterial Road Travel Time Study usingProbe Vehicle Data, Department of Civil EngineeringNagoya University (2007)

A City's Composite Foundation Building Land Suitability Evaluation

Xue-mei Li, Zeng-qin Zhang, Zhi-feng Song, and Wen-jing Chen

Hebei Prospecting Institute of Hydrogeology and Engineering Geological
050021 Shijiazhuang, China
Fcy1970@163.com

Abstract. Through In-depth analysis and research a city construction land's engineering geological conditions ,a comprehensive system evaluation for the construction land of composite foundation of the study area suitability, establish a city construction land suitability evaluation system, get the results is engineering geological evaluation and prediction of the environmental quality of the evaluation results, and fuzzy comprehensive evaluation model is introduced into construction land suitability evaluation use fuzzy comprehensive evaluation method, a city construction land is divided into four suitability level partition: Suitable areas , comparable suitable area , suitable compare poor areas and poor suitability district.

Keywords: composite foundation evaluation, Fuzzy Comprehensive Evaluation Method, soil layer bearing capacity.

This study combined with Hebei water Institute survey of a city urban geological investigation and evaluation of projects carried out. Geological Survey of the city is a major project, The engineering services in a municipal social and economic sustainable development for the purpose ,Tightly around a city facing and the urban geological problems to be solved, according to the needs of a city 's overall urban planning, tightly followed the process of urbanization pulse, Give full play to the advantage of the disciplines of geological work[1],To carry out comprehensive geological survey of the city three - dimensional geological structure , geological resources and geological environment , comprehensive evaluation of urban development resources and support capacity of the environment and urban security , to provide geological information for the overall urban planning and urban construction and management , industrial layout and material project site to provide basis for decision making , and to provide basic protection for sustainable urban development .

In this paper, the theoretical significance is reflected in :explore a suitable Construction land evaluation method for Shijiazhuang, combined with types of pile

[1] Guangyu Liu. Apply Stepwise clustering method of agricultural land suitability evaluation[J]. Huabei Agricultural Sciences,1988,3 (1): 50-55.

F. Bian et al. (Eds.): GRMSE 2013, Part I, CCIS 398, pp. 16–24, 2013.
© Springer-Verlag Berlin Heidelberg 2013

foundation 15 - 20m depth evaluation , the evaluation results more guidance construction.

The scope of this study is a city of New Area, north of the Hutuo, East of the Beijing-Zhuhai Expressway, west of the Airport Road, south of the Southern cattle Township - North San board – lijiazhuang, the area is 142 square kilometers. Take full account of the status quo conditions, Combined with urban planning [2], Fuzzy comprehensive evaluation method to establish multi-level evaluation system. this paper aim at the specific circumstances of the study area, Considering various factors, Selected five primary factors and ten secondary factors to evaluate comprehensive, Tentative construction land suitability evaluation system engineering geological conditions for suitability , good , poor, poor in four grades.

1 Composite Foundation Suitability Evaluation Method for Determining

1.1 this paper Given layer of a composite foundation holding force in the underground 15m above the soil, divided into two levels to evaluate,5-8m is the first layer,8-15m is the second layer. this paper make 5-8m as important study object. Shijiazhuang district general adopt auger drilling pump pressure pile composite ground ,Composite foundation bearing capacity stantard value's determined method, according to construction in Hebei Province standard DB13 (J) 31-2001 <<auger drilling pump pressure concrete piles composite foundation of technical regulations >> the provisions of Article 3.2.1 ,Can be determined through on-site Compound Stratum, Can also be calculated using Equation 1.for first grade building, If necessary, combine the pile-soil deformation compatibility analysis, Comprehensive determined.

$$f_{sp,k} = m\alpha R/(\gamma_0 A_p) + \beta(1-m) f_k \tag{1}$$

formulation: fsp,k—composite foundation bearing capacity standard value (kPa);

m—Area replacement ratio;

β—single pile bearing capacity Efficiency Factor, α=0.7~1.0, when the base area big, pile length shorter , full house cloth pile , the pile spacing is small , cushion thickness the desirable lower value , and vice versa preferable to a higher value

R—composite foundation Single pile bearing capacity standard value (kN);

γ0—Composite Foundation importance factor, For one, two, three buildings take γ0=1.1, 1.0, 0.9; When the value of r0 Over upper internal force analysis considered inconsistent with the provisions of this article , no longer substituting r0 Over computing: Inconsistent, should be taken here r0 Over value ratio of the superstructure the r0 Over value.

Ap—Pile cross - sectional area (m2);

---

[2] Yueguang Zong. Urban land use ecological and economic suitability evaluation - New Area of Tianjin living[J]. Urban Environment and Urban Ecology, 1993,6 (3): 26-29.

β—The pile soil strength Efficiency Factor, Should be takenβ=0.75~1.0, The deformation of the strict requirements of the building should be taken as a lower value , general building preferable to a higher value;

fk—The natural foundation bearing capacity standard value (kPa);

1.2 Single pile composite foundation vertical bearing capacity of the standard value R value, shall meet the following requirements:

(1) single pile vertical bearing capacity standard value Q_{uk} the relevant provisions of <<the existing building pile foundation technical specifications>> should be OK.

(2) Determine the single pile vertical bearing capacity standard value R, should take formulation 2 to calculate:

$$R = Q_{uk} / \gamma_{sp} \tag{2}$$

formulation: γ_{sp} —Adjustment factor, when use in situ Static load test to determine Q_{uk} γ_{sp} =1.65,When the use of empirical parameters of bearing capacity estimates Q_{uk} γ_{sp} =1.70.

(3) When determined according to the empirical relationship between the physical indicators of soil bearing capacity parameters Q_{uk} should according toformulation 3 tocalculate:

$$Q_{uk} = u_p \sum q_{sik} l_i + q_{pk} A_p \tag{3}$$

Formula: Q_{uk} —singal pile Vertical limit bearing capacity standard value;

u_p —Pile cross-section perimeter;

q_{sik} —Pile side of the i - layer soil limit side resistance standard value , value in Appendix A;

q_{pk} —Limit end of the pile end soil resistance value of the standard value, in accordance with Appendix B;

l_i —I - layer thickness of the soil;

A_p —The pile side bottom area.

2 5-8m Suitability Evaluation of Composite Foundation

2.1 5-8m Composite foundation bearing capacity of the standard to determine the value of the bearing layer

First determining held bearing layer lies within the depth of soil type;Less than 8m soil water content, void ratio , liquid index , standard penetration base weighted average ; eigenvalue distribution by the method of the upper part of the bearing capacity of the bearing stratum as follows:

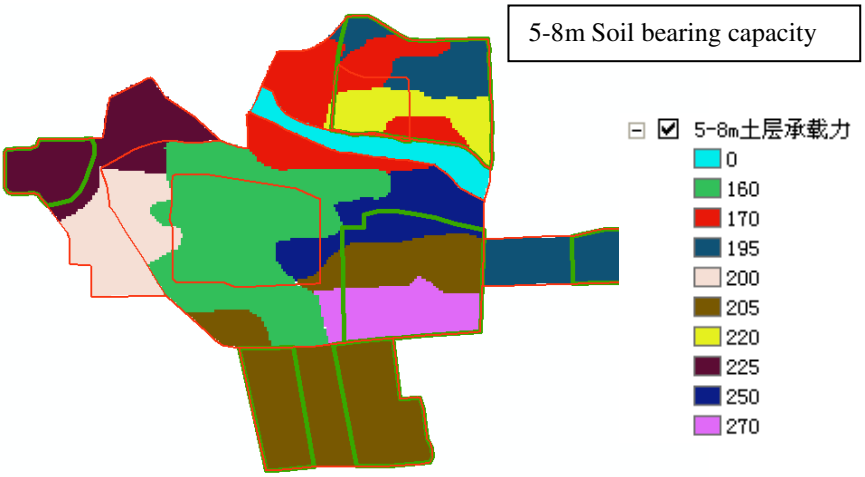

Fig. 1. 5-8mSoil layer bearing capacity maps

2.2 According to the nature of the soil and soil (liquid limit , void ratio, and sand density), Check Hebei Province, engineering construction standard DB13 (J) 31-2001 << auger drilling pump pressure concrete piles composite foundation of technical regulations>> in Appendix A, Appendix B,Ultimate Resistance of standard values determine the 5 - 8m depth range pileq_{sk} (figure 2) And pile tip resistance standard limit valueq_{sk} (figure 3). According to Equation 3 determines the vertical bearing capacity standard values (Figure 4) , and (assuming the pile diameter 0.5m, area replacement ratio m 0.5 %) .

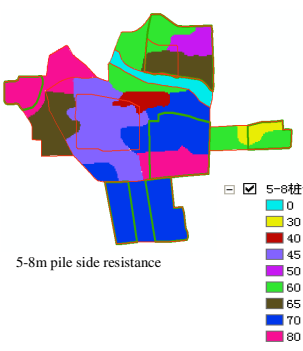

Fig. 2. 5-8m The Ultimate Resistance standard value of the pile in the depth range of

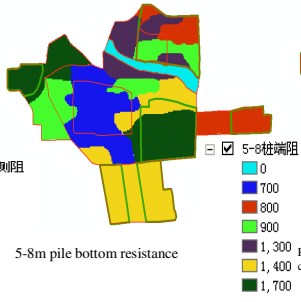

Fig. 3. 5-8m Depth range within the limits of the pile tip resistance standard value

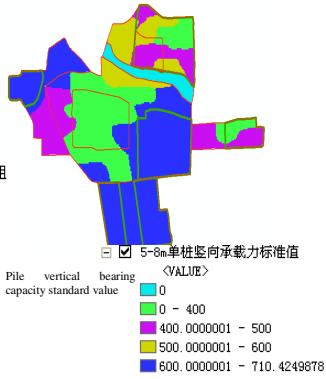

Fig. 4. 4 5-8mThe depth range of vertical bearing capacity standard value

2.3 according to formulation 1 and 2 study areaComposite foundation bearing capacity figure5

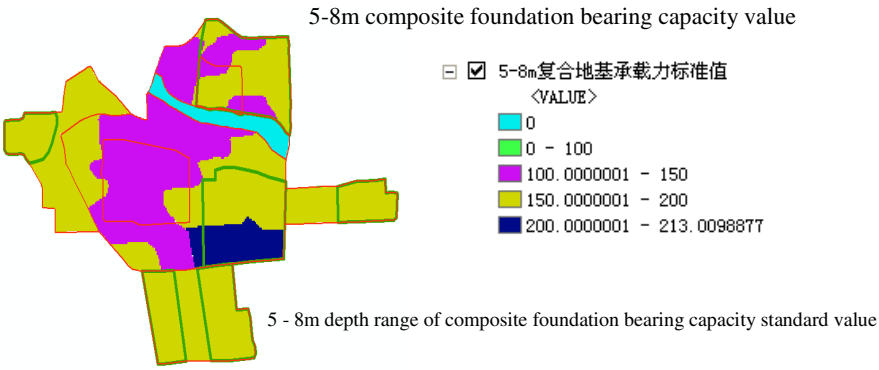

Fig. 5. 5 - 8m depth range of composite foundation bearing capacity standard value

3 Composite Foundation Suitability of Fuzzy Comprehensive Evaluation Method

Fuzzy Comprehensive Evaluation Method,Fuzzy relationship between the synthesis of the principles,from a number of factors (indicators) , a comprehensive evaluation method to evaluate things Grade of Membership Status3,According to the gray fuzzy mathematical theory and fuzzy evaluation method,Given Grey Fuzzy Comprehensive Evaluation of mathematical models and methods.

(1) Analysis of impact factor system, use AHP method of thinking,Factors affect the judge things by attribute classification, establish the hierarchical relationship of the influencing factors.Set of factors set $U = \{u_1, u_2, ..., u_m\}$, Alternative set (or sets of reviews) $V = \{v_1, v_2, ..., v_n\}$.

(2) Weight set can be regarded as gray fuzzy relationship between the evaluation object and the factors set according to the influencing factors hierarchical relationship , given the same level of each factor on a layer of criteria weights and the corresponding gray , constitute a set of weights:

$\underset{\sim}{A} = [(a_1, V_1), (a_2, V_2), ..., (a_m, V_m)]$ among, Each weight value requires normalization, namely $\sum_{i=1}^{m} a_i = 1$。

[3] Yaolin Liu、Yanfang Liu、Zaofa Xia. Fuzzy Comprehensive Evaluation in Land Suitability Evaluation[J].Journal of Wuhan University of Science and Technology of Surveying and Mapping, 1995,3 (1): 71-75.

(3) establish evaluation matrix

Evaluation matrix can be regarded as gray fuzzy relationship between the factors set alternative set.evaluation object is given based on certain factors alternative focus on the degree of membership of each element , and according to the degree of importance of the factors gives the corresponding gray[4].

$$R=(R_1\ R_2\ R_3\ R_4\ )=\begin{bmatrix} \alpha_{11}\ \alpha_{12}\ \alpha_{13}\ \alpha_{14} \\ \alpha_{21}\ \alpha_{22}\ \alpha_{23}\ \alpha_{24} \\ \cdots\cdots\cdots \\ \alpha_{j1}\ \alpha_{j2}\ \alpha_{j3}\ \alpha_{j4} \\ \alpha_{n1}\ \alpha_{n2}\ \alpha_{n3}\ \alpha_{n4} \end{bmatrix}$$

(4) Comprehensive evaluation

To make each influencing factor suitability of the geological environment is reflected,must be integrated into the evaluation factors set each factor weights and membership , take the ordinary matrix multiplication geological environment suitability level fuzzy comprehensive evaluation:

$B = W \bullet R = (b_1, b_2, ..., b_j)$, among, B_j Corresponding to the geological unit is to be evaluated the suitability of fuzzy comprehensive evaluation results.calculation results take B_j the maxima the district for the evaluation unit suitable level area.

4 Construction Land Composite Foundation Comprehensive Evaluation of the Suitability

To make each index construction land suitability is reflected, Must be integrated into the evaluation set each index weight and membership, take ordinary matrix multiplication to make construction land suitability level fuzzy comprehensive evaluation: Corresponding $S = WR = (S_1\ S_2\ ...\ S_j)$, among, S_j (j=1, 2, 3, 4) geologic unit suitability to be evaluated fuzzy comprehensive evaluation results. calculation results take S_j the maximum of the district for the evaluation unit suitable level area. A city construction land will eventually be divided into four

[4] Fuchu Dai, Xiaojun Zhang, Jun Li. Geographic Information Systems GIS support urban geological environmental assessment[J]. Journal of Engineering Geology, 2000(04): 43-49.

suitability level partition: suitable5, comparable suitability, suitability comparable poor and suitability poor district.5 - 8m composite foundation classification and quantitative criteria of evaluation are shown in table 1:

Table 1. construction land composite foundation Suitability influencing factors grading

sort	Evaluation factor	Suitability level			
		suitability	comparable suitability	suitability comparable poor	suitability poor
Engineering geology	Composite foundation bearing capacityC1/（MPa）	>0.25	0.25-0.2	0.2-0.15	<0.15
	Compression factor C2	<0.2	0.2-0.3	0.3-0.5	>0.5
	Composite foundation Pile bearing stratum thickness C3	>12	12-7.5	7.5-3	<3
	Cohesion C4	>25	25-15	5-15	<5
	Friction C5	>35°	35°- 25°	25°- 15°	<15°
	Site soil C6	Ⅰ level Assignment 10-7.5	Ⅱ A level Assignment 7.5-5	Ⅱ B level Assignment 5-2.5	Ⅲ level Assignment 2.5-0
Hydrogeological	Water level/(m) C7	>15m	15-10m	10-5m	<5m
	Water corrosion C8	no Assignment 10-7.5	weak Assignment7.5-5	center Assignment5-2.5	strong Assignment 2.5-0
Topography	Slope ration C9	<5°	5°- 10°	10°- 20°	＞20°
Geological structure	fracture C10	no Assignment10-7.5	little Assignment7.5-5	Little more Assignment5-2.5	Holocene active fault Assignment2.5-0
Dynamic geological	Earthquake influence C11	no Assignment10-7.5	weak Assignment7.5-5	Little strong Assignment5-2.5	strong Assignment2.5-0
	Earthquake Liquefaction C12	no Assignment10-7.5	weak Assignment7.5-5	little Assignment5-2.5	strong Assignment2.5-0

[5] Bingwen Qiu, Yong Zhou, Xueyuan Li. Dynamic evaluation of the suitability of geographic information systems support the regional soil resources[J].Journal of Soil, 2002, 5(3):301-307.

5 5-8m Suitability Evaluation Results 0f the Composite Foundation

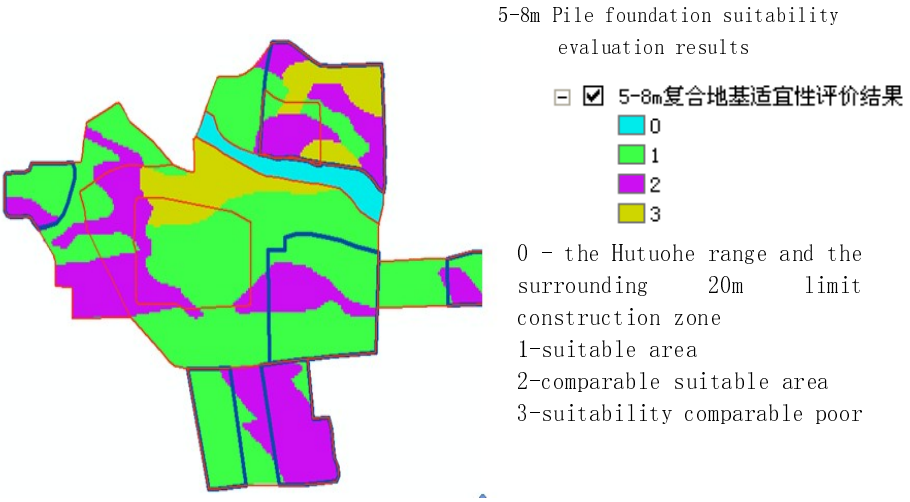

Fig. 6. 5-8m composite foundation suitability evaluation results

6 Conclusion

Through in-depth analysis and research on engineering geological conditions of the urban construction land , construction land suitability of the study area is a comprehensive evaluation of the system , the establishment of urban construction land suitability evaluation system , the fuzzy comprehensive evaluation model is introduced into the suitability of land for construction evaluation obtained engineering geological evaluation and prediction of the environmental quality of the evaluation results .

Natural foundation bearing stratum visual evaluation results can be seen , most of the study area of construction land area is more appropriate suitability poor are mainly distributed in the mountainous and Hutuo he Valley and the floodplain areas , to deal with these areas for afforestation , strengthen green .

References

1. Liu, G.: Apply Stepwise clustering method of agricultural land suitability evaluation. Huabei Agricultural Sciences 3(1), 50–55 (1988)
2. Zong, Y.: Urban land use ecological and economic suitability evaluation - New Area of Tianjin living. Urban Environment and Urban Ecology 6(3), 26–29 (1993)

3. Liu, Y., Liu, Y., Xia, Z.: Fuzzy Comprehensive Evaluation in Land Suitability Evaluation. Journal of Wuhan University of Science and Technology of Surveying and Mapping 3(1), 71–75 (1995)
4. Dai, F., Zhang, X., Li, J.: Geographic Information Systems GIS support urban geological environmental assessment. Journal of Engineering Geology (04), 43–49 (2000)
5. Qiu, B., Zhou, Y., Li, X.: Dynamic evaluation of the suitability of geographic information systems support the regional soil resources. Journal of Soil 5(3), 301–307 (2002)

The Adaptability of a City'S Natural Foundation of Fuzzy Comprehensive Evaluation

Zeng-qin Zhang, Chuang-ye Feng, Xue-mei Li, and Dou Li

Hebei Prospecting Institute of Hydrogeology and Engineering Geological
050021 Shijiazhuang, China
Fcy1970@163.com

Abstract. Through a full understanding of the current urban construction land quality, adopt fuzzy comprehensive evaluation method, Quantitative analysis of engineering geological conditions of urban construction land suitability, the paper divided existing land into a suitable area, Suitability better area, General District suitability and appropriateness of poor area four categories. Through this research, can provide Prediction and evaluation of the results for future urban planning and construction management, So as to determine the construction excellent areas, land use optimal solutions and provide the basis for development planning.

Keywords: natural foundation, Fuzzy Comprehensive Method, evaluation suitability.

The city is a regional economic,political and cultural center,the development of the city is not only affected by the constraints of the overall socio-economic development situation, but also largely dependent on the natural environment .Natural environment directly affects the structure and layout of the city, landscape, transportation and other engineering facilities construction, At the same time , the production and living of urban residents will be affected. So, it is necessary to do the engineering geological conditions in urban planning before research.

In our country evaluation of construction land began in the 1960s in the late, Three Gorges Project, The upper and middle reaches of the Yellow River basin water conservancy project、Water diversion plan and Guangdong, southern Liaoning nuclear power plant site and so on[1], Are carried out in - depth investigation and evaluation of regional engineering geological environment, The formation of urban construction land evaluation theory with Chinese characteristics, Summarized in the following aspects: in 1988, Guangyu Liu useing Stepwise clustering method of agricultural land suitability evaluation,

[1] Xiangran Li, Jinqiao Guo.Urban engineering geological environment quality evaluation theory and method of.Ningxia Engineering Technology.2002, 12.

F. Bian et al. (Eds.): GRMSE 2013, Part I, CCIS 398, pp. 25–32, 2013.
© Springer-Verlag Berlin Heidelberg 2013

Put forward the selected evaluation factors as quantitative、Standardized treatment, Cluster analysis of the use of mathematical, Through the preparation process, Computing, Separation of the reasonable level, And then according to the level of each type of cluster centers, Decided to land level; in 1993, Yueguang Zong useing of urban complex ecosystem theory, Combination of qualitative and quantitative analysis of computer-aided support, Expert advice on key indicators in the evaluation index system to filter, On the basis of land use ecological potential restriction analysis, Level merger rules Diego diagram analysis, Tianjin New Area of residence land ecological suitability level.

The scope of this study is a city of Zhengding New Area, north of the Hutuo, East of the Beijing-Zhuhai Expressway, west of the Airport Road, south of the Southern cattle Township - North San board – lijiazhuang, the area is 142 square kilometers. Take full account of the status quo conditions, Combined with urban planning, Fuzzy comprehensive evaluation method to establish multi-level evaluation system. this paper aim at the specific circumstances of the study area, Considering various factors, Selected five primary factors and ten secondary factors to evaluate comprehensive, Tentative construction land suitability evaluation system engineering geological conditions for suitability, good, poor, poor in four grades[2].

1 The Establishment of Evaluation Index Set

The fuzzy comprehensive evaluation method is a very effective method to make comprehensive evaluation of things affected by many factors. To judge the pros and cons of the suitability of the land for construction, first establish the appropriate evaluation factors set, To this end take in Figure 1 Suitability Evaluation Index System 12 index factors as the suitability evaluation factors set, that U={C1, C2,……,C12}.

2 Establish Set V and Indicators of Membership on the Reviews Set

So that construction land suitability evaluation set for the continuous interval [0,1], Urban construction land suitability level: Suitable ($0.75\leq S_j <1$); More appropriate ($0.5\leq S_j <0.75$); more Poor suitability ($0.25\leq S_j <0.5$); Poor suitability ($0\leq S_j <0.25$)。 Single factor evaluation indicators set indicators, Resulting membership of the corresponding factors on the V α_i:$0\leq \alpha_i \leq 1$. α_i Size indicates that the factors of construction land suitability how good or bad the vague concept of the degree of

[2] Zugang Li, Biao Chen, Xiaoning Chen. The Xi'an Engineering Geology Environmental Quality Assessment[J]. Gansu technology, 2004(01):112-113.

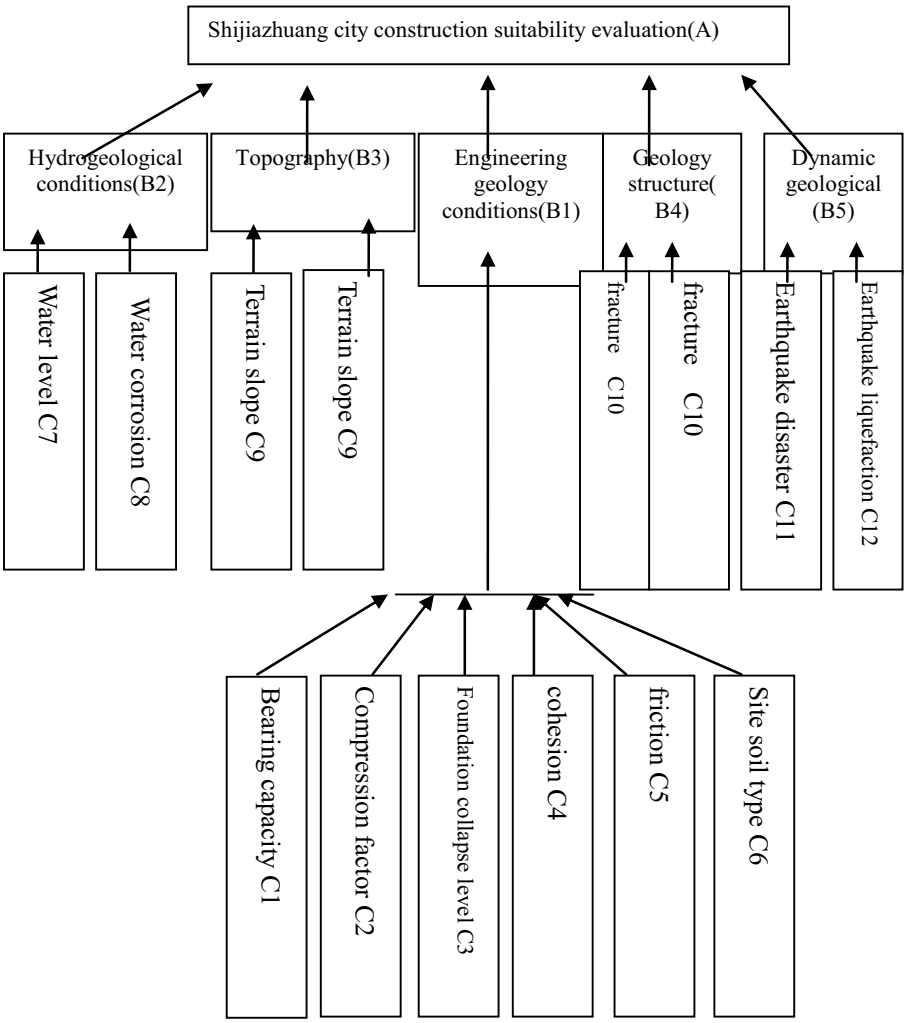

Fig. 1. A city construction land suitability evaluation analysis model

compliance , and provides for the membership value of a factor greater, indicating that factor the closer the goal of the best suitable areas , and vice versa departure from the more suitable target[3] .

To establish the basis of membership function is to establish a mathematical model, The key to it is part of the urban construction land suitability evaluation rating reflecting the individual factors, According to various factors quantized data demographics, In this paper, the trapezoidal membership function (Equation 1) This mathematical model to determine the degree of membership of these factors (Figure 2).

[3] Jinxia Wang. Olympic Park Engineering Geology Environmental Quality Analysis and Evaluation[D]. China University of Geosciences (Beijing) Journal, 2006.12.

$$\alpha_i(x)=\begin{cases}0 & x\le a\\ \dfrac{x-a}{b-a} & a<x\le b\\ 1 & x\ge b\end{cases} \quad (1)$$

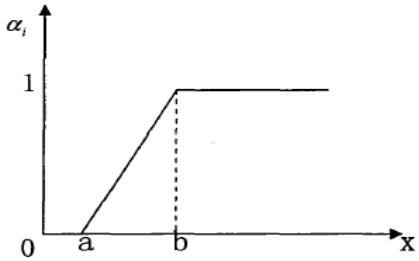

Fig. 2. Membership function curve

Note: X in the figure as the actual value of the evaluation factors, a, b , c for the factors of the upper limit or the lower limit value, α_{ij} is Membership of the factors.

3 Establish Fuzzy Evaluation Matrix

This article is divided into a city 's urban construction land suitability suitable more appropriate suitability poor , poor suitability of four levels of evaluation, Therefore, fuzzy matrix arranged in rows 12 a factor 4 the suitability level membership value, The formation of a 12 × 4 matrix of order , in the form as follows:

$$R=(R_1\ R_2\ R_3\ R_4\ )=\begin{bmatrix}\alpha_{11} & \alpha_{12} & \alpha_{13} & \alpha_{14}\\ \alpha_{21} & \alpha_{22} & \alpha_{23} & \alpha_{24}\\ & & \cdots\cdots & \\ \alpha_{j1} & \alpha_{j2} & \alpha_{j3} & \alpha_{j4}\\ \alpha_{n1} & \alpha_{n2} & \alpha_{n3} & \alpha_{n4}\end{bmatrix}$$

Among n=12, R_j Level j of the construction land suitable area (j = 1 , 2 , 3 , 4) fuzzy evaluation vector: $R_j=(\alpha_{1j}\ \alpha_{2j}\ \alpha_{3j}\ \alpha_{4j})^T$, α_{ij} is Control of the i-th this level impact factors on the level j suitability.

4 Construction Land Foundation of Nature Comprehensive Evaluation

To make each index construction land suitability is reflected, Must be integrated into the evaluation set each index weight and membership, Ordinary matrix multiplication to make construction land suitability level fuzzy comprehensive evaluation: $S=W\cdot R=(S_1\ S_2\ S_3\ S_4)$, S_j (j=1, 2, 3, 4) Corresponding geologic unit suitability to

be evaluated fuzzy comprehensive evaluation results, The results take the S_j maximum the district for the evaluation unit suitable level area.

5 Natural Foundation Suitability Classification and Quantitative Criteria of Evaluation

According to the above evaluation of the principle of selecting establish numerical criteria, According to geological data collected and the actual extraction of each index value to establish a database, Through scientific, systematic and comprehensive analysis to determine the value of each geological environment quality evaluation index grading standards, Finally according to the construction experience, Reference engaged in an urban geological environment monitoring、Engineering geological survey、 views of the city planning and Expert opinions[4], Comprehensive analysis of the development of the geotechnical engineering properties , groundwater , active faults and geotechnical environmental engineering problems geological factors distribution and its impact on the development and utilization of underground space, A city construction land suitability classification for the four grades : suitability , comparable suitability, suitability comparable poor and suitability poor , as shown in Table 1 .

6 Comprehensive Evaluations of the Concrete Steps and the Evaluation Results

1. Before evaluate a city urban construction land suitability, Engineering Geology Division is very important operation,Because it is the basis of the evaluation partition.use ArcGIS software projection the drilling coordinates within the scope of the study area and attached to each drilling indicators projected onto the base map has been imported (index value stored drilling properties) , the use of its space Kriging interpolation function for each evaluation operation , divided into 200m × 200m square grid , each grid is a small evaluation unit , a total of 23,769 evaluation unit

2. Evaluation unit attribute values exported to Excel, 0-1 standardization of data processing in matlab first , then my own in matlab created a city urban construction land suitability evaluation system for automatic evaluation . This system is written entirely in accordance with the specific situation of the city, as well as expert guidance of a teacher , the evaluation results have a certain reference value .

3. The results of the evaluation re - imported into ArcGIS , the raster attribute stored in the raster file , the resulting evaluation zoning map , as shown in Figure 3.

[4] Liancheng Sheng. Qingdao Economic and Technological Development Zone, engineering geology Environmental Assessment[D]. China Ocean University , 2004,(02).

Table 1. Natural foundation suitability factors grading

sort	Evaluation factor	Suitability level			
		suitability	Comparable suitability	Suitability comparable poor	Suitability poor
Engineering geology	Natural ground bearing capacityC1/(MPa)	>0.2	0.2-0.15	0.15-0.1	<0.1
	Compression factor C2	<0.2	0.2-0.3	0.3-0.5	>0.5
	Foundation collapsible level (total collapse settlement—mm) C3	<300	300-500	500-700	>700
	Cohesion C4	>25	25-15	5-15	<5
	frictionC5	>35°	35°- 25°	25°- 15°	<15°
	Site soil C6	Ⅰ level Assignment 10-7.5	Ⅱ A level Assignment 7.5-5	Ⅱ B level Assignment 5-2.5	Ⅲlevel Assignment 2.5-0
Hydrogeological	Water level/(m) C7	>15m	15-10m	10-5m	<5m
	Water corrosion C8	no Assignment 10-7.5	weak Assignment 7.5-5	center Assignment 5-2.5	strong Assignment 2.5-0
Topography	Slope ratio C9	<5°	5°- 10°	10°- 20°	>20°
Geological structure	fracture C10	no Assignment 10-7.5	little Assignment 7.5-5	Little more Assignment 5-2.5	Holocene active fault Assignment 2.5-0
Dynamic geological	Earthquake influence C11	no Assignment 10-7.5	weak Assignment 7.5-5	Little strong Assignment 5-2.5	More strong Assignment 2.5-0
	Earthquake Liquefaction C12	no Assignment 10-7.5	weak Assignment 7.5-5	Little strong Assignment 5-2.5	strong Assignment 2.5-0

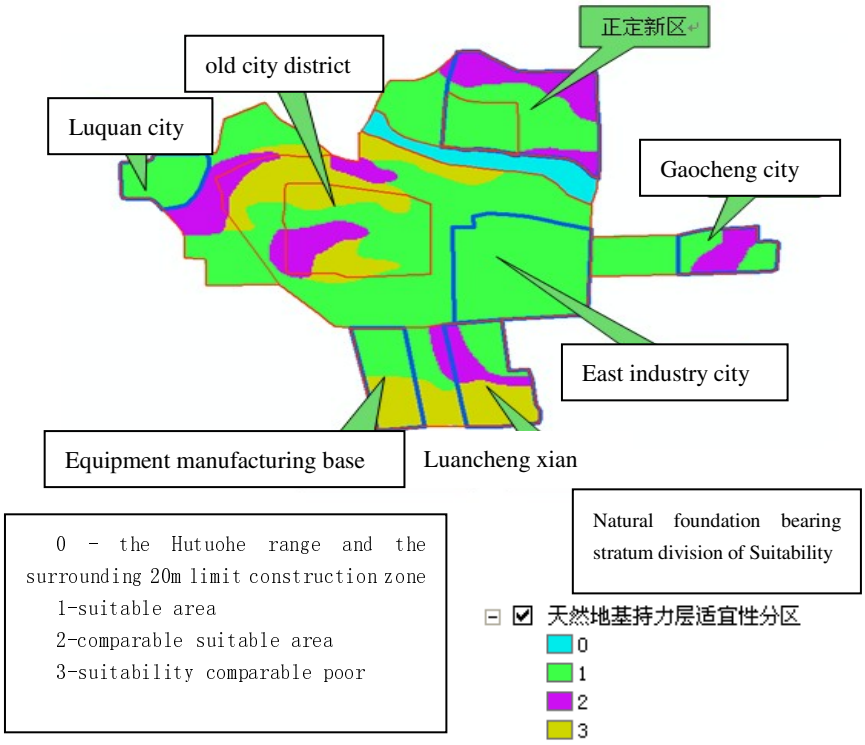

Fig. 3. Natural foundation of a city construction landsuitability evaluation Figure

7 Conclusion

Through in-depth analysis and research on engineering geological conditions of the urban construction land, construction land suitability of the study area is a comprehensive evaluation of the system, the establishment of urban construction land suitability evaluation system, the fuzzy comprehensive evaluation model is introduced into the suitability of land for construction evaluation obtained engineering geological evaluation and prediction of the environmental quality of the evaluation results .

Natural foundation bearing stratum visual evaluation results can be seen , most of the study area of construction land area is more appropriate suitability poor are mainly distributed in the mountainous and Hutuohe Valley and the floodplain areas , to deal with these areas for afforestation , strengthen green .

References

1. Li, X., Guo, J.: Urban engineering geological environment quality evaluation theory and method of. Ningxia Engineering Technology 12 (2002)
2. Li, Z., Chen, B., Chen, X.: The Xi'an Engineering Geology Environmental Quality Assessment. Gansu Technology (01), 112–113 (2004)
3. Wang, J.: Olympic Park Engineering Geology Environmental Quality Analysis and Evaluation. China University of Geosciences (Beijing) Journal 12 (2006)
4. Sheng, L.: Qingdao Economic and Technological Development Zone, engineering geology Environmental Assessment. China Ocean University (02) (2004)

The Design and Development of Object-Oriented UAV Image Change Detection System

Qing Wang*, Xiaodong Zhang, Yao Wang, Guanzhou Chen, and Fan Dan

Wuhan University,
430079 Wuhan, China
gis02@126.com

Abstract. The UAV image is characterized by high spatial resolution and few bands. It needs to use the object-oriented change detection method to detect the change of the UAV image. On the basis of the study of the key technique and process in object-oriented change detection, ArcEngine 10 is adopted for secondary development, so that the system realizes the process from the UAV image input to the ultimate detection output of change polygons and then the efficiency and automation degree of image change detection can be improved. Finally, an application example of land law enforcement displays the reliability and practicability of the system.

Keywords: change detection, UAV image, the design of change detection system.

1 Introduction

In recent years, the UAV remote sensing monitoring technology is developed rapidly and becomes a hot research at home and abroad, gradually applied to various fields of the society. UAV image is characterized by high spatial resolution and few bands. The traditional detection method based on pixel level only use the pixel gray feature and there exists some errors in terms of its detection precision due to the phenomena of objects with the same spectrum and of synonyms spectrum. In addition, there are abundant shape features, texture and shading information of high spatial resolution image. Only by the method based on pixel classification, it is difficult to use these information and the data produced is redundant; also, the automatic classification results will appear “salt and pepper noise”. Therefore, object-oriented remote sensing image classification and change detection method come into being. Their resulting object is no longer a pixel, but the one after image division.[1] Not only spectral information but also the texture and shape information fo the object are considered in classification and change detection, which greatly improves the detection accuracy. So, the extraction of object-oriented high resolution remote sensing image and the study on change detection method have become one of the concerns and hot researches in the fields of remote sensing, photogrammetry and GIS..

* Corresponding author.

F. Bian et al. (Eds.): GRMSE 2013, Part I, CCIS 398, pp. 33–42, 2013.
© Springer-Verlag Berlin Heidelberg 2013

2 Research on Key Technology

2.1 Change Detection Method

In recent years, scholars in different countries have put forward many change detection methods based on remote sensing image[3-5]. There are different classification methods according to different division methods, and the change detection method of remote sensing in this paper is divided into direct comparison method and post-classification comparison method according to whether the classification is to be made.[6] With direct comparison method, it is classified by direct observations--response spectral information of the image, which can avoid the influence on accuracy in classifying spectral information and yet can't obtain the category after the change. Post classification comparison method is actually about class comparison of the same block on remote sensing image in different periods, but not about a direct comparison of response spectrum on image. The basic process of classification comparison method is to classify first and then compare. The classifying and comparing methods are in accordance with the specific problems, which is more suitable for modular program design; meanwhile, manual intervention can be added in the whole process of change detection. So, I believe that this method is more flexible and practical in the practical application. In this article, the post-classification change detection method is adopted.

2.2 Object-Oriented Feature Extraction and Classification

UAV images, which are high resolution ones, are characterized by high spatial resolution and wavelength less. The effect is not good if the feature is extracted only by spectral information, and the geometry and texture features must be made full use of; as a result, object-oriented feature extraction and classification are adopted in the article. Its core idea is to treat image object instead of pixels as the smallest processing unit; its core technology involves the image segmentation and clustering feature space; and its basic process includes image segmentation, feature attribute classification and the feature extraction and classification. By following the principle of minimum heterogeneity, image segmentation involves integrating the neighboring pixels with similar spectral information into a homogeneous image object, and all pixels belonging to the same object after the segmentation are given the same meaning. Image segmentation method can accordingly be divided into two categories: methods based on boundary like edge growing and edge detection, and methods based on region such as thresh-holding, region growing, regional separatism-mering, etc.. Remote sensing image segmentation results have a direct impact on subsequent remote sensing image analysis and understanding, so choosing or designing the appropriate remote sensing image segmentation method to get a good image segmentation result is one of the most important factors to determine the success or failure of remote sensing image analysis and understanding. The characteristics and attributes of image objects are the primary bases of image segmentation, analysis and information extraction. Conceptually speaking, those characteristics include intrinsic

(inherent) features, topological features and context features. Splitting the image into objects and conducting a characteristic attribute calculation, you can use pattern recognition method to classifying and extracting the objects in the feature space in order to obtain the object class information. Traditional pixel-based supervision methods like nearest neighbor method, maximum likelihood method based on Bayesian discriminant rule and vector-supporting method, will still be able to achieve better classification results when they are used to automatically classify the objects after segmentation.

3 System Design and Implementation

3.1 System Design

The task of the system is to compare and analyze the UAV images in different time phases, and to identify the area changed by using the type after adopting object-oriented remote sensing change detection method; the goal of the system is to achieve the automatization and real-time and in-orbit operation of unmanned image change detection. System flow chart is shown in Figure 1.

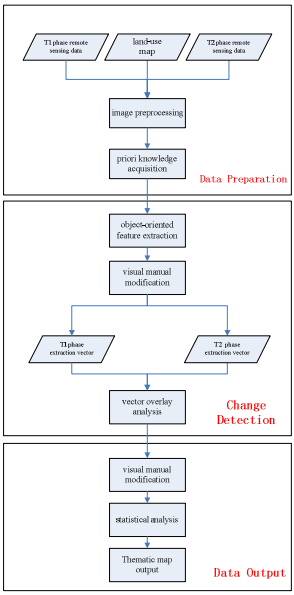

Fig. 1. Flow chart of object-oriented UAV change detection system

3.2 System Functional Design

Object-oriented UAV image detection system features include image pre-processing module, manually interactive change detection module, object-oriented change

detection module and change detection aids module, each module contains multiple functional sub-modules. The system functional design is shown in figure 2, wherein the object-oriented change detection module is the core of the system.

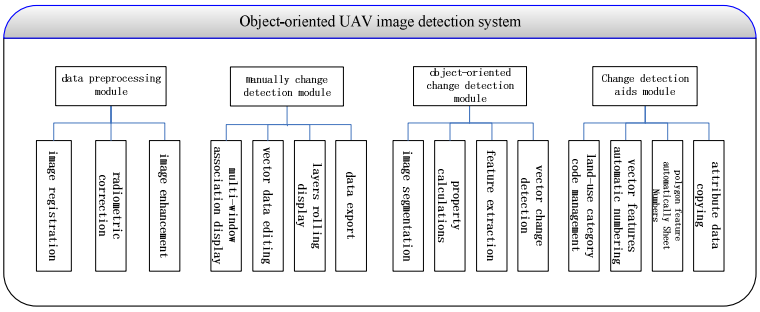

Fig. 2. System function block diagram

3.2.1 Data Preprocessing Module

The purpose of preprocessing is to truly reflect the spectral values of the data obtained at the different time in the same location, and then to improve detection abilities. In terms of remote sensing change detection, data preprocessing mainly includes image registration, radiometric correction and image enhancement [8].

1. image registration. Most change detection methods require precise temporal image registration. The accuracy of image registration has a great influence on the accuracy of change detection results. If the image registration accuracy can not meet the requirements, it will lead to a large number of spurious changes, which is caused by the image dislocation.
2. Radiative correction. Radiometric correction is to eliminate or weaken the inconsistency between the measured values obtained from the sensor and the target spectral reflectance or spectral radiance. It includes absolute radiometric calibration and relative radiometric calibration.
3. Image enhancement. It aims at improving the image quality, enriching the amount information, enhancing the results of image interpretation and recognition. The commonly used methods include linear transformation and nonlinear transformation.

3.2.2 Manually Interactive Change Detection Module

It refers to manually draw changed area by visually comparing two phase images. The functions mainly include:

1. Function of the layer management . The raster or vector layer is operated on the process of opening, displaying and closing.
2. Function of associated multi-window display . Multiple windows can be associated to display. When one of the windows is zoomed in or zoomed out or roamed, other related windows simultaneously display, so that users can easily compare and judge the multiple image data.

3. Function of vector data editing. Face data can be added or deleted or moved or edited in the vector, and the corresponding attribute data can be edited. With this function, the changing area of visual interpretation can be recorded directly.
4. Function of layers shutter display. When there are more than two layer data in the same window, shutter function can be used to compare and show more clearly the differences between different layers.

3.2.3 Object-Oriented Change Detection Module

Its main functions include:

1. image segmentation. It is the process in which the original pixel in image is divided into regions according to brightness, texture, and similarities of spectral characteristics.
2. attribute calculation. The attribute of the region divided mainly includes spectral, shape and texture characteristics. A region and the attribute value describing the region form an object. The object model is used for supervised classification or the classification based on rule set (feature extraction), differing from the common classification. Object-oriented classification considers the multiple characteristics of spatial spectrum and texture, and can also customize index, such as NDVI etc.. This greatly improves divisibility of the feature.
3. Feature extraction. Feature can extracted by supervised classification and the method based on the rule set. Different from the traditional supervised classification, object-oriented classification is to see each region as the smallest unit of classification. The system offers Bias classification, K neighbor classification, cloud parameters model classification and vector-supported classification. The classification based on rule set is on the basis of people's intuitive understanding of objects, for instance, the road has a greater extensibility, houses are usually rectangular, the NDVI of the vegetation is high, the texture of trees is more abundant than grass's, and the like. Therefore, we can set a group of rules aimed at feature to be extracted, judge the objects one by one, and then extract the target objects.
4. Vector change detection. After the data in different phase is extracted characteristically to obtain classified vector data, we can have overlay analysis on classified vector data in two different phases to result in changing patches, and can count the number and area of the change type.

3.2.4 Change Detection Tool Module

These function modules mainly include:

1. class code management. The name of the class and the code are managed in a unified way in order to realize the function of data dictionary.
2. automatic numbering of elements. It is to be realized that vector elements are automatically numbered from top to bottom and left to right and written to the specified attribute field.

3. Automatic map sheet number of surface elements. According to the rule of 1:1000 map sheet number, the map sheet number of surface number is automatically generated and written to the specified attribute field.
4. Attribute bulk copy. The attribute one of a face data is copied in a bulk way into the specified attribute field of another surface data.

4 Case Study

4.1 Experimental Data

In figure 3, there are two UAV image data from different phases after orthorectification(the spatial resolution is 0.5m). Our task is to use a system developed by the author to have a change detection on two images, find out suspected illegal use of land area, draw the scope of monitoring, and then provide a reference to the work of land enforcement.

former phase image(0.5m)

after phase image(0.5m)

Fig. 3. UAV image data

4.2 Experimental Process

1. Data preprocessin. The contrast of after phase image is low, which influence the interpretation of the land type during supervision and classification. So the system can be used to contrast and stretch the after phase images.
2. Image segmentation. The system adopts graph theory to segmentate the images. In this way, each pixel in a image is seen as a vertex, the image is represented as network diagram in graph theory, the problem of image segmentation is transformed into the optimal one in graph theory, and then use the minimum spanning tree algorithm to complete the image segmentation[2]. Segmentation results are shown in the following graph.

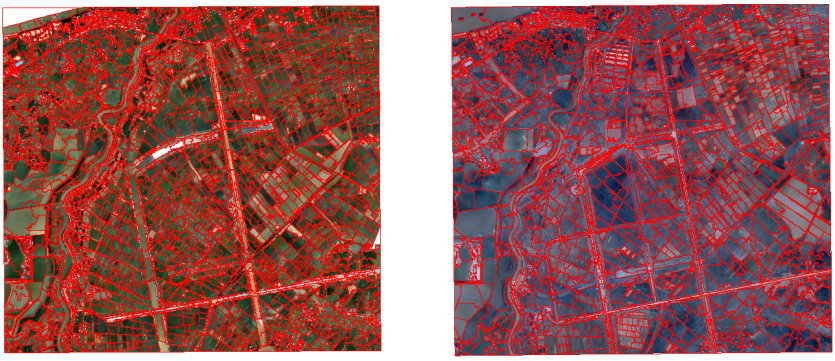

segmentation result of former phase segmentation result of after phase

Fig. 4. Segmentation result of image

3. Attribute calculation. The system extracts the spectral information of each polygon after segmentation, which include the mean, variance, maximum and minimum of three bands; it also extracts the geometric information of polygons, which include size, shape factor and squareness.
4. Supervised classification. The experiment adopts the classification method of support vector machine, and the classification result is shown in figure 5.

Fig. 5. Result after supervised classification

5. Change detection. The two vector results after classification are made an overlay analysis and the changing information needed by land enforcement is extracted. Then the result is shown in figure 6.

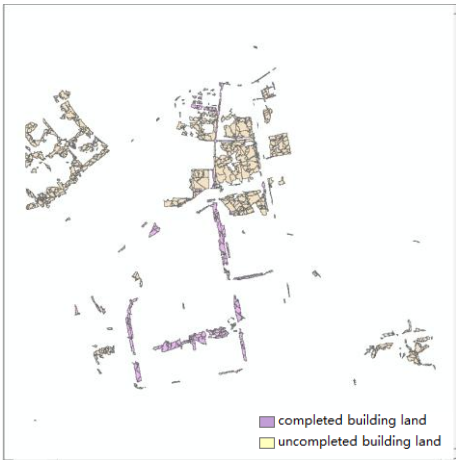

Fig. 6. Results from change detection system interpretation

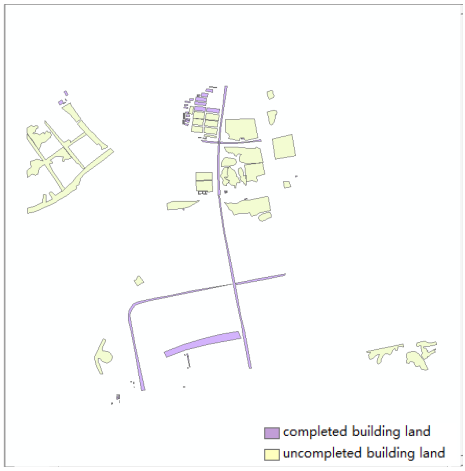

Fig. 7. Results from change detection manual interpretation

4.3 Analysis of Experimental Result

It is to be adopted in this paper to contrast system detection result with manual interpretation result (figure 7) and to evaluate the accuracy. Seized full rate and precision rate are used as indicators of accuracy assessments, and

Seized full rate = accurate detection area/ standard change area

precision rate = accurate detection area/ total detection area

Accuracy assessment result: when it is uncompleted to change agricultural land into building land, accurate detection area is 800583.785040, total detection area is

1136292.036204, standard changing area is 1103480.316716, seized full rate is 72.55%, and precision rate is 70.46%; when it is completed (including road), accurate detection area is 277070.219025, total detection area is 331184.795919, standard changing area is 300639.938261, seized full rate is 92.16% and precision rate is 83.66%.

In accordance with the accuracy of assessment results, the system can meet the needs of practical application.

5 Conclusion

On the basis of fully studying UAV image feature extraction and change detection method, it designs object-oriented UAV image change detection system. The system uses UAV image data and land-using data to achieve the extraction of change polygons and the determination of its type in object-oriented UAV image change detection technology. Through the development and application of the system, some conclusions are summarized as follows:

1. aimed at high resolution images, the change detection method, in which object-oriented post-classification contrast is made, is reliable and practical. The key steps are image segmentation and feature classification. The system uses graph theory for image segmentation, the setting of segmentation parameter requires the determination from a lot of experiments, and finally the ideal segmentation result is to be achieved. In future, through theories and experiments, the relationship between partition parameter and the image type as well as detection target will be studied and organized and then accumulated into a library, which can be reference for later setting of partition parameter. On the other hand, the system uses SVM to supervise and classify. Without considering spectral and spatial characteristics, classification effect is more ideal, but the topology and semantic and hierarchical relations of the target objects are not achieved. As a result, the future research will be carried out from these two aspects, making full use of the topology and semantic and hierarchical relations to improve the feature library.
2. The system uses modular operating mode to allow users to combine automatic and semi-automatic and manual processes, so the overall accuracy of change detection can be improved. From the final results, the overall accuracy of change detection basically meet the requirements of practical application, so it is feasible. Factors affecting the accuracy are various, generated and accumulated along with the image processing, including image radiometric correction, geometric registration errors, image segmentation errors, building extraction errors and overlay analysis errors in ArcGIS. Remote sensing image change detection is a complex and comprehensive process, so there are still many problems to be solved if automatic process and higher accuracy are to be achieved.

References

1. Du, F.-l., et al.: Object-oriented Image Classification Analysis and Evaluation. Remote Sensing Technology and Application (1), 20–23 (2004)
2. Weihong, C.: Research on Graph Theory Based Objeet-oriented High Resolution Image Segmentation, Wuhan University (2010)
3. Lu, D., et al.: Change detection techniques. International Journal of Remote Sensing 25(12), 2365–2401 (2004)
4. Radke, R.J., et al.: Image change detection algorithms: a systematic survey. IEEE Transactions on Image Processing 14(3), 294–307 (2005)
5. Hussain, M., et al.: Change detection from remotely sensed images: From pixel-based to object-based approaches. ISPRS Journal of Photogrammetry and Remote Sensing 80, 91–106 (2013)
6. Xiao-xia, S., et al.: A Summary on Current Techniques and Prospects of Remote Sensing Change Detection. Remote Sensing Information (01), 119–123 (2011)
7. Li, D.R., Tong, Q.X., Li, R.X., et al.: Current issues in high-resolution Earth observation technology. Sci. China Earth Sci. 55, 1043–1051 (2012), doi:10.1007/s11430-012-4445-9
8. Im, J., Jensen, J.R., Tullis, J.A.: Object-based change detection using correlation image analysis and image segmentation. International Journal of Remote Sensing 29(2), 399–423 (2008)

Design and Implementation of a Taxi Intelligent Service System*

Jian-cheng Ye, Ang Chen, Xian-nan Huang, Xin-yu Liu, and Hui-ling Zhou

School of Automation, Beijing University of Posts and Telecommunication, Beijing, 100876

Abstract. Based on research in the present city taxi industry, developed a taxi intelligent service system. The optimal shortest path distance and traffic information as the core parameters matching algorithm design, realizes fast and convenient taxi taxi passengers, reduce the run rate; mobile intelligent terminal based on APP and related hardware device development, realize the no-load and full-load signal acquisition, voice broadcast, response function, convenient driver driving safety and high efficiency to match the passengers; through the records in the database data, can carry on the taxi for data analysis, provides the reference for the management decision; the environmental temperature and humidity of the real-time detection of the taxi, air quality, through the mobile phone voice broadcast for the driver to provide health care for humanity.

Keywords: Taxi intelligent service, mobile terminal, bluetooth telecommunication, data acquisition, database.

1 Introduction

With the rapid development of economy in modern society, intelligent transportation gradually becomes the core content of intelligent city construction. Intelligent transportation refers to the use of advanced detection systems, communication technology, information processing technology and electronic control technology to improve traffic management, optimization of road resources, improve the traffic safety, realize the modern traffic management scientific, intelligent. Its goal is to reduce air pollution, traffic generated by reducing invalid vehicles, improve the efficiency of road, so that the sustainable development ability of fast transportation safety, keep the city. With the process of promoting the city, traffic congestion has intensified, with oil prices rising, the taxi has become an indispensable part of daily life of modern fast. Taking a taxi trip will become a major means of transportation, and how to effectively reduce the run time and taxi taxi passenger waiting time is worth our problem [1].

Network is the Internet of things most realistic, concrete, with the car for the node, application of information to the public network based, has built three national coverage of 3G network provide full support, the rapid development of mobile Internet and network provides a new means and opportunities for development.

* **[funds]:** Research Innovation Fund for College Students of Beijing University of Posts and Telecommunications.

F. Bian et al. (Eds.): GRMSE 2013, Part I, CCIS 398, pp. 43–50, 2013.
© Springer-Verlag Berlin Heidelberg 2013

This paper mainly through direct interaction between the establishment of taxi passenger service with the taxi driver, in order to reduce the run time, passenger taxi's waiting time and the driver to provide health care service for the purpose, the device for mobile intelligent terminal based on APP and related hardware, realizes the no-load and full-load signal acquisition, voice broadcast, response function, convenient driver process safe and efficient received matching passengers; through the records in the database data, can carry on the taxi for data analysis, provides the reference for the management decision; the air quality of the environment temperature and humidity, real-time detection of the taxi, through mobile phone voice broadcast for the driver to provide health care for humanity.

2 System Design

This system is composed of three parts, respectively for passengers to client, client and server driver, one passenger and driver client application client for mobile intelligent terminal based on.

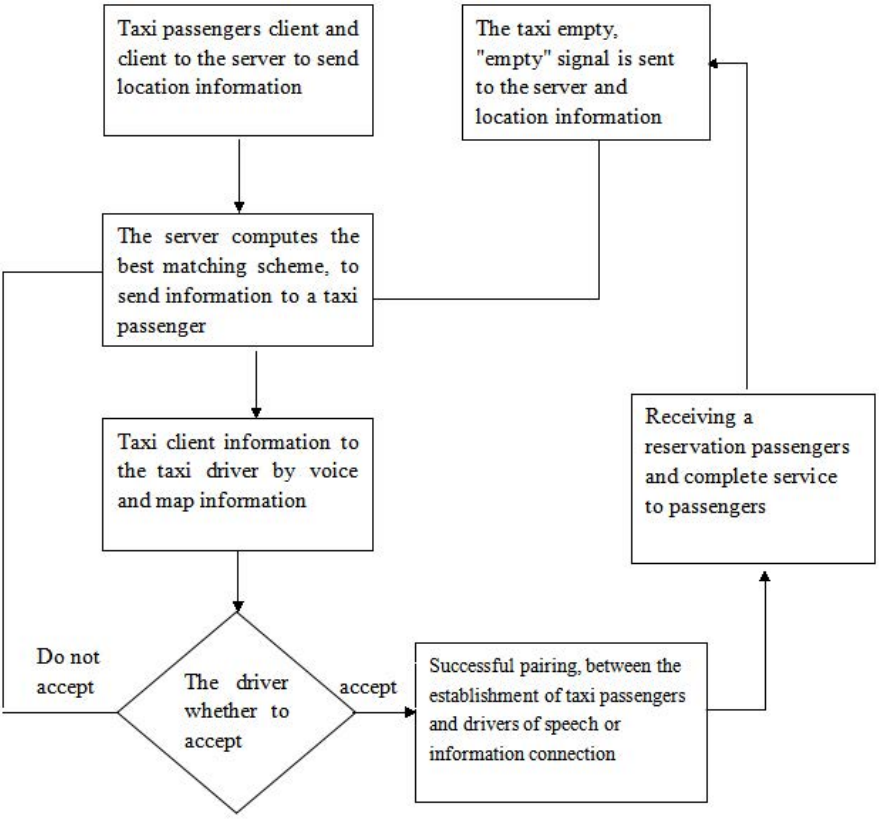

Fig. 1. A flow chart of intelligent public service system

The client is mainly responsible for the passengers to collect passengers geographical location and related information, to send the data to the server and the client is connected with the driver.

The driver client is mainly responsible for the collection of the taxi driver location information and whether the vacancy information, sending data to the server and the client connection with passengers.

Server is responsible for recording and analyzing two client to send data, through the relevant algorithm to calculate the best pair, and sends the results to the corresponding client.

3 The Client

3.1 Part of the Software

Mobile agent server is part of the system software, intelligent mobile terminal application development technology mature for the stability of the system provides some assurance [2].

Passengers client software, to obtain the geographical position information by mobile terminal GPS module or click locations on the map. Click on the taxi passengers, information is sent to the server via the Internet, at the same time, the receiving server feedback information, including the driver location (update), waiting time and with the driver of the communication and other related information [3] calculated.

The driver client software, real-time geographic position information by the GPS module of mobile intelligent terminal to obtain the driver, the client receives the sensor switch is arranged in the empty plate on the vacancy information, information is sent to the server via the Internet, while receiving the feedback information service, including a person's position, and passenger communication information [4]. At the same time, in order to guarantee the traffic safety of the driver, passenger information by voice broadcast way, inform the driver, driver can voice inform intelligent terminal whether a shuttle, intelligent terminal by correlation analysis to get instruction, operation, avoiding the driver in processing information when watching related information, intelligent terminal screen while ignoring the road ahead and unsafe factors. Of course, the driver can selectively view more specific information on the screen. The driver client driving time and multiple sensors to monitor air quality and temperature and humidity data according to the driver, timely to remind drivers to pay attention to rest and ventilation.

3.2 Part of the Hardware

Considering the driver safety during driving, not convenient to use mobile phone. So the driver picks up passengers at the empty plate down and stand up these two simple action is necessary, without changing the original structure of the taxi empty-plate, system installation angle sensor YL-38 in the empty plate, using AT89C51 MCU developed a small embedded circuit, circuit mounted Bluetooth module, sending the

machine measured angles change sensing data to the mobile phone terminal, using software background Bluetooth serial monitoring program, the client software to identify the information, can help drivers in turning empty plate by mobile phone terminal to the server to send the "empty" or "passenger" instruction, allowing drivers to safer and more convenient. The use of the system. Simple switch installed in the driver circuit part, shift circuit can stop working at any time, no longer sends information to the server, the driver is convenient safe and punctual shift.

Due to the requirements of the working environment and occupation, the taxi driver's health status is not optimistic, in order to better for the service of the driver installation, system of temperature and humidity sensor DHT11, an air quality sensor MQ-135 on the hardware circuit, the measured data is transmitted to the driver via Bluetooth client, client voice broadcast allows the driver to know health car. LCD1602display screen at the same time, the data can be in the circuit board, when the driver at the traffic lights can focus on these information.

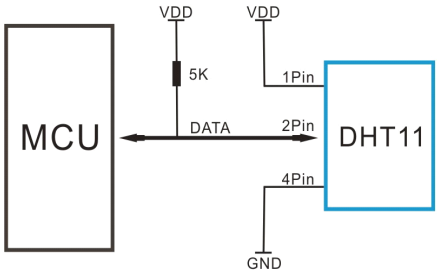

Fig. 2. DHT11 and MCU connection diagram

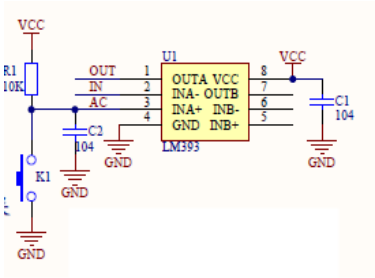

Fig. 3. Angle sensor circuit module

3.3 Part of the Server

The server is processing the information and exchange hub. It received from the mobile intelligent terminal geographic information and related data stored in the database, and through the relevant algorithm to calculate the optimal matching, relevant information will be sent separately to match the passengers client and client for processing and display driver.

The system design adopts a mode of database access in order to reduce dependence on array vector, using the database interview with a self-locking characteristic data to avoid the subscript exception occurs. Database design including the client attribute table (including ID, geographic location, matching ID) was established, and relevance constraints. The database to add produced bigger change on frame construction, by means of access to the customer ID replacing the original array access vector by the subscript mode, the database query function unified packaging into modules, to make the code more clear and easy to understand, and to the code creates a dynamic refresh panel, can match in program testing and operation of the process of real-time observation of the user and driver, effectively correct matching to detect errors of algorithm.

4 The Optimal Matching Algorithm Design

Research on taxi scheduling algorithm, mostly starting from mathematical theory [5], the constraints on the scheduling scheme [6] on-line taxi on the chart, and for complex practical application traffic and many unpredictable factors, this kind of research has only indicative significance. This paper presents a practical traffic condition based on the existing data, in technology and feasible, relatively fast best drivers and passengers matching algorithm.

All the known empty location set down as the geographical position $T=\{t_i \mid i=1,2,3....n\}$, all known taxi passengers need to set down as $C\{c_i \mid i=1,2,3....n\}$. Distance above using the longitude and latitude information calculation $d_a(v_1,v_2)$ between two points v_1,v_2 denoted by google API map calculated distance to. Taking passengers waiting time as T . Taking passengers c_i for matching the right empty Car t_i as $e(c_i,t_i)=\alpha T+\beta d_a(c_i,t_i)$. The specific process:

(1) A taxi passenger requests in a place.

(2) Taking v_s as the center, a as the length, establishment of the square area S ; If the collection of T in the presence of multiple t_i, meet $d_a(t_i,v_s)\le\sqrt{2}a$, get into the first (4) step; If the collection of T in the presence of multiple t_i, meet $d_a(t_i,v_s)\le\sqrt{2}a$, associate c_{i_s} 、 t_{i_s}, get into the first (5) step; If do not meet the above two conditions, increase the length of S, which can satisfy the $a^*=\theta a$, return the article (2) step.

(3) For each t_i , calculating $d_b(v_s,t_i)$, comparison of various d_b , get $d_b(v_s,t_{i_m})=\min(d_b(v_s,t_i))$, t_{i_m} is the nearest empty car apart from v_s. Association of c_{i_s} , t_{i_m} .step into the (5) .

(4) For t_{i_m}, if there exists except c_{i_s} outside, into the (6) step; if there is no other association other than c_{i_s} ,after the waiting time t, if t_{i_m} is no other association except c_{i_s}, remove h, I in the collection F、G, matching c_{i_s} 、 t_{i_m}, matching successfully. If the t_{i_m} has been established in other relation during the time t , transfer to the (6) step.

(5) Comparison of the t_{i_m} associated c_i weight, get the results of $e(c_{i_m}, t_{i_s}) = \max(e(c_i, t_{i_s}))$, c_{i_m} is the best passenger, other passengers c_i returns the (3) step. In the set C 、 T, remove the c_{i_m} 、 t_{i_m}, matching c_{i_m} 、 t_{i_m}, matching successfully, algorithm is end.[7] [8]

(6) The b_{i_m} connection weights of c_i, get $e(c_{i_m}, b_{i_s}) = \max(e(c_i, b_{i_s}))$, c_{i_m} is the best passenger, other passengers on the back (3) step removed.

(7) In the set C 、 B, delete c_{i_m} 、 b_{i_m} ,matching c_{i_m} and b_{i_m}, the match is successful, the algorithm terminates.

Fig. 4. The simulation graph matching scheme

In order to facilitate the solution and analysis of the model, assuming a 4 taxis and 4 passengers to match the taxi passengers, with their distance as shown in Table 1, because the system matching time is very short, think the time distance invariant [9].

Table 1. The optimal matching of taxi distance passenger distance (unit: m)

Taxi	Passenger			
	A	B	C	D
P	25	29	31	42
Q	39	38	26	20
M	34	27	28	40
N	24	42	36	23

The following optimum matching algorithm for solving process:

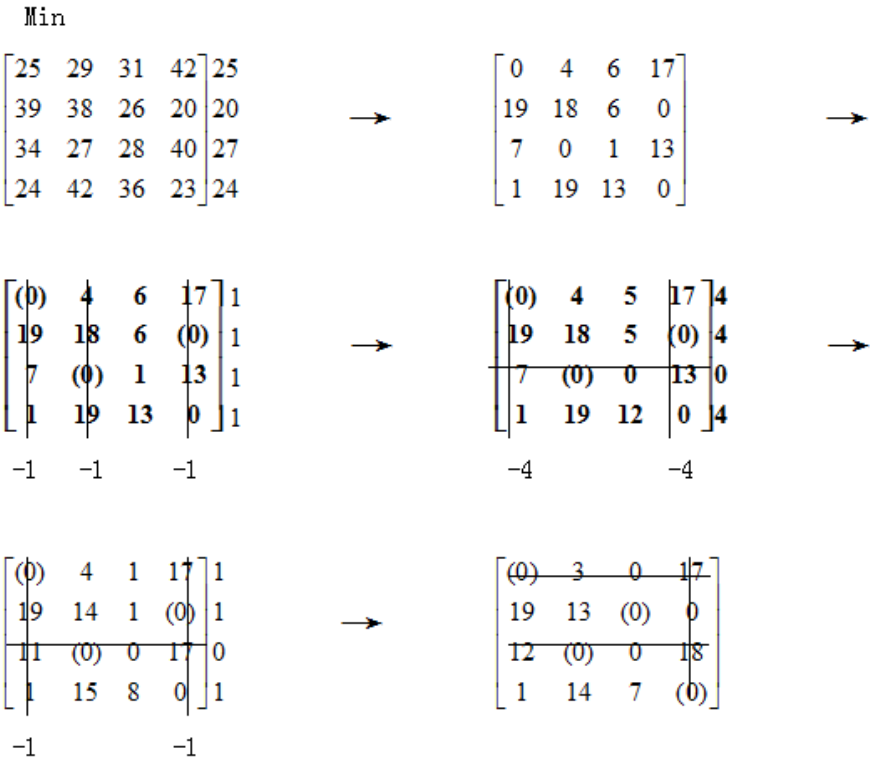

Fig. 5. The optimal matching algorithm

So the optimal solution for x11, x23,x32, x44, P matches the passengersA, Q matches the passengersC ,M matches the passengersB, Npassengers is D,he total time can enable the vehicle to travel the shortest, thereby reducing the driver run time and the waiting time of passengers, reduce energy waste. Substituting the obtained Z=25+26+27+23=101 values of objective function.

5 Conclusion

The system makes full use of wireless communication technology and electronic circuit technology, which can well solve the passengers are not easy to take a taxi, the taxi run time is long, the better use of resources to improve the development efficiency of the taxi, the taxi industry, but also to some extent alleviate the city traffic pressure. Provide support to promote the development of intelligent transportation and intelligent city.

The system could be detected in the taxi air temperature and humidity, air quality data, continuous driving time, run time, matching storage location data to passengers system settings in the database. Through the software end data integration analysis function, can obtain the driver where the car environment, driver fatigue status, different passengers more time zones, different time each road traffic congestion, the system successfully matching rate the results of data analysis, management department can pass and related analysis of these data to develop a more scientific and effective management measures, both the physical conditions of the driver and improve taxi efficiency, promote development of taxi industry. Analysis of massive data processing can add impetus to the intelligent transportation public transportation, but also for the development of intelligent city to provide data support and guide decision.

References

[1] Li, X.: The European intelligent transportation construction and Enlightenment of. City Traffic (2), 58–62 (2004)
[2] based on. Android 4 network programming. Publishing House of Electronics Industry, Beijing (2011)
[3] Wang, S.: Google introduction Android development guide. People's Posts and Telecommunications Press, Beijing (2009)
[4] Wan, Z.: Luo Minggang and implementation of. Information Technology Taxi Dispatch Radio Communication Terminal Design Based on GPS (6) (2009)
[5] Xu, Y., Wang, K.L., Ding, J.: The restrictions of the on-line taxi scheduling graph and competitive algorithm on. System Engineering 14(4) (1999)
[6] Cheung: GPS taxi dynamic management system design based on. Journal of Sichuan University of Science and Engineering (Natural Science Edition) 23(3) (2010)
[7] Liu, Y., Tong, M.: The Hungarian algorithm in multi-objective allocation in the application of. Fire Control and Command 27(4) (2002)
[8] Wu, B., Ni, W., Fan, S.: Particle swarm algorithm. Computer Integrated Manufacturing System, Open Vehicle Routing Problem in Dynamic Network 15(9), 1788–1794 (2009)
[9] Muller, J.: Approximative solutions to the bicriterion vehicle routing problem with time windows. European Journal of Operational Research 202(1), 223–231 (2010)

Design and Implementation of Digital Measurable Image Management Platform

Yinglong Du[1,2], Changfeng Jing[1,2], Mingyi Du[1,2], and Chao Jin[3]

[1] School of Geomatics and Urban Spatial Information of Beijing University of Civil Engineering and Architecture
[2] Key Laboratory for Urban Geomatics of National Administration of Surveying, Mapping and Geoinformation
[3] Beijing Institute of Surveying and Mapping
100044 Beijing, China
jingcf@bucea.edu.cn

Abstract. As a foresight application of close-range photogrammetry, digital measurable images, combining with the business data in specific field, can provide users a visible, elaborate high-efficiency system. In this paper, DMI management platform will be presented in detail about the design and implementation. On that basis, three type application based on DMI platform in urban management are put forward including advertising signboard supervision, urban management case representation, route planning and preview. DMI application takes the urban management model to a new era with multi-source spatial data.

Keywords: Digital Measurable Image, street view, urban management, measurement.

1 Introduction

In recent years, under the rapid and steady growth of Chinese economy, the level and pace of urbanization has greatly improved. Government and administrative department have increasing the investment in urban infrastructure to satisfy people's requirement for urban environment and urban functions, especially in urban components. The troubling problem for administrative departments (urban management departments) is how to rapidly find the right urban components which are damaged or disabled or illegal things. Urban Grid Management Mode is born against the background of the fast development of 'digital city'. In this model, the traditional supervision and report method is based on "urban electronic maps + components symbols". There are many shortcoming in this method : (1) lack of other useful information around the urban component. In traditional method, plane electronic map and urban component symbol only show abstract information of urban component and environment information, but for complex urban component case, the "true-fact" information and picture around component are essential. (2) overdue information. Since the update cycle of urban component is about two or three years,

F. Bian et al. (Eds.): GRMSE 2013, Part I, CCIS 398, pp. 51–57, 2013.
© Springer-Verlag Berlin Heidelberg 2013

the up-to-date of urban component is weak. In the traditional method, some urban component supervision may be missing.

For above drawbacks, with full use of DMI (Digital Measurable Image), 360-degree panoramic image and the basic city management data, we designed and implemented a street view management and business platform with rich visual, management, supervision modules. Integrating the DMI image and panoramic image, we bring forth a new supervision and report method based on “urban electronic maps + urban ortho-photo + road videos + multi-angle DMI image + panoramic image”. The rich urban spatial data featured holographic information around urban component, and can be update with a few hours. The new supervision and report method can thoroughly supervise the urban components and be promoting scientific and technological level of urban management and development of "smart city". Section 2 introduces our DMI management platform. In section 3, the applications of DMI management platform are bring forth, including advertising signboard supervision, urban management case application and route planning and preview. Finally, section 4 concludes the paper and gives ideas for future work.

2 DMI Management Platform

Digital measurable image (DMI) refers to a combination of aviation, aerospace and ground-dimensional images, which contains absolute orientation elements on the spatial and temporal sequence and is integrated with management. DMI contains interior and exterior orientation elements and is collected by Mobile Mapping Technique (MMT). Temporal parameters, API, and ground real images are integrated with DMI, either. A significant advantage of DMI is that it can be integrated with other geographical fundamental information products, especially with 4D geographical fundamental information products. Traditional 4D products are the projection of the real world in two-dimensional space, instead of the real scene, so, they do not possess the function to provide the visible, measurable, cultural and social information which DMI is able to provide. [1]

In the demand of Web 2.0, the 3rd internet waves [2] and the demand of services and information of the clients, the 5th ‘D product’, digital measurable images [3], with the properties of intuitive visual and rich information has started to integrate into the construction of digital cities. The services supplied by the DMI can better meet the needs of people in real life.

Street view with 360 degree scene such as Google Inc.’s product is a high resolution, multiple, all-dimensional "true " image, providing users with photo-holographic data and the urban managers’ decision-making support information. Comparing with street view, DMI can not only reflect the present situation as well as detailed information of components directly, but also get the spatial information (e.g. coordinates, length, height). Therefore, in our urban management design, both two type images are included. DMI is geo-information, 360 degree street view is the true situation of some interested things.

DMI Management Platform integrates multi-source images data, in addition to DMI and 360-degree panoramic view, including columnar panoramic view, GIS spatial data, urban management business data. A three-tier structure is used to design

the system framework as shown in Fig.1. Based on design, urban management business such as inspection of illegal advertising signboard, urban management cases visualization, route planning in important event are realized.

The core of system framework is three database and three core modules.

Three databases: spatial database, street view database, urban component database.

- Spatial database is the most important and basic spatial data in urban management. It has features such as full element in real world, large amount and up-to-date of spatial information.
- DMI database is the core data of system. DMI provides the precise urban component position.
- Component database is the thematic data being appropriate for specific business applications.

Three cores: GIS is associated with DMI; DMI is associated with urban component; DMI image contrast adjustment.

The three-tier framework of this system is divided into:

- Data layer: is the data basis. In our system, we design GIS database, DMI database and urban component database according to business needs. Data layer is the data support of system.
- The middle layer is business applications layer of this platform and software functions, mainly responsible for the achievement of specific business needs.
- The top application layer is the users and hardware of system. Hardware is the basis for users and execution carrier of system applications, including PC, laptops, PDA, smart phones and so on.

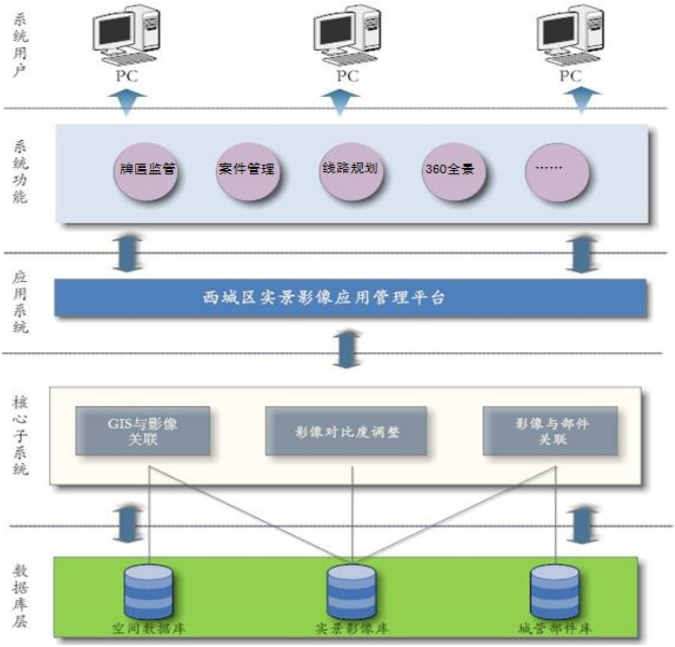

Fig. 1. General structure design of Street View Management Platform

3 Typical Applications

3.1 Advertising Signboard Supervision

According to urban management department, advertising signboard placed on the both sides of road have often violating city management regulations. These questions include placing densely, non-uniform styles, non-ruled color and size, and so on [4]. At present, these are found by many urban management supervisors. Non-uniform rule and subjectivity of supervisor are existing and affecting the advertising signboard management.

In our research, we use mobile mapping system to get the current state of advertising signboard, and the ruled style information of advertising signboard imported into database. We make the DMI analysis for comparing the ruled and current info of advertising signboard. This solution has the good visual and rapid to find the violated one.

Data Collection. In this platform, we collected all the advertising signboard about 12,200 covering Xicheng district of Beijing and handled data indoor with DMI. Fig.2 shows the information and DMI images of one advertising signboard.

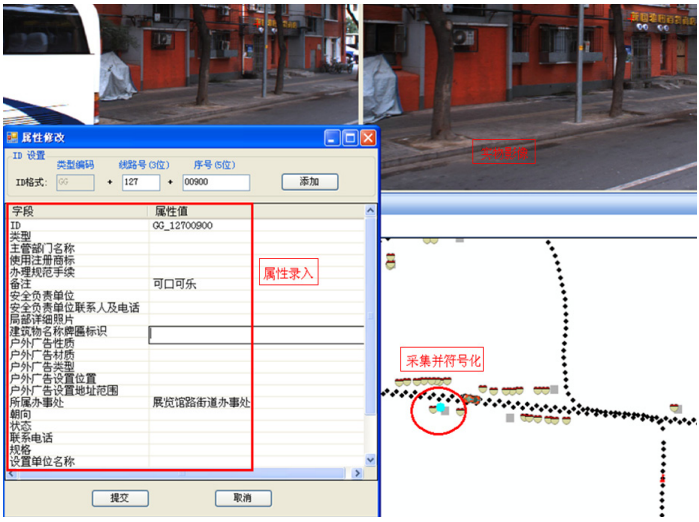

Fig. 2. Data collection, attributes input, symbolization of data

Find Irregularities Advertising Signboard. According to our statistic, the most common violated problems are non-ruled size, color and style. In our research, we import urban management rules as standard to find the illegal board. With non-ruled size as example, traditional method depends on people's field investigation, needing manpower and material resource, but the effect is not obvious. In our solution, we make the seamlessly associate between DMI and map info. Thus, as show in Fig.3, we can get the visual effect and rapidly judge.

Fig. 3. Measure the length, width, height of plaque with DMI

3.2 Case Management

A large number of cases occur every day in the city, for example, dirty roads, road caved, traffic jams and so on. The occurrences of these cases affect the normal social order, bringing a lot of inconvenience to the public life. It is becoming a difficulty puzzling administrative departments that how to manage these cases highly efficiently. In this platform, we realize some functions like multi-type query and quick positioning of cases. In addition, one algorithm which helps cases to be associated with the DMI was designed along with a complete process of dealing with case being established.

Fig. 4. The process of case management with street view

Once inspectors found cases, he would report the location, attributes and local images information about the case. We are able to present the occurred case real-timely in our platform. Moreover, urban managers can view the details of the case information, local images only through a simple point-and-click operation and invoke street view to observe surrounding environment, measure, assist in judging a case. This type of management module is helpful to achieve the high efficiency of cases from discovery to solve. Invoking street view provides the handling of the case with a strong basis.

3.3 Route Planning and Rehearsal

Xicheng district is located in the center of Beijing, and some of the major events places (e.g. churches, theaters, venues) and high risk factors places (e.g. petrol stations, gas plant) gathering here. Once major activities were held or unexpected accidents occurred, government would be faced with the work like route planning for patrol. However, in the traditional management module, the process of route planning is a procedure that contains four parts: plan your route on the two-dimensional electronic map -> confirm outside -> feedback confirmation message -> edit route. This procedure does not only waste people and material resources, but also lacks timeliness. Particularly for emergencies, its effect is minimal. In order to improve this situation, we add one function to plan route which based on associating algorithm between DMI and two-dimensional electronic map, image data extraction algorithm of road image dataset. As shown in Fig.5, the red line is planned in map, and the top frame is showing the DMI image.

Fig. 5. The scene of street view rehearsal

Using DMI route planning, the entire plan-making process is accomplished completely indoors to avoid confirming outside and feeding back information two steps. Due to reducing the workload, some valuable time is won for unexpected

events particularly. In addition, this function can also be used in the environmental inspection of the specified roads.

4 Conclusion

DMI has a good prospect in urban management. In paper, our work in DMI management platform is introduced, including some related application. Paper gives the new application model of DMI in urban management: ” urban electronic maps + urban ortho-photo + road videos + multi-angle DMI image + panoramic image”, which called multi-source spatial data. The application approves the feasibility and foresight of DMI in urban management.

In future work, the plug-in model DMI and other application business need develop. In addition, the automatic measure with mouse single click is necessary.

Acknowledgment. This research is partially supported by Beijing Natural Science Foundation (8122017, KZ201210016016) and the General Program of Science and Technology Development Project of Beijing Municipal Education Commission of China (KM201110016004) and The National Key Technology R&D Program (2012BAJ14B03).

References

1. Cong, X., Heng, L., Yun, B., Cheng, J., Zhenfeng, S.: Building Facade Measurement Service Based on Digital Measurable Image. In: 2013 Third International Conference on Intelligent System Design and Engineering Applications (ISDEA), January 16-18, pp. 406–408 (2013)
2. Goodchild, M.F.: Citizens as voluntary sensors: spatial data infrastructure in the world of Web 2.0. Int. J. Spat. Data Infrastr. Res. 2, 24–32 (2007)
3. Li, D.R., Shao, Z.F.: The new era for geo-information. Sci. China Ser. F-Inf. Sci. 4, 1233–1242 (2009)
4. Wang, W., Du, M.: Application of MMS in city outdoor advertisement information collection. Science of Surveying and Mapping 35(5), 199–201 (2010)

Feature Extraction and Filter in Handwritten Numeral Recognition

Zhu Qing and Xin He

The School of Software Engineering, Beijing University of Technology, Beijing, China

Abstract. Handwritten numeral recognition is about identifying Arabic numerals and various coding and statistical data which are composed by a few of special symbols. Feature extraction for improved recognition rate has a great influence, and effective classification can be characterized in that the feature is separability, reliability and independence. Characteristic dimension should as little as possible. To meet this requirement, classifier needs to combine various features to put them together. This article describes the extraction method of handwritten digits eigen values, based on the researches on features of several handwritten digits, discussing 6 kinds of features, they are Fourier switch features, stroke density features, contour features, projection features, the barycenter and barycenter distance feature, wide grid feature. Finally using inner and outer analogy method to select and filter the features.

Keywords: handwritten numeral recognition, feature extraction, feature filter.

1 Introduction

Digital Recognition is a branch of optical character recognition. Numeral recognition is composed by Printing digital recognition and handwritten numeral recognition. In recent years, neural network-based handwritten numeral recognition has become a hot issue. Such as zip code automatic identification system, tax tables and automatic bank check processing system. But when it comes to digital identification, it often requires a high recognition reliability, particularly when it's related to finance. Therefore, for such problems, the key for design the recognition system is to establish an algorithm of high reliability and high recognition rate of off-line handwritten numeral recognition. This field has made rapid development, partly due to better learning algorithms, partly due to looking for a new feature extraction method, to obtain a better training set. This paper mainly focused on the feature extraction and feature selection.

For improving recognition rate, feature extraction has a great influence, and effective classification can be characterized in that the feature is separability, reliability and independence. Characteristic dimension should as little as possible. To meet this requirement, classifier needs to combine various features to put them together. Specifically, separability means the difference of feature should vary greatly which is extracted from different types of the samples, this can more easily to

F. Bian et al. (Eds.): GRMSE 2013, Part I, CCIS 398, pp. 58–67, 2013.
© Springer-Verlag Berlin Heidelberg 2013

distinguish the different types of samples; Reliability means for the same type of sample, according to the characteristic of the reliability, reduced the possibility of false misjudgment for the same type of samples; independence means various features of the extracted value should be independently of each other, each feature is independent existence, this can effectively reduce the redundancy characteristic value; the characteristic dimension of as little as can increase recognition speed, reduce memory resource consumption. Therefore, in accordance with the above principles of feature extraction is also necessary to establish a standard for the selection and combination of feature values, to obtain the final optimal feature set.

This article extract a plurality of features from the digital library of MNIST handwritten training samples, and according to the characteristic value of 10,000 test samples, do the test for each class of the feature values using the inner and outer analogy method, and comparing the result to obtain the final excellent feature set. This paper is structured as follows: Chapter II handwritten numerical character of a comprehensive summary; third chapter describes feature selection methods, namely between classes within the class principles than function; fourth chapter to focus feature, for example, specific instructions for MNIST handwritten digits recognition database, how to apply the inner and outer analogy method, and ultimately get the optimal feature set; fifth chapter is about summary of the study.

2 Hand Written Numeral Recognition Feature

In the past ten years, researchers have proposed many identification methods, by the use of the characteristics' different, can be divided into: method based on structure feature and method based on statistical features. Statistical features typically include a point density measurement, moments, feature region; structural features usually include round, endpoint, intersection, stroke, contour, generally two features each has advantages. For example, the use of statistical classifier easy training, but also for the use of statistical classifier, can get comparatively high recognition rate in the training set is given; and the main advantages of structure is able to describe the character of the structure, and can effectively combine geometry and structure of knowledge in the process of recognition, therefore can obtain reliability good recognition results.

For handwritten numeral recognition, not only the numerical category is small, but also strokes is simple, especially in large differences in all handwritten digits. Digital identification key feature is the ability to find effectively, [2] gives a plurality of features for digits, they can generally describe the digits in digital way. Besides, the selected features should have the ability to distinguish effectively and can be as little as possible, that is for resolving power of computing and reducing information redundancy. Numerical characteristics of the present study are mainly including handwritten strokes density characteristics, wide grid feature, the barycenter and barycenter distance characteristics of the first black point features, characteristics and spatial domain transform projection characteristics, in addition to the above features, there are new features proposed constantly.

2.1 Strokes Density Characteristics

Density of stroke refers to for the different number's density of strokes in the horizontal direction and the vertical direction and the other angular direction. For example, the number 1 in the vertical direction, density strokes is high, strokes in the horizontal direction, density is low, and the number 8 in an oblique direction density is high. Such features can be found between the sample number of lines of horizontal and vertical scanning, recording the number of black pixels in the single line as the characteristic value, from this extraction method is easy to see that the stroke density characteristics have the ability to ignore the digital distortion, but noise immunity is weak.

2.2 Wide Grid Feature

wide grid feature extraction is mainly Segment the processed sample image into non-overlapping partial blocks, and make the black pixels in each block as a percentage of the total number of black pixels as the characteristics. This experimental study use the pictures of 28 × 28 pixels size as samples, and will be horizontally and vertically separated with a spacing of 7 pixels ,each sample in horizontal and vertical line is divided into 7 × 7 = 49 blocks, statistic each region's proportion of black pixels as the feature value. The smaller pieces separated the stronger ability to distinguish the relative number. Consider an extreme case: when the block size is only a pixel, the pixel point judgment standard is whether it is black pixel, the feature value will only be 0 or 1, there is a module that corresponds to the test numbers match.

Wide grid is characterized by a set of character images focus on the overall distribution of feature, which has a very strong noise suppression capability.

2.3 Barycenter and Barycenter Distance Feature

barycenter and barycenter distance characteristics means the position of the center of gravity , and in four-quadrant digital pixel values deviate from the center of gravity,

$$\bar{p} = \sum_{q=0}^{Q-1} \sum_{p=0}^{P-1} f_{p,q} \frac{p}{\sum_{q=0}^{Q-1} \sum_{p=0}^{P-1} f_{p,q}} \tag{1}$$

$$\bar{q} = \sum_{q=0}^{Q-1} \sum_{p=0}^{P-1} f_{p,q} \frac{q}{\sum_{q=0}^{Q-1} \sum_{p=0}^{P-1} f_{p,q}} \tag{2}$$

Which, $p = 1,2,\ldots,P-1, q = 1,2,\ldots,Q-1$. $(\bar{P},\bar{q})$Is defined as the center of gravity of the entire character.

Barycenter distance is:

$$L_{i,j} = \sum_{q=(j-1)\frac{Q}{2}}^{j\frac{Q}{2}} \sum_{p=(i-1)\frac{P}{2}}^{i\frac{P}{2}} (p - \bar{p})(q - \bar{q}) \tag{3}$$

Which $i = 1,1; j = 1,2$.

It needs to be indicated that the value should be 255 minus the pixel value, because in image of 8bits, 255 represent white, 0 represent black, if using the value of pixel directly as input into $f_{p,q}$, then the output is the barycenter of white region, not the black pixel region.

2.4 Fourier Switch Feature

The handwritten characters can generally described by closed contour consisting of many line segments. Some discrete obtained by mapping image can adequately reflect these changes of the closed contour [1]. In general, if the contour is provided with a dynamic point, and make it moves along the contour curve counterclockwise, the point coordinate transformation is a periodic function. Through the standardization later, the periodic function can be expanded into a Fourier series. In this series some of the coefficients can describe the contour shape. So Fourier coefficients can ignore character's displacement, rotation, size and other factors, is a good description of the character.

For the two-dimensional digital signal $\{f(p,q)(p = 1, \dots, P, q = 1, \dots, Q)\}$, the discrete Fourier transform is defined as:

$$F(m,n) = \frac{1}{\sqrt{P}\sqrt{Q}} \sum_{p=1}^{P} \sum_{q=1}^{Q} f(p,q)\, e^{-j2\pi\left(\frac{pm}{P} + \frac{qn}{Q}\right)} \tag{4}$$

Which, $m = 0,1, \dots, P-1, n = 0,1, \dots, Q-1$, called spatial frequency. J is the imaginary unit.

If handwritten digital image is large, you can make multiple transformation, suitable number of Fourier coefficients as the feature value:

$$F = \begin{pmatrix} F(0,0) & \cdots & F(1,Q) \\ \vdots & & \vdots \\ F(P,0) & \cdots & F(P,Q) \end{pmatrix} \tag{5}$$

2.5 Cut Off Frequency Feature

Cutoff frequency characteristic is the use of numbers 0-9 which are horizontal and vertical cutting, and recording the number of cross between the cutline and digit, the number will be the feature. You can cut image on vertical and horizontal direction, and decide the cutting interval.

Experiments using the cut line interval is 4, since the first row, first column and the last row, last column does not contain black pixels, so only truncation in the image, total 6 +6 strip cutting line, get 12 one-dimensional feature. The ability of this identified method should be very strong when is using to identify the general figures, and the number of feature is small, but because many of the handwritten digits appear broken pen, burrs, and personal writing habits are different, so there will be fluctuations in the experimental results.

3 Feature Filter

When producing the training set, there is a misunderstanding that the greater the number of feature for input which will contains more feature values , the greater recognition accuracy. In fact, this approach has two drawbacks: (1) many of the low-dimensional space with good performance classification algorithm is computationally infeasible; (2) in the training sample size under certain preconditions, the feature dimension increases will make estimate the statistical properties of the sample becomes more difficult, thereby reducing the classifier's promoting ability and generalization ability, showing the so-called "over-learning" and "overtraining" phenomenon [1].

To solving these problems, this article raise a method that using inner and outer analogy method to filter the features.

In this paper, using the Euclidean distance to calculate the Euclidean distance between the characteristic values to determine the characteristic' similarity. Euclidean distance is defined as:

$$D_e(x,y) = \sqrt{\sum_{i=1}^{d} |x_{i-} y_i|^2} \tag{6}$$

Where d is the dimension of the feature space. Obviously, if the sample x and y in the same category, the Euclidean distance will be smaller, if belonging to different categories, the Euclidean distance bigger.

When using Euclidean distance to filter the features, the filter criteria is: for similar characteristics, Euclidean distance between samples should be as small as possible, for the different categories, Euclidean distance between samples characterized bigger the better. According to this criterion, the Euclidean distance is calculated through an average of squared distances within the class and between the class, using intra-class / between class, this result is as bigger as better.

4 Research Result

In this chapter, mainly take the barycenter line feature as an example, to explain and experiment the process of filtering the features. We using the MNIST handwritten digit database samples in the experiment.

The MNIST database of handwritten digits, has a training set of 60,000 examples, and a test set of 10,000 examples. It is a subset of a larger set available from NIST. The digits have been size-normalized and centered in a fixed-size image. The original black and white images from NIST were size normalized to fit in a 20x20 pixel box while preserving their aspect ratio. The resulting images contain grey levels as a result of the anti-aliasing technique used by the normalization algorithm. the images were centered in a 28x28 image by computing the center of mass of the pixels, and translating the image so as to position this point at the center of the 28x28 field.

The probability of 0-9 digital we use to test is as the following table:

Table 1. The probability of 0-9 digital we use

digit	0	1	2	3	4
probability	0.13	0.14	0.06	0.11	0.13
digit	5	6	7	8	9
probability	0.04	0.1	0.1	0.08	0.11

Experimental data:

Table 2. Real digit and barycenter line feature

digit	**feature**	**digit**	**feature**	**digit**	**feature**
0	16.10036	0	15.74453	1	15.92683
0	15.79452	0	15.67365	1	15.77444
0	16.32258	0	15.52708	1	15.64583
0	15.87938	1	15.66935	1	15.44792
0	15.54017	1	16.272	1	15.28346
0	16.27378	1	16.05882	1	15.83688
0	15.49533	1	15.59341	1	15.82075
0	16.55405	1	15.92562	2	15.59483
0	15.71174	1	15.33951	2	15.8835
0	15.79927	1	16.02857	2	15.98227
4	15.63889	5	15.8963	6	15.64253
4	14.98387	6	15.99213	7	15.13542
4	15.41401	6	15.3	7	15.6
4	15.83654	6	15.77083	7	16.7069
4	16.00862	6	15.90854	7	15.49558
4	15.38068	6	16.33846	7	15.875
4	12.93443	6	15.96585	7	15.2439
5	15.25943	6	16.01449	7	15.00585
5	15.7047	6	16.02488	7	15.63014

Table 2. (*continued*)

5	13.07317	6	15.76339	7	14.92228
3	15.73295	3	15.85057	4	15.13043
3	15.2766	4	15.2619	4	15.896
3	16.13333	4	16.07018	4	15.8359
9	15.69136	9	15.14894	9	15.61047
9	15.69178	9	15.34868	9	15.33533
2	16.19623	8	15.88942	3	16.02
2	15.40404	8	15.09524	3	15.5035
2	16.01594	8	15.66383	3	15.84821
3	15.60081	8	15.49778	7	15.87234
3	15.19	8	15.41667	8	15.175
3	15.21154	8	15.48636	8	15.19005
3	15.70775	9	15.38547	9	16.1938
9	15.67485	4	15.02439	9	15.21905
9	15.51064				

Now let's calculate the data using the inner and outer analogy method.

Firstly calculate the average value of each kind of digit's features, the result is as the following table: ($\text{aver}_i, i = 0,1,2, \ldots 9$).

Table 3. The average value of 0-9 digits' feature

i	0	1	2	3	4
$\mathbf{aver_i}$	15.87819	15.75881	15.84613	15.64321	15.33968
i	5	6	7	8	9
$\mathbf{aver_i}$	14.9834	15.87211	15.54874	15.42679	15.52821

Secondly, using the average value to calculate the variance of each kind of digits' features, the result is a s the following table: ($\text{var}_i, i = 0,1,2, \ldots 9$).

Table 4. The variance of 0-9 digits' feature

i	0	1	2	3	4
$\mathbf{var_i}$	0.103453	0.074209	0.071655	0.093355	0.610886
i	5	6	7	8	9
$\mathbf{var_i}$	1.269705	0.06877	0.251552	0.063535	0.077654

Thirdly, using the average value and the probability to calculate the inner distance between the features, the algorithm is:

$$J_W = \sum_{k=1}^{C} P_i J_i \tag{7}$$

Which P_i is the probability of each kind of digit we used to experiment, J_i is the variance of each kind of digit, c is the number of types of the digit we have used.

And the result is:

$$J_W = \sum_{k=1}^{C} P_i J_i = 0.214267 \tag{8}$$

Fourthly, calculate the outer distance of the features. The algorithm is:

$$J_b = \sum_{j=1}^{c} P_j (m_j - m)^T (m_j - m) \tag{9}$$

and the total average square distance J_t is

$$J_t = \frac{1}{n} \sum_{j=1}^{n} (x_k - m)^T (x_k - m) \tag{10}$$

$$J_t = J_b + J_w \tag{11}$$

There are two way to calculate the outer distance of feature, the result is:

$$J_b = 2.619478 \tag{12}$$

Finally, the ratio of inner and outer distance:

$$J = \frac{J_b}{J_w} = 12.22 \tag{13}$$

In the above experiments, we extract the barycenter line as feature, use the inner and outer ratio function to calculate, the result is 12.22. To review the principles of feature selection: features should have higher separability, reliability and independence, and the ratio of inner and outer distance can well reflect the three characteristics. First of all, the same characteristics of different samples, different regional features in the feature space, feature distance is large, can reflect the strong separability; and for the same class samples, feature distance is small, show similar samples gathered intensive, meet the reliability characteristics. So the same sample density, different types of sample dispersion, meet such requirements are characterized by good characters. Reaction in the inner distance ratio function, is the molecular J_b distance between classes need bigger is better, and the denominator of J_w within class distance as small as possible, so the J should be the bigger the better.

When its value is less than 1, the distance between classes is less than the distance within classes, samples cannot be correctly distinguished, corresponding to the feature as invalid characters [1].

This feature extraction and selection method, compared with the other feature of the extraction methods, has some advantages.

First, it adds more features, including: the cutoff frequency feature and so on, the extracted features more comprehensive; secondly, through individual features were extracted, the eigen values obtained more accurate, for the following analysis and filtering of great help; finally, using the ratio of inner and outer method to compare each feature's pros and cons, eliminate invalid feature, the feature set obtained is more accurate, compared to other methods proposed, by changing the feature's coefficient to adjust feature set, this method is more efficient.

5 Summary

This paper discusses the extraction of feature and filtering the effective features in handwritten numeral recognition. Handwritten numeral recognition is a special issue of character recognition, has been widely applied in the real life.

This paper discusses the extraction methods especially for the handwritten digits, and also the feature selection, using inner and outer ratio method to remove the invalid features, to maintain the appropriate dimension of feature, reduce the amount of computation and time, improve the recognition efficiency and effectiveness.

Due to handwritten digits have many variations, there are a lot improving for me to research for obtain the more effective feature set. In the aspect of feature extraction, it needs extracting effective features characters; in feature selection, it needs to improve filtering function, compress feature dimension.

References

1. Dong, H.: Handwritten Digit Recognition feature extraction and feature selection. Beijing Universityof Posts and Telecommunications Thesis (2007)
2. Qu, H.: Handwritten Digit Recognition Method Research and Implementation. Nanjing University of Science Thesis (2005)
3. Bai, L.: Neural network ensemblehandwritten numeral recognition research. Beijing Universityof Posts and Telecommunications Thesis (2007)
4. Liu, P.: Bank notes handwritten digit string recognition preprocessing and segmentation. Nanjing University of Science Thesis (2012)
5. Shen, Y.: Bank notes Automatic Identification System. East China Normal University Thesis (2006)
6. Huang, Q.: BP neural network based handwritten numeral recognition system. Central China Normal University Thesis (2009)
7. Gao, L.: BP neural network based handwriting recognition alphabet. North University Thesis (2009)
8. Huang, Z.: Neural network cascade handwritten numeral recognition Research and Implementation. Beijing University of Posts and Telecommunications Thesis (2010)

9. Zhou, B.: Neural Networks in Handwritten Digit Recognition. Hunan Normal University Thesis (2009)
10. Yang, L.: Based on artificial neural network pattern recognition and classification of handwritten digits. North University Thesis (2012)
11. Liu, X.J.: Neural Network Based on Genetic Optimization of bank notes handwritten numeral recognition. Jilin University Thesis (2006)
12. Huang, Q.: BP neural network based handwritten numeral recognition system. Central China Normal University Thesis (2009)
13. Wu, X.: Based on Neural Network handwritten numeral character recognition. Beijing University of Posts and Telecommunications Thesis (2010)
14. Li, C.: ImprovedBP Neural Network and its Application in Handwritten Digit Recognition. Harbin Institute of Technology Thesis (2006)
15. Zhang, N.: Unconstrained Handwritten Numeral Recognition. Chinese Academy of Sciences (Institute of Computing Technology) Thesis (2000)
16. Wang, T.: BP neural network Handwritten Digit Recognition. Guizhou University Thesis (2008)
17. Kim, K.K., Kim, J.H., Suen, C.Y.: Segmentation-based recognition of handwritten touching pairs of digits using structural features. Pattern Recognition Letters 23(1-3), 13–24 (2002)
18. Kussul, E., Baidyk, T.: Improved method of handwritten digit recognition tested on MNIST database. Image and Vision Computing 22(12), 971–981 (2004)
19. Cheng, D., Yan, H.: Recognition of handwritten digits based on contour information. Pattern Recognition 31(3), 235–255 (1998)
20. Lu, Z., Chi, Z., Siu, W.-C., Shi, P.: A background-thinning-based approach for separating and recognizing connected handwritten digit strings. Pattern Recognition 32(6), 921–933 (1999)

Evaluation on Regional Competitiveness of Wuhan Modern Service Industry in the Comparative Perspective: Based on 15 Vice-Provincial Cities' Crosswise Comparison

Jialong Xie and Shuhua Hu

School of Management, Wuhan University of Technology, Wuhan, 430070 Hubei, China
xiejialong1234@126.com, sjxwhsh@163.com

Abstract. Based on the comparison and analysis of the relevant study at home and abroad, this paper designs four-level evaluation index system including 24 perform indexes, from the developmental level, developmental potential and developmental environment. Multi-step fuzzy comprehensive evaluation and K-means cluster is used to construct the evaluation model of regional competitiveness of modern service industry. Then, according to the measurement results of 15 vice-provincial cities' competitiveness in 2010, this paper compares to get the regional competitiveness level and the weaknesses of modern service industry in Wuhan from the layer indexes, which provides a theoretical reference for urban industrial policy making.

Keywords: Modern Service Industry, Regional Competitiveness, Multi-step Fuzzy Comprehensive Evaluation, K-means Cluster, Wuhan City.

1 Introduction

With the rapid development of information technology and the acceleration of economic globalization, modern service industry has dominated predominance in each country's service industry. It is becoming the important engine of the national economic growth, which developmental level has been the important criterion to measure the modern and international developmental extent of one country, region or city. In 2010, Jianghan District in Wuhan was permitted as the first experimental area to construct "national service industry comprehensive reform pilot project"; in 2011, East Lake National Innovation Model area was approved as "national modern service industry pilot project", thus the modern service industry in Wuhan has entered a new stage of development. However, we must face the competitive advantages and the developmental disadvantages of the modern service industry in Wuhan, comparing with the developmental level of other same level cities. This study has great realistic significance to promote leapfrog development of the modern service industry in Wuhan.

F. Bian et al. (Eds.): GRMSE 2013, Part I, CCIS 398, pp. 68–79, 2013.
© Springer-Verlag Berlin Heidelberg 2013

2 Literature Review

Research about the competitiveness in foreign academic circles has been for a long time, from the traditional theories of competitiveness, such as Ricardo's comparative advantage and Krugman's economies of scale, to Poter's diamond model, Tim Padmore and Hervey Gibson's GEM model[1]. But a comprehensive study on service industry and competitiveness dates from mid and late 1990s. Mark. Tomlinson and Paul. Windrum (1999) defined the nature and status of innovational industry, and pointed out the correlation between service industry and other economic activities determines the strength of innovational spillage and international competitiveness[2]. Scholars like Anton Meyer (1999) studied financial services, professional services, hotel services, hydropower services and their management model in Britain, America and Germany, then considered the service performance of all sectors was determined by the essentials and market level of corresponding departmental service in each country[3]. Rubalcaba etc. (2001) established a conceptual frameworks on the relationship between competitiveness and service industry, finding the service industrial competitiveness level associated with the cost factor, thereby it could partly explain the strength of international competitiveness[4].

The competitiveness is a reflection of the comprehensive ability, so that constructing a set of scientific evaluation system is the basis and precondition to objectively analyze the modern service industrial competitiveness. Compared with the traditional service industry, modern service industrial has remarkably knowledge-intensive and technology-intensive characteristics. Its competitiveness stresses the function of the information level and the technological strength. Huo (2007) analyzed the R&D competitiveness of Chinese modern service industry from the international and comparative perspectives, which opened a dialogue about modern service industrial competitiveness[5]. Cha (2008) used factor analysis to extract three main factors (scale, structure and growth capacity) in 17 evaluation indexes, and calculated the competitiveness level of 31 provinces[6]. Then, Cao[7] (2012) and Li[8] (2012) expanded the original three main factors foundation, technology and environment on the basis of more systematic and comprehensive evaluation indexes. In addition, Huang[9] (2013) and Zhou[10] (2013) put forward this new main factor, namely, public environment, based on empirical results of provinces in central and eastern China. Huang[11] (2011) and Zhang[12] (2012) constructed a set of evaluation index system made up of the basis, scale, structure/hierarchy, developmental speed and innovation ability, and used principal components analysis to evaluate the modern service industrial regional competitiveness of Jiangxi and Hubei on the foundation of typical provinces comparison. According to the index value during 2004-2009 and 2007-2009, Zhang[13] (2011) and Han[14] (2012) used shift-share method to evaluate respectively the competitive situation of 10 industries in Xi'an and 9 industries in Shanxi. Zhou (2012) used the fuzzy comprehensive evaluation and grey fixed weight clustering to construct competitiveness evaluation model, and analyzed the changing situation of the Pearl River Delta's Economic Areas during 2000-2010[15].

In conclusion, we can find that there are many studies on the service industrial competitiveness abroad, but seldom shows modern service industrial competitiveness,

and that the research results on each subdivided industries are more than overall service. The relevance researches at home are focus on some important provinces, such as the central and eastern regions. However, the city is important spatial carrier of modern service industrial development, so deep research obviously does not match with its important position. Meanwhile, they use the single evaluation method, for instance, factor analysis and principal component analysis, whose evaluation quality may be doubted. Therefore, based on the existing classic evaluation index system, this paper refines its key areas, and establishes the regional competitiveness evaluation model by using the multi-step fuzzy comprehensive evaluation and layer clustering. Then, this paper compares in 15 vice-provincial cities to get the regional competitiveness level and the weaknesses of modern service industry in Wuhan, thus provides a theoretical reference for its industrial policy making.

3 Index System Design

Modern service industrial competitiveness belongs to the research scope of industrial competitiveness. With reference to the explanation on industrial competitiveness by the World Economic Forum and the International Institute for Management Development in Lausanne, this paper defines the urban modern service industrial competitiveness as a reflection of the comprehensive ability to acquire and utilize the resource taking part in competitiveness and the sum total of living conditions and development potential under certain political, economic and science conditions. Therefore, the evaluation system of modern service industrial regional competitiveness is a complicated system including multi-factor. Building a set of correct and complete index system is the prerequisite and foundation to truly evaluate the modern service industrial competitiveness.

At present, the research on this field is still at a groping and primitive stage. Based on the previous research, author not only analyzes the developmental level of modern service industry, but also integrates the developmental potential and developmental environment into index system; for instance, urban disposable income per, waste recycling value, etc. Analysis of these factors can help us to thoroughly understand the deep reason for this urban difference, and fully comprehend the status and dynamics of modern service industrial competitiveness. Consequently, this paper use analysis hierarchy process to compare comprehensively modern service industrial competitiveness from all sides. Include three respects: firstly, developmental level reflects the urban modern service industrial scale, efficiency and service quality; secondly, developmental potential reflects the capacity for sustainable development in market, talents and technology; thirdly, developmental environment consists mainly of the basic resource allocation (per urban electricity consumption) and the quality of human residential environment (per capita green area).

This index system includes four levels. Urban modern service industrial competitiveness as evaluation target is divided into three first-level indexes, namely developmental level, developmental potential and developmental environment. Then, these first-level indexes are successively divided into eight second-level indexes and thirty-three third-level indexes (as shown in Table 1). Developmental level is key index to reflect the reality of urban modern service industrial competitiveness, whose

difference needs be measured from industrial scale, developmental efficiency and service quality. Developmental potential can reflect an ever-increasing capability with the existing market, talent and technology conditions. The strength of modern service industrial competitiveness is subtly influenced by urban developmental environment, which have been important judgment criteria of urban environmental quality.

Table 1. Evaluation Index System of Urban Modern Service Industrial Competitiveness

First-level Index	Second-level Index	Third-level Index
Developmental Level D	Developmental Scale D_1	D_{11} Value added of modern service industry
		D_{12} Value added of modern service industry to GDP
		D_{13} Workforce of modern service industry
		D_{14} Employees share of modern service industry
		D_{15} Fixed investments of modern service industry
	Developmental Efficiency D_2	D_{21} Per capita value added
		D_{22} Unit area value added
		D_{23} Overall labor productivity
		D_{24} Resource allocation efficiency
	Service Quality D_3	D_{31} Amount of per capita savings and loan
		D_{32} Urban premium income
		D_{33} Per capita telephone service traffic
		D_{34} Telephone amount per hundred people
		D_{35} Amount of internet access per hundred people
		D_{36} Total volume of urban transport
		D_{37} Total volume of urban freight
Developmental Potential P	Market Potential P_1	P_{11} Urban per capita disposable income
		P_{12} Urban per capita consumption expenditure
		P_{13} Urban per capita savings
		P_{14} Urban industrial added value
	Talent Potential P_2	P_{21} Amount of regular institutions of high education
		P_{22} The number of students in university
		P_{23} Amount of scientific institution
	Technology Potential P_3	P_{31} Research and development funding
		P_{32} Weighted amount of patent applications
Developmental Environment E	Basic Resource E_1	E_{11} Per urban electricity consumption
		E_{12} Per capita water resources
		E_{13} Public transport vehicles per million people
		E_{14} Per capita urban road area
	Environmental Quality E_2	E_{21} Per capita urban green area
		E_{22} Waste recycling value
		E_{23} Urban sewage processing ratio
		E_{24} Life garbage treatment ratio

4 Construction of Evaluation Model

In order to remove the influence of the subjective factor during the evaluation, the paper chooses to use multi-step fuzzy comprehensive evaluation model combined

with the multi-level feature of index system. This model is organic combination of Fuzzy Theory and classical comprehensive evaluation method, of which the advantage is primary data without pretreatment. The relative deviation fuzzy matrix established by this method eliminates dimension and order of magnitude, meanwhile gets a "benefit type" fuzzy matrix. Then it makes use of entropy method to confirm the weight of all indicators, at last figures out the comprehensive values of each city.

4.1 Weight Definition: Entropy Method

According to level difference set by index system, multi-step fuzzy comprehensive evaluation model further divide $u_{ij} = (j = 1, 2, \cdots, n)$ in evaluation factor set into several evaluation grades on the basis of evaluative aspects and evaluative factors:

$$u_{ij} = \{u_{j1}^*, u_{j2}^*, \cdots, u_{jo}^*, \cdots, u_{jp}^*\}. \tag{1}$$

In the formula, 1≤o≤p, p means the number of evaluative factors in the *i*th evaluative aspect, the *j*th evaluative element.

Then, entropy method is used to confirm the weight of all indicators based on different levels, reflecting the degree of variation through information entropy. If the degree of variation of some index value is large, it indicates resolved information more abundant and corresponding information entropy smaller, so greater weight should be assigned to this index.

The formula of entropy method confirming weight is shown as the following formula: first of all, the proportion of *j*th sample in *i*th index

$$p_{ij} = r_{ij} \Big/ \sum_{j=1}^{n} r_{ij} \ (i = 1, 2, \cdots, m; j = 1, 2, \cdots, n) \tag{2}$$

In the formula, *m* is the number of indicators, *n* is the number of given cities, r_{ij} is the evaluated value that *i*th influence factor in *j*th city is standardized.

Next, the entropy value of *i*th indicator is shown as the following formula

$$e_i = -1 \Big/ \ln n \sum_{j=1}^{n} (p_{ij} \ln p_{ij}) \tag{3}$$

At last, the weight of *i*th indicator is got by utility value $d_i = 1 - e_i$

$$\omega_i = d_i \Big/ \sum_{i=1}^{m} d_i \tag{4}$$

Because the evaluation index system is four-level structure, the utility value D_k in upper level is got by using the sums of utility values in lower levels according to entropy additive property:

$$W_k = D_k \Big/ \sum_{k=1}^{s} D_k \ (k = 1, 2, \cdots, s) \tag{5}$$

4.2 Index Evaluation: Relative Deviation Fuzzy Matrix

Given: $A=\begin{bmatrix} a_{11} & a_{12} & \cdots & a_{1n} \\ a_{21} & a_{22} & \cdots & a_{2n} \\ \vdots & \vdots & \vdots & \vdots \\ a_{m1} & a_{m2} & \cdots & a_{mn} \end{bmatrix}$, a_{ij} in the formula means the index value of the *i*th evaluation factor of *j*th city.

Firstly, establish the ideal scenario.

$$U=(u_1^o,u_2^o,\cdots,u_m^o) \tag{6}$$

when a_{ij} is benefit type index, $u_i^o=\max\{a_{ij}\}$; when a_{ij} is cost type index, $u_i^o=\min\{a_{ij}\}$.

Secondly, set up the relative deviation fuzzy matrix *R*

$$R=\begin{bmatrix} r_{11} & r_{12} & \cdots & r_{1n} \\ r_{21} & r_{22} & \cdots & r_{2n} \\ \vdots & \vdots & \vdots & \vdots \\ r_{m1} & r_{m2} & \cdots & r_{mn} \end{bmatrix}, \text{ in the formula, } r_{ij}=\frac{\left|a_{ij}-u_i^o\right|}{\max\{a_{ij}\}-\min\{a_{ij}\}} \tag{7}$$

Thirdly, use entropy method to confirm the weight ω_i of each evaluation index.

Lastly, establish comprehensive evaluation model as the following formula:

$$F_j=\sum_{i=1}^{m}\omega_i \bullet r_{ij}\,(j=1,2,\cdots,n) \tag{8}$$

Because the relative deviation fuzzy matrix is benefit type, namely, the higher the score, the stronger the urban modern service industrial competitiveness. So, if $Ft>Fz$, then the *t*th city is ahead of the *z*th city.

5 Empirical Analysis

According to the evaluation index system of urban modern service industrial competitiveness in Table 1, it uses corresponding statistical software to calculate 15 vice-provincial cities' competitiveness. Thus we can get the evaluation results and comprehensive ranking, and analyze the strength and weakness of the modern service industrial competitiveness in Wuhan through comparing the equivalent cities.

5.1 Comparison of Developmental Level

5.1.1 Remarkable Advantages in Industrial Scale

Scale advantage of modern service industry in Wuhan focus shows in industry value, quantity of employment and fixed investment. Wuhan is expanding continually

industrial scale of modern service industry by propelling the balanced development strategy, and its annual value is increasing. In 2010, added value of modern service industry in Wuhan reached 2863.07 billion RMB, accounting for more than 50% in the city's GDP. It was fourth in the same level cities after Guangzhou, Shenzhen and Hangzhou. In the aspect of employment contribution, modern service industry created 2.44 million jobs for Wuhan, accounting for 50.06% in the city's quantity of employment. Barely East Lake National Innovation Model area provided 328800 employment opportunities for high-tech talents. With the concerted efforts of the value scale and employment scale, fixed investments of modern service industry in Wuhan increased rapidly, ranking fourth, and strengthened fixed investments' leading role in economic running.

5.1.2 Low Efficiency of Resource Allocation

By Contrast with sufficient capital and labor force, labor productivity and efficiency of resource allocation of Wuhan is not positive. The whole developmental efficiency only takes tenth place in 15 vice-provincial cities. In 2010, per capita value added of Wuhan modern service industry reached 29258.59 RMB, existing a gap relative to Guangzhou(51594.46), Shenzhen(48704.88), Hangzhou(33276.16), Dlian(32397.17). This explains that labor capacity of Wuhan modern service industry has yet to translate into market value. In the aspect of resource allocation efficiency, Wuhan utilized superior labor (ranking fifth) and investment (ranking fourth) to only produce 3.49% of the resource allocation (ranking tenth), not as good as Xiamen(3.86%). So you can see that resource allocation in the process of modern service industry is irrational, likely to cause potentially industrial resource waste.

Table 2. Developmental Level and Rankings of 15 Vice-provincial Cities

City	D_1	Rank	City	D_2	Rank	City	D_3	Rank	City	D	Rank
GZ	0.8929	1	SZ	0.7553	1	SZ	0.7783	1	SZ	0.7379	1
SZ	0.6007	2	GZ	0.5208	2	GZ	0.4904	2	GZ	0.5752	2
CD	0.5689	3	SY	0.4646	3	CD	0.4314	3	CD	0.3393	3
WH	**0.5576**	**4**	XM	0.2230	4	HZ	0.2748	4	SY	0.2981	4
NJ	0.4617	5	NJ	0.2127	5	NB	0.2728	5	HZ	0.2729	5
SY	0.4554	6	QD	0.2079	6	XM	0.2576	6	NJ	0.2728	6
XA	0.4237	7	DL	0.2039	7	NJ	0.2397	7	**WH**	**0.2637**	**7**
HZ	0.4108	8	JN	0.2010	8	XA	0.2130	8	XM	0.2465	8
HEB	0.3673	9	HZ	0.1869	9	**WH**	**0.2044**	**9**	NB	0.2197	9
JN	0.3662	10	**WH**	**0.1824**	**10**	DL	0.1724	10	DL	0.2105	10
DL	0.3234	11	NB	0.1689	11	QD	0.1428	11	XA	0.1967	11
QD	0.3006	12	CD	0.0534	12	SY	0.1359	12	JN	0.1947	12
XM	0.2559	13	CC	0.0398	13	JN	0.1268	13	QD	0.1926	13
NB	0.1621	14	XA	0.0341	14	HEB	0.0282	14	HEB	0.0893	14
CC	0.1318	15	HEB	0.0205	15	CC	0.0160	15	CC	0.0451	15

Note: abbreviations in table are initials of city, such as GZ-Guangzhou, SZ-Shenzhen, CD-Chengdu, WH-Wuhan, NJ-Nanjing, SY-Shenyang, XA-Xi'an, HZ-Hangzhou, HEB-Haerbin, JN-Jinan, DL-Dalian, QD-Qingdao, XM-Xiamen, NB-Ningbo, CC-Changchun.

5.2 Comparison of Developmental Potential

5.2.1 Insufficient Purchasing Power of Urban Residents

As the core component of consumption level, purchasing power of urban residents become an important driving force for regional economic growth. Although Wuhan is the central city of central China and its output scale and tax are in the front row, such two indexes as per capita disposable income (20806 RMB) and per capita consumption expenditure (14490 RMB) ranks 12th and 13th, even less well than some cities in the West and the north-east. Meanwhile compared with Hangzhou (173219 RMB), Shenzhen (132165 RMB), Nanjing (129687 RMB), Guangzhou (128126 RMB) and Ningbo (123692 RMB), per capita savings in Wuhan (92931 RMB) is lagging. Savings is in positive correlation with the propensity to consume in China's consumption concept, so consumption momentum of modern service industry in Wuhan is suppressed by the lower per capita savings.

5.2.2 Intensive Innovative Talents Resource

Wuhan benefits from the intensive colleges and research institutes distribution, and then its talent potential index ranks first. Wuhan is the big city having rich talent resource. 78 colleges and universities locate in Wuhan, and 881400 college students study here, so the proportion of college students is the highest in China. It also has 1 National Laboratory, 1 National Centre for Scientific Research, 15 the State Key Laboratory, 15 National Enterprise Technology Center, 22 National High-tech Industrialization Base, 56 provincial key laboratories, 64 academicians, which sends plenty of innovative talents to urban modern service industry. Therefore an excellent situation is formed by extensive talents and personnel structure optimization.

5.2.3 Relatively Weak Technical Support

Advanced scientific achievements offer the powerful technical support for leapfrog development of modern service industry. In this knowledge explosion era, in particularly, technology has carried through all sectors of modern service industry,

Table 3. Developmental Potential and Rankings of 15 Vice-provincial Cities

City	P_1	Rank	City	P_2	Rank	City	P_3	Rank	City	P	Rank
SZ	0.8873	1	**WH**	**0.9931**	**1**	SZ	1.0000	1	GZ	0.7883	1
GZ	0.8658	2	GZ	0.9667	2	HZ	0.5278	2	SZ	0.6550	2
HZ	0.6879	3	NJ	0.8514	3	CD	0.4786	3	HZ	0.6036	3
NB	0.6122	4	XA	0.7198	4	GZ	0.4579	4	NJ	0.5608	4
NJ	0.5064	5	JN	0.7022	5	XA	0.4001	5	**WH**	**0.4778**	**5**
XM	0.4451	6	CD	0.6212	6	NB	0.3559	6	CD	0.4251	6
QD	0.3905	7	HEB	0.6081	7	NJ	0.3191	7	XA	0.4146	7
DL	0.3205	8	HZ	0.5487	8	**WH**	**0.2853**	**8**	JN	0.3903	8
JN	0.2956	9	SY	0.4587	9	QD	0.1918	9	NB	0.3786	9
SY	0.2940	10	CC	0.3195	10	JN	0.1904	10	SY	0.3068	10
CD	0.2564	11	QD	0.2848	11	DL	0.1729	11	QD	0.3061	11
WH	**0.2375**	**12**	DL	0.2569	12	SY	0.1548	12	DL	0.2623	12
XA	0.2118	13	XM	0.0900	13	HEB	0.0880	13	XM	0.2264	13
CC	0.0944	14	NB	0.0618	14	CC	0.0513	14	HEB	0.2120	14
HEB	0.0126	15	SZ	0.0173	15	XM	0.0227	15	CC	0.1508	15

and become key factor to determine industrial level and quality. In 2010, the government R&D expenditure in Wuhan is about one-third of that of Guangzhou, and enterprise R&D expenditure lags behind Shenzhen and Guangzhou etc. Meanwhile, the weighted amount of patent applications and granted of Wuhan only reaches 13183, ranking ninth. This situation does not match with abundantly innovative talent resource, showing relatively weak technical support for modern service industry.

5.3 Comparison of Developmental Environment

5.3.1 Complete Infrastructure

Urban infrastructure provides the material basis for normal running of modern service industry, and is indispensible external condition of competitiveness improvement. Locating the confluence of Yangtze River and Han River, Wuhan is the important hub of transportation. These natural advantages offer essential conditions for development, such as plentiful water and energy, etc. In addition, when ground traffic facilities are constantly optimized in Wuhan, 9 subway lines and 3 express subways are building, about 540 kilometers. Thus three towns of Wuhan will be linked together, and the bearing pressure of their public transport would be also significantly reduced. A new business model around the subway will come into being in these influences. But above all, there are obviously comparative advantages of basic resource in the process of Wuhan modern service industry, and these advantages will continue to be expanded.

5.3.2 Improved Environment Quality

Favorable environment quality provides elegant quarters for urban residents, and attracts a large number of enterprises and talents settling in the city. It creates a vast market demand and manpower resources for modern service industry development. The enormous improvement of Wuhan in waste recycling, urban sewage processing and life garbage treatment, etc. should be affirmed, although there are gaps between Wuhan and other cities (e.g. Hangzhou, Shenzhen, Guangzhou, Qingdao). The waste

Table 4. Developmental Environment and Rankings of 15 Vice-provincial Cities

City	E_1	Rank	City	E_2	Rank	City	E	Rank
SZ	1.0000	1	HZ	0.6331	1	SZ	0.7388	1
GZ	0.3791	2	SZ	0.4994	2	HZ	0.4223	2
NJ	0.3397	3	GZ	0.2750	3	GZ	0.3248	3
XM	0.2790	4	QD	0.1953	4	NJ	0.2620	4
WH	**0.2320**	**5**	NJ	0.1909	5	XM	0.2300	5
HZ	0.1922	6	XM	0.1852	6	**WH**	**0.2028**	**6**
DL	0.1558	7	**WH**	**0.1761**	**7**	QD	0.1684	7
NB	0.1474	8	NB	0.1679	8	NB	0.1581	8
QD	0.1390	9	CD	0.1587	9	DL	0.1430	9
SY	0.1075	10	SY	0.1383	10	CD	0.1292	10
JN	0.1075	11	JN	0.1375	11	SY	0.1236	11
CD	0.0971	12	DL	0.1312	12	JN	0.1232	12
CC	0.0728	13	CC	0.1296	13	CC	0.1024	13
XA	0.0657	14	XA	0.0885	14	XA	0.0776	14
HEB	0.0069	15	HEB	0.0240	15	HEB	0.0158	15

recycling value and the life garbage treatment ratio reach 18.83% and 9.06% respectively; the urban sewage processing ratio increased from 89.8% in 2009 to 94.96% in 2010, ranking first in the same level cities.

5.4 Comparison of Comprehensive Competitiveness

According to the data of Table5, we get that the three best cities are Shenzhen, Guangzhou and Hangzhou, and Wuhan, Chengdu are fifth equal in the list. The rankings of comprehensive competitiveness indicate that Wuhan is the front row, but it would take a while to chase after Shenzhen and Guangzhou etc.

Table 5. Value of Criteria Layer and Comprehensive Evaluation

Index / City	Developmental Level	Developmental Potential	Developmental Environment	Comprehensive Competitiveness
NJ	0.4617	0.2127	0.2397	0.3236
JN	0.3662	0.201	0.1268	0.2071
QD	0.3006	0.2079	0.1428	0.2057
GZ	0.8929	0.5208	0.4904	0.5293
SZ	0.6007	0.7553	0.7783	0.7225
HZ	0.4108	0.1869	0.2748	0.3869
NB	0.1621	0.1689	0.2728	0.2285
WH	**0.5576**	**0.1824**	**0.2044**	**0.2832**
CD	0.5689	0.0534	0.4314	0.2832
XA	0.4237	0.0341	0.213	0.1969
XM	0.2559	0.223	0.2576	0.237
SY	0.4554	0.4646	0.1359	0.2397
DL	0.3234	0.3234	0.3234	0.197
CC	0.1318	0.0398	0.016	0.0848
HEB	0.3673	0.0205	0.0282	0.0872

In order to reveal the strength characteristic of modern service industrial competitiveness in different cities, K-means clustering is used to analyze 15 vice-provincial cities. 8 second-level indexes are plugged into SPSS17.0 software, and then we directly get the clustering result including four levels, appearing “olive” shape, namely both ends is small, middle is large (as shown in Figure1).

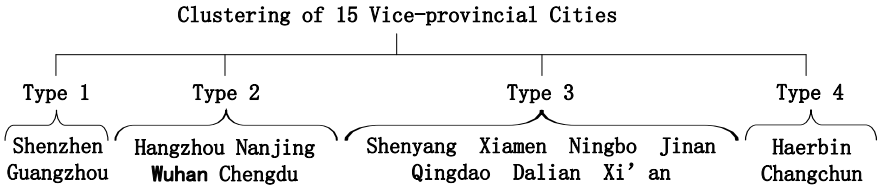

Fig. 1. K-means Clustering Result of 15 Vice-provincial Cities

The paper draws the relational graph (as shown in Figure2) in accordance with the results of first-level indexes and comprehensive competitiveness in Table5 the abscissa, the ordinate clustered sequence of 15 vice-provincial cities. The changing

trend of modern service industrial competitiveness and its developmental level are the closest, because the influence effect of developmental level to competitiveness is nearly the sum of other indexes. This complies with former research using developmental level instead of competitiveness. Meanwhile, developmental potential is the most unstable index, especially the results of Guangzhou, Xiamen and Xi'an suddenly changed larger or smaller compared with neighboring cities. The phenomenon indicates this index can drive or restrain obviously urban modern service industrial competitiveness.

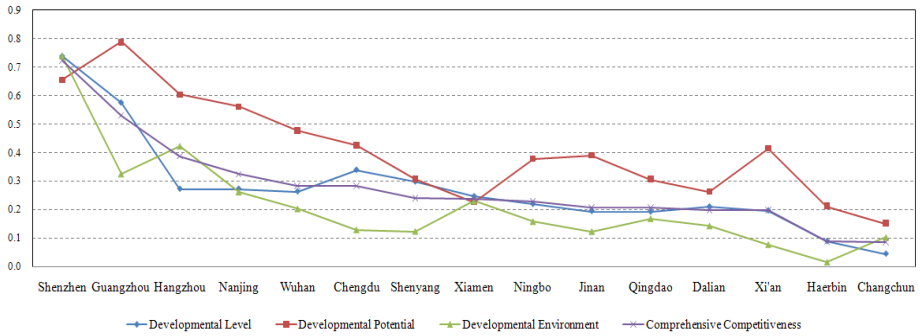

Fig. 2. Relationship between Sample and Indexes in Criteria Layer

6 Conclusion

On the basis of calculation results, we can conclude by analysis that Wuhan modern service industrial competitiveness is confronted mainly with the following advantages and disadvantages: First of all, the advantages can be easily found in remarkable industrial scale, not only strengthening the market economic aggregate and providing much employment opportunities, but also laying a solid foundation for quality upgrading and scale effect; abundant education resource and dense innovative talents create favorable intellectual support; enough material supply, smoothing transportation network and improved environment quality offer a good environment for leapfrog development.

Next, the disadvantages focus show in low efficiency of resource allocation, fall behind other same-level strong cities, and developmental level of important sectors is unbalanced; the per capita disposable income, per capita consumption expenditure and per capita savings remain low, thus restrain consumption tendency of citizen, leading to lacking consumption traction; abundant talent resource does not translate into sufficient research & development power, and is unable to play a strong supporting for technological innovation of modern service industry; although the environmental quality is improved in recent years, there are gaps between Wuhan and China's eastern coastal cities. So this requires increase investment in environmental harness and improvement to break through the environment bottleneck of modern industry.

References

1. Padmore, T., Gibson, H.: Modeling System of Innovation: A Framework for Industrial Cluster Analysis in Regions. Research Policy 26, 625–641 (1998)
2. Tomlinson, M., Windrum, P.: Knowledge-intensive Services and International Competitiveness: A Four Country Comparison. Technology Analysis and Strategic Management 3, 391–408 (1999)
3. Meyer, A., Chase, R., Roth, A., et al.: Service Competitiveness: An International Benchmarking Comparison of Service Practice and Performance in Germany, UK and USA. International Journal of Service Industry Management 4, 369–379 (1999)
4. Rubalcaba, L., Gago, D., et al.: Relationship between Services and Competitiveness: The Case of Spanish Trade. Service Industries Journal 1, 34–61 (2001)
5. Huo, J.-D., Xia, J.-C.: The International Comparison on R&D Competitiveness of Modern Service Industry. China Soft Science 10, 8–14 (2007)
6. Cha, Q.-F., Zhu, T.: The Comprehensive Evaluation on Modern Service Industrial Competitiveness Level of China. Jiangsu Commercial Forum 10, 74–76 (2008)
7. Cao, J.-Y.: Construction and Its Application of the Evaluation System of Competitiveness of Modern Service Industry. Northwes Population Journal 6, 111–115 (2012)
8. Li, X.-Q., Xin, B.-G.: Evaluation of Modern Service Industry Competitive Power of Qingdao City: Based on Data of 21 Main Cities in China. Science Technology and Management 3, 78–82 (2012)
9. Huang, M.-Y., Li, Z.-F.: Evaluation and Analysis of the Regional Competitiveness of Modern Service Industry in Hubei Province. Modern Business Trade Industry 3, 14–16 (2013)
10. Zhou, F.: Evaluation of the Competitiveness of Modern Service Industry and Its Developmental Measures: To Jinan in Shandong Province as an Example. Commercial Times 6, 27–28 (2013)
11. Hu, Y., Huang, X.-J.: Jiangxi Province Modern Service Industry Competitiveness Evaluation. Special Zone Economy 1, 191–192 (2011)
12. Zhang, X.: Analysis on Developmental Level and Competitiveness of Modern Service Industry of Hubei Province. Cooperative Economy & Science 22, 14–15 (2012)
13. Zhang, S.-X., Feng, H.-L.: Study on the Competitiveness of Xi'an Modern Service Industry Based on the industrial Structure. China Business & Trade 15, 3–4 (2011)
14. Han, Y.: Analysis of the Structure and the Competitiveness of Modern Service Industry in Shanxi Province. Science Technology and Industry 4, 7–10 (2012)
15. Zhou, J.-W., Tang, Y.-Z., Zhao, W.-Y.: An Empirical Analysis on the Competitiveness of Modern Service Industry in Pearl River Delta. Jiangsu Commercial Forum 7, 102–104 (2012)

Research of Regional Real Estate Early Warning Based on Spatial Regression

Jun Zhao, Qiqing Duan, and Zhifang Xi

School of Civil Engineering and Architecture, University of Jinan, Jinan250022, China
{Jun.Zhao,Qiqing.Duan,Zhifang.Xi,keled}@163.com

Abstract. It is important that spatial statistical analysis is used into forecasting trends of the real estate market. In this paper, we select 740 living areas in Jinan, Shandong Province for Hot-Spot analysis. Then we use Moran's I spatial autocorrelation analysis to determine spatial association for each cell. Finally spatial regression method is used to predict real estate trends in Jinan. The results present that the northwestern region show slow development, and the southeastern region show rapid development.

Keywords: real estate early warning, Hot-Spot analysis, Moran's I spatial autocorrelation, spatial regression.

1 Introduction

It is important that trends forecasting of the real estate market by spatial statistical analysis, which combine spatial data and statistical data. The spatial relationship about research objects of real estate early warning has been attracted gradually by people's attention. Through combining attribute data and spatial data, spatial regression can better explain spatial relationships of geographic things [1].

In 1970s, scholars have proposed some spatial econometric models. Then subsequently spatial econometrics in various research areas are gradually developed. Relevant results are: Spatial econometric analysis in geographic data [2]; Quantitative explore issues of spatial data sequences in spatial econometric analysis [3]; Spatial autocorrelation, spatial association, spatial statistical analysis and other methods are embedded into the GIS system and illustrates its application in regional economic analysis [4].

In this paper, we select 740 living areas in Jinan, Shandong Province for Hot-Spot analysis. Then we use Moran's I spatial autocorrelation analysis to determine spatial association for each cell. Finally spatial regression method is used to predict trends of the real estate market in Jinan.

2 Methods

2.1 Hot-Spot Analysis

Hot-Spot analysis is a kind of point pattern analysis [5]. We select 740 residential districts in central district of Jinan, and draw spatial distribution map as the basis of

F. Bian et al. (Eds.): GRMSE 2013, Part I, CCIS 398, pp. 80–87, 2013.
© Springer-Verlag Berlin Heidelberg 2013

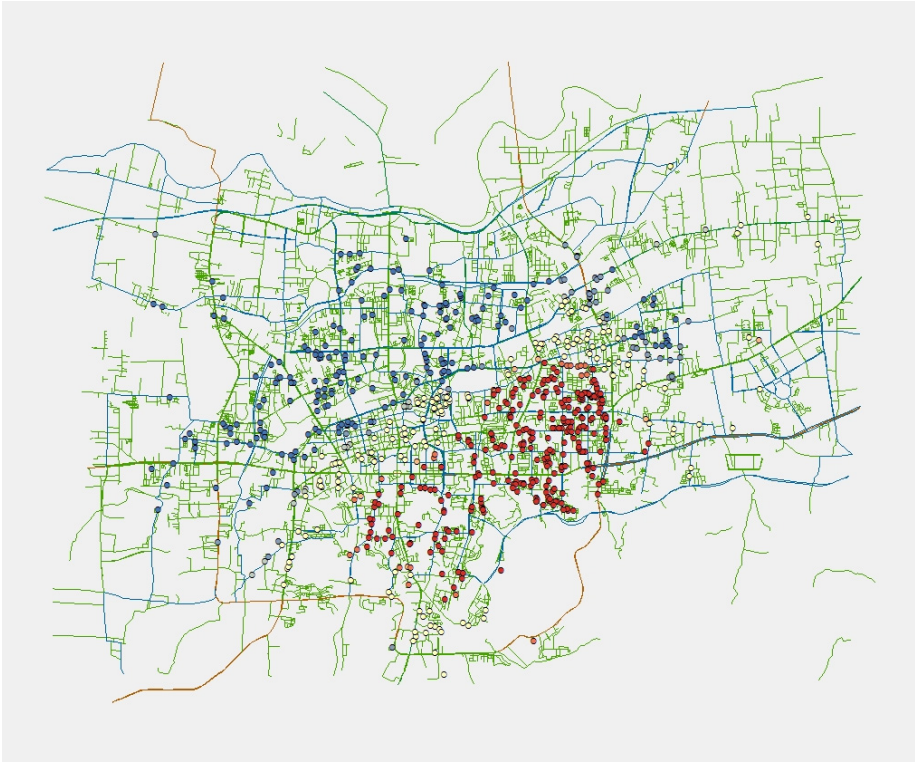

Fig. 1. Hot-Spot Analysis

spatial data sets. Then we process Hot-Spot analysis by using housing price of those districts, as shown in Figure 1.

Through Figure 1, we can see that housing price in Jinan is varies, since the geographic areas are affected by some factors such as economic, cultural, and quality of residents, etc. At the same time, it shows highly polymerized mode. Specifically, southeast region is higher price (red scatter). Central region is affordable (yellow scatter). Northwest and northern region is lower price (blue scatter).

2.2 Moran's I Spatial Autocorrelation

Moran's I spatial autocorrelation can measure the spatial correlation according both feature locations and feature values [6]. Given a set of elements and associated attributes in the case, the results of the assessment tools are clustering mode, discrete mode and random mode. Moran's I tool is used by calculating the index's value, Z-score and P-value to assess significant.

We process continuously on Moran's I spatial autocorrelation analysis, which used point elements of 740 districts . The results are shown in Figure 2.

We can see the results of point feature spatial autocorrelation is "Clustered". It indicate significant spatial autocorrelation. Table 1 and Table 2 give explanation that the point elements show significant spatial autocorrelation.

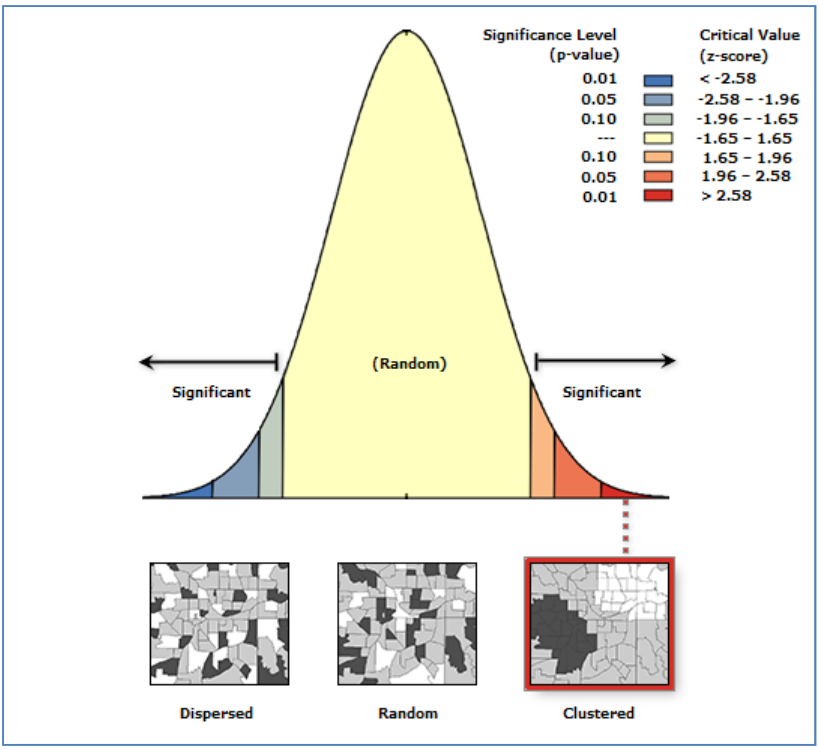

Fig. 2. Point Feature Spatial Autocorrelation

Table 1. Global Moran's I Summary

Statistics	Value
Moran's Index:	0.439919
Expected Index:	-0.034483
Variance:	0.014580
Z-score:	3.928914
P-value:	0.000085

Table 2. Dataset Information

Dataset Information	Methods
Input Feature Class	Warning Area_SpatialJoin
Input Field	AVERAGEPRICE
Conceptualization	CONTIGUITY_EDGES_ONLY
Distance Method	EUCLIDEAN
Row Standardization	True
Distance Threshold	None
Weights Matrix File	None

2.3 Spatial Regression Analysis

Through Hot-Spot analysis and spatial autocorrelation analysis, we find that the spatial distribution of point elements present regional differences. The results make possible for the spatial regression analysis in the regional real estate early warning.

The first step is to make the map pretreatment. The work map is drawn in ArcGIS desktop trial version. According to the second level road and the third level road we divide central area of Jinan into 30 warning areas, as shown in figure 3.

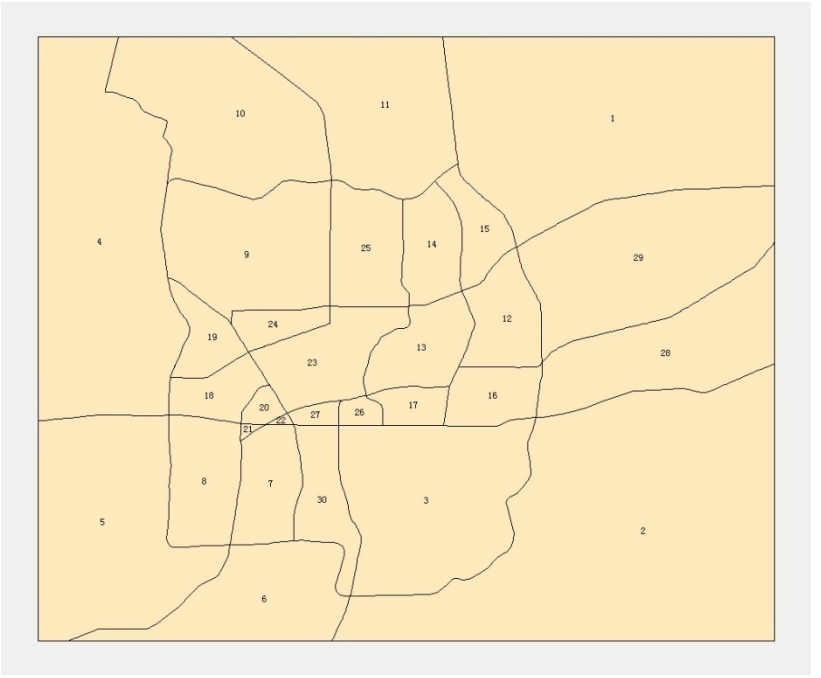

Fig. 3. Early Warning Area Division in Central of Jinan

Since differences of development levels on economic, cultural and traffic, figure 4 shows qualitative classification of the downtown, which should be a spatial visualization reference of spatial regression analysis model. Yellow color means more developed. Green color means developed .Blue color means underdeveloped.

The second step is to determine the dependent variable and the independent variables. Because housing price data of 740 living districts in warning area can reflect the current operation of the housing market, we collect the average price of the warning area by the end of 2010, obtain 30 housing price of warning area, which is average value in living area. Therefore the 30 housing price should be the dependent variable of spatial regression model.

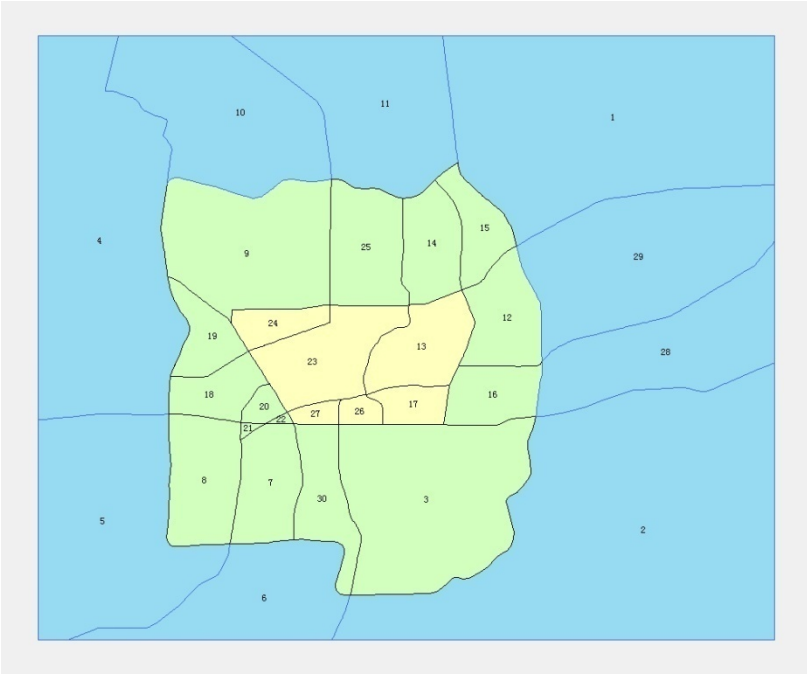

Fig. 4. Classification of Development Level

The independent variables are reflected mainly spatial relationship among warning area elements, as shown in Table 3.

Table 3. The Independent Variables of Spatial Regression Analysis

Independent variables	Fields
Number of living area	Join_Count
District category	IsCityCenter
Inverse Distance	InserseDistance
Area length	SHAPE_Lengh
Regional area	SHAPE_Area

Details are below.

(1) " Number of living area " uses the ArcGIS "Spatial Join" method to calculate the number of living area in each of warning areas ;

(2) "District category" is assigned by value. Value of yellow area is 3, which shows more developed. Value of green area is 2, which shows developed. Value of blue area is 1, which shows underdeveloped.

(3) "Inverse distance" is Euclidean distance between the center of Jinan and 30 warning area center (here we take the center of gravity).

(4) "Area length" and "Regional area" are used as a alternative argument. After preliminary analysis, we find that these two variables are no linear relationship for the dependent variable. They are redundant variables.

Therefore, the final independent variables involved in the spatial regression analysis are: Number of living area, District category, Inverse distance.

The third step, we use Ordinary Least-squares Regression(OLS), part of spatial regression models. The dependent variable is average price. Predicted results are shown in Figure 5.

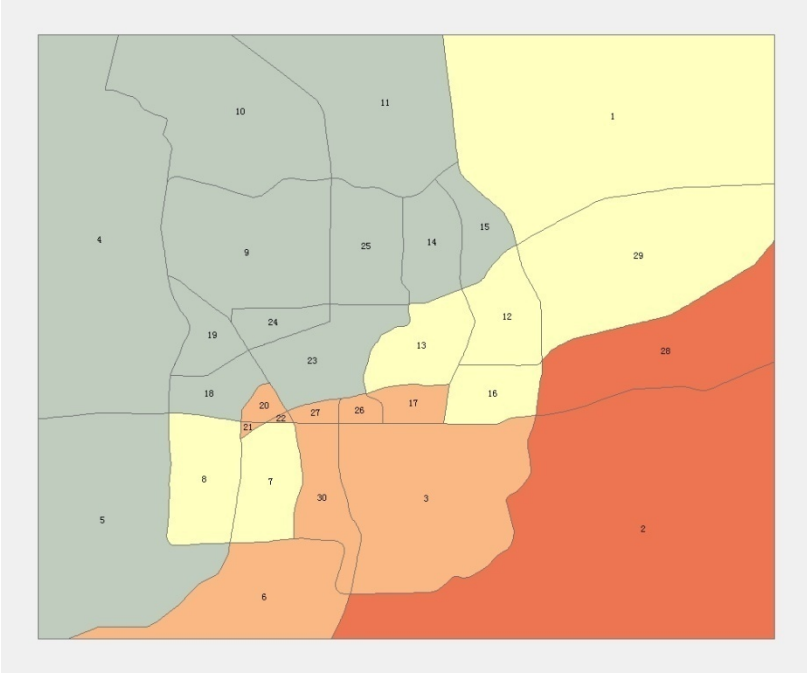

Fig. 5. Predicted Results

It can be seen that OLS model reflects clearly trends of housing market in warning area. The heatness of early warning forecast area meet the actual situation of Jinan. Northwest region(gray) is in the low price,which due to economic conditions. Southeast region(red) appears partial thermal phenomena.The prediction will provide guidance for government departments, developers, property owners, etc.

2.4 Evaluation

The evaluation of spatial regression analysis is shown in table 4.

Table 4. Evaluation of OLS Model

Content	Method	Value	Result	Reference value
Performance	Adjusted R2	0.08409	Poor	(0,1)
	AIC	504.333931		
Is independent variables are redundant	VIF	No	No redundant variables	>7.5
Significance	Joint Wald Statistic	0.028112*	Statistically significant	<0.05
Stability	Koenker (BP) Statistic	0.540405	Unstable	<0.05
Deviation	Jarque-Bera Statistic	0.280975	Biased	
Residual spatial autocorrelation	Moran's I	Randomly distributed		

3 Conclusion

Spatial regression is an extension of classical regression. The methods present visualization of the entire warning areas and surrounding areas ,which can predict trends of the real estate market. From table 4, we conclude that performance of the OLS model is poor. It does not well reflect the distribution and predict trends of warning area housing prices. Further analysis should be carried out in order to find some other indicators of regional real estate early warning.

Although the OLS model exists some problem of poor performance, we can see the following issues, which is compared between spatial regression analysis and traditional statistical regression analysis.

(1) Spatial regression analysis can provide graphical information of real estate early warning.

(2) Through comparing early warning data in different periods or different region, trend of regional economic activity can be presented visually.

(3) The method can analysis the spatial correlation of neighboring regions in warning area.

Acknowledgements. The work described in this paper is part of project supported by A Project of Shandong Province Higher Educational Science and Technology Program, China (Grant No.J10LE54 and No. J11LE01).It is also part of project supported by the Doctoral Fund for University of Jinan, Jinan , China (Grant No. XBS1222).

References

1. Liu, X., Huang, F., Wang, P., Tong, Z.: Principles and Methods of GIS Spatial Analysis. Science Press, Beijing (2006)
2. Bennett, R.J., Haining, R.P.: Spatial Structure and Spatial Interaction: Modeling Approaches to the Statistical Analysis of Geographical Data. The Royal Statistical Society. Series A (General) 148(1), 1–36 (1985)
3. Griffith, D.A.: Advance Spatial Statistics: Special Topics in the Exploration of Quantitative Spatial Data Series. Kluwer Academic Press, Dordrecht (1988)
4. Chen, F., Du, D.: Spatial Statistical Analysis and GIS in Regional Economic Analysis. Editorial Board of Geomatics and Information Science of Wuhan University (4), 391–396 (2002)
5. Illian, J.: Statistical Analysis and Modeling of Spatial Point Patterns. John Wiley & Sons, Ltd., England (2008)
6. Mao, R., Zhao, W.: Spatial Differences of Household Disposable Income and Consumption Expenditure in Sichuan Province. Journal of Southwest University for Nationalities (Humanities and Social Science) (06), 188–192 (2009)

Application of GIS and RS Techniques in Rapid Seismic Damage Prediction*

Yongmei Zhai[1] and Qianwen Ouyang[2]

[1] Shanghai Institute of Disaster Prevention and Relief,
Tongji University, Shanghai 200092, China
zymww@tongji.edu.cn
[2] Institute of Structural Engineering and DisasterReduction,
Tongji University, Shanghai 200092, China
91ouyangqianwen@tongji.edu.cn

Abstract. In order to achieve rapid large-scale seismic damage prediction, this paper studied on relevant application of high-resolution remote sensing (RS) and GIS. As this technique takes RS image as information source, investigation and improvement of existing attribute information extraction methods has been done to realize automatic extraction and precise intelligent interpretation. Moreover, software platform integration of RS and GIS is also accomplished by secondary development for seamless data transmission and further operation in GIS. Furthermore, structural vulnerability analysis method has been introduced to GIS system for calculating damage degrees of various structure forms. Thus, intuitionistic prediction results are obtained in GIS interface. In addition, this paper took a case study on a county of Henan province to verify its reliability.

Keywords: GIS, RS, Integration, Rapid Seismic Damage Prediction.

1 Introduction

Several seven-magnitude and above earthquakes occurred in China since the modern times, resulted in significant death toll and economic losses. Nowadays, rapid urbanization process causes aggregation both of population and property. Therefore, cities will suffer severer losses in earthquakes assuming no valid prevention measures.

Given the background that two-thirds of million population cities in China are confronted with a latent seismic threat of 7-intensity or above, there is a critical need to incorporate disaster prevention and reduction concept into urban planning.

Severity of seismic damage is influenced by major factors, including earthquake magnitude, focal depth, site condition, construction quality and disaster prevention facilities. When it comes to city, the immediate disaster cause is building collapse. For improving urban seismic capacity, backward buildings exposing to disproportionate high risks should be metabolized preferentially according to failure probability analysis. Such work has come to be known as seismic damage prediction. Realization

* Supported by National Natural Science Foundation of China (Project No:51178351).

F. Bian et al. (Eds.): GRMSE 2013, Part I, CCIS 398, pp. 88–94, 2013.
© Springer-Verlag Berlin Heidelberg 2013

of prediction depends on large-scale attribute information investigation. However, nowadays it is mainly implemented by manual work with a lack of effectiveness and accuracy due to the long execution period. Recently, as GIS and RS techniques develop, its time and economical efficiency become more prominent day by day—higher sampling frequency, larger map-sheet while the lower cost. Under this background, integration of RS and GIS techniques was studied for realizing rapid large-scale seismic damage prediction.

2 Methods of Building Seismic Damage Prediction

Building seismic damage prediction refers to destructiveness evaluation of a city or block in a certain seismic intensity. It is the basement of disaster reduction planning, especially in the earthquake-prone area. At present, methods of seismic damage prediction can be sorted into empirical method, theoretical method and semi-empirical theory. Domestic relevant search dated from 1980s, and made great achievements. On the basis of previous researches, Zhiqian Yin[1] put forward a kind of semi-empirical theory for damage estimation. This method summarized all previous large earthquakes' statistics and provided efficient solution for various structure forms. By introducing earthquake damage matrix concept, it couples each structure form with its failure probability in earthquake of assumed intensity. Realization of large-scale prediction by above method requires for accurate building attribute information and powerful data processing ability. Therefore, this paper adopted semi-empirical theory to do the research and discussed the application of GIS and RS techniques.

3 Attribute Information Extraction

Building attribute information, including plane and height data, can be expressed and identified in RS image. As a kind of data medium, RS owns remarkable advantages on time and economical efficiency. Recent years, domestic and foreign scholars have made many researches on RS information extraction. However, most existing methods rely on manual intervention to some extent[2]. Therefore, there are difficulties to achieve large-scale automatic operation by traditional methods. On this basis, some improvements are embodied in the study.

In this paper, object oriented multi-scale segmentation is adopted to extract plane information. This method is first put forward by Baatz[3]. It takes geometric, texture and spectral features into comprehensive consideration by setting thresholds and rules, so as to extract ground objects accurately. Image-processing software ENVI is an open platform equipped with rule classification function. By secondary development of IDL/ENVI, a rule function has been done to invoke the batch processing module for intelligent interpretation.

In aspect of height information extraction, the typical method[4] is to calculate building height data from corresponding shadow length. Tiezheng Li[5] has put forward a practical method. It realized automatic extraction by rotating RS image and searching for effective line segment. Its principle is scanning rotated image column by

column to simulate manual operation. This method requires only a scrap of intervention while provides precise results. However, its execution based on cooperation between ENVI and MATLAB, calls for manipulator's programming ability. Therefore, secondary development of IDL/ENVI has been done to improve it.

For computing building area, there is another problem, attribute matching of massive data, to be solved. For the identical image, ENVI matches shadow data with plane data automatically to meet adjacent relation[6]. Even so, the raw results require further correction. Therefore, a program for judging matching accuracy has been developed by IDL language. Uncorrelated information can be distinguished and rejected by this program so as to meet the requirement of GIS model reconstruction. Specific algorithm is shown below:

Calculate area and areal coordinate Z0(xi ,yi)of each object from extracted building plane information.

Set the point Z0(xi,yi) as origin, scan pixels from bottom to top. Record the upper boundary point Z1(xi,yi-d) and lower boundary point Z2(xi,yi-t). If there do not exist Z2, then regard Z2 as the upper frontier point.

If t-d<s, s is predetermined threshold value, then judge plane data to be match with story number calculated from shadow data. Otherwise, judge the plane data to be interference information.

4 Integrated Platform of RS and GIS

Obtained attribute information lays foundation of building seismic prediction. While its realization still requires further data processing, including classification, statistics and matrix manipulation. This complex procedure is supported by powerful spatial data processing ability of GIS[7]. However, as GIS and RS have different data formats, there are several key problems like format transformation, geometric correction and attribute transfer to be solved.

ENVI and ArcGIS are mainstream application software of RS and GIS. Several image processing modules of ENVI4.8 can be integrated seamlessly in ArcToolbox of ArcGIS 9.3 or later versions. For those reasons, this paper adopted development approach of software platform integration. Developed ENVI module was embedded into GIS through scripting language. By invoking Python Script, 3D model construction and prediction visualization can be achieved in GIS interface.

5 Case Study on RS/GIS Application

This paper took a case study on a county of Henan province, whose gross area accounting for 1393 Square Mile. South district of the county is old town, while the west is new city zone. Main structure form of existing buildings is multi-story brick-concrete, the rest contains single story workshop, reinforced concrete high-rise and civil house. Experimental area was divided into seven prediction units according to structure form and distribution, as Fig.1 shown below.

Fig. 1. Block plan of experimental area

5.1 Precision Analysis of Attribute Information Extraction

Taking real-time remote sensing image of the experimental area as information source, the integrated program automatically identified edge and shadow of urban buildings as demonstrated before. Extracted vector data was converted and transmitted into raster attribute information, including gross area and height. In order to verify accuracy of this program, 12 buildings were selected randomly. Comparison of program intelligent interpretation results and accurate attribute data provided by Planning Bureau are tabled as below.

It can be perceived that extraction accuracy of plane area is high, only 1 of these 12 buildings' relative error exceeds 10%; in aspect of height information, 2 buildings' story number has error that not exceeds 1. Overall, extraction results of brick-concrete structures are precise while civil houses' are relatively imprecise. Extraction error of old civil buildings is mainly caused by misreading slope roof eaves. Moreover, roofs of some civil houses are charcoal grey, its gray value are too similar with adjacent shadow to be distinguished. For height data extraction, errors are mainly caused by vertical irregularity of buildings, as overlapping shadow interferes accurate judgment easily. Therefore, height data extraction method needs further improvement. Nevertheless, for accomplishing seismic damage prediction, the extraction error is totally acceptable.

According to on-site survey, buildings of the experimental area can be sorted into 5 types: brick-concrete, reinforced concrete, civil house, single story workshop, and old civil house. In order to associate story number with building height, set story height of civil, communal, and industrial building to 3.0m, 3.6m, and 4.5m respectively. Moreover, structure form can be judged through comprehensive consideration of plane edge, story number and spectral features. Divisional area statistics of each structure form are verified to be satisfactory. Thus attribute assignment is done for matrix manipulation.

Table 1. Correlation table of intelligent interpretation results and accurate data

No.	Calculation area(m^2)	Actual area(m^2)	Area relative error (%)	Calculation story number	Actual story number
1	957.48	870.84	9.94	6	6
2	836.32	761.27	9.85	6	6
3	1540.65	1380.4	11.6	6	6
4	942.66	872.41	8.03	6	6
5	676.06	651.46	3.78	6	6
6	1322.07	1273.15	3.85	2	2
7	1022.64	949.44	7.65	2	2
8	269.72	251.46	7.17	5	5
9	694.63	646.49	7.43	5	6
10	860.54	799.33	7.66	3	3
11	243.42	265.34	8.26	5	5
12	354.84	374.33	5.48	5	6

5.2 Damage Index Calculation

As mentioned above, earthquake damage matrix method is adopted for probability analysis. Matrixes of the experimental area derived from field sampling survey results and structure vulnerability theory. The aim of introducing damage matrix is to compute damage index which refers to damage degree of structures or components subjected to earthquake. Damage index is a dimensionless value ranging from 0 to 1, and the greater the value, the severer the seismic damage. It is widely used as building damage state characterization method.

Calculation formula of seismic damage is shown as below:

$$D_z = \sum D_j \times P_j \tag{1}$$

Where D_Z is building damage index of one structure form under a certain seismic intensity; Dj is damage index of j-grade under a certain seismic intensity; Pj is j-grade damage probability of one structure form under a certain intensity, can be referred to corresponding damage matrix. Matrix manipulation of damage index is mainly accomplished by means of GIS attribute field function.

Table 2. Damage degree classification and corresponding damage index

Damage degree	Basically intact	Slightly damaged	Moderately damaged	Seriously damaged	Collapse
Damage index	0.00~0.10	0.10~0.30	0.30~0.55	0.55~0.85	0.85~1.00

5.3 Three-Dimensional Visualization of Damage Prediction

As fortification intensity of the experimental zone is 7-intensity, select 7 and 8-intensity for damage prediction. According to calculation results of damage index,

corresponding damage degree can be obtained and transmitted to GIS attribute list. By invoking ArcScene software, three-dimensional damage prediction graph can be done in GIS interface. Graphs of 7 and 8-intensity are shown as below, colors reflect distinct damage degree.

It can be seen, under 7-intensity, that is, fortification intensity, multi-story reinforced concrete structures are basically in state of intact, workshop and brick-concrete is slightly damaged, while civil house is moderately damaged. When the intensity is 8, reinforced concrete structures are slightly damaged, old civil houses present seriously damaged. The rest newly-built civil houses, workshops and brick-concrete structures are moderately damaged. Intuitionistic prediction results provide a significant convenience for executing earthquake disaster plans.

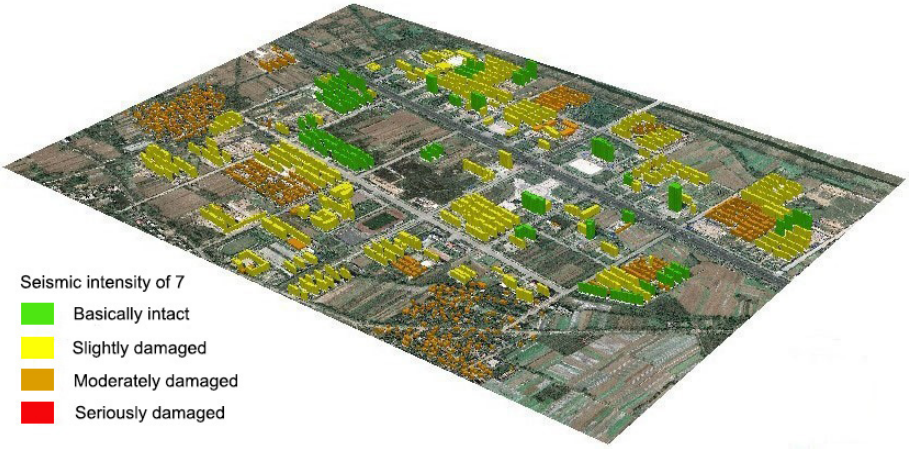

Fig. 2. Three-dimensional seismic damage prediction graph of 7-intensity

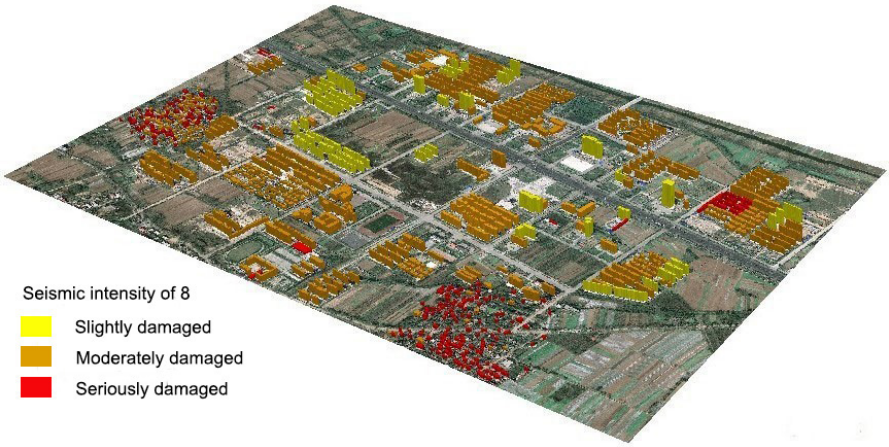

Fig. 3. Three-dimensional seismic damage prediction graph of 8-intensity

6 Conclusion

With the view to requirement of achieving rapid large-scale seismic damage prediction, this paper studied on relevant application of RS and GIS techniques. Taking real-time RS images as information source, automatic extraction and intelligent interpretation are realized by IDL/ENVI secondary development. And the results are verified to be coincident with on-site survey. Software platform integration of RS and GIS is also done for seamlessly transmitting obtained vector data. Combined with structural vulnerability analysis theory and matrix manipulation, attribute information is converted into damage index to indicate damage degree. Three-dimensional seismic damage prediction graph is finally gained in GIS interface, while supporting further interactive operation.

This processing system is definitely an interdisciplinary subject involves RS, GIS, and structural seismic analysis. However, its operation requires only a spot of manual intervention and specialized knowledge. Large-scale seismic damage prediction contributes to rational strategic decisions in earthquake-prone area to seismic disaster prevention and reduction, has remarkable theoretical and practical significance.

References

1. Yin, Z., Li, S., Yang, S., Zhao, Z.: Estimating Method of Seismic Damage and Seismic Loss. Journal of Earthquake Engineering and Engineering Vibration 1, 99–108 (1990)
2. Colwell, N.R.: History and place of photographic interpretation. Bethesda. Manual of Photographic Interpretation 33, 33–48 (1997)
3. Baatz, M., Schepe, A.: Multi resolution Segmentation: an Optimization approach for high quality multi-scale image segmentation. In: Strobl, J., Blaschke, T. (eds.) Angewandte Geogr. Information sverarbeitung XII, pp. 12–23. Wichmann, Heidelberg (2000)
4. Cheng, F., Thiel, K.H.: Delimiting the building heights in a city from the shadow in panchroma-Tic Spot-Image-Pare 1-Test of Forth Two Buildings. Int. J. Remote Sensing 16(3), 405–415 (1995)
5. Li, T., Zhai, Y.: Study on ExtractionMethod ofUrban Buildings Attributes Information in Earthquake Damage Prediction. Journal of Catastrophology 25, 300–304 (2010)
6. Kim, T., Vision, J., Muller, P.: Development of a graph-based approach for building detection. Image Vision Computing 17, 3–14 (1999)
7. Ehlers, M.: Remote Sensing And Geographic Information Systems: Towards Integrated Spatial Information Processing. IEEE Transactions on Geoscience and Remote Sensing 28, 763–763 (1990)

Research on Digital Campus Landscape Modeling of East China Jiaotong University*

Cuiyu Sun[1], Feihu Ma[1], and Ning Lei[2]

[1] School of Civil Engineering and Architecture Departments,
East China Jiaotong University, Nanchang, 330013, China
[2] The First Institute of Oceanography of State Oceanic Administration,
Qingdao, 266061, China

Abstract. In this paper we chose East China Jiaotong University as a case to study the digital campus 3D landscape modeling technology. Using the GIS and virtual reality technology and the Google SketchUp, we build 3D digital campus landscape model and design attributes database. This study laid the foundation for further research of the East Jiaotong University digital campus.

Keywords: Digital campus, 3D modeling, Google SketchUp.

1 Introduction

Virtual reality is a new developed field of computer technology, with integrated computer graphics technology, multimedia technology, sensor technology, human-computer interaction technology, network technology, stereo vision technology, simulation technology and other technologies [1-3]. Digital Campus is an important application of virtual reality technology to enable the school's topography and the real landscape reproduced in the computer. Digital Campus can build a vivid real campus environment to provide real intuitive experience to the users [4-5]. Integrated with the attributes database, the system can satisfy real-time interactive queries for a variety of related information. So for the users who want to know the campus environment or to plot the campus planning, this is more convenient and intuitive.

East China Jiaotong University covers an area of nearly 3,000 acres and construction area is about 70 million square meters. As one of "The national sector afforestation 300 good units", the university lies near the great river and fills with hills and lake in the yard. Yet the construction of digital campus has not undertaken. In the geomatics undergraduate practical teaching project we completed the main building landscape modeling and attributes database design for the Southern District of the campus. This has laid a foundation for the future work.

* Surported by the provincial teaching reform project of the colleges and universities in Jiangxi province (JXJG-10-5-32).

F. Bian et al. (Eds.): GRMSE 2013, Part I, CCIS 398, pp. 95–99, 2013.
© Springer-Verlag Berlin Heidelberg 2013

2 Data Preparation

We apply the Google SketchUp software to build 3D models. For attribute data table, we chose the Microsoft Office Access. The interactive query application program is designed under SkyLine Series software. In the process, the data related includes:

- Geomorphological data: precision DEM of the campus from photogrammetry course, as the basis of terrain
- The primary building data: building data from digital mapping course, to model the campus building and major roads, as well as the relevant information: number of floors, story height, the appearance texture images, road type…
- Other surface features data: vegetation types, street lightings, signage and other related surface features' shape information
- Attribute data: all related attribute data information, in order to design and build the property database

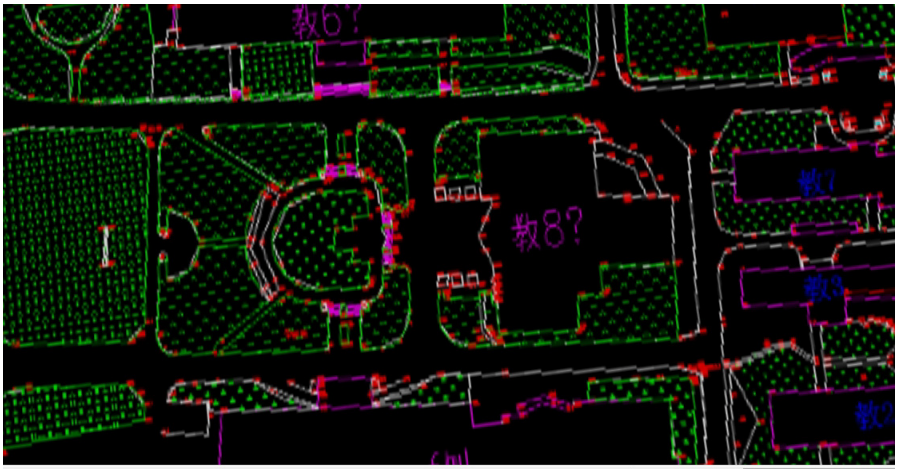

Fig. 1. CAD data for southern campus

3 Construction of 3d Model

By analyzing the data, the DEM data of the campus shows the area covers only near Maan mountain with low accuracy. So in this stage we conduct modeling without any terrain information, only build a three-dimensional landscape models.

Digital Mapping teaching focused on the Southern District of campus, we generate the map of the primary buildings and roads in CAD.

For teaching buildings, office buildings, dormitories and faculty apartments, they have simple structure and regular shape. So the modeling of these buildings, we import CAD data directly into Google SketchUp using polygonal modeling techniques to finish three-dimensional model. We add photos to the buildings as their texture to make it more real in appearance.

For those buildings have more complex structure, such as libraries, cafeterias and some office buildings, we divide the building into many simple blocks. We work on

the model in various details for each part using CAD base map and the photos. Finally we put together the blocks to complete the model. Also the textures are blocks too in order to achieve a very realistic effect. Figure 2 shows two schematic maps of the modeling, parts of the model texture has been attached in figure b.

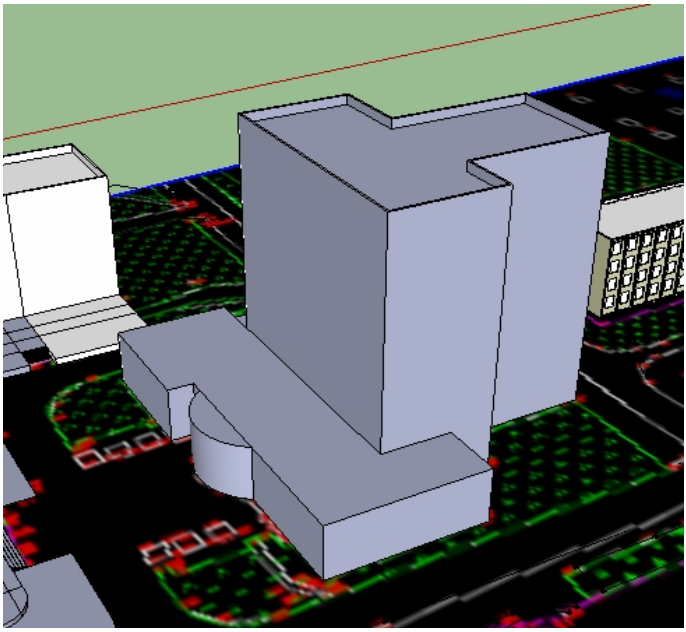

a

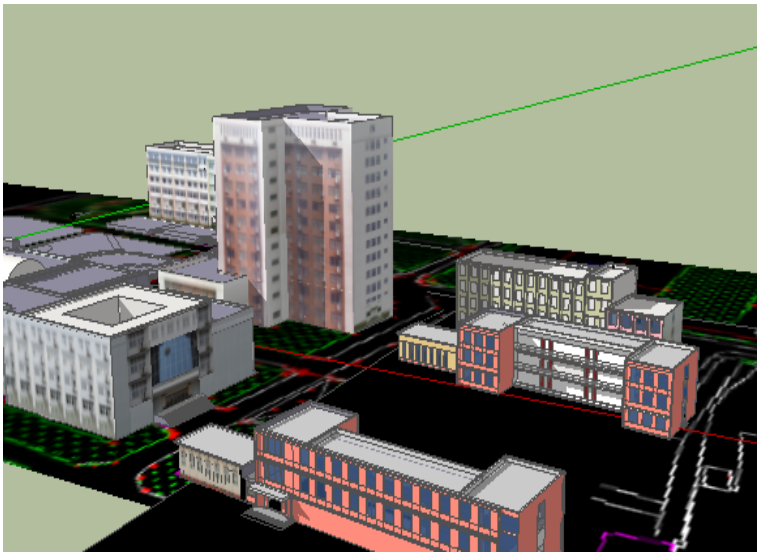

b

Fig. 2. The schematic map of buildings modeling process

The main roads in campus are concrete pavement and some roads using bricks. We select appropriate textures to achieve a campus corridor modeling according to the southern district plans. For the campus greening and street lamps feature, we can simply select the appropriate model in the model library. If there are some features are not match in the library, we can use cross face texture mapping method or Billboard polygons to ensure the scene are vivid. Figure 2 shows southern district campus landscape modeling.

Fig. 3. Southern campus teaching area modeling renderings

4 Attribute Database Structure Design and Implementation

We gather attribute information of important features such as name, category, and other information. After analyzing we design the main attribute table following the database principles and query requirements for the digital campus. The buildings have eight basic tables and the roads have two tables. Table 1 is part of the basic table of teaching buildings.During the design process the fine three-dimensional model of functional requirements are fully considered. Microsoft Office Access database is applied to build the database, some of the attribute data have been input. There are a great deal of attribute data to be collected and edited.

Table 1. Basic table of teaching buildings

ID	Name	Type	Length	constraint
1	tbName	C	16	
2	tbMumber	N	8	primary key
3	fNumber	C	8	
4	tbDepartment	C	50	foreign key
5	claNumber	N	2	
6	tbAdmin	C	20	
7	claQuan	N	8	
8	claMulti	C	2	
……	……	……	……	

5 Conclusion

Digital Campus is a three-dimensional interactive large-scale system involving a wide range of integrated technologies such as computer technology, virtual reality technology, graphics technology, GIS and databases. In this study, based on SketchUp, Access and other software we built south part of East China Jiaotong University main campus 3D landscape models using geomatics teaching achievements and design its attribute database. Subsequent work includes the refinement of existing models importing topographic data, building a complete property database and three-dimensional digital campus interactive query and analysis system based on SkyLine Series.

References

1. Wei, Y.: Design and Implementation of an Interactive Virtual Campus Roaming System Based on VRML. Jilin University, Changchun (2011)
2. Qiu, P.: Application of Google SketchUp and IMAGIS in campus three-dimensional visualization. Engineering of Surveying and Mapping 17(2), 58–61 (2008)
3. Jiang, D., Guo, D., Luo, N., et al.: Planning and Practice of New Generation Digital Campus in Tsinghua University. Journal of Xiamen University (Natural Science) 46(z2), 173–178 (2007)
4. Sun, Y., Ding, N., Wang, Q.: The research of digital campus based on 2D and 3D interactive system. Journal of Shandong Jianzhu University 24(4), 377–380 (2009)
5. Yu, Z., Hu, S.: Digtal Campus Construction of New Campus of Henan Polytechnic University. Geomatics & Spatial Information Technology 29(2), 99–102 (2006)
6. Li, F., Xiao, H., Yang, B., et al.: Design and Implementation of 3D Digital Campus. System Simulation Technology 6(1), 71–75 (2010)

Urban Green Space Landscape Pattern Evaluation Based on High Spatial Resolution Images

Xiang-wei Gao[1], Zhi-guo Zhang[2,*], and Xian-yun Fei[1]

[1] School of Geodesy & Geomatics Engineering, HuaiHai Institute of Technology, Lianyungang China 222005
[2] School of Ecology Technology and Engineering, Shanghai Institute of Technology, Shanghai, 200235
zgzhang@sit.edu.cn

Abstract. Quantity indexes can not describe green space spatial location. Landscape construction can describe the spatial location by various metrics. Two kinds of indexes reflected the quality of urban green space from different aspects, so they are important indexes for urban green space quality evaluation. In this paper, the urban green space information of Pingyi and Linsu county in Linyi city of Shandong province was obtained using SPOT5 images. Based on the information, two kinds of indexes were calculated, and the quality of urban green space was studied. The result showed that three basic quantity indexes were similar and both had no predominance. From landscape metrics, apart from public park and other green space, the green space landscape construction and function in Pingyi county was poorer than in Linsu county, though they had similar green space quantity index value.

Keywords: Urban green space, quality evaluation, SPOT5 images, quantity indexes, landscape metrics.

1 Introduction

The eco-efficiency of urban green space is not only related with urban green quantity, but also closely related with spatial construction [1]. So both the quantity and spatial construction are important indicative indexes of the quality of urban green space. Quantity indexes, including ratio of green space, percentage of greenery coverage, per capita park green space area, indicate total area quantity of urban green space. Landscape patterns could be quantified by various landscape metrics, such as patch area, patch density, edge density, component position, diversity index and evenness index et al[2],[3],[4],[5],[6],[7],[8],[9]. Using RS and GIS technology, the landscape metrics could be calculated rapidly. In this study, two counties, Pingyi and Linsu of Linyi city in Shandong province, were selected as the study areas. Using SPOT5 images, three basic quantity indexes, including ratio of green space, percentage of

* Corresponding author.

F. Bian et al. (Eds.): GRMSE 2013, Part I, CCIS 398, pp. 100–106, 2013.
© Springer-Verlag Berlin Heidelberg 2013

greenery coverage, per capita park green space area, were obtained. In the same time, the landscape metrics of urban green space were calculated in the two county regions. Using these indexes, the quality of urban green space would be evaluated from quantity and spatial construction. Based on the indexes, the quality of urban green space between the two areas was compared.

2 Study Area and Data

In this study, two counties, Pingyi and Linsu of Linyi city in Shandong province, were selected as the study areas. For the two counties, the geography location is adjacent and the urban area and population quantity is close. Because of the poor economic, the greening state is not good. Now the county governments have recognized the importance of greening for urban development and made plans to increase investment in the construction of urban greening. It would be help for the urban green space rational development to correctly evaluate the quality using RS and GIS.

SPOT5 multi-spectral and pan images were used to obtain the urban green space information. Images of Pingyin were taken in October 26, 2004, and Linsu were taken in October 15, 2008. All images have good quality and were Orthorectified by second Polynomial. Pan and multi-spectral images were merged by PCA method. Other data included 1:10000 scale topographic map and urban limit those were provided by Urban Construction Bureaus.

3 Study Methods

3.1 Three Basic Quantity Indexes Obtaining

In the year of 2000, national garden and park urban standard was published by ministry of housing and urban-rural development of the people's republic of China (MOHURD). Among the many evaluation indexes, three basic quantity indexes are most important. The three basic quantities indexed are calculated as follow [1], [10]:

(1) ratio of green space is the percentage of total green area (including public park, productive plantation area, green buffer, attached green space, residential green space, green space attached to urban road and square) accounting for urban area.

(2) percentage of greenery coverage is the ration of the all plants vertical projection area, including arbor, shrub and lawn, accounting for urban area.

(3) per capita park green space area is the average park area quantity of each urban resident possessing.

Using spot5 images, the information of each urban green space type was obtained by visual interpretation according to national garden and park urban standard. Based on the interpretation, the digital urban green space location maps of the two counties were plotted. The supervised classification method, maximum likelihood, was used to

get the green coverage information. Based on above information, three basic quantity indexes including ratio of green space, percentage of greenery coverage, per capita park green space area were calculated.

3.2 Landscape Metrics

Using RS and GIS technology, the landscape structure could be quantified by a series of metrics from three levels of patch, class and landscape, including diversity index, area/density/perimeter, and shape indices. The landscape metrics used in this study was showed as table 1.

4 Result Analysis

4.1 Three Basic Index Calculation Result

Using the digital urban green space location maps, the three basic indexes were calculated, and the result was shown as table 2. according to garden and park urban standard of Shandong province, for a county level urban, the ratio of green space should be more than 28%, the percentage of greenery coverage more than 33%, and per capita park green space area more than 7m^2/person. So according to three basic indexes calculation result, the quantity of two counties green space met the requirement of garden and park urban standard of Shandong province. The green space quantity indexes value was similar, and no county had obvious dominance.

4.2 The Landscape Metric Calculation Result

(1) Landscape diversity analysis
Showed as table 3, in Pingyi, Landscape diversity index was 1.34, the maximum dominance index was 0.66, and evenness index was 0.67. In Linsu, three Landscape index were 1.50, 0.50, and 0.75 respectively. The calculation result showed that location of various green space types in Linsu was even, and there was dominant green space type. But in Pinyi, the green space types were not even. By analyzing the quantity of each green type, it was could be showed that the residential green space had obvious dominance.

(2) landscape fractural dimension index analysis
The Landscape fractural dimension index indicates urban green space ecology function. High landscape fractural dimension index value means poor ecology function. Showed as table 3, the landscape patch density value was 71.99 and45.43 respectively in Pingyi and Linsu. The index value showed that the fragmentation in Pingyi was obvious higher than in Linsu. In Pinyi, the residential green space around urban village houses was in dominant position among all green space types. These residential green spaces were various trees growing randomly, in trial patches, and forming the higher landscape fragmentation.

Table 1. The landscape metrics used in study

Landscape metrics	Formula	Indication
Mean patch area	$MPS_i = A_i / n_i$	Indication of fragmentation and heterogeneity of a certain forest landscape type
Carrier density	$C_j = \frac{L_i}{A_j}$	Carrier density means green space length in unit area. Bigger density value means good connectivity and fine landscape construction.
Minimum distance	$N_{\min} = \frac{N_{mean}}{N_{\exp}}$	Minimum distance index means the minimum distance between landscape patches and to indicate if the landscape patch is subject to random location.
Fractural Dimension	$S = 2\ln(L_i/4)/\ln A_i$	Indication of patch shape complexity, with value from 1 to 2. S approaching to 1 means simple shape and more disturbances.
Isolation	$F = (n/A)^{0.5}/2(A_i/A)$	Indication of the spatial location isolation of all elements in a certain landscape type. Bigger value means more location deviation in the region.
Diversity	$H = -\sum_{i=1}^{n}(P_i \log_2(P_i))$	Quantifying the landscape types and the proposition difference of various types. Equal proposition of each type means highest value of diversity for landscape constructed of more than two types. When the proposition of every types increase, the diversity value will rise.
dominance	$D = \log_2 n - H$	Corresponding to diversity index Bigger value means more difference of every types and smaller value means proximity proposition. When the value becomes zero, the landscape type proposition equal.
evenness	$E = \frac{H}{H_{\max}} \times 100\%$	Evenness means the distribution uniformity of different landscape type and the value is between 0 and 1. Value approaching to 0 means extremely uneven, and approaching to 1 means extremely even.

Note: A_i representing the total area of a certain landscape type i; a_{ij} representing each patch area of a certain landscape type i, L_i representing the total perimeter of a certain landscape type i; N_i representing the minimum distance between the patch and its neighbor patches; C_i representing patch density of a certain landscape type i; n_i representing the patch number of a certain landscape type i; A representing total area of all landscape patch in study area; P_i representing proportion of one certain landscape type in entire study area; n representing the number of all the landscape types in study area.

Table 2. Urban green space index of Pingyi and Linsu

Green space indexes	Pingyi county	Linsu county
Urban area (m2)	18841125	16497800
Urban population (person)	195600	118900
ratio of green space	29.48%	28.00%
the percentage of greenery coverage	33.65%	34.48%
per capita park green space area (m2/person)	7.06	7.00

Table 3. Urban green space landscape diversity index

Landscape index	Pinyi county	Linsu county
Diversity index	1.34	1.50
Maximum diversity index	2	2
Maximum dominance index	0.66	0.50
Evenness index	0.67	0.75

Table 4. Urban green space landscape patch density index

Landscape type	Pinyi county	Linsu county
public park	20.28	10.89
productive plantation area	33.92	25.35
attached green space	202.84	109.64
green buffer	28.24	26.22
green space attached to urban road and square	30.93	35.73
Average	71.99	45.403

(3) road green space Landscape corridors density analysis

The corridor can separate landscape different parts the one hand, on the other hand it connect other parts together. Corridor not only has ecology function, but also has Recreational and economy function. Showed as table 5, the corridor density index was 2.37 that were lower than 6.56 in Linsu. Contrast to corridor of Pinggyi, the corridor has better connection and function.

Table 5. Urban green space landscape corridor density index

landscape type	Pingyi County	Linsu county
road green space	2.37	6.56

(4) landscape Minimum distance index of public park analysis

Showed as table 6, the public parks tended to be reunion distribution and the reunion was more obvious in Linsu. This index value showed that the location was concentrated in two counties and the park service blind spot was serious. The

distribution of productive plantation area was regular. The distribution of attached green space inPingyiwas random, but in Linsu was regular. The other green space in two counties tended to be random.

Table 6. Landscape Minimum distance index

Landscape type	Pingyi County	Linsu county
Public park	0. 32	0.14
productive plantation area	1.14	1. 35
attached green space	0.82	0.70
other green space	0.78	0.72

(5) Landscape dimensions index analysis

Showed as table 7, the Landscape dimensions index value was higher in Pingyi County, and the result indicated the complex shape of landscape patch in Pingyi County. By comparing the landscape dimension value of different green space type, the attached green space owned highest value. The second was other green space and the lowest value was public park.

Table 7. Urban green space Landscape dimensions

Public park	Pingyi County	Linsu county
productive plantation area	1.29	1.27
attached green space	1.34	1.32
other green space	1.45	1.43
Public park	1.32	1. 29

Only from the quantity of the green space, the index value was similar. But if evaluating from landscape construction, the quality had obvious difference in two counties, though having similar characteristics in some respect. One similarity in two counties was that the public park in two counties tended to be reunion distribution and the location was concentrated, so the park service blind spot was serious. Another similarity was that the other green space tended to be regular location and had no obvious difference in landscape construction. The difference was including: 1) the residential green space in Pingyi county had obvious dominance, but in Linsu county, the various green space types located uniformly and had no dominantly type. 2) the fragmentation of various green space in Pingyi county was obvious higher than in Linsu. Higher fragmentation would lead to simple landscape function. 3) the corridor density index in Pingyi county was lower than in Linsu county and its corridor of road green space had poor connection and function. So, apart from public park and other green space, the green space landscape construction and function in Pingyi county was poorer than in Linsu county, though they had similar green space quantity index value.

Acknowledgment. Sponsored by: 1) the National Natural Science Foundation of China (31070626, Urban green space location grid evaluation model based on high spatial RS image); 2) Jiangsu Provincial Bureau of Surveying and mapping scientific research project (JSCHKY201212); 3) The peak of six personnel in Jiangsu Province (2012) Email: gaoxw2008@126.com Corresponding author :ZHANG Zhi-guo.

References

1. Ministry of Construction. Urban construction, number 106, national park urban standard (2000)
2. Xiao, R.-B., Zhou, Z.-X., Wang, P.-C., et al.: Landscape pattern analysis and comprehensive assessment of greenbelt in Wuhan steel & iron industrial district. Acta Ecologica Sinica 24(9), 1924–1930 (2004)
3. Li, S., Geng, X., Wang, F.: The Spatial Connectivity and Distribution Regularity of the Landscape Types in Maoershan Forest Farm in Heilongjiang Province. Journal of Northeast Forestry University 30(2), 49–51 (2002)
4. Gang, Z.T., Hao, C.Y., Zhi, G.D., et al.: Fuzzy Comprehensive Method and its Application in Landscape Ecological Comprehensive Assessment of Urban Greenland System–Taking Shanghai as an Exmple. Urban Environment & Urban Ecology 12(4), 23–25 (1999)
5. Liu, P., Li, Y.-Y.: Evaluation on Greenland Landscape Based on RS and GIS in Urumqi. Journal of South China Agricultural University 28(4), 56–59 (2007)
6. Zhou, L., Zhang, Z., Wu, L., et al.: Landscape Pattern Gradient Analysis of Green Space Along the Extended Directions of Urbanization in Beijing. Forest Resources Management (5), 47–52 (2006)
7. Xiao, R.-B., Zhou, Z.-X., Wang, P.-C., et al.: Landscape pattern analysis and comprehensive assessment of greenbelt in Wuhan steel & iron industrial district. Acta Ecologica Sinica 24(9), 1924–1930 (2004)
8. Gao, J., Yang, M., Tao, K.: Analyse the pattern of urban greenary features in Shanghai. Journal of Chinese Landscape Architecture (1), 53–56 (2000)
9. Zhou, T.-G., Guo, D.-Z.: GIS-based study on spatial structure of urban greenbelt landscapes: Taking Ningbo City as an example. Acta Ecologica Sinica 23(5), 901–907 (2003)
10. Wei, B., Wang, J., Zhang, T.: Improvement of Assessment Methods for Ecological Effect of Urban Greenland. Urban Environment & Urban Ecology 10(4), 54–56 (1997)

Virtual Reality in Smart City

Chao Peng, Xicheng Tan, Meng Gao, and Yayu Yao

International School of Software,
Wuhan University, Wuhan Hubei, China
mikejay0520@163.com,
xichengtan@gmail.com

Abstract. Based on the current cutting-edge technologies, smart city becomes more and more popular in China. Briefly, smart city can provide various services for every citizens and outlanders in a lot of fields, such as tourism, transportation, management and so on. Since smart city contains so many contents, we just focus on one side of it ------ visualization. Through the help of virtual reality, the visualization can reach a new level compared to the historical systems, which just utilized common visual display devices; in the new systems, not only eyes, but also ears, hands and even nose can feel the existence of the whole city. In this paper, we'd like to put forward some opinions on the combination of virtual reality and smart city. A detail design of virtual reality framework is put forward in third section. In section four, an actual project follows the blueprint is raised up for practical discussion.

Keywords: smart city, virtual reality, visualization, interactivity.

1 Introduction

In November 2008, IBM's Chairman, CEO and President Sam Palmisano, during a speech at the Council on Foreign Relations, outlined a new agenda for building a "Smart Planet". Palmisano emphasized how the world's systems and industries are becoming more instrumented, interconnected and intelligent, and that leaders and citizens can take advantage of this state of affairs to improve current living situations.

In January 2010, Sam Palmisano gave a follow-up speech to the Chatham house called the "Decade of Smart". He highlighted dozens of initiatives in which the leaders from various fields invented smarter systems to solve the most challenging problems worldwide. 1

According to the above two speeches, the main purpose of establishing Smart Planet is providing convenient solutions to the known and unknown difficulties. City, the man-made environment, is obviously the first object which should be smarter than current state.

In China, the trend of building smart city has spread across the whole country. The central government has already organized three councils called *Chinese Smart City Convention*, and many local governments have responded to the call and proposed the development scheme in smart city, such as Beijing, Tianjin, and Wuhan.

F. Bian et al. (Eds.): GRMSE 2013, Part I, CCIS 398, pp. 107–118, 2013.
© Springer-Verlag Berlin Heidelberg 2013

Not only in China, but also in most developed and rapid developing countries around the world, the smart city has attracted leaders' concern. From Paris to New York, the seed of smart city has taken root and sprout, and will finally grow into a towering tree in the next decade. (4, 5 and 6)

2 Smart City

According to the most common definition, smart city is a city well performing in 6 characteristics: (1) Economy, (2) Mobility, (3) Environment, (4) People, (5) Living and (6) Governance 3. Fig. 1 illustrates the six axes model of smart city.

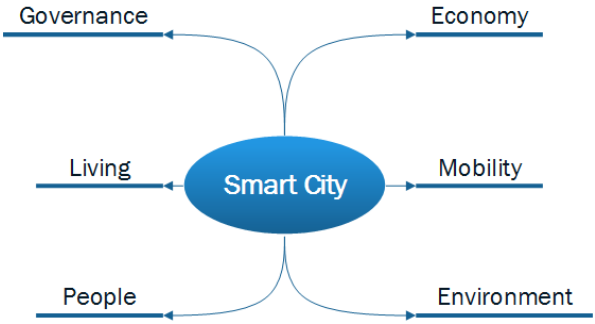

Fig. 1. Smart City Model

The six dimensions can almost summarize all aspects of the city from the leaders' opinions. In order to implement smart city, a lot of technologies should be utilized in it, from traditional mechanical industry to emerging information and communication industry (ICT) 7, especially the latter one, which is the backbone and foundation of smart city.

It is easy to see that the core of smart city is "smart". Before discussing the implementation of "smart", we should first define it. In short, "smart" is the ability to perceive the objects and use the collected information to exploit solutions of specific problem. The interconnection and perception is the main problem before 2000. However, with the prosperity of IOT (Internet of Things, 8), the key issues are solved perfectly. IOT gives every object the ability to connect Internet with a small sensor attached on it. Once the object gets the network connection, the information gathered by sensor would flow into a central server, where the desired problem would be solved when the uploaded data is analyzed and processed.

With so many technologies utilized in the establishment of smart city, a hierarchy structure of technologies is a necessity. Considering the functions and features of technologies and referring to some existed model 9, the smart city can be divided into five layers: (1) Perception Layer, (2) Basic Data Layer, (3) Application Service Layer, (4) Application Layer and (5) Network Layer as Fig. illustrating. The network layer through the model means every layer needs the support from it. The difference of (3) and (4) is that (3) just provides programming interfaces for application programmers to build the applications in (4), while (4) usually offers graphic interface for ordinary people who may not major in software.

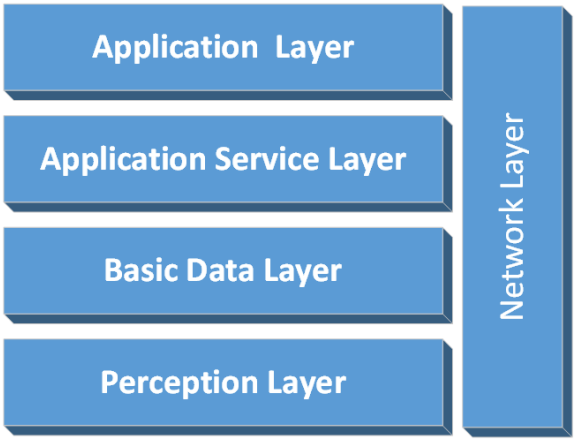

Fig. 2. Smart City Layers

3 Visualization in Smart City

Visualization is in the upper most layer of the architecture. Considering the end users can only contact the applications, the visualization becomes somewhat the core technology in terms of products.

Compared with normal visualizing methods, virtual reality is a very powerful and compelling computer application by which humans can interface and interact with computer-generated environments in a way that mimics real life and engages all the senses. Although its most widely known application is in the entertainment industry, the real promise of virtual reality can also lie in smart city and other industries. 10

Different with other platforms, virtual reality itself needs many specifically designed devices to provide multiple sense-simulations. Therefore, the framework has two parts, one is for hardware encompassed by the system, and the other one is software obviously.

The detail design of hardware can be very different with budget changing. Considering that too luxurious configuration is impractical, a list balancing between usability and budget is put forward. On the contrary, the software framework is easier to design through the help of open source movement.

There are already some platforms discussed in some papers which have been already published. For instance, in 11 the author combined *Sensor Network, OSG Engine* and some other technologies to give a clear framework of such platform. However, the software details are not talked about in 11, which maybe the key point of the whole architecture. Any the loss of detail hardware model is another problem to build such a platform.

In this paper, we advance from the foundation in 11 and give the software detail design, which is the core of framework. Since the software model and hardware model of the system are strongly correlated in terms of functions, the conceptual model should be raised first for easy discussion.

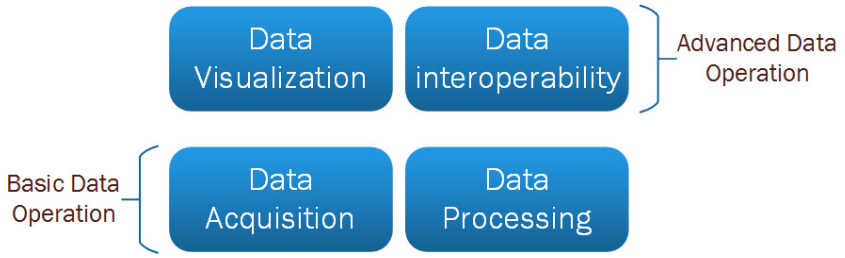

Fig. 3. Conceptual Model

As shown in Fig. 3, the conceptual model of the system includes four parts: *Data Acquisition, Data Processing, Data Visualization, and Data Interoperability.* According to the abstraction degree, the four parts can be divided into two groups. One is **basic data operation**, which includes *Data Acquisition and Data Processing* and is aimed to handling fundamental data affairs, such as data cleaning, acceleration measurement and etc. The other is **advanced data operation**, which includes *Data Visualization and Data Interoperability* and provide real interactivity, such as 3D display, gesture operation, voice control and etc.

The emphasis of the system is the **data** collected from different sources. Without the various data, the system is no more than a normal display device providing common user experience. So, how to process and exploit the **data** is obviously an important and tough task.

3.1 Hardware Model

In this paper, hardware design doesn't mean the circuit design for every device utilized in the virtual reality system. Since there are many devices dedicated in special aspect, such as 3D-display screen in vision display, Dobly Surround Sound in audition, we don't have to establish the hardware architecture from scratch. On the contrary, an assembling list is enough for construction.

Unlike the conceptual model, the detail hardware model is more complicated and sophisticated. (1) First, the data here has more than one type --- smart city data and user data. The former data is provided by some companies or departments, the latter one is collected from the user by hardware itself. (2) Second, every part in conceptual model may have more than one representatives in hardware model. (3) Third, there are some additional parts in hardware model for the actual limitations. Even though the hardware model is more complicated, the actual application of the system still needs some improvements such as wire arrangement, power setting and etc. However, the following hardware model in Fig. 4 is detailed enough guiding engineers to build such a system.

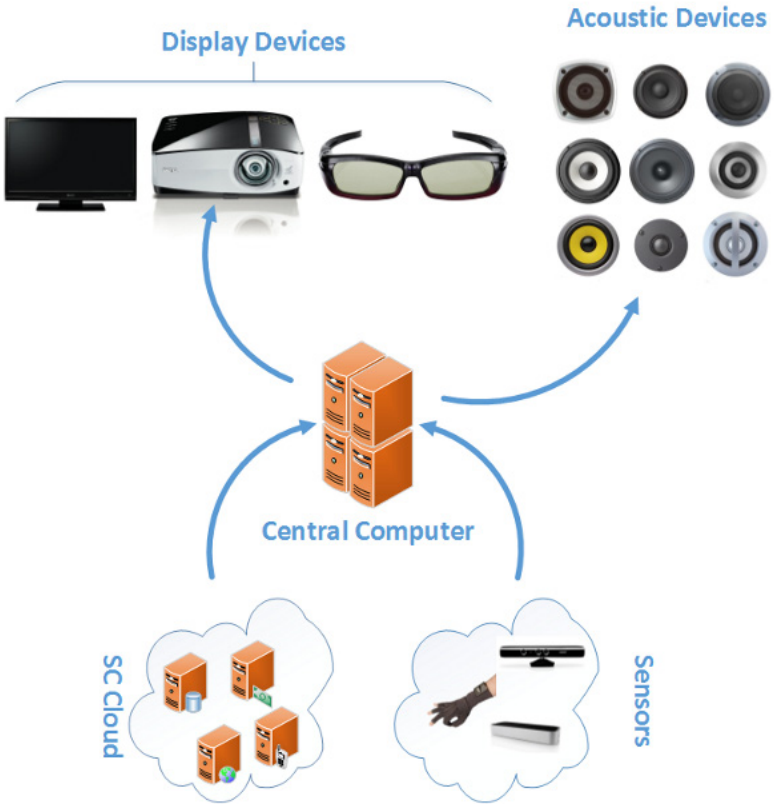

Fig. 4. Hardware Model

The equipment utilized for **Data Acquisition** has two parts in hardware design. Shown in Fig. 4, *SC Cloud* means the smart data source, where cloud means the data center storing city data. This part of hardware needs many investments to build but can be accessed through Internet with relatively small service charge; *Sensors* represents different sensors collecting user data. At present, there are many devices to choose from. For instance, *Kinect* produced by Microsoft Corp. provides a high resolution camera and an infrared sensor gathering depth information 12; *Leap Motion* produced by Leap Corp. uses two cameras to establish a 3 dimensional space and capture users' gestures. Besides these home-use devices, there are some special devices offering more functions or improving the accuracy, such as data gloves. There are many types of data gloves made by different corporations, and usually a pair of glove has 20 or more sensors to catch finger actions. Some data gloves have force feedback gears which can give users tactile feedback on hand simulating pressures 13. Of course, the traditional keyboard and mouse can also be used here.

Data Processing is simple in the hardware model, while the counterpart in software model is more complicated. In many cases, a central computer is enough for hardware tasks.

Data Visualization part has more choices in hardware model. Since 1922, one of the earliest electronic displays --- cathode ray tube (CRT) --- was created 2, the display technologies have been through many revolutions from monochrome to color, form big and heavy box to small and light tablet, from 2D to 3D. In most cases, we also need some acoustic devices to "visualize" voices and sounds. The simulation of tactility is easy with the help of data gloves. If needed, some special devices making odor and flavor can be considered in the final plan too.

The implementation of **Data Interoperability** in hardware is the most complicated section. The tasks of data interoperability need multiple devices work together. In fact, the tasks contained all the matters in other three sections. As we have described the various devices above, it is no need to repeat the configuration. However, a brief explanation of procedures is necessary.

A common task is like following:

(1) The *Sensors* collect user's action
(2) The *Central Computer* analyzes the user's action
(3) The peripheral equipment changes physically

The above three steps are simple but outline the keys of performing **Data Interoperability**. Usually, (2) is the most difficult part to implement. Many predicates and transformations are made here. Another problem is the flexibility of it. If the rules can't be altered according to user's demands, the system can't occupy the market too.

3.2 Software Model

The same as hardware design, software model here doesn't mean construct the virtual reality system from scratch. Specifically, the software model given latter is mainly the application design, which means only the programs in *Data Processing, Data Interoperability* and a part of *Data Visualization* are modelled. The rest work has been down by device manufacturers.

Despite the missing of some parts, the software design is still a huge project which needs a lot of pictures to illustrate. As the data is the key, we'd like to put forward the data-flow graph first.

Corresponding to the hardware model, the *SC Data* stored in *SC Cloud,* and the *User Data* is acquired by Sensors. In Fig. 5, the *Acquisition* represents the data access procedure. The *Aggregation* means the combination of *SC Data* and *User* Data. Then, the data is past to *Processing*, where a lot of work are done, such as coordination transformation, project transformation, scale transformation and etc. The end of data stream is visualization, which is the main work of visualizing devices themselves.

The data flow graph 14 is more like an interpretation of hardware model in software aspect. In general, there are little work for application developers in steps: *Acquisition, Aggregation, Visualization and User Data*. These work are either done by the devices themselves or follow a fixed pattern. The access to *SC Data* is a little bit more complicated than *User Data*. As *SC Data* is stored in *Cloud*, the access is through web service. This type of service are usually XML or Json based, so a powerful parser and builder is a necessity 15.

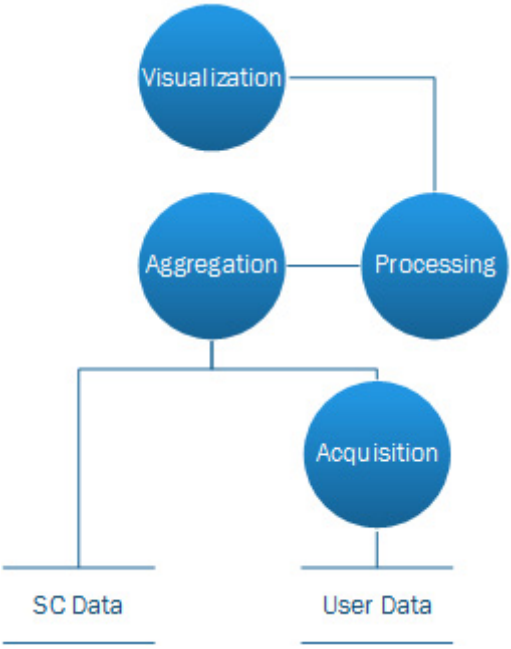

Fig. 5. Data Flow Graph in Concepet

The *Processing* is the key point of software model. Here we'd like to give an UML-Based blueprint for *Processing* and *SC Data* shown in Fig. 6. The OOA (Objective-Oriented Analysis) method has a lot of advantages when establishing actual software system. The most important one is the ability to abstract the real world. Besides the method itself, the tools related to can help a lot. Some handful tools could transform the UML 16 diagram to actual Java or C# codes which decreases a lot of boring and stupid work for developers. More discussion about OOA method can refer to 17.

The framework of software model consists of 2 parts: data handlers and data processors divided into two packages *pDataHandler* and *pDataProcessor*. The classes in *pDataHandler* are mainly aimed to get data from different sources: *SCCloudInterpreter* gets the data from Cloud, while *UserDataInterpreter* obtains the data from local devices. Other classes in *pDataHandler* are just common routines designed for specific use, such as class HttpHelper used for data exchange through http protocol.

In package *pDataProcessor*, the classes handles multiple and heavy computation tasks. For neat explanation, Fig. 7 gives the data flow diagram in these classes.

As illustrating in *Data Stream Diagram*, class *DataAggre-gator* processes the data first. The main task of it is aggregating heterologous data and outputting a formatted data. Class *DataPreprocessor* is the second processing unit, its tasks are common routines, such as data cleaning, conversion, and etc. Sometimes, if the source data is of high quality, this unit can be removed from the final system.

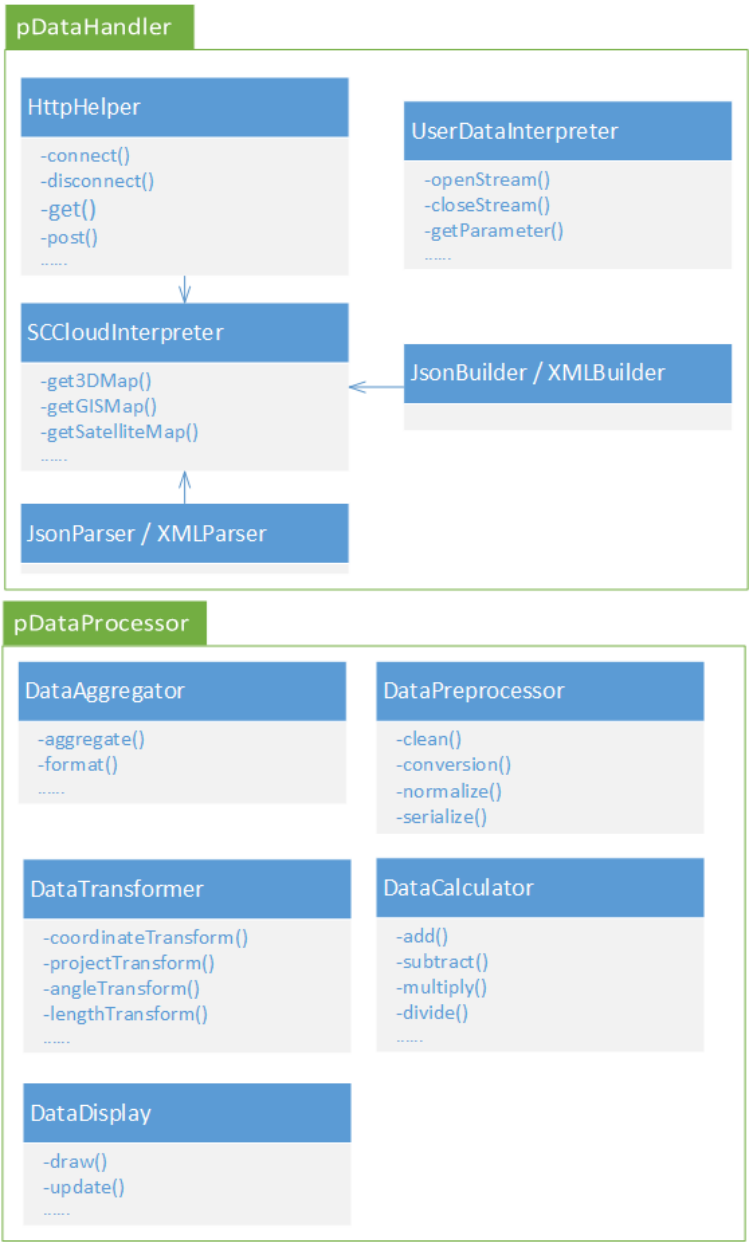

Fig. 6. UML Class Diagram

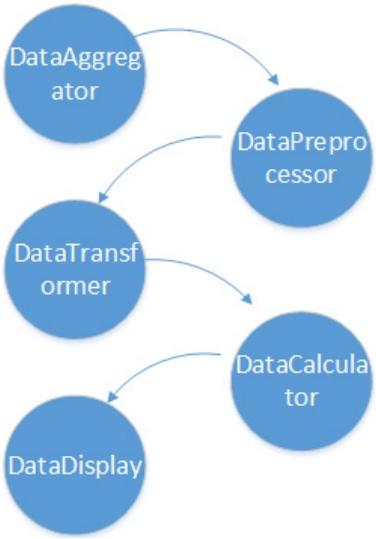

Fig. 7. Data Flow Diagram in Classes

Then, class *DataTransformer* and *DataCalculator* are united to perform advanced data processing. Class *DataTransformer* is aimed at spatial information processing, such as coordination transformation, project transformation and so on, while Class *DataCalculator* chiefly handles matrix-based transformation. Last but not the least, class *DataDisplay* gets the final data and push the byte stream into the video memory and notifies the display devices updating physical states.

This software model is a blueprint with enough structure details. In practice, there are many tradeoffs and additional modules waiting for further solutions.

4 Case Analysis

There is a project built by a company that is at the same position as theory's. And I'd like to briefly talk about the project follows the above blueprint. This project is a part of Smart City, mainly the visual parts. The chief purpose of the project is offering convenient daily life for every citizen. As the project is concerned about visualization, pictures are the best medium to describe the whole project.

The first two Fig.s, Fig. 8 and Fig. 9, show the aerial view of the city. Different with previous systems employed by government, this project uses true 3D technology 18 to construct the city model. Besides, the model generated by the project is built under the criterion of real coordinates in a specific coordinate system and even the size and shape of buildings are downscaling according to a desired ratio.

The second pair of Fig.s, Fig. 10 and Fig. 11, illustrate the road and streets of the project. The most important feature of road simulation in this project is that it can offer more functions related to roads, such as travelling along the street inside a virtual car or

Fig. 8. Aerial View of City I

Fig. 9. Aerial View of City II

Fig. 10. Road I

just by foot, simulation of dynamic traffic management 19, traffic light dispatch test and emergency events resolution test. These additional features give the related staff ability to solve severe problems on obsolete systems. It is said that more functions are under developing.

Fig. 11. Road II

The last picture, Fig. 12, shows the virtual construction of railway station. As known to all, most Chinese choose railway as their intercity communication means. Since China is the most populous country in the world, railway station management faces many challenges especially during the Spring Festival travel rush, when over a hundred million Chinese come home from working place. It is impossible to simulate every details, however, the emergency plans can be tested and verified through the system in the project, which can save various humanity and materials resources 20.

Fig. 12. Railway Station

5 Conclusion

Smart City becomes more and more important, and there are many cities introducing smart platforms to solve daily problems, such as Beijing, Toronto, Stratford and etc. When introducing virtual reality, the presentation ability of Smart City has been enforced so much that a city with intelligence is just a matter of time.

Acknowledgements. This work was supported by grants from the Guangzhou Science and Technology Plan Projects (2012Y2-00035； 2013Y2-00031). The authors are also grateful to teachers and staff of IIS of WHU for their technique and logistics support during the writing.

References

1. Wikipedia. Smarter Planet (2013), http://en.wikipedia.org/wiki/Smarter_Planet
2. Wikipedia. History of display technology (2013), http://en.wikipedia.org/wiki/History_of_display_technology
3. Smart Cities: Ranking of European Medium-Sized Cities. Centre of Regional Science, Vienna University of Technology (2007)
4. Caragliu, A., Bo, C.D., Nijkamp, P.: Smart cities in Europe. Vrije Universiteit, Faculty of Economics and Business Administration (2009)
5. Hollands, R.G.: Will the real smart city please stand up? Intelligent, progressive or entrepreneurial? City 12(3), 303–320 (2008)
6. Berce, J., Lanfranco, S., Vehovar, V.: eGovernance: Information and Communication Technology, Knowledge Management and Learning Organisation Culture. Informatica (Slovenia) 32(2), 189–205 (2008)
7. Jordan, A.G.: Frontiers of research and future directions in information and communication technology. Technology in Society 30(3), 388–396 (2008)
8. Atzori, L., Iera, A., Morabito, G.: The internet of things: A survey. Computer Networks 54(15), 2787–2805 (2010)
9. Bian, F.: Principle and Methods of Digital Engineering, pp. 91–95 (2011) ISBN 978-7-5030-2224-1
10. Burdea, G., Coiffet, P.: Virtual reality technology. Presence: Teleoperators and Virtual Environments 12(6), 663–664 (2003)
11. Hu, J., et al.: Virtual reality platform for smart city based on sensor network and OSG engine. In: 2012 International Conference on Audio, Language and Image Processing (ICALIP). IEEE (2012)
12. Smisek, J., Jancosek, M., Pajdla, T.: 3D with Kinect. In: Consumer Depth Cameras for Computer Vision, pp. 3–25. Springer, London (2013)
13. Ku, J., et al.: A data glove with tactile feedback for FMRI of virtual reality experiments. Cyberpsychology & Behavior 6(5), 497–508 (2003)
14. Choi, C., Ha, S.: Software synthesis for dynamic data flow graph. In: Proceedings of the 8th IEEE International Workshop on Rapid System Prototyping 'Shortening the Path from Specification to Prototype'. IEEE (1997)
15. Erl, T.: Service-oriented architecture: a field guide to integrating XML and web services. Prentice Hall PTR (2004)
16. Arlow, J., Neustadt, I.: UML and the unified process: Practical object-oriented analysis and design, vol. 2. Addison-Wesley, Reading (2002)
17. Liang, Y.: Approach to assessing and comparing object-oriented analysis methods, vol. 13(3), pp. 27–33 (2000)
18. Tsai, C.-H., Chen, W.-L., Hsu, W.-L.: 32.4: Invited Paper: The Pursuit of High-Definition 3D Display Technology. In: SID Symposium Digest of Technical Papers, vol. 39(1). Blackwell Publishing Ltd. (2008)
19. Yang, Q., Koutsopoulos, H.N., Ben-Akiva, M.E.: Simulation laboratory for evaluating dynamic traffic management systems. Transportation Research Record: Journal of the Transportation Research Board 1710(1), 122–130 (2000)
20. Wang, L., et al.: Simulation study of pedestrian flow in station hall during the Spring

Design of Security and Monitoring System for Prison Based on Wireless Sensor Networks

Xinyu Li

International School of Software, Wuhan University, Wuhan, China
282215143@qq.com

Abstract. With the rapid development of security systems, the security system design has been put forward higher requestments. It introduces the wireless technology into prison security system. Modern prison management and wireless sensor network are analyzed; Focus on the overall system structure, as well as the hardware and software design of the system; The key technology of implementing the system is discussed. It can notice to the related working personnel in the prison to make the prisonguard arrives on the scene for the first time to deal with the emergency.

Keywords: Security monitoring system, Wireless Sensor Network(WSN), key technology.

1 Introduction

Prison is the place that held and transforming crimimals [1],Safety is the first of all to guarantee. To protect the safety of society, and to protect the safety of personnel and stability of guards and detainees. By installing security monitoring systems, it can effectively strengthen the management of prisoners, reflect the important location of site's condition intuitively and in time; to enhance the security measures is a useful tool for modern prison management. With the extensive application of computer technology in all walks of life, making the rapid development of computer software and hardware have reached the prison monitoring system application's requirements, and gradually into the practical. By combining the new security system and the computer technology ,it can effectively strengthen the management of prisoners and reduce accident's happening[2].To strengthen security measures and strengthen prison modernization, puting forward a kind of prison security system design scheme based on wireless sensor network (WSN).

Wireless sensor network (WSN) is a collection of microelectromechanical system, sensor technology, embedded computing technology, information processing technology, modern network and wireless communication technology and digital electronics in the integration of a new generation of task oriented distributed network.It is deployed in monitoring area of a large number of tiny sensor nodes of stationary or mobile, which through wireless communication form a multiple hops self-organizing wireless network[3].Its purpose is to perceive, acquisition, processing and transmission

F. Bian et al. (Eds.): GRMSE 2013, Part I, CCIS 398, pp. 119–127, 2013.
© Springer-Verlag Berlin Heidelberg 2013

the network covering's geographical area of perception object monitoring information, collaboratively to deal with it, then delivering the information to the user terminal in the form of self-organization multiple hops. It realizes to connect the physical world, computer world and human society. With strong concealment, highreliability, self-organization's characteristic, etc

The composition of the system can notice to the related work of personnel in the prison, to make the prisonguard arrives on the scene for the first time to deal with the emergency, to ensure the safety of prison guards, to safeguard the order of the management[4].

2 Overall Structure of the System

The prison security and monitoring system overall structure: the sensor node is large deployed within or near the monitored area through artificial arrangement, each node constitutes the network by means of self-organizing. In the wireless sensor network, each sensor node are statically and randomly distributed in a particular area. Sensors collect the area's voice, luminance signal, etc. Data through simple processing jumping to transfer between neighboring nodes, monitoring data can be processed by multiple test nodes during transmission, to arrive at sink nodes after multiple hops posterior. Sink nodes transfer a network through transmission network, and finally transfer the collected data to the remote information processing center for centralized processing. Information are spread in real-time in the network. Monitoring staff is according to the computer output control signals to take corresponding measures. Figure 1 is the sensor network structure, which includes sensor nodes, sink nodes and information processing center, etc.

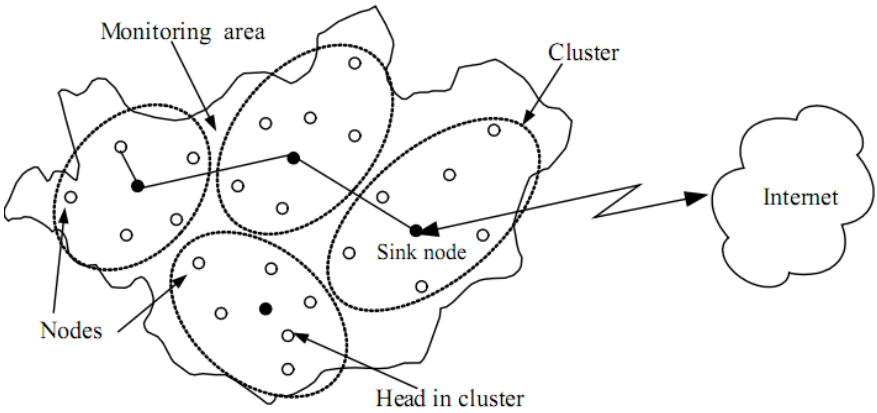

Fig. 1. Framework of WSN

Sensor nodes are usually a miniature embedded system, which through carrying limited battery power energy to supply. Restricted by the volume of node, sensor node's energy is limited. Its storage capacity, processing ability and communication ability are relatively weak. From the view of network functions, each sensor node has double functions of traditional network node terminals and routers. In addition to collect local information and process data , but also to make data forward other nodes for storage, integration and management, etc. As well as complete certain tasks by coordinating with other nodes[5].

Compared with the ordinary nodes, sink nodes are relatively stronger in storaging capacity, processing capacity and communication capacity .It connects the sensor network and external network, such as the Internet, to implement communication protocol conversion between two kinds of protocol stack, and transmit the collected data to the external network. It can send the related data to the node. Sink nodes have enough energy to supply and more memory and computing resources, so they can be either enhancemed sensor nodes, or only special gateway device with wireless communication interface without monitoring function[6].

3 The Hardware and Software Design of the System

3.1 The Hardware Design of Node

Wireless sensor network node is divided into micro controller, data acquisition, RF transceiver, power management, programming interfaces, this a few parts. The node hardware structure diagram is as shown in figure 2:

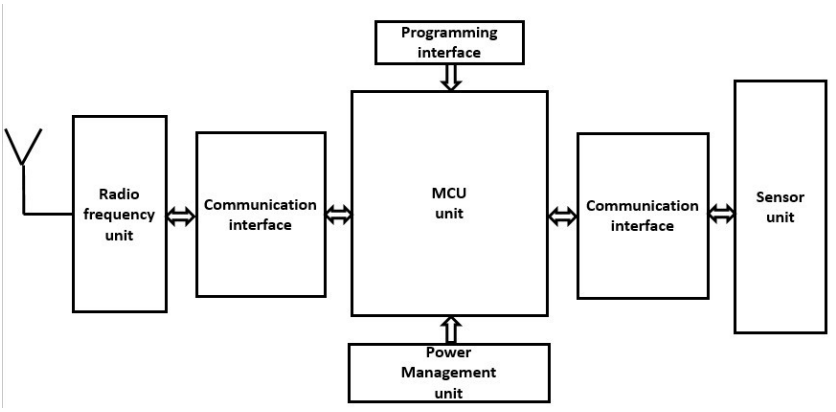

Fig. 2. The node hardware structure

The microcontroller is the core brain of the system, which is responsible for organizing the system function's realization and allocating resources, we should choose low power consumption microcontroller chip. Microprocessor is one of the core components of wireless sensor nodes, each module of the nodes must be controlled by

microprocessor to control and communicate. Therefore, the selection of the microprocessor largely determine the performance of the node. The system adopts touch Tmegal28L chip as microprocessorcomponents to implement the prison security monitoring wireless sensor nodes.

This system adopts the low cost, small volume and compatible with 51 microprocessor AT89C2051.The processor has 2 kilobytes program memory and 128 bytesdata memory. And the power supply voltage is as low as 2.7 volts, with active and free two patterns, the working current can be as low as 2 milliamperesin activepattern(when the working frequency and voltage rise, the working current increases).

Microchip Tmegal28L is 8-bit CMOS low power and high-performance AVR microprocessor launched by ATMEL company. The microprocessor is based on AVR RISC structure, and has the advanced instruction set and the single cycle instruction execution time. Its high data throughput rate greatly alleviates the contradiction between the system's processing speed and power consumption. Moreover,ATmegal28 processor has rich resources, in addition to the 128 kilobytes on chip flash program memory, 4 kilobytes data accessors, block 4 kilobytes EEPROM memory, 32 general purpose working registers, it also includes the 53 general interface, two USAR and TWI, 8 channe IO ADc, SPI serial interface, 4 which has the function of comparison model and PWM 's timer/counter, and six kinds of programmable power saving mode[7]. ATmegal28L microcontroller with its good performance and relatively rich resources is suitable for this system.

Data acquisition implements the function of applied parameter acquisition . Sensor unit outputs digital signals through the standard interface SPI and microcontroller unit. In order to implement low power consumption design, to balance the actual demand and the energy consumption's relationship. the sensor makes data acquisition periodically, and make sensors in the low power or inactive state during idle time. If the sensor has no low power modes, it reduces power consumption by controlling the power supply on and off to startup and shutdown sensors[8]. In order to reduce power consumption, save the volume, this system's sensors are all integrated sensors, a sensor can collect multiple similar signals.

Power management is used to detect the current state of battery, which is implemented by power management unit. If the voltage is lower than the threshold, it will notify the user by the alarm audible, and transmit the alarm message to the sink node, so that can inform people to replace the battery in time.

3.2 Node's Software Design

Considering from lower power consumption, the system adopts an event-driven design thought. Most of the time, the system is in low power mode, the CPU is completely shut down. Then wake up the CPU by interrupting events, enter into the phase of data processing, and then continue to enter a state of low power consumption.CPU is woken up by receiving interrupt events caused by a complete data frame which is received from RF transceiver and timer timing interrupt event, then CPU will out of the low power mode. Sensor node's program flow chart is as shown in figure 3:

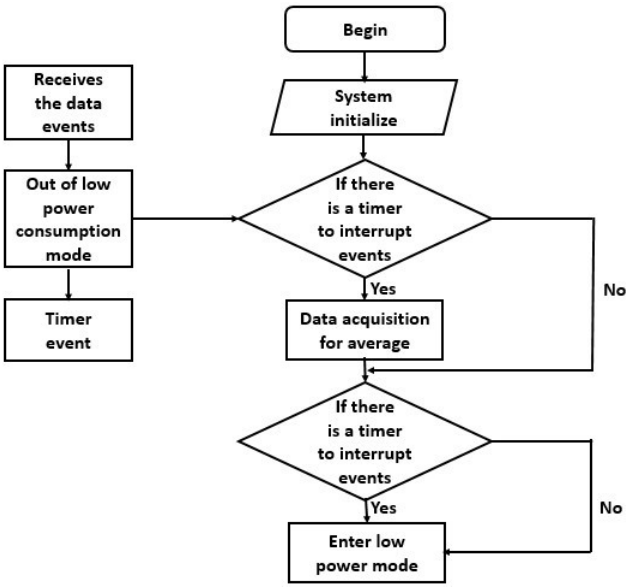

Fig. 3. The procedure flow charts of sensor nodes

The body of the application is an infinite loop, the inside of the loop can data acquisition, calculate the mean value, send out it, and then enter into sleep mode. When the timer is arriving on time, the interrupt service subprogram wake up CPU, then continue to repeat[9].

3.3 The Wireless Transmission Unit

CC2420 element is up to the standard of IEEE802.15.4 wireless transceiver RF chip launched by ChipconAS's. The chip adopts SmartRF03 technology, and works in ISM unlicensed 2.4GHz frequency band. The chip's dormancy working mode has very low energy consumption, it is suitable for the battery supplying power for a long time . At the same time, the low cost can be applied to the specific requirements of plentiful deployment. In addition, the chip adopts CSMA - CA technology in order to avoid competition and collision during data transmition. Thereby, to ensure the reliability and effectiveness of communication. In addition, the chip integrates the CRC data integrity check, the implementation of hardware's function not only increases the speed of communication, but also reduce the energy consumption. Wireless communication equipment adopted by this chip is small volume, low power consumption, high data transfer rate. It is widely used in PAN network industry and ZigBee equipment . Wireless communication as the wireless sensor node design is the key to success or failure of the system[10]. In order to meet the wireless sensor network on the system performance, efficiency, power consumption of communication's requirements, adopting CC2420 as the RF module to implement wireless communication between sensors.

4 The Key Technology

Due to the particularity of prison security work, in addition to have general key technologies of wireless sensor network (WSN), in the system's design and implementation process, there are the following key issues: sensor nodes, energy management, data sampling and collecting, energy efficient communication mechanism.

4.1 Sensor Nodes

Used to monitor prison environment's wireless sensor nodes need to satisfy the small size, high precision, long life cycle's requirements. Because of the complexity of monitoring environment and the sensitivity of monitoring environment for foreign equipment, it need to minimize the volume of asensor node. In order to obtain the exact parameters of the surroundings, sensor nodes need to equip a variety of high-precision sensors. In order to extend the sensor networks' preferentially-deployed time as much as possible, enhance the practicality of the network, sensor nodes need to have a long life cycle.

Selecting replaceable and high precision sensors is very important for environmental monitoring . In general, the same kind of sensor error of measured data is less than 3% , so that error can be controlled within 1% through certain compensation mechanism. During selecting sensor, another important factor is the sensor's start-up time. Start time refers to the sensor node's time from powering up to reading data stably. Sensors need a constant current in the start time, so the system needs to use the shorter startup time's sensor nodes to save energy. Mote node developed by the university of California, Berkeley is more usedin the current application. Mote node has a special sensor board through extension board, the board has light sensor, voice and other sensors. The system chooses the Mote node based on the above factors.

4.2 Energy Management

The prison monitoring applications require continuous months or even years of monitoring, the sensor node's energy supply put forward high demands. Most of the current sensor node use two dry batteries to supply power, the power is about 220 mAhunder the condition of 3 v. Table 2.2 lists the common operations consume energy of the sensor nodes.

In a sensor network, different nodes have different energy demands and use. Node sclose to the base station need more energy to use on the data packet's transmiting, and the edge of the network node will use the main energy in data collection. Therefore, some nodes consume energy faster, and become the bottleneck of the whole network energy. It takes a certain node redundancy measures to ensure that data transmission will not be interruptted because of individual node's failure.

Table 1. The relation between typical operation of sensor nodes and power consumption

The operating of sensor nodes	Power Consume/mAh
Transmit a data packet	20.000
Receive a data packet	8.000
Monitor the channel for 1ms	1.250
Simulation samples	1.080
Digital samples	0.347
Read the ADC sampling data at a time	0.011
Read the Flash data	1.111
Write or clear the data on the Fhsh	83.333

The main way to save energy for notes is the dormancy mechanism. When sensor nodes have no tasks and do not need to transmit datd for other nodes, it will close the node's wireless communication module,data acquisition module and computing module in order to save energy. In this way, a sensing tasks occurs, only the adjacent area of sensor nodes are active, thus forming a activity area. Active area move with data transmitted to the gateway node, so the original activity node can switch to sleep modeto save energy after leaving the movement area. .

4.3 Sample and Collect Data

Prison environment monitoring application's ultimate goal is to sample and collect data for the monitoring environment. Sampling frequency and precision are determined by the specific application, and control center gives commands to the sensor network. Sensor nodes need to consider the compromise between energy consumption and sample data. Because the node on the edge of monitoring area only need to send the collected data to the base station, the energy consumption is relatively small, but the nodes close to the base station due to need for edge node routing data at the same time, the consumption of energy is more than two orders of magnitude. Data fusion is an important aspect to reduce datacommunication's volume. Because the sensor node's deployment has redundancy, the collected data has nuch repeatability between adjacent nodes. On one hand ,it can reduce data communication' volume through the data fusion mechanism, on the other hand it can also refine single node's datacollection through the correction mechanism[11]. Therefore, edge nodes must compress and process fusion the collected data before sending to the base station.

4.4 Energy-Efficient Communication Mechanism

For the prison environment monitoring applications, energy efficient communication mechanism includes a series of routing algorithm, MAC algorithm as well as directly control and access control to the communication component. Routing algorithm needs

to guarantee efficient communication between the nodes, and maintenance the connectivity of data transmission path .The most simple and efficient routing protocol is a node directly broadcast to the base station in a fixed allocation of time slot , but this requires nodes are at distance of jump range with base,it limits the size of the sensor network, it needs more routing mechanism in larger applications.

Network lifetime is an important problem of sensor networks. The use of GAF, SPANalgorithm's network topology management mechanism can improve the survival of the entire network, but only for 2 to 3 times, and it needs to increase about 100 times for existing network lifetime in practical applications. Therefore, in addition to the routing protocol, the actual application needs low energy consumption of MAC protocol. MAC protocol need to determine the duty cycle of nodes' wireless communication module, nodes close communication module in order to save energy in most of the work cycle time.It determines the working cycle of the sampling and frequency of sensor module at the same time. Consistent between cycle of wireless module and sampling cycle of sensor module can effectively reduce the node energy consumption.

5 Summarize

In this paper, wireless sensor network technology is applied to prison security monitoring, puting forward a kind of prison security system based on wireless sensor network (WSN). The system does not need human intervention when it is at run time ,it has real-time monitoring, alarming, and the function of query historical data. Not only overcome the inconvenience caused by cable limit in security system integration process ,but also make the security system can implement many new applications[12].The way of wireless sensor network and the integration framework of wireless sensor and control network given in this paper can make the wireless network technique effectively used in the prison security system .

References

1. Prison IP network broadcast intercom, http://www.comtom.cn/ApplicationsDetail.aspx?id=10
2. Prison security system solutions, http://www.viewse.com.cn/shownews.asp?id=102
3. Typical time synchronization technology analysis of wireless sensor networks, http://www.shoukehuji.cn/a/qianrushi/yejiedongtai/jiejuefangan/2013/0104/13680.html
4. Hao, X., Kang, Y., Wang, Y.: (College of Electrical and Information Engineering, Lanzhou University of Technology, Lanzhou 730050, China): Design of security and safety system for prison based on wireless sensor networks. Transducer and Microsystem Technologies (January 2008)
5. Duan, X.: (College of Computer Science and Technology, Beijing University of Posts and Telecommunications, Beijing 100876, China): Design of the wireless image sensor node based on the Zigbee protocol. Sciencepaper Online

6. The structure of the wireless sensor network (WSN), http://www.iot101.com/tech/WSN/2012-09-26/388.html
7. Designand implementation of intelligent vehicle based on ATmegal28L(1), http://www.eeworld.com.cn/mcu/2012/0609/article_9077.html
8. Zhao, H., Yin, K.-X., Shao, J.-H.: A safe and environment monitor indoor system based on wireless sensor network. Control and Automation Publication Group 26(1), 21–22, 34 (2010)
9. Song, X.-C., Shan, Z.-Q.: Monitoring System of Oilfield Parameters Base on Wireless Sensor Network. Coal Technology 28(7), 41–43 (2009)
10. Wang, X.-M., Liu, N.-A.: 2.4 GHz RF Chip CC2420 and Its Application in Zigbee Communication. International Electronic Elements 3, 59–62 (2005)
11. Sun, L.-M., Li, J.-Z., Chen, Y., Zhu, H.-S.: Wireless Sensor Network. Tsinghua University Press 409
12. Sun, C., Zhang, S.-Q., Zhang, X.-L., Yang, J.: Wireless sensor network (WSN) application in greenhouse environmental monitoring. Journal of Agricultural Mechanization Research 9, 194–195 (2006)

Overview of Hyperspectral Remote Sensing of Impervious Surfaces in Urban Environment

Shailesh Deshpande[1], Arun Inamdar[2], and Harrick Vin[1]

[1] Tata Research Development and Design Centre,
54-B Hadapsar Industrial Estate, Pune, 411013, India
{shailesh.deshpande,harrick.vin}@tcs.com
[2] Centre of Studies in Resources Engineering,
Indian Institute of Technology, Mumbai, 400076, India
abi@iitb.ac.in

Abstract. In this paper we provide a concise overview of hyperspectral studies of impervious surface in urban environment. We highlight socio-ecological impact of urban conglomerate on the surroundings. We present few important techniques of material detection using spectral matching methods - a unique opportunity provided by hyperspectral data. The paper then discusses signatures of urban materials and reviews how various investigators have utilized hyperspectral data to study impervious surface in urban area.

Keywords: Hyperspectral, Impervious surface, SAM, EO-1.

1 Introduction

Urban areas are important conglomerates of socio-economic activities and are regarded as prime movers of any state. But at the same time, owing to their population density, they act as critical agents in changing their surroundings – on a substantial spatial and temporal scale. Urban areas act as sinks of large amount of societies' resources and major sources of environmental change. These land use-land cover (LU/LC) changes brought by urbanization bring other hosts of changes along with it namely - increased run off, ground water depletion, change in ambient temperatures (Heat Island Effect), and increase in air and water pollution.

Impervious (to water) surface is an important artifact of these changes. Impervious surface reduces quantity of ground water recharge. Ground water depletion is natural inevitable consequence if the mitigation steps are not taken. The urban runoff peak is increased and is achieved much more quickly than earlier. Urban flash floods have become a routine phenomenon now in many metros. The run off naturally adds to the non-point source pollution which ultimately reaches the natural sinks such as rivers, coastal water etc. Non-point source pollution is among the largest pollutants in United States of America (USA) [1].

Over the years, remote sensing has been successfully applied to mapping urban infrastructure, land use land cover and so on [2]. The remote sensing platforms and

F. Bian et al. (Eds.): GRMSE 2013, Part I, CCIS 398, pp. 128–140, 2013.
© Springer-Verlag Berlin Heidelberg 2013

the urban area to be monitored - both have changed since their inception. Arial photographs have been replaced by sub-meter resolution satellite imagery and mapping needs are replaced by need to understand and quantify bio-physical parameters within city area. Sound understanding of fluxes of biophysical parameters is required to provide tractable model for urban impact on its surroundings.

Advent of hyperspectral data provides new opportunities in this regard. Hyperspectral data provides many advantages over conventional multispectral data for impervious surfaces detection in urban environment. The minute details available in the spectral signature of a particular material are lost in broad band data collection (as energy is collected over a broad range). In contrast, the signatures provided by hyperspectral data are very unique (most of the times) enabling discrimination of large variety of natural and manmade materials. Direct identification of a particular material by comparing target spectrum with reference spectrum in unsupervised manner has thus become a viable option.

Weng [3] provides a comprehensive review of requirements, methods for remote sensing of impervious surfaces in urban area. The scope of this review is much broader and hence hyperspectral remote sensing of impervious surface - though reviewed – is discussed briefly. He emphasizes the fact that hyperspectral data has been underutilized for impervious surface detection. Shafri et.al. [4] provide good overview of hyperspectral remote sensing of urban area with a short review of impervious surface detection. Both these articles are intended to provide broader overview of the respective topics and hence organized accordingly.

This paper attempts to provide concise overview of hyperspectral remotes sensing of impervious surfaces in urban area with emphasis on spectral matching methods – a unique advantage provided by hyperspectral data. This discussion is not intended to be a comprehensive survey of research but to be a good starting point for hyperspectral remote sensing of impervious surfaces. This paper is organized as follows: Section 2 provides gentle introduction to hyperspectral data characteristics and provide brief introduction to few important hyperspectral sensors. Section 3 provides glimpses of important spectral matching techniques (for material detection). Section 4 provides brief overview of research efforts taken towards hyperspectral detection of impervious surfaces in urban area. Section 5 concludes the discussion.

2 Hyperspectral Data Characteristics

2.1 Hyperspectral Data Characteristics

Hyperspectral data[1] refers to the remotely sensed data collected over electromagnetic spectrum – typically in visible and infrared range from 400 nm to 2500 nm – in

[1] The terms “hyperspectral data” and “imaging spectrometric data” are used interchangeably in literature. Jet Propulsion Laboratory (JPL) prefers “imaging spectroscopy” and “imaging spectrometric data” to “hyperspectral imaging” or “hyperspectral data” to make it amenable to other science disciplines such as physics, chemistry, biology [5].

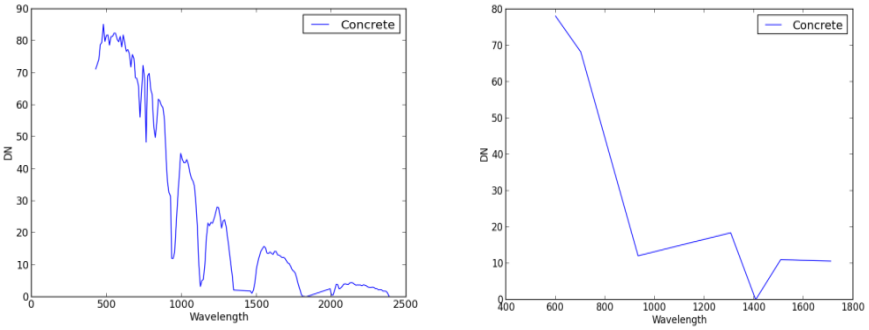

Fig. 1. Spectral curves extracted from hyperspectral (left sub-plot) and multispectral (right sub-plot) images

contiguous bands of ~10 nm widths. As can be seen from the spectral curves of concrete in hyperspectral and multispectral images from Fig.1, the band width of conventional multispectral scanners is too coarse to capture highly structured reflectance and eminence determined by electromagnetic energy and vibrational energy states in the material [6]. As the interaction between the material and electromagnetic energy is recorded at much finer resolution, diagnostic features are available which can help to detect the material. Spectral width of 10 nm (9.3 to be specific) in the spectral range of 400 nm to 2400 nm is sufficient to completely describe diagnostic features of materials [7]. Table 1 gives comparison between multispectral data and hyperspectral data.

Table 1. Comparison of hyperspectral and multispectraldata

Attribute	Hyperspectral	Multispectral
Data characteristics	Continues with app. 10 nm width	Discrete, broad bands
Data processing, analysis	High dimensional data, needs dimensionality reduction measures for computational efficiceny	High dimensionality is not an issue
Material detection	Direct material detection is possible, Spectral library can be built and used subsequently	Need to use conventional classification procedure-further signature is of insufficient details too
Quantification of bio-physical parameters	Models for variety of bio-physical parameters are possible	Broad band signatures limits the scope to few physical parameters only

2.2 Hyperspectral Sensors

One of the early sensors collecting hyperspectral data is Airborne Visible InfraRed Imaging Spectrometer (AVIRIS). AVIRIS uses four aircrafts – National Aeronautics

and Space Administration's (NASA)ER-2 (flight height app. 20 km above sea level, at 730 km/hr and Twin Otter International's turboprop aircraft (flight height ~4km, at 130 km/hr). Other two aircrafts are Scaled Composites' Proteus, and NASA's WB-57 [13].AVIRIS is whiskbroom type of scanner with Instantaneous Field of View (IFOV) of 1.0 mrad [8].

The only space-borne available sensor currently is Earth Observing-1 (EO-1)-Hyperion. NASA EO-1 satellite was launched on November 21, 2000 as a part of one-year technology demonstration mission. Though the mission was completed, NASA and the United States Geological Survey (USGS) reached an agreement to allow continuation of the EO-1 program as an Extended Mission.EO-1 is tasking satellite with onboard hyperspectral sensor Hyperion (Can service 12 request per day). It also collects information in broad bands with Advanced Land Imager (ALI) sensor simultaneously [9].

HyMap is commercial hyperspectral sensor manufactured by Integrated Spectronics Pty. Ltd. and operated by HyVista Corporation, Australia. It uses whiskbroom type of scanner and utilizes 32-element detector arrays for recording data. HyVista started providing hyperspectral data to government, academic, and commercial customers all over the word since 1999 [10], [11].

Table 2. Spectral and spatial charcteristics of hyperspectral sensors

Sensor	AVIRIS	EO1-Hyperion	HyMap
Range	400 – 2500	357 nm – 2576 nm	450 nm – 2500 nm
Number of bands	224	242 (198 calibrated)	128
Spectral resolution	10 nm	10 nm	15 – 20 nm
Spatial resolution	20m, 4m (High, Low altitude)	30 m	3 – 10 m
Image swath	11km, 1.9km (High, Low altitude)	7.5 km	~1.5 - ~5.0 km (512 pixels)
Image length	10 -100 km	42 km	

3 Spectral Matching Methods for Material Detection

The intuition of spectrum matching is straightforward - it attempts to mimic the laboratory process to identify material/s using a reflectance spectrum. Similar to laboratory spectra, suppose we have reference spectra of known materials, we can detect these materials by spectrum matching procedure. If a reference spectrum of known material matches with a particular target spectrum then we can resolve the identity of target material. Following section reviews some of such methods that employ spectral matching procedures to detect the target material.

In his early review of hyperspectral data characteristics and analysis techniques Goetz et al. [7] suggested Hamming distance as a similarity measure between reference and target spectrum. The reference spectrum and target spectrum are coded in binary format first and then Hamming distance between binary coded spectra is

calculated to see how close they are to each other. Binary coding is performed by simple operation: reflectance values in a given spectrum above its mean are coded as 1 and below its mean are coded as 0.

3.1 Spectral Angle Mapper (SAM)

SAM is one of the primary techniques that uses spectral library to classify the pixels in unsupervised manner. The goal is to identify (classify) a pixel by comparing the spectrum of that pixel with the spectrum of known material. If the pixel spectrum matches with a particular reference spectrum of the known material in the library, we can assign that pixel to that particular material class. The "matching" or "closeness" of the two spectra is decided using angle between the two spectral vectors with *m* dimensions where *m* is number of bands in a spectrum – and hence the name. More formally expressed as:

Let $L = \{l_{i=1}, l_2, l_3 \ldots l_n,\}$ set of library members where each member $l_1, l_2, \ldots l_n$ are the vectors indicating a member in the spectral library - say for example, each member represent signature for asphalt, concrete, gravel surface and so on. Each member $l_1, l_2, \ldots l_n$ is represented as a vector of reflectance values in each band as $l_i = \{r_{k=1}, r_2, r_3 \ldots r_m\}$ where *m* equals number of bands. Similarly, each pixel in the image can be represented as *m* dimensional vector as $p_j = \{r_{k=1}, r_2, r_3 \ldots r_m\}$. Then the cosine of angle between pixel vector and library member is given by:

$$\frac{l_i \,.\, p_j}{\|l_i\| \|p_j\|} \tag{1}$$

Since its initial application in Spectral Image Processing System (SIPS) developed by Kruse et al. [12], SAM is been used extensively for target detection and it provides a bench mark performance for other methods of spectral similarity. The distinct advantages of the methods are its simplicity and computational efficiency. Further the technique is amplitude invariant – the angle between the two vectors does not change with reflectance values amplitude of a particular band. This is a disadvantage as well – cases where two spectral curves are very similar in shape with difference in amplitude (reflectance) values, SAM does not differentiate those materials.

3.2 Cross Correleogram Spectral Matching (CCSM)

Cross correleogram is calculated using ordinary linear correlation between target spectrum (material to be identified) and reference spectrum (laboratory spectrum) at different positions on x axis. To achieve this, the reference spectrum is shifted on x axis and at each shifted position correlation between two spectra is calculated. By convention, negative shift indicates that the reference spectrum is shifted towards lower wavelengths. The cross correlation for m match position is given by:

$$\mathrm{r_m} = \frac{\mathrm{n}\sum \lambda_\mathrm{r}\lambda_\mathrm{t} - \sum \lambda_\mathrm{r} \sum \lambda_\mathrm{t}}{\sqrt{[\mathrm{n}\sum \lambda_\mathrm{r}^2 - (\sum \lambda_\mathrm{r})^2][\mathrm{n}\sum \lambda_\mathrm{t}^2 - (\lambda_\mathrm{t})^2]}} \tag{2}$$

Where, λ_r and λ_t are reference spectrum and target spectrum respectively, and n is number of overlapping position

Meer et al. [13] used cross correleogram to measure similarity between target spectrum and reference spectrum. They studied the method for target spectrum of kaolinite. They showed that addition of 5% noise in target spectrum didn't affect the shape (skewness) of the correleogram. Subsequent to these studies, Meer et al. [14] extended the CCSM by removal of continuum and tested it on AVIRIS target spectrum of kaolinite. They found CCSM with continuum removed is more sensitive to subtle spectral features and noise. They suggested use of appropriate wavelength interval covering single absorption instead of selecting multiple absorptions.

Senthil kumar et al. [15] combined CCSM with Variable Interval Spectral Average (VISA) method and test edits performance on two datasets: one a laboratory simulated image and the other AVIRIS sensor 92AC3C for a test site called Indian Pine in north-western Indiana (soybean, wheat, grass etc.).VISA and SAM provided almost similar results. Mixed pixel performance for VISA gave poorest classification accuracy. Though, the VISA and CCSM method applied together improved accuracy of classification of mixed pixels than their individual counterparts.

3.3 Normalized Spectral Similarity Score (NS3)

Spectra of some materials mainly differ in amplitude values (reflectance values) of spectral signature (length of vectors) rather than the angle between two spectral vectors. This drawback motivates consideration of the amplitude information for calculating similarity between target spectra and reference spectra. The NS3 algorithm developed Nidamanuri et al. [16] attempted to incorporate amplitude information while measuring the similarity between two spectra. The formulation is given below:

The spectral amplitude difference is calculated as:

$$A = \left[\frac{1}{N-1}\sum_{i=1}^{n}[\lambda_r(r_i) - \lambda_t(r_i)]^2\right]^{0.5} \tag{3}$$

Where N = number of interval and $\boldsymbol{\lambda}_r$ and $\boldsymbol{\lambda}_t$ are reference and target spectrum.

A values are further normalized using following equation:

$$\hat{A} = \frac{A - A_{min}}{A_{max} - A_{min}} \tag{4}$$

Further, this normalized spectral difference is incorporated in the formula to give a final match score as:

$$B = \sqrt{\hat{A}^2 + (1 - \cos\theta)^2} \tag{5}$$

Value of *B* range from 0 to $\sqrt{2}$ where 0 indicates perfect match. The value *B* – that is similarity score between two spectra is sufficient to detect the target material. But it is further refined to give empirical discriminative function as:

$$f = 0.6B + 0.4\,\Delta B \tag{6}$$

Where $\Delta B = \frac{B_2 - B_1}{B_2}$ and B_1 is higest similarity socre for a match and B_2 = 2nd highest similarity score for a match.

Nidamanuri et al. [16] investigated the proposed method by comparing it with SAM, CCSM methods. Spectral library was created using filed spectrometer. Historical HyMap imagery was used for validating classification of different crop types. Though the results show improvement in overall accuracies, SAM and NS^3 show similar trend for most of the crops.

SAM and other similarity measures can successfully detect materials within the pixel containing a single (or dominant) material. But in case of mixed pixels, unmixing operation is required to identify proportion of different materials within a particular mixed pixel. The discussion on unmixing techniques is not within the scope of this document as we focus on spectral matching techniques – a unique advantage provided by hyperspectral data.

4 Imaging Spectroscopy of Impervious Surface

4.1 Classification Models for Impervious Surface Detection Studies

Following models are predominant classification schemas used in impervious surface detection studies.

Vegetation-Impervious Surface-Soil (V-I-S). The V-I-S model – as it is called – is similar to the conventional diagram used for soil classification. The diagram or V-I-S model can easily characterize various aspects of urban environment under study [17].

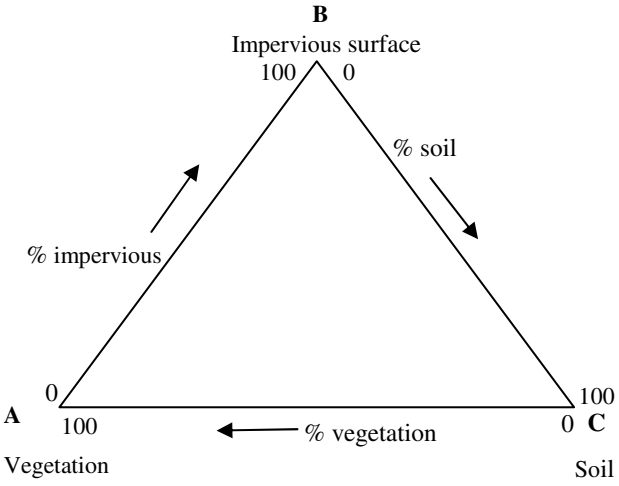

Fig. 2. Vegetation-Impervious surface-Soil model [17]

Urbanization - depending upon the initial condition at the development site and the stage of urbanization - reduces the soil component or vegetation component. Initial plot clearance activities change vegetation or soil cover to impervious surface as these plots would occupy the structure intended for public or private use (Fig. 2). As we may see, some of the conventional USGS classes [18] might coincide with V-I-S, but motivation of V-I-S model is to identify classes that reflect biophysical functions and not the conventional LULC. In fact, each such traditional class may be remodeled using V-I-S.

High Ecological Resolution Classification for Urban Landscapes and Environmental Systems (HERCLUES). Cadenasso et al. [19] discuss some of the drawbacks of existing classification systems and propose a new approach. The objective of the new approach is to complement existing approaches and enhance ecological understanding of urban systems.

HERCULES begins with first three basic classes as V-I-S and then breaks each class further into six features: (1) coarse-textured vegetation (trees and shrubs), (2) fine textured vegetation (herbs and grasses), (3) bare soil, (4) pavement, (5) buildings, and (6) the building typology. Each of these 6 components is allowed to vary independently of the other. Preliminary analysis suggests that HERCULES is better at predicting nitrate yield from urban watersheds than USGS classification [19].

4.2 Signatures of Impervious Surface Materials

Most of the impervious surface detection studies begin with signature analysis of urban materials. It serves two purposes: First it creates a spectral library – a vital component for further analysis, and second it helps in assessing if signatures are separable from each other or not. Separate study for different region is required as signatures of composite urban material vary with their raw material.

Chen et al. [20] study hyperspectral signatures of urban materials to assess their discriminating power and utility of reference spectra for image classification. Field spectra of 20 roofing materials, 12 paving materials, 23 vegetation samples, and 25 miscellaneous urban materials were collected using ASD field spectrometer. Along with the field studies, AVIRIS data was acquired for the study area – Park City, Utah. The field spectra were rescaled to magnitude 0 to 1 and were resampled to match AVIRIS field data.

Herold et al. [21] provide comprehensive analysis of spectra of specific types of materials in urban area. Over 5000 (5500) spectra for 147 uniquematerials in Santa Barbara and Goelta, CA, USA were recorded and analyzed for the signatures using statistical measure. The spectra were measured using ASD, and Full-Range (FR) spectrometer in the range of 350-2400 nm with a spectral resolution of 1.4 nm for the VNIR, and 2.0 nm for the SWIR. The spectra were recorded during 2 hrs of solar noon. The spectra were resampled with 2 nm width to create 1075 bands. Resampled 108 spectra were further analyzed for separability using Bhattacharya Distance.

We summarize below important spectral characteristics of impervious surfaces as recorded by these studies:

1. Sand, gravel, concrete are not distinguishable in broad band data [20].
2. Spectra of asphalt road, parking lots, and some roofs show fairly constant reflectance without a specific absorption. Bare soil spectrum also shows similar behavior [21].
3. New paving asphalt has overall very low reflectance (15% lower than its medium-weathered counterpart) with relatively high increase towards 2100 nm range [21]. Aging asphalt shows increased reflectance in all part of the spectrum – the increased reflectance can be attributed to loss of oil material in sealing. Aging also changes the nature of curve – aging spectral curve show concavity in the range 1000-1600 nm while new asphalt surface show convexity [20], [21].
4. Concrete surfaces have highest reflectance (among the surface types studied) and with aging the reflectance decreases. This behavior is exactly opposite of asphalt surfaces. Concrete roads have high separability. Concrete roads and some roof materials show similar signatures. Concrete shows low separability with bare soil and beach [21].
5. Urban materials lack diagnostic absorption and full spectrum matching techniques should be considered. In cases of two materials with same spectral curve with difference in reflectance magnitude, SAM would not be able to detect the difference – such as asphalt, and paving concrete [20].
6. Though the spectral reflectance of roof materials (mainly shingles) changes with illumination angle, the shape of the spectrum does not change – indicating the utility of spectra to discriminate objects under different (direction wise) illumination condition [21].

4.3 Impervious Surface Detection Using Airborne and Spaceborne Hyperspectral Data

Chen et al [20] attempted to analyze fitness of the field spectra of urban materials in discriminating AVIRIS data. SAM was used for spectral matching with unmixing analysis. They found spectral variability increases uncertainty in analysis of similar types of material. Hence they suggest hybrid spectral analysis – instead of single algorithm - to resolve the spectral ambiguity.

Xu et al. [22] compared results of vegetation and impervious surface classification using ALI and EO-1 imagery for Fremont, California. They used USGS class I classification schema for broad categories and class II for more specific ones. Direct usage of data (without any dimensionality reduction) and Mahalanobis distance classifier produced very similar results for EO-1 and ALI. However, feature reduction in EO-1 data resulted in a jump of 3 percent but ALI results didn't change. Hyperspectral data consistently outperformed ALI results for vegetation and impervious classes. Classification results were improved when class II results were transformed to class I results; jump of 5 percent for EO-1 and 7 percent for ALI was observed.

Weng et al. [23] used EO-1 and ALI data to compare the accuracy of V-I-S classification model. Data for Indianapolis, Marion County, Indiana, USA was collected and processed using principal component analysis – to reduce the size of the data and redundancy. Further using 3-4 end members, fractions of vegetation, impervious surface, and soil in the study area were identified using linear spectral mixture analysis. Both ALI and EO-1 were effective in identifying impervious surfaces and other classes. EO-1 imagery provides more accurate results – especially in case of low reflectance surfaces such as asphalt roads.

Heiden et al. [24] employed features derived from spectral signatures and used maximum likelihood classifier to detect impervious surface. The difference in their approach was twofold: Secondary features from spectral curve were derived instead of using reflectance values of each band, and each material was detected using separate classifier (employing spectral features in different wavelength ranges for different materials). For example, two of all the spectral features considered for polyethylene and roof tiles are "increase" and "absorption" over 486-880 and 1130-1259 for polyethylene and 515-2402 and 454-622 for roof tiles respectively. "Brightness" was the additional feature added to facilitate detection of spectrally bland dark surfaces such as asphalt. They created a spectral library of urban materials using HyMap imagery for Dresden City (1999, 2000, 2003), Germany and Potsdam City (1999), Germany. Four types of features namely: absorption, reflectance peak, increase and decrease of reflectance, continuity of spectral curve were extracted from the training data from spectral library (1999, 2000 images). The results were compared with grey value (or reflectance values) features as suggested by Herold et al. [21].Spectral features showed better results than the grey values.

Approach [24] - though interesting and logical extension of absorption features - needs further investigation. Their current result comparison (between spectral features and grey value features) uses different sets of wavelength ranges for extracting spectral features and grey values – grey values are always extracted from the wavelengths 445 nm, 576 nm, 638 nm, 759 nm, 1100 nm, 1316 nm, 1989 nm. The true comparison would be if the grey values are derived from the same wavelength range corresponding to the range of spectral features.

Weng [3] provides an excellent review of remote sensing of impervious layers in urban area. He rightly points out underutilization of hyperspectral data for impervious surface detection, and believes availability of data with high spectral and spatial resolution augmented with LIDAR provide excellent opportunity for changing the way urban remote sensing is performed.

5 Conclusion

Current research efforts indicate possibility of accurately detecting impervious surfaces in urban area. Most of the urban materials show spectral uniqueness with slight confusion in materials from other classes such as bare soil. Current research using spectral features is focused on feasibility studies, spectral library development, and classification methods for detecting impervious materials accurately. Naturally,

there are no specific preferences to particular spectral features. While some researchers advocate use of full spectrum [20] others use parts of the spectrum [21], [24]. Further investigations and thorough comparative assessment is required to reach maturity.

One of the possible hurdles in exploiting potential of hyperspectral data – especially using spectral matching methods - is efforts required to create spectral library of impervious (and otherwise) materials in a given region. The library using field spectrometer is effort intensive (it took 15 person years to create USGS Splib06a [25]). Creation of spectral library using image derived spectra needs accurate calibration methods that require sound atmospheric correction model and/or synchronized field measurements [26].

Motivation behind studying impervious surfaces is to assess socio-ecological impact of urbanization on its surroundings - on short term and long term basis. Hence, the detection of impervious surface is a primary step taken to understand (and quantify) spatio-temporal relations between urban area and its surroundings. Methods providing quick and consistent results are required to achieve that goal. Possibly, the approaches that use features over part of a spectrum would help better [21], [24]. Development of indices of some sorts for urban materials of our interest hence becomes ultimate objective. The way NDVI has aided study of vegetation changes on large spatio-temporal scales, we can hope urban indices would result in similar amount of insights.

References

1. Arnold Jr., C.L., Gibbons, C.J.: Impervious Surface Coverage: The Emergence of a Key Environmental Indicator. Journal of the American Planning Association 62(2), 243–258 (1996)
2. Jensen, J.R. (ed.): Urban/Suburban Land Use Analysis, Manual of Remote Sensing (R.N. Colwell, editor), 2nd edn., pp. 1571–1666. American Society of Photogrammetry, Falls Church (1983)
3. Weng, Q.: Remote Sensing of Impervious Surfaces in the Urban Areas: Requirements, Methods, and Trends. Remote Sensing of Environment (2011), doi:10.1016/j.rse.2011.02.030
4. Shafri, H.Z.M., Taherzadeh, E., Mansor, S., Ashurov, R.: Hyperspectral Remote Sensing of Urban Areas: an Overview of Techniques and Application. Research Journal of Applied Sciences, Engineering and Technology 4(11), 1557–1565 (2012)
5. Jet Propulsion Laboratory, California Institute of Technology, `http://aviris.jpl.nasa.gov/index.html`
6. Vane, G., Goetz, A.F.H.: Introduction to the Proceedings of the Airborne Imaging Spectrometer (AIS) Data Analysis Workshop. In: Proc. Airborne Imaging Spectrometer Data Analysis, Jet Propulsion Laboratory, California Institute of Technology, April 8,9,10, pp. 1–21. JPL Publication, Pasadena (1985)
7. Goetz, A.F.H., Vane, H.G., Solomon, J.E., Rock, B.N.: Imaging Spectrometry for Earth Remote Sensing. Science 228(4704), 1147–1153 (1985)

8. Jet Propulsion Laboratory, California Institute of Technology, http://aviris.jpl.nasa.gov/data/newdata.html
9. EO-1 User guide v. 2.3, Compiled by: R. Beck, Department of geography, University of Cincinnati, Cincinnati, Ohio (2003)
10. HyVista Corporation, http://www.hyvista.com/
11. Kruse, F.A., Boardman, J.W., Lefkoff, A.B., Young, J.M., Kierein-Young, K.S., Cocks, T.D., Jenssen, R., Cocks, P.A.: HyMap: An Australian Hyperspectral Sensor Solving Global Problems – Results from USA HyMap Data Acquisitions, http://www.hyvista.com/wp_11/wp-content/uploads/2011/02/10ARSPC_hymap.pdf
12. Kruse, F.A., Lakeoff, A.B., Boardman, J.W., Heidbrecht, K.B., Shapiro, A.T., Barloon, P.J., Goetz, A.F.H.: The Spectral Image Processing System (SIPS) – Interactive Visualization and Analysis of Imaging Spectrometer Data. Remote Sensing of Environment 44, 145–163 (1993)
13. Van Der Meer, F., Bakker, W.: CCSM: Cross Correleogram Spectral Matching. International Journal of Remote Sensing 18(5), 1197–1201 (1997)
14. Van Der Meer, F.: Spectral Curve Shape Matching with a Continuum Removed CCSM Algorithm. International Journal of Remote Sensing 21(16), 3179–3185 (2000)
15. Kumar, A.S., Earthy, V., Manjunath, A.S., Van Der Werff, H., Van Der Meer, F.: Hyperspectral Image Classification by a Variable Interval Spectral Average and, Spectral Curve Matching Combined Algorithm. International Journal of Applied Earth Observation and Geoinformation 12, 261–269 (2010)
16. Nidamanuri, R., Zbell, B.: Normalized Spectral Similarity Score (NS^3) as an Efficient Spectral Library Searching Method for Hyperspectral Image Classification. IEEE Journal of Selected Topics in Applied Earth Observations and Remote Sensing 4(1), 226–240 (2011)
17. Ridd, M.K.: Exploring V-I-S (Vegetation – Impervious Surface – Soil) Model for Urban Ecosystem Analysis through Remote Sensing: Comparative Anatomy of the Cities. International Journal of Remote Sensing 16(12), 2165–2185 (1995)
18. Anderson, J.R., Hardy, E.E., Roach, J.T., Witmer, R.E.: A Land Use and Land Cover Classification System for Use With Remote Sensor Data, Geological Survey Professional Paper 964. United States Government Printing Office, Washington (1976)
19. Cadenasso, M.L., Pickett, S.T.A., Schwarz, K.: Spatial Heterogeneity in Urban Ecosystems: Reconceptualizing Land Cover and a Framework for Classification. Frontiers in Ecology and the Environment 5(2), 80–88 (2007)
20. Chen, J., Hepner, G.: Investigation of Imaging Spectroscopy for Discriminating Urban Land Covers and Surface Materials. In: 2001 AVIRIS Earth Science and Applications Workshop, Palo Alto, California (2001), ftp://popo.jpl.nasa.gov/pub/docs/workshops/01_docs/2001Chen_web.pdf
21. Herold, M., Roberts, D., Gardner, M.E., Dennison, P.E.: Spectrometry for Urban Area Remote Sensing—Development and Analysis of a Spectral Library from 350 to 2400 nm. Remote Sensing of Environment 91, 304–319 (2004)
22. Xu, B., Gong, P.: Land-use/land-cover Classification with Multispectral and Hyperspectral EO-1 data. Photogrammetric Engineering and Remote Sensing 73(8), 955–965 (2007)
23. Weng, Q., Hu, X., Lu, D.: Extracting Impervious Surfaces from Medium Spatial Resolution Multispectral and Hyperspectral Imagery: a Comparison. International Journal of Remote Sensing 29(11), 3209–3232 (2008)

24. Heiden, U., Segl, K., Kaufmann, H.: Determination of Robust Spectral Features for Identification of Urban Surface Materials in Hyperspectral Remote Sensing Data. Remote Sensing of Environment 111(4), 537–552 (2007)
25. Clark, R.N., Swayze, G.A., Livo, K.E., Hoefen, T., Kolkaly, R., Sutley, S.J.: USGS Digital Spectral Library splib06a: U.S. Geological Survey. Digital Data Series, vol. 231 (2007), http://speclab.cr.usgs.gov/spectral-lib.html
26. Clark, R.N., Swayze, G.A., Livo, K.E., Kokaly, R.F., King, T.V.V., Dalton, J.B., Vance, J.S., Rockwell, B.W., Hoefen, T., McDougal, R.R.: Surface Reflectance Calibration of Terrestrial Imaging Spectroscopy Data: a Tutorial Using AVIRIS. In: Proceedings of the 10th Airborne Earth Science Workshop. JPL Publication 02-1 (2002)

The Study of the Talent Evaluation System Based on Multi-criteria Decision-Making Method of Grey Linguistic

Xin Wu[1] and ZhiFeng Li[1,2]

[1] School of Information Management, Wuhan University, Wuhan, China
wuxintt@163.net
[2] Department of Marketing, Guangdong Peizheng College, Guangzhou, China
Toyota99@21cn.com

Abstract. Due to the insufficient information in the current talent evaluation standards, and uneven evaluation standards of evaluation experts, the evaluation results vary greatly. Therefore, based on the multi-criteria decision-making models of grey linguistic, this paper re-defines the evaluation standards and evaluation models of talent evaluation system so as to make its information more complete. Through experiments, it is found the evaluation is more correct and objective.

Keywords: Talent evaluation, Multi-criteria, Grey linguistic.

1 Introduction

Innovative industry is the main economic growth point for current China. However, innovative industry needs to cultivate innovative sci-tech talents while building a large innovative team composed by sci-tech talents must first correctly define the innovative sci-tech talents. Specifically, a set of scientific, reasonable and adaptive evaluation standards for innovative sci-tech talents shall be established. Secondly, talent evaluation has already become a kind of industry abroad. However, it is not only always a challenge for Chinese human resource management field to research an innovative sci-tech talent evaluation system adaptive to Chinese economic and technological development zones based on introducing foreign mature talent evaluation technology; but also the key to maintain the competitiveness of Chinese economy and technology. Thirdly, the evaluation system for innovative sci-tech talents studied in this paper is also with important theoretical reference value for the government civil servant selection, researcher evaluation, and enterprise recruitment and employee performance assessment.

At present, the Chinese innovative talent evaluation theories are not complete and lacking of adaptive and targeted evaluation system. Consequently, under the premise of perfecting theoretical basis, it is necessary to establish a new innovative talent evaluation system and conduct case study on the detailed application of new evaluation system in the talent work of the economic and technological development zones so as to solve the above problem. This is also the research starting point of this paper.

F. Bian et al. (Eds.): GRMSE 2013, Part I, CCIS 398, pp. 141–146, 2013.
© Springer-Verlag Berlin Heidelberg 2013

2 Literature Review

2.1 Talent Evaluation

Construct the index system based on occupational analysis theory. The occupational analysis theory believes, the talent evaluation index shall be determined by collecting detailed information of the company positions such as rights and liabilities scope, needed skills and required education. Through decomposing positions into position factors, McCormick established Position Analysis Questionnaire (PAQ) system and provided important index for comprehensive evaluation for talents. From the aspect of position and task description, Fleishman(2012) built F-JAS system for talent evaluation from four angles of ability, technology, knowledge and social interpersonal relationship [1]. Based on the two important factors like added value and substitutability of talents, Zuboff(1988)put forward talent evaluation matrix. With the changes of job nature [2], Cascio(1995)pointed out that the talent evaluation system based on occupational analysis is not static but adaptive to the different positions with similar skills [3]. Sidney(1999) analyzed the American positions, formulated functional job analysis, and established talent evaluation index system including position index, reasoning logic, math ability and language ability [4]. This is widely used in the human resource field now. Through analyzing the life cycle of enterprise positions, Sloan(2003) proposed classified talent evaluation by utilizing life cycle theories [5]. From the occupational analysis perspective, Boudreau(2005) put forward the LAMP talent management frame, constructed talent evaluation index from logic structure, analysis, measurement method and process management, and applied decision-making and scientific methods to realize talent evaluation and management [6].

2.2 Multi-criteria Decision-Making Models of Grey Linguistic

A In grey system overview, Deng(1989)pointed out that grey system was a mathematical system with quantified information[7].Besides, there were white system and black system included in the grey system, in which the white system appeared when all the information in a system was transparent, and black if not. However, if the channel of information was not transparent while the system information was semitransparent, grey system was achieved. According to Huang (1999), in traditional fuzzy logic, the problem will become very complicated when there were numerous variables [8].

The improvement of network evaluation summarized from the above documents tends to be a major concern for the improvement of modern network society. To promote a more fair evaluation with large amount of information, many researchers are devoting themselves to studying the evaluation. Multi-criteria decision-making models of grey linguistic can be applied to the evaluation, as well as decision support. In conclusion, multi-criteria decision-making models of grey linguistic can be applied to the evaluation of networking products.

3 Innovative Talent Evaluation System

3.1 System Modeling

Through inputting data related to innovative talents in the front-end information system, the applicants can enter the evaluation standard model. Then the evaluation standard model can draw the evaluation standard for this type of innovative talent, experts of different domains will give criteria based on evaluation standard model, the criteria form a decision-making matrix, the relevant decision-making matrix will be input in the multi-criteria decision-making model of grey linguistic, and finally the evaluation order for innovative talents can be obtained.

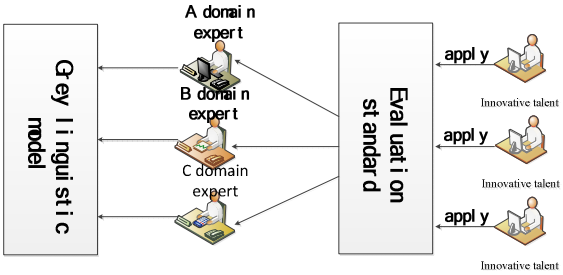

Fig. 1. Innovative evaluation system

The traditional evaluation index can only generate three kinds of evaluation for ratee: the most innovative, innovative and not innovative respectively. However, such evaluation grade is not enough for evaluating innovative talents. (1) The current evaluation index are not more enough for evaluation of all innovative talents. (2) As different experts offer different evaluation standards, the evaluation results may be different due to the changes of subjective factors. (3) Experts do not have a sufficient understanding of the ratee, and the information transparency for ratee's information is not enough.

3.2 Evaluation form Comparison

Table 1. Old Evaluation Form

Please evaluate the innovative level of the ratee		
Name:	Accept evaluation:	
○ The most innovative	○ Innovative	◉ Not innovative

The improved evaluation standard has multiple evaluation grades for innovative talents and the evaluation grade number can be from H0 to Hn+1. Moreover, the new evaluation form has certain valuator types and information transparency, which further allows experts to fill their degree of familiarity on this aspect.

Table 2. Old Evaluation Form

Give the evaluation						
Name:	Number:	Weight ( )	Talents Category ( )		The transparency of information ( )	
○ H0	○ H1	○ H3	◉ H4	○ H5	○ H6	○ H7....Hn+1

The ratee is required to submit evaluation data as innovative talents to the system. After the system collects relevant evaluation standards for innovative talents, it can be evaluated by the grey linguistic criteria made by experts of different domains. Fill the grey linguistic evaluation table, and the system will convert the evaluation of different experts into decision-making matrix and input decision-making matrix into the multi-criteria decision-making models of grey linguistic and the multi-criteria decision-making models of grey linguistic will determine the ranking of innovative talents and show the results in the front-end information system.

The standard of innovative talents is described as grey linguistic criteria in grey system. There are many evaluation dimensions for innovative talents from innovative thinking, innovative ability to innovative psychology and others. Different dimensional factors can be transferred into different criteria influencing factors. Then the criteria constitute the grey evaluation matrix and the evaluation matrix determines the innovative talents through the multi-criteria decision-making models of grey linguistic.

4 Sample Statistics and Verification

Definition Let talent $\tilde{A}(x)$ be the fuzzy subset in the space $X=\{x\}$, if the membership degree $\mu_A(x)$ of x to $\tilde{A}(x)$ is the grey in the interval $[0,1]$, and its grey is $\nu_A(x)$, then $\tilde{A}(x)$ is called the grey fuzzy set in space X (GF set, for short), denoted by $\tilde{\underset{\otimes}{A}}(x)$, as follows[8]:

$$\tilde{\underset{\otimes}{A}}(x)=\left\{(x,\mu_A(x),\nu_A(x))\middle| x\in X\right\} \tag{1}$$

The set pair mode is $\tilde{\underset{\otimes}{A}}(x)=(\tilde{A}(x),\underset{\otimes}{A}(x))$, where $\tilde{A}(x)=\left\{(x,\mu_A(x))\middle| x\in X\right\}$ is called the fuzzy part of $\tilde{\underset{\otimes}{A}}(x)$, and $\underset{\otimes}{A}(x)=\left\{(x,\nu_A(x))\middle| x\in X\right\}$ is called the grey part of $\tilde{\underset{\otimes}{A}}(x)$. So the grey fuzzy set is regarded as the generalization of the fuzzy set and the grey set [10].

Table 3. Expert 1's Evaluations Matrix

EXPERTS	A_1	A_2	A_3	A_4
E1	(H6[0.3,0.4])	(H5[0.5,0.4])	(H2[0.3,0.4])	(H7[0.3,0.4])
E2	(H4[0.5,0.7])	(H2[0.3,0.4])	(H4[0.5,0.6])	(H3[0.6,0.4])
E3	(H1[0.4,0.4])	(H4[0.7,0.5])	(H1[0.2,0.2])	(H5[0.5,0.4])
E4	(H7[0.2,0.4])	(H7[0.6,0.7])	(H7[0.3,0.6])	(H7[0.6,0.4])

Table 4. Expert 2's Evaluations Matrix

EXPERTS	A_1	A_2	A_3	A_4
E1	(H5[0.5,0.7])	(H3[0.2,0.3])	(H4[0.2,0.4])	(H5[0.3,0.5])
E2	(H6[0.3,0.4])	(H5[0.3,0.4])	(H7[0.7,0.7])	(H4[0.4,0.5])
E3	(H7[0.6,0.7])	(H6[0.6,0.6])	(H6[0.2,0.6])	(H5[0.5,0.5])
E4	(H3[0.3,0.4])	(H6[0.5,0.7])	(H5[0.3,0.4])	(H6[0.6,0.4])

Table 5. Expert 3's Evaluations Matrix

EXPERTS	A_1	A_2	A_3	A_4
E1	(H5[0.4,0.7])	(H2[0.3,0.2])	(H7[0.7,0.6])	(H4[0.3,0.4])
E2	(H1[0.1,0.1])	(H7[0.6,0.7])	(H6[0.3,0.6])	(H5[0.4,0.4])
E3	(H4[0.3,0.4])	(H6[0.3,0.4])	(H6[0.6,0.6])	(H3[0.3,0.4])
E4	(H2[0.3,0.2])	(H5[0.3,0.5])	(H5[0.3,0.4])	(H6[0.5,0.6])

We use the formula shown in upper and the variables to compute the grey linguistic model.

After using the GLWAA operator computing:

$$M=\begin{Bmatrix}[1.66,0.42,0.70][2.40,0.91,0.70][2.83,1.12,0.70][4.43,1.60,0.70]\\ [0.73,0.26,0.70][2.60,1.10,0.70][3.17,1.39,0.70][4.37,1.93,0.70]\\ [0.80,0.39,0.70][2.93,1.48,0.70][3.37,1.64,0.70][4.67,2.23,0.70]\\ [0.80,0.19,0.40][3.20,1.35,0.70][3.77,1.52,0.70][5.67,2.60,0.70]\end{Bmatrix}$$

A1=0.481; A2=0.579; A3=0.671; A4=0.781

System Talents Ranking: A4, A3 ,A2 ,A1,talent A4 is the priority selected.

5 Conclusion

The selection of innovative talents is the most important link for current talent selection. Different from the selection of other talents, the selection of innovative talents is composed by multiple dimensional innovation aspects. The evaluation of current innovative talents is far from meeting the evaluation needs. Through the multi-criteria decision-making models of grey linguistic, this paper provides construction basis and mathematical model for the evaluation of innovative talents.

References

1. Fleishman, E.A., Quaintance, M.K., Broedling, L.A.: Taxonomies of human performance: The description of human tasks (EB/OL) (1984), http://siop.org/tip/Archives/online/TIP%20Volume%2021,%20Issue%204.pdf (March 20, 2012)
2. Zuboff, S.: In the age of the smart machine: The future of work and power. Basic Books, New York (1988)
3. Cascio, W.F.: Whither industrial and organizational psychology in a changing world of work? American Psychologist 50(11), 928–939 (1995)
4. Fine Sidney, A., Cronshaw Steven, F.: Functional job analysis: A foundation for human resources management. Lawrence Erlbaum Associates Publishers, Mahwah (1999)
5. Sloan, E.B., Lewis, R.E.: Managing succession successfully. In: Workshop presented at the Annual Conference of the Society for Industrial/Organizational Psychology, Orlando, FL (2003)
6. Boudreau, J.W.: Talentship and the New Paradigm for Human Resource Management: From Professional Practices to Strategic Talent Decision Science. Human Resource Planning 28, 23 (2005)
7. Deng, J.L.: Introduction to grey system. The Journal of Grey System (UK) 1(1), 1–24 (1989)
8. Huang, Y.-P., Chu, H.-C.: Simplifying fuzzy modeling by both grey relational analysis and data transformation methods. Fuzzy Sets and Systems 104(2), 183–197 (1999)

Extenic Image Classifier and Its Application in the Land Use Classification

Jiafa Tang and Han Xie

Dept. Remote Sensing and Geospatial Information,
Southwest Jiaotong University, Chengdu, P.R. China, 610031
tajava@home.swjtu.edu.cn,
1045372604@qq.com

Abstract. The theory of Extenic was put forward by the Chinese scientist, Prof. Cai wen, in 1983. As a new kind of artificial intelligence method, it has been used in the many areas, this paper use it to extract the land use information from the remote sensing image. The research area in this paper is the plan area of city of the Du Jiang Yan, which locates in the northwest of the Sichuan basin and the data used here is the HJ satellite image. It has four kinds of land use type in the ground, the forest land, the water body, the built-up land and the farm land, different land use type in the ground has different color in the false color image, and the 11 subtypes are divided according to the relationship analysis of the land use type and the pixel color of the image. The 11 standard matter-element models, which corresponding to 11 subtypes of the land use, are built at first, then calculate the extension correlation degrees of each pixel in the image to the 11 standard matter-element models and finally, and finally the pixel is determined to belong the land use type which has the biggest extension correlation degree. The right rate of the classification is about 87.2% and the Kappa index is 0.86, it shows that the classifier based on the theory of the Extenic has the high precision in the classification of the remote sensing images.

Keywords: Extenic image classifier, Remote sensing image, Land use.

1 Introduction

Classification is regarded as a fundamental process in remote sensing, which lies at the heart of the transformation from satellite image to usable geographic product [1]. The traditional classification methods include supervised and unsupervised classification methods, and they are both belonging to the statistical method [2, 3]. Some new classification methods, such as the neural network method [4], fuzzy mathematics method [5], the genetic algorithm method [6], support vector machines [7], the object-oriented method [8] etc., have been used in the classification of the remote sensing images in the recent years. Because there is still considerable scope for further increases in accuracy to be obtained and a strong desire to maximize the degree of land cover information extraction from remotely sensed data, the research into new methods of classification has continued [7].

F. Bian et al. (Eds.): GRMSE 2013, Part I, CCIS 398, pp. 147–154, 2013.
© Springer-Verlag Berlin Heidelberg 2013

The theory of extenic was put forward by the Chinese scientist, Prof. Cai wen, in 1983 [9]. As a new kind of artificial intelligence method, it has been used in many areas, such as the system control [10], decision technique [11] and so on. The objective of this paper are to develop a new image classification method based the theory of extenic, and try to use it to extract the land use information from the image of the HJ satellite. The research area is the plan area of city of the Du Jiang Yan city, which is located in the northwest of the Sichuan basin. The results of the classification show that the classifier based on the theory of the extenic has the high precision in the image classification.

2 The Theory and Method of the Extenic Image Classifier

Using formalized model to describe the problem and solve the problem with extenic logic is the character of the extenic theory. In order to use the extenic theory in the classification of the remote sensing image, two kinds of matter-element models, one is about the land use types that used as standard pattern in the classification and the other is about the pixel of the image, should be set up at first. Then, calculate the correlation degrees of the pixel model to the land use models using the extenic method and the pixel's belonging is determined by the maxim of the correlation degree.

2.1 Building the Matter-Element Model

Matter element is the basic logic unit of the extenic theory to describe the real world. In the view of the extenic theory, the object in the real world can be abstracted as three parts: the object, the characteristics, and their corresponding values. Thus, the object can be noted as:

$$R = (\text{Object, Characters, Values}) = (N, C, C(v)) \tag{1}$$

where N denotes the matter's name, C represents the characteristics of the matter and v denotes the value corresponding to the characteristic.

In this way, an object of the real world can be expressed by the numerous characters with the corresponding value which are defined by the observer, and the process of this abstraction is so called the "building matter-element model" according to the extenic theory.

There are two kinds of the matter-element of the image information should be set up. The first one is the typical land use model, which is the reflection of the prior knowledge about the land use types in the ground and their characters in the image, and in this paper, it refers the spectral characters of the image. So the matter-element model about the land use type is:

$$L = \begin{bmatrix} Landuse & band_1 & v_1 \\ & band_2 & v_2 \\ & \cdots & \cdots \\ & band_n & v_n \end{bmatrix} \tag{2}$$

where *Landuse* is the name of the land use type, $band_{i(i=1,2,...,n)}$ is the spectral band that contained in the remote sensing image, $v_{i(i=1,2,...,n)}$ is the DN (Digital Number) value or value domain of the corresponding spectral band, and in this paper, it refers the value domain.

The numbers of this kind model is corresponding to the land use types that will be used in the image classification, and each type has one model.

The second model is the image pixel model. The matter-element model of the pixel is:

$$P = \begin{bmatrix} Pixel & band_1 & v_1 \\ & band_2 & v_2 \\ & \cdots & \cdots \\ & band_n & v_n \end{bmatrix} \tag{3}$$

where *Pixel* is the name of the pixel, $band_{i(i=1,2,...,n)}$ is the spectral band that contained in the remote sensing image, $v_{i(i=1,2,...,n)}$ is the pixel DN value of the corresponding spectral band in the image

Each pixel in the image is waiting for the determination, so each pixel has its own matter-element model.

2.2 Setting Up the Correlation Function

Correlation function is the basic tool that used to measure the relationship of the different objects in the extension set.

Supposed, $X_0 =< a,b >, X =< c,d >, X_0 \subset X$ and they have no common end points,

$$K(x) = \frac{\rho(x, X_0)}{D(x, X_0, X)} \tag{4}$$

where,

$$\rho(x, X_0) = \left| x - \frac{a+b}{2} \right| - \frac{1}{2}(b-a)$$

$$D(x, X_0, X) = \begin{cases} \rho(x, X) - \rho(x, X_0), x \notin X_0 \\ -1, x \in X_0 \end{cases}$$

2.3 Calculate the Correlation Degree and Determine the Pixel'S Belonging

Equation 4 is the way of calculating the extenic distance. Each matter-element model has several elements, so the extension correlation degree of the pixel model to each land use model is the weight sum of the extension distance of each element, and it can be calculated through the equation 5.

$$K(P) = \sum_{i=1}^{n} \alpha_i K\ (v_i) \tag{5}$$

where, n equals to the numbers of the elements in the matter-element models, α is weight coefficient.

The extension correlation degree is the index of the extenic image classifier and the land use type that the pixel belonged can be determined by the maxim of the total extension correlations degree (Equation 6).

$$K_{j_0}(P) = \max_{j_0 \in \{1,2,\ldots,n\}} K_j(P) \tag{6}$$

where n equals to the numbers of the land use type models.

The whole image is scanned and each pixel is determined to what the type it should be through the equation 4.

3 Application of the Extenic Image Classifier in the Land Use Classification Using the Remote Sensing Image

In this paper, the extenic image classifier is used to extract the land use information from the image of the HJ satellite. The research area is the plan area of city of the Du Jiang Yan city, with the geographic coordinate of 103°25′42″E ~ 103°47′0″E and 31°44′54″N ~31°02′9″N. The northwest of the city is the mountain area; the southeast is the plan area, which is the research area of this paper. The population density in plan area is fairly high with strong economic activity; this character is enhanced along with the large-scale reconstruction after the earthquake of the 2008, and the land use pattern has changed a lot since 2008.

3.1 Data Preparation and the Image Character Analysis

Data Preparation

The remote sensing image used for the research is the HJ satellite image with the spatial resolution of 30m, it has four bands: blue light, red light, green light and infra-red light. The data used in this paper is got by the HJ-A satellite in 2009-04-29(Path number: 13-80).The satellite image is registered with the administrative map of Du

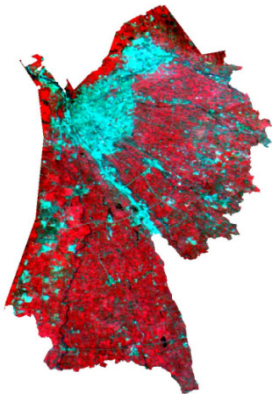

Fig. 1. The false color image of the plan area of the Du Jiang Yan city

Jiangyan (the scale is 1:100,000) and the Aster DEM which is got from the USGS website, then the area with the altitude lower than 800m of the city is subset from the image.

Image Analysis

There are four kinds of land use types in the research area, the farmland, the built-up land, the water body and the forest land. Because the imaging time is the early spring, so the crops in the farmland are the dry crops, such as the vegetable, rape, wheat and so on, these crops have pink color in the false color image. The main water bodies in the area are the rivers and irrigate channels, and they have the blue black color in the false color image. The residential area are widely spread in the whole area, the color of them is steel grey or white, some buildings under the construction have the deep green or fresh green color. The road can also be regarded as a kind of built-up land, and it has the same color with residential area in the false color image. The forest land has two colors: deep red and fresh red in the image, it may be caused by the variety or the age of the forest.

The pixels in the image responding to the typical land use type of the ground have the typical colors, and these pixels are easy to be interpreted. All the land use types are mixed together in the ground and the imaging time is the early spring, for these reasons, some pixels in the images which responding to the edges of the different types don't have the typical color, it brings some confusion to the interpretation of these pixels.

3.2 Building the Matter-Element Models for the Land Use Types and the Image Pixels

In order to improve the accuracy of the classification, each land use type is divided into several subtypes according the image analysis. The farm land has 2 subtypes, the forest land has 2 subtypes, the water body has 2 subtypes and the built-up land had 5 subtypes. So, there are totally 11 matter-element models, which represent 11 subtypes of land use subtypes, should be set up, and the equation 2 is the sample of the land use matter-element model.

The false color remote sensing image has three bands: infrared light band, red light band and green light band, so the land use matter-element model has three elements: the IR, the RED and the Green. The partial domain of each element can be got from the image through the statistic of the ROIs, which are collected by means of on-screen selection of the point mode using the software of ENVI. In the RGB color space of the image, the digital number (DN) of each band varies from 0 to 255, so the classical domain of the each element is [0, 255].All these models are showed in the table 1.

The matter-element model of the pixels can also be set up as the sample in equation 3. It also has the three elements, and its DN value in the image is the value of each element. Each pixel in the image has its own matter-element model

$$P = \begin{bmatrix} Piexl & P & \text{IR} & \text{DN}_1 \\ & & \text{RED} & \text{DN}_2 \\ & & \text{GREEN} & \text{DN}_3 \end{bmatrix}$$

Table 1. The standard land use matter-element models

Land use types	Matter-element model
Forest land	$R_1 = \begin{bmatrix} \{Deep\ \text{red frest land A}, & \text{IR}, & <90,94> \\ & \text{RED}, & <43,45> \\ & \text{GREEN} & <43,45> \end{bmatrix}$
	$R_2 = \begin{bmatrix} \{Fresh\ \text{red froest land B}\}, & \text{IR}, & <109,121> \\ & \text{RED}, & <41,47> \\ & \text{GREEN} & <42,46> \end{bmatrix}$
Farm land	$R_3 = \begin{bmatrix} \{Pink\ \text{farmland C}\}, & \text{IR}, & <104,111> \\ & \text{RED}, & <49,52> \\ & \text{GREEN} & <49,52> \end{bmatrix}$
	$R_4 = \begin{bmatrix} \{Pink\ \text{farm land D}\}, & \text{IR}, & <91,98> \\ & \text{RED}, & <47,50> \\ & \text{GREEN} & <47,50> \end{bmatrix}$
Water body	$R_5 = \begin{bmatrix} \{Blue\ \text{water body F}\}, & \text{IR}, & <60,73> \\ & \text{RED}, & <52,57> \\ & \text{GREEN} & <53,56> \end{bmatrix}$
	$R_6 = \begin{bmatrix} \{Blue\ \text{water body G}\}, & \text{IR}, & <42,58> \\ & \text{RED}, & <48,52> \\ & \text{GREEN} & <51,54> \end{bmatrix}$
Built-up land	$R_7 = \begin{bmatrix} \{White\ \text{Built - up land J}\}, & \text{IR}, & <99,136> \\ & \text{RED}, & <87,118> \\ & \text{GREEN} & <66,104> \end{bmatrix}$
	$R_8 = \begin{bmatrix} \{Cyan\ \text{blue built - up land K}\}, & \text{IR}, & <60,75> \\ & \text{RED}, & <66,73> \\ & \text{GREEN} & <57,64> \end{bmatrix}$
	$R_9 = \begin{bmatrix} Cyan\ \text{blue built - up land } L\}, & \text{IR}, & <75,86 \\ & \text{RED}, & <56,63> \\ & \text{GREEN} & <52,57> \end{bmatrix}$
	$R_{10} = \begin{bmatrix} \{Deep\ \text{green built - up land N}\} & \text{IR}, & <60,69 \\ & \text{RED}, & <51,55> \\ & \text{GREEN} & <47,50> \end{bmatrix}$
	$R_{11} = \begin{bmatrix} \{Fresh\ \text{green buiilt - up land O}\} & \text{IR}, & <60,72 \\ & \text{RED}, & <60,66> \\ & \text{GREEN} & <51,55 \end{bmatrix}$
Classical domain of each element	$R_P = \begin{bmatrix} \{Objects\ \}, & IR, & <0,255> \\ & RED, & <0,255> \\ & GREEN, & <0,255> \end{bmatrix}$

3.3 Result and Discussion

Result of the Image Classification

The whole image is scanned and each pixel is determined to what the subtypes it should be through the equation 4-6. It has 3 elements in the matter-element models and each one has the equal importance, so in the calculation of the equation 5, the n = 3, and the α=(1/3, 1/3, 1/3). There are 11 models in the table 1, so in the calculation of the equation 6, the n = 11. After that, the subtypes are merged according to the table 1. The Fig.2 is final map of the land use classification.

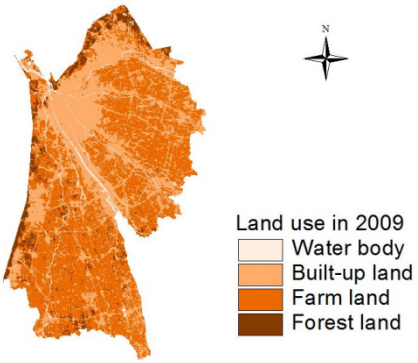

Fig. 2. The land use classification of the plan area of the Du Jiang Yan city

The Analysis of the Classification Accuracy

Generally, the land use types in the classification map have the same space distribution with the original remote sensing image; it means that extenic classifier works well in the land use classification, and the right rate of the classification is about 87.2%. The Kappa index is another way to estimate the classification accuracy, it is up to 0.86 in this paper, and that means the extenic classifier has the high classification accuracy.

4 Conclusion

In this paper, a classification based on the extenic theory is used to extract the land use information from the remote sensing image. The key of this method is how to set up the matter-element model of the land use types, which related the land use type in the ground and the pixel in the image. The research area of this paper is the Du Jiang Yan's plan area, and the final result of the land use classification shows that the method used in this paper has a high precision in the classification of the remote sensing images.

The elements in the model are spectral band, so in the classification of the image, it cannot avoid the errors which caused by the phenomenon of "same object with different spectra" and "'same spectral for different objects", and getting the partial domain of the land use types accurately is the key to reduce these errors.

Acknowledgment. This paper is supported by the Ministry of education of Humanities and social science fund plan (12YJAZH124) and the Fundamental Research Funds for the Central Universities (A0920502051308-12).

References

1. Wilkinson, G.G.: Results and implications of a study of fifteen years of satellite image classification experiments. IEEE Transactions on Geoscience and Remote Sensing 43(3), 433–440 (2005)

2. Strahler, A.H.: The use of prior probabilities in maximum likelihood classification of remotely sensed data. Remote Sensing of Environment 10(2), 135–163 (1980)
3. Aksoy, S., Koperski, K., Tusk, C., et al.: Learning bayesian classifiers for scene classification with a visual grammar. IEEE Transactions on Geoscience and Remote Sensing 43(3), 581–589 (2005)
4. Frizzelle, B.G., Moody, A.: Mapping continuous distributions of land cover: a comparison of maximum-likelihood estimation and artificial neural networks. Photogrammetric Engineering & Remote Sensing 67(6), 693–705 (2001)
5. Wang, F.: Fuzzy supervised classification of remote sensing images. IEEE Transactions on Geoscience and Remote Sensing 28(2), 194–201 (1990)
6. Bandyopadhyay, S., Pal, S.: Pixel classification using variable string genetic algorithms with chromosome differentiation. IEEE Transactions on Geoscience and Remote Sensing 39(2), 303–308 (2001)
7. Foody, G.M., Mathur, A.: A relative evaluation of multi class image classification by support vector machines. IEEE Transactions on Geoscience and Remote Sensing 42(6), 1335–1343 (2004)
8. Hai-yang, Y., Gang, C., Xiao-San, G., Xiao-Ping, L.: Object oriented land cover classification using ALS and GeoEye imagery over mining area. Original Research Article Transactions of Nonferrous Metals Society of China 21(3), 733–737 (2011)
9. Cai, W., Yang, C.Y., Ling, W.C.: The Extension Engineering Method, pp. 17–18. Since Press, Beijing (2000)
10. Zheng, H., Sun, Y., Xian, C.: Research of multi-mode extension control for pump-control electro-hydraulic servo system. China Metal Forming Equipment & Manufacturing Technology (5), 86–90 (2011)
11. Shi, K., Diao, C., Sun, X.: Evaluation of soil-water resources carrying capacity based on entropy weight extension decision model in the Three Gorges Reservoir Region of Chongqing. Acta Scientiae Circumstantiae 33(2), 609–616 (2013)

Classification Method for Object Feature Extraction Based on Laser Scanning Data

Kun Yu, Ting Li, Jie Chen, Fang Wu, and Changkui Sun

China Aero Geophysical Survey & Remote Sensing Centre for Land and Resources, Beijing, 10083, China
{211544,6592296}@qq.com,
tingziforever@foxmail.com,
{wufang027,sunchangkui}@163.com

Abstract. Mobile laser scanning has many advantages compared to traditional survey technology. These characteristics make it possible to rapidly acquire large-area high-precision 3D spatial data for reconstruction of 3D model. In this paper, we focus on the classification and recognition of mobile laser scanning data. We present a method based on object feature extraction. The main workflow of this method is made up by extraction of geometric feature from scanning data, foundation of objects feature knowledge database, extraction of main feature by PCA (Principal Component Analysis) to match geometric features, multi-level classification according to object's principal feature at last. This method has been applied to data points obtained by mobile laser scanning system; the experiment results show that the proposed classification method is promising.

Keywords: mobile laser scanning data, classification, feature extraction, PCA.

1 Introduction

With the rising demand of city digitalizing and informationization, how to use high efficient and accurate method to reconstruct 3D city model is becoming the key step and difficulty in achieving those. Mobile laser scanning has advantages of rapid, non-contact, real-time, dynamic, active, high-density, high precision and so on [1], which can quickly capture a large area of high-precise 3D spatial data, and get the surface information of buildings, roads, vegetation and other cities' objects. In addition, it provided a new idea for 3D modelling while traditional photogrammetric methods encountered a series of bottlenecks.

The main workflow of point clouds processing includes pre-processing, segmentation, classification (recognition), modelling. Rapid and accurate classification can provide more precise and reliable information for various applications. Classification has become an urgent problem to be solved in 3D model filed. This paper focuses on the classification and recognition parts.

F. Bian et al. (Eds.): GRMSE 2013, Part I, CCIS 398, pp. 155–165, 2013.
© Springer-Verlag Berlin Heidelberg 2013

2 The Status of Research on Point Clouds Classification at Home and Abroad

Researches on the automatic classification and recognition of the laser scanner data is still in its early stage in China. The early research focused on multi-sensor data integration and feature extraction and recognition based on the image information, while taking the Laser technology only as an auxiliary tool. With the development of the Laser Scanner technology, more and more researches were made on the classification and recognition of point clouds. Li Bijun et al. (2003) proposed a method for information mining based on the geometric features of buildings, but we have to make a rough estimate on the observations according to prior known information when making classification between the terrain and the above-ground objects and denoising for point clouds [2]. Shi Wenzhong et al. (2005) proposed an image segmentation method for ALS distance based on the density of projective points [3]. Li Yongqiang et al. (2008) proposed a method for 3D-road information extraction based on point clouds, but this method over depends on artificial interaction, and is unsuitable for complicated urban environment [4].

Studies in this field started earlier at abroad. Many robot researchers have already developed fairly ideal algorithms for automatic recognition of point clouds. MANANDHAR.D and SHUBASAKIR (2001) proposed an algorithm that classifies laser data into different groups according to the Spatial distribution of the points(such as the geometric features, degree of dispersion, density information) [5], however, further study should be made because the application for the mixed arranged point still seems to be very complicated. Shi Pu and George Vosselman (2009) proposed a method for point clouds feature detection based on building semantics. The algorithm aims at extracting semantic features such as wall, gate, window, the projecting portion and indented part and roof, from point clouds to forming buildings. Firstly, the point clouds were divided so that each data group included only one semantic feature. Then classification was made, according to the size, location, orientation topology or the point's density of the semantic features, to extracting different semantic features for realizing the 3D building reconstruction [6].

In this paper, we designed a relatively integrated model for laser scanning data classification based on features of urban block objects. First of all, various semantic features of block objects were extracted to establish classification rules for block objects. In the next step, the established rules should be transformed to feature constraints that can be easily understood by computer. Then we extracted the principle features via the PCA. Finally a hierarchical classification mode was established.

3 Classification Method Based on PCA

Principal Component Analysis means finding out the most "principal" elements and components effectively. This procedure can remove noise and redundancy, revealing

the simple structure hidden behind complex data [7]. The main steps of the proposed method based on PCA is listed as following:

The 1st step, extracting of geometric features from scanning data and segmented points plane, this features include elevation, normal vector, planer fitting residual, Planar projection area and density in XOY plane, etc.

The 2nd step, taking the spatial distribution and geometric structure characteristics of block objects into consideration, summarizing knowledge rules.

The 3rd step, extracting main feature according to geometric features of corresponding object class.

The 4th step, using PCA method to classify raw point clouds into different classes and recognizing it.

3.1 Extraction of Geometric Features

The raw data obtained by mobile laser scanner are scatter points, involve coordinates, colour, and intensity etc. This makes a single point cloud data unable to reveal the overall characteristics of the object. So raw data requires pre-process such as segmentation before classification. We use point proximity and the local smoothness of the surface as two standards for determining the surface extension and seed growth. After processing, point cloud data of the same or similar properties and space adjacent is divided into a segmented points plane [8]

Taking the spatial distribution and geometry structure characteristics of block objects and segmented points plane into consideration, we can extract features including elevation, normal vector, planer fitting residual, Planar projection area and density in XOY plane, etc.

3.1.1 Planar Fitting. We usually use least squares method for planar fitting, this make the square of vertical distance between all points to the fitting planar minimum. Although most surface estimation is nonlinear, we can use plane equation for fitting in order to reduce the number of parameters and speed up the processing speed. The slant range-type formula used for plane fitting of LIDAR point clouds is as bellow:

$$Z = aX + bY + c \tag{1}$$

But for urban blocks data, planes vertical to or near vertical to XOY plane is of very high frequency. Equation 3.1 may results in some wrongly-fitted planes. So we search for other parameter equation. Taking into account that there are little planes precisely through the origin, so we use equation 2 for the least squares plane fitting:

$$aX + bY + cZ = 1 \tag{2}$$

3.1.2 Normal Vector. As presented, we use formula $aX + bY + cZ = 1$ to realize least squares plane fitting of a certain number of points in the neighbourhood of a point. Then we can get the equation parameters: a,b,c,(a,b,c)is the normal vector of this point。

3.1.3 Residual. Residual value refers to the difference between the observed value and regression estimated value. Regression estimated value equals to the average of observed value.

$$\delta_i = y_i - \bar{y}, (i = 1, 2, \cdots, n) \tag{3}$$

When it comes to the residual estimation of plane fitting result, we can't take the average of observed value as regression estimated value, we may take the square of vertical distance between all points to the fitting plane as residual of plane fitting. Equation 4 indicates vertical distance between all points to the fitting plane. Equation 5 is the calculation of residuals, δ_i means the vertical distance between one point among them to the fitting plane.

$$\delta_i = \frac{|ax_i + by_i + cz_i - 1|}{\sqrt{a^2 + b^2 + c^2}}, (i = 1,2,3.....,n) \tag{4}$$

$$\sigma = \sum_1^n \delta_i^2, (i = 1, 2, 3 \cdots, n) \tag{5}$$

3.1.4 Planar Projection Area and Density in XOY Plane. Imaging the points contained in the segmented points plane project to the XOY plane, there is a outline of polygons enclosed by point clouds. We can use the minimum area bounding rectangle to replace its external contour; the smallest rectangle's area can be regarded as the planar projection area. Planar projection density equals to the number of points divided by its projected area.

3.2 Summary of Surface Features Knowledge

3.2.1 Classification System of Urban Blocks. According to the typical urban surroundings, especially the urban truck road and streetscape on both sides, urban basic features can be classified as roads, buildings, vegetation and other scattered ones.

3.2.2 Modelling Objects of Urban Blocks Features. Mode is defined as the regularity we discover and abstract from continuously appeared events as well as the summary of experience we use to solve problems [9]. Based on the analysis of both spatial distribution characteristics and geometric structure characteristics, modelling urban blocks features denotes a formation of knowledge rules support classification as well as identification and then basic knowledge with respect to the classification of urban features. Table 1 shows a knowledge base on identification and reconstruction of urban features, which are merged and extracted based on the spatial distribution characteristics as well as geometric structure ones of features objects of city blocks.

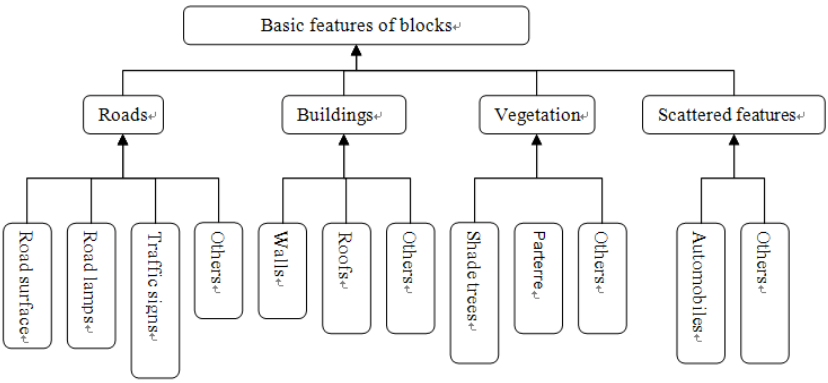

Fig. 1. Classification system of urban blocks

Table 1. Characteristics knowledge base of features objects

objects	Description of characteristic modes
Ground	1. Usually owns a lower elevation compared with other surface features in the scene; 2. with small ups and downs and smooth altitude change; 3. parallel to the plane; 4. generally throughout the whole scanning scene, takes on a stripe distribution in the middle of the scene
Buildings	1. Above the surface, on both sides of the road ,with a regular shape; 2. Smooth walls, perpendicular to the plane, planar projection for linear; 3. Metope is commonly regular blocks of rectangular or surface with a big width as well as right-angle corner; 4. Rectangular windows are uniformly embedded in the wall bodies in a certain interval
Trees	1. Between the buildings and roads, stand in rows at certain interval; 2. Elevation is usually taller than surface but lower than buildings; 3. Divided into the trunk and the crown, crowns are umbellate or tapered, planar projections are irregular circles; 4. Leaves are dense but distributed without rules
Parterres	1. Between the buildings and roads; 2. long and narrow in shape; 3. the low shrubs are close to the surface but lower than shade trees; vegetation usually takes on a irregular spatial distribution
Traffic signs	1. stand in rows with regular intervals in front of the buildings or fences; slightly close to the trees in height; 2. Poles are long and thin regular cylinder while panels are smooth rectangular

3.2.3 Knowledge Rules of Urban Blocks Features. Feature constraints that can be easily understood by computer are showed in Table 2, which is transformed by the knowledge base of various objects in Table 1.

Table 2. Features knowledge rules for various objects

Rules / Objects	Elevation	Planar projection area in XOY plane	Planar projection density in XOY plane	Normal vector	Planar fitting residual
Grounds	Highest	The area is large	small, evenly distributed	vertical	small
Buildings	Lowest	Linear, the area is large	big, linear	horizontal	small
Trees	higher than parterres but lower than buildings	Irregular circles, the area is larger	larger, diffused distribution	come in different directions	big
Parterres	Usually lower than shade trees but higher than surface	Oblong, the area is larger	larger	come in different directions	big
Traffic signs	Lower than parterres but higher than buildings	The area is smaller	larger	vertical	bigger

3.2.4 Extraction of Main Features. PCA aims at resolving the main influence factors from multiple things, revealing the nature of things and simplifying complicated problems. In order to improve the effectiveness of identification, we can summarize the characteristics of every feature which shows a biggest difference compared with other features based on the analysis of point clouds characteristics of various features. In other words, with extracting one or two main characteristics and auxiliary ones, we can make the hierarchical classification strategy. The main characteristics of several typical features are concluded as follows (Table3 ★ for main, ☆ for auxiliary):

Table 3. Conclusions of main characteristics of features objects

Features / Objects	Elevation	Planar projection area	Planar projection density	Normal vector	Planar fitting residual
Ground	★				
Buildings		☆	☆	★	☆
Trees	☆			★	☆
Parterres	☆			★	☆
Traffic signs	☆			★	

Comprehensively considering the principal feature which plays the crucial role in classifying and recognizing the various ground objects summarized above, a hierarchical classification mode can be established. The designed algorithm flow is as follows:

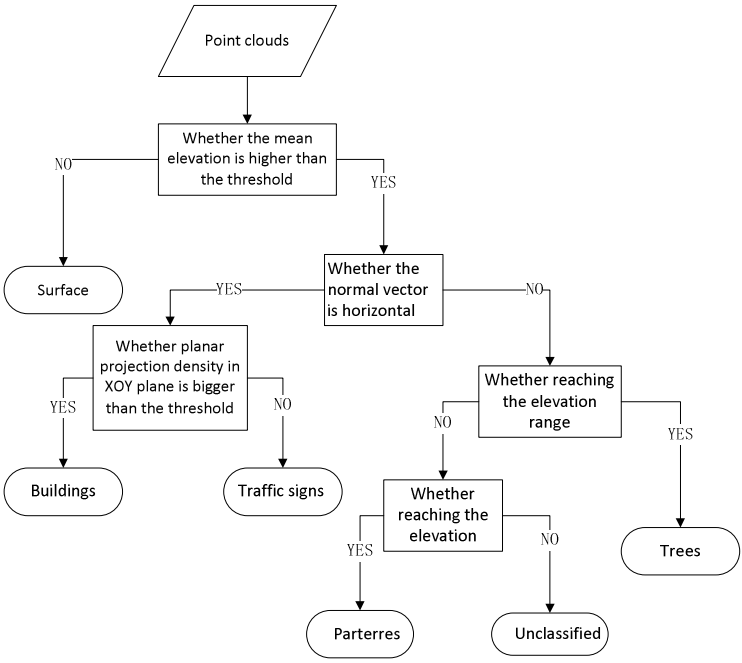

Fig. 2. Hierarchical Classification Mode

4 Experiment AND Analysis

The raw point set is acquired by 3D mobile laser scanner LYNX.

In this test, we use 30 points for planar fitting when searching radius is 0.5m, Angle threshold is 15°, and the percentage of residual threshold is 95%. After process of segmentation, we can get segmentation result showed in figure 3. On the basis of

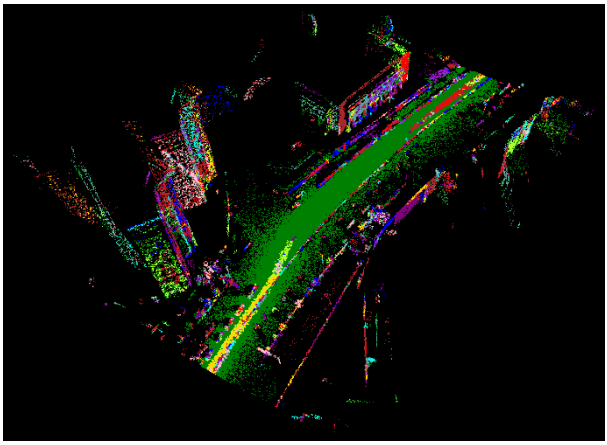

Fig. 3. Segmented Result

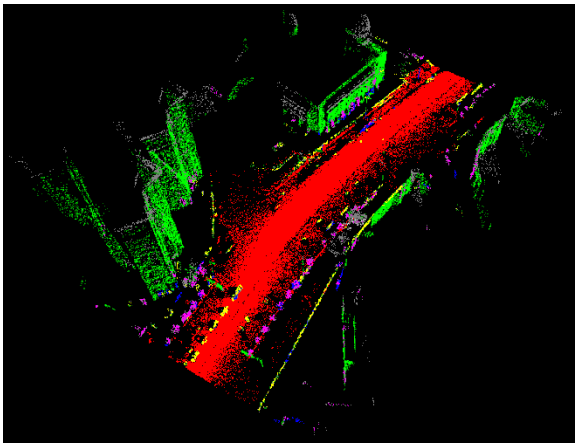

Fig. 4. Automatic Classification (Recognition) results

segmentation, we using PCA method to classify raw point clouds into different classes and recognize them, then we can get the automatic classification result showed in figure 4.

In above figures, the red part means ground. The green means buildings. The blue means artificial coverings (such as Large billboards, Traffic badges).The yellow indicates irregular surface features (such as parterres, cars).The purple is on behalf of irregular surface features (such as streets trees).In addition, the gray means other objects.

The artificial classification result by an interactive is showed in the Figure5.

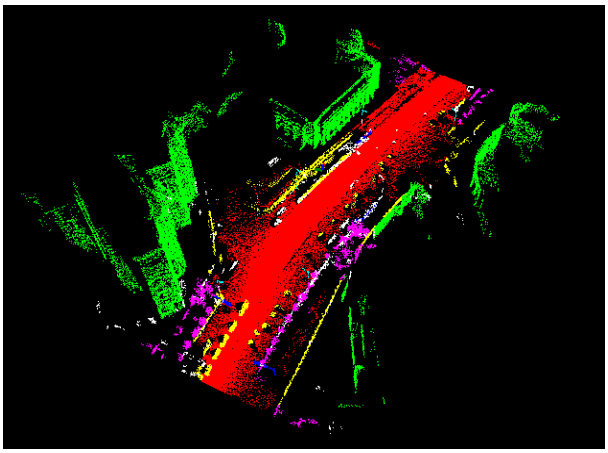

Fig. 5. Artificial classification(Recognition) results

Following is the confusion matrix (table 4) showing the result of the comparative analysis between automatic classification using the proposed method with the artificial classification.

Table 4. Confusion matrix

Automatic classification / Artificial classification	Ground	Building	Traffic signs	Parterres	Trees	Others	Total	Accuracy 1(%)
Ground	303	0	4	22	1	0	330	91.8
Building	0	186	12	8	5	118	329	56.5
Traffic signs	2	17	56	0	8	0	83	67.5
Parterres	65	0	6	103	5	0	179	57.5
Trees	9	11	8	22	92	38	180	51.1
Others	121	5	12	13	42	43	236	18.2
Total	500	219	98	168	153	199	1337	
Accuracy2 (%)	60.6	84.9	57.1	61.3	60.1	21.6		58.5

The above confusion matrix shows the confused results of automatic and artificial classification of block objects.

1. The buildings and traffic signs are wrongly classified: there exist some segmented points plane on the building, the height of which are relatively close with the traffic signs. Meanwhile the normal vector of the traffic signs is also nearly horizontal, therefore to some extent overlapping with the classification rules of building.
2. The number of buildings blocks with artificial classification exceeds the result with the method mentioned above: the roof of the building has an arched dome, pitched roof and other irregularly shaped adjuncts; also some walls of the building are archly shaped. Describing the points plane are relatively segmented and features are different from that of the features of the database.
3. The parterres and street trees are somewhat wrongly classified: the normal vector of the parterres and trees are differentiated and abnormally shaped, thus the trunk and some parts of the crown are likely to be segmented into independent planes .what's more, the height and features of trees are close to that of the flowerbed, thus leading to wrongly classification.
4. Lower objects on the ground: modern streets are normally higher in the middle and lower on two sides, so as to facilitate draining; therefore the threshold value of the height is hard to define: if defined too low, the middle part will not be accounted as streets; if too high, the objects along the street will also be accounted.

As the ground objects are of various kinds and with different structures, many segmented points planes are not classified in this experiment. And as the features cannot exactly reflect what the object is, the experiment cannot classify and identify the objects with high definition. This experiment justifies the feasibility of the application of proposed classification method based on PCA, but its accuracy still need to be improved.

5 Conclusion

The method proposed in this paper, extracting various semantic features of urban block objects to establish classification rules for ground objects, then transforms the

established rules to feature constraint that can be easily understood by computer. The method made a breakthrough at constrain of single-parameter classification, comparing to the traditional algorithms for feature detection and classification which were based on echo intensity or the gray information. Based on PCA, it discussed the strategy of the hierarchical classification and through a stepwise classification for principle features of various objects; it successfully avoided redundancy of feature information in constraints and also improved the efficiency in recognition and classification. For further research, several feature parameters can be considered and can be set with different weight for classification. Moreover, threshold value for feature parameters can also be set through a prior statistics by manual classification, and can be taken as a prior knowledge for classification of other scenes to improve the classification precision.

As for the complex category of ground objects of streets in urban area, extracting building information from the massive LiDAR data and acquiring the height information of buildings can help to ensure whether the height is beyond the threshold. And the recognition of trees along the streets can help to acquire the information of trees and decide their location and height. Besides, the classified data of roads can be used for monitoring and maintenance of the states of road. In conclusion, the technology of recognition and classification for urban blocks objects enjoys a broad application prospect, and it is certain that the reconstruction of models and textures for ground objects on streets will become the hotpot as well as difficulty for further researches.

Acknowledgment. This research is sponsored by China Aero Geophysical Survey & Remote Sensing Center for Land and Resources.

References

1. Wu, F.: Survying on feature extraction of buildings based on Mobile laser scanning data. Master Thesis. Wuhan University, Wuhan (2005) (in Chinese)
2. Manandhar, D., Shibasaki, R.: Mobile Laser Mapping System (VLMS) -A New Observation System for 3-D Mapping. In: Remote Sensing and Data Fusion over Urban Areas, IEEE/ISPRS Joint Workshop (2001) (Rome)
3. Shi Pu, G.V.: Knowledge based reconstruction of building models from terrestrial laser. ISPRS Journal of Photogrammetry and Remote Sensing (64), 575–584 (2009)
4. Li, B.J., Fang, Z.J., Ren, J.: Survying on feature extraction of buildings based on Mobile laser scanning data. Geomatics and Information Science of Wuhan University 28(1), 65–69 (2003) (in Chinese)
5. Shi, W., Li, B.J., Li, Q.Q.: A Method for Segmentation of Range Image Captured by Mobile Laserscanning Based on the Density of Projected Points. Acta Geodaetica et Cartographica Sinica 34(2), 95–100 (2003) (in Chinese)
6. Li, Y., Sheng, Y., Liu, H., et al.: 3D road information extraction based on mobile laser scanning. Science of Surveying and Mapping 33(4), 23–25 (2008)

7. Baidu Encyclopedia.PCA, http://baike.baidu.com/view/852194.htm (in Chinese)
8. Liu, Y., Xiong, Y.: Automatic segmentation of unorganized noisy point clouds based on the Gaussian map. Computer-Aided Design 40(5), 576–594 (2008)
9. Pang, Q.: Knowledge_rased 3D reconstruction of histrical buildings using point Cloud. PhD thesis. Wuhan University, Wuhan (2009)

Spatial Expansion and Sprawl Quantitative Analysis of Mountain City Built-Up Area

Pengfei Ren[1], Shu Gan[2,*], Xiping Yuan[2], Huilin Zong[1], and Xianqi Xie[1]

[1] Faculty of Land Resource Engineering, Kunming University of Science and Technology, Kunming, Yunnan Province, 650093, China
494590944@qq.com
[2] Faculty of Land Resource Engineering, Kunming University of Science and Technology, Professor, Kunming, China
n1480@qq.com

Abstract. Urban expansion is a spatial and demographic process and refers to the increased importance of cities as a concentration of population within a particular economy and society. Urban expansion can be mapped, measured and modeled by using remote sensing data and GIS techniques along with statistical measures. In this study three temporal satellite images of 8 years interval (2002, 2006 and 2010) have been classified to determine the urban expansion of Kunming in eight different directions. Pearson's chi-square test and Shannon's entropy method have been applied to calculate the degree of freedom and degree of sprawl towards the analysis of urban expansion and the urban expansion intensity index towards the expansion rate. The result shows that the city of Kunming has a high degree of freedom, high sprawl but a decreasing tendency. With a rapid development rate, the city gradually tends to be more compact.

Keywords: Urban Built-up area, Remote Sensing, Urban expansion, Degree of sprawl, Expansion intensity.

1 Introduction

Urban expansion is a process of urban development; it makes a tremendous impact on social and economic development and has aroused widespread concern. Remote sensing data and GIS technology has been widely used in the analysis. Remote sensing data was used to determine the rate of urban growth and the spatial structure [1]. GIS technology has a wide spectrum of application in urban analysis, because the discipline embraces space in analysis and modeling [2]. Related researches involve urban sprawl model, processes, causes and results, strategies and so on. Most of the current statistical models are non-spatial; there are many problems, such as the failure of most conventional statistics to adequately summarize location information, the lack of independence and inherent stickiness of spatial data, and the implications of shape and representation in spatial analysis. To solve these problems, a new approach was

* Corresponding author.

F. Bian et al. (Eds.): GRMSE 2013, Part I, CCIS 398, pp. 166–176, 2013.
© Springer-Verlag Berlin Heidelberg 2013

adopted-spatial statistics, which accounts spatial dimensions and the statistical measures as well. Pa´ez and Scott [3] documented the confluence between urban analysis and spatial statistics.

According to statistics, there are currently some twenty or more applications of analytic and simulation models to cities, such as in the diffusion or migration of resident populations, competitive location of economic activities, joint expansion of urban surface and traffic network, generic urban growth, urban land-use dynamics and so on [4]. Using these models can better understand urban growth, but in most cases they require a lot of input data and in many countries, especially the developing countries, general lack of basic data which can be effectively utilized. In addition, previous studies about urban expansion analysis mostly from sprawl or process alone, but urban expansion should not be only for a moment or a certain time period changes in the spatial structure, it should be analyzed as a combination of both.

This study is aimed to analyze the urban expansion, by using the current and historical remote sensing data with the help of statistical models that can be applied on different spatial and temporal dimensions. In this study, remotely sensed satellite imageries of three temporal instants were used to determine the urban land-cover class over the study area. These data were then used for spatial analysis by using Pearson's chi-square, Shannon's entropy and urban expansion intensity index. Pearson's chi-square statistics can reveal the disparity in growth [5], Shannon's entropy method can determine the sprawl [6], and urban expansion intensity index was used to determine the rate of urban expansion. And then the urban expansion conditions were analyzed from the pattern, the process and the overall situation.

2 Study Area

Kunming is the capital and largest city of Yunnan province in Southwest China. It is the political, economic, communications and cultural center of Yunnan, and is the seat of the provincial government. It is located between north latitude 24°23´ and 26°22´N, and east longitude 102°10´and 103°40´E, with a total area of 21,473 km^2. It is located at an altitude of 1,900 m above sea level and at latitude just north of the Tropic of Cancer. The urban area covers about 2,622 km^2 and the main city area includes 5 regions (Wuhua, Panlong, Xishan, Guandu, Chenggong), and is located at the northern edge of the large Lake Dian, surrounded by temples and lake-and-limestone hill landscapes. In this study, the study area is the main city of Kunming.

Landsat-7 ETM+ imageries (09 February 2002, 03 January 2006 and 30 January 2010) with 4 years temporal interval have been used to execute the study. The images were obtains as standard product-that is, geometrically and radiometric corrected. The quality of three images were better, no clouds obscured the selected study area. This research was executed through ENVI and ARCGIS. Landsat-7 ETM+ data contains eight bands , in which , band1-band3 was the optical band, band4 was the near-infrared band, band5 and band7 were the shortwave infrared bands, the spatial resolution of these six bands was 30m; band8 is pan band with 15m resolution. Band6 is thermal infrared band which divided into band61 and band62 was not considered for the analysis.

3 Information Extraction of Urban Built-Up Area

The growth of urban built-up area is a clear sign of Urban expansion, including residential land, commercial buildings, municipal facilities and public infrastructure, and its most notable feature is the increase of impervious surface concomitantly, so in this study impervious surface was used to carry out research on behalf of built-up area. Impervious surface is an artificial surface, including urban roads, car parks, plazas, roof and other buildings [7, 8]. The area percentage of impervious surface can be directly reflects the growth of the city state, as opposed to less developed regions, the developed areas has a higher ratio [9].

In this study, MNDWI [10] (Modified normalized Difference water Index) and Fc [11] (Vegetation coverage) were used to obtain vegetation cover images and then according the negative correlation between impervious surface and vegetation coverage to obtain impervious surface [12, 13]. The relevant formulas are:

$$MNDWI = (Green – MIR) / (Green + MIR) . \quad (1)$$

$$Fc = (NDVI - NDVI_{soil}) / (NDVIveg - NDVI_{soil}) . \quad (2)$$

$$NDVI = (NIR-Red) / (NIR + Red) . \quad (3)$$

$$NDVI_{soil} = (Fc_{max} * NDVI_{min} - Fc_{min} * NDVI_{max}) / (Fc_{max} - Fc_{min}) . \quad (4)$$

$$NDVI_{veg} = ((1- Fc_{min}) * NDVI_{max} - (1 - VFC_{max}) * NDVI_{min}) / (Fc_{max} - Fc_{min}) . \quad (5)$$

$$ISA = (1- Fc)_{dev} . \quad (6)$$

In the above formulas: Green represents green band, MIR represents the mid-infrared, NIR represents near-infrared bands, and Red represents the red band. NDVI represents the normalized difference vegetation index. $NDVI_{veg}$ represents the NDVI value of pixels which covered by vegetation, $NDVI_{soil}$ represents the NDVI value of bare ground or areas without vegetation cover. Subscript dev represents the formula only was applied to the urban built-up area.

$NDVI_{veg}$ and $NDVI_{soil}$ take fixed values; it is means that $NDVI_{max}$ and $NDVI_{min}$ represent the largest and smallest NDVI values of study area. Then setting Fc_{max} = 100%, Fc_{min} = 0% to calculate the vegetation coverage. Due to the unavoidable presence of noise, $NDVI_{max}$ and $NDVI_{min}$ generally take the maximum and minimum values in a certain range of confidence. After several comparative analyses, this study selects the NDVI values which in the vicinity of 5 % and 95 % as $NDVI_{min}$ and $NDVI_{max}$. As shown in Table 1:

Table 1. NDVI values of each temporal span

	2002.02.09	2006.01.03	2010.01.30
$NDVI_{min}$	-0.102676	-0.061893	-0.103478
$NDVI_{max}$	0.412192	0.460870	0.421154

Though repeated experiments, the study choose the threshold value of 0.8. The image was divided into two parts which greater than 0.8 was the impervious surface and the other was the pervious surface. Then the classification image of each period was acquired. Take 2010's classification image for example, shown in Figure 1.

Upon examination, the classification images of each period which acquired from the above step have much higher classification accuracy. In the classification image of 2006, for example, we randomly selected 1579 pixels to verify. There were 232 errors. The total accuracy was 85.31% and Kappa coefficient was 0.8265. So the classification images can meet research requirements.

4 Spatial Quadrant Division and Characteristics Analysis

4.1 Spatial Quadrant Division and Statistics

The expansion of urban built-up area depends on the conflict between growing urban area and limited regional, which often tend to be few directions, and the "pie" type of expansion was rare [14]. Quadrant statistics was used to acquire the impervious surface information. We choose central business district as the center of Kunming and make a radius of 26 Km circular statistical area. Then it was been divided into eight equal parts, namely the north, northeast, east, southeast, south, southwest, west and northwest. The eight quadrants were shown in Figure 2. The radius was selected from the latest remote sense image, and the statistical date of each image and each zone are furnished in Table 2 that directly shows the status of built-up areas.

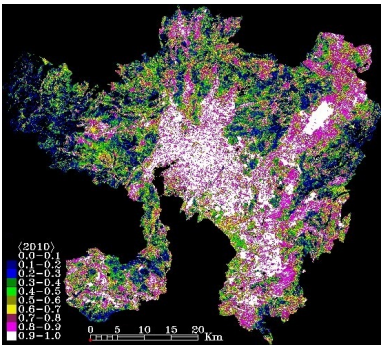

Fig. 1. Classified image of 2010

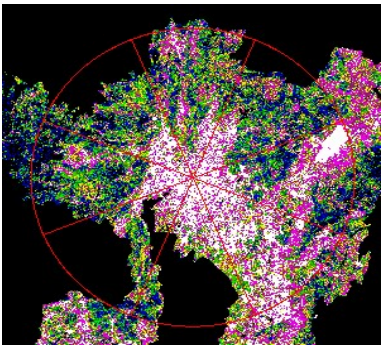

Fig. 2. Diagram of space quadrant divided

Table 2. Built-up areas of study area in different directions (in km^2)

	N	NE	E	SE	S	SW	W	NW	Total
2002	11.51	14.01	13.74	40.12	16.78	13.49	17.62	12.66	139.93
2006	15.30	18.11	20.52	52.60	22.69	15.43	19.14	15.80	179.59
2010	23.03	20.78	48.28	87.23	32.06	15.67	19.93	19.26	266.24

4.2 Statistical Analysis of Spatial Features

It can be seen from Table 2 that the development of each period and each direction has significant differences. Observed expansion of Built-up area in different zones (Table 3) was calculated for the time spans 2002-2006 and 2006-2010. The percentage of increase in built-up area can also been calculated. This clearly shows that the urban own a rapid expansion speed in recent years. There was a significant growth in north, east, southeast, south four directions especially, while a relatively slower growth in west and southwest. Urban growth rate was accelerating trend and larger differences in each direction.

Table 3. Observed expansion of Built-up area in different zones (in km^2)

	N	NE	E	SE	S	SW	W	NW	Total
02-06	3.79	4.1	6.78	12.48	5.91	1.94	1.52	3.14	39.66
06-10	7.73	2.67	27.76	34.63	9.37	0.24	0.79	3.46	86.65
Total	11.52	6.77	34.54	47.11	15.28	2.18	2.31	6.6	126.31

4.3 The Study of Spatial Expansion

4.3.1 Theoretical Value Calculation of Urban Expected Expansion

To further understand the differences of regional expansion, this study conducts a comparative analysis of observed and theoretical values. The expected built-up growth for each variable was calculated by the products of marginal totals, divided by the grand total [15]. Let the Table 3 be called matrix M, with elements M_{ij}, where i = 1, 2 (rows of the table) and j = 1, 2...8 (columns of the table).From Table 3, the theoretical expected urban expansion can be calculated statistically by employing the Eq. 7. The results are shown in Table 4.

$$M_{ij}^{E} = \frac{M_i^S \times M_j^S}{M_g} \quad . \tag{7}$$

In the above formula: M_i^S represents row total, M_j^S represents column total, M_g represents grand total.

Table 4. Expected expansion of built-up area in each period (In km^2)

	N	NE	E	SE	S	SW	W	NW
02-06	3.62	2.13	10.85	14.79	4.80	0.68	0.73	2.07
06-10	7.90	4.64	23.69	32.32	10.48	1.50	1.58	4.53

We can identify the discrepancy of urban expansion for each zone and each temporal span by subtract observed values from expected values. Negative values indicate less growth and positive values show more growth than the expectations. Clearly, the discrepancy is much large in E and SE two directions regions.

4.3.2 Pearson's Chi-Square Statistics

Pearson's chi-square statistics takes into account the checking of freedom amongst pairs of variables chosen to explain the same category of land-cover change [15]. The expression: (observed expected) ^{2}/expected. It reveals the freedom or degree of deviation for the observed urban growth over the expected. The lower limit value is 0, that is, when observed and predicted values are equal. This model was used to determine the regional total degree of freedom by Bonham-Carter [5] and Almeida [15]. This study extends the model to analyze the pattern, process and the overall situation of urban expansion.

For Table 3 and Table 4, the chi-square statistics for each temporal span (shown in Table 5) was calculated by Eq. 8. Replacing column by row, we can determine the degree of freedom for each zone (shown in Table 6).

$$x_i^2 = \sum_{j=1}^{m} \frac{\left(M_j - M_j^E\right)^2}{M_j^E} \quad . \tag{8}$$

In the above formula: x_i^2 represents the degree-of-freedom of i-th temporal span, M_j represents observed built-up area in j-th column, M_j^E represents expected built-up area in j-th column.

Table 5. Degree-of-freedom of each temporal span

Time span	Freedom(x_i^2)
02-06	7.72
06-10	3.53

Table 6. Degree-of-freedom for urban expansion in each zone

Zoom	N	NE	E	SE	S	SW	W	NW
Freedom(x_i^2)	0.01	2.66	2.23	0.53	0.38	3.39	1.25	0.81

The overall degree of freedom can also be estimated by Eq. 9. The calculation result was 11.25.

$$x^2 = \sum_{i=1}^{n} \sum_{j=1}^{m} \frac{\left(M_{ij} - M_{ij}^E\right)^2}{M_{ij}^E} \quad . \tag{9}$$

In the above formula: x^2 represents the overall degree-of-freedom, M_{ij} represents observed values in i-th row and j-th column, M_{ij}^E represents expected values in i-th row and j-th column.

As can be seen from the table, the study area in the two periods has higher degrees of freedom. The freedom of N, SE, S, NW areas are low, while NE, E, SW, W are much higher. Higher degree of freedom indicates that the regional development process is unsustainable. The overall degree of freedom was 11.25, indicating that the urban total planning was unbalanced and lack of coherence. Each period degree of freedom was

higher, indicating that the freedom was much higher among regions in the time dimension relatively. It should be noted that the high degree of freedom reflects the differences of regional expansion patterns or process but not spread.

4.3.3 Shannon's Entropy

Shannon's entropy is a well accepted method for determining the sprawled urban pattern [6]. The degree of sprawl can be identified by the magnitudes of entropy value. The value of entropy ranges from 0 to $\log_e(m)$.Value 0 indicates that the distribution of built-up is compact, while values closer to $\log_e(m)$ reveal that the distribution of built-up is dispersed. Higher values of entropy indicate the occurrence of sprawl [16]. In this study, the Shannon's entropy for each temporal span (shown in Table 7) has been calculated by using Eq. 10. Replacing column by row, we can determine the entropy value for each zone (shown in Table 8).

$$H_i = -\sum_{j=1}^{m} p_j \log_e(p_j) \quad . \tag{10}$$

In the above formula: H_i represents the Shannon's entropy for each temporal span. p_j represents the proportion of the variable in the j-th column (i.e., proportion of built-up growth rate in j-th zone).

Table 7. Shannon's entropy of each temporal span

	Entropy (H_i)	$\log_e(m)$	$\log_e(m)/2$
02-06	1.98	2.08	1.04
06-10	1.62	2.08	1.04

Table 8. Shannon's entropy for different zones

	N	NE	E	SE	S	SW	W	NW
Entropy (H_i)	0.67	0.64	0.58	0.63	0.69	0.32	0.63	0.69
$\log_e(n)$	0.69	0.69	0.69	0.69	0.69	0.69	0.69	0.69
$\log_e(n)/2$	0.35	0.35	0.35	0.35	0.35	0.35	0.35	0.35

The overall Shannon's entropy (H) can also be estimated by Eq. 11. The calculation result was 2.44.

$$H = -\sum_{i=1}^{n}\sum_{j=1}^{m} p_{ij} \log_e(p_{ij}) \quad . \tag{11}$$

In the above formula: p_{ij} represents the proportion of the variable in i-th row and j-th column (i.e., proportion of built-up growth rate in i-th temporal span and j-th zone)

As can be seen from the table, the entropy of N, NE, E, SE, S, W, NW directions were much higher than the half of maximum limits, especially in the S and NW direction, indicating that the growth of regions showed sprawled state. Only the SW direction was non-sprawling in the whole study area. In addition, the Shannon entropy values for each period are much larger than the half of the maximum limit value, which

can be determined that the expansion of study area is sprawling. The results show that the development of the study area becomes more compact gradually and the sprawling is decreasing. The decreasing tendency should not be interpreted as non-sprawling; it can be said that the city is non-sprawling only when the entropy value goes below the half-way mark of $\log_e(m)$.

4.3.4 Urban Expansion Intensity Index

In the process of urban development, due to the impact of road network, terrain, economic development and social factors, the development often become unique in each direction which be called preference of urban development. Urban expansion intensity index can be used to analyze the spatial extension differences of regional land use quantitatively and understand the preference of urban development in a certain period. It refers to the percentage that the urban expansion area occupied of the total land area in a specific area or a specific period [17].

The index can reflect the future direction and potential of urban expansion, and it compares the intensity or speed of urban land use in different periods. The division standard of UEI as: >1.92, high-speed development; 1.05-1.92, fast development; 0.59-1.05, medium-speed development; 0.28-0.59, low-speed development; 0-0.28, slow development. The calculation expression as following:

$$UEI_{it} = [(ULA_{i,b} - ULA_{i,a})/t\ ] / TLA_i * 100\ . \quad (12)$$

In the formula: UEI_{it} represents the annual average expansion intensity index of i-th spatial zone during the time quantum t; $ULA_{i,a}$ and $ULA_{i,b}$ represent the beginning and ending built-up area of i-th spatial zone. TLA_i represents the total land area of i-th spatial zone.

Table 9. UEI of each temporal span

Time span	UTI
02-06	0.55
06-10	1.20

Table 10. UEI for different zones

Zoom	N	NE	E	SE	S	SW	W	NW
UTI	0.59	0.38	1.63	2.22	0.72	0.22	0.12	0.45

Results shown that the expansion intensity index of five zones (including N, NE, NW, SW, W) were much lower, that means these zones have slow expansion rate, especially in the SW and W directions. E and SE zones expanded quickly, where E was fast development and SE direction was high-speed development. In addition, the overall index showed a medium-speed expansion of study area that means the city had a relatively stable rate of expansion but differences in directions.

5 Conclusions

The study area was selected by a circle and divided into eight fan-shaped areas that can help us better understanding the growth of the city in each direction. Urban development often radially expands from the central business district, so the center of the study area was selected in the central of district. The selected condition of radius was that the urban built-up area was maximum contained. In recent years, the new air port of Kunming is a larger urban construction project, which covers much larger area. Considering its importance, the study determined the study area of 26 km radius though numerous tests.

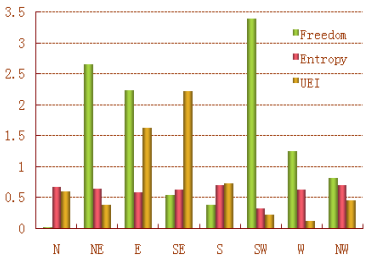

Fig. 3. Degree-of-freedom, entropy and UEI in each zone

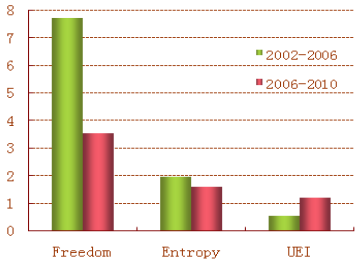

Fig. 4. Degree-of-freedom, entropy and UEI in each span

From the perspective of regional (shown in Figure 3), we can see that the NE and SW directions had a much higher degree of freedom but a quite low expansion intensity, indicating that the freedom of development is high but the expansion speed is slow and the region land are not be effectively used. The degree of freedom, sprawl and expansion intensity of zone E all were high, that means the speed of development was fast and had less policy limits. N direction has a higher degree of sprawl and expansion intensity but an extremely low freedom, indicating that the region development is gradual and sustainable.

From the perspective of time span (shown in Figure 4), it can be seen that the urban development had lass limits from the policy, urban planning and other factors. The development showed a higher spread trend and a lower expansion rate between 2002 and 2006, namely develop relatively slow. From 2006 to 2010, the urban growth rate has accelerated, but the sprawl and freedom have a significant decline. The city developed rapidly and tended to be more compact and intensive gradually, which accord to the overall trend of sustainable urban development.

In this study, several statistical models were used to analyze the urban development from the pattern, process and overall situation three levels. The results show that there had no significant increase in W and SW zones, where the Lake Dian located, so the space of development was small and reflected by the topographical factors significantly. Due to the policy planning of Chenggong area, E, SE and S zones had a rapid development.

The limit of the analysis in this study is that the statistical models did not consider the impact of policy-oriented factors. But the expected values of urban expansion were calculated by observed values, namely the research indirectly reflects the existing policies of urban and mainly lacks the influences of expected policy. Thus we should determine the weighting of expected impact when the statistical models are used for other large cities in the further study. In addition, the study also not considered the impact of other factors, such as urban traffic network and terrain. Collecting more comprehensive data and setting the appropriate weight coefficient of impact factors to arrive a more detailed and accurate experimental results will be the emphasis of further research.

Acknowledgments. This study was supported by China National Natural Science Research Fund Project (No.71163023, No.41261092).

References

1. Maktav, D., Erbek, F.S., Jurgens, C.: Remote sensing of urban areas. International Journal of Remote Sensing. 26(4), 655–659 (2005)
2. Fotheringham, A.S., Wegener, M.: Spatial models and GIS: New potential and new models. Taylor and Francis, London (2000)
3. Páez, A., Scott, D.M.: Spatial statistics for urban analysis: a review of techniques with examples. Geo Journal 61, 53–67 (2004)
4. Batty, M.: GeoComputation using cellular automata. In: Openshaw, S., Abrahart, R.J. (eds.) Geocomputation, pp. 95–126. Taylor & Francis, New York (2000)
5. Bonham-Carter, G.F.: Geographic information systems for geoscientists: Modelling with GIS. Pergamon, Ontario (1994)
6. Yeh, A.G.O., Li, X.: Measurement and monitoring of urban sprawl in a rapidly growing region using entropy. Photogrammetric Engineering and Remote Sensing 67(1), 83–90 (2001)
7. Espy, W.H., Morgan, W.C., Masch, F.D.: A study of some effects of urbanization on storm runoff from a small water shed. Texas Water Development Board, Austin (1966)
8. Stankowski, S.J.: Population density as an indirect indicator or urban and suburban land-surface modifications. U. S. Geological Survey Professional Paper 800-B, U.S. Geological Survey (1972)
9. Sudhira, H.S., Ramachandra, T.V., Jagdish, K.S.: Urban sprawl: metrics, dynamics and modelling using GIS. International Journal of Applied Earth Observation and Geoinformation 5, 29–39 (2004)
10. Xu, H.: A Study on Information Extraction of Water Body with the Modified Normalized Difference Water Index (MNDWI). Journal of Remote Sensing 9(5), 589–595 (2005)
11. Li, M., Wu, B., Yan, C., et al.: Estimation of Vegetation Fraction in the Upper Basin of Miyun Reservoir by Remote Sensing. Resources Science 26(4), 153–159 (2004)
12. Carlson, T.N., Arthur, S.T.: The Impact of Land Use land Cover Changes Due to Urbanization on Surface Microclimate and Hydrology: A Satellite Perspective. Global and Planetary Change 25, 49–65 (2000)
13. Owen, T.W., Carlson, T.N., Gillies, R.R.: Remotely-sensed Surface Parameters Governing Urban Climate Change. International Journal of Remote Sensing 19, 1663–1681 (1998)

14. Pan, J.-H., Han, W.-C.: Spatial-temporal Changes of Urban Morphology of Provincial Capital Cities or above in China. Journal of Natural Resources 28(3), 470–480 (2013)
15. Almeida, C.M., Monteiro, A.M.V., Mara, G., et al.: GIS and remote sensing as tools for the simulation of urban land-use change. International Journal of Remote Sensing 26(4), 759–774 (2005)
16. Bhatta, B., Saraswati, S., Bandyopadhyay, D.: Quantifying the degree-of-freedom, degree-of-sprawl, and degree-of-goodness of urban growth from remote sensing data. Applied Geography 30(1), 96–111 (2010)
17. Liu, H.-H.: Remote monitoring of urban expansion and Smart Growth strategic analysis. D. Kunming University of Science and Technology, China (2012)

Vegetation Patch Structure and Dynamics at Gudong Oil Field of the Yellow River Delta, China

Qingsheng Liu*, Gaohuan Liu, Chong Huang, and Chuanjie Xie

State Key Laboratory of Resources and Environmental Information System,
Institute of Geographic Science and Natural Resources Research,
Chinese Academy of Sciences, Beijing 100101, China
{liuqs,liugh,huangch,xiecj}@lreis.ac.cn

Abstract. It is well known that the vegetation communities are damaged and subsided by oil field developments. However, the extending phenomenon of vegetation community caused by oil field explorations is rarely reported. In this paper, we used the high spatial resolution images to describe the patch structure and dynamics. The results indicate that: (1) it is sufficient to identify patch structure and analyze dynamic using high spatial resolution SPOT5 image data. (2) The patches are isodiametric or have irregular circular shapes which represent approximately 10.1% of the study area. (3) Without exogenous disturbance, the patches don't decrease and the time of quick extensions of patches is less than five years, and the new patches don't randomly grow at some certain location. Of course, to further study vegetation ring completeness and spatial distribution and the relationships with soil and water and nutrients benefit the restoration of wetland ecosystems of the study area.

Keywords: Patch structure, Spotted patter, Patch dynamics, SPOT5 image, Yellow River Delta.

1 Introduction

The Yellow River Delta (YRD), one of China's three major river deltas, is a piece of the youngest land that has been formed since 1855. With the courses of the Yellow River changed, large amounts of sands and sediments transported by the Yellow River have produced the different depositional layers of sand and clay. Therefore, the unique YRD wetland ecosystem is formed by continuous oscillation of the Yellow River promontories with interaction between land and sea, which makes ecosystem boundary of the Delta change frequently [1, 2]. Wetland ecosystems are ecologically important for their hydrologic attributes and their roles as an ecological exchange interface between terrestrial and aquatic ecosystems [3]. In 1992, The Yellow River Delta Nature Reserve (YRDNR) was established by the central government with the aim of protecting the young coastal wetland ecosystem, and rare and endangered birds, which is a home to several species of birds receiving the topmost priority for conservation [2]

* Corresponding author.

F. Bian et al. (Eds.): GRMSE 2013, Part I, CCIS 398, pp. 177–187, 2013.
© Springer-Verlag Berlin Heidelberg 2013

and is also identified by satellite tracking as one of the most important rest sites for red-crowned cranes in the western autumn migration routes [4].

However, over the last three decades, many parts of the natural wetlands have been transformed to other uses, such as aquaculture ponds, salt pans, industrial land and agricultural fields [5]. As one of the most important regions of petroleum production in China, the YRDNR has been subject to increasing human disturbance (e.g., petroleum exploitation and production) since the early 1960s. Oil wells and roads have made the considerable fragmentation of protected wetlands in the YRDNR [6] and damaged the vegetation communities at Gudong Oil Field. In order to protect and restore the wetland ecosystem, the wetlands restoration project on the YRDNR via pumping the Yellow River water to the downstream wetlands owing to the low channel runoff during the dry seasons of March–May and September–November annually was initiated in July 2002. Typically, wetland restoration focuses on restoring three key components—hydrology, biology (vegetations and animals) and soil of wetlands. Five years of restoration efforts has significantly improved the wetland ecosystem (e.g., reduced water salinity, better soil quality and re-establishment of vegetation communities) [7]. Detailed investigation of the components of wetland ecosystem and how they change during wetland ecosystem development is required. These changes include vegetation composition and structure, percent cover, biomass, plant diversity associated with re-establishment of species and so on.

Affected by seawater intrusion and fresh ground water from the Yellow River, vegetation and landscape in YRDNR are zonated from starting in the sea, sequentially sea water, tidal flats, estuarine emergent wetland, shrub land, grassland, forest, palustrine emergent wetland, and the Yellow River [8]. The natural succession of plant community in the YRD belongs to primary succession without human disturbance. The succession series of plant community in the YRD is as follows: saline bare land -> *community S. salsa* -> *community T. chinensis* -> grassland [9]. The plant communities have not the apparent different spatial distribution along meridional or zonal direction in the YRD. However, recently some types of patchy vegetations have been found and proved by high spatial resolution satellite remote sensing images and field investigations at Gudong Oil Field of the YRD (see Fig.1), which in fact is the secondary successions of vegetation communities in the abandoned lands surrounded by Gudong Oil Field cofferdam and caused by the seismic exploration of Oil Field. To understand the vegetation succession mechanism infected by oil field development benefit further wetland vegetation re-establishment and restoration at the oil field development regions or the others of the YRD, firstly detailed studies are required to analyze the patch structure and dynamics of vegetation. The pattern and dynamics of the patches represent fundamental attributes of vegetation, and patch structure is an important determinant of ecosystem function [10]. Therefore, the objectives of this study are to: (1) identify the vegetation patches and analyze the size, shape, and spatial distribution of vegetation patches; (2) monitor the dynamics of the vegetation pattern over time. These results help further refinements and improvements for management of wetland restoration in the future, and help to better coordinate the contradiction between the oil field development and the wetland ecosystem protection in the YRD.

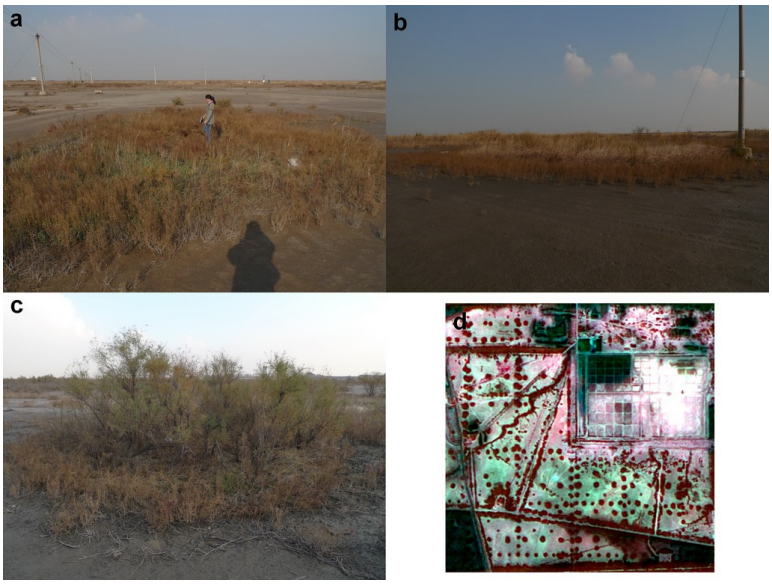

Fig. 1. Examples of three patch types of Gudong Oil Field of the Yellow River Delta. (a) Suaeda salsa and scattered Tamarix chinensis. (b) Tamarix chinensis, Phragmites australis and Imperata cylindrica encircled by two rings of Limonium bicolor (Bge.) e. Ktze and Suaeda salsa. (c) Tamarix chenensis encircled by a ring of Suaeda salsa. (d) Spotted vegetation recorded by the SPOT5 images on September 7, 2005.

2 Materials and Methods

2.1 Study Area

The YRD (118°7′E to 119°10′E, and 37°20′N to 38°10′N) is located in the northern part of Shandong Province, China, and on the southwest coast of the Bohai Sea. The massive silt from erosion of the Loess Plateau created the continuous, fast-growing natural delta at the mouth of the Yellow River. The current course of the Yellow River was formed from artificially changing the old course from Diaokouhe River to Qingshuigou Gully in 1976. This area has a warm temperate continental monsoon climate with distinctive seasons and a rainy summer (June–August). Annual temperature averages 12.1°C. It receives an annual rainfall of 551.6 mm, against an annual evaporation of 1,962 mm. It has an aridity index of up to 3.56, belongs to arid ecosystem. The most common soil is Glyic Solonchaks with high salt content in the tidal flats. The Suaeda salsa and Tamarix chinensis and Phragmites australis are three main native vegetations which occur widely across the YRD.

The study area (the area is about 225 ha) is part of Gudong oil field, located in the northeast of the Yellow River Delta (See Fig.2). Gudong Oil Field, which belongs to Shengli Oil field (the second largest oil field of China), has been largely exploited since 1984. In order to reduce the cost of petroleum exploration, the cofferdam was

begun to build in May, 1985 and finished in February, 1986, which was 13.5 km long, 5.0 m tall and 10 m wide. Therefore, except oil wells and construction lands the abandoned lands are formed in Gudong Oil Field where the secondary successions of vegetation communities have happened.

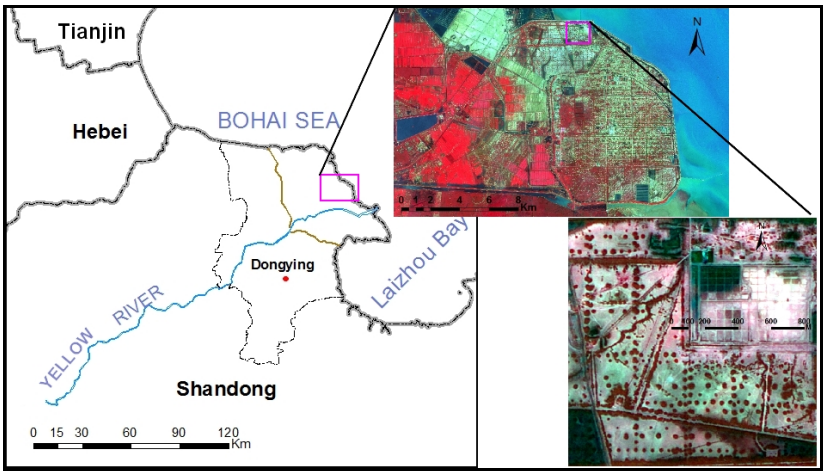

Fig. 2. Location of the Yellow River Delta and Gudong Oil Field (The study area lies on the north of Gudong Oil Field.)

2.2 Remote Sensing Data

Kadmon & Harari-Kremer (1999) demonstrate the viability of image texture derived from aerial photography as a means for characterizing vegetation structure, particularly in heterogeneous environments. Such images allow for analysis of canopy cluster size, fraction of tree cover, and when time series of data are present, rates of woody cover change [11]. Barbier et al (2006) find that panchromatic contacts digitized into grayscale levels with a pixel size of 2 m is sufficient to study decametric-scale vegetation patterns, and tests with higher resolution, i.e. 1 m pixel or less led to similar results for all analyses [12]. Compared with sparse aerial photography, satellite images from high spatial resolution sensors meet three important criteria in regards to vegetation patch structure observation and dynamic change detection: they have high spatial resolution, are regional in extent, and are old enough to extract historical rates of change. So the multi-temporal SPOT5 images with a pixel size of 2.5 m are selected to use in this paper.

The SPOT5 satellite was placed in orbit in May 2002, and is the fifth of five SPOT satellites. The SPOT image is a view of the Earth seen through one of the satellite's high-resolution imaging instruments in five spectral bands (Multispectral: Band 1 (green, 500-590 nm); Band 2 (red, 610-680 nm); Band 3 (near infrared, 780-890 nm); Band 4 (short-wave infrared, 1580-1750 nm); P (panchromatic, 480-710 nm)). By combining imagery from all five SPOT satellites, it is now possible to generate data at

four levels of resolution (2.5 m, 5 m, 10 m, and 20 m) in black and white and in color across the same 60 km swath. Spot Image is now offering SPOT Globe products for use in Google Earth Enterpise and SPOT Globe products are fusion-ready data sets ready for use in Google Earth Enterprise. Over 15 million km2 of SPOTMaps products, Spot Image's high quality 2.5m natural color seamless mosaic products, are now available and ready-to-use in your Google Earth Enterprise system. With Google Earth used widely, SPOTMaps product in fusion-ready format will be often used and popularized. In this paper, we are interested in monitoring the vegetation patch dynamics over time. This requires the use of spatially overlapping, summer coverage from multi-temporal images that are located at Gudong Oil Field. The image acquired on July 7, 2000, September 7, 2005 and May 27, 2012 is selected. Firstly we perform the geometric rectification of the image acquired on September 7, 2005 with 27 ground control points collected by the Differential GPS (DGPS) within the image range. Then the other two images (acquired on July 7, 2000 and May 27, 2012) are registered according to the image acquired on September 7, 2005 after geometric rectification. Finally, the three subset images of fusion-ready SPOT 5 images with the resolution of 2.5m (acquired on July 7, 2000, September 7, 2005 and May 27, 2012; 600×600 pixels; area is about 225 ha) are selected as the experiment image (shown in Fig.3).

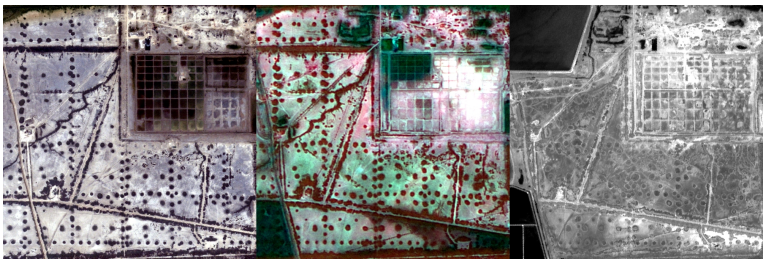

Fig. 3. Maps of vegetation patch patterns illustrating the temporal dynamics in the study area: the left and middle and the right are the images acquired on July 9, 2000 and September 7, 2005 and May 27, 2012 respectively.

2.3 Patch Structure and Pattern Detection

Arid ecosystems present a two-phase mosaic structure of high- and low-cover patches. Vegetation patterns in arid ecosystems are characterized by the size, shape and spatial distribution of high plant-cover patches. Low-cover patches are usually considered as a matrix, in which denser patches are distributed. In some ecosystems, the dense vegetation patches are irregular in shape, and form patches or spots presenting this pattern are referred as spotted or ‘leopard’ vegetation [10]. Vegetation patches differ in size and shape among ecosystems. Vegetation patterns play an important role on determining the location of runoff and sediment source and sink areas. Natural vegetation patterns that take decades to hundreds of years to evolve provide stabilizing properties for ecosystems as they are efficient in reducing overland

flow and land degradation, and help ecosystems to recover from disturbance and to resist stressors. Therefore the state of natural vegetation patterns constitutes an important indicator of ecosystem health, and is necessary to understand the relative importance of prospective drivers of land cover change. In spotted or leopard vegetation patterns, high-cover patches or spots are isodiametric or have irregular circular shapes. Vegetation spots range from 1 m to less than 100 m in diameter. As the above figures of this paper, vegetation pattern in study area where vegetation is composed of a two-phase (high pant cover and bare land) mosaic can be called as spotted vegetation. According to the components and shape, the general structure of the community may be characterized as a combination of three patch types: (1) Suaeda salsa and scattered Tamarix chinensis (Fig.1a); (2) Tamarix chinensis, Phragmites australis and Imperata cylindrica encircled by two rings of Limonium bicolor (Bge.) e. Ktze and Suaeda salsa (Fig.1b) and (3) Tamarix chenensis encircled by a ring of Suaeda salsa (Fig.1c). Three aspects of the patch types stand out from general field observation: (1) Tamarix chinensis is present in the three patch types; (2) Suaeda salsa is present in the three patch types in the outer part of rings and (3) different degrees of grass ring completeness are apparent. Taking into account these aspects, we hypothesized that the structure of vegetation is the spatial manifestation of different phases of a cyclical succession. Because the first and third patch types are confused among the neighbor vegetation communities and environment, only the second patch type is discussed in this paper. However, with limited spatial resolution of the used images, the patch is only identified as a whole circular patch not a ring. To describe the patch structure of the community, the patch is identified firstly.

On the SPOT5 panchromatic images, bright pixels correspond to bare soil, whereas dark pixels result from water, and intermediate grayscale pixels relate to vegetation. Both the spectral differences and shape differences between vegetation patches and the other objects in the image can be used to detect the patches. Because the vegetation patches in the study area are quasi-circular which is obviously different from the other objects in the images, so the quasi-circular vegetation patches can be detected based on shape differences, which is done in MATLAB software.

Firstly, use the Function ToGray in MATLAB software to transform the color image into the grayscale image. According to the color difference of vegetation patches and the other objects, one appropriate threshold (DN<75) is selected to classify the grayscale image into binary image. The color of vegetation is white and the others are black after inverting the color using the Function InvertBinary in MATLAB.

Secondly, use the Function BWBOUNDAREIES in MATLAB trace the exterior edges of targets and label the targets. Then the centroid coordinates of the targets are calculated and saved. The actual areas of targets are calculated through accumulation of pixels of targets, and the theoretical areas of the targets are calculated according to the area equation of ellipse too.

Finally, the ratio between the actual and theoretical area of each target are calculated. When the ratio between the actual and theoretical area of the target is dropped into the given certain interval range (0.7-1.2), the quasi-circular vegetation patches are detected very well (shown in Fig.4). After the interactive post-classifications of the above Fig.4,

the overall detection accuracy of the year 2000, 2005 and 2012 are 90.1%, 84.9% and 73.4%. This is enough for the needs of monitoring and identifying the vegetation community patches.

Use average nearest neighbor method in ArcGIS 10 (the famous commercial geographic information system software in the world) to analyze the patch patterns of the year 2000, 2005 and 2012. The Average Nearest Neighbor tool measures the distance between each feature centroid and its nearest neighbor's centroid location (see ArcGIS 10 help documents). It then averages all these nearest neighbor distances. If the average distance is less than the average for a hypothetical random distribution, the distribution of the features being analyzed is considered clustered. If the average distance is greater than a hypothetical random distribution, the features are considered dispersed. The average nearest neighbor ratio is calculated as the observed average distance divided by the expected average distance (with expected average distance being based on a hypothetical random distribution with the same number of features covering the same total area). If the index (average nearest neighbor ratio) is less than 1, the pattern exhibits clustering. If the index is greater than 1, the trend is toward dispersion. The null hypothesis for the pattern analysis tools is complete spatial randomness. The p-value is a probability and the z-score is simply standard deviations. When it yields small p-values and either a very high or a very low z-score from spatial pattern analysis, this indicates that the null hypothesis is rejected and the observed spatial pattern unlikely reflects the theoretical random pattern represented by null hypothesis. In this paper, given the z-score of -0.55 of the year 2000 and 0.45 of the year 2005, the pattern does not appear to be significantly different than random. Given the z-score of 1.90 of the year 2012, there is less than 10% likelihood that this dispersed pattern could be the result of random change.

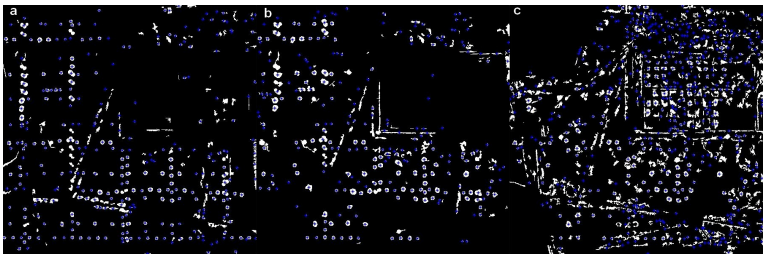

Fig. 4. Maps of vegetation patch detection (patches labeled with the blue *). (a) the detection results of July 9, 2000. (b) the detection results of September 7, 2005. (c) the detection results of May 27, 2012.

3 Results

3.1 Patch Structure and Patterns

In order to analyze the patch structure and spatial patterns more accurately, visual interpretation is used to get the real amount of patches of the year 2000, 2005 and

2012 year which is 252, 270 and 218 respectively (shown in Fig.5). In general, high-cover patches or spots are isodiametric or have irregular circular shapes which represent approximately 10.1% of the study area. Many vegetation spots distribute along the four edges of the square whose edge is about 290 m long, which are bigger in size than the other spots (see Fig.5). Vegetation spots range from 2.9 m to 31.5 m in diameter, and the minimum and maximum area of spots is 26 m^2 and 3122 m^2, and the areas of percent 50 of vegetation spots range from 284 m^2 to 766 m^2 (see Table 1 and Fig.6). The average distance between each patch centroid and its nearest neighbor's patch centroid location is about 44 m.

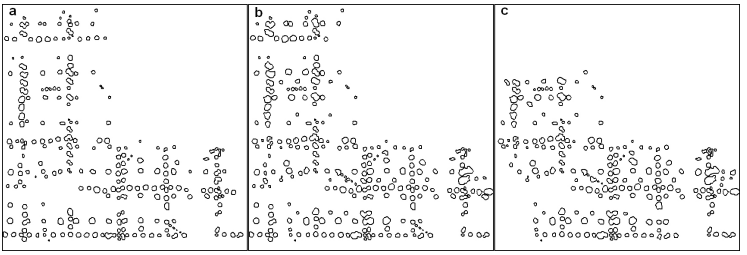

Fig. 5. Three visual interpretation result maps of spotted pattern in the different years. (a) the view of July 9, 2000. (b) the view of September 7, 2005. (c) the view of May 27, 2012.

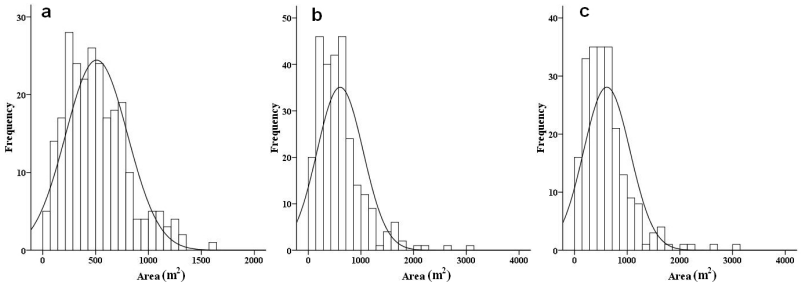

Fig. 6. The frequency histogram of the area of spotted patch. (a) the histogram of July 9, 2000. (b) the histogram of September 7, 2005. (c) the histogram of May 27, 2012.

3.2 Patch Temporal Dynamics

Changes in the vegetation pattern and state in arid regions are among the main indicators of the state of land degradation leading to desertification. In general, patch dynamics include both a building and a degenerative phase. The degenerative phase starts with the death of the dominant individuals. If the vegetation cover is removed, the redistribution of water is altered inducing higher runoff rates and causing soil erosion during intense rainstorms. The image displayed in Fig.3 and Fig.5 illustrates the temporal dynamic in patch patterns in the study area. Compared with the 2000, there was a slight, yet significant, increase of patches in 2005. These new patches

don't distributed randomly, and fill up the blanks among the primary patches regularly. This indicates that the extension of the patches is affected by some or other factor. A decrease of patches was also noted, as a consequence of several patches coming into being a big patch. Compared with the 2000 and the 2005, there was not an increase of patches in 2012. An dramatic decrease was noted in the upper left and lower left areas, as a consequence of the impacts of human occupation. During the 2000 to 2012 interval, the area of patches didn't change significantly except the new patches (in 2000, the area of percent 50 of patches range from 284 m^2 to 686 m^2; in 2005, the area of percent 50 of patches range from 292 m^2 to 743 m^2; In 2012, the area of percent 50 of patches range from 332 m^2 to 766 m^2; see Fig. 6). The area of new patches in 2005 during the 2005 to 2012 interval was not significantly changed too. These important spatial extensions of patches indicate: (1) without human disturbance, the patches can't decrease; (2) the time of quick extensions of patches is less than five years; (3) the new patches grow at some certain location, not randomly.

Table 1. The statistical analysis of the areas of spotted patches in the different years

Date	July 7, 2000	September 7, 2005	May 27, 2012
Area (m^2)			
Minimum	26	26	48
Maximum	1594	3122	3122
Sum	128869	163216	133804
Mean	511	605	614
Standard Deviation	294	440	442
Count	**252**	**270**	**218**

4 Discussion

4.1 Vegetation Extension and Ecological Restoration

With the increase of human development activities, except that the vegetation communities are directly destroyed, the vegetation habitats also are changed indirectly, which has made some vegetation communities disappear and the other vegetation communities extend [13]. Therefore, it is necessary to study the phenomenon caused by development activities in order to the negative effects of development activities on ecological environment. In fact, the extension phenomenon of vegetation patches caused by oil field development activities has been found in the many areas of the YRD. From the ecological role, such extension of plant community is beneficial to the ecological restoration and protection and re-vegetation of the YRD. The YRD belongs to the area lack of fresh water. It is impossible to fully use the fresh water supply to make the restoration and re-vegetation of the wetland ecosystem. This vegetation extension, obviating the need for additional funds, is necessary to lucubrate, and look for the countermeasures which make it change from

spontaneous state into artificial coordinating for maximum extension in the suitable areas, which will help to better coordinate the contradiction between the oil field development and the wetland ecosystem protection.

4.2 Patch Pattern and oil Field Development

Each patch in the mosaic has its own dynamics and there is no unidirectional overall landscape pattern. But many vegetation patches distribute along the four edges of the square whose edge is about 290 m long, which are bigger in size than the spots at the other locations (see Fig. 5). This is possibly as a consequence of seismic exploration at Gudong Oil Field since 1980's. The seismic exploration changes the local soil structure and geomorphology due to drilling and blasting for burying detectors regularly for receiving the seismic waves, and forms irregular circular geomorphology where is suitable for the vegetation patch growth. Martin (1999) reported that in the spotted patterns, the building phase starts with the establishment and growth of woody plants in a certain location, and patch dynamics are associated with growth and mortality of woody plants [14]. This is true in the evolution of vegetation patches of Gudong Oil Field? To further study vegetation ring completeness and spatial distribution and the relationships with soil and water and nutrients, may make a valuable contribution to the answer of this question and the monitoring of the impacts of seismic exploration of oil field.

5 Conclusions

It is sufficient to study decametric-scale vegetation patterns using high spatial resolution remote sensing data. The spotted pattern of vegetation in Gudong Oil Field of the YRD is first identified and described using high spatial resolution SPOT5 satellite image data. We have shown that the image acquired in summer or autumn (from July to October of every year) is more suitable for identifying the patches of the study area, which is better in detection accuracy than the image acquired in winter or spring (from November of every year to June of the next year). There are three patch types in Gudong Oil Field, which are the spatial manifestation of different phases of a cyclical succession. In general, high-cover patches or spots are isodiametric or have irregular circular shapes which represent approximately 10.1% of the study area. Vegetation spots range from 2.9 m to 31.5 m in diameter, and the minimum and maximum area of spots is 26 m^2 and 3122 m^2, and the areas of percent 50 of vegetation spots range from 284 m^2 to 766 m^2 (see Table 1 and Fig. 6). By comparing changes in vegetation patterns during the 2000 to 2012 interval, we have shown that without exogenous disturbance, the patches don't decrease and the time of quick extensions of patches is less than five years, and the new patches grow at some certain location, not randomly. A slight increase of patches is noted in 2005 and a dramatic decrease is in the upper left and lower left areas in 2012, as a consequence of human occupations. These research results should be considered for the restoration of vegetation in the future.

Because every vegetation community patch actually had a ring layer structure (range from 0.5 m to less than 5 m in diameter), which needed use higher spatial resolution remote sensing image such as Geoeye-1 with 0.41m spatial resolution to study in the future. Of course, the vegetation patch extension mechanism and speed would be studied in detail through using the high resolution images acquired during 2000 to 2005.

Acknowledgments. This research work was jointly supported by a grant from the National Science-Technology Support Plan Projects (Project No. 2013BAD05B03) and a grant from the National Natural Science Foundation of China (Project No. 41023010, 41271407) and a grant from the Research Fund of Field Station of IGSNRR, CAS.

References

1. Xu, X.G., Guo, H.H., Chen, X.L., et al.: A multi–scale study on land use and land cover quality change: the case of the Yellow River Delta in China. Geo Journal 56(3), 177–183 (2002)
2. Shi, L.Q., Li, J.F., Ying, M., et al.: Advances in researches on the modern Yellow River Delta development and evolution. Advances in Marine Science 23, 96–104 (2005)
3. Pascoe, G.A.: Wetland risk assessment. Environmental Toxicology Chemistry 12, 2293–2307 (1993)
4. Hiroyoshi, H., Yuri, S., Jason, M., et al.: Satellite tracking of the migration of the red-crowned crane Grus japonensis. Ecology Research 13(3), 273–282 (1998)
5. Li, S.N., Wang, G.X., Deng, W., et al.: Influence of hydrology process on wetland landscape pattern: a case study in the Yellow River Delta. Ecology Engineering 35(12), 1719–1726 (2009)
6. Bi, X.L., Wang, B., Lu, Q.S.: Fragmentation effects of oil wells and roads on the Yellow River Delta, North China. Ocean & Coast Management 54(3), 256–264 (2011)
7. Cui, B.S., Yang, Q.C., Yang, Z.F., et al.: Evaluating the ecological performance of wetland restoration in the Yellow River Delta, China. Ecological Engineering 35, 1090–1103 (2009)
8. Fang, H.L., Xu, J.: Land cover and vegetation change in the Yellow River Delta Nature Reserve analyzed with Landsat thematic mapper data. Geocarto International 15(4), 1–7 (2000)
9. Zhang, G.S., Wang, R.Q., Song, B.M.: Plant community succession in modern Yellow River Delta, China. Journal of Zhejiang University Sciences B 8(8), 540–548 (2007)
10. Soriano, A., Osvaldo, E.S., Perelman, S.B.: Patch structure and dynamics in a Patagonian arid steppe. Vegetatio 111, 127–135 (1994)
11. Kadmon, R., Harari-Kremer, R.: Studying long-term vegetation dynamics using digital processing of historical aerial photographs. Remote Sensing of Environment 6(8), 164–176 (1999)
12. Barbier, N., Couteron, P., Lejoly, J., et al.: Self-organized vegetation patterning as a fingerprint of climate and human impact on semi-arid ecosystems. Journal of Ecology 94, 537–547 (2006)
13. Peiyou, H., Ruiru, G.: Research on the Extension of Tamarix Shrubs Resulted from Development Projects in Arid area. Journal of Forestry Research 15(1), 45–48 (2004)
14. Martin, R.A., Osvaldo, E.S.: Patch structure, dynamics and implications for the functioning of arid ecosystems. Tree 14(7), 273–277 (1999)

RPNOS: Reliable Pedestrian Navigation on a Smartphone

Jiuchao Qian, Jiabin Ma, Rendong Ying, and Peilin Liu

School of Electronic Information and Electrical Engineering,
Shanghai Jiao Tong University (SJTU), Shanghai, China
andychin9@gmail.com

Abstract. This paper presents a novel solution using smartphone inertial sensors for pedestrian navigation application. Pedestrian dead reckoning (PDR), which determines the relative location of a pedestrian without the need for additional infrastructure assistance, is utilized to locate pedestrians in our work. A robust step detection technique leaves out the preprocessing of raw signal and reduces complex computation. Since the estimation model is related to different walking modes, a stride length estimation algorithm using a linear combination of step frequency and acceleration variance is developed. Heading determination is carried out by detecting the gravity crossings of acceleration, which is effective to infer the heading form smartphone's yaw angle. The experimental results indicate that the displacement is estimated with 1.79 % error of distance travelled in the best situation and 3.86 % in the worst situation.

Keywords: Pedestrian navigation, smartphone inertial sensors, PDR.

1 Introduction

As one of the most challenging application in the development of navigation technologies, pedestrian navigation has gained great concern in recent years. Pedestrian navigation system (PNS) is generally required to provide continuous positioning capability in all environments including urban canyons, indoors and undergrounds, where GPS and other radio navigation signals may degrade or even outage, due to the weak signal or non-line-of-sight (NLOS) conditions between the pedestrian and satellites or base stations. Therefore, an accurate and reliable PNS is an important and emerging technology for many location-based services (LBS) applications, such as commercial, public-safety and military fields [1]. As we known, most of existing PNS approaches rely on the dedicated inertial measurement units (IMUs) fixed on user body (e.g. foot and waist) for pedestrian tracking [2, 3]. Although the so-called zero velocity update (ZUPT) methodology is an effective way to reduce the error drift of an inertial sensor-based navigation system, the main drawback of this method related to inconvenience has been discussed by several researchers [4, 5]. They point out that the IMU module, in the ZUPT algorithm, has to be attached on the foot in all the experiment, which may bring some uncomfortable feelings for the pedestrian and thus limit its widely application in the actual situation.

F. Bian et al. (Eds.): GRMSE 2013, Part I, CCIS 398, pp. 188–199, 2013.
© Springer-Verlag Berlin Heidelberg 2013

With the development of micro electromechanical system (MEMS) technologies and the evolution of the capabilities in handheld devices, it becomes universal to integrate MEMS sensors (e.g. accelerometers, gyroscopes and magnetometers) into personal navigation devices, such as smartphones and tablets. Consequently, pedestrian navigation relies on smartphones only becomes a potential solution with acceptable accuracy using reliable PDR algorithms. Moreover, pedestrian navigation on a smartphone embedded with MEMS sensors has several advantages over the GPS system, such as small size, light weight and especially low power consumption, which are the major concerns for pedestrian navigation applications. However, to achieve reliable positioning of pedestrians using smartphones, we face several significant challenges as follows:

- Low-cost MEMS inertial sensors in smartphones are only able to provide required accuracy for brief moments due to the sensor errors arise from random zero bias and oscillation noise.
- During walking, the smartphone can be placed in different positions including the pedestrian's hand and pocket, which leads different smartphone orientations and affects the heading determination of PDR algorithm.
- While the smartphone is in the pedestrian's hand, the flexibility and complexity of hands activities make the reliable step detection difficult. Furthermore, the pedestrian may switch modes such as from swinging the hand to texting or taking a phone call.

In the recent years, several pedestrian navigation technologies that leverage MEMS sensor in a smartphone have been researched [5-7]. However, there exist many unsolved problems that arise from the challenges mentioned above in these systems, such as limited degree of freedom of smartphone orientations, constant stride length estimation, and lacking heading determination, etc.

In this paper, we present Reliable Pedestrian Navigation on a Smartphone (RPNOS), a scheme using PDR algorithm for pedestrian navigation application. To tackle the low-cost inertial sensors, RPNOS focuses on the topic of the designing of a robust step detection algorithm. Using the local gravity value crossings detection and autocorrelation operation of measured acceleration signals, we detect steps with low false alarm probability, which makes sure that the algorithm is not susceptible to the actual situation and independent of walking patterns, routes, distances and terrains. Then the stride length is estimated in RPNOS based on the relationship between stride length and stride interval (reciprocal of stride frequency). In order to find out the most appropriate parameters for the pedestrians, the stride length estimation models are established and are tested repeatedly according to extensive experiments that were performed by subjects with different physical profiles such as gender, height and weight. Heading determination is acquired through inferring the offset between the pedestrian and her smartphone and gained from the yaw angle of the smartphone sensors.

In the rest of this paper, we describe first the position principle of PDR module and it is followed by detailed description of the algorithms for step detection, stride length

estimation and heading determination. Afterward, the performance of proposed algorithms is evaluated through an outdoor experiment and is compared with ground truth. Finally, the conclusion and future works are drawn.

2 PDR Algorithm

Pedestrian dead reckoning (PDR) is a relative navigation technique, which determines the relative location of a pedestrian by using step detection, stride length estimation, and heading determination. The PDR algorithm can provide means of reducing the inertial error accumulation to the navigation solution by taking advantage of the sequential characteristics of the pedestrian motion [7]. Typically, the accelerometer measurements are utilized to implement step detection and stride length estimation, and heading determination is simultaneously implemented by fusing the information from gyroscopes and magnetometers. The block diagram of RPNOS system proposed in this paper is shown in Fig. 1.

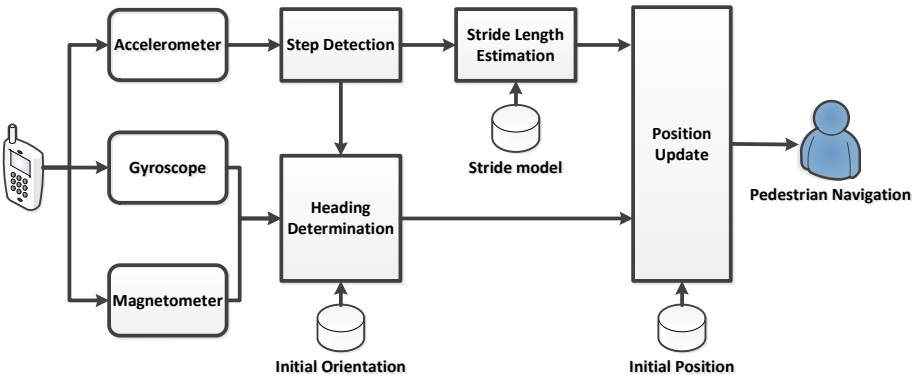

Fig. 1. Block diagram of RPNOS system

As shown in Fig. 1, the sensor data collected from a smartphone is used by the PDR modules for pedestrian navigation. Note that the stride model is trained offline and inputted to update the stride length online according to the stride frequency and acceleration variance. In addition, the system needs to get the initial position and orientation of the pedestrian in advance through GPS or user input, and then updates the position of the pedestrian at each step.

In the PDR system, the position of the pedestrian can be propagated as the following equations:

$$\begin{cases} X_{k+1} = X_k + SL * \sin(\theta_{k^*}) \\ Y_{k+1} = Y_k + SL * \cos(\theta_{k^*}) \end{cases} \tag{1}$$

where X and Y are the coordinates in north and east directions, SL is the stride length and θ is the heading at epoch k^*, which is not necessary same as subscript k that denotes the index of steps and defined in Heading Determination section. From the Equation 1, it is shown that we can estimate the position of the pedestrian at any moment provided that the initial position, the stride length and the heading of the pedestrian are known.

2.1 Step Detection

Step detection algorithm, as a basic technique of PDR system, is crucial to influence the performance of the pedestrian navigation system. As previously mentioned, the accelerometer signal is usually used to detect the steps of the pedestrian. A number of papers have described the methods of step detecting for PDR systems, such as peak detection and Fourier transformation [8, 9]. However, with regards to the low-cost MEMS sensors in a smartphone and the flexibility of hands activities, the performance of these methods cannot be guaranteed when the experimental measurements are collected from accelerometers of smartphones.

In general, the output of accelerometer may present harmonic oscillation waveforms that result from walking behaviors. Fig. 2 shows the triaxial acceleration signal collected from a smartphone in hand during normal walking and its total acceleration magnitude.

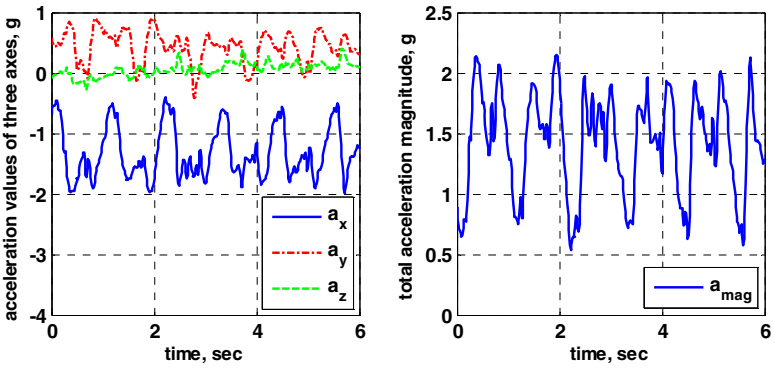

(a) (b)

Fig. 2. Acceleration signal and its total magnitude during walking

As shown in Fig. 2, the total acceleration magnitude, as well as all the output acceleration signals of three axes, has approximately bimodal oscillation mode with interferences that arise from perturbations of the hand. And the magnitude a_{mag} can be expressed as:

$$a_{mag,k} = \sqrt{a_{x,k}^2 + a_{y,k}^2 + a_{z,k}^2} \tag{2}$$

where $a_{x,k}$, $a_{y,k}$ and $a_{z,k}$ are the measurements from the triaxial accelerometer. Unlike other approaches that use vertical direction of the acceleration to detect steps, the total acceleration magnitude is used in our algorithm, in view of its advantage of being insensitive to the orientation of the accelerometer sensor.

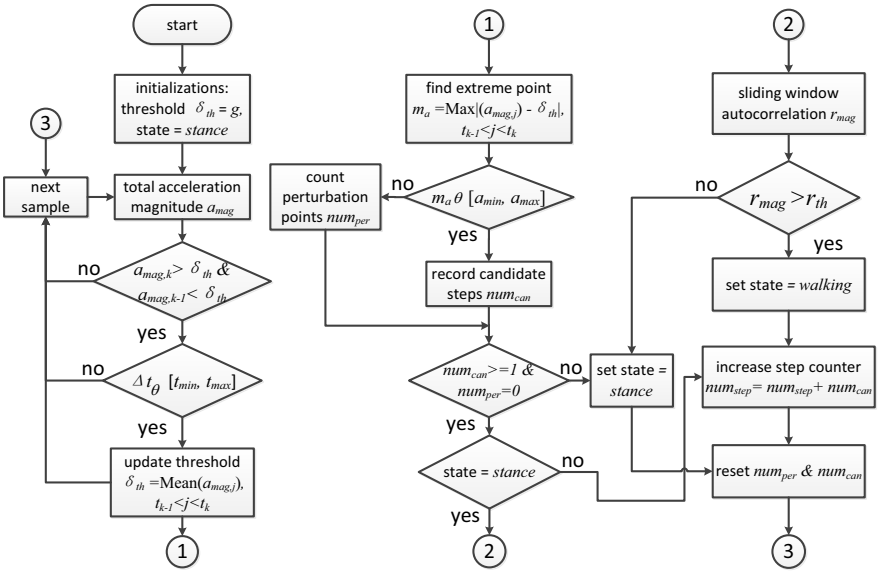

Fig. 3. Proposed step detection algorithm

Fig. 3 shows the flowchart of the proposed step detection algorithm. At the beginning of the algorithm, the thresholdδ_{th} is initialized to the local gravity acceleration value and the total acceleration magnitude a_{mag} is calculated. A candidate step is identified by following criterions:

C1. The total acceleration magnitude a_{mag} has to cross the thresholdδ_{th} from negative to positive.

C2. The time intervalΔt between two consecutive steps defined by C1 must be within t_{min} to t_{max}.

C3. The extreme value of a_{mag} during a step phase, denoted as ma, compared with the thresholdδ_{th}, has to be among a_{min} to a_{max}, otherwise a perturbation point is recorded.

The thresholdδ_{th} in C3 is updated dynamically according to the mean value over a step period. Then a sliding window of appropriate size is created and a finite state machine (FSM) is actuated. Under the premise that all the candidate steps and perturbation points in the sliding window have been recorded, the state can be determined as follows:

S1. *Stance*: there is no candidate step or there exists perturbation points in the sliding window.

S2. *Walking*: the candidate step number is more than one and there is not any perturbation point within the sliding window, and the autocorrelation value r_{mag} is more than threshold r_{th}.

The autocorrelation in S2 is used for distinguish walking motions from other pedestrian activities (refer to Fig. 4), and it needs to be computed only when the state transits from *stance* to *walking*. The purpose of this scheme is to effectively reduce unnecessary calculations. As a result, the step counter num_{step} is incremented if the state is *walking* and the candidate steps counter num_{can} and the perturbation points counter num_{per} are reset to zero for the next sample.

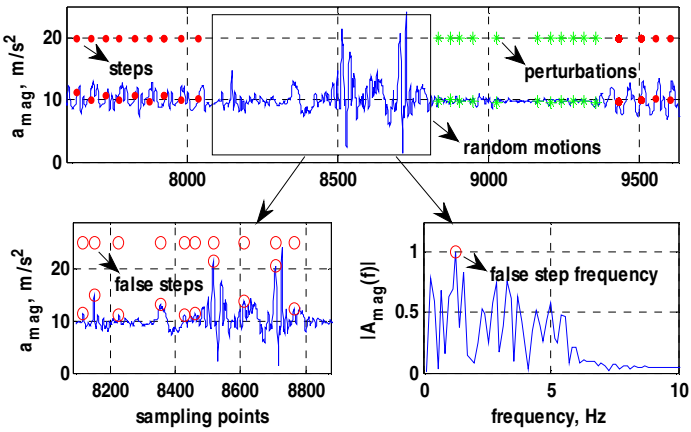

Fig. 4. Step detection for activities during actual walking

The top of Fig. 4 shows that the experimental results of step detection using proposed algorithm by which activities including steps, perturbations and random motions all can be detected and classified with high accuracy. However, for peak detection and FFT, random motions that occur during changing actions are difficult to be distinguished from real walking behaviors. As a result, a large number of false steps are introduced into the detection process (see the bottom of Fig. 4). Therefore, compared with peak detection and FFT, the algorithm proposed in this letter is more adaptive to the flexible and complex hands activities during walking motions.

2.2 Stride Length Estimation

In the PDR system, stride length estimation, combined with heading determination, is utilized to compute the traveled distance and update the position of the pedestrian on condition that the previous position is known. As described in related IMUs based PDR system, the step length of a pedestrian is not constant and varies with walking speed, step frequency, and inclination of the walking route [10]. In order to estimate

the travel distance of the PDR system accurately, adaptive stride length estimation must be adopted according to these variations.

In RPNOS, the stride length is estimated using a linear combination of step frequency and acceleration variance [11]. The stride length is estimated through following equations:

$$\text{Stride Length } L = \alpha \cdot f + \beta \cdot v + \gamma \tag{3}$$

where f is step frequency, v is acceleration variance during one step; α and β are weighting factors of step frequency and acceleration variance; γ is constant. And the step frequency and acceleration variance in Equation 3 are obtained as:

$$\begin{aligned} f_k &= 1/(t_k - t_{k-1}) \\ v_k &= \sum_{t=t_{k-1}}^{t_k} \frac{(a_k - \overline{a}_k)^2}{n} \end{aligned} \tag{4}$$

where f_k and v_k are step frequency and acceleration variance at t_k ; t_k means timestamp of the step k ; a_k is acceleration signal and $\overline{a}_k$ is average acceleration during on step; n is the number of sensor sampling points.

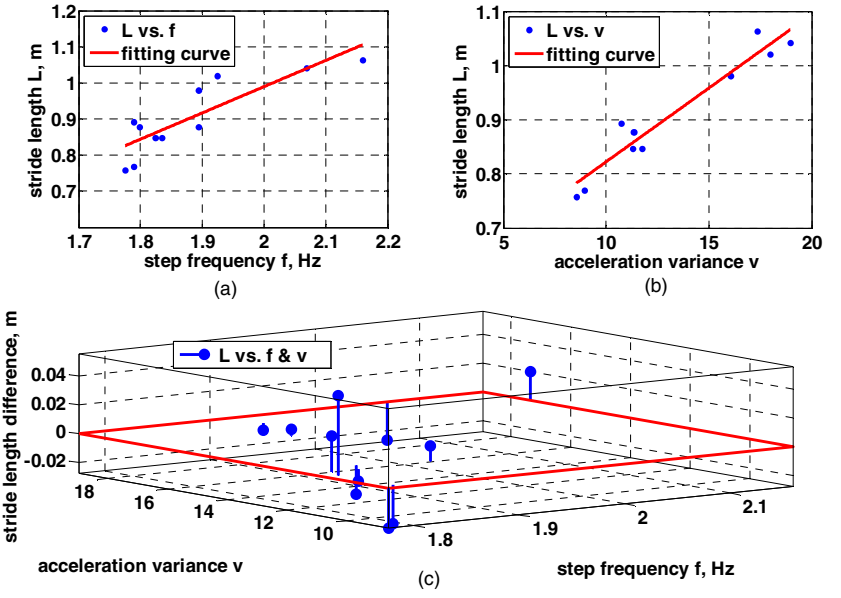

Fig. 5. Unary and binary polynomial fitting of step frequency and acceleration variance for stride length estimation

Fig. 5 shows that the relations between stride length and variations including step frequency and acceleration variance. From this figure, we can find that stride length is approximately proportional to the step frequency and acceleration variance. And the binary polynomial fitting is better than unary fitting due to the root mean square error (RMSE) decrease from 0.0571 to 0.02937.

2.3 Heading Determination

Heading determination in PDR is like heart in a body, because the error in heading leads to quadratic growth of localization error. To obtain the heading of phone, one has to deal with the altitude of the sensor which can be represented in the form of quaternion. RPNOS calculates the altitude quaternion by adopting a gradient-descent attitude and heading reference system (AHRS) algorithm using MARG sensor arrays (including accelerometers, gyroscopes and magnetometers) [12], which calm to be both computationally inexpensive and effective at low sampling rates. Some PDR systems use body mounted MARG to provide accurate heading information. However, a smartphone has ways of placements and much higher degree of freedom. We usually use it to text, to make a call; it may be swinging with hands or be placed in pocket.

RPNOS deals with these situations and provides reliable heading determination in following four scenarios:

- Compass: User is holding the smartphone stably with the screen up. She/he may be checking the map or texting.
- Calling: User is making a call, so the smartphone is close to her ear.
- Pocket: Smartphone is placed in the user's trousers' pocket.
- Hand-swinging: User is holding the smartphone in hand, and the smartphone is swinging with the hand.

We first assume that the offset between sensor yaw and pedestrian heading is known. This is reasonable because there always be a chance for the user to check her smartphone when he points the smartphone at her direction. With the knowledge of heading offset, first two situations can be solved. However, in the situation 3 and 4, even the user walks straight ahead, sensor's yaw angle still can change dynamically. To determine the heading in dynamic state, RPNOS takes advantage of the characteristics of walking behaviors.

As demonstrated before, when a pedestrian is walking, the MARG attached to her body will give a periodic signal which represents the walking motion. The magnitude of acceleration is not only useful in detecting steps but also effective in determining the pedestrian's heading when the smartphone is in pocket or swinging with the hand. As illustrated in Fig. 6, despite of the dynamic changing of sensor's yaw angle, the moment to access the true heading is determined by the time when the magnitude of acceleration cross the threshold of gravity. This is reasonable since smartphone will have the same offset heading to pedestrian when the magnitude of acceleration crosses the gravity. Fig. 7 shows the result of heading determination according to gravity value crossings of acceleration. As can be seen in this figure, the algorithm estimates the heading well due to accurate crossings detection.

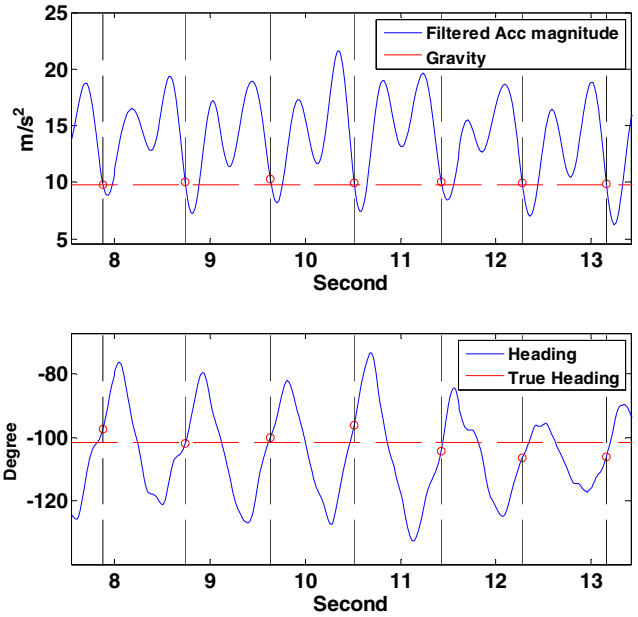

Fig. 6. Heading determination corresponding to acceleration magnitude

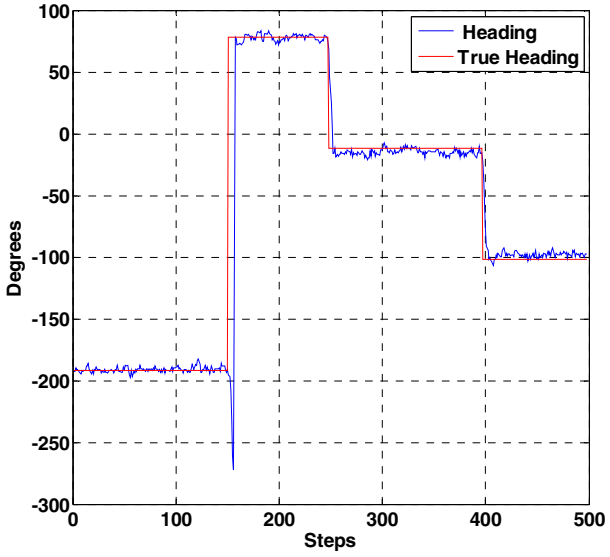

Fig. 7. Heading determination and its true heading

3 Experimental Results

In this section, to verify the performance of RPNOS in practical situations, an experiment with long distance was performed. The experiment site was situated at the football stadium of our university where the total length of one lap was about 345 m. The subjects, who participated in the experiment, walked in different postures naturally each lap as descriptions in heading determination section. In the experiment, an iPhone was utilized and the output rate of the smartphone was set to 32 Hz (the output rate of the data was increased to 64 Hz by interpolation when RPNOS system was in operation).

Fig. 8 shows that the estimated trajectory using RPNOS. The blue line, red line, yellow line and green line represent Compass, Calling, Pocket and Hand-swinging situations respectively. The results indicate that in most situations, the positioning accuracy of RPNOS is reliable and accurate. However, when the smartphone is placed in the pocket, it is hard to estimation the exact positions of pedestrians especially the headings due to the random shaking of the smartphone. Table 1 lists the detailed results of the experiments in four scenarios. Obviously, the best result is Compass situation, the maximum error is 11.6358 m and the error of distance travelled is only 1.79 %. And the worst one is Pocket situation, the maximum error is 19.4688 m and the error of distance travelled is 3.86 %.

Fig. 8. Estimated trajectory of pedestrian around the football stadium

Table 1. Estimated errors in four scenarios

Scenarios	Maximum error	Error of distance travelled
Compass	11.6358 m	1.79 %
Calling	15.0683 m	3.7 %
Hand-swinging	15.346 m	2.31 %
Pocket	19.4688 m	3.86 %

4 Conclusion

In this paper, a reliable smartphone based pedestrian navigation system named RPNOS is proposed. The system possesses an efficient performance in step detection and heading determination, and allows us to positioning pedestrians accurately using PDR algorithm with comparatively less amount of calculation. Experimental results show that RPNOS, which is applicable to diverse usage scenarios of smartphones, could be a prospective system for pedestrian navigation applications.

For future work, the system will be improved in all aspects of PDR algorithm and be tested in indoor environment where the heading determination may be seriously affected by various magnetic interferences, such as electric equipment, reinforced concrete, and so on. On the other hand, other technologies, such as WLAN, Bluetooth, RFID, etc., can be fused into RPNOS to improve the positioning accuracy.

Acknowledgments. This work is supported by Shanghai Key Laboratory of Navigation and Location Based Services.

References

1. Beauregard, S., Haas, H.: Pedestrian dead reckoning: a basis for personal positioning. In: Proceeding of the 3rd Workshop on Positioning, Navigation and Communication, Hannover, Germany, pp. 27–36 (2006)
2. Zhang, S., Xiong, Y., Ma, J., Song, Z., Wang, W.: Indoor location based on independent sensors and WIFI. In: International Conference on Computer Science and Network Technology, vol. 4, pp. 2640–2643. IEEE (2011)
3. Lan, K.C., Shih, W.Y.: Using simple harmonic motion to estimate walking distance for waist-mounted PDR. In: Wireless Communications and Networking Conference, pp. 2445–2450. IEEE (2012)
4. Cui, Y., Ariyur, K.B.: Pedestrian navigation with INS measurements and gait models. In: ION GNSS, Portland, OR, pp. 1328–1337 (2011)
5. Alzantot, M., Youssef, M.: UPTIME: ubiquitous pedestrian tracking using mobile phones. In: Wireless Communications and Networking Conference, pp. 3204–3209. IEEE (2012)
6. Constandache, I., Choudhury, R.R., Rhee, I.: Towards mobile phone localization without war-driving. In: 2010 Proceeding of the IEEE INFOCOM, pp. 1–9. IEEE (2010)
7. Bylemans, I., Weyn, M., Klepal, M.: Mobile phone-base displacement estimation for opportunistic localization systems. In: 3rd International Conference on Mobile Ubiquitous Computing, Systems, Services and Technologies, pp. 113–118. IEEE (2009)

8. Jang, H.J., Kim, J.W., Hwang, D.H.: Robust step detection method for pedestrian navigation systems. J. Electronics Letters 43, 14 (2007)
9. Levi, R.W., Judd, T.: Dead reckoning navigational system using accelerometer to measure foot impacts. U.S. Patent No. 5,583,776, Washington, DC (1996)
10. Leppakoski, H., Kappi, J., Syrjarinne, J.: Error analysis of step length estimation in pedestrian dead reckoning. In: Proceedings of the 15th International Technical Meeting of the Satellite Division of the Institute of Navigation, Portland, OR, pp. 1136–1142 (2002)
11. Shin, S.H., Park, C.G., Kim, J.W., Hong, H.S., Lee, J.M.: Adaptive step length estimation algorithm using low-cost MEMS inertial sensors. In: Sensors Application Symposium, pp. 1–5. IEEE (2007)
12. Madgwick, S.: An efficient orientation filter for inertial and inertial/magnetic sensor arrays. Technical report, Department of Mechanical Engineering, University of Bristol (2010)

Study of Water Quality in Dubai Creek Using DubaiSat-1 Multispectral Imagery

Tarig A. Ali, Md. Maruf Mortula, and Serter Atabay

Department of Civil Engineering, American University of Sharjah,
Sharjah, United Arab Emirates
atarig@aus.edu

Abstract. Dubai has witnessed enormous infrastructural developments within the recent decades resulting in rapid changes, which have detrimental effects on the environment. A major attraction in Dubai is Dubai Creek, which is a saltwater stream that divides the city into two major sub-areas known as Bur Dubai and Deira. The creek is playing a major role in commerce and tourism following a few successful dredging efforts. Due to high level of anthropogenic activities, the creek has been viewed as a source of concern. Study of the variability of water quality parameters can help in understanding the pattern of changes and assessing the sustainability of the creek. DubaiSat-1 imagery and field data for monitoring stations along the creek have been utilized to study the variability of chlorophyll-a as essential algal growth indicator. Based on this study, the implications of the urban development on the variability of the concentrations of chlorophyll-a, phosphates, and total nitrogen in the creek are evident. The analysis shows a high correlation between the spectral-based chlorophyll-a concentrations, field-based phosphates and total nitrogen concentrations; as expected. Given the study timeframe, the fluctuation pattern of the concentrations of chlorophyll-a and the limiting nutrients calls for the implementation of a mitigation plan, which will ensure the sustainability of the creek.

Keywords: DubaiSat, Water Quality, Dubai Creek.

1 Introduction

The City of Dubai, United Arab Emirates has witnessed huge developments and intense growth within the last two decades, which have transformed it from a small fishing town into a modern, urbanized city. This transformation has resulted in economic, social, demographic, cultural and societal changes. The petroleum discovery in the sixties uplifted the economy; enabling for the execution of major projects, which have resulted in a modern infrastructural and industrial establishments. Given the unique geographic location of Dubai, commerce has coupled the oil industry in revolutionizing the economy; making the city a major hub for trade and tourism in the Middle East. The economic growth led to a population evolution that was fuelled by the demand of the oil and commercial industries for foreign labor and expertise. This rapid infrastructural development of Dubai is being

F. Bian et al. (Eds.): GRMSE 2013, Part I, CCIS 398, pp. 200–210, 2013.
© Springer-Verlag Berlin Heidelberg 2013

executed according to a strategic plan, which specifies a spatial scale of urbanization (Pacione, 2005).

A natural derivative of the economic growth and infrastructural development of Dubai is environmental pollution resulting mainly from two sources: solid waste disposal and industrial and domestic effluent into the Dubai coast and Dubai Creek. Major sources of pollution into the creek include the effluent from Al Awir wastewater treatment plant (AWWTP), industrial waste from Port Saeed and the Dubai Ship Docking Yard (DSDY), and waste from commercial and tourism vessels. The AWWTP is the major source of pollution to the creek (Saunders et al., 2007). In an effort to closely monitor the Dubai Creek water quality, Dubai Municipality has established numerous monitoring stations across the creek and along the Dubai coast. In this study, parameters measured at the monitoring stations have been used as ground truth data for model calibration and verification.

Water quality parameters are commonly measured through field sampling techniques followed by laboratory analysis. Field sampling is normally performed at monitoring stations established at fixed or mobile locations (e.g. buoy-based). Some of the water quality parameters typically measured at monitoring stations include chlorophyll-a, suspended/dissolved solids/sediments, dissolved organic material, temperature, dissolved oxygen, nitrate, phosphate, pH, salinity, and turbidity. Although field sampling provides accurate measurements, it is a costly method that only provides point-based measurements. Satellite remote sensing techniques, which utilize the spectral property of the water column to derive the concentrations of parameters such as suspended material, sediment, and chlorophyll-a, have emerged as a cost-effective water quality monitoring method (Dekker and. Peters, 1993; Brivio, et al., 2001; Salama et al., 2012).

Presence of high concentrations of water quality parameters; specially limiting nutrients (nitrate and phosphate) accelerate the growth of phytoplankton and algae. Phytoplankton and algae are a group of photosynthesizing marine organisms, the biggest form of which is called seaweeds (May et al., 2003). Seaweed can release hydrogen sulfide; a highly toxic gas, which can cause vomiting and diarrhea when inhaled. The existence of phytoplankton and algae is normally characterized by a greenish water color due to the presence of chlorophyll-a in their cells, but another type of algae known as harmful algal blooms (HABs) turns water color to red. HABs, also known as the red tide, is a type of algae that can cause catastrophic fish kills as it creates a nontransparent layer on the surface of the water that wouldn't allow sunlight to pass through and into the subsurface layers of the water column. Research has shown a high correlation between high levels of nutrients; specifically phosphate (measured as Phosphorus) and HABs (Anderson, et al., 2002; Anderson, et al., 2008; O'Neil et al., 2012).

2 Study Area and Datasets

The study area of this research is Dubai Creek (or Khor Dubai); a 14 km long saltwater stream, which occupies an area of about 8 km^2 and consists of a wide downstream lagoon and a narrow upstream channel with an average depth of about 3 meters (Figure 1). The creek embraces Port Saeed, Dubai Creek Park, and Ras Al Khor Wildlife Sanctuary, and several malls and hotels.

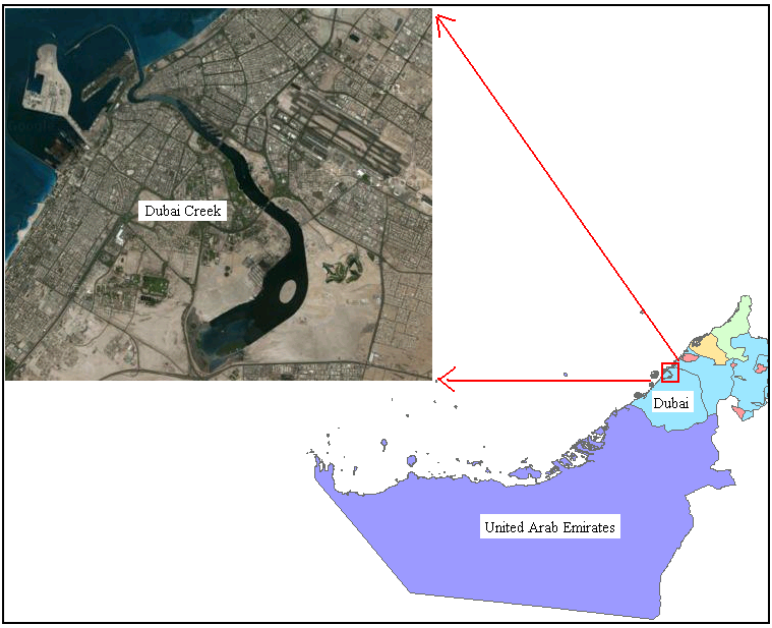

Fig. 1. Study area: Dubai Creek, Dubai, UAE

Table 1. Chlorophyll-a, turbidity, and the limiting nutrients measurements at 5 monitoring stations along Dubai Creek (April-June, 2010)

Station	Northing	Easting	Chlorophyll-a (ug/L)	Turbidity N.T.U	Total Nitrogenmg/L	Phosphates as P (mg/L)
Creek mouth (CM)	2797486.926	495785	0.1	0.5	0.46	0.02
Hyat Regency (HR)	2797345.594	497361	10.8	1	0.29	0.02
Abra (AB)	2795589.528	497081	6.4	0.5	0.69	0.02
Wharfage (WH)	2794425.83	498580	9.2	1.5	1.03	0.07
Floating Bridge (FB)	2793618.334	499200	7.7	1.5	1.2	0.08

The datasets used in this study includes a 5m resolution DubaiSat-1 multispectral imagery obtained from the Emirates Institution for Advanced Science and Technology (EIAST). DubaiSat-1 has one panchromatic (420-720nm) and four multi-spectral bands (B: 420-510nm, G: 510-580nm, R: 600-720nm, NIR: 760-890nm). The multi-spectral DubaiSat-1 images used in this study have been taken for the study area on June 15, 2010 and 2011 respectively. The water quality data was obtained from the Dubai Municipality (DM) for monitoring stations along the creek (Tables 1 & 2). Water quality data include concentrations of chlorophyll-a, phosphate, nitrate, turbidity, total nitrogen, salinity, pH, dissolved oxygen, and petroleum hydrocarbon as chrysene.

Table 2. Chlorophyll-a, turbidity, and limiting nutrients measurements at 5 monitoring stations along Dubai Creek (April-June, 2011)

Station	Northing	Easting	Chlorophyll-a (ug/L)	Turbidity N.T.U	Total Nitrogen (mg/L)	Phosphates as P (mg/L)
Creek mouth (CM)	2797486.926	495785	8.1	0.5	1.51	0.05
Hyat Regency (HR)	2797345.594	497361	11.2	1	0.8	<0.02
Abra (AB)	2795589.528	497081	29.8	1.5	1.98	0.07
Wharfage (WH)	2794425.83	498580	32.8	1.5	2.26	0.09
Floating Bridge (FB)	2793618.334	499200	22.4	1.5	2.22	0.1

3 Methodology

The DubaiSat-1 data used in this study were first pre-processed by correcting for geometric distortions followed by atmospheric and radiometric corrections. The images were geometrically corrected using seven ground control points (GCPs) identified on a 2009 orthophotograph of the study area and a Dubai Municipality (DM) roads map. All GCPs are basically roads intersections that were clearly identified on DubaiSat-1 imagers and are well-distributed in the study area. A two-dimensional affine transformation was carried out to register the images into Dubai Spatial Reference System (Table 3). To minimize the radiometric degradation, the nearest neighbor resampling (NNR) method was then applied to the imagery in order to re-assign digital numbers (DN) to the output imagery

Table 3. Parameters of the Dubai Spatial Reference System

Spatial Reference	Dubai Local Transverse Mercator (DLTM)
Linear Unit	Meter
Angular Unit	Degree
False Easting	500000
False Northing	0
Central Meridian	55.3333
Scale Factor	1
Latitude of Origin	0
Datum	WGS 1984

To perform atmospheric correction, the DNs of the images were used to derive the surface normal and roughness values from all four bands and later the ratios between these bands were computed. These images-derived surface normal and surface roughness values were analyzed, and later checked and corrected using a 4-meter resolution Digital Terrain Model (DTM) developed for the study area from a 2-meter interval contour map obtained from DM. Sensor calibration was then performed on the imagery to convert the DN to absolute radiances (L) using the linear model shown below:

$$L = o + gDN \quad (1)$$

Where "o" and "g" are the offset and gain parameters respectively. Erdas software was used to generate the values of these two parameters using the known spectrum of different objects in the images. Due to the unavailability of the default values of the offset and gain parameters, Erdas-estimated values were used to compute the absolute radiances (L) of the two images.

Linear spectral-based chlorophyll-a model of the following form was developed from the imagery; specifically from the reflectance in the Green, Red, and Infra-red bands of DubaiSat-1 imagery and the field data:

$$\text{Spectral-based Chlorophyll-a} = c1.\text{Green\_L} + c2.\text{Red\_L} + c3.\text{Infra-Red\_L} \quad (2)$$

Where c1, c2, and c3 are constants and Green_L, Red_L, and Infra-Red_L are the absolute radiance values in the green, red, and infra-red bands.

4 Results and Discussion

A least squares adjustment approach was used to estimate the values of the three constants in equation (2) for eight different combinations of the field data for 5, 4 (four combinations), and 3 data points (three combinations) at the five stations in the study area in 2010 and 2011. R-square values for the eight combinations of data points used to develop the model are shown in Table 4 below. Spectral-based chlorophyll-a maps for April-June, 2010 and 2011 using field values at all five stations are shown in Figures 2 and 3 below (R-square values:87.7%, 89.1%; respectively) .

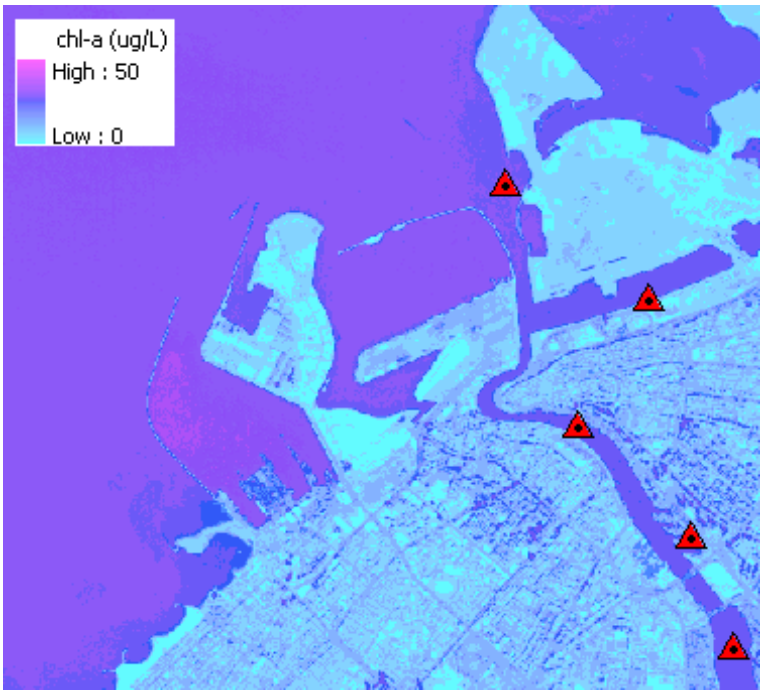

Fig. 2. The spectral-based chlorophyll-a map overlaid with the field values (April-June, 2010)

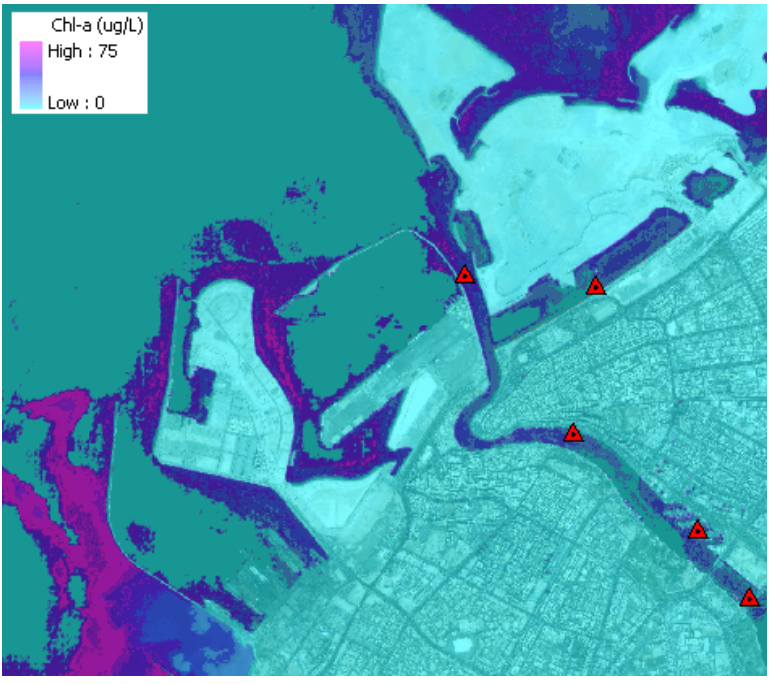

Fig. 3. The spectral-based chlorophyll-a map overlaid with the field values (April-June, 2011)

Table 4. R-square values for the eight combinations of field data points used in the study

Number of points	Station Combination	R-Square (%) - 2010	R-Square (%)- 2011
5	All Stations	87.7	89.1
4	CM, HR, AB, WH	90.1	89.4
4	HR, AB, WH, FB	85.6	88.7
4	CM, HR, WH, FB	84.4	85.1
4	CM, AB, WH, FB	81.6	84.6
3	CM, HR, AB	78.8	83.8
3	HR, AB, WH	79.1	83.5
3	AB, WH, FB	81.2	85.5

Creek mouth (CM), Hyat Regency (HR), Abra (AB), Wharfage (WH), Floating Bridge (FB)

Spectral-based and field measured chlorophyll-a concentrations at all five stations for the maps shown in Figures 2 and 3 above were plotted in Figures 4 and 5 below. The spectral-based chlorophyll-a models seem to estimate the values at all stations to within 1.0 ug/L in 2011 and to within 1.8 ug/L in 2010. An analysis of the relationship between the spectral-based chlorophyll-a concentrations and the phosphates values at the five monitoring stations illustrated a high correlation (94.3%) in 2011 (Figures 6) and rather a low correlation (34.3%). The analysis showed consistently high correlations of 98.2% between the spectral-based chlorophyll-a concentrations and total nitrogen values at the five stations in 2010 and 2011 (Figures 7 and 8). The analysis results confirmed the close correlation between algal growth (chlorophyll-a) and the limiting nutrients (essentially phosphates and nitrogen).

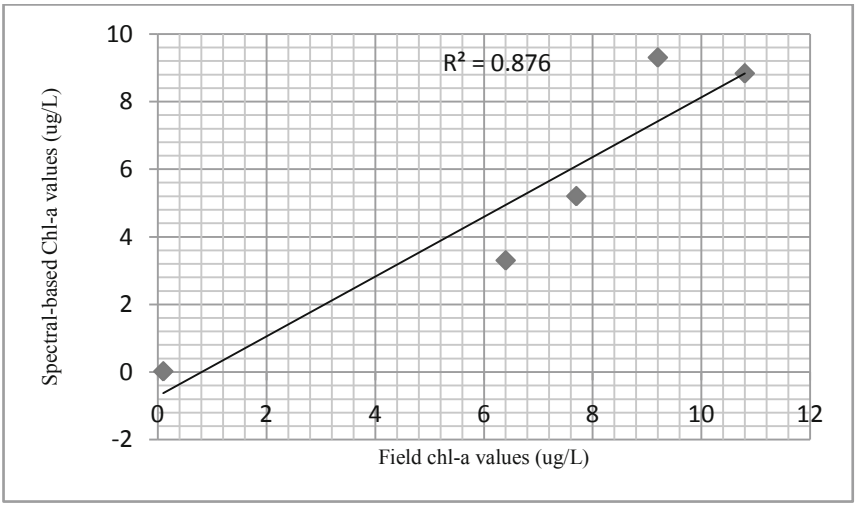

Fig. 4. Spectral- versus field-based Chlorophyll-a concentrations (April-June, 2010)

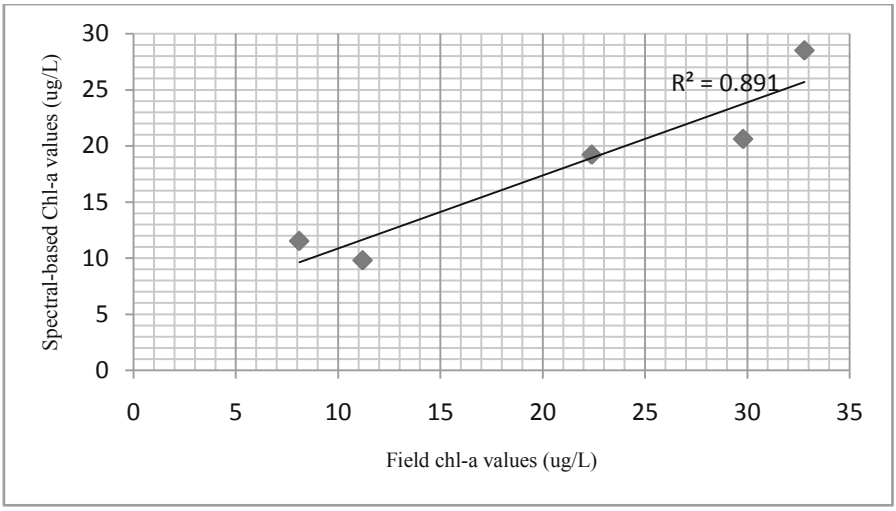

Fig. 5. Spectral- versus field-based Chlorophyll-a concentrations (April-June, 2011)

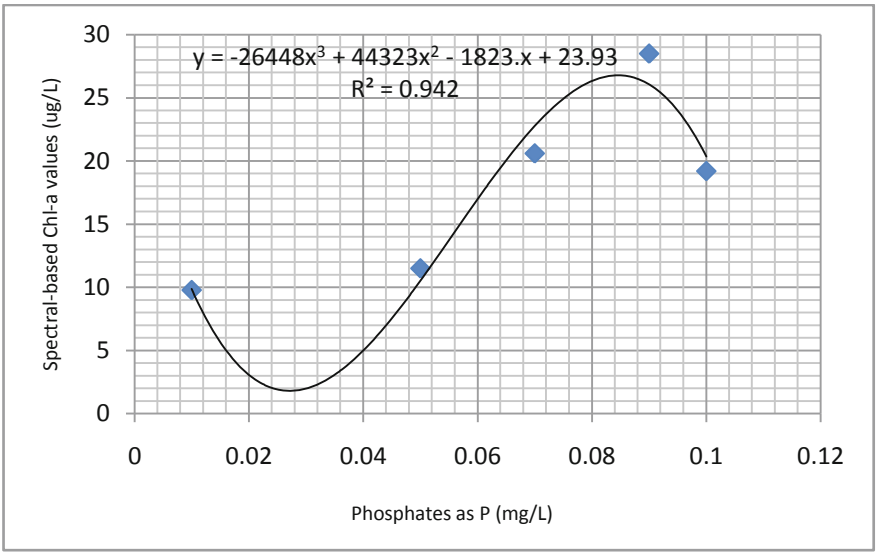

Fig. 6. Concentrations of spectral-based chlorophyll-a versus field phosphates as P (April-June, 2011)

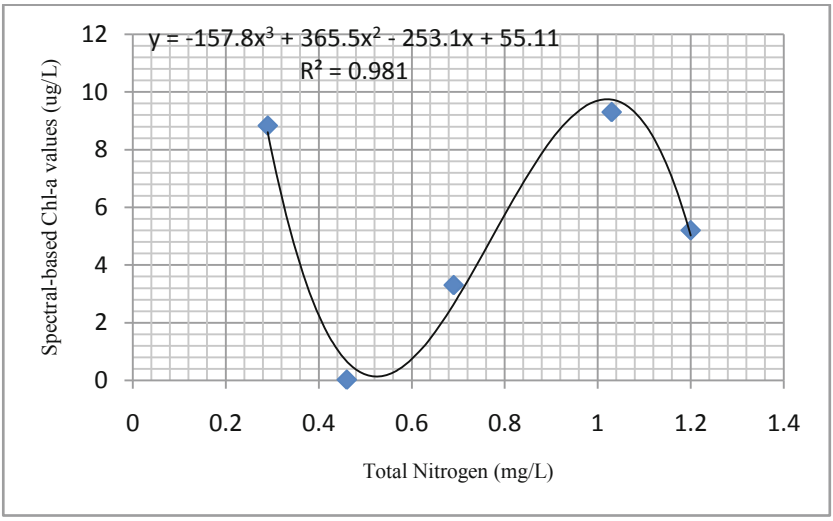

Fig. 7. Concentrations of spectral-based chlorophyll-a versus total nitrogen (April-June, 2010)

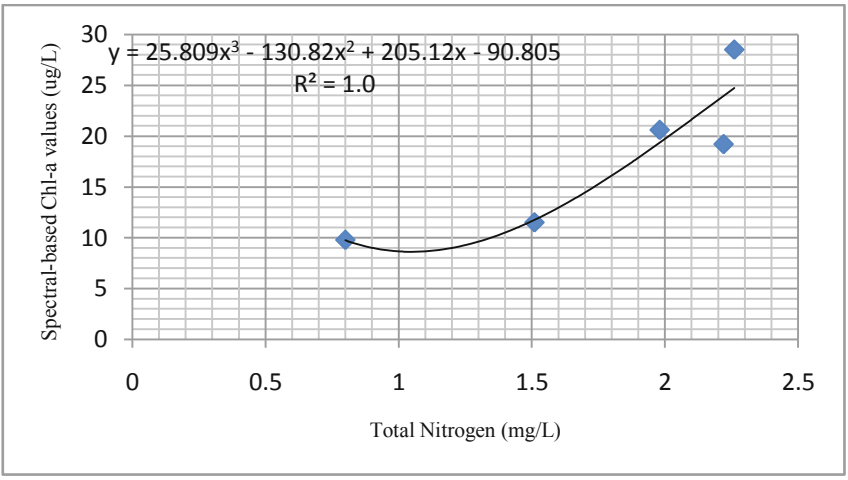

Fig. 8. Concentrations of spectral-based chlorophyll-a versus total nitrogen (April-June, 2011)

The spectral-based chlorophyll-a map of 2011 (Figure 3) shows a high rate of algal growth at the mouth of the creek and in the south-western coasts of Dubai compared to that inside the creek. Given the role of the creek as a source of nutrients (major sources of nutrients include the discharge from Al Awir Plant and the waste from tourism boats) to the Dubai coasts and the spectral-based chlorophyll-models developed in this study, it seems this part of the Arabian Gulf coasts is characterized with irregular circulations and wave patterns, which can lead to redundant eutrophication in this area. This is confirmed by phosphates concentrations at the

mouth of the creek in 2011 (measured: 0.07 mg/L; modeled: 0.11 mg/L) that exceeds the United States Environmental Protection Agency (EPA) water quality criteria, which limits phosphates concentration to 0.05 mg/L for streams that discharge into lakes. To ensure the sustainability of the Dubai Creek given the results of this short-term study, it is certain that a mitigation plan is much needed.

5 Concluding Remarks

The implication of rapid urban development on the Dubai Creek is evident given the pattern of short-term spatio-temporal variability of the concentrations of chlorophyll-a and the limiting nutrients in the creek. The fluctuation of the concentrations of chlorophyll-a and the nutrients in the creek and along the south-western Dubai coasts calls for the implementation of a mitigation plan, which will ensure the sustainability of the creek. Such a mitigation plan would limit phosphates and nitrogen concentrations inside and at the mouth of the creek to levels that would allow for the control of the increased algal growth. This is really important given the role the creek plays in tourism and commerce.

Acknowledgments. The authors would like to acknowledge the support of the Emirates Institution for Advanced Science and Technology (EIAST) and the Dubai Municipality (DM) by providing the datasets used in this study.

References

1. Anderson, D., Burkholder, J., Cochlan, W., Glibert, P., Gobler, C., Heil, C., Kudela, R., Parsons, M., Rensel, J., Townsend, D., Trainer, V., Vargo, G.: Harmful algal blooms and eutrophication: Examining linkages from selected coastal regions of the United States. Harmful Algae 8(1), 39–53 (2008)
2. Anderson, D., Glibert, P., Burkholder, J.: Harmful algal blooms and eutrophication: nutrient sources, composition and consequences. Estuaries 25, 562–584 (2002)
3. Brivio, P.A., Giardino, C., Zilioli, E.: Validation of satellite data for quality assurance in lake monitoring applications. Sci. Total Environ. 268, 3–18 (2001)
4. Dekker, A., Peters, S.: The use of the Thematic Mapper for the analysis of Eutrophic Lakes-A case study in the Netherlands. Int. J. Remote Sens. 14, 799–821 (1993)
5. May, L., Koseff, J., Lucas, V., Cloern, E., Schoellhamer, H.: Effects of spatial and temporal variability of turbidity on phytoplankton blooms, Marine Ecology. Progress Series 254, 111–128 (2003)
6. O'Neil, J., Davis, T., Burford, M., Gobler, C.: The rise of harmful cyanobacteria blooms: The potential roles of eutrophication and climate change. Harmful Algae 14, 313–334 (2012)
7. Pacione, M.: Dubai. Cities 22(3), 255–265 (2005)
8. Prato, T.: Assessing ecosystem sustainability and management using fuzzy logic. Ecological Economics 61(1), 171–177 (2007)

9. Salama, M., Radwan, M., van der Velde, R.: A hydro-optical model for deriving water quality variables from satellite images (HydroSat): A case study of the Nile River demonstrating the future Sentinel-2 capabilities. Physics and Chemistry of the Earth, 50-52, 224–232 (2012)
10. Saunders, J., Al Zahed, K., Paterson, D.: The impact of organic pollution on the macrobenthic fauna of Dubai Creek (UAE). Marine Pollution Bulletin 54, 1715–1723 (2007)
11. Walker, N., Schulze, R.: Climate change impacts on agro-ecosystem sustainability across three climate regions in the maize belt of South Africa, Agriculture. Ecosystems & Environment 124(1-2), 114–124 (2008)

Correlation Analysis of the Four Photo Themes in Five Layers

Alaa A. Jabbar[1], Shahrin Bin Sahib[1], and Mazdak Zamani[2]

[1] Faculty of Information & Communication Technology, Universiti Teknikal Malaysia Melaka, 76100 Melaka, Malaysia
[2] Advanced Informatics School, Universiti Teknologi Malaysia, 54100 Kuala Lumpur, Malaysia
alaaj@student.utem.edu.my, shahrinsahib@utem.edu.my, mazdak@utm.my

Abstract. This paper intends to analyze the correlation of the four photo themes in five layers based on statistical analysis of pixel correlation evaluation.

Keywords: Pixel Correlation, Steganography, Watermarking, Steganalysis, Photo Themes.

1 Introduction

The photos in different themes have different level of correlativity based on the offered correlativity analysis methods. Even photos with wide flat regions would represent higher level of correlativity until certain level of embedding in comparison with edgy photos [1-4].

Therefore to have accurate steganalysis, photos should be examined based on their themes and content. To perform the correlativity analysis of a photo in offered method it firstly should be classified according its theme and then analyzed based on properties and criteria of that photo theme. Despite embedding external data within a photo will reduce its correlativity, but correlativity of a photo after embedding up to particular ratio can be higher than original photo in another photo theme. Therefore is a vital need for an accurate steganalysis method to analyze a photo based on its theme to achieve accurate results. The photos with big areas of flat colors have maximum correlativity and edgy photos, as they have least connected areas and various colors, have minimum value of it. Smooth photos and partially flat or smooth photos are located in between. Following sections describe properties of each of counted photo themes and then analyze behavior of each one of the themes based on proposed correlativity analysis methods [5-11].

2 Wide Flat Region

This type of photos has big areas filled with a flat color. The background color is almost constant or with slight change that is not easily recognizable with human

F. Bian et al. (Eds.): GRMSE 2013, Part I, CCIS 398, pp. 211–222, 2013.
© Springer-Verlag Berlin Heidelberg 2013

visual system. Red, green, and blue color code of the pixels will be the same or with slight changes between central pixel and each of the neighbor pixels in the background area [12-18].

This photo theme has highest level of correlativity as there are many identical or similar pixels in the background area. For low ratios of data embedding this kind of photos still will have more correlativity among the pixels than original photos in other photo themes. This type of photos is made by computer graphic software [19-24].

To find red, green and blue correlation between pixels, the code values of each pixel is compared with neighbors up to five layers in two ways. In first way percentage of result of AND comparison between each central pixel with the neighbors is calculated. For each layer ff from layer one up to the chosen layer any pixel with exactly the same RGB code of central pixel was found, then that pixel for that layer would be counted as genuine pixel [25-31].

The second way does the same process of analysis except computing OR comparison of RGB colors. Equality of any of red, green, or blue values of central pixel with the neighbor pixels is enough to count that pixel as genuine one for that particular layer.

Table 1 reflects computed results of analyzing photos with wide or big flat regions. To make a reliable dataset fifty photos analyzed and the results presented in the Table 1. Last row shows total number of analyzed pixels and average value of this analysis on fifty samples.

Figure 1 shows the scattering of AND analysis results of wide flat region photos. The minimum and maximum values for each layer are slightly different, but they are almost between 60 and 100.

Figure 2 reflects OR correlation evaluation of wide flat region photos. Since in OR evaluation always there is more likeliness of finding related pixels, then percentage of related pixels is more than AND correlation. As is visible in the figure bellow except for first layer the rest of the results are between 90 and 100.

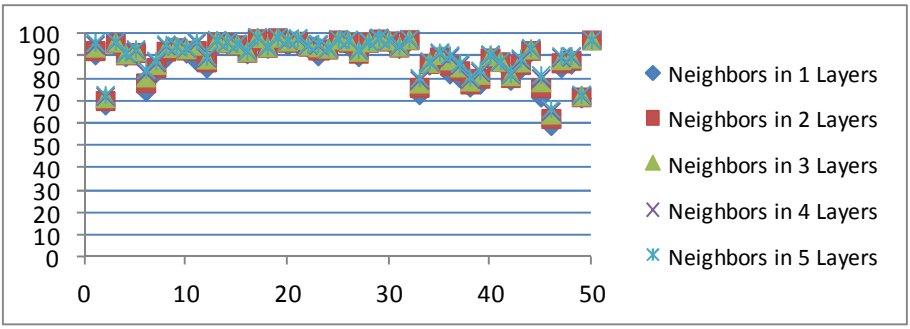

Fig. 1. Analysis of AND correlation in wide flat region photos

Table 1. OR & AND analysis of wide flat region photos up to 5 layers

File No	Total Analyzed Pixels	Neighbor-1		Neighbor-2		Neighbor-3		Neighbor-4		Neighbor-5	
		AND	OR	AND	OR	AND	OR	AND	OR	AND	OR
1	1892100	90.65	90.65	92.59	92.59	94.07	94.07	95.26	95.26	96.26	96.26
2	1892100	68.19	90.59	70.23	96.9	71.47	98.72	72.24	99.35	72.87	99.62
3	1892100	94.9	96.97	95.94	98.08	96.38	98.48	96.64	98.68	96.82	98.81
4	4054500	89.88	93.58	90.68	95.69	91.16	96.89	91.51	97.72	91.8	98.28
5	1892100	90.58	99.3	91.75	99.75	92.46	99.87	92.98	99.91	93.37	99.93
6	4054500	74.3	91.89	78.2	94.78	80.78	96.42	82.68	97.38	84.16	98.02
7	2272900	82.75	96.65	84.98	98.59	86.42	99.16	87.41	99.44	88.16	99.61
8	2043700	89.4	92.89	92.4	95.88	93.95	97.3	94.85	98.08	95.44	98.57
9	2043700	93.45	97.5	93.98	98.78	94.4	99.33	94.69	99.56	94.88	99.67
10	1892100	91.49	96.11	92.81	98.16	93.48	98.92	93.86	99.25	94.15	99.44
11	1892100	87.91	88.33	92.71	93.15	95.03	95.48	96.24	96.67	96.99	97.42
12	1892100	84.88	90.16	87.47	94.51	88.77	96.12	89.55	96.94	90.12	97.51
13	2272900	95.28	96.83	96.47	98.22	97.02	98.75	97.32	99.02	97.5	99.16
14	768612	95.6	98.41	96.08	99.07	96.36	99.36	96.55	99.52	96.69	99.6
15	1287780	94.75	99.34	95.23	99.77	95.5	99.89	95.69	99.94	95.83	99.96
16	1736800	91.13	98.13	91.79	99.21	92.2	99.6	92.5	99.78	92.75	99.86
17	1892100	97.18	97.54	98.02	98.42	98.44	98.84	98.68	99.08	98.84	99.23
18	1892100	93.64	97.92	94.04	98.94	94.28	99.32	94.47	99.53	94.64	99.65
19	1892100	98.14	98.8	98.39	99.21	98.54	99.4	98.65	99.5	98.74	99.57
20	1892100	94.93	95.75	96.22	97.26	96.93	98.04	97.36	98.5	97.66	98.81
21	1892100	95.34	95.53	96.76	97.01	97.55	97.81	98.01	98.28	98.32	98.59
22	1892100	93.91	98.29	94.54	99.15	94.93	99.48	95.19	99.65	95.4	99.75
23	1892100	90.21	91.64	92.79	94.42	94.24	95.91	95.15	96.83	95.78	97.43
24	1892100	92.78	97.6	93.31	98.81	93.67	99.3	93.93	99.52	94.15	99.65
25	1892100	96.93	98.71	97.43	99.41	97.69	99.64	97.83	99.74	97.94	99.8
26	1892100	94.65	96.14	96.35	98.16	97.05	98.88	97.4	99.18	97.61	99.35
27	1892100	89.88	95.28	91.42	98.05	92.3	98.98	92.8	99.37	93.17	99.57
28	1892100	95.98	98.72	96.33	99.4	96.53	99.62	96.67	99.72	96.78	99.78
29	1892100	96.86	98.18	97.75	99.02	98.13	99.35	98.33	99.52	98.48	99.63
30	1892100	96.44	99.08	96.92	99.53	97.22	99.68	97.39	99.76	97.53	99.8
31	1892100	93.51	99.18	94.17	99.69	94.5	99.85	94.75	99.92	94.96	99.95
32	1892100	96.94	98.43	97.48	99.13	97.76	99.41	97.91	99.53	98.01	99.59
33	1287780	72.81	86.67	76.09	93.17	78.09	96.1	79.45	97.53	80.48	98.36
34	1892100	86.08	93.24	86.84	96.5	87.29	98.09	87.61	98.86	87.89	99.26
35	1892100	88.3	91.31	89.85	95.24	90.89	97.28	91.45	98.26	91.88	98.81
36	1892100	82.03	86.87	85.98	93.17	88.39	96.56	89.76	98.13	90.62	98.88
37	1892100	80.43	88.26	83.65	92.84	85.19	94.47	86.23	95.57	87.01	96.44
38	1892100	76.23	93.85	77.69	96.79	78.89	97.89	79.88	98.44	80.72	98.8
39	1892100	77.47	86.03	80.2	92.8	81.89	95.68	82.95	97.15	83.71	97.98
40	2272900	87.93	93.28	89.41	97.01	90.24	**98.49**	90.71	99.13	91.03	99.44
41	6697600	87.38	93.86	87.64	96.21	87.83	97.6	87.97	98.46	88.11	98.98
42	2043700	79.26	95.01	80.57	98.58	81.39	99.39	81.9	99.67	82.3	99.78
43	2272900	84.57	97.59	86.34	99.29	87.6	99.7	88.46	99.83	89.23	99.89
44	2043700	92	96.87	92.7	98.52	93.22	99.04	93.57	99.27	93.87	99.4
45	1892100	71.74	85.67	76.07	93.31	78.57	96.16	80.3	97.53	81.76	98.35
46	1892100	58.97	84.89	62.17	94.04	64.19	97.24	65.43	98.47	66.57	99.05
47	1287780	84.88	97.8	87.17	99.2	88.59	99.62	89.56	99.78	90.26	99.86
48	1287780	86.5	92.62	88.26	96.74	89.28	98.27	89.91	98.93	90.38	99.29
49	1736800	71.31	88.69	71.87	94.22	72.32	96.63	72.68	97.93	73.04	98.69
50	1892100	97.32	99.16	97.39	99.65	97.44	99.81	97.49	99.87	97.54	99.9
	102013532	87.73	94.16	89.36	96.94	90.32	98.13	90.92	98.73	91.38	99.07

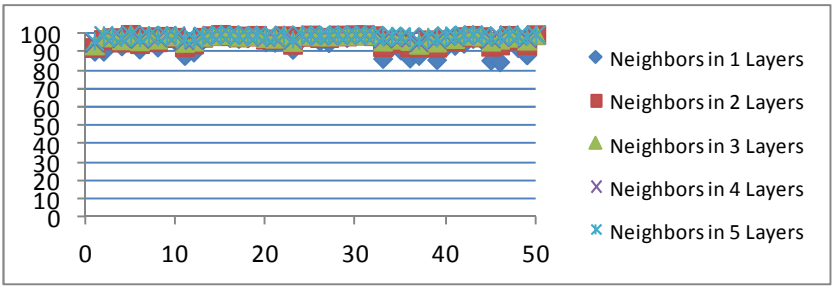

Fig. 2. Analysis of OR correlation in wide flat region photos

3 Wide Smooth Region

In this category of photos majority of the photo is covered by spectrum of a color or gradually the background changes from one color to another one. Source of photos in this class could be both natural and computer made ones. Since normally the background gradually changes from one color to another one or from lighter to darker, then the correlation among the pixels is not as strong as the photos with flat background.

Table 2. OR & AND analysis of wide smooth region photos up to 5 layers

File No	Total Analyzed Pixels	Neighbor-1		Neighbor-2		Neighbor-3		Neighbor-4		Neighbor-5	
		AND	OR	AND	OR	AND	OR	AND	OR	AND	OR
1	6311890	60.73	96.86	68.78	98.96	73.26	99.48	76.31	99.69	78.66	99.80
2	1287780	87.11	95.21	89.29	98.34	90.52	99.22	91.31	99.55	91.92	99.73
3	1892100	5.99	89.54	10.15	96.52	14.76	98.38	19.79	99.11	24.91	99.47
4	2043700	92.71	96.96	93.82	98.63	94.45	99.18	94.86	99.45	95.17	99.60
5	4054500	85.30	91.16	86.83	95.05	87.78	96.96	88.45	98.01	89.00	98.67
6	1736800	91.65	97.47	92.62	99.21	93.10	99.64	93.40	99.81	93.64	99.88
7	2272900	87.54	96.99	88.39	98.71	88.98	99.28	89.45	99.51	89.86	99.64
8	4054500	83.23	96.55	84.21	98.78	84.94	99.52	85.57	99.76	86.14	99.86
9	2272900	84.63	88.03	88.46	92.95	90.47	95.29	91.67	96.56	92.47	97.36
10	1892100	80.43	93.31	84.14	96.95	86.12	98.29	87.38	98.90	88.30	99.38
11	4662252	35.08	61.29	51.26	84.08	58.25	91.85	61.91	95.23	64.29	96.98
12	1892100	97.43	98.56	98.43	99.46	98.76	99.70	98.95	99.80	99.08	99.87
13	2272900	86.41	89.24	89.89	93.38	91.73	95.46	92.90	96.72	93.74	97.61
14	1892100	84.16	94.90	86.17	98.12	87.42	99.08	88.09	99.45	88.56	99.64
15	2272900	68.36	77.50	78.37	91.21	82.02	95.48	83.77	97.28	84.81	98.21
16	2272900	79.77	89.05	81.88	94.49	83.14	97.04	84.01	98.30	84.72	98.98
17	2272900	83.42	93.69	84.48	96.64	85.09	97.93	85.52	98.62	85.83	99.04
18	1287780	89.11	95.04	90.66	97.58	91.54	98.63	92.14	99.14	92.60	99.42
19	709700	95.40	99.10	95.99	99.67	96.30	99.82	96.52	99.88	96.68	99.92
20	1892100	87.39	96.58	88.40	98.78	88.99	99.45	89.45	99.71	89.82	99.83
21	1287780	82.85	93.11	84.07	96.57	84.79	98.03	85.32	98.77	85.73	99.20
22	1287780	90.68	97.37	91.90	99.41	92.57	99.78	93.06	99.89	93.42	99.93
23	1892100	87.28	94.92	88.86	97.81	89.67	98.79	90.23	99.22	90.66	99.44
24	1892100	86.10	93.19	88.28	96.21	89.42	97.66	90.04	98.42	90.49	98.95
25	1892100	64.15	84.84	66.63	92.35	68.21	95.54	69.39	97.19	70.32	98.15
26	1892100	93.12	96.44	94.33	98.21	94.98	98.89	95.39	99.22	95.68	99.42
27	1892100	79.36	90.34	80.87	95.16	81.76	97.21	82.40	98.21	82.92	98.79
28	1892100	85.76	94.65	86.64	97.42	87.18	98.45	87.58	98.95	87.90	99.24
29	1892100	89.95	90.81	94.25	95.44	96.25	97.51	97.26	98.46	97.85	98.98
30	2272900	75.49	95.42	78.90	98.33	80.83	99.09	82.02	99.40	82.89	99.58
31	1892100	95.62	99.26	97.28	99.71	98.02	99.83	98.36	99.87	98.58	99.90
32	2272900	96.80	99.20	97.40	99.51	97.80	99.68	98.03	99.76	98.21	99.82
33	2272900	87.53	96.21	88.91	98.44	89.65	99.18	90.12	99.52	90.43	99.70
34	2272900	69.22	78.81	81.56	92.69	86.77	96.97	88.94	98.35	90.13	98.93
35	1892100	54.22	73.80	74.55	91.72	79.90	94.20	83.31	95.74	85.15	96.20
36	768612	75.14	86.19	80.75	93.47	83.69	96.44	85.24	97.78	86.22	98.48
37	1892100	65.18	83.24	77.55	93.82	82.64	96.79	85.14	98.00	86.69	98.66
38	768612	71.12	88.87	80.86	96.16	84.26	97.90	86.08	98.63	87.34	99.06
39	2043700	66.52	92.58	70.65	96.59	73.37	97.80	75.25	98.44	76.64	98.88
40	2272900	74.91	87.98	78.03	93.97	80.08	96.65	81.25	97.94	82.22	98.65
41	3109988	88.92	94.81	89.17	97.31	89.36	98.37	89.51	98.90	89.64	99.21
42	2272900	64.25	72.68	70.87	83.74	74.48	89.28	76.66	92.57	78.12	94.69
43	2272900	65.76	84.63	66.60	91.93	67.13	95.62	67.49	97.56	67.79	98.61
44	2043700	33.35	87.96	40.67	96.01	46.08	98.12	50.50	98.95	54.24	99.36
45	4054500	96.99	98.79	97.87	99.56	98.32	99.79	98.57	99.86	98.72	99.88
46	1892100	97.17	98.53	97.37	99.31	97.51	99.59	97.62	99.72	97.70	99.80
47	1287780	73.89	90.52	79.17	95.44	82.29	97.35	84.12	98.28	85.29	98.74
48	2043700	66.34	85.84	70.89	94.93	73.34	97.56	74.82	98.62	75.85	99.12
49	2272900	43.58	88.05	53.66	95.07	60.29	97.34	65.04	98.42	68.61	99.01
50	1736800	41.23	45.73	62.72	69.80	76.21	83.72	83.86	90.77	88.06	94.20
	108676054	73.77	90.40	78.27	95.67	80.72	97.58	82.33	98.48	83.53	98.97

Table 2 represents analysis results of fifty samples of wide smooth region photos in dataset. Last row of this table shows number of total analyzed pixels and average value of all fifty analyze samples for both AND and OR analysis up to 5 layers. For wide smooth region photos the majority of AND analysis values are between sixty and hundred while correlativity in only few percent of the photos is less than sixty. In flat region photos all the marks of pixel correlativity were condensed between sixty and hundred while here the values are more dispersed. Except OR analysis results of first layer the rest of values are located between ninety and hundred and for upper layers the values are more close to hundred. OR analysis of flat region photos showed more correlativity among the pixels.

Figure 3 shows the scattering of AND analysis results of wide smooth region photos. The minimum and maximum values for each layer are slightly different, but they are almost between 60 and 100.

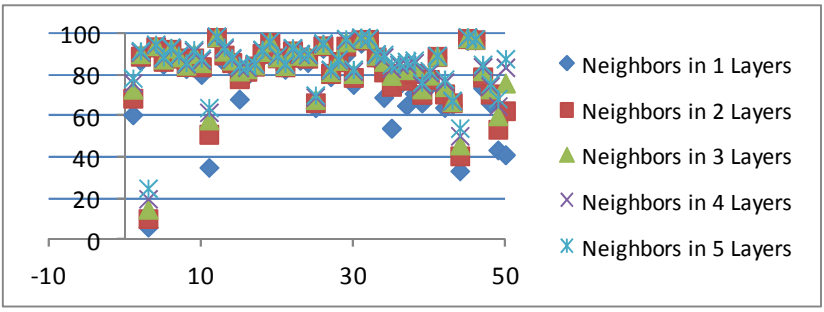

Fig. 3. Analysis of AND correlation in wide smooth region photos

Figure 4 reflects OR correlation evaluation of wide smooth region photos. Since in OR evaluation always there is more likeliness of finding related pixels, then percentage of related pixels is more than AND correlation. As is visible in the figure bellow except for first layer the rest of the results are between 90 and 100.

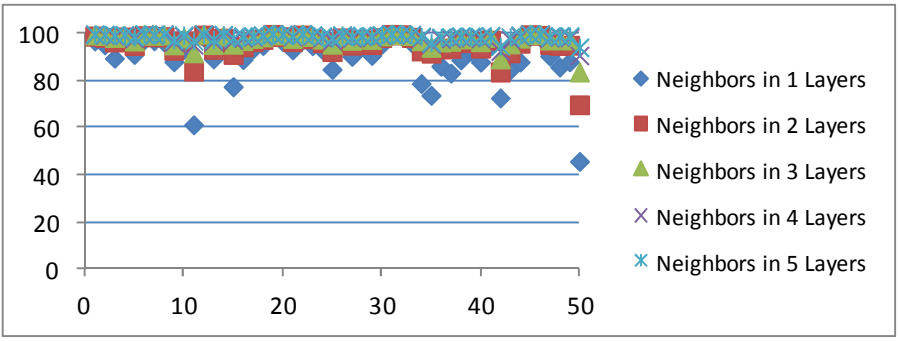

Fig. 4. Analysis of OR correlation in wide smooth region photos

4 Partial Smooth Region Photos

In this category of photos there are numerous small smooth or sometimes flat regions. The flat/smooth regions in this photo theme are smaller than flat/smooth regions in wide smooth regions photo theme while number of the regions is more. Normally the regions are separated with other colors and inside of each region the color changes from lighter to darker. Correlativity of pixels in this type is less than the two prior categories as there is no big and connected spectrum in it. Source of this theme of photos could be natural or computer made photos.

Table 3. OR & AND analysis of partial smooth region photos up to 5 layers

File No	Total Analyzed Pixels	Neighbor-1		Neighbor-2		Neighbor-3		Neighbor-4		Neighbor-5	
		AND	OR	AND	OR	AND	OR	AND	OR	AND	OR
1	2272900	59.53	79.70	63.79	90.24	65.88	94.73	67.08	96.99	67.85	98.25
2	1892100	78.13	93.77	80.01	98.17	81.03	99.29	81.72	99.66	82.30	99.82
3	5594290	46.89	83.54	49.93	92.73	51.60	96.43	52.74	98.08	53.66	98.87
4	975268	35.32	60.35	37.80	81.25	39.48	90.99	40.51	95.43	41.39	97.52
5	768612	41.14	70.17	47.96	88.64	52.14	95.00	54.47	97.26	56.16	98.24
6	768612	51.22	70.72	59.56	86.64	64.17	92.87	66.57	95.69	68.21	97.25
7	768612	42.31	69.72	48.68	86.61	52.44	92.78	54.50	95.51	56.02	96.95
8	5953090	59.20	88.07	63.85	94.24	67.16	96.95	69.03	98.29	70.52	99.00
9	5830500	46.18	81.15	49.71	92.21	51.72	96.40	52.91	98.17	53.81	98.98
10	2272900	34.64	62.94	44.01	81.89	49.29	90.27	52.30	94.65	54.31	97.00
11	2272900	12.24	46.56	17.04	73.52	20.32	87.14	22.69	93.36	24.78	96.25
12	1736800	48.25	82.20	53.38	93.55	56.38	96.84	58.22	98.13	59.67	98.75
13	1736800	57.88	80.72	62.74	90.17	65.75	94.85	67.72	97.24	69.25	98.45
14	2272900	71.17	93.79	75.54	98.13	78.42	99.11	80.27	99.51	81.67	99.70
15	2272900	48.05	82.67	53.58	94.22	57.87	97.48	61.00	98.74	63.60	99.30
16	1736800	55.12	81.29	62.34	91.91	66.17	95.65	68.43	97.35	70.09	98.24
17	1736800	59.63	81.70	64.72	91.67	67.66	95.75	69.59	97.61	71.05	98.53
18	2272900	38.14	79.83	50.20	95.15	57.16	98.43	60.82	99.27	63.36	99.61
19	2272900	29.91	71.75	40.54	85.92	46.87	91.84	51.19	95.04	54.51	96.85
20	2272900	23.23	54.61	29.26	77.18	32.89	88.71	35.45	94.20	37.61	96.83
21	2272900	32.63	65.59	40.00	85.54	44.57	93.78	48.04	96.98	51.02	98.30
22	2043700	68.35	90.59	73.25	95.95	76.72	97.63	78.98	98.56	80.72	99.11
23	2043700	63.72	95.75	68.39	99.46	72.32	99.77	75.40	99.87	78.11	99.92
24	1892100	45.13	63.06	56.40	81.04	62.30	89.31	65.60	93.60	67.91	95.96
25	2043700	45.20	78.89	48.58	91.26	51.21	95.41	53.15	97.43	54.87	98.41
26	1892100	40.01	74.82	49.94	91.00	55.37	95.97	58.20	97.76	60.14	98.63
27	2272900	46.79	83.53	54.42	94.25	59.15	97.65	62.26	98.86	64.76	99.37
28	1892100	37.13	68.87	42.25	86.66	45.39	93.81	47.40	96.76	49.07	98.11
29	2272900	38.92	97.22	52.26	99.14	61.44	99.55	67.75	99.73	72.24	99.82
30	2272900	10.80	79.11	14.04	95.08	16.80	98.63	19.34	99.47	21.74	99.74
31	1892100	13.88	42.53	21.72	72.59	27.13	87.30	31.13	93.59	34.46	96.30
32	2272900	90.13	93.88	91.97	96.91	92.89	98.27	93.38	98.98	93.70	99.37
33	1736800	82.88	92.86	87.47	97.50	89.70	98.88	90.92	99.39	91.72	99.62
34	1736800	20.43	55.94	29.35	84.47	35.58	94.13	39.91	97.12	43.53	98.29
35	2043700	57.97	78.75	64.90	91.63	69.00	95.83	71.15	97.46	72.70	98.25
36	2043700	33.09	60.44	40.93	82.40	48.20	91.22	54.30	94.95	59.25	96.73
37	2272900	77.13	97.73	78.84	99.38	79.87	99.72	80.68	99.85	81.36	99.91
38	2272900	79.70	95.43	82.82	98.48	84.45	99.31	85.45	99.63	86.19	99.78
39	4054500	49.63	83.21	58.28	94.37	63.93	97.16	67.63	98.39	70.45	99.03
40	4054500	55.22	79.86	68.08	94.76	74.38	98.08	77.48	99.08	79.53	99.50
41	2272900	69.67	90.69	73.27	96.69	74.75	98.36	75.68	99.10	76.33	99.47
42	2272900	56.40	78.22	66.25	91.78	71.62	96.24	74.70	98.00	76.94	98.77
43	2272900	69.16	84.43	80.93	95.67	85.98	98.24	88.48	99.14	89.94	99.53
44	2272900	44.09	68.80	50.73	82.75	55.08	89.74	58.09	93.64	60.41	95.88
45	2272900	68.15	90.89	70.10	96.34	71.02	98.12	71.50	98.93	71.88	99.37
46	2272900	69.24	92.08	72.48	97.30	74.04	98.67	74.94	99.27	75.57	99.58
47	768612	36.92	69.07	47.58	89.69	53.66	95.60	57.06	97.70	59.42	98.61
48	768612	26.66	49.10	39.95	77.82	49.04	90.94	53.91	95.62	56.97	97.52
49	2272900	72.13	87.82	75.00	95.07	76.71	97.51	77.70	98.59	78.46	99.13
50	1892100	91.41	96.61	92.15	98.85	92.64	99.56	92.97	99.78	93.23	99.87
	112300908	51.48	79.79	57.58	91.55	61.28	95.89	63.62	97.76	65.40	98.66

Table 3 shows fifty analysis results of partial smooth region photos. As is visible in the presented results there is less pixel correlativity in this category than wide flat and smooth region photos. The average of AND correlativity is almost about fifty percent while for wide flat and smooth photos this value was about eighty percent. The result individually can help to distinguish this type of photo from the counted types. Last row of Table 3 shows total number of analyzed photos and average values of analysis of fifty photos.

Figure 5 illustrates AND correlativity values dispersal of partial smooth region photos. Unlike the two prior categories the values are not condensed and vary from almost ten to ninety.

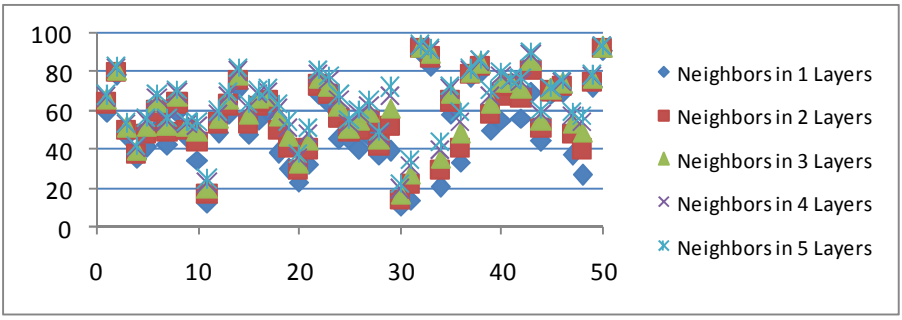

Fig. 5. Analysis of AND correlation in partial smooth region photos

In Figure 6, OR correlativity analysis of this category shows more classified results and despite there are overlapped areas for each analyzed layer but the values are more separated than first two categories.

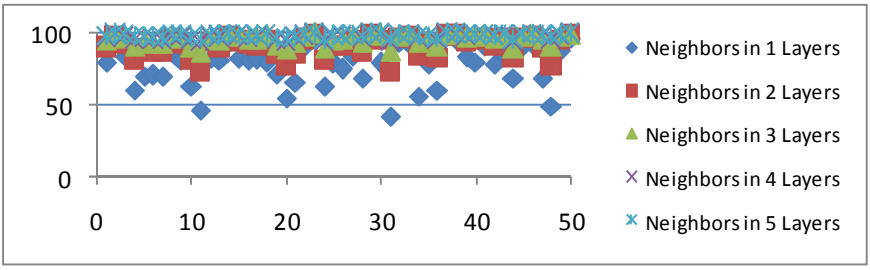

Fig. 6. Analysis of OR correlation in partial smooth region photos

5 Edgy Photos

Photos of this theme have least pixel correlativity. These photos continuously are changing from one color to another one and the smooth or flat regions either are very

small or do not exist. Since in the small smooth regions the colors will change from lighter to darker, or from one color to another one in fewer steps than prior categories the correlativity of pixels is less than other three counted types. Original edgy photos may have less correlativity result than stego objects made from photos in previously described photo themes.

Table 4 shows AND and OR analysis values for fifty analyzed photos in this theme from neighbors of first layer to fifth layer. The average results of analyzing fifty samples in the last row show the minimum connectivity among the pixels in comparison with other themes.

Table 4. OR & AND analysis edgy region photos up to 5 layers

File No	Total Analyzed Pixels	Neighbor-1		Neighbor-2		Neighbor-3		Neighbor-4		Neighbor-5	
		AND	OR	AND	OR	AND	OR	AND	OR	AND	OR
1	4827630	23.69	54.77	30.07	76.28	34.13	87.10	37.15	92.73	39.51	95.74
2	5941130	25.83	84.13	32.71	93.53	36.97	96.54	40.05	97.86	42.54	98.57
3	5941130	57.67	95.94	63.42	98.90	66.62	99.59	68.73	99.81	70.29	99.90
4	2272900	7.83	42.02	9.54	70.27	10.87	85.61	11.87	92.68	12.80	95.92
5	2272900	27.30	59.21	35.59	79.67	40.51	89.06	43.85	93.50	46.33	95.87
6	2043700	62.21	82.38	68.49	93.32	71.81	97.11	73.65	98.61	75.01	99.25
7	4054500	0.20	48.59	0.41	81.00	0.65	93.82	0.93	98.08	1.21	99.31
8	747650	25.37	56.56	28.87	77.84	30.96	87.16	32.13	91.89	32.98	94.61
9	1736800	17.47	49.46	21.81	73.05	24.09	86.32	25.54	92.96	26.70	96.14
10	1027848	15.40	52.01	19.46	81.02	22.24	92.77	23.90	96.94	25.26	98.47
11	4054500	23.96	76.53	31.02	91.68	35.50	96.16	38.53	97.98	40.77	98.86
12	2272900	20.00	49.01	29.13	74.12	35.06	86.52	39.36	92.70	42.82	95.84
13	2043700	10.41	73.85	14.23	91.94	17.99	97.05	21.63	98.62	25.06	99.21
14	2272900	32.96	63.82	37.41	83.50	40.37	91.67	42.48	95.39	44.20	97.26
15	1892100	38.10	82.83	41.44	92.79	43.73	96.40	45.67	97.99	47.37	98.78
16	1892100	26.01	67.45	31.97	86.89	35.33	94.01	37.77	96.86	39.63	98.15
17	1736800	42.90	90.20	50.66	97.66	54.71	99.06	57.20	99.54	59.02	99.73
18	6057740	31.89	64.86	37.08	82.86	39.99	91.01	41.74	94.94	43.09	96.95
19	5576350	2.63	47.21	3.75	73.71	4.55	87.63	5.17	94.03	5.67	96.82
20	2272900	14.70	55.20	17.51	78.95	19.52	90.09	21.16	95.01	22.65	97.22
21	768612	17.72	44.25	23.74	72.81	27.83	86.68	30.17	92.87	32.08	95.75
22	1272700	9.73	42.98	11.23	70.52	12.35	84.68	13.16	91.75	13.94	95.40
23	1003300	29.61	65.48	33.64	84.72	36.04	92.38	37.41	95.88	38.48	97.64
24	638820	7.91	44.42	9.19	70.11	10.08	84.02	10.65	91.33	11.19	95.12
25	768612	26.45	57.28	28.10	78.55	29.21	89.10	29.88	94.20	30.48	96.69
26	2272900	14.21	71.55	20.98	90.54	26.60	96.20	31.12	98.07	35.04	98.87
27	2272900	6.19	40.52	9.06	71.57	11.77	89.27	14.18	95.55	16.53	97.36
28	1892100	37.62	67.23	46.65	85.21	52.12	92.79	55.44	96.03	57.77	97.55
29	4054500	73.51	93.75	77.11	98.31	79.08	99.31	80.30	99.64	81.20	99.77
30	2272900	38.48	67.91	47.03	86.96	51.62	93.80	53.95	96.72	55.64	98.13
31	4054500	25.68	65.41	31.38	84.47	34.71	92.22	36.75	95.80	38.37	97.55
32	4054500	32.67	88.24	40.28	97.91	45.40	99.46	48.78	99.81	51.57	99.91
33	4054500	45.83	85.68	50.63	95.46	53.64	97.96	55.61	98.89	57.22	99.31
34	2043700	49.77	73.44	54.71	87.54	57.28	93.66	58.81	96.63	60.03	98.08
35	2272900	3.80	41.49	4.79	64.95	5.46	78.95	6.04	87.41	6.59	92.48
36	2272900	26.83	74.31	33.82	90.08	37.92	95.13	40.37	97.36	42.21	98.51
37	4054500	41.75	95.90	47.52	99.32	51.82	99.77	55.01	99.88	57.68	99.93
38	2043700	24.27	64.73	34.94	91.08	41.45	97.11	45.04	98.76	47.71	99.37
39	4054500	29.72	65.30	39.03	86.46	43.85	93.34	46.65	96.29	48.73	97.80
40	4054500	49.37	80.13	54.78	91.69	57.59	95.98	59.25	97.90	60.46	98.84
41	2272900	34.30	78.42	38.81	93.64	41.49	97.69	43.05	99.04	44.26	99.53
42	1003300	33.66	62.44	39.89	82.23	43.66	90.76	45.70	94.80	47.42	96.80
43	1003300	20.78	48.53	28.77	76.86	34.26	89.22	37.73	94.36	40.62	96.69
44	1206500	46.74	79.93	51.49	92.67	54.28	96.51	55.87	98.08	57.09	98.79
45	768612	48.44	64.53	64.59	86.08	73.14	93.91	77.42	96.78	79.99	98.02
46	768612	7.58	25.97	10.00	48.97	11.84	67.00	13.09	79.32	14.16	87.10
47	768612	37.60	52.08	50.45	75.08	58.33	86.73	63.01	92.51	66.29	95.48
48	768612	11.54	34.80	15.16	59.37	17.69	75.56	19.37	85.46	20.63	91.14
49	1027848	8.81	39.75	11.03	68.29	12.54	82.87	13.62	90.43	14.56	94.48
50	2087500	33.38	63.41	38.74	84.70	42.13	93.35	44.31	96.85	46.08	98.35
	122791518	29.52	68.29	34.91	85.75	38.24	93.04	40.45	96.30	42.21	97.85

Figure 7 illustrates AND correlativity values dispersal of edgy photos. Unlike the two prior categories the values are not condensed and vary from almost ten to ninety.

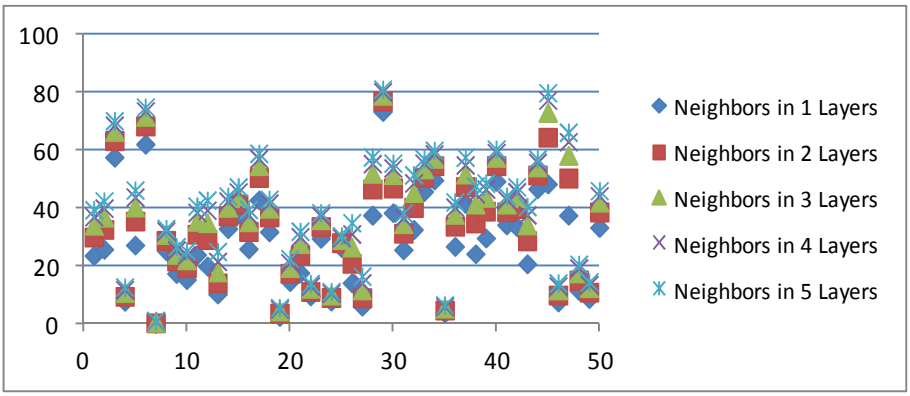

Fig. 7. Analysis of AND correlation in edgy photos

In Figure 8, OR correlativity analysis of this category shows more classified results and despite there are overlapped areas for each analyzed layer but the values are more separated than first three categories.

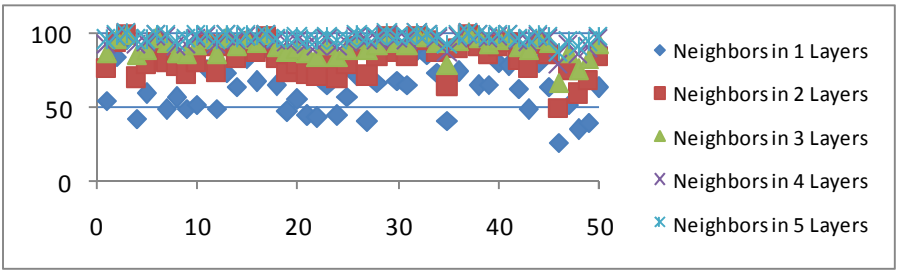

Fig. 8. Analysis of OR correlation in edgy photos

6 Conclusion

By moving from wide smooth and flat photos toward edgy photos, AND analysis marks tended to move down in the charts. The marks in the figures of wide flat region were located in upper side. In figures of wide smooth region, it was in upper side but lower than first category. In third category values were almost in the middle of chart and for fourth category the most density is in the lower half.

AND analysis results of different neighbor layers in different photo themes are mixed together and only for far neighbors the values are higher, while OR analysis results of photos in all four categories show that results are layered based on analyzed

layer of neighbors. When correlation of pixels is higher the results are more condensed. OR analysis chart of wide flat and wide smooth region photos show condensed and overlapped results. For partial smooth photos and edgy photos the results are more separated and layered.

Flat and smooth areas in photos increase percentage of pixel correlativity. Analysis tables of the four photo types revealed this fact and according to the results the pixel correlativity values decreases from first category toward fourth one. When a photo has more colors and smaller connected areas, RGB pixel values vary more than photos with wider connected areas. Table 5 shows average values of analysis of fifty samples of the four photo categories from one up to five layers. The values in each column are decreased from top to down. Since likelihood of finding a neighbor with the same either red, green, or blue values is higher than finding a neighbor with the same red, green, and blue values, then results of OR analysis are higher and more close together than AND values.

Table 5. Average OR & AND correlation analysis of the four themes from one to fifth layer

Photo type	Neighbor-1		Neighbor-2		Neighbor-3		Neighbor-4		Neighbor-5	
	AND	OR	AND	OR	AND	OR	AND	OR	AND	OR
Wide Flat Region	87.73	94.16	89.36	96.94	90.32	98.13	90.92	98.73	91.38	99.07
Wide Smooth Region	73.77	90.4	78.27	95.67	80.72	97.58	82.33	98.48	83.53	98.97
Partial Smooth Region	51.48	79.79	57.58	91.55	61.28	95.89	63.62	97.76	65.4	98.66
Edgy	29.52	68.29	34.91	85.75	38.24	93.04	40.45	96.3	42.21	97.85

References

1. Zamani, M., Manaf, A.B.A., Ahmad, R.B., Jaryani, F., Chaeikar, S.S., Zeidanloo, H.R.: Genetic audio watermarking. In: Das, V.V., Vijayakumar, R., Debnath, N.C., Stephen, J., Meghanathan, N., Sankaranarayanan, S., Thankachan, P.M., Gaol, F.L., Thankachan, N. (eds.) BAIP 2010. CCIS, vol. 70, pp. 514–517. Springer, Heidelberg (2010)
2. Zamani, M., Manaf, A.B.A., Abdullah, S.M., Chaeikar, S.S.: Mazdak Technique for PSNR Estimation in Audio Steganography. In: Applied Mechanics and Materials, vol. 229-231, pp. 2798–2803. Trans Tech Publications, Switzerland (2012)
3. Zamani, M., Manaf, A.A., Ahmad, R., Zeki, A., Abdullah, S.: A Genetic-Algorithm-Based Approach for Audio Steganography, June 24-26. World Academy of Science, pp. 355–358. Engineering and Technology (2009)
4. Zamani, M., Taherdoost, H., Manaf, A.A., Ahmad, R.B., Zeki, A.M.: An Artificial-Intelligence-Based Approach for Audio Steganography. Journal of Open Problems in Science and Engineering 1(1), 64–68 (2009)
5. Zamani, M., Manaf, A.A., Ahmad, R., Jaryani, F., Taherdoost, H., Chaeikar, S.S., Zeidanloo, H.R.: A Novel Approach for Genetic Audio Watermarking. Journal of Information Assurance and Security 5, 102–111 (2010)
6. Zamani, M., Manaf, A.A., Ahmad, R., Jaryani, F., Taherdoost, H., Chaeikar, S.S., Zeidanloo, H.R.: Genetic Audio Steganography. International Journal on Recent Trends in Engineering & Technology 3(2), 89–91 (2010) ISSN: 2158-5563

7. Abdullah, S.M., Manaf, A.A., Zamani, M.: Recursive Reversible Image Watermarking Using Enhancement of Difference Expansion Techniques. Journal of Information Security Research 1(2), 64–70 (2010)
8. Zamani, M., Manaf, A.A., Zeidanloo, H.R., Chaeikar, S.S.: Genetic Subtitution-Based Audio Steganography for High-Capacity Applications. International Journal for Internet Technology and Secured Transactions 3(1), 97–110 (2011)
9. Zeki, A.M., Manaf, A.A., Ibrahim, A.A., Zamani, M.: A Robust Watermark Embedding in Smooth Areas. Research Journal of Information Technology 3(2), 123–131 (2011)
10. Zamani, M., Manaf, A.A., Ahmad, R.: Knots of Substitution Techniques of Audio Steganography. In: International Proceedings of Computer Science and Information Technology, vol. 2, pp. 370–374. IACSIT Press, Singapore (2011)
11. Zamani, M., Manaf, A.B.A., Abdullah, S.M.: An Overview on Audio Steganography Techniques. Journal of Digital Content Technology and its Applications. Advanced Institute of Convergence Information Technology (2012)
12. Zamani, M., Manaf, A.A.: Genetic algorithm for fragile audio watermarking. In: Telecommunication Systems, Special Issue on Innovations in Emerging Multimedia Communication Systems. Springer (in press) ISSN: 1018-4864
13. Zamani, M., Manaf, A.A., Ahmad, R.: Knots of Substitution Techniques of Audio Steganography. In: The 2009 International Conference on Telecom Technology and Applications, Manila, Philippines, June 6-8, pp. 415–419 (2009)
14. Zamani, M., Manaf, A.A., Ahmad, R.: Current Problems of Substitution Technique of Audio Steganography. In: International Conference on Artificial Intelligence and Pattern Recognition, Orlando, Florida, USA, July 13-16, pp. 154–160 (2009)
15. Zamani, M., Manaf, A.A., Ahmad, R., Zeki, A., Abdullah, S.: Genetic Algorithm as an Approach to Resolve the Problems of Substitution Techniques of Audio Steganography. In: The 2009 International Conference on Genetic and Evolutionary Methods, Las Vegas, Nevada, USA, July 13-16, pp. 170–175 (2009)
16. Zamani, M., Manaf, A.A.: Azizah's Method to Measure the Efficiency of Steganography Techniques. In: 2nd International Conference on Information and Multimedia Technology (ICIMT 2010), Hong Kong, China, December 28-30, pp. 385–389 (2010)
17. Zamani, M., Manaf, A.A., Ahmad, R., Zeki, A.: An Approach to Improve the Robustness of Substitution Techniques of Audio Steganography. In: 2nd IEEE International Conference on Computer Science and Information Technology, Beijing, China, August 8-11, vol. 2, pp. 5–9 (2009)
18. Zamani, M., Taherdoost, H., Manaf, A.A., Ahmad, R., Zeki, A.: Robust Audio Steganography via Genetic Algorithm. In: Third International Conference on Information & Communication Technologies, Karachi, Pakistan, August 15-16, pp. 149–153 (2009)
19. Zamani, M., Manaf, A.A., Ahmad, R., Zeki, A., Magalingam, P.: A Novel Approach for Audio Watermarking. In: Fifth International Conference on Information Assurance and Security, Xi'an, China, August 18-20, pp. 83–86 (2009)
20. Zamani, M., Manaf, A.A., Ahmad, R., Jaryani, F., Taherdoost, H., Zeki, A.: A Secure Audio Steganography Approach. In: The 4th International Conference for Internet Technology and Secured Transactions, November 9-12, pp. 501–506 (2009)
21. Zeki, A.M., Manaf, A.A., Zamani, M.: Bit-Plane Model: Theory and Implementation. In: Engineering Conference 2010, Kuching, Malaysia, April 14-16 (2010)
22. Abokhdair, N.O., Manaf, A.B.A., Zamani, M.: Integration of Chaotic Map and Confusion Technique for Color Medical Image Encryption. In: 6th International Conference on Digital Content, Multimedia Technology and its Applications, Seoul, Korea, August 16-18, pp. 20–23 (2010)

23. Abdullah, S.M., Manaf, A.A., Zamani, M.: Capacity and Quality Improvement in Reversible Image Watermarking Approach. In: 6th International Conference on Networked Computing and Advanced Information Management, Seoul, Korea, August 16-18, pp. 81–85 (2010)
24. Zamani, M., Manaf, A.A.: "Mazdak's Method for PSNR Estimation in Audio Steganography". In: International Conference on Computer and Computational Intelligence, Nanning, China, December 25-26, pp. 574–577 (2010)
25. Zamani, M., Manaf, A.B.A., Abdullah, S.M., Chaeikar, S.S.: Correlation between PSNR and Bit per Sample Rate in Audio Steganography. In: 11th International Conference on Signal Processing, Saint Malo, Mont Saint-Michel, France, April 2-4, pp. 163–168 (2012)
26. Zamani, M., Manaf, A.B.A., Abdullah, S.M.: Correlation between PSNR and Size Ratio in Audio Steganography. In: 11th International Conference on Telecommunications and Informatics, France, April 2-4, pp. 82–87 (2012)
27. Zamani, M., Manaf, A.A., Shahidan, M.A.: Efficient Embedding for Audio Steganography. In: 2nd International Conference on Environment, Economics, Energy, Devices, Systems, Communications, Computers, Mathematics, April 2-4, pp. 195–199 (2012)
28. Zamani, M., Manaf, A.A., Daruis, R.: Azizah Technique for Efficiency Measurement in Steganography. In: 8th International Conference on Information Science and Digital Content Technology, Jeju, Korea, June 26-28, vol. 3, pp. 480–484 (2012)
29. Jabbar, A.A., Sahib, S.B., Zamani, M.: An Introduction to Image Steganography Techniques. In: International Conference on Advanced Computer Science Applications and Technologies (ACSAT 2012), November 26-28 (2012)
30. Jabbar, A.A., Sahib, S.B., Zamani, M.: Multimedia Data Hiding Evaluation Metrics. In: 7th WSEAS International Conference on Computer Engineering and Applications (CEA 2013), Milan, Italy, January 9-11 (2013)
31. Jabbar, A.A., Sahib, S.B., Zamani, M.: An Introduction to Watermarking Techniques. In: 12th WSEAS International Conference on Applications of Computer Engineering (ACE 2013), Cambridge, MA, USA, January 30-February 1 (2013)

Pixel Correlation Behavior in Different Themes

Alaa A. Jabbar[1], Shahrin Bin Sahib[1], and Mazdak Zamani[2]

[1] Faculty of Information & Communication Technology, Universiti Teknikal Malaysia Melaka, 76100 Melaka, Malaysia
[2] Advanced Informatics School, Universiti Teknologi Malaysia, 54100 Kuala Lumpur, Malaysia
alaaj@student.utem.edu.my, shahrinsahib@utem.edu.my, mazdak@utm.my

Abstract. This paper intends to study pixel correlation behavior of photos in different themes based on statistical analysis of pixel correlation evaluation.

Keywords: Pixel Correlation, Steganography, Watermarking, Steganalysis, Photo Themes.

1 Introduction

Conducted statistical analysis of proposed pixel correlation evaluation revealed that photos in different themes show different pixel correlation behavior. Therefore for more accurate steganalysis it is very important to analyze a photo based on its content. To do so, it is required to analyze original photos and their stego copies to discover the relations and patterns [1-4].

The known themes of photos are solid, smooth, and edgy photos. Furthermore, results of pixel's correlation analysis shows that there is difference between photos with wide smooth area and photos with partial smooth area. Thus the four analyzed photo themes for extracting patterns are wide flat region, wide smooth region, partial smooth region, and edgy photos [5-9].

2 Correlativity Analysis of Pixels

Layer is the main concept for correlativity analysis in offered method. All the pixels located in the same layer of neighbors have same importance and if only one of the pixels in the layer be correlated to central pixel then that layer and all outer layers would be counted as correlated. To approve correlativity of a layer at least one of the pixels in that layer or one of the pixels in inner layers should be correlated to central pixel [10-14].

Figure 1 illustrates concept of layer by separating pixels of each layer in different colors. Central pixel is a single pixel colored in red. All the pixels next to the central pixel constitute first layer and the outer adjacent pixels to the pixels of first layer constitute second layer.

F. Bian et al. (Eds.): GRMSE 2013, Part I, CCIS 398, pp. 223–234, 2013.
© Springer-Verlag Berlin Heidelberg 2013

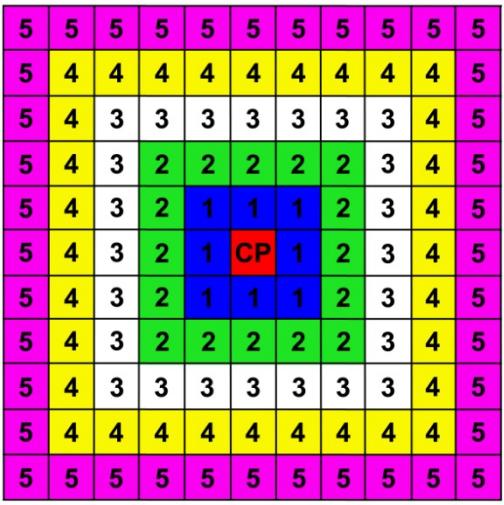

Fig. 1. Illustration of layer concept

White pixels are in third layer and the pixels numbered by 4 are located in fourth layer. Pixels of last layer, fifth layer, are colored in violet and numbered as 5. If any correlativity exist in one of the layers then from that particular layer up to fifth layer would be counted as correlated layers. For instance, we assume no correlativity exists between central pixel and the pixels in first layer, but there is a correlated pixel in second layer. Therefore second, third, fourth, and fifth layers would be seen as correlated layers to the central pixel as at least one correlated pixel has been found in their internal territory. Since there is no correlated pixel in first layer also it has no inner layer containing correlated pixel then first layer is not correlated.

Pixel color matching and channel color matching are the two proposed pixel's correlativity evaluation methods to discover the correlativity of a pixel with the neighbor pixels in different layers. Since in pixel matching all three color channels of Red, Green, and Blue (RGB) between central pixel and one of the neighbor pixels must be the same, then logically this comparison could also be called as AND correlativity analysis. In second way, if either of Red, Green, or Blue be the same between central pixel and one of neighbor pixels then they could be considered as correlated pixels. In view of the fact that the neighbor pixels would be analyzed up to five layers then first five rows and column of pixels from top and left, and last five rows and columns from bottom and right side of photo will be ignored in analysis process as they do not have enough neighbors for analysis.

In the Figure 2 the pixels in small yellow, blue, and white squares have enough neighbors to be considered for analysis process while the small violet square only has four layers of neighbors in left and down sides and therefore is not qualified for analysis.

2.1 AND Correlativity Analysis

Pixel color matching or in another word AND color analysis examines the correlativity of the central pixel with neighbors in different layers in a way that all red, green, and blue channels of both pixels should be same. This analysis starts from comparing the central pixel with first neighbor pixel in first layer. Then the process continues with comparing color channels of the central pixel with next neighbors in the same layer and then the neighbors in next layers up to fifth layer [15-19].

If there is a correlated pixel in boundary of first layer, then this correlativity also exists in boundary of second, third, fourth and fifth layers. Therefore there is no need to continue pixel color matching correlation analysis process for outer layers if any similar pixel be found in inner layers. This fact also speeds up the process of correlativity analysis [20-24].

In case there was any pixel with the same color channels of the central one, the comparison process will stop and from that particular layer until last layer flags of finding correlated pixel would change to true. For each layer proportion of correlated pixels to total number of analyzed pixels gives correlativity percentage of photo for that particular layer [25-31]. Following pseudo code shows process of AND correlativity analysis of a pixel. The used variables are:

Found: a flag to verify whether the loop should continue or not based on finding a correlated pixel. Value of true means that correlativity is found and there is no need to continue the process.

Layer_Flagi: value of this flag shows whether there is any correlated pixel for the layer of i.

Layer: identifier of layer which will vary from 1 to 5

layer.n: number of pixels in particular layer (not whole territory of the layer)

```
Found= false
For i=1 to 5 do
 Layer_Flagi =false
For layer =1 to 5 do
Begin
For Neighbor =1 to layer.n do
Begin
If ((CentralPixel.Red = Layer.Neighbor.Red) and (CentralPixel.Green = Layer.Neighbor.Green) and (CentralPixel.Blue = Layer.Neighbor.Blue) ) then
Begin
For i=layer to 5 do
 Layer_Flagi =true
Found= true
End
If found then break
End
If found then break
End
```

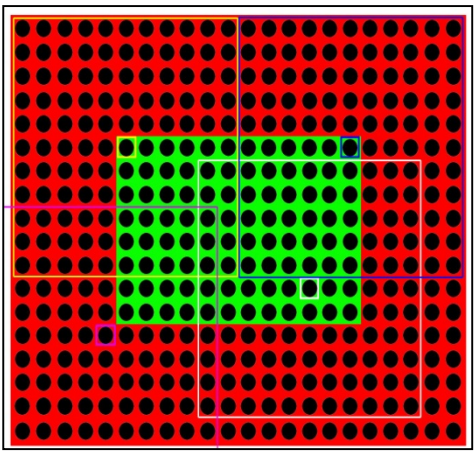

Fig. 2. Pixel analysis area

Figure 3 illustrates how the pixels would be analyzed for AND correlation analysis. In upper half there is a photo and in lower half a rectangle of 11*11 pixels of it is zoomed in. The numbers in red square show red, green, and blue values of the central pixel. The 8 pixels between red and green squares are first layer neighbors.

The 16 pixels between blue and green squares are second layer neighbors and this order continues until last layer which is constituted from 40 pixels between orange and black squares. RGB values of each pixel are written in top-down order in yellow color. RGB values of central pixel and similar values in other pixels are highlighted by white color. As is visible in the Figure 3 there is no similar value of central pixel in the first layer. In second layer only red value of one pixel is the same but since in AND pixel correlativity analysis all three values should be the same then there is no correlated pixel in second layer. In third layer three pixels have the same red or green or blue value, but only one of them has the same red and green and blue codes.

Therefore in layer three there is a correlated pixel to the central pixel which means the layers of three, four, and five are correlated to the central pixel as there is at least one correlated pixel in their territories. After finding correlated pixel in third layer there is no need to continue RGB comparison process for fourth and fifth layers and they would be considered as correlated layers to the central pixel despite there is no correlated pixel to the central one in those particular layers.

To calculate percentage of correlated pixels of this photo, both layer one and layer two have the value of zero and third, fourth, and fifth layers have value of one. Total number of pixels which are RGB correlated in layer (i) timed by 100 and divided by total number of analyzed pixels gives correlativity percentage of that layer.

Layer (i) R|G|B pixel correlativity =
[total number of layer (i) R|G|B correlated pixels*100] / [total number of analyzed pixels]%

Fig. 3. AND pixel correlativity analysis illustration

2.2 OR Correlativity Analysis

Channel color matching, or in other hand OR correlativity analysis, measures correlativity of the central pixel with neighbor pixels up to five layers in a way that if red, green, or blue channel values of the central pixel be the same as one of neighbors then that layer up to fifth layer would be considered as OR correlated layers [25-31].

The comparison process starts from first pixel in first layer and continues spiral like until the last pixel of the fifth layer. Since the inner layers are located into territory of outer layers then as soon as finding first identical color channel between the central pixel and one of neighbors the analysis process will stop and flags of finding correlated pixel of that layer and outer ones will convert into true. For each of layers proportion of correlated ones to total number of analyzed pixels will give correlativity percentage of that layer. Following pseudo code shows color channel correlativity analysis method for a pixel. The used variables are:

Found: a flag to verify whether the loop should continue or not based on finding a correlated pixel. Value of true means that correlativity is found and there is no need to continue the process.

Layer_Flagi : value of this flag shows whether there is any correlated pixel for the layer of i.

Layer: identifier of layer which will vary from 1 to 5.

Layer.n: number of pixels in particular layer (not whole territory of the layer)

```
Found= false
For i=1 to 5 do
Layer_Flagi =false
For layer =1 to 5 do
Begin
For Neighbor =1 to layer.n do
Begin
If ((CentralPixel.Red = Layer.Neighbor.Red) or (CentralPixel.Green = Layer.Neighbor.Green) or (CentralPixel.Blue = Layer.Neighbor.Blue) ) then
Begin
For i=layer to 5 do
Layer_Flagi =true
Found= true
End
If found then break
End
If found then break
End
```

Figure 4 illustrates process of color channel correlativity analysis. Upper half of this figure has a photo which a 11*11 square of its pixels is zoomed in lower half for color channel OR correlativity analysis.

Central pixel is highlighted by a red square and the layers of one to five are separated respectively in blue, green, white, orange, and black squares. Pixels of each layer are located between the squares but to consider a layer as correlated is enough to find a correlated pixel either in the layer or in inner layers.

Fig. 4. OR pixel correlativity analysis illustration

Numbers of the pixels in layers of one to five are respectively 8, 16, 24, 32, and 40. Numbers of whole pixels in territories of layers of one to five respectively are 8, 24, 48, 80, and 120. It means that, for example, for fifth layer if any of 120 pixels be OR correlated to the central one then this layer will considered as correlated layer regardless of exact location of the pixel.

In Figure 4 the central pixel RGB values respectively are 104, 112, and 61. In first and second layers there is no channel with the same value of central channels. Therefore first and second channels are not correlated. In third channel red value of one of pixels, which is highlighted by white color, is the same as red value of central pixel. Hence layer three and outer layers will be considered as correlated layers and there is no need to continue analysis process after finding the first match channel.

Layer (i) R|G|B pixel correlativity =
*[total number of layer (i) R|G|B correlated pixels*100] / [total number of analyzed pixels]%*

3 Correlativity Patterns

Pixels of photos naturally are correlated to the neighbor pixels. Photos with wide flat regions have strongest correlativity and then it follows by wide smooth region, partial smooth region, and edgy photos.

When an external object manipulates RGB values of the pixels to embed external data, correlativity of the pixels would be affected and for higher embedding bit-rates correlativity will be degraded more. Farness of pixels' correlativity from its average values in natural photos can be used as steganalysis measurement for both recognizing stego images than original ones, and in more advanced stage predicting ratio of data embedment.

To find measurements of steganalysis, correlativity of stego images should be compared with average correlativity of original images in that particular photo theme. Proposed pixel color and channel color correlativity examination methods can be used to define pattern of each photo theme.

In addition of the original photos, stego photos also will have different patterns than original ones as their correlativity is affected through insertion of data. In more depth, stego photos with different bit-rates and different photo themes will have different pattern of correlativity than other types.

Therefore to have accurate steganalysis method based on pixel color and channel color correlativity of pixels, stego photos in different photo themes with different embedding rates should be analyzed for extracting patterns. After extraction of the patterns they can be used for analysis of photos to firstly distinguish stego ones from original images and secondly predict bit-rate of embedded data into the object.

3.1 Determining Layer Examination Threshold

Correlativity analysis will examine the pixels in five layers but for higher performance and enhancing speed of steganalysis system best threshold of analysis of layers should be determined based on experimental results.

By moving from first layer toward fifth layer likelihood of having correlated layer increases as there are more pixels. It increases chance of finding correlation and correlation of inner layers automatically will be inherited to outer layers.

Therefore probability of having correlated layers for outer layers is higher and they will overlap each other. Experimental correlation analysis on data set can determine the best analysis threshold layer.

3.2 Pattern Matching System

After determination of the best threshold for correlativity analysis, patterns of different original photos themes and their embedded copies must be extracted. Since some samples of data set in correlativity analysis may have results far than normal behavior of that category then through a statistical process the generated results must be purified. Standard deviation can be used to filter out abnormal results from generated analysis results.

The standard deviation of a data set, statistical population, random variable, or probability distribution can be calculated by computing the square root of its variance. Unlike variance, an important property of standard deviation is that its result is in the same unit as the data is. It is commonly utilized to measure margin of errors and statistical conclusions confidence. The reported error margin is normally about twice of the standard deviation.

In researches generally standard deviation of the experimental data will be reported and the data located outside of the range will be ignored or only will be statistically significant. Standard deviation distinguishes normal error or variation from casual variation.

To calculate standard deviation firstly average of data set values must be computed and then the mean will be used to calculate variance. Square root of the variance is standard deviation. The variables used are as follow:

X_i = item of the dataset
f_i = plenty of the item in dataset
N= number of the items in the dataset
$\overline{X}$= arithmetic mean
S^2: Variance
S: standard deviation

$$\overline{X} = \frac{1}{N}\sum_{i=1}^{K} f_i X_i$$

$$S^2 = \frac{1}{N-1}\sum_{i=1}^{k} f_i(x_i - \bar{x})^2$$

$$S = \sqrt{S^2}$$

Standard deviation gives range of the most reliable data from mean. Therefore values in both right and left sides of average with the range of standard deviation would be reliable data.

The values are located from border of mean value minus standard deviation toward minimum and mean value plus standard deviation toward maximum value will lose their importance and reliability. Therefore, to extract the patterns from each category in the data set mean value, standard deviation, minimum, and maximum values are required. After extracting patterns a marking system should measure the new samples to find the most similar pattern to correlativity behavior of analyzed photo. Since the results in the boundaries of standard deviation are considered as genuine values then in the evaluation system they should have maximum worth and from the boundaries toward maximum and minimum the analysis results should lose their importance.

If the results in the reliable area get the full mark, then the results out of the boundaries of standard deviation from mean point should lose their importance based on their distance to the genuine area. Therefore as is shown in the Figure 5 the analysis results in the genuine area will get full mark of one and other results based on their distance will have a value between 0 and 1.

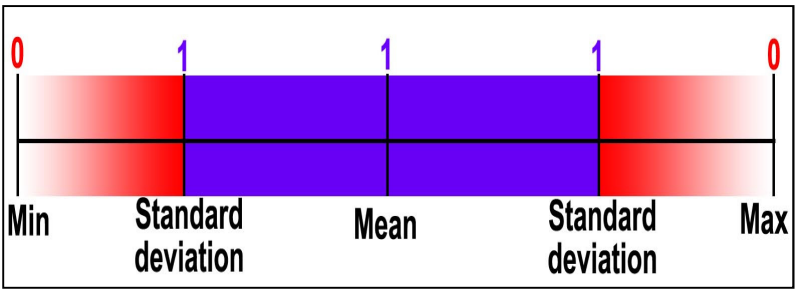

Fig. 5. Pattern analysis marking system

Analysis of a photo from first layer to the last layer will generate separate results for each layer. Comparing the results with each of the extracted patterns will lead in having separate mark for matching to each pattern. Sum of the similarity marks of each layer will determine similarity of the results to that particular pattern. By comparing the results with each of the patterns and sorting them in descending order the marking system will find the most similar pattern and determine whether the photo is original or with which embedding bit-rate if recognized as stego image.

4 Conclusion

This paper starts with elaborating details of proposed pixel color and color channel correlativity analysis methods. Based on the proposed method each type of photo and their embedded copies will have two correlativity patterns which should be extracted.

The extracted patterns later can be utilized to distinguish original photos from stego objects and also prediction of embedding rate. To assess photos a proposed pattern matching system based on standard deviation will examine similarity of the given object with the extracted patterns to firstly recognize stego files and secondly predict the embedment rate if the given file is stego object.

References

1. Zamani, M., Manaf, A.B.A., Ahmad, R.B., Jaryani, F., Chaeikar, S.S., Zeidanloo, H.R.: Genetic audio watermarking. In: Das, V.V., Vijayakumar, R., Debnath, N.C., Stephen, J., Meghanathan, N., Sankaranarayanan, S., Thankachan, P.M., Gaol, F.L., Thankachan, N. (eds.) BAIP 2010. CCIS, vol. 70, pp. 514–517. Springer, Heidelberg (2010)
2. Zamani, M., Manaf, A.B.A., Abdullah, S.M., Chaeikar, S.S.: Mazdak Technique for PSNR Estimation in Audio Steganography. In: Applied Mechanics and Materials, vol. 229-231, pp. 2798–2803. Trans Tech Publications, Switzerland (2012)
3. Zamani, M., Manaf, A.A., Ahmad, R., Zeki, A., Abdullah, S.: A Genetic-Algorithm-Based Approach for Audio Steganography. In: World Academy of Science, Engineering and Technology, June 24-26, pp. 355–358 (2009)

4. Zamani, M., Taherdoost, H., Manaf, A.A., Ahmad, R.B., Zeki, A.M.: An Artificial-Intelligence-Based Approach for Audio Steganography. Journal of Open Problems in Science and Engineering 1(1), 64–68 (2009)
5. Zamani, M., Manaf, A.A., Ahmad, R., Jaryani, F., Taherdoost, H., Chaeikar, S.S., Zeidanloo, H.R.: A Novel Approach for Genetic Audio Watermarking. Journal of Information Assurance and Security 5, 102–111 (2010)
6. Zamani, M., Manaf, A.A., Ahmad, R., Jaryani, F., Taherdoost, H., Chaeikar, S.S., Zeidanloo, H.R.: Genetic Audio Steganography. International Journal on Recent Trends in Engineering & Technology 3(2), 89–91 (2010) ISSN: 2158-5563
7. Abdullah, S.M., Manaf, A.A., Zamani, M.: Recursive Reversible Image Watermarking Using Enhancement of Difference Expansion Techniques. Journal of Information Security Research 1(2), 64–70 (2010)
8. Zamani, M., Manaf, A.A., Zeidanloo, H.R., Chaeikar, S.S.: Genetic Subtitution-Based Audio Steganography for High-Capacity Applications. International Journal for Internet Technology and Secured Transactions 3(1), 97–110 (2011)
9. Zeki, A.M., Manaf, A.A., Ibrahim, A.A., Zamani, M.: A Robust Watermark Embedding in Smooth Areas. Research Journal of Information Technology 3(2), 123–131 (2011)
10. Zamani, M., Manaf, A.A., Ahmad, R.: Knots of Substitution Techniques of Audio Steganography. In: International Proceedings of Computer Science and Information Technology, vol. 2, pp. 370–374. IACSIT Press, Singapore (2011)
11. Zamani, M., Manaf, A.B.A., Abdullah, S.M.: An Overview on Audio Steganography Techniques. Journal of Digital Content Technology and its Applications. Advanced Institute of Convergence Information Technology (2012)
12. Zamani, M., Manaf, A.A.: Genetic algorithm for fragile audio watermarking. In: Telecommunication Systems, Special Issue on Innovations in Emerging Multimedia Communication Systems. Springer (in press) ISSN: 1018-4864
13. Zamani, M., Manaf, A.A., Ahmad, R.: Knots of Substitution Techniques of Audio Steganography. In: The 2009 International Conference on Telecom Technology and Applications, Manila, Philippines, June 6-8, pp. 415–419 (2009)
14. Zamani, M., Manaf, A.A., Ahmad, R.: Current Problems of Substitution Technique of Audio Steganography. In: International Conference on Artificial Intelligence and Pattern Recognition, Orlando, Florida, USA, July 13-16, pp. 154–160 (2009)
15. Zamani, M., Manaf, A.A., Ahmad, R., Zeki, A., Abdullah, S.: Genetic Algorithm as an Approach to Resolve the Problems of Substitution Techniques of Audio Steganography. In: The 2009 International Conference on Genetic and Evolutionary Methods, Las Vegas, Nevada, USA, July 13-16, pp. 170–175 (2009)
16. Zamani, M., Manaf, A.A.: Azizah's Method to Measure the Efficiency of Steganography Techniques. In: 2nd International Conference on Information and Multimedia Technology (ICIMT 2010), Hong Kong, China, December 28-30, pp. 385–389 (2010)
17. Zamani, M., Manaf, A.A., Ahmad, R., Zeki, A.: An Approach to Improve the Robustness of Substitution Techniques of Audio Steganography. In: 2nd IEEE International Conference on Computer Science and Information Technology, Beijing, China, August 8-11, vol. 2, pp. 5–9 (2009)
18. Zamani, M., Taherdoost, H., Manaf, A.A., Ahmad, R., Zeki, A.: Robust Audio Steganography via Genetic Algorithm. In: Third International Conference on Information & Communication Technologies, Karachi, Pakistan, August 15-16, pp. 149–153 (2009)
19. Zamani, M., Manaf, A.A., Ahmad, R., Zeki, A., Magalingam, P.: A Novel Approach for Audio Watermarking. In: Fifth International Conference on Information Assurance and Security, Xi'an, China, August 18-20, pp. 83–86 (2009)

20. Zamani, M., Manaf, A.A., Ahmad, R., Jaryani, F., Taherdoost, H., Zeki, A.: A Secure Audio Steganography Approach. In: The 4th International Conference for Internet Technology and Secured Transactions, November 9-12, pp. 501–506 (2009)
21. Zeki, A.M., Manaf, A.A., Zamani, M.: Bit-Plane Model: Theory and Implementation. In: Engineering Conference 2010, Kuching, Malaysia, April 14-16 (2010)
22. Abokhdair, N.O., Manaf, A.B.A., Zamani, M.: Integration of Chaotic Map and Confusion Technique for Color Medical Image Encryption. In: 6th International Conference on Digital Content, Multimedia Technology and its Applications, Seoul, Korea, August 16-18, pp. 20–23 (2010)
23. Abdullah, S.M., Manaf, A.A., Zamani, M.: Capacity and Quality Improvement in Reversible Image Watermarking Approach. In: 6th International Conference on Networked Computing and Advanced Information Management, Seoul, Korea, August 16-18, pp. 81–85 (2010)
24. Zamani, M., Manaf, A.A.: "Mazdak's Method for PSNR Estimation in Audio Steganography". In: International Conference on Computer and Computational Intelligence, Nanning, China, December 25-26, pp. 574–577 (2010)
25. Zamani, M., Manaf, A.B.A., Abdullah, S.M., Chaeikar, S.S.: Correlation between PSNR and Bit per Sample Rate in Audio Steganography. In: 11th International Conference on Signal Processing, Saint Malo, Mont Saint-Michel, France, April 2-4, pp. 163–168 (2012)
26. Zamani, M., Manaf, A.B.A., Abdullah, S.M.: Correlation between PSNR and Size Ratio in Audio Steganography. In: 11th International Conference on Telecommunications and Informatics, France, April 2-4, pp. 82–87 (2012)
27. Zamani, M., Manaf, A.A., Shahidan, M.A.: Efficient Embedding for Audio Steganography. In: 2nd International Conference on Environment, Economics, Energy, Devices, Systems, Communications, Computers, Mathematics, April 2-4, pp. 195–199 (2012)
28. Zamani, M., Manaf, A.A., Daruis, R.: Azizah Technique for Efficiency Measurement in Steganography. In: 8th International Conference on Information Science and Digital Content Technology, Jeju, Korea, June 26-28, vol. 3, pp. 480–484 (2012)
29. Jabbar, A.A., Sahib, S.B., Zamani, M.: An Introduction to Image Steganography Techniques. In: International Conference on Advanced Computer Science Applications and Technologies (ACSAT 2012), November 26-28 (2012)
30. Jabbar, A.A., Sahib, S.B., Zamani, M.: Multimedia Data Hiding Evaluation Metrics. In: 7th WSEAS International Conference on Computer Engineering and Applications (CEA 2013), Milan, Italy, January 9-11 (2013)
31. Alaa, A.: Jabbar, Shahrin Bin Sahib, Mazdak Zamani. An Introduction to Watermarking Techniques. In: 12th WSEAS International Conference on Applications of Computer Engineering (ACE 2013), Cambridge, MA, USA, January 30-February 1 (2013)

The Evolution of Poyang Lake Wetland Hydroecology

Zhimin Deng, Xiang Zhang, and Yang Xiao

State Key Laboratory of Water Resources and Hydropower Engineering Science, Wuhan University, Wuhan, China

Abstract. This study used remote sensing technology, employing Landsat-TM image covering the Poyang Lake wetland during fall and winter of 1991-2009, to investigate the water level variation characteristics of the Poyang Lake before and after the Three Gorges Reservoir water storage. And then the CoupModel was used to simulate the respiration amount of the wetland typical vegetation during 1990-2009. The results indicate that the water body area of Poyang Lake wetland shows a downward trend, while the grass lands the tendency of expansion. The average value of the percentage share of water body area before and after the Three Gorges Reservoir water storage are 56.62% and 29.35%, respectively, the percentage share of the thick grass land are 22.98% and 34.6%, respectively. The typical wetland vegetation respiration amount also shows a downward trend during September to November of 1990-2009, namely the typical vegetation biomass is reduced, thereby destroying the habitat and food chain of migratory birds. It is concluded that the Three Gorges Reservoir operation makes the decline of the Poyang Lake water level which reduces the typical vegetation biomass.

Keywords: Poyang Lake wetland, CoupModel, remote sensing, water level, vegetation respiration.

1 Introduction

Poyang Lake is the largest freshwater lake in China and international important wetland, and is also the largest habitat of migratory birds, so it is paid widespread international attention. The water level fluctuation of Poyang Lake **is** subject to the interaction of the five rivers flow into Poyang Lake and exchanging water with the Yangtze River. Poyang Lake servers as an important regulator for water balance and ecological safety of the Yangtze River, due to intensive human activities and the Yangtze River water level influenced by factors like the Three Gorges Reservoir water storage, Poyang Lake has emerged some phenomena such as outflow increase and inflow decrease to lake, low water level in advance and duration extension, wetland degradation, biodiversity loss and water quality deterioration and so on, which are widespread concerned, so many scholars have carried out the research in Poyang Lake. Jinbao wan[1], Xuchun Ye[2], Min Qian[3] and WAN Zhong-ying[4] et al analyzed the water level change of Poyang Lake; Huifang Guo[5], Zhao Xiujiang[6], Jiang Jiahu[7] and Liu Wenbiao[8] et al analyzed the impact of the Three Gorges Project operation on

F. Bian et al. (Eds.): GRMSE 2013, Part I, CCIS 398, pp. 235–245, 2013.
© Springer-Verlag Berlin Heidelberg 2013

the Poyang Lake water level; Q. Zhang[9] revealed the considerable effects on the Poyang Lake water level, particularly a reduced level over the dry period from late summer to autumn, and pointed out that the Three Gorges dam impact needs to be further assessed based on long-term monitoring of the lake ecosystem.

Wetlands are an important component of ecosystems because of its role in the maintenance of environmental quality and biodiversity. Wetland vegetation biomass is an important part of wetland ecosystems and is the important indicator of the health status of the wetland ecosystems. Therefore to estimate **the** wetland vegetation biomass aids in understanding the dynamics of **the** wetland ecosystems. Conventional field method of wetland observation and estimation are often time consuming, labor intensive and inaccessibility. However, along with the increase in remote sensing data sources and the development of remote sensing inversion method, relevant scholars have applied the remote sensing data to study the wetland. YU Li et al[10] employed Landsat-TM image to analyze the effects of the Three Gorges Project on the evolution law of the typical wetlands vegetation in the Poyang Lake, the results showed that with the running of the Three Gorges Project, the effects on the succession of the wetlands were very different depending on the distance from Hukou; LI Jian[11] and WANG Qing[12] et al also employed the remote sensing technology to establish the wetland vegetation biomass model and estimate the wetland vegetation biomass, respectively.

However, most of the study in retrieving vegetation biomass has been focused on the implement of linear and non-linear regression models. But the obtainment of vegetation biomass is always very complex, and the semi-empirical regression model cannot reflect on the evolution of the vegetation biomass from the physiological function point of view. Hongxiu Wan[13] et al estimated the carbon fluxes from the Poyang Lake wetlands vegetation in the growing season, the results demonstrated that carbon dioxide flux **had** closer relationship with vegetation change than methane flux does, **the** vegetation biomass maybe controlled the magnitude of $\mathbf{CO_2}$ fluxes. So this **study** simulated the vegetation respiration (carbon) using CoupModel instead of linear or non-linear models.

Poyang Lake is rich in wetland vegetations, vegetation community structure variety, the seasonal change abundant, and is a rare giant lake marsh wetland landscape in the subtropical area. However, Carex community is the largest area and the most widely distributed community types in the Poyang Lake. Carex has two vigorous growth seasons from April to May and September to November separately due to the flooding[14]. So the ecological characteristics of Carex adapts to the ecological environment under the specific hydrological condition of Poyang Lake, seasonal change in water level and climate are **the** controlling factors for the growth of Carex.

On this basis, the comprehensive of the Three Gorges Reservoir operation characteristics and **the** Carex growth characteristics, this **study** chose the duration from September to November each year as the research period, with the aid of **the** remote sensing technology platform and **the** application of CoupModel model, to analyze **the** Poyang Lake water level variation characteristics before and after the Three Gorges Reservoir water storage in 2006 and explore the ecological effect generated by the water level change.

2 Study Area and Data

2.1 Study Area

Poyang Lake(115°49′ to 116°46′E, 28°21′ to 29°52′N) is the largest freshwater lake in China and international important wetland, located in the southern bank of the lower reach of the Yangtze River and the northern part of Jiangxi Province. Poyang Lake receives water flows mainly from the five rivers: Ganjiang, Fuhe, Xinjiang, Raohe and Xiuhe, and exchanges water with Yangtze River in Hukou. Poyang Lake's water level is affected by Yangtze River and five rivers. The high water level of Poyang Lake occurs in the period from April to September, and the flood season of five rivers is in the period from April to June. Water flow from five rivers into lake reduces from July to September, but Yangtze River is in the flood season, the occurrence of backflow from Yangtze River to Poyang Lake induces the rise of the Poyang Lake's water level rapidly. In this **study**, the study area is Poyang Lake National Nature Reserve, which administers nine lakes such as Dahuchi, Shahu, Banghu, Zhushihu, Meixihu, Zhonghuchi, Dachahu, Xianghu and Changhuchi, and is the most important wintering habitat for migratory birds in the world today and the main wintering sites for crane and Oriental white stork, and is an international important wetland and the global important ecological regions. The water level drops and bottomland comes out and only several wandering watercourses remain from October to next March, which provides a suitable habitat and food for waterfowl. At a scale of the whole lake, from the ratio of the dominant community point of view, Carex community is the largest area and the most widely distributed community types in the Poyang Lake.

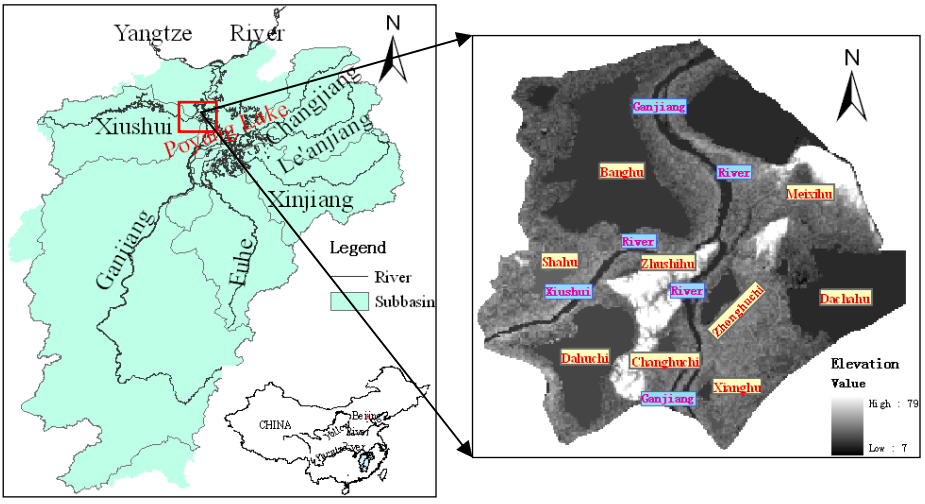

Fig. 1. Location and Scratch Map of Poyang Lake

2.2 Data Acquisition and Preparation

Total 13 Landsat TM images for path121/row40 of the Poyang Lake wetland from fall and winter of 1991 to 2009 are derived from USGS and Institute of Remote Sensing and Digital Earth Chinese Academy of Sciences. Area covered by clouds or cloud shadows in any image were small or seldom. Preprocessing of data mainly includes data input, orthorectification, registration and mask, and so on.

The meteorological data (daily precipitation, sunshine duration, average relative humidity, average temperature and average wind speed) were provided by China Meteorological Data Sharing Service System. The daily data was processed by inverse distance weighted interpolation (IDW), and then masked by shape file of the study area, the calculated average value of meteorological data was used as the model input with the format of PG file.

Soil properties database refers to Harmonized World Soil Database and literature [15]. Soil maps of China are obtained from Institute of Soil Science, Chinese Academy of Sciences, Nanjing, China for the Second National Soil Survey of China at a scale of 1:1 million. Soil classification system is delineated based on the soil family definitions and the FAO-90. Porosity ranges from 0.41 to 0.52 and saturated hydraulic conductivity varies from 0.14 to 0.97m/d. The vegetation database refers to the literatures [11-12, 16-17] and is obtained by the field observation and sampling.

Based on the daily water level data of Xingzi hydrological station in the Poyang Lake which **was** derived from Jiangxi Provincial Water Conservancy Planning and Designing Insititute.

3 Coup Model

3.1 Coup Model Profile

The CoupModel is a one-dimensional dynamic model, which can simulate heat and water transfer process and also simulate C and N in a soil-plant-atmosphere-transfer system. Two coupled differential equations for water and heat flow represent the central part of the model. These equations are solved with an explicit numerical method. There are two basic assumptions behind these equations as follows: (1) the law of conservation of mass and energy; (2) flows occur as a result of gradients in water potential(Darcy's law) or temperature(Fourier's law). The model takes many properties into account, which are represented as corresponding parameter values. The model needs to enter the three major database (meteorological data, vegetation characteristics and soil properties) beside parameters input when the model simulates.

3.2 Design of the Model

The main options of the model switch are shown in the following table:

Table 1. The Switch of the CoupModel

Model Structure		Plant Growth		Meteorological Data	
Items	Switches	Items	Switches	Items	Switches
Evaporation	Radiation input style	Growth	Water use efficiency	RadGlo-bInput	Estimat-ed
GroundWater Flow	On	Litter fall dynamics	f(Growth TempSum)	Vapour-AirInput	As relative humidity
Nitrogen and Carbon	Dynamic interaction with abiotics	PlantRespiration	Growth and Maintenance		
PlantType	Explicit one big leaf	Resp Temp Response	Q10 whole range		
SnowPack	On	Winter regulation	On	Others	Read from PG-file
WaterEq	On with complete soil profile	Terminating Harvest	On		

Part of the model parameters are set as follows in table 2:

Table 2. Part of the CoupModel parameters

Items	Value	Items	Value
Altitude of meteorological station	15m	The number of soil layers	7
Altitude of simulated site	13m,Literature [16]	The thickness of each layer	0.1m
Amplitude of air temperature	40.3℃	Maximal cover of the plant	0.88,Literature [11]
Mean temperatures	17.5℃	Canopy height (mean)	0.44m
Latitude	29°	Length of the roots	0.2m
The radiation use efficiency	2 gDw/MJ	The water use efficiency	3 gDW/mm
The growth respiration coefficient	0.21/d	The respiration rate coefficient	0.001/d

In this **study**, the meteorological data input used the above preprocessing meteorological database, the vegetation characteristics data was set by the growth parameters of the Poyang Lake wetland typical vegetation (Carex), some parameters of the soil propertied in the model were chosen as fixed value or were default values due to their minor sensitivity on the investigated output.

4 Results and Discuss

4.1 Classification of the Poyang Lake Wetland and Water Body Change

Wetland classification is the basis of all wetland researches. Scientific classification of wetland is a frontier field of international wetland scientific research. This **study** referred to the definition of the wetland, classification system[14,18,19]used in the domestic study and the specific situation of the Poyang Lake, and considered the interpretation of Landsat TM remote sensing image. Firstly, **the** Poyang Lake wetland classification **was** established by the man-machine interactive interpretation: 1 water body; 2 mudflat; 3 thick grass land; 4 sparse grass land; 5 sand. Secondly, the Poyang Lake wetland classification map was obtained by using Arcgis with mask and mapping (Fig.2). Due to the limitation of space, part of the wetland classification maps was listed as follows.

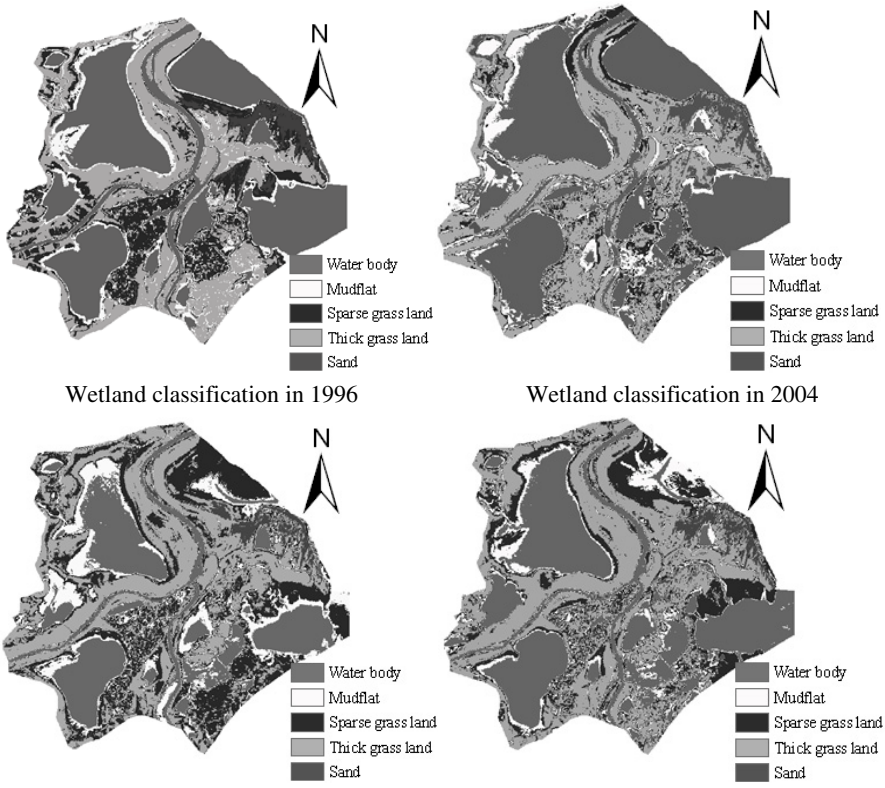

Fig. 2. Poyang Lake wetland classification in fall and winter

The number of pixels of each category was obtained through class statistics, and the percentage share of each category was calculated (as shown in Fig.3).

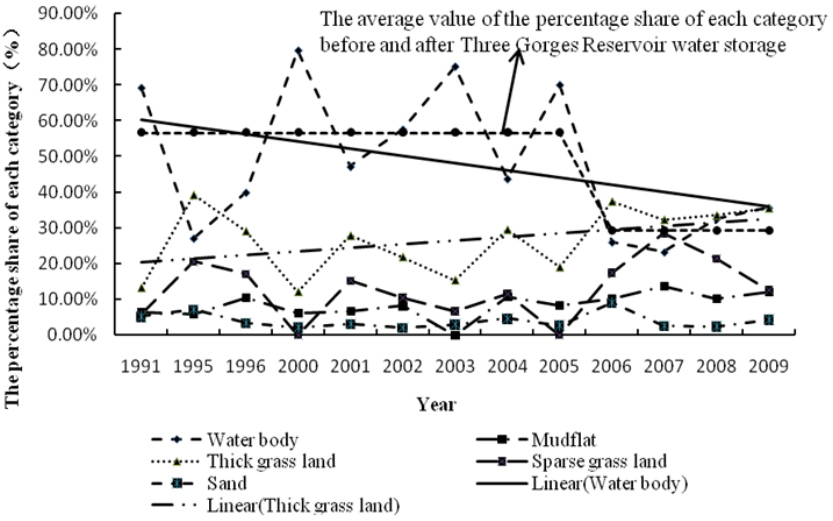

Fig. 3. The schematic representation of the percentage share of each category of the Poyang Lake wetland

As shown in Fig.3, the percentage share of water bodies generally **shows** a downward trend from fall and winter of 1991 to 2009, which **is** in close agreement with the simultaneously measured water level of Xingzi hydrological station (Fig.4). Area of water bodies gradually **reduces** at a rate of 2.03%/a, from the percentage share of 57.57% on Nov 8,2002 to 26% on Nov 3, 2006, the magnitude of water level fluctuation is rather **large**. However, the percentage share of thick grass land shows an upward trend at a rate of 1.01%/a. Trial impounding of Three Gorges Project started in

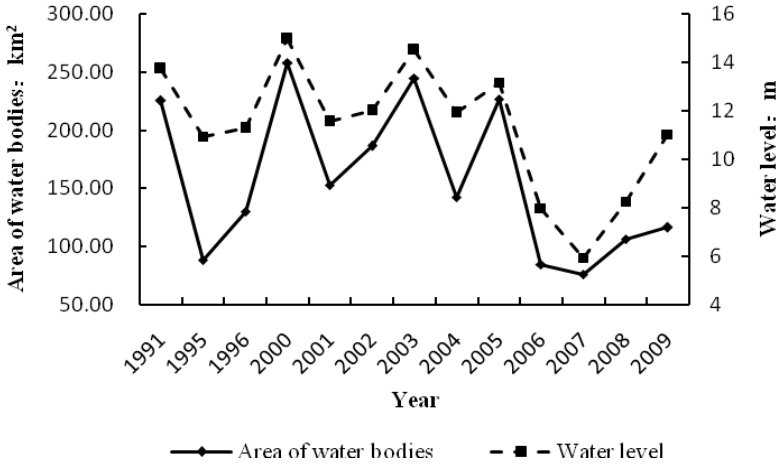

Fig. 4. The relationship between the water body area of Poyang Lake and the water level of Xingzi hydrological station

2006, the water level 135m on 20 September 2006 rose up to 155.77m on 4 December 2006. The average value of the percentage share of water bodies and the thick grass land in fall and winter is 56.62% and 22.98% before 2006, respectively, but 29.35% and 34.6% after 2006, respectively. water bodies reduces as much as 27.27%, however, the thick grass land **rises** by 11.62% and sparse grass land by 10.26%, water bodies gradually transfer into the grass land. Thus it can be seen, Three Gorges Project has exerted a great influence over the Poyang Lake water level since it started water storage, which reduced the water level of the typical wetland bottomland, and promoted the expansion of the wetland grass land.

4.2 CoupModel Test

The simulation runs from1990 to 2011(except 2010) with daily output values. Due to lack of the measured soil properties data, so this **study** only tested the simulation effect of meteorological database module in the model, model performance was evaluated for a liner regression between simulated and observed values. The results **are** shown as follows, the simulation **generates** good results in the comparison with measured data.

Table 3. The CoupModel test

Meteorological factors	Sunshine duration (minutes)	Average relative humidity(%)	Average temperature(℃)	Average wind speed(m/s)
Liner regression coefficients R^2	0.78	0.87	0.98	0.72

4.3 Accumulated Vegetation Respiration Output

According to the Three Gorges Reservoir operation characteristics and **the** Carex growth characteristics, time from 10 September to 29 November each year was selected as a simulated period to calculate the accumulated vegetation respiration, which was represented by the accumulated amount carbon from vegetation respiration including root respiration, unit: gc. The results **are** shown in Fig.5 below, which **are** close to the study results of the literature [13].

As can be seen from Fig.5 and 6, the accumulated vegetation respiration **amount** generally **shows** a downward trend from 1990 to 2011. The average value of the accumulated vegetation respiration **amount** is 47.39gc before the Three Gorges Reservoir water storage, however, the average value of the accumulated vegetation respiration **amount** is 44.44gc after the Three Gorges Reservoir water storage, which **decreases** by 2.95gc. The accumulated vegetation respiration **amount** is the largest in 1998, the smallest in 1992. Because both the highest water level and the magnitude of the water level fluctuation in 1998 are the biggest, 18.95m and 12.21m, respectively, and the smallest in 1992, 11.3m and 4.97m, respectively. However, the growth and development of the vegetation always are restricted by its ecological environment, **the**

change of which will inevitably lead to the vegetation occurs the corresponding evolution. Among the natural factors inducing the vegetation evolution, changes in water level fluctuation is always dominant. Its influence degree will depend on the magnitude of water level fluctuation, duration with different water level and its expiration of the period (season)[14]. The accumulated vegetation respiration **amount** gradually decrease from 2005 to 2009, mainly because the impoundment of the Three Gorges Reservoir started since 2006, resulting in the Hukou water lever pulling empty and the decline of Poyang Lake water level, and then affecting the growth of the wetland typical vegetation.

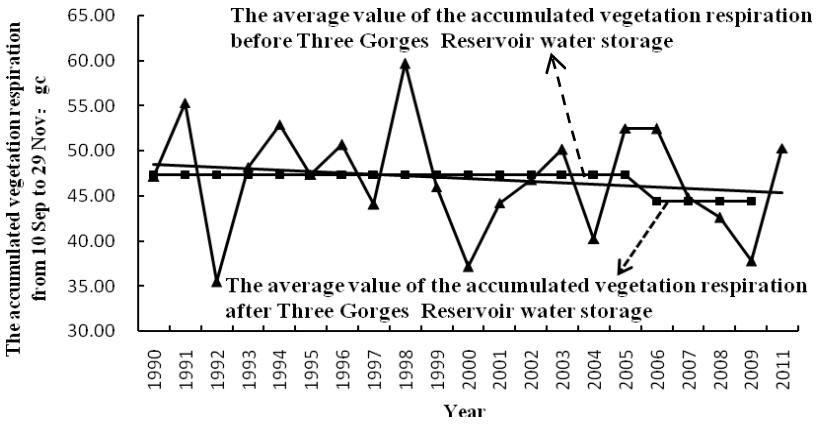

Fig. 5. The accumulated vegetation respiration from10 September to 29 November each year

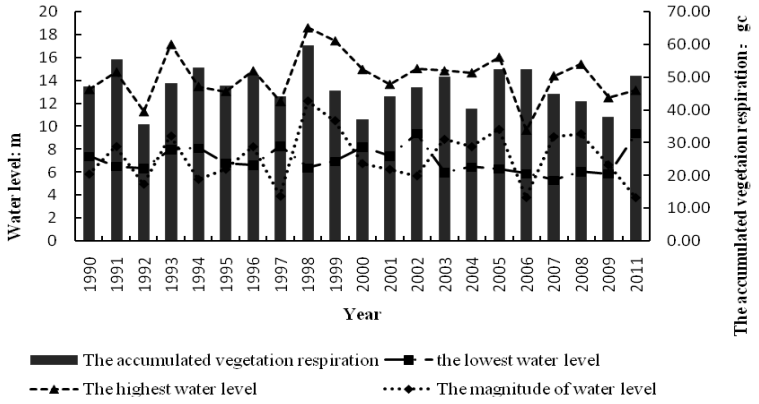

Fig. 6. The relationship between the water level and the accumulated vegetation respiration

5 Conclusions and Outlook

The aim of this study is to investigate the water level variation characteristics and the variation trend of the wetland typical vegetation biomass in the Poyang Lake. This study analyzed the water level change by employing the total 13 Landsat TM images during the fall and winter of 1991-2009. The wetland typical vegetation respiration amount, instead of the vegetation biomass, was simulated by applying the CoupModel, the research results helped to make the following important conclusions:

The percentage share of water bodies generally **shows** a downward trend from fall and winter of 1991 to 2009, the area of water bodies gradually drops at a rate of 2.03%/a, namely **the** water level **presents** a tendency of decline. However, the percentage share of the thick grass land shows an upward trend.

The accumulated vegetation respiration **amount** generally shows a downward trend from 1990 to 2011, which is the largest in 1998, the smallest in 1992. The trend of water level change was consistent with the vegetation respiration amount, indicating that as the continuous decline of water level, the extension of low water level duration is not conductive to the growth of the wetland typical vegetation-Carex. However, **the variation trend of the grass lands and the vegetation respiration amount presents** an opposite trend, because the parameters of the model were set according to the physiological characteristics of the Carex, so the simulated **vegetation** respiration amount represented the respiration amount of Carex. Although the area of the grass land increased, Carex gradually was shrinking because of inter-ethnic competition, thus the **vegetation** respiration amount decreased.

Poyang Lake wetland provides the habitat and food for waterfowl, however, as the area of water bodies drops and the area of the grass land increases, human will plant and graze on the grass land, resulting in the decline of the wetland area and the destruction of habitat for birds and threatening the survival of birds. Therefore, the restoration and protection of the Poyang Lake wetland should be strengthened.

This **study** simply determined the water level succession of the Poyang Lake wetland by using **the** remote sensing image and simulated the wetland typical vegetation respiration **amount** by applying the CoupModel, but the relationship between water level and the vegetation respiration **amount** has been not established, **which** may be taken into account in the future. **And** then the growth condition of the wetland typical vegetation can be predicted according to the water level data, to provide a reference for the restoration and protection of the Poyang Lake wetland.

References

1. Wan, J.B., Chen, L., Lan, X.Y., Lai, X.J.: Effects of the Water Level Change of Poyang Lake on Characteristics of Water Quality. In: International Conference on Remote Sensing, Environment and Transportation Engineering (RSETE), pp. 6818–6820. IEEE (2011)
2. Ye, X.C., Zhang, Q., Guo, H., Bai, L.: Long-term Trend Analysis of Effect of the Yangtze River on Water Level Variation of Poyang Lake(1960 to 2007). In: International Symposium on Water Resource and Environment Protection (ISWREP), vol. 1, pp. 543–545. IEEE (2011)

3. Min, Q., Wang, Z.P.: The Varying Tendency of the Water Level of the Poyang Lake in Recent 40 Years. Jiangxi Hydraulic Science & Technology 4, 360–364 (1992)
4. Wan, Z.Y., Zhong, M.S., Wang, M.W., Ding, S.L., Huang, S.E.: Dynamic Prediction Model of Poyang Lake's Water Level. Journal of Jiangxi Normal Universtiy 3, 232–236 (2003)
5. Guo, H.F., Dong, Z.C., Chen, X., Ma, X.X., Zhang, P.Y.: Impact analysis of Poyang Lake after Three Gorges Project's running by using ANFIS. In: International Conference on Multimedia and Information Technology, pp. 741–743 (2008)
6. Zhao, X.J., Sun, Z.Y., Gao, Y.: Three Gorges Reservoir Operation Effects on Water Level and Ecological Function of Poyang Lake. Three Gorges Forum 5, 19–22 (2010)
7. Jiang, J.H., Huang, Q.: A Study of the Impact of the Three Gorges Project on the Water Level of Poyang Lake. Journal of Natural Resouces 3, 219–224 (1997)
8. Liu, W.B.: Study on the Impacts of the Three Gorges Reservoir Running in Initial Stages on the Trend of High Water Level in Poyang Lake, Nanchang University (2007)
9. Zhang, Q., Li, L., Wang, Y.G., Werner, A.D., Xin, P., Jiang, T., Barry, D.A.: Has the Three-Gorges Dam made the Poyang Lake wetlands wetter and drier? Geophysical Research Letters 39, L20402 (2012)
10. Yu, L., He, L.H., Zhang, Q., Chen, Y.W., Wang, X.L.: Effects of the Three Gorges Project on the typical wetland vegetation of Poyang Lake. Geographical Reserch 1, 134–144 (2011)
11. Li, J., Shu, X.B., Chen, S.S.: Establishment of wetland vegetation biomass model by in-situ and remote sensing observation in Poyang Lake area. Journal of Guangzhou University (National Science Edition) 6, 494–498 (2005)
12. Wang, Q., Lian, J.J.: Estimation of Wetland Vegetation Biomass in the Poyang Lake Area Using Landsat TM and Envisat Asar Data. Journal of Geo-Imformation Science 2, 282–291 (2010)
13. Wan, H.X., Qin, Z.H., Liu, Y.B., Xu, Y.M.: Estimates of carbon fluxes from Poyang Lake wetlands vegetation in the growing season. In: Proceeding of SPIE-The International Society for Optical Engineering. Remote Sensing of the Coastal Ocean, Land, and Atmosphere Environment, vol. 7858 (2010)
14. Zhu, H.H., Zhang, B.: Poyang Lake-Hydrology Biology Deposit Wetland Development and rehabilitation. China Science and Technology University Press (1997) (in Chinese)
15. Ye, X.C., Zhang, Q., Bai, L., Hum, Q.: A modeling study of catchment discharge to Poyang Lake under future climate in China. Quaternary International, 221–229 (2011)
16. Zhou, W.B., Wan, J.B., Jiang, J.H.: The impact of water level change between Yangtze River and Lake in Poyang Lake on the ecosystem. Science Press (2011) (in Chinese)
17. Yu, X.G.: Study on ecological processes of Carex cinerascens Kukenth in the Wetland of Poyang Lake, Jiangxi Normal University (2010)
18. Poyang Lake research Editor Board.: Poyang Lake Research. Shanghai Science and Technology Press (1988) (in Chinese)
19. Hu, Z.P., Ge, G., Liu, C.L., Chen, F.S., Li, S.: Structure of Poyang Lake Wetland Plants Ecosystem and Influence of Lake Water Level for The Structure. Resources and Environment in the Yangtze Basin 6, 597–605 (2010)

Eco-environment Quality Evaluation of Rare Earth Ore Mining Area Based on Remote Sensing Techniques

Yan Peng[1,*], GuoJin He[1], and Wei Jiang[1,2]

[1] The Institute of Remote Sensing and Digital Earth, Chinese Academy of Science, Beijing 100094
[2] University of Chinese Academy of Science, Beijing 100049

Abstract. In this paper, we took LongNan County in JiangXi Province as a study area, and built up an eco-environment equality evaluation mode based on grids using remote sensing techniques to get the regional features of eco-environment and to assess the ecological and environmental equality of rare earth ore mining area. The result shows that 62.16% of the whole area in LongNan County is a better grade of the eco-environmental equality. However, 10.54% of the whole area maintained a bad or worse grade. There into, 0.59% of the total area is a worse grade. From the spatial distribution, the area which is a better grade of the eco-environmental equality mainly concentrated in forestland with high vegetation coverage and high biological abundance; on the contrary, the area which is a worst grade mainly located in the rare earth ore mining area. It was concluded that the status of eco-environment quality of LongNan County in 2010 was in a good grade, and rare earth ore mining activities destroyed the eco-environment status seriously. The study will provide a support and decision-making for the relevant department to set up plans for mineral resource exploitation, it has an important significance.

Keywords: rare earth ore mining area, remote sensing, eco-environmental quality, land use and land cover.

1 Introduction

Mineral Resource plays an important role in national economy and social development of our country. On one hand, the exploitation of mineral resource contribute to the development of national economy and society, on the other hand, it caused various ecological environment problems, such as lots of cultivated lands which were occupied, waste pollution and so on. These problems have affected people's work and life of the surrounding area, and have restricted regional sustainable development of social economy in a certain degree. Traditional means of mining area ecological environment monitoring is single, and far behind the requirements of environmental protection on the environmental information processing. The Remote Sensing techniques has characteristics of fast, macroscopic, multitemporal, comprehensive and short cycle.

* Corresponding author.

F. Bian et al. (Eds.): GRMSE 2013, Part I, CCIS 398, pp. 246–257, 2013.
© Springer-Verlag Berlin Heidelberg 2013

These characteristics make the remote sensing techniques become a powerful means for mine exploitation and environmental monitoring. Therefore, the eco-environment quality of rare earth ore mining area using remote sensing techniques was analyzed in LongNan County, Jiangxi Province.

In this paper, we assessed the eco-environment equality of the study area mainly by reference to Technical Criterion for Eco-environmental Status Evaluation (on trail) (HJ/T192-2006) [1]. The criterion provides a certain guidance and reference for monitoring ecological environment status using remote sensing and GIS. Some researchers evaluated the eco-environmental quality for a large area like a province or a city using the technical criterion [2-3], at the same time, some assessed the ecological and environmental quality for county region or below county region using the technical criterion [4-5]. Whatever the study area is large or small, the final result is a synthetic eco-environment index of the whole area. The value can only reflect the ecological and environmental status of the whole, not everywhere of the whole. In addition, we took a county as a study area, and focused on analyzing the effect of rare earth ore mining to the eco-environment quality. So, if we analyze the ecological and environmental status of the study area only with an index, the effect of rare earth ore mining to the eco-environment quality will be ignored easily. It will go against the research purpose. However, some researchers [6] proposed a new ecological environment condition evaluation model of county region based on grids using remote sensing techniques by reference to the criterion. The model can reflect the concrete eco-environment status of the study area. Thus, we applied the idea of the model to evaluate the eco-environment status in the study area, and focus on analyzing the effect of rare earth ore mining to the eco-environment quality.

2 Study Area and Data Processing

2.1 Study Area

LongNan County is located in the south of Jiangxi Province, which connects LianPing County and HePing County in GuanDong Province, extending between 24°26′8″N to 25°5′3″N latitude and 114°29′15″E to 114°57′43″E longitude. The study area is hilly area, the total area is about 1640 square kilometres. The study area is one of the maize zone of Gannan navel orange, and is rich in mineral resources especially in rare earth ore, and has became one of the first national rare earth ore planning counties.

2.2 Date Processing

The main data used in this paper, including remote sensing image and related non-remote sensing data. The remote sensing images are the multi-spectral bands and pan band of ALOS high spatial resolution remote sensing images on November in 2010 and Landsat TM low spatial resolution remote sensing images on October in 2010.

For the characteristics of ALOS, we carried out ortho-rectification, data fusion, image mosaic and image cut. The production level of selection ALOS data is 1B2 level, so the ALOS data was orthorectified by Rational Function Model with RPC. And the

error of the orthorectified images is within 10 meters. The fused images were obtained using PANSHARP transform, as show in Fig.1. PANSHARP transform is a popular fusion algorithm recently, it found the matching gray value between the fused bands mainly using the least squares method, and adjust the contribution values of individual band, to keep its color best and to make it be close to natural color [7-8]. And it estimated the gray value relationship among all bands using statistical method to remove the data gap problem [7-8].

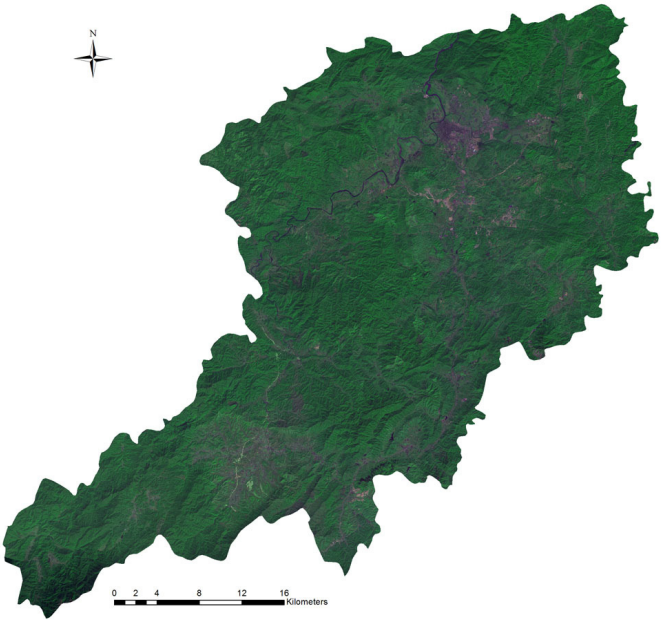

Fig. 1. ALOS fusion image of study area in 2010

3 Methodology

Aiming at the regional features of eco-environment and environmental equality of rare earth ore mining area, an co-environment equality evaluation mode based on grids using remote sensing techniques was set up. And the study area's map of land use in 2010 must be obtained for the following various abstracted eco-environment indexes.

3.1 Abstraction of EQI

Eco-environment indexes included biological abundance index (BAI), vegetation fraction (VF), water density index (WDI), human activity index (HAI) and soil erosion intensity (SEI) according to Technical Criterion for Ecol-environmental Status Evaluation (on trail) (HJ/T192-2006) and literatures at home and abroad about eco-environment quality evaluation. Fig. 2 shows the flow of calculating eco-environment indexes.

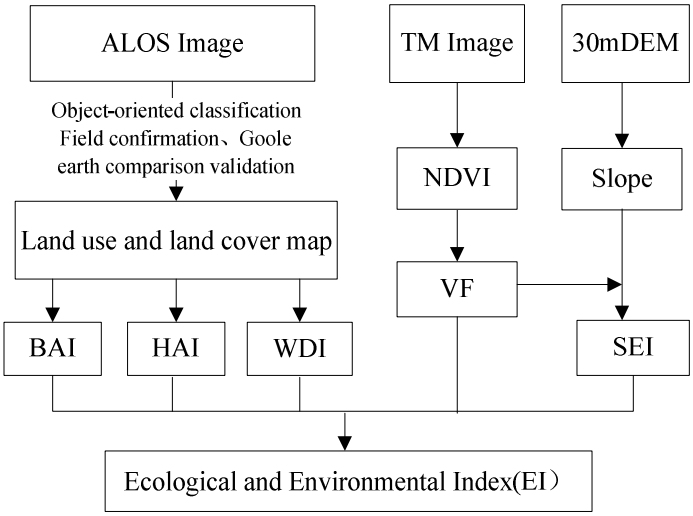

Fig. 2. The flow of calculating ecological and environmental indexes

According to Fig.3, it's obvious that biological abundance index, human activity index and water density index can be obtained on the basis of land use and land cover map. So, an objects-oriented classification approach combining with object size, context features and texture information extracted by Gray Level Co-occurrence Matrix (GLCM) was applied to classify the remote sensing imagery. Object-oriented classification method is suitable for medium or high resolution satellite imagery. It

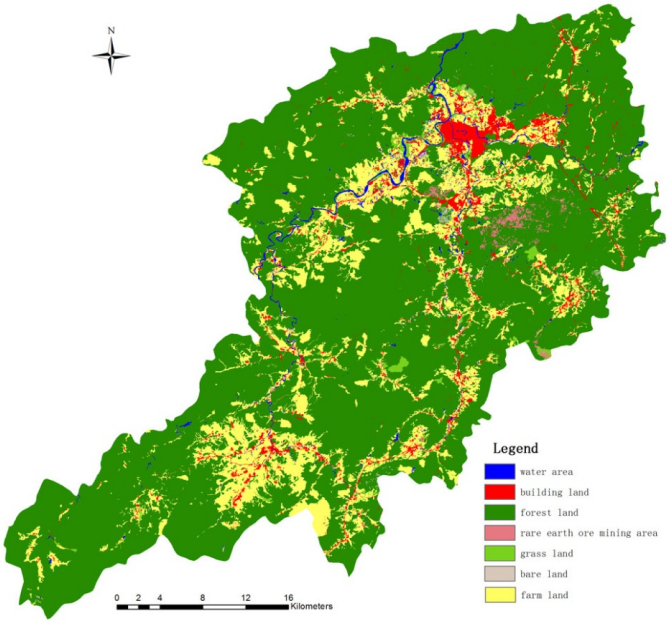

Fig. 3. The land use and land cover map of the study area

involves segmenting an image into objects (groups of pixels). These objects have geographical features such as shape and length, and topological entities such as adjacency and found within [6] . These attributes make a knowledge base for example objects, which can be called on in the classification process. And the fused ALOS imagery was classified as building land, forest land, grassland, farmland, water area, bare land and rare earth ore mining area based on the requirement. Fig.3 is the final classification result. Then the accuracy of the classification result was verified using confusion matrix with field survey and Gooleearth image. As a result, it showed the overall classification accuracy is as high as 90% and the Kappa value is 0.9033. The accuracy can meet the research's need.

Biological Abundance Index. Biological Abundance Index reflects the abundance poverty degree of the evaluated area indirectly through the difference in number of species with different ecological system types on unit [1]. According to the different ecological system types which pixels are belonged to, the weights of the different biological abundance indexes are given. Weights were determined according to the criterion. At the same time, some weights were adjusted with the classification result of the study area. The value of the weight is as show in Table 1. And the biological abundance index distribution map (As Fig.4 show) could be obtained according to the biological abundance index weight table (As Table.1show).

Table 1. The biological abundance index weight table of the ecological system types

types	forestland	grassland	water area	farmland	building land	bare land	REO mining area
weights	0.35	0.21	0.28	0.11	0.035	0.01	0.005

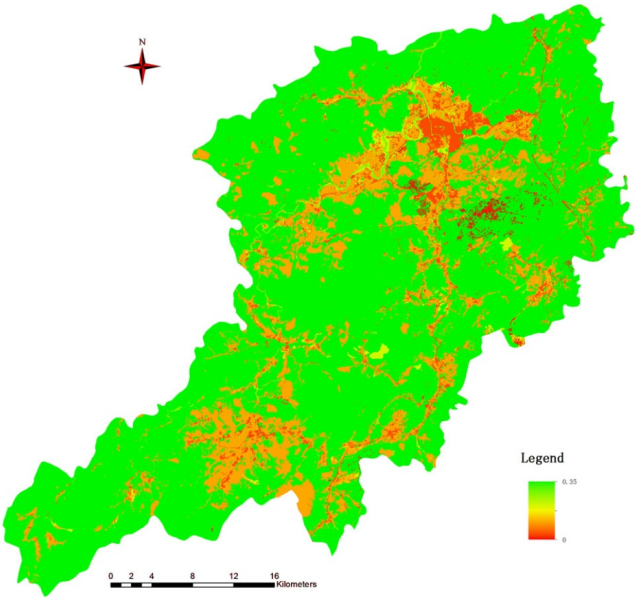

Fig. 4. The biological abundance index of distribution map of the study area

Water Density. Water Density Index is a proportion of the water area accounting for the total area. And the water area includes area of rivers, reservoirs, lakes and ponds. The study area was divided into 0.3*0.3km grid, and all pixels' value of a grid was assigned by the ratio of the water area of a grid accounting for the grid [9]. So, the water density index distribution map was obtained (As Fig.5 show).

Human Activity Exponents. The interference of human activity has a direct impact on the eco-environmental structure and function. The land use type reflects the process of nature ecological system being disturbed by human activities. The disturbing of human activities to eco-environment is more intense, the eco-environment status is worse. By taking it as a principle, different land use types are given the corresponding score [6] [10], as Table 2 shows. The Human Activity Index distribution map can be got by combining the land use and land cover map and the weights of human activity index, as Fig.6 show.

Table 2. Human activity index weights of the study area

type	Forest land	Grass land	Water area	Farm land	bare land	REO mining area	Building land
weights	90	80	68	48	42	20	30

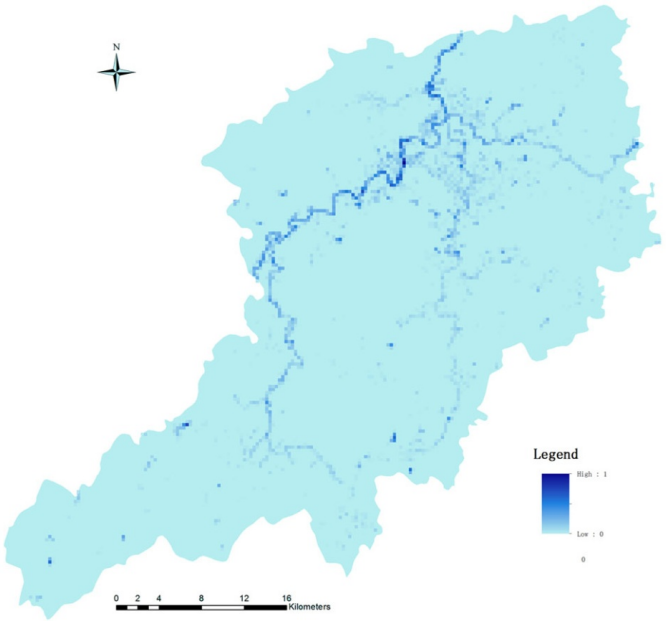

Fig. 5. The water density index distribution map of the study area

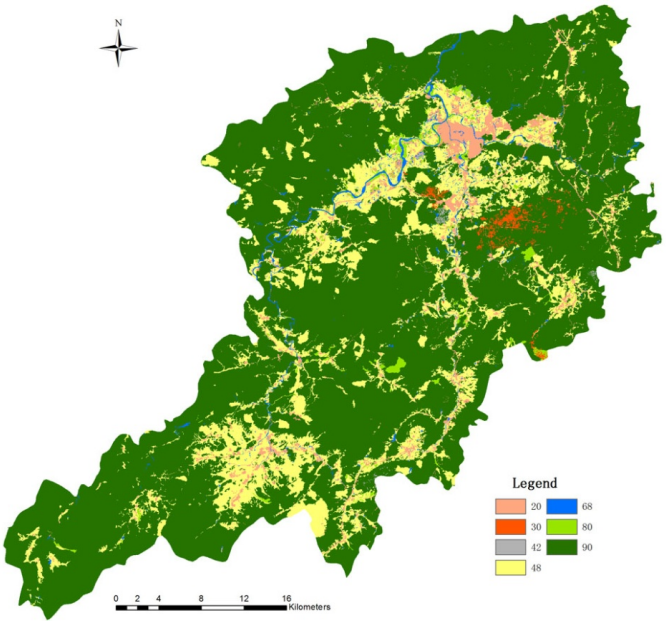

Fig. 6. The human activity index distribution map of the study area

Vegetation Fraction. Vegetation Fraction is one of the indicators which can reflect the vegetation cover degree of a study area, and it is also the required parameters for calculating soil erosion intensity. The model using normalized differential vegetation index (NDVI) to estimate vegetation fraction was adopted on the basis of derivation the two important parameters of dimidiate pixel model [11], according to the principle for vegetation index estimating vegetation fraction. The expression is as below.

$$FC = \frac{NDVI - NDVI_{veg}}{NDVI_{veg} - NDVI_{soil}} \tag{1}$$

Among them, FC means vegetation fraction; NDVI is pixel normalized differential vegetation index; $NDVI_{soil}$ is the NDVI value of bare land; $NDVI_{veg}$ is the NDVI value of areas which is completely covered with vegetation. $NDVI_{soil}$ is got by calculating the average of NDVI of these typical bare land area selected from image; $NDVI_{veg}$ is got by calculating the average of NDVI of these selected typical area which is completely covered with vegetation. So, $NDVI_{soil}$ is 0.032865 and $NDVI_{veg}$ is 0.559667 through calculating. Finally, the vegetation fraction distribution map is as Fig.7 show.

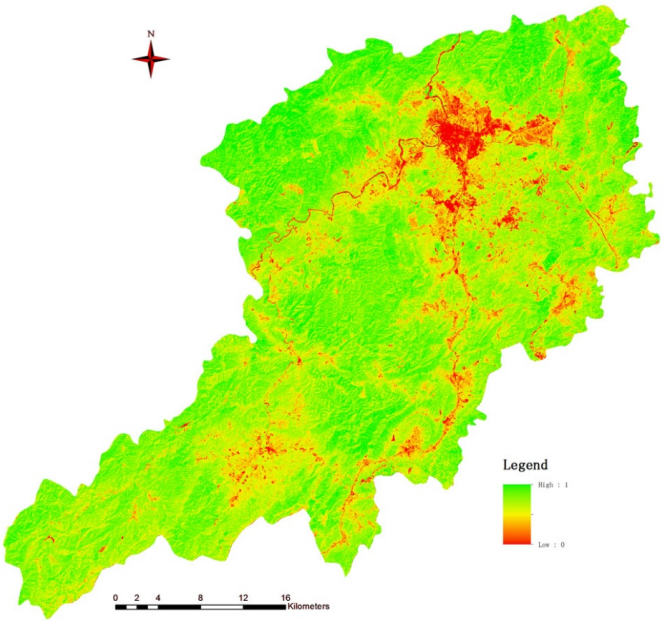

Fig. 7. The vegetation fraction distribution map of the study area

Soil Erosion Intensity. Soil erosion intensity and vegetation fraction are inversely proportional relationship under other constant conditions. Soil erosion intensity is calculated using vegetation fraction and slope factors in Standards for Classification and Gradation of Soil erosion [12]. In this paper, the soil erosion intensity is classified as slight erosion, moderate erosion and severe erosion according to the standards and considering the actual situation of the study area. Considering the ecological system types, the soil erosion intensity was calculated using fraction and slope factors for forest land, grass land, farm land, bare land and rare earth ore mining area, as Table 3 show; the soil erosion of other types including water area and building land are determined to be inapparent soil erosion area. To quantitatively evaluate the soil erosion intensity, these three soil erosion intensity degrees weights are assigned different values according to the criterion [1], as Table 4 show. Finally, the soil erosion distribution map of study area is got, as Fig.8 show.

Table 3. The gradation table of soil erosion intensity in LongNan County

VF (%)	Slope (°)					
	<5	5~8	8~15	15~25	25~35	>35
>75	slight	slight	slight	slight	slight	slight
60~75	slight	slight	slight	slight	moderate	moderate
40~60	slight	slight	slight	moderate	moderate	severe
30~45	slight	slight	moderate	moderate	severe	severe
<30	slight	moderate	moderate	severe	severe	severe

Table 4. The weights of soil erosion intensity

type	Slight	moderate	severe
weight	0.05	0.25	0.7

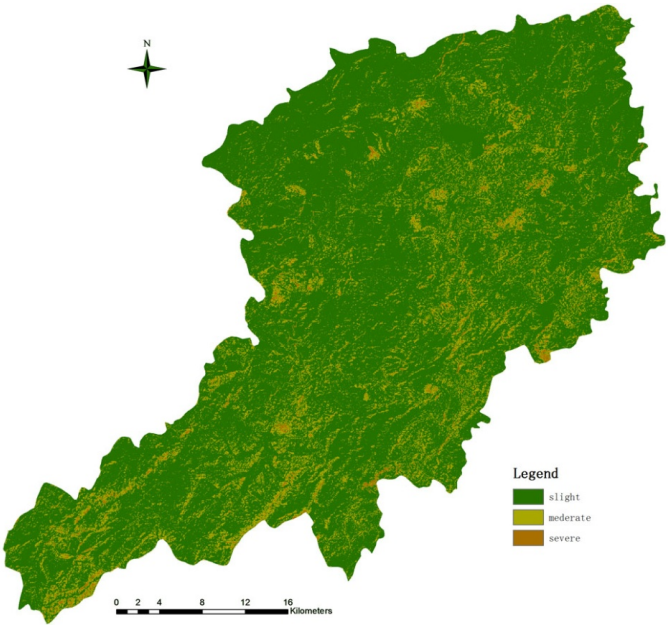

Fig. 8. The soil erosion intensity distribution of the study area

3.2 Eco-environment Quality Evaluation

The expression of ecological environment quality is as following according to the criterion.

$$EI = \sum_i u_i \left(\frac{100}{(A_i)_{\max}} A_i \right) \tag{2}$$

In above equation, u_i is a weight of a evaluation factor, the detail is as table 5 show; A_i is one factor of all, $(A_i)_{\max}$ is the max value of these factors, $\frac{100}{(A_i)_{\max}}$ is the normalization of these factors, its range is from 0 to 100.

So, the eco-environment quality index can be calculated through these five ecological environment index distribution maps according to above mentioned expression. And the eco-environment status of the study area is classified as five degrees by reference to Table 6 [1]. Finally, the eco-environment status distribution map can be obtained as Fig.9 shows.

Table 5. The weight table of eco-environment index in LongNan County

EI	BAI	VF	WDI	HAI	SEI
weight	0.25	0.2	0.2	0.15	0.2

Table 6. The gradation table of eco-environment status in LongNan County

gradation	Best	better	general	worse	worst
	>=75	55~75	35~55	20~35	<20
status	the most suitable for human survival	more suitable for human survival	suitable for human survival	there are significant restriction factors for human survival	bad human survival environment

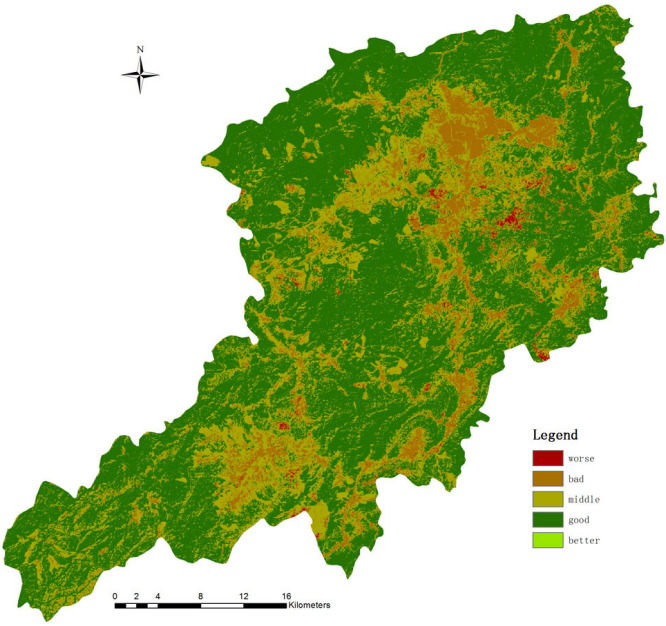

Fig. 9. The eco-environment status distribution map of the Study Area

4 Results and Discussion

The percent of each ecological environment status area accounting for the total area can be calculated through statistics, as Table 7 shows.

Table 7. The percent of each eco-environment status area accounting for the whole

gradation	better	good	middle	bad	worse
percent	0	62.16%	27.3%	9.95%	0.59%

The results of eco-environment quality evaluation showed that the regions at good were 62.16% of the total area of LongNan county, which indicated a better level of integral eco-environment quality. The good quality of eco-environment in LongNan county mainly concentrated in the forest land with high vegetation coverage and high biological abundance. However, it hardly exist regions at better grade of eco-environment quality, which showed that the study area still has room for improvement in eco-environment status. The regions at middle maintained 27.3%, and they mainly located in these areas which are rich in water resources, such as water areas and paddy fields of lower slope. These areas are rich in biology and less affected by human activities. However, the regions at bad were 9.95%, and they mainly concentrated in building land, high slope farmland and so on. These areas are largely affected by human activities and have low biology abundance, low vegetation fraction and high slope which can cause water and soil less easily. And the regions at worse maintained 0.59% , they mainly located in the rare earth ore mining area which are lower vegetation fraction, lower biology abundance and higher slope, and more seriously affected by human activities, which suggested that rare earth ore mining activity destroyed the eco-environment quality seriously in the study area.

In conclusion, rare earth ore mining activity has negative impact on ecological environment status in LongNan County. It made the vegetation be destroyed, caused water and soil loss easily and made the ecological environment status become worse. Even so, the status of eco-environment quality of LongNan County in 2010 was main in a good grade, and the study area was suitable for human survival.

5 Conclusion

The eco-environmental quality evaluation model based on grids can reflect the concrete eco-environment status in the study area, so it is more suitable for evaluating the ecological environment status in mining area. At the same time, all of these evaluated factors can be obtained through remote sensing data, which solved the problem that the eco-environmental data of a county region or below county region is difficult to obtain.

The results of eco-environment quality evaluation showed that: ①the status of eco-environment quality of LongNan County in 2010 was main in a good grade. The regions at good quality mainly concentrated in forestland with high vegetation coverage and high biological abundance. ②0.59% of the total area is a worse grade of eco-environmental quality. And the area at a worse quality mainly located in the rare earth ore mining area, which shows that the rare earth ore mining activity has negative impact on ecological environment status in study area.

Acknowledgements. The work was supported by the Ecological Status and Ten Years Change of the Typical Area of Mineral Resources Exploitation Project under grant number STSN-10-03.

References

1. Environmental protection industry of the People's Republic of China (HJ/T 192-2006), Technical Criterion for Eco-environmental Status Evaluation (on trail) (2006)
2. Wang, Y., Gong, H.-L., Li, X.-J.: The Monitoring and Analysis of Ecological Environment Quality of Beijing Based on GIS. Remote Sensing for Land & Resources (1), 91–97 (2008)
3. Jiang, Z.-L., Sha, J.-M., Yang, W.-N.: Multiple Factors-Based on Remote Sensing Evaluation of Ecological Environment in Fuzhou. Remote Sensing for Land & Resources 61(3), 46–48 (2004)
4. Tao, X.: Eco-environment evaluation based on 3S technology in Linfen city. In: ShanXi Normal University, Master Dissertation (2012)
5. Hu, Y.-L., Wang, P., Zhang, L.-P., et al.: Application of Remote Sensing in Mining Area Ecology Environment Evaluation. Resource Development & Market 27(7), 584–586 (2011)
6. Wang, S.-X., Zhou, Y., Yao, Y., et al.: Ecological environment condition evaluation mode of county region based on remote sensing techniques. China Environmental Science 32(1), 181–186 (2012)
7. Li, H., Manjunath, B.S., Mitra, S.K.: Multesensor Image Fusion Using the Wavelet Transform. Graphical Models and Image Processing 57(3), 235–245 (1995)
8. Zhang, Z., Blum, R.S.A.: Categorization of multiscale-decomposition-based image fusion schemes with a performance study for a digital camera application. Proceeding of IEEE 87(8), 1305–1326 (1999)
9. Baatz, M., Benz, U., Dehghani, S., Heynen, M., et al.: eCognition Professional: User Guide4. Defiiens-Imaging, Munich (2004)
10. Meng, Y., Zhao, G.-X.: Ecological environment condition evaluation of estuarine area based on quantitative remote sensing. China Environmental Science 29(2), 163–167 (2009)
11. Miao-miao, L.I., Bing-fang, W.U., Chang-zhen, Y.A.N., et al.: Estimation of Vegetation Fraction in the Upper Basin of Miyun Reservior by Remote Sensing. Resources Science 26(4), 153–159 (2004)
12. Water Conservancy industry Standard of the People's Republic of China, Standards for Classification and gradation of Soil erosion (SL 190-2007). In: Water Resources Ministry of the People's Republic of China Publication (2007)

Comparison of Four Models on Forest above Ground Biomass Estimation Based on Remote Sensing

Jinjin Dong*, Liang Wang, Shenghua Xu, and Rong Zhao

Research Center of Government GIS, Chinese Academy of Surveying and Mapping,
No. 28 Lianhuachi West Road, Haidian District, Beijing, China
{Jinjin Dong,jinjind1118}@163.com

Abstract. The estimating of forest biomass can help us to find out the carbon storage of our country, gradually raise the level of carbon emissions constraints, reduce the concentration of the greenhouse gases in the atmosphere, slow down the global warming process and will be conducive to the formation of resource saving, environment friendly modes of production, lifestyles and consumption patterns, and realize sustainable development. Here, several common estimation methods of forest above ground biomass with remote sensing were used respectively, and were compared. 150 sample data which received by CASA model and 45 variables achieved by remote sensing and meteorological data in Mount Tai scenic area are applied in these models. The results showed that the fittings, estimating precisions and root mean square errors of multi-stepwise regression model, traditional BP neutral network model, RBF neutral network model and K-NN method were 72.1%, 79.2%, 22.805 $t \cdot m^{-2}$; 79.3%, 84.7%, 20.854 $t \cdot m^{-2}$; 81.6%, 87.1%, 19.195 $t \cdot m^{-2}$ and73.2%, 79.6%, 24.092 $t \cdot m^{-2}$ respectively. Above all, this paper provides the reference for forest above ground biomass estimation with high precision of the further research.

Keywords: BP neural network, RBF neural network, K-NN, estimating precision.

1 Introduction

The global carbon cycle is one of the core issues of global climate change research. As the largest terrestrial ecosystem, the forest ecosystem carbon exchange has an important influence on the global carbon balance. Therefore, the quantitative estimating of forest biomass also provides important reference for global carbon and carbon cycle research.

Traditional forest biomass statistics based on the measured data need a lot of field investigation. With the character of big-workload, long-cycle and certain damage of physicals, the traditional methods are not conducive to study the spatial distribution and change of biomass. Furthermore, the problems such as forestry measuring instrument error in practice increase the difficulties of forest above ground biomass (AGB)

* Corresponding author.

F. Bian et al. (Eds.): GRMSE 2013, Part I, CCIS 398, pp. 258–263, 2013.
© Springer-Verlag Berlin Heidelberg 2013

estimation in study area scale. But with the rapid development of remote sensing technology, it provides a fast, economic and convenient way for large-scale forest biomass estimation and dynamic change for a long time study.

Currently, forest AGB estimation based on remote sensing mainly has four kinds of methods: multi-stepwise regression model, the process model fitting method, the artificial neural network model and K nearest neighbors (K-NN method) [3]. This paper will use the Landsat TM data and meteorological data to estimate the forest AGB respectively by the above methods, and then compare their estimated results.

2 Study Area and Data

The study area was located in Mount Tai scenic area (36.25°N, 117.09°E), which is in Shandong province with the data of Landsat TM on September 23, 2009. The plantation in Mount Tai is mostly built in the 1950s in addition to a small amount of ancient trees. It is the typical representative of artificial ecological public welfare forest in northern mountain, and also is the powerhouse of ecological balance maintaining in the northern province which has little plantation. As one of the five big seed plants area, Mount Tai area contains various common ecosystem types in the northern. As a result, there are both regional representative and the importance of study in estimating the forest biomass in Mount Tai scenic area.

3 Methods and Results

3.1 Data Processing and Variables Selection

To get the needed data of Mount Tai scenic area, the TM data and meteorological data should be processed by radiation correction, atmospheric correction, geometric correction, topographic correction and interpolation, etc. The sample data of forest AGB are obtained from the CASA model for the reason that there are little sample data on hand temporarily.

This paper selected 150 samples in Mount Tai scenic, 144 samples were reserved after the outlier removal that 115 as the train samples, 29 as test samples.

The variables in the model mainly include two parts: remote sensing variables and geological variables. Remote sensing variables include the original bands information, bands transformation, vegetation index and texture. Geological variables include the elevation, slope and slope direction, etc which are highly correlated with spatial distribution. In this paper, 45 variables were extracted from remote sensing and geological data. At last, 22 variables are selected.

3.2 Multi-stepwise Regression Model

Multi-stepwise regression model obtain linear equation by correlation analysis and regression. Different variables combine different models. After achieving the models, we should calculate the test samples' prediction accuracy and the root mean square

error for further analysis [4]. Prediction accuracy and root mean square error (RMSE) are given by eqn (1) and (2):

$$precision = \frac{1}{n}\sum_{i=1}^{n}(1 - abs(\frac{x_i - y_i}{x_i}) \times 100\%) \tag{1}$$

$$RMSE = \sqrt{\frac{1}{n} \times \sum_{i=1}^{n}(x_i - y_i)^2} \tag{2}$$

where Xi is the real biomass of test sample i, YI is the predicted biomass of test sample i.

Finally, the variables combination of NDVI, PCA2, band1mean and band7mean which are significant in associating with biomass but weak correlation between each other were chosen as variables of this model through analysis on the precision. The model is given by eqn (3):

$$\begin{aligned} Biomass &= 287.172 * NDVI + 0.0022 * PCA2 - 2.944 * band1mean \\ &+ 1.953 * band7mean + 33.658 \end{aligned} \tag{3}$$

3.3 The Traditional BP Neural Network Model Multi-stepwise Regression Model

Back propagation (BP) was created by generalizing the Winrow-Hoff learning rule to multiple-layer networks and nonlinear differentiable transfer functions. The difference between BP neural network and other neural network is mainly its self learning rules, namely using the error back propagation algorithm to adjust the weights and thresholds. BP network can realize any nonlinear mapping of the input and output because its neurons use the transfer function of Sigmoid differentiable function.

The BP neural network model chosen in this paper is set up by 3 layers, including input layer, hidden layer and output layer. The input layer of this network is 22 kinds of variables which have been normalized from 0 to 1. The number of neurons in hidden layer was obtained by the test.

3.4 RBF Neural Network Model

The hidden layer of RBF network transfer function is radial basis function which can make the nodes in the hidden layer response to the input [1]. RBF network is a kind of approximation theory of three layers structure, with a single hidden layer feed-forward neural network. The training time of RBF is much less than the BP neural network while it may need more number of neurons.

There are two kinds of RBF neural network including exact network which has the number of functions as the same as the inputs and approximate network which has

the number of functions increased generally. The input and the output are also normalized while it covers the scope. This paper chose the exact network to create and train the network. And the distribution density of radial basis function which called spread was obtained by the test.

3.5 K Nearest Neighbors Method

K-NN method used in estimating forest AGB is to calculate the Euclidean distance or Markov distance between each pixel and sample area (the value of single pixel is Zp = [z1, z2,…, zn] and sample value is Xi). The equation of Euclidean distance is |Zp-Zpi|t, where t is the specified constant, in this work, t = 2. Find the K minimum distances of samples, and then calculate their weights by the equation given by equn (4):

$$w_{i,p} = \begin{cases} \dfrac{1/d^{t}_{p_i,p}}{\sum_{j\in\{i_1(p),i_2(p),\ldots i_k(p)\}} 1/d^{t}_{p_i,p}}, & if \quad i \in \{i_1(p), i_2(p), \ldots i_k(p)\} \\ 0, & else \end{cases} \tag{4}$$

then the AGB estimation of this pixel is $m_p = \sum_{j\in\{i_1(p),i_2(p),\ldots i_k(p)\}} w_{j,p} \times m_j$, where mj is the AGB of sample, mp is the estimate of pixel p [6].

In this paper, samples have 22 parameters of feature space. The Euclidean distance between 29 test samples and 115 train samples are calculated respectively to choose the k train samples and calculate their weights. Then the test samples' biomass is $bio^{'} = \sum_{i=1\ldots k} w_i \times bio_{yd}$, where bio_{yd} is the train samples' biomass. Different k values obtained different prediction of biomass and have different fitting precision. In this paper, when the k is 10, the estimated accuracy is highest.

3.6 Comparing

The AGB in Mount Tai was estimated by above four models. The results of test samples are shown in Figure 1. As is shown in Table 1, Multi-stepwise regression model is lowest in the simulation accuracy. Owing to the choice of test samples, while the test sample fitting accuracy reached 79.2%, its fitting precision is 72.1%, but this model can intuitively show the relationship between forest AGB and variables. Compared with the multi-stepwise regression model, BP neural network model has been greatly improved, but it can be better on the estimated accuracy and the training speed. RBF neural network is the best in this paper for its improved estimated accuracy and fast estimated speed. The estimated precision of K-NN method can be much higher, but the KNN method is totally dependent on the choice and precision of sample data.

Table 1. The comparing of four models

model	Fitting R2	Prediction R2	RMSE
Multi-Stepwise Regression Model	0.721	0.792	22.805
BP neural network model	0.793	0.847	20.854
RBF neural network model	0.816	0.871	19.195
K nearest neighbors method	0.732	0.796	24.092

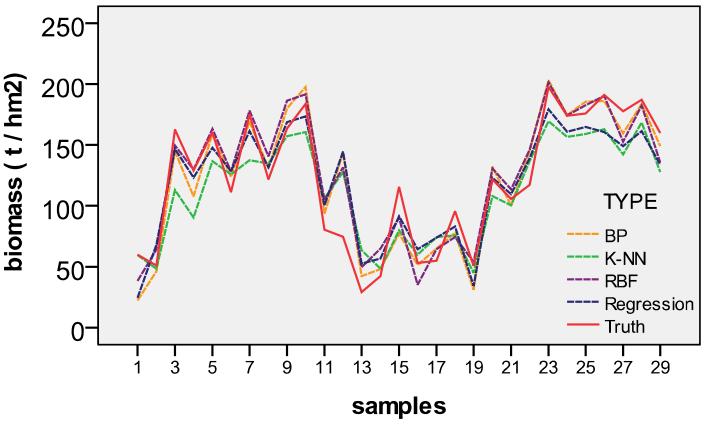

Fig. 1. The test samples' line graphic of four models

4 Conclusions

This paper estimate the AGB based on remote sensing in Mount Tai scenic area by four kinds of common models. Multi-stepwise regression model in forest AGB estimation has a lot of research both at home and abroad. Even through its estimation accuracy is low, its intuitive is strong which can reflect the relationship between the parameters and biomass. K-NN method has attracted much attention abroad, but domestic research on this method is not so much. The estimated accuracy of K-NN method can be higher, but its calculation is very big for computing the distance between each pixel and train samples. According to a variety of processing methods and algorithm, neural network model can be improved in the network convergence speed, stability, estimated accuracy and generalization, etc. In addition, how to use neural network with physiology, ecology significance that can reflect the relationship between biomass and remote sensing parameters is one of the development direction in future. Moreover, removing the abnormal sample points is necessary because the estimated precision of several kinds of model has obvious increased after the outlier remove. In conclusion, this paper provides the reference for the further research on high precision in the forest AGB estimation based on remote sensing.

Acknowledgement. This research was funded by National High-tech R&D Program of China (863 Program) under grant No. 2012AA12A309 and No. 2013AA122003, the National Science & Technology Pillar Program under grant No. 2012BAB16B01, Basic Research Fund of CASM.

References

1. Liu, Y., Zhang, L.: Implementation of BP and RBF neural network and their performance comparison. Electronic Measurement Technology 30(4), 77–80 (2007)
2. Fan, W., Zhang, H., Yu, Y.: Comparison of three models of forest biomass estimation. Chinese Journal of Plant Ecology 35(4), 402–410 (2011)
3. Xu, X., Cao, M.: An Analysis of the Applications of Remote Sensing Method to the Forest Biomass Estimation. Geo-Information Science 8(4), 122–128 (2006)
4. Li, M.: Estimation and analysis of forest biomass in northest forest region using remote sensing technology, Northeast Forestry University (2010)
5. Shen, A.: Prediction method of BP and RBF neural network based data, Central South University (2007)
6. Chen, E., Li, Z., Wu, H., Han, A.: Forest volume estimation method for small areas based on K-NN and Landsat Data. Forest Research 21(6), 745–750 (2008)
7. Cutler, M.E.J., Boyd, D.S., Foody, G.M., Vetrivel, A.: Estimating tropical forest biomass with a combination of SAR image texture and Landsat TM data: An assessment of predictions between regions. ISPRS Journal of Photogrammetry and Remote Sensing 70, 66–77 (2012)
8. Zhao, F., Guo, Q., Kelly, M.: Allometric equation choice impacts lidar-based forest biomass estimates: a case study from the Sierra National Forest, CA. Agricultural and Forest Meteorology 165, 64–72 (2012)
9. Rheinhardt, R., Brinson, M., Meyer, G., Miller, K.: Integrating forest biomass and distance from channel to develop an indicator of riparian condition. Ecological Indicators 23, 46–55 (2012)
10. Paladinic, E., Vuletic, D., Martinic, I.: Forest biomass and sequestered carbon estimation according to main tree components on the forest stand scale. Preiodicum Biologorum 111(4), 459–466 (2009)

Assessing the Surface Urban Heat Island Effect in Xining, China

Yinling Zhang[1,2,*], Zhongke Bai[1], and Weibo Liu[2]

[1] School of Land Science and Technology, China University of Geosciences (Beijing), Beijing, 100083, China
[2] Department of Geography, University of Kansas, Lawrence, KS, 66045, USA
zylcugb@gmail.com

Abstract. This study focuses on using remotely sensed land surface temperature (LST) to assess the surface urban heat island effect (SUHI) in Xining, Qinghai. Cloud-freeLandsat TM data acquired on 30 June 2002 and 17 July 2009 were selected to generate LSTmaps. Analysis of the SUHI characteristics from these two images reveals that1) there was a mean LST growth in magnitude of 0.63 ℃, or 2.09%. 2) The center of Xining did not exhibit the highest LST. But apart from the arid and semi-arid areas, the spatial pattern of the SUHI shows that higher temperatures in urban than in rural areas.3) The strong negative correlations were found between LST and NDVI. Based on the findings, potential design strategies are proposed in an effort to mitigate SUHI effect.

Keywords: Surface urban heat island, Land surface temperature, Normalized difference vegetation index.

1 Introduction

Xining, as the Summer Resort Capital of China, is experiencing a rapid urban transition. As a tourism city, it attracts more and more people going there for sightseeing, investment and retirement, which are important factors to enhance its urban development and also significantly affect the quality of life of urban inhabitants. However, as city continues to grow in population and physical size, these urban-rural differences in temperature also increase[1]. And the influence of urban surfaces on temperature patterns in urban areas as opposed to surrounding areas is the urban heat island (UHI) effect[2].

The UHI is generally evaluated in two ways: (1) measuring the UHI in air temperature through the use of automobile transects and weather station networks and (2) measuring the UHI in surface temperature through the use of airborne or satellite remote sensing[3]. Rao (1972) was the first to demonstrate that urban thermal feature could be identified from remote sensing data [4]. Satellite remote sensing overcomes

* Corresponding author.

F. Bian et al. (Eds.): GRMSE 2013, Part I, CCIS 398, pp. 264–273, 2013.
© Springer-Verlag Berlin Heidelberg 2013

some problems of in-situ measurements generally with wider sources, broader coverage, and steadier periodicity [5]. And when UHI is monitored with remote sensing data, we should focus on surface urban heat island (SUHI) because the parameter studied is no longer the air temperature but the land surface temperature (LST)[6]. A variety of LST related to SUHI studies were carried out [7-10]. Moderate and high spatial resolution thermal infrared imagery, such as Landsat TM/ETM+, MODIS and so forth, has been extensively employed to study SUHI and LST distribution [11, 12].

However, in Xining, only a few studies have been conducted to investigate the UHI. Guo (1994), studied the mechanism of action among landforms, climate, hydrology, human activities and environmental ecological system in Xining, and mentioned UHI in his research[13]. Even though without many details about UHI effect, it mentioned that the layout and density of build-up have a great impact on UHI. Then the first study specifically on UHI in Xining was conducted by Zhang (1997), which explored the relationship between urbanization and temperature change[14]. It mainly discussed four factors:city population, build-up area, roads, and public transportations vehicles, which have impacts on the urban temperature change. The most recent one done in Xining was conducted by Yu (2008), which studied on UHI dynamics from 1961 to 2004[15]. It found that the average temperature showed the rising tendency. Furthermore, from 1961 to 2004, the average temperature had risen by 0.40°C. All the above researches were carried out by air temperature measurements and without any consideration on remote sensing images. That's the reason why there is not any research about the spatial pattern of UHI in Xining.

As the biggest city in Qinghai province, Xining is selected for this study. In order to avoid the impact of clouds, we focused on case studies in a short time period by selecting representative cloud-free LST images, which were utilized to study spatial patterns of LST and the relationship between LST and NDVI, measure the change of LST and examine the SUHI effect. This study carried out in Xining also could be expanded the scope of the SUHI study to other tourism cities and help to integrate the knowledge in decision-making process for future development of the city.

2 Data and Methods

2.1 Study Area

The city of Xining (36°34′N, 101°49′E), the capital of Qinghai province is in west China (Fig.1). The city is located on the eastern edge of Qinghai-Tibet Plateau, with an average altitude of about 2,000 m in a valley, which is bounded on the north and south by mountains. Conditions are influenced by the aridity and high elevation. Due to the semiarid climate, bare soil is exposed between sparse vegetation cover.

Today, with a population of about 2.2 million, the city is a major center of tourism, culture, industry, commerce and transportation. Xining, exhibiting rapid population growth and urban expansion in the form of encroachment to the limited agricultural areas in limited directions, is selected for this study.

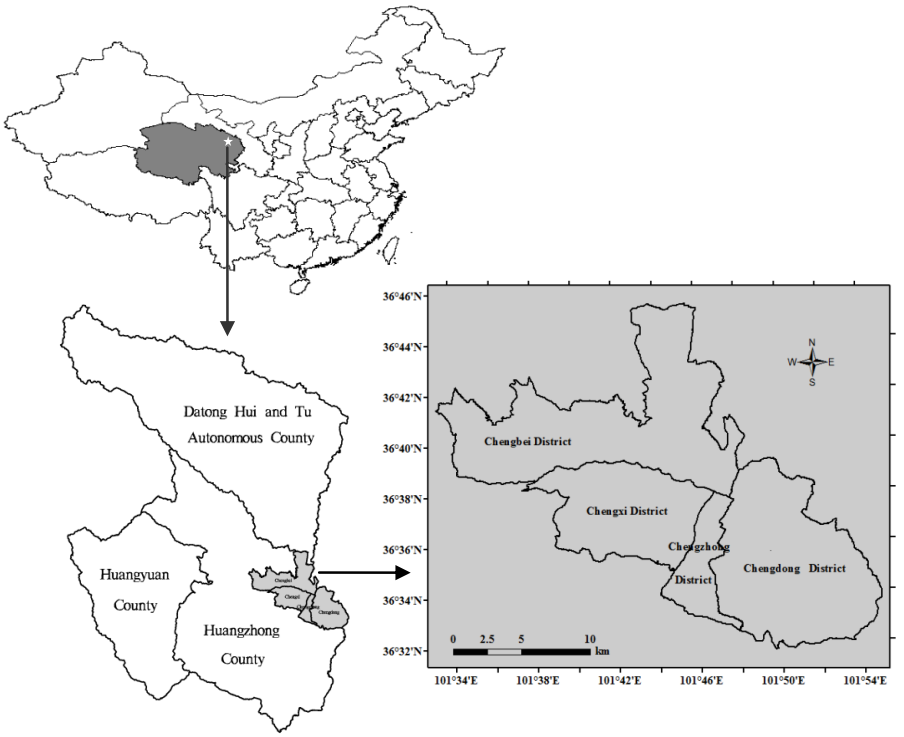

Fig. 1. Location of the study area

2.2 Data Used and Image Pre-processing

Landsat TM images (Row/Path:132/35) dated on 30 June 2002 and 17 July 2009 were chosen in this study, because June and July are typical months for UHI study. The images were rectified to a common UTM coordinate system and were resampled to 30 m resolution for all bands. The resultant root mean square error (RMSE) of 2002 and 2009 images was estimated to be 0.34 and 0.29 respectively.

NDVI was used to express the density of vegetation. It was calculated by using:

$$NDVI = \big(\rho(band4) - \rho(band3)\big)/\big(\rho(band4) + \rho(band3)\big) \quad (1)$$

Where, ρ represents the radiance in reflectance units, band 3 and band 4 represent the spectral bands of the Landsat images.

2.3 LST Computation

For Landsat 5, the high gain thermal infrared image was transformed to surface temperature in a pixel-based manner in two steps:

First, at-sensor radiant temperatures for TM thermal band were calculated from emitted spectral radiance (R_{TM6}) using Planck's equation:

$$\mathrm{R_{TM6}} = \mathrm{R_{min}} + (\mathrm{R_{max}} - \mathrm{R_{min}}) \times \mathrm{DN_6}/255 \tag{2}$$

$$\mathrm{T} = \mathrm{K_2}/\ln(1 + \mathrm{K_1}/\mathrm{R_{TM6}}) \tag{3}$$

Where, T is the radiant temperature in Kelvin for the pixel in band 6. For Landsat 5, $\mathrm{K_1}$ is 607.76 $\mathrm{mW \cdot cm^{-2} \cdot Sr^{-1} \cdot \mu m^{-1}}$,$\mathrm{K_2}$ is 1260.56 K, $\mathrm{R_{max}}$ is 15.303 μm, $\mathrm{R_{min}}$ is 1.238 μm.

The radiant temperature value computed using Eq. (3) is referenced to an internal black body. The LST was derived after correcting for spectral emissivity of different land covers. Landsat 5 LST was derived from the corrected [16]

$$\mathrm{T_s} = \frac{\mathrm{T}}{\left(1 + \left(\lambda * \frac{\mathrm{T}}{\rho}\right) \ln\varepsilon\right)} - 273.15 \tag{4}$$

Where $\mathrm{T_s}$ is the LST in Celsius, ε is the surface emissivity, λ is the wavelength of emitted radiance and value of 11.5 was used. $\rho = \mathrm{hc}/\sigma\mathrm{mk}$, σ is the Boltzmann constant (1.3806×10-23$\mathrm{J \cdot K^{-1}}$), h is the Planck's constants (6.626×10-34 $\mathrm{J \cdot S}$) and c is the velocity of light (2.2998×108 $\mathrm{m \cdot s^{-1}}$).

The emissivity was calculated with a simplification of NDVI Thresholds Method introduced by Qin et al. (2004)[17]. The NDVI Thresholds Method uses certain NDVI values (thresholds) to distinguish between soil pixels (NDVI < $NDVI_S$), pixels of full vegetation (NDVI > $NDVI_V$), and mixed pixels ($\mathrm{NDVI_S} \leq \mathrm{NDVI} \leq \mathrm{NDVI_V}$), assuming the typical threshold values of $\mathrm{NDVI_V} = 0.7$ and $\mathrm{NDVI_S} = 0.05$.

For Landsat TM

- If NDVI <0.05 then ε=0.995
- If 0.05< $NDVI$ <0.7 then $\varepsilon = 0.9589 + 0.086 * \mathrm{P_v} - 0.0671 * \mathrm{P_v^2}$
- If NDVI >0.7 then $\varepsilon = 0.9625 + 0.0614 * \mathrm{P_v} - 0.0461 * \mathrm{P_v^2}$

where $\mathrm{P_v}$ is referred to as fractional vegetation cover, and is given by[18]

$$\mathrm{P_v} = \frac{\mathrm{NDVI} - \mathrm{NDVI_S}}{\mathrm{NDVI_V} - \mathrm{NDVI_S}} \tag{5}$$

2.4 Transect Analysis

The transect analysis was carried out to identify the spatial distribution of urban LST and demonstrate the existence of the SUHI effect. For this purpose, two transects were drawn (Fig. 2), which avoid arid and semi-arid land areas. Transect 1 was from north to south and crossed Chengbei district and Chengdong district. Transect 2 was from northwest to southeast and crossed all of the four districts. And the LST distributions and SUHI effect were showed in Fig. 2a, b.

3 Results and Discussion

3.1 Analysis of the SUHI Spatial Distribution

Satellite-based method provides not only a measure of the magnitude of LST in the entire area, but also the spatial distribution of LST (Fig.2a, b). The LST map ranges from 18.95 to 43.99 °C on 30 June 2002, from 16.68 to 42.88 °C on 17 July 2009, respectively. The extreme LST decreased, which includes both the hottest and the coldest, but the average LST increased from 30.14 to 30.77 °C, with a 2.09% increase. Inspect the distribution of LST, some characters can be found as follows: (1) the center of Xining did not exhibit the highest LST. From the center of the urban city to both west and east, the LST decreased gradually, which showed striking SUHI effects by the contrasts between urban and rural surface temperature. From the center to the north and south, however, the change of LST presented irregularly. The LST in mountain area was significantly higher than the central area, which implied that the majority of pixels belonged to a bare or semi-bare natural background in mountain areas. (2) On 30 June 2002, most of the low LST pixels were concentrated in the

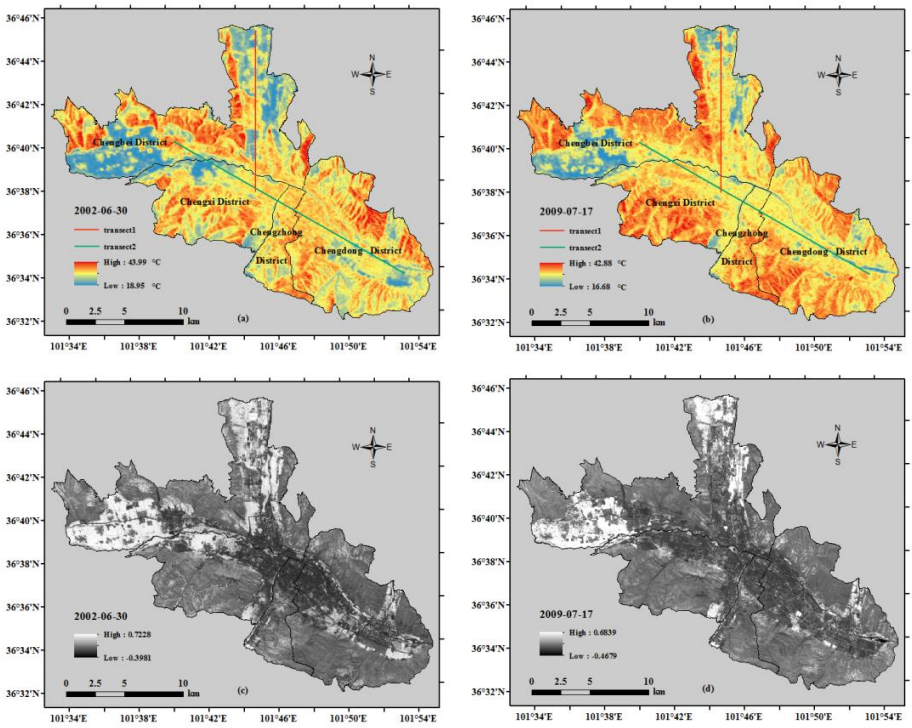

Fig. 2. Land surface temperature (LST) and normalized difference vegetation index (NDVI) in Xining retrieved from 30 June 30,2002 and 13 July,2009, respectively.* (a) and (b) are LSTderived from the 2002 and 2009 images;(c) and (d) are NDVI indices derived from the 2002 and 2009 images.

Chengbei district, which is a major agricultural region. Low LST of this district was due to a large number of cultivated lands. On 17 July 2009, the urbanization occurredat the expense of irrigated green space and started by removing cultivated lands. Thus the LST changed significantly. (3) By comparing the two images (Fig.2a b), a striking increase of LST in the west of Chengxi district and in the east of Chengdong district can be found. And a small increase of LST in the south as well as a small decrease in the north of Chengzhong district. (4)HuangShui River runs through Xining, which can weaken the role of the urban heat island effect. Meanwhile, the recreational parks with water bodies located in the center of the urban city also create cool surfaces.

For further study of urban thermal environment characteristics, the transect analysis method (Fig.2a b) was used to qualitatively demonstrate the existence of the SUHI effect. Comparing the data of 30June 2002 and 17 July of 2009 (Fig.3), the LST fluctuated strongly, but it generally displayed as a convex shape. For transect 1(Fig.3a, c), some pixels with low LST on 30 June 2002 became higher on 17 July 2009, which was caused by the land use of corresponding pixels changed from cultivated land to built-up land, such as urban expansion in the form of encroachment

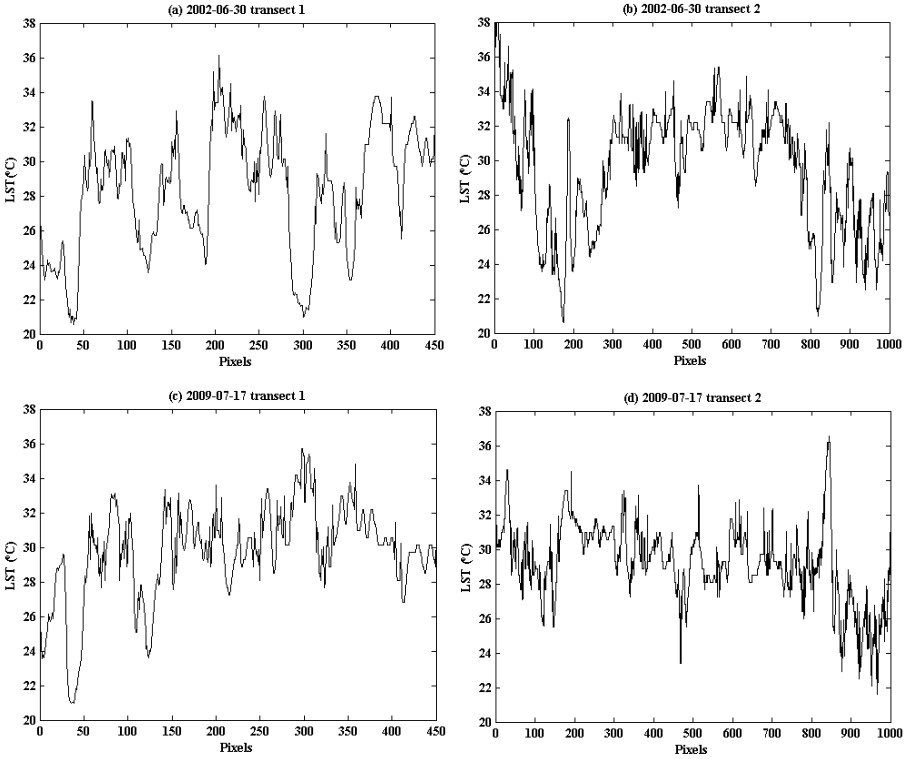

Fig. 3. Profiles of Land surface temperature (1,2). *(a) and (c) are LST derived from the pixels on transect 1 of 2002 and 2009 images; (b) and (d) are LST derived from the pixels on transect 2 of 2002 and 2009 images.

of the limited agricultural areas in Chengbei district. Pixels, numbered from 150 to 400 on the transect 1, were concentrated in urban area and had higher LST than the other pixels concentrated in rural areas. For transect 2 (Fig.3b, d), from 30 June 2002 to 17 July 2009, the maximum LST decreased, while the mean LST increased. On 30 June 2002, pixels numbered from 100 to 300 on transect 2 were concentrated in rural area in Chengxi district. However, with the construction of Haihu district, the land use type was changed to built-up land with these pixels on 17 July 2009. And the LST of corresponding pixels showed a great increase. So apart from the arid and semi-arid areas, the SUHI shows higher temperatures in urban than in rural areas, which was also found in other study [19].

3.2 LST and NDVI Variation in Four Districts

According to the administrative boundary, four districts can be defined for the Xining city and analyses of mean LST and NDVI were carried out in these four districts respectively. From 30.3718 to 31.6375 °C, with a 2.09% increase, the biggest change of mean LST happened in Chengxi district. And the mean NDVI dropped from 0.1606 to 0.0406 and also ranked the first with a 74.72% decrease among the four districts. Based on the distribution of LST and NDVI (Fig.2), same conclusions can be drawn. NDVI indices derived from the 30 June 2002 and 17 July 2009 images (Fig.2c, d) revealed that a large scope of cultivated land in the northwest of Chengxi district disappeared, which was attributed to the construction of Haihu district. The urbanization took place in Chengxi district at the expense of the cultivated land, so the corresponding LST increased. Meanwhile, it also can be found that the southwest of Chengxi district showed higher LST than the other area in the same district. Chengbei district, as an important agricultural region in the city, the change of mean LST ranked second while the change of NDVI ranked the last among the four districts. The quantity of cultivated land decreasedat the center of this area by comparing the NDVI images (Fig.2c, d) of 30 June 2002 and 17 July 2009. Chengzhong district and Chengdong district had a small increase in mean LST, but an obvious decrease in mean NDVI.As a consequence, the decrease of NDVI didn't induce a striking increase of LST in these two districts.

Table 1. Land surface temperature and normalized difference vegetation index change

Date	Mean LST				Mean NDVI			
	Chengbei district	Chengzhong district	Chengxi district	Chengdong district	Chengbei district	Chengzhong district	Chengxi district	Chengdong district
2002	29.11	31.22	30.37	31.02	0.26	0.10	0.16	0.10
2009	29.91	31.53	31.64	31.14	0.14	0.03	0.04	0.04
	2.75%	0.99%	4.17%	0.38%	-46.89%	-70.49%	-74.72%	-57.65%

3.3 Relationship between LST and NDVI

By plotting the parameter images in a LST vs. NDVI scatterplot, the overall distribution of the pixels depicted the typical triangular shape (Fig.4a, b). Three vertexes of the triangle reflect the physical conditions of the area. The upper left corner corresponded to the pixels representing hot conditions (high LST and low NDVI) and lower right corner was formed by pixels suffering cool conditions (low LST and high NDVI). A clear 'warm edge' was defined by the right side of the pixel envelope. The well-known inverse relationship between LST and NDVI occurred in the direction of warm edge along the points where an increase in NDVI caused a decrease in LST. For a further study to analyze the relationship between LST and NDVI, scatter plots were used. Pixels of NDVI values were queried out by 0.02 intervals and the corresponding pixels for their LST values were averaged. The results were presented in Fig.4c, d. And the regression analysis between Mean LST and NDVI present the relationships quantitatively (Eq.5, 6). Then strong negative correlations were found between them (Fig.4c, d). R square value of 2002 was 0.9577 and R square value of 2009 was 0.9592. However, based on the results in Section 3.2 and according to the change of mean LST and mean NDVI among Chengbei, Chengzhong and Chengdong districts, it would be better to study the relationship between LST and NDVI among the four districts respectively.

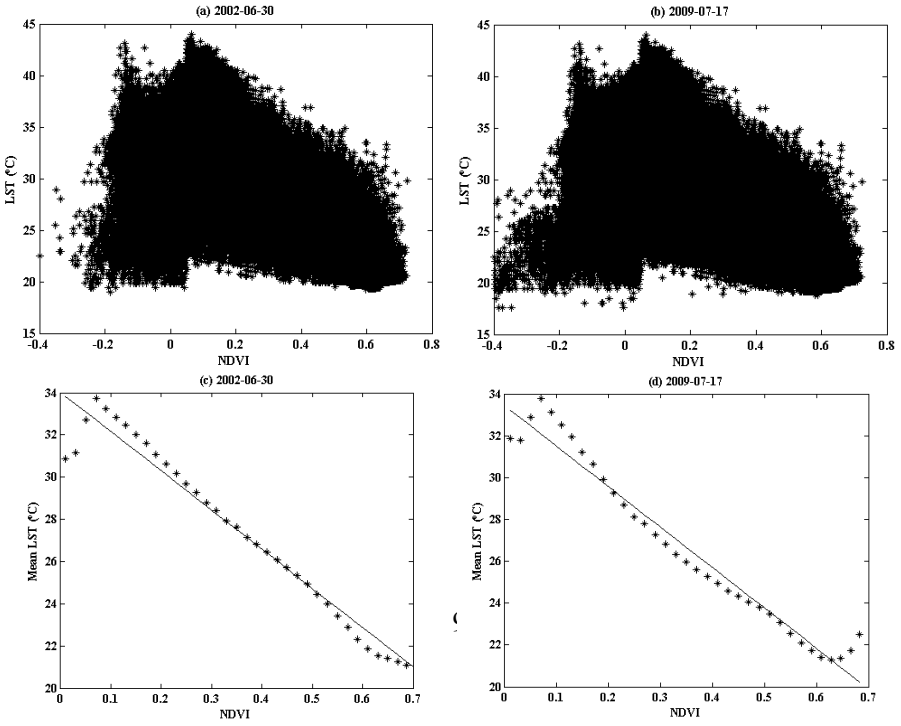

Fig. 4. Scatter Diagram of LST and NDVI. *(c) and (d) are relationships between LST and NDVI, average by NDVI of 0.02 intervals.

$$T_s = 34.0123 - 18.582 * \text{NDVI} \quad (6)$$

$$T_s = 33.4215 - 19.3097 * \text{NDVI} \quad (7)$$

Where T_s in Eq.6 refers to the temperature of 2002 and T_s in Eq.7refers to the temperature of 2009.

4 Conclusions

This paper studied the spatial pattern of LST and measured the change of LST by using Landsat thermal infrared and reflective data. Results showed that, from 30 June 2002 to 17 July 2009, the mean LST increased. Meanwhile, the spatial distribution of LST also changed due to land cover changes. Transects analysis was introduced to demonstrate the existence of SUHI effects and showed that apart from arid and semi-arid areas, the SUHI shows higher temperatures in urban area than in rural area. This was observed by using two transects to depict a convex shape of LST on 30 June 2002 and 17 July 2009 respectively. And with the same transect on different date, the LST fluctuated among different pixels because of the various land use alteration. The temporal analysis of the LST and NDVI in four districts showed that the biggest increase of mean LST and decrease of NDVI happened in Chengxi district. The analysis of relationship between LST and NDVI carried out here could be the assessment of the consequences of future green space changes associated with urbanization on the surface thermal environment of the city. It implied that vegetation could serve as a good remedy for warming surfaces. The increase in the NDVI could stimulate the migration of LST in opposite direction.

In the future study, some work needs to be focused. The impact of the different land use types in the urbanized area on SUHI needs to be studied. And it would better to carry out all the researches on a small scale, such as focusing on the four districts respectively.

References

1. Tran, H., Uchihama, D., Ochi, S., Yasuoka, Y.: Assessment with satellite data of the urban heat island effects in Asian mega cities. International Journal of Applied Earth Observation and Geoinformation 8, 34–48 (2006)
2. Oke, T.R.: The energetic basis of the urban heat-island. Quarterly Journal of the Royal Meteorological Society 108(455), 1–24 (1982)
3. Voogt, J.A., Oke, T.R.: Thermal remote sensing of urban climate. Remote Sensing of Environment 86, 370–384 (2003)
4. Rao, P.K.: Remote sensing of urban “heat islands” from an environmental satellite. Bulletin of the American Meteorological Society 53, 647–648 (1972)
5. Hu, L., Brunsell, A.: The impact of temporal aggregation of land surface temperature data for surface urban heat island (SUHI) monitoring. Remote Sensing of Environment 134, 162–174 (2013)

6. Sobrino, J.A., Oltra-Carrio, R., Soria, G., Bianchi, R., Paganini, M.: Impact of spatial resolution and satellite overpass time on evaluation of the surface urban heat island effects. Remote Sensing of Environment 117, 50–56 (2012)
7. Gallo, K.P., McNab, A.L., Karl, T.R., Brown, J.F., Hood, J.J., Tarpley, J.D.: The use of NOAA AVHRR data for assessment of the urban heat-island effect. Journal of Applied Meteorology 32(5), 899–908 (1993)
8. Quattrochi, D.A., Luvall, J.C., Rickman, D.L., Estes, M.G., Laymon, C.A., Howell, B.F.: A decision support information system for urban landscape management using thermal infrared data. Photogrammetric Engineering and Remote Sensing 66(10), 1195–1207 (2000)
9. Streutker, D.: Satellite-measured growth of the urban heat island of Houston, Texas. Remote Sensing of Environment 85, 282–289 (2003)
10. Chen, X., Zhao, H., Li, P., Yin, Z.: Remote sensing image-based analysis of the relationship between urban heat island and land use /cover changes. Remote Sensing of Environment 104, 133–146 (2006)
11. Aniello, C., Morgan, K., Busbey, A., Newland, L.: Mapping micro Urban Heat Islands using Landsat TM and a GIS. Comparative Geoscience 21, 965–969 (1995)
12. Stathopoulou, M., Cartalis, C.: Daytime Urban Heat Islands from Landsat ETM+ and Corine land cover data: An application to major cities in Greece. Solar Energy 81, 358–368 (2007)
13. Guo, H.: Preliminary study of the action's mechanism of urban nature system, antropogenic action and the urban environmental system in xining. Journal of Qinghai Normal University (Natural Science), 54–59 (1994) (in Chinese)
14. Zhang, J., Zhou, L.: On the Effect of Urban Climate in Xining City. Journal of Xuzhou Normal University (Natural Sciences) 15, 47–51 (1997) (in Chinese)
15. Yu, B., Liu, F., Zhou, Q., Liang, J.: Analysis of the Air Temperature Changes and Heat Island Effect in Xining City. Journal of Anhui Agriculture Science 36, 16031–16033 (2003) (in Chinese)
16. Artis, D.A., Carnahan, W.H.: Survey of emissivity variability in thermography of urban area. Remote Sensing of Environment 12, 313–329 (1982)
17. Qin, Z., Li, W., Xu, B., Chen, Z., Liu, J.: The estimation of land surface emissivity for Landsat TM6. Remote Sensing for Land and Resources 3, 28–42 (1982) (2004)
18. Kerr, Y.H., Lagouarde, J.P., Imbernon, J.: Accurate land surface temperature retrieval from AVHRR data with use of an improved split window algorithm. Remote Sensing of Environment 41(2), 197–209 (1992)
19. Jin, M., Dickinson, R.E., Zhang, D.A.: The footprint of urban areas on global climate as characterized by MODIS. Journal of Climate 18(10), 1551–1565 (2013)

A Study of the Application of Data Mining on the Spatial Landscape Allocation of Crime Hot Spots

Shu-Meng Huang

No. 101, Sec. 1, Fenliao Rd., LinKou District, New Taipei City 24452, Taiwan (R.O.C.)
simon@mail.hwu.edu.tw

Abstract. This study uses the crime hot spots announced by the Taipei police as an example. With the combination of the geographic information system and data mining technologies, it can effectively find out the association rules between the crime hot spots and spatial landscape, and the distance between them. This paper could provide information to the public-security organizations for enhanced patrol of the potential crime hot spots, but is also served as references of urban renewal. It reduces the crime hot spots by avoiding programming the spatial landscape of crime hot spots, therefore promoting safety and happiness of the society.

Keywords: Geographic Information Systems, Spatial Data Mining, Crime hot spots.

1 Introduction

People needs determines what objects exist in space according to their own needs, and who has become one of the spatial composition of objects, when the composition of space objects - people and buildings are met, naturally extended The security incidents, and prone to security incidents has become the space of public order. At present, many researches on Crime hot spots were analyzed through Criminology and Statistics. Criminologists use the term “Hot Spot” to describe Crime hot spots.

Criminologists discovered that the time and space distribution of crime matches the time and space distribution of adolescents do. The time distribution is at dawn and night. The space distribution of crime concentrated on the place which only occupies 3% of city. Similarly, the time distribution concentrated on Hot Days Of Week and Hot Time Of Day. Therefore, most places and the places around Crime hot spots have barely no crime occuring there (Hsu,1998). To reach our research purpose, we used Geographic Information Systems to analyze the information gathered from police unit. We used Spatial Data Mining method to explore the rule within the information.

2 Related Work

Accompanying with the development of information technology, varieties of types of information contents was saved in different kinds of information systems. Such as

F. Bian et al. (Eds.): GRMSE 2013, Part I, CCIS 398, pp. 274–286, 2013.
© Springer-Verlag Berlin Heidelberg 2013

transaction records in POS system, consumer behavior research in CRM system, and industrial operation information in ERP system. Many information was saved permanently in electromagnetic type. However, the capability of traditional method for analyzing information effectively is going to be limited as database is getting larger. Therefore, Data Mining method was developed to analyze information within database. Because of its great ability in filtering, calculating, analyzing, and inducing information , it can help researchers discover more endogenous knowledge from database than traditional methods. In 2000, MIT Technology Review had predicted that Data Mining is one of the most influential technologies in the future. The above notion was also announced by TIME (Hu & Yi, 2004).

Data mining techniques are classified as predictive and descriptive methods. The former uses Decision Tree and non-Decision Tree methods to classify data and predict experiment result (Han`Kamber,2000; Berry`Linoff,1997). Decision tree based classification method includes ID3, PRISM, Gini Index. non-Decision Tree classification methods includes Baye's Rule, K-Nearest Neighbor, Neural network classification. Descriptive data mining technique has focused on describing, understanding, explaining data which had happened. Association rule mining discovers relationship between data that had already exisited to provide a basis or reference for decision making. With the development of Data Mining technique, data type which can be analyzed by Data Mining technique is extent from transaction data to non-transaction data which was previously only can be analyzed by GIS.

There is a concept in management science that is “a chart worth a thousand words”. GIS has powerful capacity in dealing with spatial object. Thus it makes the accumulation of a variety of spatial data access speed to go beyond the traditional manual measurement. However, its data analysis capability is relatively weak. In spatial data analysis, statistical analysis is the most common method to be adopted. However, due to the assumption that statistical distribution between data is independent each other, and such assumption contrary to Spatial Autocorrelation.

With the demand of analysis of spatial data, Spatial Data Mining technique is developed with the combination of spatial data and Spatial Data Mining technique. Data in the relational data base algorithm model is assumed to be independent each other, however this assumption does not conform to the characteristics of spatial data. Because the data attribute of spatial data exists Distance and Topology. Thus, the techniques in dealing with space-related data must have space knowledge, geometry and spatial reasoning technique. Non-spatial data can be mined with the combination of spatial data to find the relationship between spatial and non-spatial data. Spatial autocorrelation analysis now can analyze from spatial objects to non-spatial objects, for example, the distribution of spatial objects from the aging of the population characteristics and the relative temporal relationship between migration(Hsieh & Chou,2002), using spatial data mining technique to select Metro MRT station site. (Huang,2008).

That is, objects may aggregate due to a certain object presenting in a specified range of space. Or because the properties of objects that already exist in the specified range of space affect the properties of the follow-up increased objects, making the spatial information is often with a strong symbiotic relationship. Spatial information is often

made with a strong symbiotic, dependent relationship, such as school districts and the tutorial, or mutually exclusive relationship, such as industrial and residential areas, making the statistical methods was limited in spatial data mining.

Spatial association rules is used to represent the relationship between objects. The objects mentioned here are entity in space or abstract event occurred in space. The abstract event is composed of spatial data or non-spatial data, such as transactions occurred in stores and occurrence of crime. And attributes of spatial properties includes topology, distance, relative location, and direction.

The composition between spatial objects can be construct by point, line, and surface Even with the need of analyzing the phenomenon of classical space, the methods used are clustering, trend detection and classification. These data collection in accordance with the traditional way to design out of the classical way to analyze the demand for spatial data mining analysis, immediately after the adjustment algorithm is applied to the analysis of the phenomenon of space needs, rather than to re-design of a new algorithm to achieve the purpose . However, when operating calculation, we still need to have knowledge and understanding of space as a basis to be the correct interpretation of the connotation of spatial data. Currently there have been various types of expert systems incorporating with GIS (Zhu,1999). In the event, the analysis result is better than that analyzed by simply using GIS. And in a larger extent it solves the problem of expression and application of knowledge, but knowledge still exist limitations (Tsou & Sun,2005). By combining Spatial Data Mining and Data base, we can get more general and refined knowledge, even the implicit knowledge and rules so that the knowledge gained more in line with human thinking. So far, there are many research which method is Spatial Data Mining technique, such as the relationship between earthquakes and landslides. (Tsou & Sun,2005), Metro Area Rapid Transit Site Selection(Huang,2008), Mining census data space(Jung & Sun,2005), Improving the risk of fire and rescue services (Kairasov′a, Krisp and Virrantaus,2005).

3 Research Frame and Methods

People needs determines what objects exist in space according to their own needs, and who has become one of the spatial composition of objects, when the composition of space objects - people and buildings are met, naturally extended The security incidents, and prone to security incidents has become the space of public order. At present, many researches on Crime hot spots were analyzed through Criminology and Statistics. Criminologists use the term “Hot Spot” to describe Crime hot spots.

Criminologists discovered that the time and space distribution of crime matches the time and space distribution of adolescents do. The time distribution is at dawn and night. The space distribution of crime concentrated on the place which only occupies 3% of city. Similarly, the time distribution concentrated on Hot Days Of Week and Hot Time Of Day. Therefore, most places and the places around Crime hot spots have barely no crime occuring there(Hsu,1998). To reach our research purpose, we used Geographic Information Systems to analyze the information gatherd from police unit. We used Spatial Data Mining method to explore the rule within the information.

3.1 Research Steps

(1) Data collection

This step focused on collecting raw data. Raw data came from database system, information system, and Manual sorting data. After collecting data we need, we reposit it to our database system.

(2) Data preprocessing

As real-world data is very messy, and data collection accuracy of the tool itself may exist errors, leading to the information collected, and unlikely to be fully utilized.

Therefore, the purpose of this step focused on the purification of data, fulfilling missing data, and eliminating noise data. And decide how to transform spatial data to generalized data.

(3) Data conversion

Because of the space with a spatial attribute data mining related information, and this type of information needed to make this sudden transformation of the action, determine the standardized way of converting, finishing in accordance with the rules and add or remove spatial attributes of the property given.

(4) Data mining

Using statistical analysis and modeling methods, mining from the data useful to focus on the pattern and relevance.

(5) Pattern analysis

View the results of data mining, the hidden information may be meaningful, or may be meaningless, and meaningful information also must comply with the fun or interesting features.

In this stage, information has been filtered to see if it is meaningful to provide to user.

3.2 Association Rule

In this study, we transformed spatial data into transactional data to apply data mining. Association rule mining aims to identify transactions that may be associated items, the association rule is also known as Market Basket Analysis (Agrawal et al.,1993). The original idea was used to analyze consumer behavior, according to consumer transactions in the store. Association rule can be tapped through a similar Implicit knowledge, that is "75% of customers after the purchase of a product A also buy product B ". Bottom to the data mining (Tseng, etc, 2005) under Chapter VII of the contents of the book to a brief introduction to association rules and algorithms.

(1) The definition of association rules:

Taking shopping trade as an example to illustrate the interpretation, in a store selling goods in the project (Items) is a collection of I, called the project set (Itemssets), in the

transaction database records each transaction T, containing the transaction number and a subset of items to be purchased. Suppose that X is a collection of items, if all the items in X are included in the transaction T. It means that T supports project set X. the statement is as follows.

$$X \Rightarrow Y \text{ (Support, Confidence)}$$

Where X and Y on behalf of a collection of items, X stands for "conditional", Y as the "conclusion sentence. " Support expressed support, on behalf of "a collection of X's support for the project the total number of transactions the total amount in the proportion of records of transactions". Confidence stands for reliability, on behalf of the accuracy of a number of laws, "Project X, in the purchase of the project will also purchase the proportion of Y", the higher the reliability of this rule that the higher reference value. The association rule must meet two pre-set parameters: minimum support (Minsupport) and the minimum reliability (Minconfidence). Its existence is to eliminate rules not going beyond the minimum support and fail to reach the confidence threshold.

(2) Apriori algorithm

Apriori algorithm (Agrawal et al., 1994) is the core of the definition of "a large collection of items in any collection. It must have been homozygous for a collection of large-scale projects". Suppose {A, B} is a large collection of items, the {A, B} disassembled into a collection of items and item set {A} {B}, in the transaction history database, the project supported by a collection of the number of {A} Collection of items will be greater than or equal to {A, B}, so the project must be the set {A} a collection of large-scale projects, same reason, the project will surely set {B} is a collection of large-scale projects. The spirit of Apriori algorithm is " Join " and " Prune ", the first record of the database in the transaction table to create a single project, and view the number of its projects there over the minimum support threshold, if so, Stand the project is retained; if not, then remove from the project table. After viewing, The project will be retained items combined into a collection of candidate (Candidate Itemsets), and then calculated for each candidate item set minimum support and see if over the threshold, through constant repetition of the "merger" and "delete " action, not directly Generate a new set of candidate projects to date.

(3) LqiTid algorithm

In transactional database, transactional data consists of purchasing items and purchasing quantity. For example "75% of customers buy a package of diapers will then purchase of six bottles of beer", this rule is known as "the number of related laws ". Since taking into account the "project" and "Quantity" will result in across the minimum support threshold has become less a collection of items, or collection of items without any threshold can be crossed. Therefore, "the number of association rules, " divided quantity into several intervals (Intervals), to improve the collection of each project within its own range of support, the focus will be divided into a number corresponding to the respective intervals Integer. We will use LqiTid algorithm for mining large-scale projects set 1 under the list of 15 document data record from the transaction database is the sorting out of the mining in the database with the backup.

Table 1. Transaction database

Tid	q_itemset
1	<B,1> <C,2> <F,1> <G,3>
2	<C,1> <D,1> <G,1>
3	<C,1> <F,3> <G,1>
4	<A,2> <B,1> <C,3> <G,2>
5	<A,1> <B,1>
6	<B,3> <C,2>
7	<B,3> <C,2> <D,1> <E,5> <F,1>
8	<B,1> <C,2> <G,3>
9	<B,4> <F,2>
10	<A,2> <B,2> <C,3> <F,1>
11	<B,2> <C,3> <F,1>
12	<A,1> <B,2> <G,2>
13	<B,2> <C,2> <G,4>
14	<A,1> <B,2> <C,3> <F,3> <G,5>
15	<A,3> <C,4> <G,3>

SOURCE: Modified from Tseng, 2005

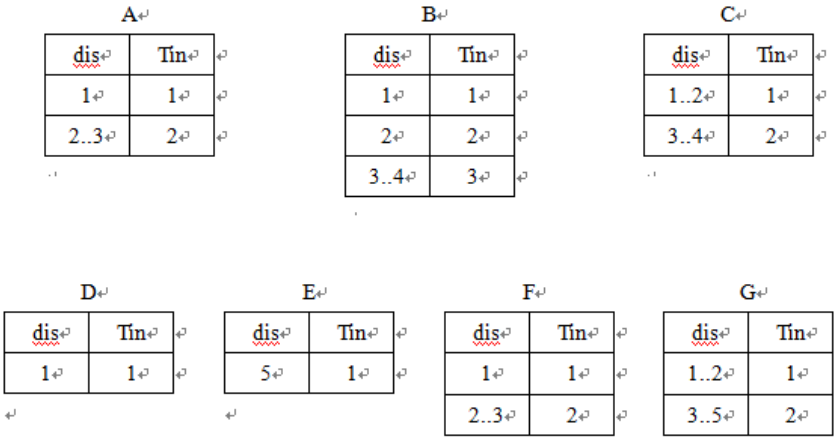

Fig. 1. Interval integer table of item (SOURCE: Modified from Tseng, 2005)

After transforming the minimum support of Operational definition into the numbers of minimum support, we can divide each item. When completed, it will generate the number of items in Figure 2 corresponds to an integer table interval.

Get the corresponding number of items in the entire table after the interval, so that an integer can be used to replace the corresponding transaction data table out of the original number of transactions, and so can be converted in Table 2 record the transaction database DB.

Table 2. Transformed transaction database

Tid	q_itemset
1	<B,1> <C,1> <F,1> <G,2>
2	<C,1> <D,1> <G,1>
3	<C,1> <F,2> <G,1>
4	<A,2> <B,1> <C,2> <G,1>
5	<A,1> <B,1>
6	<B,3> <C,1>
7	<B,3> <C,1> <D,1> <E,1> <F,1>
8	<B,1> <C,1> <G,2>
9	<B,3> <F,2>
10	<A,2> <B,2> <C,2> <F,1>
11	<B,2> <C,2> <F,1>
12	<A,1> <B,2> <G,1>
13	<B,2> <C,1> <G,2>
14	<A,1> <B,2> <C,2> <F,2> <G,2>
15	<A,2> <C,2> <G,2>

SOURCE: Modified from Tseng, 2005

After acquiring transactional database, data can be “joined” and “delete” in aids of data mining technique.

3.3 Spatial Material Acquisition

In research we usually check charts to see the way how spatial objects being constructed (Estivill-Castro and Lee, 2001), cut the looking down areas into different checks by 50m * 50m, then indicate the spots that each exit check’s spatial material and events, see Figure 2. The event that check indicates (the red dot in Figure 2) belong to the user wants to observe the event, add all the spatial objects in this check

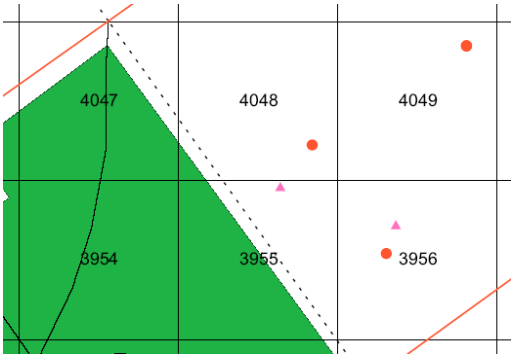

Fig. 2. Grid map with spatial data (Source: Karasov’a, Krisp and Virrantaus, 2005)

(the triangle in Figure 2) in database. However, this way to collect data doesn't take the spots and spatial objects distance into consideration, maybe it because the spots is on the check's left bottom, the indicated spatial objects are on the top right-hand corner or the spots are on the check's margins, but the nearest spatial objects from the spots are disregard.

Karasov'a, Krisp and Virrantaus, (2005) above the check's foundation, they brought up that the spots are considered to examine the spatial objects' central place, see the Figure 3, use 50m as radius outward to draw a circle area (the yellow area in Figure 3), put all the spatial objects (light purple triangle in Figure 3) into database, in this way, the focus can be much stronger on each relation between the spots and spatial objects.

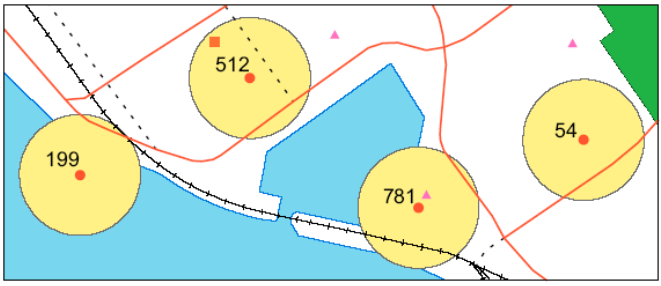

Fig. 3. Circle area with spatial data (Source: Karasov'a, Krisp and Virrantaus, 2005)

3.4 Research Materials

(1) AcrView 3.1

ArcView is a GIS system made by Environmental Systems Research Institute, ESRI, products of the company can apply in Desktop, Server, Motion platform, in the research we use ArcView 3.1 of ArcGis Desktop series, the materials provides the use of GIS information, charting, making forms and the basic of GIS analysis, and support Net、VB、VC++.

(2) DMAS 2.6

DMAS is data mining tool use JAVA made by Dr.Tseng, the version is 2.6.2, besides association mining modules, it also provides the data modules, classified models modules, cluster analysis modules.

4 Confirmation Feasibility

The research follow the former steps to proceed data mining, see figure 4.

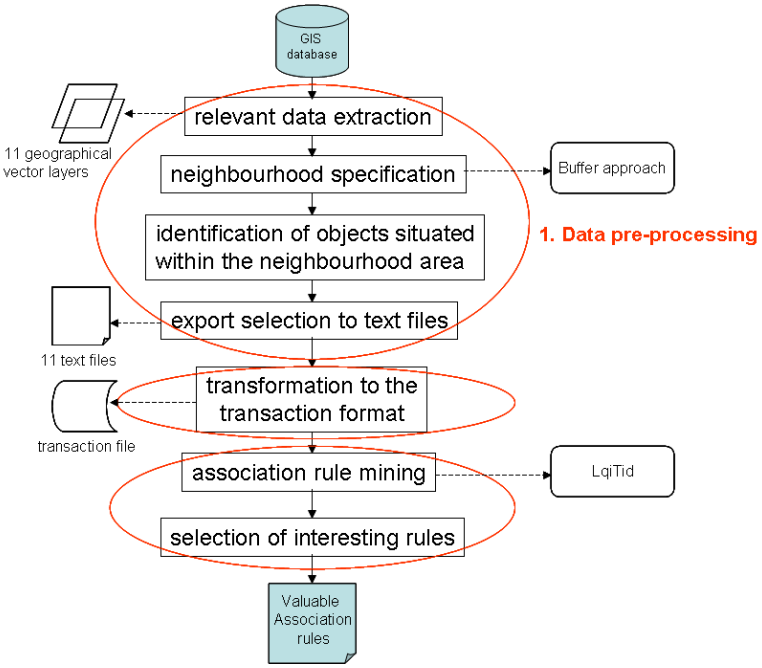

Fig. 4. Research framework

Fig. 5. Crime hot spots

4.1 Data Collection

The resource comes from Taipei City Police Department announce crime hot spots, we draw the crime hot spots to make GIS graphic layers, see Figure 5, GIS layers illustrates scope's spatial objects, see Figure 6, survey the distance between the crime hot spots and nearby spatial objects, see Figure 7.

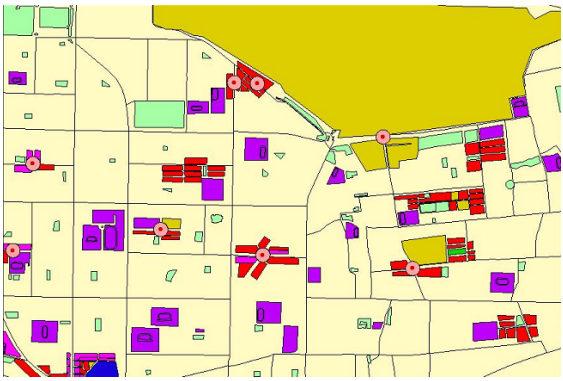

Fig. 6. The crime hot spots and nearby spatial objects

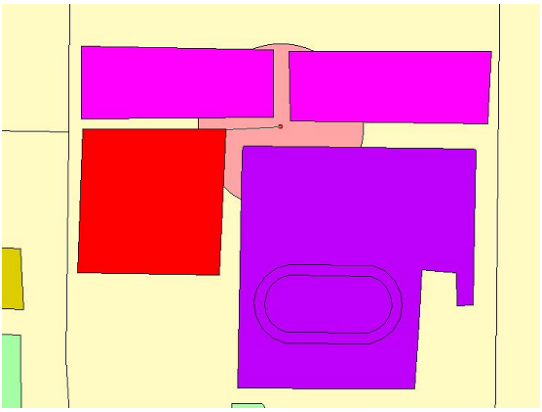

Fig. 7. Survey the distance between the crime hot spots and nearby spatial objects

4.2 Data Processing

After collecting the distance of the spots and spatial objects, the information has decimal fraction (table 3.) according to the rules of round off to arrange the whole numbers also use codes to replace original neighborhoods' names table 3.

Table 3. Original files format examples

Wang Shi Li	<A,19> <D,0> <E,30>
Sin Guang Li	<A,0> <D,0> <E,10.6>
Jiou Jhuang Li	<A,3.77> <B,12.08> <D,6.34>
Sing Fong Li	<A,0> <B,1.59> <E,5.57>
Jian Gong Li	<A,9> <B,7.32> <D,0>
Guo Ye Li	<A,1> <B,3.92>

Table 4. Round-off, given the neighborhood's names codes files format examples

80	<A,19> <D,0> <E,30>
81	<A,4> <D,0> <E,11>
82	<A,4> <B,12> <D,6>
83	<A,0> <B,2> <E,6>
84	<A,9> <B,7> <D,0>
85	<A,1> <B,4>

4.3 Information Transformation

In this research we adopt "quantification association rules" to reduce the numbers of items by using the interval division. We use 40m as a unit of interval transformation, the example is as follow:

<A,19> <A,51> => <A,1> <A,2>

After transferring all the spatial objects distance into interval codes by interval division, the information contents transform to ideals type format, the example of the difference of before and after is as follow:

001|<A,1> <A,2> <A,3> => 001|<A,1>001|<A,2>001|<A,3>

4.4 Information Mining

Then transform to ideals type information, see table 4, use LqiTid algorithm to proceed mining association rules, we set min-support count is 30 this time, min-confidence is 50%, the mining result get 3 association rules, see table 5.

Table 5. The mining result

Number	Association Rules	Min-Support Count	Min- Confidence
1	<B,1> => <A,1>	28	68%
2	<A,1> => <D,1>	30	52%

4.5 Types Patterns

In this mining we find that inside 50m radius and inside 0~40m has crime hot spots also exists residential sites (A) business section (B) spatial objects combination or residential sites (A) and industrial area (B) spatial objects combination, the analysis reason is this business section and industrial area are sparsely populated except normal work and rest, the crime hot spots happens easily when the victim go back to residential sites from business section or industrial area in non work and rest, or the same time go to business section and industrial area.

5 Conclusions and Suggestions

After confirmation feasibility, 3 conclusions come by:

(1) By combining mining skills and geographic information systems, we can mine the events and spatial objects efficiently.
(2) In research, we can take the distance between spatial relation and objects into consideration, states the result between the events and spatial objects relation.
(3) In the present study found that the combination of spatial objects and their distance from the composition of public order for the production of a certain relationship exists, therefore, the negative side can dig out the research methods in line with the position space constitutes a point of time to strengthen arrangements patrols to prevent the occurrence of security incidents of public order and generate a new generation. On the positive side, the urban planning should try to avoid mining results consistent with the combination of spatial objects

Among this study, only taking into consideration of public order and the distance between spatial objects, not deep space objects and space considerations to the relative relationship between objects, such as spatial objects A and B space object distance, or space object C in Spatial orientation of the object D such relationship, so the next time studying the relationship between spatial objects can be included in the study range.

References

1. Hsu, Introduction to Police Administration. San Min Books, Taipei (1998)
2. Hu, Yi: SQL Server Business Intelligence Bible. Xbook Marketing Co. Ltd., Taipei (2004)

3. Hsieh, C.-Y., Chou, K.-P.: A Spatial Autocorrelation Analysis of Aging Distribution and Transition. Journal of Population Studies 25, 91–119 (2002)
4. Huang, S.-M., Hsu, P.-Y., Chen, C.-C.: Use Spatial Data Mining for Planning Urban Mass Rapid Transit System. Journal of e-Business 10, 491–506 (2005)
5. Tsou, M.-C., Sun, C.-H.: Mining Association Pattern from Spatial Database. Journal of Taiwan Geographic Information Science 3, 27–41 (2005)
6. Tsou, M.-C., Sun, C.-H.: Discerning Chi-Chi Earthquake-induced Landslide Using Data Mining Technique. Journal of Taiwan Geographic Information Science 36, 117–131 (2004)
7. Jung, C.-T., Sun, C.-H.: Spatial Data Mining on Census Data —A Case Study for Location Analysis of Convenience Stores in Taipei City
8. Tseng, et al.: Data Mining. Flag Publishing Co. Ltd., Taipei (2005)
9. Agrawal, R., Imielinske, T., Swami, A.: Mining Association Rules between Sets of Items in Large Database, pp. 207–216. ACM (1993)
10. Agrawal, R., Srikant, R.: Fast Algorithms for Mining Association Rules in Large Database. In: Proceedings of the 20th International Conference on Very Large Data Bases, pp. 487–499 (1994)
11. Berry, M., Linoff, G.S.: Data Mining Techniques for Marketing, Sales and Customer Support. John Wiley and Sons, New York (1997)
12. Ester, M., Kriegel, H.-P., Sander, J.: Algorithms and applications for spatial data mining. In: Miller, H.J., Han, J. (eds.) Geographic Data Mining and Knowledge Discovery. Taylor & Francis, New York (2001)
13. Estivill-Castro, V., Lee, I.: Data Mining Techniques for Autonomous Exploration of Large Volumes of Geo-referenced Crime Data. In: Proceedings 6th International Conference on Geocomputaion (2001)
14. Han, J., Kamber, M., Tung, A.K.H.: Spatial clustering methods in data mining. In: Miller, H.J., Han, J. (eds.) Geographic Data Mining and Knowledge Discovery. Taylor & Francis, New York (2001)
15. Han, J., Kamber, M.: Data Mining: Concepts and Techniques. Morgan Kaufmann Publishers, San Francisco (2000)
16. Karasová, V., Krisp, J.M., Virrantaus, K.: Application of Spatial Association Rules for Improvement of a Risk Model for Fire and Rescue Services. In: Proceedings 10th Scandinavian Research Conference on Geographical Information Science, ScanGIS 2005 (2005)
17. Shekhar, S., Chawla, S.: Introduction to Spatial DataMining. In: Shekhar, S., Chawla, S. (eds.) Spatial Databases: A tour. Prentice Hall, London (2003)
18. Zhu, A.-X.: A personal construct-based knowledge acquisition process for natural resource mapping. In: Proceedings Geographical Information Science, vol. 13(2), pp. 119–141 (1999)

Designing Baiguo Landslide Disaster Monitoring and Pre-warning System Based on GIS

Zhanshi Liu[1], Zhigang Li[2], and Bo Li[2]

[1] Geological Environmental Monitoring Institute of Henan Province, Zhengzhou, Henan, China
[2] Engineering Faculty, China University of Geosciences, Wuhan, Hubei, China
{747104420,7338744}@qq.com, lzgdyy@163.com

Abstract. This paper aims to design Baiguo Landslide disaster monitoring and early warning system on considering both the safety and the funding. MAPGIS is selected as the foundation platform. This software's basic function is taken full advantage of in managing geological information. Then realize the early warning function on base of a secondary development library of MAPGIS. This forecasting system contains database design and early warning function module design. It colligates middle or short term system and approaching disaster system these two types, including 6 kinds of models. The system could manage the disaster information automatically. And it provides the basis for Baiguo landslide early warning.

Keywords: landslide, monitor, early warning system, Baiguo Village, GIS.

1 Introduction

Baiguo Landslide is a large-scale but moderately thick soil landslide located in Baiguo Village, Xixia County, Henan province. Its deformation and fracture is obvious now, threatening 576 people's lives and property in Baiguo Village. This paper aims to design the disaster monitoring and early warning system so that to guarantee the safety and reduce the fund as well.

2 The Characteristic of Baiguo Landslide

The elevations of the slip mass leading and trailing edge are 408m and 618m separately. Its width is 385m and length is 447m. This slide mass' maximum thickness is 20m, its volume is about 120*104m³. The main sliding direction is about 100°, shown in Figure 1. The emergence stratum around the landslide mainly belong Erlangping Group lower Palaeozoic erathem in Sinian System, short for Pz1E, including Huoshenmiao Formation, short for Pz1h, Damiao Formation, short for Pz1d and Erjingou Formation, short for Pz1e. The hydrogeological condition here is simple relatively. The groundwater contains pore phreatic water in loose rock mass and frature water in bedrock.

F. Bian et al. (Eds.): GRMSE 2013, Part I, CCIS 398, pp. 287–297, 2013.
© Springer-Verlag Berlin Heidelberg 2013

The slide mass' main scarp has been appeared and a semi-closed depression is initially shaped there. There are some regional uplifts in the slip mass surface. The slip tongue and drumlin are formed in leading edge of the slide. The constructions around it are pushed to incline. The terraced fields are interrupted. Some individual trees become slanting. The rim is not formed overall but it is clear in some sections.

The slip mass is mainly made up of thick weathered layer and slope wash. There's silty clay in its surface. It's thick in the trailing edge and middle part but thinner in the leading edge as a whole, shown in Figure 2. Its slide bed is quartz schist. The slip soil is silty clay performing massive or broken structure with fracture development.

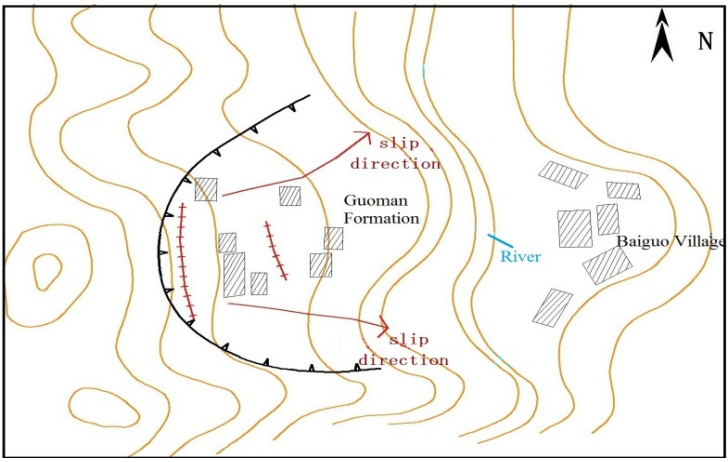

Fig. 1. Baiguo landslide plan

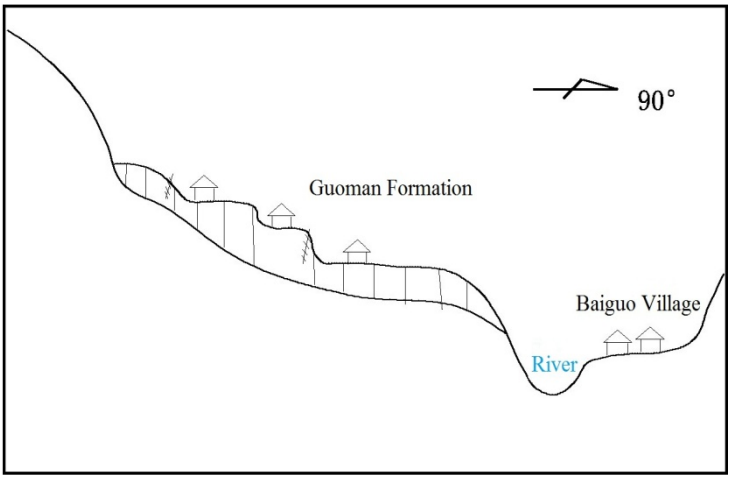

Fig. 2. Baiguo landslide profile map

3 Disaster Monitoring Scheme of Baiguo Landslide

This landslide monitoring scheme contains 7 GPS monitoring points according to Baiguo landslide geological data at present. These datum points lay down along the southwest out of slide mass where the bedrock exposed in the stable area, shown in Figure 3. The monitoring period is one month as usual. However, the observation frequency will increase in special circumstances. In addition, an automatic rain gauge is equipped to monitor rainfall capacity. Two monitoring points are fitted to monitor the underground and surface water level separately.

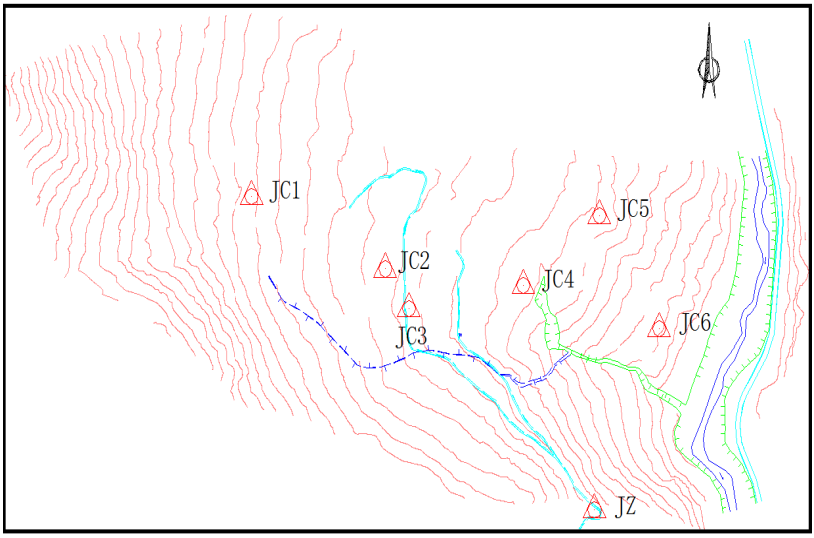

Fig. 3. GPS monitoring points' distribution diagram

4 Designing Pre-warning System Schematic of Baiguo Landslide

4.1 Designing System Objectives

The monitoring and early warning system based on GIS is on the foundation of dynamic monitoring data. This pre-warning system has the advantages of establishing an approaching slide model as well as the technical support offered by GIS. Its two objectives are:

(1) Realizing information management, including essential information and dynamic monitoring information.

(2) Realizing landslide forecast by comparing the criterions of forecasting model and pre-warning of approaching slide model on base of dynamic monitoring information.

4.2 Designing System Organization

The monitoring and early warning system structure of Baiguo landslide is shown in Figure 4.

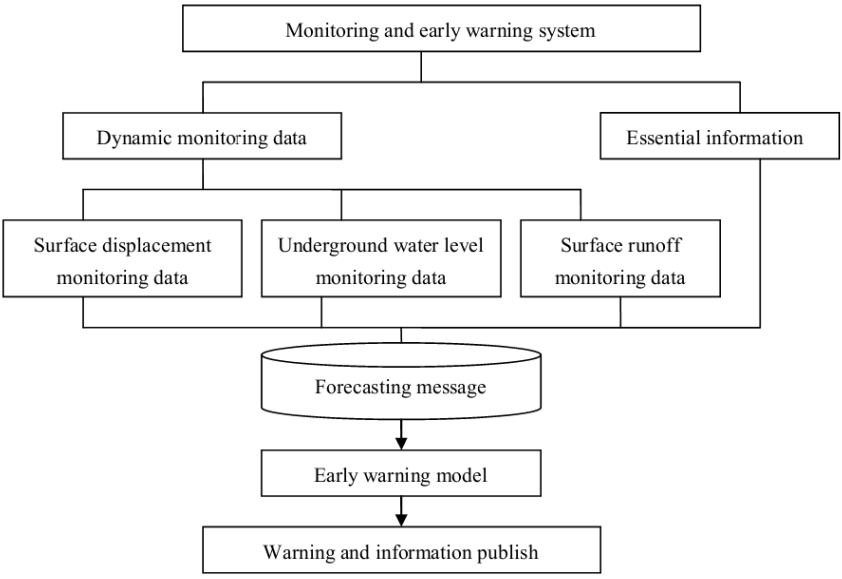

Fig. 4. Monitoring and early warning system

4.3 Designing System Database

The system database is one of the keys in system research and development. Its quality influences the property of function module directly as well as its transplant and broadening in the future. According to the design philosophy of data base, the monitoring objectives are classified into the system data type and the relationship between data types. The system data are classified into monitoring and management data as well as monitoring data these two parts. Monitoring and management data mainly manage essential information of monitoring points. These data includes surface displacement, underground water level, surface water level and rainfall capacity. According to data classification, the basic information property database and the monitoring information database are established separately. They restore monitoring management data and monitoring data accordingly. [1] The attribute data design of monitoring point, displacement, rainfall capacity, underground water level and surface water level are shown orderly in Table 1, Table 2, Table 3, Table 4 and Table 5.

Table 1. Monitoring point attribute data design

Field name	Field type	Field Length	Decimal place
ID	long int	8	/
Point	Character string	5	/
Type code	short int	2	/
Instrument type	Character string	20	/
Mainframe No.	Character string	20	/
Remarks	Character string	20	/

Table 2. Displacement monitoring attribute data design

Field name	Field type	Field Length	Decimal place
Point	Character string	5	/
Type code	short int	2	/
Instrument type	Character string	20	/
Monitor time	Data Time		
X	Float	8	3
Y	Float	8	3
H	Float	8	3
delta X	Float	8	3
delta Y	Float	8	3
delta H	Float	8	3
delta S	Float	8	3
Alfa	Float	8	3

Table 3. Rainfall capacity attribute data design

Field name	Field type	Field Length	Decimal place
Point	Character string	5	/
Type code	short int	2	/
Monitor time	Data Time		
Rainfall capacity	Float	8	3

Table 4. Underground water level attribute data design

Field name	Field type	Field Length	Decimal place
Point	Character string	5	/
Type code	short int	2	/
Monitor time	Data Time		
Buried depth of groundwater	Float	8	3
Elevation of groundwater	Float	8	3

Table 5. Surface water level attribute data design

Field name	Field type	Field Length	Decimal place
Point	Character string	5	/
Type code	short int	2	/
Monitor time	Data Time		
Buried depth of surface water	Float	8	3
Elevation of surface water	Float	8	3

4.4 Designing Function Module of Early Warning System

4.4.1 Designing Function Module of Pre-processing Monitoring Data

When the monitoring data intervals are not equal, we should make these data at regular intervals in order to improve the prediction accuracy. The time series is rough when it is seriously affected by random factors. We should smooth it so that to get rid of interference from random factors.[2] The software could offer equal spaced processing, normalization processing and step function processing these three methods. Their computational formulas are as follows:

(1) Equal spaced processing
Its transformation formula is

$$X^{(0)}(t_i) = X_0^{(0)}(t_i) - \Delta X_0^{(0)}(t_i) \quad (i = 1, 2, \cdots n) \tag{1}$$

$$\Delta X_0^{(0)}(t_i) = \theta(t_i)[X_0^{(0)}(t_i) - X^{(0)}(t_i - 1)] \tag{2}$$

$$\theta(t_i) = [t_i - (i - 1)\Delta t_0]/\Delta t_0 \tag{3}$$

Where $X_0^{(0)}(t_i)$ is initial displacement, $X^{(0)}(t_i)$ is output displacement, Δt_0 is mean time interval.

(2) Normalization processing
Its transformation formula is

$$X^{(0)}(i) = \frac{X(i) - \bar{X}}{s} \quad (i = 1, 2, \cdots n) \tag{4}$$

$$\bar{X} = \frac{1}{n}\sum_{i=1}^{n} X(i) \tag{5}$$

$$s = \sqrt{\frac{1}{n}\sum_{i=1}^{n}\left(X(i) - \bar{X}\right)^2} \tag{6}$$

Where X(i) is initial displacement, $X^{(0)}(i)$ is output displacement.

(3) Step function paraded processing
Its transformation formula is

$$Y(k) = X(k) - \sum_{i=1}^{n} b_i \cdot h(k) \quad . \tag{7}$$

Where Y(k) and X(k) are the displacements of after and before filtering separately. b_i is the step elevation at the very moment, h(k) is the unit step function.

4.4.2 Designing Forecast System Module

This landslide is in steady creep upon its deformation. The landslide forecasting model colligates middle or short term system and approaching disaster system these two types, including 6 kinds of models. The middle or short term system consists of Verhulst model, nonlinear regression analysis model, GM(1,1) model and exponential smoothing model. [3][4][5] The approaching disaster system consists of Saitou model and collaborative model. [3][6] These model computational formulas are as follows:

(1) Verhulst model
The nolinear differential equation of dynamic forecasting model is

$$\hat{X}^{(1)}(t) = \frac{\frac{a}{b}}{1 + \left(\frac{a}{b} \bullet \frac{1}{x^{(0)}(1)} - 1\right)e^{-a(t - t_0)}} \quad . \tag{8}$$

Make the critical value of creatures from mature to die, a/2b, as the critical displacement of landslide, substituted to the equation above, leads to

$$t = \frac{1}{a} \ln\left(\frac{a}{bx^{(0)}(1)} - 1\right) + t_0 \quad . \tag{9}$$

$$t' = t \bullet \Delta t \quad . \tag{10}$$

Where t is the ordinal time in landslide monitoring. t' is the time to rupture. Δt is the average interval time in monitoring.

(2) Nonlinear regression analysis method
Assume a group of displacement corresponding to time, y_i, t_i, where t_i means each time stage, and y_i means corresponding displacement in each time stage. Fitting y_i and t_i these two group of data by polynomial. And assume the polynomial of regression equation is

$$y = a_0 + a_1 t + a_2 t^2 + a_3 t^3 + \cdots + a_n t^n \quad . \tag{11}$$

Where n is the power exponent, and the larger n is, the higher fitting precision will be. In general, n>=3 will satisfy the engineering requirement. Here we select n=3, then determine a_0, a_1, a_2, a_3 by the least square method. Substitute a_0, a_1, a_2, a_3 to the above equation. Then we can forecast landslide displacement at any time.

(3) Grey theory GM (1,1) model

The expression of this model is

$$\hat{x}^{(1)}(k+1) = [x^{(0)}(1) - \frac{b}{a}]e^{-ak} + \frac{b}{a} \quad (k = 1, 2, \cdots n) \quad . \tag{12}$$

The predicted value of landslide displacement is

$$\hat{x}^{(0)}(k+1) = \hat{x}^{(1)}(k+1) - \hat{x}^{(1)}(k) \quad . \tag{13}$$

Where a and b are undetermined coefficients. They are determined by least square method.

(4) Exponential smoothing

Given that monitoring displacement values of first t periods' stage. Forecast the latter m periods. It means the t+m period.

$$F_{t+m} = A_t + B_t m + \frac{1}{2} C_t m^2 \quad . \tag{14}$$

Where m is a positive integer, m>=1, A_t is the value in the t period. B_t is the linear increment in the t period. C_t is the parabola increment in the t period.

(5) Saitou model

The empirical formula of slide time and creep rate in the stage of constant speed creep deformation is

$$\lg t = 2.23 - 0.196 \lg \varepsilon \pm 0.59 \quad . \tag{15}$$

Where ε is the constant creep rate.

(6) Synergetic model

The expression of synergetic model is

$$x^{(1)}(t) = \sqrt{\frac{a}{\frac{1}{\frac{x^{(1)}(0)}{[a - b[x^{(1)}(0)]^2]} e^{2at}} + b}} \quad (k = 1, 2, \cdots n) \tag{16}$$

Make the time point where the rate of deformation is maximal as the landslide forecast time. x is the corresponding displacement at this time point.

$$x^{(1)}(t) = \sqrt{\frac{a}{3b}} \quad . \tag{17}$$

Then obtain the slip time

$$t = \frac{1}{2a} \ln\left[\frac{a - b[x^{(1)}(0)]^2}{2b[x^{(1)}(0)]^2}\right] + t_0 \quad . \tag{18}$$

Where t_0 is the initial time, a and b are undetermined constants obtained by least square method.

4.4.3 Designing Prediction Criterion Module of This Landslide

Prediction criterion is the core in forecasting. Prediction criterion is classified into three classes, security coefficient and reliable probability criterion, rate of deformation criterion as well as summarized information forecast criterion. [3] This paper selects four criterions, critical rainfall intensity criterion, underground water level criterion, rate of deformation criterion and acceleration criterion. We take the highest grade of deformation, rate of deformation and acceleration as the forecast criterion. Critical rainfall intensity criterion mainly refers to the statistics achievement of landslide occurrence with precipitation as well as similar landslide's rainfall intensity. The selections of underground water level criterion, rate of deformation criterion and acceleration criterion all refer to similar landslide's occurrence conditions.

(1) Rate of deformation criterion

Baiguo landslide belongs to a localized landslip in slope wash layer of completely weathered granodiorite. The rate of deformation criterion selects system default values:

1) When v>0.02mm/d, red alert, danger classes is Grade I.
2) When v≥0.005mm/d, orange alert, danger classes is Grade II.
3) When v<0.005mm/d, green, safety.

(2) Acceleration criterion

1) When the rate of displacement declines, $d^2u/dt^2<0$, safety

2) When the rate of displacement is an invariant, $d^2u/dt^2<0 =0$, orange alert, danger classes is Grade II.

3) When the rate of displacement increases, $d^2u/dt^2>0$, red alert, danger classes is Grade I.

(3) Critical rainfall intensity criterion is shown in Chart 6.

Table 6. Critical rainfall intensity criterion

Danger classes	Early warning classes	Cumulative rainfall in one precipitation process (mm)	Rainfall in an hour (mm/h)	Rainfall in a day (mm/d)
I	Red alert	>50	>6	>30
II	Orange alert	>25	>3	>15
III	Green	<25	<3	<15

(4) Comprehensive criterion

We should judge the grades of rate of deformation, acceleration and critical rainfall intensity comprehensively. Then select the highest grade of these three grades as the final grade for early warning.

4.5 Realization Process of Landslide Early Warning

Landslide forecast database platform is established on the foundation of essential data and real-time monitoring data. Each model selects the very data and calculates it. Then forecast it according to the comparison between the model's results and approaching slide criterion. Report the final result to superior unity to publish. The detail realization process of landslide early warning system of Baiguo landslide is shown in Figure 5.

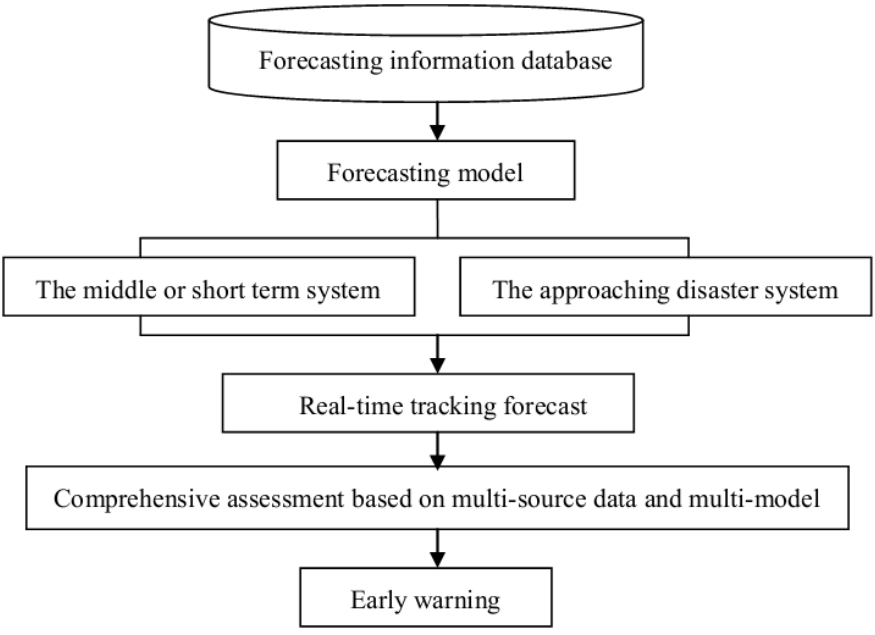

Fig. 5. Realization process of landslide early warning system

5 Conclusions

It's high cost performance in science of disaster to apply geographic information system to geological disaster early warning. The utilization potentiality of GIS expands unceasingly. In the disaster forecast system of Baiguo landslide, the prediction model is the core. In this system, the basic information data and dynamic monitoring data are the foundation, and the GIS is the technology platform. Then the geological disaster processes including data input, data management, model calculation and automatic evaluation are realized.

The combination of high-end monitoring instrument, deep geological analysis and Web GIS platform is an effective method via the monitoring and early warning system of Baiguo landslide above.

Acknowledgements. Financial supports from the project of Geological disaster monitoring and early warning technique application research on Baiguo village landslide control project in Xixia County (2011—622—29) that scientific and technological project in Office of Land and Resources in Henan province.

References

1. Li, X., Li, Y.: Design of GIS-based Monitoring and Early-warning System of Landslide Hazard in Diao Zhongba. Energy Procedia 16(pt. B), 1174–1179 (2012)
2. Li, Y.: Landslide forecasting system development and applied research based on GIS, Chengdu Univerisity of Technology (2003)
3. Sun, H.: Landslide forecasting model base development and applied research based on GIS, Taiyuan University of Technology (2002)
4. Xu, C.: The comparative analysis of landslide forecasting model, Harbin Engineering University (2011)
5. Zhang, Y., Li, H., Sheng, Q., Wu, K., Chen, G.: Real time remote monitoring and pre-warning system for Highway landslide in mountain area. Journal of Environmental Sciences 23(suppl.), S100–S105 (2011)
6. Lu, J.: Slope forecasting model research and its application in engineering, Hefei University of Technology (2006)

A Heterogeneous Data Integration Model

Hai Liu, Yunzhen Liu, Qunhui Wu, and Shilong Ma

Department of Computer Science and Technology,
Beihang University, 37 Xueyuan Road,
100083 Beijing, China
{Liuhai,Liuyunzhen,Wuqh,slma}@nlsde.buaa.edu.cn

Abstract. With the rapid development of the Internet of Things (IOT), the data management, data mining and data analysis in IOT systems require improving the usability of the multi-sourced, distributed, autonomous and heterogeneous data from the subsystems, making the aggregation, integration and collaboration of the data a focus in research. According to the characteristics of basic IOT data environment, a HDIM is proposed based on the comparison and analysis of the current existing data integration approaches. This model can not only mask the data heterogeneity in distributions, but also provide the customized application view for the upper applications, which can decouple the programs and data structures; additionally, the model can maintain the integrity and consistency of the data. Based on this HDIM model, a pattern-mapping-based system with the name of UDMP is designed and implemented. The experiments show that the proposed model and the corresponding system can address the features of the IOT with relative good performance.

Keywords: Internet Of Things; data integration; view mapping.

1 Introduction

With the rapid development of the Internet of Things (IOT), and the growing demands of data management, data mining, data analysis in the application layer of IOT, the business data in both intra-industry and inter-industry need to be integrated. The integration of databases in the various distributed and heterogeneous subsystems has become a hot research topic. As the technical basis of data integration in IOT, Data middleware is the key technique to the integration and management of the distributed and heterogeneous data. Therefore, the study on data middleware has important significance for data integration.

For the current practical applications, along with the continuous system integration, the linkage and collaboration between subsystems, there are a large number of different types of application units in the application layer. Meanwhile, the storage formats and data specifications are diverse in the data layer, which constitute a number of heterogeneous data sources. These heterogeneous data sources make the data manipulation and data exchange more difficult.

The current research works take the implementation of "Query" as the main purpose of data integration. Data query is a "top-bottom" vertical process, because

F. Bian et al. (Eds.): GRMSE 2013, Part I, CCIS 398, pp. 298–312, 2013.
© Springer-Verlag Berlin Heidelberg 2013

one query operation does not affect the existence of data in another schema. This form of model construction and organization take the data as isolated objects during data manipulation and cannot establish mutual relations between these data in the patterns. However, in the systems of IOT, the basic data supporting environment calls for the maintenance of the global data integrity and consistency. This requires the data integration platform not only to achieve the unified query of heterogeneous data, but also to maintain the integrity and consistency of the heterogeneous data without violating the autonomy of the data resources in the global scope. Compared with data queries, operations which modify the data would cause more complex checks for data integrity and the corresponding modifications for data consistency. In this process, it is required not only to rewrite and decompose the data operation tasks to finish the current task, but also to establish corresponding operational tasks in order to maintain global integrity and consistency. Take the seismic industry as an example, the distributed data sources in various regions nationwide constitute the basic data supporting environment for the system. The organization and management of these data sources may be different.

Firstly, data models needs to be constructed so as to be mapped into every data source based on the business needs. The integrity and consistency constraints in the data model should be established so as to check the global data integrity together with the trigger mechanism of each data source, thereby integrating the entire data sources to ensuring the integrity, consistency and validity of data in the basic data supporting environment.

Secondly, more and more applications for IOT systems are written in the object-oriented way. These applications cannot seamlessly work together the rational databases because of the differences in their models, To overcome this impedance mismatch between the object model and the relational model, an object / relational mapping is essential for the system.

Thirdly, the data source has poor scalability, when a new data source is added, it is difficult to facilitate the integration of the new data or to dynamically adjust to the changes of the data sources. The traditional middleware mainly adapts the "black box" mechanism. The "black box" implementation mechanism cannot make an external application to access the system's internal structure and state behavior, and thus cannot be dynamically adjusted according to the relevant changes of the application layer or the data source layer. This limits the system’s scalability and adaptability to the dynamic environment.

The pattern is the basic starting point in heterogeneous data integration approach. Pattern mapping is the core technology to achieve integration of heterogeneous data sources [1-7].According to the different mapping styles, there are Global-As-View mode(GAV), Local-As-View mode(LAV) and Global-Local-As-View mode (GLAV).GAV defines the target mode as a view above the data source mode; LAV defines the data source mode as a view above target mode; GLAV combines the characteristics of both GAV and LAV.GAV inquires data through unfolding technology. One of the typical GAV projects is TSIMMIS. GAV performs high efficiency but poor scalability, which is unsuitable for IOT data environment.LAV queries data by the rewriting technology. The typical LAV project is the Information

Manifold.LAV can easily adapt to the dynamic changes of the underlying data. However, the process of transforming global data query into a local data query in LAV is much more complex than in GAV, which results in lower efficiency. GLAV focuses on the characteristics of those two former methods[7].The pattern matching and mapping generation are two key points of pattern mapping .Pattern matching is looking for different modes of mapping between data elements following particular rules. Study [8] proposes a method using machine learning to find the relationship between the global view and the data sources. This method is based on a global schema rules directory automatically finds between the source schema mapping between elements; This method automatically finds relationship the between the global view and the data source elements based on a rules directory; Study[9] proposes a value-based method for generating the corresponding mapping. The method establishes mapping by utilizing the relationship between the elements and semantic constraints of patterns.

The rest part of the paper is constructed as follows: Section 2 gives a detailed instruction of HDIM. Section 3 provides detailed design and implementation of original data middleware system UDMP. Section 4 conducts experiments and evaluation of UDMP. And Section 5 concludes the paper.

2 Data Integration Model HDIM

2.1 Definition of HDIM

This paper presents a Heterogeneous Data Integration Model(HDIM) based on pattern mapping. First, HDIM creates a globally unified view for all underlying data sources so as to shield the heterogeneous data sources and data structures through mapping. Second, HDIM provides a appropriate application view above the unified view so that all applications can be customized according to their needs.

Definition 1.Unified key. A unified key is the basic element to constitute a Unified data table, it establishes a direct mapping relationship with Keys in the entity data source. Unified key consists of four-tuple form: Ukey = (Ukname, Utname, {KMap}, {Fk});Ukname represents for unified key name, Utname is the name of unified data table which unified key belongs to, {KMap} is the mapping path from unified key to a set of key in data sources;

Definition 2.Mapping paths of the unified key. KMap consists of four-tuple: KMap = (Ukname, UVname, tname, kname); Ukname is the name of the unified key, UVname is Unified view name, tname is the original table name which unified table is mapping to, kname is the original key name which the unified key is mapping to. A unified key establishes mapping relationship to the original key by KMap.

Definition 3.Integrity relationship. Integrity relationship is defined by triple form: Fk = {parentUkey, dependentUkey, F}; ParentUkey represents for parent key, dependent Ukey represents for the sub-key; both of them are made of tuple form: parentUkey = dependentUkey = UKRef = (Utname, Ukname). Ukname represents for

unified key name, Utname is the name of unified data table which the unified key belongs to; F is a constrained label. When a parent key generates value changes, it will affect the value of sub-key. There are a set of integrity relationships in each unified key. For each change of the key value, HDIM checks the integrity relationship of the key in a global scope. Data changes cannot be carried out unless the integrity relations is satisfied.

Definition 4.The Unified table. Unified table is the globally unified logical and virtual table in the system. It defines all the underlying data source data in standards so that the system can adapt to the changes of database product or the database structure. The unified table is defined as follows: Utable = (Utname, {Ukey}).

Definition 5.The Unified data view. The Unified data view consists of triple form: UnifiedView = (UVname, Addr, {Utable}); UVname is the name of unified view; Addr contains the access information to the original data source, Addr aims at addressing and connection to the original data source. Utable stands for the unified data table. A unified key in the unified table may map to different original key in the underlying data source.

Definition 6.The Application view. The Application view consists of application data object. Data object is the specific logical data model of the application itself, which has the following form: DataObj = (DOname {Items}); DOname represents data object name,{Items} stands for a collection of attributes of the data object.

Definition 7.Attributes of data object. Data object attributes are the basic elements that constitute the application view, they each consists of a triple form: Item = (Itemname, DOname, {IMap}); Itemname is the attribute name, DOname is data object name, {IMap} path sets for the object attribute mapping;{IMap} is the mapping path from object attribute to a set of unified key in unified view. One object attribute has a unique name in the object, it can mapping to multiple data sources, however, the same data source path has only one mapping.

Definition 8.Mapping paths of object attribute. IMap consists of four-tuple: IMap = (Itemname, DOname, Utname, Ukname); Iternname is the attribute name, DOname is object name,Utname is the unified table name which attributes mapping to, Ukname is the unified key name which attributes mapping to. One object attribute unified key establishes the mapping relationship to one or several unified key by IMap.

Definition 9.Data resource integration model. The data resource integration model consists of a tuple form: GV = (DOs, UVs);DOs is the application data view for the application data set, UVs is the unified view of application data set.

Unified table and unified key establish a globally unified expression for heterogeneous and distributed data sources. Ukey defines integrity and consistency relationship of data. Applications submitted data objects DataObj for data access request. HDIM realizes the task mapping, decomposition and resolution according to IMap and KMap. Ukey establishes the integrity constraint relationship in order to maintain the global integrity of the data in case of data changes. Uview masks the differences between heterogeneous data sources. HDIM improves the flexibility and scalability of data integration in a view mapping way.

2.2 HDIM Mapping

In HDIM, there are three views: the application view, the unified view and the original data view; it also has two maps: IMap , KMap. IMap maps data objects in application view to the unified key in the unified view. The uniform access to data through a unified view of heterogeneous data entry defines a unified expression, KMap maps unified key in the unified view to the key in the original data source. The unified table and unified key establish a globally a unified expression for heterogeneous and distributed data sources. The unified view masks the differences between heterogeneous data sources and improves flexibility and scalability of HDIM. The applications view can provide customized data access service for specific applications. During the mapping process, DOname and Item specify application data objects and their attributes name, Utname and Ukname specify unified key name and unified table which the unified key belongs to, Addr realizes the data source location in the unified view, tname and kname represent the corresponding key in the original data source respectively, which the unified key is mapping to. Fig.1 shows a mapping between a data object and a table in the original data source.

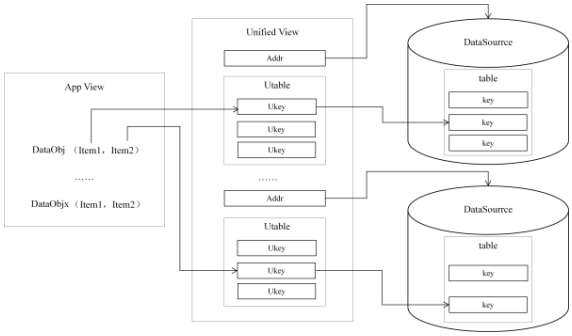

Fig. 1. Mapping of HDIM

Mapping process from data object to original key can be formalized as follows:

ForwardFullLink: item × GV→ Key

ForwardFullLink(item,GV)=ForwardLowerLink((ForwardUpperLink(item,GV)),UV)

ForwardUpperLink :item × GV→ Ukey

let utname = Getutname(Obj,item,Imap)

let ukname = Getukname(Obj,item,Imap)

ForwardUpperlink(item,GV)=GetUkey(Utname,Ukname,GV)

Getutname：Obj×item×Imap → utname

Getukname = Imap(Objname,itemname)

Getukname：Obj×item×Imap → ukname

Getutname = Imap(Objname,itemname)

GetUkey:utname × ukname× GV → Ukey

GetUkey(utn, ukn, GV)= let Uks = Ut(Utn)

let results = findUKey(ukn,Uks) in result

findUKey: ukname × Ukey* → Ukey

findUKey(ukn,Uk(Ukn,Utn,km*,fk*))=MatchName(ukn, Ukn) → Uk,null

findUKey(ukn,Uk:Uks)=findUKey(ukn,Uk):findUKey(ukn, Uks)=

let r = findUkey(ukn, Uk) in;

r = null→findUkey(ukn, Uks)

MatchName: string × string → Boolean

MatchName(s1, s2) =

s1 = s2 → true,false;

ForwardLowerlink :Ukey × UV→ Key

let tname = Gettname(Utname,Ukname,Kmap)

let kname = Getkname(Utname,Ukname,Kmap)

ForwardLowerlink(Ukey,UV)=Getkey(tname,kname,UV)

Gettname：Utname×Ukname×Kmap → tname

Getkname =Kmap-1(Utname, Ukname)

Getkname：Utname×Ukname×Kmap →kname

Gettname = Kmap-1(Utname, Ukname)

GetKey:tname × kname× UV → Key

GetKey(tn, kn, UV)= let ks = T(Tn)

let results = findKey(kn,ks) in result

findKey: kname × Key* → Key

findKey(kn,K(Kn,Tn))=MatchName(kn, Kn) → Key,null

findKey(kn,K:Ks)=findKey(kn,K):findKey(kn, Ks)=

let r = findKey(kn, K) in;

r = null→findKey(kn, Ks)

2.3 Data Manipulation Tasks of HDIM

A data manipulation task takes the application data object as an entity, through mapping, to do data extraction or modification operation in one or more corresponding original data source.

Definition 10.Task.A task is constituted by a four-tuple: GTask = (op, A, Obj, W),op stands for the data operation type, and its possible value can be: "SELECT" (data extraction), "DELETE" (data deletion), "INSERT" (add data), "UPDATE" (data update); A is the collection of data attribute which is constituted by object attribute definition: A = {attribute}; attribute = (item, value),item is the object attribute name, value is the data value, when op is UPDATE or INSERT, value is data record values which the object attribute is mapping to, when op is a SELECT or DELETE, value is null; O is a collection of data objects, Obj = {objname}; W is a set of constraints which consists of four-tuple form: (item, Obj, f, comp),item for the object attribute names, Obj for the data object name, f is the constraint value, comp is the constraint relationship.

In the task execution process, firstly select all objects properties in the task, and then transform the GTask into UTask or Task by mapping these properties. The selection of object properties can be formalized as follows:

GetItemFromTask：GTask× GV → {Item}

GetItemFromTask(gt,GV)=GetItemFromTask((op,A,O,W))=GetItemFromA(A,GV)∪GetItemFromW(W,GV)

GetItemFromW：W*× GV →Item*

GetItemFromW(w,GV)=

let result = FindItem(itemname,items,GV) in result

GetItemFromW(w:ws,GV)=GetItemFromW(w,GV)∪

GetItemFromW(ws,GV)

GetItemFromTask：GTask × GV→ {Item}

GetItemTask(GT,GV)=

let result = FindItem (itemname,items,GV) in result

FindItem: Itemname* × item*× GV →{ item}

FindItem(Itemname,item:items,GV)=GetItem(Itemname,item,GV)∪

GetItem (Itemname, items,GV)

FindItem(Itemname:Itemnames,items,GV)=FindItem(Itemname,items,GV)∪

FindVkeys(Itemname s, items,GV)

HDIM constructs the data model and submits the data access request based on application requirements. When the task engine accepts this request, it decomposes for each data source to perform a sub-task in accordance with the mapping of the data object. These sub-tasks execute in the distributed original data source. Final results of the sub-task are collected and return to the application. Data access process is shown in Fig.2:

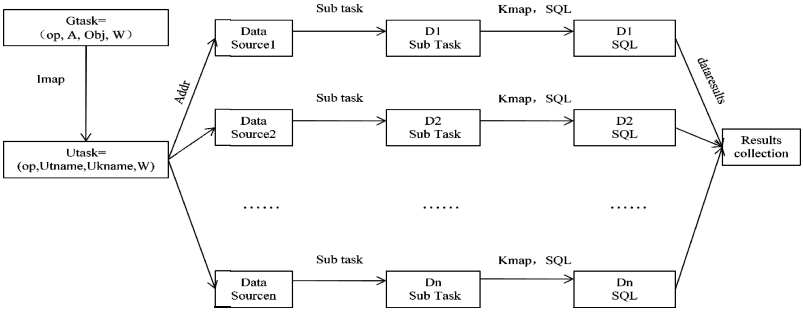

Fig. 2. GTask execution process

Task execution process can be formalized as follows:

ImplTask：GTask → dataresult

ImplTask(GT)=

letutsks = IMapTasks(GT) in;

let tsks = KMapTasks(utsks) in;

letrtsks= RelateTask(utsks) in;

let subresults = ImplsubTask(tsks:rtsks) in ;

collectData(subresults) ;

IMapTasks：GTask →UTask*

IMapTasks(GT) = let uv= FilterSource1(GT) in ;

letresult=CreateUTasks(GT,uv)) in;

FilterSource1: GTask →UVname *

CreateUTasks：GTask ×UVname* → UTasks

KMapTasks：UTask → Task*

KMapTasks(UT) = let uv= FilterSource2(UT) in ;

let result=CreateUTasks(UT,uv)) in;

FilterSource2: UTask →kname *

CreateTasks：UTask ×kname* →Tasks

RelateTasks：UTask → Task*

ImplsubTask: Task* → dataset *

ImplsubTask(tsks:rtsks)=ImplsubTask(tsks)∪

ImplsubTask(rtsks)

ImplsubTask(tsk:tsks)=ImplsubTask(tsk)∪ImplsubTask(tsks)

```
ImplsubTask(tsk) =
    let Sql = createSQLFromTask(tsk) in ;
    let con = createSQLConnection(tsk) in ;
    let d =execuSQL(con, Sql) in;
    letsubresult = d(con,tinfo,d)
```

2.4 Integrity Constraint Relationship Maintenance of HDIM

The entire data environment can be considered as a virtual database that consists of a large number of heterogeneous data sources. Each key of this virtual database is mapped to a real physical key in physical data sources. Constraint relationship exists between tables and keys in this virtual database, which forms a integrity constraints in the Unified View. When a unified key in the physical data generates changes, the value of other unified key will be influenced, which has the integrity or consistency relationships with it in a global scope. Integrity relationship is defined by triple form: Fk = {parentUkey, dependentUkey, F}; ParentUkey represents for parent key, dependentUkey represents for the sub-key; both of them made by tuple form: parentUkey = dependentUkey = UKRef = (Utname, Ukname).Ukname represents for unified key name, Utname is the name of unified data table which the unified key belongs to; F is a constrained label.

In the Unified View all integrity constraint relations constitute a diagram, where the unified keys are the vertex and the constraint relationship Fk between unified keys are the edges. Fig.3 is an example of the relationship diagram:

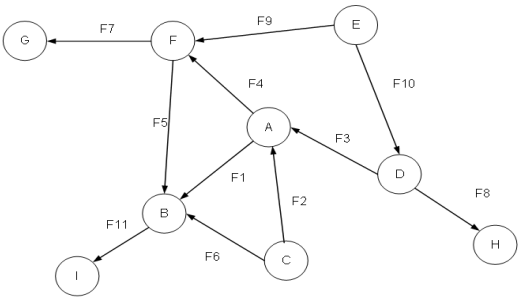

Fig. 3. Constraint relation tree of node A

In the figure, Point A, B, ...stand for unified key, while Edge F1, F2, ... stand for the relationship definition between unified keys. In the definition of integrity constraint relationship, if a unified key is a sub-key, the integrity relationship of this unified key is considered as an inverse relationship, then the relationship of the edges corresponding to the unified key is called backward edge. On the contrary, if a unified key is a parent-key, the integrity relationship of this unified key is then considered as an forward relationship, the relationship of the edges corresponding to the unified key is called forward edge. During the execution of the task, HDIM needs to the select the corresponding constraint relationships according to operate type to complete data integrity checks.

According to the operate type, data integrity check can lead to the following different occasions:

- Select operation: since there are no data changes, so do not make any integrity checks in the global scope.
- Delete operation, Needs to do forward integrity checks in global scope on the unified key which is about to change.
- Insert operation, Needs to do backward integrity checks in global scope on the unified key which is about to change.
- Update operation, Needs to do forward and backward integrity checks in global scope on the unified key which is about to change.

Forward and backward relationship tree are shown as follows:

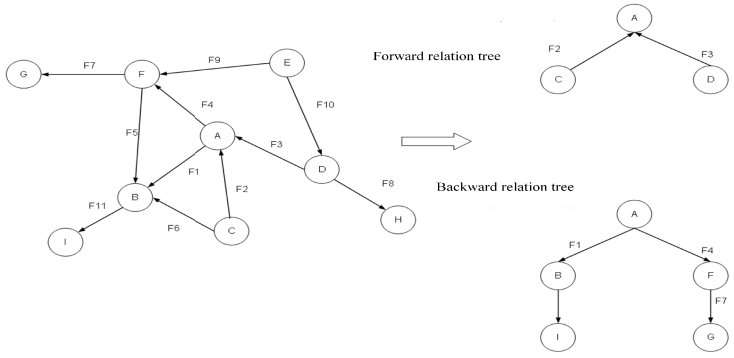

Fig. 4. Forward and Backward relationship tree of node A

In the integrity relationship tree, Each node stands for a unified key, a branch represents the constraints between a parent node and a child node. Relationship tree is defined as: RTree = (UK, {node});UK is the root node, UK = (Utname, Ukname), {node} is the set of nodes. In Rtree, one node corresponds to a unified key, while edge is the integrity relationship Fk. Node consists of a triple form: node = (UK, Fk, {node}),{node} is a set of its child nodes.

Forward integrity relationship check process can be formalized as follows:

CheckPKs：Ukey *× GV× RTree→ Boolean

CheckPKs(Uk, GV ,GT) = CheckPK(Uk , GV ,GT)

CheckPKs(Uks,G,GT)=CheckPKs(Uk:Uks,GV,GT)=CheckPK(Uk,GV,GT)∪

CheckPKs(Vks , GV ,GT)

CheckPK：Ukey × GV × RTree→Boolean

CheckPK(Uk,GV,RTree)=CheckPK(Uk,GV,CreatePTree(Uk,GV))

CreatePTree:Ukey × GV →RTree

CreatePTree (Uk, GV) =

ukn' (Ukn, Utn,-,-)= Uk ;

let nodes = CreateNodes(GetPFk(Uk,GV)) in ;

RTree((ukn,utn) , nodes) ;

CreatePNodes：Ukey × Fk* → node *

CreatePNodes(Uk, fk)= CreatePNode(Uk, fk)

CreatePNodes(Uk,fk:fks)=CreatePNode(Uk,fk)∪

CreatePNodes(Uk, fks)

CreatePNode：Ukey ×Fk ×GV → node

CreatePNode(Uk, fk , GV)=

letukref (utn,ukn)= GetPairKey (Uk , fk) in ;

letuk=GetUkey(utn,ukn,GV) in ;

let pnodes = CreatePNodes(uk,GetPFk(uk,GV)) in ;

let result = n(ukref, fk , pnodes)

3 Design and Implementation of Prototype System UDMP

In this section we designs and implements a three-view two maps UDMP(unified data management platform). It supports unified data manipulation and aggregation for all heterogeneous data sources, and allows the users to configure the view themselves. UMDP creates a unified global logical view for heterogeneous data objects in the system. Through this unified global logical view it masks underlying data heterogeneity. Above the logical view, UMDP provides specific application theme view for different applications so that each application can customize specific data objects to do CRUD(Create, Retrieve, Update, Delete) operations according to their needs. The platform architecture is shown in Figure 1:

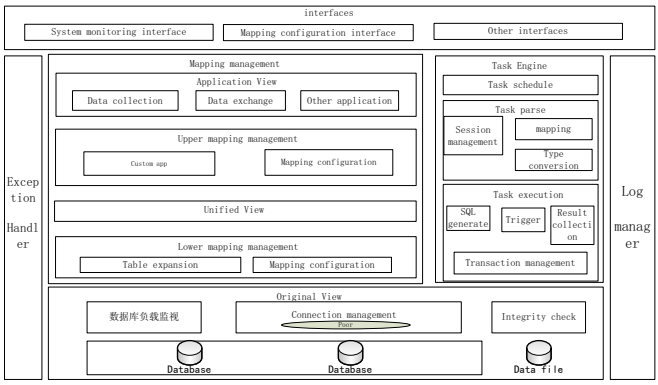

Fig. 5. System structure of UDMP

UMDP is composed by four major components: the mapping management, the execution engine, the application interfaces and the database interfaces.

Mapping management includes three data views: the database original view, the unified view and the application theme view. Unified data view is the global unified logical view of the data. Unified view mapping to the original view can mask differences in the way data is stored and the data structural isomers. Meanwhile, Application theme view mapping to unified view can provide convenient operation of customized data set to applications, which increase the flexibility of data manipulation.

Task execution engine includes the task scheduling, task analysis and task implementation. When a task arrives, it is queued by its priority first. In the implementation phase, the object data is parsed to original data sheet and SQL statement and then be executed.

System users can edit view mapping content through mapping configuration, including add, delete and modify the data object in the application theme, data sheet in the unified view and original view. This makes UDMP to some extent a white box, which increases system flexibility and scalability. In addition, the platform provides transaction support to data collection interface, and corresponding trigger mechanism supports the data exchanging.

4 Experiment and Analysis

4.1 Experimental Environment

The setup of both the hardware and software environment for the test are listed as follows:

Table 1. Experimental environment

Nodes	Ip	Hardware	Software
Middle node database server	10.2.101.100	cpu: 8-core;	1.Suse Linux Enterprise
Middle node application server	10.2.101.101	memory: 4G;	10 2.Oracle10g
Lower node2 database+application	10.2.101.102	hard dsisk:	for Suse Linux
Lower node3 database+application	10.2.101.103	120G	3.jdk-/1.6
Lower node1 database server	10.2.101.104		
Upper node1 application server	10.2.101.105		
Upper node1 database+application	10.2.101.106		
Lower node4 database+application	10.18.220.220		

4.2 Experiment Result

In this chapter we compare the performance of UDMP and hibernate data platform[10], which is the mainstream data middleware using O/R mapping and command persistence management.

Experiments are as follows: 20,000 data records are randomly generated, each with the size 1K.We insert, query, modify and delete these records by 100 concurrent threads. The selected database is Oracle.

Table 2. Experimental result

No	Experiment	*UDMP*	*Hibernate*
1	Insert 20,000 records, each 1k, record average time-consuming	158314ms	193585ms
2	Select those record, record average time-consuming	31240ms	35086ms
3	Update those record, record average time-consuming	39344ms	43190ms
4	Delete those record, record time-consuming	33773ms	34536ms
5	Simultaneous 100 concurrent data access continuously for 300 minutes to see whether there is abnormal situation	stable, no exception	stable, no exception
6	Insert 100 records, each 30M, record average time-consuming	388942ms	305351ms

The performance diagram of UDMP and hibernate is shown in figure 6.

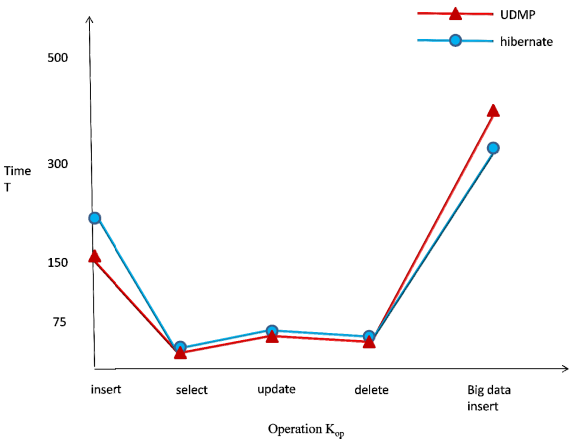

Fig. 6. Experiment results

Comparative results show that the performance of UDMP is better than that of hibernate in case there are data objects of very large size. In the manipulation process of large size data objects, object reconstruction during task parsing, type conversion, memory management and other aspects of pressure make the efficiency of UDMP slightly lower than hibernate, but it is still in line with the standard range.

This chapter selects an application scenario of national earthquake precursors platform as a test scenario to conduct the experiment and evaluate the performance of UDMP practically. Test results shows that UDMP can achieve uniform data access and data management, and give a better performance than hibernate.

5 Conclusions

Although relatively distributed, heterogeneous, the data resources within the basic data supporting environment of IOT systems still demand unified organization and management. The previous research works in data integration focus on the data query and modeling, while the studies in the constraints relationships among the heterogeneous data within the environment is insufficient. To address these issues, a HDIM model is proposed for the collaboration and integration of heterogeneous data. HDIM model builds the hierarchical presentations of the Applied View – the Unified View –the Original Data View, wherein, the corresponding data access objects are generated in the Applied View to provide the customized data access service for applications; the global unified standard logical view is built in the Unified View; through the above 3-level mappings, the data is processed. Additionally, the constraints check model is built among the Unified data item within the Unified View, so as to construct the complete integrity relationship for the entire data supporting environment, realize the maintenance of the integrity and ensure the data collaborations among the distributed heterogeneous data sources. After that, the HDIM-model-based prototype system UDMP is designed and implemented considering the actual requirements and characteristics of the data and business in seismic field. UDMP sets the unified and formal data storage format and data access standard for transparent access to the data sources; it also decomposes the applications and the data structures and objectifies the upper-layer applications for efficiency improvement; it provides the configuration functionalities for view mappings and convert the data middleware into a “white-box” to allow the flexible replacement and expansion of the underlying databases by configuring the parameters. Experiments show UDMP can fulfill all the required functionalities and its efficiency for data operation is relative high.

References

1. Liu, L., Li, H.: Metadata Model in Grid Database and its Application. In: The 9th International Conference on Computer Supported Cooperative Work in Design, UK, pp. 362–366 (2005)

2. Guo, H.-M., Ma, S.-L.: Functional demand-driven resource aggregation method and implementation. Journal of Beihang University 34(5), 260–262 (2008)
3. Yang, Y.-Q., Ma, S.-L., Wen, J.: Method for data integration mechanism for maintaining data integrity. Journal of Beihang University 34(9), 1045–1048 (2008)
4. Guo, H.-M., Hao, G.-S.: Heterogeneous data integration and coordination in NGG. Journal of Beihang University 34(2), 180–182 (2008)
5. Wang, G.-L., Li, Y.-S., et al.: A service Grid Dynamic Information Aggregation Model and Its Application. Journal of Computers 28(4), 541–548 (2005)
6. Yeom, K.-W., Park, J.-H.: An Evolutionary Approach for Dynamic Reconfiguration in Heterogeneous Database Schemas. In: IEEE Congress on Evolutionary Computation Sheraton, Vancouver, Canada, pp. 162–166 (2006)
7. Nguyen, T.N.: Object—Oriented Software Configuration Management. In: 22nd IEEE International Conference on Software Maintenance, ICSM 2006, pp. 351–354 (2006)
8. Lenzerini, M.: Data Integration: A Theoertieal Pesrpective. In: Proceedings of the 21st ACM SIGMOD-SIGACT-SIGART Symposium on Principles of Database Systems, pp. 233–246. ACM, New York (2002)
9. Hu, C.-M., Huai, J.-P., Wo, T.-Y.: An end to end Support Service Grid Architecture. Journal of Software 17(5), 1448–1458 (2006)
10. King, G., Baue, C.: Hibernate in Action. Manning Publications Co. (2004)

Geoinformatics Production for Urban Disasters Risk Reduction: A Zero Cost Solution*

Zhichong Zou[1] and Xunguo Lin[2]

[1] Department of Urban Planning, School of Architecture,
Harbin Institute of Technology. Harbin 150001, Heilongjiang, China
[2] CSIRO Computational Informatics,
Canberra 2601, Australian Capital Territory, Australia
{zhichong.zou,xunguo.lin}@csiro.au

Abstract. Catastrophic events (such as natural disasters) bring more damages to urban area than rural places because of high density of human population, properties and infrastructures. Geo-informatics is critical for all stages of disaster management. It is critical for risk assessment of natural disasters. Based on a research project of urban natural disaster vulnerability measurement and risk assessment, this paper illustrates a zero cost solution of geo-informatics semi-automatic production by using open-source and free-access geo-software. In order to enrich attributes to meet the requirements of risk assessment, methods of combining the produced geo-informatics with other format of geo-data (e.g. DEM, raster layers, vector layers, Microsoft Excel files, etc.) are introduced. The geo-informatics developed from this research forms a basis for disaster vulnerability measurement which is a part of disaster risk assessment.

Keywords: Geo-informatics, GIS data production, natural disasters, urban risk reduction.

1 Introduction

One of the priority purposes of the Hyogo Framework for Action 2005-2015 for disaster risk reduction is the use of knowledge, innovation and education to build a culture of safety and resilience at all levels of government [1].

According to the United Nations International Strategy for Disaster Reduction (UNISDR) disaster data and statistics report, in the past three decades (1980 2011) there were 3455 floods, 2689 storms, 470 droughts, and 395 extreme temperature events occurred around the world. In the last 12 years (2000 - 2011), natural disasters have caused about 1.3 trillion USD losses, affected 2.7 billion people, and killed 1.1 million people[2].

Since all natural hazards risk components locate specifically and vary spatially, accurate risk assessment relies on geo-informatics. Geo-informatics as the basis of decision-making information was proved to be critical and essential to natural, technological and man-made disaster risk assessments.

* This paper is supported by China Postdoctoral Science Foundation funded project.

F. Bian et al. (Eds.): GRMSE 2013, Part I, CCIS 398, pp. 313–324, 2013.
© Springer-Verlag Berlin Heidelberg 2013

Expenses of geo-informatics ranges vastly with different updating frequency, quality, and total amount of information it carries. Contrasting with commercial sources, free geo-data and geo-software have limited comparable features. However, they are free to add new features by further development.

Based on a study of urban natural disaster risk assessment and vulnerability mapping which aims at improving community safety and resilience to natural hazards, this paper shares our experience on a zero cost method for semiautomatic geo-informatics production by using free Internet resources of Google Maps, Google Earth, and free and open-source software including QGIS, and Orfeo Toolbox (OTB).

The rest of this paper is organized as follows. In Section 2, a method of acquiring Google high resolution satellite images and a fast geo-referencing approach introduced. In Section 3, a pixel based Support Vector Machine (SVM) supervised classification procedure for satellite imagery feature detection and extraction is illustrated. In Section 4, QGIS based semiautomatic procedure for large dataset processing is demonstrated. Finally, in Section 5, a method to enrich attributes from raster layers, vector layers, and MS Excel files is introduced.

2 High Resolution Satellite Images Acquisition from Google Maps

Google Maps is a web mapping service application and technology provided by Google. Google Maps powers in many map-based services, including the Google Maps website, Maps for mobile, and maps embedded on third party website by using Google Maps API.

Higher resolution images are used for more interesting locations and more populated places, such as urban areas. And rural areas tend to have less detail available in the imagery. The best resolution is less than 60cm per pixel and the worst is about 450cm per pixel.

Google Earth and Google Maps share the same satellite image database. The satellite images are not updated in real time, but rather they are several months or years old. From our experience, images of some areas may be updated more frequently.

Google allows the use of satellite images for non-commercial, non-violent, non-invasive purposes only. Google obscures sensitive or private information and will not allow any commercial use of their images.

Google satellite images are accessible by both API and Internet browsers. Method of acquiring satellite imagery form Google Maps with Firefox and its add-on screen grab tool is published on website of DetailDesignOnline[1] [3].

For a following process of urban disaster risk assessment, satellite images need to be geo-referenced. In our example, QGIS (Quantum GIS) as a free and open-source GIS is employed for this task.

To geo-reference satellite images, normally at least three Ground Control Points (GCPs) are needed. While in our case there is not such existing (known)

[1] DetailDesignOnline website: `http://www.detaildesignonline.com`

GCP on the satellite images which were captured from Internet browsers. The only (geo-coordinate) known point of each image is its central point, which can also be used for geo-reference processing by QGIS with its 'OpenLayers' Plugin. See Figure 1.

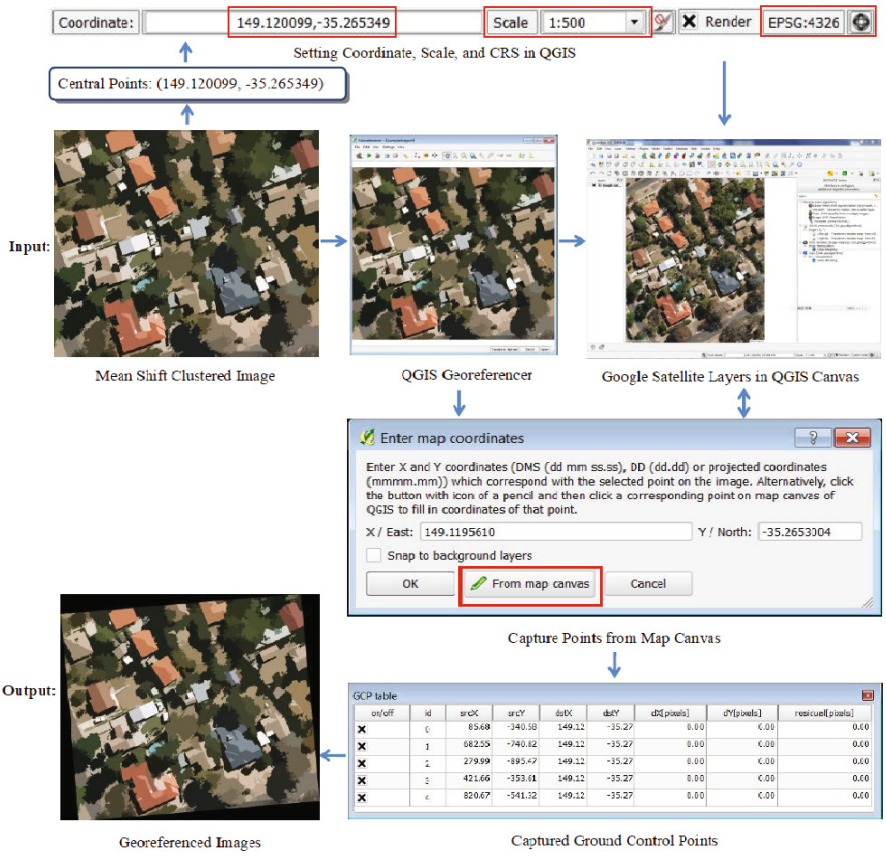

Fig. 1. Image Geo-referencing in QGIS

3 Feature Detection and Extraction

To protect both public and private properties, geo-informatics of houses, buildings, streets, vegetation and other land covers are required for vulnerability measurements and risk modelling. The high resolution Google satellite images acquired by the above method could not directly provide such information.

For free and open-source geo-software solution consideration, Orfeo Toolbox is used for this task. OTB is a library for (both optical and radar) remote sensing

image processing, which is implemented in C++ and based on ITK [2]. The OTB project was initiated by CNES (French Space Agency) in 2006 and is under heavy developments and the participation from the open source community.

The library was originally targeted at high resolution images acquired by the Orfeo Constellation. OTB provides image access, data access, filtering, feature extraction, image segmentation, classification, change detection, map projections, radiometric indices, principal component analysis computation, flexible visualization, and more functionality is under development[4].

Besides the OTB development team, great contribution was from its user group who aimed at improving OTB algorithms for more flexible use in the real world [5] [6] [7] [8] [9] [10].

Because of its advantages of efficient performance, free license, and open-source, OTB is utilized globally for multiple purposes of research, teaching, and even commercial usages. On disaster risk and relative researches, OTB has been broadly used in change detection [11] , object counting [7], building detection for disaster response [12], road extraction [13], urban area detection [14], and urban critical infrastructure protection [15].

3.1 Segmentation

Segmentation produces homogeneous clusters or objects each of which is associated with additional attributes such as mean, variance, shape index, textural measures, etc. depending on the segmentation methods. Aim of segmentation is to lower the complexity of the input data and increase accuracy of classification.

The level of details of details available in high resolution images can have a strong negative effect at some stages of the processing. For instance roof superstructures are irrelevant when trying to extract the whole building.

The mean-shift algorithm provides an efficient way to simplify such images [**?**]. In addition, mean Shift segmentation also helps to open the original image into a multi-scale space to allow the incorporation of scale into classification [16].

In our example, Monteverdi (GUI version OTB) is employed for mean-shift segmentation. A demonstration example of OTB mean-shift segmentation is shown as Figure 2(with parameters settings: spatial radius is 30, spectral value is 45.5, and minimum region size is 100).

3.2 Pixel-Based Processing and Object-Based Detection

There are two main methods to achieve feature extraction from remote sensed imagery: pixel-based processing and object-based detection [12].

Pixel-based processing is a procedure analyses the spectral properties of every pixel or picture element within the area of interest [17]. Pixel-based analysis was originally designed for use with coarse resolution imagery.

Problems and limitations of using pixel-based procedure on Very High Resolution (VHR) imagery analyzing were pointed out [18]. Pixel-based methodology

[2] ITK (Insight Toolkit): `http://www.itk.org`

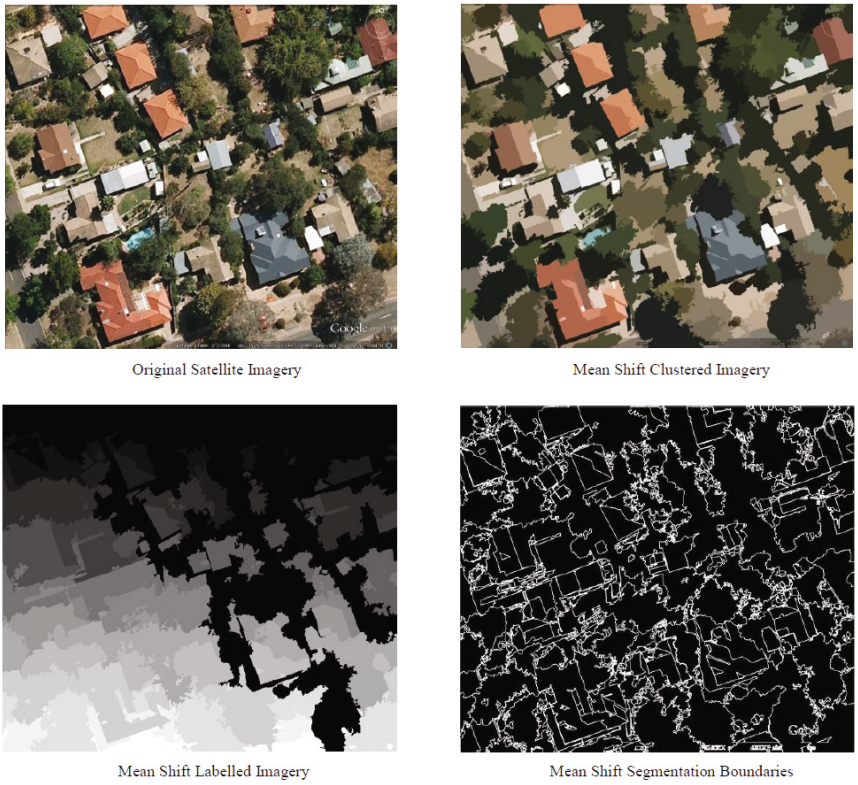

Fig. 2. OTB mean-shift segmentation and edge extraction

cannot set a minimum mapping unit, resulting in an over-classification of individual pixels. Advantage of this method is straightforward and fast, which is much suitable for comparison of a pair images of pre- and post- disaster.

Object-based detection is a method to analysis spectral, spatial, and contextual properties of pixels. It uses a segmentation process and iterative learning algorithm to achieve a semi-automatic classification procedure.

OTB object detection is a supervised object detection chain adapted to limited extent object with strong shape features, such as planes, boats, roundabouts, and fixed-shape buildings. OTB object detection applications are not published in its latest version 3.16, while the illustration of this method was shared on international conference of IGRASS 2011 [19].

In our example, pixel-based detection method is used for classification task. In Canberra many roofs are covered or shadowed by trees leaves. Houses with shadows on roofs are near to plants, which are regarded fuel in bushfire. Such houses are in higher physical vulnerability ranks. Roof shapes of those exposed parts are irregular. And object-based detection method is not suitable for irregular shape detection.

Although pixel-based detection has limitation in VHR images processing; such as errors appear when roofs are in same colour with ground surface. Most of those errors can be corrected in the following geo-analysis and geo-processing.

3.3 Support Vector Machines (SVM) Classification

In OTB statistical classification, each object is represented by d features, and the goal of classification becomes finding compact and decision regions for classes in a d-dimensional feature space. Such decision regions are defined by decision rules that are known or can be trained with a priori knowledge [4].

OTB SVM classification provides a supervised pixel-based classification chain based on learning from multiple images. It supports large images through streaming and multi-threading [20]. The classification chain performs a SVM training steps based on the intensities of each pixel. Standard OTB SVM classification chain concludes steps: (1) images statistics estimation; (2) building up training dataset; (3) training SVM model; and (4) SVM classification.

Comparison of the original satellite image, SVM labelled result, and colour mapped SVM classification image are shown as Figure 3. In colour mapped result image, red colour represents roofs, green represents vegetations, yellow represents land, and blue represents road.

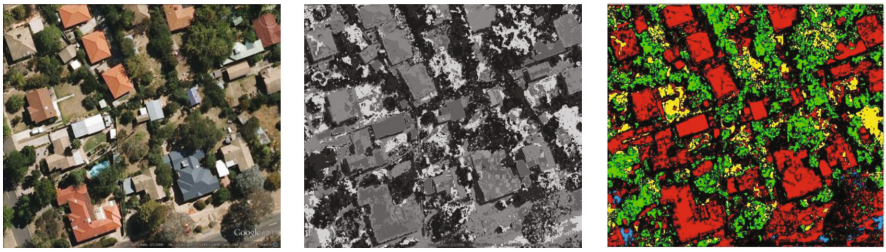

Fig. 3. Comparison of original satellite image, SVM labelled result, and colour mapped result

Limited by the original data sources and acquisition method, elevation of buildings and houses cannot be extracted from the captured Google satellite imagery. Elevation also cannot be estimated by produced geo-informatics. Although it was pointed out building elevation can be estimated by its shadow length, we found it is hardly to measure shadows length. Because trees and houses are too adjacent to each other, their shadows are either mixed together or projected on the walls. It is impossible to use shadow length for elevation estimation in this condition. Individual building height can be probably estimated by Google Building Maker and Google SketchUp, while for massive geo-data producing it is difficult to get elevation information of all buildings.

4 Semiautomatic Procedure for Large Dataset

According to our experience, it has been proofed there are two efficient methods for large dataset processing automatically or semi-automatically.

Automatic method is to use OTB-wrapping and bind it with other languages. OTB is an open-source library compiled by C language. Its source code is free to download and use at OTB website.

By binding with other languages, almost all OTB applications are available and can be used flexible according to users purposes.

Semiautomatic method is to use OTB applications on QGIS platform with spatial analysis plugin 'Sextante'. Actually, Sextante supports more external applications than OTB algorithms, such as GRASS, SAGA, PostGIS, and LIDAR images processing functionalities. And it supports Python scripts and R scripts running as flexibility for users own algorithms applications.

Conveniently Sextante has a graphic modeller tool, which allows user generate models as processing procedures with combining algorithms, scripts, and models. Sextante is suitable for large dataset processing because all of its algorithms and models can be execute as batch process.

In our example, we devide the 800 pieces of images into 20 groups (begin with the same letter). Each group has 40 images. A designed Sextante model runs 20 times in batch execution would finish all processing.

Three modules are designed by Sextante graphic modeller, and named as Module I, II, and III. Module I is designed with functionality of images SVM classification and polygonization. Module II is to set attribute values to extracted features from Module II, such as acreage and area, boundary perimeters, and geometry coordinate. Module III is for features extraction and errors correction. Structures and functionalities of these three modules are shown as Figure 4, Figure 5, and Figure 6 separately.

5 Attributes Enrichment

Necessary attributes of features relative to location information and disaster characters need to be endowed for further calculation and computation. By merging with other geographic and demographic information on QGIS the produced geo-informatics can be enriched in attributes.

5.1 Attributes Enrichment from Raster Layers

Extracted features attributes can be enriched with information carried by all raster files. As an example,90 m Digital Elevation Model (DEM) raster layer is combined to attribute tables by a core QGIS plugin tool called 'Zonal Statistics', as shown in Figure 7.

To assign correct elevation value to each feature, the DEM raster and produced vector must be in the same CRS. Zonal Statistics has only few fixed statistics computation, as count, sum, and mean. More statistics complex calculation can be performed by Grid Statistics from SAGA GIS. It is also accessible from Sextante toolbox.

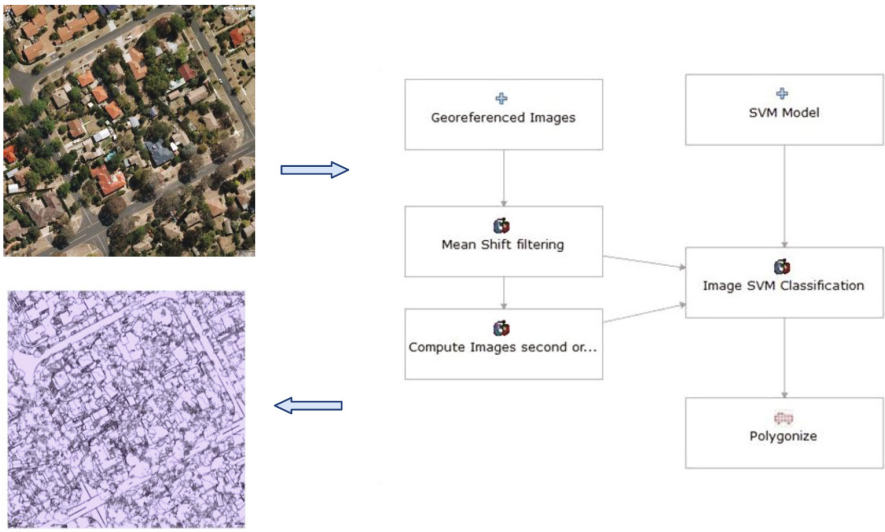

Fig. 4. Structure and functionality of Module I

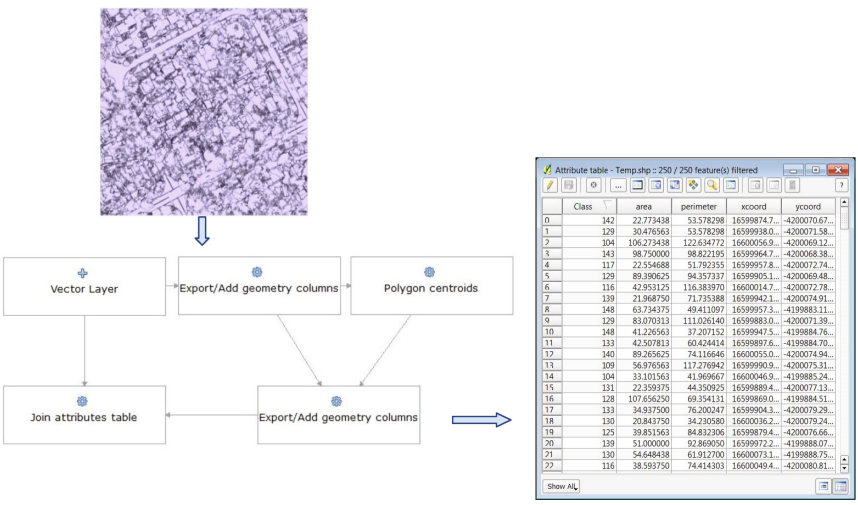

Fig. 5. Structure and functionality of Module II

5.2 Enrichment from Vector Layers

Attributes can also be enriched from all vector layers, which contain a lot of useful information can be used to enrich the produced geo-data. QGIS plugin 'Join Attributes by Location' combines attributes of two vector layers according

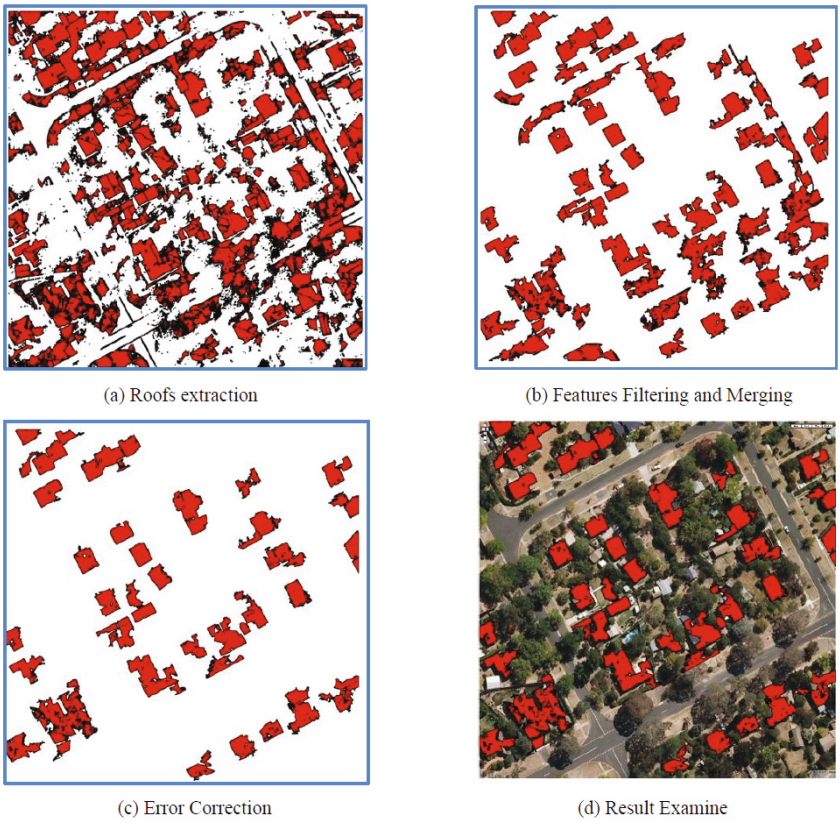

Fig. 6. Functionalities of Module III (roofs layer example)

to their locations. By joining a point layer into a polygon layer, the attributes combined together where their representative features are at the same location. See Figure 8.

5.3 Combining with Excel Tables

The produced vector layers can also be enriched by combining with Microsoft Excel file (or other formats can be convert into Excel files), which must have columns of x and y coordinate. To read and write Excel tables, python libraries of python-xlrd and python-xlwt are necessary. A QGIS plugin named x-y tool can convert Excel tables and x-y point layers by import and export functions. By x-y tool a Excel file is accessible to convert to a point layer in QGIS.

Attributes of the produced geo-informatics can be enriched from multiple sources of data, by converting them into raster layers, vector layers, and Excel files. More comprehensive, attributes of produced geo-informatics can be enriched from all tables by language R with spatial analysis packages.

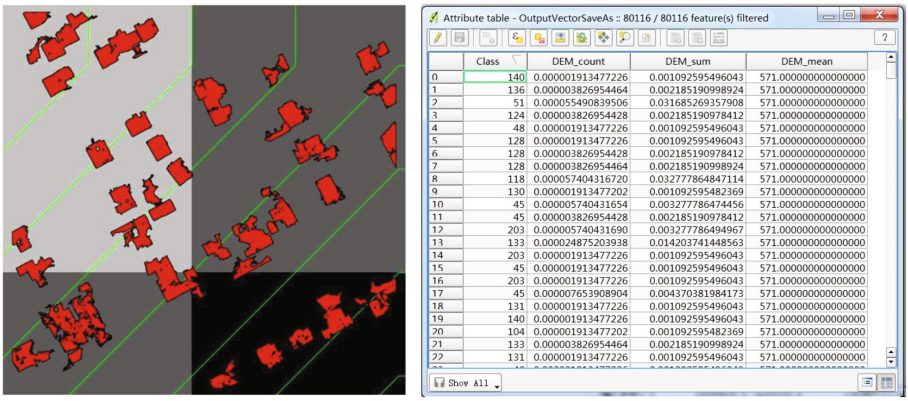

Fig. 7. Acquiring elevation values form DEM raster layer

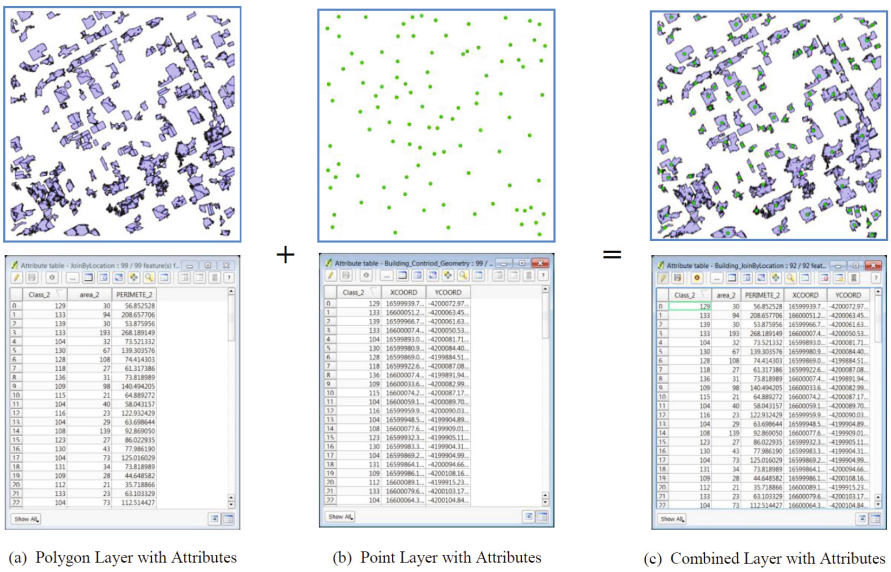

Fig. 8. Attributes combination from vector layers at the same location

6 Conclusion

Experience and approaches of a zero cost solution for semiautomatic geo-informatics production is introduced based on a research project of urban natural disaster risk assessment and vulnerability mapping. As raw material to produce geo-data, timely high resolution satellite images can be acquired from Google Maps and Google Earth by several approaches. In this paper a Internet browser based acquisition method is introduced. Orfeo Toolbox as a free and

open-source library for remote sensing task is handy and helpful for satellite imagery analysis and features extraction. OTB pixel based SVM classification is employed for satellite image analysis and feature extraction where would be used for urban disaster risk assessment in our project as illustrated in paper. Fundamental and necessary attributes of the produced geo-data can be enriched from other data source by QGIS. Although there are limited comparable features to the commercial resources, free geo-data and open-source geo-software can be developed to meet multiple demands with large flexibility.

Acknowledgments. The research of Urban Natural Disasters Risk Assessment and Community Vulnerability Measurement Mapping is supported by both Chinese Scholarship Council and Australian Commonwealth Scientific and Industrial Research Organisation (CSIRO). The authors thank to Dr. Warren Jin (CSIRO, Division of Computational Informatics) for his administration of QGIS on a super computer, which was used to produce the geo-informatics introduced in this paper.

References

1. Zschocke, T., de León, J.C.V.: Towards an ontology for the description of learning resources on disaster risk reduction. In: Lytras, M.D., Ordonez De Pablos, P., Ziderman, A., Roulstone, A., Maurer, H., Imber, J.B. (eds.) WSKS 2010. CCIS, vol. 111, pp. 60–74. Springer, Heidelberg (2010)
2. UNISDR. Statistics of Natrual Diasters (1980-2011) (2012)
3. Bimpson, A.: Capturing High Resolution Satellite Imagery from Google Maps (2010)
4. OTB Development Team. The ORFEO Tool Box Software Guide Updated for OTB-3.16. Centre National D'etudes Spatiales, France (2013)
5. Christophe, E., Inglada, J.: Open source remote sensing: Increasing the usability of cutting-edge algorithms. IEEE Geoscience Remote Sensing Society Newsletter 4, 9–15 (2009)
6. Ferson, S., Siegrist, J., Agarwal, J., Liu, M., Blockley, D.: Copyright ASCE 2011 ICVRAM and ISUMA 2011 VULNERABILITY, UNCERTAINTY, AND RISK Copyright ASCE 2011 ICVRAM and ISUMA 2011 (1981), 62–69 (2011)
7. Inglada, J., Christophe, E.: Object counting in high resolution remote sensing images with OTB. In: 2009 IEEE International Geoscience and Remote Sensing Symposium, IGARSS 2009, pp. 737–740 (2009)
8. Lahlou, O., Michel, J., Pichard, D., Inglada, J.: Assessment of interest points detection algorithms in OTB. In: 2009 IEEE International Geoscience and Remote Sensing Symposium, IGARSS 2009, vol. 4, pp. IV–749. IEEE (2009)
9. Michel, J., Feuvrier, T., Inglada, J.: Reference algorithm implementations in OTB: Textbook cases. In: 2009 IEEE International Geoscience and Remote Sensing Symposium, IGARSS 2009, vol. 4, pp. IV–741. IEEE (2009)
10. Tinel, C., Fontannaz, D., de Boissezon, H., Grizonnet, M., Michel, J., Boissezon, H.: The ORFEO acompaniment program and ORFEO ToolBox. In: 2012 IEEE International Geoscience and Remote Sensing Symposium (IGARSS), pp. 7102–7105. IEEE (March 2012)

11. Mercier, G., Inglada, J.: Change Detection with Misregistration Errors and Heterogeneous Data Through the Orfeo Toolbox. gregoire-mercier.fr, 1–11 (2008)
12. Dubois, D., Lepage, R., De, É.: Object- Versus Pixel-Based Building Detection for Disaster Response. In: The 11th International Conference on Information Sciences, Signal Processing and their Application, pp. 5–10 (2012)
13. Christophe, E., Inglada, J.: Robust road extraction for high resolution satellite images. In: IEEE International Conference on Image Processing, ICIP 2007, vol. 5, pp. 437–440. IEEE (2007)
14. May, S., Inglada, J.: Urban area detection and segmentation using OTB. In: 2009 IEEE International Geoscience and Remote Sensing Symposium, IGARSS 2009, vol. 4, pp. IV–928. IEEE (2009)
15. Lukas, L., Hromada, M.: Utilization of the EASI model in the matters of critical infrastructure protection and its verification via the OTB SAF simulation tool. In: 13th WSEAS International Conference on AUTOMATIC, Canary Islands, Spain, pp. 131–136 (2011)
16. Vu, T.T.: Object-Based Remote Sensing Image Analysis with OSGeo Tools. In: AGSE 2012 FOSS4G-SEA, p. 79 (2012)
17. Riggan Jr., N.D., Weih Jr., R.C.: A comparison of pixel-based versus object-based land use/land cover classification methodologies. Journal of the Arkansas Academy of Science 63, 145–152 (2009)
18. Whiteside, T., Ahmad, W.: A comparison of object-oriented and pixel-based classification methods for mapping land cover in northern Australia. In: Proceedings of SSC 2005 Spatial Intelligence Innovation and Praxis The National Biennial Conference of the Spatial Sciences Institute, Melbourne, Australia, pp. 1225–1231 (2005); Spacial Sciences Institute
19. Christophe, E., Michel, J., Inglada, J.: Remote Sensing Processing: From Multicore to GPU. IEEE Journal of Selected Topics in Applied Earth Observations and Remote Sensing 4(3), 643–652 (2011)
20. OTB Development Team. The Orfeo ToolBox Cookbook, a guide for non-developers Updated for OTB-3.14. Centre National D'etudes Spatiales, France (2012)

A Joint Weight Based Dynamic Clustering Algorithm for Wireless Sensor Networks*

LeiChun Wang, YanMei Li, and GuoYu Zhou

Faculty of Mathematics & Computer Science, Hubei University, 430062 Wuhan, China
wlc2345702@163.com

Abstract. Wireless sensor networks (simply WSN) is required to save the energy and prolong network lifetime when aggregating and transmitting data efficiently sampled by nodes. This paper put forwards a joint weight based dynamic clustering algorithm for WSN, JWDC. In cluster head selection phase, JWDC selects appropriate nodes as cluster heads by the weight model for cluster heads selection. In cluster formation phase, a sensor node chooses a proper cluster head to be one of its members according to the weight model of nodes clustering. Simulation results show that JWDC outperforms CDN and PPC in terms of network lifetime, data traffic and average quality of data aggregation.

Keywords: WSN, Spatial Correlation, Joint weight, Clustering.

1 Introduction

Sensor nodes in WSN have extremely limited energy, and they are frequently discarded or failure because their power energy is exhausted. Therefore, it is the key task to save energy and prolong network lifetime when aggregating and transmitting data sampled by nodes in WSN.

In WSN, advantages of cluster schemes are good network extension, smaller expenditure of route and control, distributed applications and load balance, and convenient data aggregation, and so on [1~2]. At present, clustering algorithms in WSN [1~6] usually cluster nodes in the network by residual energy, times as cluster heads and the distance between a node and a cluster head. The cluster techniques can reduce and balance energy consumption in the network and prolong the network life. However, the algorithms can lead to uneven distribution in cluster heads and bigger differences among data sampled by nodes from the same cluster since they don't consider the distance and spatial correlation between nodes when clustering nodes in the network. Therefore, it is more difficult to aggregate and transmit data in the network.

This paper proposes a joint weight based dynamic clustering algorithm For WSN, JWDC which tries to cluster nodes in the network to save network energy, to aggregate and transmit data efficiently by joint weight models.

* This work is partially funded by Hubei Province Department of Education Foundation (Q20111003).

F. Bian et al. (Eds.): GRMSE 2013, Part I, CCIS 398, pp. 325–335, 2013.
© Springer-Verlag Berlin Heidelberg 2013

The rest of the paper is organized as follows. We describe some of the related work on clustering algorithms in Section 2. In Section 3, we give a network structure based on large-scale WSN. In Section 4, we provide data model of jointed weight. In Section 5, we describe joint weight for dynamic clustering algorithm, JWDC. We present and analyze the simulation results in Section 6. Selection 7 concludes this paper and discusses our future work.

2 Related Work

Clustering technology is an essential part of many WSN applications. Over the years, many researchers have proposed many different solutions for this problem (for example, [1]~[10]).

[3] proposes a simple and practical clustering scheme by min-max optimization and approximate optimization. In the scheme, neighboring nodes form a cluster in which data from the same node are transmitted to the cluster head by the shortest route tree, and then are aggregated, and eventually are sent to sink. [4] puts forward a distributed timer-based clustering algorithm that selects cluster heads by residual energy. [5] gives a clustering hierarchy arithmetic based on energy prediction for WSN. [6] suggests a clustering algorithm based on the hexagons virtual grid, which is suitable for the non-uniformly distributed LS-WSN.

In [7,8], nodes are clustered according to correlation among them that is on the basis of assumption modes. [7] uses rainfall model that computes correlation among nodes by practical learning. [8] calculates correlation coefficient by joint Gauss model to. However, the two algorithms don't involve correlation among dynamic, online data. In another related work, Li et all. [9] propose a dynamic clustering algorithm PPC which cluster nodes in WSN by aggregation gains, energy and transmission distance. Xie et al. [10] provides a novel clustering algorithm DCAM (Distributed Clustering Auto Model) which constructs clusters based on area. In DCAM, clusters are connective and can cover all nodes in the network.

Different from above clustering algorithms, JWDC algorithm by this paper clusters nodes in WSN according to residual energy of cluster heads, spatial correlation and clustering distance between nodes and cluster heads. This can greatly reduce energy consumption and raise the quality of data aggregation in the network.

3 Network Structure

Assume that N sensor nodes are randomly deployed in a area $L \times L$. Sensor nodes send data from sensing environments to *Sink* periodically. *Sink* is at the verge of monitoring area and in charge of receiving and dealing with sampling data. In order to analyze and describe the model conveniently, we make the following assumptions in this paper:

(1) nodes are static and deployed densely in WSN.
(2) all nodes are isomorphic, namely they has same initial battery energy, sensing ability, communication one and computing one.
(3) nodes can be aware of their own location by localization technology.

4 Data Model

4.1 Definition

Spatial Correlation. *Definition 1 (Spatial correlation among nodes)* In WSN, Spatial correlation among nodes is the similarity among data sampled by nodes at the same time which monitor the same spatial area.

Definition 2 (Spatial reading vector, SRV). In WSN, SRV of a node N_i is made of a series of readings in a time window Δt. A reading can be expressed as $v_i(t) = \{d_i(t-\Delta t+1),\ d_i(t-\Delta t+2),...,d_i(t)\}$, where $d_i(t)$ is the data sampled by the node N_i at time t.

Definition 3 (Similarity of spatial reading vector, SSRV). In WSN, SSRV is defined as the similarity between two SRVs, and be expressed as $S_{i,j}$. $S_{i,j}$ can be calculated in equation (1).

$$S_{i,j} = \frac{v_i(t)v_j(t)}{\|v_i(t)\|_2^2 + \|v_j(t)\|_2^2 - v_i(t)v_j(t)},\quad \|v_i(t)\|_2^2 = |d_i(t-\Delta t+1)|^2 + ... + |d_i(t)|^2 \tag{1}$$

where $v_i(t)$ and $v_j(t)$ are SRVs of N_i and N_j respectively, and $S_{i,j} \in [0,1]$.

Criterion 1 (Criterion of spatial correlation between two nodes) Two nodes N_i and N_j are spatial-correlation if and only if $S_{i,j} \geq S_\theta$, and S_θ is the threshold of spatial correlation between two nodes.

Transmission Distance. *Definition 4 (Candidate distance).* Candidate distance is the practical distance between two candidate cluster heads CCH_i and CCH_j in cluster head selection phase, and can be expressed by d_{CCH_i,CCH_j}.

Definition 5 (Energy consumption distance). Energy consumption distance d'_{N,CH_i} is the distance considering energy between a node N and a cluster head CH_i in cluster formation phase. d'_{N,CH_i} can be calculated by the following equation.

$$d'_{N,CH_i} = \begin{cases} d^2_{N,CH_i}\ d_{N,CH_i} \leq d_0 \\ d^4_{N,CH_i}\ d_{N,CH_i} > d_0 \end{cases} \tag{2}$$

where d_0 is the threshold that is be related to sensor hardware, and d_{N,CH_i} is the real distance between N and CH_i.

Residual Energy. *Definition 6 (Energy of candidate cluster head).* Energy of a candidate cluster head is the energy of a node that compete for a cluster head in cluster head selection phase, and it can be expressed by e_{CCH} .

Definition 7 (energy of cluster head). Energy of a cluster head is the residual energy of a node as cluster head in cluster formation phase. It can be expressed by e_{CH} .

4.2 Joint Weight Model

This paper gives two joint weight modes, weight model for cluster head selection (WMCHS) and weight model for nodes clustering (WMNC). The former is the basics for a node to compete for a cluster head in cluster heads selection phase, and the latter is used by a node to choose a cluster in cluster formation phase.

Weight Model for Candidate Cluster Heads Competition. In cluster head selection phase, the goal is to choose the nodes with more residual energy as cluster heads and to guarantee cluster heads to be even in WSN. Considering residual energy candidate cluster heads, spatial correlation and energy distance, this paper puts forward weight model for candidate cluster head competition W_{CCH_i} . W_{CCH_i} can be expressed by following equation (3).

$$W_{CCH_i} = (\frac{e_{CCH_i}}{e})^{\alpha_{CCH}} \times (\tau_{CCH_i,CCH_j})^{\beta_{CCH}} \times (\theta_{CCH_i,CCH_j})^{\gamma_{CCH}} \tag{3}$$

The symbols in equation (3) are explained as following.

- $\frac{e_{CCH_i}}{e}$ is a energy factor whose value is decided by the ratio between the residual energy and the initial energy of CCH_i .
- τ_{CCH_i,CCH_j} is a spatial correlation factor whose value is decided by S_{CCH_i,CCH_j} . $S_{\max}$ and $S_{\min}$ are respectively the maximum and the minimum of the distance between CCH_i and its neighboring $CCHs$, and S_{th} is the threshold in advance. τ_{CCH_i,CCH_j} can be calculated by the following equation.

$$\tau_{CCH_i,CCH_j} = \begin{cases} \frac{S_{\max} - S_{CCH_i,CCH_j}}{S_{\max} - S_{\min}} & S_{\min} \le S_{CCH_i,CCH_j} \le S_{\max} \quad and \quad S_{CCH_i,CCH_j} \le S_{th} \\ 0 & other \end{cases}$$

- θ_{CCH_i,CCH_j} is a distance factor whose value is decided by the real distance d_{CCH_i,CCH_j} between CCH_i and CCH_j . $d_{\max}$ and $d_{\min}$ are respectively the maximum and the minimum of the distance between CCH_i and its neighboring CCH_j , and d_{th} is the threshold in advance. θ_{CCH_i,CCH_j} can be calculated by the following equation.

$$\theta_{CCH_i,CCH_j}=\begin{cases}\dfrac{d_{\max}-d_{CCH_i,CCH_j}}{d_{\max}-d_{\min}} & d_{\min}\le d_{CCH_i,CCH_j}\le d_{\max}\ and\ d_{CCH_i,CCH_j}\le d_{th}\\ 0 & other\end{cases}$$

- α_{CCH} , β_{CCH} and γ_{CCH} are the adjustment coefficients and their values belong to $[1,2]$. In initial stage, energy of a node is enough, so β_{CCH} and γ_{CCH} are the same, and α_{CCH} is bigger than β_{CCH} and γ_{CCH} . In steady phase, α_{CCH} , β_{CCH} and γ_{CCH} are the same. In last stage, the key task is to guarantee the connectivity of the network by residual energy of candidate cluster heads. β_{CCH} and γ_{CCH} is the same, and α_{CCH} is smaller than β_{CCH} and γ_{CCH} .

It can be known from W_{CCH_i} that a node with more energy is prior to other nodes in cluster head selection, and a node can compete for a cluster head only when its τ_{CCH_i,CCH_j} and θ_{CCH_i,CCH_j} is in the appropriate range.

Weight Model for Nodes Clustering. The key task of cluster formation is to save energy and efficiently aggregate data sampled by nodes when WSN is running. Therefore, this paper puts forward a weight model for nodes clustering considering residual energy of cluster heads, spatial correlation and energy consumption distance between a node and a cluster head , W_{CH_i} . W_{CH_i} can be calculated by the following equation.

$$W_{CH_i}=(\frac{e_{CH_i}}{e})^{\alpha_{CH}}\times(\tau_{N,CH_i})^{\beta_{CH}}\times(\theta_{N,CH_i})^{\gamma_{CH}} \tag{4}$$

The symbols in equation (4) are explained as following.

- $\dfrac{e_{CH_i}}{e}$ is a energy factor whose is decided by the ratio between the residual energy and the initial energy of CH_i .
- τ_{N,CH_i} is a spatial correlation factor whose value is decided by S_{N,CH_i} . $S_{\max}$ and $S_{\min}$ are respectively the maximum and the minimum of the spatial similarity between N and CH_i . τ_{N,CH_i} can be calculated by the following equation.

$$\tau_{N,CH_i}=\begin{cases}\dfrac{S_{N,CH_i}-S_{\min}}{S_{\max}-S_{\min}} & S_{\min}\le S_{N,CH_j}\le S_{\max}\\ 0 & other\end{cases}$$

- θ_{N,CH_i} is a transmission factor whose value is decided by the energy consumption distance between a node N and a cluster head CH_i d'_{N,CH_i} . $d'_{\max}$ and $d'_{\min}$ respectively the maximum and the minimum of the spatial similarity between N and CH_i . θ_{N,CH_i} can be calculated by the following equation.

$$\theta_{N,CH_i} = \begin{cases} \dfrac{d'_{N,CH_i} - d'_{\min}}{d'_{\max} - d'_{\min}} & d'_{\min} \le d'_{N,CH_i} \le d'_{\max} \\ 0 & other \end{cases}$$

- α_{CH}, β_{CH} and γ_{CH} are the adjustment coefficients and their values belong to [0,1]. In initial stage, energy of a node is enough, so value of γ_{CH} is bigger than the value of β_{CH}, and the value of α_{CH} is bigger than γ_{CH}. In steady phase, the value of γ_{CH} is smaller than the value of β_{CH}, and the value of β_{CH} is smaller than α_{CH}. In last stage, γ_{CH} is smaller than the value of β_{CH}, and the value of α_{CH} is smaller than γ_{CH}.

Equation (4) indicates that a node will choose the cluster head with more residual energy, stronger spatial correlation and nearer distance, and act as its member.

5 Joint Weight Based Dynamic Clustering Algorithm

JWDC includes two parts: cluster head selection algorithm based on WMCHS and cluster formation algorithm based on WMNC.

5.1 Cluster Head Selection Algorithm Based on WMCHS

In cluster head selection algorithm based on WMCHS, the key task is to choose candidate cluster heads with most energy as cluster heads in cluster head selection phase. The detailed steps can be described as follows.

(1) A node N_i is a CCH_i after cluster head selection begins.

(2) CCH_i sends neighboring nodes $M_{CH_i\_complete}$ that contains node number Num_{CH_i}, residual energy e_{CH_i}, spatial reading vector SRV_{CH_i} and the location Loc_{CH_i}.

(3) CCH_i receives $M_{CH_j\_complete}$ from other CCH_j, and calculate W_{CCH_i} and $\{W_{CCH_j}\}$ of CCH_j according to equation (3).

(4) CCH_i compares W_{CCH_i} to one of $\{W_{CCH_j}\}$. If W_{CCH_i} is bigger than any one of $\{W_{CCH_j}\}$, CCH_i acts as a cluster head and broadcasts M_{CH_i}. Or else, CCH_i acts as a normal node, and broadcasts M_{quit}.

(5) If CCH_i receives M_{quit} of CCH_j whose W_{CCH_j} is bigger than W_{CCH_i}, CCH_i acts as a cluster head and broadcasts M_{CH_i}.

5.2 Cluster Formation Algorithm Based on WMNC

In cluster formation algorithm based on WMNC, a node receives clustering information from cluster heads, and then selects an appropriate cluster head with best weight W_{CH_i} to be its member in cluster formation phase. The detailed steps can be described as following.

(1) A cluster head CH_i sends clustering information M_{CH_i} to its neighboring nodes using biggest power.
(2) A normal node N receives M_{CH_i} from CH_i.
(3) N calculates W_{CH_i} between N and CH_i according to equation (4), and then adds W_{CH_i} to cluster weight set $\{W_{CH_i}\}$.
(4) N chooses the cluster head with the maximal W_{CH_i} of $\{W_{CH_i}\}$ to join, and becomes its member.

After clustering nodes, WSN will run steadily for some time. Then, it will go into the next period in which CCH_i and W_{CH_i} are calculated again, and choose new cluster heads and cluster nodes.

6 Experimental Results

To evaluate and analyze the performances of JWDC, the experiment implement the clustering algorithms JWDC, CDN[8] and PPC[9]. One thousand sensor nodes are placed randomly in an area of $600m \times 600m$ where JWDC, CDN and PPC algorithms are simulated separately. In the experiment, parameters of energy consumption model are from illiterate [2], and other parameters are listed in Table. 1.

Table 1. Simulation parameters

parameters	value
Network field	600m×600m
Nodes distribution	random and even
communication radius	15m
nodes	900
E_{elec}	$50nJ/bit$
ε_{fs}	$10pJ/bit/m^2$
ε_{amp}	$0.013pJ/bit/m^4$
E_{DA}	$50nJ/bit/signal$
Data package size	500Byte
Initial energy	2J

According to the characters of WSN, the experiment divides the process into three phases, namely initial formation phase (phase I)、steady phase (Phase II) and end phase (phase III). Table.2 lists adjustment factors in different phases.

Table 2. Adjustment parameters

Phase (Rounds)	Phase I (1~200)	Phase II (201~700)	Phase III (701~1000)
α_{CCH}	1.3	1.0	0.8
β_{CCH}	1.0	1.0	1.0
γ_{CCH}	1.0	1.0	1.0
α_{CH}	1.0	0.9	0.8
β_{CH}	0.7	0.8	1.0
γ_{CH}	0.8	0.7	0.9

The experiments compare the performances of JWDC, CDN and PC in network lifetime, network data traffic and average quality of data aggregation. The results are shown in Fig.1~Fig.3.

6.1 Network Lifetime

Fig.1 plots number of alive nodes in three clustering algorithms. It can seen from Fig.1 that the network lifetime of PPC is longer than one of CDN, and the death time of the first node and all nodes in JWDC is later that CDN and PPC. In addition, JWDC has smaller time span than CDN and PPC. This indicates that JWDC makes better balances in energy consumption of all nodes in WSN. Compared with CDN, PPC can save energy in the network because it considers aggregation benefit of data sampled by nodes in last round when clustering nodes in the network. JWDC clusters

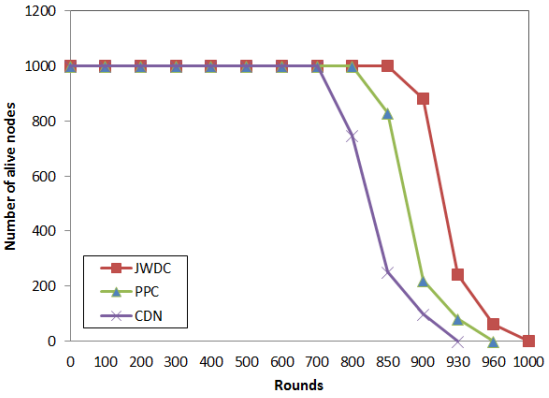

Fig. 1. Comparison of network lifetime

nodes by considering residual energy of cluster heads, energy consumption distance, and spatial correlation, so it can better save and balance energy consumption in the network.

6.2 Network Data Traffic

Fig.2 compares JWDC with CDN and PPC in comparisons among network data traffic. As is shown in Fig.2 that network data traffic in three clustering algorithms decline as the reduction of alive nodes in WSN, and JWDC has least network data traffic. The reason is that data sampled by nodes and transmitted become less as more dead nodes. What's more, JWDC considers spatial correlation among nodes when clustering nodes in the network, so JWDC has best data aggregation and network data traffic.

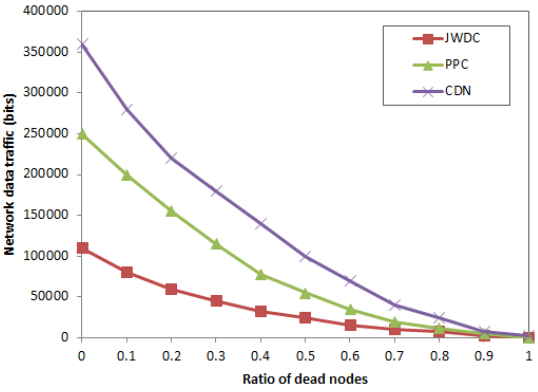

Fig. 2. Comparison of network data traffic

6.3 Average Quality of Data Aggregation

Definition 8 (Average quality of data aggregation). Average quality of data aggregation q_{da} can be defined as $q_{da} = \frac{\overline{d_a}}{\overline{d_r}}$. Here, $\overline{d_a}$ is the average result of data aggregation using JWDC algorithm, and $\overline{d_r}$ is the average of the real result of data aggregation in the network.

Fig.3 shows average quality of data aggregation with the range of the percentage of dead nodes in three clustering algorithms. Compared with CDN and PPC algorithms, JWDC provides better average quality of data aggregation and slower decline as the rise of dead nodes. That's because JWDC considers spatial correlation among nodes from the same cluster when clustering nodes in WSN, so there is small difference among data sampled nodes. This can aggregate data sampled by nodes more conveniently, and provide better performance when dead nodes increase.

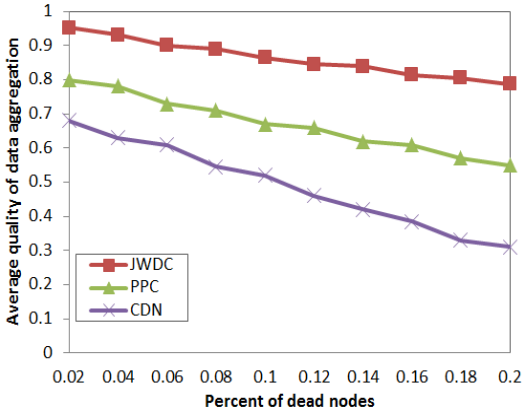

Fig. 3. Comparison of average quality of data aggregation

7 Conclusions and Future Work

This paper proposes a joint weight based dynamic clustering algorithm for WSN, JWDC. Taking into consideration residual energy of cluster heads, spatial correlation and distance of energy consumption between nodes and cluster heads, JWDC respectively establishes the weight model for competition of cluster heads in cluster head selection phase, and the weight model for clustering in cluster formation phase. Simulation results show that JWDC can aggregate data sampled by nodes, reduce data traffic, and save and balance energy consumption in WSN. Future work is to implement JWDC algorithm in real system, and to validate and improve it.

References

1. Heinzelman, W., Chandrakasan, A., Balakrishnan, H.: Energy-efficient communication protocol for wireless microsensor networks. In: Proceedings of the 33rd Annual Hawaii International Conference on System Sciences, pp. 3005–3014. IEEE Computer Society, Maui (2000)
2. Heinzelman, W.R., Chandrakasan, A., Balakrishnan, H.: An application-specific protocol architecture for wireless micro-sensor networks. IEEE Transactions on Wireless Communications 1(4), 660–670 (2002)
3. Pattem, S., Krishnamachari, B., Govindan, R.: The impact of spatial correlation on routing with compression in wireless sensor networks. ACM Transactions on Sensor Networks 4(4), 195–227 (2008)
4. Cao, Y.T., He, C., Jiang, L.G.: A Distributed Timer-Based Clustering Algorithm for Wireless Sensor Networks. Acta Electronical Sinica 9(35), 1718–1723 (2007)
5. Lin, K., Zhao, H., Yin, Z.Y., Luo, D.D.: A Clustering Hierarchy Arithmetic Based on Energy Prediction for Wireless Sensor Networks. Acta Electronical Sinica 4(36), 824–828 (2008)

6. Zhang, X.D., Kang, G.X., Zhang, P., Zhang, H.: Game Theoretic Clustering Algorithm for Large Scale WSN. Journal of Electronics & Information Technology 33(10), 2516–2520 (2011)
7. Zhang, C.Q., Wang, B.G., Fang, S.: Spatial data correlation based clustering algorithms for wireless sensor networks. In: The 3rd International Conference on Innovative Computing Information and Control, p. 593. IEEE Computing Society, Dalian (2008)
8. Lin, K., Zhao, H., Yin, Z.Y.: A clustering hierarchy arithmetic based energy prediction for wireless sensor networks. Acta Electronical Sinica 4(36), 824–828 (2008)
9. Li, B., Lin, Y.P., Hu, Y.P.: A Dynamic Clustering Algorithm Based on Polymerization Proceeds for Wireless Sensor Networks. Acta Electronical Sinica 38(2A), 128–132 (2008)
10. Xie, Z.J., Qian, J.B.: Researches on Area Based Distributed Clustering Auto Modeling Sensor Networks. Acta Electronica Sinica 38(1), 218–221 (2010)

Towards Open Source Remote Sensing Software – A Survey

Yinghui Zhao[1,2]

[1] Department of Water Resources,
Zhejiang Tongji Vocational College of Science and Technology,
Hangzhou, 311231, China
[2] School of Earth Sciences and Engineering, Hohai University,
Nanjing, 210098, China
zhaoyinghuihust@gmail.com

Abstract. Remote sensing is one of the best ways for earth observation and environment monitoring due to its spatial and temporal capability for long term and large scale regions. Typical remote sensing software consists of modules including image preprocessing, pixel manipulation, complicated calculation and transformation, interactions with other GIS/RS software, etc. Currently, open source remote sensing is emerging as a promising solution for commercial, governmental, and scientific applications. In this paper we review the state of some open source remote sensing software and make a comprehensive comparison on their general functionalities.

Keywords: remote sensing, open source, spectral image processing.

1 Introduction

Remote sensing is the acquisition of information about an object or phenomenon on Earth (on the surface, in the atmosphere or oceans) from a distance, typically from aircrafts or satellites [1-4]. Passive remote sensing and active remote sensing are main types of remote sensing, where passive sensors detect natural radiation that is emitted or reflected by the targeted object or surrounding areas, especially based on the reflected sunlight of radiation. Typical examples of passive remote sensors include film photography, infrared, charge-coupled devices (CCDs), and radiometers. Since passive remote sensing records radiation that is reflected from Earth's surface, usually from the sun, passive sensors can only be used to collect data during daylight hours. In contrary, active remote sensing uses sensors to emit energy to scan targeted objects and areas then detects and measures the radiation that is reflected or backscattered from the targets. A typical laser based sensing system projects a laser onto the surface of the target (usually the Earth) and then measures the time delay that it takes for the laser to reflect back to its sensor (the laser source). Typical active remote sensing examples include RADAR and LiDAR where the time delay between emission and return is measured, establishing the location, speed and direction of the targeted object [5]. Due to its non-contact nature, remote sensing is widely used in various

F. Bian et al. (Eds.): GRMSE 2013, Part I, CCIS 398, pp. 336–347, 2013.
© Springer-Verlag Berlin Heidelberg 2013

fields, especially in conditions where it's dangerous or inaccessible to collect data on targeted areas, for an instance, earth observation. Moreover, remote sensing is the best way to monitor very large scale areas in variable spatial and temporal resolutions. For example, remote sensing is the best way to monitor coastal deforestation, glacial features in Arctic and Antarctic regions, global climate change, land use and transformation, hazard assessment, natural resource management, etc.[6,7]. Currently, remote sensing has changed, even replaced the costly and slow ways of data acquisition in many fields, including meteorology, ecology, hydrology, agriculture, military, city planning, public health, archaeological investigations, disease mapping, military observation and geomorphological surveying, etc.

By satellite, aircraft, spacecraft, ship, and helicopter, data is acquired and created automatically from the sensed target by means of various kinds of acquisition systems. The acquired satellite and aerial images are geospatial data and contain more raw data and information than can be easily dealt with, for example, for direct visualization and human interpretation. The information explosion of raw data about our earth does us no good if we cannot turn it into understandable information. Therefore, the acquired data, mostly, the images are processed by computer software, sometimes with the help from human [8-12]. GPU based computing cluster is one of the promising paradigm for large scale remote sensing image mining and analysis with better performance-price ratio [13-17].

A substantial challenge and considerable efforts have been made over the past 4 decades to develop remote sensing related techniques. With the advances in sensor technologies, the spatial resolution(the size of a pixel that is recorded in a raster image – typically pixels may correspond to square areas ranging in side length, for example, 1 pixel stands for a 30 meters by 30 meters area), spectral resolution(the wavelength width of the different frequency bands recorded – usually, this is related to the number of frequency bands recorded by the remote sensing platform and specific devices), radiometric resolution(the number of different intensities of radiation the sensor is able to distinguish), and the temporal resolution are greatly improved. Hence the size of sensed image is becoming larger and larger. They also demand tremendous computing power for sensed image processing and complicated analysis. For an instance, large-scale remote sensing observation and data analysis system requires technique support of high performance computing due to the processing and storage requirements, especially parallel processing techniques and massive data storage and management.

Remote sensing software is almost developed simultaneously with the advances in remote sensing technologies and computer science. The remote sensing software has been developed for decades and commercial software packages have been successfully developed, such as ERDAS Imagine [18], ENVI [19], ER Mapper [20], PCI Geomatic [21], etc. They provide powerful functionalities for calculation and analysis, including mapping, imaginary, tracking, and complicated fusion analysis.

Meanwhile, in the last several decades the open source software movement has received enormous attention from the academia and industry [22-25]. It is often regarded as a fundamentally new way to develop high quality software and it also poses a serious challenge to the conventional commercial software businesses that dominate most software markets today, sometimes even the whole software

ecosystem. Nowadays, in the software ecosystem, open source software plays an important role as alternatives for commercial software. From the cost point of view, the open source software development enables the development of software algorithms without spending thousands of dollars for commercial applications. Moreover, open source software development speeds up the development time, produces high-quality codes and allows for the maintenance and distribution of the software to be completed by users from around the world on the internet. In fact, academic institutions, government organizations, entrepreneurial developers and the business communities have benefited a lot from open source software.

Open source remote sensing software is one of the reflection of the open source software movement where many open source remote sensing software are as high as quality with commercial software [26-29].For example, the open source GeoTIFF [30] project is the leading commercial standard for geospatial tiff files adopted by most of the existing commercial remote sensing and GIS software.

The rest of the paper is organized as follows: In Section 2, we present the introductions of some selected open source remote sensing software. We made a comprehensive comparison on the selected open source remote sensing software in Section 3. Finally, we summarize the paper in Section 4.

2 Examples of Selected Open Source Remote Sensing Software and Programming Libraries

In this section, we will select some open source remote sensing software for introduction and comparison. Thanks to the advances in computer programming, all these software evolves after their initial version, some of them even for decades. Most of them are object or component oriented software [31-33].

2.1 OSSIM

OSSIM(Open Source Software Image Map) [34]is a library set that provides high performance remote sensing, mapping and image processing capabilities[35]. OSSIM provides the capability to process images from satellite and aerial cameras and transform them into accurate image maps associated with three-dimensional positions on the Earth. Usually the remote sensing instruments are capable of capturing spectral information from the electromagnetic spectrum outside of human visual range. OSSIM allows this information to be processed for a wide variety of applications, including precision farming, environmental assessment and urban planning. The library is capable of concurrently handling many large image files of arbitrary pixel depth. It has been designed from the ground up to support high performance parallel processing, map projections, three-dimensional models and scientific applications. The library can serve as the basis for a number of significant applications and tools in the remote sensing and geographical information systems areas. The OSSIM library is implemented in C++ language and provides bindings to several libraries, including wxWindows[36], GDAL[37] and GRASS[38]. wxWindows is a framework that

provides a generic GUI(graphical user interface) interface for programmers. The resulting code can then be targeted to Windows, UNIX and Mac platforms respectively. Python and XML support are also provided in the OSSIM library. For example, OSSIM viewer can display a wide range of imagery and can also map data sets, roam, zoom, pan and track the latitude and longitude coordinates of the cursor. OSSIM has been designed to support dynamic linking of image chains. Images can be opened in their native format and sampled on demand to fill a viewport on the screen or to generate an output product. The dynamic linking allows for reprojections, filters, combiners and other image processing functions to be added or removed easily to produce the desired result. Multiple image chains can be linked together to provide more complex analysis products and views such as mosaics and fusions. OSSIM is also designed to provide nondestructive processing, parameter driven options and a state-management system that allow for taking snapshots of a work in progress and restoring them during later sessions. Functions from the library can be linked together dynamically and combined with other image chains to create the desired product or view. The end of those chains can be combined to create composite processing products. OSSIM can also attach imagery and maps in their native map projections, window into a geographic area of interest (AOI) and resample to common scales and orientations [34].

2.2 GRASS

GRASS (Geographic Resources Analysis Support System)[38], is Geographic Information System and Remote Sensing software used for data management, image processing, graphics production, spatial modeling, and visualization of many types of data. GRASS contains over 350 modules to render maps and images on monitor and paper. It also provides functions such as: manipulate raster and vector data including vector networks; process multispectral image data; and create, manage, and store spatial data. GRASS also offers both an intuitive GUI as well as command line syntax for ease of operations. GRASS GIS can interface with printers, plotters, digitizers, and databases to develop new data as well as manage existing data[38].

In GRASS, imagery data is treated as raster maps but there are a number of special modules specifically designed to help with image processing. GRASS has tremendous capabilities, including raster analysis,3D-Raster (voxel) analysis, vector analysis, point data analysis, image processing, DTM-analysis, geocoding, visualization, map creation, SQL-support, geostatistics, erosion modeling, landscape structure analysis, solution transport, watershed analysis, etc.

2.3 ORFEO Toolbox

The vision of the Orfeo Toolbox (OTB)[39] is a set of algorithmic components, adapted to large remote sensing images, which allow to capitalize the methodological know how, and therefore use an incremental approach to benefit from the results of the methodological research. OTB is distributed as an open source library of image processing algorithms. In OTB, all the details of all the algorithms

are open source. OTB is based on the medical image processing library ITK and offers particular functionalities for remote sensing image processing in general and for high spatial resolution images in particular. Targeted algorithms for high resolution optical images (SPOT, Quickbird, Worldview, Landsat, Ikonos), hyperspectral sensors (Hyperion) or SAR (TerraSarX, ERS, Palsar) are available. Most functionalities are also adapted to process huge images without the need for a supercomputer by using streaming and multi-threading as often as possible. Moreover, OTB provides a number of heavily documented functionalities, such as image access (optimized read/write access for most of remote sensing image formats, meta-data access, and visualization), standard remote sensing preprocessing, filtering, feature extraction, image segmentation, classification, change detection, information extraction for integration in GIS and mapping systems [39].

2.4 Opticks

Opticks[40] is an expandable remote sensing and imagery analysis software platform that supports imagery, video (motion imagery), Synthetic Aperture Radar (SAR), multi-spectral, hyper-spectral, and other types of remote sensing data. Opticks supports processing remote sensing video in the same manner as it supports imagery, which differentiates it from other remote sensing applications. Opticks can also be used as a remote sensing software development framework. Developers can extend Opticks functionality using its plug-in architecture and public APIs.

Opticks can also be used as a software development framework. The Opticks community provides and supports a public SDK which includes a documented API as well as several extension tutorials. The Opticks website hosts a variety of extensions, some of which are developed and maintained by the same development team as Opticks.

Opticks supports more than 20 image formats, provides manipulations like zoom, pan, rotate of spatially large datasets and huge images, has quickly layer GIS features, annotations, results, and other information ,image display controls such as colormap, histogram, transparency, etc. It also supports for datasets larger than 4GB and combines steps using graphical wizards, processing data in its native interleave of BIP, BSQ or BIL and various extensions to drop in new capability.

2.5 LibGeoTIFF

TIFF format is the most popular and versatile raster data format in the world today. TIFF is an industry class format for storage, transfer, display, and printing of raster images, such as clipart, logotypes, and scanned documents. Today, TIFF is being used for storage of map information, too.

GeoTIFF[30] is a public domain metadata standard which allows georeferencing information to be embedded within a TIFF file. It's a TIFF based interchange format for georeferenced raster imagery. The potential additional information includes map projection, coordinate systems, ellipsoids, data, and everything else necessary to establish the exact spatial reference for the file. The GeoTIFF format is fully

compliant with TIFF 6.0 specification, so software incapable of reading and interpreting the specialized metadata will still be able to open a GeoTIFF format file.

The TIFF imagery file format can be used to store and transfer digital satellite imagery, scanned aerial photos, elevation models, scanned maps or the results of many types of geographic analysis products. Over the past several years many users of such images have urged geographic data suppliers to provide imagery in TIFF format. TIFF is the only full-featured format in the public domain, capable of supporting compression, tiling, and extension to include geographic metadata. GeoTIFF implements the geographic metadata formally, using compliant TIFF tags and structures.

GeoTIFF refers to TIFF files which have geographic (or cartographic) data embedded as tags within the TIFF file. The geographic data can then be used to position the image in the correct location and geometry on the screen of a geographic information display. GeoTIFF is a metadata format, which provides geographic information to associate with the image data. But the TIFF file structure allows both the metadata and the image data to be encoded into the same file. GeoTIFF makes use of a public tag structure which is platform interoperable between any and all GeoTIFF-savvy readers. Any GIS, CAD, Image Processing, Desktop Mapping and any other types of systems using geographic images can read any GeoTIFF files created on any system according to the GeoTIFF specification [30].

Libgeotiff is an open source library normally hosted on top of libtiff for reading, and writing GeoTIFF information tags.

2.6 GDAL

Image manipulation libraries play a crucial role in all the remote sensing software and they provide base functions for pixel-level image manipulation and calculation. GDAL [37] is the geospatial data access library that provides read/write access to a large number of geospatial data formats including raster and vector data. GDAL is a translator library for raster geospatial data formats and provides a single abstract data model to the calling application for all supported formats. Within the GDAL source tree, there is another library, i.e., the OGR library which provides a similar capability for vector data. The GDAL/OGR libraries are backend supporting libraries in many remote sensing and GIS software including ArcGIS[41], FWTools[42], GRASS GIS[38], MapServer[43], OSSIM[34], OpenEV[44], Orfeo toolbox(also known as OTB)[39], Quantum GIS(i.e., QGIS)[45],etc.

In GDAL, the data model is the type of information that a GDAL data store can contain, and their semantics. A dataset (represented by the GDAL Dataset class) is an assembly of related raster bands and some information common to them all. In particular the dataset has a concept of the raster size (in pixels and lines) that applies to all the bands [37]. The dataset is also responsible for the georeferencing transform and coordinate system definition of all bands. The dataset itself can also have associated metadata, a list of name/value pairs in string form. The GDAL dataset, and raster band data model is loosely based on the OpenGIS Grid coverage specification.

2.7 GEOTRANS

The National Imagery and Mapping Agency (NIMA) GEOTRANS(Geographic Translator)[46] package provides a valuable tool chest of certified map projection transformations, file formats and useful functionality that has been subsequently modernized to object-oriented code. GEOTRANS provide function to convert geographic coordinates among a wide variety of coordinate systems, map projections, and data. To convert a set of coordinates, simply select the coordinate system or map projection, the datum, in which the coordinates are defined, then enter the source coordinates, select the coordinate system or map projection, and the datum, to which the user want the coordinates to be converted, and then can start the convert procedure. Currently, there are twenty-five different coordinate systems, map projections, grids, and coding schemes, and over two hundred different datums that are supported.

GEOTRANS can also be used to efficiently convert large numbers of coordinates contained in either text files (.txt) or comma separated values (.csv). A multiline file header defines the coordinate system or map projection, and datum, of the coordinates contained in the file. Following the header, each line contains a single set of coordinates, separated by commas. Using the GEOTRANS file processing interface, the user can select an existing file of coordinates to be converted, define the coordinate system or map projection, and the datum, to which the user want to convert the coordinates, and specify the name and location of the output file that is to be created. GEOTRANS then converts the input file and creates the output file as a single operation.

3 Comparison of Selected Open Source Remote Sensing Software and Programming Libraries

Table 1 and table 2 compare the open source remote sensing software and libraries surveyed in this paper including various attributes.

Table 1. Comprehensive comparison for Open Source Remote Sensing Software

Software	Language	License	Support Platform	Library	Parallel Processing	Features	GUI/CLI	Plug-in	Image Support	Image Format	Backend Institution/ Developer
OPTICKS	C++	LGPL	W/S	N/A	N/A	ABCD	GUI/CLI	Yes	ABC	A	NASIC
OTB	C++	CeCILL	U/L/W/M/S	N/A	N/A	ABCD	GUI/CLI	Yes	ABC	A	CNES
OSSIM	C++	LGPL	L/W/M	GDAL	Yes	ABCD	GUI/CLI	Yes	ABC	A	OSGeo
NEST[47]	Java	GPL	L/W/M	N/A	Yes	ABCD	GUI/CLI	Yes	C	AB	ESA
BEAM[48]	Java	GPL	L/W/M	N/A	Yes	ABCD	GUI/CLI	Yes	C	AB	ESA
GRASS	C	GPL	L/W/M	GDAL	Yes	ABCD	GUI/CLI	Yes	ABC	AB	CERL/ OSGeo
QGIS	C++	GPL	L/U/M/W/A	GDAL	N/A	ABCD	GUI/CLI	Yes	ABC	A	OSGeo
OpenEV	Python	LGPL	L/W/S/I	GDAL	N/A	N/A	CLI	Yes	ABC	A	CGDI
Parbat[49]	Java	N/A	L/W/S	GDAL	N/A	A	GUI/CLI	No	A	A	A. Lucieer
PolSARpro[50]	C	GPL	L/U/M/W/S	ActiveTcl	N/A	A	GUI/CLI	Yes	SAR	A	ESA
ILWIS Open[51]	C++	GPL	L/U/M/W/S	N/A	N/A	ABCD	GUI/CLI	Yes	ABC	AB	ITC

Table 2. Comprehensive comparison for Open Source Remote Sensing Libraries

Libraries	Language	Binding language	License	Support Platform	Parallel Processing	GUI /CLI	Plug-in Extension	Image Source Support	Backend Institution Developer
GDAL	C++	C/C++/Perl/Python/VB6 /Ruby/Java/C#/R	X/MIT	U/ L/S/M/W	Yes	CLI	Yes	N/A	OSGeo
libgeotiff	C	C/Java	X/MIT	U/ L/S/M/W	N/A	N/A	Yes	GeoTIFF	OSGeo
GCTP	C	Fortran/C	N/A	U/ L/W	N/A	N/A	N/A	N/A	NASA
Proj/PROJ4[52]	C	C	MIT	U/ L/W	N/A	CLI	N/A	N/A	USGS
GeoTools[53]	Java	Java	LGPL	U/ L/W	N/A	GUI /CLI	N/A	NA/	OSGeo
LASlib[54]/ LASzip[55]	C++	C++	LGPL	U/ L/W	N/A	CLI	N/A	LAS	rapidlasso
libLAS[56]	C/C++	Python/C++/C#/VB.Net /Ruby	BSD	U/ L/W/M	N/A	CLI	N/A	LAS	IGSB
GeoTrans	C++	C/C++/Python	N/A	U/ W	N/A	CLI	N/A	N/A	NIMA

Note:

1. Licensing marked N/A means fully free for public domain and not dedicated to a specific license like GPL or LGPL or X/MIT. GPL means version greater than 2.0 except specified explicitly.

2. We define the features of the software as three categories as follows:

Type A: General features and functions for remote sensing image processing, including:

(1)Image manipulation: zoom, pan, rotate, metadata access, image visualization;

(2)sensor geometry: sensor models, cartographic projections;

(3)radiometry: atmospheric corrections, vegetation indices;

(4)filtering: blurring, denoising, enhancement;

(5)fusion: image pansharpening;

(6)feature extraction: interest points, alignments, lines;

(7)image segmentation: region growing, watershed, level sets;

(8)classification: K-means, SVM, Markov random fields;

(9)change detection.

(10)object based image analysis.

(11)geospatial analysis.

Type B: GIS support, GIS layer constructions, annotations,

Type C: Special functions, in memory and on disk processing, Batch processing

Type D: Scripting,IDL,Python

3. We classify the images source used in the software or libraries into three categories as follows:

Type A: optical images

Type B: hyperspectral sensors

Type C: SAR

4. We classify the images formats used in the software or libraries into three categories as follows:

Type A: NITF2.0/2.1, ASPAM/PAR, CGM, DTED, ENVI, Generic RAW, ESRI Shapefile, HDF5, AVI, MPEG, JPEG, GIF, PNG, BMP, TIFF, GeoTIFF

Type B: NetCDF, CEOS

Type C: others

5. In Support platform, W is Windows, U is Unix, L is Linux, S is Solaris, M is MacOS,A is Android,I is IRIX

4 Conclusion and Future Work

The open source software challenge is often described as much more fundamental, and goes to the basic motivations, economics, market structure, and philosophy of the institutions that develop, market, and use software. In the remote sensing area, the open source remote sensing software plays an important role for commercial, personal and scientific applications. In this paper we review the state of some open source remote sensing software and make a comprehensive comparison on their general functionalities.

In this paper we do not compare the selected software exhaustively but we compare some functionality aspects that are import for software selection and implementation in real remote sensing system development. We also present some discussions for open source software selection in the following except for the comparison in the above sections.

(1) Parallel processing support is very import for remote sensing software. Large scale remote sensing image processing, especially for the high resolution images is highly computing-intensive and time-consuming and it poses serve computational challenges for modern computing systems. The inherent nature of raster data makes it very suitable for parallel processing of large number of images. However, different domain specific applications demands different processing methods and analysis. For example, different applications demand increasing amounts of spatial, temporal, and spectral resolution images for different reception, archival, cataloging, user query, processing, manipulation, and analysis of the remote sensing image data. Currently there is no standard high performance parallel remote sensing image processing specifications or implementation references. Usually the researchers and developers use standard parallel computing techniques to accomplish parallel performance and speedups. Multi-threaded image processing is often used in real applications by using of super computers, clusters, and multi-core PC servers[57-59]. However, how to tune the performance of the target high performance computing infrastructure for remote sensing image processing should be addressed further[60,61].GRASS is one of the open source remote sensing software that has capabilities of parallel processing for remote sensing images[62,63].

(2) Scripting and customized development support is another consideration for real world remote sensing applications. Support for scripting language including JavaScript, Python and Perl is essential for customized development and image processing in various environments.

Acknowledgments. The funding support of this work by Natural Science Fund of Zhejiang Province (ZJNSF, Grant No. LY12E09009), Science and Technology Planning Project in Water Resources of Zhejiang Province, China (Grant No. RC1218), and 2012 Special Funding Program in Water Resources of Zhejiang Provincial Departments, are greatly appreciated.

References

1. Davis, S.M., Landgrebe, D.A., Phillips, T.L.: Remote Sensing: the Quantitative Approach. McGraw Press, New York (1978)
2. Goetz, A.F.H., Vane, G., Solomon, J.E., Rock, B.N.: Imaging Spectrometry for Earth Remote Sensing. Science 228, 1147–1153 (1985)
3. Pohl, C., Van Genderen, J.L.: Multisensor Image Fusion in Remote Sensing: Concepts, Methods and Applications. International Journal of Remote Sensing (1998)
4. Green, R.O., Eastwood, M.L., Sarture, C.M., Chrien, T.G., Aronsson, M., Chippendale, B.J., Faust, J.A., Pavri, B.E., Chovit, C.J., Solis, M.: Imaging Spectroscopy and the Airborne Visible/Infrared Imaging Spectrometer (AVIRIS). Remote Sensing of Environment 65(3), 227–248 (1998)
5. http://en.wikipedia.org/wiki/Remote_sensing
6. Ehlers, M., Janowsky, R., Gähler, M.: New Remote Sensing Concepts for Environmental Monitoring. In: The Conference on Remote Sensing for Environmental Monitoring, GIS Applications, and Geology, Toulouse, France, pp. 1–12 (2002)
7. Ren, H., Chang, C.-I.: Automatic Spectral Target Recognition in Hyperspectral Imagery. IEEE Transactions on Aerospace and Electronic Systems 39, 1232–1249 (2003)
8. Jiang, C., Xu, X., Wan, J., Zhang, J., Li, Y.: Java Multi Threaded Based Parallel Remote Sensing Image Interpretation in Desktop Grid. In: 5th Annual ChinaGrid Conference (China Grid 2010), pp. 51–59. IEEE Press, New York (2010)
9. Plaza, A., Valencia, D., Plaza, J., Martinez, P.: Commodity Cluster-Based Parallel Processing of Hyperspectral Imagery. Journal of Parallel Distributed Computing 66, 345–358 (2005)
10. Plaza, A., Chang, C.-I.: High Performance Computing in Remote Sensing. Taylor & Francis, Boca Raton (2007)
11. Plaza, A., Du, Q., Chang, Y.-L., King, R.L.: High Performance Computing for Hyperspectral Remote Sensing. IEEE Journal of Selected Topics in Applied Earth Observations and Remote Sensing 4, 528–544 (2011)
12. Plaza, A., Plaza, J., Paz, A., Sanchez, S.: Parallel Hyperspectral Image and Signal Processing. IEEE Signal Processing Magazine 28, 119–126 (2011)
13. Sanchez, S., Paz, A., Martin, G., Plaza, A.: Parallel Unmixing of Remotely Sensed Hyperspectral Images on Commodity Graphics Processing Units. Concurrency and Computation: Practice and Experience 23, 1538–1557 (2011)
14. Lee, C.A., Gasster, S.D., Plaza, A., Chang, C.-I., Huang, B.: Recent Developments in High Performance Computing for Remote Sensing: A Review. IEEE Journal of Selected Topics in Applied Earth Observations and Remote Sensing 4, 508–527 (2011)
15. Christophe, E., Michel, J., Inglada, J.: Remote Sensing Processing: From Multicore to GPU. IEEE Journal of Selected Topics in Applied Earth Observations and Remote Sensing 4, 643–652 (2011)
16. Mielikainen, J., Huang, B., Huang, A.: GPU-Accelerated Multi-Profile Radiative Transfer Model for the Infrared Atmospheric Sounding Interferometer. IEEE Journal of Selected Topics in Applied Earth Observations and Remote Sensing 4, 691–700 (2011)
17. Chang, C.-C., Chang, Y.-L., Huang, M.-Y., Huang, B.: Accelerating Regular LDPC Code Decoders on GPUs. IEEE Journal of Selected Topics in Applied Earth Observations and Remote Sensing 4, 653–659 (2011)
18. ERDAS Imagine, http://geospatial.intergraph.com/
19. ENVI, http://www.exelisvis.com
20. ER Mapper, http://geospatial.intergraph.com/
21. PCI Geomatics (2013), http://www.pcigeomatics.com

22. McIlhagga, D., Zeiss, G.: Open Source Geospatial An Alternative Business Model for Municipal Governments
23. Dibona, C., Ockman, S., Stone, M.: Open Sources: Voices from the Open Source Revolution. O'Reilly, Sebastopol (1999)
24. Raymond, E.S.: The cathedral and the bazaar (1999), http://www.tuxedo.org/esr/writings/cathedral-bazaar/
25. Vixie, P.: Software Engineering. In: Dibona, C., Ockman, S., Stone, M. (eds.) Open Sources: Voices from the Open Source Revolution, pp. 91–100. O'Reilly, Sebastopol (1999)
26. Christophe, E., Inglada, J.: Open Source Remote Sensing: Increasing the Usability of Cutting-Edge Algorithms. IEEE Geoscience and Remote Sensing Society Newsletter, 9–15 (2009)
27. Steiniger, S., Bocher, E.: An Overview on Current Free and Open Source Desktop GIS Developments. International Journal of Geographical Information Science 23, 1345–1370 (2009)
28. Open Source Initiative, http://www.opensource.org/
29. Paul Ramsey. The state of Open Source GIS.FOSS4G (2007)
30. http://trac.osgeo.org/geotiff/
31. Câmara, G., Souza, R.C.M., Freitas, U.M., Garrido, J.: SPRING: Integrating Remote Sensing and GIS by Object-Oriented Data Modeling. Computers & Graphics 20, 395–403 (1996)
32. Blaschke, T.: Object Based Image Analysis for Remote Ssensing. ISPRS Journal of Photogrammetry and Remote Sensing 65, 2–16 (2010)
33. DeBardeleben, N.A., Ligon, W.B., Stanzione, D.C.: The Component Based Environment for Remote Sensing. In: Proceedings of 2002 IEEE Aerospace Conference, vol. 6, pp. 2661–2670. IEEE Press (January 2002)
34. OSSIM, http://www.ossim.org
35. http://www.remotesensing.org
36. wxWindows, http://www.wxwidgets.org
37. GDAL, GDAL - Geospatial Data Abstraction Library: Version 1.9.2, Open Source Geospatial Foundation (2012), http://gdal.osgeo.org
38. http://grass.osgeo.org/
39. http://www.orfeo-toolbox.org/
40. http://opticks.org/
41. ArcGIS, http://www.esri.com/
42. FWTools, http://fwtools.maptools.org/
43. MapServer, http://mapserver.org/
44. OpenEV, http://openev.sourceforge.net/
45. QGIS, http://www.qgis.org/
46. http://earth-info.nga.mil/GandG/geotrans/
47. The Next ESA SAR Toolbox, http://nest.array.ca/web/nest
48. BEAM, http://www.brockmann-consult.de/cms/web/beam/
49. Parbat, http://parbat.lucieer.net/
50. PolSARpro, http://earth.eo.esa.int/polsarpro/
51. ILWIS Open, http://ilwis.org/
52. Proj/PROJ4, http://trac.osgeo.org/proj/
53. GeoTools, http://www.geotools.org/
54. LASlib, http://www.cs.unc.edu/~isenburg/lastools/
55. LASzip, http://www.laszip.org/

56. libLAS, http://www.liblas.org/
57. Wei, S.-C., Huang, B.: GPU Acceleration of Predictive Partitioned Vector Quantization for Ultraspectral Sounder Data Compression. IEEE Journal of Selected Topics in Applied Earth Observations and Remote Sensing 4, 677–682 (2011)
58. Yang, H., Du, Q., Chen, G.: Unsupervised Hyperspectral Band Selection Using Graphics Processing Units. IEEE Journal of Selected Topics in Applied Earth Observations and Remote Sensing 4, 660–668 (2011)
59. Goodman, J.A., Kaeli, D., Schaa, D.: Accelerating an Imaging Spectroscopy Algorithm for Submerged Marine Environments Using Graphics Processing Units. IEEE Journal of Selected Topics in Applied Earth Observations and Remote Sensing 4, 669–676 (2011)
60. Ray, S., Simion, B., Brown, A.D.: Jackpine A Benchmark to Evaluate Spatial Database Performance. In: IEEE 27th International Conference on Data Engineering (ICDE 2011), pp. 1139–1150 (2011)
61. Simion, B., Ray, S., Brown, A.D.: Surveying the Landscape: an In-depth Analysis of Spatial Database Workloads. In: The 20th International Conference on Advances in Geographic Information Systems (SIGSpatial 2012), pp. 376–385 (2012)
62. Osterman, A.: Open Source GIS A GRASS GIS Approach Implementation of the r.cuda.los Module in the Open Source GRASS GIS by Using Parallel Computation on the NVIDIA CUDA Graphic Cards. Elektrotehniski Vestnik 79, 19–24 (2012)
63. Sorokine, A.: Implementation of a Parallel High-Performance Visualization Technique in GRASS GIS. Computers & Geosciences 33, 685–695 (2007)

Monitoring Soil Moisture in Typical North China Region Using Modified Perpendicular Drought Index and MODIS Satellite Data

Jiahua Zhang[1,2,3], Zhengming Zhou[3], Fengmei Yao[4,*], and Zhenming He[1]

[1] College of Geosciences, Yangtze University, Wuhan, 430100, China
[2] Institute of Remote Sensing and Digital Earth, Chinese Academy of Sciences, Beijing 100094, China
jhzhang@ceode.ac.cn
[3] Chinese Academy of Meteorological Sciences, Beijing, 100081, China
[4] College of Geosciences, University of Chinese Academy of Sciences, Beijing, 100049, China
yaofm@ucas.ac.cn

Abstract. Soil moisture is one of the most important and direct index for assessing drought. In this study, we performed a monitor of soil moisture in typical North China region using modified perpendicular drought index (MPDI) and the MODIS satellite data, and Henan Province was selected as the study area. Firstly, the parameters of MPDI and fraction of vegetation (f_v) were description; Secondly, the validation of MPDI for monitoring the soil moisture from different ranges of depth and time-lagged impact were analyzed; Thirdly, the comparison were carried out for observing the area of the same soil texture and different types. The results showed that the MPDI had a negative correlation with soil moisture in winter wheat growing area of Henan, and the MPDI presented its better feature for estimating soil moisture in 10cm soil depth. When calculated the time-lag effect from 0 to 4 days delay length, the results demonstrated that the MPDI corresponded soil moisture rapidly with no obvious time-lag effect from 0-3days time-lag length, and soil moisture changed obviously at 4-daytime-lagin 10cm depth.

Keywords: MPDI, soil moisture, drought index, time-lag effect, MODIS data, Henan.

1 Introduction

As an important parameter of agricultural and hydrological drought researches, soil moisture has its limitation in retrieving the spatial variation from the insitu measurements of the agro meteorological stations [1,2]. Thus, the estimation of soil moisture from remote sensing images isvery important [3-5]. The soil moisture was first retrieved from the Normalized Difference Vegetation Index (NDVI) of AVHRR, and then estimated by the Land Surface Temperature (LST) [6] or the combination of NDVI and LST [7,8] derived from remote sensing data. Nemani et al. (1993) developed

* Corresponding author.

F. Bian et al. (Eds.): GRMSE 2013, Part I, CCIS 398, pp. 348–358, 2013.
© Springer-Verlag Berlin Heidelberg 2013

the AVHRR-NDVI and temperature images to estimate soil moisture [7], and then the Enhanced Vegetation Index (EVI) was developed by Huete et al.(1994) and proved to be better in the estimation of soil moisture [9]. Wang et al. (2004) used the temperature-vegetation dryness index (TVDI) to evaluate the soil moisture status in China [10]. Mallick et al. (2009) used a soil wetness index considering surface and NDVI to estimate soil moisture of crop land [11]. In last decades, the spectral water indexes such as the Normalized Difference Water Index (NDWI) derived from NIR near-infrared (NIR) and shortwave infrared(SWIR), which incorporates the water content information in the plant canopy, was proposed by Gao (1996) to describe the of vegetation liquid water characteristic[12]; Zhang et al. (2006) developed a new DRSI, calculated as R(1640,2130) /ND(855,555), and examined it by field experiments in Northern China [13].The Perpendicular Drought Index (PDI) was developed based on the reflective and absorptive features of the canopy and bare soils in the NIR and Red spectral domain[14] by Ghulam et al. (2007a), with the advantage of its robustness in monitoring bare soil and real time monitoring of drought conditions.

Winter wheat grows during September to June next year in North China Plain. In different growth stages, vegetation fraction of winter wheat varies from low to high. Normalized spectral indexes derived from remote sensing data retrieve sole meteorological factor such as precipitation and temperature much better than soil moisture. Normally, the PDI is developed based on the soil line theorem in red-near infrared feature space. It performs precisely on condition of low vegetation fraction, especially in the same soil texture. However, on condition of high vegetation fraction, the PDI performs poorly to retrieve soil moisture, because no vegetation fraction factor is designed in PDI. Thus, the PDI need to be modified taking vegetation fraction into consideration. Ghulam et al. (2007b) developed a Modified Perpendicular Drought Index (MPDI) to estimate the soil moisture under high vegetation fraction condition [15], and the normalized spectral index is used as a parameter in the MPDI to estimate vegetation fraction.

In this study, we performed an estimation of soil moisture under high vegetation coverage stages in Henan Province by using the MPDI soil moisture index. Considering since there exists time-lag in the response of vegetation growth to the change of soil moisture, the time-lag effect of MPDI in observation on the condition of high vegetation fraction were discussed. In addition, the spectral information varies in different soil textures, and soil textures differ spatially with non-continuity in a large area. Therefore, the effect of soil texture on soil moisture estimated by MPDI was also discussed in current study. In this analysis, observation performance was performed in the same and different soil textures fields in various sites, respectively.

2 Study Area and Method

2.1 Study Area

Henan Province is located in North China, on the plain between the Yellow and Huaihe rivers. Agriculture has been a pillar of the economy of Henan Province. Main planting crops include winter wheat and summer maize. Climatically, Henan is located between

the northern sub-tropical zone and warm temperate zone, Henan has distinctive four seasons with complicated weather conditions characterized with a hot and rainy summer. Southern Henan is in the northern sub-tropical zone. The province's average temperature of the year is 13~15℃; the average annual rainfall is 807 mm; and its frost-free period lasts 308~275 days.

2.2 Data

In this study, the soil moisture data was collected from 16 agro meteorological station with the depth ranging from 10cm to 50cm, the dates on 8th, 18th and 28th in each month from 2001 to 2010 respectively (Figure 1). Institute of Henan Meteorological Sciences provided parameters related to soil moisture, including field water capacity, wilting humidity and types of soil texture in each range of depth from 10cm to 50cm. the weight of soil moisture and comprehensive drought index (K) is calculated using the data collected above.

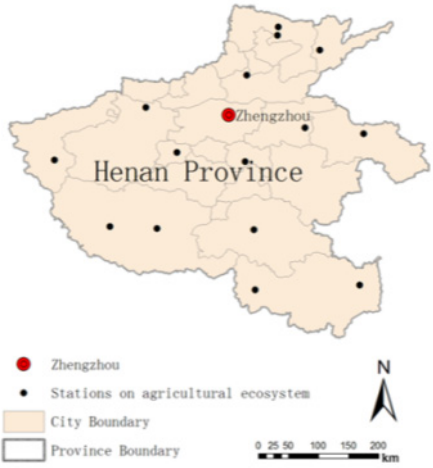

Fig. 1. Distribution of agro meteorological stations in Henan Province

The MODIS 500-meter surface reflectance data (MOD09GA and MOD 09A1) were used in this study. In validation, daily products are used for the purpose of ground-satellite synchronous observation. When analysing drought in Henan Province, 8-day composite products are used for minimizing the effect from cloud cover.

2.3 Method

2.3.1 Calculation of MPDI

The PDI calculates the distance of each scatter point to the specific line which is perpendicular to the soil line at origin point in red-near infrared feature space. It

contains no factor of vegetation fraction in PDI. However, scatter points distribute triangular in shape based on soil line and scatters derived from high vegetation fraction gather in the opposite vertex apart from soil line. Therefore, the distance to the perpendicular to the soil line is not sufficient to retrieve soil moisture in different vegetation fraction. Two-component model is used to decompose mixed pixels in red and near-infrared wavelength, thus considering vegetation fraction in MPDI. And by replacing R_{red}, R_{nir} to $R_{red,s}, R_{nir,s}$, PDI is modified as MPDI[15],

$$MPDI = \frac{1}{\sqrt{M^2+1}}\left(R_{red,s} + R_{nir,s}\right) \quad (1)$$

Where, M is the slope of soil line. Here, slope of soil line (M) is evaluated from East China winter-wheat planting area, and is defined as$M = 1.1054$.$R_{i,s}$ is expressed as,

$$R_{i,s} = \frac{R_i - f_v R_{i,v}}{1 - f_v} \quad (2)$$

Where f_v is fraction of vegetation. PROSAIL is a radiative transfer model simulating spectral reflectance of vegetation canopy. Using PROSAIL to simulate reflectance at the wavelength of red (648nm) and near-infrared (858nm), reflectance of typical vegetation is no larger than 0.05 and 0.50 respectively.

2.3.2 Calculation of Vegetation Fraction

All the parameters of MPDI are determined except forf_v. Baret et al.(1995) used PROSAIL to simulate a dataset of vegetation reflectance, and get a semi-empirical relationship by training and predicting that dataset with two-layer neutral network[16]. Then f_v is expressed as,

$$f_v = 1 - \left(\frac{NDVI_{MAX} - NDVI}{NDVI_{MAX} - NDVI_{MIN}}\right)^{0.6175} \quad (3)$$

Since NDVI reduced atmospheric effect due to its ratio expression, and semi-empirical relationship based on physical radiative transfer model and neutral network is more robust, third method of vegetation fraction estimation is adopted in calculation. Based on the theory of Boolean, f_v approaches to 1 when LAI getting close to infinite. Therefore, f_v never reaches to 1, and the denominator of MPDI never equals to zero. In the estimation of f_v, f_v is set as 0.99 when NDVI equals to $NDVI_{MAX}$. $NDVI_{MAX}$ and $NDVI_{MIN}$ are determined by visual interpretation from pure pixels of vegetation and bare soil. In Henan Province, $NDVI_{MAX}$ and $NDVI_{MIN}$ are set as 0.7 and 0.0, respectively.

2.3.3 Cloud Detection

Daily reflectance data derived from remote sensors at red and near-infrared are disturbed by cloud cover. For single band of red and near-infrared, reflectance under

clear sky is much smaller than that with cloud cover. Under clear sky reflectance at red and near-infrared bands show the characteristics of landscapes, while the reflectance of cloud is high at both bands of red and near-infrared. Therefore, the ratio of cloud reflectance between near-infrared and red is approaching to 1, which makes a difference to the ratio of landscape. Threshold of reflectance at red band and that of the ratio between reflectance of near-infrared and red are determined by visual interpretation.

2.3.4 Validation

Using soil moisture observed in situ and MPDI derived from remote sensing data, four steps of validation are processed. Longitudes and latitudes of each station in Henan are collected to select corresponding pixel in remote sensing image. Then corresponding pixels affected by cloud cover are removed.

First, soil moisture data of different depth at Zhengzhou station in 2008 and ground-satellite synchronous MPDI are calculated. The relationship between MPDI and soil moisture of different depth is discussed. Second, growing periods with different vegetation fraction of tillering period and heading period are chosen to do validation, using soil moisture data and MPDI derived from remote sensing data during the year of 2001 to 2010. And the data with clear-sky are analyzed by calculating the correlation of the corresponding soil moisture and MPDI at the depth with the best correlation. Third, choosing the depth of soil moisture with the best correlation of all, time validity of MPDI observation is discussed for no time-lag to 4-day time-lag. The result is analyzed for validate the time-lag of MPDI observation, and the change rate of soil moisture is analyzed. Then, in Henan Province, soil texture type varies spatially. Loam spreads in most parts of Henan Province. Therefore, soil moisture is used to do validation among stations with the same soil texture type, and comprehensive drought index (K) derived from soil moisture is used to do validation among stations with different soil texture types,

$$K = 1 - \frac{W - W_p}{W_h - W_p} \tag{4}$$

Where, K is the comprehensive drought index, W is soil moisture, W_h is field water capacity, and W_p is the wilting point of corresponding soil type. K reflects the necessity for soil moisture of plants with different soil texture types. When K=1, it indicates drought, while K=0, it indicates no drought occurs.

3 Result and Discussion

3.1 Cloud Detection Result

The False color image of Henan Province on 8th May 2006 is derived from MODIS daily reflectance data. It is adopted to determine the threshold to distinguish cloud in daily data. The result shows that at the single band of red, the threshold to distinguish

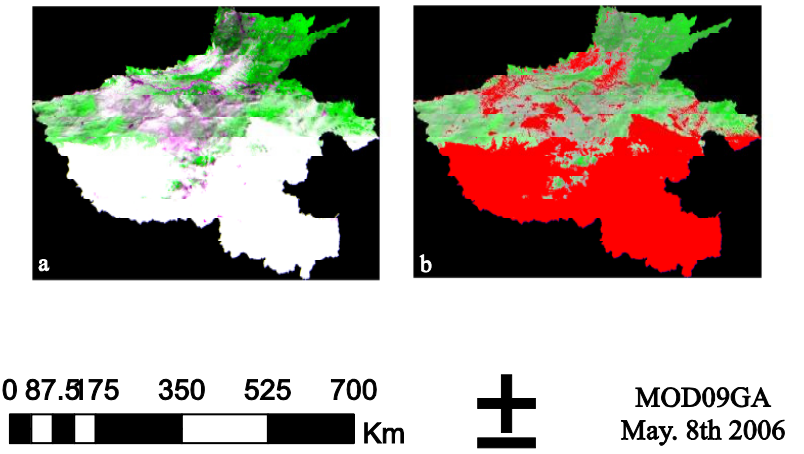

Fig. 2. (a) False color composite observation derived from MOD09GA in Henan Province on May. 8th 2006,(b) Cloud cover observation (in red) detected from MOD09GA in Henan Province on May. 8th 2006.

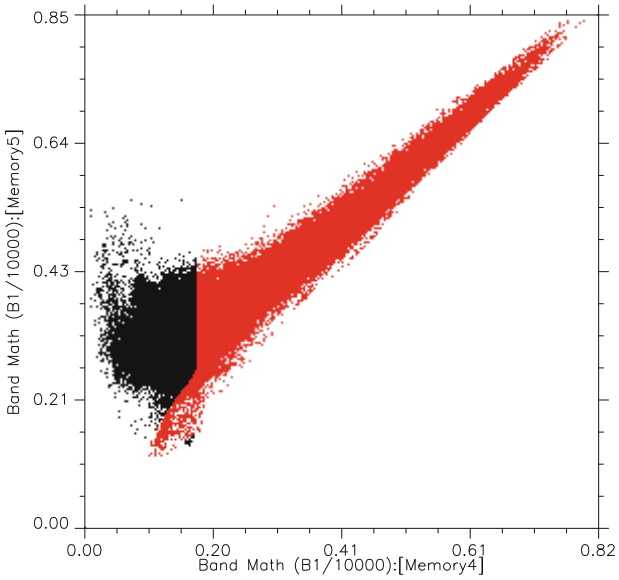

Fig. 3. Cloud cover detection from MOD09GA in red-nir feature space in Henan Province on May. 8th 2006, cloud cover in red, clear-sky in black

cloud is 0.18. When the reflectance of red is greater than 0.18, the pixel is regarded as covered by cloud. And the ratio between reflectance of near-infrared and red to distinguish cloud is 1.45. When the ratio is less than 1.45, the pixel is regarded as covered by cloud. Then all the pixels in validation and observation use these two principles to remove cloud pixels.

3.2 MPDI Observation in Different Soil Depth

The thresholds are adopted to remove pixels disturbed by cloud cover at Zhengzhou Station in the whole year of 2008. Dates with soil moisture observation in situ are collected to calculate the correlation between MPDI and soil moisture in different depths. The result shows that, among all the 36 pairs of ground-satellite synchronous data, 12 pairs are under clear sky condition. These 12 pairs of data are used to do validation in the depth of 10cm, 20cm, 50cm and 10-20cm. The result shows that MPDI corresponds well with shallow depth of soil moisture. The coefficients in the depth of 10cm, 20cm and 10-20cm are -0.8873, -0.6840 and -0.8226, respectively. And the coefficient in the depth of 50cm is insufficient as -0.1645. Therefore, MPDI has strong correlation with shallow soil moisture in different seasons of the whole year, while the correlation with soil moisture in depth of 50cm is weak.

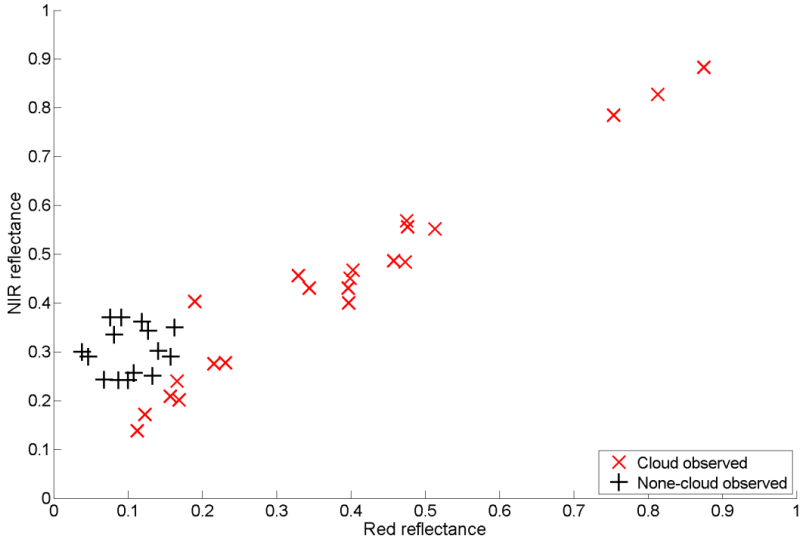

Fig. 4. Cloud cover detection from MOD09GA ground-satellite synchronous data in red-nir feature space at Zhengzhou station in 2008. × denotes observation disturbed by cloud cover, + denotes observation in clear-sky.

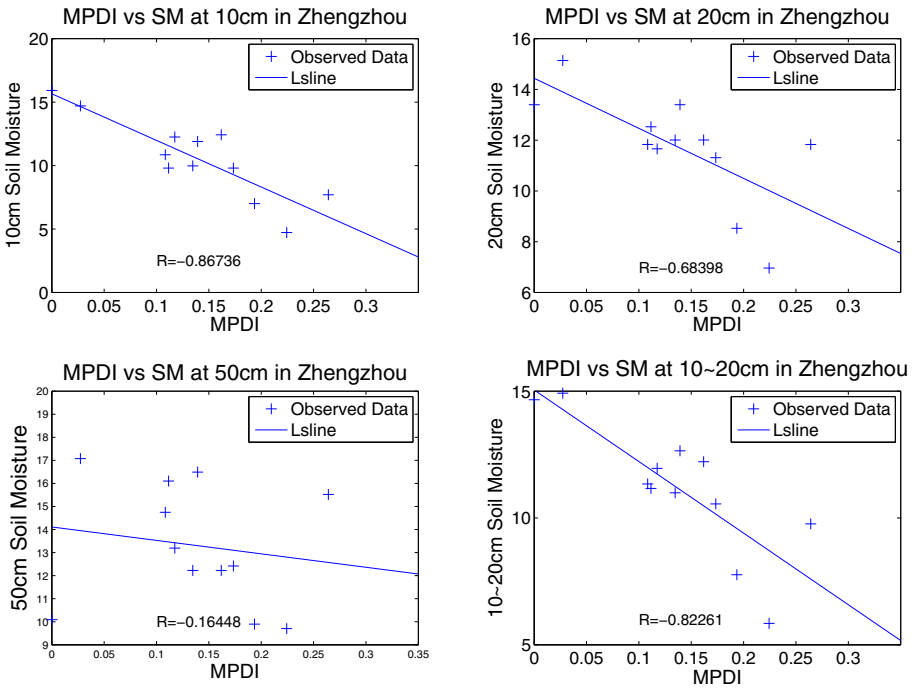

Fig. 5. Correlationship analysis between MPDI and soil moisture in different depths at Zhengzhou station: (upper left) linear fitting for MPDI and soil moisture in depth of 10cm, (upper right) linear fitting for MPDI and soil moisture in depth of 20cm, (bottom left) linear fitting for MPDI and soil moisture in depth of 50cm, (bottom right) linear fitting for MPDI and soil moisture in depth of 10-20cm.

3.3 Sensitivity of Time-Lag Effect

Soil moisture in the depth of 10cm is used to do validation of time validity. Since there is few data in clear sky condition with 1-day time-lag, validation of time validity is processed with no time-lag, 2-day, 3-day and 4-day time-lag. The result shows that the coefficient with no time-lag is -0.8873, which means remote sensing data corresponding soil moisture in time. The coefficient with 2-day time-lag is -0.4587. And the coefficients with more than 3-day time-lag are insufficient to observe the soil moisture. Therefore, MPDI derived from remote sensing data observed soil moisture in time, and soil moisture in shallow depth changes rapidly within 1 to 4 days, thus no effective observation is made after more than 3-day delay.

3.4 Effect of Soil Texture and Vegetation Fraction

Using data in Henan Province from the year of 2001 to 2010, validation of MPDI is performed on tillering stage (middle of November) and heading stage (early in May),

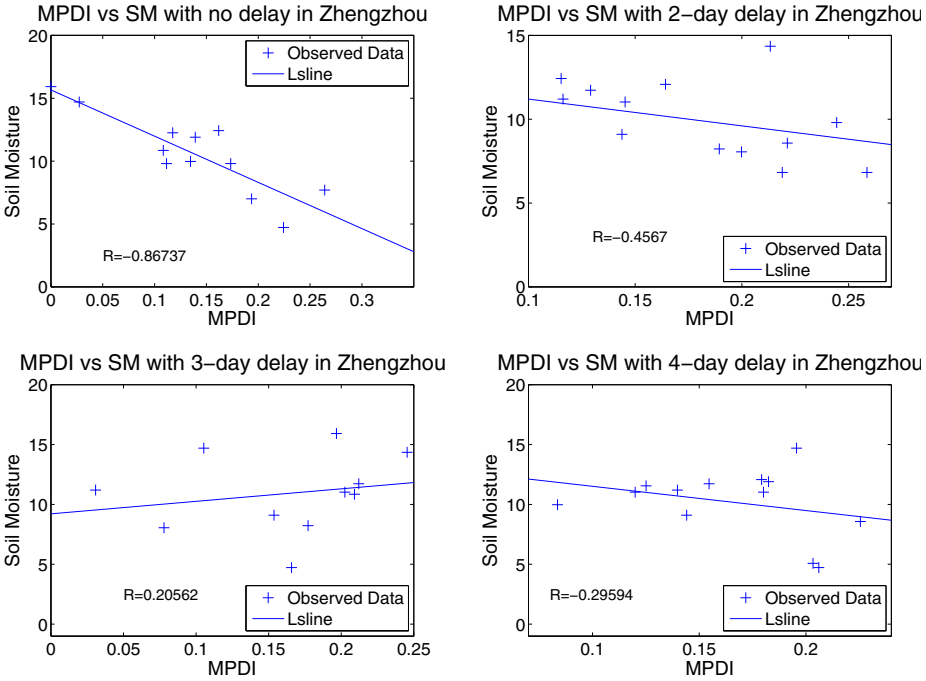

Fig. 6. validation of time validity at Zhengzhou station in 2008: (upper left) linear fitting for MPDI and soil moisture in depth of 10cm with no time-lag, (upper right) linear fitting for MPDI and soil moisture in depth of 10cm with 2-day time-lag, (bottom left) linear fitting for MPDI and soil moisture in depth of 10cm with 3-day time-lag, (bottom right) linear fitting for MPDI and soil moisture in depth of 10cm with 4-day time-lag.

respectively. On tillering stage, validation was processed for the stations of different soil texture types with no cloud cover, the coefficient between MPDI and comprehensive drought index (K) is 0.47378. For the stations of the same soil texture type of loam, coefficient between MPDI and soil moisture is -0.52275 in clear sky condition. On heading stage, validation was processed for the stations of different soil texture types with no cloud cover, the coefficient between MPDI and comprehensive drought index (K) is 0.51554. For the stations of the same soil texture type of loam, coefficient between MPDI and soil moisture is -0.81308 in clear sky condition. Vegetation fraction is low in tillering stage, when LAI is less than 2. And vegetation fraction is relatively high in heading stage, when LAI is greater than 2. The results show that MPDI performs better in high vegetation fraction condition than low vegetation fraction condition. And MPDI performs better in the same soil texture type condition than in different soil type condition both on tillering stage and heading stage.

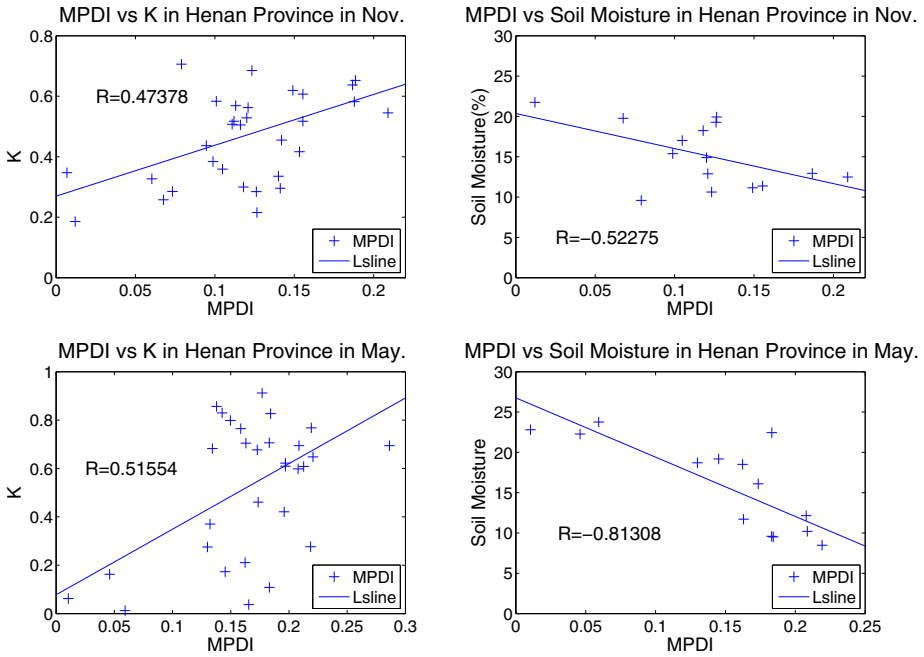

Fig. 7. (upper left) linear fitting for MPDI and comprehensive drought index K at stations with different soil textures in tillering stage, (upper right) linear fitting for MPDI and soil moisture at stations with the same soil texture of loam in tillering stage, (bottom left) linear fitting for MPDI and comprehensive drought index K at stations with different soil textures in heading stage, (upper right) linear fitting for MPDI and soil moisture at stations with the same soil texture of loam in heading stage.

4 Conclusion

The MODIS reflectance data and observed soil moisture information in the agro meteorological stations were used in the investigation. The Modified Perpendicular Drought Index (MPDI) was calculated and validation in Henan Province. We concluded that the MPDI showed a negative correlation with soil moisture in winter wheat growing area of Henan, and MPDI presented its better feature for estimating soil moisture in 10cm soil depth than others depths of soil. When examining the effect of the time-lag, we demonstrated that the MPDI corresponded soil moisture rapidly with no time-lag effect from 0-3 days time-lag; however, soil moisture changed obviously on a 4-daytime-lag in 10cm depth. For the sensitive of soil texture types to the soil moisture estimation, we found that, for the stations of the same soil texture type of loam, the coefficient between MPDI and soil moisture is -0.81308 in clear sky condition. It indicated that accuracy of estimated soil moisture will be improved if the soil texture maps are added into the analysis process.

Acknowledgements. This study is supported the Social Commonweal Meteorological Research Project (Grant No. GYHY201106027), the Fund of Agricultural Science &Technology Achievements (No.2011GB249100), the Global Change Global Research Key Project of the National Science Plan (Grant No. 2010CB951302), and 100 Talent Program of Chinese Academy of Sciences.

References

1. Brubaker, K.L., Entekhabi, D.: Analysis of feedback mechanisms in land-atmosphere interaction. Water Resour. Res. 32, 1343–1357 (1996)
2. Hosseini, M., Saradjian, M.R.: Multi-index-based soil moisture estimation using MODIS images. Inter. J. Remote Sens. 32, 6799–6809 (2011)
3. Goward, S.N., Cruickshanks, G.D., Hope, A.S.: Observed relation between thermal emission and reflected spectral radiance of a complex vegetated landscape. Remote Sens. Environ. 18, 137–146 (1985)
4. Price, J.C.: Using spatial context in satellite data to infer regional scale evapotranspiration. IEEE Trans. Geosci. Remote Sens. 28, 940–948 (1990)
5. Vicente-Serrano, S.M., Pons-Fernandez, X., Cuadrat-Prats, J.: Mapping soil moisture in the central Ebro river valley (northeast Spain) with Landsat and NOAA satellite imagery: a comparison with meteorological data. Inter. J. Remote Sens. 25, 4325–4350 (2004)
6. Jackson, R.D., Idso, S., Reginato, R., Pinter, J.P.: Canopy temperature as a crop water stress indicator. Water Res. Res. 17, 1133–1138 (1981)
7. Gillies, R., Kustas, W., Humes, K.: A verification of the'triangle'method for obtaining surface soil water content and energy fluxes from remote measurements of the Normalized Difference Vegetation Index (NDVI) and surface. Inter. J. Remote Sens. 18, 3145–3166 (1997)
8. Goward, S.N., Hope, A.: Evapotranspiration from combined reflected solar and emitted terrestrial radiation: preliminary FIFE results from AVHRR data. Advan. Space Res. 9, 239–249 (1989)
9. Huete, A., Justice, C., Liu, H.: Development of vegetation and soil indices for MODIS-EOS. Remote Sens. Environ. 49, 224–234 (1994)
10. Wang, C.Y., Qi, S.H., Niu, Z., Wang, J.B.: Evaluating soil moisture status in China using the temperature–vegetation dryness index (TVDI). Can. J. Remote Sens. 30(5), 671–679 (2004)
11. Mallick, K., Bhattacharya, B.K., Patel, N.K.: Estimating volume surface moisture content for cropped soils using a soil wetness index based on surface temperature and NDVI. Agri. Forest Meteo. 149, 1327–1342 (2009)
12. Gao, B.C.: NDWI–A normalized difference water index for remote sensing of vegetation liquid water from space. Remote Sens. Environ. 58, 257–266 (1996)
13. Zhang, J.H., Guo, W.J.: Studying on spectral characteristics of winter wheat with different soil moisture condition. In: The 2nd Inter. Sym. Recent Adv. Quan. Remote Sen. RAQRS'II, Spain (2006)
14. Ghulam, A., Qin, Q., Zhan, Z.: Designing of the perpendicular drought index. Environ. Geol. 52(6), 1045–1052 (2007a)
15. Ghulam, A., Qin, Q., Teyip, T., Li, Z.L.: Modified perpendicular drought index (MPDI): a real-timedrought monitoring method. ISPRS J. Photo. Remote Sens. 62, 150–164 (2007b)
16. Baret, F., Clevers, J.P.W., Steven, M.D.: The robustness of canopy gap fraction estimates from red and near-infrared reflectances: A comparison of approaches. Remote Sens. Envir. 54, 141–151 (1995)

MMS-IU Model for Incremental Update of Spatial Database

Yaqin Ye[1], Bo Chen[2], Bo Wan[1], Shunping Zhou[1], and Zejun Zuo[1]

[1] China University of Geoscience(Wuhan), 388 Lumo Road, Wuhan, China 430074
yeyaqin@126.com
[2] Wuhan Zondycyber Co., Wuhan, China 430074
galey@tom.com

Abstract. The update quality of spatial database determines the data's value. Combined with the characteristics of the spatial database updating, we studied incremental updates modeling of the spatial database and supported a multi-mode update model, which referred to as the MMS-IU. The model has two features: (1) it contains two different update ways to enhance the applicability of the model; (2) we combine time and events with the version management mechanism, which let the model becomes an event-based and object-oriented update model. The article elaborated the basic principle of an updated way supported by the MMS-IU model - that is based-edit update way. Aimed at the obtainment for changes information, incremental information fusion, concurrency control such key issues which existed in updating process, we proposed a reasonable solution.

Keywords: incremental update, obtainment for changes information, incremental information fusion, concurrency control.

1 Introduction

The key technologies of database incremental update modeling include incremental data storage model, the incremental information and historical data organizational issues, as well as version generates and space-time retrieval. But how organizations incremental information and the version of the database is the primary problem.

There are certain outcomes appear in incremental update model on the spatial data. ZL Fu and JH Wu (2007) proposed a multi-scale spatial database updating solution based CHT_EUR spatial database model. It can identify automatically change data by data matching and attributes contrasting between spatial elements. Jun Chen, Xiaoguang Zhou (2008) proposed an incremental update method based on the topological linkage, which infers the rules of the entity change type by topological relationship between the targets before and after the change. The article also designed several update operations for local linkage updating and topological consistency maintenance in database. However, it did not propose any access method of incremental information. Feng Zhang (2010) chose cadastral data for the study, and discussed the linkage changes which occurred in various elements during update

F. Bian et al. (Eds.): GRMSE 2013, Part I, CCIS 398, pp. 359–370, 2013.
© Springer-Verlag Berlin Heidelberg 2013

operations, and established a data consistency detection method. However, the incremental information access methods are singled.

According to the different ways of incremental data acquisition, Incremental update mode of spatial data can be divided into two types: one is based on data comparison update mode; the other is based-edit update mode. The common of the two modes is that are using incremental information to update the master database, and further to format the current potential files. The difference between the two is that the access methods for incremental data. Based on data comparison update mode will not store the incremental data after finishing the master database's updating, which resulting in the loss of the incremental data. When there are required for incremental data again to update the user database, it will find them by data comparison. This incremental update mode of spatial database is common. Thus based-edit update mode will store incremental information as soon as they are produced, and release them to the user database.

The purpose of the modeling is designed to a multi-mode incremental update model, which thinks about characteristics of access ways of current file and the update operations in reality. Such model is more in line with the actual update business processes at one hand. On the other hand, it can improve automation degree of the update process, and improve the accuracy and efficiency of updating.

2 MMS-IU Update Process Model

Incremental update process modeling is actually the further renovation and expansion based on the spatial data model, which is designed to meet the incremental update and management characters of a digital model of the storage.

Vector spatial database update must be designed and considered from the data's accuracy, consistency, security, user operating convenience. Based on the study of the data production process and the existing matching algorithms, considering the efficiency and feasibility of the algorithm, and applying synthesizing technologies such as version comparison, spatial object matching, geospatial reasoning, an effective rule processing and so on. A spatial database update model supporting multi-mode, called Multi-Mode Supported Incremental Updating model, in short MMS-IU.

The multi-mode of this model reflected in the supporting two update modes: based on data comparison mode and based-edit mode. Two update modes are different in incremental data acquisition as well as efficiency and functionality of data editing. Users should choose different editing modes depending on the business requirements.

Based on data comparison mode refers to using current version of the data to complete updating. Typically, users can get a current snapshot of the data by making a vectorization from the latest remote sensing image data or re-measuring topographic mapping. Then, how to find the incremental data is the core to complete the spatial database' updating. This update mode finds the incremental information through object matching algorithm. Unfortunately, the matching algorithm is often relatively

complexity and time-consuming. So only regional updates with a small amount of data, for example, nobody mountain area, are suitable to using this incremental update mode. However, when you want to update for heavy task area, this update model is insufficient.

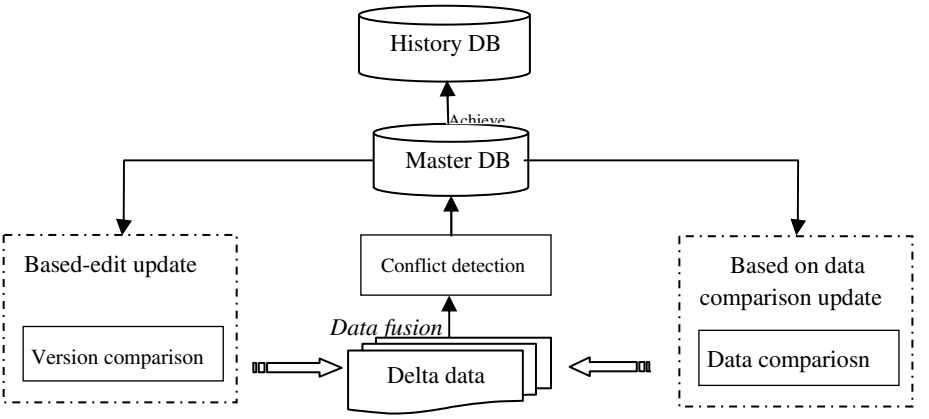

Fig. 1. Summary of the Update Model of MMS-IU

While based-edit incremental update mode means completing the extraction of changed data in the stage of data collection, and using certain format to store these data in the database. That mode puts spatial objects into a particular version, and allows the user to check out any range of data from the master database to a local edit database and updates the data in offline. This updating mode copied the data to be edited, extended editing from connection to offline, extended the incremental detection mechanism to the edit database, and reduced the pressure of the master database. Basic geographic information databases for urban planning, land management departments want to need several requires. On the one hand they want to meet the day-to-day requirements of the query. On the other hand, they must meet the requirements of daily data updates. Based-edit update can reduce the conflict between the two and the burden of database server.

3 The Principle of Based-Edit Incremental Update

In the process of database updating, data producers can determine the changes of geographic objects directly during spot mapping. When they obtain the new data by mapping equipment, the incremental data by human intervention has been identified. These results can realize incremental update of the spatial database directly, thereby eliminating the need for space target matching process, improving accuracy and discovery efficiency of the incremental information.

What's more, in reality, spatial data updating need several even many departments to work together. The various departments who are in charge of producing data have

obvious characteristics of the geographical distribution and administrative classification. Collaborative performance between them are as follow: the superior departments manage the entire database; while a superior department distributed the data to subordinate departments who are responsible to collect and update data respectively; and then complete synchronize of all branches' update to a master database. Therefore, how to ensure a superior-subordinate departments access to the transmission data update efficiency by MAN or LAN, must be considered.

The traditional editing way of online is making the updating always connect to the superior database server. This model needs to load a large amount of real-time data, and if concurrency control is not in place, other users cannot access and update. The better solution is to obtain only from a far superiors database need to edit the data to a local database, and then disconnect the connection to the server, in the case of off-line to continue editing. This way can improve the utilization of the transmission of data, and support on the lower level organizations to centrally manage the data block to update and maintain. What's more, it can ensure the completeness and correctness of the data updating process. In summary, the based-edit update mode is the solution in line with the actual application demand, providing a feasible idea for remote editing update and outdoors data collection in distributed environment.

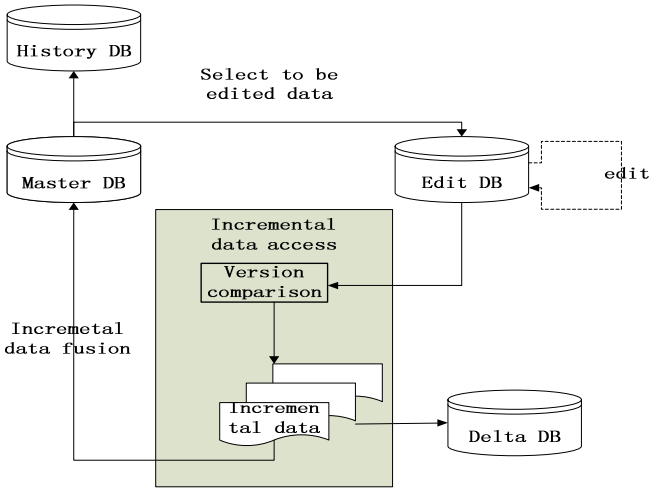

Fig. 2. Schematic Incremental Update Method of Based-edit

Let's familiar with the basic process of based-edit incremental updating. The entire update is generally divided into three steps. The first step is to obtain the data to be updated from the master database. The second step is to update the master database by using incremental information. The third step is to archive the old data. In case of the user definite the update range, apply to the master database after connecting to the internet and logging in. After the approval of the application, the user checks out the data to be updated from the master database in a window form and stores in the edit database. Now the user can be disconnected from the network, edit and update data in

the edit database. Since the data update has been completed, the user can import the incremental data from the edit database into the delta database. Next, the user needs to connect to the internet again, and uses the delta database to updates the master database. This update is suitable for the update of onerous task regional.

Actually, after data editing is completed, the user can directly use edit database to update the master database. Then what is the significance of the incremental database? This is considered two factors.

(1) In edit database, there is a lot of redundant data, which may increase the burden on the network and be time-consuming in update process.
(2) The edit database is not suitable for releasing incremental data.

So we designed incremental database, which smaller than the edit database and more suitable for network transmission. Moreover, its formation also provides technical support for incremental data release.

Based-edit incremental update methods are based on the state management mechanism of the spatial data. State is the basic concept. It is the identity of a moment in geographic database. Editing causes GDB to transit from one state to another state. Spatial database operation will generate a number of states, which can be represented by a set of states. The finite state machine consists of a set of states, an initial state, the input, and a conversion function transit the input and present status to the next state. A finite state machine M can be represented as a five-tuple:

$$M = \{S, \Sigma, l, s0, F\};$$

S represents a non-empty set of states, Σ represents a limited set of input, I is a mapping $S \times \Sigma \rightarrow P(S)$, i.e., a state transit to another state, $S0 \in S$ is the initial state, F is the end state of a group of state machine, but meets the $F \subseteq S$. Method based on this expression can formalize the change of spatial entities as the state tree, which can be used as the basis of query and relevant policy research.

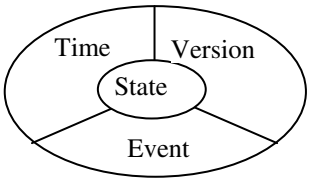

Fig. 3. Event-based or Object-oriented Incremental Update Expression.

In order to achieve a data change management of the different scales, the version is added based on the states. A version corresponds to a particular state. We also combine time and event to the model so as to enhance the expressive power on the spatial-temporal data. Thus kneading the time, event, version management uniformly to form the state of the data as the core concept, time, version and event co-expressed (as Figure3 shown), achieving the incremental update mechanism based on events and entities, which is more conducive to the management of the temporal and spatial information. In implementation, these three types of information are stored in the state data dictionary table.

4 The Key Technologies of Based-Edit Incremental Update

The master database is used to store fresh data. The update for it completes by the producer or deliverer of basic geographic information database by obtaining change data through measuring directly or indirectly. This process includes insert new features, delete disappears, and update some of changes in the original database.

The update methods of master database can be divided into two categories. One is update directly with changes draw from the same scale data, the other is update small-scale data by an updated large-scale data. This article focuses on the former method. When you use based-edit incremental updating method to deal with the same scale data, there are several key technologies, such as how to find the changed data, how to fuse changed data with the master database, and how to male concurrency control in the update process.

4.1 The Evolution of the Data State in Updating Process

Version management mechanism of spatial data is the research foundation for the realization of based-edit incremental updating. The whole process involves three databases: master database, edit database and incremental database. The design of the update process is as follows: choose one version (the check-out version) to edit, copy edit data on this version from master database to edit database. As the meanwhile, two versions will be created on edit database: reference version and check-out version. The reference version is sub version inherit from default version of edit database, and the check-out version is sub version inherit from the reference version.

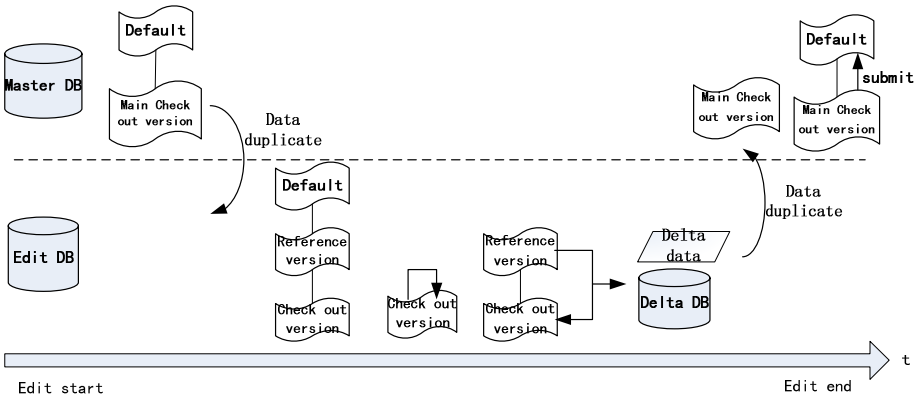

Fig. 4. Based-edit updating process at different times

Then user offline edit on the check-out version, and complete the check-in by any father and son version comparison algorithm and detect all changes (incremental) checked in to the master database, a version of the potential data are made. When a check-out action occurred, a relationship would be automatically established between

the master database and edit database for a data replication. The master database specified a version, then selected to be edited data and associated data on the version from the master database to edit database. The master database marked a main check-out version, which was the sub version of the editing version in the master database when offline action occurred. The main check-out version would be used later to access the changes by version comparison when the data was check-in.

Now let's back to the data replication. When data replication was completed, two versions were created immediately in edit database, which were the reference version and check-out version. The reference version was created as the sub-version of the default version in edit database. It reflected the state of the master database at checked-out instantly. This version cannot be edited, just be used to compare with check-out version to access delta data when check in. The check-out version was inherited from the reference version. User edited on this check-out version, and only this version can be checked back to the master database. By comparing the check-out version with the reference version, we could access all the changes in the editing operations (incremental data). The incremental data would be checked in to the master database on main check-out version. After incremental data was checked in, data replication relationship between the master database and edit database was deleted. That was the whole updating procedure. The actions are shown in Figure 4. The detailed description of correspondence version relationship is shown in Table 1.

Table 1. Geographic database version relational tables

Geographic Database	Correspondence Version	effect
The master DB	Main check-out version	1. When the data was checked out, a sub-version as the current version was created, while check in complete it would not be automatically deleted. 2. It received changes from the check-out version.
The edit DB	Reference version	1. It was created when check out, and cannot be edited. 2. When the data was checked in, it compared with checkout version to determine the changes in the data. It would be automatically deleted after the completion of the check in.
	Check-out version	1. To record user's editing operation in the edit database. 2. It would be automatically deleted after Checked in completed.

4.2 Incremental Data Access

Once users selected to be edited data from the master database to the edit database, they could edit the data in the edit database. After editing, users need to complete the update of the master database. The key of this step is how to find changes of spatial data. When the data was edited, the edit database could automatically maintain records of the incremental data by version management mechanism. We could find changed data by querying on the relationship between states and versions. Version management is to record changes by increasing the table A and table D. When users add an object to the database, there will add a record in Table A. When users delete an object from the database, there will add a record in Table D. When users update one object, there will add a record both Table A and Table D. Meanwhile two records associate by the same state ID. To do so, we converted incremental data access into two arbitrary states query problem. Of course, the two states must belong to the same linear branch in the state tree, so the states have the parent-child relationship.

It was not complicated to find changed information between two sons states based on this principle, but the difficulty was how to improve the efficiency of the algorithm. Generally speaking, the search algorithms between two states to find changed information needed to perform multiple complex SQL clauses. With the serious study of the principles of the search algorithm, we combined basic operations of relational tables, such as selections, projections and connections and finally the algorithm had been optimized. The ultimate realization of the algorithm could find any changes (add, update, delete) data only execute one SQL clause. That improved the efficiency of the algorithm greatly. The algorithm steps are as follows:

(1) Get exactly state IDs that the check-out version and reference version existed in the edit database pointed to. We assumed they were STATE_CHECKOUT and STATE_REF;
(2) Query linear branch IDs from the state tree that these two states belonged to. We assumed they were CHECKOUT_BRANCH_ID and REF_BRANCH_ID;
(3) Query the states list start from STATE_REF, which belong to the same branch. We assumed it was SL_REF;

$$SL\_REF \leftarrow \Pi_{StateID}\left(\sigma_{(BranchID = REF\_BRANCH\_ID \wedge StateID \leq STATE\_REF)}(BRANCH\_TBL)\right)$$

(4) Find out intersect branch ID between STATE_CHECKOUT and STATE_REF state. We assumed it was STATE_CROSS. The formula could be showed as follow;

$$STATE\_CROSS \leftarrow MAX_{stateID}(\sigma_{stateID \leq STATE\_CHECKOUT \wedge stateID \in SL\_REF}(BRANCH\_TBL))$$

(5) Query the states list SL between STATE_REF and STATE_CHECKOUT states on this branch;

$$SL \leftarrow \prod_{stateID}\left(\sigma_{(stateID \in SL\_REF \wedge stateID > STATE\_CROSS)}(BRANCH\_TBL)\right)$$

(6) Query all the records from Table A and D under states list SL to find the collection of added features. Added features exist in table A and do not exist in table D. We formula added features collection CAt as follow:

$$CA_t \leftarrow \Pi_{u.FID}(\sigma_{(u.StateID \in SL \wedge d.FID\ IS\ NULL)} (\rho_d(D) \overset{\bowtie\sqsubset}{d.FID = u.FID \wedge d.existStateID = u.StateID} \rho_u(A)))$$

(7) Query all the records from Table A and D under states list SL to find the collection of deleted features. Deleted features exist in table D and do not exist in table A. We formula deleted features collection CDt as follow:

$$CD_t \leftarrow \Pi_{d.FID}(\sigma_{(d.existStateID \in SL \wedge u.FID\ IS\ NULL)} (\rho_d(D) \overset{\sqsupset\bowtie}{d.FID = u.FID \wedge d.existStateID = u.StateID} \rho_u(A)))$$

(8) Query all the records from Table A and D under states list SL to find the collection of updated features. Updated features exist in table A and table D. We formula updated features collection CUt as follow:

$$CU_t \leftarrow \Pi_{u.FID}(\sigma_{(u.StateID \in SL)} (\rho_d(D) \overset{\bowtie}{d.FID = u.FID \wedge d.existStateID = u.StateID} \rho_u(A)))$$

(9) A collection of incremental information between two states is the total of CAt, CDt and CUt.

4.3 Incremental Information Fusion

Now we had incremental information collection. How to use this collection to update the master database in order to form the present potential data? Fig. 5 depicted the version and status changes in the main database and edit database when incremental data fusion process occurred:

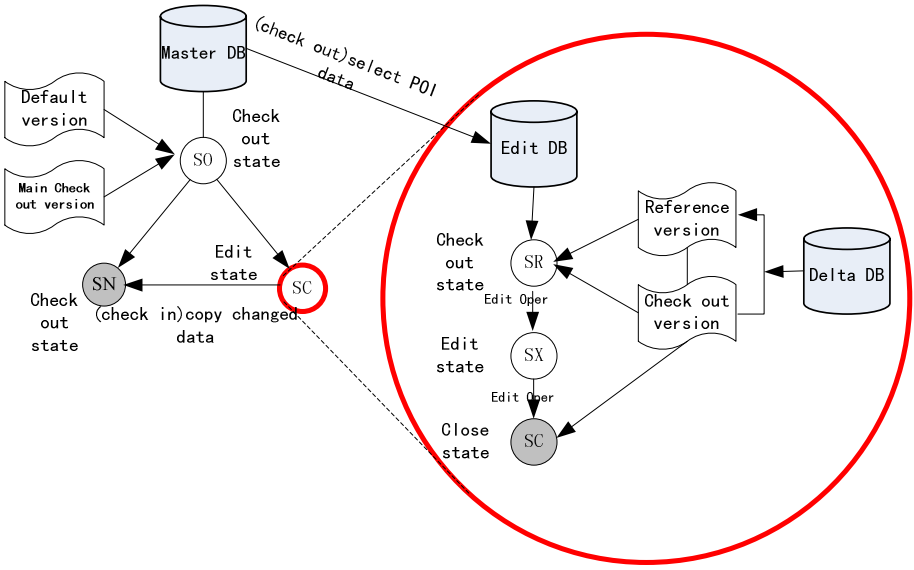

Fig. 5. Edit state diagram

(1) The main check-out version in the master database was state SO. When data was checked in, SO created a sub state SC. Then the main database started to receive the incremental data checked in from the edit database. At the same time, another state SN was created, which was the checked-in state. The main check-out version and state SC belong to the same state branches in the case of no editing. If editing is performed, the SC and SO will be in a different state branch.
(2) Before the edit database performed check-in operation, it would determine incremental information between check-out state SR and edit ending state SC by the states comparison algorithm. Then it would replicate the incremental information to the master database state SC. When replication was completed, the states of Table A and Table D will point to the new state SN. The main check-out version would also point to that state after checking in. So long, the check-in process was completed.

Next, we tested with real data to validate the feasibility of the process (shown as Fig.6).

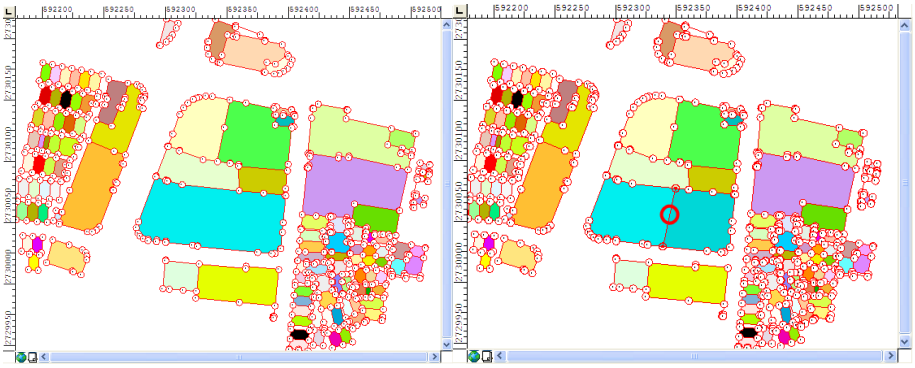

Fig. 6. Before updating land use data (left), and the updated chart (right)

4.4 Concurrency Control in Update Process

Modern GIS is adapted to the network environment and supports multi-user concurrent operation. Therefore, concurrency issues must be taken into account in the design of any of the functions of the GIS. It may last a long time when users start to edit data checked out from the master database. Other users' access to the same regional data throughout the update process will not be affected. Common offline solutions are needed to put multi-scale object locks to the data, but version management realized in geographic database, however, provides a no lock solution. This solution can be achieved throughout the updating. What's more, it makes information centralized management and highly concurrent update tool.

The object-oriented version management simplifies the process of editing. Because when several users access the database, it does not require the extraction of the data or locking objects. In the process of based-edit incremental updating, the two versions of the master database named the default version and the main check-out version are of

their duties. The main check-out version receives changes while the default version can receive the assessments from other users, such as read and update operation. That is the solution to online editing exclusive of resources. Users to apply a piece of data in the master database for offline editing process, other users can read or edit the same data on the master database unrestrictedly.

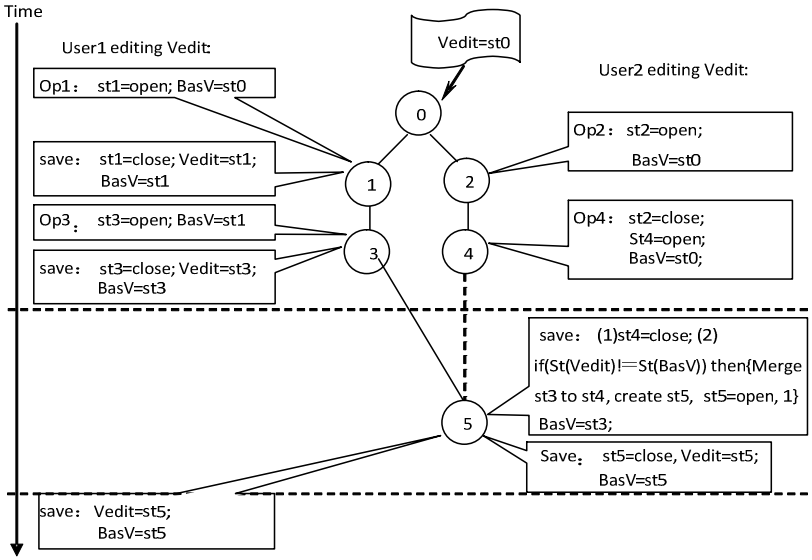

Fig. 7. Version Concurrency Schematic Diagram.

In summary, based-edit incremental update mode is a complete solution to the multi-user concurrent operation on the master database. It gives full play to the advantages of version management techniques. The algorithms of change detection and change integration are high efficiency. It is suitable for the actual maintenance. On the one hand, the offline editing can usually avoid enormous pressure of the network communication caused by synchronous operations to the database. On the other hand offline operations will faster than online ones. For example, the speed of layers loaded with graphic display will be better than in line form. The improvement in these two aspects contributes to enhance the efficiency of database updating.

5 Conclusion

Combining the characteristics of spatial data update process, we supported a multi-mode incremental update process model, which referred to as the MMS-IU. This study focuses on key issues of an MMS-IU model update mode –based-edit incremental updating model.

(1) Times and events were added to the version management mechanism in order to realize an event-based or object-oriented incremental update mechanism.

(2) A clear state evolution of the data update process was given.
(3) The optimization algorithm to obtain changes information based on version management has been proposed. Any two states changes query algorithm has been optimized based on the operations of the relational table, such as selection, projection and connection. The ultimate realization of the algorithm to find any changes (add, update, delete) data, only need to execute one SQL clause, which improved the efficiency of the algorithm greatly.
(4) The incremental data fusion mechanism has been analyzed. The focus point was analysis of incremental data to the main database integration process and the version evolution.

Acknowledgment. This project was supported by Wuhan Science and Technology Project (No. 2013010501010123), the Special Fund for Basic Scientific Research of Central Colleges, China University of Geosciences (No. CUGL130255).

References

1. Bobzien, M., Burghardt, D., Petzold, I.: Re-Generalisation and Construction Two Alternative Approaches to Automated Incremental Updating in MRDB. In: International Cartographic Conference: Mapping Approaches into a Changing World (2005)
2. Jiang, J., Chen, J., Li, Z.-L.: Continuous Updating of Geo-spatial Databases. Geomatics World 5(2), 1–5 (2004)
3. Fu, Z., Wu, J.: Update Technologies for Multi-scale Spatial Database. Geomatics and Information Science of Wuhan University 32(12), 1115–1118 (2007)
4. Chen, J., Zhou, X.: Incremental Updating of Spatial Database Based on Topological Linkage, Taking Cadastral Database's Updating as an Example. Acta Geodaetica et Cartographica Sinica 37(3), 321–329, 337 (2008)
5. Zhang, F., Liu, N., Liu, R., et al.: Research of Cadastral Data Modelling and Database Updating Based on Spatio-temporal Press. Acta Geodaetica et Cartographica Sinica 39(3) (2010)
6. Wu, J., Fu, Z.: Methodology of Feature Change Detect ion and Matching in Data Updating. Journal of Computer Applications 28(6), 1612–1615 (2008)
7. Cooper, A.: The Concepts of Incremental Updating and Versioning. In: Proceedings of the 21st International Cartographic Conference, Durban, August 10-16 (2003)
8. Anders, K.-H.: MRDB Approach for Automatic Incremental Update ICA Workshop on Generalisation and Multiple Representation, Leicester, August 20-21 (2004), `http://ica.ign.fr/Leicester/paper/Anders-v1-ICAWorkshop.pdf` (accessed February 2005)
9. Wan, B., Zhou, S., Chen, B., Fang, F.: Design and Realization of MAPGIS7.0 Version Management Based on DBMS. Earth Science 31(5) (2006)
10. Peled, A., Cooper, A.: Incremental Updating and Versioning. In: Proceedings of 20th International Cartographic Conference, Beijing, pp. 2806–2809 (2001)
11. Badard, T.: On the automatic retrieval of updates in geographic databases based on geographic data matching tools. In: ICA 1999 Proceedings, Ottawa, Canada, pp. 47–56 (1999)
12. Jahard, Y., Lemarié, C., Lecordix, F.: The Implementation of New Technology to Automate Map Generalisation And incremental Updating Processes. In: Proceedings of the 21st International Cartographic Conference, Durban, August 10-16, pp. 1449–1459 (2003)
13. Zeiler, M.: Modeling Our World: The ESRI Guide to Geodatabase Design. ESRI Press (1999)

Research on Meteorological Application Oriented Vectorization of Raster Datasets*

Lujin Hu[1,2] , Kunwang Tao[2], and Agen Qiu[2]

[1] School of Resource and Environmental Science, Wuhan University, Wuhan, China
[2] Research Center of Government GIS,
Chinese Academy of Surveying & Mapping, Beijing, China
hulujin5388@163.com

Abstract. The meteorological data always display hierarchically, and its feature value is shown as planar pattern, which borderline is smooth and continuous. Based on these characteristics, a meteorological application oriented method for vectorization of raster data is brought out in this paper. With this method, the meteorological data storage format is described, a topographic data structure is designed, and traditional border-tracing algorithm is optimized. Meanwhile, the problems generated during the vectorization are solved, which conclude the data hierarchically display, edge smoothing, edge self intersection, closed angle, single point handling. Finally, with the tests in the disaster prevention and mitigation geographic information system, this method has a good practicability at weather forecast, rainfall warning meteorological disaster protection and other aspects of meteorological applications.

Keywords: vectorization, meteorological application, raster datasets.

1 Introduction

For the various types of data sources, the meteorological data always have heterogeneous data formats, which result in many difficulties when integration and sharing data [1]. To solve this problem, vectorization of raster datasets become one of isomorphic ways for the heterogeneous meteorological data. In addition, vectorization of meteorological raster datasets is of significance in the field of Meteorology, GIS, disaster modeling, and Ecology. E.g. the visualization representation of meteorological data requires the overlay analysis of base map and the meteorological thematic map, if the meteorological map is show as the raster data format, when the map is zoom in, the raster edges will become jagged and ambiguous, which destroy the beauty of the map overlay, in other wise, when in the vector format, however degree the map zooms in, it will still show smooth and clear edges. In general, the vectorization of the meteorological data can realize a high accuracy visualization representation, which can play an adequate role in the weather forecast, rainfall warning, disaster protection and other aspects.

* Supported by the National science and technology support project (2012AA12A309).

F. Bian et al. (Eds.): GRMSE 2013, Part I, CCIS 398, pp. 371–383, 2013.
© Springer-Verlag Berlin Heidelberg 2013

In the application of GIS, e.g. the regional or national prevention and mitigation system, the vectorization meteorological data often refers to the weather forecast data, rainfall data, the temperature data, pressure data, and so on. All the data listed above shows the characteristics as follows: (1) It is visualized hierarchically, vary types of meteorological data are represented hierarchically according to specified values. E.g. the rainfall data can be divided into levels based on rainfall deepness, 0-10 mm, 10-20mm, 20-50mm, 50-100mm, 100-250mm, more than 250mm, and the level of more than 250mm will be thought to cause the meteorological disaster. (2) After the hierarchically showing of the meteorological data, it always display as lower level polygons consists of the higher level polygons, e.g. in the application of rainfall data, the definite level increases with the rainfall deepness, the first feature layer consists of the second level, and the second feature layer consists of the third level, and so on, meanwhile, different level polygon's edges will not intersect with each other, which can be showed in the Fig.1. (3) After the vectorization of the meteorological data, all levels of boundary is continuous and smoothly.

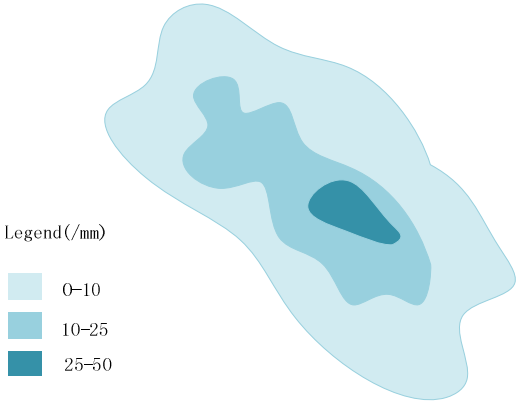

Fig. 1. Rainfall data were showing hierarchically

Review the vectorization algorithms of the raster datasets: Shen Zhangquan's research shows a method of obtaining the arc points coordinate and other vector information by scanning the raster datasets, then junk the coordinate points to lines or the polygon[2-3]; Vectorization technology is summarized in Zhang Xiaocan's paper[4]; In the research of Xie Shunping[5], a run-length encoding algorithm was put forward based on run-length encoding of raster datasets, the vector information can be extracted from the source data, which is suitable to remote sensing image analysis and the special analysis; Fu Qinghua focus on the problem of polygon edges self intersection and the holes in the polygon during the vectorization[6]; An optimized algorithm is brought out based on the arithmetic of Shen Zhangquan by Zhang Xinghua[7]; Liu Renwu brought out an automatic tracking algorithm based on the method of thinning the edges level by level[8]; From the research described above, they mostly focus on the optimization of the vectorization arithmetic, and applied in

the processing of remote sensing data and the geographic spatial data, while in this paper, meteorological application oriented is one of the main aspects, a hieratical vectorization method is described in detail, the same as the realization and experimental analysis of this method, which consist of the reading of the data source, the design of the topographic data structure and boundary tracking arithmetic description, solution for the problem during the vectorization. Meanwhile, the traditional vectorization method was optimized in this paper, and it improved the efficiency of data processing.

2 Method Description

The vectorization Method of meteorological application oriented will be described from four aspects: meteorological data source analysis, topographic data structure design, boundary-tracking algorithm optimization and the follow-up problems solution design. Then, the four aspects will be expounded in details.

2.1 Meteorological Data Source Analysis

Meteorological data mostly rely on the data gathered from the weather stations, if the quality of the metadata is good enough, it can be used to the vector analysis directly, but, in most cases, the meteorological data cannot meet the requirement of the data quality, because of the small quality of the distribution of the weather stations. Then, the meteorological data need to the further interpolation analysis. The data source used in this paper just was the data that have been interpolated or done the other processing, and the data is stores as the *.img format.

*.img format use the data node to store the data, each data node conclude its head files, and each data node can be related with the head files [9]. In this paper, *.img files were read with the library of GDAL.

2.2 Topographic Storage Structure Design

After vectorization of the meteorological data, every level of polygon always exits the holes. For the processing and visualising of the data with holes, the topographic storage structure was designed for the hierarchal vectorization algorithm, which considerate the characteristics of the meteorological data. Topographic storage data structure stores the point data, simple polygon data, complex polygon data and their spatial relationship.

Point storage structure stores the coordinate of the point, the index codes, and its attributes, which shows in the Table 1.

Table 1. Point Storage Structure

Index codes	Attribute codes	Coordinates
P_index	P_type	(x,y)

Simple polygon storage structure was designed to store the outer boundary of every level data. It consists of the lists of coordinates, the attribute codes and the Index codes of the polygon. Just as shown in Table2.

Table 2. Simple Polygon Storage Structure

Index codes	Attributes codes	Outer boundary's coordinates
Poly_index	Poly_type	(0,x,y)(1,x,y)…(n,x,y)

Complex polygon storage structure was designed to store the inner boundary of every level data. It consists of the outer boundary's coordinates, the inner boundary's coordinates, its index codes and Attributes codes. It can be showed in Table3.

Table 3. Multiple Polygon Storage Structure

Index codes	Attributes codes	Outer boundary's coordinates	Inner boundary's coordinates
MPoly_index	MPoly_type	(0,x,y)(1,x,y)…(n,x,y)	(0,x,y)(1,x,y)…(n,x,y)

Meanwhile, a rule was set as: every polygon has one outer boundary and one or many inner boundaries, which can be showed at Fig.2.

Fig. 2. Inner and outer boundary of the polygons

2.3 Optimization of Boundary-Tracking Algorithm

Boundary-tracking algorithm is the core of the method for converting raster data to vector data. The optimization of the algorithm is of great significance for improving the efficiency of the vectorization program. So, some optimizations of the boundary-tracking algorithm were put forward, and the algorithm's efficiency was improved.

2.3.1 Principle of the 8-Connected Tracking Algorithm

the main steps of the 8-connected tracking algorithm can be described as follows: (1) the first level's threshold value should be determined, with this value the image pixel value can be divided into two parts, which are greater than the threshold value and another part smaller than the threshold value, i.e. binary the images, and setting the

background color and the target object color. (2) It is important to make sure the start tracking point, the tracking rules always from the left to the right, and the top to the bottom of the raster images, when traced to the point whose color different from the background color, the point can be determined as the start point. (3)From the start point, tracing at the eight neighborhood direction pixel point, among the eight pixel, the pixel which at the direction of 45 degree, i.e. the right top pixel, if it is the target point, come to the point which rotate 90 degree at the clockwise direction, if it is not the target point, come to the point which rotate to 45 degree at the anticlockwise direction. When coming to the point which is not the target point, the next target point will be the boundary point, and store the data. Just show in the Fig.3, the start point just set as the center, you can trace to 45 degree the direction of the center point, just as the red arrow point at. Then, we can see it is the target point, you can rotate 90 degree clockwise, then it comes to the background point, it should rotate 45 degree anticlockwise, and comes to the target point, it is the point which found after the point is not the target point and meet the condition of the becoming the boundary point. You can store it in the boundary entity structure, and begin with this point as the new start point and seek for other boundary points.

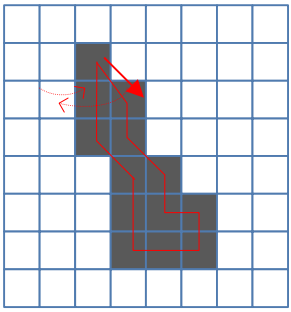

Fig. 3. Schematic of eight neighborhood border-tracing algorithm

2.3.2 Shortcomings of the 8-Connected Tracking Algorithm in Meteorological Application and Their Solutions

During the implementation of the 8-connected boundary tracking arithmetic, two shortcomings were found. First of all, when the area contain single line region, after the vectorization, the whole polygon region will be divided into two parts, which can be showed as Fig.4. The second, when the polygon area is small, its boundary will be show as point or just single lines, and this will not according with the meteorological characteristics of showing planar. In order to solve these two problems, two correspondent solutions were brought out in this paper, which can be expounded as follows.

In allusion to the first problem, which can be showed in Fig.4.(a), and Fig4.(b). When the boundary point 2 is found out, the boundary point 1 will be circulated seek out, which can lead to the tracking end is coming in advance, the boundary points are not all found, and the whole planar feature will be divided into two parts. Finally it

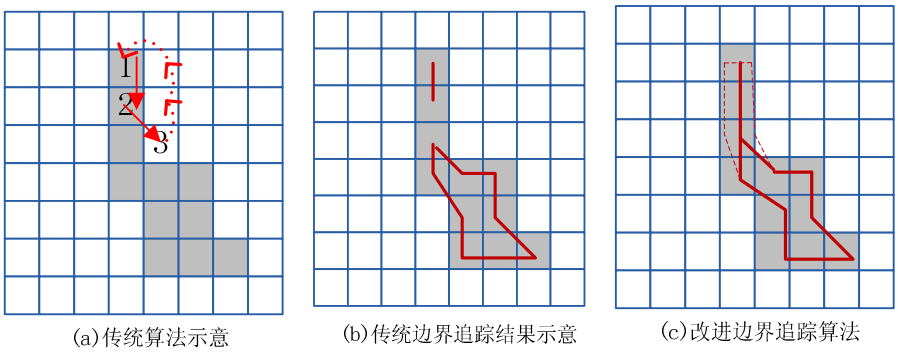

Fig. 4. Improved algorithm of Border-tracing

result in much data redundancy, as Fig.4.(b). The main principle to solve this problem is to moving the start point to the left pixel, i.e. if the origin start point is (x, y), now it will be (x-1, y). And if the boundary point is found to (x, y) again, the tracking is stopped. Just as the Fig.4.(c), the red dotted lines shows the result of optimized algorithm.

In allusion to the second problem, which can be showed in Fig.4.(b). As the exit of single pixel and the single line pixels in the raster datasets, the vectorization results are always single point and lines, which are not meet the characteristic of planar showing with the meteorological data. The solution for this problem was to adding an condition when storing the boundary point in the boundary data structure, i.e. when storing the boundary point, do the judgment, whether the point is overlap with the point which have been stored in the boundary structure, if it overlap with the exit boundary point, correct the exiting point's x coordinate, reduce half pixel, i.e. correct x to (x-0.5), and to the new found point, increase half pixel, i.e. convert x to (x+0.5), and store the new point. Then in the process of vectorization, the origin width will not changed, just as shown in the Fig.4.(c) the red dotted line.

2.3.3 Implementation Steps of the Improved Vectorization Arithmetic

The main implementation steps will be described as follows, the step which marked * is the added step to optimized the traditional vectorization arithmetic.

Step 1: `setBGcolor=0; setTargetcolor=255;`

// Do the binary process for the raster datasets, the target object color was set to white, which RGB is(255,255,255), respectively, the background color was set to black, which RGB is (0,0,0).

Step 2: `for(i: 0-(column-1), j: 0-(row-1));`

// Seek for the first start point from the left to the right and top to the bottom.

```
if(value[i, j]==255)
          { xstart=i, ystart = j;}
```

// if the pixel color is black, i.e. RGB is(255,255,255), it is the target point, and store the start point's coordinate (xstart, ystart).

* Step 3: `xpstartnext=i-1;ypsatrtnext=j;`

// if the first target pixels is the boundary pixels, record the first target pixel's left pixel i.e. Pstartnext(xstart-1,ystart).

```
xpcenter= xpstartnext;ypcenter=ypstartnext;
```

//the Pcenter (xcenter, ycenter) is the center point.

Step 4: mark point Pcenter's eight neighborhood directID as shown in the Fig.5, at the same time to record each neighborhood pixel's offset to center pixel i.e. the direction [direcID, 2] = {(1, 1), (1, 0), (1, 1), (0, 1), (1, 1), (1, 0), (1, 1), (0, 1)}.

Step 5: define the initial direction is StartDrect = 0, i.e. 0 direction shown in Fig.5. If the StartDirect coordinate values is (255,255,255), you can store this point as a boundary point and come to the step6, meanwhile set StartDirect = StartDirect - 2 judging other direction at the same time, otherwise StartDirect = StartDirect + 1, go to the step4;

*Step 6: for(i: 0 - border. num){If (borderx = = border [i]){borderx = borderx + 0.5; Border [i].x = border [i].x-0.5; // when a new boundary point was overlap with the existing boundary point, the original boundary point minus the half pixel, the new point increase half a pixel coordinates.

Step 7: if (borderx == xstart && bordery == ystart) BorderSearchOver = true; //if the finding boundary point as the starting point, a polygon's bpundary seeking get to the end, jump out of the seeking loop and begin another polygon.

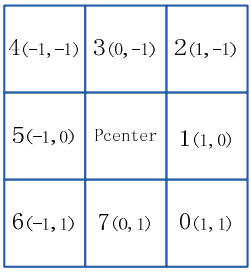

Fig. 5. The mark of eight neighborhood direction

2.4 Problems and Solutions during the Vectrization Process

After the polygon edges were tracked out with the 8-coonected tracking arithmetic, there are some problems exist in the vector data, which conclude the problem of how to display the meteorological vector data in hierarchal layers, how to smooth the polygon edges, and how to process the edges' self intersection, closed angles and single pixel point. The following will be expounded the solutions one by one.

2.4.1 Displaying the Meteorological Data Hierarchal Polygon Layers

In allusion to characteristic of the meteorological data which is showing in hierarchal layers, besides of the topographic data storage structure, the overall meteorological data structure was designed. The binary building blocks were used to store the vector

data, which is convenient to the data loading at the computer server-side in GIS. The hierarchical layers' data storage structure can be described as: each level data stores as a few geometric entities, and each geometric entities is consists of multiple complex polygon data, and the corresponding attribute data. The binary building blocks structure of hierarchical Data is shown in the Fig.6. Blob's head file was used to store the following data: the number of geometric entities (i.e., meteorological data classification number), number of the complicated polygons in one geometric entity (i.e., number of each level of meteorological data's polygons), and each entity's storage location. The body of the Binary file is mainly stored the coordinates lists of each complex polygon in each geometric entities

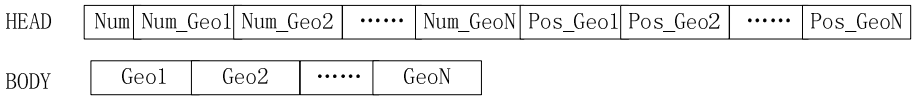

Fig. 6. Meteorological layer data's storage structure in binary file

2.4.2 Smoothing the Polygon Edges

Due to vector data extracted by the arithmetic were the pixel coordinates, so if the curvilinear interpolation was done directly, it will lead to shaking lines at the polygon edges. So before curvilinear interpolation, you can do the data compression processing first, Douglas-poker algorithm was used for data compression in this paper, and at the same time, using the parabolic weighted curvilinear algorithm as the edge smooth interpolation method.

The principle of Douglas poker algorithm can be depicted as follows: Connect the begin point and end point of the lists of points, then calculate the distance between the rest points to the lines, find maximum distance, if it is less than the distance tolerance, delete all the points list, otherwise retain that point, and split the line into two curves and do the same operation.

The principle of the parabolic weighted curvilinear algorithm: according to the point of series, each three adjacent points connect as a parabola, the curve which overlapped by every two adjacent parabolic curve, can be show as the final interpolation curve. As shown in Fig.7. And the following formula 1 is the curvilinear interpolation formula.

$$\begin{cases} X_{i\sim i+1}(t) = x_i - (x_{i-1} - x_{i+1})t + 2(2x_{i-1} - 5x_i + 4x_{i+1} - x_{i+2})t^2 \\ -4(x_{i-1} - 3x_i + 3x_{i+1} - x_{i+2})t^3 \\ Y_{i\sim i+1}(t) = y_i - (y_{i-1} - y_{i+1})t + 2(2y_{i-1} - 5y_i + 4y_{i+1} - y_{i+2})t^2 \\ -4(y_{i-1} - 3y_i + 3y_{i+1} - y_{i+2})t^3 \end{cases} \quad (1)$$

At the above formula, $X_{i\sim i+1}(t)$ represents the x coordinate which interpolated between i point and i+1 point. t is the number between 0 to 1, which represent the number according to the interpolated location.

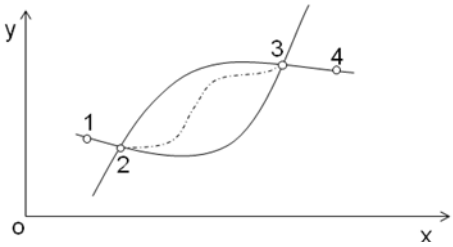

Fig. 7. Weighted average curve

2.4.3 Processing the Edges' Self-intersection

For the states below shows in Fig.8.(a), to a large extent, edge self intersection would be happened after edge extracted with curve compression and curve smoothing, which is due to boundary's overlay. Therefore, a theory based on cross product is used to decide whether edge self-intersection is happened, and delete the intersection point if happened. The procedure is described as Fig.8.

Fig. 8. Dealing with the edge self-intersection

2.4.4 Handing of the Close Angles

Closed angle, which means the angle less than 30 degree, would be happened in the states below shows in Fig.9.(a). In this paper, the problem is improved by a algorithm based on bisector of angle, first, the angle should be decided whether its value is less than 30 degree or not, if less than 30, pan the edges inwards pivot on to the bisector of angle until its value is more than 30. As Shown in Fig.9.

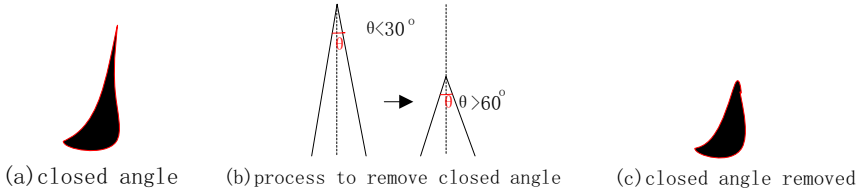

Fig. 9. Diagrams of handling the closed angle

2.4.5 Dealing with the Isolated Pixel

The single pixel point always exits in the raster datasets, as shown in Fig.10. If you just convert this single raster point into vector point, when zoom in or zoom out, it will still just a vector point. So you can preprocess the single raster point when convert it to the vector data. One simple way is to convert it into a circle which radius

is specified, but if in this way, on one hand, it will influence the beauty of the whole map, and on the other hand, it will reduce the accuracy of the vectorization. So in this paper an 8-beighborhood process method is brought out, according to this method, all the influence the lower level influences will be considerate.

The principle of the 8-beighborhood single point processing method can be depicted as follows: judging the center single point and its 8-beighborhood pixels' hierarchal level grade, if the center point's grade and one of its direction neighborhood pixel is differ by one grade, then the radius of this neighbor direction can be set one pixel, if more than one grade, e.g. n grade, the radius can be set one pixel per n, i.e. 1/n pixel. As shown in the Fig.10, the blue single pixel, its level grade is 2, gray area's level grade is 1, white as the background area, and level grade 0. With different neighbor directions, the smaller grade differences the lower radius value.

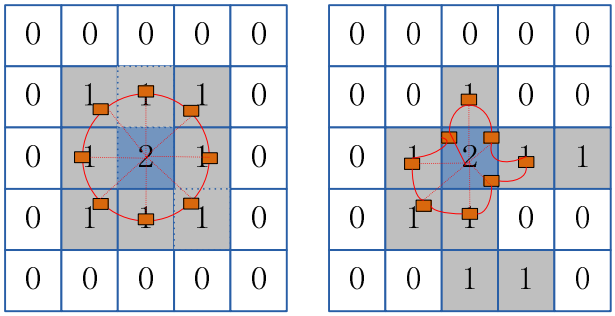

Fig. 10. Diagram of handling the single pixel

3 Method Implementation

3.1 Realization of Hierarchically Displaying with the Meteorological Data

Just as rainfall data (.IMG) as the meteorological data, the procedures of vectorization hierarchically can be depicted as follows: (1) Reading the IMG data and storing it with two-dimensional array which represent the column and the row. (2) Set the level threshold values for the whole raster datasets, which in according with the data type. (3) Do the binarization processing for the raster datasets. (4) Post processing such as data compression with stabilization, line smoothing, sharp corner removing, self intersection removing and isolated pixel point removing. (5) Storing data in the hierarchical data structure. In order to reading and loading the data from server.

3.2 Data Structure Design

3.2.1 Point Data Structure

Point data structure is used to store the vertex latitude and longitude coordinate of polygon, and point data structure is used for simple or complex polygon structure. The structure is described as below:

```
class GeoPoint
{    double x; //latitude coordinate
     double y;  // longitude coordinate      }
```

3.2.2 Design of Simple Polygon Data Structure

Simple polygon data structure is used to store the data unit of polygon without inner boundary. This data structure is used for the construction of complex polygon data structure and geometry entity data structure. The structure is described as below:

```
class Polygon
{    List<GeoPoint> point; //store the point in order of data list
}
```

3.2.3 Design of Complex Polygon Data Structure

Complex polygon data structure is made up of outer boundary and inner boundary, which are stored with simple polygon data structure. Just shown as below:

```
calss MultiPolygon
{    Polygon Outboard; //store outer boundary
     List<Polygon> Inboard; //store inner boundaries
}
```

3.2.4 Design of Geometry Entity Data Structure

Geometry entity data structure is used to store meteorological data of every level like meteorological polygon or meteorological attributes. it can be described as below:

```
class Geometry
{    public Multipolygon multi;
     public string attributes;
}
```

4 Experimental Analysis

With the platform of the disaster prevention and mitigation GIS, this paper test the algorithm of hierarchical vectorization which oriented to meteorological application. In the client, the original raster data is processed and written to database in form of binary files, the result is displayed and invoked in server. Below is the result map after hierarchical vectorization of raster meteorological data with the algorithm.

The pictures show the result of overlay analysis between vector meteorological data and remote sensing data, and between vector meteorological data and vector map data. From the picture, the method not only make the overlay display accurately between vectorization and image or map, but also satisfy the unity of space vision and the data structure satisfy the display efficiency in data invoking.

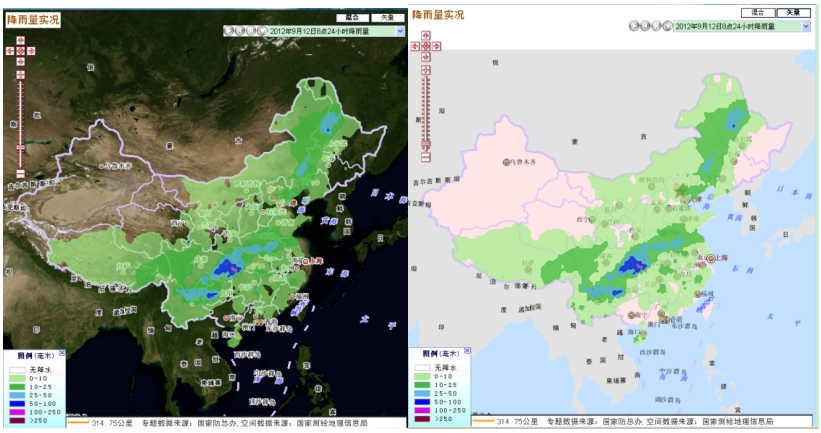

Fig. 11. Results of the algorithm

5 Conclusion

To solve the low-precision overlay display of meteorological raster data with image tile data or vector map data in GIS, this paper propose a meteorological application oriented vectorization method. A topological data structure is designed according to the features of meteorological data in this paper, and the boundary tracking algorithm was improved in this paper. Simultaneously, this paper analyze the problem after vectorization of meteorological data, such as hierarchal vectorization, hole processing, boundary self intersection, shape corner processing, isolated pixel processing, and propose a stable solution to improve the vectorization algorithm. Finally, with the test through the disaster prevention and mitigation GIS, the result shows the method get a good stability and efficiency.

References

1. Xu, G.: Design and Implementation of Meteorological data Management and Forcast System. Dongbei University (2008)
2. Shen, Z., Wang, R.: A New Approach for Converting Raster to Vector–Node. Journal of Image and Graphics 3(4), 318–321 (1998)
3. Shen, Z., Wang, R.: Research on the Method of Converting Raster to Vector based on Topographic Principle. Journal of Remote Sensing 3(2), 38–42 (1999)
4. Zhang, X., Pan, Y.: Vectorization Technique for GIS Grid Data Based on “Grid Technique”. Jour. of Computer-Aided Design and Computer Graphics 13(10), 895–900 (2001)
5. Xie, S., Dou, J., Wang, L., Go, G.: Approach of Vectorization for GIS Raster Data Based on Run-length Encoding System. Acta Geodetic Cartographic Sinica 33(4), 323–327 (2004)

6. Fu, Q., Ni, S., Guo, J.: Vectorization of Raster Data and Solving of its Problems. Modern Surveying and Mapping 27(3), 8–11 (2004)
7. Zhang, X., Wang, M., Jiang, S.: A Novel Approach for Raster Data Vectorization. Geo-information and Science 10(6), 730–735 (2008)
8. Liu, R., Li, Y.: Study of Auto-vectorization based on Scan-thinning Algorithm. Acta Geodaetica et Cartographic Sinica 41(2), 309–314 (2012)
9. Zhang, Z., Liu, R., Liu, N.: Analysis of Img Format and Method of Reading for the Large Image. Computer Application 41(2), 60–61 (2003)

Principle and Error Analysis of Doppler Acoustic Omni-directional Beacon

Kun Fang, Sen Zhang, and Jie Liu

Electronic Engineering Department, Naval University of Engineering
Wuhan, China
fk827728@126.com

Abstract. In this paper, a new underwater acoustic navigation method is proposed, which is named Doppler Acoustic Omni-directional Beacon (DAOB). It is borrowed from the idea of Doppler VHF Omni-directional Range (DVOR) and based on the Doppler principle. To overcome the serious multipath effect, a new signal mode which uses FM signal as reference signal and is named from FM mode is presented. The system error of is analyzed. Some simulation is presented to verify the performance.

Keywords: DAOB, Error Analysis, Principle, FM Model.

1 Introduction

Underwater navigation is to make the underwater vehicle or body obtaining absolute coordinates or the relative coordinates. Underwater navigation is a key technique in the research of underwater vehicle [1].

With the development of the exploitation of ocean and marine research, It is important to provide navigation information for a variety of underwater bodies, which put forward more and more requirements for the underwater navigation system: Low cost, convenient use and placement of any number of user access etc. At present long baseline is the mainly underwater navigation method, but it is need to put at least three beacons. It is high cost and complex to lay on and recover.

In this case, single beacon underwater navigation system has focused more and more attention based on. It is only need to put one beacon to provide navigation information [2]. Obviously, the navigation system based on the single beacon is economical and easy to use.

At present single beacon underwater acoustic navigation can be divided into three parts. (1) Underwater navigation system based on a single responder + USBL. (2) Underwater navigation system based on single beacon, pure distance calculation. (3) Single beacon underwater navigation system based on spiral array.

In this paper a new single beacon system based on the Doppler principle is introduced. This system has the same characteristics as single beacon system based on spiral array[3]. This beacon system could provide range and azimuth information for underwater vehicle with assistance of the synchronous clock or response equipment.

F. Bian et al. (Eds.): GRMSE 2013, Part I, CCIS 398, pp. 384–392, 2013.
© Springer-Verlag Berlin Heidelberg 2013

The idea of the single beacon system mainly borrowed from the one of Doppler VHF Omni-directional Radio Range(DVOR). We call it Doppler Acoustic Omni-directional Beacon(DAOB).

2 Principle of DAOB

A point source beacon moves around the center O clockwise in a circle, the angular velocity is ω. The coordinate system definition diagram is shown in Fig. 1.

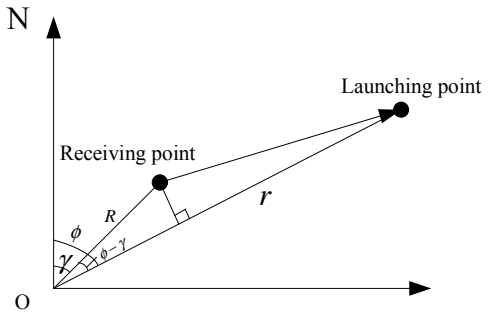

Fig. 1. The Coordinate System Definition of DAOB

In the picture, r is the rotation radius of the circle. The azimuth angle of receiving point is ϕ. The azimuth angle of launching point is γ. The distance between underwater vehicle and the rotation center of the circle is R. Provided the launching point always send a single frequency signal of which the sending frequency is f_v. The delay phase from the launching point source to the receiving point is shown in Formula 1.

$$\varphi = \frac{2\pi f_v}{c}\sqrt{\left[r - R\cos(\phi-\gamma)\right]^2 + \left[R\sin(\phi-\gamma)\right]^2} \tag{1}$$

Equation Chapter (Next) Section 2In the formula 1, c is the speed of sound. Because $\gamma = \omega t$, the receiving signal can be expressed as Formula 2.

$$s_v(t) = \cos\left[2\pi f_v\left(t - \frac{\sqrt{\left[r - R\cos(\phi-\omega t)\right]^2 + \left[R\sin(\phi-\omega t)\right]^2}}{c}\right)\right] \tag{2}$$

At this time, the instantaneous frequency of the signal is shown in Formula 3.

$$f(t) = \frac{1}{2\pi}\frac{d}{dt}\left[2\pi f_v\left(t - \frac{\sqrt{\left[r - R\cos(\phi-\omega t)\right]^2 + \left[R\sin(\phi-\omega t)\right]^2}}{c}\right)\right] \\ = f_v + f_d \tag{3}$$

The variable f_d is the Doppler frequency caused by the motion of point source, and it can be expressed as Formula 4.

$$f_d = -\frac{f_v}{c}\frac{d}{dt}\sqrt{\left[r - R\cos(\phi-\omega t)\right]^2 + \left[R\sin(\phi-\omega t)\right]^2} \\ = -\frac{f_v}{c}\frac{-\omega R\left[r - R\cos(\phi-\omega t)\right]\sin(\phi-\omega t) - \omega R^2\sin(\phi-\omega t)\cos(\phi-\omega t)}{\sqrt{\left[r - R\cos(\phi-\omega t)\right]^2 + \left[R\sin(\phi-\omega t)\right]^2}} \\ = \frac{f_v}{c}\frac{\omega R\sin(\phi-\omega t)}{\sqrt{\left[1 - \frac{R\cos(\phi-\omega t)}{r}\right]^2 + \left[\frac{R\sin(\phi-\omega t)}{r}\right]^2}} \tag{4}$$

In normal case, $R \ll r$, and Formula 4 can be simplified to Formula 5.

$$f_d \approx \frac{\omega R f_v \sin(\phi-\omega t)}{C} \tag{5}$$

From Formula 5, it can be found that a frequency modulation(FM) signal is formed because of the Doppler Effect, when a transmitting single frequency signal source moves around a circular. The initial phase of modulation signal depends on azimuth of receiving point. The FM signal is called "variable phase signal". At the receiving point, a sinusoidal modulation signal is received after phase demodulation. The modulation frequency of the signal is rotating frequency, and the initial phase of the signal is the azimuth angle[4].

DAOB provides the navigation information by the principle above. Another launching point source is placed on the circle. This FM signal is called “reference phase signal”, and the signal can be expressed as formula 6.

$$s_{Rs}(t) = \cos\left[2\pi f_R\left(t + \frac{r\cos(\omega t)}{C}\right)\right] \tag{6}$$

The reference phase signal frequency is f_0, and the initial phase of the modulation signal for reference phase signal is 0.

At the receiving point, the variable phase signal and the reference phase signal through band-pass filter with different center frequency respectively. The two demodulated signal can be obtained through phase detection. The azimuth angle can be estimated from the phase different of the two modulated signal.

Of course, the reference phase signal can also be used in other forms such as the use of signal, broadband signal (such as narrow pulse or LFM). Its rising edge of the rotating source indicates the initial phase for the 0 time. Reference phase signal is used to provide the variable phases signal with a zero phase reference. Comparing the zero phase delay with the variable phase modulation signal at the receiving unit, the zero phase difference can be obtained to estimate the azimuth angle[5].

3 Error Analysis of DAOB (FM Model)

In order to analysis system error more delicately, considering the sound velocity in water is much less than the speed of light in air, therefore, here the accurate model of system error analysis is used[6].

We are concerned only with the phase part of FM mode, In Formula 2, the received signal can be expressed as the form of Formula 7.

$$s(t)=\cos\left[2\pi f_v\left(t-\frac{\sqrt{\left[r-R\cos(\phi-\omega t)\right]^2+\left[R\sin(\phi-\omega t)\right]^2}}{c}\right)\right] \tag{7}$$

First we simplified the delay term, using two Taylor to expand. $(R/r)^2$ and the high order terms can be neglected because it is very small. So we can get Formula 8.

$$\begin{aligned}\Delta t&=\frac{1}{c}\sqrt{\left[r-R\cos(\phi-\omega t)\right]^2+\left[R\sin(\phi-\omega t)\right]^2}\\&=\frac{r}{c}\sqrt{1-2R\cos(\phi-\omega t)/r+(R/r)^2}\\&\approx\frac{r}{c}\left[1-\frac{R\cos(\phi-\omega t)}{r}+\frac{1}{2}\left(\frac{R\cos(\phi-\omega t)}{r}\right)^2\right]\end{aligned} \tag{8}$$

So $s(t)$ can be expressed in Formula 9.

$$s(t)=\cos\left\{2\pi f_v\left[t-\frac{r}{c}\left(1-\frac{R\cos(\phi-\omega t)}{r}+\frac{1}{2}\left(\frac{R\cos(\phi-\omega t)}{r}\right)^2\right)\right]\right\} \tag{9}$$

instantaneous phase φ_{pr} is:

$$\varphi_{pr}=2\pi f_v\left[-\frac{r}{c}\left(1-\frac{R\cos(\phi-\omega t)}{r}+\frac{1}{2}\left(\frac{R\cos(\phi-\omega t)}{r}\right)^2\right)\right] \tag{10}$$

Because after filtering, the received signal will pass an ideal detector. It means that the instantaneous phase is differentiated. Therefore, the output signal is:

$$i_{pr} = \frac{1}{2\pi}\frac{d\varphi_{pr}}{dt} = \frac{f_v \omega R}{c}\left[\sin(\phi-\omega t) - \frac{R}{2r}\sin(2\phi-2\omega t)\right]$$
$$= \frac{f_v \omega R}{c}\sqrt{1+\left(\frac{R}{2r}\right)^2 - \left(\frac{R}{r}\right)\cdot\cos(\phi-\omega t)} \tag{11}$$
$$\cdot\sin\left\{(\phi-\omega t) - \tan^{-1}\left[\frac{(R/2r)\cdot\sin(\phi-\omega t)}{1-(R/2r)\cdot\cos(\phi-\omega t)}\right]\right\}$$

In the formula, $-\tan^{-1}$ is the error term:

$$e = -\tan^{-1}\left[\frac{(R/2r)\cdot\sin(\phi-\omega t)}{1-(R/2r)\cdot\cos(\phi-\omega t)}\right] \tag{12}$$

Because $\left(\frac{R}{2r}\right)$ is far less than 1, the error term is similar to $-(R/2r)\cdot\sin(\phi-\omega t)$, the error is very small.

The following is a simulation of the error, and the parameters are shown in the following Table 1.

Table 1. The Parameters of Simulation

parameter	Q	R	ω	fr	fA	fB
value	0.2	0.2米	2π	60KHz	55KHz	65KHz

The result of the simulation is shown in Fig. 2.

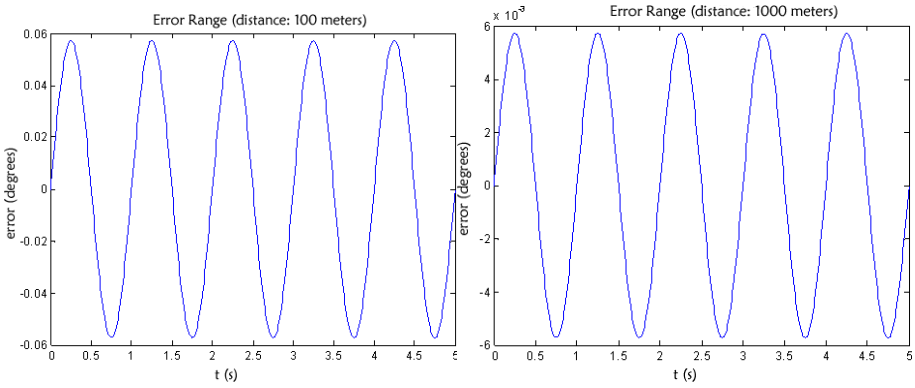

Fig. 2. The Result of Smulation

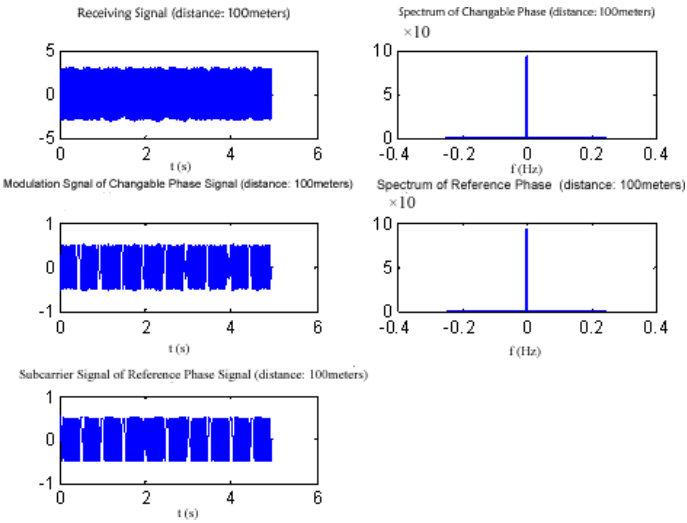

Fig. 3. The Receiving Signal under Ideal Conditions（r=100meters）

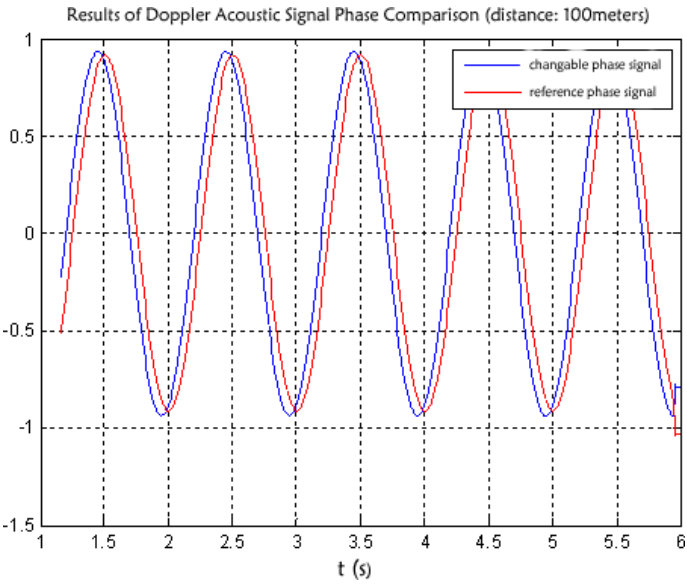

Fig. 4. The Result Figure of Reference Phase compared to Changeable Phase

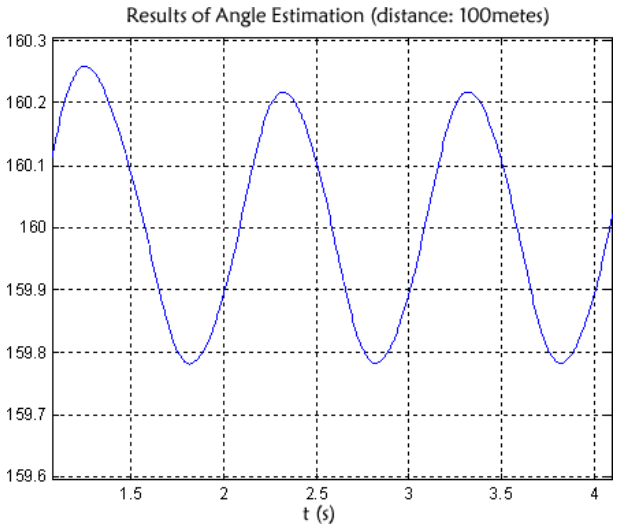

Fig. 5. The Result of Angle Estimation（r=100meters）

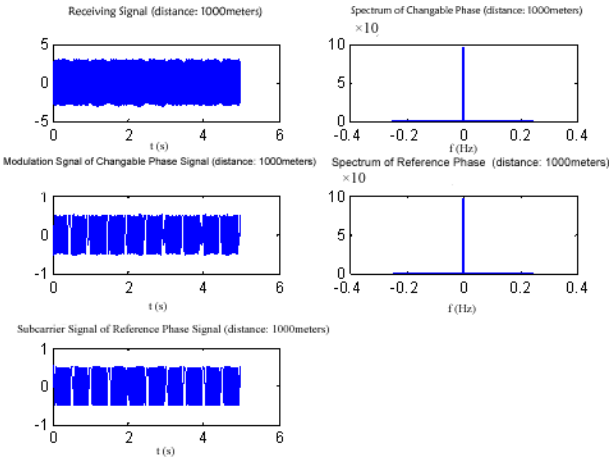

Fig. 6. The Receiving Signal under Ideal Conditions（r=1000meters）

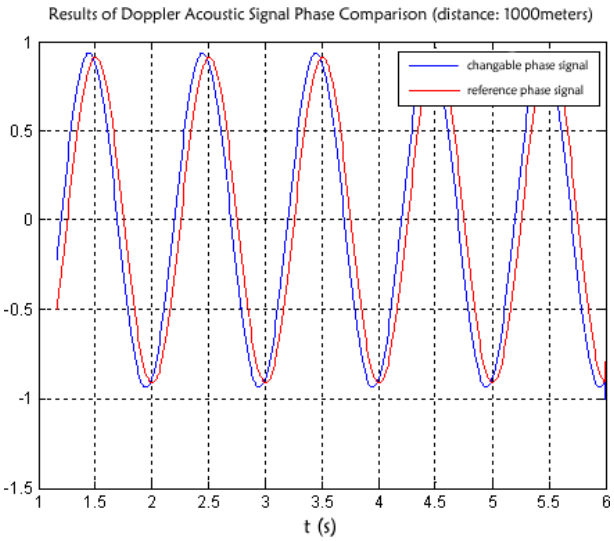

Fig. 7. The Result Figure of Reference Phase compared to Changeable Phase

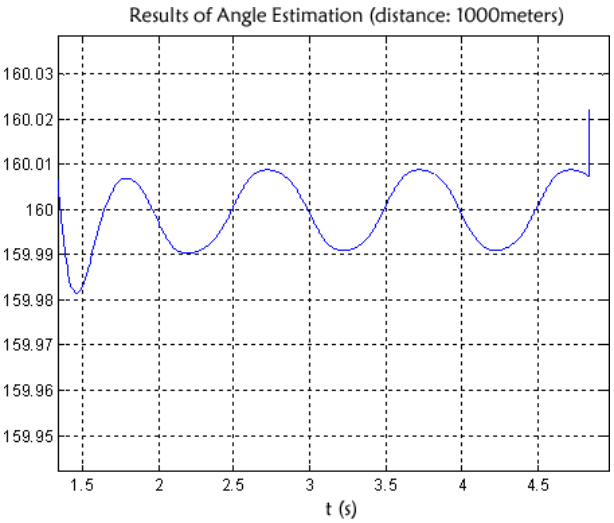

Fig. 8. The Result of Angle Estimation（r=1000meters）

4 Conclusion

In this paper, a new underwater acoustic navigation method is proposed, which utilizes Doppler Effect of a moving source. It causes the receiver receive different signal in different direction. To overcome the serious multipath effect, a new signal mode which uses FM signal as reference signal and is named from FM mode is presented. The system error of is analyzed. Some simulation is presented to verify the performance.

References

1. Hahn, M.J.: Undersea Navigation Via a Distributed Acoustic Communications Network. Naval Postgraduate School Master's Thesis (2005)
2. Rice, J.A.: Seaweb Acoustic Communication and Navigation Networks. In: Proceedings of the International Conference "Underwater Acoustic Measurements: Technologies & Results" (2005)
3. Rice, J.A.: Undersea Networked Acoustic Communication and Navigation for Autonomous Mine-Countermeasure Systems. In: Proc. 5th International Symposium on Technology and the Mine Problem (April 2002)
4. Webster, S.E.: Decentralized Single-Beacon Acoustic Navigation: Combined Communication and Navigation for Underwater Vehicles. Johns Hopkins University Ph. D's Thesis (2010)
5. Eustice, R.M., Whitcomb, L.L.: Recent Advances in Synchronous-Clock One-Way-Travel-Time Acoustic Navigation. In: Proceedings of the IEEE Oceans, pp. 1–6 (2006)
6. Eustice, R.M., Singh, H., Whitcomb, L.L.: Synchronous-Clock, One-Way-Travel-Time Acoustic Navigation for Underwater Vehicles. Journal of Field Robotics 28(1), 121–136 (2011)

Retracted: The Discrimination of Cloud Using the Data of Calipso Based on SVM Method

Jingbo Wang and Xiaoyi Li

International School of Software, Wuhan University, Wuhan, China
Jingbowang.whu@gmail.com, 2496282640@qq.com

Abstract. Cloud is a natural physical phenomenon, and its growth is a very complicated process, knowing how to recognize the cloud in the atmosphere correctly is very important for understanding the physical conditions in the air. The launch of satellite is for a better research of the cloud layer around the earth and for new type of three dimensions observation of aerosol, and have a better understanding of how cloud layer affect the atmosphere and global warming, acquiring new knowledge concerning the distribution and evolvement. Besides, it can also help how cloud and aerosol is formed, developed and its influence on water resource supply, climate, weather and air quality. Our passage here is based on data from CALIPSO satellite, and we chose some parameters from it, using SVM classifying method to do the cloud discrimination. After that, we select testing samples to detect the correction rate of it and get our final result.

Keywords: CALIPSO, Support vector machine, Cloud discrimination.

Retracted

1 Introduction

Cloud is water vapor which condenses into water droplets, supercooledwater droplets and ice crystals or a visible slurry mixture of them.

The formation and growth of cloud is a complex physical process, the interaction of many factors like the temperature, humidity, airflow, condensation nuclei and ice nuclei in the atmosphere caused the formation of colorful cloud.

Cloud has an important influence on global climate change, it is the key to the earth's hydrologic cycle. Cloud can bring water from the air to the ground by influencing the radiation of the sun and the earth to control the intake and emission of heat on earth.

The formation of cloud, its appearance characteristic, the quantity, distribution and evolvement, not only reflects the atmospheric movement, stability and water vapor condition and so on of that time, it is also an important feature of the prediction of future climate change. Observing and analyzing the general evolution of cloud correctly and objectively is an important task of understanding the status of the physical condition of atmosphere, and also essential for grasping the law of weather changes.

F. Bian et al. (Eds.): GRMSE 2013, Part I, CCIS 398, pp. 393–402, 2013.
© Springer-Verlag Berlin Heidelberg 2013

For that reason, early in the 1990s, the US, Europe and Japan united to carry out a huge MTPE plan. By launching several satellites and form a rigorous global earth observation net of the earth's environment to carry out a full-scale, long-term observation. Its aim is to find out the changing rules so that they can solve environment problem fundamentally. Its core task is to build the EOS system.

There are 6 satellites in the EOS system, using the method of satellite formation, just like lining a train in a line. Those satellites are all polar-orbiting satellites, though their spatial resolution is very high, their temporal resolution is relatively low, with repeat observation time interval as long as 16 days.

Through the way of satellites formation, we can use its advantages and at the same time use satellite relay to implement repeated observation of the same spot to improve temporal resolution. This six satellites using this kind of working method, formed the "A-Train" satellites formation together.

2 Data

Cloud Aerosol Lidar and Infrared Pathfinder Satellite Observations (CALIPSO) is a member of "A-Train". CALIPSO satellite is used to observe the aerosol in the air that have an influence on weather and climate, which is called aerosol particles. It can provide critical data information of the characteristics of aerosol and cloud, radiation flux and atmospheric conditions, besides, it also provide lots of information concerning the height of cloud.

There are three main lowest point observation instruments carried on CALIPSO satellite, namely Cloud-Aerosol Lidar with Orthogonal Polarization(CALIOP), Wide Field Camera(WFC) and Imaging Infrared Radiometer(IIR).

WFC camera is a refined type of commercial off-the-shelf CT-633 star tracker camera produced by Ball Aerospace company. It is a kind of perpendicular to the imager which uses a single spectrum, covering an area of 620 to 670 nm. With a bandwidth of 50nm, it is mainly used to match a certain spectrum with the perpendicular to the imaging resolution imaging spectrometer on the "water" satellite, whose instantaneous field of view is 125m, bandwidth is 61m and data transfer rate is 26kb/s. IIR radiation meter is supplied by French Spatial Research Center, is belongs to the vertical scanning to the imager. The pixel resolution of IIR is 1km, and its bandwidth is 64km. It uses a micro detector array of radiation measurement, the rotate lens provides three measuring thermal infrared channel, with 8.65, 10.6 and 12.0 micron.

In this passage, the data we use is observed by 7249 observation spot ranging from 30°N to 70°, 110°E to 150°provide by CALIPSO satellite with the resolution of 5000m.

3 Research Method

SVM is a new kind of high efficiency machine learning algorithm, is an implementation to statistic learning principle, belonging to feedforward network in neural network. By introducing core function, it can map the feature space of the

Retracted

original sample to a high dimensional feature space. Using SVM algorithm can solve the problem of pattern recognition and non-linear regression. Here in the passage we are trying to use SVM algorithm to solve pattern recognition problem of cloud classification. Pattern recognition can be divided into linear separable pattern and linear inseparable pattern, below is a detailed description of them.

The main point of SVM algorithm is to find a optimal hyper plane in the multi-dimensional space, and separate the point having different characteristics in separate side of the plane and at the same time make those point be as far as possible to the plane. The distance between planes formed by the points whose names are support vectors that is nearest to the plane is called margin. Since those support vectors are nearest to the decision plane, we usually choose the points that are most difficult to classify as support vectors.

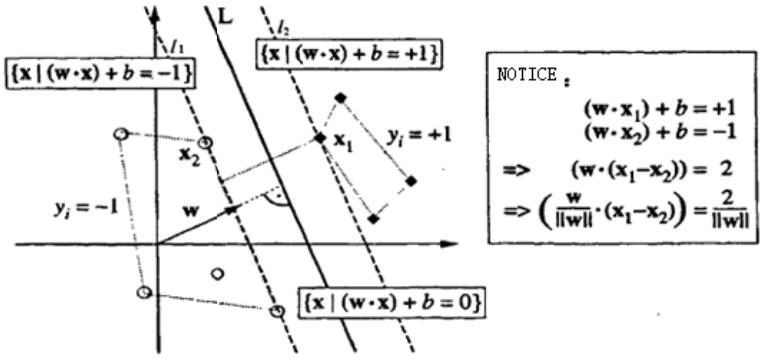

Fig. 1. The optimal classification

3.1 Linear Classification

Support vector machine defines an optimal linear hyper plane, and tries to convert the problem of finding an optimal one into solving quadratic programming. Moreover, based on Mercer theorem, through non-linear mapping of core function, it maps the sample space into a multi-dimensional feature space. And in this way it solves the highly non-linear problem in sample space in a linear manner. Support vector machine is put forward mainly aimed at two kinds of classification problems. Suppose given training samples{xi,yi}, i=1,...l,x∈R,yi∈{-1,1}, and there exists classification hyper plane $\omega * X + b = 0$, in order for all of the samples to be classified in the right side and have enough classification margin, they must satisfy (1) [1]

$$y_i[(w \cdot x_i) + b] \geq 0 \tag{1}$$

classification margin must satisfy the (2)

$$\min_{\{x_i|y_i=+1\}} \frac{(w\cdot x_i)+b}{\|w\|} - \min_{\{x_i|y_i=-1\}} \frac{(w\cdot x_i)+b}{\|w\|} = \frac{2}{\|w\|} \tag{2}$$

in order to maximize the classification margin $2/\|\omega\|$, that is minimize $\|\omega\|$, so that solve the optimal classification hyper plane problem is converted to constrained optimization problem, meaning under the constraint of (3), to minimize the (3)

$$\Psi(w) = \frac{1}{2}\|w\|^2 = \frac{1}{2}(w\cdot w) \tag{3}$$

By introducing the Lagrange function, we get the (4)

$$L = \frac{1}{2}\|w\|^2 - \sum_{i=1}^{l} a_i y_i (w\cdot x_i + b) + \sum_{i=1}^{l} a_i \tag{4}$$

Among them, ai>0 is Lagrange coefficient. Use (4) and calculate the partial derivatives for b and w respectively, we can convert the above problem to dual problem, just like (5) and (6)

$$\frac{\partial L}{\partial w} = w - \sum_{i=1}^{l} a_i y_i x_i = 0 \tag{5}$$

$$\frac{\partial L}{\partial b} = -\sum_{i=1}^{l} a_i y_i = 0 \tag{6}$$

Put (5) and (6) into (4), we will get the dual optimization problem, and calculate the maximum of the following function.

$$W(a) = \sum_{i=1}^{l} a_i - \frac{1}{2}\sum_{i,j=1}^{l} a_i a_j y_i y_j (x_i \cdot x_j) \tag{7}$$

$$\text{s.t.} \quad y_i[(w\cdot x_i)+b] \geq 0 \tag{8}$$

$$\sum_{i=1}^{l} y_i a_i = 0 \tag{9}$$

Among them, $a_i \geq 0; i = 1,...,l$

Rejected

The above equation is a quadratic programming under the constraints of an inequation. According to Karush. Kuhn. Tucker condition, this optimization problem must satisfy (10)

$$a_i\{y_i[(w\cdot x_i)+b]-1\}=0\,,\quad i=1,\cdots,l \tag{10}$$

Therefore, the corresponding Lagrange argument aiof most samples are 0, and indicates those samples whose ai≠0in (1) and call them support vectors (SVs). In SVM algorithms, SVs is the critical elements in training sets, they are nearest to the decision edge. And even if we delete all the training samples except those SVs and train again, we can get the same classification hyper plane.

After solving the above quadratic programming, the classification decision function can be described by (11). The sum in (11) is only applied to those SVs, that is those training samples whose corresponding Lagrange argument ai is not 0 determines the classification result, and all the other samples have nothing to do with classification result. b is class-based thresholds, when the training samples are not linear separable, we introduce non-negative slack variables, $\delta_i, i=1,...,l$,the optimization of classification hyper plane is as (12)

$$\min_{w,\xi_i}\frac{1}{2}\|w\|^2+C\sum_{i=1}^{l}\xi_i \tag{12}$$

The dual problem is to calculate the maximum α of the following function.

$$\sum_{i=1}^{l}a_i-\frac{1}{2}\sum_{i,j=1}^{l}a_ia_jy_iy_j(x_i\cdot x_j) \tag{13}$$

$$\text{s.t.}\quad y_i[(w\cdot x_i)+b]\geq 1-\xi_i \tag{14}$$

$$\sum_{i=1}^{l}y_ia_i=0 \tag{15}$$

Among them, $0\leq a_i\leq C,\delta_i\geq 0,i=1,...l$ and C>0 is a constant, and we call it error penalty parameter or regularization parameter, it is used control the degree of penalty for wrongly classified samples. When the training samples are not linear separable, we introduce slack variable, at that time, the classification decision function can also be expressed in the form of (11).

3.2 Non-linear Classification

As for non-linear classification problem, we can choose proper inner product function K(xi,xj)to implement a linear classification after some non-linear transformation. Then the optimized objective function becomes (16)

Rejected

$$Q(a) = \sum_{i=1}^{l} a_i - \frac{1}{2} \sum_{i,j=1}^{l} a_i a_j y_i y_j K(x_i, x_j) \tag{16}$$

And the corresponding classification decision function can be expressed as (17)

$$f(x) = \operatorname{sgn}\left[\sum_{i=1}^{l} a_i^* y_i K(x_i, x) + b^* \right] \tag{17}$$

So the above classification decision function is called SVM.

After the above analysis, we conclude the basic thought of SVM as follows: First of all, define a proper inner product function to implement a kind of non-linear transformation. After that, using this non-linear transformation to transform the input feature space into a multi-dimensional feature space. The last step is to get the optimal linear classification plane in the new space. The form of SVM classification function is somewhat similar to neural network, its output is a combination of several inner layer nodes, and every inner layer node is connected with the production of a support vector and input sample, as shown in the Fig 2[2]

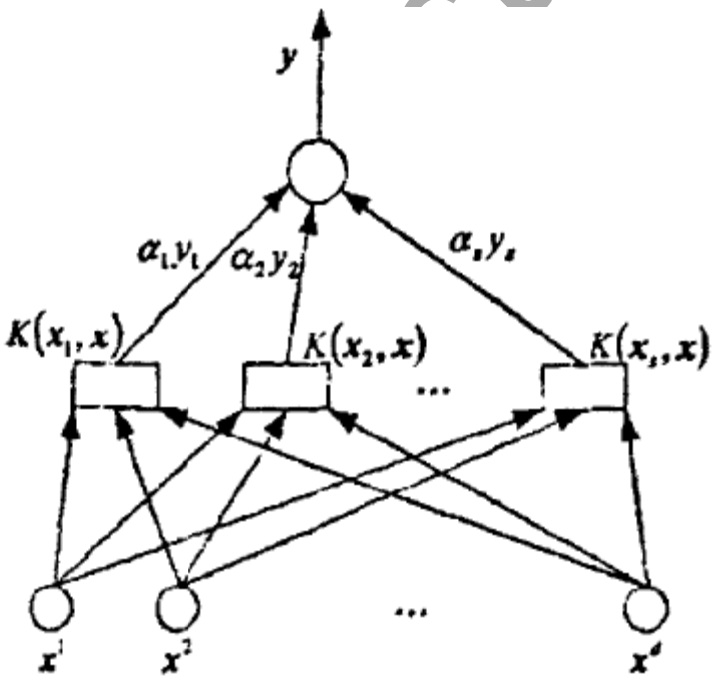

Fig. 2. The Input Process of SVM

Weight: $w_i = a_i y_i$ diagram2.2 the input process of SVM

the non-linear transformation based on s support vectors

Input Vector: $x=(x^1,x^2,..x^d)$

3.3 Classifier Training

After a brief knowledge of SVM basic principle, since we can SVM algorithm to conduct pattern recognition efficiently, here the task is to distinguish whether a point we observed is cloud or not. And that problem is just a pattern recognition problem. Patter recognition is defined formally as a process, we use the patter or signal received during the process to determine the class it belongs. So now, we need to use SVM principle to design and train a classifier and use it to conduct the classification task. [3-7]

The design of a classifier usually include several phases, namely data collecting, feature choosing, classifier training, classification decision and classifier judgement.

First of all, the data collecting phase, as we have introduce before, we use the data collected by CALIPSO satellite with a resolution of 5000m between 30°N to 70°,110°E to 150°.

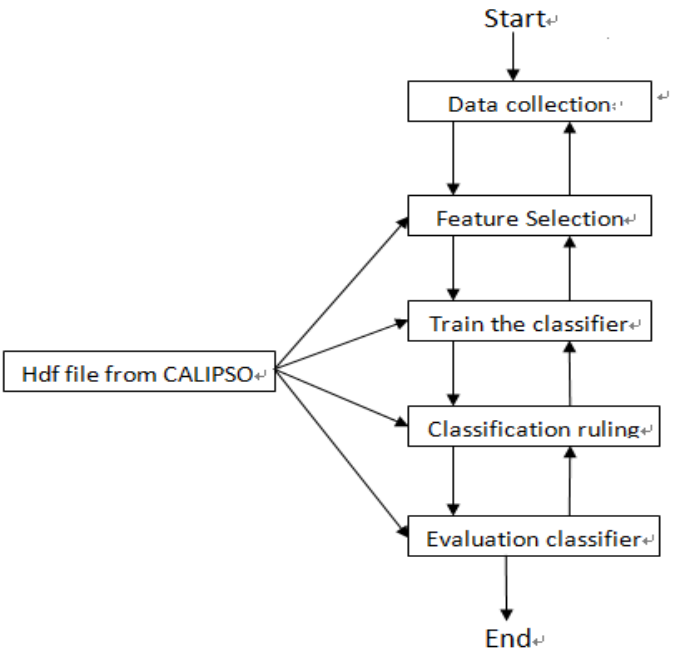

Fig. 3. Design the Flow of classifier

According to the content of the hdf file, the data we use consists of 88 attributes and 7248 sample points. But as for this experiment, though use all of the attributes to design a classifier may increase the correct rate, as the increase of number of eigenvalue, the complication of the design of the classifier and the efficiency of conducting the experiment will greatly reduce. Therefore, we need to filter those eigenvalue.

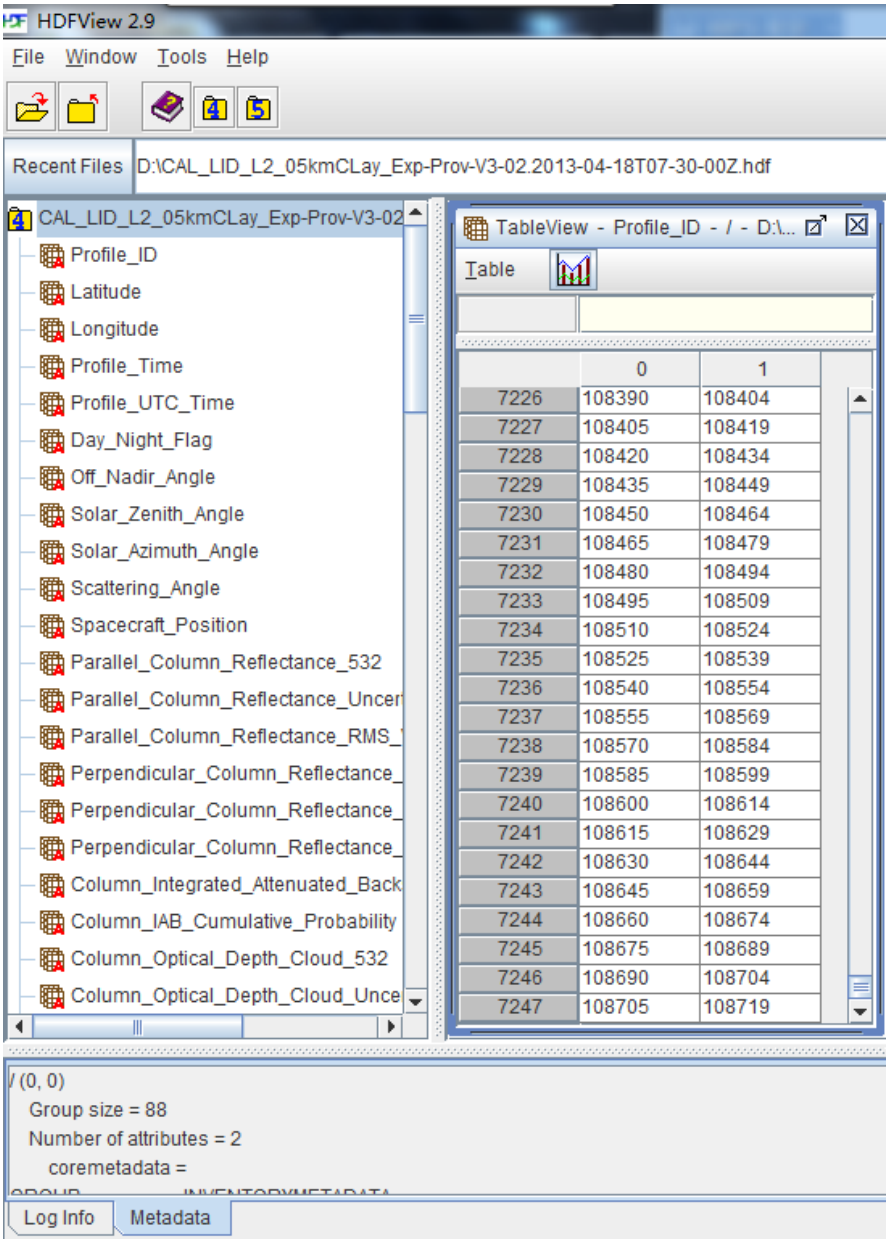

Fig. 4. Open hdf File

At the same time, choosing the appropriate eigenvalues will dense the distribution of the sample point of the same group, separating points that belong to different types. So when choosing eigenvalues, be careful to choose only the valid features and abandon redundant features under the condition of not losing any useful information. What's more, the selected eigenvalues should be able to classify better than other features.

The training of the classifier is the core phase of the designing process. In our paper, the method we use is supervised learning based on samples. Since we have selected part of the attributes in the previous phase, we successfully lowered the dimensions of the data and therefore improved the efficiency of the classification.

The last phase is to judgethe classifier. There are many ways to conduct it like holdout, leaving one out, bootstrap and so on. In our experiment, we choose the holdout method, that is choose two sample sets, one is used as training sets and another is used as testing sets. And the standard we use is an attribute called "Column_Optical_Depth_Cloud".

We can use correct rate or rate of deviation as the norm of judging classification model. The method to calculate is as follows:

correct rate=number of corrected predicted sample／total number of predicted sample

rate of deviation=number of not corrected predicted sample／total number of predicted sample

4 Experiment and Results

In this experiment, we used the CALIPSO data, and selected 12 of the attributes as eigenvalue. First of all, we filtered the experiment data and deleted some data that is apparently not correct, and then used a group of them to train the classifier. After that, we used another group of data to test them.

After repeating the experiment several times, in the process, we improved the correct rate from 81.2362% to 86.0927 through optimization model.

The result is as follows:

When the "option" parameter we choose is "-s 0 -t 2", the predicted correct rate is:
Accuracy = 81.2362% (5888/7248) (classification)
And when it is adjusted to "-s 1 -t 2", the predicted correct rate is refined to
Accuracy = 86.0927% (6240/7248) (classification)

In the experiment, the weight of characteristic dimension is acquired by SVM learning. In this way, we included much calculation cost, while in theory, only once of the learning process is enough. However, this only meets the need if the type of training samples are distributed evenly and outliers less. So basically, every training it need to relearn the training samples to gain new weights. Therefore, if we can find a way that is less costly, the learning efficiency will greatly be improved.

While at the same, the correct rate in the result of the experiment result is not ideal is because there is still improvement in the optimization of core function. We will further discuss and explore them in the following experiment in the future.

Retracted

At the moment, the technology of cloud discrimination is still at the exploration stage, so there is still time before it can be applied in reality. However, since cloud play an essential role in our daily life, so finding a better technology or method of discriminate cloud play a vital part in the climate research in the future.

5 Conclusion

In this experiment, we used SVM algorithm to help us classify cloud and it proved to be an effective way of doing it. Since cloud is an essential part in the weather and climate research, so it has lots of meaning to conduct experiments like that. And our experiment proved somewhat successful and helpful to improve classify method.

While at the same, the correct rate in the result of the experiment result is not ideal is because there is still improvement in the optimization of core function. We will further discuss and explore them in the following experiment in the future.

At the moment, the technology of cloud discrimination is still at the exploration stage, so there is still time before it can be applied in reality. However, since cloud play an essential role in our daily life, so finding a better technology or method of discriminate cloud play a vital part in the climate research in the future.

Retracted

References

1. Liu, J., Cheng, J., Cheng, J.: General Description of Support Vector Machine algorithm. Information and Control 31(1), 45–50 (2002)
2. Yu, J.: Cloud Discrimination, tornado division and center location research based on Satellite Cloud Image. Wuhan University of Technology, Wuhan (2008)
3. Hao, Y., Wang, H., Jiang, Z.: The Application of SVM in Cloud Testing. Journal of PLA University of Science and Technology (2009)
4. Huo, J., Lv, D.: The simulation of clear sky and clour-related air radiation distribution and the application of the cloud discrimination of the whole sky
5. Zheng, J., Huang, F., Zhang, Y.: Cloud Classification Research Based on Artificial Neural Network. Computer Engineering 30(18), 24–25 (2004)
6. Qi, H.: A general Statement of SVM and its Application. Computer Engineering 30(1) (2004)
7. Ma, Y., Gong, W.: Evaluating the Performance of SVM in Dust Aerosol Discrimination and Testing its Ability in an Extended Area. IEEE Journal of Selected Topics in Applied Earth Observations and Remote Sensing (5) (2012)
8. Ma, Y., Gong, W., Zhu, Z., et al.: Cloud amount and aerosol characteristic research in the atmosphere over Hubei province. In: 2009 IEEE International Geoscience and Remote Sensing Symposium, IGARSS, China, vol. 3, pIII-631–III-634. IEEE (2009)
9. Mao, F., Gong, W., Zhu, Z.: Simple multiscale algorithm for layer detection with lidar. Applied Optics 50(36), 6591–6598 (2011)
10. Ma, Y., Gong, W., Zhu, Z.: Cloud Amount and Aerosol Characteristic Resarch in the Atmosphere Over Hubei Province, China. IEEE (2009)

Retracted: Analysis of Transmission Line's Scattering Characteristics in High Resolution Radar Satelite Image

Jingbo Wang, Qi Chen, and Shuaishuai Deng

International School of Software,Wuhan University,Wuhan,China
Jingbowang.whu@gmail.com, {731996261,1518254262}@qq.com

Retracted

Abstract. Since the reform and opening up policy,the development of China's economy has been accelerating. People's demand as well as the size of the national grid is growing and expanding.Our nation makes vigorous effort in building UHV, EHV transmission lines to meet the demand. 1000kV southeastern Shanxi - Nanyang - Jingmen UHV AC pilot demonstration project was put into operation in 2009, which brings significance to the adjustment of the layout construction and optimal allocation of China's recourses. However, in recent years, the occurrence of extreme weather and geological disasters leads to great damage to people, which is increasing and becoming more and more fierce. At the beginning of 2008, snow disaster occurred in large scale of central and southern part of China, as well as Wenchuan earthquake in May 2008, the 2010 earthquake in Yushu in Qinghai Province, Ya'an, Sichuan earthquake in 2013, during which time the overturning of the transmission line tower caused abnormal run of the grid of those affected areas for a long time, which caused huge losses of national economy and people's lives.

Synthetic Aperture Radar (SAR) can handle remote sensing observations through microwave, with features of all-day, round-the-clock work, high resolution, strong penetration and rich characteristic signal, etc. The region has its unique advantages in a wide range of natural disasters. Real-time and on-time feature drawings provided can be reduce the losses caused by disasters when used in emergency command and rescue work.

In this paper, research on 3m resolution TerraSAR images UHV transmission line scattering characteristics focuses on the discipline of bright spots offset by scattered wires. The study shows that the high-resolution SAR images, transmission towers and power lines can be used as a basis for target recognition for it's high scattering intensity. In 3m image resolution, when the angle between the direction of flight is greater than 0°, the overall transmission line bright spot shift tower to the south; when less than 0°, the overall to the north. By processing the data, we found that the change of the angle formed by bright spots---caused by scattered power lines is facing an offset, while the overall offset is affected by other factors, which needs further research and analysis.

Keywords: High-resolution, TerraSAR, UHV, Transmission Tower, Transmission, Lline, Scattering Characteristics, Offset.

F. Bian et al. (Eds.): GRMSE 2013, Part I, CCIS 398, pp. 403–417, 2013.
© Springer-Verlag Berlin Heidelberg 2013

1 Introduction

1.1 Research Background

In recent years, due to the global warming trend, our country appeared many extreme weather events with the trend of intensified. The features of state grid UHV transmission lines are wide covering area, long line transmission distance, built through the complex regional climate that topography, and natural disasters, which are serious threats to the safe and stable operation of transmission line, or even causes large area power outage of power grid. Across a wide range of disasters, monitoring the safety of power grid transmission line and tower for the assessment of the disaster and post-disaster reconstruction provides real-time scientific data, which is significance to the disaster prevention and mitigation.

SAR (Synthetic Aperture Radar, SAR) is a kind of active sensors using microwave remote sensing observation, compared with the optical, infrared and other sensors, not affected by the weather and day and night. Therefore, SAR has its unique superiorityin ice and snow disasters, earthquake, flood disaster, etc. in a wide range under the condition of natural disasters.

1.2 Research Status and Development Trend at Home and Abroad

With remote sensing technology, aerospace standards as well as the development of data processing capacity, modern remote sensing technology has entered a fast, accurate, dynamic, more means to provide a variety of new stage of earth observation data. The image data of the temporal resolution, spatial resolution and spectral resolution got rapid increase and development.

Early resolution of the SAR satellite is lower, for UHV transmission tower target recognition technology related research is much less. In science and technology research projects of national grid, Liu Yan and other researchers used information in high resolution SAR image for the analysis of transmission tower and the safety of the line under the condition of the disaster condition (damaged, ice, etc.). Monitoring of transmission line and tower is proved feasibility of ice and safe state provides a new technical scheme [17] for large-scale disasters of UHV transmission tower under the condition of wide area monitoring .

In recent ten years, there are more and more high precision remote sensing satellite launches. Optical remote sensing, multispectral remote sensing, and radar remote sensing technology have been widely used in electric power system at home and abroad.

1.3 Paper's Research Content and Arrangement

In this paper, the research area is constrained to part of southeast Shanxi - Jinmen 1000 kV UHV AC demonstration project that is in hubei province, in the study area

Retracted

was 1000 kv uhv tower base 260, but there are still some invisible in Google Earth, nor it is in the SAR images, which is so chosen a more continuous 151 steel tower as the main research object of thesis. Data source for the two phases of 3 m resolution TerraSAR -x stripe pattern image, respectively, on January 30, 2009 and November 1, 2009.

The main research contents are as follows:

1. Geocoding of SAR image via combining with the Google Earth high resolution optical image.
2. Use 3m resolution satellite images to analyse the radar on the scattering characteristics of uhv transmission tower and transmission line.

2 SAR and Imagery Features

2.1 Characteristics and Development of SAR

Synthetic aperture radar (SAR) is a kind of perception of active sensors using microwave. Compared with optical and infrared, and other sensors, the SAR has its unique advantages:

1. Throughout the day, all-weather work ability for the energy is emitted by a radar active, do not need to rely on the sun.
2. SAR has the surface penetration that can imaging in vegetation areas and can detect the surface or target certain depth below the water.
3. Can get more precise ground 3D information. By means of two or more fork points interference processing of SAR images, SAR can obtain coverage of digital elevation model data, and can extract high precision surface deformation.

Synthetic aperture radar bearing flight platform can be divided into according to airborne and space-borne two kinds. Airborne system is loaded on the plane with the height between a few hundred meters to several kilometers. Space-borne system carry on satellites or the space shuttle, running in the hundreds of kilometers of high altitude orbit. In June 1978, NASA launched the first star SeaSat satellite synthetic aperture radar surveying and mapping of 100 million square meters of the surface of the earth, which caused the attention of the remote sensing community. The successful launch of SEASAT is a symbol of the space-borne SAR technology is changing from the laboratory to the key of the application research. After that, Japan, Russia, Canada and other states have launched their own SAR with the high-speed development on the applications.

2.2 Image-Forming Principle of SAR

Image-forming principle of SAR is gaining a high-resolution radar image by compressing the Doppler echo in azimuth direction and the linear frequency modulation (LFM) signal in range direction.

Retracted

2.3 Geocoding of SAR Image

In the field of remote sensing, location model is generally applied to SAR image resampling. The process of being from image space coordinate transformation to the geographic coordinate space is the Geocoding. After geocoding, SAR image can be turned into a geocoding image. SAR geocoding generally used J.C.Curlander R-D positioning model that adopts the tight range equation and Doppler equation [25]. It is based on the earth ellipsoid model and become a standard of most SAR positioning model. R - D positioning model is illustrated below.

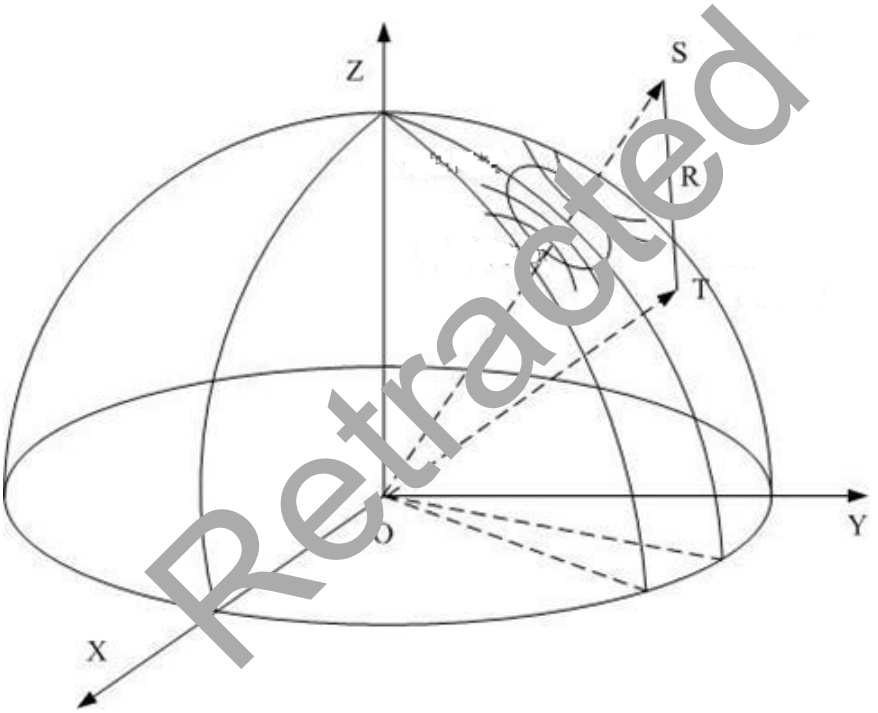

Retracted

Fig. 1. R - D positioning model

2.4 Chapter Summary

This chapter firstly introduces the history of satellite synthetic aperture radar and the basic principle of SAR imaging. Finally elaborated the geocoding principle, in this paper, which is also the key technologies of satellite image preprocessing used for analysis of scattering characteristics of transmission lines.

3 UHV Transmission Lines and the SAR Image Preprocessing

3.1 UHV Transmission Lines and the SAR Image Data

3.1.1 1000KV UHV Transmission Lines

1000KV Southeast Shanxi - Jinmen UHV AC testing demonstration project up in southeast Shanxi, check in hubei jingmen substation with the total length of 654km.

1000KV transmission line iron tower of the basic form of free-standing dual-circuits power tower type glass tower, single loop and single loop V type anchor tower, etc. Southeast shanxi - jingmen circuit adopts the form of the free-standing dual-circuits power tower, not only in the steep mountain terrain to ensure flawless foundation but also more economic.For 1000 kv transmission lines, high field caused by corona noise near the surface of the conductor is reduced, not only need to consider the transmission capacity and mechanical strength, but also need to consider when rain on the surface of the conductor corona and the radio interference.Best wire arrangement for eight root area by using the 810 mm squared s23 split steel core aluminum stranded wire spacing of 0.4 m is octagonal eight division lead [18]. Due to the weight of wire and considering the principle of heat bilges cold shrink, power lines have a certain degree of sag amplitude. The size of it depends on the real time environment temperature of the wire, the physical strength, the transmission power, and the distance [23, 24].Fig 2 is for UHV transmission tower mounted power line.

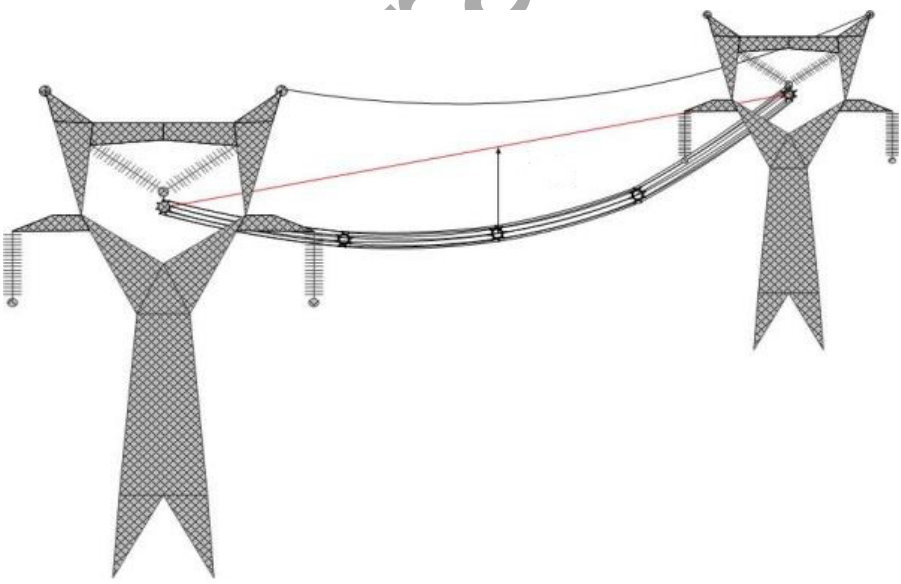

Fig. 2. UHV transmission tower mounted power line

3.1.2 3m Resolution Banding Pattern Image

Experimental data used in this paper are two terrasar-x SSC. Image data processing can be done in own programming or via software, in this paper, by means of GAMMA, NEST software to implement the data read.

Below image 200901301, for example, reading standard SSC images from the GAMMA software the basic task of the header information and imaging parameters:

1, The basic task information includes the SAR sensor type, imaging time (the 2009-1-30 22:36:37. 7570), track number, track number, lift rail (item first-just), polarization mode (HH), etc.

2, Imaging parameters as shown in Table 1.

Table 1. On January 30, 2009, imaging parameters of SAR image

Sensor type: TSX-1	Range zoom factor: 1.0000000e+00
Image acquisition time: 2009-1-30 22：36：37.7570	Azimuth zoom factor: 1.0000000e+00
Initial Imaging moment: 81397.757000s	Central latitude: 32.1537691°
Intermediate imaging moment: 81401.826901s	Central longitude112.5173303°
Final image moment: 81405.896802s	Sensor-Image distance: 581356.4560m
Azimuth row imaging time: 2.9208418e-04 s	Sensor-Image's center distance: 589642.4852m
Total row: 18224	Sensor-Image' long haul: 597928.5143m
Total Line: 27869	Azimuth angle: 90.0000°
Image format: SCOMPLEX	Radar wave frequency: 9.6500000e+09Hz
Range pixel size: 0.909403m	Radar ave bandwidth: 1.5000000e+08Hz
Azimuth pixel size: 2.070334m	Pulse repletion frenquency: 3423.670489Hz
Azimuth bandwidth: 2765.00000Hz	Receive gain: 18.0000db
Radar satellite-Geocenter distance：6884164.7895m	Revision gain: 48.9271db
Earth radius: 6372316.6013m	Vector number of satellite position: 12
Earth semi-major axis: 6378137.0000m	Initial time of satellite position vector: 81355.00000s
Earth semi-minor axis: 6356752.3141m	Time interval of satellite position vector: 10.000000s

Retracted

3.2 Data Preprocessing

In SSC, the received signal data is decomposed into two parts, $a(t)\cos\phi(t)$ and $a(t)\sin\phi(t)$. $a(t)$ is the amplitude for the compositon of I while $\phi(t)$ is phase for the composition of Q. SAR images usually is the result of the amplitude data visualization. Fig 3 for the January 30, 2009, the three pieces of the whole scene SAR shadow without any processing.

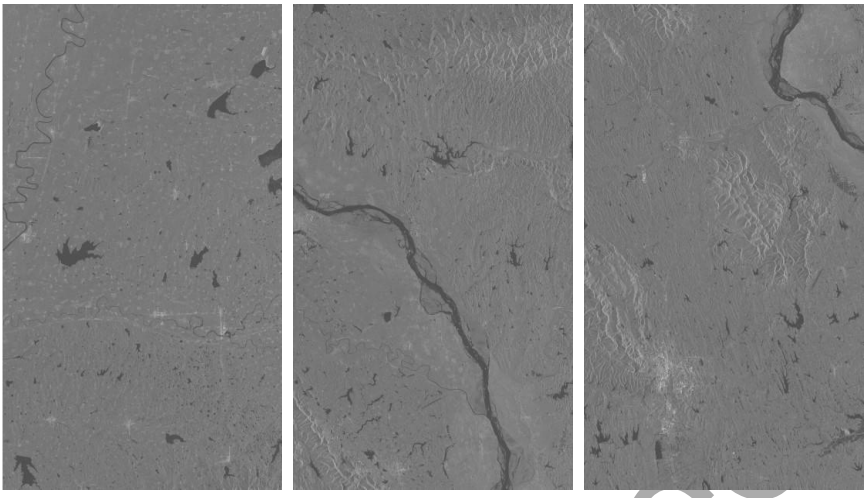

Fig. 3. January 30, 2009, the three pieces of the whole scene SAR shadow

File in SLC data, in addition to the parameters for the geographical scope of the image, the SSC does not contain any geographic information. But after geocoding image contains the geographic coordinates of information. 200901301 images, for example, Figure 3.3 first picture for the SSC results after data visualization, a total of 27869 lines of 18224 columns. The second picture is after dealing with the distance and the mirror image contains a resolution of 2.1 meters and a total of 27869 lines of 15534 columns. The third picture for the geocoding image resolution and sampling to 3m that includes a total of 20725 lines of 13822 columns.

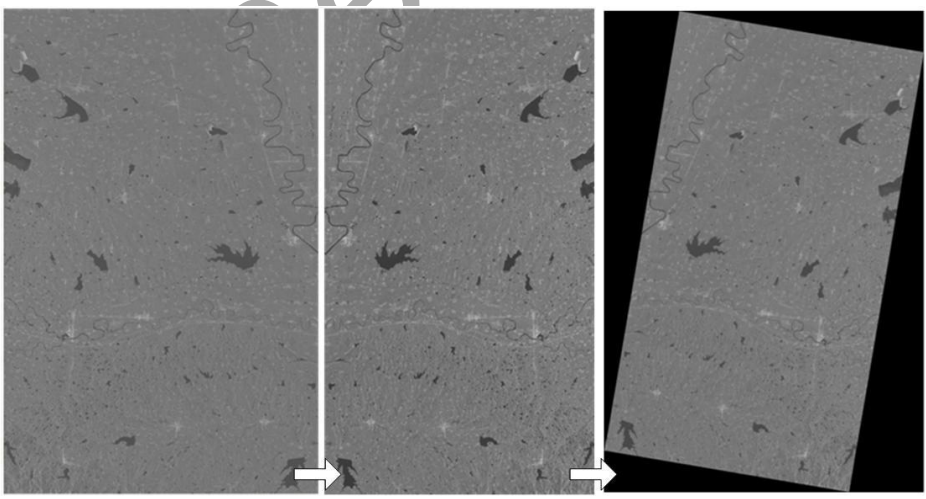

Fig. 4. SSC>PRI>GEC

For SAR image, after finished the geocoding image of each pixels, with geographical location information, SAR images can be made into KMZ files and analysed the combination of high resolution optical images. For two holograms in January 2009, for example, figure 4 for SAR holograms superimposed to the Google Earth image.

Fig. 5. SAR image compared with Google Earth

3.3 Chapter Summary

1000 kv uhv ac demonstrative project of basic situation, then introduces the experimental zone for 3 m resolution of SAR image. Finally on the original data pre-processing, after geocoding SAR images, combined with Google Earth high resolution optical images, to prepare for the next analysis.

4 Transmission Line Scattering Characteristics Analysis

4.1 3m Resolution Scattering Characteristics Analysis of Transmission Tower

In 3m resolution SAR images, 1000 kv uhv transmission lines are north-south direction while the direction of the radar scanning is east-west influenced the effect of image

with intense backscatter. In general, while large transmission tower targets are in the region of lush vegetation, the radar scattering intensity is higher than the background intensity and the target is easy to identify. When in plains across villages and buildings, background reflection features of high strength lead to the difficult recognition.

4.2 3m Resolution Scattering Characteristics Analysis of Transmission Lines

In 3 m resolution terrasar-x image, scattering of the transmission line is more special, is usually as a hard target with strong echo signal. Therefore, some slender artificial linear features such as railway, highway guardrail, power lines, Bridges, etc. have been attributed to a hard target. They are often characterized by a certain shape in the image of the bright line or a series of bright spots. Because of the characteristic of the side-looking SAR imaging, there will be a bigger change to the scattering characteristics if the flight direction of the trend is different from the sensor. In fig 6, we can clearly see the transmission line formed by the scattering of light spot.

Fig. 6. Contrast diagram

2009013 data, the information in this article were taken in January 2009.

1、When bright spot is located between two base tower:

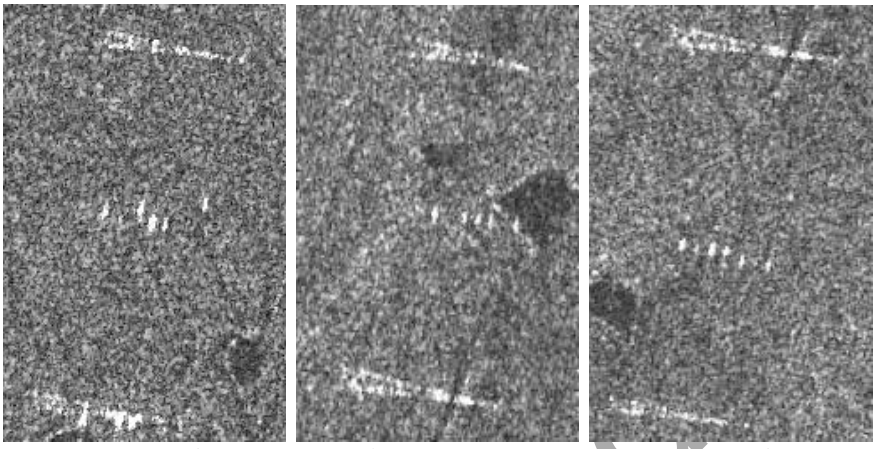

(a)314-315 (b)343-344 (c)344-345

Fig. 7. Bright spot located between two base tower

As shown in figure 4.2, power transmission conductor and bright spot basic into parallel the whole columns. The height difference of two adjacent tower base is smaller. Above three wires and satellite flight direction Angle are shown in Table 2

Table 2. The parameters of the bright spot in the middle position

Starting tower			Termination tower			Coordinates azimuth(°)	With satellite Angle(°)
num	type	Height (m)	num	type	Height (m)		
314	Straight line tower	118	315	Straight line tower	117	188.4956837	-0.5043163
343	Straight line tower	142	344	Straight line tower	136	188.0394078	-0.9605922
344	Straight line tower	136	345	Straight line tower	135	188.8304296	-0.1695704

2、Bright spot near the north tower:

As shown in fig 8, some power lines in the image appeared with large deviation. Can be seen from table 4.2, the three file relative to the flight direction of satellite wires by west.

Retracted

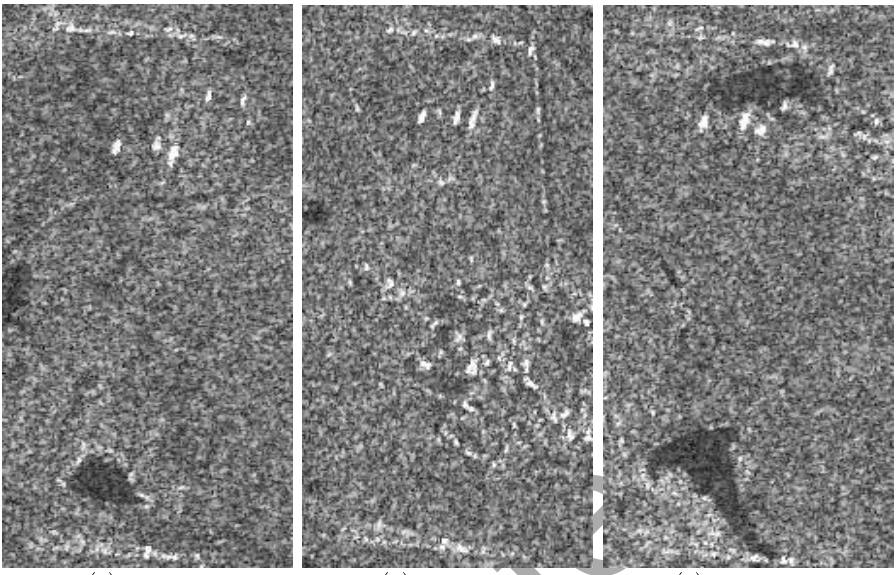

(a) 292-293 (b) 308-309 (c) 318-319

Fig. 8. Bright spot near the north tower

Table 3. The parameters of the bright spot near the north tower

Starting tower			Termination tower			Coordinates azimuth(°)	With satellite Angle(°)
num	type	Height (m)	num	type	Height (m)		
292	Straight line tower	118	293	Straight line tower	117	180.4222247	-8.8315598
308	Straight line tower	103	309	Straight line tower	100	181.1112351	-7.8887649
318	Straight line tower	127	319	Straight line tower	134	181.0138737	-7.9861263

3、near the south tower:

As can be seen from fig 9 bright spot appeared larger deviation, to be near the south tower. From Table 3, these three wires with respect to the direction of flight satellite easterly, maximum angle is 9 degrees, and the minimum of about 4.4 °.

Retracted

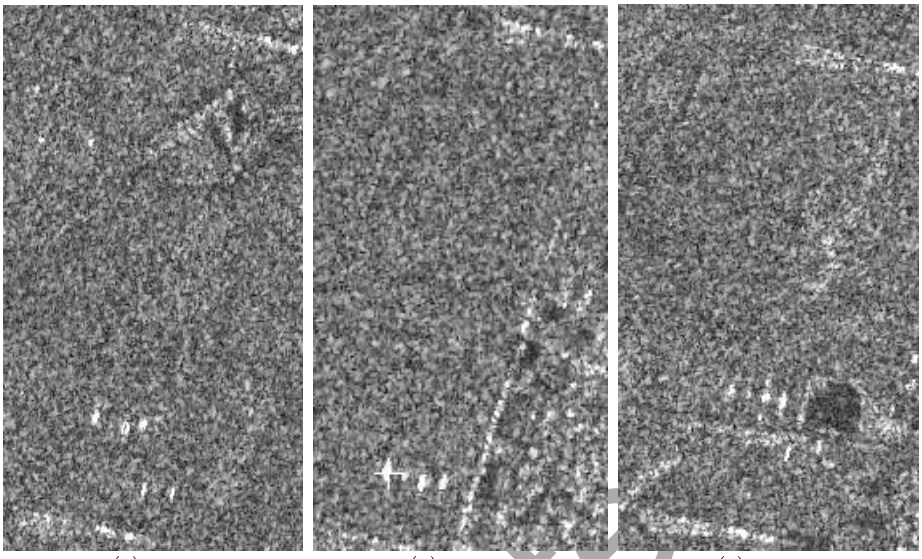

(a) 204 (b) 211 (c) 265

Fig. 9. Near the south tower

Table 4. The parameters of the bright spot near the tower

Starting tower			Termination tower			Coordinates azimuth(°)	With satellite Angle(°)
num	type	Height (m)	num	type	Height (m)		
204	Straight line tower	91	205	Straight line tower	91	196.5875942	7.5875942
211	Straight line tower	92	212	Straight line tower	93	197.9514406	8.9514406
265	Straight line tower	102	266	Straight line tower	98	193.3820743	4.3820743

4、Transmission line on relationship between spot offset and lightning line offset

The transmission wire scattering spots offset Ds as the abscissa axis and lightning protection line scattering spots offset Df as the ordinate axis. Analysis the relationship between the two statistics150 gear transmission line. As show in the fig 10:

Retracted

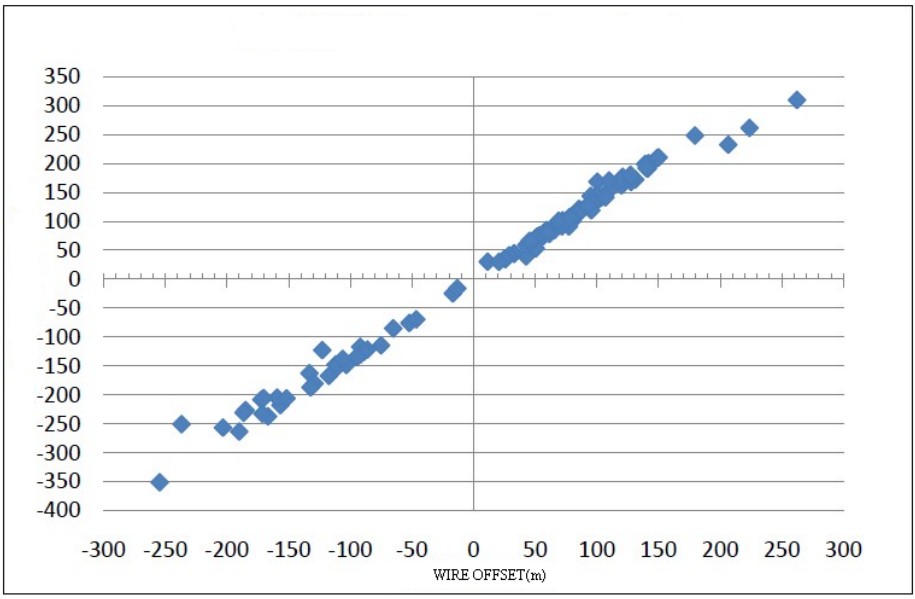

Fig. 10. Relationship wire offset and lightning protection line offset

Through statistical analysis of scattering signal 143 geartransmission lines, obtained the following conclusions：

1. If the transmission line and the flight direction of approximate parallel and adjacent two base tower height difference is not big, the scattering light will be located in the middle of two base tower.
2. Trend of transmission line affects the direction of the light spot. relative to the flight direction is right, the overall shift to the south tower deviation.
3. Conductor and ground wire each scattering form bright spot, a linear relationship with the offset

Retrac

4.3 Conclusion

Resolution of this chapter is based on 3m TerraSAR images, studying the scattering characteristic of 1000 kv uhv transmission line, and analyzed 3 m resolution image in scattering characteristics of high-voltage transmission line. The migration characteristics of scattering were summarized, validated using field measurement results, the identification of a transmission line and the whole transmission lines for the future of wide-area monitoring to provide technical support.

References

1. Binaghi, E., Gallo, I., Pepe, M., et al.: Neural classification of high resolution remote sensing imagery for power transmission lines surveillance. In: 2002 IEEE International Geoscience and Remote Sensing Symposium, IGARSS 2002, Toronto, Ont, Canada, pp. 500–502 (2002)

2. Earp, G.: Condition based risk assessment of electricity towers using high resolution images from ahelicopte. In: Eighteenth International Conference and Exhibition on Electricity Distribution, CIRED 2005, Turin, Italy. Technical Reports - Session 1: Network Components, pp. 91–95 (2005)
3. Frost, P., Annegarn, H.: Providing satellite-based early warnings of fires to reduce fire flashovers onsouth Africa's transmission lines. In: 2007 IEEE International Geoscience and Remote Sensing Symposium, IGARSS 2007, Barcelona, Spain, pp. 2443–2446 (2008)
4. Jardini, M.G.M., Jardini, J.A., et al.: Use of geo-referenced images for the surveillance of transmission lines right-of-way. In: 2004 IEEE International Geoscience and Remote Sensing Symposium Proceedings, Sao Paulo, Brazil, pp. 711–716 (2004)
5. Liao, J., Shao, Y., Wang, S.: Monitoring for 2003 Huai River Flood in China Using Multisource SAR Data. In: Geoscience and Remote Sensing Symposium, vol. 4, pp. 2260–2263 (2004)
6. Yan, L., Tao, L., et al.: Power transmission tower monitoring technology based on TerraSAR-X products. In: International Symposium on Lidar and Radar Mapping 2011: Technologies and Applications, Proceedings of SPIE - The International Society for Optical Engineering, vol. 8286 (2011)
7. Eineder, M., Minet, C., Steigenbenger, P.: Imaging geodesy-toward centimeter level ranging accuracy with TerraSAR-X. IEEE Trans. on Geoscience and Remote Sensing 4(2), 661–671 (2011)
8. Novak, L.M., Owirka, G.J., Netishen, C.M.: Performance of a High resolution Polarimetric SAR Automatic Target Recognition System. The Lincoln Laboratory Journal 6, 11224 (1993)
9. Sarabandi, K., et al.: Extraction of power line maps from millimeter-wave polarimetric SAR images. IEEE Trans. on Antenna and Propagation 48(12), 1802–1809 (2000)
10. Sarabandi, K., et al.: Power lines: radar measurement and detection algorithm for polarimetric SAR images. IEEE Trans. on Aerospace and Electronic System 30(2), 4 (1994)
11. Yang, W., Zhang, H., Chen, J., et al.: Automatic Detection of Power Transmission Seriesin Full Polarimetric SAR Imagery. In: Radar Conference, 2007, IEEE, Boston (2007)
12. He, R.: Research on Spaceborne Synthetic Aperture Radar Interferometry Processing Technique. Doctoral Dissertation of Hunan University (2007)
13. Rui, H., et al.: New high resolution spaceborne SAR satellite: TerraSAR-X.Sciencepaper Online of China. Project of National Natural Science Fund of China (40772191)
14. Shiqi, H.: Research on Microwave Remote sensing SAR Military Detection Technology (2005)
15. Yan, L., et al.: Surveillance for 1000kV Transmission Tower Deformation Using High-resolution SAR Satellite. Project Supported by National Natural Science Fund of China (40604002), Programme of Introducing Talents of Discipline to Universities, B07037 (2009)
16. Yan, L.: Research on Detection Technology of 1000kV Transmission Lines and Tower Using High-resolution SAR Image. Doctoral Dissertation of Wuhan University (2009)
17. Yan, L., et al.: Monitoring Damage of State Grid Transmission Tower in Bad Weather by High-Resolution SAR Satellites. Geomatics and Information Science of Wuhan Uinversity 34(11) (November 2009)
18. Design of 1000kV Power Transmission Line in Japan. Guangdong Power Design Institute. Pan Chuping Lin Fangxing
19. Lichun, S., et al.: System and Applicationd of German Radar Satellite TerraSAR-X. Journal of Zhengzhou Institute of Surveying and Mapping 24(5) (October 2007)

Retracted

20. Sui, L.: Active Radar and Lidar Remote Sensing. Surveying and Mapping Press, Beijing (2009)
21. Su, N.: Priciples of Microwave Remote Sensing. Wuhan Uinversity Press, Wuhan (2000)
22. Wei, J., et al.: Research on Methods of TerraSAR-X Image Direct Geolocation. Bulletin of Surverying and Mapping, 11–14 (September 2009)
23. Xia, K., et al.: Structual Analysis and Testing Research UHV AC Transmission Tower. High Voltage Engineering 33(11) (November 2007)
24. Xu, J., Xing, L., Pan, J.: The Application of Remote sensing Technology to the Route Selection of the High Voltage Transmission Lines. Remote Sensing Technology and Application 21(2), 168–172 (2006)
25. Xu, H.: Research on the Target Location of Space-borne Synthetic Aperture Radar Image. Graduate University of Chinese Academy of Sciences, Beijing (2005)
26. Li, Y., Li, Z.: Research on the Production and Accuracy Analysis of TerraSAR-X DOM. Bulletin of Surverying and Mapping (8), 1–3 (2010)
27. Wen, Y., et al.: Discussion on Interpretation of SAR Imagery. Space Electronic Technology (1) (2004)
28. Hong, Z., Chao, W., et al.: High Resolution SAR Imagery Target Recognition. Science Press, Beijing (2009)
29. Zhang, Y.: Synthetic Aperture Radar Imaging Geometry Understanding and Processing. Doctoral Dissertation of Wuhan University (2001)
30. Zhu, J.: Research on Data Fusion of High-Resolution Optical and SAR Image and Extraction of Typical Object. Graduate University of Chinese Academy of Sciences, Beijing (2005)

Retracted

A Multi-scale Progressive Framework for Ground Segmentation of Airborne LiDAR Data

Likun Liu and Zhenfeng Shao

State Key Laboratory of Information Engineering in Surveying,
Mapping and Remote Sensing LIESMARS, Wuhan University,
430079 Wuhan, P.R. China
{rpbtiger,shaozhenfeng}@whu.edu.cn

Abstract. LiDAR technology can be used to carry out ground extraction with higher resolutions. The technique can penetrate the topping of vegetation and collect ground points for bare land estimation. But for thick forest, the simple selection of return echoes to generate ground is not accurate. To solve the problem, this paper presents a progressive framework to segment ground out of densely-vegetated area from LiDAR data. A morphological filter is applied to the process by a multi-scale representation which can adaptively respond to different environment with the parameter of the structure element is progressively increased by one pixel from the starting value at each step. The proposed method also incorporates image inpainting in the implementation of a smooth initial data grid and missing point data restoration. After all, the performances of the framework are tested against different data of densely-vegetated and sloped terrain, and yield a better result.

Keywords: Airborne LiDAR, ground segmentation, multi-scale representation.

1 Introduction

Among several geodetic imaging technologies of the Earth's surface, LiDAR (Light Detection And Ranging) is a fast evolving field for acquiring millions of points from ground features [1]. It can be used to extract accurate and three-dimensional information directly. Various LiDAR sensors on different platforms can provide coarse to fine point cloud data at respect observing height [1]. The Airborne LiDAR acquisition is becoming a major source for extracting ground at large scale, compared with Terrestrial Laser Scanning (TLS) and Mobile Laser Scanning (MLS) especially.

As the capability and frequency of acquiring instruments drastically increase along with the price of owning the device and cost of carrying out a flight campaign decrease expectedly, airborne LiDAR surveying can be implemented routinely after certain periods to monitor ground surface change and land inventory. The point clouds collectively combining with precise geo-spatial coordinates and other useful attributes have being utilized to reveal and delineate the contours of real-life terrain, utility infrastructure, forestry and other above-ground features in the surrounding environment.

F. Bian et al. (Eds.): GRMSE 2013, Part I, CCIS 398, pp. 418–424, 2013.
© Springer-Verlag Berlin Heidelberg 2013

For these applications, a significant step before concrete process is to separate bare earth and other non-ground features (e.g. vegetation and artificial objects) from LiDAR returns for generating the digital terrain models (DTM, here synonymously with Digital Elevation Model, or DEM). Compared with traditional optical image extraction method which is greatly annoyed by vegetation canopy disturbance, the LiDAR technique can penetrate the topping of vegetation and collect information of ground point for bare land estimation. Normally, the discrete return echoes of LiDAR data can reflect different parts of tree crowns, branches, trunks, unburied roots or bare ground vertically. But for thick forest area, the simple selection of return echoes to generate DEM is not suitable for accurate ground extraction. As for the generation of DTM, different filtering methods have been researched and evaluated which can be found in [4, 5]. And a progressive morphological approach has been developed by Zhang [6] to detect above-ground LiDAR data by gradually modifying the window size of the filter.

Based on above-mentioned researches, this paper puts forward a progressive framework to segment ground out of densely-vegetated area from LiDAR data. A morphological filter is applied to the process by a multi-scale representation which can adaptively respond to different environment. The structural element (SE) of the morphological filter is chosen as a disk-shaped SE, and the parameter of the SE is progressively increased by one pixel from the starting value at each step. The proposed method also incorporates image inpainting techniques in the implementation of a smooth initial data grid and missing point data restoration. After all, the performances of the proposed method are tested against two different data of densely-vegetated and sloped terrain, and yield a better result with current state-of-the-art solution.

2 Methodology

The proposed framework contains four stages representing a progressive approach. Concisely speaking, Stage 1 is the generation of the initial minimal surface $InitS_{min}$. Stage 2 is deciding whether the cells in $InitS_{min}$ are bare earth. Stage 3 is creating the transitional DEM temporarily. Stage 4 is the classification of ground points.

For the $InitS_{min}$ in the Stage 1, all scanned points in each cell of the LiDAR data with lowest elevations are preserved and those empty cells are filled by inpainting technique. The creation of $InitS_{min}$ takes the first and last returns of the point cloud data for the thought that the last return of one wave may happen to hit an object at one location, while the first return of another wave may possibly touch closer to the ground at the same spot. Therefore, both first and last returns will be employed to remove outliers. Then, the minimal ground grid $InitS_{min}$ is filled with proximal and lowest elevation from the original point cloud only when the distance to the nearest point is not beyond the given cell size threshold. So there might exist empty and unfilled grid cells. Those cells are to be fixed by image inpainting technique [2] which is a kind of data interpolation method.

In the Stage 2, there are four sections sequentially comprising the core of the framework to apply a progressive morphological filter to the initial ground surface $InitS_{min}$. The first section is to create a duplicate of the $InitS_{min}$ which is called *lastGround* here for convenience. Then the second section is to generate a vector which is provided by the given largest window size (radius). And the vector increases starting from one pixel to the value which is produced by the maximum in distance divided by the cell size one by one. For each value of window size in the vector, there are also four processing steps: (a). calculate the height threshold which is equal to the given slope parameter multiplied by the product of the window size times the cell size of minimal ground surface grid. (b). create *thisGround*, and this ground surface is produced after morphological opening operation [3] by disk-shaped structural element with current window size. (c). add any cell generated by subtracting the *thisGround* from the *lastGround* whose difference is larger than the elevation threshold in (a) to the labeled ground feature unit set. (d). set the *lastGround* as the *thisGround.* Then the fourth section is processed by inverting the ground surface and applying the section 1 and section 2 for single small window and large elevation threshold to locate lower outliers in $InitS_{min}$.

After the above kernel of the framework, a transitional DEM can be created in the Stage 3. It is carried out by retaining cells which is considered as bare earth in $InitS_{min}$, and removing artifact cells from the original surface $InitS_{min}$, then empty cells are inpainted by the technique mentioned in the Stage 1.

The Stage 4 is the classification of ground surface points. The original laser-scanning point cloud data is classified as bare earth or non-ground features according to the required vertical distance parameter and optional scaling parameter.

A schematic flow chart of the framework is visualized in figure 1.

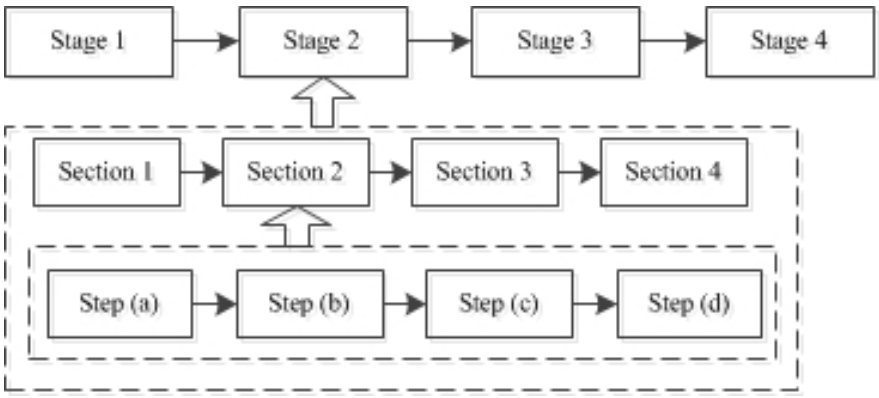

Fig. 1. The visual flow chart of the proposed multi-scale progressive framework. Specific contents and processing techniques are described in the above paragraphs.

3 Experiments

Two different high resolution LiDAR data acquired from sloped vegetative terrain are used to test the proposed framework. The source of data can be found from G-LiHT team at Goddard Space Flight Center, NASA[7].One of them is a natural slope environment without human buildings in Phillipston, MA, the other one is a vegetative hump surrounded by roads and artifacts in Bowie, MD. The gridded result of two samples is illustrated in Figure 2 with height coloring respectively.

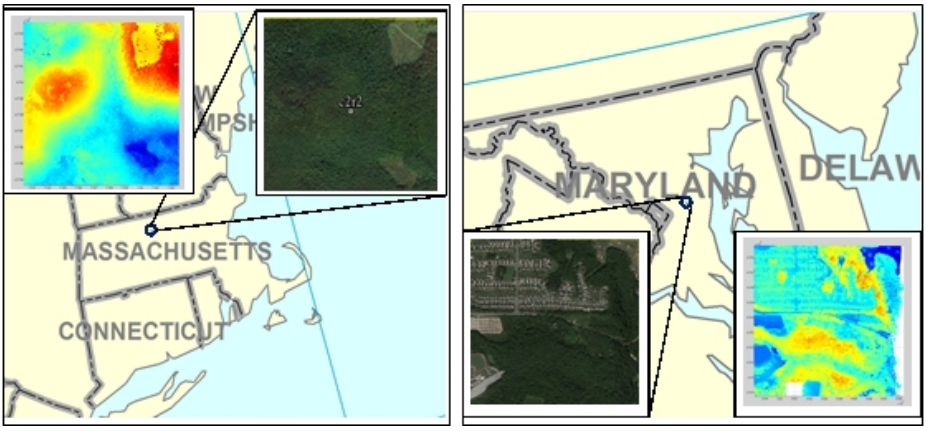

Fig. 2. The Illustration of high resolution gridded LiDAR point data with elevation coloring. The left one is natural sloped environment, the right one is vegetative hump with roads and other artifacts.

The processed results of the two samples are compared with the results generated by FUSION software [8] developed by Vegetation Monitoring and Remote Sensing Team of Pacific Northwest Research Station, USDA Forest Service. The core functionality of the FUSION which can produce DTM automatically is based on the method proposed by Kraus and Pfeifer [9]. The intermediate product of ground grid $InitS_{min}$ which is the portal of the proposed framework is given to show how the method evolves. The ultimate processed LiDAR samples are placed with their FUSION's results respectively in Figure 3 and Figure 4. Apparent differences between the results from the proposed framework and the FUSION's computation are delineated in red circle.

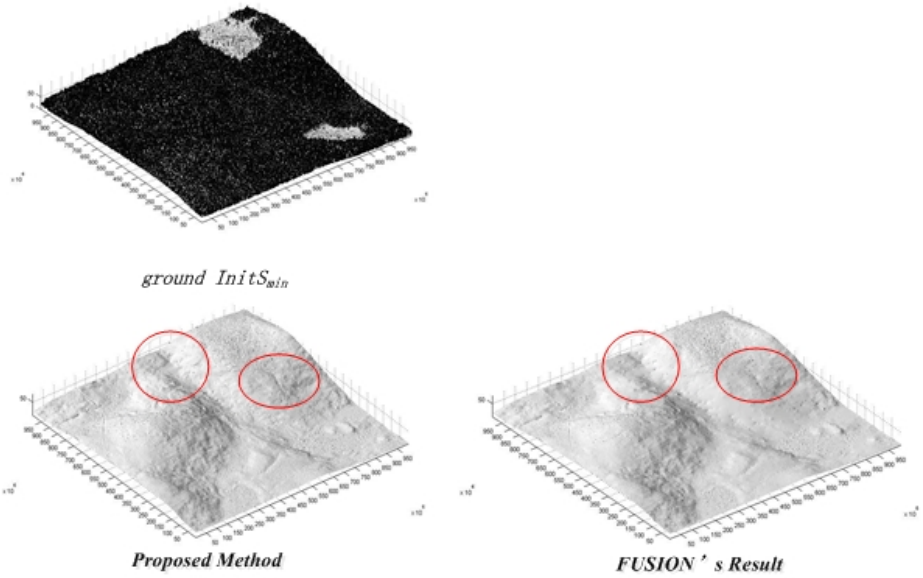

Fig. 3. The Experimental results. (a) The Phillipston's results.

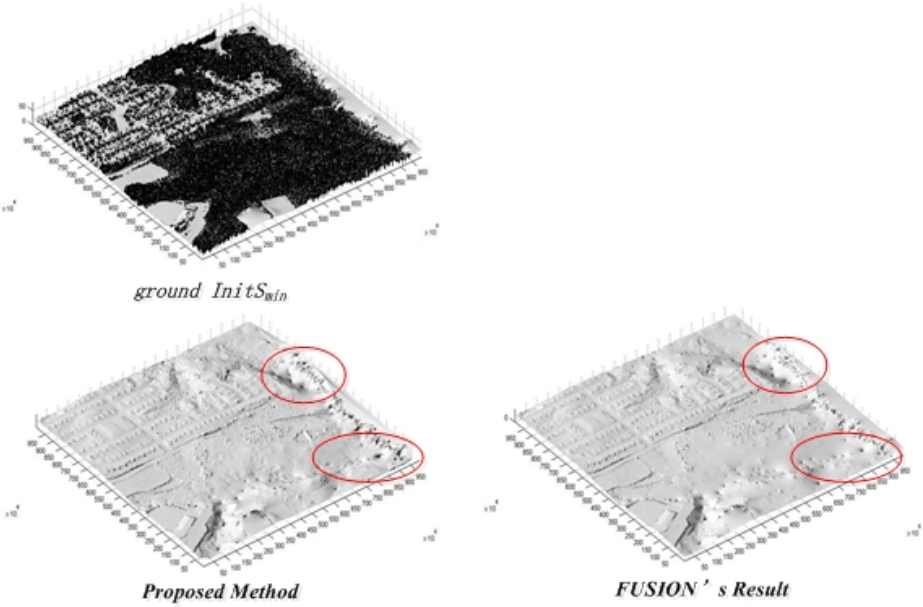

Fig. 4. The Experimental results of (b) The Bowie's results

4 Discussion

In our experiments, two sloped terrains with different ground features are tested for the proposed ground separation framework. Conspicuous red regions in the two results demonstrate that the proposed method can deal with acute sloped terrain even it is densely-vegetated and yield a better outcome than the state-of-the-art professional software from the perspective of human inspection. And the processed ground surface is more vivid to the natural environment from other sources of optical modalities

5 Conclusions

In this paper, we presented a framework to determine bare earth in LiDAR data acquired from sloped and densely-vegetated terrain. It can extract the lowest ground surface to produce DTM automatically. Experiments were carried out by testing different data samples from two distinct ground features, and we demonstrated better results than the state-of-the-art professional software FUSION from the perspective of human perception. Further studies will be stressed in quantitative assessment and more comparisons with current solutions. Moreover, combining with optical images will be tested again other data sources.

Acknowledgements. The research is funded and supported by the National Basic Research Program of China (973 Program, No. 2010CB731800), the National Natural Science Foundation Program of China (No. 61172174), the National Science and Technology Specific Projects (No. 2012YQ16018505 and No. 2013BAH42F03), Open Fund of The Key Laboratory of Digital Oceanic Science and Technology, SOA (KLDO201307). Special thanks to the support from the PhD Short-time Mobility Program at Wuhan University.

References

1. Glennie, C.L., Carter, W.E., Shrestha, R.L., Dietrich, W.E.: Geodetic imaging with airborne LiDAR: the Earth's surface revealed. Rep. Prog. Phys. 76, 086801 (2013)
2. Bertalmio, M., Guillermo, S., Caselles, V., Ballester, C.: Image inpainting. In: Proceedings of the 27th Annual Conference on Computer Graphics and Interactive Techniques (SIGGRAPH 2000), New Orleans, LA, July 23-28, pp. 417–424 (2000)
3. Cho, H.-C., Kampa, K., Slatton, K.C.: Morphological segmentation of Lidar Digital Elevation Models to extract stream channels in forested terrain. In: IGARSS, July 23-28, pp. 3182–3185 (2007)
4. Sithole, G., Vosselmann, G.: Experimental comparison of filter algorithms for bare earth extraction from airborne laser scanning point clouds. ISPRS J. Photogramm. Remote Sens. 59, 85–101 (2004)
5. Meng, X., Currit, N., Zhao, K.: Ground filtering algorithms for airborne LiDAR data: a review of critical issues. Remote Sens. 2, 833–860 (2010)

6. Zhang, K., Chen, S., Whitman, D., Yan, J., Shu, M., Zhang, C.: A progressive morphological filter for removing nonground measurements from airborne LIDAR data. IEEE Trans. Geosci. Remot. Sen. 41(4), 872–882 (2003)
7. G-LiHT team at Goddard Space Flight Center, NASA, http://gliht.gsfc.nasa.gov
8. Vegetation Monitoring and Remote Sensing Team of Pacific Northwest Research Station, USDA Forest Service, http://forsys.cfr.washington.edu/fusion/fusionlatest.html
9. Kraus, K., Pfeifer, N.: Determination of terrain models in wooded areas with airborne laser scanner data. ISPRS J. Photogramm. Remote Sens. 53(4), 193–203 (1998)

Web-Based Remote Sensing Image Processing Tools – A Study of Change Detection Using Landsat Imagery

Jin Hu and Xiaoliang Meng

International School of Software, Wuhan University,
No. 37, Luoyu Road, Wuhan, Hubei Province 430079, China
{huj,xmeng}@whu.edu.cn

Abstract. Taking advantages of web service, remote sensing image distributed processing occurs, which aims at the shortcomings of standalone solutions. In this paper, efforts have focused on interaction as well as efficiency of web-based remote sensing image change detection. The system framework consists of OGC WCS specification, Browser-Server three-tiered structure, and image change detection workflow. A pair of 4-3-2 TM bands combination images have been taken to execute an experiment. The result corresponds to actual condition.

Keywords: Remote Sensing, Image Processing, Change Detection, Web-based, Landsat Imagery.

1 Introduction

An increasing pace of geospatial research leads to demand for heavy load and easy access data processing. Besides, since no software or service can cover entire requirements from past to future throughout potential and existent users, expansibility should also be considered.

eXtensible Markup Language (XML) is a way to format documents in order to realize both human-readable and machine-readable. When delivering remote sensing data between servers and clients to meet requirements of processing on demand, XML can be used. [1]

Considering the difference between Image Information Mining (IIM) systems about web-service and request, standardization has been called on, based on Services Oriented Architecture (SOA) and extends several existing Open Geospatial Consortium (OGC) services via schemas in XML, which facilitates interoperability between web services, and foster business logic layer to separate with presentation layer. [2]

Distributed remote sensing parallel processing service is put up in order to meet network-based demands, under a basic job framework named Spatial Information Grid Runtime Environment (SIGRE), which is founded based on components involving JRE, web server and servlet container. SIGRE plays an important rule as the middleware between services and end users, managing distributed processing services. [3]

Web service is able to be applied to remote sensing image process for its superiority, which can be embodied when handling data in large volume especially within network computing environment. [4]

F. Bian et al. (Eds.): GRMSE 2013, Part I, CCIS 398, pp. 425–434, 2013.
© Springer-Verlag Berlin Heidelberg 2013

The usage of Java Native Interface (JNI) makes it practical to reuse processing modules programed in other language such as C and C++. Also, algorithms are packaged as Web Processing Service (WPS) for users to request from client browsers. [5]

Another instance of embracing geospatial contents and capabilities within SOA is the Geospatial Online Analysis System (GeOnAs), which is extensible and takes advantage of web-services that are standardized and open, so users are able to process under latest generic protocols. This web-based system can discover, retrieve, analyze and visualize geospatial network data. A platform which allows multi-user processing, data sharing and exchanging is also built to solve problems about multi-tasking. The GeOnAs takes Geographic Resources Analysis Support System (GRASS) to achieve processing, Apache to balance load, RAID disks that directly installed in a processing server to store data. Transmission of large piece of geospatial data is to be investigated. [6]

Research on efficiency has also been paid attention to. An overview on the developing, deploying and operating of a geo-processing web is provided with features of light-weight protocols, crowd sourcing, real-time processing and interoperation. [7]

Web service technology supports data processing via network so as to make it realizable to exchange information between various terminals or even systems. It's convenient for service providers to update and upgrade services while it's the same with users to get access and execute on-demand processing. Taking advantages of web service, remote sensing image distributed processing involves large amount of data, computing and also data transfer under the framework consisting of servers, storages, standardized protocols and lightweight clients. In a distributed processing case, requirements for a client environment are always reduced, and high efficiency is practically implemented.

This paper firstly provides an overview on existing subjects about web-based remote sensing image processing. Then, change detection processing is specially illustrated following traditional standalone solutions. Further step is taken to an implementation to supply the proposal tools by experiments.

2 Web-Based Remote Sensing Image Change Detection

Image Change detection is a procedure that compare given images of a certain area during a certain period of time with that of another period, aiming to acquire information about statistics as well as details of change.

Existing achievements have implemented various algorithms for change detection based on traditional form of standalone processing platform. The ENVI is a desktop platform that processes and analyzes imagery; it also integrates with ArcGIS, which helps to design and manage solutions through the application of geographic. The ERDAS Imagine is a system that incorporates image processing into a package with add-ons offered to expand core functionality. For particular users that have no need for processing other than change detection, making use of languages such as C++ or MATLAB to program dedicated software is also feasible. It should be noted that most of standalone change detection tools are unable to adapt to multi-user environments or integrate with other systems within simple steps.

One of key features that web-based tools differ from previous standalone ones is the separation of modules, namely distributed processing consists of server, user client and network.

Protocols link these separated modules. OGC is an international standardized organization leading the progression of geospatial standard. WCS is a specification formulated by OGC involving the following three operations: GetCapabilities to return XML documents that describe service and data, GetCoverage to return value or property of geoinformation, DescribeCoverageType to enable clients forwarding integrated description to WCS service.

To achieve fully automated change detection analysis based on web, GeoCDX is designed for very large volume of data processing and results are present in various ways by an easy-to-use web application. It's web-accessible which adds interfaces in Google Earth, Web Map Service (WMS) and a SOA based on XML. [8]

In this paper, efforts have focused on interaction as well as efficiency; as a result, the web-based remote sensing image change detection tools built using JAVA Development Kit. The framework consists of OGC WCS specification, Browser-Server (B/S) three-tiered structure, and image change detection workflow.

The advantages, disadvantages and features between traditional standalone and web-based methods are compared in Table 1.

Table 1. Compare between standalone and web-based change detection processing

Change detection processing method	ENVI (commercial)	ERDAS (commercial)	Standalone change detection software (noncommercial)	Web-based change detection tool (noncommercial)
Processing speed	Very high	Very high	Very high	High
Portability	No	No	Yes with platform independent language	Yes with platform independent language
Reusability	Yes with ArcGIS	No	Yes	Yes
Scope of application	Wide-ranged	Wide-ranged	Specialized for change detection	Specialized for change detection
Price	Very high	Very high	Very low with open-source development kits	Very low with open-source development kits
Demand for operation	Not very high	Not very high	Very low	Very low
Demand for data management	High	High	High	Very low for users
Support multi-user	No	No	No	Yes
Support distribute deployment	Yes with ArcGIS	No	No	Yes
Update	Inconvenient	Inconvenient	Inconvenient	Very convenient for users

Web-based tools may take extra time to transmit data between the application server and the data server via Ethernet, while it's not as fast as transmitting data with local drives. Benefiting from simplified system infrastructure, specialized tools are able to realize portability and reusability. It should also be highlighted that commercial systems are usually costly and complex for the sake of wide-ranged application, which may be unnecessary for users concentrated only on change detection. Moreover, as for web-based processing, the separation of processing modules simplifies data management, enables multi-user and distribute support, makes the tools convenient to update, especially for user end: just login right after the administrator finished updating the server end.

3 Study Area

Images that acquired by instruments on the Landsat satellites have been widely used for global change research in fields of agriculture, regional planning and so forth. Types of sensors equipped in Landsat satellites are Multi Spectral Scanner (MSS), Thematic Mapper (TM) and Enhanced Thematic Mapper Plus (ETM+). [9]

There are various forms of band combination in order to meet specific requirements. For instance, 4/3/2 TM bands composite image, which is called a false color composite image, is extraordinary in embodying characteristic of vegetation.

The region of XiLinGuoLe, Inner Mongolian, China locates in the middle of Inner Mongolian Plateau with the majority type of topographic being plain plateau. Covering 180 thousand square kilometers while ranging from 5 types, prairie in this area is well-preserved so it's fit for research on variation of vegetation.

Fig. 1a. 4-3-2 Bands Combination 1

Fig. 1b. 4-3-2 Bands Combination 2

In this paper we select remote sensing images acquired by Landsat TM sensor in the area of XiLinGuoLe belonging to two periods, then composite 4/3/2 bands of each image aiming at variation of vegetation. The composite image of first period in 2010 is shown as Fig. 1a, and image of the other period later in 2011 is shown as Fig. 1b.

Geographic coordinate of the upper left corner is (115°18' 5" E, 43°50' 25" N) in geodetic coordinate, that of the bottom right is (116°58' 50" E, 42°34' 50" N). The region covers 134 kilometers in east/west direction and 141 kilometers in south/north direction. Geographic Coordinate System is WGS1984, projection is Transverse Mercator, and geometric resolution is 30 meters. Images are used after several means of corrections; file size of image1 is 67.7 MB, while that of image2 is 60.1 MB.

4 Implementation

4.1 Hardware and Software Requirements

To fix hardware/software requirement equals to determine construct, operate as well as maintain of whole system. There are two computers being used as web (application) server and data server, each one has at least processor of 8 cores and memory of 6 Gigabytes by recommend. Servers' operating system is Ubuntu 12.10, Apache Tomcat is used as Java web server, and the software development uses Java Development Kit 7. Benefited from web-based architecture, no more than a computer joint network with one of popular browsers is required for a client, so that user group is readily to expand.

4.2 Network Architecture

Considering transmission rate and data security, network architecture is divided into three tiers: server tier, user tier and network tier. And the tiers are linked by 1Gbps Ethernet as shown in Fig. 2.

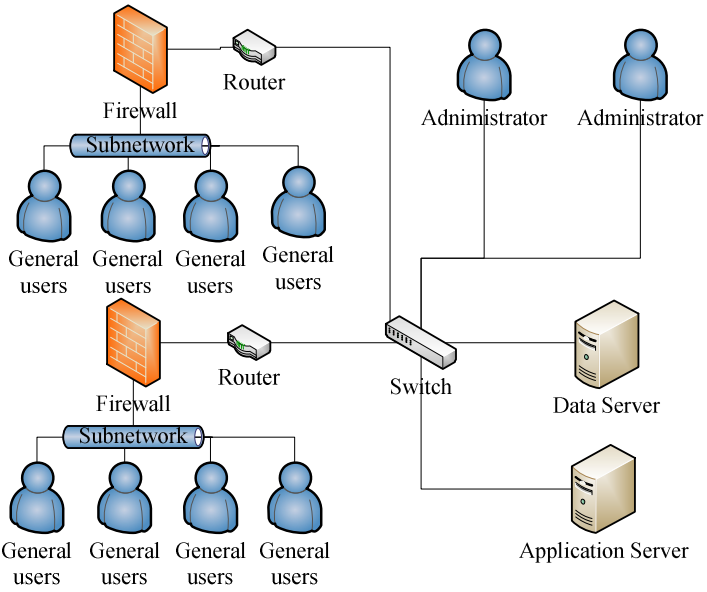

Fig. 2. Network Architecture

On server tier, images, statistics, results, logs and other data are stored on and load from the data server, which is continuously in communication with application server, while on the latter disposes applications including runtime environment, processing program, service and user authenticate. On user tier, different users can apply for authentication and get access to services by creating accounts. General users together with administrators are both involved in the same network but divided into sub-networks by limits of authority. On network tier, high performance switches are used to set up fast Ethernet, ensuring large throughout capacity under frequent data transmission and act as entrance and exit of the whole network with external modules. Redundancy is also taken into account in case of overload or accidently crash. Firewall and router are deployed between general users and switches in a sub-network to keep servers and other users out of threating operations or data.

4.3 System Infrastructure

The system infrastructure consists of network, Browser-Server (B/S) three tiers structure, several data processing modules (Fig. 3) and image change detection workflow (Fig. 4) deployed in the application server.

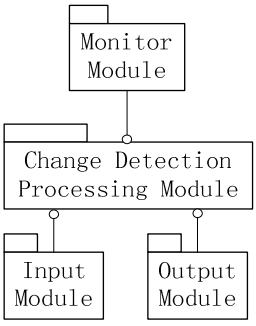

Fig. 3. Data Processing Modules

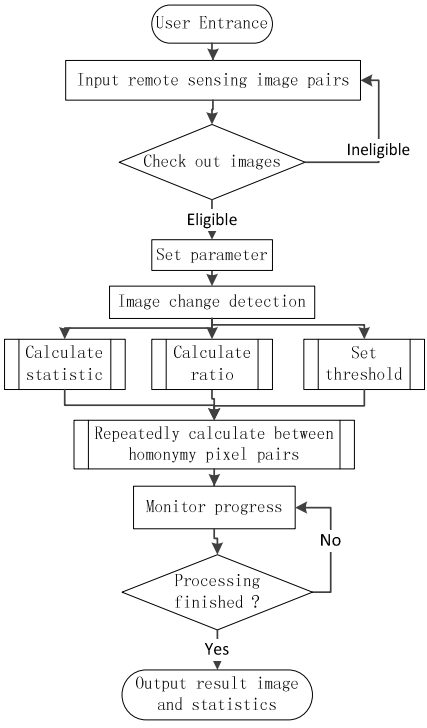

Fig. 4. Change Detection Workflow

In addition to advantages that B/S three-tiered structure takes by general realization, it also carries forward beneficial aspects specially in remote sensing image processing. Firstly, image up to 1Gbytes turns easier to transmit and process, users only need to send request and receive result files that are much smaller in size. Moreover, image data only transmit between servers, direct access by user lessens to ensure safety and up-to-date feature. Furthermore, high workload processing only executes on high performance servers, as a result, the processing runs much more efficient than runs on local user terminal computers. Then, benefiting from modular system, the remote sensing change detection tools are easy to be integrated in other systems.

The input module imports image from catalogue provided by the data server in the form of packages. It also receives requests for processing via XML. Requests are linked then organized with relevant images, and sent to the application server run queue.

The output module packages the calculated results together with processed images, transmits to data server, meanwhile, reveals in browser at the user end.

The change detection processing module detects changes between homonymy pixel pairs of different time in the same band by ratio or difference at certain value, which depends on user preferences. Domain of variation is marked in a processed image and parameters of change are listed in the calculated result. The monitor module runs daemon in the background, returning progress to system interface simultaneously.

4.4 System Interface

To establish communication between change detection tools and users, system interface include user interface (Fig. 5), and communication interface (Fig. 6).

User interface serves as control panel and also monitor of the system. Each step is visual and friendly with default parameters proposed. Besides, processing stage synchronously renew on user interface, informing users of percent completed.

The change detection workflow starts with selecting image pairs, no files other than a pair of GeoTIFF images in the same size, and under the same reference are eligible. Wave bands are analyzed afterwards for users to pick and a threshold about change is available to set. When the application server finished contradistinction, results are then stored on the data server.

Communication interface links modules or devices. In this paper, OGC service serves to provide images and information. Images are organized with GeoTIFF format, which is supported by OGC WCS to transmit. Information is organized with XML, which makes it convenient while generic to send and acquire requests.

Also, because of web-based B/S three-tiered structure, network protocols including TCP/IP, HTTP and FTP contribute to system integrating.

Fig. 5. User Interface

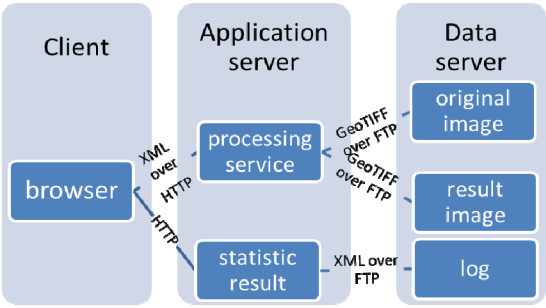

Fig. 6. Communication Interface

4.5 Experimental Result

Based on the actual research work, remote sensing image change detection tools are implemented. To assess the effectiveness of the proposed method, a pair of remote sensing images acquired by Landsat TM in combination of 4-3-2 bands in the region of XiLinGuoLe as described in section 3 has been taken to execute the experiment.

Between two moments those images are acquired, vegetation in this region was affected by climate changing, sunshine changing together with human activities, thus the vegetation distribution change occurred. Considering change detection accuracy, threshold is set as 20 percent.

The result image of change detection is shown as Fig. 7. Pixels in color red represent area that vegetation decreases while color green pixels represent increase. The result corresponds to actual condition.

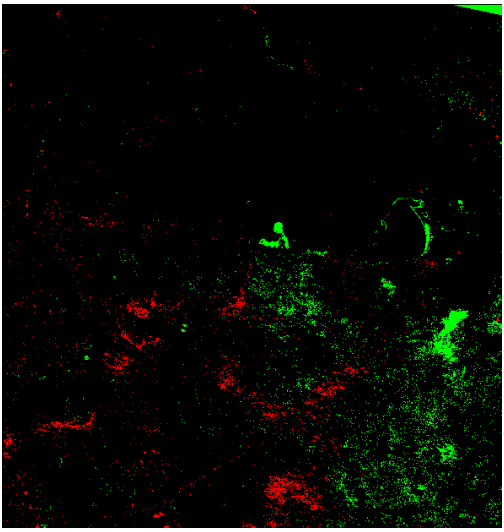

Fig. 7. Experimental Result of Change Detection

5 Conclusion

In this paper, an overview of remote sensing image processing is given, followed by highlighting the possibility and necessity of applying the web-service technique. Then change detection, as a specific kind of remote sensing image processing, is surveyed resulting a proposal to implement web-based remote sensing image change detection tools. Typical remote sensing images reflecting variation on vegetation in the region XiLinGuoLe are selected for experiment.

Due to the works mentioned above, the web-based remote sensing image change detection tools, which achieve interactivity, interoperability, visualization, efficiency and convenience, are designed, developed then implemented for the experiment. The experiment obtains images that correctly show change of vegetation in selected region.

It remains to be seen, however, if the algorithm accuracy and efficiency of tools in this paper can still be satisfying when dealing with remote sensing images that reflect complex landform or sharp change. To deal with accuracy, advanced algorithms could be introduced such as spatial neighborhood relativity and edge detection. To overcome efficiency loss, further steps should be taken toward multi-thread transmitting and processing.

References

1. Aloisio, G., Milillo, G., Williams, R.D.: An XML architecture for high-performance web-based analysis of remote-sensing archives. Future Generation Computer Systems 16(1), 91–100 (1999)
2. Durbha, S.S., King, R.L., Gokaraju, B., Younan, N.H.: A Proposal for the Standardization of Image Information Mining Systems via OGC Web Services Frame-work. In: International Geoscience and Remote Sensing Symposium (IGARSS), vol. 3(1), pp. III648–III651 (2008)
3. Guang, D., Zhenchun, H., Xianlin, Q., Xu, Z., Zengyuan, L.: Research on a Kind of Web Based Distributed Forest Remote Sensing Parallel Processing Service. In: Tan, H., Zhou, M. (eds.) CSE 2011, Part I. CCIS, vol. 201, pp. 593–600. Springer, Heidelberg (2011)
4. Shen, Z., Ming, D., Li, J.: Remotely sensed image distributed processing system design with Web Services technology. In: International Geoscience and Remote Sensing Symposium (IGARSS), vol. 6, pp. 4244–4247 (2005)
5. Jiang, C., Geng, Z.-X., Wei, X.-F., Shen, C.: Research on networked integration technology of remote sensing image processing. In: Zhang, W., Yang, X., Xu, Z., An, P., Liu, Q., Lu, Y. (eds.) IFTC 2012. CCIS, vol. 331, pp. 1–8. Springer, Heidelberg (2012)
6. Zhao, P., Di, L.: Building a Web-Services Based Geospatial Online Analysis System. IEEE Journal of Selected Topics in Applied Earth Observations and Remote Sensing 5(6), 1780–1792 (2012)
7. Zhao, P., Foerster, T., Yue, P.: The Geoprocessing Web. Computers and Geosciences 47, 3–12 (2012)
8. Klaric, M.N., Claywell, B.C., Scott, G.J., Hudson, N.J., Sjahputera, O., Li, Y., Barratt, S.T., Keller, J.M., Davis, C.H.: GeoCDX: An Automated Change Detection and Exploitation System for High-Resolution Satallite Imagery. IEEE Transactions on Geoscience and Remote Sensing 51(4), 2067–2086 (2013)
9. Landsat Project Information, `http://landsat.usgs.gov`

A System Dynamic Based Utilization Effectiveness Assessment Method of Marine Functional Zones in Qindao, China

Haihong Wang[1,*], Miru Li[1], Naiping Hu[1], and Yamming Gao[2]

[1] Academy of Information Science and Technology,
Qingdao University of Science and Technology, 266061, Qingdao China
wanghaihong@qust.edu.cn, {leemiru,hunaiping}@163.com
[2] Key Laboratory of Marine Ecological Environment and Disaster Prevention and Reduction of Shandong Province, North China Sea Branch of the State Oceanic Administration, 266033, Qingdao China
gaoyanming@163.com

Abstract. The marine functional zoning (MFZ) for China is a new large-scale, ecosystem-based zoning policy for management of development and use in the marine environment. The system dynamic (SD) method is used to evaluate the utilization effectiveness of existed marine functional zones (MFZs) quantitatively for China. As a case study, an impact assessment system is constructed to obtain the cause and effect feedback chart of the mariculture functional zones in Qingdao city, China. A feedback SD model and the main control loops are developed to analyze the utilization effectiveness of the mariculture functional zones. Vensim software is applied to the assessment for the mariculture functional zones of Qingdao. Analysis results and simulations are presented to verify and validate the proposed model.

Keywords: Marine functional zoning, System dynamics, Utilization effectiveness, Marine policy.

1 Introduction

In recent years, the need for balancing the various demands on marine areas and resources has become critical. The health of ocean resources is vital for both economic and environmental sustainability. Comprehensive planning is required to protect marine resources. Protection can be achieved through MFZ, which is an integrated, multi-sector (e.g., fisheries, energy, transport) and multi-disciplinary (e.g., engineers, scientists, policy analysts, planners) process of the allocation and assessment of anthropogenic ocean uses to achieve and meet ecological, economic, and social objectives [1]. MFZ enables the country to have better control of its marine areas, protect and improve its marine environment, ensure the rational exploitation of its marine resources, and allow for the sustainable development of the marine economy.

* Corresponding author.

F. Bian et al. (Eds.): GRMSE 2013, Part I, CCIS 398, pp. 435–445, 2013.
© Springer-Verlag Berlin Heidelberg 2013

The division of MFZs is directly related to the rational development and sustainable use of the oceans. Therefore, assessing the effectiveness of existing MFZs is of great importance. However, accessing the utilization effectiveness of MFZs can be difficult because the systems need to deal with complex data often seen in most facets of anthropogenic ocean uses, such as marine ecology and biological modeling, mapping, and associated analyses, using a variety of modeling and data management tools. The impact assessment of MFZs is a complicate system involving many factors and constraints, which require a variety of modeling and data management tools [2,3].

Qingdao historically known as Tsingtao is a major city in eastern Shandong province, Eastern China, with a population of over 8.715 million (2010 census). Lying across the Shandong Peninsula while looking out to the Yellow Sea, Qingdao is a major seaport, naval base, and industrial centre. Qingdao has abundant marine resources and a good industrial base. In 2004, Qingdao designated a total of 191 MFZs in nine categories. Of the 191 MFZs, 33 are fisheries resource utilization zones and conservation zones (including fishing ports and fishing facilities, fishing bases, breeding areas, proliferation areas, and fishing area). The total area is 385.1585 square kilometers in Qingdao, and comprises 29.2% of the entire MFZs of Qingdao. Qingdao fishery output value accounted for 22.3% of the marine economy, whereas marine aquaculture production accounted for 73% of the total output of aquatic products in 2009. However, with the booming marine economy and tourism, and the rapid development of port and shipping services, the aquaculture area is shrinking [4]. Since aquaculture has expanded and intensified in almost all regions of the world and has grown to about 43 percent of current global fish consumption, an inevitable question arises: how one can knows the polices are right for keeping an sustainable development while conserving places that are critical for the health of the marine environment and its biodiversity? Therefore, analyzing the utilization effectiveness of the marine aquaculture is of great importance.

At present, most studies are focused on the principles, methods, and zoning processes of MFZs. Division methods of MFZs in China are more concentrated in the indicator method, superposition method, and coordination method [2-5]. For example, a project with the marine and MFZ compliance criteria is studied in [3]. An analytic hierarchy process is proposed to establish the assessment indices systems for the exploration potential of MFZs [6]. Analyzes marine environmental impacts of the ports and establishes the indicators of functional characteristics of ports.

Worldwide marine spatial plans (MSP) have been prepared with various objectives, similar to Chinese MFZ. MSP is a process that brings together multiple users of the ocean-including energy, industry, government, conservation and recreation-to make informed and coordinated decisions about how to use marine resources sustainably [7-12]. In Australia Marine bioregional plans are developed as a new focus for marine planning and have been developed for four of Australia's marine regions [7]. Canada provides an integrated ocean management through marine spatial planning based on the national legislative and policy context [8]. In the United States, marine spatial planning is being addressed at the national, regional, and state levels. In 2002, EU Recommendations on Integrated Coastal Zone Management, the EU issued the EU Green Paper on Future Maritime Policy. In 2006, the EU Marine

integrated Policy Blue Book in 2007, respectively [10]. Above the EU policy to promote, a number of European countries carried out the management of marine spatial planning and achieved good results [11]. The North Sea, Belgium, Netherlands, Germany, the United Kingdom has been initially completed the proposal of sea-use planning and the zoning within the scope of the territorial sea [12-14], One may refer to [15, 16] and the references therein for some other introduction about MSP in practice.

In all the initiatives taken in MFZ or MSP, most studies and research tools are focused on the principles, methods, and zoning processes [17] no clear socio-economic factors and assessment models have been considered. Recently evaluation is generally recognized as an essential step for learning and improvement in MSP, Practical guidance and experience relative to evaluation in MSP is, however, very limited. The division methods of MFZs in China most focus on the fuzzy method, quantitative method, and analytic hierarchy method [5, 17]. Moreover, these initiatives were implemented before the division of the MFZs. The utilization effectiveness and impacts of MFZs are not considered in China [18].

The present paper aims at assessing and modeling the utilization effectiveness for MFZs in Qingdao using the SD method. SD is an approach used to understand the behavior of complex systems over time and created in the mid-1950s by Professor Jay Forrester of the Massachusetts Institute of Technology, The approach is very useful to conceptualize a comprehensive understanding and explanation of human interactions and complicated phenomena [19]. The impact assessment system is constructed to obtain the cause and effect feedback chart of the marine culture functional zone. Data are processed using statistical method and geographic information system. A feedback SD model and the main control loops for the utilization effects evaluation are presented based on the obtained results. Simulations are conducted to verify the proposed model. The models are implemented with Vensim and the programs use stock and flow icons to help one see where the accumulations of the system take place.

2 Impact Assessment of the Utilization Effectiveness of MFZs

The price of aquatic products is the most important factor in determining the extent of breeding activities in MFZs [14]. In addition, the price of aquatic products production is also affected by aquiculture, catching costs, social economic conditions, per capital annual expenditure on consumption, and consumption habits. However, these factors also affect the fishery price in one or two years, depending on the growth cycle of aquiculture products.

Even among the same aquatic products, the price of edible fish in the lowest category is far less affected by the economic situation than that of the high quality seafood. Many marine economic function zones, such as mariculture zones, tourism zones, and others, are also affected by the regional marine environment, marine weather conditions, and other major environmental conditions. Thus, the unitization effectiveness of MFZs should be taken into account.

In addition, various types of MFZs affect each other. In creating MFZs, the authorities need to consider the cumulative effect of maritime industries on the seas, seek to make industries more sustainable, and proactively minimize conflicts between industries seeking to utilize the same sea area, and promote the economic development of the zones that are closely related to the key industries. Wastewater and pollution in ports and sailing areas can affect nearby breeding areas. The sediment and water power also affect the tourist zones.

To summarize, the system state variables are selected according to urban population, aquatic products price, energy cost, production materials cost, feed cost, human resource cost, consumption desire, and marine capture production, shipping throughout, tourism income, marine aquaculture area, and marine aquaculture production.

The system decision variables include the growth rates of the following: urban population, first industry, second industry, third industry, agricultural products price, aquaculture cost, consumption per capita, expected consumption, marine capture, freshwater aquaculture, and freshwater capture.

3 SD Model for the Utilization Effectiveness of Qingdao Mariculture Functional Zone

The causal loop diagram can express the feedbacks in the system better than the causal relation model. The price of aquatic products is divided into six categories, and each category is refined. Each system branch description is analyzed based on the categories divided before. The causal loop diagrams are then obtained using Vensim.

The branch circuits of SD modeling Qingdao MFZ are as follows:

1) Urban GDP (branch circuit: Urban population, total values).
2) Per capita aquatic consumption (branch circuit: GDP, per capita GDP, per capita income, per capita aquatic consumption).
3) Average price of aquatic products (branch circuit: calculated using aquatic products cost, per capita aquatic consumption, the difference between desired yield and actual yield).
4) Aquatic products cost (branch circuit: decided by energy, production materials, feed and human resource costs).
5) Desired consumption of aquatic products (branch circuit: calculated using per capita aquatic consumption and price).
6) Desired yield of marine aquatic products (branch circuit: marine aquaculture area, desired marine aquaculture yield, desired consumption of aquatic products, fresh water yield).

Not all the variables can be used in this model. Hence, only some important factors are selected to build the model, as shown in Figure 1. By adjusting the loop parameter, the future economic benefits can be predicted using historical data. Figure 2 shows the SD model of the utilization effectiveness of Qingdao MFZs, where GDP is gross domestic product which consist of the primary industry(GDP1), the secondary industry(GDP2) and tertiary industrial (GDP3).

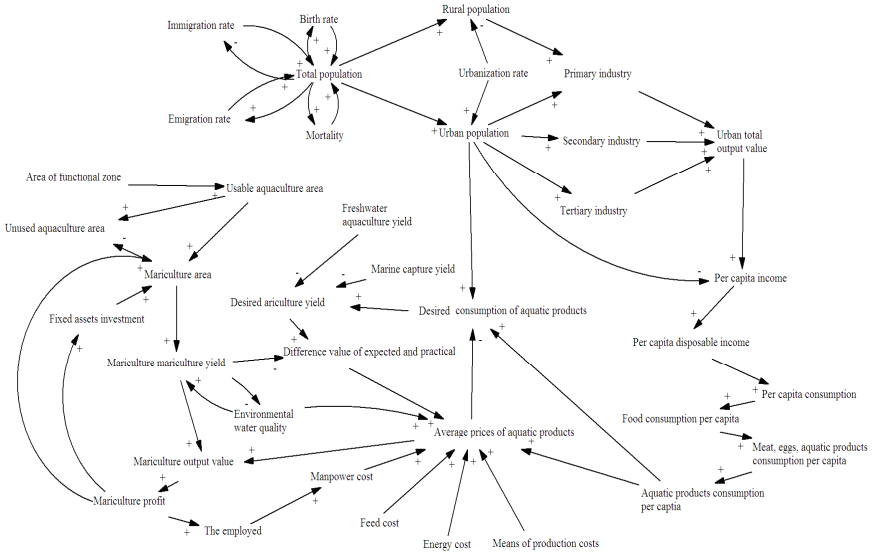

Fig. 1. Feedback structure for the utilization effectiveness of Qingdao MFZs

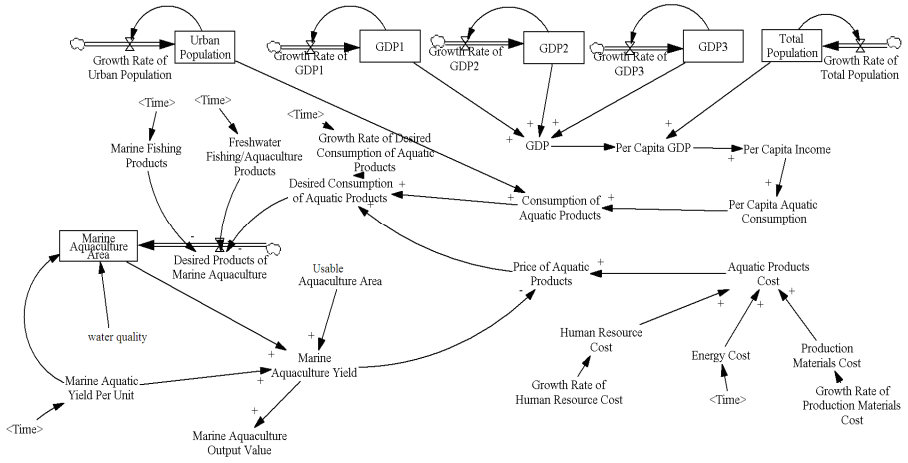

Fig. 2. System flow diagram of the utilization effectiveness of Qingdao MFZs

4 Simulations

Mathematically, the basic structure of a formal SD computer simulation model is a system of coupled, nonlinear, first-order differential (or integral) equations.

The simulation of such systems is easily accomplished by partitioning simulated time into discrete intervals. State variable is computed from its previous value and its net rate of change.

4.1 Additional Information Required by the Volume Editor

To validate the simulation model, the historical data from year 2000 to 2011 in Qingdao are used. Five subsystems are established to simulate three main state variables, namely, human resource costs, production costs, and energy costs. In addition, urban population, aquatic products price, marine aquaculture production, and per capital consumption costs are verified. The verified data are shown in Tables 1 and 2. Table 1 describes the errors between marine aquaculture area and marine aquaculture production from 2000 to 2011. Table 1 shows that the main factors will change even in the same year; the actual errors are more obvious if using the same single parameter matrix in the model. Table 2 describes the errors between aquatic products price and marine aquaculture production from 2000 to 2011. Table 1 and 2 show that the prediction accuracy of the SD model can be guaranteed (more than 91%) even if the annual main parameters and impact index matrix are unchanged. Verifying variables for the proposed model is satisfied.

Table 1. Simulation errors of the SD model of Qingdao MFZs between Marine Aquaculture Area and Production

Year	Mariculture Area (Ha)			Mariculture yield (Ton)		
	Actual Value	Simulation Value	Error (%)	Actual Value	Simulation Value	Error (%)
2000	55387	57584.6	3.97	783503	829955.6	5.93
2001	59456	66025	8.6	827228	906583.4	8.6
2002	58355	63902.5	2.52	858536	896189.2	2.52
2003	42460	42621.37	0.86	817176	826577.8	0.86
2004	44789	47494.39	5.75	821744	854998.5	5.75
2005	45368	50757.68	7.26	806198	851189.2	7.26
2006	45602	49586.66	6.83	800482	893560	6.83
2007	41416	44197.38	1.93	755466	763008	1.93
2008	35954	36324.74	6.8	755843	804455.8	6.8
2009	37098	41319.45	7.75	794168	809608.1	7.75
2010	40101	41831.3	4.31	812642	840947.9	3.48
2011	38743	41542.2	7.23	823080	896998.2	8.98

Table 2. Simulation errors of the SD model of Qingdao MFZs between Marine Aquaculture Area and Production

Year	Mariculture output value (Ton)			Aquatic products Price Index		
	Actual Value	Simulation Value	Error (%)	Actual Value	Simulation Value	Error (%)
2000	323160	359422.5	1.12	106.6	117.69	10.4
2001	392665	435245.7	8.6	108.09	119.41	10.4
2002	438771	460379.2	2.52	103.55	104.01	0.44
2003	471366	502171.2	0.86	105.73	116.67	10.3
2004	487952	502171.2	5.75	116.62	123.05	5.51
2005	511659	563390.5	7.26	120.58	133.67	10.8
2006	584037	589848.3	6.83	124.68	138.58	11.1
2007	570395	610289.2	1.93	130.79	144.74	10.6
2008	571171	587435.9	6.80	147.53	148.01	0.33
2009	646790	662769.9	7.75	150.93	152.29	0.90
2010	751788	795264.03	5.78	161.19	171.27	6.25
2011	862643	905685.16	4.99	184.41	197.29	6.98

4.2 Sensitivity Analysis

Sensitivity analysis shows how a particular scenario may be affected by multiple variables. For example, in modeling a home mortgage, sensitivity analysis could forecast situations if interest rates rise and/or property values decline.

From a different point of view, the sensitivity of the model can be divided into three types, namely, value sensitivity, behavior sensitivity, and policy sensitivity, all of which can determine the robustness of the model.

Figure 3 shows the sensitivity analysis results of the utilization effects for Qingdao MFZ. The simulation curve in each variable bracket means the trends from 2000 to 2011. And the variables in blue background such as marine fishing products, freshwater fishing products and desired consumption of aquatic products are influenced by time. The variation of the variables with a slider can cause changes with its associated variables in the feedbacks, or even to the whole system.

The main factors of the aquatic products cost include human resource, production, and energy costs. The first two factors are regular. The curve of energy costs is growth, but the changes are irregular. The change rate is used in the calculations of the cost of human resources, and the look-up table method is used in energy fuel costs calculations.

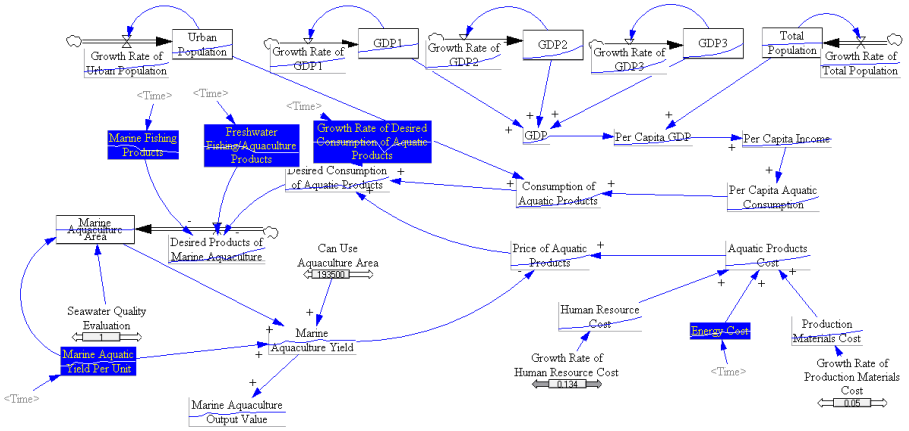

Fig. 3. Sensitivity analysis of the utilization effects for Qingdao MFZ

As the production cost has increased significantly in 2011, the increasing rate of the production materials costs in the sliding model is set as about 10% in the simulation data. Figure 4 shows the simulation curves of average aquatic products price in Qingdao at different growth rates of human resource costs and Figure 5 shows the simulation curves of expected consumption of aquatic products in Qingdao at different growth rates of human resource costs. From Figure 4, 5 and Table 1 we conclude that with the increasing price of aquatic products, the expected consumption is reduced.

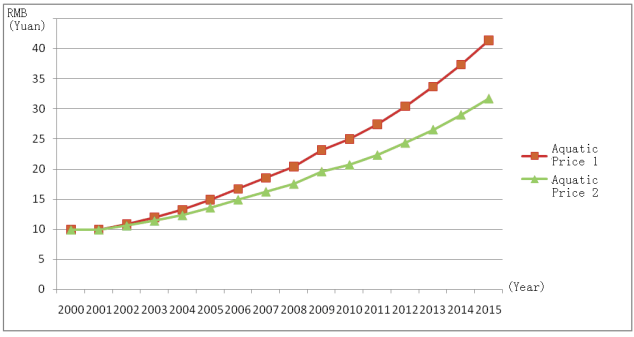

Fig. 4. Simulation curves of average aquatic products price in Qingdao at different growth rates of human resource costs (Aquatic Price 1 represents the simulation curves when human resource costs growth rate is 0.1, in red; Aquatic Price 2 represents the simulation curves when human resource costs growth rate is 0.11, in green)

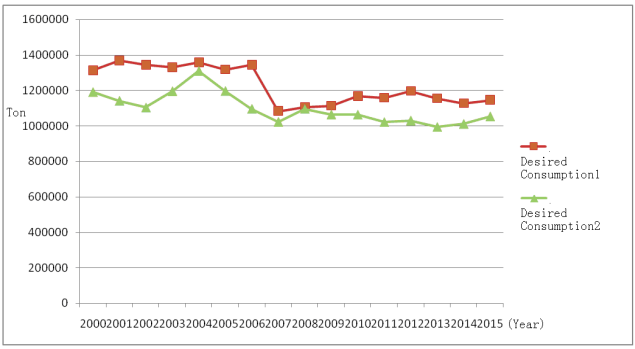

Fig. 5. Comparison chart of expected consumption of aquatic products in Qingdao (Desired consumption 1 represents the simulation curves when human resource costs growth rate is 0.1, in red; Desired consumption 2 represents the simulation curves when h human resource costs growth rate is 0.11, in green)

From the analysis above, the impact factors of aquatic products is more than scientific-technological progress and prices. Scientific and technological progress is a long process. The price of aquatic products and the level of consumption are processes of continuous volatility. Under the influence of aquatic growth cycle, the trend in information delay and the aquatic price undergoes fluctuation for four to five years per period. In order to further verify the conclusions above, we add a ratio factor γ which represents "purchasing desire of aquatic product" in the model proposed. The initial value $\gamma_0 = 1$. When a similar marine culture quality incidents happen, the ratio factor is adjusted to (0, 1) depending on the influence of the incident, when the other similar products (meat and eggs) quality incidents happen, γ is increased to (1, 2) depends on the influence. γ may be the largest when some incidents happens, and in the second year, third year, γ moves down accordingly. Figure 6 is the simulation and prediction curve of the total marine culture production after two mariculture quality accident in 2003 and 2008, and figure 6 shows that the lag affects of the yield changes obviously.

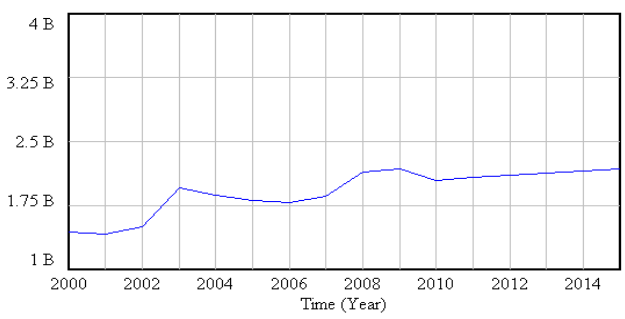

Fig. 6. Simulation of the total mariculture yields of Qingdao (The mariculture yields of Qingdao in 2013 and 2014 are predictive values)

In summary, the detailed conclusions obtained are as follows:

1. Qingdao marine aquatic area is reduced by 33% in the past decade, and aquaculture production would not change much.
2. The effect of the aquatic products price and other factors translates to an aquaculture fluctuation period of five to six years.
3. The aquatic production and output value of Qingdao have been increasing recently. However, this surge is not a real performance boost affected by the increasing energy price, production materials, feed, and human resource costs. With the economic development of Qingdao and the extension of the city, aquaculture will be further marginalized. Therefore, factory aquaculture will be very important for the future development of aquaculture.

5 Conclusions

This paper provides an integrated assessment model on the utilization effectiveness of Qingdao MFZs using SD. The impact assessment system is established. Simulations are conducted using historical data from year 2000 to 2011. The results indicate that simulations can assess the utilization effectiveness and predict the development trend of Qingdao MFZs with satisfactory accuracy. The model may be more effective if the values of the assessment system are changed annually. The proposed model provides an effective means to analyze the MFZs quantitatively.

Acknowledgments. This work is supported in part by open funds of Marine Ecological Environment and Disaster Prevention and Reduction key Laboratory of Shandong Province under Grants 2011014, Young Scientists Award Funds of Shandong Province under Grants BS2012HZ003 and Major Program Foundation for Youths of State Oceanic Administration under Grants 2009602.

References

1. Luan WX, A.D.: The functional programs of marine functional division of China. Human Geography 17, 93–95 (2002)
2. Wei, X.: On the determination standards of the compliance between sea areas for developing projects and marine functional zoning. Ocean Development and Management 7, 4–7 (2010)
3. Wang, J.T., Xu, W.: Construction and evaluation of the assessment indicator system of exploration potential of marine functional zone. Marine Science Bulletin 6, 1–6 (2009)
4. Zhang, G.H., Li, X.: Marine Functional Division in Qingdao City. Territory and Natural Resources Study 4, 5–7 (2006)
5. Miao, L.J., Li, S.Y.A.: Discussion of method of classified sea area use grading. Management Geological Science and Technology 22, 75–77 (2005)
6. Wang, J.J.T., Liu, B.Q.: Preliminary study on the compatibility discrimination methods of marine function zoning: A case study of port functional zones. Marine Science Bulletin 30, 496–501 (2011)

7. Vince, J.: The South East regional marine plan: Implementing Australia's oceans policy. Marine Policy 30, 420–430 (2006)
8. Hall, T.: Advancing objectives-based, Integrated Ocean Management through Marine spatial planning: current and future directions on the Scotian Shelf off Nova Scotia, Canada. Journal of Coastal Conservation 15, 247–255 (2011)
9. Gopnik, M., Fieseler, C., Cantral, L.: Coming to the table: Early stakeholder engagement in marine spatial planning. Marine Policy 36(5), 1139–1149 (2012)
10. Douvere, F., Ehler, C.N.: New perspectives on sea use management: Initial findings from European experience with marine spatial planning. Journal of Environmental Management 9, 77–88 (2009)
11. Qiu, W.F., Jones, P.J.: The emerging policy landscape for marine spatial planning in Europe. Marine Policy 39, 182–190 (2013)
12. Wang, Q.M., Miao, F.M.: Overview of foreign marine spatial planning and its impact on Chinese marine functional zoning. Ocean Development and Management 25, 45–49 (2008)
13. Gimpel, A., Stelzenmüller, V., Cormier, et al.: A spatially explicit risk approach to support marine spatial planning in the German EEZ. A spatially explicit risk approach to support marine spatial planning in the German EEZ. Marine Environmental Research 13 (2013)
14. Suárez de Vivero, J.L., Rodríguez Mateos, J.C.: The Spanish approach to marine spatial planning. Marine Strategy Framework Directive vs. EU Integrated Maritime Policy. Marine Policy 36, 18–27 (2012)
15. Collie, J.S., Adamowicz, W.L., Beck, M.W., et al.: Marine spatial planning in practice. Estuarine, Coastal and Shelf Science 117, 1–11 (2012)
16. Halpern, B.S., Diamond, J., Gaines, S.: Near-term priorities for the science, policy and practice of Coastal and Marine Spatial Planning (CMSP). Marine Policy 36, 198–205 (2012)
17. Stelzenmüller, V., Lee, J., South, A., et al.: Practical tools to support marine spatial planning: A review and some prototype tools. Marine Policy 38, 214–227 (2013)
18. Gao, Y.M., Zhou, L., Qu, P.: Evaluations on the utilization effects of marine functional zones based on system dynamics. Journal of Ocean University of China (Social Sciences) 4, 15–20 (2011)
19. Sterman, J.D.: System Dynamics Modeling. California Management Review 43, 8–25 (2001)

Carbon Dynamics of *Pinus Massoniana* Plantations Following a Thinning Treatment 5 Years and 10 Years Before

Zhiwei Ge, Danyan Zhou, Yushan Hao, Xiaochi Ma, Qingwei Guan*, Ruixia Li, and Dong Wang

College of Forest Resources and Environment, Nanjing Forestry University, Nanjing 210037, China

Abstract. The change of carbon storage in *Pinus massoniana* plantations after thinning is important to improve the plantation management. The forest biomass distribution, biodiversity, soil respiration, and soil total carbon (STC) were investigated in Lishui *Pinus massoniana* plantations after thinning, the results are as follows: (1)the total community biomass has significantly growth, while the biomass in herb layer has decreased in stands thinned 10 years earlier. (2) Soil total carbon increased first and then decreased, while soil total nitrogen had the opposite trend. And thinning had little influence on soil C/N ratio. (3)The carbon storage of *Pinus massoniana* plantations in different thinning periods from large to small is as follows: 10 years after thinning > unthinned > 5 years after thinning.

Keywords: Pinus massoniana plantation, thinning, biodiversity, carbon storage.

1 Introduction

To fully understand the role forest landscapes play in regional, continental, or global carbon dynamics it is necessary to consider constraints on biogenic carbon fluxes, the impacts of disturbance on the stocks of live and dead biomass, and the interactions between disturbance and biogenic carbon fluxes [1]. Thinning is an important management measure to adjust the structure of plantations. It can provide favorable growing environment for forests, promote the growth of individual trees, increase the plant diversity of plantations and enhance the stability of forest community and productivity of forest ecosystem by improving foraging space of the canopy and supply condition of the underground fertilizer [2-4]. The study of the effects of thinning on carbon storage of plantations is important to improve the plantation management.

Thinning can remove a certain ratio of timber storage from forests, thus decreasing the carbon storage of vegetation. Some research indicates that the NEP of ponderosa pine forests in Canada is down by a third after thinning and not recovered to the level

* Corresponding author.

F. Bian et al. (Eds.): GRMSE 2013, Part I, CCIS 398, pp. 446–455, 2013.
© Springer-Verlag Berlin Heidelberg 2013

before thinning even after 16 years[1]. Model research finds that the carbon storage of vegetation can reach the original level 60 years after thinning. However, thinning can increase the light utilization of forests by 60% and forest regeneration can compensate for the missing carbon storage [5]. A research using Sima model finds that with the intensification of thinning, the carbon storage of forest ecosystem in Finland is about to decrease 100 years later [6]. Some scholars believe in order to improve the comprehensive benefits of forests, it is necessary to determine appropriate thinning intensity and management model according to the characteristic of species while thinning [7-10].

Pinus massoniana is one of the main afforestation species in southern China. It has an area of 7.74% of the national forest area and plays a vital role in the restoration and reconstruction of degraded forest ecosystem in subtropical zone.

Questions remain as to how much and for how long these apparent alterations impact gross primary production (GPP), the allocation of GPP among functionally different growth forms and plant component (i.e. roots, stems, and foliage), and the subsequent magnitude of ecosystem respiration (Re) and net ecosystem production (NEP) have no definite conclusion.

This research analyses the effects of thinning on carbon dynamics of plantations and provides theoretical basis for determining thinning periods of *Pinus massoniana* plantations in forest management.

1.1 Study Site

The study site was located in Lishui plantation basin（31°36′N, 119°01′E）. The total area is 1333 hm^2. The average elevation is 100m and the highest peak is 209.8m. This location experiences an average annual air temperature of 16.1℃ and precipitation of 1119.2mm. The vegetation is dominated by plantations and secondary forests made by forest closing.

1.2 Methods

1.2.1 Plot Design

According to the principle of typicality and representativenezss, we chose the representative block, 10-20meters away from forest edge, as the sample plot to set 9 blocks in Lishui 43-year-old pure masson pine plantations measured 5 years after thinning, 10 years after thinning and unthinned respectively (the thinning intensity was about 30%) and each plot had an area of 40×50m. We did tally to the tree layer in the 9 blocks. That was to record names of tree species, diameter, height, crown width and growth. Record habitat Factors like altitude, slope and aspect of each sample plot at the same time.

1.2.2 Biomass Estimation of the Tree Layer

According to the average diameter and height data of stands in each block, we calculated the biomass of different parts like stems and foliage of the tree layer respectively using the aboveground biomass formula [11]:

$$W_S=0.0459(D^2H)^{0.8867} \quad W_B=0.0127(D^2H)^{0.7886}$$
$$W_L=0.0283(D^2H)^{0.6012} \quad W_T=W_S+W_B+W_L$$

Among them: WS—trunk biomass, WB—branch biomass, WL—foliage biomass, WT—aboveground total biomass, D—average diameter/cm, H—average height/m.

1.2.3 Biomass Estimation of Understory Vegetation

Randomly locate three 1×1m plots in each sample plot, dig out the root of all shrubs and herbs and test weight using the harvest method. Then, take 30% of the mixed sample of stems, foliage and roots respectively, put them in the labeled sealed pocket and take them back to the lab after calculating the fresh weight using electronic scales. Dry those at 75℃, measure the dry mass, calculate the moisture content and converse the biomass.

1.2.4 Estimation of Underground Biomass

We used the mining harvest method to estimate the underground biomass. Select 3 points in each sample plot randomly and take 81 pieces (9×3×3)of 20cm×20cm clods from 0-10cm, 10-20cm, 20-30cm layer of soil respectively using shovels 50cm away from the tree. Put these clods on white plastic sheets immediately and make sure that the roots are complete. Pick up all the roots carefully, put them in the labeled sealed pocked, slot them in the storage with ice and take them back to the lab the same day. Collect all the soil that contains roots from the same sample plot into a container, put them in test sieves or nylon bags and then wash. Separate, dry and weigh the roots after washing to get the root biomass of a certain amount of soil.

1.2.5 Estimation of Soil Total Carbon and Nitrogen

We used Elementar Vario EL to estimate soil total carbon and nitrogen. Select 5 points randomly using the S-form-spacing method in each sample plot. Collect soil sample from 0-10cm, 10-20cm and 20-30cm layer of soil respectively using drills with a 2cm diameter. Mix up the soil from the 5 points to form a sample and the total number of soil samples is 135(9×5×3). Air dry the soil samples and make them go through the 100 mesh screen after abrading. Use Elementar Vario EL to estimate soil total carbon and nitrogen. Estimate soil bulk density using the cutting ring method at the same time.

1.2.6 Calculation of Carbon Storage of *Pinus massoniana* Plantations

Carbon storage of *Pinus massoniana* plantations is composed mainly of carbon storage of vegetation and carbon storage of soil.

Carbon storage of vegetation was acquired by multiplying vegetation biomass by carbon content rate of vegetation:

Carbon storage of vegetation (t/hm^2) = vegetation biomass×carbon content rate of vegetation (%)

The common 0.47 carbon conversion rate was adopted by the carbon content rate of trees, shrubs and herbs in *Pinus massoniana* plantations (ICPP.2006).

2 Results and Analyses

Since the soil layer of the study site was thin, the estimation of soil carbon storage of this research was constrained within 30cm depth of epipedon and aboveground litter excluded. The forum is as follows:

$$S_d = \sum_{i=1}^{d} D_i C_i H_i$$

Among them:

S_d—Soil carbon storage of per unit area within d depth of epipedon.
D_i—Soil bulk density of the i soil layer.
C_i—Carbon content rate of the i soil layer.
H_i—Thickness of the i soil layer.

2.1 Vegetation Biomass of *Pinus massoniana* Plantations in Different Thinning Periods

Thinning increased the vegetation biomass of *Pinus massoniana* plantations remarkably. Compared with the unthinned control stand, the shrub and herb biomasses of *Pinus massoniana* plantations thinned 10 years earlier were increased by 90.62% and 71.43% respectively. This is the same as the result of the study about Chinese fir forest and larch and spruce mixed forest[9,12]. The shrub biomass and total biomass of *Pinus massoniana* plantations thinned 10 years before were 24.49% and 11.72% above that of *Pinus massoniana* plantations measured 5 years after thinning while the herb biomass was 8.70% lower. This may be that *Pinus massoniana* plantations did not have crown closure 10 years after thinning, thus providing necessary resources and spaces for the growth of shrubs. However, herbs are more sensitive to environmental changes than shrubs. The raise of species and numbers of shrubs will definitely constraint the growth of herbs, which leads to the result that the shrub biomass of *Pinus massoniana* plantations thinned 10 years earlier was increased but the herb biomass was lower than that of *Pinus massoniana* plantations measured 5 years after thinning. At the same time, since the accumulated

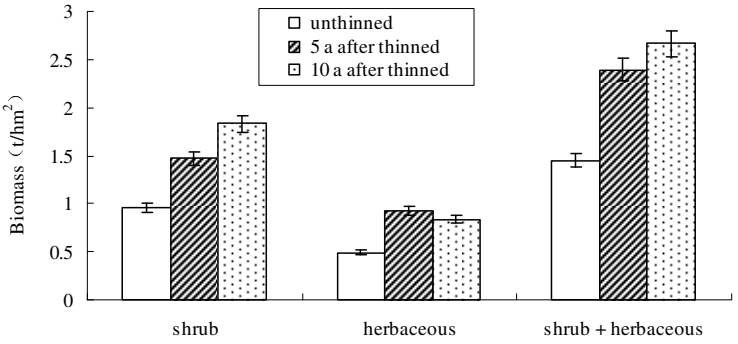

Fig. 1. The understory biomass (shrub, herb) of *Pinus massoniana* plantations in different thinning periods

biomass of shrubs was greater than the reduced biomass of herbs of *Pinus massoniana* plantations thinned 10 years earlier, so the total forest vegetation biomass was higher than that of *Pinus massoniana* plantations measured 5 years after thinning finally.

2.2 Root Biomass of *Pinus massoniana* Plantations in Different Thinning Periods

Root biomass of *Pinus massoniana* plantations in different thinning periods is shown in figure 2. Compared with the unthinned control stand, root biomass of *Pinus massoniana* plantations measured 5 years after thinning was reduced. The possible reason is that thinning itself can decrease the stand biomass[13-14]. According to figure 2, root biomass of 10-20cm and 10-20cm layer of soil of *Pinus massoniana* plantations thinned 10 years earlier is higher than that of *Pinus massoniana* plantations measured 5 years after thinning. What is more, the total root biomass of 0-20cm layer of soil of *Pinus massoniana* plantations thinned 10 years earlier are remarkably higher than that of *Pinus massoniana* plantations measured 5 years after thinning. That is to say, with the raise of thinning periods, root biomass of *Pinus massoniana* plantations was accumulating significantly. This is because the stand coverage was enhanced of *Pinus massoniana* plantations thinned 10 years earlier and the microclimate in the stand was improved continuously, which was good for the result of carbon storage of *Pinusmassoniana* plantations.

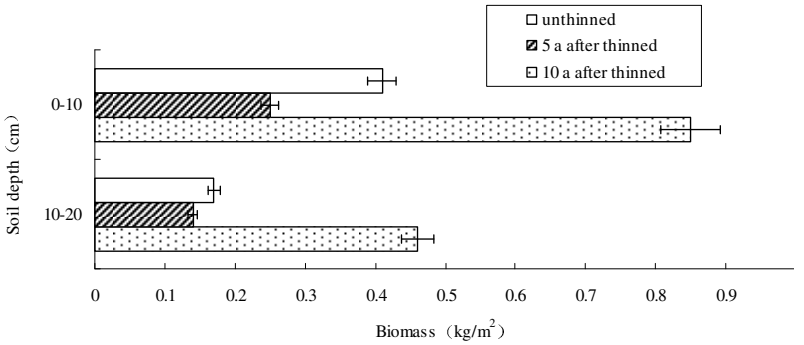

Fig. 2. The underground biomass of *Pinus massoniana* plantations in different thinning periods

2.3 Soil Total Carbon and Nitrogen Content of *Pinus massoniana* Plantations in Different Thinning Periods

Soil total carbon content of *Pinus massoniana* plantations in different soil depth and thinning periods is shown as figure 3. The change of soil total carbon content of 0-10cm layer with the change of thinning periods was the same as that of 10-20cm layer. Soil total carbon content increased first and then decreased with the raise of thinning periods; soil total carbon content was highest in *Pinus massoniana* plantations measured 5 years after thinning and was 2.22% and 0.35% above that of the unthinned control stand; soil total carbon content was lowest in *Pinus massoniana* plantations thinned 10 years earlier and was 2.68% and 2.84% lower than that in the unthinned control stand. 5 years after thinning, soil carbon content increased and there

were two possible reasons. With the raise of thinning periods, total carbon of the 20-30cm layer of soil decreased first and then increased; it reached the lowest point 5 years after thinning and 2.08% lower than that of the soil in the unthinned control *Pinus massoniana* plantations; soil total carbon content of *Pinus massoniana* plantations thinned 10 years earlier showed no remarkable difference with that of the unthinned control group.

Soil C/N ratio is generally considered as an index of the mineralization ability of soil nitrogen and has certain influence on the activity ability of soil microorganisms[15]. As is shown in figure 4, soil C/N ratio decreased gradually with the deepening of soil; for the 0-10cm and 10-20cm layer of soil, soil C/N ratio increased first and then decreased with the raise of thinning periods and arrived at the level before thinning 10 years after thinning. The change of soil C/N ratio with the change of thinning periods was the same as that of soil carbon content. However, the result of variance analysis indicated that differences between soil C/N ratio of the same soil in different thinning periods were not remarkable ($P > 0.05$), that is to say thinning did not have a great influence on soil C/N ratio.

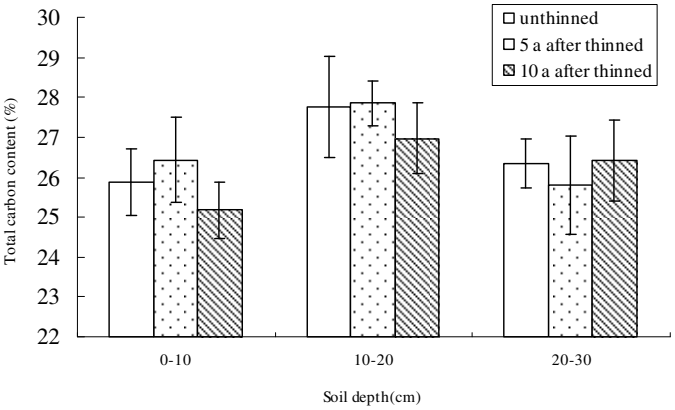

Fig. 3. The soil total carbon content in *Pinus massoniana* plantations in different thinning periods

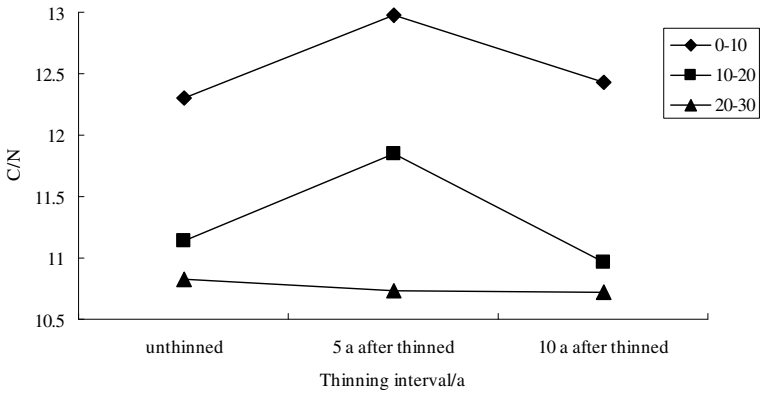

Fig. 4. The soil C/N in *Pinus massoniana* plantations in different thinning periods

2.4 Carbon Storage of *Pinus massoniana* Plantations in Different Thinning Periods

Carbon storage of the ecosystem of *Pinus massoniana* plantations are mainly composed of carbon storage of vegetation layer and soil layer. Among carbon storage of vegetation layer, tree layer has a distinct advantage and makes up more than 58.70% of all the carbon storage of the ecosystem. Carbon storage of tree layer and the root in different thinning periods from large to small is as follows: 10 years after thinning > unthinned > 5 years after thinning. The carbon storage of forest vegetation layer in different thinning periods from large to small is as follows: 10 years after thinning > 5 years after thinning > unthinned. Carbon storage of the ecosystem was lowest in the *Pinus massoniana* plantations measured 5 years after thinning, highest in the stand thinned 10 years earlier and intermediate in the unthinned control group. Among them, carbon storage of vegetation layer and soil layer in the stand measured 5 years after thinning were reduced by 5.51% and 9.47% respectively, 1.57t/hm^2 and 1.35t/hm^2 lower than that in the unthinned control group.10 years after thinning, the raise of carbon storage of the ecosystem of *Pinus massoniana* plantations was mainly due to the raise of carbon storage of vegetation layer. It made up 75.68% of all carbon storage of the ecosystem and tree layer had a distinct advantage.

Table 1. The carbon stocks and its distribution of the ecosystem in different thinning periods

Time after thinning (a)	Carbon stocks (t/hm^2)		
	Aboveground layer	Understory layer	Root layer
CK	25.13 (58.70)	0.68 (1.59)	2.73 (6.37)
5	24.01 (60.19)	1.12 (2.82)	1.83 (4.59)
10	33.02 (61.81)	1.25 (2.35)	6.16 (11.53)
Time after thinning (a)	Carbon stocks (t/hm^2)		
	Vegetation layer	Soil layer	Ecosystem
CK	28.54 (66.65)	14.28 (33.35)	42.82 (100)
5	26.97 (67.60)	12.93 (32.40)	39.90 (100)
10	40.43 (75.68)	12.99 (24.32)	53.42 (100)

PS: Numbers in the brackets were the percentage of carbon stocks in different layers.

3 Discussion

(1) Effects of thinning on tree layer and forest vegetation of *Pinus massoniana* plantations. At the beginning of thinning, the aboveground biomass of the stand was reduced. With the raise of thinning periods, stand biomass of *Pinus massoniana* plantations thinned 10 years earlier was increased remarkably. Stand vegetation biomass of *Pinus massoniana* plantations thinned 10 years earlier was still in its accumulation stage and the proportion of shrubs was increased. Compared with *Pinus massoniana* plantations measured 5 years after thinning, shrub biomass of *Pinus massoniana* plantations thinned 10 years earlier was increased, herb biomass was decreased and total biomass of forest vegetation was enhanced.

(2) Soil total carbon content increased first and then decreased with the raise of thinning periods; thinning did not have a great influence on soil C/N ratio. At the beginning of thinning, soil carbon content increased and there were two possible reasons. On the one hand, the residue produced after thinning became the main resource of soil carbon[16]. On the other hand, the number of *Pinus massoniana* was decreased, the amount of soil organic carbon exhausted by root was reduced, litters of shrub layer was increased and the input of soil organic carbon was enhanced. The growth of root and vegetation of *Pinus massoniana* plantations was vigorous and the use of organic matters was increasing. Both of them led to the reduction of soil carbon storage of stands, especially in surface soil. The remove of some trees reduced the nutrient input of the stand and the vigorous growth of plants increased the use of soil nutrients. Both of them led to the reduction of soil total nitrogen content. Soil C/N ratio was not affected by thinning. However, soil total nitrogen content showed a tendency that decreased first and then increased, especially of the surface soil. The reason for this phenomenon may be that *Pinus massoniana* plantations had certain promoting effects on the mineralization process of soil nitrogen[17].

(3) Effects of thinning on carbon storage of *Pinus massoniana* plantations. Carbon storage of the ecosystem of *Pinus massoniana* plantations in different thinning periods from large to small is as follows: 10 years after thinning＞unthinned＞5 years after thinning. Thinning provided more growth space for individuals, relieved intraspecific competition, supplied enough light for stands, made photosynthesis proceed more effective and accelerated accumulation of organic matters. The accumulation of biomass and carbon storage of individuals of the thinned stand was much higher than that of the unthinned sample plot[18]. Forest vegetation biomass is one of the indexes to measure the growth of forest vegetation.Meanwhile, biomass can reflect the species richness to some degree[19-21].

(4)The raise of soil C/N ratio has certain restriction on the activity ability of soil microorganisms. It can reduce the decomposition and mineralization speed of organic matters and nitrogen, increase the ability of soil to fix organic carbon and is good for the ability of soil to collect carbon and nitrogen[22]

(5)The raise of species and numbers of shrubs would definitely constraint the growth of herbs[23-24], which led that shrub biomass of *Pinus massoniana* plantations thinned 10 years earlier was increased but herb biomass was lower than that of *Pinus massoniana* plantations measured 5 years after thinning.Since thinning adjusted the relationship between forests, it reduced the coverage of stands, improved light, temperature and humidity conditions in stands, increased environmental heterogeneity, renewed shrubs and herbs of *Pinus massoniana* plantations and enhanced biodiversity of the community[25-27].Affected by the constraint of environmental conditions and competitions among species, evenness index of herbs of *Pinus massoniana* plantations thinned 10 years earlier was lower than that of the control group [28].

4 Conclusions

Effects of thinning on the ecosystem of *Pinus massoniana* plantations: (1) Rise of stem volume and forest vegetation biomass, remarkable accumulation of root biomass and enhancement of stand biomass of *Pinus massoniana* plantations caused by

thinning. (2) The structure of soil carbon pool is changed to a certain degree. With the raise of thinning periods, soil total carbon content increases first and then decreases, total nitrogen content decreases first and then recovers to the level before thinning while the change of soil C/N ratio is not remarkable. (3) Total carbon storage of the ecosystem reduces first and then achieves stability. So, it is necessary to select the method and intensity of thinning according to the goal of forest management. Especially for the difficult construction of carbon sink forest. One should be careful to choose the management method to avoid unnecessary carbon loss of the ecosystem.

Acknowledgments. We thank the staff of the Forest Farm of Lishui County, Jiangsu Province, China for field assistance. This study was supported by Forestry public welfare projects Fund of State Forestry Administration (No. 201104075) and the Major State Basic Research Development Program of China (973 Program) (No. 2012CB416904).

References

[1] Campbell, J., Alberti, G., Martin, J., Law, B.E.: Carbon dynamics of a ponderosa pine plantation following a thinning treatment in the northern Sierra Nevada. Forest Ecology and Management 257, 453–463 (2009)
[2] Yang, L.G., Wang, W.M., Liu, H.: Effect of Thinning on Natural Forest Growth. Forestry Science and Technology Information 41(2), 26–27 (2009)
[3] Mack, M.C., Schuur, E.A.G., Bret-Harte, M.S., et al.: Ecosystem carbon storage in arctic tundra reduced by long-term nutrient fertilization. Nature 431, 440–443 (2004)
[4] Liu, S.R., Wang, H., Luan, J.: A review of research progress and future prospective of forest soil carbon stock and soil carbon process in China. Acta Ecologica Sinica 31(19), 5437–5448 (2011)
[5] Comfort, E.J., Roberts, S.D., Harrington, C.A.: Midcanopy growth following thinning in young-growth conifer forests on the Olympic Peninsula western Washington. Forest Ecology and Management 259, 1606–1614 (2010)
[6] Paquette, A., Messier, C.: The role of plantations in managing the world's forests in the Anthropocene. Frontiers in Ecology and the Environment 8, 27–34 (2010)
[7] Wang, Z.H., Li, R.X., Wang, X.J., et al.: Effects of thinning on biomass and species diversity of understory in Chinese fir plantations. Ecology and Environmental Sciences 19(12), 2778–2782 (2010)
[8] Chen, D.L., Guo, J.P., Du, N.N.: Effect of Thinning Intensity on Biodiversity of Undergrowth Vegetation in a Larix principis-rupprechatii Plantation. Journal of Northeast Forestry University 41(2), 26–27 (2009)
[9] Li, S.H., Yang, J.C., Liu, Y.Y.: Forest Research of Thinning. Journal of Heilongjiang Vocational Institute of Ecological Engineering 23(1), 31–32 (2010)
[10] Zhang, X.J., Wang, Q.C., Hao, L.F., et al.: Effect of Gap Thinning on the Regeneration and Plant Species Diversity in Larix olgensis Plantation. Scientia Silvae Sinicae 47(8), 7–13 (2011)
[11] Carbon Accounting of Afforestation Project and Guidance for testing. National Forestry Bureau Climate (2010)

[12] Lei, X., Lu, Y., Peng, C., Zhang, X., Chang, J., Hong, L.: Growth and structure development of semi-natural larch-spruce-fir (Larix olgensis–Picea jezoensis–Abies nephrolepis) forests in northeast China: 12-year results after thinning. Forest Ecology and Management 240, 165–177 (2007)
[13] Powersa, M.D., Palik, B.J., Bradford, J.B., Fraver, S., Webster, C.R.: Thinning method and intensity influence long-term mortality trends in a red pine forest. Forest Ecology and Management 260, 1138–1148 (2010)
[14] Picchio, R., Neri, F., Maesano, M., Savelli, S., Sirna, A., Blasi, S., Baldini, S., Marchi, E.: Growth effects of thinning damage in a Corsican pine (Pinus laricio Poiret) stand in central Italy. Forest Ecology and Management 262, 237–243 (2011)
[15] Liao, L.P., Gao, H., Wang, S.L., et al.: The effect of nitrogen addition on soil nutrient leaching and the decomposition of Chinese fir leaf litter. Acta Phytoecologica Sinica 24(1), 34–39 (2000)
[16] Cao, Y.K.: Effects of logging slash treatments on ecosystem carbon storage of the second rotation Chinese fir plantations. D. Fujian Agriculture & Forestry University (2008)
[17] Zhang, D.H., Ye, Z.F., Fan, B.Y., et al.: Influence of thinning on soil fertility in artificial forests. Chinese Journal of Applied Ecology 12(5), 672–676 (2001)
[18] Shi, C.: The factor on carbon stocks of Platyclatdus orientalis plantation in Xuzhou. D.Nanjing Forestry University (2012)
[19] Nilsen, P., Strand, L.T.: Thinning intensity effects on carbon and nitrogen stores and fluxes in a Norway spruce (Piceaabies L.) stand after 33 years. Forest Ecology and Management 256, 201–208 (2008)
[20] Verschuyla, J., Riffell, S., Miller, D., Wigley, T.B.: Biodiversity response to intensive biomass production from forest thinning in North American forests-A meta-analysis. Forest Ecology and Management 261, 221–232 (2011)
[21] Liao, Y.C., Fan, H.B., Li, Y.Y., et al.: Effects of simulated nitrogen deposition on growth and photosynthesis of 1-year-old Chinese fir (Cunninghamia lanceolata) seedlings. Acta Ecologica Sinica 30, 150–154 (2010)
[22] Zhang, C.H., Wang, Z.M., Ju, W.M., et al.: Spatial and temporal variability of soil C / N ratio in Songnen Plain maize belt. Environment Science 32(5), 1407–1414 (2011)
[23] Mao, Z.H., Zhu, J.J., Liu, Z.G., et al.: Effects of thinning on species diversity and composition of understory herbs in a larch plantation. Chinese Journal of Ecology 25(10), 1201–1207 (2006)
[24] Wang, Q.K., Wang, S.L., Huang, Y.: Comparisons of litter fall, litter decomposition and nutrient return in a monoculture Cunninghamia lanceolata and a mixed stand in southern China, China. Forest Ecology and Management 255, 1210–1218 (2008)
[25] Sartor, I.F., Lal, R., Ebinger, M.H., et al.: Changes in soil carbon and nutrient pools along a chrono sequence of poplar plantations in the Columbia Plateau, Oregon. Agriculture, Ecosystem and Environment 122, 325–339 (2007)
[26] Inagaki, Y., Kuramoto, S., Torii, A., Shinomiya, Y., Fukata, H.: Effects of thinning on leaf-fall and leaf-litter nitrogen concentration in hinoki cypress (Chamaecyparis obtusa Endlicher) plantation stands in Japan. Forest Ecology and Management 255, 1859–1867 (2008)
[27] Cao, Y., Yang, Y., Song, B.Y., et al.: Effects of artificial tending on Pinus tabulaeformis forest growth and its structural characteristics. Chinese Journal of Applied Ecology 16(3), 397–402 (2005)
[28] Duan, J., Ma, L.Y., Jia, L.M., et al.: Effect of thinning on Platycladus orientalis plantation and the diversity of undergrowth vegetation. Acta Ecologica Sinica 31(6), 1431–1441 (2010)

Dynamic Monitoring Technique for Remote-Sensing Image of Invasive Alien Plant Species

Rabigul Hesen[1], Zhenhong Jia[1,*], Jie Yang[2], and Raphael Hu[3]

[1] College of Information Science and Engineering, Xinjiang University, Urumqi 830046, China
[2] Institute of Image Processing and Pattern Recognition, Shanghai Jiao Tong University, Shanghai 200240, China
[3] Knowledge Engineering and Discovery Research Institute, Auckland University of Technology, Auckland 1020, New Zealand
976250588@qq.com, jzhh@xju.edu.cn

Abstract. Invasive Alien Plant Species (IAPS) could seriously affect the local ecosystem balance, and pose a threat to the ecological security. In order to effectively monitor and control invasive alien plants, it needs to monitor the spatial distribution and dynamic changes of IAPS. It will cite the method of nonsubsampled contourlet transform (NSCT) combination with fuzzy C-means clustering algorithm in this paper, which is used in remote sensing image change detection, for monitoring the dynamic changes of biological invasive species in this paper, to get a better detection result.

Keywords: Invasive Alien Plant Species, dynamic monitoring, nonsubsampled contourlet transform, fuzzy C-means clustering algorithm.

1 Introduction

Invasive Alien Plant Species (IAPS) mean the alien species which migrate because of intentional or unintentional acts of human activities, and establish populations in natural or semi-natural ecosystems or habitat to cause change and a threat to the native biological diversity [1]. IAPS has a strong influence on growth and reproduction and resource allocation of indigenous plants, and even can replace the indigenous plants [2,3], and it results in changes in community structure and diversity reduction of indigenous plants [4]. IAPS had already had a serious impact on social progress and economic development of the local, and cause huge economic losses. According to rough statistics, several major IAPS cause China's annual economic losses up to one hundred billion Yuan [5-8]. Therefore, it will have very important significance on China's agricultural production and ecosystem stability with studying on monitoring technique for IAPS, to establish a nationwide IAPS control system.

Remote-sensing monitoring technique has made up the flaw and difficulties [9] on large space-time interval, high labor costs, difficult to have the overall or general

* Corresponding author.

F. Bian et al. (Eds.): GRMSE 2013, Part I, CCIS 398, pp. 456–462, 2013.
© Springer-Verlag Berlin Heidelberg 2013

sense and the high cost of traditional monitoring methods to a certain degree. According to different periods of satellite remote sensing images with image change detection, it is a very effective monitoring technique [10] for IAPS by analyzing distribution changes of IAPS. It will apply the method of nonsubsampled contourlet transform (NSCT) combination with fuzzy C-means clustering algorithm for biological species invasion change detection, to achieve the dynamic monitoring of the biological species invasion.

2 Algorithm Summarization and Expected Result of Experiment

2.1 Algorithm Summarization

Nonsubsampled Contourlet Transform (NSCT) is composed of Nonsubsampled Pyramid Filter Bank (NSPFB) and Nonsubsampled Directional Filter Bank (NSDFB) [11, 12]. The front part ensures the multi-scale characteristics of the application of dual-channel nonsubsampled filter bank, the latter part is permitted to decompose into 2n directions band-pass sub-band. NSCT is a kind of improved contourlet transforms, which makes it has translation invariance, directionality, and anisotropy, etc. It is more suitable for feature extraction in noisy environments. It decomposes the input image into low-pass sub-bands and high-pass sub-bands by NSPFB first, then the high-pass sub-bands are decomposed into direction sub-bands. Finally, by repeating the above operations on each layer of low-pass sub-bands, we can get multi-scale, multi-directional decomposition of input image.

Fuzzy C-means clustering is an algorithm that determines each data point belongs to a cluster by degree of membership, which presented by Bezdek in 1973, it can be used in vector clustering [13]. It is flexible to divide the data, while K-means clustering is rigid.

FCM clustering algorithm is a fuzzy classification that is to find the given data by minimizing the objective function. Suppose there is a set of p-dimensional data X, which is divided into k fuzzy groups by the FCM method, and to solve the cluster centers of each group for minimizing the objective function. For each given data point, it has the value of between 0 to 1 of degree of membership to determine the degree of belonging to each group, to adapt the fuzzy partition introduced, membership matrix is permitted to have the elements of the value of between 0 to 1. Plus normalized stipulation, the sum of degree of membership of a data set is equal 1, that is

$$\sum_{i=1}^{c} u_{ij} = 1, \forall j = 1 \cdots n \tag{1}$$

the objective function of FCM is

$$J\left(U, c_1, \cdots, c_c\right) = \sum_{i=1}^{c} J_i = \sum_{i=1}^{c} \sum_{j}^{n} u_{ij}^{m} p_{ij}^{2} \tag{2}$$

where $u_{ij} \in [0, 1]$, c_i is the cluster center of fuzzy group, $p_{ij} = \left\| c_i - x_j \right\|$ is the Euclidean distance between the *i*-th cluster center and the j-th data point, and $m \in [1, \infty]$ is a weighted index. Form, which is a flexible control algorithm parameter, if the value of *m* is too large, clustering effect will be very poor, and if it is too small, the algorithm will be close to C-means clustering algorithm. And there is no theoretical guidance on selecting the value of *m* [14]. According to the result [15] of cluster validity studies by J C Bezdek, the value range of *m* can be limited between 1.5 and 2.5.

Constructing a new objective function to minimize formula (2), we can get

$$\begin{aligned} &\overline{J}\left(U, c_1, \cdots, c_c, \lambda_1, \cdots, \lambda_n\right) \\ &= J\left(U, c_1, \cdots, c_c\right) + \sum_{j=1}^{n} \lambda_j \left(\sum_{i=1}^{c} u_{ij} - 1 \right) \\ &= \sum_{i=1}^{c} \sum_{j}^{n} u_{ij}^{m} p_{ij}^{2} + \sum_{j=1}^{n} \lambda_j \left(\sum_{i=1}^{c} u_{ij} - 1 \right) \end{aligned} \tag{3}$$

where λ_j (j=1, 2, …n) is n Constrained Lagrange multipliers of formula (2), when minimizing formula (3) with the derivation of all input parameters, it is the following:

$$c_i = \frac{\sum_{j=1}^{n} u_{ij}^{m} x_j}{\sum_{j=1}^{n} u_{ij}^{m}} \tag{4}$$

$$u_{ij} = \frac{1}{\sum_{k=1}^{c} \left(\frac{p_{ij}}{p_{kj}} \right)^{2/(m-1)}} \tag{5}$$

By the two necessary conditions above-mentioned, we know that Fuzzy C-Means clustering algorithm is an iterative process, so it needs to repeat the calculation of membership matrix until the output of the optimal cluster center, to display the final change detection image. When the advantage of NSCT in the feature extraction and that of fuzzy C-means clustering algorithm combining with the method, we can get a better experimental results [16].

2.2 Specific Steps of Algorithm

Let X_1 and X_2 denote calibrated two different periods of the same area of the shooting images of biologicalspecies. $X_1 = \{X_1(i,j), 1 < i < H, 1 < j < W\}$, $X_2 = \{X_2(i,j), 1 < i < H, 1 < j < W\}$, and image size is $H \times W$.

Specific steps of experiment:

(1) By subtracting the input reference image X_1 and detection image X_2, we can get difference image X_D, that is $X_D = |X_1 - X_2|$.

(2) Transforming the difference image by NSCT, and decomposing into couples of layers according to actual situation, we can get different sub-band images. If the number of layers is too large, it will blur detail and waste time, if it is too small, then it will lose some details again. Therefore, it can be shown by experimental analysis that it will be better to be decomposed into 3 layers.

$$NSCT(X_D) = \{d_{1,1}, d_{2,1}, d_{2,2}, d_{3,1}, d_{3,2}, d_{3,3}, d_{3,4}, a\} \tag{6}$$

Where d_{ij} denotes the i-th directional high-frequency sub-band image of j scale, and a denotes low-frequency sub-band. By three layers of decomposing in this paper, which combined with difference image X_D and each sub- band coefficients, the eigenvectors can be constructed.

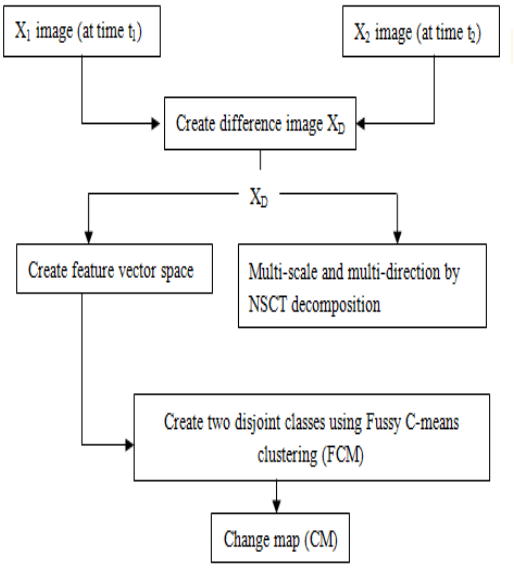

Fig. 1. General scheme of the proposed approach

(3) For each eigenvector, it needs to consider neighborhood information adequately, and it takes sliding window by 3×3 for average to determine a new eigenvector.

$$\Delta' = \{X_D', d_{1,1}', d_{2,1}', d_{2,2}', d_{3,1}', d_{3,2}', d_{3,3}', d_{3,4}', a'\} \tag{7}$$

(4) Feature vector space is classified by classic fuzzy C-means clustering algorithm [16], to determine each pixel`s category (changed or unchanged). Fuzzy C-means clustering algorithm classify the feature vector space into two disjoint categories. The

number of cluster centers C=2, and each feature vector is clustered into an appropriate category by Euclidean distance. U_C and U_U are final membership of FCM clustering for changed and unchanged of each feature vector. We can get a binary image by comparing U_C with U_U, that is $jieguo=\{jieguo(i,j)|1\le i\le N, 1\le j\le N\}$,where "0" denotes the position of unchanged, and "1"denotes the position of changed. The formula is shown as follows:

$$jieguo(i,j)=\begin{cases}0, & u_c \le u_u \\ 1, & otherwise\end{cases} \tag{8}$$

2.3 Experimental Results

In order to test the performance of the method proposed in dynamic monitoring of biological invasive species, we do experiment on the satellite image [17] data of

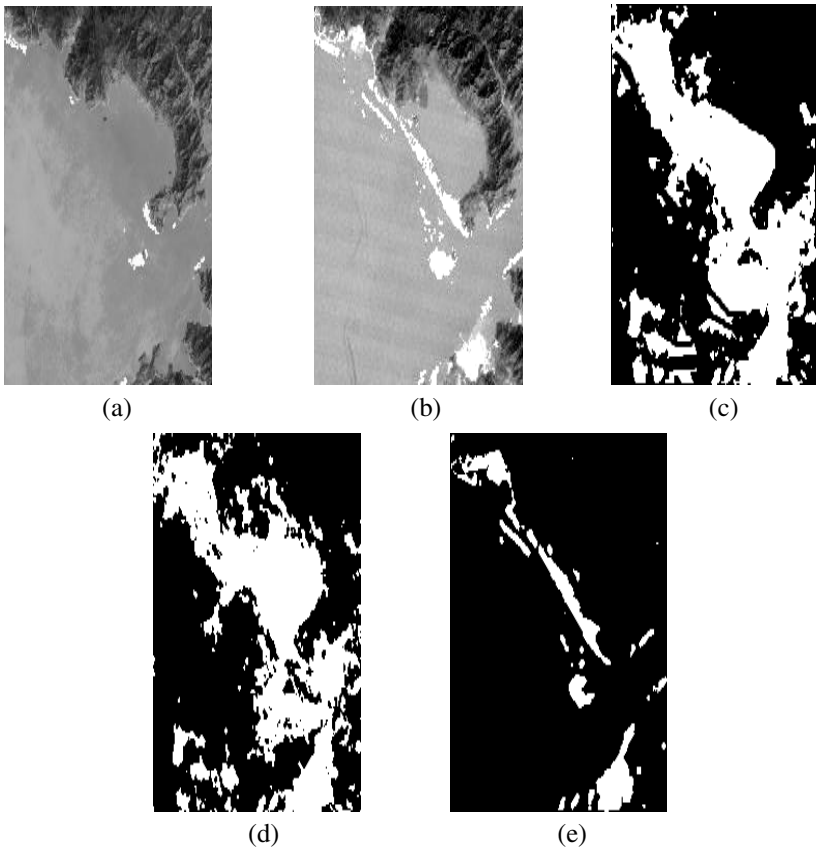

Fig. 2. (a) Remote-sensing distribution image of Spartina alterniflora in Luoyuan Bay in 2000. (b) Remote-sensing distribution image of Spartina alterniflora in Luoyuan Bay in 2006. (c) UDWTKMEANS algorithm. (d) NSCTPCNN algorithm. (e) Present algorithm.

information that distributed at different times of Spartina alterniflora in Luoyuan Bay area. Comparison algorithms are proposed in reference [18] and [19]. The abbreviation of the algorithm proposed in reference [18] is UDWTKMEANS, which is the combination of discrete wavelet transform and K Means clustering algorithm, and the abbreviation of the algorithm proposed in reference [19] is NSCTPCNN, which is the combination of nonsubsampled contourlet transform and pulse coupled neural network. The qualitative comparison results of these three algorithms are shown in Fig.1.In figure (a) and (b), the black expresses the land, the gray expresses water and tidal flats, while the white for Spartina alterniflora.

It can be seen qualitatively that the present algorithm has a definite breakthrough in dynamic monitoring of invasive species, which can detect precisely the change information of Spartina alterniflora.

Comparing with the traditional methods, it can save manpower and resources, and can more quickly and accurately provide the proliferation information of invasive species. In addition, the detection effect will get better and better with the improvement of the algorithm, and it provides a scientific basis [20] for better protection of the ecological environment and biodiversity.

3 Conclusion

The application of the technique of remote-sensing image change detection can be more effective to study on the spatial distribution and dynamic changes of invasive alien species population. It took full advantage of multi-scale decomposition characteristics of NSCT and the feature of retaining more information of initial image of FCM, and it realized change detection of remote sensing image well to achieve better results.

Acknowledgements. We gratefully thank the financial support by International Cooperative Research and Personnel Training Projects of the Ministry of Education of the People's Republic of China.

References

1. Li, Z., Xie, Z.: Chinese invasive species. China Forestry Publishing House, Beijing (2002)
2. Nejd, V., Antoniou Metal, D.: Mech is underlying the impacts of exotic plant invasion. Proceeding of the Roy Society of nod: Biological Sciences 23(270), 775–781
3. Kareivap: Developing a predictive ecology for non indigenous species a decological invasions. Geology 88(1), 651–652 (1996)
4. Chaynbe, R.M., Mderson, L.A., Saltonstal, K.: Expansion of Phragllitesaus into tidal wetland of North Area. Amati Botany 64(21), 261–273 (1999)
5. Peng, S.: To the words. Plants invasive species and their impact on the ecosystem. Geology 19(4), 560–568 (1999)
6. Cao, H., Ge, X., Ye, W.: Odorata invasive species distribution and damage in Guangdong. Guangdong Forestry Science and Technology 20(2), 57–59 (2010)

7. Chen, B., Wang, R., Huang, X., et al.: Boisiana a Newly Recorded Species in Guangdong. Tropical and Subtropical Botany 13(1), 76–77 (2005)
8. Guo, W., Chao, T., Zhou, G., et al.: Biological Invasion of Xinjiang Agricultural Situation Trends and Countermeasures. Xinjiang Agricultural Sciences 49(1), 86–100 (2012)
9. Idawo, C., Laneve, G.: Hyperspectral analysis of multispectral ETM+data:SMA using spectral field measurements in mapping of emergent macrophytes. In: Proceedings of the 2004 Geoscience and Remote Sensing Symposium, vol. 1(3), pp. 246–249 (2004), Li, Z., Xie, Z.: Chinese invasive species. China Forestry Publishing House, Beijing (2002)
10. Chen, H., Chen, L.: Using remote sensing and GIS methods to predict the potential distribution of invasive alien species. Journal of Remote Sensing 11(3), 426–432 (2007)
11. Li, S., Fang, L.: Mutitemporal Image Change Detection Using a Detail-Enhancing Approach With Nonsubsampled Contourlet Transform. IEEE Geoscience and Remote Sensing 9(5), 836–840 (2012)
12. Po, D.D.-Y., Do, M.N.: Directional multiscale modeling of images using the Contourlet transform. IEEE Transaction on Image Processing 15(6), 1610–1620 (2006)
13. Zhao, L., Wang, B., Zhang, L.: Based on Fuzzy C-Means clustering and neighborhood analysis unsupervised multi-channel remote sensing image change detection. Data Acquisition and Processing 26(4), 395–401 (2011)
14. Fan, J., Wu, C.: The new explanation of membership degree in FCM and its applications. Acta Electronica Sinica 32(3), 350–352 (2004)
15. Pal, N.R., Bezdek, J.C.: On cluster validity for the fuzzy c-means model. IEEE Transactions Fuzzy Systems 3, 370–379 (1995)
16. Wu, C., Wu, Y.: Multitemporal Images Change Detection Using Nonsubsampled Contourlet Transform and Kernel Fuzzy C-Mean Clustering. In: International Symposium on Intelligence Information Processing and Trusted Computing, pp. 96–99 (2011)
17. Pan, W., Chen, J., Li, L., Wang, J.: Fujian Luoyuanwan Spartina Remote Sensing Dynamic Monitoring. Chinese Agricultural Science Bulletin 25(13), 216–219 (2009)
18. Celik, T.: Multiscale Change Detection in Multitemporal Satellite Images. IEEE Geoscience Remote Sensing Letters 6(4), 820–840 (2009)
19. Yu, Y., Jia, Z.: Research on Remote Sensing Images Change Detection Algorithm. Computer Engineering and Applications 47(25), 168–175 (2011)
20. Macleod, R.D.: A Quantitative Comparison of Change Detection Algorithms for Monitoring Eelgrass from Remotely Sensed Data. PE&RS 47(25), 207–216 (1998)

Effects of Straw and Simulated Root Exudates on Aggregate Dynamics and Aggregate-Associated Carbon in Consideration of FACE Condition

Hong-liang Ma[1,3,*], Jian-guo Zhu[2], Zu-bin Xie[2], and Ren Gao[1,3]

[1] Key Laboratory of Humid Subtropical Eco-geographical Process, Ministry of Education, Fuzhou 350007, China
mhl936@163.com
[2] State Key Laboratory of Soil and Sustainable Agriculture, Institute of Soil Science, Chinese Academy of Sciences, Nanjing 210008, China
jgzhu@issas.ac.cn
[3] School of Geographical Sciences, Fujian Normal University, Fuzhou 350007, China
ren.gao@fjnu.edu.cn

Abstract. In order to investigate the role of residue and root carbon inputs in soil carbon changes due to elevated CO_2, soil sample weighted 500 g collected from field under elevated CO_2 and ambient CO_2 condition, respectively, were incubation for one year with addition of straw and chemical matters, and then examined the different aggregates fraction and aggregated-associated carbon in soil. The results showed that the soil carbon for macro- (>250 μm) and micro-aggregates (250-53 μm) increased by 8.8-73.1% due to the addition of straw and by 11.2-111.7% (p<0.05) due to the exudates. Conversely, soil carbon in the clay and silt-sized particles (<53 μm) was decreased by 12.3-22.1% (p<0.05) by glucose and decreased even further with the addition of straw, whereas it was increased only by 5.8-11.8% with phenol and organic acid. These results could help to understand deeply the effects of elevated CO_2 on the dynamics of both soil aggregates and carbon in a field due to variations in the crop straws and root exudates forms.

Keywords: Elevated CO_2, aggregate dynamics, carbon content, glucose, phenol, organic acid.

1 Introduction

Elevated atmospheric CO_2 concentration causes global climate change [1] and it is important to stimulate the potential climate change induced by CO_2 escalation and reveal its impact on a variety of ecosystems. Therefore, the FACE (Free-Air Carbon dioxide Enrichment) system has been established worldwide to perform experimental simulations and modeling [2, 3]. An extensive review of the FACE investigations over the past 15 years showed that elevated CO_2 would increase plant biomass to a

* Corresponding author.

F. Bian et al. (Eds.): GRMSE 2013, Part I, CCIS 398, pp. 463–474, 2013.
© Springer-Verlag Berlin Heidelberg 2013

significant level [3, 4]. Our previous FACE experiment in China has shown that a 200 μmol mol^{-1} increase in the atmospheric CO_2 concentration increased the aboveground litter production of rice and wheat biomass by 21%, significantly increasing the flux of labile and non-labile C in the soil [5, 6].

The Third International Conference on Mechanisms of Organic Matter Stabilization and Destabilization was the first attempt to categorize the specific mechanisms in the soil, most of which is well documented [7]. Furthermore, much of the research of the changes in the SOM (Soil Organic Matter) triggered by climate change includes the analyses of pools of samples over a large number of areas for a specific interval of time [8]. Other studies have made attempts to measure the changes in the soil C and N stores under elevated CO_2 regimes [9]. Indeed, a detailed understanding of the C cycling in the soil and the mechanisms underlying the stabilization of soil organic matter is necessary to predict the consequences of CO_2 flux between the atmosphere and soil and how the organic C stores are affected by global climate change.

The total and fresh organic carbon distribution in soil macro-aggregates was identified in soil of 24 years following the crop conversion from C3 to C4 and 6 weeks greenhouse plant growth after conversion from C3 to C4 and vice-versa considering the effects of fresh material from plants [10]. Residue carbon mineralization in different aggregate size classes and determination of size and turnover of a slow pool in different aggregate size classes was studied [11]. The chemical characteristics of residue also changed under elevated CO_2 conditions, including increases in the lignin and tannin contents [12]. Under natural conditions, such changes would diminish the decomposition in the soil and affect the carbon cycling [6] and other active carbon exudates from the roots [13]. Moreover, elevated CO_2 induced changes in the root length, ratio of root turnover and root biomass [4, 14], factors that play important roles in the turnover of soil carbon when combined with root exudates.

To date, many factors that affected the stabilization of organic matter through the interaction with soil minerals have been highlighted [7,15], including the effects of root exudates and organic inputs on the stability, dynamics and carbon sequestration of soil aggregates [16-18]. Importantly, no consistent responses of the SOC under elevated CO_2 have been reported based on FACE experiments, and the underlying mechanisms are difficult to discriminate clearly. Although increases in the soil C content [9,19] and in root exudates [20, 21] by CO_2 enrichment, and significant increase of litter decomposition due to addition of labile root exudate components [17] were found, the information regarding the contribution of crops straw and root exudate components to aggregate dynamics is insufficient.

Regardless of whether the observed enhancement in NPP (Net Primary Productivity) is persistent, it is uncertain whether the increased NPP will lead to significant increases in the soil C storage from a long-term perspective [19]. In particular, little is known about how increased residue inputs to soils affect the long-term storage of the soil organic C (SOC) in agricultural ecosystems [19, 22] and whether the additional carbon input may affect the formation of soil aggregates [14, 23]. Thus, on the base of our study [24], the present study investigated the impacts of the addition of straw and three compounds on: (1) the soil aggregates distribution, (2) changes of the carbon concentration in soil aggregate fractions, and (3) aggregate-associated carbon.

2 Materials and Methods

2.1 Field Experimental Description

The FACE experiments were conducted at the Wuxi Experimental Station (Jiangsu Province, China, 31° 35' N, 120º 30' E) according to reports [25, 26], with modifications, in June 2001 for the rice season. The soil properties were analyzed prior to the FACE experiments, with the following results: sand (0.05–1 mm), 92 g kg^{-1}; silt (0.001–0.05 mm), 657 g kg^{-1}; clay (<0.001 mm), 251 g kg^{-1}; bulk density, 1.2 g cm^{-1}; soil organic carbon (SOC), 1.5%; total nitrogen, 1.59 g kg^{-1}; total phosphorous, 1.23 g kg^{-1}; available phosphorous, 10.4 mg kg^{-1} and a pH of 6.8. This field has not been subjected to any substantial agronomic changes in the past 50 years and represents the majority of agricultural lands in Jiangsu Province, a key rice-production area in China.

After two years of rice and winter wheat rotation under the FACE system, in June 2003, soil samples were grinded (1 cm in diameter) and blended, and the biomass was collected, dried and crushed for <1 cm, then mixed to put into a nylon net bag (15×15×7 cm, depth×length×width) with 50μm mesh size, and placed at 0–15 cm depth to perform experimental incubations in the field for one year, as reported [24] with three FACE plots and three ambient plots.

In June 2004, soil samples (500 g) under ambient CO_2 (sample A) and elevated CO_2 (sample F) were collected and incubated in plastic bottles in triplicate placed in a greenhouse under a fertilization level of 184 mg N kg^{-1} soil. The soils from fields (A, F) treated without the addition of straw (treatment C) and with addition of straw (treatment S) were evaluated. The characteristics of the straw added to the soil are presented in Table 1. On the base of biomass increasing under a condition of elevated CO_2 [5, 27], in order to simulate the effects of elevated CO_2 by biomass on soil aggregate and carbon cycling during one year, after harvesting wheat straw (4.6 g and 3.9 g) in June 2004 and rice straw (8.2 g and 7.1 g) from November 2004 to June 2005 were added differently to the soil surface, respectively.

2.2 Experimental Design

To evaluate the effects of the carbon from root exudates and elevated CO_2 (F), carbon (glucose, treatment G) was added to the F sample three times as 50 mL, 100 mL, and 50 mL of a solution of 50 mg mL^{-1}. Similarly, phenol (p-hydroxybenzoic acid, treatment P) or organic acid (citric acid, treatment O) was added as 1 mL, 2 mL, and 1 mL of a solution of 0.5 mg mL^{-1}. These chemical matters amounts were based on our study [28] and were added accompanying with water to keep soil moisture content as following.

To simulate the effects of elevated CO_2 due to the straw and root exudates of rice or wheat in comparison to the ambient CO_2 (A), we compared the treatments of the straw and compounds added to sample F to the A sample with added straw.

During the incubation, the soil was kept to submerge by water for two months and dry for 3 times per one month and then was kept wet of 25-35% in rice season. Soil water content was kept wet of 10-20% in wheat season. After one year (June, 2005), the soil was collected for further analysis.

Table 1. The characteristics of the rice and wheat straw added to the soil

CO_2	Winter wheat straw				Rice straw			
	C g kg^{-1}	N g kg^{-1}	C/N	Polyphenol g kg^{-1}	C g kg^{-1}	N g kg^{-1}	C/N	Polyphenol g kg^{-1}
F	435	5.7	76.2	30.1	419*	12.5***	33.5***	28.9
A	425	7.0	61.1	29.4	410	13.7	29.9	25.9

F, Free-air CO_2 enrichment (FACE). A, ambient CO_2. *$p \leq 0.05$, ***$p \leq 0.001$ differences between F and A.

2.3 Soil Fractionation and Analysis

The fractionation of the soil by size was performed using <4 mm material after the removal of visible root remnants and aboveground residue [29-31]; low-energy ultrasonic dispersion was used to obtain aggregate fractions of the tested soils. A 100 g soil sample was wetted with 500 ml distilled water for 5 min and treated with ultrasonication (300 W, 15 min) before wet sieving. The floatable particulate organic matter on the surface was removed with a polypropylene sponge and discarded, and the resulting mixture was stroked on a 250 μm sieve at a vertical distance of 3 cm for 50 oscillations over 2 min. The soil collected on the sieve was recovered using distilled water as the >250 μm fraction (macro-aggregates), whereas the rest of the material was further stroked on a 53 μm sieve at a vertical distance of 3 cm for 35 oscillations over 2 min. The 53-250 μm fraction (micro-aggregates) on the sieve was recovered using distilled water, and the remaining material was centrifuged at 6000 rpm for 10 min to generate the <53 μm fraction (clay and silt-sized particles). All of the fractions were dried (60 °C), weighed and finely ground before subjected to an elemental analysis using a CHNS/O element analyzer (PE2400). After this process, the soil carbon concentration of each soil fraction was obtained and denoted as Ci. According to Ci, the contribution of carbon and nitrogen in each soil fraction to the entire soil sample, denoted as Si, was calculated as Si=Ci*Mi/Ms, where Mi is the weight of each fraction and Ms is the weight of the entire soil sample before the physical fractionation.

The mean weight diameter (MWD) was calculated for each treatment and for the mean of three treatments by the relationship $MWD=\Sigma(X_iW_i)$.

In the above equation, X (in millimeters) is the average diameter of the openings of the two consecutive sieves and W is the weight ratio of the aggregates remaining on the *i*th sieve.

2.4 Statistical Analysis

A one-way ANOVA (SPSS 10.0) was used to determine the differences between the treatments, i.e., straw, glucose, phenol and organic acid. Differences were considered significant only when $p < 0.05$. The data are expressed as the mean±SD and are presented in the figures.

3 Results

3.1 Soil Aggregate Fractions Change under Different Treatments

The soil fraction distributions of the >250 µm and 250-53 µm aggregates were increased by 22.8-162.2% and 1.2-36.4%, respectively, and decreased by 5.1-16.4% for the <53 µm aggregates with the addition of straw (S) compared to the treatment without straw (C) (Fig. 1). Compared to A, the distributions of the >250 µm and 250-53 µm soil aggregates in F were increased by 45.5% and decreased by 17.7%, respectively, under the C treatment and were decreased by 31.9% ($P < 0.05$) and 20.0% ($P < 0.05$), respectively, under the S treatment. When compared with F, the soil fraction distributions of macro-aggregates (>250 µm) and micro-aggregates (53–250 µm) were increased by 146.6% ($P<0.01$) and 83.8% ($P< 0.01$) under the C treatment, by 164.2% ($P< 0.01$) and 40.3% ($P< 0.01$) under the S treatment, respectively, with the addition of glucose (G). The fraction distribution for the clay and silt-sized particles (<53 µm) was decreased by 20.7% ($P< 0.01$) and 26.3% ($P< 0.01$) under the C and S treatments, respectively. Conversely, there were no significant changes found with the addition of phenol (P), and the significant effect of the addition of organic acid (O) was similar to that of glucose, with a low degree of change.

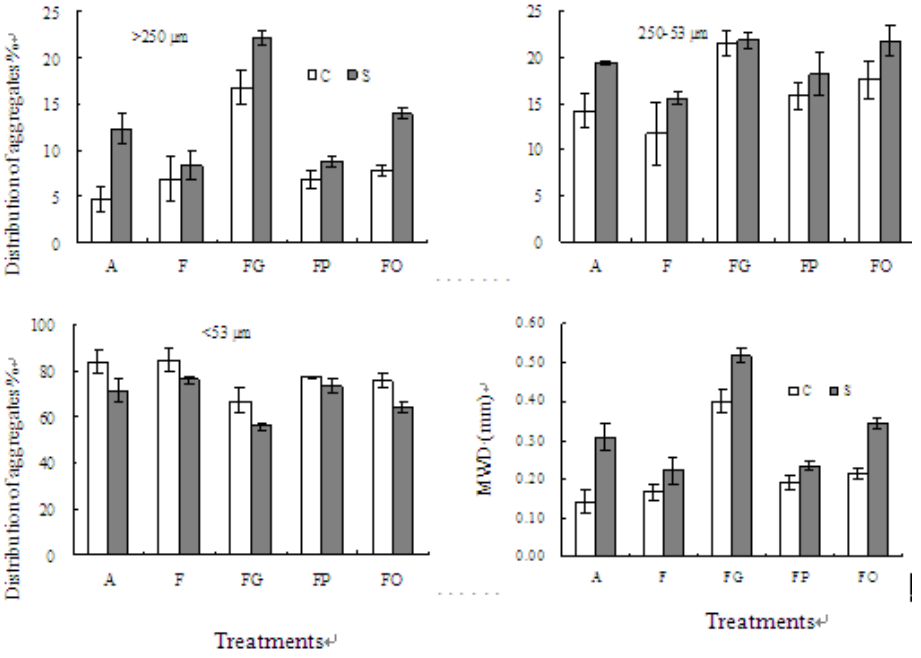

Fig. 1. The distribution (%) of soil aggregates and the mean weight diameter (MWD, mm) affected by straw (C - without straw addition, S - with straw addition) and root exudates (G - glucose, P - phenol, and O - organic acid) based on soil under ambient CO_2 (A) and elevated CO_2 (F). The error bars represent the standard deviation ($n = 3$).

The addition of straw increased the MWD (Mean Weight Diameter) by 23.7-116.4% and the extent was greater in A than F and in O than G and P. Compared with A, the F treatment increased the MWD by 16.8% under the C treatment but decreased it by 28.3% ($P< 0.05$) under the S treatment. Compared with F, the MWD was increased by 139.8% ($P< 0.01$) and 134.0% ($P< 0.01$) under the G treatment, only by 13.8% and 5.9% under the P treatment and by 27.8% and 55.9% ($P< 0.05$) under the O treatment, with C and S, respectively.

3.2 Changes of the Carbon Concentration in Soil Aggregate Fractions under Different Treatments

As indicated in Figure 2, the soil carbon concentration was decreased by 66.6% ($P < 0.01$) and 49.4% ($P < 0.01$) due to addition of straw at A and F, respectively, only for the >250 μm aggregates. No significant effects of the straw on the carbon concentration of the 250-53 μm and <53 μm aggregates under the G, P and O treatments were observed. Compared with F, the addition of glucose decreased the soil carbon concentration in the macro-aggregates (>250 μm) and micro-aggregates (53–250 μm) by 69.6% ($P< 0.01$) and 15.2% ($P< 0.05$) under the C treatment and by 12.6% and 7.5% under the S treatment, respectively. However, the soil carbon concentration in the macro-aggregates (>250 μm) showed an increase of 101.4% ($P< 0.01$) due to the phenol and of 60.1% ($P< 0.01$) due to the organic acid under the C treatment. The soil carbon concentration in the <53 μm aggregates was increased by 18.4% ($P < 0.05$) and 12.2% ($P< 0.05$) under the C treatment and by 16.4% ($P< 0.05$) and 20.3% ($P< 0.05$) under the S treatment due to the addition of phenol and organic acid, respectively.

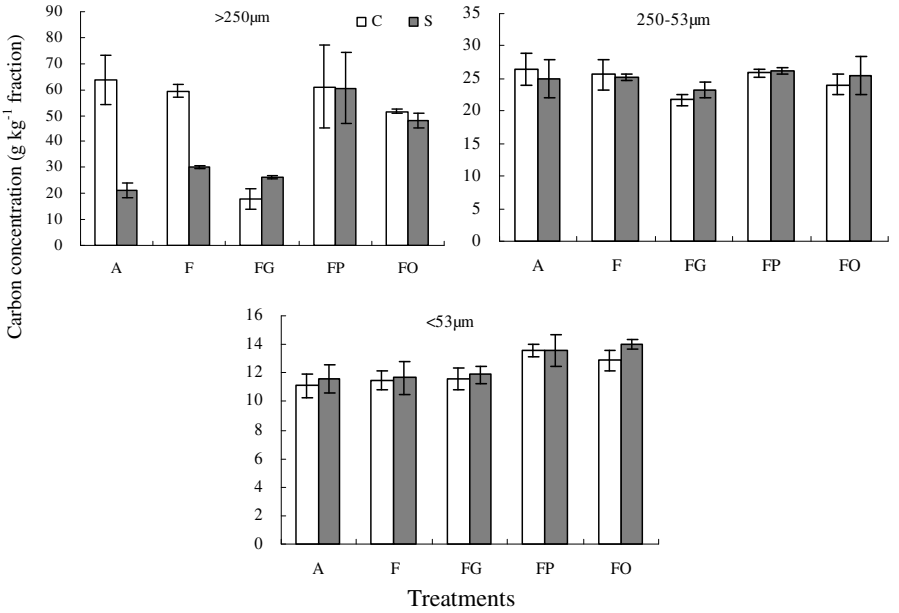

Fig. 2. Changes of the carbon concentration in soil aggregates due to straw (C - without straw addition, S - with straw addition) and root exudates (G - glucose, P - phenol, and O - organic acid) based on soil under ambient CO_2 (A) and elevated CO_2 (F). The error bars represent the standard deviation ($n = 3$).

3.3 Changes of the Soil Carbon in Aggregate Fractions under Different Treatments

The soil carbon was increased by 20.2%-73.1% for the >250 μm aggregates and by 8.8%-40.8% for the 250-53 μm aggregates in the A and F samples, respectively, due to the addition of straw (Fig. 3). Compared with F, the soil carbon in the macro-aggregates (>250 μm) was increased due to the addition of the compounds by 52.4-90.5% ($P<$ 0.05) under the C treatment and by 76.5%-111.7% ($P<$ 0.01) under the S treatment. Similarly, the soil carbon was increased by 11.2-30.9% ($P<$ 0.05) and by 31.1-42.6% ($P<$ 0.01) for the 250-53 μm aggregates under the C and S treatments, respectively. However, the soil carbon in the <53 μm aggregates showed a decrease of 12.3% and 22.1% ($P<$ 0.01) under the G treatment, an increase of 6.3% and 10.4% ($P<$ 0.05) under the P treatment and an increase of 11.8% ($P<$ 0.05) and 5.8% under the O treatment, with C and S, respectively.

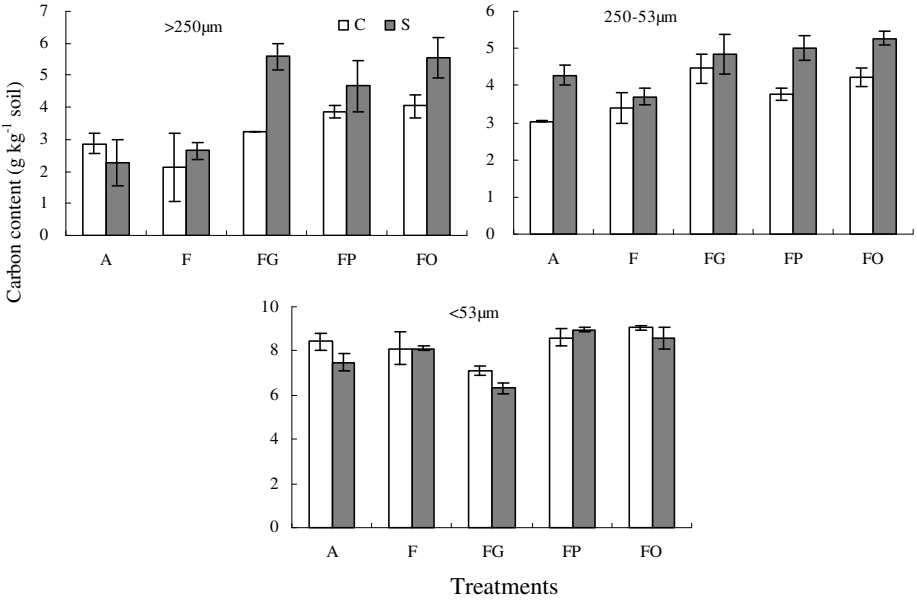

Fig. 3. Changes of the carbon content in aggregates per unit soil due to straw (C - without straw addition, S - with straw addition) and root exudates (G - glucose, P - phenol, and O - organic acid) based on soil under ambient CO_2 (A) and elevated CO_2 (F). The error bars represent the standard deviation (n = 3).

4 Discussion

It is well known that additional carbon input to soil may affect the formation of soil aggregates [23, 32]. Our previous FACE experiment in China and the reports of others [5, 6] showed that there were significant increases of labile and non-labile C fluxes in

the soil. Thus, the effects of increased biomass due to elevated CO_2 are important when considering the dynamics of aggregates. Our results showed that the addition of straw increased the distribution of >53 μm aggregates, independent of the presence of specific compounds, particularly for the >250 μm aggregates, a result that was consistent with previously reported results [33]. On the one hand, the primary effects of litter addition to the soil on the decomposition of original organic matter in soil and the dispersion of macro-aggregates will affect the soil aggregate turnover [34]. On the other hand, organic residues could act as catalysts for microbial activity and induce the complexation of soil particles into macro-aggregates [32, 35] to promote the accumulation of macro-aggregate [36]. According to the model of aggregate formation, more clay and silt-sized particles (<53 μm) from the plant debris entered the soil to form micro- or macro-aggregates (Fig. 1), which resulted in a significant decrease in the distribution of the <53 μm particles, with the exception of the phenol treatment.

The soil carbon concentration varied with the change of the soil aggregate distribution. Residue input increased the carbon concentration mainly due to the decomposition of the plant residue [33], which was necessary for both soil C sequestration and also to alleviate soil degradation by improving the soil structure [32]. However, the carbon concentration did not significantly increase accordingly, even though the macro-aggregate distribution significantly increased due to the addition of straw (Fig. 2). This can be explained by the evidence of the small aggregates (with low carbon concentrations) transforming into large aggregates, resulting in a decrease or no change of their overall carbon concentration. Simultaneously, the effects of the straw on the carbon concentration were dependent on the addition of glucose in that the carbon concentration increased with the straw and the addition of glucose, which was consistent with reports that root exudate components change the litter decomposition [17]. However, the addition of glucose decreased the carbon concentration in the >53 μm aggregates and was decreased with the addition of straw. In contrast, phenol and organic acid increased the carbon concentration in the >250 μm aggregates with the addition of straw and increased it in the <53 μm aggregates, independent of straw, which mainly contributed to the effects of the addition of the compounds (R^2=0.9324). We found that the effects of root exudates on the carbon concentration with the addition of straw were positive, indicating that exudates could induce the decomposition of the litter to increase the carbon concentration [17], particularly for the >250 μm aggregates.

Our results show that adding straw to the soil increased the carbon content in the >53 μm aggregates, mainly with the addition of compounds, a finding that has not been mentioned in other studies [9, 19, 22]. Interestingly the soil carbon in the <53 μm particles did not increase (Fig. 3), and the change was dependent on the management [24, 37]; particularly, the addition of glucose resulted in more soil carbon under conditions of elevated CO_2. Our results show that the carbon content was significantly increased for the >250 μm aggregates and 250-53 μm aggregates and that the effects was enhanced by the addition of the straw and compounds. More water soluble carbon and active carbon (alkaline $KMnO_4$ oxidizable C) in macroaggregates than in micro-aggregates has been reported [11]. The carbon content in the <53 μm particles was decreased by the addition of glucose, but it was increased by the phenols and organic acids, which could contribute to the different C availability, chemical structure

and stability of the aggregate dynamics. Because most enzymes were enriched in the clay fraction, but high activities of enzymes involved in the degradation of cellulose and chitin were also found in the macro-aggregates. And the different distributions of organic C in soils affected in turn enzyme production and activity, leading to higher activity rates within macro-aggregates. In addition, the nature of inputs also plays a different role in distributions of organic C [38]. It was reported that the significantly increased biomass at an elevated CO_2 was one major element in soil carbon storage [3]. However, considering the input of residues with different chemical characteristics under different CO_2 concentrations, the changes in the carbon content closely parallels the additional input of organic material [39] and the chemical characteristics [36]. In particular, the change in the carbon content of the <53 μm particles mainly contributed to the effects of the addition of compounds (R^2=0.8328).

Some reports showed that the increased soil C storage under elevated CO_2 was due to the increased C/N ratio that accompanied an increase of the biomass [12]; in contrast, others argued that more available carbon from root biomass would induce microorganism activity, resulting in the decomposition of more soil carbon [40]. Thus, the different C/N ratios in the plant residue under different CO_2 concentrations may be one way to affect the soil carbon and nitrogen cycling when residues are input to the soil. However, the extent of the influence of CO_2 on the C/N ratio and other chemical characteristics was less than that of the biomass [5]. Although Williams et al. [41] reported that elevated CO_2 increased the soil carbon by reducing the decomposition of the carbon pool, our results showed that the increase might be due to the increasing turnover of carbon. The soil carbon was more significantly affected by the simulated root exudates than the straw in this experiment, which partly did not support a previous argument [42] that the change in the biomass was more important than that of the plant chemical characteristics for soil carbon storage under elevated CO_2. Combined with the effects of the addition of straw during field incubation [24], our results suggested that compounds that are increased under elevated CO_2, such as glucose, phenol and organic acid, play important roles in carbon cycling.

5 Conclusions

The soil carbon content for the >53 μm aggregates was increased when straw as added. The effects of the simulated exudates were significant and variable. The addition of glucose significantly increased the soil carbon content for the >53 μm and decreased it for <53 μm, and the effect was greater with the addition of straw. However, the influence of phenol and organic acid on the soil carbon was not exactly the same as that of glucose for all the aggregates (>53 μm and <53 μm). Furthermore, crops residue should be considered when to assess the effects of root exudates. These results could help to explore the effects of elevated CO_2 on the dynamics of both soil aggregates and carbon that may occur in a field due to variations in the crop straw and root exudate levels. The effects of elevated CO_2 concentration on the storage of the soil organic C (SOC) and the dynamics of soil aggregates in agricultural ecosystems are still uncertain.

Acknowledgments. This research was supported financially by the National Natural Science Foundation of China (40901115, 31070548, 31070549 and 31170578), the project for innovation team of Ministry of education (IRT0960), Foundation for University young Key Teachers from Fujian Normal University (fjsdjk2012069) and Foundation for Distinguished Young Scholars Program of Higher Education of Fujian Province (JA12058).

References

1. Keeling, C.D., Whorf, T.P.: Atmospheric CO2 records from sites in the SIO air sampling network, trends: A compendium of data on global change. Carbon Dioxide Information Analysis Center, Oak Ridge National Laboratory, US Department of Energy, USA (2004)
2. Kimball, B.A., Kobayashi, K., Bindi, M.: Responses of agricultural crops to free-air CO2 enrichment. Advances in Agronomy 77, 293–368 (2002)
3. Ainsworth, E.A., Long, S.P.: What have we learned from 15 years of free-air CO2 enrichment (FACE)? A meta-analytic review of the responses of photosynthesis, canopy properties and plant production to rising CO2. New Phytologist 165, 351–372 (2005)
4. Pendall, E., Bridgham, S., Hanson, P.J., Hungate, B., Kicklighter, D.W., Johnson, D.W., Law, B.E., Luo, Y., Megonigal, J.P., Olsrud, M., Ryan, M.G., Wan, S.: Research review Below-ground process responses to elevated CO2 and temperature: a discussion of observations, measurement methods, and models. New Phytologist 162, 311–322 (2004)
5. Ma, H.L., Zhu, J.G., Xie, Z.B., Liu, G., Zeng, Q., Han, Y.: Responses of rice and winter wheat to free-air CO2 enrichment (China FACE) at rice/wheat rotation system. Plant Soil 294, 137–146 (2007)
6. Kasurinen, A., Peltonen, P.A., Julkunen-Tiitto, R., Vapaavuori, E., Nuutinen, V., Holopainen, T., Holopainen, J.K.: Effects of elevated CO2 and O3 on leaf litter phenolics and subsequent performance of litter-feeding soil macrofauna. Plant Soil 292, 25–43 (2007)
7. Sollins, P., Swanston, C., Kramer, M.: Stabilization and destabilization of soil organic matter—a new focus. Biogeochemistry 85, 1–7 (2007)
8. Bellamy, P.H., Loveland, P.J., Bradley, R.I., Lark, R.M., Kirk, G.J.D.: Carbon losses from all soils across England and Wales 1978–2003. Nature 437, 245–248 (2005)
9. Jastrow, J.D., Miller, R.M., Matamala, R., Norby, R.J., Boutton, T.W., Rice, C.W., Owensby, C.E.: Elevated atmospheric carbon dioxide increases soil carbon. Global Change Biology 11, 2057–2064 (2005)
10. Urbanek, E., Smucker, A.J.M., Horn, R.: Total and fresh organic carbon distribution in aggregate size classes and single aggregate regions using natural $^{13}C/^{12}C$ tracer. Geoderma 64, 164–171 (2011)
11. Jha, P., Garg, N., Lakaria, B.L., Biswas, A.K., Subba Rao, A.: Soil and residue carbon mineralization as affected by soil aggregate size. Soil & Tillage Research 121, 57–62 (2012)
12. Cotrufo, M.F., Ineson, P.: Does elevated atmospheric CO_2 concentrations affect wood decomposition? Plant Soil 224, 51–57 (2000)
13. Carney, K.M., Hungate, B.A., Drake, B.G., Megonigal, J.P.: Altered soil microbial community at elevated CO_2 leads to loss of soil carbon. PNAS 104, 4990–4995 (2007)
14. Pendall, E., Mosier, A.R., Morgan, J.A.: Rhizodeposition stimulated by elevated CO_2 in a semi-arid grassland. New Phytologist 162, 447–458 (2004)
15. Smernik, R., Skjemstad, J.: Mechanisms of organic matter stabilization and destabilization in soils and sediments: conference introduction. Biogeochemistry 92, 3–8 (2009)

16. Cheng, W., Kuzyakov, Y.: Root effects on soil organic matter decomposition. In: Wright, S., Zobel, R. (eds.) Roots and Soil Management: Interactions Between Roots and the Soil. Agronomy Monograph, vol. (48), pp. 119–143. American Society of Agronomy, Madison (2005)
17. Kuzyakov, Y., Hill, P.W., Jones, D.L.: Root exudate components change litter decomposition in a simulated rhizosphere depending on temperature. Plant Soil 290, 293–305 (2007)
18. Bandyopadhyay, P.K., Saha, S., Mani, P.K., Mandal, B.: Effect of organic inputs on aggregate associated organic carbon concentration under long-term rice–wheat cropping system. Geoderma 154, 379–386 (2010)
19. Lichter, J., Barron, S.H., Bevacqua, C.E., Finzli, A.C., Irving, K.E., Stemmler, E.A., Schlesinger, W.H.: Soil carbon sequestration and turnover in a pine forest after six years of atmospheric CO_2 enrichment. Ecology 86, 1835–1847 (2005)
20. Phillips, R.P., Bernhardt, E.S., Schlesinger, W.H.: Elevated CO_2 increases root exudation from loblolly pine (Pinus taeda) seedlings as an N-mediated response. Tree Physiology 29, 1513–1523 (2009)
21. Phillips, R.P., Finzi, A.C., Bernhardt, E.S.: Enhanced root exudation induces microbial feedbacks to N cycling in a pine forest under long-term CO_2 fumigation. Ecology Letters 14, 187–194 (2011)
22. De Graaff, M.A., Van Groenigen, K.J., Six, J., Hungate, B., Van Kessel, C.: Interactions between plant growth and soil nutrient cycling under elevated CO_2: A meta-analysis. Global Change Biology 12, 2077–2091 (2006)
23. Prior, S.A., Runion, G.B., Torbert, H.A., Rogers, H.H.: Elevated atmospheric CO_2 in agroecosystems: Soil physical properties. Soil Science 169, 434–439 (2004)
24. Ma, H.L., Zhu, J.G., Xie, Z.B., Liu, G., Zeng, Q.: Effects of increased residue biomass under elevated CO_2 on carbon and nitrogen in soil aggregate size classes (rice-wheat rotation system, China). Canadian Journal of Soil Science 89, 567–577 (2009)
25. Liu, G., Han, Y., Zhu, J.G., Okada, M., Nakamura, H., Yoshimoto, H.: Rice–wheat rotational FACE platform: system structure and control. Chinese Journal of Applied Ecology 13, 253–1258 (2002) (in Chinese)
26. Okada, M., Lieffering, M., Nakamura, H., Yoshimoto, M., Kim, H.Y., Kobayashi, K.: Free air CO_2 enrichment (FACE) using pure CO_2 injection: System description. New Phytologist 150, 251–260 (2001)
27. Ma, H.L., Zhu, J.G., Liu, G., Xie, Z.B., Wang, Y.L., Yang, L.X., Zeng, Q.: Availability of Soil Nitrogen and Phosphorus in a Typical Rice-Wheat Rotation System under Elevated Atmospheric [CO_2]. Field Crops Research 100, 44–51 (2007)
28. Ma, H.L., Zhu, J.G., Xie, Z.B., Zhang, Y.L., Liu, G., Zeng, Q.: Effect of FACE (Free Air Carbon-dioxide Enrichment) on available C, N and P in soil during rice growing. Soil 36, 392–397 (2004) (in Chinese)
29. Wright, A.L., Hons, F.M.: Carbon and nitrogen sequestration and soil aggregation under sorghum cropping sequences. Biology and Fertility of Soils 41, 95–100 (2005)
30. Cambardella, C.A., Elliott, E.T.: Methods for physical separation and characterization of soil organic matter fractions. Geoderma 56, 449–457 (1993)
31. Christensen, B.T.: Physical fractionation of soil and structural and functional complexity in organic matter turnover. European Journal of Soil Science 52, 345–353 (2001)
32. Yu, H., Ding, W., Luo, J., Geng, R., Cai, Z.: Long-term application of organic manure and mineral fertilizers on aggregation and aggregate-associated carbon in a sandy loam soil. Soil & Tillage Research 124, 170–177 (2012)

33. Sodhi, G.P.S., Beri, V., Benbi, D.K.: Soil aggregation and distribution of carbon and nitrogen in different fractions under long-term application of compost in rice–wheat system. Soil and Tillage Research 103, 412–418 (2009)
34. Hoosbeek, M.R., Scarascia-Mugnozza, G.E.: Increased Litter Build Up and Soil Organic Matter Stabilization in a Poplar Plantation After 6 Years of Atmospheric CO_2 Enrichment (FACE): Final Results of POP-EuroFACE Compared to Other Forest FACE Experiments. Ecosystems 12, 220–239 (2009)
35. Six, J., Elliott, E.T., Paustian, K.: Soil macroaggregate turnover and microaggregate formation: A mechanism for C equestration under no-tillage agriculture. Soil Biology and Biochemistry 32, 2009–2013 (2000)
36. Chivenge, P., Vanlauwe, B., Gentile, R., Six, J.: Organic resource quality influences short-term aggregate dynamics and soil organic carbon and nitrogen accumulation. Soil Biology & Biochemistry 43, 657–666 (2011)
37. Bronick, C.J., Lal, R.: Soil structure and management: A review. Geoderma 124, 3–22 (2005)
38. Lagomarsino, A., Grego, S., Kandeler, E.: Soil organic carbon distribution drives microbial activity and functional diversity in particle and aggregate-size fractions. Pedobiologia 55, 101–110 (2012)
39. Oelbermann, M., Voroney, R.P., Kass, D.C.L., Schlönvoigt, A.M.: Above- and below-ground carbon inputs in 19-, 10- and 4-year-old Costa Rican Alley cropping systems. Agriculture, Ecosystems & Environment 105, 163–172 (2005)
40. Zak, D.R., Pregitaer, K.S., Curtis, P.S., Teeri, J.A., Fogel, R., Randlett, D.L.: Elevated atmospheric CO_2 and feedback between carbon and nitrogen cycles. Plant Soil 151, 105–117 (1993)
41. Williams, M.A., Rice, C.W., Omay, A., Owensby, C.: Carbon and nitrogen pools in a Tallgrass Prairie Soil under elevated carbon dioxide. Soil Science Society of America Journal 68, 148–153 (2004)
42. Van Vuuren, M.M.I., Robinson, D., Scrimgeour, C.M., Raven, J.A., Fitter, A.H.: Decompostition of ^{13}C-labelled wheat root systems following growth at different CO_2 concentrations. Soil Biology and Biochemistry 32, 403–413 (2000)

Sea Level Rise-Drived Simulations of Social and Economic Impact on Taihu Lake Basin

Lin Yi, Linwang Yuan, and Zhaoyuan Yu

Key Laboratory of Virtual Geographic Environment (Ministry of Education),
Nanjing Normal University, Nanjing, 210023, China
yilin57@163.com

Abstract. This paper takes Taihu Lake Basin as the research area, predicting population and GDP values of every city and county until 2030 with Bootstrap method. Based on sea level-ground system evolution model, it further carries on multi-scenario simulation and evaluation of social and economic impact on the areas where sea level rises until 2030. The result shows: when the value of sea level rise is 23cm, 31cm and 60cm, the affected area, population, and GDP loss will amount to 13.2% ~ 24.0%, 8.6% ~ 16.3% and 15.7% ~ 26.9% respectively. The potential impact of sea level rise in Taihu Lake Basin is characterized by regional differentiation. As cities and counties with developed social economy are located in low and flat areas, the impact of sea level rise is more significant. Strategies like area-classified management and regional cooperation should be taken into consideration in future regional development to respond the potential threats from sea level rise.

Keywords: Taihu Lake Basin, Sea Level-Ground System, Bootstrap Method, Impact Evaluation.

1 Introduction

Variation of sea level-ground system is one of the most important control factors in the process of geographical and cultural history evolution in coastal areas. Many achievements in regional impact research of sea level rise have been made [1]. The value of sea level ground and that of rise in different areas are different, and all kinds of social and economic indexes in potentially affected areas during prediction period are variables [2, 3]. Evolution and impact evaluation of actual sea level-ground system should take overall consideration of several interrelated and indivisible organic compositions such as sea level rise prediction, ground subsidence prediction, prediction of affected areas, prediction of regional social and economic development, prediction of impact on regional social and economic development, etc. [4]. Therefore, based on sea level-ground system model, by simulating the response mechanism and variation trend of social and economic system to sea level and ground subsidence represented as population and economy factors to carry on scenario prediction and estimation, virtual experiment, and strategy research of regional social

F. Bian et al. (Eds.): GRMSE 2013, Part I, CCIS 398, pp. 475–485, 2013.
© Springer-Verlag Berlin Heidelberg 2013

and economic impact are important means to effectively deal with sea level rise and reduce the losses it causes.

Delta as greatly affected area by multi-circle coupling effect and man-ground interaction, its evolution process, mechanism, discipline, and modeling and simulation research of trend are more typical and exemplary [2,5]. Taihu Lake Basin as the main body of Yangtze River Delta, is an area of high environmental pressure and high sensitiveness with typical strong sea-ground-man interactivity. With the dual impact of sea level rise and ground subsidence, this area is facing several security problems such as land loss in coastal zone, level loss in plain and low-lying areas, degradation of water quality in coasts and river mouths, etc. [6] . As one of most developed areas in social and economic aspects in our country, impacts of human activities not only have intensified complexity of variation, but also increased the potential threats from sea level rise. Under the frame of global change, from the point of view of sea level-ground system, research on social and economic impact of sea level-ground system evolution in this area is helpful to sort out how to deal with situation and impact of sea level-ground system variation under the conditions of dual impacts of nature and humanity culture, further providing lessons and thoughts for management and strategies.

Sea level-ground system, from being researched by now, can simulate simultaneously time+3D sea level variation, and do dynamic control [4, 7]. Comprehensive and integrated researches of virtual experiment and impact prediction are still rarely found. With the technology of geographic information and geographic modeling, based on geology and history records, it is expected to achieve revealing of history scenes of regional environmental changes and virtual experiment eventually through introducing dynamic simulation and visible technology, integrating related spatio-temporal analysis model. This paper takes Taihu Lake Basin as an example, and predicts population and GDP variation value by means of Bootstrap over the years in every city and county until 2030. Then it obtains the potentially affected area range until 2030 in Taihu Lake Basin under the condition of rise in value on different sea levels with evaluation model of sea level-ground system variation impact, and evaluates social and economic impact. Finally, the paper analyzes preliminarily the correlation between spatio-temporal pattern evolution of social and economic factors in this area and sea level rise, and proposes corresponding countermeasures.

2 Data and Method

2.1 Data

This paper simulates the affected area range in Taihu Lake Basin until 2030 by sea level rise under different scenarios with sea level-ground system virtual experiment platform. Via clearing up and organizing relative basic data needed, It adopts 1:200,000 around lake remote sensing interpretation diagram in Taihu Lake Basin edited by Institute of Geography and Limnology, Chinese Academy of Sciences, transfers the data into 50m×50m DEM grid data after encryption processing of contour lines. After that, land-water boundary binary data is overlapped on it to form

grid form 50×50m raster data for final analysis. The background value of future sea level rise is obtained from Wusong Tide Station, provided by Shanghai Maritime Safety Administration Sea Survey Team, adopting the annual average high tide level value 3.25m from 1990 to 2002 (Wusong base level). Sea level rise value is the comprehensive evaluation value of sea level rise in the area near Yangtze River Estuary. Three evaluation values are high evaluation value 60m, average evaluation value 31m and low evaluation value 23m respectively. Data of ground subsidence speed rate is obtained based on 1:2,000,000 modern vertical crustal movement speed rate in areas of Yangtze River Estuary. Social and economic statistics data are from statistics yearbook of every province and city in Taihu Lake Basin. It selects population and GDP data from 1992 to 2008 as basic data, and works out a forecast for future values of population and GDP from 2009 to 2030 (In order to obtain relatively accurate GDP growth rate, transform all yearly GDP to a comparable price in 1992 based on inflation index).

2.2 Bootstrap Method and K-Means Cluster

Bootstrap method is a commonly used and important statistics method in statistic variance evaluation and then in interval estimation [8]. The basic thought of this method is: Under the condition of good representativeness of samples but with little total sum, through stochastic returning re-sampling of smaller sample with good representativeness, replace overall distribution by empirical distribution of re-sampling sample, then to achieve parameter evaluation, and obtain confidence interval of statistics to be evaluated more accurately. As Bootstrap method does not need hypothesis or analytic formula of deriving statistics beforehand to overall distribution [9], and can be applied in computer, it is widely used in several research areas like hypothesis testing, parameter estimation, statistics inference, etc.

Cluster method of data is helpful in disclosing the overall distribution mode and interrelation of data properties, and the most common methods are K-means, hierarchical cluster, etc. K-means algorithm obtains the best geometric gravity center and divided semi-diameter through constant iteration of geometric gravity center of original sample point, to make effective classification on data. Hierarchical cluster is to make hierarchical decomposition to set off the given data objects. K-means algorithm is capable of dealing with big data set without relying on sequence [10]. If an initiated distribution is given, the same data classification will be obtained no matter what the sequence of sample point is. The algorithm is relatively scalable and effective. Although hierarchical cluster method is relatively simple, problems of merge points or splitting point selection occur very often, and without high scalability.

2.3 Sea Level-Forced Simulation

From integrity and correlativity of environmental system, Xie (1997) first built the physical concept and mathematic model of sea-ground-ice unified sea level-ground system [11]. Zhong (2007) and Xin (2005) built a new sea level-ground simulation

system in Yangtze River Delta areas with the self-adapting 3D paleo-ground variation model as the core [4, 7]. The system calculated and generated 2D and 3D paleotopographic map under corresponding conditions at any given moment or period with regulation and control of control parameters like paleo-sea level elevation, sub-time sedimentation speed rate, crustal movement mode, etc. Based on this, method of manual intervention by experts can be taken to adjust the original control parameters with verification data like paleo-coast trace, archaeological site, etc. and then new graphical output result will generate automatically. The prediction data of population and GDP until 2030 in Taihu Lake Basin are obtained based on Bootstrap method, and the sea level-ground system evolution impact evaluation model is applied in order to obtain land area covered by seawater under different scenarios in 2030. Then the distribution of possibly affected area in Taihu Lake Basin based on binary graph quadrature of this area and land-water boundary is obtained. Analysis is applied to conduct spatial discretization to the population and GDP of the affected area and obtain the potentially affected data of population and GDP in every county and city. Finally, to analyze the correlation between temporal and spatial pattern inversion of social and economic factors and sea level rise in this area through overlapping analysis and evaluation of affected condition.

3 Social and Economic Spatio-temporal Pattern and Future Prediction in Taihu Lake Basin

3.1 Spatio-temporal Pattern of Social and Economic Factors

Spatio-Temporal pattern of social and economic factors in Taihu Lake Basin at this stage is the premise and background of future impacts and evaluation research. Therefore, spatio-temporal cluster to population and GDP data in Taihu Lake Basin is conducted with K-Means cluster method. And then social and economic spatio-temporal structure characteristics in Taihu Lake Basin is analyzed. Stochastic simulation needs to be conducted repeatedly for 200 times to obtain the average silhourtte width statistics with number of types from 2 to 10 respectively. The results show that cluster result discrimination is relatively good and cluster result is relatively stable when number of types is 6. Then the spatial distribution of population and GDP of different types of regions can be produced (Fig. 1). The population cluster result shows that Shanghai, as a special type for its most dense population (the sixth type), the mean center variation range is among 9,270,900 ~ 9,535,300 people. The fifth type of cities include Changzhou, Wuxi, Suzhou and Hangzhou, while the mean center variation range is among 1,842,700 ~ 2,304,600 people. The mean center variation range of the second, third and fourth type of counties and cities is among 561,800 ~ 1,104,500 people, and this type of counties and cities include Yixing, Jiangyin, Huzhou, Lin'an, Yuhang, Wujiang and Jiaxing, etc. Counties and cities with relatively less population can be treated as the first type, including Taicang, Qingpu, Jiashan, Pinghu, Haiyan, Deqing and Anji seven counties and cities, while the mean center variation range is among 420,800 ~ 434,600 people. The GDP cluster result shows that urban Shanghai has the largest GDP volume, and its mean center variation

range is among CNY 97,000 million ~ 455,000 million (the sixth type). And GDP of the fourth and fifth type of counties and cities rank only second to urban Shanghai, while it's mean center variation range is among CNY 7,800 million ~ 104,800 million, counties or cities such as Wuxi and Hangzhou. GDP of the first or second type counties and cities are relatively low, while the mean center variation range is among CNY 1,300 million ~ 16,000 million. This type of counties and cities include Jintan to the northwest of the Basin, as well as Anji, Lin'an, Deqing, Tongxiang, Haining, etc. to the southwest of the Basin. From the point of view of spatial pattern of population and GDP cluster result, counties and cities with large population and developed economy mostly are close to Taihu Lake Basin or seas, and the topography is relatively low, and they are relatively more affected by sea level variation.

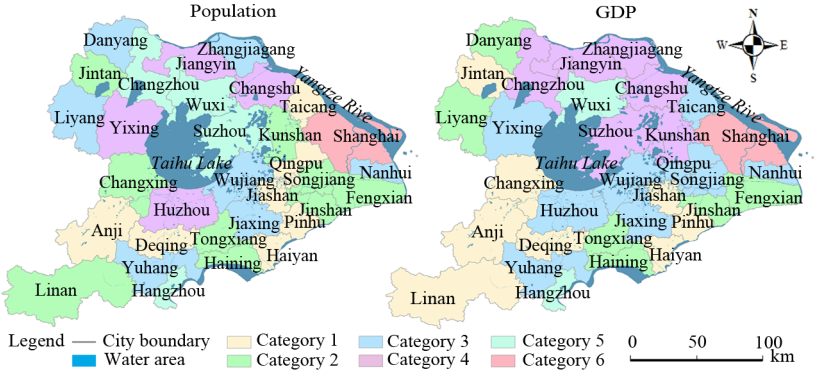

Fig. 1. Spatial distribution of population and GDP of different types of regions

3.2 Prediction on Population and GDP Until 2030

Characteristics of diverse impact factors of social and economic development and complexity of mechanism lead to irregular nonlinear growth trend of population and GDP sequences. Since generally the sample size of population and GDP sequences is relatively small, the commonly used time sequences prediction model is difficult to obtain good prediction result. And it's more difficult to conduct multi-scenario prediction. Bootstrap, as a nonparametric statistical method, can estimate specific statistics and confidence interval accurately under the premise of lacking prior information of sample distribution itself and sample size. So it can be used for population and GDP prediction. With the synthesization of conciseness and prediction accuracy of model, in this paper, it conducts stochastic re-sampling including returning for annulus sequence of population and GDP of every county and city from 1992 to 2008 respectively, and obtains annulus bootstrap distribution. The distribution reflects variation process information of population and GDP at this stage. The average state and possible range of population and GDP variation at this stage are represented by Bootstrap average value calculated and 95% of the bootstrap confidence interval in order to obtain average annulus of medium, high and low scheme and further to build annulus growth rate based population and GDP prediction model.

The predicted population values in Taihu Lake Basin are 37,635,000, 42,382,000 and 49,862,000 under the low, medium and high schemes respectively until 2030. It is anastomotic to 42,230,000 in Taihu Lake Basin predicted by Huang (2001) [2]. The predicted values of population of urban Shanghai are respectively 8,108,000, 9,920,000 and 10,579,000. The prediction range of total population of Shanghai and the districts and counties under its administration is among 10,791,000 ~ 13,655,000 and it's anastomotic to Shanghai prediction value of 13,761,800 by Wang (2000) [12]. With respect to GDP prediction, the total GDP under low, medium and high schemes in Taihu Lake Basin is respectively CNY 12,415,420 million, CNY 24,364,690 million and CNY 60,072,660 million until 2030, among which, the prediction of total GDP of urban Shanghai and the districts and counties under its administration is among CNY 4,142,980 ~ 14,380,270 million. The annual population and GDP growth rate and prediction in Jiangsu, Zhejiang province, etc. can be contrasted with related research results [13].

Table 1. Sea level rise impacts of Taihu lake basin until 2030 under the three scenarios

Scenarios Sea	Level Rise(cm)	Area(km^2)	%	Population	%	GDP	%
Low	23	5215.6	13.2	621.04	8.61	56751.59	15.73
Medium	31	7420.3	18.7	877.95	12.17	80560.35	22.33
High	6	9530.3	24.0	1175.38	16.29	97036.79	26.90

The population unit is Ten Thousand and the unit of GDP is Hundred Million Yuan.

4 Evaluation and Analysis of Social and Economic Impact

4.1 Impact Evaluation

In the evolution impact evaluation model of sea level-ground system, its comprehensive social and economic impact evaluation module flow is: Take prediction data as input, calculate the social and economic index value of unit area according to the area of every county and city, and conduct overlay analysis on layer data of potentially affected areas and obtain the layer data of future social and economic index of the affected areas in unit area of every county and city. And then potentially affected areas of different counties and cities are picked up, to calculate their areas and social and economic index quadrature of unit area, and then to obtain potential impact data on population and GDP of every county and city in Taihu Lake Basin until 2030. The background tide level value is 3.25 m, sea level rise value and the overall evaluation result of total potential impacts on Taihu Lake Basin until 2030. And Fig. 2 shows the potential impacts on population and GDP of Taihu Lake Basin under the three scenarios.

13.2% ~ 24.0% of Taihu Lake Basin will be affected at different degrees under the three scenarios up to 2030. The most severe two places that are potentially affected will be Huzhou and Wujiang located at the middle of the area. The impact values of these two cities under medium scenario are 867.08 km^2 and 851.02 km^2 respectively. With regard to the degree of impact of the sea level rise on social and economic

factors in this area, a population of 6,210,400 ~ 11,753,800 will be affected in this area until 2030, and the expected GDP loss will be CNY 5,675,159 ~ 9,703,679 million (Table 1); and the population of urban Shanghai will the most severely affected that 3,225,900 people will be affected under medium scenario; and GDP of Kunshan will be the most severely and potentially affected that GDP loss will be around CNY 2,793,332 million; and the second biggest GDP loss will be in urban Shanghai, about CNY 1,269,525 million.

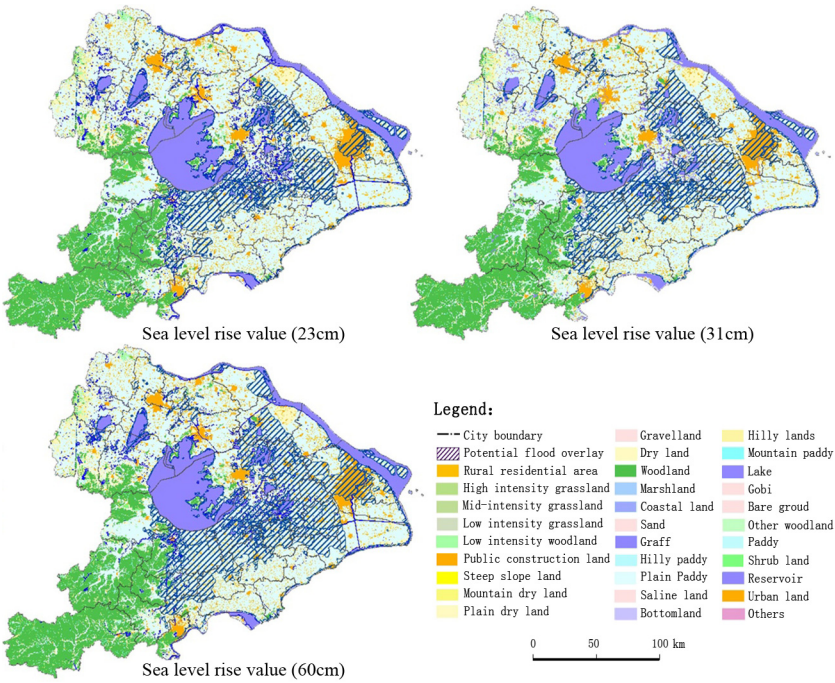

Fig. 2. Spatial Distributions of Potential Impacts under the Three Scenarios

In general, the affected areas expand outwards with Taihu Lake, Yangtze River and its branches as the center. Under the influence of dish landform in this area, the plains and the low-lying lands are affected badly, such as Wujiang, Huzhou, etc. 575,200 people are affected with an estimated GDP loss of CNY 508,612 million in Wujiang, while 643,300 people are potentially affected with an estimated GDP loss of CNY 140,176 million in Huzhou. In contrast, counties and cities with higher altitude in northern and eastern outskirts are less affected, for example, Danyang and Taicang are less affected thanks to higher altitude. Besides, potential impacts on population and GDP by sea level rise are highly regional. Potential impacts on the population and GDP of some neighboring areas are equal, such as the population of Danyang, Jintan and Liyang in the Northwest, and the population of counties and cities like Haining, Haiyan, Pinghu etc. in the South, as well as GDP of Changshu, Kunshan and Suzhou in the Northeast.

4.2 Spatio-temporal Pattern Comparasion

According to current spatio-temporal cluster results of social and economic factors in Taihu Lake Basin, we may classify the potentially affected situations in this region in 2030 to reveal how the population and GDP (Fig.3) factors of different types of regions under different scenarios are affected. Based on the above classification results, under low, medium and high scenarios, urban Shanghai of the sixth type will be affected greatly up to 2030 for its big population base, economic base, and low land. Under the three scenarios of low, medium and high, affected population will be 1,860,000 ~ 2,440,000, 2,630,000 ~ 3,440,000 and 3,910,000 ~ 5,110,000 respectively; and in other types of regions, the variation of affected population is relatively small. In the above regions, the counties and cities in the northwestern part, southern part and northern part of its outskirts with high lands are less affected; counties and cities with low lands near Taihu Lake are greatly affected, and the affected population scopes of Huzhou, Wujiang and Kunshan are in the interval of 421,000 ~ 838,000; while Anji and Lin'an are basically unaffected.

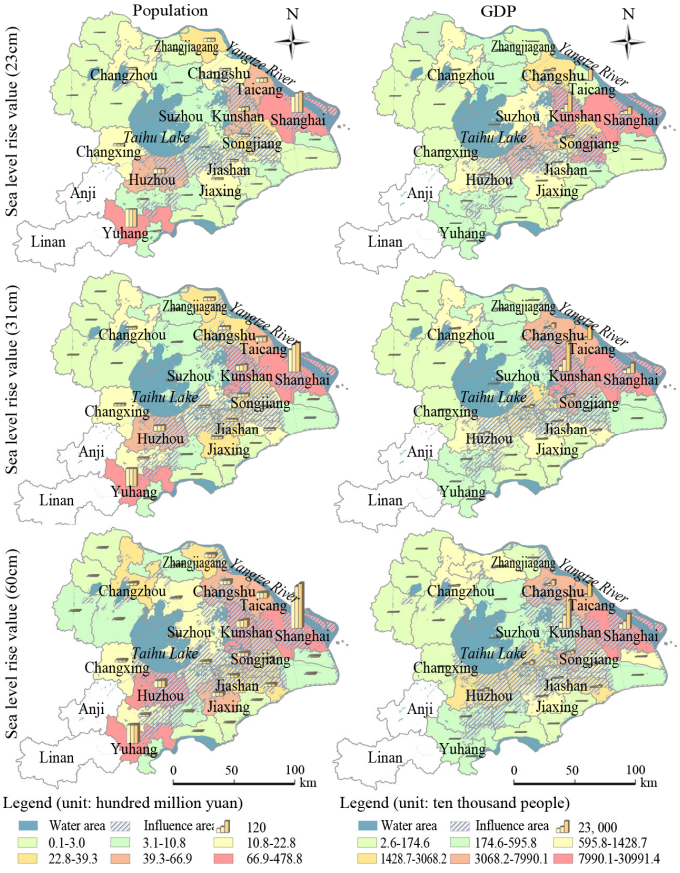

Fig. 3. Potential Impacts of Population Distribution under the Three Scenarios

In contrast to the population distribution, affected spatial variation of GDP is more uneven. From the absolute numerical value, urban Shanghai is still the most greatly affected region, under the three scenarios, the affected GDP are CNY 596,200 ~ 1,734,700 million, CNY 842,600 ~ 2,451,800 million and CNY 1,250,700 ~ 3,639,100 million respectively. The affected GDP of the fifth type cities such as Hangzhou and Wuxi is small for their affected areas are small. The whole mean value of fourth type cities is a little lower than that of Shanghai, but the spatial variation is quite obvious. This type of cities is mainly concentrated in southern Jiangsu province, especially in Suzhou. Where, Kunshan is the most severely affected while Jiangyin is the least affected. In the three types of cities, Songjiang District, Qingpu District and Wujiang City are greatly affected, and the other cities are relatively less affected.

The above analysis shows that: The evolution of regional sea level-ground system affects regional society and economy differently. On one hand, the impact degree is determined by landforms and geography of each county and city; on the other hand, it is restricted by their own population and economic development. Because the altitude of Taihu Lake Basin is low in general, especially the developed counties and cities are in low and flat and even relatively low-lying areas, so that generally speaking, larger GDP and population base, and faster development will be subject to bigger impact by the sea level-ground system evolution, but the impact degree of counties and cities with slower economic development is relatively smaller. The impact analysis on sea level-ground system evolution and the research on its differentiation features can be referred to making decisions and planning for regional sustainable development.

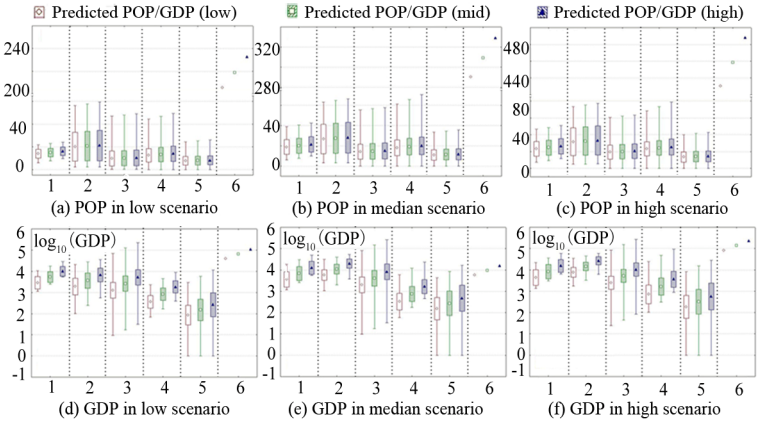

Fig. 4. Statistics of Potential Impacts of Different Scenarios

5 Conclusion and Discussion

With the deepening research of global change, regional integration research is becoming important. Under the situation of global change, regional environment evolution process and mechanism, quota and simulation of regional nature and humanity coupling process, the research on regional system sensibility and spatio-temporal difference have

been attached more and more importance to Fan (2004) and Liu(2003) [14,15]. Constructing different simulation and prediction scenarios, simulating the range of impact area under different scenarios and making dynamic evaluation of modifiable input condition on the impact of society and economy accordingly are the main objectives and important method of applying sea level-ground system theory effectively to carry out impact evaluation and simulation experiment. Under the background of global change and especially sea level rise caused by global warming, sea-level system evolution has an important theoretical and realistic significance to the research on sustainable development of regional society and economy in coastal areas, especially in low-lying areas.

This paper takes K-Means cluster method to discuss spatio-temporal pattern and evolution process of social and economic factors in Taihu Lake Basin, and applies Bootstrap method to predict the population and GDP of each county and city until 2030. Based on the sea level-ground system evolution evaluation model, under three scenarios of high, medium and low sea level rise, it conducts simulation and evaluation on social and economic impact area range until 2030 for sea level rise. The research shows: Sea level rise has an significant impact on regional social and economic development in Taihu Lake Basin: When the sea level rise value is 23cm, the population and GDP affected are approximately 6,210,000 and CNY 5,675,200 million; when the sea level rise value is 31cm, the area affected is 18.7% of the total regional area, about 8,780,000 people are affected, and GDP loss is about CNY 8,056,000 million; when sea level rise value reaches up to 60cm, the population and GDP loss possibly affected will amount to 11,750,000 and CNY 9,703,700 million.

Under the influence of dish landform in this area, central plain and low-lying land are badly affected, the northern and eastern part of outskirts are slightly affected, and the southwest mountainous and hilly areas are almost not affected for its higher terrain. Through the contrast and analysis between social and economic spatio-temporal pattern and sea level rise impacts, sea level rise may be disastrous and its impacts have strong regionality. Where: relatively economically developed counties and cities, such as urban Shanghai and its administrated districts, developed counties and cities in southern Jiangsu province, and Huzhou, Zhejiang Province, etc. On which, sea level rise impacts are determined by their own population and economic development. The impact degree of counties and cities with relatively slow economic development is not only determined by their topography and landforms, but also controlled by their own population and economic development degree. This research shows that the GDPs of Shanghai, Wujiang, Songjiang, and Kunshan, etc. will be greatly affected potentially. When considering the economic benefit and social benefit in regional development, disasters and problems caused possibly by future sea level rise should be fully considered, and especially joint prevention and control among counties and cities within the area should be focused on so as to minimize the possible impacts caused by sea level rise and to ensure coordinated development of regional society and economy.

Acknowledgement. This work is supported by the Special Project of Sub Project of Key Projects in the National Science & Technology Pillar Program of China (Grant no. 2012BAC07B01).

References

1. Mousavi, M.E., Irish, J.L., Frey, A.E., et al.: Global warming and hurricanes: the potential impact of hurricane intensification and sea level rise on coastal flooding. Climate Change 104, 575–597 (2011)
2. Huang, Z., Zhang, W., Fan, J., et al.: Areas In uenced by Sea Level Rise in Zhujiang Delta. Oceanologia et Limnologia Sinica 32, 225–232 (2001)
3. Werner, A.D., Craig, T.: Simmons Impact of Sea-Level Rise on Sea Water Intrusion in Coastal Aquifers. Ground Water 47, 197–204 (2009)
4. Zhong, H., Xie, Z.: The Research of Appraisals Model of In fluence of The Sea Level-Land Surface's System Change. Hydrographic Surveying And Charting 27, 30–33 (2007)
5. Weng, Q.: Land Use Change Analysis In The Zhujiang Delta Of China Using Satellite Remote Sensing, GIS And Stochastic Modelling. J. Environ. Manage 64, 273–284 (2002)
6. Chen, S., Chen, L., Liu, Q., et al.: Remote Sensing And GIS-Based Integrated Analysis Of Coastal Changes And Their Environmental Impacts In Lingding Bay,Pearl River Estuary, South China. Ocean & Coastal Management 48, 65–83 (2005)
7. Xin, Z., Xie, Z., Jiang, W.: Construction and Experiment for Sea-Level & Land Surface System Model in The Yangtze Delta Region. Geographical Research 24, 513–520 (2005)
8. Manly, B.F.J.: Randomization, Bootstrap And Monte Carlo Methods In Biology, 3rd edn. Chapman & Hall/CRC, Boca Raton (2007)
9. Staszewska-Bystrovaa, A., Winkerb, P.: Constructing narrowest pathwise bootstrap prediction bands using threshold accepting. Int. J. Forecast. 29, 221C–233C (2013)
10. Huang, Z., Yuan, L., Yu, Z., et al.: The Spatio-Temporal Evolution And Character-istics Analysis of Tourist Flow In Eco-Tourism Area: A Case Study of Yancheng Eco-Tourism Area For David's Deer. Geographical Research 27, 55–64 (2008)
11. Xie, Z., Xia, S.: Future Oriented Research On Sea Level Changes. Earth Science Frontiers 4, 235–246 (1997)
12. Wang, G.: On the Reasonable Size of the Future Population in Shanghai. Journal of East China Normal University (Philosophy And Social Sciences) 1, 107–117 (2000)
13. Yang, L., Yang, G., Yuan, S.: Application Of Mathematical Models In Predication of The Population-Taking Jiangsu Province As An Example. Resources And Environment In The Yangtze Basin 15, 387–391 (2006)
14. Fan, J.: Comprehensiveness of Geography And Integrated Research on Regional Development. Scientia Geographica Sinica 59, 33–40 (2004)
15. Liu, Y., Xu, X.: Duality of Chinese Geography. Scientia Geographica Sinica 28, 587–593 (2008)

The Application of the Sensor Model Language in the HeiHe Watershed Allied Telemetry Experimental Research

Ting Liu[1,2], Wanming Luo[1], and Baoping Yan[1]

[1] Computer Network Information Center, Chinese Academy of Sciences, 100190, Beijing, China
[2] University of Chinese Academy of Sciences 100190, Beijing, China
{liuting,luowanming,ybp}@cnic.cn

Abstract. The HeiHe Watershed Allied Telemetry Experimental Research (HiWATER) is a research project that builds a world-class watershed observing system to improve the observability of hydrological and ecological processes. To achieve this goal, some observation stations and sensor networks were established. In order to make these disparate sensors in the networks easily discoverable and accessible, we used the Sensor Model Language (SensorML) to model these sensors and sensor systems in the stations. In this paper, we firstly introduce the SensorML and then mainly present a model of the HiWATER based on SensorML. In order to meet some special requirements of the project, we customize some element of the metadata group and design the particular processes for the model. The model laid a solid foundation for later design and study in HiWATER.

Keywords: SensorML, SWE, Sensor Web, XML, HeiHe Watershed.

1 Introduction

As the sensor technology is advancing, various sensor systems and sensor networks, which use sensors to sense, collect, process and transfer the sensing information, are emerged in many domains, such as military, environment monitoring and geo-spatial explore. However, since different sensor systems and sensor networks contain many different sensor types, it is difficult to discover, access, and process sensors within the heterogeneous systems. The heterogeneity of these systems also means that interoperability between them is very hard.

To solve this problem, members of the Open Geospatial Consortium, Inc. (OGC) proposed the Sensor Model Language (SensorML) which specifies a suit of information model and XML schema for the description of all kinds of sensor systems to achieve the interoperability between the sensors in the heterogeneous networks.

In the HeiHe Watershed Allied Telemetry Experimental Research (HiWATER), which is a research project to build a world-class watershed observing system to

F. Bian et al. (Eds.): GRMSE 2013, Part I, CCIS 398, pp. 486–497, 2013.
© Springer-Verlag Berlin Heidelberg 2013

improve the observability of hydrological and ecological processes, we have established several observation stations and sensor networks for ecological and hydrological observation. In order to make these disparate sensors in the observation stations easily discoverable and accessible, it is an efficient way to use the SensorML to model these sensors and sensor systems. This paper mainly introduces the SensorML and proposes the model of the stations in the HiWATER based on SensorML.

The remainder of the paper is organized as follows. In Section 2, we present the concept and structure of the SensorML. The model of the HeiHe Watershed Allied Telemetry Experimental Research is presented in the Section 3 and conclusions are drawn in Section 4.

2 SensorML Standard Models

SensorML defines models and XML Schema for describing sensors and measurement processes, including measurement by a sensor system, as well as post-measurement processing [1]. Moreover, it also provides information needed for discovery of sensors, location of sensor observations and listing of taskable properties. It is one of the OGC Sensor Web Enablement (SWE) [2] suites of standards. While SensorML serves as a component within the SWE framework, SensorML does not depend upon the presence of the other SWE components. It is a standard that can be used independently.

Conceptually, SensorML consists of two aspects: one is the standard concept models for describing the sensors or sensor systems, and the other is the XML schema which encoded the models as XML schema documents.

The SensorML schema provides concrete elements and rules for creating instance documents for sensors and sensor components. The http://www.opengis.net/sensorML/1.0 namespace of the schema is used for fundamental core SensorML elements that can be applicable for a wide range of sensors. In additional, The SensorML schema also utilizes components from two external XML schemas: the Geography Markup Language (GML) with the http://www.opengis.net/gml namespace and the SWE Common data components with the http://www.opengis.net/swe/1.0 namespace to reference some useful and common elements and data types.

In the following parts of the section, we primarily introduce the concept model of the SensorML.

2.1 SWE Common Conceptual Models

The SWE common models define several basic value types and data encodings that exist in the Sensor Web Enablement (SWE) Common namespace. These definitions include the primitive data types, aggregate data types with specialized semantics like position, curve, and time-aggregates as well as the standard encodings to add semantics, quality indication and constraints to both primitive and aggregate types. The set of data types and related components SWE Common provides are required in

various places across the suite of OGC SWE standards. In the SensorML, they are used to define the type of data used by the inputs, outputs and parameters properties in processes which is the core component of SensorML.

2.2 SensorML Conceptual Model

In SensorML sensors are modeled as processes that convert physical phenomena to data. These processes often contain input, output, parameter and metadata Group properties. The input and output properties represent sensor data measurements or connections to other processes. The parameter property is used to configure the process or provide other inputs that are not sensor measurements. The Metadata Group generally used to assist humans in understanding the sensor system. These processes are conceptually divided into two types: physical processes and non-physical or "pure" processes.

Non-physical Processes. Non-physical or "pure" processes can be treated as merely mathematical operations. Besides including the common properties, the pure processes also contain the method property that provides the methodology by which one transforms input values to appropriate output values, based on the provided parameter values.

Process Model. The atomic non-physical processes modeled by the ProcessModel type and usually used within a more complex Process Chain. It is associated to a Process Method which defines the process interface as well as how to execute the model. It also precisely defines its own inputs, outputs and parameters.

Process Chain. Process chain is a collection of the atomic non-physical processes that are executable in a sequential manner to obtain a desired result. While the Process chain consists of the other processes, it itself is a process that can participate as a component within other process chains. The process chain describes the processes in the chain as well as the connections between the components. The connection property includes a collection of Link objects that provide references to the source and destination "ports" within the various component processes.

Physical Processes. In addition to describing purely mathematical processes, SensorML also describes the physical processes that have some relationship to space and time. Physical processes provide physical information, such as location, temporal and spatial reference, which can be used in processing if required.

Component. The atomic physical process is modeled by the Component type. A component is the physical process that either cannot be subdivided into smaller sub-processes, or if one chooses to treat it as a single indivisible process. It can be considered as a real-world equivalent of a Process Model and can participate as part of a Process Chain or System.

System. System can be seen as a physical equivalent of a Process Chain. It can include several physical and non-physical processes that all act to provide a certain set of System outputs, based on the System inputs and parameters. Like Process Chain, System provides a list of processes and the links between these processes by using the components and connections properties. In addition, System can provide relative positions of its components through the positions property.

Metadata Group. All the processes depicted in the SensorML contain a group of metadata named Metadata Group. It is generally used to assist humans in understanding the sensor system, discovering the resources and assessing the process results. These metadata primarily include the general information of keywords, identifications and classifications, the constraints information, the references information and the history information.

3 Modeling in the HiWATER Based on Sensor ML

3.1 Overview of HiWATER

The Heihe River Basin is the second largest inland river basin in Gansu province of China, which has a total area of 295, 000 km^2. It has diverse nature landscape including the ice, frozen soil, forests, grasslands, rivers, lakes, oases, desert, Gobi. Meanwhile, the Heihe River Basin has a long history of human activities affected by the hydrological environment. The intersection of the natural and human processes make the Research conducted in the Heihe River Basin becomes a significant experimental watershed.

The HiWATER is just a research project that conducted in the Heihe River basin. It is a watershed-scale eco-hydrological experiment designed from an interdisciplinary perspective to address problems including heterogeneity, scaling, and closing water cycle at the watershed scale. With found by the National Natural Science Foundation (NSFC), the objective of the HiWATER is to improve the observability of hydrological and ecological processes, to build a world-class watershed observing system and to enhance the applicability of remote sensing in integrated eco-hydrological studies and water recourse management at the basin scale. To achieve these goals, an eco-hydrological wireless sensor network is built to capture multi-scale heterogeneities and to address complex problems. The observation sites of the sensor networks are distributed in both the Babaohe River Basin in the upstream and the Daman /Yingke irrigation districts in the middle stream of the Heihe River basin. The sensor network deployment of the middle reaches in the Heihe is showed in the Fig. 1. Fifty sets of the sensor nodes are deployed in these observation stations. The instrument configuration of the station is showed in Fig.2. To easily discover and access the various sensors and heterogeneous sensor data in the observation stations through the Internet, we use the SensorML to model the stations in a standard way .Since the sensor types are the same in each station, in this paper, we mainly take each station as a whole to modeling.

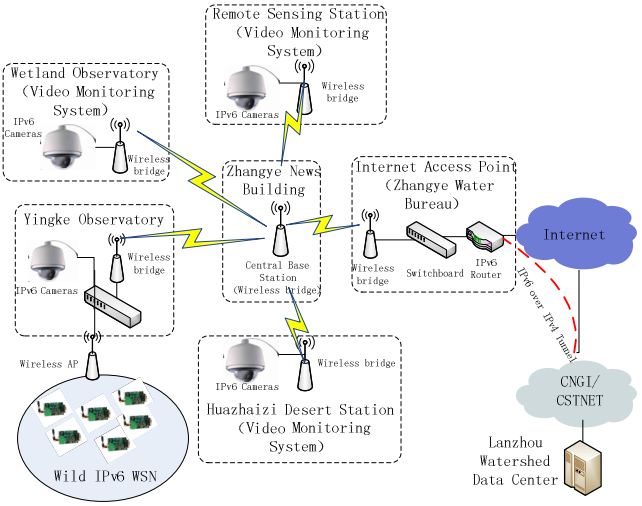

Fig. 1. The network topology about the middle of the Heihe

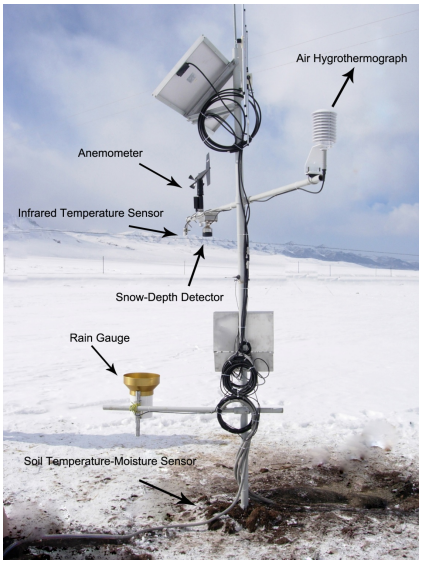

Fig. 2. The instrument configuration of the station

3.2 System Modeling

As show in the Fig.2, the station includes sensors for rain volume, wind direction and speed, soil temperature, humidity and salt, air temperature and humidity, snow depth as well as Infrared surface temperature. We modeled the station as a System which allows a very accurate description of the observation station. In the System, there are

two sub-systems: one consists of all the components and the other includes the processes or process chains. The distinct sensors of the station are separately modeled as Components which are the part of the ComponentSystem and associated with the whole System. The ComponentSystem model logically incorporates the components just match the real distinct sensors assembled on the station. It is a good way to simplify the component modeling. For the details of data processing, we put them into the processes sections of the component. The ProcessChainSystem includes processes or process chains that design for the particular applications. All the components of the both sub-systems contain the Metadata Group that describes the related information. The overall architecture of the system model is showed in Fig.3. The XML encodings of the System list in Fig.4.

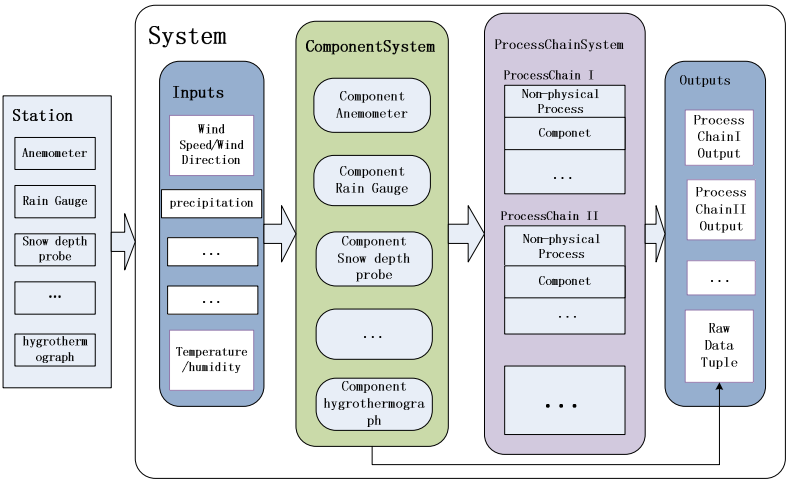

Fig. 3. The overall architecture of the model

```
<components>
  <ComponentList>
    <component name="componentSystem" xlink:href="ComponentSystem.xml">
    </component>
    <component name="processChainSystem" xlink:href="processChainSystem.xml">
    </component>
  </ComponentList>
</components>
```

Fig. 4. XML encoding of the System

3.3 Metadata Group Modeling

The metadata group provides a common collection of metadata elements that can be used within the any system, components or processes. It is a compulsory and important part in the components of the model to describe the basic information for discovery. It contains the General information of the identifier, description and the classifier, the Constraints information of the securityConstraints, vaildTime and

legalConstraints, the Properties information of Characteristics and Capabilities, the References information and the History information. The elements of the metadata group are provided in the Fig.5.The identification property of the general information specifies the unique ID or Name for the resources. The classification property provides a list of possible classifiers that might aid in the rapid discovery of processes, sensors, or sensor systems. The capabilities property is intended for the definition of parameters that further qualify the output of the process, component, or system and the characteristics use to define the parameters that may not directly qualify the output.

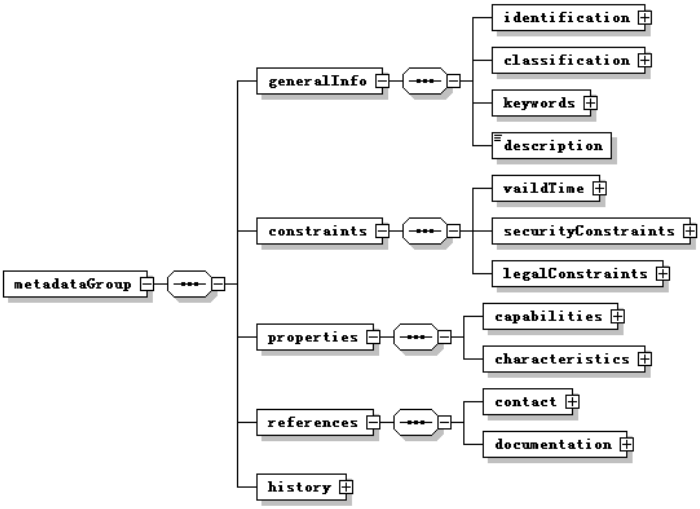

Fig. 5. The schema of the metadata group

While some of the elements in metadata group of the SensorML just provide abstract descriptions for the resource, we customize these metadata elements according to the requirements in the project. We define the identification in the metadata group of the non-physical process including two elements: longName and shortName, while the classification has the element processType. The capabilities and the characteristics properties could have different values according to the different processes. Unlike the non-physical process, the metadata of the component should include some information about the sensors and the physical properties. The metadata group of the components is showing in the Fig. 6, in which the elements not showed are the same with the metadata group of the SensorML. In the identification property, the modelNumber is the nodeID of the sensor modeled in the component, and the manufacturer is the name of the factory produced the sensor. The sensorType in the classification specifies the type of the sensor. The physicalProperties in the characteristic describe the weight, diameter or length of the sensor, and the measurementProperties in the capabilities specify the dynamic range and accuracy of the data got from the sensor. Additionally, the manufacturer in the contact of the references provides the information about the sensor producer. The XML encoding sections of the component is provided in the Fig.7.

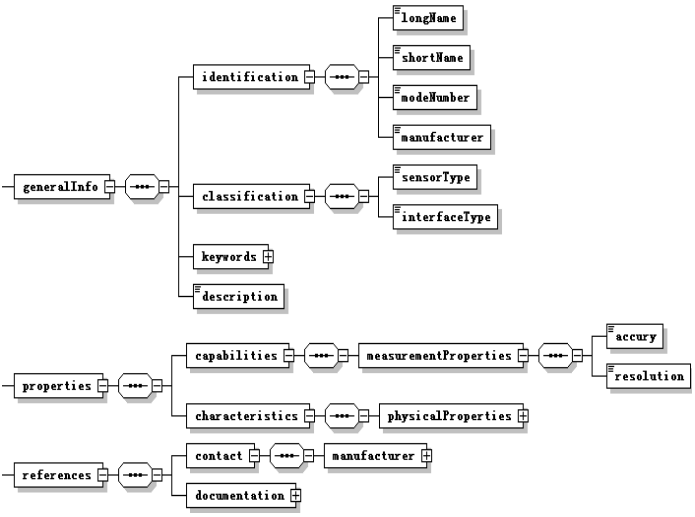

Fig. 6. The schema of the component metadata

```
<identification>
  <IdentifierList>
    <identifier name="longName">
      <Term definition="urn:ogc:def:identifier:OGC:longname">
        <value>R.M Young TR-525M 52203 Rain Gauge</value>
      </Term>
    </identifier>
    <identifier name="shortName">
      <Term definition="urn:ogc:def:identifier:OGC:shortname">
        <value>TR-525M Rain Gauge</value>
      </Term>
    </identifier>
    <identifier name="modelNumber">
      <Term definition="urn:ogc:def:identifier:OGC:modelNumber">
        <value>52203</value>
      </Term>
    </identifier>
    <identifier name="manufacturer">
      <Term definition="urn:ogc:def:identifier:OGC:manufacturer">
        <value>R.M Young</value>
      </Term>
    </identifier>
  </IdentifierList>
</identification>
<classification>
  <ClassifierList>
    <classifier name="sensorType">
      <Term definition="urn:sensor:classifier:sensorType">
        <codeSpace xlink:href="urn:x-ceos:def:GCMD:sensors"/>
        <value>hyetometrograph</value>
      </Term>
    </classifier>
</ClassifierList>
```

Fig. 7. The metadata description of the component

3.4 Component System Modeling

The ComponentSystem is a collection of sensors that modeled as components. As the sensors are deployed in different position in the station, besides including the metadata information, the component model in the system has the position properties

and interface properties describing the physical process. As showing in the Fig.3, in our project the output of the componentSystem is the raw data tuple, we model the process of the components in a simple way without parameters. For the components that measure the single type value, the process section only has one input and one output. For the components that measure multiple phenomena, the outputs can have more than one. The XML encoding sections of this process using the xml based on the SensorML schema provided in the Fig. 8.

```
<inputs>
  <InputList>
    <input name="AnemometerInput_speed">
      <swe:ObservableProperty definition="urn:ogc:def:property:OGC:windSpeed"/>
    </input>
    <input name="AnemometerInput_Dir">
      <swe:ObservableProperty definition="urn:ogc:def:property:OGC:windDirection"/>
    </input>
  </InputList>
</inputs>
<outputs>
  <OutputList>
    <output name="measuredWindSpeed">
      <swe:Quantity definition="urn:ogc:def:property:OGC:windSpeed"/>
      <swe:uom code="m/s"/>
    </output>
    <output name="measuredWindDirection">
      <swe:Quantity definition="urn:ogc:def:property:OGC:windDirection"/>
      <swe:uom code="deg"/>
    </output>
  </OutputList>
</outputs>
```

Fig. 8. The inputs and outputs section of the component

These components are connected to the ComponentSystem by using the connections property. The XML codes are showed in the Fig.9.

```
    <connection name="inputToWindDirection">
      <Link>
        <source ref="this/inputs/windDirection"/>
        <destination ref="windDirectionDetector/inputs/windDirection"/>
      </Link>
    </connection>
    <connection name="windDirectionToOutput">
      <Link>
        <source ref="windDirectionDetector/outputs/measuredWindDirection"/>
        <destination ref="this/outputs/weatherMeasurements/windDirection"/>
      </Link>
    </connection>
    <connection name="inputToRainGauge">
      <Link>
        <source ref="this/inputs/rainFall"/>
        <destination ref="rainGauge/inputs/rainFall"/>
      </Link>
    </connection>
    <connection name="rainGaugeToOutput">
      <Link>
        <source ref="rainGauge/outputs/measuredRainFall"/>
        <destination ref="this/outputs/weatherMeasurements/rainFall"/>
      </Link>
    </connection>
  </ConnectionList>
</connections>
```

Fig. 9. The connections section

3.5 Process Chain System Modeling

The process chain system model is one of the most important and complicated parts in the station modeling. The process chains contain two types of the process: one is the

physical process which is just the component; the other process is the non-physical process that is just considered as the merely mathematical operations. These processes can form several process chains for particular purposes. These process chains are based on the given applications.

At present, there are mainly four basic applications from the ecological hydrology scientists. The first one is to develop the evapotranspiration models in the heterogeneous surface. In the arid zones, especially in arid inland river basin like Heihe that lack of water resources, the mainly form of the water dissipation is evaporation. The evapotranspiration provides important information to guide agricultural irrigation and drainage, improve the utilization of water resources. The second application is the irrigation management which combines the different control standards and the amount of the irrigation using the real-time moisture data the soil moisture sensors probed to decide the irrigation water required. It is an innovative way to use the sensor networks to replace the traditional irrigation management system. In additional, the researches on crops growth model and agricultural output assessment are all relied on the observation data.

In our model, all the applications are modeled as process chains consisted of a series of other process chains, processes or components. Since these applications are so complicated and may have different processes in different cases, we just model these applications as process chains at a very high level of abstraction. Take evapotranspiration model as an example, from the abstract level, the inputs of the evapotranspiration model is a set of values that calculating the evaporation needed. The output is the value of the evaporation. Since different evapotranspiration model needs different parameters and may have various inputs, in our model, we just describe the common inputs and parameters. The XML codes are showed in the Fig. 10.

```
<inputs>
  <InputList>
    <input name="temperatureInput">
      <swe:Quantity/>
    </input>
    <input name="precipitationInput">
      <swe:Quantity/>
    </input>
    <input name="moistureInput">
      <swe:Quantity/>
    </input>
    <input name="saltInput">
      <swe:Quantity/>
    </input>
    <input name="soiltemperatureInput">
      <swe:Quantity/>
    </input>
  </InputList>
</inputs>
<!-- ================================== -->
<!-- Evapotranspiration computing outputs -->
<!-- ================================== -->
<outputs>
  <OutputList>
    <output name="evapOutput">
      <swe:Quantity/>
    </output>
  </OutputList>
</outputs>
```

Fig. 10. The inputs and outputs of the evapotranspiration

While the application is modeled as the process chain, it is just a descriptive process of the application, the concrete process model depend on the specific implementation. Although the implementation of the application is the next step we

intended to do, the process chains proposed here provide a basic framework for the applications and can be extended easily.

After completion of the process modeling, the last thing is to connect these processes, process chains into the process chains system. This xml encoding is showed in the Fig.11.

```
<components>
  <ComponentList>
    <component name="processChain_Evap" xlink:href="processChain_Evap.xml">
    </component>
    <component name="processChain_IMOD" xlink:href="processChain_IMOD.xml">
    </component>
    <component name="processChain_CORM" xlink:href="processChain_CORM.xml">
    </component>
    <component name="processChain_CORA" xlink:href="processChain_CORA.xml">
    </component>
  </ComponentList>
</components>
```

Fig. 11. The componetList of the ProcessChainSystem

4 Conclusions

In this paper, we present the OGC standards SensorML and model the observation stations in the project of the (HiWATER) based on the modeling language. To describe the component in more detail and make the resources more likely to be found, we customize some elements in the metadata group of the non-physical process and component. In additional, some particular processes are designed in our model to meet the requirements for the eco-hydrology studies. While the processes modeled are not used to do researches directly, it provides a standard and uniform ways to implement them. Since the SensorML is a part of the Sensor Web Enablement (SWE) initiative, the model we designed could be used in the project with the SWE framework or dependent of the SWE. In a word, the model based on the SensorML laid a solid foundation for later design and study in HiWATER.

Acknowledgments. This work is jointly supported by National Grand Fundamental Research Program of China (973) under Grant No.2009CB320502; the Development Program “Ecological Hydrology - Ground Remote Sensing Observation Experiment and Comprehensive Simulation in the Heihe River Basin” of China Next Generation Internet (CNGI); the project “The Integrated Research on Hydrological and Ecological Processes in the Heihe River Basin” founded by National Natural Science Foundation of China (NSFC) under Grant No.40925004.

References

1. Botts, M., Robin, A.: OpenGIS Sensor Model Language (SensorML) Implementation Specification 1.0.0. Open Geospatial Consortium Inc., Wayland (2007b)
2. Botts, M., Percivall, G., Reed, C., Davidson, J.: OGC Sensor Web Enablement: Overview And High Level Architecture. Open Geospatial Consortium Inc., Wayland

3. Jirka, S., Bröring, A.: SensorML Profile for Discovery Engineering Report. Open Geospatial Consortium, Inc. (July 29, 2009)
4. Palmer, C.: SensorML on SenseTile (2010)
5. Aloisio, G., Conte, D., Elefante, C., et al.: Globus monitoring and discovery service and sensorML for grid sensor networks. In: 15th IEEE International Workshops on IEEE, pp. 201–206 (2006)
6. Li, X., Cheng, G., Liu, S., et al.: Heihe Watershed Allied Telemetry Experimental Research (HiWATER): Scientific Objectives and Experimental Design. Bulletin of the American Meteorological Society (2013), doi:10.1175/BAMS-D-12-00154
7. Hu, C., Chen, N., Wang, C.: Remote sensing satellite sensor information retrieval and visualization based on SensorML. In: 2011 IEEE International Geoscience and Remote Sensing Symposium (IGARSS), pp. 3425–3428 (2011)
8. Chen, J., Chen, N., Wang, W., Hu, C., Zheng, Z.: Remote satellite sensor modeling design and implementation based on the sensor modeling language. In: International Symposium on Spatial Analysis, Spatial-Temporal Data Modeling, and Data Mining, pp. 74922V–74922V
9. Hu, C., Chen, J., Chen, N.: Application of Sensor Model Language in Antarctic Zhongshan Weather Station. Bulletin of Surveying and Mapping (10), 31–34 (2010) (in Chinese)
10. Luo, W., Li, X., Jin, R., Yan, B.: A Comprehensive Design of IPv6 Wireless Sensor Network for Ecological and Hydrological Watershed-scale Research. In: Zhang, Y. (ed.) Future Wireless Networks and Information Systems. LNEE, vol. 143, pp. 673–680. Springer, Heidelberg (2012)
11. Luo, W., Yan, B.: Metadata Modeling of IPv6 Wireless Sensor Network in Heihe River Watershed. In: The 1st ICSU World Data System Conference (ICSU WDS 2011), September 3-6, Kyoto University, Kyoto, Japan (2011)

A Novel Change Detection Method Based on Direction Feature and Fuzzy Clustering for Remote Sensing Images and Its Application in Biological Invasions

Qingsong Li[1], Xizhong Qin[1], Zhenhong Jia[1,*], Jie Yang[2], and Raphael Hu[3]

[1] College of Information Science and Engineering, Xinjiang University, 830046 Urumqi, China
{lantiang12,qmqqxz}@163.com, jzhh@xju.edu.cn
[2] Institute of Image Processing and Pattern Recognition, Shanghai Jiao Tong University, 200240 Shanghai, China
jieyang@sjtu.edu.cn
[3] Knowledge Engineering and Discovery Research Institute, Auckland University of Technology, 1020 Auckland, New Zealand
rhu@aut.ac.nz

Abstract. Change detection techniques attempt to be used for remote sensing monitoring of invasive plants. A novel change detection method based on direction feature and RFLICM (an improved fuzzy C-means clustering) is proposed. Firstly, the difference image is acquired from multitemporal images. The pixel values of the difference image are updated using the template of directional neighborhood based on direction feature. The final change detection map is achieved by clustering the pixel values of the difference image using RFLICM algorithm into two disjoint classes: changed and unchanged. The results obtained by experiment are compared with some other existing state of the art methods. It is observed that the proposed method outperforms the other methods. Finally, the proposed change detection technique is applied to remote sensing monitoring of invasive plants.

Keywords: Change detection, invasive plants, Remote sensing monitoring, Spartina alterniflora, Direction feature, RFLICM.

1 Introduction

In the context of global economic integration of the 21st century, biological invasions have become the major scientific issues which are closely associated with each country's economic development and ecological security [1]. This has attracted international attention. As soon as harmful alien species invade new zones where it is suitable for the growth of the alien species, its population would sire rapidly, destroying the local ecological environment seriously and reducing biodiversity [2]. Invasive plants mainly refers to the harmful plants which brings hazards and threats to agriculture, forestry, wetlands, grasslands, freshwater, marine and other different

* Corresponding author.

F. Bian et al. (Eds.): GRMSE 2013, Part I, CCIS 398, pp. 498–509, 2013.
© Springer-Verlag Berlin Heidelberg 2013

ecosystems. Such as herbs, vines, shrubs, algae and other plants ands some obvious hazard trees. In early 2003, the list of 16 kinds of serious harm alien species is firstly announced by China, including nine kinds of plants. Spartina alterniflora is one of them [1], [3]. Estuaries bay and coastal zones are the interplay of various processes of important area among terrestrial, marine and atmospheric, and are ecosystem types of the highest value of ecosystem services per unit area. But they are also easy to be an invasion of alien species. Spartina alterniflora, which is native to the Atlantic coast, is gramineae belonging to perennial herb [4]. For promoting siltation and protecting land, etc., it was introduced from the United States in 1979. In recent years, due to the fast propagation and no local natural enemies of spartina alterniflora, spartina alterniflora occupies large swamp and wetland. Coastal environment and aquaculture sector suffer serious harm in the spreading area, now it has become an important invasive specie of the world's coastal salt marsh ecosystems [5]. In order to effectively control and legitimately take advantage of invasive alien species, spatial distribution and dynamics of the species populations that needs to be monitored and counted [6]. Personnel and boats can not walk in the growth area of the lush spartina alterniflora on the beach. It is difficult to obtain measured data. Only in the local site and at specific time, conventional field observers can obtain the relevant environmental data. Involving to large-scale species invasion, this method not only consumes time and funds, statistical accuracy and timeliness also cannot be guaranteed. Because of its accuracy and timeliness, breadth and completeness of coverage, remote sensing data has been widely used in the classification and mapping of vegetation [4]. Conventional remote sensing projects should be broken at the application level, they should make breakthroughs in new fields, for example, species diversity, biological invasions, public health, monitoring of changes in air and water quality. Study of practical and automation should be comprehensively and systematically strengthened at the technical level [7]. With the development of remote sensing technology, it provides a new option for us to monitor invasive species. Remote sensing technology can directly monitor hazard information on invasive species. The vegetation maps of host plants of invasive species are obtained after remote sensing interpretation. Potential risks and invasive channel of invasive species are assessed to achieve early warning [8]. Related research which takes advantage of remote sensing technology to obtain information of spartina alterniflora has emerged at home and abroad currently [3], [4], [5], [9], [10]. Weihua Pan *et al*. proposed a method based on a decision tree classification which can quickly and accurately monitor the growth and distribution of spartina alterniflora in the study area. Finally remote sensing distribution of spartina alterniflora is obtained at Luoyuan bay, Fu Jian, China in 2000 and 2006, respectively [3]. However, the information is not exhaustive enough. With this in mind, we propose a change detection method which can accurately calculate diffusion range, diffusion location and the boundary of the diffusion region of spartina alterniflora at Luoyuan bay, Fu Jian, China from 2000 to 2006. This provides accurate remote sensing data for prevention and management of spartina alterniflora.

2 Change Detection

In remote sensing applications, change detection aims at identifying differences in the state of a land cover by analyzing a pair of images acquired in the same geographical area at different times. Remote sensing image change detection is widely utilized to study land use/land cover dynamic, analysis of deforestation processes, assessment of vegetation changes, etc. [11]. Change detection involving remote sensing image processing includes radiometric correction, geometric correction, registration, classification, feature extraction, etc. [12]. Common change detection methods include image difference method, image ratio method, correlation coefficient method, histogram comparison method, image entropy method, etc. However, the current study shows that no single change detection method has an absolute advantage [13]. In practical applications, the appropriate change detection method should be selected according to the specific application purpose. In this paper, a direction feature and fuzzy clustering (RFLICM)-based change detection method for remote sensing monitoring of spartina alterniflora is proposed. The general scheme of the proposed method is shown in Fig. 1.

3 The Proposed Method

Consider coregistered satellite intensity images, $X_1=\{X_1(i,j),1<i<M,1<j<N\}$ and $X_2=\{X_2(i,j),1<i<M,1<j<N\}$, with a size of $M\times N$. Each is acquired at the same geographical area but at two different time instances t_1 and t_2 ($t_1<t_2$), respectively. The first step of the proposed method is to generate the difference image. Let X_D be the difference image, X_D is defined as absolute valued difference of gray value of two remote sensing images, that is $X_D=|X_2-X_1|$.

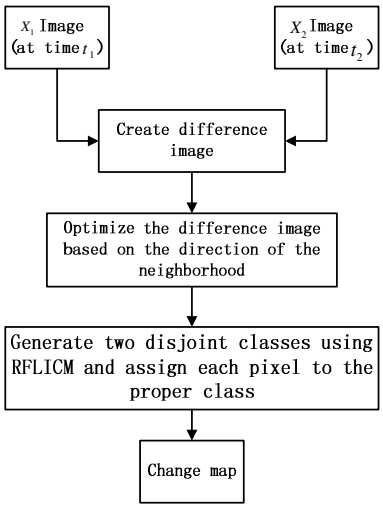

Fig. 1. The diagram of the proposed method

3.1 Direction Feature

Since remote sensing images contain both spectral and spatial information. Only the spectral information of the pixel is utilized. The influence of the space neighborhood relations among the pixels on noise, registration error and other factors is not considered. Research shows that if contextual information is fully utilized, it will help suppress speckle noise and improve the accuracy of change detection for remote sensing images [14]. As such, we use a change detection method based on neighborhood similarity [15]. It is precise since there are smooth region and edge in the images, each pixel of the images is not independent. In the smooth region, the distribution of pixel is uniform. Edge point is directional; the direction of a point needs to be determined. Ratio operator is utilized to determine the pixel direction in this paper. The average value of similar points is used to update values of the image pixel after determining the neighborhood similar point of the image pixel. For each point in the image, processing steps are as follows.

Step 1 Current point is the center. Let the size of the scale of the window 3×3, the window is a neighborhood of the center. According to the angle of 0°, 45°, 90° and 135° four different directions, the window is divided into two equal regions f_1 and f_2. In each direction $\theta = 0°, 45°, 90°, 135°$, the window is divided into two regions as a group, a total of four groups (see Fig. 2).

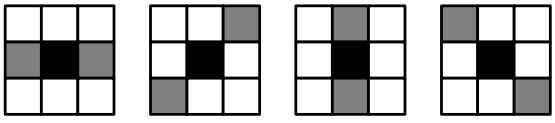

Fig. 2. Four directions. (a) 0°. (b) 45°. (c) 90°. (d) 135°.

Step 2 The average pixel values $\mu_1(\theta)$ and $\mu_2(\theta)$ in the two different areas of each group are calculated, respectively.

Step 3 The ratio of these two means of each group are calculated $r_{12} = \mu_1(\theta)/\mu_2(\theta)$, $r_{21}=\mu_2(\theta)/\mu_1(\theta)$, and let $r(\theta) = \min(r_{12}(\theta),r_{21}(\theta))$.

Step 4 Direction of the point is $\theta=\arg(\min(r(\theta)))$, i.e. the corresponding direction of $\min(r(\theta))$, $\theta = 0°, 45°, 90°, 135°$ is the direction of the pixels.

Step 5 According to the above method to determine the direction of pixels, similarity points of the current point is found in this directional neighborhood of the pixels. The template of directional neighborhood is shown in Fig. 3. The average value of points of similarity is used to update values of the image pixel after determining the neighborhood similar point of the image pixel.

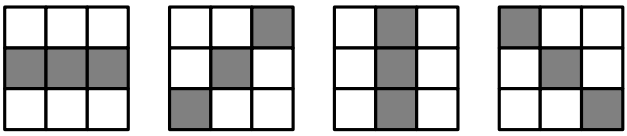

Fig. 3. Four templates of directional neighborhood. (a) 0°. (b) 45°. (c) 90°. (d) 135°.

Regarding points of the image smoothing area, after determining the direction by the Ratio operator, the result is not very different. Any determination of directional neighborhood can be selected to determine points of similarity. This has no effect on the final result of the change detection. However, taking into account the edge points, each edge point has a respective direction. In order to achieve a more accurate result of change detection, different edge points should select the respective template of directional neighborhood according to the corresponding direction.

3.2 RFLICM Algorithm

The purpose to process the difference image is to distinguish changed area from unchanged area. In this letter, we attempt to apply a fuzzy clustering-based classification algorithm to produce a binary image corresponding to the two classes, i.e., change and unchanged. Among the fuzzy clustering algorithms, fuzzy c-means (FCM) algorithm is one of the most popular clustering methods. However, the traditional FCM is very sensitive to noise since it does not consider any information about spatial context. In [16], S. Krindis *et al.* proposed a robust fuzzy local information C-means clustering algorithm (FLICM) for image segmentation. The characteristic of FLICM is the use of a fuzzy local similarity measure for guaranteeing noise insensitiveness and image detail preservation. In particular, a novel fuzzy factor is introduced into its objective function to enhance the clustering performance [17]. Recently, an improved FLICM (RFLICM) is proposed for classifying changed and unchanged regions of the change detection problem in [18]. This reformulated FLICM (RFLICM) incorporates the information about the spatial context by adding a new fuzzy factor in its objective function, in order to enhance the changed information and reduce the effect of speckle noise. The highlight of it lies in the modification of the objective function.

This algorithm is characterized by preserving image details and providing noise immunity. A novel fuzzy factor G_{ki} is introduced into the object function of RFLICM to enhance the clustering performance. This factor is formulated without setting any artificial parameter that controls the balance between the image noise and the image details. This fuzzy factor can be mathematically defined as follows.

$$G_{ki}=\begin{cases}\sum_{j\in N_i}\dfrac{1}{2+\min((c_u^j/c_u)^2,(c_u/c_u^j))^2}\times(1-u_{kj})^m\left\|x_j-v_k\right\|^2, & if \quad c_u^j\geq\overline{c_u}\\ \sum_{j\in N_i}\dfrac{1}{2-\min((c_u^j/c_u)^2,(c_u/c_u^j))^2}\times(1-u_{kj})^m\left\|x_j-v_k\right\|^2, & if \quad c_u^j\geq\overline{c_u}\end{cases} \tag{1}$$

where the ith pixel is the center of the local window, the jth pixel represents the neighboring pixels falling into the window around the ith pixel, v_k represents the prototype of the center of cluster k, and u_{kj} represents the fuzzy membership of the gray value j with respect to the kth cluster, C_u is the local coefficient of variation of the

central pixel, C_u^j represents the local coefficient of variation of neighboring pixels, $\overline{C}_u$ and is the mean value of C_u^j that is located in a local window. Here, C_u is defined as

$$C_u = \frac{\mathrm{var}(x)}{(\overline{x})^2}, \tag{2}$$

where var(x) and $\overline{x}$ are the intensity variance and the mean in a local window of the image, respectively. Let $X=\{x_1,x_2,\ldots,x_N\}$ is the set of N patterns, x_i is the ith pattern $\in X$ and $\| x_i - v_k \|^2$ (Euclidean norm) is the dissimilarity measure between the sample x_i and the kth cluster center. By using the definition of G_{ki}, the objective function of the RFLICM can be defined in terms of

$$J_m(X;U,V) = \sum_{i=1}^{N}\sum_{k=1}^{c}\left[u_{ki}^m \|x_i - v_k\|^2 + G_{ki}\right], \tag{3}$$

where $U=[u_{ki}]\in M_{fcn}$, fuzzy partition matrix of X, following two constraints must be satisfied as

$$\sum_{k=1}^{c} u_{ki} = 1, \tag{4}$$

where $u_{ki}\in[0,1]$. The calculation of the membership partition matrix and the cluster centers are performed as

$$u_{ki} = \frac{1}{\sum_{j=1}^{c}\left(\frac{\|x_i - v_k\|^2 + G_{ki}}{\|x_i - v_j\|^2 + G_{ji}}\right)} \tag{5}$$

and

$$v_k = \frac{\sum_{i=1}^{N} u_{ki}^m x_i}{\sum_{i=1}^{N} u_{ki}^m}, \tag{6}$$

respectively, where $m(>1)$ is a parameter, called fuzzifier, which controls the fuzziness of the algorithm. The RFLICM algorithm is putted in Table 1.

4 Experimental Results

Firstly the effectiveness of the proposed algorithm is validated, and then the proposed algorithm is applied to remote sensing monitoring of plant invasions. We compare the proposed method with the following two well-known change detection approaches, i.e., UDWT-KMEANS [19] and NSCT-KFCM [20]. The two experiments have been carried out for different purposes.

Table 1. RFLICM algorithm

Input: Unlabeled data set consisting of N patterns.
Output: Prototypes V and fuzzy partition matrix U.
Step 1: Set the number C of the cluster prototypes, fuzzification parameter m and the stopping condition ε.
Step 2: Initialize random the fuzzy partial matrix.
Step 3: Compute each cluster center using (**6**).
Step 4: Compute all possible distances $\|x_i - v_k\|^2$:k=1,2,…,C; i=1,2,…,N.
Step 5: Update fuzzy partition matrix using (**5**).
Step 6: Compute $\Delta=\|U_t - U_{t-1}\|$; t denotes tth iteration.
Step 7: Check if $\Delta<\varepsilon$;
Step 8: If the above condition is not true go to Step 3; otherwise, Stop.

4.1 Algorithm Verification

The first experiment aims at the analysis of the effectiveness of the proposed change detection algorithm. In order to analyze the performance of the proposed approach both qualitatively and quantitatively, we consider a real data set. For Mexico data remote sensing images (of size 512×512) acquired by the Landsat Enhanced Thematic Mapper Plus (ETM+) sensor of the Landsat-7 satellite, in an area of Mexico on April 2000 and May 2002 are considered. Fig. 4(a) and Fig. 4(b) show channel 4 of the 2000 and 2002 images, respectively. In order to make a quantitative evaluation of the proposed method, the available ground truth (reference image) is given (see Fig. 4(c)).

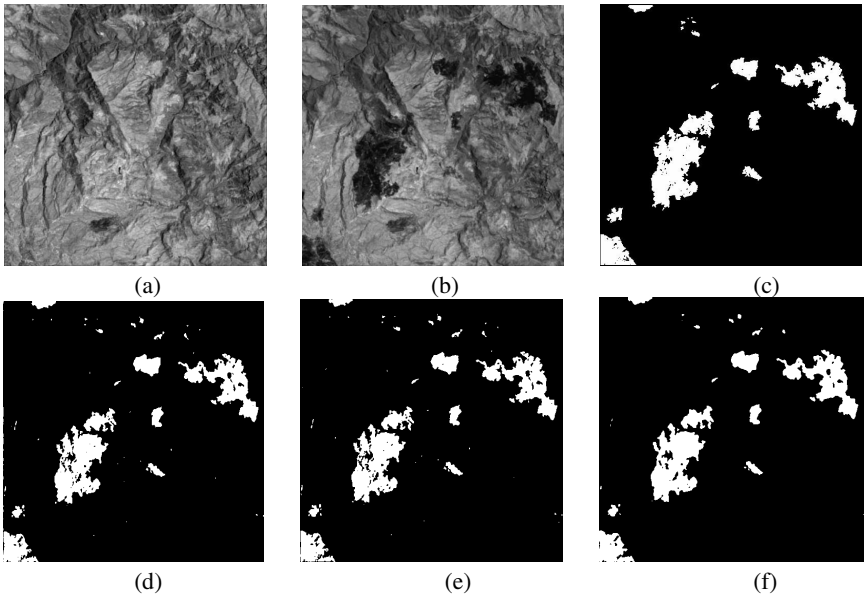

Fig. 4. Change detection result of the Mexico data. (a) April 2000. (b) May 2002. (c) Reference image. (d) UDWT-KMEANS. (e) NSCT-KFCM. (f) The proposed method.

The qualitative results of the various methods are shown in Fig. 4(d)-(f). Fig. 4(d) and Fig. 4(e) show the result of UDWT-KMEANS method and the result of NSCT-KFCM method, respectively. Fig. 4(f) shows the result of our proposed method. The result of the proposed method is likely to be better than the other two methods because of noise plaques in Fig. 4(f) are less than those in Fig. 4(d) and Fig.4(e). Moreover, Fig. 4(f) is the closest to the reference image.

For the quantitative assessment, the following quantities have been computed for each change map. *TP* (True Positive) is the number of correctly identified changed pixels, *TN* (True Negative) is the number of correctly identified unchanged pixels, *FN* (False Negative) is the number of wrongly identified changed pixels, *FP* (False Positive) is the number of wrongly identified unchanged pixels. Several metrics are derived from the above quantities to assess the performance of an algorithm [21]. In this paper, the following metrics are adopted.

1 Undetected rate:

$$P_{Ur} = \frac{FP}{TP + FN + FP} \times 100\% \quad . \tag{7}$$

2 False alarm rate:

$$P_{Ur} = \frac{FP}{TP + FN + FP} \times 100\% \quad . \tag{8}$$

3 Percentage correct classifications (PCC):

$$PCC = \frac{TP + TN}{TP + FP + TN + FN} \quad . \tag{9}$$

4 Kappa coefficient:

$$\begin{aligned} &Kappa = \frac{pr_0 - pr_c}{pr_c} \\ &pr_0 = \frac{N - FN - FP}{N}, \quad pr_c = \frac{TP + FN}{N} \times \frac{TP + FP}{N} \times \frac{TN + FP}{N} \times \frac{TN + FN}{N} \end{aligned} \quad , \tag{10}$$

where the concordance rate Pr_c is concordance rate of expectation, N is the total number of pixels in the image.

Above results of qualitative analysis gives a rough idea about the quality of change detection method, and the quantitative comparison is given in Table 2. It can be seen from Table 2 that the proposed method provides an overall accuracy better than that obtained by UDWT-KMEANS method and NSCT-KFCM method. The comparison shows the superiority of the proposed method.

Table 2. Quantitative comparison of change detection results

Method	Undetected rate	False alarm rate	PCC	Kappa
UDWT-KMEANS	13.78	4.85	0.9809	0.8868
NSCT-KFCM	14.18	3.45	0.9822	0.8936
The proposed method	12.82	3.56	0.9834	0.9017

4.2 Application

In the second experiment, the proposed change detection method is applied to remote monitoring of plant invasions. The rapid spreading and soaring of spartina alterniflora has seriously endangered the safety of the local farming areas and waterways in Luoyuan bay, Fujian, China. The data set is acquired in 2000 and 2006 by Landsat TM/ETM+ in Luoyuan bay, Fujian, China. There is a lot of character information about the earth's surface in original remote sensing images. The vegetation spectral characteristics which are among the characteristic information coexist with other non-vegetation information. To this end, Weihua Pan *et al.* put Landsat TM / ETM + images in 2000 and 2006 as data source. First the geometric correction and other processing in implemented by taking advantage of 1:5000 topographic maps, and then the normalized difference vegetation index and tasseled cap transformation processing of images are carried out. Weihua Pan *et al.* proposed spartina alterniflora remote sensing monitoring method based on decision tree classification. The distribution and change trends of Luoyuan bay's spartina alterniflora is obtained from 2000 to 2006 in Fujian, China (see Fig. 5). We apply the change detection techniques for remote sensing monitoring of spartina alterniflora.

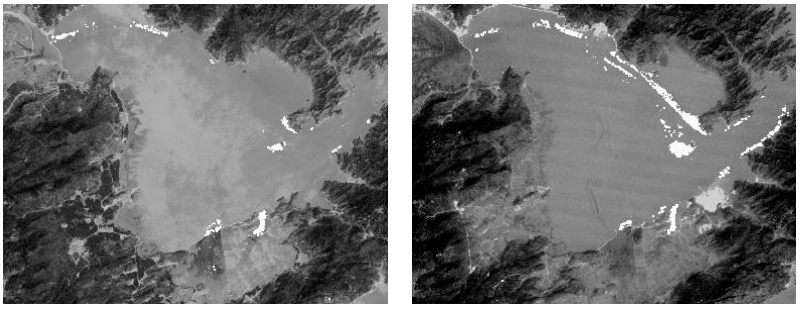

(a) (b)

Fig. 5. Remote sensing distribution map of spartina alterniflora in Luoyuan bay, Fujian, China. (a) In 2000. (b) In 2006.

Two o'clock remote sensing images are matched by ENVI Software. There are changes of some areas due to the earth's surface changes caused by other factors in the images. So we only study the growing areas of spartina alterniflora (see Fig. 6). After

the pretreatment, our proposed change detection method, UDWT-KMEANS method and NSCT-KFCM method are applied to growing area monitoring of spartina alterniflora. The results of three different methods are shown in Fig. 7. From comparison of the results, there are less white spots in Fig. 7(c) than in Fig. 7(a) and in Fig. 7(b). The proposed method is better than the other two methods, and with good robustness to the noise. Feasibility of change detection for remote sensing monitoring of invasive plants is validated.

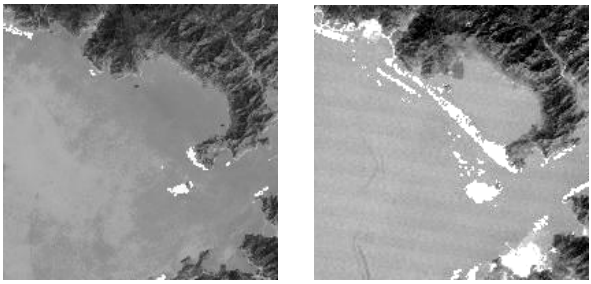

(a) (b)

Fig. 6. Remote sensing distribution map of spartina alterniflora after coregistration. (a) In 2000. (b) In 2006.

(a) (b) (c)

Fig. 7. Experimental results of three different methods. (a) UDWT-KMEANS. (b) NSCT-KFCM. (c) The proposed method.

5 Conclusion

A change detection method based on direction feature and fuzzy clustering (RFLICM) is proposed for remote sensing monitoring of spartina alterniflora in this paper. The proposed change detection method has following advantages: 1) this method not only takes into account the direction of pixels, but also the relations of spatial neighborhood among pixel. The Influence of noise, registration errors and other factors is effectively suppressed. Detection accuracy of the edge of change region is guaranteed; 2) RFLICM is robust to outliers, the characteristics of RFLICM include noise immunity, preserving image details without setting any artificial parameter and being applied directly to the

original image. Experimental results have shown that the proposed method owns acceptable performances on change-detection tasks, and outperforms comparison algorithm.

The proposed change detection algorithm has been successfully applied in the remote sensing monitoring of invasive plants. Experimental results show that change detection results of a spreading region of Spartina alterniflora are consistent with the actual results. Compared with the visual interpretation, change detection results can accurately express the boundary and location spreading region of invasive plants. Change detection techniques not only improve the efficiency of monitoring for invasive plants, but also the accuracy of monitoring. In this paper, change detection techniques for monitoring invasive plants is an attempt, the experimental results are valid. Change detection techniques for monitoring invasive plants need to be more widely extended and validated.

Acknowledgements. We gratefully thank the financial support by International Cooperative Research and Personnel Training Projects of the Ministry of Education of the People's Republic of China.

References

1. Li, X., Jin, H.: Study on Invasive Plant Species. Journal of Agriculture 3(03), 39–43 (2013)
2. Wan, H., Wang, C., Ya, L., et al.: Monitoring an invasive plant using hyperspectral remote sensing data. Transactions of the CSAE 26 (suppl. 2), 59–63 (2010)
3. Pan, W., Chen, J., Li, L., Jiayi, W.: Dynamical Monitoring of Spartina Alterniflora Invasion by Using Remote Sensing Data in Luoyuan Bay, Fujian. Chinese Agricultural Science Bulletin 25(13), 216–219 (2009)
4. Zhang, Y., Lu, J.: Progress on Monitoring of Two Invasive Species Smooth Cordgrass (Spatina alterniflora) and Water Hyacinth (Eichhornia crassipes) by Remote Sensing. Bulletin of Science and Technology 26(1), 130–137 (2010)
5. Pan, W., Chen, J., Zhang, C., et al.: Dynamic Monitoring Analysis of Expansion of Spartina alterniflora in Fujian. Chinese Journal of Agrometeorology 32 (supp.1), 174–177 (2011)
6. Mack, R.N., Von Holle, B., Meyerson, L.A.: Assessing invasive alien species across multiple spatial scales: Working globally and locally. Frontiers in Ecology and the Environment 5(4), 217–220 (2007)
7. Gong, P.: Remote sensing of environmental change over China: A review. Chinese Science Bulletin 57(16), 1379–1387 (2012)
8. Xu, R.: A few thoughts about biological invasions. Journal of Environmental Entomology 30(1), 80–82 (2008)
9. Huang, H., Zhang, L.: Remote sensing analysis of range expansion of spartina alterniflora at Jiuduansha shoals in Shanghai, China. Journal of Plant Ecology 31(1), 75–82 (2007)
10. Pu, R., Gong, P., Tian, Y., Miao, X., Carruthers, R.I., Anderson, G.L.: Invasive species change detection using artificial neural networks and CASI hyperspectral imagery. Environ. Monit. Assess. 140, 15–32 (2008)
11. Mishra, N.S., Ghosh, S., Ghosh, A.: Fuzzy clustering algorithms incorporating local information for change detection in remotely sensed images. Applied Soft Computing 12(8), 2683–2692 (2012)

12. Radke, R.J., Andra, S., Al-Kofahi, O., et al.: Image Chang Detection Algorithms: A Systematic Survey. IEEE Trans on Image Process 14(3), 294–307 (2005)
13. Li, S., Li, Y., An, Y.: Automatic Recognition of Landslides Based on Change Detection. Remote Sensing Information 1, 27–31 (2010)
14. Jiang, L., Liao, M., Zhang, L., et al.: Change Detection in Multitemporal SAR Images Using MRF Models. Geomatics and Information Science of Wuhan University 31(4), 312–315 (2006)
15. Zhang, X., Li, H., Jiao, L.: A change detection algorithm based on object feature for SAR image. In: The Second International Asia-Pacific Conference on Synthetic Aperture Radar, APSAR 2009, Xian, China, pp. 693–696 (2009)
16. Krinidis, S., Chatzis, V.: A robust fuzzy local information C-means clustering algorithm. IEEE Trans. Image Process. 19(5), 1328–1337 (2010)
17. Ma, J., Gong, M., Zhou, Z.: Wavelet Fusion on Ratio Images for Change Detection in SAR Images. IEEE Geoscience and Remote Sensing Letters 9(6), 1122–1126 (2012)
18. Gong, M., Zhou, Z., Ma, J.: Change Detection in Synthetic Aperture Radar Images based on Image Fusion and Fuzzy Clustering. IEEE Trans. Image Process. 21(4), 2141–2151 (2012)
19. Celik, T.: Multiscale Change Detection in Multitemporal Satellite Images. IEEE Geoscience and Remote Sensing Letters 6(4), 820–824 (2009)
20. Wu, C., Wu, Y.: Multitemporal images Change Detection using nonsubsampled contourlet Transform and Kernel Fuzzy C-Mean Clustering. In: International Symposium on Intelligence Information Processing and Trusted Computing, TPTC 2011, Wuhan, China, pp. 96–99 (2011)
21. Xin, F.: Change Detection in Remote Sensing Imagery Based on Fisher Classifier and Computational Intelligence. Xidian University, Xian (2011)

Approach to Real-Time Mapping, Using a Fuzzy Information Function

Stanislav Belyakov, Igor Rozenberg, and Marina Belyakova

Southern Federal University, Chekhova st., 22, 347928, Taganrog, Russian Federation
beliacov@yandex.ru

Abstract. In this article we consider the problem of real-time mapping that is to create a digital map of situations, recognized from the source of information of not a cartographic character. An approach to mapping is offered, it is based on a special imaging procedure that maximizes the information content of the working area of the map. The model of the visualization control is described. The model is based on the intelligent estimation procedures informative. Estimation uses a granular representation of fuzzy function of information content. Cartographic description of the informativeness is considered. Image defects caused by the imperfection of algorithms for automatic mapping are alanyzed. Visual and procedural defects were marked. The model of the map visualization with defects of displaying of uncertain situations is built. The proposed approach will reduce the risk of making wrong decisions due to the incomplete and irrelevant maps of geographic information systems.

Keywords: real-time mapping, geographic intellectual system, automatic mapping, uncertainty, fuzzy function.

1 Introduction

Mapping plays an important role in the analysis and management of ecosystems. On the one hand, the maps are the basis of a visual representation of spatial data collected, on the other hand, an instrument for decision-making in difficult situations. In the first case, the user-analyst is exploring the real world through a graphical image of the data. In the second case, the user builds cartographic objects that show the solution of the application. Required software tools for these tasks are provided by modern geographic information systems (GIS) [1-3].

The use of cartographic visualization is important in cases where the hard forming problems are solved in uncertainty and a lack of information. Visual mapping images of situations, processes and objects are useful because they stimulate the intuitive creative thinking and encourage the use of deep knowledge of the decision-maker. In this case the main mode of GIS is the dialogue with the user-analyst, aimed at building and studying map images. Visual analysis of the working area of the map, using all sorts of software tools for analysis, the combination of layers and types of cartographic image creates specific conditions for the solution of complicated intellectual problems [2].

F. Bian et al. (Eds.): GRMSE 2013, Part I, CCIS 398, pp. 510–521, 2013.
© Springer-Verlag Berlin Heidelberg 2013

Maps of any part of the earth's surface are continuously becoming obsolete. Every geographical map published by the time of its use contains incomplete data. This is caused by the rupture of the rate of the environment changing and the speed of creating and updating maps. Cartographic production standards require updating and adjustment of cards in a period of 5-7 years or more, which eliminates the fixation of the event in present. For example, the events of a week or a month ago might be reflected on the map after several years in average [4].

Updating the GIS map data promptly is difficult for a number of objective reasons. In particular, the individual steps of creating a map cannot be formalized because it involves the use of knowledge, skills and experience of expert cartographers. This increases the time map updates. In addition, for mapping territories the problem of the displaying the "fast" processes and events is not set. Every geographical map is a generalization of the observations made over a long period of time. The frequency of updating the content of each map is determined by the relevant regulations [6].

In order to make effective decisions in the management of ecosystems completeness, reliability and relevance of the map data are required. The low quality of the map creates the risk of damage due to an incorrect decision. This raises the problem of real-time mapping, suggesting the creation of cartographic images in the flow rate of the real processes. This problem is known for a long time and an effective solution is not found yet [3-7]. Manual mapping in real time has high cost and does not provide the required level of reliability. Automatic mapping gives a low quality of the final product [6,7].

2 Setting a Problem

The problem of real-time mapping can be considered as a problem of providing the required quality of mapping spatial data visualization [8]. The difference of this approach is the use of procedures of maximizing the information content of cartographic images. It is supposed that the function of building the most informative version of the map is assigned to the GIS, including inconsistent and possibly incorrect objects of the map in terms of standards of mapping. Analysis has shown that this approach has not previously been investigated.

The further presentation of results of research is built in the following way:

- the concept of information content is introduced and the task of managing cartographic visualization is formalized;
- the way of describing the function of information content in a fuzzy way is offered;
- the image defects that occur when visualizing incorrectly defined map objects are considered;
- the effectiveness of the proposed approach is estimated.

3 The Model of Visualization of the Working Map Area

Solving the applied problem with the help of GIS, the user implements a procedure of mapping analysis [9]. At the heart of the procedure is the creation of a working area of the global map, which the GIS contains.

The working map area $\Omega = \{ \omega_1, \omega_2, ... \omega_n \}$ that consists of map objects ω_i is a subset of objects $m_W \subseteq \Omega$ that describes the fragment of a map with boundaries

$$L_W = \{ S_W, T_W, C_W, E_W \},$$

where S_W - spatial boundary, T_W - temporal boundary, C_W -semantic boundary, E_W - pragmatic boundary. The semantic boundary C_W is a set of classes of objects and relationships, which are described in the GIS, E_W is a description of the limits of applicability of the map constructed. The specific work area with boundaries is generated by the sequence of request from the client to the GIS server:

$$Q_i(X_S, X_T, X_C, X_E), i = \overline{0, N},$$

where X_* are, accordingly, the spatial, temporal, semantic and pragmatic parameters of a single request. $Q_i(X_S, X_T, X_C, X_E)$ is a predicate of the request which in modern GIS is built by user through the system of dialogue menus or is directly set as an expression in SQL.

The structure of the workspace $m_W \subseteq \Omega$ can be represented as the union of two sets:

$$m_W = B \bigcup E ,$$

$$B \subseteq \Omega : \forall \omega_i \in B \Rightarrow \exists Q_j(X_S, X_T, X_C, X_E) = true, j = \overline{1, N}, i = \overline{1, |\Omega|},$$

$$B \bigcap E = \varnothing, E \subseteq \Omega.$$

The set B is a skeleton of the request which is determined by predicates of requests, E - environment of the skeleton, in other words, it is subset of map objects that provides the continuity of maps [4], and semantic entirety of the work area. The entirety is formed by using the expert rules of construction of the image of expert response $K(B, \Omega)$ to the skeleton of request B :

$$\omega_i \in E \Rightarrow K(B, \Omega) = true, i = \overline{1, |m_W|}.$$

Expert rules $K(B, \Omega)$ represent knowledge about how to construct the mapping images useful for solving the problem. Application of the rules $K(B, \Omega)$ leads to a reduction in redundancy of cartographic images and improvement of their informational content.

Information content $I(m_W)$ of any work area is a related, subject determined value. Its value is validly estimated only in the narrow confines of a particular class of

applied problems that can be solved by a certain group of users. General restrictions following from the specification of a person's perception of graphic images are as follows:

$$| m_W \models 0 \Rightarrow I(m_W) = 0 ,$$
$$| m_W \models \infty \Rightarrow I(m_W) = 0 .$$

The level of information content cannot be estimated by any other way except a set of expert rules $K_I(m_W)$. Rules reflect the subjectivity and ambiguity that is inherent in the evaluation of information content.

Expert knowledge in the form of rules $K(B,\Omega)$ and $K_I(m_W)$ represent the "reasonable" rendering of map images strategy [10]. The difference between described "intellectual" visualization and the traditional one is in support of subjective utility of map images. Not only the objects that meet the predicate of the request are visualized, but all those who fill a cartographic image with a meaning.

The management of visualization is in solving the problem

$$\begin{cases} I(m_W) \to max, \\ | m_W \models m^*, \\ m_W : Q_i(Xs, X_T , X_C , X_E) = true, i = \overline{1, N} \end{cases}$$

To solve the problem, the GIS should be equipped with software mechanism of expert evaluation $I(m_W)$ and a mechanism of adding and removing mapping objects in the working area. The GIS works in a following way:

• The user authenticates himself at the beginning of a session with GIS. This allows us to classify and choose it from a database of expert rules $K(B,\Omega)$ and $K_I(m_W)$. The effectiveness of further work in the session depends on how adequate classification is. If necessary, you can perform a "reclassification", i.e. start a new session;

• The GIS server builds workspace m_W of maximal information content and sends it to the client for each of the next request from the client. Accounting of the limited resources of the client $m_W \models m^*$ ensures the completeness of the result and security of interaction.

4 The Description of Information Function

Estimating the information content of the workspace $I(m_W)$ is the basis of the process of visualization control. Setting the function of information content is dependent on a number of factors:

- the total number of map objects in the work area;
- the distribution of copies and classes of objects by the level of significance of the problem to be solved;

- the distribution by the level of importance of instances and classes of relations between objects;
- the user's work experience with cartographic materials;

It can be said that information function depends on many variables $X = \{ x_1, x_2, ..., x_M \}$:

$$I(m_W) = F(X).$$

The number of variables is not known beforehand. The multidimensionality of the space of factors $\{ x_1, x_2, ..., x_M \}$ creates serious difficulties in finding the analytical relationship $I(m_W)$. Therefore it is proposed to evaluate the informative content by a fuzzy description. The description is based on expert data. This approach is explained by the high degree of incompleteness and uncertainty about the behavior of the function $F(x_1, x_2, ..., x_M)$. Let us consider the model of granular representation of the information function [11,12].

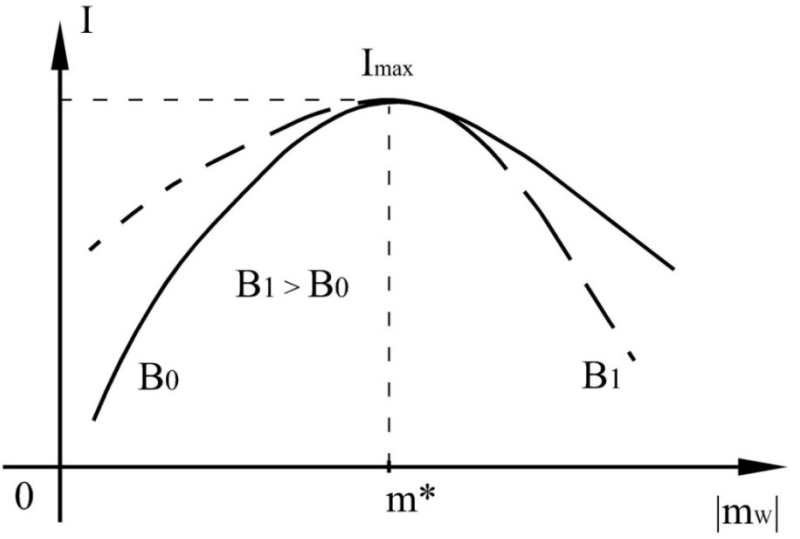

Fig. 1. The information function

The analysis of the analysts' behavior shows that the function $I(m_W)$ can be characterized by the curve in Fig. 1. The shape of the curve reproduces the qualitative features of the information content changes. With a small number of graphic objects in the workspace m_W information content is not high and grows as you add new items. The growth rate of information content should be related to the adding of objects from the environment (*E*), because the information content of skeleton *B* represents the minimum level that the workspace gets by the user's request.

The dotted line shows the information curve for skeleton B_1 with a large number of objects ($| B_1 |\rangi| B_0 |$).

Where I_{max} is the highest possible level of workspace's m_W information content. Qualitative analysis of the curve in Fig. 1 allows us to enter at least three granules $\{ I_L, I_M, I_R \}$. Each granule defines the area in space $I \times N$ in a fuzzy way:

$$I_L = \{ \mu_{Lk} / (i_{Lk}, N_{Lk}) \}, I_L \subset I \times N,$$
$$I_M = \{ \mu_{Mk} / (i_{Mk}, N_{Mk}) \}, I_M \subset I \times N,$$
$$I_R = \{ \mu_{Rk} / (i_{Rk}, N_{Rk}) \}, I_R \subset I \times N.$$

Where μ_{Ak} is the degree of belonging of the point (i_{Ak}, N_{Ak}) with the number k to a granule with an index A, an each pair (i_{Ak}, N_{Ak}) is a value of information content i_{Ak} with a number of objects N_{Ak}.

Please note that the definition of function in the space $I \times N$ is a simplification. Simplification is used deliberately to implement controls.

Granule I_L represents an area of increasing information content for cartographic images of low complexity of perception. Granule I_M is the area of the most informative images with the utmost level of perception. Granule I_R is the area of falling informative content of images difficult to perceive.

For the use and description of the granules $\{ I_L, I_M, I_R \}$, we suggest using the way of cartographic representation. The essence of method is in constructing figurative and symbolic model of granules. The model describes the distribution of the importance of classes and copies of objects and relations of the work area; also it describes the relationship between the grade of information content and the total number of objects in the workspace. Demonstrativeness of the cartographic representation, from our point of view, plays a decisive role in obtaining reliable and coordinated knowledge from expert GIS users [6,7].

Cartographic representation has a form of atlas - a set of maps that show the behavior of informativeness. Formally, this means that the information function is a superposition of functions

$$I(m_W) = F(x_1, x_2, ..., x_M) = F(Y_1, Y_2, ..., Y_H),$$

where

$$H < M, Y_i = Y_i(X_i), X_i \subset X, i = \overline{1, M}.$$

Each map of atlas shows the dependence $Y_i(X_i)$. The coordinate axes can deal with terms of different complexity. Each map is a graphic "projection" of the multidimensional space of concepts “problem domain”. The problem of mapping $I(m_W)$ thus reduces to the determination of a set of "projections" with the required properties.

Let us consider the example of mapping. We assume that the atlas consists of two maps: the first allows determining a preliminary assessment of informativeness, the second determines the granule, which contains the analyzed workspace of the map. Formally

$$I(m_W) = F(I_P, |m_W|), I_P = Y_1(\hat{n}, \hat{c}).$$

The value of I_P is determined from the set {«Low», «Middle», «Sufficient», «High»}. Any value of I_P subjectively displays a preliminary evaluation of informativeness. The value of I_P depends on the use of layers, objects and relations of the workspace map. Fig. 2 shows the example of a map that binds used layers, objects and relationships that are clustered into three clusters $\{C_0, C_1, C_2\}$. The coordinates of any point on the map is $(\hat{n}, \hat{c})$ where $\hat{n}$ is a fuzzy evaluation of the relative number of objects and workspace relations, $\hat{c}$ is the name of the most significant cluster of objects and relations in the work area. For example in Fig. 3 point I_{Pk} displays workspace that contains some $\hat{n} = 40\%$ elements of the cluster $\hat{c} = C_0$. In a cluster C_0, for example, were included:

- examples of "Automobile filling station";
- examples of the relation "located near businesses of repairing of motor vehicles";
- layers of "parking", "motorway", "Restaurants", "repair", "Hotels", "ATM";
- relations "Crosses", "Attached", "Located in the danger zone."

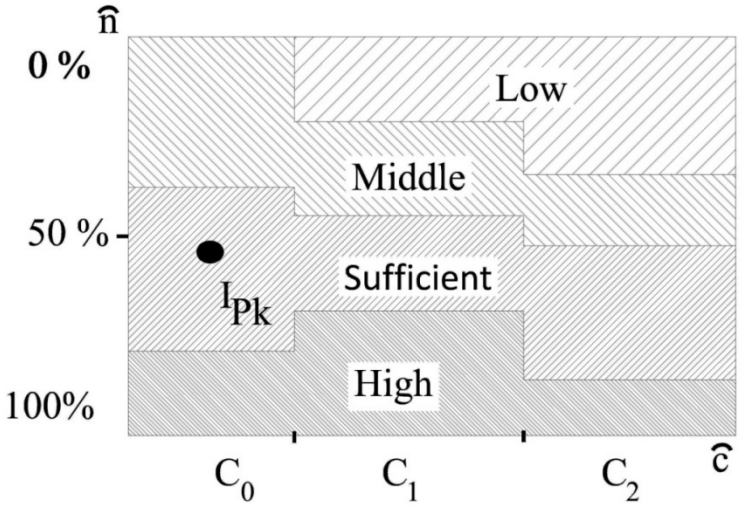

Fig. 2. The map of preliminary informativeness

The map of prepaid informative content is zoned. Each area corresponds to one of the values of the set {«Low», «Middle», «Sufficient», «High»}.

Figure 3 shows a map of zoned granules of information content $F(I_P,|m_W|)$. In this example of the map the fuzziness of granules is not displayed for the sake of simplicity. The coordinates of any point $(I_P,|m_W|)$ clearly belong to a single granule. Having determined I_{Pk} on the map (Fig. 2), counting the total number of objects in the workspace m_W, you can accurately match the workspace to the granule of information content on the map (Fig. 3). All procedures are implemented in software.

5 The Visualization of not Completely Certain Situations

Getting the operational spatial data creates a necessity to access heterogeneous systems, fixing things and events of the real world. The Internet plays a special role [13]. For example, the information about the natural anomalous situation can be got as a message from the news flow (RSS), published space or aerial photos, video streams from Web-cameras, reports from the electronic media, from personal blogs, from specialized communities in social networks, as well as from the map services. Often this information is not metric and does not contain an explicit gridding. However, its value in the case of responsible decision-making is very high. The importance of information is able to compensate for the lack of accuracy and completeness.

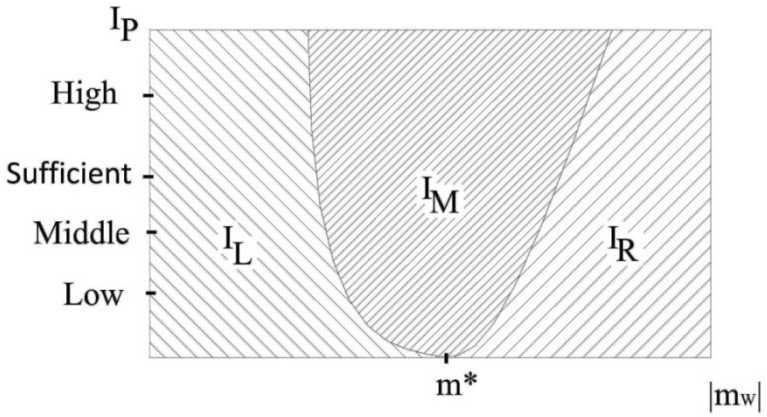

Fig. 3. The map of the arrangement of information content granules

Let us assume that GIS has a search engine that can find information resources for later retrieval of spatial data. GIS also has a set of programs for identification and mapping of situations. As is well known [6], automatic mapping is not perfect. Created mapping objects can disrupt the logic of the map.

Let us consider the model of visualization for the case when the objects are added to the map, images of which are not consistent with the rest of the map.

Let us describe the set of mapping objects built by the recognition of situations outside the world as $S = \{ s_i \}$. The information base of GIS in the process of real-time mapping is complemented by multiple map objects S:

$$\overline{\Omega} = \Omega \cup S \ .$$

Unlike any other object $\omega_i \in \Omega$, the space-time coordinates and semantic attributes $s_i \in S$ are not completely reliable because of the limited capacity of the subsystem recognition [11].

Adding situations to the work area and its visualization with maximizing of information content

$$I(B \cup E \cup S)$$

Cannot be done by a method discussed above. The reason is that the visualization of situations $s_i \in S$ creates defects of cartographic displaying. The defect appears, for example, like an overlay of images of situations $V(s_i)$ and objects of cartographic basis:

$$V(s_i) \cap V(\omega_j) \neq \varnothing \ .$$

Analysis has shown that defects in the mapping image can be divided into two classes.

Fig. 4. The example if image with situation $s_i \in S$

Defects of the first class are visual defects that create a misconception about the objects whose images are overlapped on each other. There is a danger that any of the objects involved in the overlapping during the visual analysis of the map would be

perceived incorrectly. Fig. 4 shows an example of a map with the representation of two situations: the both are displayed as polygonal objects of different colors. The situation depicted in gray overlapped on the line of the railway. However, the map is recognized by the analyst's truly. In contrast, the situation displayed by an area objects in black, hides an important object to analyze - the bend of the road. The visual recognition of the road would be incorrect.

Procedural defects form a second class. Defects of this class produce incorrect results when the procedures of cartographic analysis are performed. The example in Figure 4 shows how an error of estimation of the topological relation "to be around" occurs. If you request "to find all objects of situations that are close to the railway," the result will be incorrect. The object of situation shown in gray is for "overlap". The functionality of a particular GIS determines the possibility of procedural defects. It may be that the GIS does not have evaluation procedures of topological relations. Then the procedural defects are not possible.

Despite the fundamental differences in the causes of occurring and influence of defects, we can claim that any defect reduces the information content of the cartographic image. In this case the procedure of maximizing the information content can take one of two actions:

- Removing the object $s_i \in S$ that raises the defect;
- Correct the defect by removing the objects $\omega_i \in \Omega$.

The information content of each option for selection of the desired action should be estimated. Suppose that after the elimination of defects the set $D = \{ d_i \}$ of objects removed from the workspace is formed. Then the modified work area described by the set

$$\tilde{m}_W = B \cup E \cup S \setminus D .$$

Adding uncertain situations to the workspace has the effect, if the following inequality is right:

$$I(B \cup E \cup S \setminus D) > I(B \cup E).$$

Finally, the procedure of visualization control can be described as follows:

- to build for the next request $Q_i(X_S, X_T, X_C, X_E)$ skeleton B and the environment E;
- assess the information content of the constructed workspace;
- to construct objects $S = \{ s_i \}$ that display information from external sources;
- to identify the visual and procedural defects and to find objects which removing will increase the information content of cartographic images by a linear search.
- to synchronize the workspace with the GIS client.

6 Conclusion and Discussion

The effect of the using of the proposed approach is defined as follows.

The main factor in improving the quality of real-time mapping should be considered as the adequacy of the expert description of information content to subjective perception of cartographic images. Granular representation of the information function represents unclearness and incompleteness that are specific for expert knowledge about the information content.

An important factor in the quality of real-time mapping is also the presence of a search GIS engine, able to extract spatial data from data sources of different nature. The more important are the data, the greater may be deviation from the standards of cartographic representation. The proposed approach puts the visual analysis of maps first. With the support of GIS activates a powerful mechanism inherent to men - an intuitive understanding of the meaning of the map.

Some of the quantitative evaluations of the gain from using the approach can be done as follows. We assume that the wrong decision leads to damage U . The damage occurs when the map contains no objects $S = \{ s_i \}$. The damage is reduced if such objects appear on the map and analyst successfully identifies the state of the outside world. Because the information content is maximized, it can be assumed that an absolutely accurate identification can be prevented only by the lack of the effectiveness of programs of the recognition of external situations. We denote p the probability of correct recognition of individual situation. Then, using the formula of the binomial distribution

$$P_N(k) = \binom{N}{k} p^k (1-p)^{N-k}$$

we can calculate the probability of that k situation would be recognized from N actually existing ones. Medium damage in this case is calculated as

$$\overline{U} = (1 - P_N(k))U \ .$$

This expression allows you to evaluate the effect depending on the parameters of the recognition system (probability p), and the specific of the decision making process (values N and k).

References

1. Egenhofer, M.J.: Toward the Semantic Geospatial Web. In: 10th ACM International Symposium on Advances in Geographic Information Systems (ACM-GIS-2002), pp. 1–4. ACM Press, Virginia (2002)
2. Erle, S., Gibson, R., Walsh, J.: Mapping Hacks – Tips & Tools for Electronic Cartography. O'Reilly Press, Sebastopol (2005)
3. Cartwright, W., Peterson, M.P., Gartner, G.: Multimedia cartography. Springer, Berlin (2007)

4. Li, W., Li, L., Goodchild, M.F., Anselin, L.: A geospatial cyberinfrastructure for urban economic analysis and spatial decision-making. ISPRS International Journal of Geo-Information 2, 413–431 (2013)
5. Konecný, M., Bandrova, T.: Proposal for a Standard in Cartographic Visualization of Natural Risks and Disasters. In: Joint Symposium of Seoul Metropolitan Fora and Second International Workshop on Ubiquitous, Pervasive and Internet Mapping, Seoul, Korea, pp. 165–173 (2006)
6. Harrie, L., Weibel, R.: Modelling the overall process of generalisation. In: Ruas (2007)
7. Mackaness, W.A., Sarjakoski, L.T. (eds.): Generalisation of Geographic Information:Cartographic Modelling and Applications. Series of International Cartographic Association, pp. 67–87. Elsevier
8. Pettit, C., Cartwright, W., Bishop, I., Lowell, K., Puller, D., Duncan, D. (eds.): Landscape Analysis and Visualisation, Spatial Models for Natural Resource Management and Planning. Springer, Berlin (2008)
9. Dent, B.D.: Cartography: Thematic map design, 2nd edn. Wm. C. Brown Publishers, Dubuque (1990)
10. Sowa, J.F.: Knowledge representation: Logical, philosophical, and computational foundations. Brooks Cole Publishing Co., Pacific Grove (1999)
11. Luger, G.F.: Artificial Intelligence: Structures and Strategies for Complex Problem Solving. Addison Wesley (2004)
12. Zadeh, L.: Towards a Theory of Fuzzy Information Granulation and its Centrality in Human Reasoning and Fuzzy Logic. Fuzzy Sets and Systems 90, 111–127 (1997)
13. Sui, D., Elwood, S., Goodchild, M. (eds.): Crowdsourcing Geographic Knowledge: Volunteered Geographic Information (VGI) in Theory and Practice. Springer (2012)

Machine Learning Based Urban Change Detection by Fusing High Resolution Aerial Images and Lidar Data

Kaibin Zong[1], Arcot Sowmya[1], and John Trinder[2]

[1] School of Computer Science and Engineering, The University of New South Wales, Sydney 2052, Australia
{kaibinz,sowmya}@cse.unsw.edu.au
[2] School of Civil and Environmental Engineering, The University of New South Wales, Sydney 2052, Australia
j.trinder@unsw.edu.au

Abstract. Map databases usually suffer from obsolete scene details due to frequently occurring changes, therefore automatic change detection has become vital. Generally, change detection is done by spectral analysis of multi temporal images without including elevation information. In this paper, we describe a method for urban change detection by fusing high resolution aerial images with airborne lidar data which provides elevation information. For dealing with radiometric differences, three supervised learning algorithms are introduced which reduce the need for radiometric corrections. Three experiments are conducted on different training sets for each algorithm, to evaluate their performance on change detection and their sensitivity to unbalanced and noisy datasets. All algorithms are also compared with the standard PCA method. Experimental results demonstrate the capabilities of these methods and a detailed theoretical analysis of the achieved results is also presented.

Keywords: Remote sensing, change detection, supervised learning, Lidar.

1 Introduction

City mapping and GIS are widely used in many fields and have also become the focus of recent research [3]. However, the databases usually suffer from obsolete scene details due to frequently occurring changes and require timely updating. Therefore, the development of change detection technology is critical. Change detection is the process of identifying differences in the state of an object or phenomenon by observing it at different times [1]. Traditionally, changes are detected from multi-temporal images using spectral information alone. Many algorithms have been developed for dealing with this problem, such as image difference, PCA and post-classification comparison [2]. However, with developments in sensor technology, high resolution images bring more challenges for those traditional algorithms and make their performance unstable. By using images alone, it is difficult to distinguish between classes with similar spectral features, or to separate objects made of the same material but with different semantic meaning [3].

F. Bian et al. (Eds.): GRMSE 2013, Part I, CCIS 398, pp. 522–532, 2013.
© Springer-Verlag Berlin Heidelberg 2013

Airborne lidar (Light Detection and Ranging) is an active acquisition system that scans the terrain normal to the flight direction by emitting infrared laser pulses at high frequency [4]. By exploiting the elevation information provided by lidar, researchers have explored change detection by image and lidar data fusion [5-6]. Trinder and Salah [4] evaluated the contribution of aerial images and lidar data to pixel level change detection using four methods, namely image difference, principal component analysis (PCA), minimum noise fraction transformation (MNF) and post-classification (P-C) comparison. For each method, their results show an improvement in terms of best detection accuracy and omission and commission errors when the two data sources are fused. By fusing image and airborne lidar data, low contrast and shadow effects in images can be compensated for by the more accurately defined planes in lidar, and the poorly defined edges in lidar data can be compensated for by the accurately defined edges in aerial images [4]. However, the performance of P-C comparison is highly reliant on the classification accuracy in each individual image. For the other three methods, a thresholding step must to be implemented, which usually lacks justification. Besides, the choosing of the most suitable components is still problematic when using PCA and MNF methods.

In this paper, we consider fusion of high resolution aerial images and airborne lidar data for urban change detection due to their complementary advantages. In order to overcome the drawbacks of traditional methods and make full use of lidar elevation data, three supervised learning algorithms are utilized for pixel level change detection, namely artificial neural network (ANN) [7], support vector machine (SVM) [8] and Logitboost [9]. ANN and SVM are well known off-the-shelf algorithms that can handle the nonlinear relationships and noise in the training set. Logitboost has been rarely used so far for change detection. It combines the ideas of additive models and logistic regression [9] and the performance of the base learner can usually be improved by the boosting process. By using supervised learning techniques, changes can be predicted directly without using thresholds and the radiometric differences between two images can be handled robustly as well.

In order to demonstrate the capability of these algorithms, we conducted three experiments using different training sets. All algorithms were first tested on a dataset that contains 8 manually selected sub-images. Then, to address the imbalance in the data, we decreased the number of unchanged training instances using random sampling. Finally, some patches were hand-selected from those sub-images to create the third training set. All the three experiments were repeated 10 times with 10-fold cross validation (CV). After that, we further tested the performance of the three learning algorithms on all 8 sub-images based on the best model built in each experiment.

The remainder of this paper is organized as follows. A brief overview of the three learning algorithms is presented in Section 2. The experiments and results of applying those algorithms to change detection are reported in Section 3 followed by detailed results discussion. Finally, conclusions are drawn and some perspectives are given in Section 4.

2 Learning Algorithms

2.1 Artificial Neural Network

Artificial neural network (ANN) is an information processing algorithm inspired by biological nervous systems [7]. It is composed of a large number of interconnected neurons with different weights on the edges. Such a network is able to learn highly complex and nonlinear relationships among data. This is achieved by a nonlinear transformation of the weighted sum of inputs at each individual unit and then combining them together. Among all structures of ANN, the Multi-Layer Perceptron (MLP) with back propagation learning algorithm is the best known [7]. The weights in the network are initialized to small values randomly and are optimized iteratively by minimizing the sum of squared errors. In order to avoid being trapped in local minima, a momentum term is added so that the neural network can step over local minima or flat regions during the gradient descent process and may achieve better performance.

2.2 Support Vector Machine

Support vector machine (SVM) is a statistical learning algorithm aimed at finding a linear separating hyperplane between two classes [8]. This hyperplane can be described using the function:

$$f(x) = sign(< w, x > + b) \tag{1}$$

SVM searches for the best hyperplane among all candidates by maximizing the geometric margins. This results in a classifier that separates training instances of different classes with the largest gap. SVM handles nonlinear relationships by adopting the kernel trick. It maps the feature vector into a higher dimensional space using a nonlinear function and then creates the hyperplane for separation, which corresponds to a nonlinear decision surface in the original feature space. When considering potential outliers in the dataset, a regularization term is added into the target function and the optimal plane is the one that provides the best trade-off between training errors and complexity of the decision surface.

2.3 Logitboost

Logitboost algorithm was introduced by Friedman et al. [9] and combines the ideas of additive model and logistic regression [9]. Logitboost fits its model by maximizing the binomial log-likelihood using a generalized backfitting algorithm called "Local Scoring". Instead of using a weighted linear combination of input attributes, the posterior class probability is estimated based on a sum of smooth functions in the following form:

$$p(x) = P(y = 1|x) = \frac{e^{F(x)}}{1 + e^{F(x)}}$$
$$F(x) = \sum_{m=1}^{M} f_m(x) \tag{2}$$

Similar to Boosting, in each loop, a separate Logistic regression model is built based on a reweighted training set and is added into the ensemble classifier for maximizing the probability in (2). Cross validation is used in this process to avoid overfitting.

3 Experiments and Results

3.1 General Introduction

In order to demonstrate the capabilities of the three supervised learning algorithms on change detection, bi-temporal high resolution aerial images of Coffs Harbour in NSW Australia and corresponding airborne lidar datasets were used (provided by NSW Department of Land and Property Information). Data information is summarized in Table 1.

Table 1. Dataset information

First set of aerial images	Resolution Time	50cm 9/2009
Second set of aerial images	Resolution Time	10cm 12/2009
Two date aerial lidar data	Density Time	1.5pts/m^2 9/2009 & 12/2009

This dataset covers an urban area that includes buildings, roads, trees, water and ground. Due to the short time interval of 3 months between the bi-temporal data acquisition, newly constructed buildings are the main changes estimated by visual interpretation. Hence, the change detection problem can be simplified to a binary classification task. Firstly, a digital surface model (DSM) was generated from the first return lidar data using nearest neighbor interpolation to avoid creating new height values and keeping the well-defined planes. This step results in a lidar image in which pixel values denote ground surface heights (see Fig. 1). After resampling the second aerial image to 50cm resolution with bilinear interpolation, the two images were registered to each other and matched against their corresponding lidar DSM by using a projection transformation.

In this paper, we used a feature vector that consists of 8 attributes for each pixel. The first 3 attributes are the original pixel values (3 colour image bands) in the first aerial image and the fourth attribute is its height information in the DSM. The remaining 4 attributes were derived from the second aerial image and DSM in the same order. As can be seen in Fig. 1, due to the different seasons and sun angle, the radiometric characteristics and shadows are different in the images. Instead of using any pre-processing technique, we aim to overcome these confusing factors by using lidar elevation information and the flexibility of the learning algorithms.

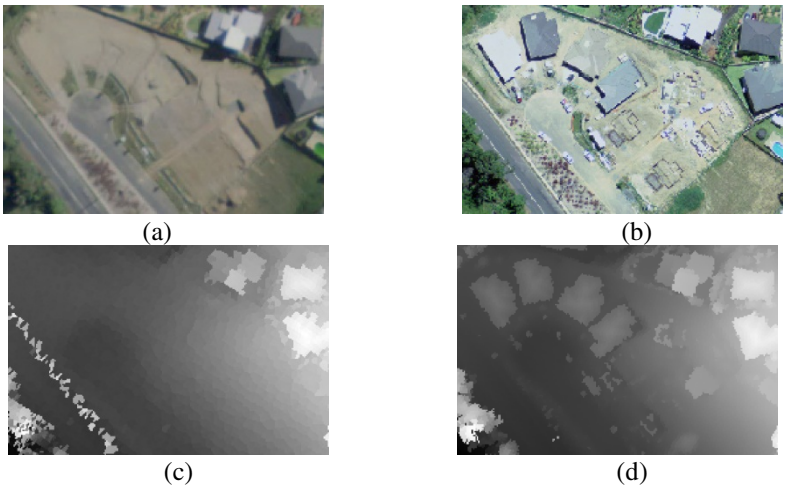

Fig. 1. Sample sub-image (a) The old aerial image; (b) The new aerial image; (c) The old Lidar DSM; (d) The new Lidar DSM

3.2 Experimental Design

Three experiments were conducted for each algorithm based on different training sets. We used 10 times 10-fold CV in all three experiments. For the first experiment, 8 sub-images were selected manually from the whole dataset and combined together as the training set. Among them were 5 sub-images with both changed and unchanged contents, and 3 other sub-images without changes. No sampling process was used in this part. Therefore, the training set in *Experiment 1* is highly unbalanced. Many more unchanged instances were found in the dataset due to the small time interval between the acquisition of two images. This makes the classifier more likely to label a test instance as the majority class in the training set [10]. To address this problem, random sampling was used in *Experiment 2* to decrease the size of the unchanged class. Due to the relatively small number of changed instances, all pixels belonging to this class were retained. The unchanged class was randomly sampled to obtain twice the number of samples of the changed class, in order to tradeoff between the imbalance and representativeness of the training data. In *Experiment 3*, we manually selected some patches from the 8 sub-images to create the training set. Changed patches were selected from all 5 sub-images that contain changes, and unchanged patches were selected from 7 of them. Those instances with outlier values were removed in this step. For further testing of the performance of the three algorithms, all methods were tested on all 8 original sub-images using the best models built in each experiment.

For the neural network, the learning rate was set to 0.01 and momentum was 0.1 in all experiments. Only one hidden layer was constructed with the number of hidden units equals to the average of the number of input and output units. Two output units were used to represent changed and unchanged classes. Weights in the network were updated based on the back propagation algorithm. The second method was SVM,

implemented in the "libsvm" package [11]. All attributes were scaled into the range between -1 and 1 before feeding into the classifier. A polynomial kernel function was chosen for nonlinear mapping and the penalty term was also considered. The best parameter values of degree d and coefficient C in the optimization function were determined based on grid search and 5-fold cross-validation. For Logitboost algorithm, the only parameter that needs to be defined is the maximum iteration number for boosting, which was set to 500 in all experiments. Cross validation was used for choosing the best stopping point and avoiding overfitting. All detection results are compared against the manually created ground truth map and numerical comparisons are carried out based on the confusion matrix (see Table 2). The following criteria (derived from confusion matrix) are used in each experiment, namely the overall accuracy, true negative (TN) rate, false negative (FN) rate, completeness and false alarm rate, and their definitions are listed below.

Table 2. Confusion matrix

	Predicted Class	
Actual Class	Changed	Unchanged
Changed	True positive (TP)	False negative (FN)
Unchanged	False positive (FP)	True negative (TN)

$$Overall\_accuracy = \frac{TP + TN}{TP + TN + FP + FN}$$

$$Completeness = \frac{TP}{TP + FN} \quad FN\_rate = \frac{FN}{TP + FN} \tag{3}$$

$$TN\_rate = \frac{TN}{TN + FP} \quad False\_alarm\_rate = \frac{FP}{TN + FP}$$

3.3 Results and Analysis

The averaged results of different learning algorithms in the three experiments are listed in Tables 3, 4 and 5 and the averaged results of testing the best models of all three methods on the 8 original sub-images are summarized in Tables 6, 7 and 8.

Table 3. Averaged performance of three learning algorithms in Experiment 1 using 10 times 10-fold CV

Method	ANN	SVM	Logitboost
Overall Accuracy	0.9913	0.9914	0.972
Completeness	0.9048	0.9	0.5844
FN rate	0.0952	0.1	0.4156
TN rate	0.996	0.996	0.992
False alarm rate	0.004	0.004	0.008

Table 4. Averaged performance of three learning algorithms in Experiment 2 using 10 times 10-fold CV

Method	ANN	SVM	Logitboost
Overall Accuracy	0.9771	0.9758	0.94
Completeness	0.9614	0.9588	0.8939
FN rate	0.0386	0.0412	0.1061
TN rate	0.985	0.9843	0.9631
False alarm rate	0.015	0.0157	0.0369

Table 5. Averaged performance of three learning algorithms in Experiment 3 using 10 times 10-fold CV

Method	ANN	SVM	Logitboost
Overall Accuracy	0.9997	0.9996	0.9991
Completeness	0.9988	0.998	0.9942
FN rate	0.0012	0.002	0.0058
TN rate	1	1	1
False alarm rate	0	0	0

Table 6. Averaged test results of three learning algorithms using their corresponding best models built in Experiment 1

Method	ANN	SVM	Logitboost
Overall Accuracy	0.9921	0.9925	0.9752
Completeness	0.8206	0.795	0.3706
FN rate	0.1794	0.205	0.6294
TN rate	0.9956	0.9966	0.9925
False alarm rate	0.0044	0.0034	0.0075

Table 7. Averaged test results of three learning algorithms using their corresponding best models built in Experiment 2

Method	ANN	SVM	Logitboost
Overall Accuracy	0.9843	0.9848	0.9623
Completeness	0.9228	0.9094	0.7854
FN rate	0.0772	0.0906	0.2146
TN rate	0.9852	0.986	0.965
False alarm rate	0.0147	0.014	0.035

Table 8. Averaged test results of three learning algorithms using their corresponding best models built in Experiment 3

Method	ANN	SVM	Logitboost
Overall Accuracy	0.9421	0.939	0.9424
Completeness	0.9214	0.93	0.8978
FN rate	0.0786	0.07	0.1022
TN rate	0.941	0.939	0.9418
False alarm rate	0.059	0.061	0.0583

From Table 3 one can see that both ANN and SVM achieved good detection results with overall accuracy of 99.13% and 99.14% respectively. More than 90% of changes (completeness) can be detected using either method. In contrast, although Logitboost achieved 97.2% overall accuracy, only 58.44% of real change was detected; this shows that overall accuracy by itself is not a good performance evaluation criterion for unbalanced datasets. When testing the best model of the three algorithms built in Experiment 1 on all sub-images (see Table 6), all the overall accuracies were higher than 97%. However, the completeness decreased to 82.06%, 79.5% and 37.06% when using ANN, SVM and Logitboost respectively.

The detection results using a randomly sampled training set are shown in Table 4. From Tables 3 and 4, one can claim that random sampling of training instances improves the completeness markedly, while the TN rate drops just a little. When testing on sub-images with the best model built on a randomly sampled training set (see Table 7), both ANN and SVM detected more than 90% of changes and the completeness of Logitboost is 78.54%, which is an improvement by more than 40% compared with the 37.06% in Table 6. This is because the imbalance in the training dataset was reduced during the sampling process, and the performance of all three algorithms improved.

In Experiment 3, we manually selected some patches for creating the training dataset. This can be viewed as a kind of spatial sampling. As can be seen from Tables 7 and 8, compared with using a randomly sampled dataset, the completeness for SVM and Logitboost were further enhanced by 2.1% and 11.2% respectively, while remaining the same for neural network. This improvement is due to the data cleaning during the manual selection process. On the patch based training set (see Table 8), SVM outperformed the other two methods in terms of completeness, although its overall accuracy and TN rate were lower.

For comparison purposes, traditional PCA method was tested on the same datasets. Bi-temporal datasets were stacked together (with 8 attributes for each pixel) followed by PCA transformation to detect changed parts. The component with the best contrast was selected manually and changes were separated from the background using thresholds. The averaged results of PCA are listed in Table 9. The testing results of the three algorithms using their best model built in each experiment on the sub-image shown in Fig. 1 are listed in Fig. 2 (a) ~ (i) and the result using traditional PCA method is shown in Fig. 2 (j).

Table 9. Averaged detection results of PCA method

Method	Overall Accuracy	Completeness	FN rate	TN rate	False alarm rate
PCA	0.8753	0.7742	0.2258	0.8838	0.1162

To sum up, both ANN and SVM outperform Logitboost, but it is difficult to choose between ANN and SVM. Moreover, Logitboost is more sensitive to the unbalanced and noisy datasets compared with ANN and SVM. When fusing high resolution images with lidar data, both ANN and SVM exceed PCA even on highly unbalanced and noisy datasets and Logitboost can also outperform PCA as long as the dataset is relatively clean and balanced. This may be explained by the underlying mechanism of

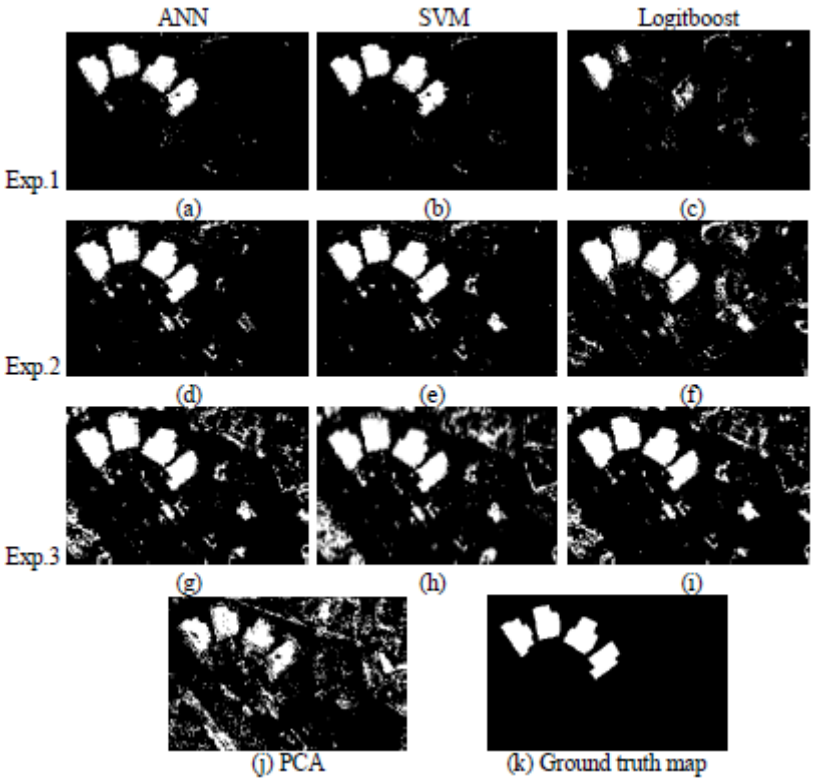

Fig. 1. Testing results of three algorithms using the best model built in each experiment on the sub-image shown in Fig. 1

each method. SVM is designed to maximize the separation margin between two classes, and is thus robust to noise, and the global optimum solution is found by solving the quadratic programming problem. A nonlinear boundary is achieved using the kernel trick and performance is further improved after adding a regularization term. For ANN, as a nonlinear mapping function is used in the network, it has the ability to model complex relationships. Although it cannot guarantee convergence to the global optima, it still works well on many real problems, and this drawback can be partially solved by adding a momentum term. Benefitting from the boosting process, Logitboost is able to model the nonlinear mapping even using a single linear base learner. However, since AdaBoost is sensitive to noise, Logitboost reveals weaker robustness compared with ANN and SVM. In contrast, PCA is based on a linear transformation and cannot handle nonlinear models well. Besides, covariance matrix estimation in PCA is based on the whole image and the noise in the process is known to have impacts. All of these factors together determine the better performance of the supervised learning algorithms.

4 Conclusions

In this paper, the capabilities of three supervised learning algorithms for urban change detection were evaluated. Experimental results illustrate that the performance of all algorithms can be enhanced using random sampling to improve the imbalance in training instances. Moreover, when spatial sampling of training samples is employed, both SVM and Logitboost algorithms work even better. Logitboost shows more sensitivity to imbalance and noise and is not as robust as the other two supervised methods. When compared with PCA, substantial improvements can be found and results can be interpreted from a theoretical point of view. In future, other kinds of features can be considered and cost-sensitive methods for handling unbalanced datasets (e.g. cost-sensitive SVM) can be developed as well. Besides, although the TP rate of changed class increases after sampling, more pseudo detections also appeared (see Fig. 2). This problem should be addressed in future to further improve the result. Finally, due to the success of spatial sampling, we will move from pixel to region based recognition in future research.

Acknowledgments. The authors wish to thank NSW Department of Land and Property Information for the images and lidar data.

References

1. Singh, A.: Digital Change Detection Techniques Using Remotely-sensed Data. International Journal of Remote Sensing 10, 989–1004 (1989)
2. Lu, D., Mausel, P., Brondízio, E., Moran, E.: Change Detection Techniques. International Journal of Remote Sensing 25, 2365–2401 (2004)
3. Luo, B., Chanussot, J.: Geometrical Features for the Classification of Very High Resolution Multispectral Remote-sensing Images. In: 17th IEEE International Conference on Image Processing, pp. 1045–1048. IEEE Press, Hong Kong (2010)
4. Trinder, J., Salah, M.: Aerial Images and Lidar Data Fusion for Disaster Change Detection. In: The XXII Congress of the International Society for Photogrammetry and Remote Sensing, Melbourne, pp. 227–232 (2012)
5. Li, M.C., Cheng, L., Gong, J.Y., Liu, Y.X., Chen, Z.J., Li, F.X., Chen, G., Song, X.G.: Post-earthquake Assessment of Building Damage Degree Using Lidar Data and Imagery. Science in China, Series E: Technological Sciences 51, 133–143 (2008)
6. Chen, L.C., Lin, L.J.: Detection of Building Changes from Aerial Images and Light Detection and Ranging (LIDAR) Data. Journal of Applied Remote Sensing 4, art. no. 041870 (2010)
7. Zometzer, S.F., Davis, J.L., Lau, C.: An Introduction to Neural and Electronic Networks, 2nd edn. Academic Press, New York (1994)
8. Vapnik, V.N.: Universal Learning Technology: Support Vector Machines. NEC Journal of Advanced Technology 2, 137–144 (2005)

9. Friedman, J., Hastie, T., Tibshirani, R.: Additive Logistic Regression: A Statistical View of Boosting. Annals of Statistics 28, 337–407 (2000)
10. Ng, W., Dash, M.: An Evaluation of Progressive Sampling for Unbalanced Data Sets. In: 6th IEEE International Conference on Data Mining Workshops, pp. 657–661. IEEE Press, Hong Kong (2006)
11. LIBSVM: A Library for Support Vector Machines, http://www.csie.ntu.edu.tw/~cjlin/libsvm

Parallel Access Optimization Technique for Geographic Raster Data

Liu Ouyang, Jinli Huang, Xiaohe Wu, and Bohu Yu

Northwest Institute of Nuclear Technology,
Xi'an 710024, Shanxi, China
oyangliu@mail.ustc.edu.cn

Abstract. In the field of geographic raster data processing, the performance of data access determines the overall performance of the parallel geographic program, especially when data are massive. Currently, the research on parallel optimizations for geographic raster data I/O is quite limited. By combining the data access paradigms in parallel geographic programs with the characteristics of the geographic raster logical and physical models, a parallel access architecture for geographic raster data is proposed in this paper, and four parallel access algorithms for geographic raster data is implemented on message passing model. Contrast tests are carried out, it is verified that the parallel access methods outperform not only the conventional sequential access method but also the time-sharing multi-processes data access method. This new architecture can be used to promote the access efficiency of the parallel raster processing algorithm and thus improve the parallel performance of the program.

Keywords: Geographic raster data, Parallel data access, Parallel raster processing, Message passing model.

1 Introduction

In the recent years, parallel Geo-Computation, which is the combination of geographic analysis and high-performance computing technology, gradually attracts more attention. High-performance processing capabilities and geographic spatial data analysis capabilities can be reached by using parallel thought in the Geo-spatial data calculation process. So far, there have been lots of investigations carried out on the parallel computing, for instance, Q.Guan [1] developed a number of parallel algorithms based on the existing geographic algorithms and models; Hawick et al. (2003) developed GIS middleware DISCWorld, which supports distributed parallel geographic computing for large scale geospatial data (such as remote sensing data, etc.). However, with the spatial data processing capabilities improving, the performance of data access can't match the computing capability, which has become the bottleneck in the overall efficiency of Geo-Computation. Along with the development of the earth observation technology, geo-spatial data increase sharply, therefore how to improve the performance of data access is particularly important when we are in the face of large-scale and high-precision geospatial data. Currently,

F. Bian et al. (Eds.): GRMSE 2013, Part I, CCIS 398, pp. 533–542, 2013.
© Springer-Verlag Berlin Heidelberg 2013

there have been many correlative studies on access to scientific matrix, yet research on geographic raster data access is still limited. In the aim of improving the overall performance of the geographic program, new parallel access optimization algorithms are proposed in this paper to enhance the access speed of geographic raster data. The author aims to use the parallel data access methods to achieve parallel geographic computing, thus to help investigators develop parallel raster processing algorithms of high access efficiency.

2 Geographic Raster Data Access Parallelization Techniques and Realization

2.1 Geographic Raster Data Access Parallelization Mechanism

During geographic calculation process, the data access is an essential step and plays a very important role in the overall time efficiency. There are two mainstream data access patterns in the parallel geographic computing: Distribution/Collection (D/C) and Parallel Access (PA). Compared to the traditional D/C mode, PA mode eliminates the performance bottleneck which is caused by the traditional reading and writing pattern which only carried out by the master process. What's more, the master and slave process transfer lightweight data, therefore the traffic congestion between them is avoided. In summary, based on the parallel file system with good parallel throughput performance, the parallel geographic program using PA mode can greatly reduce the time cost of data reading, thereby improves the performance of data access significantly.

For instance, geographic raster data with a given width w, and a given height h, it's a w×h two-dimensional matrix structure logically, and a w·h one-dimensional array structure physically. Because the image data is typically stored as row priority storage, i.e. each point in the two-dimensional matrix can be mapped to a one-dimensional array in order of row. In parallel geographic program, we'll choose a kind of method to divide large-scale image data, and then each process handles a small data block after division. We assume that the data is divided into m·n blocks using block partition, i.e. this program needs m·n processes, shown in Figure 1. For any process P_x it handles a collection of a series of points actually, after mapped from the two-dimensional matrix to one-dimensional array, the set of corresponding physical offset of these points is,

$$S(P_x) = \{ f(x,y) \mid x \in [x_0, x_0 + \frac{h}{n}], y \in [y_0, y_0 + \frac{w}{m}] \} \quad . \tag{1}$$

Where, x_0 and y_0 could be calculated through row No. and column No. of P_x , f(x, y) means the physical offset of any point (x, y) mapped to the one-dimensional array,

$$f(x,y) = (x \cdot w + y) \cdot sizeof(pixel) \quad . \tag{2}$$

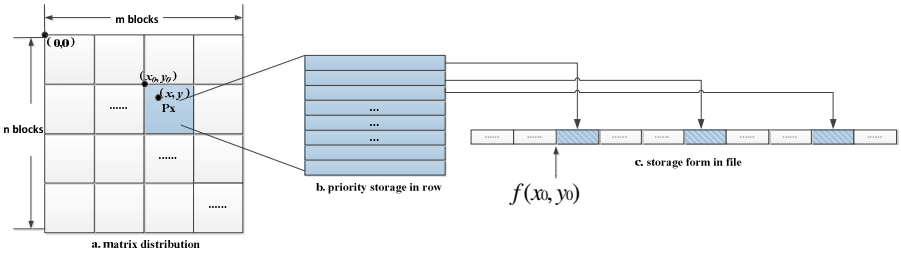

Fig. 1. Map from logical structure to physical structure

In order to achieve the parallel access mode mentioned in the previous section, we need to know physical offsets in the data file of these points handled by each process, these sets of physical offsets could be calculated through equation (1) and (2). By analyzing the two equations, we know that width、height and data type are very important, so the foundation of parallel data access is analyzing geographic raster data and obtaining useful metadata. This paper chooses the common format---Tagged Image File Format, TIFF. Because of its flexibility and scalability, TIFF is widely used in digital imaging、remote sensing、medical and other fields.

By combining the PA mode with the mapping equations, we build parallel access architecture for geographic raster data, shown in Figure 2.

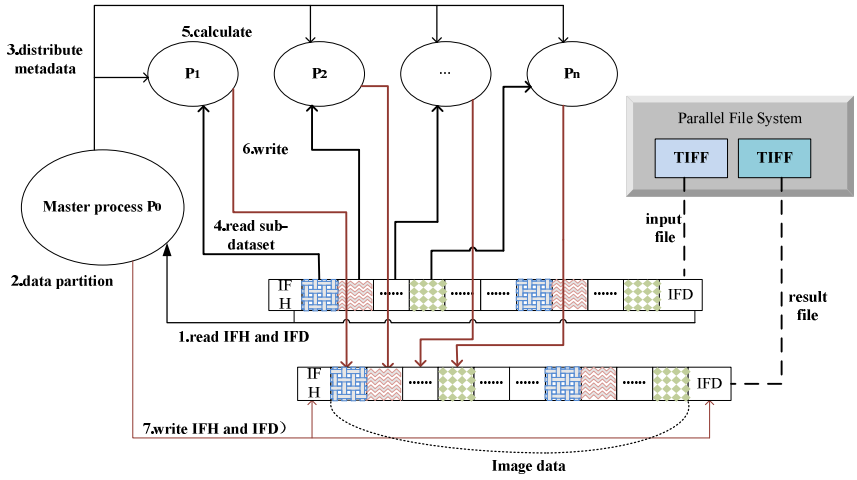

Fig. 2. Parallel access architecture for geographic raster data

2.2 Optimization Design of Parallel Access Algorithm for Geographic Raster Data

As a part of MPI-2 specification[2], MPI-IO offers effective and portable data access interface, and provides strong support to parallel access to spatial data. After the deep

analysis of the characteristics of geographic raster data, based on the proposed parallel access architecture, four parallel access optimization algorithms for geographic raster data are summarized, where the interface of MPI-IO is used. This section will introduce the principles and features of these four algorithms, and analyze their applicable conditions. As shown in Figure 3, this paper defines four algorithms as: Multi-process Independent Non-continuous Data Access(MINDA), Multi-process Gather Together Data Access(MGTDA), Multi-process Independent Continuous Data Access(MICDA) and Multi-process Aggregation Continuity Data Access(MACDA).

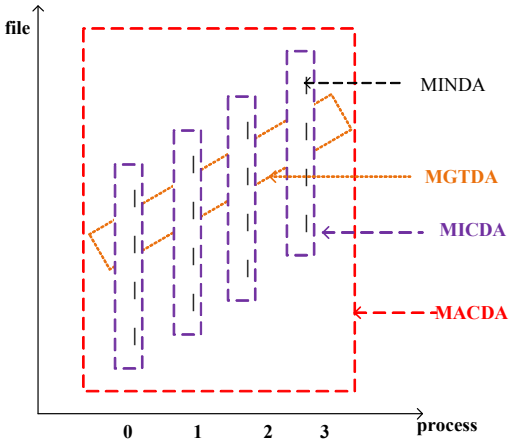

Fig. 3. Principles of four parallel access algorithms

In MINDA, each separate I/O request corresponds to a row in the local array. Firstly, each process calculates the physical offset of starting point of the data block, and reads or writes the first line, and then calculates the next physical offset, and reads or writes the second line, and so on. The I/O times of each process equal to the rows of data block.

MINDA Algorithm:

Step 1: Parsing a variety of geographic spatial metadata information;

Step 2: The master process divides each band image data by choosing a partitioning strategy;

Step 3: The master process distributes related metadata to each slave process;

Step 4: After receiving metadata, each slave process calculates their own physical offset, then reads the sub-datasets from disk concurrently;

This step will call the functions: `MPI_File_seek();` `MPI_File_read();`

Step 5: Each slave process parallel deals with the geographic raster data, such as digital terrain analysis, etc.

Step 6: Each slave process parallel writes local calculations to the result file;

This step will call the function: `MPI_File_write();`

Step 7: If spatial metadata is modified, the master process will write the modification to the result file.

MGTDA is similar to MINDA, but MGTDA refers to the theory of centralized I/O[3], by calling collective-I/O function, all processes will open a raster file together, and then access their own data independently at the same time. 'Collective' means that each process in the communicator must call this function, which is a group operation. Unlike MINDA, before accessing and distributing message, MGTDA will collective all process's request, thus the number of I/O request will be reduced. On the other hand, when a process uses collective operation, it knows that the other processes will call the same function, and then it will wait for all the processes, which will substantially increase the waiting time. If the parallel geographic program opens too many processes, its data access performance will degrade. The algorithm flow of MGTDA is similar to MINDA, but in step 4 and 6, MGTDA calls functions: `MPI_File_read_all()` and `MPI_File_write_all()`.

The core thought of MICDA is that each process has its own file view of the opened file, which means a virtualization description of accessing scope by making use of an abstract data structure[4]. Therefore, when the process access its own data block, although these data being accessed are discrete physically, in the logical description it's continuous. Compared to MINDA, MICDA is more flexible. In MICDA, multiple I/O operations of the same process are consolidated into one data access, the amount of data access equals to the size of this process's file view. The total I/O times are equal to the number of processes, which greatly decreases I/O times and reduces access overhead.

MICDA Algorithm:

Step 1~Step 3: Same with MINDA;
Step 4: According to the received metadata, each slave process set the file view;
This step calls functions:
`MPI_Type_create_subarray();`
`MPI_File_set_view();`
`MPI_File_read();`
Step 5: parallel geographic computing, as the same with MINDA;
Step 6: Each slave process parallel writes local calculations to the result file;
This step calls function: Same with Step 4; `MPI_File_write();`

MACDA is similar to MICDA in general idea, but MACDA uses the thought of centralized I/O. I.e. based on MICDA, all I/O operations are merged into one I/O operation, the amount of data access is the size of this accessed file, and the performance is further improved.

As shown in Figure 3, from MINDA to MACDA, the amount of data of each access increases gradually. As we all know, more data one I/O requests means better performance. Therefore, theoretically, performance of parallel geographic program using MACDA is better than using MINDA.

Via the above analysis, we know that these four access algorithms have different thoughts and principles. They are adapted to different practical situations, and not all

cases need to set file view for processes. If a parallel geographic program needs to access a large number of continuous data, MINDA and MICDA achieve the same effect, and MGTDA equals to MACDA. Below we will design a set of comparative experiments on the proposed parallel access algorithms for geographic raster data to verify these algorithms' effectiveness and efficiency, and then analyze and summarize the applicable conditions of these data access algorithms.

3 Experiment

3.1 Experiment Environment and Description

In order to verify the effectiveness of these proposed algorithms, we implement a set of comparative experiments based on an IBM high-performance computing cluster and datasets of different sizes. Details of experiments are shown as Table 1.

Table 1. Hardware, Software and Dataset

Details	Configuration details
Master node	x3650M3: 2* Intel Xeon 4C X5540 2.4GHz, 6* 4GB DDR3 LP RDIMM
I/O Control node	4*x3550M3: 2* Intel Xeon 4C X5570 2.80GHz, 6* 2GB DDR3 LP RDIMM
Compute nodes	28*Blade HS22: 2* Intel Xeon 4C X5570 2.80GHz, 6* 2GB DDR3 LP RDIMM
Network	Infiniband
Shared File System	GPFS
Software System	RedHat Enterprise Server 5.0、GCC 4.1.2、OpenMPI 1.4.3、GDAL 1.8.0
Datasets	Dataset 1(50MB)、Dataset 2(300MB)、Dataset 3(900MB)、Dataset 4(1.56GB)

All experiments are implemented under the same cluster environment. Test results are the average of 10 measurements. In all following result figures, Abscissa axis is the number of processes *n* that run in parallel, which is the number of currently used computing cores, $n=2^k, k\in N$. When n=1, it represents tests of serial geographic procedure; when n>1, it represents tests of parallel geographic procedure. Ordinate axis represents running time of t serial program t_1、parallel running time t_n、and Speedup $Sp=t_1/t_n$、parallel efficiency $E=Sp/n=t_1/(n\cdot t_n)$.

3.2 Experiment Results and Analysis

We choose traditional row partitioning strategy, i.e. the geographic raster data is divided into sub-blocks with the same number of processes, and each process is responsible for a sub-block. So, the rows of each sub-block is sub_row=h/n, where h is the height of original raster data, n is the number of processes. Next, based on cluster environment and dataset 2 in Table 1, we test serial reading time and parallel reading time with different number of processes. The result is shown in Figure 4, experimental analysis is as follows:

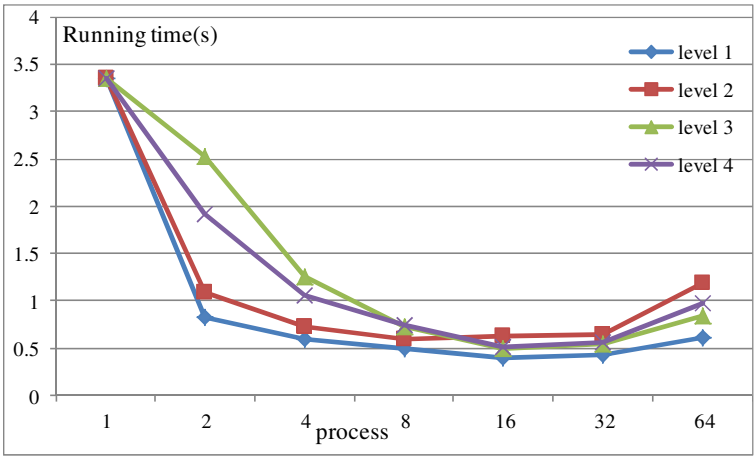

Fig. 4. Reading time of four data access algorithms with different number of processes

1. n=1, only one process accesses raster data serially, its running time is the longest. n>1, there are multiple processes accessing parallel. With n increasing, parallel reading time of four algorithms decrease gradually, which means our parallel access algorithms is effective, they can reduce the accessing time, and enhance the overall performance of parallel geographic procedure.

2. Four curves almost have the same trend, when n increases to 32, they reach the lowest point, and then gradually increase. The reasons are: (1) the cluster has four I/O nodes, 32 cores in total. While n≤32, as n increases, the size of sub data block for each processor decreases, which makes a corresponding decline in reading time; (2) When n>32, there aren't enough I/O cores providing support to parallel access. Although the size of each sub-block is smaller, parallel access speed becomes slower, which causes the overall reading time no longer reduces, or even gradually increases.

The open source data model Geospatial Data Access Library (GDAL)[5] has support function of parallel reading in version 1.9. But parallel reading of GDAL is actually a multi-process turning serial read, which is essentially a pseudo-parallel data access method. In order to compare the performance between the proposed parallel access algorithms and GDAL, based on the above experiments, we further implement an experiment with GDAL, and name it GDALDA. Because GDAL includes cache optimization and block optimization mechanisms, its performance is competitive. The result is shown in Figure 5(a), and the experiment conclusions are as follows.

By comparing the parallel reading time of the five kinds of access methods, we find that running time of GDALDA is very short, its performance is better than other three methods except MINDA. This result does not mean that our approach is not feasible, it is because that each process's data block stores contiguously in physical memory when we take row partitions; and for the data which is stored contiguously in physical memory, our algorithms takes no significant advantage. As a mature open source geographic raster data access library, GDAL includes a variety of optimization strategies, so GDALDA still has a competitive performance. However, its performance still lags behind the proposed MINDA.

To verify the above analysis, with the same dataset, we design and implement another experiment with column partitioning strategy (columns of sub data block: sub_col=w/n), the result is shown in figure 5(b).

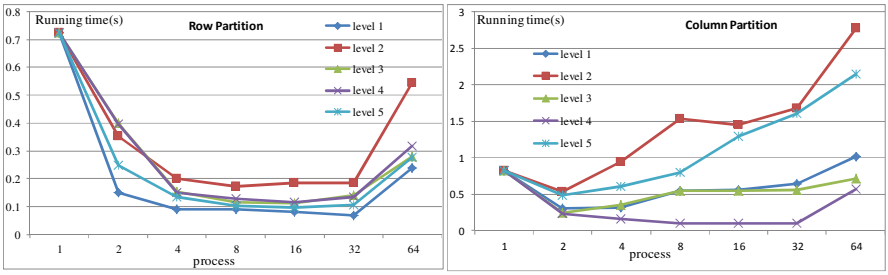

Fig. 5. Parallel reading time of five access algorithms: a. row partition; b. column partition

1. The performance of MINDA、MICDA and MACDA is better than that of GDALDA. In the case of column partitions, sub data block of each process is stored non-continuous in the physical memory. When GDALDA mode access data, firstly each process navigates to the appropriate location in the file, reads a line of data, and then navigates to the next position, reads the next line, and so on. So in the case of column partition, parallel geographic program with GDALDA will greatly increase the addressing time. This pseudo parallel I/O based on GDAL does not support multi-process and multi-pointer to access the file in parallel, thus with the number of process increasing, the performance of the program drops significantly.

2. For MINDA、MICDA、MACDA and GDALDA, with the increasing number of processes, their performance declines. Because the increase of process number allows the number of divided columns to increase, size of each sub data block decreases, but the I/O requests do not change, so the total time increases slowly.

3. In all the five algorithms, MGTDA has the worst performance. This is because MGTDA uses the aggregation thought, all I/O requests should call this collective-I/O function, therefore the waiting time is sharply increased. And the size of each I/O request equals to a line of sub data block, this could cause the waiting cost between processes is greater than that of each independent request, thus degrade the access performance.

4. MICDA sets file view for each process, for each process, the size of one I/O request equals to the size of the file view. And the total requests are equal to the number of processes, compared to MINDA and MGTDA, MICDA reduces the I/O times, its performance is better.

5. MACDA's performance is the best. Because based on setting file view, MACDA also uses the aggregation thought, the size of one I/O request equals to the size of the whole file.

To prove that the size of dataset doesn't affect above experimental results, this paper design a set of experiments to compare the performance between MACDA and GDALDA with four different dataset (as shown in Table 1), the result is shown in Figure 6.

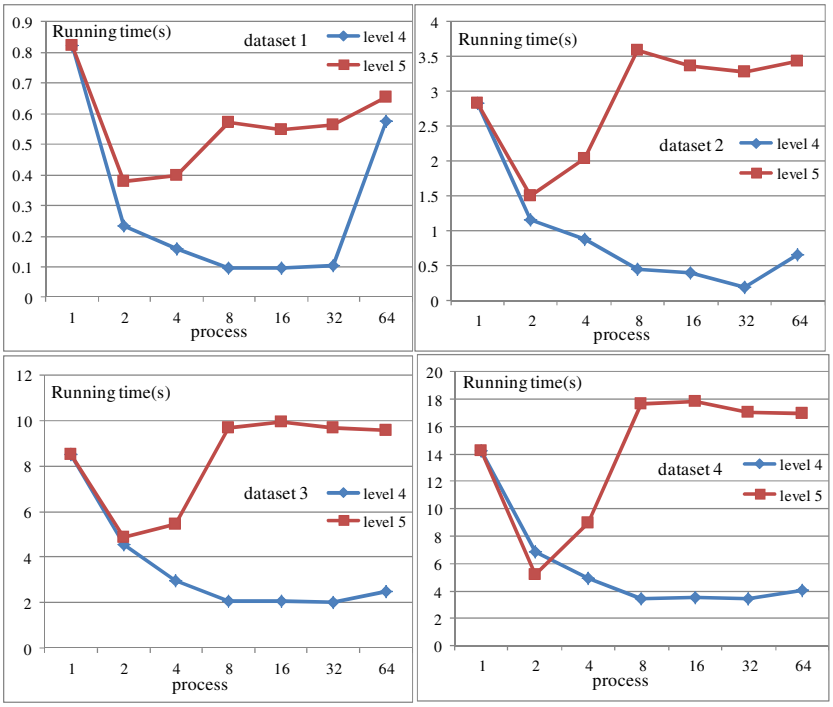

Fig. 6. Performance comparison of MACDA and GDALDA

By analyzing the experimental result shown in figure 6, it is conclude that, in the case of column partition, with any dataset, the performance of proposed MACDA is better than GDALDA, and larger dataset makes the performance difference more obvious.

In summary, we can see that MACDA designed in this paper has the best effect in the parallel geographic program. Its parallel running time、parallel speedup and parallel efficiency are shown in Figure 7.

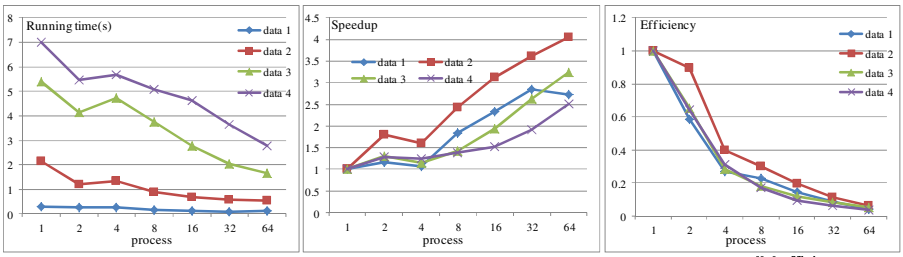

a. parallel running time b. parallel speedup c. parallel efficiency

Fig. 7. Parallel access performance of four datasets with MACDA

Figure 7(a) shows that the parallel access time reduces with the increasing number of processes; figure 7(b) shows that the parallel speedup increases with the increasing number of processes; figure 7(c) shows the parallel efficiency decreases with the increasing number of processes. When n>32, the decreasing trend of parallel running time becomes gentle, parallel speedup grow slowly, whereas while the parallel efficiency gets much lower, even as low as zero. Because the cluster has four I/O nodes, and 32 cores in total, we can see from figure 7 that under the experimental environment, the maximum number of processors that parallel geographic program can effectively utilize is 32, at this time the composite indicator of parallel application reaches the highest.

4 Conclusion

Data access has become a key issue that restricts the overall performance of parallel geographic program, the proposed parallel access algorithms for geographic raster data have great advantages in application. This paper builds a parallel access architecture and proposes four parallel access algorithms for geographic raster data. Experimental results demonstrate that the proposed algorithms are effective and efficient. The result of this paper can be applied to parallel processing algorithms for raster data to improve spatial data access performance.

References

1. Guan, Q.: pRPL: an open-source general-purpose parallel Raster Processing programming Library, pp. 57–62. ACM (2009)
2. The MPI-IO Committee. MPI-IO: A Parallel File I/O Interface for MPI, Version 0.5 (April 1996), World-Wide Web at `http://lovelace.nas.nasa.gov/MPI-IO`
3. Nitzberg, B., Lo, V.: Collective Buffering: Improving Parallel I/O Performance. In: Proceedings of the Sixth IEEE International Symposium on High Performance Distributed Computing, vol. 8, pp. 148–157 (1997)
4. Thakur, R., et al.: A case for using MPI's derived datatypes to improve I/O performance, pp. 1–10. Computer Society (1998)
5. Warmerdam, F.: The geospatial data abstraction library open source approaches in spatial data handling. In: Hall, G.B., Leahy, M.G. (eds.) Open Source Approaches in Spatial Data Handling, pp. 87–104. Springer, Heidelberg (2008)

Topological Relationship Extraction by Two Improved Image Segmentation Methods*

Xiaoli Liu[1], Guobin Zhu[2], and Xue Li[1]

[1] Key Laboratory of Earthquake Geodesy, Institute of Seismology, CEA,
40 Hongshance Road, Wuhan, 430071, China
[2] International School of Software, Wuhan University, Wuhan 430079, China
{Liuxl.j,gbzhuu}@gmail.com

Abstract. Topological maps are graph-like spatial representations. To mitigate the above drawbacks of existing image segmentation algorithms, we propose a general theory of topological maps based on the abstract data structure whereby sensory input, topological and local metrical information are combined to define the topological maps explaining such information. In order to put the theory here proposed into computational practice, we provide two improvement algorithms on conventional region-based and edge-based image segmentation methods, which aim to extract directly regional boundaries and topological maps from the pixel sets in the processing of remote sensing image segmentation. The experimental results show that the two algorithms support different exploration strategies and facilitates map disambiguation when perceptual aliasing arises, and remain well the geometric topology information.

Keywords: Topological maps, Spatial representations, Region-based image segmentation, Edge-based image segmentation, Remote sensing imagery.

1 Introduction

Image segmentation aim to subdivide the image into disjoint subsets of pixels, called regions, on the basis of some homogeneity criterion. Many types of segmentation techniques have been proposed in literatures [1, 2]. In general, two outputs of remote sensing imagery segmentation can be typically divided into two classes: region-based segmented images and edge-based segmented images. Nevertheless, a drawback of most of these approaches is that they don't take into account that a region must be topologically connected[3, 4]. As a consequence, pixels belonging to separate and different regions could be assigned to the same cluster. However, connectivity obtained from conventional segmentation methods are generally not consistent with the topological relationships[5]. Based on complex theories, Liu build a multi-level hierarchical image representation framework that preserves spatial relationships and, so raises a suitable condition for image segmentation to incorporate spatial

* The research is supported by the Director Fund (IS201116002) from Institute of Seismology, China Earthquake Administration, and the National Science and Technology Support Project (2012BAH01F02) from Ministry of Science and Technology of the People's Republic of China.

F. Bian et al. (Eds.): GRMSE 2013, Part I, CCIS 398, pp. 543–552, 2013.
© Springer-Verlag Berlin Heidelberg 2013

information related to adjacency between pixels[6]. This method of topological representation is based on finite topological space and, leads to low efficiency and high data volume for remote sensing imagery.

Currently, the most image segmentation algorithms turn to heuristic methods for the problem on topology. The outputs of edge-based segmentation algorithms, such as the Canny method, are edge-based images, of which edge points are pixels and not the intervals between of pixels. The outputs of region-based segmentation algorithms are region-marked images and not edges of marked regions. The watershed transformation algorithm also marks regions and their boundaries. However, this kind of boundaries still belong to the closed regional boundary of a single-pixel width [7, 8]. In the case of lacking a priori knowledge of the target, because there are a large number of transitional region in the processing of remote sensing image segmentation, it is more difficult to detect pixels of regional boundaries. Therefore, the results often appear discontinuous regional edges and drift phenomenon. In summary, the output images by the existing image segmentation algorithms are not low-dimensional boundary element on the theoretical significance. In consideration of this, this paper presents an improvement on conventional region-based and edge-based image segmentation methods based on the abstract data structures[6], which aim to extract directly regional boundaries and topological maps from the pixel sets in the processing of remote sensing image segmentation.

2 The Abstract Data Structures

A topological model is used to explicitly specify adjacency and inclusion relationships between the different cells of a geometrical object. The kernel of our modeler is based on the topology of abstract cell complexes (ACC) which is introduced by Kovalevsky as a means of solving certain connectivity paradoxes in digital topology, and to this extent provides an improved theoretical basis for image analysis [6]. Introductory material on ACC could be found in [6, 9]. Here we briefly summarize the definition on the GeoTopo which is an abstract data structure.

Definition of the GeoTopo: For uniform description topology and geometry of the segmented image, let GeoTopo=(P, T, ρ) be an abstract data structure, where P stands for the set of basic units, T is used to describe the topological map induced by basic units, $\rho : V \cup E \cup F \rightarrow 2^P$ is an assignment relationship between block units and the set of basic units included.

3 Topological Maps Extraction of Region-Marked Images

Region-based methods segment images by grouping neighboring pixels or regions according to certain similarity (homogeneity) criteria, defined on such features as gray level, color information, or wavelet coefficient, such as the region-growing algorithm[10], the splitting and merging algorithm[11]. As a result, several 4-connected components are created and marked, the output of the segmentation is a region-marked image. In theory, regional boundaries are edge zone between two

regions and, that is the gap between neighborhood pixels with a different marks. Because the region-marked images themselves don't contain addressable entities representing inter-pixel gaps, which are only coded by an implicit way. This way hardly represents regional topology. For example, "Seeded Region Growing" [12] is a method for image segmentation. It begins with a set of marked seed pixels (or regions) which are grown until all the image pixels have been processed. This growth is controlled by a priority queue mechanism which is dependent on the similarity of pixels within regions. Of which the outermost pixels make up boundaries of target regions. How to code inter-pixel edge elements by an explicit way based on traditional region segmentation, and extract topological maps and application to constraint the segmentation processing, is a contradiction between the image segmentation and segmented image representation.

Based on the abstract data structure [6, 9], topology relations are directly encoded by an explicit way in the tree structure and provide, coupled with the ACC approach a consistent and "natural" object description in different scales. Pixel sets with the same mark are called connected components and forms block units, therefore the proposed algorithm to extract regional topological maps from a regional marked image consists of two steps:

(1) interval entities are inserted by an explicit way in the region-marked image;
(2) Corresponding regional topological maps are built.

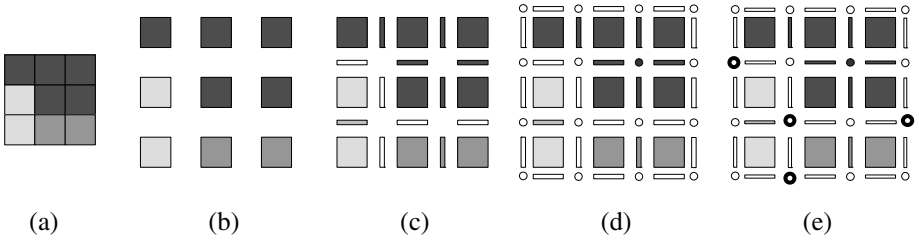

Fig. 1. Extraction topological maps based on a region-marked image: (a)a region-marked image; (b) a super-raster image; (c) an image with marked edges; (d) an image with marked nodes; (e) an image with marked branching nodes.

3.1 Inserting Interval Entities

Input: A n×m(i=1, 2,…,n; j=1, 2,…,m) region-marked image composed by 4-connected regions.

Output: A 4-connected segmented image is composed by the elements of 4-connected regions, each of which is with the same mark. Each element of 4-connected regional boundaries is called an edge or a node.

Step 1. To building a (2n-1)×(2m-1) super-raster image and copy the mark of the pixel p(x×y) on region-marked image to the super raster q(2x×2y).

Step 2. For each super-raster element with the coordinate (2i, 2j+1), if two neighboring pixels of this element in the vertical direction have the same mark, the mark is copied to the element; if not, the element is assigned by a specific edge mark.

Step 3. For each super-raster element with the coordinate (2i+1, 2j), if two neighboring pixels of this element in the horizontal direction have the same mark, the mark is copied to the element; if not, the element is assigned by a specific edge mark.

Step 4. For each super-raster element with the coordinate (2i+1, 2j+1), if the mark of any neighboring pixels of this element is an edge mark, the element is assigned by a specific node mark; if not, the mark of the corresponding neighborhood is copied to the element.

3.2 Extracting Topological Maps

Input: Results of the inserting algorithm of interval entities.

Output: Topological maps of segmented images.

Step 1. To expand the super-raster image with a pixel-width boundary, if coordinates of the edge element are both odd, which is marked by a node; if not, marked by an edge. And then, a new (2n+1)×(2m+1) super-raster image is built.

Step 2. In the process of searching boundary sets, the connected components are marked super-raster elements of edges and nodes, and each of which generates a component of the topological map.

Step 3. To simplify the topological map, and delete all corresponding nodes of non-branching points. Let d be a correlative half-line of the node C, if $|\langle \alpha_1, \alpha_2 \rangle(d)|$ is not equal to 6, the node is deleted.

Step 4. For each edge of any components, a pair of corresponding half-lines is generated, and their relationship of which is defined by α_0 replacement. For each node, the relationship of two correlative half-line is defined by α_1 replacement.

Step 5. By the type of half-lines on components, the external relationship and containment relationship of each component are built.

4 Topological Maps Extraction of Edge-Marked Images

The outputs of the edge-based segmentation methods are often edge-based images, such as the Canny algorithm and the topological refinement algorithm. Here edge is a pixel and not an interval between pixels. In practical applications, false edge points have been often detected due to the impact of noise and unknown disturbances in the process of edge detection. Edge connections can cause problems that connection errors and the edges are not closed. Hence, the output of edge detection is not as a segmentation result in direct, and is post-processed to merge edges to edge-based chains[1, 7], which will corresponds better boundaries of segmented images. Especially a zero-crossing case occurs between pixels, the most natural way is to use the inter-pixel interval, such as the interval-inserting algorithm. In general, the practice is used to sign the nearest pixel from the zero crossing as the edge pixels, such as the Canny algorithm. This requires edge connection algorithms are able to distinguish what is the edge points, and which are not. In fact, this is extremely difficult.

Pixel's 8-neighborhood is a norm to determine whether a pixel of the boundary belongs to the edge pixels. In general, edges can't appear inside the objects and must occur between different objects. Therefore, edges between regions should be refined, and don't contain a simple pixel. In other words, when doesn't change the connectivity of the regions and the boundaries, a boundary pixel can not be changed into regional pixels. Refinement example of a watershed transformation algorithm is a good, simple point based on gradient operator or Laplacian operator removes the order.

Watershed transformation algorithm is a refinement of the good example, the simple point removal order is determine based on gradient operator or Laplacian operator. But traditional watershed transformation in a flood way was not actually a local transformation. Only when the entire image is processed, it Is the time to determine whether a pixel is water pixels[8]. In addition, the Canny algorithm is not belong to refinement methods, the result of edge images remains many simple points, and therefore these simple points must be removed before the image classification.

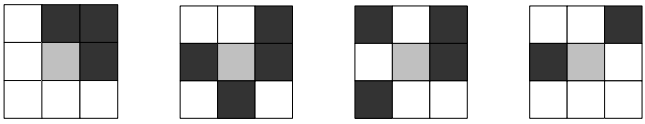

Fig. 2. Topological maps extraction of edge-marked images: (a) non-refinement pixels; (b) node pixels (can be reduced); (c) node pixels; (d) edge pixels

The other hand, in order to test the edge pixels, in the process of analyzing distribution pattern in 8-neighborhoods of regional and edge pixels, there will be 2^8=256 possible cases. Although, we can remove some equivalent cases, there are still 51 cases that need to determine whether the edge pixels are node pixels or boundary pixels. For remote sensing images, in addition to the maximum and minimum regions, there are often contains a lot of transition zones which mainly come from three aspects: (1) unknown disturbance and noise in the image acquisition process causes the transition zone within the objects; (2) Limitation of spatial resolution of the sensor and complex diversity of features commonly lead to mixed pixels in common found in in remote sensing image[13], as a result, transition zones appear around the edges of the object; (3) for some real objects occurring in the image, but their gray are neither the maximum value nor the minimum value, and between the light and dark objects. The transition zones created by the first case and the second case are in larger quantities, many types and small sizes. Because there is less contrast of transition between these transition zones and their surrounding area, they are often eliminated or reduced in the segmentation process. While the transition zone created by the third case is itself real objects, so such regions are significantly different from the surrounding area, sizes of which are often larger than the first two categories and should be remained.

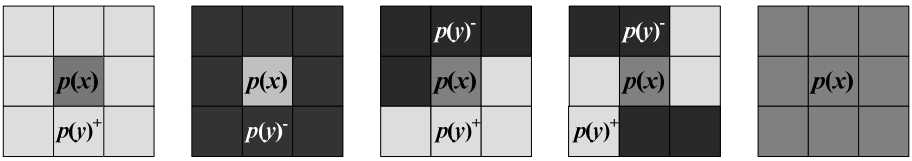

Fig. 3. Topological types of points in the image domain: (a) the minimum critical point; (b) the maximum critical point; (c) standard critical points; (d) saddle critical points; (e) flat points

In the scale space, topological changes always occur at critical points [14]. These point is local single points in implicit surfaces and an extension of non-simple points of the binary image. In general, there are classified into five categories: regular point, flat point, saddle point, maximum point and minimum point[14]. If some irregular points occur inside the image, of which topology is generally more complex. Once the contours be changed, there will give rise to drastic changes. This results in so-called "topological noise", this is the topologies of the image may cause great instability with a small change [5]. Fig. 7 illustrates all possible cases which are sufficient to detect all topology changes. Based on the above analysis, if most of the critical points in the image domain are rule points, it can be say that topology is smooth. In other words, topological properties of the image may only change at a few of the contours. For minimum point, maximum point, and saddle points, they can be replaced by their topological neighbors, as a result, their topology types are changed at the same time. Among them, the saddle point can be changed in two ways: reducing the pixel value to its neighbor's value or increasing the value of its neighbors. For raw images, there are two appropriate implementations: splitting and merging. Both options are valid, but the value closer to the neighbor are generally selected. Flat points remains the same. So, we hope to get rule points.

In summary, segmentation algorithms can not rely on and don't need limiting to the occurrence of these modes, in instead, the standard refinement mode and algorithm need to be appropriately changed. In consideration of this, we propose a extended definition of refinement mode, which is called Irreducible pattern. In traditional image segmentation algorithms, for avoiding connectivity contradictions, the types of foreground and background are often classified into two categories: 4-adjacency type and 8-adjacency type. For this reason, here is a convention that connectivity of regions and boundaries are respectively assigned with 4-adjacency and 8-adjacency types. In addition, in order to avoid dealing with special situations, the border image is firstly broadened by a pixel-width boundary, and then all pixels are marked as pixels of the border. If broadening the border image brings about some pixels can be reduced, these pixels should be removed by implementing specially iterative refinement algorithm. Therefore, if the part of 8-neighborhoods is outside of the broadened image, removed pixels are always called pixels of the infinite area. As a result, we can use the general classification procedure. Based on the above agreement, a Irreducible pattern can be categorized as follows.

Definition of irreducible pattern: A boundary pixel in the marked image with refinement edges is a edge pixel, if one of the following conditions is meet: (1) its 8-neighborhood is made up of four 4-connected components; (2) other components are made up of boundary pixels, and contain at least a 4-neighbor. Otherwise, this pixel is a node pixel, if one of the following conditions is meet: (1) it is to ensure that each edge pixel have exactly two neighbors, so that the edge pixels can be connected to edge chains in practical applications; (2) the case that no pixel is classified as the node pixel is avoided.

Based on the extended definition of refinement mode, the appropriate topological map is extracted from the edge-marked image. The algorithm will be described in detail as follows:

Input: a edge-marked image. of which boundaries are 8-connected and irreducible, and regions are 4-connected.

Step 1. Broadening the image. the edge-marked image is broadened by a pixel-width boundary, and then all pixels are marked as boundary pixels.

Step 2. Searching for 8-connected components of complete boundaries, that is the set of all pixels, and building every component of corresponding topological maps of boundary components.

Step 3. The classification of the boundary pixels is carried out based on the definition of irreducible pattern.

Step 4. The node pixels of 8-connected components are marked until each component is a simple connectivity. Otherwise, these pixels are reclassified. Each result component become a node of the topological map.

Step 5. The edge pixels of 8-connected components are marked. In order to avoid to merge different edge chains, the marked algorithm is improved as following modification: if the edge pixels is adjacent to the same node pixel, it is can be said that it is not connected. Each result component is an chain of edges and as a side of the topological map.

Step 6. For each component of the topological map, the following operations are needed to implement:

Step 6.1 For each edge chain of any components, a pair of corresponding half-lines is generated, and their relationship of which is defined by α_0 replacement. Most of edge chains have two unique endpoint pixels, which can be used to identify half-lines. In the case of degradation of pixel chains, the position and direction are used to identify half-lines. For a closed loop with non-node pixels, any edge pixel of edge chains must be reclassified as node pixels.

Step 6.2 For each node of any components, the relationship of two correlative half-line is defined by α_1 replacement. The method similar to the $\langle \alpha_1, \alpha_2 \rangle(\sigma)$ way can be used to shrink the half line.

Step 7. By the type of half-lines on components, the external relationship and containment relationship of each component are built.

5 Experimental Results and Conclusions

After the above analysis, the segmented regions are merged to eliminates the over-segmentation phenomenon after the region growing in the process of the region-based segmentation. While over-segmentation also occurs due to the high sensitivity of the watershed algorithm to image pixel intensity variations, thus contours of objects are buried in the clutter of the watershed line. To mitigate the above drawbacks of over-segmentation, we propose a new hybrid similarity measure based on the two criterions in terms of the gray similarity and boundary topological connectivity of regions and edges, which is used to further optimize the initial segmentation results for the above two algorithms. In this study, experiments with SPOT data of downtown Wuhan (Figure 2a) show that spatial information plays an important role in RS image segmentation. These images are used for testing the results proved the validity of the two improved methods.

As shown in Fig. 4, the top left figure is an image after region growing, the top right figure is an image after region segmentation with constraints on topological map, the following diagram is an enlarged figure. As can be seen from the figure, region-growing segmentation is implemented by two criterions: a global criteria on the gray similarity of regions and a local criteria on the continuity and contiguity between regions or pixels. the segmentation result is more in line with human visual perception, and also eliminates the over-segmentation phenomenon after region-growing process.

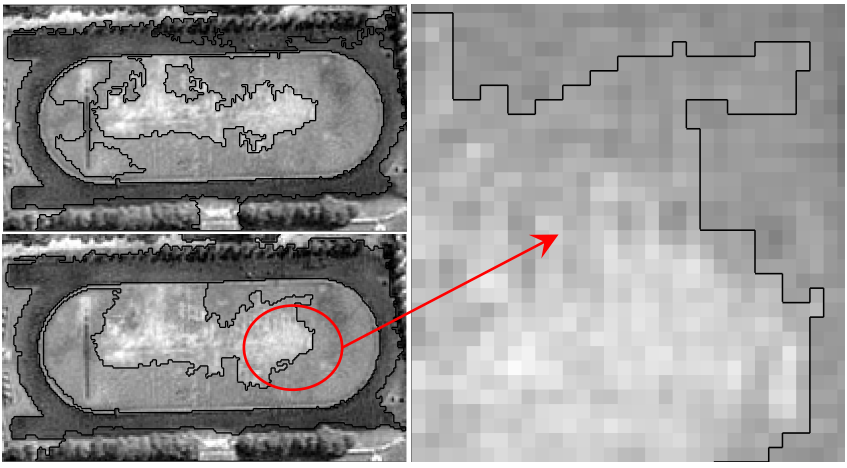

Fig. 4. Segmented result of the region growing based on 4-connectivity

As shown in Fig. 5, the top left figure is an image after the watershed transformation, the top right figure is an image after region segmentation with constraints on topological map, the following diagram is an enlarged figure. Based on two criterions of the gray similarity and boundary topological connectivity, connectivity analysis is implemented for segmented image after watershed transformation to remove noise and to mark boundaries of connecting regions.

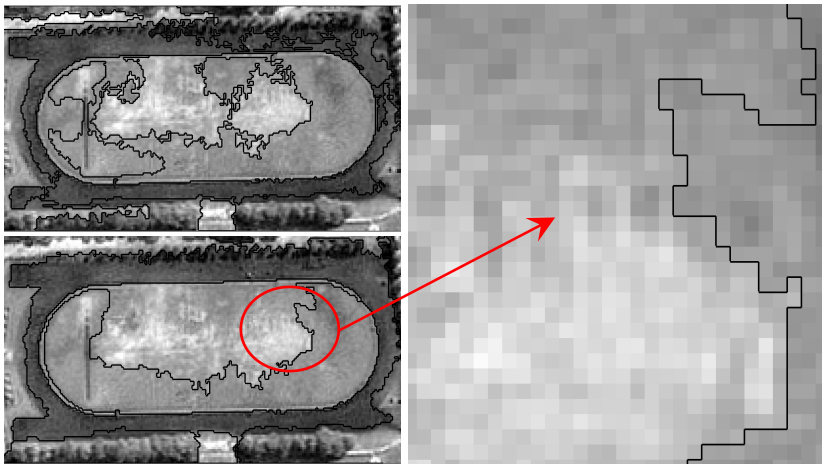

Fig. 5. Segmented result of the watershed transform based on 8-connectivity

Test results show that the algorithm with constraints of topological map save better the geometric topology information and most of the feature information of the image, have access to continuous and complete boundary of the closed contour. Moreover, the simplify image obtained by region merging well maintain the edges of connected regions remaining in the image. These edges are already existing in the image, rather than later.

References

1. Bleau, A., Leon, L.J.: Watershed-based Segmentation and Region Merging. Computer Vision and Image Understanding 77(3), 317–370 (2000)
2. Makrogiannis, S., Economou, G., Fotopoulos, S.: A Region Dissimilarity Relation That Combines Feature-Space and Spatial Information for Color Image Segmentation. IEEE Transactions on Systems, Man, and Cybernetics, Part B 35(1), 44–53 (2005)
3. Marfil, R., Molina-Tanco, L., Bandera, A., et al.: Pyramid Segmentation Algorithms Revisited. Pattern Recognition 39(8), 1430–1451 (2006)
4. David, P., Les, K.: Soft Image Segmentation by Weighted Linked Pyramid. Pattern Recognition Letters 22(2), 123–132 (2001)
5. Bazin, P.-L., Pham, D.L.: Topology Smoothing for Segmentation and Surface Reconstruction. In: Barillot, C., Haynor, D.R., Hellier, P. (eds.) MICCAI 2004. LNCS, vol. 3216, pp. 111–118. Springer, Heidelberg (2004)
6. Liu, X., Zhu, G., Jia, Z., Li, Q.: Hierarchical Image Representation Based on Digital Topology for Bridging Remote Sensing and GIS. In: First International Congress on Image and Signal Processing, pp. 736–740 (2008)
7. Bertrand, G.: On Topological Watersheds. Journal of Mathematical Imaging and Vision 22, 217–230 (2005)
8. Lotufo, R., Silva, W.: Minimal Set of Markers for the Watershed Transform. In: International Symposium on Mathematical Morphology, pp. 359–368 (2002)

9. Zhu, G., Liu, X., Jia, Z.: A Multi-level Image Description Model Scheme Based on Digital Topology. In: PIA 2007, 36(3/W49B), International Archives of Photogrammetry, Remote Sensing and Spatial Information Sciences, Munich, Germany, pp. 185–190 (2007)
10. Pavlidis, T., Liow, Y.-T.: Integrating Region Growing and Edge Detection. IEEE Transactions on Pattern Analysis and Machine Intelligence, PAMI 12, 225–233 (1990)
11. Baldacci, F., Braquelaire, A., Desbarats, P., Domenger, J.-P.: 3D Image Topological Structuring with an Oriented Boundary Graph for Split and Merge Segmentation. In: Coeurjolly, D., Sivignon, I., Tougne, L., Dupont, F. (eds.) DGCI 2008. LNCS, vol. 4992, pp. 541–552. Springer, Heidelberg (2008)
12. Sun, Y.F., Chen, Y., Zhang, Y.Z., Li, Y.X.: Automated Seeded Region Growing Method for Document Image Binarization Based on Topographic Features. In: Campilho, A.C., Kamel, M.S. (eds.) ICIAR 2004. LNCS, vol. 3212, pp. 200–208. Springer, Heidelberg (2004)
13. Hsieh, P.-F., Lee, L.C., Chen, N.-Y.: Effect of Spatial Resolution on Classification Errors of Pure and Mixed Pixels in Remote Sensing. IEEE Transactions on Geoscience and Remote Sensing 39(12), 2657–2663 (2001)
14. Weber, G.H., Scheuermann, G., Hamann, B.: Detecting critical regions in scalar fields. In: EUROGRAPHICS - IEEE TCVG Symposium on Visualization, pp. 1–11 (2003)

A Conversion Method between Wind Erosivity Values Estimated from Different Wind Datasets

Zhongling Guo[1], Chunping Chang[1], and Rende Wang[2]

[1] College of Resource and Environmental Sciences/Hebei Key Laboratory of Environmental Change and Ecological Construction, Hebei Normal University, 050024 Shijiazhuang, P.R. China
[2] Institute of Geographical Science, Hebei Academy of Sciences, 050011 Shijiazhuang, P.R. China
{Zhongling.Guo,Chunping.Chang,Rende.Wang gzldhr}@gmail.com

Abstract. Average wind erosivity is defined by a wind factor (Wf) in the Revised Wind Erosion Equation (RWEQ) model. To accurately compute the Wf, 1 min average wind data are needed. In this study, the Wf calculated from 1, 5, 10, 15, 30, 60 min average wind data and daily wind statistics (daily average, maximum and minimum wind speeds) were used to convert values of Wf estimated from different wind data type. The conversion methods, which establish the functional correlations between Wf values calculated from 1 min average wind speed data and the Wf values calculated from 5, 10, 15, 30, 60 min average wind speed data and daily wind statistics are described. So that the values of the Wf calculated from 1 min average wind speed data can be predicted from 5, 10, 15, 30, 60 min average wind speed data or daily wind statistics, respectively.

Keywords: RWEQ, wind factor, wind data type, conversion method.

1 Introduction

The Revised Wind Erosion Equation (RWEQ) is one of the most widely used models for computing field-scale wind erosion processes [1,2]. The model was developed by the USDA Agricultural Research Service (USDA-ARS) to evaluate annual or period wind erosion. Wind is the primary driver in RWEQ. Wind erosivity is the wind energy component of mass transport equations [3]. In RWEQ [1], wind erosivity is computed from a wind factor (Wf) where Wf is calculated as:

$$Wf = \sum_{i=1}^{N} \rho \frac{(U_i - U_t)^2 U_i}{gN} \tag{1}$$

where U_i is 2-m wind speed (m s^{-1}), U_t is threshold wind speed assumed as a constant of 5.0 m s^{-1}. If wind speed is below 5.0 m s^{-1}, then W for the period is zero, ρ is air density (kg m^{-3}), g is acceleration due to gravity (m s^{-2}), and N is the number of wind observations.

F. Bian et al. (Eds.): GRMSE 2013, Part I, CCIS 398, pp. 553–563, 2013.
© Springer-Verlag Berlin Heidelberg 2013

Originally, the single event version of RWEQ requires 1 min average wind data [1]. However, 1 min average wind data are not always available for some sites. Meteorological observations with averaging times of 10 min, hourly, or sometimes even daily values may only be available for some locations.

Generally, there may be two method to apply 10 min, hourly, or even daily wind statistics to the single event version of RWEQ: (1) the users could employ longer periods wind data to estimate the values of the Wf for RWEQ, or (2) convert longer-period (such as 10 min, an hour, or a day) wind speed data to 1 min wind speed data and then compute Wf. Yet several researches have shown that averaging wind data have significant impacts on wind erosivity prediction [4-6]. Moreover, theoretically, predictions of short-term variability in wind flows from wind data averaged over relatively long time are extremely difficult [7-9]. Figure 1 illustrates that a mean wind speed for a longer averaging interval (a day) could show different short-term fluctuations with different values of wind erosivity (Wf). Mathematically, one mean wind speed for a relatively long period can be derived from countless short-term wind fluctuations, which accordingly produce innumerable values of wind erosivity (Wf) (Figure 1). Our analysis has implied that a fixed short-term (1 min) wind fluctuation with a determined value of wind erosivity (Wf) cannot be precisely estimated from the longer-term (such as 10 min or an hour) wind data. Some gusts with regard to wind erosion can be lost during the conversion of different wind data types. Therefore, we cannot directly use or convert wind data averaged over longer periods, such as 10 min, 60 min or a day, to estimate the Wf for RWEQ.

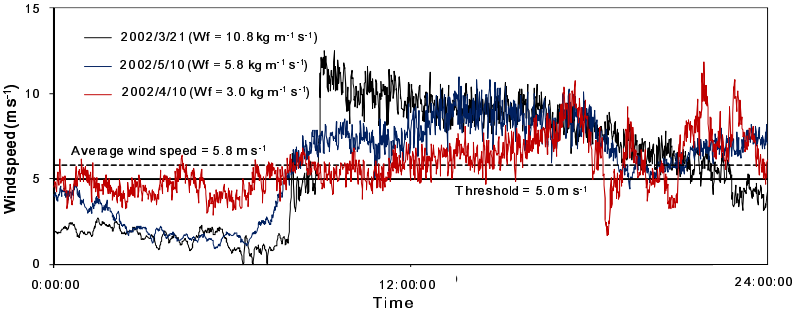

Fig. 1. Different wind flows with the same daily average wind speed (5.8 m s^{-1}) but different wind erosivity (Wf) for a daily period. Note that the relatively long averaging time obscure the short-term variability in wind flows when the erosive wind speeds may occur. Here a fixed value of 5.0 m s^{-1} was used for Wf estimation.

The challenge for application of the RWEQ to various sites without 1 min wind data still remains. A method for transforming between Wf values obtained from different wind datasets may be feasible. So far, no attempt has been made to develop the functional relationships between Wf values calculated from different wind datasets. The purpose of this study is to develop a method of converting between Wf values calculated from different types of wind data.

2 Data

An automated meteorological tower was placed on an experimental site located in a partially vegetated grass field in Lubbock County, Texas (33.599241 N, 102.057681 W) (Figure 2). The sampling site lies on the level plains of the Llano Estacado, a region known for its windy conditions and associated wind erosion problems [10]. Wind speed was measured at a height of 2 m using a propeller-type anemometer. The sampling frequency was 1 Hz and values were averaged each minute. The full sampling period extended over a period of 175 days from March 13 to September 3, 2002. During this time, only 19 min of wind data scattered over three days were lost due to instrument problems. Thus, we obtained a fairly continuous wind record, with only a few minor gaps, over the 175-day sampling period.

Fig. 2. The automated meteorological tower placed on an experimental site located in a partially vegetated grass field

The 5, 10 15, 30, and 60 min average wind speeds are calculated from the measured 1 min average wind speed data. The daily wind statistics (daily average, maximum and minimum wind speeds) dataset is extracted from the 10 min average wind speed data, since the standard wind speed is based upon a 10 min average [11]. Equation 1 was used to calculate daily values of Wf. Air density (ρ) and the acceleration of gravity (g) were assumed as 1.293 kg m^{-3} and 9.8 m s^{-2}, respectively. Values of daily Wf for each dataset were computed to develop the method of conversion.

Wind erosivity varies widely from year (season) to year (season). For our sampling location on the Llano Estacado, west Texas, USA, high wind erosivity generally occurs in spring and low wind erosivity generally occurs in summer. Accordingly, it

may be irrational that using the wind data sampled in spring (summer) to validate the conversion methods that are calibrated from the wind data sampled in summer (spring). Therefore, the days of April (spring) and August (summer) (61 days) were chosen to validate the conversion methods, and the other days for the sampling period (114 days) were used to develop the conversion methods.

3 Conversion Method

For some places, hourly or sub-hourly wind data are available. Here we attempt to explore a method that converts Wf values calculated from 5, 10, 15, 30, and 60 min (hourly) average wind data to Wf values calculated from 1 min average wind data. The relative error between Wf values calculated from different averaged wind data was calculated by [4]:

$$RE_n = (Wf_1 - Wf_n) / Wf_1 \tag{2}$$

where Wf_1 is Wf computed from 1 min average wind data, Wf_n is the Wf computed from 5, 10, 15, 30 and 60 min average wind data (Wf-5, 10, 15, 30, 60 min), and RE_n is relative error between Wf_1 and Wf_n. By rearranging Equation 2 we obtain:

$$Wf_1 = Wf_n / (1- RE_n) \tag{3}$$

Equation 3 states that Wf_1 is a function of Wf_n and RE_n. Wf_n can be calculated from 5, 10, 15, 30 or 60 min wind data directly. To obtain Wf_1, one needs to compute values of RE_n. Thus, we further examined the relationship between the RE_n for the Wf-5, 10, 15, 30, 60 min and the daily wind summary statistics for the wind speed data averaged over 5, 10, 15, 30 and 60 min, respectively. Daily wind summary statistics typically include average wind speed (AWS), the average of the wind speeds greater than threshold (AWST), turbulence intensity (I_u), Weibull coefficients *k*, *c*. Regression analysis was used to explore the relationship between RE_n and these variables. It was found that the RE_n for the Wf-5, 10, 15, 30, 60 min were closely associated with the AWST for 5, 10, 15, 30, 60 min average wind speed data, respectively. Plots of the RE_n as a function of the AWST are shown in Figure 3. Note that RE_n decreased as the AWST increased. A close examination of the data suggests that the RE_n increased exponentially with decreasing AWST. The best-fitting nonlinear regression equations from the plots were presented in Figure 3. The high values of R-square suggest that the RE_n can be extrapolated from the AWST for 5, 10, 15, 30, 60 min average wind speed data using these regression equations (Figure 3), respectively. Accordingly, we can use the Wf-5, 10, 15, 30, 60 min and the corresponding AWST for 5, 10, 15, 30, 60 min average wind speed data to estimate the Wf-1 min based on the Equation 3. This method is used to make the conversion between the Wf-5, 10, 15, 30, 60 min and Wf-1 min.

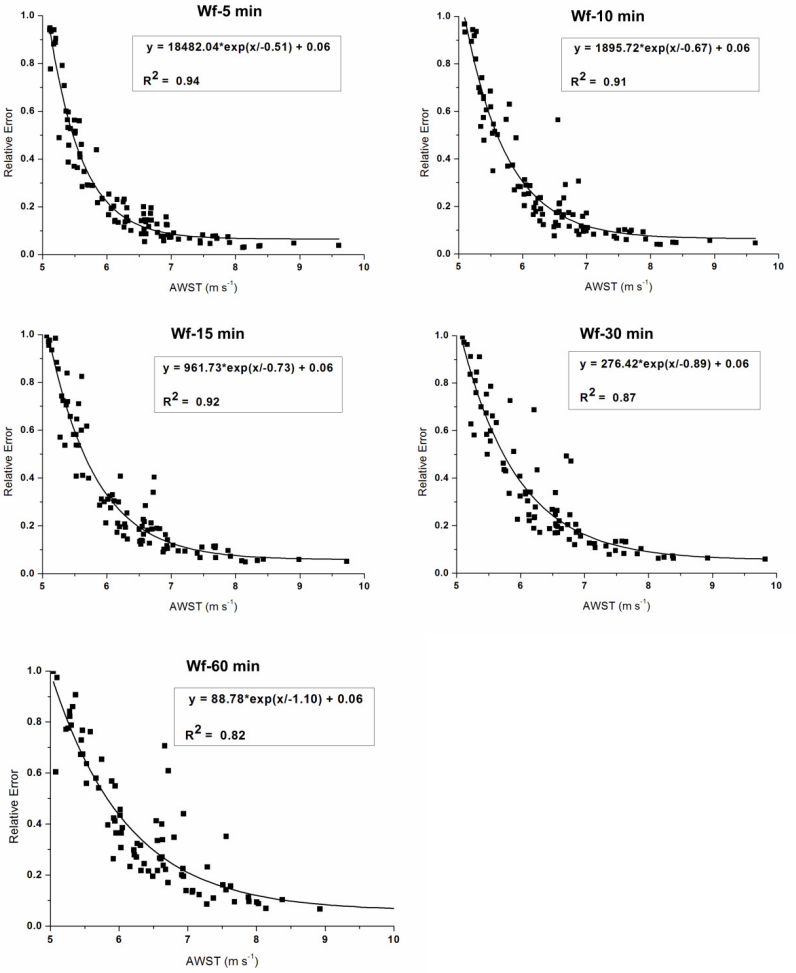

Fig. 3. Plots of the relative errors (RE_n) of the daily Wf for different averaging time as a function of the average of the wind speeds greater than threshold (AWST) for corresponding average wind speed data. Wf-5 min, Wf-10 min, Wf-15 min, Wf-30 min and Wf-60 min represent the relative errors (RE_n) of the daily Wf for 5, 10, 15, 30 and 60 min average wind speeds as a function of the AWST of corresponding average wind speed data, respectively. Note that the threshold for Wf is 5 m s^{-1}.

Note that an important input variable for the conversion method mentioned above is the average of wind speeds greater than threshold (AWST), but this important variable may not always be available. Thus, we cannot use these periods that lack daily AWST to develop and validate the conversion method. Finally, the days with the AWST for 5, 10, 15, 30 or 60 min average wind data were actually used to develop and validate the conversion method (Table 1).

Table 1. The days used to develop and validate the conversion method for different dataset. 5 min, 10 min, 15 min, 30 min and 60 min represent 5, 10, 15, 30 and 60 min average wind dataset, respectively. Daily represent daily wind statistics dataset.

Dataset type	5 min	10 min	15 min	30 min	60 min	Daily
Calibration days number	94	90	90	84	81	114
Validation days number	52	48	47	46	43	61

For some sites, only daily wind statistics are available. Here we discuss a general case where the daily average, maximum and minimum wind speed are available and how to use these daily wind statistics to predict the values of Wf-1 min.

The diurnal wind speed curve may be described by:

$$W_n = W_{ave} + \frac{1}{2}(W_{\max} - W_{\min})COS(\frac{n \cdot \pi}{12}) \tag{4}$$

where W_n is wind speed at hour of n, W_{ave} is the daily average wind speed, W_{max} is the daily maximum wind speed, W_{min} is the daily minimum wind speed. Using Equation 4, 24 values of wind speed were computed for a day using (n varies from 0 to 23). Estimates of Wf computed from the 24 generated wind speeds (Wf-daily) were used to further derive a relationship between the Wf-1 min and the Wf-daily. Plots of the Wf-1 min as a function of the Wf-daily are shown in Figure 4. Regression analysis reveals that the response of the Wf-1 min is linear for the input of the Wf-daily (Figure 4). Thus, a linear regression equation, shown in Figure 4, was used to estimate the Wf-1 min from Wf-daily. Here, the quantitative relationship between the Wf-1 min and daily wind statistics was established from an intermediate variable, the Wf-daily. This method is used to perform the conversion between the Wf-1 min and the daily wind statistics. The calibration and validation days number are shown in Table 1.

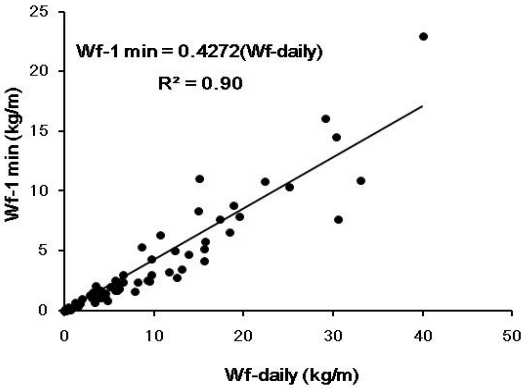

Fig. 4. Plots of the Wf-1 min as a function of the Wf-daily estimated from daily average, maximum and minimum wind speeds

4 Validation and Discussion

The following statistical parameters were used to quantify the performance of the conversion methods. Values of Wf-1 min calculated directly from 1 min average wind data was used as the observed Wf-1 min values, and the Wf-1 min estimated from the conversion method formed the predicted Wf-1 min values.

The mean absolute relative error (MARE) was used to evaluate the average difference between observed and predicted values.

$$MARE = \frac{\sum_{i=1}^{n} \left| (O_i - P_i) / O_i \right|}{n} \times 100\% \tag{5}$$

where MARE (%) is the mean absolute relative error, O_i are the observed values, and P_i are the predicted values. But MARE may cancel out the underestimation or overestimation of wind erosivity. Therefore, relative error (RE) was used to estimate the actual bias for wind erosivity.

$$RE = \frac{O_i - P_i}{O_i} \times 100\% \tag{6}$$

where RE (%) is the relative error. The Nash-Sutcliffe coefficient [12] was also used to access the models efficiency.

$$NSC = 1 - \frac{\sum_{i=1}^{n} (O_i - P_i)^2}{\sum_{i=1}^{n} (O_i - O_m)^2} \tag{7}$$

where NSC is Nash-Sutcliffe coefficient and O_m is the mean of the observed values.

Comparisons between predicted and observed Wf-1 min values are presented in Table 2 and Figure 5 for different wind datasets. The MARE of the conversion methods varies from 12.8% to 60.41% for different dataset. The RE of the conversion methods vary widely, but typically vary from -100% to 100% except for the daily wind dataset. The NSC is very high and values only change slightly for all wind datasets. The predicted Wf-1 min fit observed counterparts very well (Figure 5). Good agreement is shown in Figure 5 due to the good performance of the conversion methods for large Wf-1 min values (Table 3). For different Wf-1 min values, the larger the values of Wf-1 min, the better the conversion methods performance (Table 3). The results, as presented in Table 3, indicate that the conversion method may not be suitable for the small values of Wf-1 min, such as the values less than 0.5 kg/m. However, the large values of Wf-1 min associated with serious wind erosion storms are generally more important for period wind erosion estimation. Overall, the performance of the conversion methods is satisfactory, especially for the large Wf-1 min values greater than 0.5 kg m^{-1} s^{-1}.

Table 2. Statistics between observed and predicted Wf-1 min values for different wind dataset

Wind dataset	MARE (%)	RE (%)	NSC
5 min	12.80	-44.51 - 81.53	0.9987
10 min	14.77	-50.80 - 74.44	0.9988
15 min	14.52	-58.48 - 55.49	0.9990
30 min	17.95	-54.53 - 85.13	0.9982
60 min	25.06	-51.86 - 98.69	0.9950
daily	60.41	-230.74 - 100.00	0.9877

Table 3. The mean absolute relative error for different Wf-1 min values class for different wind dataset

Wf-1 min ($kg\ m^{-1}\ s^{-1}$)	Mean absolute relative error (MARE) (%)					
	5 min	10 min	15 min	30 min	60 min	daily
>10.0	2.19	1.94	1.81	2.37	1.56	5.31
5.0-10.0	1.64	1.66	1.71	2.39	6.94	6.29
1.0-5.0	2.99	4.91	5.25	8.79	15.77	17.98
0.5-1.0	7.37	13.30	14.56	14.79	13.44	56.19
<0.5	21.38	24.62	24.05	32.75	48.37	86.90

The conversion methods may span the gap between Wf values calculated from different wind dataset. In general, different sites may have different wind dataset. For example, 10 min average is the WMO standard wind speed [11]. Hourly average wind series can be estimated based on several mathematical models for regions lacking wind data [12-15]. For some sites, only the daily wind statistics are available. With the conversion methods, we can estimate the Wf-1 min from some rough wind data, such as hourly or daily wind dataset.

Limitation of the conversion methods is that all these parameters of the regression equations as shown in Figure 3 and 4 may have different values at different geographical regions, or perhaps they may also vary between seasons or years. The main requirement for using the conversion methods is therefore to determine the values of these parameters. Thus, it may be risky to use the regression formulas to convert Wf values for other sites with different wind fluctuations. Further studies are needed to examine the conversion methods using inter-annual and inter-site wind data.

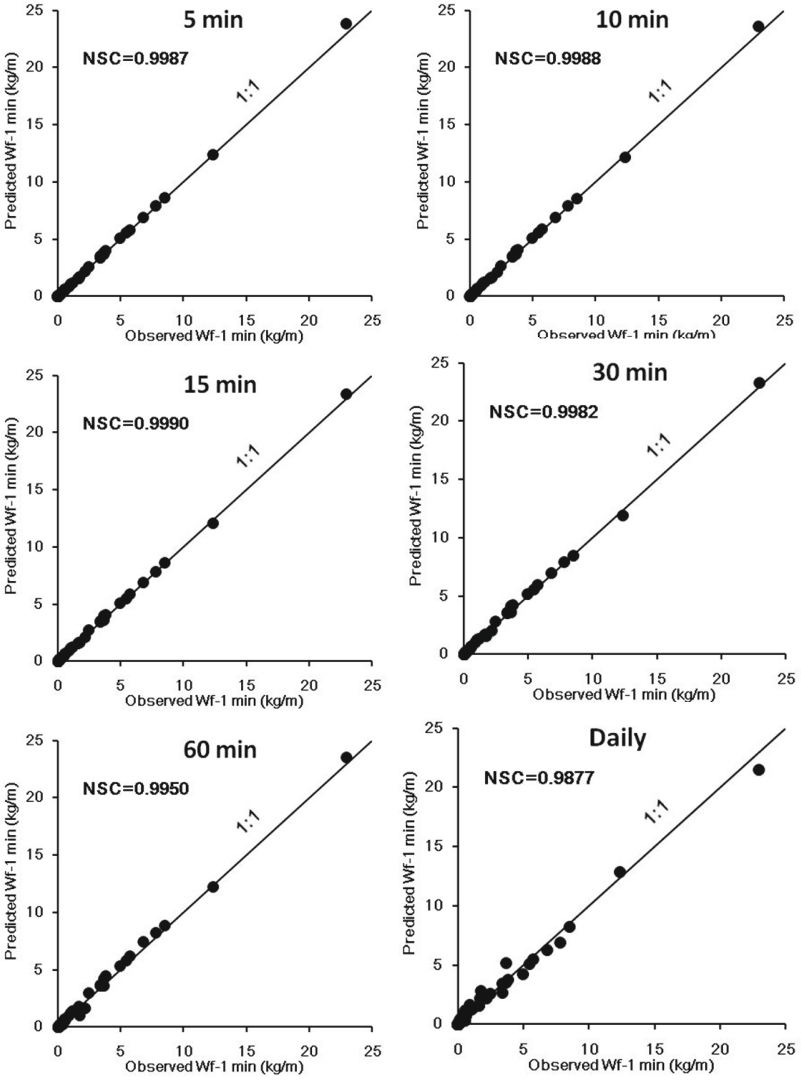

Fig. 5. Observed VS predicted Wf-1 min values. 5 min, 10 min, 15 min, 30 min and 60 min represent the predicted Wf-1 min were estimated from 5 min, 10 min, 15 min, 30 min, 60 min average wind data, respectively. Daily represent the predicted Wf-1 min was estimated from the daily average, maximum and minimum wind speeds. NSC is Nash-Sutcliffe coefficient.

5 Conclusion

In this study, we used the Wf values computed from 1, 5, 10, 15, 30 and 60 min average wind data or daily wind statistics to develop the conversion methods between the values of Wf estimated from different datasets.

The conversion methods were developed to transform the Wf values estimated from different wind datasets. Validation of the conversion methods indicated that the conversion methods are able to predict the required Wf-1 min, especially for the big Wf-1 min values. The conversion methods could help to extend and apply the RWEQ to the regions where 5, 10, 15, 30 and 60 min average wind data or daily wind statistics are available.

Acknowledgments. This research was funded by the Doctoral Starting up Foundation of Hebei Normal University, China, Natural Science Foundation for Young Scientists of China (Grant No. 41101251), Natural Science Foundation for Young Scientists of Hebei Province, China (Grant No. 41101251 and 41301291), and Science Program of the Hebei Academy of Sciences of China (Grant No.13109). The authors would like to thank J.E. Stout and T.M. Zobeck for supplying the field data used in this paper.

References

1. Fryrear, D.W., Saleh, A., Bilbro, J.D.: A single event wind erosion model. Tran. of ASAE 41(5), 1369–1374 (1998)
2. Fryrear, D.W., Saleh, A., Bilbro, J.D., Schomberg, H.M., Stout, J.E., Zobeck, T.M.: Revised Wind Erosion Equation (RWEQ). Technical Bulletin 1. Lubbock, TX: Southern Plains Area Cropping Systems Research Laboratory, Wind Erosion and Water Conservation Research Unit, USDA-ARS (1998)
3. Greeley, R., Iversen, J.D.: Wind as a Geological Process: On Earth, Mars, Venus and Titan. Cambridge University, New York (1985)
4. Guo, Z., Zobeck, T.M., Stout, J.E., Zhang, K.: The effect of wind averaging time on wind erosivity estimation. Earth Surface Process and Landforms 37(7), 797–802 (2012)
5. Larsén, X.G., Mann, J.: The effects of disjunct sampling and averaging time on maximum mean wind speeds. J. of Wind Engineering and Industrial Aerodynamics 94, 581–602 (2006)
6. Namikas, S.L., Bauer, B.O., Sherman, D.J.: Influence of averaging interval on shear velocity estimates for aeolian transport modelling. Geomorphology 53, 235–246 (2003)
7. Pavlik, D., Söhl, D., Pluntke, T., Mykhnovych, A., Bernhofer, C.: Dynamic downscaling of global climate projections for Eastern Europe with a horizontal resolution of 7 km. Environmental Earth Science 65(5), 1475–1482 (2011)
8. Ephrath, J.E., Goudriaan, J., Marani, A.: Modelling diurnal patterns of air temperature, radiation, wind speed, and relative humidity by equations from daily characteristics. Agric. Systems 51(4), 377–393 (1996)
9. Sailor, D.J., Smith, M., Hart, M.: Climate change implications for wind power resources in the Northwest United States. Renewable Energy 33(11), 2393–2406 (2008)
10. Stout, J.E.: Diurnal patterns of blowing sand. Earth Surface Processes and Landforms 35, 314–318 (2010)
11. World Meteorological Organization (WMO).: Guide to meteorological instruments and methods of observation, 7th edn. World Meteorological Organization No. 8, Geneva (2008)
12. Nash, J.E., Sutcliffe, J.V.: River flow forecasting through conceptual models part I – A discussion of principles. J. of Hydrology 10, 282–290 (1970)

13. Ma, L., Luan, S., Jiang, C., Liu, H., Zhang, Y.: A review on the forecasting of wind speed and generated power. Renewable and Sustainable Energy Rev. 13(4), 915–920 (2009)
14. Sfetsos, A.: A comparison of various forecasting techniques applied to mean hourly wind speed time series. Renewable Energy 21, 23–35 (2000)
15. Guo, Z., Zobeck, T.M., Zhang, K., Li, F.: Estimating potential wind erosion of agricultural lands in northern China using the Revised Wind Erosion Equation (RWEQ) and geographic information systems. J. of Soil and Water Conservation 68(1), 13–21 (2013)

Studying on Denoising of Chaotic Signal Using ICA and EMD

Xiang Li[1] and Wenbo Wang[1,2]

[1] College of Sciences, Wuhan University of Science and Technology, 430065, Wuhan, China
[2] State Key Laboratory of Remote Sensing science, 100101, Beijing, China

Abstract. In this paper, a new method for reducing noise within chaotic signal based on ICA (Independent Component Analysis) and EMD (Empirical Mode Decomposition) is proposed. The basic idea is decomposing chaotic signal and constructing multidimensional input vectors, firstly, on the base of EMD and its translation invariance. Then, it makes the independent component analysis on the input vectors, which means a self adapting denoising is carried out for the intrinsic mode functions (IMFs) of chaotic signal. At last, all the IMFs composed the new denoised chaotic signal. An experiment on Lorenz chaotic signal which is composed as different Gaussian noises and monthly observed chaotic sequence on sunspots was put into practice. The result proved the method proposed by this paper is effective in denoising of chaotic signal. Moreover, it can correct the center point in the phase space effectively, which makes it approach the real track of the chaotic attractor.

Keywords: ICA, EMD, Chaotic signal, Denoising.

PACS: 02.30.Nw, 31.70.Hq.

1 Introduction

Under the influence of measuring accuracy and external environment, actual measured chaotic signal will inevitably be mixed with noise. Thus, the real dynamic behavior of chaotic signal will be concealed, which has great effect on the parameter calculation and the precision of prediction. How to reconstruct chaotic signal from noisy signal and how to achieve real attractor structure utilizing the geometry characteristic of the manifold of the original chaotic attractor have been an urgent problem to be resolved[1,2]. However, chaotic signal is actually broadband and familiar with noise and its frequency band is always partly overlapped with other signals'. So it is difficult to separate the signals using traditional methods such as frequency spectrum analysis and linear filtering. And new ways must be found to distinguish chaotic signal between other signals. So far, some methods of noise reduction have been recommended to separate noise from chaotic background.

Some of these methods like structural cost function method and statistical model method are both based on existing chaotic dynamic characteristics[3-7]. The denoising of chaotic signal based on wavelet transform has a good result[8-10] . It has a great

F. Bian et al. (Eds.): GRMSE 2013, Part I, CCIS 398, pp. 564–572, 2013.
© Springer-Verlag Berlin Heidelberg 2013

ability to analyze local characteristics of signals in time-frequency field while the calculation is simply. However, the wavelet base and the number of decomposition level, which play an important part in the result according to the researches[11,12], must be selected before the denoising. Thus, wavelet transform is limited to denoise the signal. A new method called empirical mode decomposition (EMD) proposed by Huang is better than wavelet transform. It is a data driven and self-adapting denoising method. EMD can decompose original signal into a group of physical meaningful intrinsic mode function (IMF). The most competitive advantage of EMD over wavelet transform is that the base function and the number of decomposition level in EMD don't need to be given and the algorithm itself can get these parameters according to the characteristics of signals. So far, EMD has been widely used in extraction and prediction of chaotic signal[14,15]. In this article, EMD will be utilized to denoise the chaotic signal[16,17].

As a matter of fact, it's not so easy to analyze coefficient distribution model and noise variance efficiently because the EMD theory is imperfect. This causes it difficult to denoise IMFs. Therefore, the way to denoise IMFs based on their statistical property is the way to optimize the denoising results. Independent component analysis (ICA) which is proposed in the research of blind signal separation is known as a self-adaptive optimal algorithm[19]. ICA is now widely concerned in the area of redundancy reduction and denoising[20,21]. It is able to separate the desired signal from noises with the original independent signal components integrated in both time and frequency domain just under the condition that observational signal is the addition of independent desired signal and noises. Consequently, ICA is quite appropriate for IMF denoising[22] . In this article, we raise a denoising algorithm combining ICA with EMD. It decomposes original signal into IMFs using EMD firstly, and denoises the IMFs with ICA secondly, then composes the denoised IMFs. According to the experiment, this algorithm can denoise chaotic signal effectively while the midpoint position in phase space can be exactly corrected.

2 The Independent Component Analysis Theory

Independent component analysis (ICA) is a kind of new method for signal processing, which have been used widely recently in many aspects including signal filtering[19-21]. The basic ideal of ICA is to obtain the independent approximate value of original signal by estimating it utilizing its higher statistical characteristics. Suppose that $\mathbf{x}_1, \mathbf{x}_2, \ldots, \mathbf{x}_M$ are M random observational vectors which are combined linearly by N unknown independent components namely $\mathbf{s}_1, \mathbf{s}_2, \ldots, \mathbf{s}_N$. The mathematical model of ICA can be expressed as:

$$X = AS \tag{1}$$

Where $\mathbf{X} = [\mathbf{x}_1, \mathbf{x}_2, \cdots, \mathbf{x}_M]^T$, $\mathbf{S} = [\mathbf{s}_1, \mathbf{s}_2, \cdots, \mathbf{s}_N]^T$, $\mathbf{A}$ is a $M \times N$ mixed matrix, and $\mathbf{A}$ and $\mathbf{S}$ is unknown. What ICA can solve is to estimate $\mathbf{A}$ and $\mathbf{S}$ with $\mathbf{x}_i$ and

prior knowledge of $\mathbf{S}$. Generally, assume that: (1) original signals needed to be estimated are independent statistically; (2) no more than one original signal obeys Gaussian distribution. In fact, ICA is used to construct a disjunctive matrix $\mathbf{W}$ so as to make $\mathbf{y}_i$ that is a component of M -dimensional output vector $\mathbf{Y} = \mathbf{WX}$ be mutual independent. Thus, an estimate of original signal $\mathbf{s}_i$ will be got as $\hat{\mathbf{s}}_i = \mathbf{y}_i$. FastICA and Infomax are two most usually used algorithms in ICA [23]. For extraneous variable, the approximate negative entropy is defined as[19] :

$$J(\mathbf{y}) \propto \{E[G(\mathbf{y})] - E[G(\mathbf{v})]\}^2 \quad , \tag{2}$$

Where $\mathbf{y}$ is centralized and decorrelation processed observational signal, $\mathbf{v}$ is a Gaussian variable of zero-mean elemental variance, and G is a non-quadratic function. The workflow of FastICA can be described as below:

(1) Centralization and decorrelation. These two processes make observational signal have a zero-mean and an elemental variance.

(2) Initializing $\mathbf{W} = (\mathbf{w}_1, \mathbf{w}_2, \cdots, \mathbf{w}_n)$, making it a 1 norm random matrix. In the formula n is the number of row vectors.

(3) Updating every $\mathbf{w}_i$ by next formula:

$$\mathbf{w}_i^+ \leftarrow E\{\mathbf{x}g(\mathbf{w}_i^T\mathbf{x})\} - E\{g'(\mathbf{w}_i^T\mathbf{x})\}\mathbf{w}_i^T \ ,$$

$$\mathbf{w}_i \leftarrow \mathbf{w}_i^+ / \| \mathbf{w}_i^+ \|$$

(4) Symmetric orthogonalization of matrix $\mathbf{W}$:

$$\mathbf{W} \leftarrow (\mathbf{W}\mathbf{W}^T)^{-1/2}\mathbf{W} .$$

(5) Judging the convergence property of $\mathbf{W}$. If the value of the formula defined as $1 - \min\{abs[diag(\mathbf{W}(k+1)^T) * \mathbf{W}(k)]\}$ is smaller than the condition of convergence, then $\mathbf{W}$ is the desired matrix. Or, go back to step (3).

(6) Obtaining all independent components by $\mathbf{Y} = \mathbf{WX}$.

3 Denoising of Chaotic Signal Based on ICA and EMD

3.1 The Empirical Mode Decomposition of Chaotic Signal

Empirical Mode Decomposition (EMD) is aimed at decomposing origin signal into a series of intrinsic mode functions (IMF) with time scale feature. The IMFs must require the following two conditions: one is that the difference between the number of IMFs' extreme points and the number of its zero points is no more than 1; another is that the envelope line made up by maximum value points and minimum value points has a zero mean[13]. Decomposed with EMD, the chaotic signal $\mathbf{x}(t)$ can be expressed by addition of a series of IMFs and a remainder term. That is

$$\mathbf{x}(t) = \sum_{k=1}^{K} \mathbf{imf}_k(t) + \mathbf{r}_K(t) \ , \tag{3}$$

Where $\mathbf{imf}_k$ is the k th IMF component, and $\mathbf{r}_K(t)$ is the remainder term. If $\mathbf{x}(t)$ is polluted by additive noises, the noises in $\mathbf{imf}_k$ obey the additive noise model approximately too[24] . Namely

$$\mathbf{imf}_k = \mathbf{y}_k + \mathbf{n}_k \ , \tag{4}$$

Where $\mathbf{y}_k$ is unpolluted signal, $\mathbf{n}_k$ is noises, $\mathbf{y}_k$ and $\mathbf{n}_k$ is mutual independent.

3.2 Multi-dimensional Input Vectors Constructing Using ICA in IMFs Denoising

After the process of EMD, chaotic signal will be decomposed into a series of IMFs which have different frequency. Every IMF is a mono-component with a single form. After decomposition, the noises of the chaotic signal are distributed in every IMF. If the IMFs can be effectively filtered, the noises will be eliminated either. And the composition of the filtered IMFs is just the denoised chaotic signal. In this article, ICA is used to filter IMFs. To ensure ICA can work normally the number of signals must be more than the number of independent sources, that is, the input vectors must be multi-dimensional. However, the decomposed signal has only one IMF in every frequency layer. Li H[22] have solved this problem by constructing virtual noise channels.

In reality, of all the IMFs the first layer of IMF is almost made up of noises. We raise a new constructing method adapted from the idea of translation invariable EMD to construct multi-dimensional input vectors[18]. After the process of EMD, different noise samples will be obtained by cyclic shift of the first layer of IMF. Superimpose the noise samples with remainder IMFs, and a group of noisy signals which have the same signal to noise ratio will be made. The concrete steps of constructing these multi-dimensional input vectors in ICA denoising can be described as follow.

Step1: Decomposing chaotic signal $\mathbf{x}(t)$ by EMD, and we will get L IMFs. Denoting them by $\mathbf{imf}_1$, $\mathbf{imf}_2$, $\cdots$, $\mathbf{imf}_L$, then marking

$$\mathbf{x}_p(t) = \sum_{i=2}^{L} \mathbf{imf}_i \ (t) \, ;$$

Step2: Cyclic shifting the first IMF for P times, and P shifted data will be got as

$$\mathbf{imf}_1^{\alpha} = \text{Circulate} \ (\mathbf{imf}_1 \ ), \ \alpha = 1, 2, \cdots, P \, ;$$

Step3: Constructing new noisy signal $\mathbf{x}^{\alpha}(t) = \mathbf{x}_p(t) + \mathbf{imf}_1^{\alpha}(t)$;

Step4: Decomposing $\mathbf{x}^{\alpha}(t)$ $(\alpha = 1, 2, \cdots, P)$ into L IMFs, namely $\mathbf{imf}_1^{\alpha}$, $\mathbf{imf}_2^{\alpha}, \cdots, \mathbf{imf}_L^{\alpha}$ ($\alpha = 1, 2, \cdots, P$).

A P-dimensional vector collection $\mathbf{h}_i = \left\{\mathbf{imf}_i^1, \mathbf{imf}_i^2, \cdots, \mathbf{imf}_i^P\right\}$ is used as input vector in this paper. In the collection, $i = 1, 2, \cdots, L$. By now, the input vector has been constructed, and ICA can be carried out to denoise every layer of IMFs.

4 Experiment Analysis of Chaotic Signal Denoising

In order to verify the validity of the method proposed by this paper, a Lorenz chaotic signal composed as different Gaussian noises and monthly observational chaotic sequence on sunspots have been researched. In contrast, EMD threshold denoising method based on coefficient [17] and EMD threshold denoising method based on module unit[18] have also been used to do experiments.

4.1 Chaotic Signal Denoising of Lorenz System

The dynamic equation of Lorenz system is:

$$\begin{cases} \dot{x} = -\sigma(x - y) \\ \dot{y} = -xz + \gamma x - y \\ \dot{z} = xy - bz \end{cases}$$

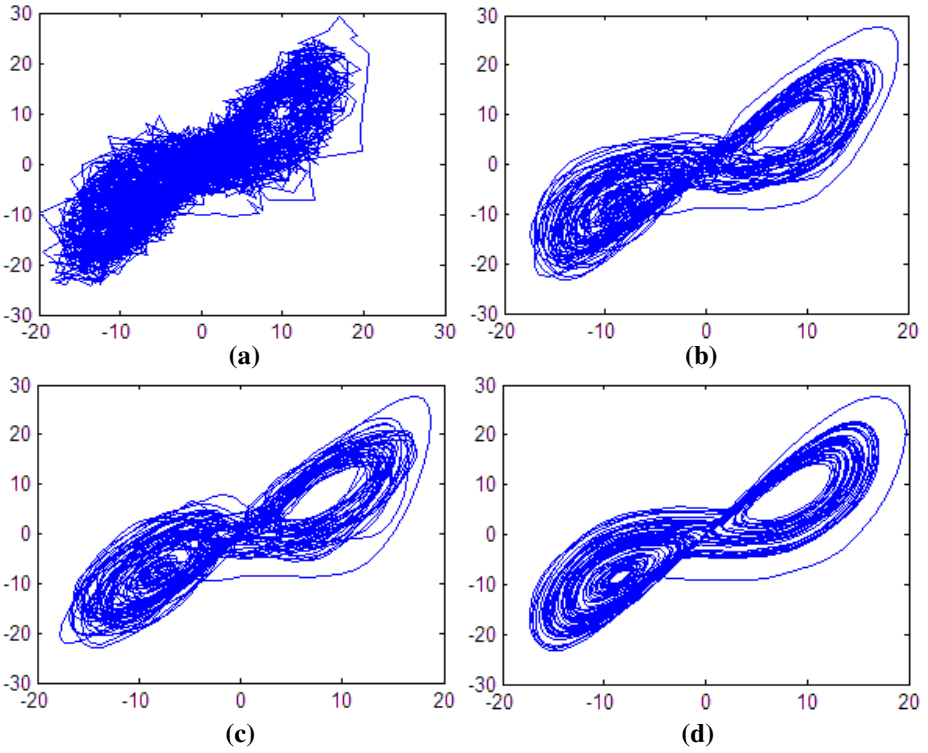

Fig. 1. 2-dimensional phase graph of noisy and denoised Lorenz signal (a) 60% noisy signal; (b) EMD threshold denoising; (c) EMD mode threshold denoising; (d) EMD-ICA denoising

Table 1. SNR(dB) and RMSE of denoised signals

Noise intensity	EMD coefficient threshold SNR/RMSE	EMD Mode Threshod SNR/RMSE	The proposed method SNR/RMSE
20%	38.9846/0.6244	41.5037/0.5586	42.8225/0.4913
40%	27.1105/1.1513	28.3427/0.9988	29.2362/0.8933
60%	21.3486/1.5985	24.1612/1.4077	25.1809/1.2527
80%	15.5768/3.0768	16.6562/2.7024	18.9117/2.4341
Monthly sunpot	12.5889/14.3135	13.1734/14.1051	13.6288/13.5098

Let $\sigma = 10$, $\gamma = 28$, $b = 8/3$, then this system is chaotic. This system is numerically simulated using Matlab by four-order Runge-Kutta method. The step length was set to 0.01, and the initial value was $y(1,1) = 10$; $y(1,2) = 1$; $y(1,3) = 0$. To simulate the chaotic signal, 50000 points was generated. These points stand out clearly in Figure 1(a). Firstly, three methods mentioned above were used to denoise 60% noisy Lorenz signal. The denoised time series signal and its 2-dimensional phase graphs are shown as Figure 1. SNR and RMSE of denoised signal are shown in Table 1.By comparing phase graph (b), (c) and (d) in above two figures, the signal denoised by method proposed in this paper is more similar to the origin signal (shown in Figure 1(a)). That is to say, EMD-ICA denoising method can show the geometric structure of original signal's chaotic attractors more clearly. As is shown in Table 1, EMD-ICA method has least SNR and most RMSE. In support of this experimental result, those three methods have been implemented respectively in 20%, 40% and 80% Gaussian noisy Lorenz chaotic signal. The results shown in Table 1 have given evidence to the experiment. In conclusion, for a model known chaotic system, EMD-ICA method can eliminate the noises hiding in it more effectively.

4.2 Denoising of Monthly Sunspot Signal

Recently, with the development of the theory of chaos, the research on chaotic characteristics of sunspot is increasing. During the observation, the observed value is always mixed with noises. So denoising must be executed to origin data. In our experiment, sunspot data observed from Jan. 1749 to Mar. 2007 is chosen. Also, three method mentioned above are utilized to denoise sunspot signal. The time series graph and the phase graph of noisy and denoised signal are shown in Figure 2.

As is shown in Figure 2, the noisy signal has a rambling pseudorandom characteristic while the denoised signal has clear and regular geometric structure of chaotic attractors. The intrinsic certainty of the denoised chaotic signal is increased, and the dynamic characteristics of the chaotic system are appeared. This smooth and regular structure gives evidence to the method raised in this paper. SNR and RMSE of denoised sunspot signal are listed in Table 1. EMD-ICA denoised signal has the most SNR and the least RMSE. In conclusion, for real signals, EMD-ICA denoising is also the most effective method of all.

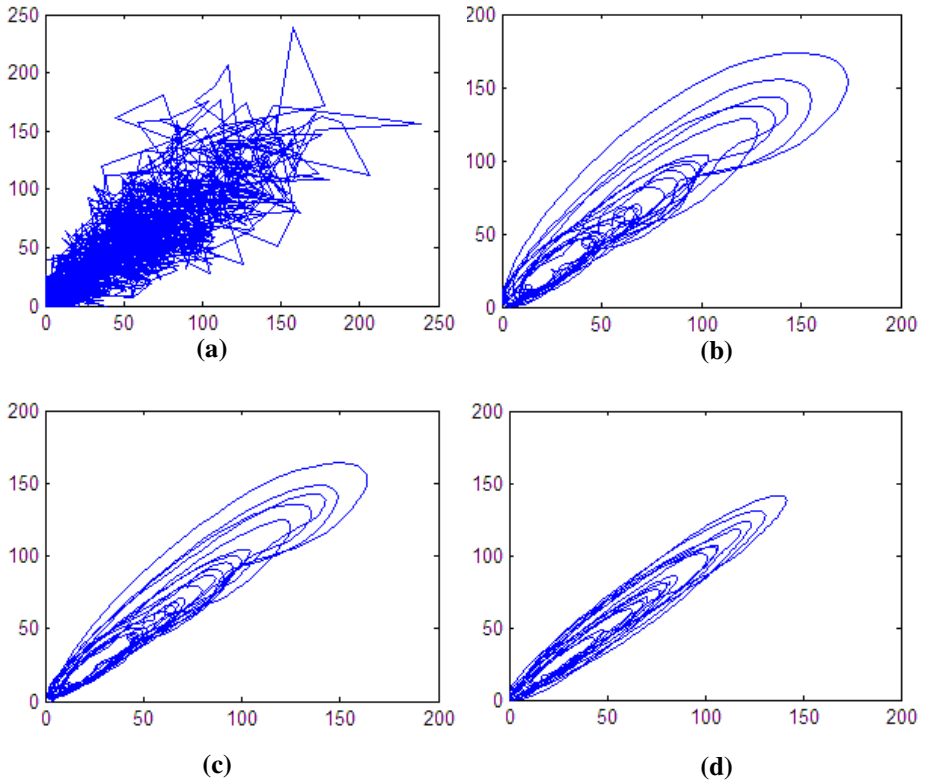

Fig. 2. 2-dimensional phase graph of noisy and denoised monthly sunspot signal (a) Observed signal; (b)2-dimensional phase graph after EMD threshold denoising; (c) 2-dimensional phase graph after EMD mode threshold denoising; (d) 2-dimensional phase graph after EMD-ICA denoising

5 Conclusions

For the problem occurred in the EMD threshold denoising of chaotic signal that the threshold is difficult to choose and the denoising accuracy is just low, it combines ICA with EMD to analyze the denoising of chaotic signal in this paper. This method eliminates the noises effectively and maintains useful information better by denoising IMFs with ICA. An experiment on Lorenz chaotic signal which is composed as different Gaussian noises and monthly observed chaotic sunspots signal was carried out. The experiment shows that the method proposed by this paper is more effective in denoising of chaotic signal in comparison with existed methods. Moreover, signal denoised by this method shows a clearer geometric structure of chaotic attractors, which is good for further application such as chaotic signal prediction and chaotic parameter extracting.

Acknowledgement. Project supported by the National nature science foundation (No. 41071270, No. 11201354); the Chenguang Foundation of Wuhan City (No. 201150431096); the open foundation of information engineering in surveying, Mapping and remote (No. 11R01) ; the open foundation of state key laboratory of remote sensing science (No. OFSLRSS201209);

References

1. Li, G.-L., Chen, X.-Y.: Design of Piecewise Linear Chaotic System. Acta Electronica Sinica 36(9), 1814–1818 (2008)
2. Vicha, T., Dohnal, M.: Qualitative identification of chaotic systems behaviours. Chaos, Solitons & Fractals 38(1), 70–78 (2008)
3. Dedieu, H., Kisel, A.: Communications with chaotic time series: probabilistic methods for noise reduction. International Journal of Circuit Theory and Applications (S1097-007X) 27(6), 577–587 (1999)
4. Jako, Z., Kis, G.: Application of Noise Reduction to Chaotic Communications: A Case Study. IEEE Transactions on Circuits and Systems-I: Fundamental Theory and Applications (S1057-7122) 47(12), 1720–1725 (2000)
5. Schreiber, T.: Extremely Simple Nonlinear Noise Reduction Method. Physical Review E (S1063-651X) 47(4), 2401–2404 (1993)
6. Han, M., Liu, Y.-H., Shi, Z.-W., Xiang, M.: The Study of Chaotic Noise Reduction Method with Improved Local Projection. Journal of System Simulation 19(2), 364–368 (2007)
7. Leontitsis, A., Bountis, T., Pagge, J.: An Adaptive Way for Improving Noise Reduction using Local Geometric Projection. Chaos (S1054-1500) 14(1), 106–110 (2004)
8. Huang, X.-G., Xu, J.-X., He, D.-H.: Reduction of noise in chaotic systems by wavelet Multiscaling decomposition algorithm. Acta Physica Sinica 48(10), 1810–1817 (1999)
9. Murguia, J.S., Campos, C.E.: Wavelet analysis of chaotic time series. Revista Mexicana De Fisica 52(2), 155–162 (2006)
10. Liu, Y.-X., Yang, G.-S., Jia, Q.: Adaptive Noise Reduction for Chaotic Signals Based on Dual-Lifting Wavelet Transform. Acta Electronica Sinica 39(1), 13–17 (2011)
11. Zhang, L., Bao, P., Wu, X.: Multiscale LMMSE-based image denoising with optimal wavelet selection. IEEE Transactions on Circuits and Systems for Video Technology 15(4), 469–481 (2005)
12. Zhang, H., Chen, X.-H., Yang, H.-Y.: Optimistic wavelet basis selection in seismic signal noise elimination. Oil Geophysical Prospecting 46(1), 70–75 (2011)
13. Huang, N.E., Shen, Z., Long, S.R., et al.: The empirical mode decomposition and the Hilbert spectrum for nonlinear and nonstationary time series analysis. Proc. of the Royal Society of London A454, 903–995 (1998)
14. Yang, Y., Ren, X., Qin, W., Wu, Y., Zhi, X.: Prediction of chaotic time series based on EMD method. Acta Physica Sinica 57(10), 6139–6144 (2008)
15. An, X.L., Jiang, D.X., Zhao, M.H., Liu, C.: Short-term prediction of wind power using EMD and chaotic theory 17(2), 1036–1042 (2011)
16. Boudraa, A., Cexus, J.: EMD-based signal filtering. IEEE Transaction on Instrumentation and Measurement 56(6), 2196–2202 (2007)
17. Olufemi, A., Vladimir, A., Auroop, R.: Empirical mode decomposition technique with conditional mutual information for denoising operational sensor data. IEEE Sensors Journal 11(10), 2565–2575 (2011)

18. Kopsinis, Y., Mclaughli, S.: Development of EMD-based denoising methods inspired by wavelet thresholding. IEEE Transactions on Signal Processing 57(4), 1351–1362 (2009)
19. Hyvarinen, A., Oja, E.: Independent component analysis: Algorithms and applications. Neural Networks 13(45), 411–430 (2000)
20. Li, P., Jin, H., Song, B.: Filtering of Ultra-Low Electromagnetic Detection Signal Using Independent Component Analysis. Acta Scientiarum Naturalium Universitatis Pekinensis 4, 45–51 (2008)
21. Zhang, Z., Yu, J., Yan, Q., Meng, Y., Zhao, Z.: Research on Polarimetric SAR Image Speckle Reduction Using Kernel Independent Component Analysis. Acta Geodaetica et Cartographica Sinica 40(3), 289–295 (2011)
22. Li, H., Sun, Y.-L.: Denoising by ICA Based on EMD Virtual Channel. Journal of Beijing University of Posts and Telecommunications 30(5), 33–36 (2007)
23. Aapo, H.: Fast and robust fixed-point algorithms for independent component analysis. IEEE Trans. on Neural Networks 10(3), 626–634 (1999)
24. Norden, E.H.: A study of the characteristics of white noise using the empirical mode decomposition method. Proc. R. Soc. Lond. A8 460(2046), 1597–1611 (2004)

A Nearest-Neighbor Delta Compression Method for GML Spatial Data

Qingting Wei[1,2], Jihong Guan[2,⋆], Ming Luo[1], and Hong Zou[3]

[1] School of Software, Nanchang University, Nanchang, Jiangxi
[2] Dept. of Computer Science and Technology, Tongji University, Shanghai
[3] Hospital of Jiangxi Provincial Unit of Chinese People's Armed Police Force
qtwei2008@gmail.com, jhguan@tongji.edu.cn

Abstract. GML has become an international encoding standard for exchanging geographic data. Whereas GML documents are often of huge size for containing high redundant spatial data. To reduce the cost for storing and transmitting GML documents, in this paper, we propose a nearest-neighbor delta compression method for GML spatial data. In parsing spatial data items into sequences of coordinates, ordered dictionaries are constructed to collect unique coordinates in each dimension. Coordinate points in the spatial reference system are mapped to points in the dictionary reference system. Each coordinate in the dictionaries is encoded as the floating-point offset from its previous coordinate. Each point in the boundaries of features is encoded as the reversed Z-order offset from its previous point. The proposed nearest-neighbor delta compression method is implemented in the GML compressor GDeltaC. Experiments on 20 GML documents show that GDeltaC outperforms the typical plain-text compressor gzip, the state-of-the-art XML compressor XMill, as well as the first GML compressor GPress in compression ratio.

Keywords: GML, spatial data, nearest-neighbor delta compression, coordinate.

1 Introduction

Geography Markup Language (GML) is proposed by Open Geospatial Consortium for modeling and representing geographic information. Nowadays, GML has a widespread application in spatial information services as a standard format of exchanging geographic data [1]. Based on XML, the latest GML 3.2.1 specification provides abundant object types to describe geographic features and their properties such as geometry, topology, time, reference system, coverage and style. Internationally, the governments and organizations in many countries have specified GML as the data standard in Spatial Data Infrastructure.

Nevertheless, the verbosity of GML documents troubles the application and spreading of GML. One important factor causing the verbosity is spatial data, i.e., sequences of high-precision coordinates in GML documents for describing

⋆ Corresponding author.

F. Bian et al. (Eds.): GRMSE 2013, Part I, CCIS 398, pp. 573–584, 2013.
© Springer-Verlag Berlin Heidelberg 2013

positions and shapes of geographic features. Each floating-point coordinate that could be represented by several bytes is expressed as characters in tens of bytes in GML documents. Moreover, spatial data often contains many similar or identical coordinates or points (tuples of coordinates). Once they are stored as characters, a number of repeated strings will be included in GML documents. As a result, GML documents usually occupy times more space than other geographic data documents carrying the same amount of information. Once GML is used for sharing and cooperating geospatial information, the transport of massive GML data in network is bound to consume excessive time and bandwidth.

Figure 1 shows a sample GML document for modeling two water features. The shape of each water feature is described by a "gml:LineString" element. The shape boundary of each water feature is represented by a "gml:posList" element which encloses a coordinate sequence of 6 points. Each point has a pair of X-coordinate and Y-coordinate. Coordinates in the same dimension are similar. There are 24 coordinates totaly while only 7 X-coordinates and 8 Y-coordinates are unique. The third, fourth and fifth points in the boundary of the first water feature are identical to the first three points in the boundary of the second water feature. If all coordinates are stored as floating-point numbers, the total space requirement is 96 bytes. However in the GML document, the space cost for all coordinates is 286 bytes.

```
<?xml version="1.0"  encoding="UTF-8"?>
<ex:Map xmlns:gml="http://www.opengis.net/gml"
        xmlns:ex="http://www.opengis.net/examples">
 <ex:Layer name="water1">
  <gml:featureMember>
    <ex:Feature fid="f100334437">
      <ex:GeometryProperty><gml:LineString><gml:posList>
        278001.5500 186941.3000 278006.1000 186918.1000
        278007.8500 186917.6000 278011.8300 186909.7300
        278016.5000 186911.3100 278019.6000 186900.9000
        </gml:posList></gml:LineString>
      </ex:GeometryProperty>
    </ex:Feature>
  </gml:featureMember>
  <gml:featureMember>
    <ex:Feature fid="f100334499">
      <ex:GeometryProperty><gml:LineString><gml:posList>
        278007.8500 186917.6000 278011.8300 186909.7300
        278016.5000 186911.3100 278014.3500 186903.2000
        278007.8500 186905.2000 278007.8500 186917.6000
        </gml:posList></gml:LineString>
      </ex:GeometryProperty>
    </ex:Feature>
  </gml:featureMember>
 </ex:Layer>
</ex:Map>
```

Fig. 1. A sample GML document

Since GML documents are a special kind of XML-grammar based text files, the existing plain text compression methods Huffman [2], LZ77 [3], Arithmetic Encoder [4], PPM [5], XML compression methods XMill [6], XMLPPM [7], and XWRT [8] are applicable to GML documents compression. However, the plain text compression methods do not distinguish structural tags and data in GML documents. The XML compression methods are conscious of structural tags while lack a specific compression on spatial data in GML documents. Therefore those compression methods are not suitable for the compression of GML documents containing a great amount of spatial data.

GML spatial data is actually vector data. The existing compression methods for vector data such as vector quantization (VQ) [9], cluster-based compression [10] are related to GML documents compression. Nevertheless those compression methods are mostly lossy because they remove redundant geometric data in compression, and the decompression can not recovery the original vector data. GML documents compression demands for a lossless compression, thus most of the existing compression methods for vector data can not be applied to the compression of spatial data in GML documents.

These years, some GML compressors are proposed such as GPress [11,12] and GSCPress [13]. Those GML compressors employ a delta compression of spatial data. Concretely, they encode each coordinate in sequences as the floating-point offset from the previous coordinate in the same dimension. Whereas, delta compression in this way is not very effective. On one hand, the offset of each coordinate in sequences from the previous coordinate is not always the lowest, and there may exist repeated coordinates. On the other hand, coordinate points may be similar or identical to each other. The existing delta compression scheme involves only the compression of coordinates without a consideration of compressing points.

Towards solving the problems above, a nearest-neighbor delta compression (NNDC) method for GML spatial data is presented in this paper. The NNDC method adopts the following compression principles:

- Collecting unique coordinates in each dimension by ordered coordinate dictionaries.
- Mapping points in the spatial reference system to points in the dictionary reference system.
- Encoding each coordinate in the coordinate dictionaries as the floating-point offset from its previous coordinate.
- Encoding each point in the dictionary reference system as the reversed Z-order offset from the previous point.

We implemented the NNDC method in the GML compressor GDeltaC and conducted extensive experiments on real GML documents to evaluate the performance of GDeltaC, which is also compared with a number of the existing compressors. Experimental results show that the GDeltaC compressor outperforms the typical plain text compressor and the state-of-the-art XML and GML document compressors in compression ratio, whiling maintaining an acceptable compression efficiency.

The rest of this paper is organized as follows. Section 2 presents a overview of the proposed NNDC method. Section 3 describes the implementation of the NNDC method. Section 4 gives the experimental results. Finally, Section 5 concludes the paper.

2 The Nearest-Neighbor Delta Compression Method

The nearest neighbor refers to the object nearest to the target position in a reference system. In this paper, the nearest neighbor of each coordinate is defined as the previous coordinate in the same ordered coordinate dictionary; the nearest neighbor of each point is defined as the previous point in the same feature boundary. To reduce the verbosity of coordinates and points, coordinates in the coordinate dictionaries are encoded as the floating-point offsets from their nearest neighbor coordinates, and points in the boundaries of geographic features are encoded as the reversed Z-order offsets from their nearest neighbor points.

2.1 Constructing Ordered Coordinate Dictionaries

For coordinates in each dimension, an ordered coordinate dictionary is constructed to collect unique coordinates. In the coordinate dictionary, any two coordinates are not equal and all coordinates are sorted by their values. Taking an example, when the GML document shown in Figure 1 is being compressed, the X-coordinate dictionary D_x and the Y-coordinate dictionary D_y are constructed as shown in the left of Figure 2. The dictionaries D_x and D_y include 7 unique sorted X-coordinates and 8 unique sorted Y-coordinates respectively.

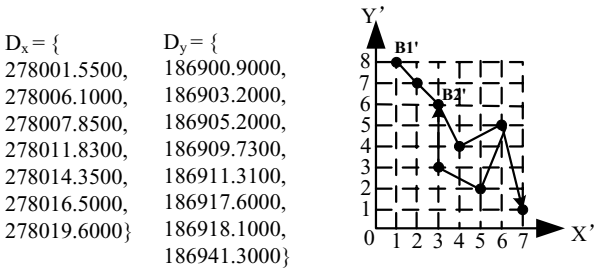

Fig. 2. Coordinate dictionaries and points mapped into the dictionary reference system

2.2 Mapping Coordinate Points into the Dictionary Reference System

Based on coordinate dictionaries, a two-dimensional or three-dimensional dictionary reference system is constructed. Points in the geometric boundaries of

features are mapped from the spatial reference system to the dictionary reference system.

Considering a feature A in a two-dimensional geographic space, the boundary is represented by a point sequence $B = (x_1, y_1), ...(x_i, y_i), ..., (x_u, y_u)$. B consists of u points where the i-th point is expressed as a pair (x_i, y_i) of the X-coordinate and Y-coordinate. Assuming the X-coordinate dictionary $D_x = \{X_j | j = 1..m\}$ consisting of m unique X-coordinates and the Y-coordinate dictionary $D_y = \{Y_k | k = 1..n\}$ consisting of n unique Y-coordinates. D_x and D_y constitute a dictionary reference system where each point is represented as (x', y'), $x' \in [0, m]$ and $y' \in [0, n]$. Then every point (x_i, y_i) in the original spatial reference system is mapped to a point (x'_i, y'_i) in the dictionary reference system. The mapping functions $F(x_i)$ and $F(y_i)$ are defined as follows:

$$F(x_i) = rank(x_i, D_x) = x'_i, \qquad F(y_i) = rank(y_i, D_y) = y'_i. \tag{1}$$

The rank function is for computing the order of a coordinate in the specified coordinate dictionary.

As shown in the right of Figure 2, the dictionary reference system based on the coordinate dictionaries D_x and D_y has X' coordinates in $[0, 7]$ and Y' coordinates in $[0, 8]$. The point sequences:$B1$=(278001.5500,186941.3000),(278006.1000, 186918.1000),...,(278019.6000,186900.9000) and $B2$=(278007.8500,186917.6000), (278011.8300,186909.7300), ..., (278007.8500,186917.6000) for describing the boundaries of the features in Figure 1 are transformed to the mapped point sequences: $B1'$=(1,8),(2,7),(3,6),(4,4), (6,5),(7,1); $B2'$=(3,6),(4,4),(6,5),(5,2), (3,3),(3,6).

2.3 Floating-Point Offset Encoding of Coordinates

To reduce the storage space for coordinate dictionaries in compressed files, we encode each coordinate in the dictionaries as the floating-point offset from the previous coordinate.

As shown in Figure 3, the first byte of encodings is necessary where the first bit saves a flag $f1$ to indicate whether the current coordinate has the same precision and sign to the previous coordinate, and the rest bits record the length of offset. The offset is an integer-type number calculating by subtracting the previous coordinate from the current coordinate without considering the sign and radix point. The second byte is optional. If the flag $f1$ in the first byte has a zero value, then the second byte will be skipped; otherwise the first bit of the second byte saves a flag $f2$ to indicate whether the current coordinate is positive or negative (0 for positive and 1 for negative). The rest bits of the second byte record the position of radix point. The third and the following bytes store the offset.

For instance, in the coordinate dictionary D_x shown in Figure 2, the number of the first coordinate "278001.5500" requires 4 bytes when the sign and the radix point are omitted. Therefore the floating-point offset encoding of the first coordinate costs 6 bytes. For each of the other coordinates "278006.1000,278007.8500, ...", the storage of the offset requires 2 bytes because the position of radix point

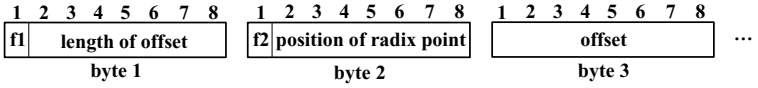

Fig. 3. Floating-point offset encoding of coordinates

and the sign are identical to the previous one. As result, the floating-point offset encoding of the other six coordinates occupies 18 bytes totally.

2.4 Reversed Z-Order Offset Encoding of Points

To decrease the storage space for point sequences in compressed files, we encode each point in the dictionary reference system as the reverse Z-order offset from the previous point in the same sequence.

Z-order curve is a kind of multi-dimensional space filling curve [14]. Each point in the curve has a number (called Morton code), which is generated by interleaving binary bits of coordinates in different dimensions. Since the numbers of points in Z-order curve keep local proximity of points in multi-dimensional space, Z-order curve is often used to transform multi-dimensional data to single-dimensional data.

We reverse the Z order of filling space, and link all points in the dictionary reference system in the reversed Z-order. Each point has a reversed Z-order number and is encoded as the offset of that number from the previous point in the same sequence. A reversed Z-order offset is represented by variable-length binary codes where the first bits of all bytes indicate whether the current byte is the last byte (1 for the last byte), and the second bit of the first byte records the sign of the offset (0 for positive,1 for negative). Figure 4 gives an example of the reversed Z-order offset encoding.

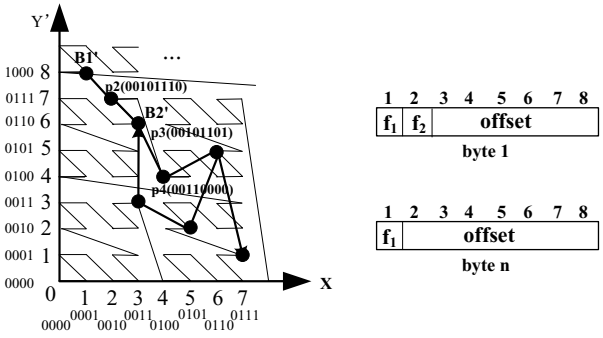

Fig. 4. Reversed Z-order offset encoding of points

As shown in the left of Figure 4, the dictionary reference system has the X' coordinates $x' \in [0, 7]$ and the Y' coordinates $y' \in [0, 8]$. The binary codes of x'

and y' are both represented by four bits in the format $a_1a_2a_3a_4$ or $b_1b_2b_3b_4$. When all points in the system are linked in the reversed Z order, each point is assigned a Morton code in 8 bits, which is generated by interleaving binary bits of x' and y', represented as $b_1a_1b_2a_2b_3a_3b_4a_4$. For the second, third and fourth points (i.e., $p2$, $p3$ and $p4$) in the point sequence $B1'$, their Morton codes are 00101110, 00101101 and 00110000 respectively, corresponding to the decimal numbers 46, 45 and 48. Then the point $p3$ is encoded as the binary code 11000001 corresponding to the decimal number -1, which is the offset of Morton codes from the previous point $p2$. Similarly, the point $p4$ is encoded as 10000011 corresponding to the decimal number 3, which is the offset from the previous point $p3$.

3 Implementation of the Compressor

We implemented the NNDC method in the GML compressor GDeltaC, which improves the compression of spatial data on the basis of the GML compressor GPress. The architecture of GDeltaC is shown in Figure 5.

Similar to GPress, GDeltaC comprises the *Document Parser* module, the *Path Processor* module and *Back-end Compressors* module. While doing compression, GDeltaC parses a GML document by the *Document Parser* and separates structural tags and characters data. The *Path Processor* encodes structural tags as integers and directs them into the *Structure Container*. Characters data is divided into different groups by the *Path Processor* through comparing the paths to the root element with the *Container Expressions*. Data in each group is saved into the corresponding *Data Containers*. All containers are allocated in memory. The *Back-end Compressors* employ a set of the plain text compressor *gzip* to compress the container contents and write the output to the compressed GML documents finally. Different from GPress, GDeltaC gathers spatial data items in the paths to the root element with the tag "`gml:coordinates`", "`gml:pos`", "`gml:poslist`", "`gml:X`" , "`gml:Y`" or "`gml:Z`", and compresses them into the *Spatial Container* by using the *NNDC Compressor*.

The *NNDC Compressor* has five sub-modules including the *Coordinate Parser*, the *Coordinate Dictionary*, the *Point Mapper*, the *Floating-point Offset Encoder* and the *Reversed Z-order Offset Encoder*. As shown in Figure 5, in the first scan of spatial data items, the *Coordinate Parser* transforms spatial data items into coordinate sequences. Accompanying the transforming, the *Coordinate Dictionary* collects and sorts unique coordinates in each dimension. In the second scan of spatial data items, the *Point Mapper* maps point sequences in the space reference system to the point sequences in the dictionary reference system. Next, the *Floating-point Offset Encoder* compresses coordinates in the coordinate dictionaries. The *Reversed Z-order Offset Encoder* compresses points in the dictionary reference system. Finally, the encodings of coordinates and points are forwarded to the *Spatial Container*.

We outline the compression procedure of the *NNDC Compressor* in Algorithm 1. Algorithm 1 accepts as inputs spatial data items from a GML document, and writes compressed spatial data items to the spatial container. The decompression

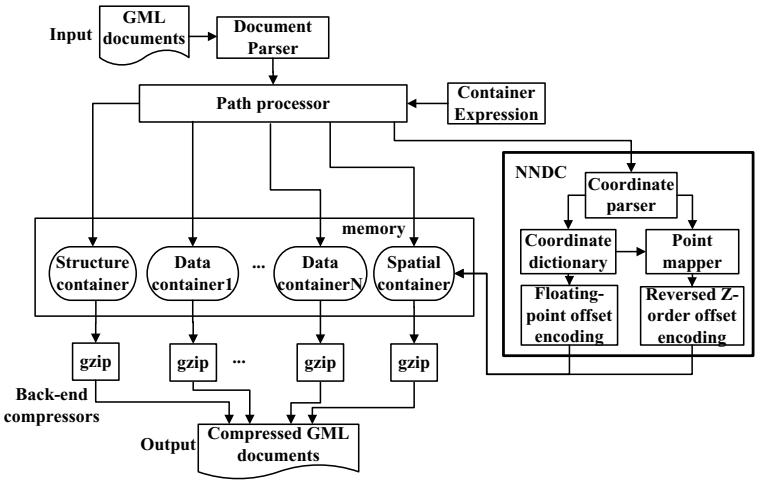

Fig. 5. Architecture of the GML compressor GDeltaC

Algorithm 1. NNDC(d) for compressing spatial data items

input : spatial data item d
output : compressed spatial data item e

Let $Barray$ be an array of coordinates representing a coordinate block, $BLOCKSIZE$ be the const maximum size of $Barray$, t be the last parsed tag name, d be the dimension, $Xset$,$Yset$ and $Zset$ be three coordinate dictionaries, $Parray$ be an array of integer-type points, c be the spatial container.

Parse d into m coordinates $b_1, b_2, ..., b_m$
for i = *1 to* m **do**
  if size of $Barray = BLOCKSIZE$ **then**
    for j = *1 to* size of $Barray$ **do**
      if $Barray[j] = \varepsilon$ **then** append 0 to $Parray$
      else
        $c_1 \leftarrow$ ordinal number of $Barray[j]$ in $Xset$
        $c_2 \leftarrow$ ordinal number of $Barray[j+1]$ in $Yset$
        if d = *3* **then** $c_3 \leftarrow$ ordinal number of $Barray[j+2]$ in $Zset$
        append an integer combining c_1,c_2 and/or c_3 to $Parray$
    end
    `FOffsetEncode` ($Xset$,e) and `FOffsetEncode` ($Yset$,e)
    if d = *3* **then** `FOffsetEncode` ($Zset$,e)
    `RZOffsetEncode` ($Parray$,e)
    write e to c and clear elements in $Barray, Parray, Xset, Yset$ and $Zset$

  if t = `gml:X` or t = `gml:Y` or t = `gml:Z` **then** add b_i to $Barray$ and the corresponding coordinate dictionaries
  else
    add b_i to $Barray$, $Xset$ and add b_{i+1} to $Barray$, $Yset$
    if d = *3* **then** add b_{i+2} to $Barray$ and $Zset$

  append ε to $Barray$
end

procedure is inverse to the compression procedure. Due to limitations of space, the decompression algorithm is not given in this paper.

Considering a GML document D having v spatial data items, each point is represented by d dimensional coordinates and the total number of coordinates is m.

For each dimension, a coordinate dictionary C is constructed, $|C|$ being the size of the C. The space requirement of the NNDC algorithm will include: 1) $O(m+v)$ for representing sequences of coordinates; 2) $O(d|C|)$ for representing d coordinate dictionaries; 3) $O(\frac{m}{d}+v)$ for represent sequences of points; 4) $O(d|C|)$ for saving the floating-point offset encodings and $O(\frac{m}{d}+v)$ for saving the reversed Z-order offset encodings. In compression, spatial data items are parsed into sequences of coordinates in $O(v)$ time. The construction of coordinate dictionaries costs $O(mlog|C|)$ time. Coordinate points are mapped from the spatial reference system to the dictionary reference system in $O(mlog|C|+v)$ time. The floating-point offset encoding of coordinate dictionaries requires $O(d|C|)$ time. The reversed Z-order offset encoding of the point sequence requires $O(\frac{m}{d}+v)$ time.

4 Experimental Evaluations

To evaluate the performance of the proposed GML compressor GDeltaC, we conduct compression and decompression experiments on 20 GML documents and compare the performance of GDeltaC with that of the typical plain text compressor gzip [15], the state-of-art XML compressor XMill [6] and the first GML compressor GPress [11,12]. All experiments are conducted on a PC with a 3.10GHz Intel Core i3-2100 CPU and 3GB RAM, running Windows XP OS.

GML Datasets. The 20 test GML documents come from four GML datasets, including CityGML [16], GeoSciML [17], OSMasterMap [18] and Synthetic. CityGML is a dataset of modeling virtual 3D cities by GML. The GeoSciML dataset describes geologic features of Eastern Australia using GML. OSMasterMap is a dataset of Great Britain's digital map in GML format. The Synthetic dataset comprises GML documents transformed from the Oracle Spatial sample files about the road network in Canada. We select randomly five GML documents from each of the first three datasets to obtain the first 15 test documents. And we select randomly one Synthetic document and repeat the features in the document to generate the last five test documents. The sizes of the 20 test documents range from 212KB to 1GB. Table 1 presents the detail of the 20 test GML documents, including document name, size, the storage ratios of structural tags, spatial data items, non-spatial data items and whitespace characters.

Performance Metrics. We evaluate the performance of compressors by the compression ratio (CR) and compression/decompression speed (CS/DCS) metrics as follows:

$$CR = \frac{\text{size of compressed document} \times 8}{\text{size of original document}}(bits/byte). \tag{2}$$

$$CS/DCS = \frac{\text{size of original document}}{\text{elapsed time}}(KB/ms). \tag{3}$$

A compressor performs better if it achieves lower CR values and is more efficient if it achieves higher CS/DCS values.

Table 1. Test GML datasets and documents

Document	Size (KB)	struc. ratio	spatial ratio	non-spatial ratio	white-space ratio	dataset
AC11-FZK-Haus	10957	0.2743	0.3113	0.1232	0.2912	CityGML (79.3M)
Berlin_Pariser	4084	0.2784	0.3373	0.1247	0.2596	
Castle_Herten	2664	0.3788	0.1729	0.2016	0.2467	
Gebaeude-Gruppe	13580	0.2658	0.3208	0.1194	0.2940	
Stadt-Ettenheim	49896	0.2932	0.3111	0.1259	0.2698	
TB3.1_UC2A_GA	706	0.0155	0.9745	0.0060	0.0040	GeoSciML (3.1M)
TB3_UC2A_GSC	212	0.1374	0.7798	0.0388	0.0440	
TB3_UC2B_Exemplar	728	0.0360	0.9453	0.0109	0.0078	
TB3_UC2B_GA_1M	723	0.0304	0.9525	0.0100	0.0071	
TB3_UC3A_GSC	802	0.1585	0.6775	0.0368	0.1272	
49287-SU6152-5i1	23353	0.7197	0.1449	0.1124	0.0230	OSMasterMap (194.2M)
49299-SS7886-5i1	25145	0.6418	0.2384	0.0992	0.0206	
6745-SU5951-2c4	33683	0.7095	0.1573	0.1106	0.0226	
6745-SU6151-2c1	85900	0.7157	0.1508	0.1107	0.0228	
6745-SU6153-2c3	30795	0.6722	0.2016	0.1048	0.0214	
ROAD_4M	2582	0.4843	0.2484	0.0026	0.2647	Synthetic (1358.9M)
ROAD_16M	15490	0.4838	0.2486	0.0023	0.2653	
ROAD_64M	64540	0.4844	0.2489	0.0024	0.2643	
ROAD_256M	260743	0.4841	0.2477	0.0028	0.2654	
ROAD_1024M	1048133	0.4845	0.2480	0.0027	0.2648	

Compression Ratio. Figure 6 illustrates the average CR results of the four compared compressors over 20 test documents. The averaged CRs of all compressors lie between 0.2 and 2.5, and GDeltaC outperforms the other compressors in averaged CRs over all datasets. Especially, on the Synthetic dataset, GDeltaC achieves a 77.8% improvement on gzip and a 34.2% improvement on GPress in averaged CR. The reasons may be as follows:

- All the test datasets keep an amount of spatial data items. GDeltaC employs an effective nearest-neighbor delta compression method, so outperforms the other compressors in averaged CRs over all datasets.
- The Synthetic dataset has an extreme high repeating frequency of coordinates and points. GDeltaC can reduce the verbosity of coordinates and points in this dataset greatly. Hence, on Synthetic, GDeltaC defeats the other compressors in averaged CR apparently.

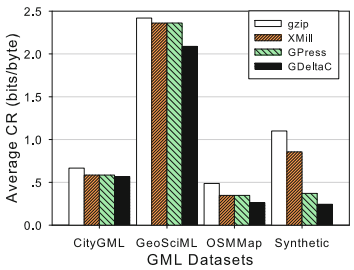

Fig. 6. Average compression ratio *vs.* dataset

Compression/Decompression Speed. Figure 7(a) and Figure 7(b) illustrates the averaged CS and DCS results of the four compared compressors over 20 test documents. The averaged CS values of all compressors lie between 5.6 to 60.0, and the averaged DCS values lie between 12.1 to 142.2. GDeltaC performs moderately in averaged CS or DCS while runs faster than GPress when compresses the the GeoSciML dataset, the Synthetic dataset and decompresses the Synthetic dataset. Especially, on the Synthetic dataset, the averaged DCS of GDeltaC is twice that of GPress. The results above may attribute to the following reasons:

- GDeltaC spends much time on constructing and searching coordinate dictionaries in compression or decompression, thus performs moderately in averaged CS or DCS over all the test datasets.
- In decompressing the compressed Synthetic documents, GPress has to decode all coordinates in the sequence one by one. On the contrary, GDeltaC only need decode few unique coordinates in the coordinate dictionaries. Therefore GDeltaC decompresses the Synthetic dataset much faster than GPress.

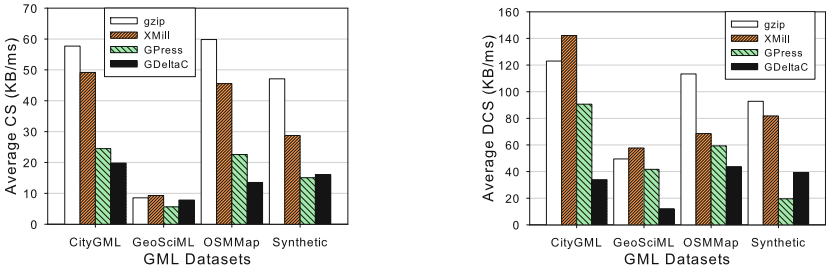

(a) Average CS *vs.* dataset (b) Average DCS *vs.* dataset

Fig. 7. Average compression/decompression speed *vs.* dataset

5 Conclusion

Similar or repeated spatial coordinates and points in GML documents increase verbosity of GML documents and often make the storage and transport of GML documents extensive. In this paper, we propose a nearest-neighbor delta compression method for GML spatial data, which reduces the verbosity of spatial data by constructing ordered coordinate dictionaries, mapping coordinate points into the dictionary reference system, floating-point offset encoding of coordinates and reversed Z-order offset encoding of points. Experiments over 20 GML documents show that averagely the proposed method outperforms the major existing compressors, including the typical plain text compressor gzip, the state-of-the-art XML compressors XMill and the first GML compressor GPress in compression ratio, while maintaining an acceptable compression efficiency.

Acknowledgments. This research was partially supported by the National Natural Science Foundation of China (NSFC) under grant No. 61173118. Qingting Wei and Ming Luo were also supported by the Science and Technology Project of Jiangxi Provincial Department of Education (Grant No. GJJ12147) and the Tianyuan Fund for Mathematics of NSFC (Grant No. 11226042)

References

1. Geospatial information – Geography Markup Language (GML). ISO 19136:2007 (2007)
2. Huffman, D.A.: A Method for the Construction of Minimum-Redundancy Codes. Proceedings of the IRE 40(9), 1098–1101 (1952)
3. Ziv, J., Lempel, A.: A universal algorithm for sequential data compression. IEEE Transactions on Information Theory IT-23(3), 337–343 (1977)
4. Witten, I.H., Neal, R.M., Cleary, J.G.: Arithmetic coding for data compression. Communications of the ACM 30(6), 520–540 (1987)
5. Cleary, J.G., Witten, I.H.: Data compression using adaptive coding and partial string matching. IEEE Transactions on Communications 32(4), 396–402 (1984)
6. Hartmut, L., Suciu, D.: XMill: an efficient compressor for XML data. In: ACM SIGMOD 2000, pp. 153–164. ACM Press, New York (2000)
7. Cheney, J.: Compressing XML with multiplexed hierarchical PPM models. In: DCC 2001, pp. 163–172. IEEE Press, New York (2001)
8. Skibiński, P., Grabowski, S., Swacha, J.: Effective asymmetric XML compression. Software: Practice and Experience 38(10), 1024–1047 (2008)
9. Gersho, A., Gray, R.M.: Vector Quantization and Signal Compression. Kluwer Academic Publishers, Norwell (1991)
10. Shekhar, S., Huang, Y., Djugash, J., Zhou, C.: Vector map compression: a clustering approach. In: ACM SIGSPATIAL GIS 2002, pp. 74–80. ACM Press, New York (2002)
11. Guan, J., Zhou, S.: GPress: Towards effective GML documents compresssion. In: ICDE 2007, pp. 1473–1474. IEEE Press, New York (2007)
12. Guan, J., Zhou, S., Chen, Y.: An effective GML documents compressor. IEICE Transactions on Information and Systems E91-D(7), 1982–1990 (2008)
13. Yu, Y., Li, Y., Zhou, S.: A GML Documents Stream Compressor. In: Xu, J., Yu, G., Zhou, S., Unland, R. (eds.) DASFAA Workshops 2011. LNCS, vol. 6637, pp. 65–76. Springer, Heidelberg (2011)
14. Morton, G.M.: A computer oriented geodetic data base and a new technique in file sequencing. Technical report, IBM Ltd. (1966)
15. GZip 1.2.4, `http://www.gzip.org`
16. Kolbe, T.H.: CityGML - Exchange and Storage of Virutual 3D City Models (2002), `http://www.citygml.org`
17. CGI Interoperability Working Group: The GeoSciML project (2003), `http://www.geosciml.org`
18. Ordnance Survey: OS MasterMap (2001), `http://www.ordnancesurvey.co.uk`

Integration of Hyperspectral Image and Lidar Data through Tri-training for Land Cover Semi-supervised Classification

Rui Huang and Jiangtao Zhu

School of Communication and Information Engineering, Shanghai University
Shanghai, China
huangr@shu.edu.cn

Abstract. The topology information derived from lidar sensors is an important complement to classification of the optic remote sensed imageries. In the paper, we investigate the joint use of hyperspectral and lidar data to extract information of spectra, texture and elevation for landcover discrimination. A semi-supervised fusion method using tri-training is proposed to integrate the different features. The DSM (Digital Surface Model) derived from the lidar data is first interpolated to the same spatial resolution as the hyperspectral image. The co-registration of DSM and hyperspectral image is followed by the spatial feature extraction using three different morphological profiles. Each kind of textural feature is concatenated with the spectral and altimetry features into a stacked feature vector, and thus three types of vectors are obtained. Subsequently, three supervised classifiers are built based on the three kinds of vectors, respectively. These classifiers are refined with help of the unlabeled samples in the tri-training process. Finally, an improvement in the final classification accuracy is achieved. The experimental results show that the proposed method can effectively integrate the information both from the spectral-positional-textural features and the labeled-unlabeled data.

Keywords: Hyperspectral image, lidar data, tri-training, morphological profiles, data fusion.

1 Introduction

Hyperspectral imaging has become an effective means of earth observation by providing the accurate spectral description of objects. However, with the increase in the spatial resolution, classification based on pure spectral information often fails in identifying different objects with similar radiation characteristics and same objects with distinct radiation characteristics. The topology information derived from lidar sensors is highly complementary to the spectral data and helps to get better performance.

Recent researches have presented some promising results about fusing the two different kinds of data [12, 1, 16]. Two different schemes of integrating hyperspectral

F. Bian et al. (Eds.): GRMSE 2013, Part I, CCIS 398, pp. 585–593, 2013.
© Springer-Verlag Berlin Heidelberg 2013

images and lidar data are usually applied. One is to concatenate the spectral and altimetry features into a new vector. In [5], elevation and intensity features derived from lidar multi-returns along with spectral features consisted of the stacked features, and the experimental results showed the elevation channel of the first lidar return was effective for separation of tree species. Coren et al jointly used lidar, hyperspectral data and four indices generated from the latter to identify cultural heritage [4]. In addition, the spatial information (such as GLCM and morphological profiles) from optical and lidar images are considered and combined with the spectra and elevation into new features [14, 15]. In the other scheme, different information is applied in different steps to generate final map. In [13], separation of ground surface and vegetation based on digital surface model (DSM) generated from the Lidar data was followed by vegetation analysis through vegetation indices. Ref. [10] adopted a similar processing procedure for roof surface classification.

In the paper, we investigate the performances of different ways of fusing information of the spectra, elevation and their textures from the two distinct data sources. A semi-supervised integration method using tri-training is proposed to combine the different features. The DSM (Digital Surface Model) derived from the lidar data and hyperspectral image are first co-registered. Then, spatial features are extracted based on three different morphological profiles. Each kind of textural feature is concatenated with the spectral and altimetric features into a stacked feature vector, and thus three types of vectors are obtained. Subsequently, three supervised classifiers are built based on the three kinds of vectors, respectively. These classifiers are retrained with help of the unlabeled samples in the tri-training process. Finally, an improvement in the final classification accuracy is achieved. The experimental results demonstrate that the proposed method can effectively integrate the information both from the spectral-positional-textural features and the labeled-unlabeled data.

2 Data Set Description

Both the hyperspectral and lidar data used were collected by the project of Watershed Allied Telemetry Experimental Research (WATER). The considered test site was Zhangye, Gansu Province, China, where the data were acquired in June 2008 [6, 11]. The hyperspectral image used is a 200200 segment of one OMIS-II data scene composed of 64 bands ranging from 460 nm to 1100 nm. The spectral resolution is 10 nm and the spatial resolution is 4 m. The lidar data were collected by the LiteMapper 5600 system with a mean density of 3 points per square meter. The DSM (Digital Surface Model) derived from the lidar data was interpolated to the same spatial resolution as the hyperspectral image. The optical images were registered to the DSM where 51 ground control points were selected and RMS error was 0.3434. The pseudo-color image of hyperspectral data and the corresponding DSM are shown in Fig. 1.

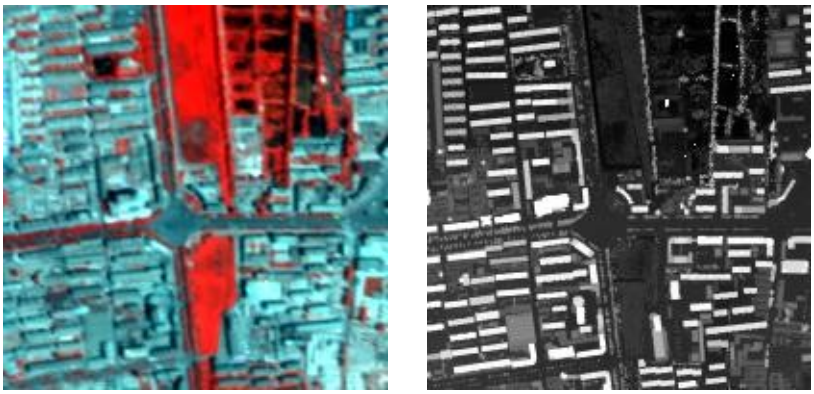

Fig. 1. (a) Pseudo-color image of hyperspectral data. (b) DSM image.

3 Methodology

Fig. 3 presents the flow chart of the proposed method. The lidar-derived DSM is first interpolated to the same spatial resolution as the hyperspectral image. To cut down the computation load, dimensionality reduction is executed for the hyperspectral data. The co-registration of DSM and reduced optical image is followed by the spatial feature extraction using three different morphological profiles, namely extend morphological profiles (EMP), derivative morphological profiles (DMP) and normalized derivative morphological profiles (NDMP). After the feature extraction step, each kind of textural feature is concatenated with the spectral and corresponding altimetric features into a stacked feature vector, and thus three types of vectors are obtained. Subsequently, three supervised classifiers are built based on these three kinds of vectors, respectively. These classifiers are refined with help of the unlabeled samples in the tri-training process and the final map is generated by combining the three classification outputs. In the rest of the section, we mainly describe the extraction of the spatial features and the tri-training scheme.

3.1 Textural Extractors

Before extraction of spatial features, PCA is first applied to reduce the dimensionality of hyperspectral data. The transformation projects the data from a higher dimension space into a lower one by keeping the first several Principal Components (PCs) with highest eigenvalues. The number of PCs to be preserved is decided by the accumulative sum of the corresponding eigenvalues exceeding 99 percent of the total sum.

Three morphological profiles, namely EMP [7], DMP [2] and NDMP, are used for extraction of textural information. All extractors are based on concepts of morphological profiles (MP) where two morphological operators, opening and closing

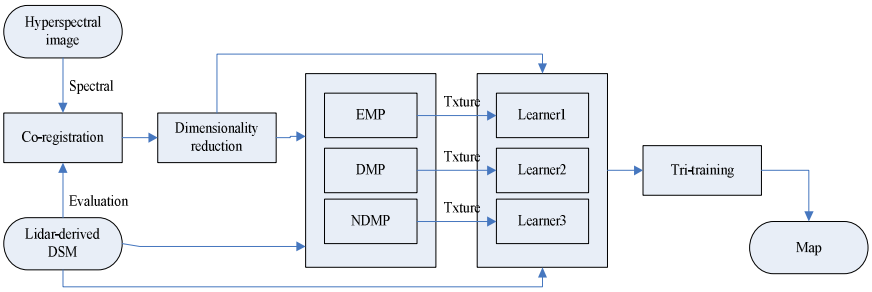

Fig. 2. Block diagram of the proposed method

are applied to the first principal component with a structuring element (SE) of increasing radius. An MP at the pixel x of the image I consist of the opening profile (OP) and the closing profile (CP), and can be defined as a 2n + 1dimensional vector:

$$MP(x) = \{CP_n(x), ..., I(x), ..., OP_n(x)\} \tag{1}$$

where CPi(x) and OPi(x) are constructed by the morphological closing and opening operators with an SE of size i ($1 \leqslant i \leqslant n$), respectively. When MP is applied on the first m PCs, EMP is an m (2n + 1)-dimensional vector:

$$EMP(x) = \{MP_{PC^1}(x), ..., MP_{PC^m}(x)\} \tag{2}$$

DMP is defined as a n+1-dimensional vector where the measures of the slope of the opening-closing profiles are stored for every step of an increasing SE series:

$$DMP(x) = \{I(x), |CP_1(x) - OP_1(x)|, ..., |CP_n(x) - OP_n(x)|\} \tag{3}$$

When DMP is applied on the first m PCs, an m(n + 1)-dimensional vector can be obtained. NDMP is a normalized version of DMP. It can be defined a n+1-dimensional vector

$$NDMP(x) = \{I(x), \frac{|cp_1(x) - op_1(x)|}{|cp_1(x) + op_1(x)|}, ..., \frac{|cp_n(x) - op_n(x)|}{|cp_n(x) + op_n(x)|}\} \tag{4}$$

When NDMP is applied on the first m PCs, an m(n + 1)-dimensional vector can be obtained. After textual extraction, feature concatenation is carried out to combine multiple features.

3.2 Information Fusion through Tri-training

Compared with the co-training learning idea [3], tri-training requires the two different views without any constrains on the supervised learning algorithm [17]. The algorithm trains three classifiers via bootstrap sampling from the original labeled

examples and refines them using unlabeled ones in the tri-training process. In each round of tri-training, an unlabeled example is labeled for a classifier if the other two classifiers agree on the labeling. Through the help of the unlabeled examples with labels, the classifier is re-trained. The work repeats until none of classifier changes. The final prediction is made through decision fusing process among all the learners.

In tri-training, a condition should be satisfied to avoid an excessive amount of unlabeled samples to be labeled in every round. Take classifier h1 as an example, and the condition is presented as follows:

$$0 < \frac{\check{e}_1(t)}{\check{e}_1(t-1)} < \frac{\left|L_1^{'}(t-1)\right|}{L_1^{'}(t)} < 1 \tag{5}$$

where |L ´ 1(t)| denotes the cardinality of the unlabeled sample set L′ 1(t) which are labeled for h1, and ě1(t) denotes the upper bound of the classifier error rate of h2&h3 in the t-round. This classifier error is estimated based on the original labeled samples as:

$$\check{e}_1(t) = \frac{\text{number of samples misclassified by h2\&h3}}{\text{number of samples assigned same labels by h2\&h3}} \tag{6}$$

The initial value ě1(0) is set 0.5. To handle the ill-posed classification problem, Eq. (6) is improved as follows [9]:

$$E_1(t) = \partial \check{e}^{L}{}_1(t) + (1-\partial)\check{e}^{U}{}_1(t) \tag{7}$$

where $\check{e}^{L}{}_1(t)$ and $\check{e}^{U}{}_1(t)$ denote the classification error based on labeled and unlabeled samples, respectively; ∂ is a weighting factor to balance the effects of the two items. $\check{e}^{L}{}_1(t)$ can be obtained by Eq. (6). Since it is difficult to calculate the exact error values for the unlabeled set, the voting rule is adopted to approximate $\check{e}^{U}{}_1(t)$ based on the unlabeled samples as follows:

$$\check{e}^{U}{}_1(t) = \frac{\text{number of samples assigned diff. labels by h2\&h3}}{\text{number of samples}} \tag{8}$$

If Eq. (5) could not hold, s samples should be randomly selected from $L_1^{'}(t)$ as follows:

$$s = \left\lceil \frac{\check{e}_1(t-1)\,|\,L_1^{'}(t-1)\,|}{\check{e}_1(t)} - 1 \right\rceil \tag{9}$$

where $\lceil . \rceil$ means to round up to the nearest whole number.

4 Experiments

The experiments are carried out for performance comparison where different features of hyperspectral and lidar data are combined through or not through tri-training. Nine land covers are selected, namely, 'Grass' (2495), 'Tree' (259), 'Water' (129), 'Road', 801, 'Roof' (2272), 'Soil' (541), 'Parking lots' (134), 'Asphalt' (212), and 'Shadow' (108), as displayed in Fig. 4. We evaluate the presented method in different ill-posed scenarios where 2%, 5% and 10% labeled samples are randomly chosen for training and the rest for testing. 3 PCs of hyperspectral data and DSM are used for EMP, DMP and NDMP to extract textural features with an SE size of 2, 4, 6 and 8. Adaboost [8] with knn (k = 5) is applied as the classifier. In tri-training, we use major voting to generate the final classification results. Three performance indices including the overall accuracy (OA), average accuracy (AA) and kappa value are calculated and averaged over 10 random realizations.

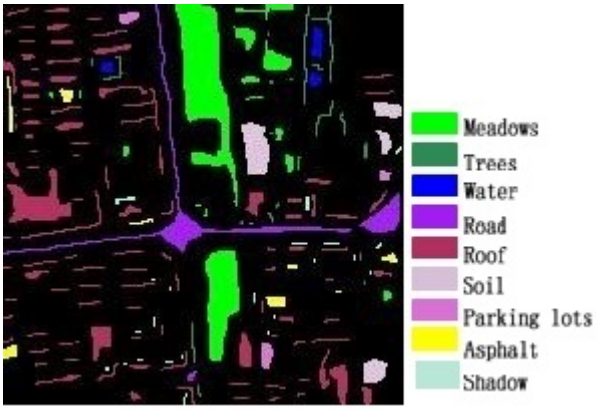

Fig. 3. Ground-truth map

Tab.1 lists the accuracy comparison among different forms of feature combinations when 2%, 5% and 10% training samples used. Here, S and E stand for the spectra and elevation features, respectively. From this table, it can be seen that: (1) the altimetric features are complementary to spectral and textural data for land cover classification; (2) DMP features seem more helpful to achieve higher accuracies; (3) the proposed method perform best among distinct ways of fusing information since it exploit not only the spectral-positional-textural features but also the labeled-unlabeled samples. Fig. 4 gives the classification results using our method when 10% labeled samples are used.

Table 1. Performance comparison among different feature combinations when different numbers of training samples used

		S+EMP	S+DMP	S+NDMP	S+E+EMP	S+E+DMP	S+E+NDMP	Tri
2%	OA	52.44	61.08	58.07	56.79	63.80	62.28	**66.26**
	AA	38.02	42.74	41.99	38.43	43.47	42.48	**44.29**
	Kappa	36.60	47.04	43.89	41.71	50.80	48.57	**52.92**
5%	OA	62.91	69.91	67.77	66.99	74.44	72.85	**76.04**
	AA	48.71	56.27	53.58	50.30	58.70	57.57	**58.76**
	Kappa	50.22	59.46	56.63	55.37	65.41	63.26	**67.00**
10%	OA	71.79	78.01	74.38	95.93	89.48	88.29	**93.97**
	AA	58.62	66.65	62.13	71.39	77.68	75.77	**83.18**
	Kappa	61.95	70.38	65.57	80.29	85.40	83.71	**91.71**

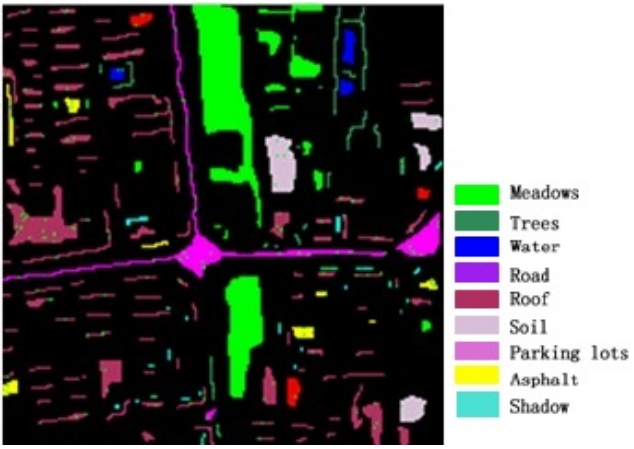

Fig. 4. Classification maps using the proposed method

5 Conclusion

The paper proposes an integration method based on tri-training learning scheme to fuse optical and altimetric features from the hyperspectral and lidar data. PCA is first applied to the hyperspectral image to reduce the computational complexity. Then, three kinds of textural features are extracted from the reduced images and the lidar-derived DSM through EMP, DMP and NDMP. Subsequently, each kind of spatial features are combined with features of spectra and altitude into new vectors which act as the three input data for corresponding classifiers in tri-training learning. These classifiers are refined with help of unlabeled samples. The experimental results show that the proposed method can effectively combine the information from the spectra, elevation and texture, as well as labeled and unlabeled data.

Acknowledgments. The research is supported by the National Natural Science Fund in China (No.61001162). The data sets used in the paper is provided by "Environmental & Ecological Science Data Center for West China, National Natural Science Foundation of China".

References

1. Asner, G.P., Knapp, D.E., Kennedy-Bowdoin, T., Jones, M.O., Martin, R.E., Boardman, J., Field, C.B.: Carnegie airborne observatory: in-flight fusion of hyperspectral imaging and waveform light detection and ranging (wilder) for three-dimensional studies of ecosystems. Journal of Applied Remote Sensing 1(1), 1–21 (2007)
2. Benediktsson, J.A., Palmason, J.A., Sveinsson, J.R.: Classification of hyperspectral data from urban areas based on extended morphological profiles. IEEE Transactions on Geoscience and Remote Sensing 43(3), 480–491 (2005)
3. Blum, A., Mitchell, T.: Combining labeled and unlabeled data with co-training. In: Proc. 11th Annual Conference on Computational Learning Theory, Madison, WI, pp. 92–100 (1998)
4. Coren, F., Visintini, D., Prearo, G., Sterzai, P.: Integrating lidar intensity measures and hyperspectral data for extraction of cultural heritage. In: Workshop Italy- Canada for 3D Digital Imaging and Modeling: Applications of Heritage, Industry, Medicine and Land, Padova, Italy (2005)
5. Dalponte, M., Bruzzone, L., Gianelle, D.: Fusion of hyperspectral and lidar remote sensing data for classification of complex forest areas. IEEE Transactions on Geoscience and Remote Sensing 46(5), 1416–1427 (2008)
6. Du, Q., Yang, Y., Liu, Q., Xiao, Q., Li, X., Ma, M.: Water: Dataset of airborne imaging spectrometer (omis-ii) mission in the zhangye-yingke-huazhaizi flightzone, Shanghai Institute of Technical Physics, Chinese Academy of Sciences; Institute of Remote Sensing Applications, Chinese Academy of Sciences; Cold and Arid Regions Environmental and Engineering Research Institute, Chinese Academy of Sciences(June 4, 2008)
7. Fauvel, M., Benediktsson, J., Chanussot, J., Sveinsson, J.: Spectral and spatial classification of hyperspectral data using svms and morphological profiles. IEEE Transactions on Geoscience and Remote Sensing 46(11), 3804–3814 (2008)
8. Freund, Y., Schapire, R.E.: A decision-theoretic generalization of on-line learning and an application to boosting. Journal of Computer and System Sciences 55(1), 119–139 (1997)
9. Huang, R., He, W.: Using tri-training to exploit spectral and spatial information for hyperspectral data classification. In: Proc. International Conference of Computer Vision in Remote Sensing, Xiamen, China, pp. 30–33 (2012)
10. Lemp, D., Weidner, U.: Improvements of roof surface classification using hyperspectral and laser scanning data. In: Proc. 3rd Int. Symp. Remote Sens. Data Fusion Over Urban Areas (URBAN) and 5th Int. Symp. Remote Sens. Urban Areas (URS), Tempe, AZ, USA, pp. 14–16 (2005)
11. Liu, Q., Pang, Y., Chen, E., Xiao, Q., Zhong, K., Li, X., Ma, M.: Water: Dataset of airborne lidar mission in the zhangye-yingke flight zone. Beijing Normal University; Institute of Forest Resource Information Techniques, Chinese Academy of Forestry; Institute of Remote Sensing Applications, Chinese Academy of Sciences; Cold and Arid Regions Environmental and Engineering Research Institute, Chinese Academy of Sciences (June 20, 2008)

12. Mundt, J.T., Streutker, D.R., Glenn, N.F.: Mapping sagebrush distribution using fusion of hyperspectral and lidar classification. Photogrammetric Engineering & Remote Sensing 72(1), 47–54 (2006)
13. Niemann, K.O., Frazer, G., Loos, R., Visintini, F., Stephen, R.: Integration of first and last return lidar with hyperspectral data to characterize forested environments. In: Proc. IEEE International Geoscience and Remote Sensing Symposium, Barcelona, Spain, pp. 1537–1540 (2007)
14. Onojeghuo, A.O., Blackburn, G.A.: Optimising the use of hyperspectral and lidar data for mapping reedbed habitats. Remote Sensing of Environment 115, 2025–2034 (2011)
15. Pedergnana, M., Marpu, P.R., Mura, M.D., Benediktsson, J.A., Bruzzone, L.: Classification of remote sensing optical and lidar data using extended attribute profiles. EEE Journal of Selected Topics in Signal Processing 6(7), 856–865 (2012)
16. Sun, X., Chen, W., Fischer, R.L., Jones, M., Eichholz, J.C., Richards, J.E., Shu, P., Jhabvala, M., La, A., Kahle, D., Adams, J.: An advanced airborne multisensory imaging system for fast mapping and change detection applications. In: Proc. IEEE International Geoscience and Remote Sensing Symposium, Barcelona, Spain, pp. 600–605 (2007)
17. Zhou, Z., Li, M.: Tri-training: exploiting unlabeled data using three classifiers. IEEE Transactions on Knowledge and Data Engineering 17(11), 1529–1541 (2005)

Automatically Construct the Surface Visualization Model with DEM and the Geological Survey Data

Xiangyu Yu and Yixian Xu

Institute of Geophysics & Geomatics,China University of Geosciences,
Wuhan Hubei 430074, China
yuxiangyu@2008.sina.com

Abstract. As the surface visualization model is an important part of the three-dimensional geological mapping, automatically surface visualization modeling has very strong practicability. Using the elevation information provided by DEM (Digital Elevation Model), the surface visualization model which represents geological properties can be constructed costly and effectively. The paper discussed some data processing technologies in the application of geological surface modeling from the authors' development work. And gave a detail description about how to automatically implementing the geological surface visualization modeling with DEM and the geological survey data.

Keywords: DEM, three-dimensional geological mapping, geological surface visualization modeling.

1 Introduction

Currently, the expression of geological information has been changed from the paper geological map to the digital geological map. But with the deepening of applications, it is widely believed that the geological plane map based on GIS (Geographic Information System) is lack of dimensional sense and sufficient information expressed in some extent. How to make the geological map having more sense of hierarchy and showing more information becomes an important problem. Thus the three-dimensional geological mapping based on the technology of computer visualization has attracted more attentions [1].

Conceptually, the three-dimensional geological mapping is aim to storing the geological information throughout surface to subsurface for resource management, hazard mitigation, mineral and petroleum exploration, etc [2]. As a result, it requires a large amount of sampling data and a lot of manual post-processing work to meet the needs. However, in many practical geological works such as the geological survey, people usually can't acquire more geological sampling data especially the drilling sampling costly and effectively. Therefore as an important part of the three-dimensional mapping, building the geological surface visualization model has more practicability [3].

In the geological survey, the geological sampling data is usually acquired from a freely sampling process. The outside staff carries out the field sampling along the prepared route or region to determine geological properties (such as lithology,

F. Bian et al. (Eds.): GRMSE 2013, Part I, CCIS 398, pp. 594–602, 2013.
© Springer-Verlag Berlin Heidelberg 2013

stratum, etc) of a block or section [4]. For them, boundaries of each geological property which mostly formed as polygons need to be clearly recorded. In other words, the sampling data in the geological survey is not specialized for visualization modeling. In this case, people usually need to process the geological sampling data manually to construct the surface visualization model with other data such as DEM which is the first choice for its cost-effective data acquisition [5].

As we all know, DEM can simulate the continuous terrain surface by the elevation information which has been recorded structurally. So it can effectively improve the dimensional sense of geological mapping. Since the DEM visualization technology has matured, the request of automatically constructing the surface visualization model with DEM and sampling data in the geological survey has been proposed. For example, in a real geological survey project the authors have faced with the requirement of automatically constructing the geological surface visualization model with the geological sampling data as quickly as possible. After some research and testing repeated, the authors have got a satisfactory effect and they have applied these research results in a developed three-dimensional geological mapping system named GCCS.

The paper will elaborate the method and technology which the authors used in the developed system for the automatically geological surface visualization modeling. The rest parts are organized as follows: Sec.2 mainly introduces the authors' modeling ideas; Sec.3 discusses some concrete technical details in the process of implementation. Sec.4 shows the implement result and makes a summary.

2 Modeling Ideas and Process

2.1 Modeling Ideas

In the geological survey work, because of the large survey area and workload, the staff usually records the survey result about geological properties conveniently. In the record, one of the most important information is the collection of point coordinates which constitute the feature polygon to represent some geological property. These feature polygons are adjacent to each other and having similar sampling intervals. Since different mapping accuracy requirements determines the interval between sampling points, when it treated with the DEM data used in the survey area both cases will emerged as shown in Fig.1 and Fig.2.

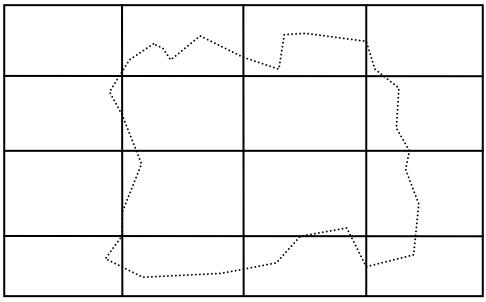

Fig. 1. The first case of the geological survey sampling data integrates with the DEM data

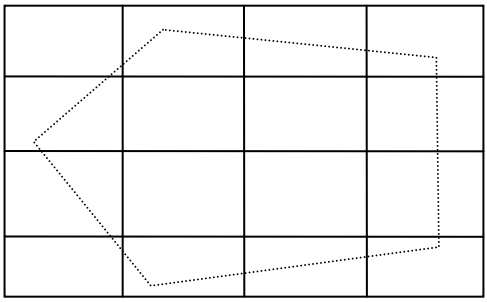

Fig. 2. The second case of the geological survey sampling data integrates with the DEM data

In the first case, the geological sampling interval is less than the spacing distance between the points of the DEM grid. So in the modeling implementation, we need to establish the TIN （Triangulated Irregular Network） with sampling points which form the feature polygon and the DEM grid points which fall in the polygon as shown in Fig.3. The specific algorithm can use the point gradually added method which based Delaunay triangulation [6]. With the TIN, the geological feature polygon can be expressed as a collection of triangles, and then all collection of triangles can be rendered to produce the visualization model.

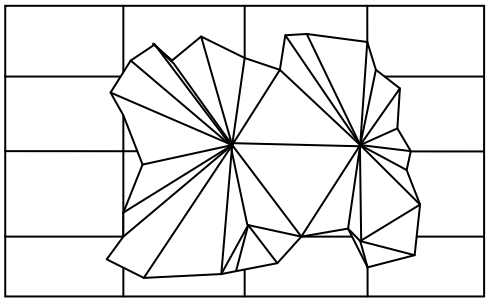

Fig. 3. TIN established for the first case

In the other case, the point's interval of the geological feature polygon is much larger than the point's spacing of the DEM grid. We carry out a resampling operation to these points, which replace the original geological survey sampling point with the nearest grid point in DEM. Such reorganized polygon (the original polygon is shown as Fig.2) is shown as Fig.4. Then we construct the visualization model based on the technology of DEM visualization. First set the predefined scalar value which represents a geological property to DEM grid points which locate in the reorganized feature polygon (display as circles in Fig.4). Then use the contour extraction algorithm [7] to the DEM surface visualization model (which built by warp the DEM grid data [8]) to get the visualization model of geological attributes. Finally, smoothing the normal of each cell in the visualization model can get a better visualization result.

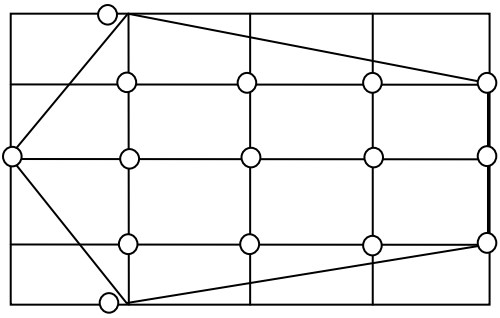

Fig. 4. Polygon reorganized for the second case

2.2 Implementation Process

In the GCCS, the process of automatically constructing the geological surface visualization model is as follows. The first step is importing the DEM data of the geological survey area. Since the whole survey area is usually very large, the imported DEM data can easily exceed 100M. While the DEM data is imported, we conduct some operations which described in Sec.3 to improve the interpolation efficiency in DEM grids. The next step is importing the geological sampling data which has been saved in the GIS file (as the ARCGIS shape file) or some specification text file (as the GPS record) obtained from the geological survey. Then the modeling procedure checks the sampling data for irregular topological relations. In addition, some sampling points may lack the elevation coordinates, of course it can be calculated from the imported DEM data.

Using modeling ideas mentioned above, the subsequent implementation process is as follows:

```
   calculate the average distance between points on
feature  polygons;
    switch(distance)
{
      case 1:
      for(each polygon recorded in the sampling data)
     {
  get the envelope of  the polygon
         determine which DEM grid points inside the
envelope is located in the polygon
         establish TIN with the polygon points and the
DEM grid points found by the previous step
         render these cell of triangles with special
color to construct the visualization model
      }
```

```
          case 2:
     for(each polygon recorded in the sampling data)
     {
  get the nearest DEM grid points to the polygon points
         reorganize the polygon with DEM grid points
gotten by the previous step
         assign the specified scalar value to the DEM
grid points which is inside the reorganize polygon
         construct the DEM visualization model
         extract the contour band to get the
visualization model
     }
   }
```

3 Technical Details

3.1 Massive Data Visualization

For the large area of the actual geological survey work, we often encounter the problem of massive data operation during the visualization modeling. If the large amounts of DEM data and geological sampling data are directly read into memory for rendering, it will be greatly affected performance even if no error occurs. To solve this problem, researchers have presented the LOD model which saves different details through hierarchical data like a pyramid [9]. And then display different visualization details to users according to their different needs of observed scenes.

We applied the idea of LOD in the visualization modeling of the GCCS. We first assume the maximum number of points which can be rendered in a scene and assign several values to the predefined shrink coefficient. Then the number of points which locate in the range of the active camera will be calculated when the viewport changes. If this number exceeds the assumed value, the data visualization model will be shrunk. Take the DEM data as an instance. Assuming at the current viewport, some DEM grid points are rendered, when zoom out the camera, the number of grid points in the camera is gradually increased. While the number reaches a setting value, the shrinking event takes place such as points in four grids are merged into one grid to be rendered. For the geological sampling data, we use a simple way to achieve the effect of shrinking. When shrinking happens, if a geological block is fully or partially falls in the shrinking grid area, we use the rectangular grid after shrinking instead of the original polygon. If not, the TIN need to be rebuilt by the sampling points and the reduction DEM grid points. This visualization result in the GCCS is shown as Fig.5 and Fig.6.

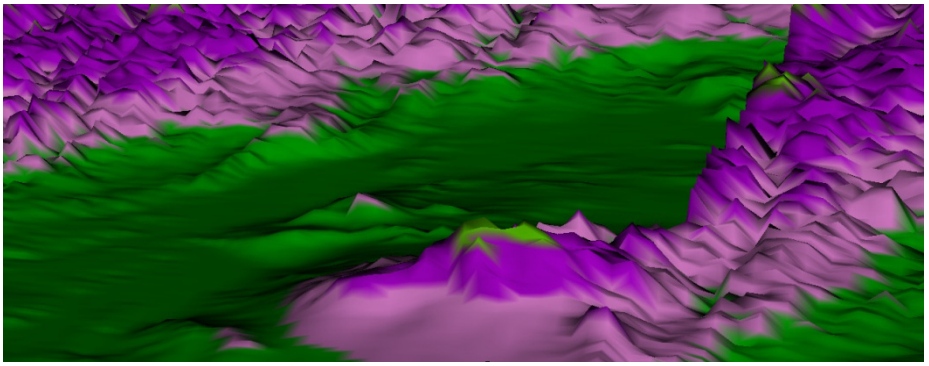

Fig. 5. The visualization model expressed all details

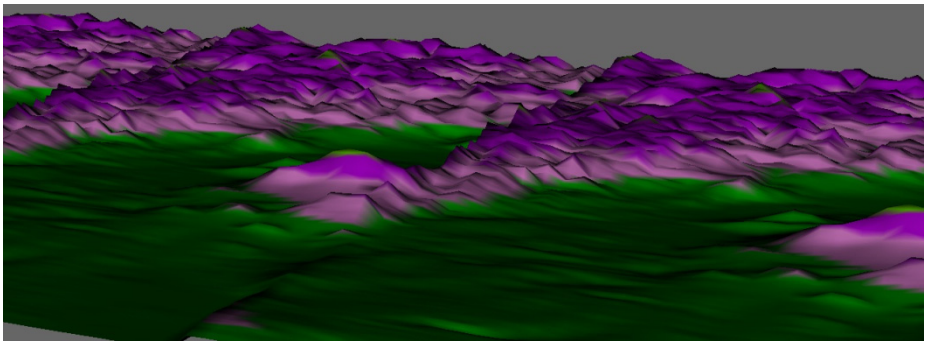

Fig. 6. The shrinking effect occurred to the visualization model shown as Fig. 5

3.2 DEM Data Manage

In the process of constructing the surface visualization model automatically, the DEM data is often used to interpolation and calculation such as finding the nearest DEM grid points to each sampling point in the feature polygon. It's usually a very time-consuming task because the DEM data can't be read into memory disposable and it's difficult to be random read when it is stored out of memory. Especially in our develop work, DEM data has saved in the document, I/O operation is more inefficient. For this similar case, some researchers have adopted the document segmentation strategy to break a large DEM data file down into several smaller DEM data files [10]. But in our practice, this strategy hasn't achieved a satisfactory result. The reason is: To improve search efficiency we must reduce the segmentation file size; when the file size reduced, more small files are produced; too many files are not conducive to management and indexing. So we must look for new ideas to manage the DEM data.

Finally, our implement ideas are inspired from NOSQL [11] that is storing the DEM data in a big table. The storage schema of DEM is very simple which can be represented as the tuple (ID, elevation). Here ID represents the index value (line index

in the DEM grid multiple column index in the DEM grid) of the grid point in DEM. We choose the JDBM [12] which is a key-value based embeddable storage to manage the DEM data.

The GCCS firstly use a wizard to guide the user importing the new DEM file, then the system parses the file and save data into the JDBM with the above-mentioned schema. The whole process may take a long time and the generated data block managed by JDBM is approximately 2 times larger than the original DEM file. In addition, the GCCS record the Meta data about the DEM data such as the number of rows, the number of columns in a simple XML file. In subsequent operations, the elevation information of the grid point can be gotten quickly by the calculated index.

4 Results and Conclusions

4.1 Results

Based on the author's modeling ideas mentioned above, the GCCS can better express geological features with the surface visualization model in areas of the geological survey. The surface visualization model based on DEM and geological sampling data can be automatically constructed as Fig.7 (the instance of case1) and Fig.8 (the instance of case2) in the system. And the different color represents the different geological property of stratum in the two figures.

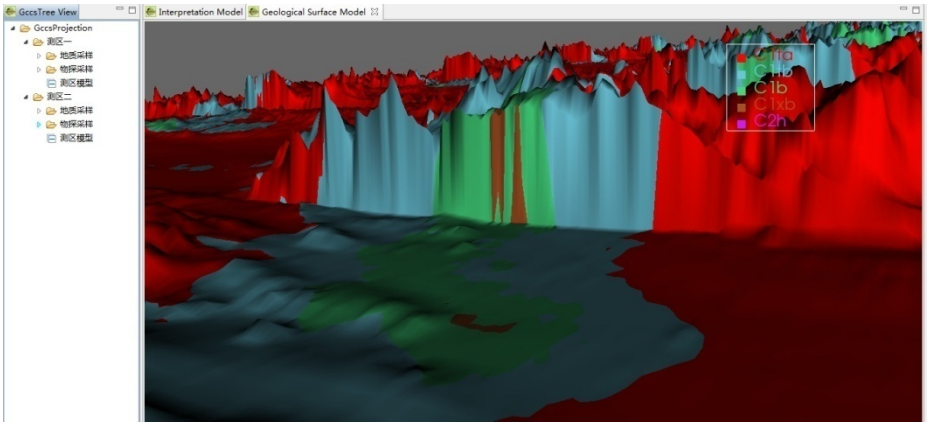

Fig. 7. An example of constructed model

Concerned about the other implement methods, the GCCS implement the visualization modeling based on VTK (The Visualization Toolkit [13]) for its good performance in related fields. About the presentation layer, it chooses Eclipse RCP [14] as the UI framework.

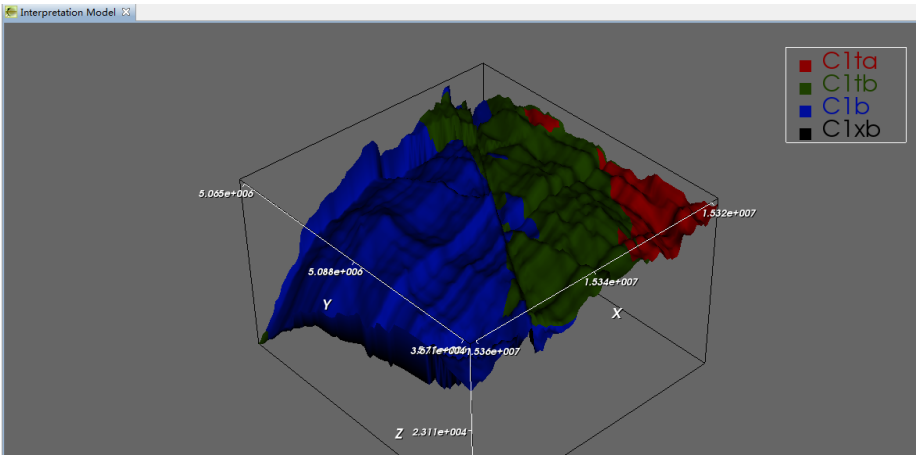

Fig. 8. Another example of constructed model

4.2 Conclusions

The system built with the modeling ideas discussed in this paper has greatly improved the data's visualization modeling and processing in the practical work (the geological survey work in the area of Karamay Xinjiang China). In the user's evaluation report, it has pointed out that with the modeling approach of the authors users can quickly get the distribution of geological properties on the surface with a better visual impression. And compared with other software used in the same project, the GCCS can achieve the three-dimensional effect with the minimum sampling data processing.

But after all, the geological surface visualization model is only a part of three-dimensional geological mapping. At current stage, people can't construct a complete three-dimensional geological model without manual intervention. The authors' modeling method and their corresponding system also needs to improve some abilities as following in later work.

a) It needs enhance editing functions to allow the user freely and manually adding or delete surfaces to the constructed model for their own needs.

b) Users often need to splice together several visualization models in the actual work; the author will complete this solution in the follow-up research.

Acknowledgment. This paper was supported by the central university research fund: CUGL130208.

References

1. Martelet, G., Calcagno, P., Gumiaux, C., et al.: Integrated 3D geophysical and geological modelling of the Hercynian Suture Zone in the Champtoceaux area (south Brittany, France). Tectonophysics 382(1), 117–128 (2004)

2. Xue, Y., Sun, M., Ma, A.: On the reconstruction of three-dimensional complex geological objects using Delaunay triangulation. Future Generation Computer Systems 20(7), 1227–1234 (2004)
3. Marschallinger, R.: Three-dimensional reconstruction and visualization of geological materials with IDL-examples and source code. Computers & Geosciences 27(4), 418–426 (2001)
4. Wu, Q., Xu, H., Zou, X.: An effective method for 3D geological modeling with multi-source data integration. Computers & Geosciences 31(1), 35–43 (2005)
5. Mark, J.: Three-dimensional geological modeling of potential-field data. Computers & Geosciences 27(4), 455–465 (2001)
6. Watson, D.F.: Computing the N-dimensional Delaunay tessellation with application to voronoi polytopes. Comput. 24(2), 167–172 (1981)
7. Wu, H.S., Barba, J.: An efficient semi-automatic algorithm for cell contour extraction. Journal of Microscopy 179(3), 270–276 (1995)
8. Kobbelt, L.P., Vorsatz, J., Labsik, U.: A shrink wrapping approach to remeshing polygonal surfaces. Computer Graphics Forum. 18(3), 119–130 (1999)
9. Varadhan, G., Manocha, D.: Out-of-core Rendering of Massive Geometric Datasets. Proceedings of IEEE Visualization, 69–76 (2002)
10. Ueng, S., Sikorski, K., Ma, K.-L.: Out-of-core Streamline Visualization on Large Unstructured Meshes. IEEE Transactions on Visualization and Computer Graphics 3(4), 370–380 (1997)
11. NOSQL Databases (2013), `http://nosql-database.org/`
12. JDBM-Embedded Key Value Java database (2013), `http://code.google.com/p/jdbm2/`
13. VTK - The Visualization Toolkit (2013), `http://www.vtk.org/`
14. Eclipse RCP (2013), `http://www.eclipse.org/home/categories/rcp.php`

Metadata Management of Models for Resources and Environment Based on Web 2.0 Technology

YiMin Lu[1], Ling Sheng[1], Sheng Wu[1], and TianXiang Yue[2]

[1] Key Laboratory of Data Mining & Information Sharing of Ministry of Education, Spatial Information Research Center of Fujian Province, Fuzhou University, Fuzhou 350002, China
[2] State Key Lab. of Resources & Environmental Information System, Institute of Geographic Sciences and Nature Resources Research, CAS. Beijing 100101, China

Abstract. The papers firstly introduce the standard framework of model metadata as well as its composition, content and meaning. It is held that model metadata should consist of an identifier, sphere of application, model parameters, principles, performances, run conditions, management information, references, and case information. Then we explained the virtual community for model metadata publishing, sharing and maintaining. Finally, we expatiated on the expression of model metadata standard based on XML schema Definition (XSD), the extended-metadata based on Tag and the publishing of model metadata based on Wiki. Based on Web 2.0 technology, the traditional model metadata which just create by modeler was extended to support extended-metadata created by model users or domain experts, which includes the feedback on model evaluation and suggestion. The user-metadata was refined from massive messy individual tags, which reflect the implicit knowledge of models.

Keywords: Model Metadata, XSD, Tag, Wiki, Extended-metadata.

1 Introduction

In recent years, the studies have advanced from quantitative description to qualitative analysis, from field investigation to mathematical model. There have been amounts of mathematical models developed in order to solve major resource and environment problem in recent years [1] such as spatial interpolation model for quantitative expression and analysis of complex environment problem. However, the model builder doesn't care about the integration and sharing of the model. Most different models often distribute on heterogeneous carriers. It's difficult to apply (or share) these models for their poor flexibility [2]. At present, there are a lot of research achievement of resources and environment information sharing both at home and abroad and relevant metadata standards have been produced. But there are some troubles as well such as the overlook of model, lack of standardization of model metadata and restricted coupling sharing. Kwon and Park [3] developed inverse prototype model system based on concept of model metadata [4]. Yoder and Razavi [5] used metadata model to construct adaptive object model and provide ideas for model reuse. SU

F. Bian et al. (Eds.): GRMSE 2013, Part I, CCIS 398, pp. 603–615, 2013.
© Springer-Verlag Berlin Heidelberg 2013

Li-hong pointed out that the integrated metadata frame should consist of the metadata about the data and the method metadata about models, and then put forward the concept of method metadata to standardize descriptive information about environment modeling for the first time in China [6],[7]. TANG Shihao [8] not only discussed the methods of remote sensing model metadata, but also advanced management of remote sensing model and operation mechanism based on metadata. YUE Tianxiang etc. considered that model metadata is the core content of model base management [9], [10]. LIN Jiaxiang provided a basic framework for grid services model metadata in grid environment, and explained the principle of model metadata organization and management by using XML as the description language [11]. Based on the open concept framework and its building foundations, model metadata, a method is designed to verify the spatial and temporal consistency between the coupling models, and the matching between the input and output variables by ZHANG Zimin [12]. Metadata criterion describing for resources and environment model are also studied recently. YUE Tian-xiang discussed further study about the effective integration between mathematical model and GIS, established mathematical modeling specification and provided a guideline for standard classification [1], [2]. YANG Hui etc. designed standard framework of geographic analysis model to achieve the standardization of grammar and structure [13]. The model metadata mentioned above is traditionally created by the modeler only; the eventual model users of the metadata are disconnected from the process. It is costly time and effort to produce only by model builder, so this makes it very difficult to scale and update [14]. Nowadays, In the Web2.0 times User created metadata is another approach. Web 2.0 is not a technical standard, but a term that explain technical shifts [15]. It is considered that web 2.0 is based on new theories such as "Long Tail", "Copyleft" and "Six Degrees of Separation". Applications such as Tag, Wiki, XML, Blog and RSS are its core. It blurred the boundaries of information providers and consumers [16]. Web 2.0 is a rapidly developing area with contributions from not only the field of IT [15], but also other disciplines such as clinical medicine [17], biology [18],[19], preservation and presentation of cultural heritage [20]. Web 2.0 is changing the ways of thinking and working [21]. Based on tag and wiki etc., the traditional model metadata which just create by modeler was extended to support extended-metadata (user metadata, or social metadata) created by model users or domain experts, which includes the feedback on model evaluation and suggestion. TANG Zhong-shi etc. used tag categories to meet the needs of different users' requirements, and open category was applied to the model sharing platform [22]. Kim presented a dynamic model of collaborative tagging by which many users add metadata in the form of keywords to shared content [23]. Zarro proposed a classification scheme to manage contributions and mitigate information overload issues [24]. He considered comments and notes are types of "descriptive metadata" that describe, identify, and add context to a resource. User metadata enhances the identification of resources, connects resources to similar holdings in a private collection, and supports the retrieval of a resource through search and browsing.

2 Standard Framework of Model Metadata

Metadata is explained as being "data about data" more generally, describes an information source, which helps users locate resources that meet their specific needs. Model metadata, or "data that describes model", is essential for use in analysis and modeling. Model metadata is critical for model resource description, discovery, and management. It also helps us to understand the model we find and helps us to evaluate what we should spend our time evaluating. Model metadata is not only used to describe the features and properties of the model, but also indicate the scope, ideas, implement, requirements and formats of the model [7]. In this paper, traditional metadata model was extended to the extended-metadata that is feedback by users on the evaluation and suggestion in web 2.0. The extended-metadata, or user created metadata, is often implicit, which helps user find, understand, or evaluate the content. User metadata, sometime named social metadata, refer to additional information about a resource (such as models) resulting from user contributions and web 2.0 technology. The user contributions that would enrich the traditional metadata could come from students, experts, or enthusiasts.

2.1 Composition of Model Metadata

Traditional standard-based model metadata is explained by the modeler in existing model. It often describes the model based on a certain standard or specification in detail. The comprehensive and complex resource environment model determines the complicacy of its model metadata. It has been unable to form a standardized model metadata so far, due to the uniform of the understanding of complexities. According to the existing references [10], [13], we determine the required model metadata which consists of nine subsets to identify the resource environment model. It contains an identifier, sphere of application, model parameters, model principles, model performances, run conditions, management information, references, and case information.

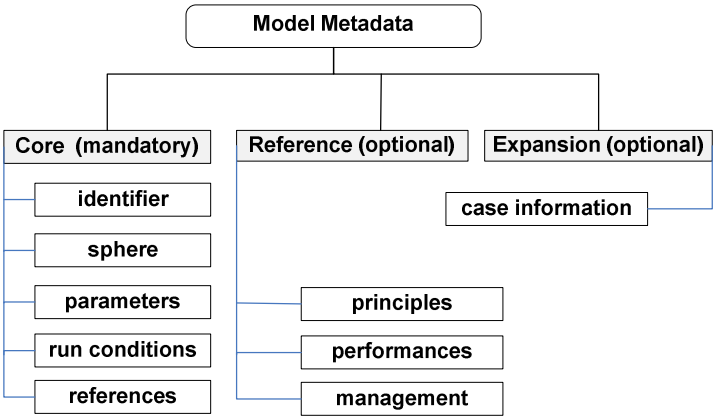

Fig. 1. Standard framework of model metadata

In order to improve the creation efficiency in the model integration environment, metadata is divided into core metadata, reference metadata and extended metadata in this paper, as in the figure 1 above. Core metadata is mandatory (M), which is necessary information about resources and environment model by model builder, manager and users to manage or use in the future. It mainly contains the information about identifier, sphere of application, model parameters, references and run conditions. Reference metadata is optional (O), mainly including information about model principles, performances, management. It comprehensively describes the model information in detail and constitutes a complete metadata framework with core metadata. Extended metadata is optional (O), which is a subset of case information. It is a dynamic expansion to traditional metadata. It includes comments, suggestions and other feedback based on users' perspective in web 2.0.

Table 1. Composition of resource and environmental models metadata standard

Subset name	Definition	Co	MO	Data type	Range
Identifier	It's the basic and unique identify information about the model, such as model ID, model name, brief description of function and so on.	M	1	compound	References / Management information / Sphere
Sphere of application	Specific application field, application problem, scope and model error of the model.	M	1	string	Free Text
Model parameters	I/O parameter sets, control parameter sets and their physical meaning, variable format, range, dimension and units and so on.	M	1	string	Free Text
Model principles	The method, basic principle, algorithm and mathematical expression of constructing model.	O	1	string	Free Text
Model performances	Evaluate the capability of model, including the stability, reliability, and accuracy, qualitative and quantitative overview about processing capability.	O	n	string	Free Text
Run conditions	Required software, hardware, network environment, personnel requirement, conditions of use and other descriptive content to run the model.	M	1	string	Free Text
Management information	Describe contact information between researchers and developers, construction, maintenance and copyright status of model.	O	1	compound	Free Text
References	References information and publishing logo of model, model reference mode and interactive interfaces, model online name, link address, protocol etc.	M	n	string	Free Text
Case information	Contain operating conditions, solution process and result illustration of model; comments, suggestions and other feedback information about extended model users' application result.	O	n	compound	References / Run conditions

2.2 The Content and Meaning of Model Metadata

The content and meaning of model metadata are described detailedly in definition, constrains, range, data type, and maximum occurrences etc. as follows. In the Table 1, "Co" refers to Constrains, and "MO" refers to Maximum Occurrences.

3 Design and Implement of Model Metadata Management

In this paper, we developed a virtual community for resource and environmental modeling to realize the management, publishing and sharing of model metadata. Howard Rheingold, the British scholar proposed the concept of virtual community in 1985. Virtual community has experienced through traditional virtual academic application to virtual academic application in web 2.0(Scientific Social Community, SSC) [19]. Traditional disciplinary information portal that mainly achieve resource navigation can't bring about greater user experience and value-added information for researchers. Virtual academic community in web 2.0 not only strengths the interaction among majority researchers and peers [18], but also provides free space for those interests and informal academic exchanges [14], [16], [20].

3.1 The Design of Model Metadata Management

Model builders edit core and reference metadata in the model metadata editor based on Wiki engine, extract theme directory automatically through core metadata, and then publish metadata model (except extended data) and theme catalog to sharing model virtual community. Model metadata management system that generates extended metadata by folksonomy collect and construct tags database, update and extend existing metadata content model.

We refer existing experience of constructing virtual academic community [16], [21], accomplish publishing and sharing of model metadata based on Wiki and Tag combined with database technology, achieve registration model services with Windows Server 2003, construct model sharing virtual community to support communication, collaboration, integrated use, problem solving and other academic activities among researchers and model users. The model is B/S three-tier architecture: client layer, business logic layer and data access layer. Customer layer is common browser; logic layer is the core that provides connection to presentation layer and data layer and displays to Client application in encapsulation; data layer is used to define, maintain, access, update data and meet the requirements of application service. Its architecture is shown as Figure 2. The core business logic layer of the community main includes Wiki engine, Tag tools and UDDI. Wiki engine supports edit, preview and retrieval data, upload local picture, insert text and link documents. Tag tools provide tag function for users to mark or remove labels, open category and show hotspots resources in Tag Cloud [21].

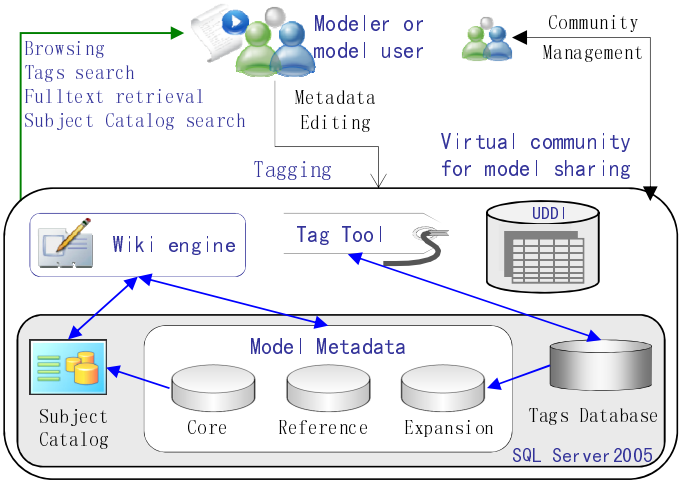

Fig. 2. Architecture of model sharing virtual community

The design of virtual community is entirely Web-based so that there are no complex algorithms, costly queries and excessive overhead. The open design of backend database makes it easy for users to get and write data. All registered users have their own independent data. Community resists destructive activities and reduces noise through a series of technical mechanisms such as version control, page lock, entry inspections and permission management. It includes five modules:

(1)Model Metadata Publishing: It is a Wiki-based text editor. Its functions are editing, modify, preview, upload and insert local picture documents. What you see is what you want. Users will publish and perfect model metadata easily.

(2) Revision control: Users control historical version of model metadata by it. It contains versions back and comparison. Backend database saves all changes from a previous version to a new one. Each version can revert to corresponding version from the record even though the users delete the entire page.

(3)Model Metadata Search: It includes full-text retrieval, subject retrieval and tags retrieval. Users use full-text retrieval to search all information comprehensively; subject retrieval is used to search name of model. Tag search consists of searching relevant tags based on the specified model, searching relevant models based on specified tag and searching all tags that tagged by specified user.

(4)Note Recommended: It realizes or removes targets through Tag and Untag, recommends active topics through statistics and displays tag cloud.

(5)Community Management: Community administrators, whose main task is to ban the intruders' IP and delete online advertisement, manage it independently. It provides Sand Box for users and entrance of graphical model integrated sharing platform for registered users.

3.2 The Expression of Model Metadata Standard Based on XSD

Extensible Markup Language (XML) is a markup language that defines a set of rules for encoding documents in a format that is both human-readable and machine-readable. Document Type Definition (DTD) and XML schema Definition (XSD) are main languages of describing XML structure and constraint. XML Schema is an XML document so that we can parse XML Schema through XML API (such as DOM, SAX or JDOM etc.) easily. It achieves consistency between XML document and description which is good for data transmission and exchange. XSD supports integrated namespace and uses a rich datatype. Navigate and position rapidly by using XPath and path expression according to data content constraint, data format and hierarchies of XSD document. We use XSD as defined standards in this paper.

XSD consist of Simple Type Element and Complex Type Element. Simple elements are features that locate in a leaf node. Complex element contains other node features and can be used to define relation between metadata. There are different ML language which is used to display, communicate, integrate, aggregate and release scientific data and label in different discipline field based on XML technology currently. For example, Chemical Markup Language (CML), Bioinformatics Sequence Markup Language (BSML), Biopolymer Markup Language (BioML), Astronomical Data Markup Language (ADML), and Geography Markup Language (GML). Mathematical Markup Language (MathML) is a XML application for mathematical equation. It is recommended by W3C and used as XML representation of mathematic expression. Mathematical expressions were generally displayed and stored in the form of graphic files before MathML existed. The form of expression is lack of flexibility and scalability so that it is impossible to edit, modify, query, index and share, which is disadvantage of resource reuse. The capacity of picture file occupies so much space that will affect network transmission speed. MathML is basic standard of mathematical information exchanged among computers. It describes structure and content of mathematical expression by XML definition, shows content in recursive tree structure, saves symbol, formulas and special characters in the form of text so that it overcomes disadvantage of traditional image files effectively. In this study, some metadata subset includes mathematical expression; other standard or specified elements that need to refer Mathematical Markup Language (MathML) Definition are used in the definition of metadata standards. For example, effective coefficient of temperature, a sub model in food provisioning services of grassland ecosystem is described as the formula (1) below. f(T) in the formula (1) is Logistic Curve Modified Coefficients (%); T(°C) is mean annual temperature. When T less than −10, f(T) is equivalent to 0. In term of the MathML specification, formula (1) expressed in form of presentation markup like XML fragment showed below. In the XML fragment: (1)<mfrac></mfrac> represent fraction; (2) <mrow></mrow> represent one row display; (3) <mn></mn> represent numeral; (4) <mo></mo> represent operator; (5) < msup ></ msup > represent superior figures; (6) <mi></mi> represent variable.

$$f(T) = \frac{1}{1 + e^{2.052 - 0.161 \cdot T}} \tag{1}$$

```
<?xml version="1.0" encoding="utf-8" ?>
- <Model Metadata for Resources and Environment>
+ <Identifier>
+ <Sphere of application>
+ <Model parameters>
- <Principles>
  + <Modeling Method>
  + <Modeling Fundamental>
  + <Modeling Algorithm>
  - <Mathematical Expression>
    -<math display="block" xmlns=
      "http://www.w3.org/1998/Math/MathML">
     - <mfrac>
        - <mrow>
            <mn>1</mn>
          </mrow>
        - <mrow>
            <mn>1</mn>
            <mo>+<mo/>
          - <msup>
            - <mrow>
                <mi>e</mi>
              </mrow>
            - <mrow>
                <mn>2.052</mn>
                <mo>-<mo/>
                <mn>0.161</mn>
                <mo>×<mo/>
                <mi>T</mi>
              </mrow>
            </msup>
          </mrow>
      </mfrac>
    </math>
  </Mathematical Expression>
</Principles>
+ <Performances>
+ <Run conditions>
+ <Management>
+ <References>
+ <Case>
</Model Metadata for Resources and Environment>
```

3.3 The Extended-Metadata Based on Tag

Model extended metadata reveals multifaceted connotation and enriches content of model metadata. Model metadata was extended from the users' point of view so that metadata based on tags base are mainly from users' ideas. Model extended metadata is supplemented and secondary information of model. It is formed by community tools with debris semantic colors, "well-formed micro content"; it is formed after creating clustering tags database and frequency statistics unconsciously when users add tag to model information viewed in Web. Referring domestic and abroad reference [22], [25], this design was to form tags database through accumulating a large number of tags and write it into case information subset through clustering Tag Tool. Metadata providers and users give a certain number of labels which are tag-based to extend model descriptive information voluntarily. System adopts varieties of algorithms and mechanisms including mathematical statistical methods in order to achieve folksonomy, automatic classification and automatic clustering process of model resource published in community. Tag technology can promote users' comment, feedback and classification of resources effectively. Label may be the result of users' thinking. Good tag flickers personal wisdom so that experienced tagger has his owns unique way of thinking and labeling model. For example, HASM-AD may appear "efficient"; Multi-grid algorithm may appear "elliptic equation"; "Estimation of potential crop production" may appear commentary labels such as "solar radiation", "temperature", "precipitation" and "lack of social impact factor". Natural and plain tag contains huge energy; when users search for a certain tag, all models in virtual community that label the tag will appear so that they can share other users' collection labels. It achieves self-organization and interactive sharing of model information when users create extended model metadata inadvertently.

Extended model metadata sharing is accomplished based on tag. Publication and sharing of extend model metadata includes not only tag tool that realize and cancel label, but also Tag Cloud display that statistic and recommend active subject. Users can retrieve all labels of specified model (e.g. "HASM" model), all relevant models (e.g. "iterative solution" label) of specified label and specified user. Figure 3 retrieved tags and its Tag Cloud display interface of "luym". Tag Cloud marks the heat of label with different size and thickness of font. The bigger and the thicker of font mean the more frequency use. Some popular generic model (HASM, Kriging) will be given to hundreds of Tag by different users. The huge number of Tag lead to the widespread and prevalence of the model in the respective academic fields [16].Users can not only see their counterparts with the same tag, but also understand outstanding model resource and hot issue in community.

Constraint of creating tag-based extended model metadata, generally, label of the same model subject is different due to various modelers. Different label information extends content of model subject, and then shares knowledge of tag participants. Tag is free, but there are certain constraints of a label that can aggregate into extended metadata. Rules and recommendations of the design are described as follows: (1) Labels should be relevant to subject and content. For example, "spline interpolation model" can label "spatial interpolation", "regularized spline". It has no meaning to

label "fairy tale". (2) Label should have a basic significance of the word. For instance, be avoiding of using "so so" and "〖". (3) Label was recommended to use refined and concise words in order to cluster easily. For instance, use "mechanism model" instead of "physical and complex model based on its principles" will be more ideal. (4) Don't use "Martian language" as model label, prohibit garbled. (5) Recommend to use professional common vocabulary as tag label in order to strengthen its sharing.

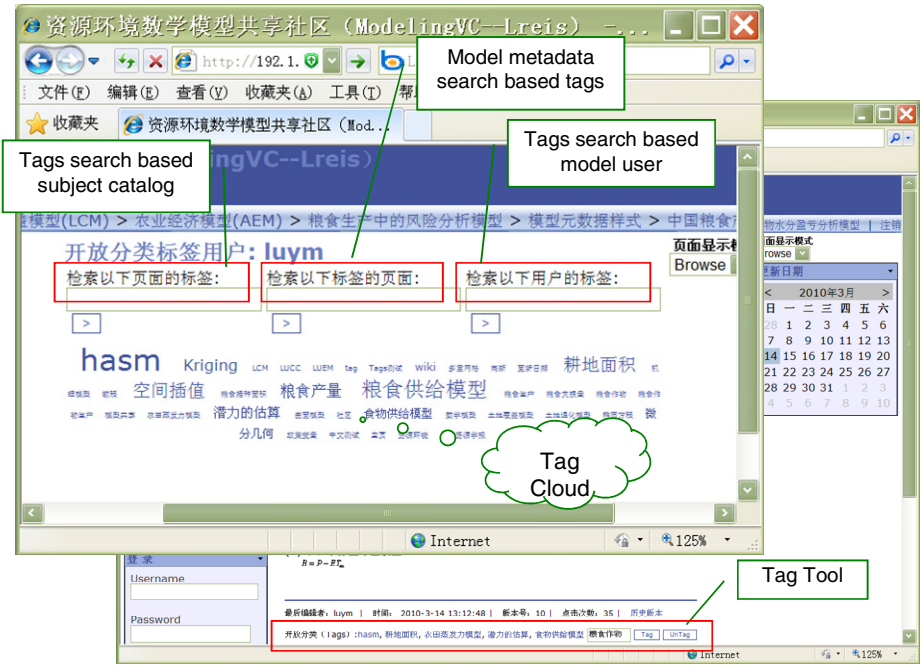

Fig. 3. Model info searching based Tags and displaying with Tag Cloud

3.4 The Publishing of Model Metadata Based on Wiki

Wiki engine is the core of model metadata management, publishing and sharing in virtual community. Wiki engine and open database support model metadata management which not only includes a system that create and change web page simply, but also a system that records all changes and provides restore function. Wiki engine is backend system program, in general, it is software that can achieve internet collaboration and integrate a complete database at last. Wiki engine supports collaborative creation orient virtual community. It includes a series of auxiliary tools that supports discussion and communication of the creation.

Model metadata management separates source file editor from content formatting, uses WYSIWYG (What You See Is What You Get) format instead of complex HTML format. Wiki engine achieves collaboration security through traced back. Model metadata management system achieves version control, saves version, version

comparison and updating description of changes every time and allows editor to modify. System developed through editing link aggregation, extending model metadata content, integrating and enriching information about model rapidly. System extracts subject theme which is model theme published on virtual community through model core metadata. It involves version management, resource retrieval and resource label recommendation. Its implement interface is shown as figure 4. Users of virtual community cooperate, create and maintain domain model metadata; achieve update model information rapidly through gather a large number of model followers.

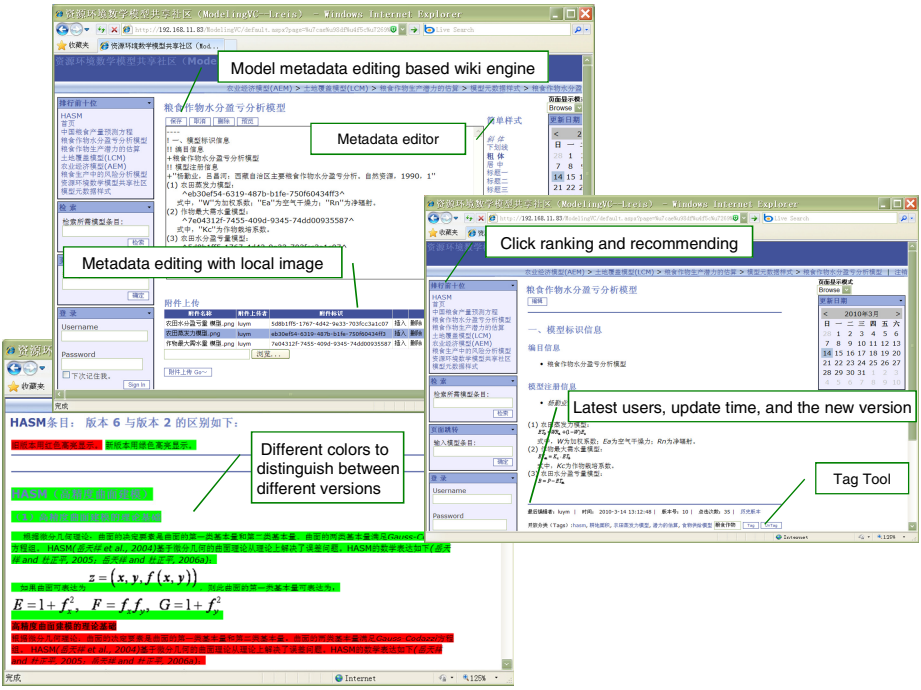

Fig. 4. Screenshots of model metadata publishing, sharing and maintaining

4 Conclusion and Prospect

In this paper, traditional model metadata created only by modeler is extend to model users who may be students, experts, or enthusiasts based on Tag, Wiki and other Web2.0 technologies. Folksonomy based on tag technology, assist modeler or model user in creating metadata, as is a new attempt at metadata research. There are many advantages of extended metadata or user metadata which extends based on traditional metadata. Extended model metadata comes from private label of personal understanding. It is an analysis and refining after practicing relevant model resource and reflection of the implicit knowledge about model resource. Metadata created by users reflect most users' suggestion and experience. The function of extended metadata is no longer navigation, but full realization of shared core and common values. On the

other hand, model metadata based on traditional standard is created by modeler or user so that creation of model and its metadata is completed once and will not update. Web 2.0 can add metadata, extend and update metadata content many times. Indeed, the openness, ease of use and scalability of web 2.0 also brings questionable shortcomings. For instance, the user's permission set very low because of openness or credibility of model resource will be jeopardized due to the mistake of tags, comments, reviews of some users. User management, control of authority and other information security leave much to be desired. In addition, the tags in database, which usually is used to generate user metadata, come from tags or comments of many people, is decompacting, even mess. So, there is need for improvement in the algorithm and mechanism to support folksonomy.

Acknowledgements. The work was supported by a grant from Provincial Natural Science Foundation of Fujian (2011J01268), a grant from Qualified Personnel Foundation of Fuzhou University (XRC-1030), a grant from Open Foundation of State Key Laboratory of Resources and Environmental Information System (2010KF0008SA).

References

1. Yue, T.X.: Handbook of mathematical model of resources and environment. Science Press, Beijing (2003)
2. Yue, T.X.: Standardized documentation of models for resources and environment and their integration with GIS. Acta Geographica Sinica 56(1), 107–112 (2001)
3. Kwon, O.B., Park, S.J.: RMT: A modeling support system for model reuse. Decision Support Systems 16(2), 131–153 (1996)
4. Keller, R.M., Dungan, J.L.: Meta-modeling: A knowledge-based approach to facilitating process model construction and reuse. Ecological Modeling 119(2-3), 89–116 (1999)
5. Yoder, J.W., Razavi, R.S.: Metadata and Adaptive Object-Models. In: Moisan, S., Yu, H.-J. (eds.) ECOOP 2000 Workshops. LNCS, vol. 1964, pp. 104–112. Springer, Heidelberg (2000)
6. Su, L., Huang, Y., Ke, Z.: Model Metadata and Its Management for Resources and Environment Information System. Resources Science 22(6), 14–21 (2000)
7. Su, L., Huang, Y.: Management and Usage of Metadata and Method Metadata in Resources and Environment Information System. Journal of Image and Graphics 6(10), 1021–1025 (2001)
8. Tang, S., Su, L., Shuai, Y., Wang, Z., Long, K.: Construction of Distributed Web-based Remote Sensing Model Library and Its Operational Mechanism. Geo-Information Science 6(1), 89–93 (2004)
9. Fan, Z., Yue, T.: Framework for the Integration of Resource and Environmental Modelbase. Geo-Information Science 6(2), 17–22 (2004)
10. Huang, H., Yue, T.: Web-based Metadata Management of Spatial Models. Geo-Information Science 8(3), 94–97 (2006)
11. Lin, J., Ma, W., Wu, X., Chen, C., Wang, W.: Model Metadata Management and Its Application in Knowledge Services Grid Platform. Journal of Geo-Information Science 12(2), 200–206 (2010)

12. Zhan, Z., Zhou, Y., Li, Q., Mao, X.: Design of an Icon-based Modelling Environment Prototype for Coupling Geoscience Models. Journal of Geo-Information Science 13(1), 48–57 (2011)
13. Yan, H., Sheng, Y., Wen, Y., Hu, Y., Wang, J., Yang, Y.: Research on Standardization and Formalization of Heterogeneous Geo-analysis Models in Web Space. Geo-Information Science 10(3), 382–389 (2008)
14. Mathes, A.: Folksonomies-cooperative classification and communication through shared metadata. Computer Mediated Communication, 1–13 (2004)
15. O'Reilly, T.: What is Web 2.0: Design patterns and business models for the next generation of software? Communications & Strategies 65(1), 17–37 (2007)
16. Pierce, M.E., Fox, G.C., Choi, J.Y., Guo, Z., Gao, X., Ma, Y.: Using Web 2.0 for scientific applications and scientific communities. Concurrency and Computation-Practice & Experience 21(5), 583–603 (2009)
17. Wright, A., Bates, D.W., Middleton, B., Hongsermeier, T., Kashyap, V., Thomas, S.M., Sittig, D.F.: Creating and sharing clinical decision support content with Web 2.0: Issues and examples. Journal of Biomedical Informatics 42(2), 334–346 (2009)
18. Csősz, É., Meskó, B., Fésüs, L.: Transdab wiki: the interactive transglutaminase substrate database on web 2.0 surface. Amino Acids 36(4), 615–617 (2009)
19. Zhang, Z., Cheung, K.H., Townsend, J.P.: Bringing Web 2.0 to bioinformatics. Briefings in Bioinformatics 10(1), 1–10 (2009)
20. Barak, M., Orit, H., Zvia, K., Dori, Y.J.: MOSAICA: A web-2.0 based system for the preservation and presentation of cultural heritage. Computers & Education 53(3), 841–852 (2009)
21. Chu, H.T., Xu, C.: Web 2.0 and its dimensions in the scholarly world. Scientometrics 80(3), 717–729 (2009)
22. Tang, Z., Rao, S., Xie, Z., Zhao, H., Wang, H.: The research of GIS model sharing platform based on Web 2.0. Science of Surveying and Mapping 33(4), 181–183 (2008)
23. Kim, H.L., Decker, S., Breslin, J.G.: Representing and sharing folksonomies with semantics. Journal of Information Science 36(1), 57–72 (2010)
24. Zarro, M.A., Allen, R.B.: User-Contributed Descriptive Metadata for Libraries and Cultural Institutions. In: Lalmas, M., Jose, J., Rauber, A., Sebastiani, F., Frommholz, I. (eds.) ECDL 2010. LNCS, vol. 6273, pp. 46–54. Springer, Heidelberg (2010)
25. Rahman, J.M., Seaton, S.P., Cuddy, S.M.: Making frameworks more useable: using model introspection and metadata to develop model processing tools. Environmental Modelling & Software 19(3), 275–284 (2004)

Final Fill Ratio Inversion of Backfilling Materials in Solid Backfilling Mining Using Surface Subsidence Data

Xiaojun Zhu, Guangli Guo, Jianfeng Zha, and Qingbiao Guo

Key Laboratory for Land Environment and Disaster Monitoring of SBSM,
China University of Mining & Technology, Xuzhou 221008, China
The Main Laboratory of Resource Environment Information of Jiangsu,
Xuzhou 221008, China

Abstract. Solid backfilling mining is a sustainable mining technology for subsidence control. Compression ratio of backfilling materials is an important index to evaluate the goaf backfilling effectiveness and its accuracy has an important influence on the plan optimization of solid backfilling mining. In this paper, two methods were proposed to obtain compression ratio with surface subsidence data and their principle and procedures were described in detail. Furthermore, it was confirmed that two inverse methods were feasible by an engineering application, which provided new monitoring methods for quality evaluation of solid backfilling mining. Ultimately, the superiority-inferiority and application conditions of the inverse methods were analyzed.

Keywords: solid backfilling mining, final fill ratio, surface subsidence data, inverse method.

1 Introduction

Coal resources exploitation satisfies world energy demand but causes a serious of geological disaster and environment problems, such as surface subsidence, landslide, groundwater pollution etc. Under the contradictory relationship between environment protection and resource exploitation, the concept of green mining [1] was proposed, which plays a positive role in sustainable coal mining in China, including solid backfilling mining. Solid backfilling mining [2, 3] is a new technology for mining subsidence control. By this technology, solid waste, such as the gangue, coal ash and loess, is filled in the goaf to replace the coal resource, which successfully achieves the aims of waste reduction and environmental protection, as well as subsidence control.

Final fill ratio of backfilling materials is an important index to evaluate the goaf backfilling effectiveness and its accuracy has an important influence on the plan optimization of solid backfilling mining. Therefore, some methods were proposed to monitor the final fill ratio. The stowing ratios[4] (the weight ratio of backfilling materials and coal) is proposed as the index of backfill quality, but the relationship between the stowing ratio and final fill ratio has not been thoroughly confirmed so that it is hard to estimate the reliability of this method. Furthermore, the monitoring

F. Bian et al. (Eds.): GRMSE 2013, Part I, CCIS 398, pp. 616–625, 2013.
© Springer-Verlag Berlin Heidelberg 2013

method of strata movements in the overburden was used to obtain final fill ratio, which involved the field monitoring of strata movement above the working face or in the backfilling face. But the method costs too much and is difficult to be implemented in the complex underground environment. Since surface subsidence is a manifestation of the results of overburden movement, two methods were proposed to obtain final fill ratio with surface subsidence data, and their principle and procedures were described in detail. Ultimately, the superiority-inferiority and application conditions of the inverse methods were analyzed.

2 Final Fill Ratio of Backfilling Materials and Inversion Methods

2.1 Final Fill Ratio of Backfilling Materials

To evaluate the goaf backfilling effectiveness with solid wastes, the final compression ratio of backfilling materials was proposed as the technical measurement index. Compression ratio is defined as the ratio of the average thickness when backfilling materials are compacted and the average thickness of coal seam. It is shown in formula

$$\varepsilon = \frac{m_r}{m} \quad . \tag{1}$$

Where ε is the final fill ratio, m is the thickness of coal seam, m_r is the average thickness of the compacted backfilling materials.

Due to three factors, including the roof displacement, the unfilled space in goaf and the amount of compression value of backfilling materials, the effective height of backfilling materials is always smaller than the average thickness of coal seam. So, the detailed formula of final fill ratio is given as follows:

$$\varepsilon = \frac{m - (h_t + h_q + h_k)}{m} \quad . \tag{2}$$

Where h_t is the roof displacement, h_q is the unfilled height in goaf, h_k is the amount of compression value of the filling material.

2.2 Final Fill Ratio Inverse Method Using Numerical Simulation

With the development of rock mechanics and computer technology, numerical simulation has become an important research tool to solve the problems about mining engineering and geotechnical engineering, especially it has been cost-effective approach to study the theory foundation of coal mining subsidence and predict ground deformation [5-8].

When developing a numerical model, one of the challenges is to identify appropriate input parameters for modeling the rock mass. Laboratory test method is currently a common method to determine mechanics parameters of rock mass. However, laboratory-determined test results do not necessarily represent the properties of the large-scale rock mass because there are a lot of fractures, joints, bedding and weak

planes inside the rock mass. Therefore, laboratory mechanical parameters of rock block must be corrected before solving engineering field by numerical simulation.

In this paper, the procedure of final fill ratio inversion using numerical simulation is proposed. The flow diagram is given shown in fig.1 and the procedure is shown as follows:

Step1. Develop the initial numerical model with the bore histogram and laboratory mechanical property of strata.

Step2. Obtain the surface subsidence values W_1' and the height of caved zones H'_{m1} by numerical simulation after coal seam is extracted.

Step3. Compare the subsidence values, the edge of subsidence basin and the height of caved zones in real and computer-simulated environments. If the simulated value has great difference with the measured or empirical value (the surface subsidence values W_1 and the caved zone height H_{m1}), we should adjust the rock parameters and go to step 2. If $W_1' \approx W_1$ and $H'_{m1} \approx H_{m1}$, it indicates that the simulated mechanical parameters can represent the properties of the large-scale rock mass.

Step4. Obtain the simulated subsidence values at the observation stations by the numerical simulation of backfilling mining at initial final fill ratio, where the rock parameters are the corrected mechanical parameters got from step3.

Step5. Compare the real subsidence W with the simulated subsidence values W_2'. If there were large differences between W_2' and W, we should adjust the final fill ratio and go to step4. If $W_2' \approx W$ not, it indicates that the simulated ratio can represent the actual final fill ratio.

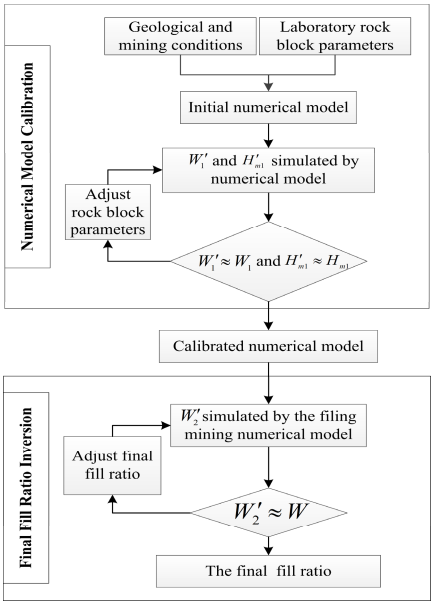

Fig. 1. Flow diagram of final fill ratio inverse method numerical simulation

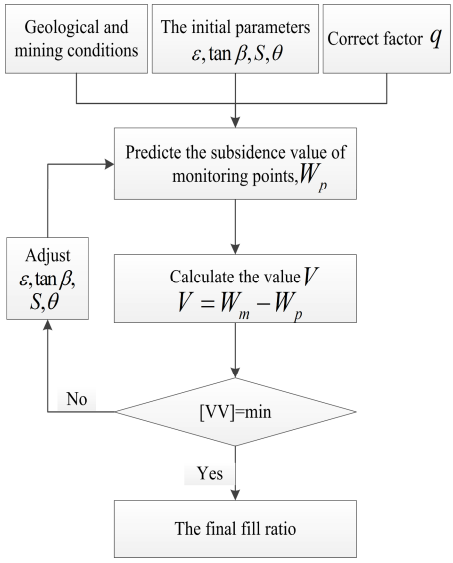

Fig. 2. Flow diagram of final fill ratio using inverse method using probability integration method

2.3 Final Fill Ratio Inverse Method Using Probability Integration Method

Probability integration method, based on the extraction of infinitesimal elements of area, is one of the influence function methods. In general, this method is the most widely applied in subsidence prediction in mining areas in China. Five predication parameters of this method are shown as follows: subsidence coefficient, q, horizontal displacement coefficient, b, tangent of major influence angle, tanβ, offset of inflection point, s and propagation angle of extraction, θ. The equation of probability integration method to calculate the surface subsidence at any point is given as follows:

$$W(x,y)=\frac{mq\cos\alpha}{\sqrt{\pi}}\int_{\frac{\sqrt{\pi}}{r}(x-l)}^{\frac{\sqrt{\pi}}{r}x}e^{-u^2}du\int_{\frac{\sqrt{\pi}}{r}(y-s)}^{\frac{\sqrt{\pi}}{r}y}e^{-v^2}dv \quad . \tag{3}$$

Where $W(x,y)$ is subsidence at the surface point with coordinates x and y, m is mining height, α is seam inclination, r is the radius of major influence, r=H/tanβ, l and s are the computing width and length of the opening.

In order to study overburden strata movements and establish a simple and precise subsidence prediction method, the probability integration method based on the equivalent mining height was proposed and has been applied in mining areas. As for solid backfilling mining, the goaf is filled by backfilling materials and the subsidence space of overlying strata is reduced. So we can explain it in another way that the subsidence is caused by mining coal with an equivalent height. In a mathematic way, equivalent mining height is the height of backfilling working face minus the height of backfilling materials after compaction. Thus, we can use the equivalent mining height to predict the surface subsidence by probability integration method. The equivalent mining height can be expressed as:

$$m_e=(1-\varepsilon)m \quad . \tag{4}$$

Where m_e is the equivalent mining height, ε is the compression ratio.

Substituting Eq. (2) into Eq. (1), we can get subsidence's equation of any point based by solid backfilling mining.

$$W_e(x,y)=\frac{(1-\varepsilon)mq_e\cos\alpha}{\sqrt{\pi}}\int_{\frac{\sqrt{\pi}}{r_e}(x-l)}^{\frac{\sqrt{\pi}}{r_e}x}e^{-u^2}du\int_{\frac{\sqrt{\pi}}{r_e}(y-s)}^{\frac{\sqrt{\pi}}{r_e}y}e^{-v^2}dv \quad . \tag{5}$$

Where $W(x,y)$ is subsidence at the surface point with coordinates x and y by solid backfilling mining, q_e、r_e is subsidence coefficient and the radius of major influence based on the equivalent mining height theory.

The characteristics of prediction parameters by the physical experiments of backfilling mining were studied in detail and some characteristics had been concluded as follow: the process of overburden movement of backfilling mining is similar to that of thin seam mining and the equivalent subsidence coefficient q_e is 1%~2% bigger than the subsidence coefficient of thin seam mining.

In this paper, we correct the equivalent subsidence coefficient q_e according to the subsidence coefficient of thin seam mining with the same or similar geological and mining conditions, then predict surface subsidence with a optimized final fill ratio and other parameters of probability integration method, ultimately compare with the measured subsidence values and the predicted values. The flow diagram is given in fig.2 and the procedure is shown as follows:

Step1. Determine the initial parameters including ε, tanβ, θ and s.

Step2. Predict the subsidence values at observation stations.

Step3. Evaluate the predicting accuracy. [VV] is a precision index for evaluation of parameters, where V represents the residual difference between the measured value and the predicted value.

Step4. Judge whether [VV] meets the termination condition. If [VV] is minimal, εis the optimal final fill ratio. If not, we should adjust ε, tanβ, θ and s and go to Step2 until [VV] is minimal.

3 Engineering Practice

3.1 The Surface Subsidence Data

1312 and 1316 working faces are the fully mechanized solid backfilling mining face, which has the average thickness of 3.01m and the average depth of 560 m. 1312 working face with the incline width of 34m and the strike advancing length of 239m and 1316 working face with the incline width of 100m and the strike advancing length of 222m were adopted the technology of overhand mining and underhand filling.

In order to obtain the precise and reliable surface subsidence data, the observation stations of 5 survey lines had been installed on the subsidence basin of 1312 and 1316 working faces, where three generally straight and linear survey lines and two irregular

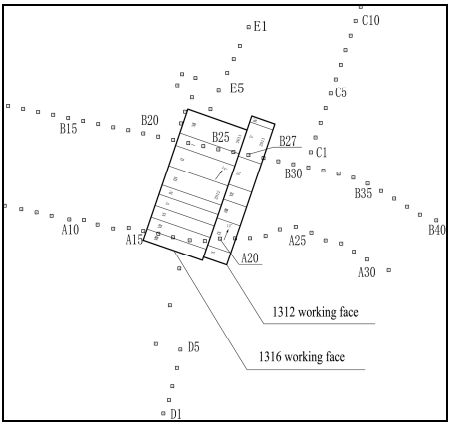

Fig. 3. Surface observation stations locations

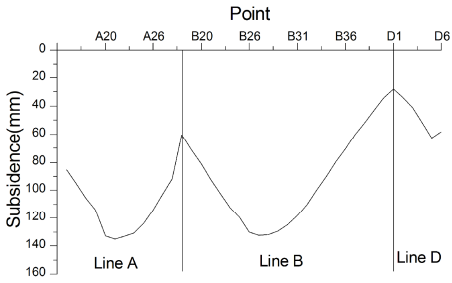

Fig. 4. Surface subsidence profiles

shaped survey lines of them were irregular. Line A and line B are in transverse direction, line C is in longitudinal direction, and line D and line E are irregular survey lines. The survey lines are shown in Fig. 3 and the partial surface subsidence profiles are shown in Fig. 4.

3.2 The First Final Fill Ratio Inverse Method

The modeling software FLAC3D is used in this paper to simulate surface subsidence of backfilling mining, and most important of all, it incorporates a lot of conceivable material behavioral models in mining engineering. Therefore considering the complex geologic and mining conditions encountered, this software has been widely used to simulate the surface subsidence.

Numerical Model Calibration. According to the borehole data, the rock structure of the numerical model from top to bottom consists of epipedon, sand layer, clay layer, sandy mudstone, medium sandstone (the roof), coal seam and clay layer (the floor). In order to efficiently inverse model parameters, uniform design method is used in this paper to design different plans with different initial parameters of rock mass (tensile strength, cohesion and elastic modulus), then the simulated subsidence values are compared with the measured subsidence values of different plans. The mined out gob should reach the critical dimension or nearly in the numerical model calibration, because the characteristic parameters of the subsidence basin, like the maximum subsidence, angle of draw and the height of caved zone, are almost calculated for the critical or supercritical subsidence, which were obtained in this paper from empirical method according to the geological and mining conditions and the working face dimension. These parameters were calculated as follows: the maximum surface subsidence is 2520mm, angle of draw is 57°, and the height of caved zone is 7~11m. After the numerical model calibration, the corrected mechanics parameters of rock mass are shown in table 1.

Table 1. The corrected mechanics parameters of rock mass

Rock mass	Thickness /m	Density /kg·m^{-3}	Bulk modulus /GPa	Shear modulus /GPa	Cohesion /MPa	Angle of internal friction /°	Tensile strength /MPa
Epipedon	280	1800	0.020	0.023	0.006	17	0.12
Sand layer	80	1870	0.045	0.030	0.057	25	0.48
Clay layer	60	2140	0.125	0.067	0.155	30	4.80
Sandy mudstone	100	2340	0.239	0.110	0.300	35	4.60
Roof	40	2540	0.362	0.196	0.859	32	6.12
Coal seam	3	1400	0.470	0.147	0.300	28	1.20
Floor	10	2140	0.440	0.281	0.590	30	4.80

Final Fill Ratio Inversion of Backfilling Materials Using the First Method. Establishing appropriate compression behavior of backfilling materials can be a challenge in the numerical simulation of backfilling mining. The material behavioral model of backfilling materials was the double-yield model according with the nonlinear characteristics. The numerical model of solid backfilling mining was developed in which the backfilling materials were described by the double-yield model and the overburden strata were simulated by Mohr-Coulomb model. Then, the final fill ratio was adjusted constantly until the simulated subsidence is most close to the surface subsidence. Finally, the numerical simulation result is shown that the average displacement of roof is 527mm and the final simulated final fill ratio is 82.4%.

3.3 The Second Final Fill Ratio Inverse Method

The second method employs the prediction equations of probability integration method at any surface point to inverse the final fill ratio, and optimizes continually parameters, like ε, tanβ, S and θ through comparing the prediction values with the measured values. The challenge in the process of this parameters inversion method is actually to solve parameter optimization problem. Besides the analytic method, the common iterative optimization methods include orthogonal experiment, gradient method, step acceleration method and so on. But when the final fill ratio is obtained by the above methods, there exist some problems, such as the divergence of iteration and the initial value problem. The cause of the problem is that probability integration method is a complex and nonlinear function. Thence the genetic algorithm is used to optimize the final fill ratio, which can solve multiple solutions problems, deal with highly nonlinear problems and has the flexibility and robustness as a global search method.

The equivalent subsidence coefficient is corrected according to the subsidence coefficient of thin seam mining with the similar geological conditions in Yanzhou Mine, and its value is 0.94.

Table 2. The range of iteration parameters

Parameters	ε	tanβ	S	θ
The minimal value	70%	1.0	-20m	80°
The maximum value	95%	2.0	20m	90°

The optimal results are obtained according to the process in fig.1 and they are shown as follows:

Table 3. The optimal results based on genetic algorithm

Parameters	ε	tanβ	S/H	θ
The optimal results	82.2%	1.25	-0.07	86°

The fitting curve with the predicted values and the measured values is shown in fig.6.

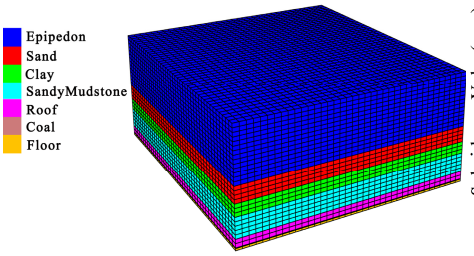

Fig. 5. Example of a numerical model used to simulate the surface subsidence

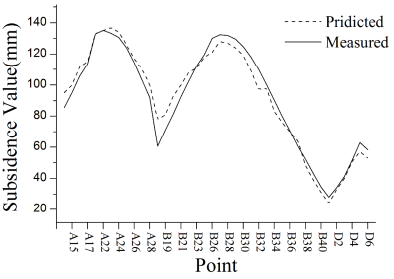

Fig. 6. The fitting curve with the predicted values and the measured values

Figure 6 shows that that fitting effect between predicted values and measured values is satisfactory. Mean square error of fitting is 5.3mm which indicates that the final fill ratio is reliable.

4 Comparison of the Two Inverse Methods

The results of final fill ratio inversion obtained by the two methods are as follows: inversion final fill ratio obtained by the first method is 82.4% and that obtained by the second method is 82.2%. Comparing the final fill ratio obtained by these two methods with the design ratio 81.7% obtained by Eq. (2) where the final fill ratio is 15%, the roof displacement is 100mm and the unfilled height is 0, the maximum error are both less than 5%. The result indicates that the two inverse methods could meet the requirements of the engineering applications.

The advantages and disadvantages, precision and application conditions between the two inverse methods were analyzed as follows:

(1) The first method is essentially the process for simulate surface deformation and overburden movements with different final fill ratio by an appropriate numerical model. On the one hand, it can simulate the actual geological conditions, especially the complex geological and mining conditions. On the other hand, it can obtain other massive amounts of data simulated data besides the final fill ratio, such as the stress-strain behavior of the rock mass, surface subsidence and overburden strata movements by solid backfilling mining. Then these mass data could provide scientific evidence to research strata control theory of solid backfilling mining.

The precision of the first method is closely related to the accuracy of mechanics parameters of rock mass. The behavior of rock strata would be changed from continuum model to discontinuous or discrete model when the gob size is large enough, which is different from the behavior of rock strata simulated by the numerical model. And rock parameters calibration is affected greatly by factitious factors and

fuzzy randomness. So, this method is low stable and time-consuming caused by the above problems.

(2) The second method based on probability integration method is higher computational efficiency and is easier to apply than the first method. Its precision is closely related to the accuracy of the selected parameters of probability integral method. Most of mining areas in china have established numerous surface observation stations for obtaining the prediction parameters of probability integration method which are suitable for conditions geological and mining conditions. Meanwhile, a large number of accurate measured data also provide reliable parameters for the second method.

However, filling mining hasn't been widely applied in china, especially solid backfilling mining which was proposed and developed in recent years. So surface subsidence measured data of filling mining are scarce and the characteristic of parameters of probability integration method in different geological and mining conditions still remain unknown. Therefore the range of applications needs further study. Meanwhile, probability integration method is a complex function with strong nonlinearity and multiple parameters. So, strong correlation between the predicted parameters may bring multi-solution problem when the gob doesn't reach the critical dimension. The above problems bring difficulties to inverse final fill ratio.

Table 4. The comparison of the two inverse methods

Evaluation Criteria	Workload	Stability	Precision	Problems	Final output information
The first method	Heavy workload and inefficiency	Instability	Medium	The numerical model calibration is difficult	Final fill ratio, overburden movement and mine pressure
The second method	Less workload and efficient	Relative stability	High	Predicted function has strong nonlinearity and multiple parameters	Final fill ratio and predicted parameters of probability integration method

(3) On the basis of the above analysis, the differences between two inverse methods were analyzed in table 4 from workload, stability, veracity, problems and final output information. Furthermore, the applicable conditions of the two methods were discussed as follows: if the geological and mining conditions are complex or the process of strata movement needs to further analyze, we can choose the first method to inverse final fill ratio; if there are correct and detailed data of probability integration method are correct and, we can choose the second method.

5 Conclusion

In the paper, two methods to inverse final fill ratio with surface subsidence data were proposed and the principle and procedure of these methods were introduced in detail. Ultimately, it was confirmed that two inverse methods were feasible by an engineering application and the superiority-inferiority and application conditions of the methods were also analyzed. The main conclusions are shown as follows: the second method is more efficient and higher reliable than the first method. If there are accurate parameters of probability integral, we can choose the second method. If the geological and mining conditions are complex or the process of strata movement is needed to further analyze, we can choose the first one. The two methods provide new feasible methods to obtain the final fill ratio

Acknowledgments. Financial support for this work, provided by the national scientific and technical supporting programs funded of China (NO.2012BAB13B03), the fundamental research funds for the central universities (2012LWB32) and the priority academic program development of Jiangsu higher education institutions (SZBF2011-6-B35), are gratefully acknowledged.

References

1. Qian, M.G., Xu, J.L., Miao, X.X.: Green Technique in Coal Mining. Journal of China University of Mining and Technology 32, 343–348 (2003)
2. Guo, G.L., Feng, W.K., Zha, J.F., Liu, Y.X., Wang, Q.: Subsidence control and farmland conservation by solid backfilling mining technology. Transactions of Nonferrous Metals Society of China 213, S665–S669 (2011)
3. Guo, G.L., Zha, J.F., Miao, X.X., Wang, Q.A., Zhang, X.N.: Similar material and numerical simulation of strata movement laws with long wall fully mechanized gangue backfilling. Procedia Earth and Plantetary Science 1, 1089–1094 (2009)
4. Zhou, Y.J., Chen, Y., Zhang, J.X., He, Q.: Control Principle and Technology of Final Compression Ratio of Backfilling Materials. Journal of Mining Safety Engineering 29, 256–352 (2012)
5. Xie, H.P., Zhou, H.W., Wang, J.A., Li, L.Z., Kwasniewski, M.A.: Application of FLAC to Predict Gound Surface Displacements due to Coal Extraction and Its Comparative Analysis. Chinese Journal of Rock Mechanics and Engineering 5, 29–33 (1999)
6. Li, P.X., Tan, Z.X., Wang, L., Deng, K.Z.: Evaluation on Stability of Building Foundation over Old-goaf with FLAC. Safety in Coal Mines 40, 11–14 (2009)
7. Wang, S.J., Jia, X.M., Han, W.F., Cui, S.M.: A Flac3d Method for Calculation of Residual Subsidence in A Mining Area Beneath An Expressway. Chinese Journal of Rock Mechanics and Engineering 24, 3545–3550 (2005)
8. Wang, J.L., Ding, C.J., Wu, S.L.: 3D Geological Modeling of Complex Landforms based on Flac3d. Journal of Geomechanics 14, 149–157 (2008)

Detection of Water Area Change Based on Remote Sensing Images

Hongxu Ma*, Shenglian Guo, and Yanlai Zhou

State Key Laboratory of Water Resources and Hydropower Engineering Science,
Wuhan University, Wuhan, PR China
mahongxu@whu.edu.cn

Abstract. A new water area detection method has been proposed by interconnecting Normalized Difference Water Index (NDWI) method, Normalized Difference Vegetation Index (NDVI) method and mathematical morphology method. Taking Poyang lake as an example, the water area change and rainfall data during the year of 2010 to 2011 are analyzed through water information recognition of remote sensing images. It is shown that the proposed method can improve estimation accuracy by an average 9.43% than the other three methods. The conjoint analysis proves the extracted water area change can highly match the actual hydrological measurement.

Keywords: water area recognition, change detection, remote sensing images.

1 Introduction

The water area detection is an important and basic task in hydrometric and hydrological computation. There are several advantages, such as promptness, speediness and high accuracy, for recognition and change detection of water area by using remote sensing data series. Many researchers have made efforts in this field. McFeeters explained the application of Normalized Difference Water Index (NDWI) into the delineation of open water features [1]. Jiang came up with a sharp-based approach to detect change of lakes using time series of remote sensing images [2]. In the research field of water recognition, Xu enhanced the NDWI method and improved the accuracy [3]. Zhai applied the morphologic method to extract water area from the remote sensing images [4]. Ma dynamically monitored the Lake group in Ruoqiang country, Xinjiang region by utilizing high-resolution remote sensing data [5]. Ma put forward a method to recognize water by combining NDWI and Normalized Difference Vegetation Index (NDVI) [6]. Cao further enhanced the sensitivity of water recognition by using NDWI [7]. However, in water recognition and water change detection, employing NDWI and NDVI separately will cause water features recognized wrongly due to the respective shortages of NDWI and NDVI methods. Moreover, few researches have focused on the match of the change detection of water area and the hydrological measurement. Therefore, it is essential to derive a method that combines NDWI, NDVI and other methods to integrate their advantages for water surface features recognition.

* Corresponding author.

F. Bian et al. (Eds.): GRMSE 2013, Part I, CCIS 398, pp. 626–636, 2013.
© Springer-Verlag Berlin Heidelberg 2013

2 Proposed Method

2.1 The Limitations of Current Methods

It has been proved that both NDVI method and NDWI method can be used to recognize water with a very high accuracy in some situations. However, neither NDWI nor NDVI method uses remote sensing images of more than two bands to calculate the index, in which some non-water features are easily misrecognized as their index values are so closed to the index values of water features.

In the test of using NDWI and NDVI methods to recognize water features, two main kinds of non-water features are found to be easily misrecognized. It is discovered that the calculated NDVI values of the building features in red band and NIR band are very near to those of the water features, which will cause building features misrecognized as water features when using NDVI method, as shown in Figure 1(a) and (b). There is apparent difference between the results of NDVI method and NDWI method. A huge number of mistaken features can be seen in Figure 1(b), while few mistaken features appear in Figure 1(c).

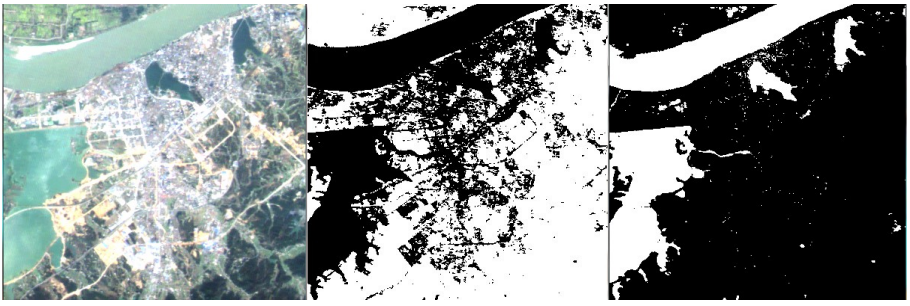

(a) (b) (c)

Fig. 1. (a) The remote sensing image of studied area with water and building features (b) NDVI Extracts land and the luildings by mistake. (c) The contrast image which use the NDWI method.

(a) Remote sensing image (b) Water extraction using NDVI (c) Water extraction using NDWI

Fig. 2. Comparison of water surface area extraction by using NDVI and NDWI methods

By analyzing the binary images and water recognition confusion matrix, it can be easily found errors are composed of two main aspects, point errors and linear errors. The point errors largely arise in NDVI method as the point features are misrecognized, in other words, the non-water features are misrecognized as water features, as shown in Figure 2(b). The linear errors mainly appear in NDWI method as the linear features are ignored, as shown in Figure 2(c).

2.2 Algorithm of Proposed Method

Although NDWI and NDVI methods can effectively recognize water features in some particular situations, while they also have some disadvantages and limitations. The NDVI method is oversensitivity of building features, while NDWI method is insensitive to small tributary streams. Some particular non-water pixels in water extraction images satisfy the conditions used to recognize water, which thus causes relatively small-scale and irregular errors.

A new water area recognition method as shown in Figure 3 is proposed to improve the qualification of water area recognition. The NDWI and NDVI methods are

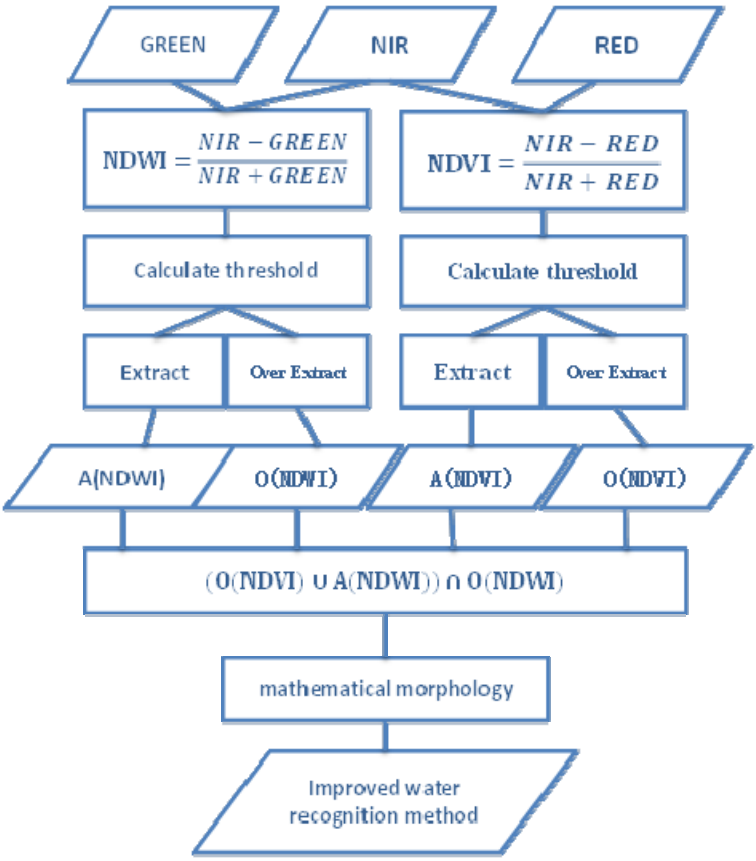

Fig. 3. The flowchart of new water area detection method

interconnected so as to increase the contrast between building and water features, as well as to raise the sensibility to small tributary streams. The mathematical morphology method is used to remove errors by calculating shape index or using corrosion expansion algorithm.

In the proposed method, NDVI and NDWI values are calculated at first. The threshold values can be defined either by automatic way or artificial interpretation way. Then the determined threshold values are used to extract water features. The extracted water features with optimum threshold values are defined as A (NDWI) and A (NDVI). The over-extracted water features with values higher than the threshold values are named as O (NDWI) and O (NDVI). Then the calculation is carried out according to Formula (1). Thus, the building features can be eliminated by Formula (1). Meanwhile, by over extracting the water features, the small tributaries steams can be enhanced.

$$(O(NDVI) \cup A(NDWI)) \cap O(NDWI) \tag{1}$$

However, after the process of the improved method, there are still some noises. The noises can be divided into two main types. One is some particular value matching with the extracting index by coincidence, which happens dispersedly. The other is the misrecognition of NDWI method and NDVI method. Both kinds of the above noises have the characteristic of small scales (Less than 20 pixels in a row). Thereby, the mathematical morphology method can be used to remove such kind of errors. The pixels are classified by the Euclidean distance between each band. The region grows when edge pixels fit the classifying threshold value. Then the number of pixels in each individual region is calculated region. The pixels are deleted if the number is less than the eliminating threshold value, as shown in Figure 4 and Figure 5.

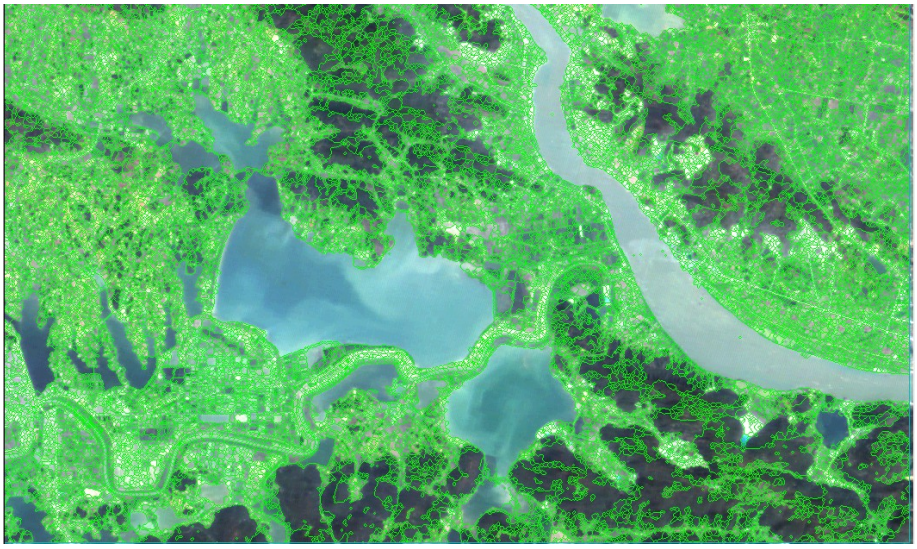

Fig. 4. The Pixels are classified based on the distance between each wave bandy

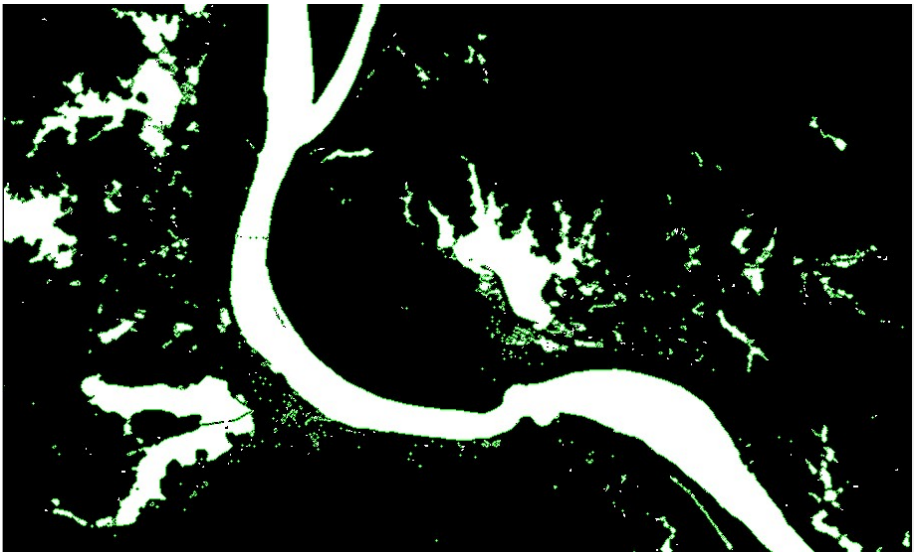

Fig. 5. Extracting pixels group of small area using the improved method

2.3 Analysis of Water Change

Considering the difference of water levels in different water parts, especially, the difference of water levels in low water level period, these polygons are created to divide the water area into several parts. By using relationship between water level and time of each part and analyzing the relationship between water level and water area, the area and the volume of the water region can be ascertained. Then, the relationship between the water level of one single hydrological station, and the water area of the whole region can be established.

The improved water recognition method can be used to extract water features, and then count up the number of pixels representing for the water. Firstly, the exact water area is calculated according to the sampling interval of the satellite. Then the extracted water areas from remote sensing images are matched with the water level of one single hydrological station for analysis and calculation. Thus it is feasible to calculate the change of water area between several time periods which are divided evenly spaced.

3 Case Study

The experimental area is Poyang lake, located in north of Jiangxi province. Poyang lake is the largest fresh lake in China. Geographic coordinates range from 115°49′E to 116° 46′E and from 28° 24′N to 29°46′N, with an area of 162225 km^2.

The experiment quotes the remote sensing images of HJ-1A from March 2010 to December 2011. The other employed data include vector diagram of Poyang Lake, the water level and the rainfall data of Xingzi hydrological station.

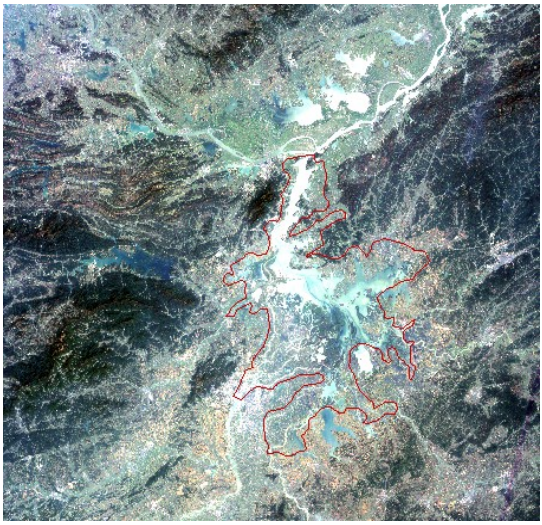

Fig. 6. The remote sensing image of the studied area

Recognition of Water Features

The remote sensing images of each period are treated to recognize water features with NDWI method, NDVI method, supervised classification method, and improved method. Then the images from recognition of water features are analyzed and compared.

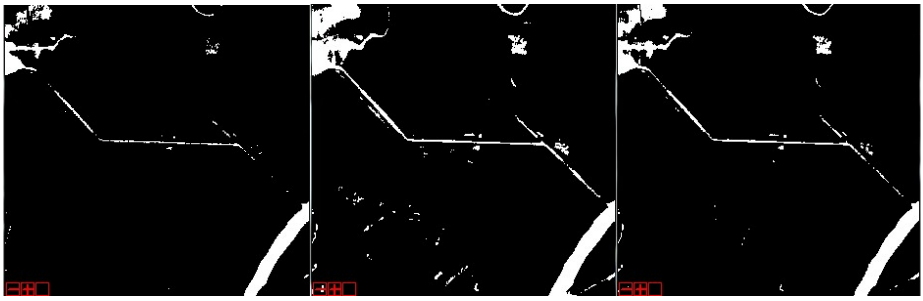

Fig. 7. NDWI method **Fig.8.** NDVI method **Fig. 9** The improved method

The extracted image of water features recognized by NDWI method is shown in Figure 7. It can be seen that the building features are obviously separated from the water features and few error pixels are misrecognized. However, the information of small tributary streams is suppressed so seriously that the tiny branches in some particular areas are ignored.

As shown in Figure 8, the small tributary streams are perfectly extracted with NDVI method. However, lots of building features and land features are misrecognized as noises, which are not shown in the image of NDWI method.

The extracted image of water features recognition by improved method is shown in Figure 9. The small tributary streams are sufficiently extracted and the errors appearing

in NDVI method are eliminated at the same time. Therefore, it is concluded that this improved method combines the advantages of NDWI method and NDVI method; meanwhile, the disadvantages of NDWI and NDVI are suppressed through interaction.

In this paper, confusion matrix is used to assess the accuracy of each method. Firstly, the false color image is made up by remote sensing images of red, green, blue band. Secondly, the water features and the non-water features are classified by artificial visual discriminant. Thirdly, 10000 pixels are taken as samples. In the test, the water pixels are set as 1, non-water pixels are set as -1, and the other pixels which will not be used to test are set as 0.

During the test, the water images with different water extraction methods are pre-processed, with the water extraction pixels evaluated as 255, the non-water extraction pixels evaluated as -1. Then the values of tested image are multiplied with the values of extraction image. The obtained image values turn out to be the confusion matrix which can be used to assess the accuracy.

Table 1. Results of confusion matrix used to assess accuracy the Methods

	water (1)	Non-water (-1)	Not be used (0)
water (255)	255	-255	0
Non-water (-1)	-1	1	0

As shown in Table 1, the value of water pixels which are extracted as water features is 255, the values of non-water pixels which are extracted as non-water features is 1, the value of water pixels which are misrecognized as non-water features is -1, and the value of non-water pixels which are misrecognized as water features is -255. It can be known that the values of pixels which are recognized properly are positive, and the values of misrecognized pixels are negative. Thus the accuracy can be assessed by counting the number of positive and calculating the percentage, as shown in Table 2.

Table 2. The Confusion Matrix of Each Methods

The account of confusion matrix		Water pixels	Non-water pixels
NDWI	Extract as water feature	5617	833
NDWI	Extract as non-water feature	1126	2724
NDVI	Extract as water feature	5406	612
NDVI	Extract as non-water feature	1337	2645
Supervised classify	Extract as water feature	5778	466
Supervised classify	Extract as non-water feature	965	2791
proposed method	Extract as water feature	6270	262
proposed method	Extract as non-water feature	473	2995

It is defined that the percentage of the pixels which are exactly extracted represents for the accuracy, as shown in Table 3. It can be seen that the improved extraction method is better than NDVI method by 15% in accuracy, better than NDWI method by 11%, better than supervised classification by 8%.

Table 3. The Accuracy Comparison between The Improved Method and The Others

Methods	proposed method	NDVI	NDWI	Supervised classify
accuracy	92.65%	80.51%	83.41%	85.69%

Analysis of Water Change Detection

In the experiment, the time-series remote sensing images are taken from the HJ-1A, with the time step length set as 3 months. The data from March 2010 to December 2011 were used to process. The data of water level were consulted s according to the day the remote sensing image was taken.

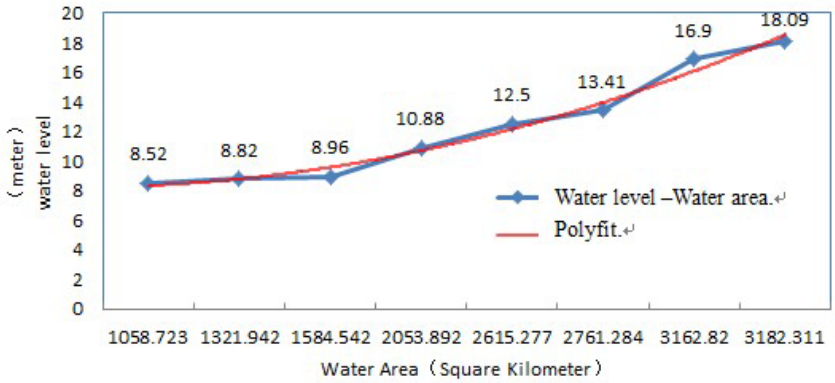

Fig. 10. The relation curve and polyfit curve of water level vs. water area by Xing-Zi Hydrologic Station.

As shown in Figure 10, the relation line between water level and the water area are plotted and fitted by quadratic polynomial.

The analysis of the relationship between the change of water area and the sum of rainfall in a period is same to the process discussed above. Because rainfall is a long influence factor for the change of water area, the time within which the remote sensing images were taken are divided into several periods. Then the sum of the rainfall in each period is calculated.

As the water area will change during this period, the change of water area during the period is considered as the value of the area of latter time node minus the area of former time node.

By analyzing the relationship between the change of water area and the rainfall in the same period, a corresponding relationship curve can be established, showing that they have strong relevancy.

Table 4. The Water Extraction Area using The Improved Method

Date	2010/3/21	2010/6/13	2010/9/22	2010/12/3
Area(km^2)	2615.277	3182.311	3162.82	1584.542
Data	2011/2/21	2011/5/27	2011/8/17	2011/12/9
Area(km^2)	1321.942	1053.892	2761.284	1058.723

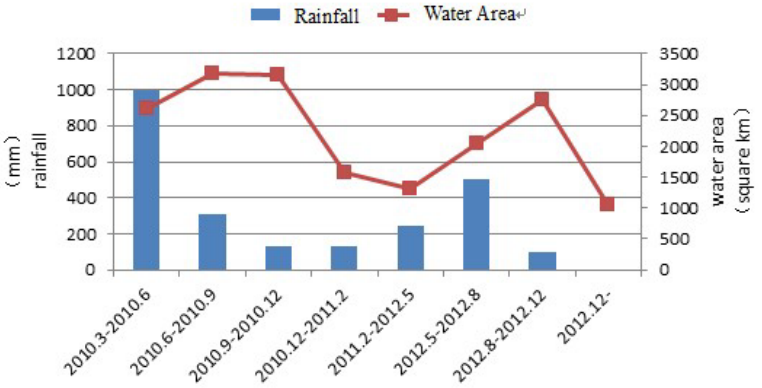

Fig. 11. The diagram of rainfall and water area

As shown in Figure 11 and Table 4, the relation curve between rainfall and water area is established first, and then the variation tendency can be analyzed. It is presented that the water area increased or remained unchanged with the rise of rainfall, and the water area decreased with the reduction of rainfall. The water area increased when rainfall reached some exact threshold value. Therefore, the rainfall can only match the change of water area in trend. For further research, evaporation should be considered.

Table 5. The Change of Water Area and The Rainfall Summed Up in Each Periods

Period	Rainfalls	Water area change
2010.3-2010.6	997.5	567.034
2010.6-2010.9	305.5	-19.491
2010.9-2010.12	131.5	-1578.28
2010.12-2011.2	127	-262.6
2011.2-2011.5	245	731.95
2011.5-2011.8	501	707.392
2011.8-2011.12	98.5	-1702.56

Taking the time when remote sensing images were taken as time node, the experiment time is divided into several periods. The change of water area and the sum of rainfall in each period are calculated, as shown in Figure 12. It suggests that great relevance exists between the change of water area and the sum of rainfall in each period.

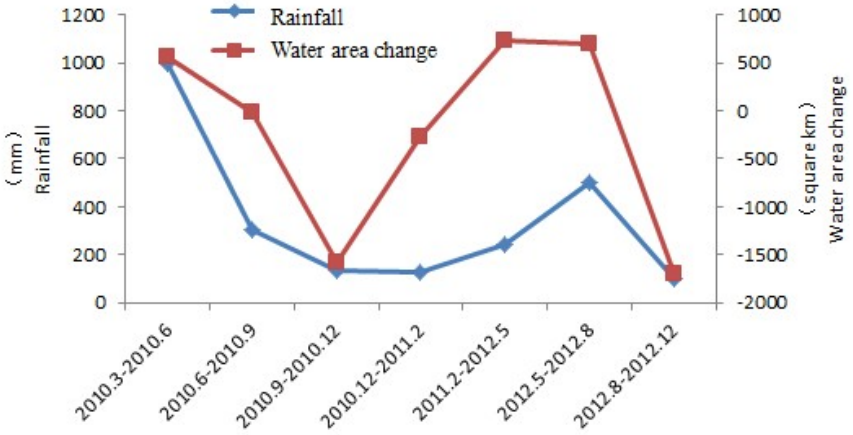

Fig. 12. The diagram of water area change and the rainfall

4 Conclusions

Interconnecting NDWI, NDVI and mathematical morphology methods, a new water area detection method is proposed and applied to Poyang lake based on the time series remote sensing images from March 2011 to December 2012. The conjoint analysis is focused on the relationship between the change of water area and the rainfall. It proves that the change of water area can highly match the hydrological measurement. The following conclusions are obtained:

(1) Comparing with NDWI, NDVI, and supervised classification methods, the proposed method is not only good at differing the building features from the water features, but also sensitive to the small tributary streams. It is shown that the proposed method is more accurate than other three methods by an average of 9.43%.

(2) Taking the Xing-Zi Hydrological Station as a sample, the research focuses on the relevancy analysis between water area and water level. The curve shows water level highly matches the change of water area, with an error limited to 5%. In the relevancy analysis between the change of water area and rainfall, it comes up with an apparent accompanying relationship which is obviously influenced by weather and seasons, such as that the amount of evaporation is high in summer and low in winter. The impact of evaporation should be considered in further relevancy analysis between water area change and hydrological data, which is an important research orientation.

References

[1] McFeeters, S.K.: The Use of Normalized Difference Water Index (NDWI) in the Delineation of Open Water Features. International Journal of Remote Sensing 17, 1425–1432 (1996)

[2] Jiang, L., Narayanan, R.M.: A Shape-based Approach to Change Detection of Lakes Using Time Series Remote Sensing Images. Transactions on Geosciences and Remote Sensing November 41, 2466–2477 (2003)
[3] Xu, H.Q.: Modification of Normalized Difference Water Index (NDWI) to Enhance Open Water Features in Remotely Sensed Imagery. International Journal of Remote Sensing 27, 3025–3033 (2006)
[4] Zhai, H.Q.: A new Algorithm for Water Area Extracting from the Remote Sensing Image Based on Morphologic Method. Science of Surveying and Mapping 31, 22–24 (2006)
[5] Ma, M.G., Song, Y., Wang, X.M.: Dynamically Monitoring the Lake Group in Ruoqiang County, Xinjiang Region. Journal of Glaciology and Geocryology 30, 189–195 (2008)
[6] Ma, M.: Change in Area of Ebinur Lake During the 1998-2005 Period. International Journal of Remote Sensing 28, 5523–5533 (2007)
[7] Cao, R.L., Li, C.J., Liu, L.Y.: Extracting Miyun Reservoir's Water Area and Monitoring Its Change Based on a Revised Normalized Different Water Index. Science of Surveying and Mapping 33, 158–160 (2008)
[8] Ke, C.Q.: A Review of Monitoring Lake Environment Change by Mass of Remote Sensing. Transactions of Oceanology and Limnology 23, 81–86 (2004)
[9] Wu, S., Zhang, Q.W.: Method and Model of Water Body Extraction Based on Remote Sensing Data of MODIS. Computer and Data Engineering 22, 1–4 (2005)
[10] He, Z.Y., Zhang, X.C., Huang, Z.C., et al.: A Water Extraction Technique Based on High-spatial Remote Sensing Images. Journal of Zhejiang University (Science Edition) 31, 701–707 (2004)
[11] Zhu, J.J., Guo, H.D., Fan, X.T., et al.: Water Detection with High-resolution SAR Image Based on Texture and Imaging Knowledge. Advances in Water Science 17, 525–530 (2006)

CFD Analysis on Ecology Function of Vertical Planting in Shenyang

Tiemao Shi[1] and Caiping Ju[2]

[1] Shenyang Jianzhu University, Vice-principal, Professor of architecture, Hunnan road.9, 110168 Shenyang, China
[2] Shenyang Jianzhu University, Master of architecture, Hunnan road.9, 110168 Shenyang, China
tiemaos@sjzu.edu.cn

Abstract. Improving the urban green rate、green coverage rate is the effective measure to the environmental. As the urban construction land being more nervous, vertical planting as a supplement of urban green space system will be more advantage. Restricted by climatic conditions in Shenyang, vertical planting has not yet been formed scale. The article is simulated the environment of a high-rise residential quarter in Shenyang by using CFD software. According to the simulation results, the author puts forward the vertical planting transformation plan, and simulating test. The result proved that vertical planting could improve the environment of the high-rise buildings obviously.

Keywords: vertical planting, ecology function, CFD, Shenyang.

1 Introduction

In the rapid development of urban economy and construction, the environmental problems have become increasingly prominent, the heat island effect, city waterlogging phenomenon began to appear, the air quality is also declining, many cities have emerged in the haze phenomenon. Plant as the only producer in ecosystem, can play to their ecological benefits, can play a role to improve the environment. The urban can be built green area is limited, so the vertical planting as the supplement of city green space system has a lot of advantages. In the Shenyang region of China, restricted by climate conditions, the ecology function of vertical planting cannot make full use in winter. How to play the ecological function of the vertical planting in growing season is worthy of discussion.

2 Urban Vertical Planting System

2.1 Urban Vertical Planting System and Urban Green Space System

The urban vertical planting system is a part of urban green space system. From the view of function, the use function, landscape function and ecological function of

F. Bian et al. (Eds.): GRMSE 2013, Part I, CCIS 398, pp. 637–645, 2013.
© Springer-Verlag Berlin Heidelberg 2013

urban vertical planting system is the same as urban green space system. From the character, the vertical planting system is a part of attached green space. [1] Unlike other part of urban green space system, the urban vertical planting system is often in the air. The characteristic of urban vertical planting is the vegetation planted on the walls, roofs or balconies. It dose not take up space on the ground.

2.2 Function of Urban Green Space System

Urban green space is an important carrier of city landscape ecological balance, it is also the main nature elements to improve the environmental quality. Through the conversion of solar energy by photosynthesis, the urban green space system realizes energy recycling. The ecology function of urban green space system is mainly the natural services. Urban green natural services reflected in the health maintenance of the natural system, the maintenance of biological diversity and human social material and spiritual service.

The function of urban green space system usually include: purify the air and water, Floods and drought hazard mitigation, degradation of waste and detoxification, promoting soil fertility and regeneration, maintenance of biological diversity, regulating local climate, ease of extreme climate and so on.

2.3 Supplement of Urban Green Space

City will be the emergence of various problems in the course of development, urban green space system will be limited. City Central District population is more and more intensive, the pollution is more serious, but the green area is the smallest, and there is no more space to expand the green. So the advantage of vertical planting will be reflected. We can use the bare walls, roof as carrier to expand the green area, enhance the city green coverage rate. Say so, in the increasingly tense today, vertical planting system is not only the supplement of urban green space system, but also exert enormous ecological benefits.

3 Actuality of Vertical Planting in Shenyang

3.1 Supplement of Urban Green Space

In order to improve the environment of Shenyang, government developed urban green planning system. The urban green coverage rate will be improved to 45% in urban center. However, the land resource is very precious. To build green area is less and less. The development of green space system can take the form of" stick in a pin wherever there's room". It is closed to be limit to find green space from the fallen building city area. They also use the way of close planting in the limited ground to increase green quantity. The result of close planting affected cultivation of scientific rationality. But with the development of the city, this way of green space construction cannot meet the need of environment. So the development of urban vertical planting

system becomes an effective method to increasing green coverage rate and improving the urban environment.

Shenyang had made some progress in the construction of vertical planting, but the coverage rate of vertical planting is only 3‰. And there is no integrity plans target of vertical planting. But some other city had a clear target on the vertical planting. For example, shanghai make the target that the coverage rate of vertical planting will reach 1% of the roofs to develop the vertical planting. Vertical planting only reaches a certain size, can better play its ecological benefit.

3.2 Vertical Planting in Shenyang Has Not Enough Benefit

The main reason to restrict the ecological benefits of vertical planting in Shenyang is its climate. Shenyang has long, cold winter. Summer there is short and cool. The annual temperature in Shenyang ranged greatly. The freezing period is very long. It is always blowing in winter. This kind of climate makes the plant species selection of vertical planting limited. Vertical planting is always in more than ten meters or more above, the level of wind there was more than ground. So tall plants is not suitable for planting on the roof. So plant selection should choose the one that was shallow roots, dwarf, slow growth, resistance to barren, drought tolerance, cold resistance. This kind of plant can overwinter safely in winter, and be easy maintenance.

Except the climate reason, government supporting is also important impetus vertical planting system development and makes it play the ecological benefits. Such like Beijing, the city that has begun to take shape of vertical planting, has launched a roof greening standards. It can guide the design and construction of vertical planting. And the government has published some policy to the construction of vertical planting. Shenyang has not yet issued related standards. The system about is to be perfect.

4 Vertical Planting Ecological Simulation Analysis of High-Rise Residential Quarter in Shenyang

4.1 Status of Outdoor Environment Simulation Analysis of High-Rise Residential Quarter

In this paper, the gambit software drew the urban model; the size of building model is the same as the actual size. In order to simplify the model for calculation, the green area of residential quarter is simplified into two pieces of equal size and actual according to the actual situation. [2] Height is set to 10m.

Shenyang belongs to cold region, and the winter there is long and cold. Plants are dormant in winter, they cannot play the ecological benefits, so the author only discusses the ecology function in summer. [3] The Outdoor temperature of ventilation is 28.2℃ in summer in Shenyang, the average wind speed is 2.9m/s. The predominating wind direction is southern in summer. The temperature of the appearance of the construction is 31.5℃ on the basis of experience value.

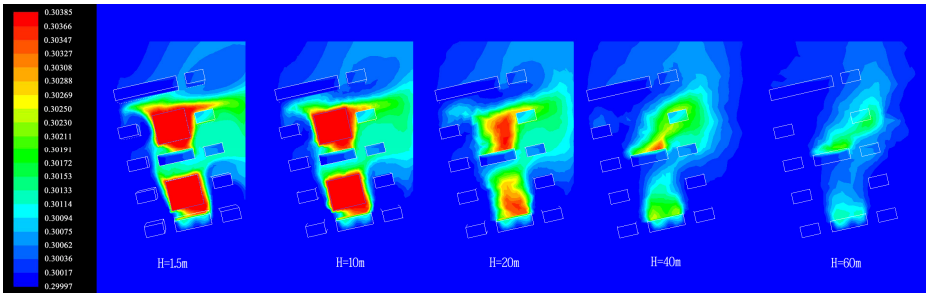

Fig. 1. Stasus of oxygen concentration distribution map

The concentration of oxygen was highest in the green space and it's surrounding. The oxygen concentration in that area ranged from 0.30327 to 0.30385. Diffusion of oxygen was to the northeast. So the oxygen environment of the buildings, which was in the northeast side of the residential quarter, was the best. The oxygen concentration in that area ranged from 0.30094 to 0.30230. On the contrary the oxygen environment of the buildings, which was in the southwest side of the residential quarter, was the worst. The oxygen concentration in that area ranged from 0.29997 to 0.30036.The oxygen that the green released has not spread to that area. With the rise of the height, the oxygen content was less and less. In the 60m heights, the phenomenon that the oxygen concentration improved obviously appeared to only one of the buildings. Can be seen from the simulation results that oxygen distribution was affected by wind and green space layout actually.

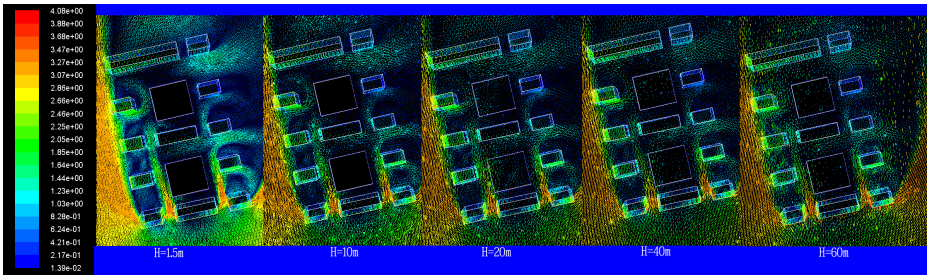

Fig. 2. Stasus of wind concentration distribution map

As can be seen from the wind speed distribution map that wind speed was large on the windward side, the wind speed was too low between the buildings that was in the east of the residential quarter and there was vortex phenomenon, the wind speed was moderate between the buildings that was in the west of the residential quarter and there was also vortex phenomenon, it was not conducive to the discharge of pollutants.

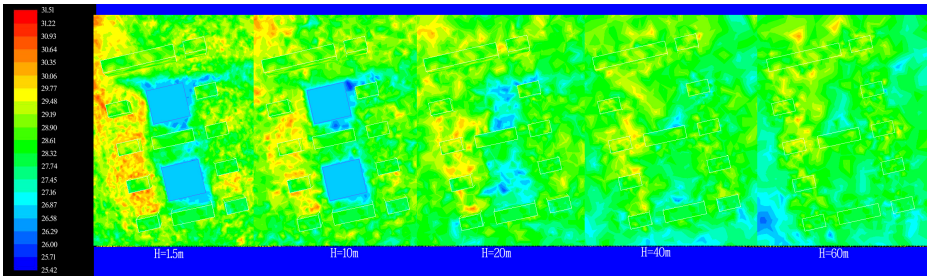

Fig. 3. Stasus of temperature concentration distribution map

As can be seen from the temperature distribution map that the cooling effect of greening was spectacular. The temperature was lowest in the green space and its surrounding. The temperature in that area ranges from 26.58℃ to 27.74℃. The temperature was high between the buildings that were in the west of the residential quarter because of the wind direction, it ranged from 30.06℃ to 31.51℃, people there cannot get comfortable condition. The temperature fell a little with the increase of height. The temperature was still high between the buildings that were in the east of the residential quarter in the 40m heights. The temperature there ranged from 29.77℃ to 30.35℃. Ground greening cannot affect the temperature in the 60m heights. The temperature ranged from 28.61℃ to 29.77℃ between the buildings that were in the northeast of the residential quarter, it was a little higher than the average temperature in the 10m heights.

From the simulation above, for a high-rise residential quarter, regulating effect of ground greening on the residential environment was not entire. The architectural environment with no surrounding dense green was not improved. [4] With the rise of the height, regulating effect of ground greening on the residential environment was more and more weak. On the roof of the building height, regulating effect of ground greening on the residential environment was zero.

4.2 Outdoor Environment Reconstruction Scheme for High-Rise Residential Quarter

According to the analysis of the results of simulation area, the author put forward a reform scheme as follow: we built vertical greening and roof greening on the buildings that were in the west of the residential quarter in order to improve the thermal environment and the oxygen environment there. In order to weaken the vortex phenomenon between the buildings that were in the northeast of the residential quarter, we built vertical greening there. We built vertical greening on the buildings that were in the north of the residential quarter to reduce the wind blowing in cold winter. Considering the environment of upper air cannot be improved by the ground greening, we built roof greening on several buildings. The specific scheme as shown below:

Fig. 4. Specific scheme of the residential quarter

4.3 The Simulation Results and Analysis on the Outdoor Environment Reconstruction

The author simulated the environment after reconstruction by using CFD software under the same boundary condition to detect the improvement of oxygen, heat and wind environment.

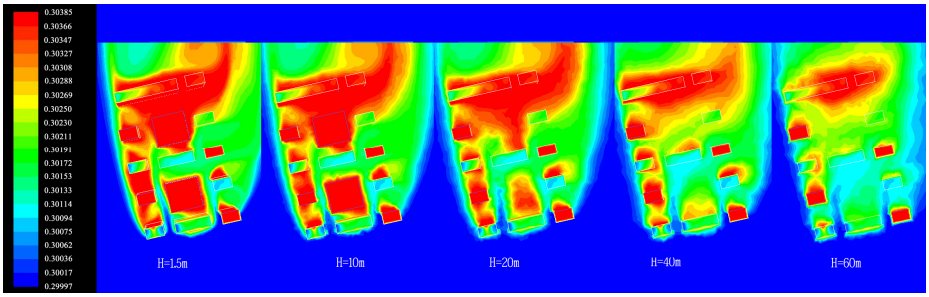

Fig. 5. Oxygen concentration distribution map

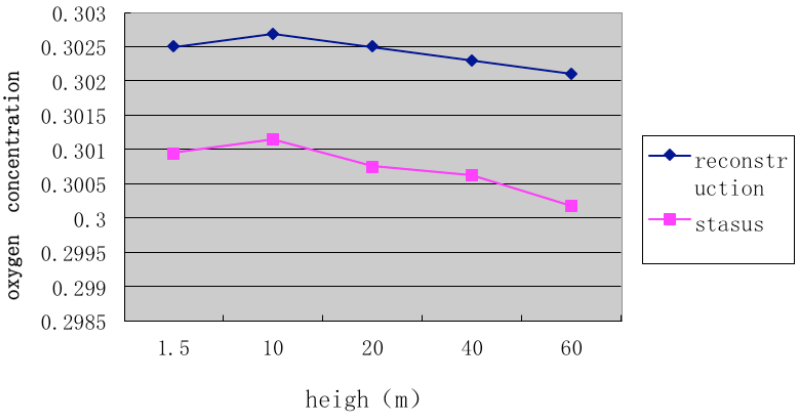

Fig. 6. Oxygen change chart

From the view of the distribution of oxygen, at the height of 1.5m, the average oxygen concentration of the residential quarter increased to 0.30250; at the height of 10m, the average oxygen concentration of the residential quarter increased to 0.30269; at the height of 20m, the average oxygen concentration of the residential quarter increased to 0.30250; at the height of 40m, the average oxygen concentration of the residential quarter increased to 0.30230; at the height of 60m, the average oxygen concentration of the residential quarter increased to 0.30211. With the rise of the height, the average oxygen concentration was still decreased, but the promotion effect of oxygen concentration is obvious overall.

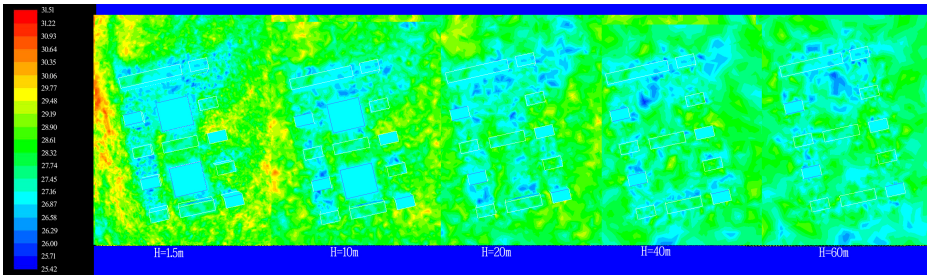

Fig. 7. Temperature concentration distribution map

From the view of the distribution of temperature, the average temperature and the highest temperature of the residential quarter were both reduced. At the height of 1.5m, the average temperature of the residential quarter was 27.16℃, the highest temperature of the residential quarter was 29.77℃. At the height of 10m, the average temperature of the residential quarter was 26.87℃, the highest temperature of the residential quarter was 29.48℃. At the height of 20m, the average temperature of the residential quarter was 26.38℃, the highest temperature of the residential quarter was 29.48℃. At the height of 40m, the average temperature of the residential quarter was

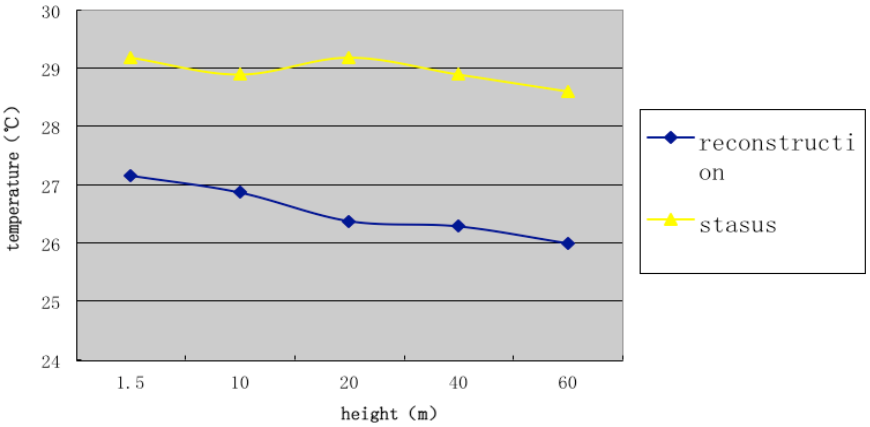

Fig. 8. Temperature change chart

26.29℃, the highest temperature of the residential quarter was 28.90℃. At the height of 60, the average temperature of the residential quarter was 26.00℃, the highest temperature of the residential quarter was 28.1℃. The average temperature of the residential quarter was reduced 2℃ in each height, it was between 26℃ and 27℃, people will feel comfortable there.

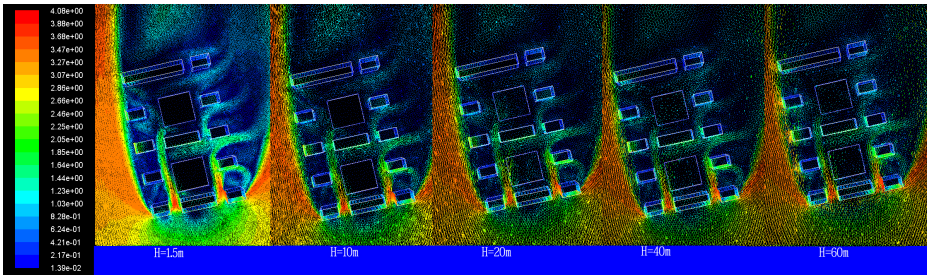

Fig. 9. Wind concentration distribution map

From the view of the distribution of wind, vertical planting constructions mainly ameliorate the wind speed. They can decrease the wind speed. The vortex phenomenon became weak after vertical planting construct. The effect that vertical planting improved the wind environment was more obvious in the high sky. From the view of the distribution of wind speed, at the height of 40m, the average wind speed of the residential quarter was reduced from 1.85m/s to 0.83m/s; at the height of 60m, the average wind speed of the residential quarter was reduced from 2.05m/s to 1.03m/s.

To sum up, the way of building vertical planting can improve the ecological environment within the district. Vertical planting as the oxygen source can enhance the oxygen content within the district. It also can reduce the temperature there. And vertical planting mainly ameliorate the wind speed in the high sky.

5 Conclusion

Vertical planting in terms of use and ecological benefit has the absolute advantage. Today, urban ecological environment worsening is becoming more and more serious, vertical planting should be vigorously promoted. The winter in Shenyang is cold and long, plants are dormant. [5] But the growing season of plants in Shenyang is eight months. The plants still bring significant ecological benefits. In urban space, the environment of mid-rise buildings was usually comfortable if there were enough ground greening around them. But the environment of high-rise buildings was usually bad even though there were enough ground greening around them. Because the rise of the height, regulating effect of ground greening on the architectural environment was more and more weak. [6] We can use vertical planting to solve this problem. The development of vertical planting was restricted by the special climate condition of Shenyang, but if we could select reasonable species of plants, construct according to the structure strictly, maintain it periodically, Vertical planting can be well established.

References

1. Kong, F., Yin, H., Nakagoshi, N., et al.: Urban green space network development for biodiversity conservation: identification based on graph theory and gravity modeling. Landscape and Urban Planning 95(1/2), 16–27 (2010)
2. Sadeghi, R., Mohebbi, A., Baniasadi, M., et al.: CFD modeling of the launder of settler of an industrial copper solvent extraction plant: A case study on Sarcheshmeh copper complex, Iran. International Journal of Mineral Processing 98(1/2), 55–65 (2011)
3. Sadeghi, R., Mohebbi, A., Sarrafi, A., et al.: CFD simulation and optimization of the settler of an industrial copper solvent extraction plant: A case study. Hydrometallurgy 106(3/4), 148–158 (2011)
4. Cao, Y., Lehto, T., Repo, T., et al.: Effects of planting orientation and density of willows on biomass production and nutrient leaching. New Forests 41(3), 361–377 (2011)
5. Jokimaki, J., Kaisanlahti-Jokimaki, M.L., Suhonen, J., et al.: Merging wildlife community ecology with animal behavioral ecology for a better urban landscape planning (Special Issue: Landscape and Urban Planing at 100). Landscape and Urban Planning 100(4), 383–385 (2011)
6. Knoll, J.E., Anderson, W.F.: Vegetative propagation of napiergrass and energycane for biomass production in the southeastern United States. Agronomy Journal 104(2), 518–522 (2012)

Publicly Verify the Integrity of the Geographical Data Using Public Watermarking Scheme

Qingzhan Zhao, Lili Sui, Chuanjian Wang, and Xiaojun Yin

College of Information Science and Technology, Shihezi University,
Shihezi, Xinjiang, P.R. China
zqz_inf@shzu.edu.cn, lily289sui@sina.cn, wangchj@gmail.com

Abstract. Geographical data is under an unsecure environment after released by data owner. The data may be modified in an illegal ways. In this paper, we propose a public watermarking scheme which can verify the integrity of geographical data. The public watermarking scheme contains two algorithms: watermark embedding algorithm and watermark detection algorithm. In the watermark embedding algorithm, a verification vector set is generated based on the dataset, and released to the public. Any end-user can verify the integrity of the dataset by watermark detection algorithm. Experiment results demonstrate that the watermarking scheme has good performance to detection several modifications efficiently, and evaluate the integrity rate at different modification amplitudes.

Keywords: geographical data, public watermarking, integrity, verification vector set.

1 Introduction

Nowadays, various geographical information systems such as digital maps, navigation and location services are widely used. Geographical data is the most important infrastructure of GIS applications. The quality of GIS applications and services is directly influenced by the quality of geographical data. The integrity is an important factor of the quality of geographical data. Adversaries launch attacks for many reasons, most importantly, profit. Unauthorized changes to such data might result in significant losses for organizations and individuals. The end-user of the data such as the provider of GIS services must verify the integrity of geographical data to ensure the data is correct and not tampered before they determine to select and use the data. Furthermore, the end-user can verify the integrity of the data as many times as necessary without having any prior knowledge of the secret parameters about the data. Recently, database research community proposed various database watermarking methods to protect the integrity of database published in web [1-5].

In this paper, we propose a public watermarking scheme, which can be used to verify the integrity of geographical data openly and repeatedly. The public watermarking scheme contains two algorithms: watermark embedding algorithm

F. Bian et al. (Eds.): GRMSE 2013, Part I, CCIS 398, pp. 646–652, 2013.
© Springer-Verlag Berlin Heidelberg 2013

and watermark detection algorithm. In the watermark embedding algorithm, a vector set is generated from the dataset, and the vector set is released to the public. In the watermark detection algorithm, any end-user can judge whether the data is complete, using the publicly released verification vector set. In the process of generating the vector set, the dataset is not modified, so the proposed scheme is distortion free.

The remainder of the paper is organized as follows. Section 2 presents in detail the proposed fragile watermarking scheme. Section 3 gives the experimental results, and Section 4 concludes the paper.

2 The Proposed Public Watermarking Scheme

2.1 The Outline of the Scheme

Geographical database instance can be defined as $D=\{R,P\}$, where R denotes reference system(WGS84), and $P=\{P_1,P_2,\ldots,P_n\}$, which denotes a set of n polygons or polylines. Polygon P_i, denoted as $P_i = \{p_{i1}, p_{i2},\ldots, p_{il-1}, p_{il} = p_{i1}\}$, $i \in \{1,2,\ldots,l\}$, consists of l vertices. Similarly, polyline P_i, denoted as $P_i = \{p_{i1}, p_{i2},\ldots, p_{il}\}$, $i \in \{1,2,\ldots,l\}$, consists of l vertices. A vertex is defined by its 2-dimension coordinates (x,y). In geographical database, one geographical object corresponds to a tuple in relational database. The number of vertices in different geographical object is not equal, so the tuple is not fixed-length.

The proposed public watermarking scheme consists of two algorithms: watermark embedding algorithm and watermark detection algorithm. In the watermarking embedding algorithm, a verification vector set is computed, in which the number of verification vector equals the number of the geographical objects in the dataset. The vector set is released to the public by the data owner. Any end-user can verify the integrity of the dataset according to the vector set and the watermarking detection algorithm. In the watermarking detection algorithm, we compute a verification vector set based on the dataset, and compare the verification vector set with the one released by the data owner, then to judge whether the dataset is complete according to the comparison results.

2.2 The Watermark Embedding Algorithm

In the watermark embedding algorithm, given the dataset $P=\{P_1,P_2,\ldots,P_n\}$, we compute a verification vector set, which contains n verification vector, and any verification vector corresponds to one geographical object. Each verification vector contains two parts: verification vector identifier and several bits. The details of the algorithm are explained as follows.

Computing Object Identifier. For each geographical object $P_i = \{p_{i1}, p_{i2},\ldots, p_{il-1}, p_{il}= p_{i1}\}$, compute its center point O_i, and its x,y coordinate is given respectively as formula (1) and (2).

$$O_{ix} = \frac{1}{l}\sum_{j=1}^{l} p_{ijx} \tag{1}$$

$$O_{iy} = \frac{1}{l}\sum_{j=1}^{l} p_{ijy} \tag{2}$$

For each geographical object P_i, its object identifier FID_i is defined as the higher part of the coordinate of P_i's center point which can distinguish all objects. Object identifier FID_i is given as formula (3).

$$FID_i = msb(O_i, h) = msb(O_{ix}, h) \,\|\, msb(O_{iy}, h) \tag{3}$$

Where $msb(\ )$ is used to get the higher part of the coordinate. And h values are determined by the dataset.

Generating a Verification Vector Set. The dataset $P=\{P_1,P_2,\ldots,P_n\}$ consists of n geographical object. Table.1 gives the algorithm which generates the verification vector set.

Table 1. Generate the verification vector set

	Algorithm 1. *generate_verification_vector_set*
	Input: $P=\{P_1, P_2,\ldots, P_n\}$, h
	Output: verification vector set $V=\{V_1,V_2,\ldots V_n\}$
1.	**for** i= 1 to n
2.	V_i.id = FID_i
3.	len = compute_length(P_i) // P_i consists of len vertices
4.	H = hash(FID_i , len)
5.	**for** j = 1 to len
6.	$FID_{ij} = msb(P_{ij},h)$
7.	s = hash($FID_i \,\|\, PID_{ij}$) mod h // PID_{ij} is the jth vertice in P_i
8.	V_i (j) = the sth bit of coordinate of P_{ij} $\otimes H[j]$
9.	**endfor**
10.	**endfor**
11.	**return** V

Given a geographical object P_i, we compute a verification vector V_i. Verification vector contains two parts: verification vector identifier and a binary string. The identifier of V_i equals the identifier of P_i. The computing step of the binary string is shown as follow.

Step1. We construct a watermark string W which length equals to the number of vertices in P_i.

Step2. Generate a verification bit for each vertex in the geographical object P_j. Given the jth vertex P_{ij} in P_i, choose the length h of higher part of its coordinates as vertex identifier, denoted as PID_{ij}. Then XOR the sth bit of vertex P_{ij}'s coordinates and $W_i[j]$, and derive the jth verification bit, denoted as $V_i(j)$. The parameter s is computed as formula (5).

$$s = hash(FID_i \,||\, PID_{ij}) \bmod h \tag{5}$$

Step3. Repeating Step2, we get the verification vector V_i, which is corresponding to geographical object P_i.

Step4. Repeating Step3, we can get the verification vector set V, which is corresponding to dataset P.

2.3 The Watermark Detection Algorithm

In the proposed watermarking scheme, the watermark detection algorithm is used to verify the integrity of the geographical data. Given the suspected dataset $P'=\{P_1,P_2,\ldots,P_m\}$ to be verified, which verification vector set is $V=\{V_1,V_2,\ldots V_n\}$. m may not be equal to n. The end-user can judge whether the dataset is modified by the watermark detection algorithm. The step of verification is described as follow. Firstly, perform the watermark embedding algorithm on the dataset P', and compute the verification vector set $V'=\{V_1,V_2,\ldots V_m\}$. Secondly, compare the two verification vector set V and V'. Traverse all the vectors in V and V', and find the identical vectors. For these identical vectors, we judge the corresponding geographical objects are not modified. For those vectors not matched, we judge the corresponding geographical objects are modified.

To evaluate the degree of the integrity of the data, integrity rate is introduced in this paper. In this paper, we focus three kinds of modifications which result in the incompleteness of dataset. The first kind of modification is geometric transformation, which contains translation, rotation, and scaling. The second kind of modification is vertex operation, such as simplification, noise addition. The third kind of modification is tuple operation, such tuple addition, and tuple deletion or cropping.

Integrity rate is defined as formula (6).

$$IR = k / l \tag{6}$$

Where the parameter k is the number of identical vectors in V and V', and the parameter l is the larger one between n and m.

3 Experiment Results

The proposed watermarking scheme is used to verify the integrity of geographical data. In other words, if the data is modified, the watermarking scheme can detection

the modification. In this section, we design some experiment to demonstrate the performance of the watermarking scheme.

The dataset is Shanghai street map, which contains 3515 polygons, 118748 vertices. The map is shown as Fig.1.

We perform the watermarking embedding algorithm on the dataset. Then do some modifications with different amplitude described in section 2.3 to the dataset. Then perform the watermark detection algorithm after each modification, and compute the integrity rate of the dataset.

(1) Geometric transformation.

Geometric transformation contains translation, scaling and rotation. For any amplitude of translation except 0, the integrity rate is 0. For any amplitude of scaling except 1, the integrity rate is 0. For any amplitude of rotation except 0 and 360 degree, the integrity rate is 0.

Fig. 1. The original dataset

(2) Vertex operation

Vertex operation contains simplification and noise addition. The experiment results are shown as Fig.2 and Fig.3. Vertex operations with small amplitudes make little changes to the dataset, so the integrity rate is close to 1. With the increase of the modification amplitude, the integrity rate decreases.

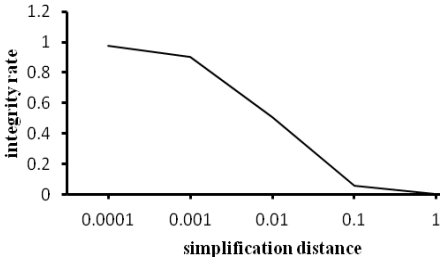

Fig. 2. Simplification operation

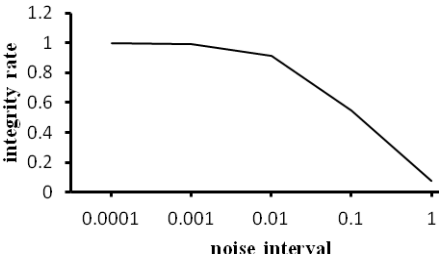

Fig. 3. Noise addition operation

(3) Tuple operation

Vertex operation contains tuple addition and tuple deletion or cropping. The experiment results are shown as Fig.4 and Fig.5. Because tuple operation doesn't modify the existing geographical objects, these objects provide buffer for tuple operation. With the increase of the proportion of tuple addition or deletion, the integrity rate decreases linearly.

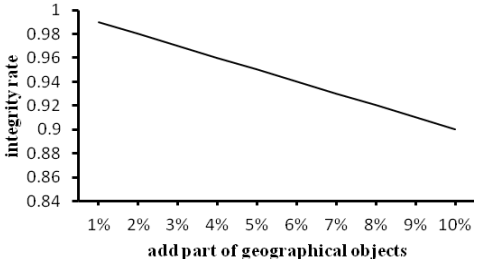

Fig. 4. Tuple addition

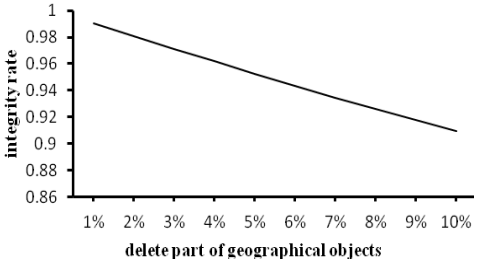

Fig. 5. Tuple deletion

4 Conclusions

Geographical data is under an unsecure environment after released by data owner. The data may be modified in an illegal ways. In this paper, a public watermarking scheme is proposed. Based on the dataset, a verification vector set is generated in

watermark embedding algorithm, and released to the public. Any end-user can verify the integrity of the dataset. Experiment results demonstrate that the watermarking scheme has good performance to detect several modifications efficiently and evaluate the integrity rate at different modification amplitudes.

Acknowledgments. This research was supported by the two research projects from China Ministry of Science and Technology (No.2012BAH27B02, 2012BAH27B03), and two research grants from National Natural Science Foundation of China (No. 31260291, 61262021) and Natural Science and Technology Innovation of Shihezi University(No. ZRKXYB-11).

References

1. Kamel, I.: A schema for protecting the integrity of databases. Computers & Security 28, 698–709 (2009)
2. Li, Y., Guo, H., Jajodia, S.: Tamper detection and localization for categorical data using fragile watermarks. In: Proceedings of the 4th ACM Workshop on Digital Rights Management (DRM 2004), pp. 73–82. ACM Press, Washington (2004)
3. Guo, H., Li, Y., Liu, A., Jajodia, S.: A Fragile watermarking scheme for detecting malicious modifications of database relations. Information Sciences 176, 1350–1378 (2006)
4. Guo, H., Li, Y., Jajodia, S.: Chaining watermarks for detecting malicious modifications to streaming data. Inf. Sci. 177(1), 281–298 (2007)
5. Niu, X., et al.: GIS Watermarking: Hiding Data in 2D Vector Maps. Studies in Computational Intelligence 58, 123–155 (2007)

An Approach for Geospatial Data Organization and Management Based on Multi-grid Model

Yongzhi Zhang[1], Qiuwen Zhang[1,*], and Yan Zhang[2]

[1] College of Hydropower and Information Engineering, Huazhong University of Science and Technology, 1037 Luoyu Road, Wuhan 430074, P.R. China
[2] Institute of Disaster Prevention, East Yanjiao, Beijing 101601, P.R. China
{zyzhust,qwzhang_hust}@163.com, shanshizhang@sohu.com

Abstract. How to establish a scientific and rational organization and management platform for geospatial data is undoubtedly the premise and basis of geo-informatics applications. Because of their special classes and characteristics, it is very difficult for traditional database to organize and manage geospatial data effectively. In order to solve the problem, the multi-grid model was introduced in this paper, including the construction principle, encoding method and the superiority of multi-grid. A new organization and management approach for geospatial data based on multi-grid model was then proposed. Combining the traditional database technology with multi-grid model, the proposed approach not only significantly achieves the integrated storage and management of different types of geospatial data, but also greatly improves the interaction and visualization of geospatial data organization and management.

Keywords: geospatial data, multi-grid, data organization and management, spatial database, level of details.

1 Introduction

With the rapid development of spatial information technology such as RS, GPS and GIS, the acquisition of massive geospatial data (in GB or TB) is becoming easier and easier, which has provided powerful foundation data support for dynamic monitoring and early warning forecast in various fields such as smart city, eco-environment and so on. However, most of these precious data were stored in different departments independently and can't be fully utilized. In order to get rid of the status, some advanced data management schemas such as ArcSDE, Geodatabase and Oracle spatial have been applied for the geospatial data [1,2]. However, faced with the explosive growth of the spatial data, the traditional management models have shown obvious shortages due to overloaded and inefficiency in data maintenance and visualization.

In recent years, with the unceasing development of distributed theory and grid technology, the centralized management models are turning to distributed model.

* Corresponding author.

F. Bian et al. (Eds.): GRMSE 2013, Part I, CCIS 398, pp. 653–661, 2013.
© Springer-Verlag Berlin Heidelberg 2013

Meanwhile, the grid technology was applied in data organization and management [3, 4].Through reviewing and summarizing the main results and problems on the field of geographic information system in nearly two decades, a significant new concept named spatial information multilevel grid (SIMG) was proposed by Li Deren[5,6]. According to the characteristics of geospatial data, the ArcSDE Geodatabase and the multi-grid model was combined to achieve a new data management approach in this paper. With the uniform data standard and spatial reference, all the data can distribute into the corresponding grid with different resolution and spatial position[7,8]. Based on SIMG, the proposed approach will improve the efficiency and visualization of the organization and management for geospatial data.

2 Classification and Characteristic of Geospatial Data

2.1 Data Classification

Compared with general data, the geospatial data has diverse types and complicated data structure. Generally, it can be divided into two parts: spatial data and non-spatial data (Fig. 1).

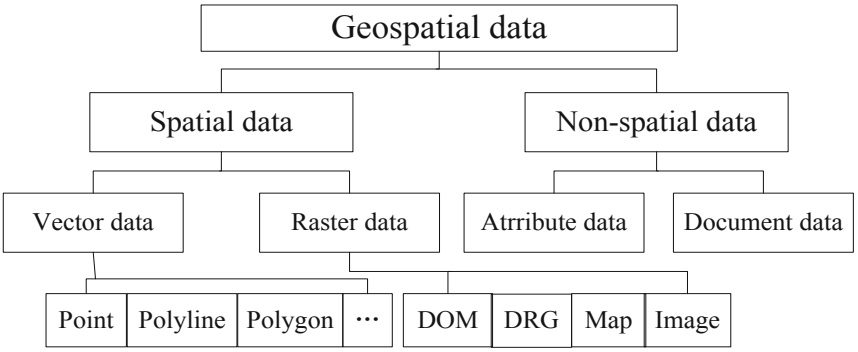

Fig. 1. The main types of geospatial data

Fig.1 presents the classification of geospatial data. It is obvious that there are both spatial data and attribute data, both structured data and unstructured data. It is quite necessary to provide corresponding method of organization and management for different types of geospatial data.

2.2 Data Characteristic

It is very necessary to analyze their characteristics of geospatial data before building the model of organization and management. There are a lot of special characteristics in geospatial data as follows:

(1) Spatial characteristic. Geospatial data are widely distributed and often associated with the position, their coordinates will be uniquely determined when the

spatial reference is specified. In addition, we also described it by the spatial relationship between each other such as intersection, contains etc.

(2) Various and massive. In addition to some structure data type such as character and text data, there are a lot of unstructured data such as vector and raster data structure, which include large-scale and high-resolution and let to huge data amounts.

(3) Multi-scale and hierarchical. Spatial and graphic data are usually expressed by way of layers, and have many different levels of detail showing multiple resolutions or scale.

(4) Attribute characteristic. Attribute is adopted to describe the spatial object in a qualitative or quantitative way. Without it, spatial data would be meaningless.

3 The Principle of Multi-grid Model

The classification and characteristics of geospatial data indicate that a scientific and rational data geospatial data model must meet the following three requirements[9,10]: First, it is required to store and manage all different types of data and provided data exchange between client and server. Second, it can achieve multi-level management for multi-resolution data. Third, partial update and efficient maintain should be operated easily in large-scale region.

3.1 Construction and Coding for Grid-Pyramid

Due to the requirements above, traditional management schemas can't satisfy the demands of their management. In order to improve the problem and meet the proposed requirements, we add a multi-grid layer above the traditional models so as to extend it. In this process, the key problem is the construction and coding for grid-pyramid. Based on quadtree structure, the way of multi-layers and multi-blocks is respectively adopted in vertical and horizontal so as to construct the grid-pyramid (Fig. 2). With the features of regularity, hierarchy and nested, it can be better to meet the organization and management requirements of geospatial data.

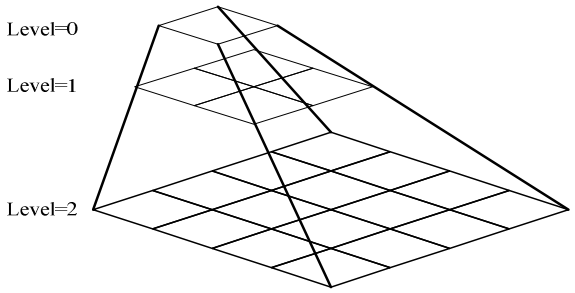

Fig. 2. The structure of grid pyramid according to quadtree segmentation

Grid coding is another important issue for the grid-pyramid. In this paper, the grid is coded separately for each level with the sequential coding method (Fig. 3). According the hierarchy relationship, from level 0 to level n (n≥0), the number of grid is increased by $4^i(0 \le i \le n)$ per level. In this model, lower-left grid is defined as the original grid and the value of grid unit is increased (from 0) by 1 from left to right and bottom to top.

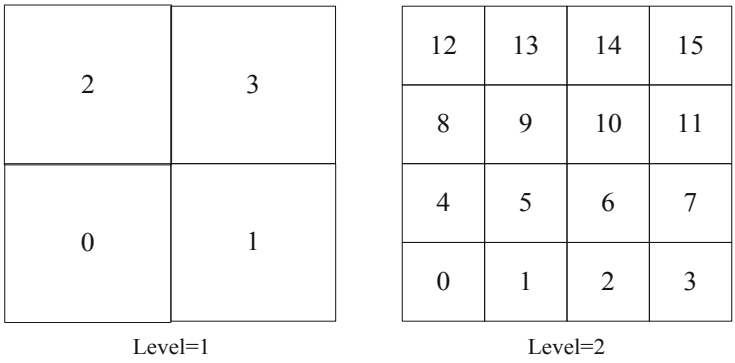

Fig. 3. The sequential coding method of multi-grid

3.2 Model Architecture

The introduction of grid-pyramid is mainly used to deal with the massive and hierarchy characteristics of geospatial data. It aims to build a Level of details (LOD) for massive database and attain greater efficiency. But the other characteristics of geospatial data should be met by inheriting the superior storage performance of traditional models[11,12]. Therefore, the proposed model is divided into three parts: the data layer, multi-grid layer and presentation layer (Fig. 4).

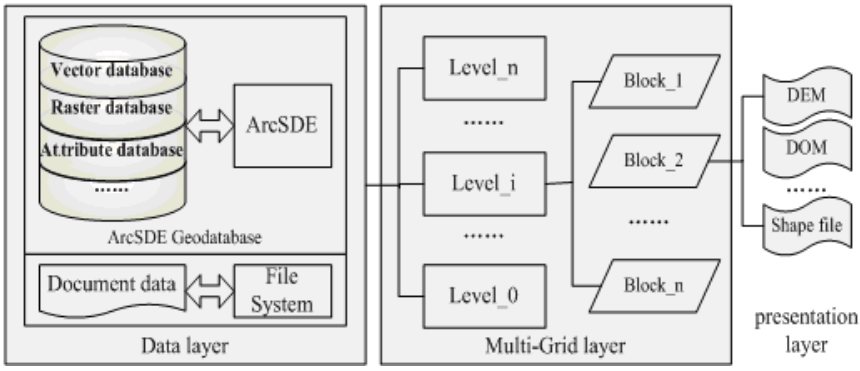

Fig. 4. The architecture of multi-grid model for geospatial data organization and management

Data layer: All types of data are collected and retrieved by corresponding grid unit and are stored in backend database or sever disk. Geodatabase model is used to store various data in RDBMS such as Oracle, SQL Sever etc. ArcSDE is adopted to extend the RDBMS. By this way, the superiorities of RDBMS and ArcSDE are inherited so as to organize and manage data better.

Multi-grid layer: This part constructs the grid-pyramid, and is the core of this article too. All the data in RDBMS is distributed into corresponding grid unit based on their resolution, coordinates or file path. In this model, grid block is considered as a unit to organize and manage geospatial data, and it will improve their efficiencies greatly.

Presentation layer: The actual data which are stored in backend database will be displayed in this layer by special clients.

4 Multi-grid Based Data Organization and Management

Grid-pyramid is used to construct the LOD of massive geospatial data, all types of data is collected by corresponding grid unit. In this model, the interaction between grids and data are realized through the following correlative tables (Fig. 5):

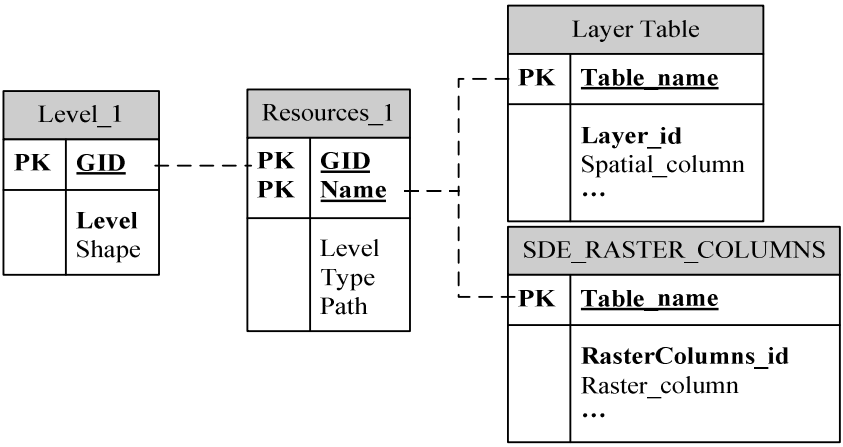

Fig. 5. The inter-relationships among different tables of multi-grid

Level table is the attribute table of each grid layer. Field "GID" is the unique code of each grid unit, which is a primary key and used to relate other tables.

Layer table and SDE_RASTER_CLOUMNS are internal tables of ArcSDE which are used to store vector data and raster data in Geodatabase respectively (see section 4.1 for more).

Resources table is one of the most important tables in the model. "GID" and "Name" are related to Level table and two ArcSDE tables respectively (Fig. 5). In addition, it plays a significant role in the description of the inter-relationships between grid units and types of data. The principle of resource distribution can be divided into

the following conditions: if a dataset is only contained by one grid, then it's described by the grid only; if a dataset crosses more grids, all the grids should record it. By the way, the null grid is nothing to do for you (Fig. 6).

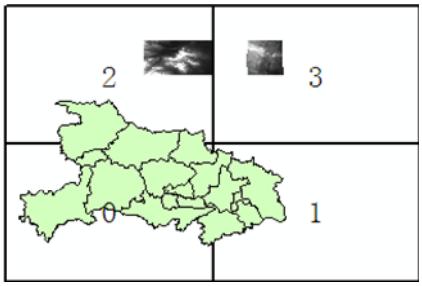

GID	Name	Level	Type	Path
0	HuBei	1	1	
1	HuBei	1	1	
2	HuBei	1	1	
2	DEM1	1	0	
2	DEM2	1	0	
3	DEM3	1	0	

Fig. 6. The principle of resource distribution for different levels of grid

From the figure above, the first level grid layer, as an example, is expounded: three raster datasets are complete contained in the 2nd and 3rd grid respectively and they are recorded with three rows in the resources table. However, the vector dataset crosses three grids, so it should have three records in the resources table.

4.1 Organization and Management of Spatial Data

Spatial data include both unstructured data and structured data. All types of these data are stored in RDBMS by ArcSDE Geodatabse based on multi-grid. The unstructured data mainly include two types: vector data and raster data.

For vector data, ArcSDE stored them in RDBMS through a series of inter-related tables. These internal tables are related with each other by corresponding field (Fig. 7). Layer Table records the number of layers in database; Business Table records the features of one of a vector layer, namely one row is one feature such as point, polyline or polygon; Feature Table stores the geometric shape itself which is a binary block; Spatial Index Table, as the name implies, describes the indexes of every element.

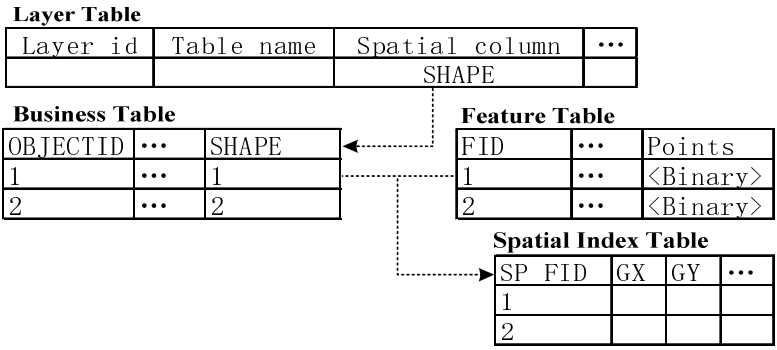

Fig. 7. Organization and management of vector dataset

Specifically, the gird blocks retrieve vector data from ArcSDE database with the inter-relation of the field "Name" of Resources Table and the filed "Table_name" of Layer Table (Fig. 5).

Similarly, ArcSDE provides a series of internal table to store the raster dataset too (Fig. 8). Once a new raster dataset is added to database, the Business Table (DEM1 in this case) subsequently increases a new row. Specifically, in order to retrieve the raster data with grid unit, the filed "Table_name" of SDE_RASTER_COLUMNS is related to the field "Name" of Resources Table (Fig. 5).

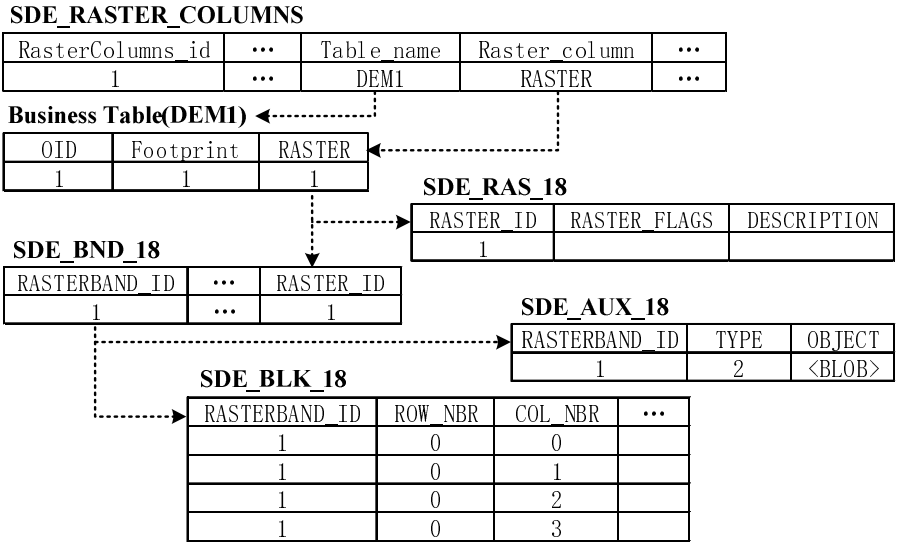

Fig. 8. Organization and management of raster dataset

SDE_RAS_<ID#>,SDE_BND_<ID#>,SDE_BLK_<ID#> and SDE_AUX_<ID#> are created when the field "RASTER" is add in SDE_RASTER_COLUMNS. These tables describe bands, blocks, metadata etc. of the raster dataset.

4.2 Organization and Management of Non-spatial Data

Non-spatial data are usually used to describe the spatial data with the quantitative or qualitative approach such as slope, gradient, humidity etc. It can be said that without non-spatial data, spatial data will lose their meanings. Therefore, the organization and management of non-spatial data are also very important.

Non-spatial data mainly indicate basic table and file documents. Due to no spatial reference, it can't collect to grid unit directly based on geographic coordinates. In order to solve this problem, the resource table is added a "path" field to relate the non-spatial data by its storage path (Fig.5). For example, if you want to get a file which is stored in the sever disk and its path is "D:\Files\slope.doc", you can fill the "path" field of resource table with "D:\Files\slope.doc". If the data is stored in database, it only needs to change the file path into database path.

5 Conclusions

The proposed multi-grid model of geospatial data organization and management is mainly composed of ArcSDE Geodatabase and grid-pyramid, which integrates the superiority of traditional RDBMS and spatial advantages of ArcSDE. Vector data, raster data and basic table are stored by RDBMS with the Geodatabase model. Meanwhile, ArcSDE, as a spatial data engine, extends the functions of RDBMS, so it can exchange data between client and sever easily and efficiently. In short, the integrality, consistency and security of existing data models are kept well and the data are unlimited in capacity.

In addition to these, it's particularly worth mentioning that multi-grid is integrated in the traditional relationship data model. In this way, the proposed approach is formed and makes it possible for massive and multi-scale geospatial data to build LOD when needed. Anyway, massive geospatial data are distributed into corresponding level of grid blocks and the grid is processed as a unit to access database, so only the affected data are returned, which reduces the visiting traffic of programs greatly and improves the organization and management efficiency for geospatial data.

Acknowledgments. The authors would like to appreciate the financial supports for this study from the National Natural Science Foundation of China (Grant#41072199, 41101258), the Natural Science Foundation for Outstanding Scholarship of Hubei Province in China (Grant#2008CDB364), the National Key Technology R&D Program of China (Grant#2008BAC36B01) and the Program for New Century Excellent Talent of Ministry of Education of China (Grant#NCET-07-0340).

References

[1] Wenbo, W., Yuanyuan, B.: DOM Database Based on ArcSDE. In: Geoinformatics 2008 and Joint Conference on GIS and Built Environment: Advanced Spatial Data Models and Analyses, vol. 7146 (2009)

[2] Lijuan, Z., Fu, Z.: Vector Geographic Data Encapsulated Based on ArcSDE. Advanced Mechanical Design 479-481, 640–643 (2012)

[3] Cheng, G., Wei, X., Jing, N.: A Grid-based Approach to Massive Geospatial Data Management. In: Proceedings of the 2012 IEEE International Conference on Computer Science and Automation Engineering (CSAE 2012), pp. 783–787 (2012)

[4] Jane, W.Q., YipWah C: Spherical Multi-Grid Technique (SMG). Encyclopedia of Tribology 3225 (2013)

[5] Deren, L., Zhifeng, X., Xinyan, Z.: Research on Grid Division and Encoding of Spatial Information Multi-Grids. Acta Geodaetica et Cartographica Sinica 35 (2006)

[6] Shao, Z., Li, D.: Spatial Information Multi-grid for Data Mining. In: Li, X., Wang, S., Dong, Z.Y. (eds.) ADMA 2005. LNCS (LNAI), vol. 3584, pp. 777–784. Springer, Heidelberg (2005)

[7] Fangfang, Z., Jun, Z.: Analysis on Multi-scale Spatial Data Index Structure. Engineering of Surveying and Mapping 17 (2008)

[8] Michael, F.G., Yang, S.: A Hierarchical Data Structure for Global Geographic Information Systems. Computer Graphics, Vision and Image Processing 54, 31–44 (1992)
[9] Zhaoting, M., Mao, P., Jinxing, H.: A Fast Walkthrough Method for Massive Terrain Based on Data Block Partition. Acta Scientiarum Naturalium Universitatis Pekinensis 40 (2004)
[10] Hongmei, Z., Yu, L.: Spatial-temporal Database Model Based on Geodatabase. In: Proceedings of SPIE - The International Society for Optical Engineering, vol. 7492 (2009)
[11] Yu, F., Zhou, H., Bin, C., Lun, W., DaFei, Y.: Architecture and Key Technologies of Grid Geographic Information System. Science in China Series E: Technological Sciences 51, 102–113 (2008)
[12] Cuiling, X.: Methods and Practice of Building Database for Digital Geological Map Based on Geodatabase. Science of Surveying and Mapping 208 (2008)

A Progressive Coding Algorithm Based on Wavelet Domain Dual Bi-tree Set for Graphics Data*

Shigao Li and Cong Zhang

School of Mathematic & Computer Science Wuhan Polytechnic University
No.68, Xuefu Road (South) Changqin Garden,
Wuhan City, Hubei Province, China
sg51@163.com

Abstract. In this paper, we present a multiscale representation and coding algorithm based on wavelet transform for graphics data. Considering the correlation of inter-band wavelet coefficients, this coding algorithm is based on a set of hierarchical bi-trees similar with the SPIHT algorithm. A graph entity in a plane composed of a sequence of points is organized as dual vectors. The first is used to represent horizontal coordinates and the second is used to represent vertical coordinates. And wavelet transform is applied to the two vectors respectively. And then the coding algorithm based on dual bi-tree sets is used to encode the wavelet coefficients. Because this algorithm encodes bit-planes one by one, the code-stream is progressive. In addition, an exact reconstructive error analysis is presented to cater the application in the field of geospatial data organization. Experiments proved the proposed algorithm is a practicable coding method of graphics data.

Keywords: Spatial Data Compression, Geospatial Data Organization, SPIHT, Wavelet.

1 Introduction

Curves are used to represent digital line graphics in many domains such as GIS. With the development of information technology, various resolution and scale versions are needed by various people. In general, a high resolution electronic map consists of plenty of curve data, and a low resolution version consists of less data. How to organize and represent the mass data for various kind applications are challenging. In the latest several decades, many researchers have sought the solution of this problem. A common solution is to store several different versions for various applications. It's obvious that the organization of data is redundant and far from efficient. In order to avoid the redundancy of the organization, digital generalization and multiscale representation were proposed by many researchers.

A famous method is Douglas-Peucker algorithm [1]. The algorithm recursively divides the line of map. Initially it is given all the points between the first and last

* This work has been supported by the National Natural Science Foundation of China (Grant No.61201452, No. 61272278).

F. Bian et al. (Eds.): GRMSE 2013, Part I, CCIS 398, pp. 662–673, 2013.
© Springer-Verlag Berlin Heidelberg 2013

point. It automatically marks the first and last point to be kept. It then finds the point that is furthest from the line segment with the first and last points as end points. If the point furthest from the line segment is greater than a pre-defined threshold, that point is kept. The algorithm recursively calls itself with the first point and the kept point and then with the kept point and the last point. Then a small threshold is set and a supplement point set is gotten by the recursive operation. Finally, the original line graphics is organized to a multiscale one.

In the last decade, due to the successful application in image compression, wavelet transform was also applied to the generalization and representation for vector graphics data. Because wavelet transform can divide the original data into a coarse one with low resolution and the detail supplement information, a multiscale organization and representation can be gotten by recursive wavelet transform in the coarse one. Although wavelet provides a multiresolution representation for signals as well as vector graphics data, how to organize and encode wavelet coefficients becomes a key problem to compress signals and vector graphics data based on wavelet.

Because various applications and situations need varied resolution data set, vector graphics data such as digital line graphics in GIS is commonly organized in the multi-level form. Compared with original data set, the high-resolution data set makes a smaller error than the low-resolution data set at the cost of big-scale data. In the fact, due to the smoothing effect of wavelet transform, the coarse version generated by the wavelet transform is distorted compared with the original. In order to solve this problem, a supplement method by adding the wavelet coefficients of detail information near those feature points is used in general [6]. Unfortunately, this supplement wavelet coefficients lead to a coding problem, because to locate these coefficients may be very costly. In [12], Li proposed a tree-based method to decrease the bit cost of addressing remained coefficients. However, it's difficult to quantify the reconstruction error. In [7], Huang encodes the individual quantized wavelet coefficients using an encoder called FFEP coding. Although low complexity and a big compression ratio were reported, it can't produce a progressive code-stream. As a matter of fact, heretofore, no efficient progressive coding method has been proposed for wavelet-based compression of graphics data.

In [2], J.M.Shapiro organizes the wavelet coefficients as quad-tree sets across different level subbands called zero-trees and gives an efficient coding method called EZW for image compression. And Amir Said followed the organization of quad-trees and proposed an improved algorithm called SPIHT [3]. Due to the high correlation of wavelet coefficients across different scales, these algorithms indicated good performance. Followed the idea, this paper introduces wavelet transform into the code of vector data and organizes wavelet coefficients in the form of dual bi-tree set (see Fig.1). Thereinto, the first set is for horizontal coordinates and the second is for vertical coordinates. Then, we present a coding algorithm based on zero-trees to encode the dual bi-tree set. This algorithm is similar with SPIHT. However, to get a progressive code-stream, it must encode two bi-tree sets side by side. Another advantage to encode two bi-tree sets simultaneously is that the reconstructive error analysis can be readily performed.

In the practice, pre-defined tolerance may be given and a simple version of the original should be produced by a generalization procedure. When it comes to compression, how to truncate a full code-stream to get the minimal size code-stream,

which can be used to reconstruct an approximation constrained by the pre-given tolerance, is a key problem. Accordingly, this paper presents an exact reconstructive error analysis corresponding to a synthesis filterbank.

The rest of this paper is organized as follows. In next section, we review multiresolution approximation by using wavelet transform. And the coding algorithm constitutes the content of the 3rd section. The 4th section is devoted into the reconstructive error analysis. In the 5th section, we test the proposed algorithm by several experiments. In the last section, we summarize this paper and give a direction of future study.

2 Multi-resolution Representation of Curve Data by Wavelet

Wavelet transform provides a multi-resolution representation for signals [4]. If $f \in L_2$, we can formulate the decomposition as follow

$$f = \sum_{V^0} c_{0,k}\phi_{0,k} + \sum_{j=0}^{N} \sum_{W^j} d_{j,k}\psi_{j,k} \,. \tag{1}$$

In (1), $c_{0,k} =< f, \phi_{0,k} >$, $d_{j,k} =< f, \psi_{j,k} >$ and V^j represents the approximation space with a complete orthogonal space spanned by Φ_j. And V^j is contained by V^{j+1}. And W^j represents the complementary space. The relation can be formulated with $\mathbf{v}^{j+1} = \mathbf{v}^j \oplus \mathbf{w}^j$. Consequently, V^0 represents the coarsest projection approximation space for signal f. In (1), we assume $f = P_{V^N} f$, that is to say, $f \in V^N$. A multiresolution representation of f can also be exhibited as (2).

$$f = P_{V^N} f = P_{V^{N-1}} f + P_{W^{N-1}} f = P_{V^0} f + \sum_{i=0}^{N} P_{W^i} f \tag{2}$$

The bi-scale equations make a bridge between wavelet and sub-band decomposition [9]. The descrete wavelet transform can be identical to sub-band decomposition and synthesis like the following

$$c_{j,m} = \sum_k c_{j-1,k} g_0(m-2k) + \sum_k d_{j-1,k} g_1(m-2k) \tag{3}$$

where g_0 and g_1 represent the filter coefficients of synthesis filterbank.

Each entity of graphics is composed of a sequence of points. Firstly, the sequence of points is organized as dual 1D-vectors (or signal). The first vector is for horizontal coordinates, denoted as f_0 and the second vector is for vertical coordinates, denoted as f_1. Then the 1D discrete wavelet transform is applied to the two 1D-vectors respectively. We can get two low-frequency subbands like a coarse version of the original and several high-frequency subbands with the detail information. This can be exhibited as Fig.1. Two levels of dyadic wavelet decomposition are applied in the two 1D-vectors respectively. As Fig.1 shows, wavelet coefficients of two 1D-vectors construct a dual-coefficient tree set. How to encode the dual-coefficient tree set will be illustrated in the next section.

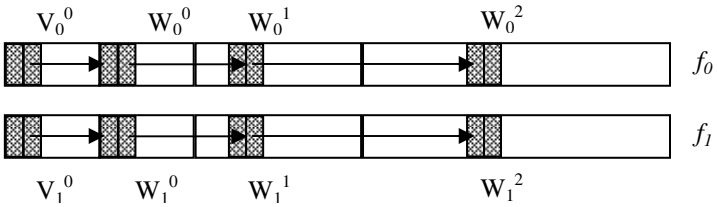

Fig. 1. Subbands of wavelet transform of horizontal and vertical coordinate vectors

3 Dual Bi-tree Set-Based Codec for Graphics Data

Like [2][3], we organize the wavelet coefficients as a bi-tree set. To illustrate the coding order of coefficient nodes clearly, the dual bi-tree set is redemonstrated as Fig.2. As shown in Fig.2, the coefficient nodes are encoded from the root to the leaves. And the bi-trees (coefficient groups) are encoded one by one. To get a progressive bit stream, those coefficients are encoded from most significant bit-plane (MSB) to least significant bit-plane (LSB).

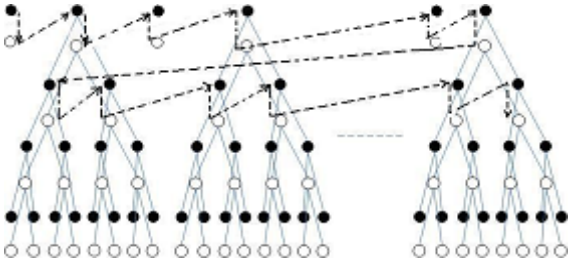

Fig. 2. Dual bi-tree set of wavelet coefficients, black dots denote the coefficients for horizontal coordinate vector and white dots denote the coefficients for vertical coordinate vector. The dash line indicates the scanning order of the top two level coefficients.

It's different from 2D case that each node except for leaves has only two children. In addition, in top level subband (low-frequency subband), odd position nodes have no children. The coding algorithm is as follow. At first, we must present several notations. $S_n(I)$ represents the nth bit value of the coefficient addressed by I. If there are several coefficients addressed by I, the logical OR operation carry out. The O(i,j) is defined as the set of coordinates of two offspring of node (i,j); D(i,j) denotes the set of coordinates of all descendants of the node (i,j); H denotes the set of tree roots which constitutes the low-frequency subband. In addition, we set L(i,j)=D(i,j)-O(i,j). The j is 0 or 1, in which 0 is for horizontal coordinate vector and 1 is for vertical coordinate vector.

Following [3], we use three class lists to store the significance. We quote them as follow. The one called LIS represents the positions of roots of those coefficients in the set D(i,j) or L(i,j), the LIP contains those individual insignificant coefficients, and the LSP includes individual significant coefficients. In the next algorithm, two coding

passes are contained when encoding a bit-plane. The first pass is called sorting pass. It's used to encode those coefficients remained insignificant after the previous pass. And the second pass is refinement pass. It's used to encode those coefficients which have become significant in the previous pass. The algorithm encodes the bit-planes of sub-band coefficients from MSB to LSB. Then a progressive code-stream is generated.

Algorithm

•.Initialization:

a) Extract the sign bit of all coefficients and set the coefficients to their absolute value, i.e. c(i,j)=abs(c(i,j));

b) Calculate and output the max bitplane number, i.e. $n = \left\lfloor \log_2(\max_{(i,j)}\{|c_{i,j}|\}) \right\rfloor$;

c) Set the LSP as an empty list, and add the coordinates (i,j)∈H to the LIP, and add also those coordinates which have descendants to LIS as type A. The order of this process is column first (see Fig.2), like this sequence (0,0), (0,1), (1,0), (1,1), (2,0), (2,1)…….

ii **.Sorting pass:**

a) For each entry i in the LIP do:
output Sn(i);
if Sn(i)=1, move i to LSP and output the sign of C_i;

b) For each entry i in the LIS do:

b1) If the entry is of type A then
Output Sn(D(i));
If Sn(D(i,j))=1 then
{
For each (k,l)∈O(i,j) do:
{
Output Sn(k,l);
If Sn(k,l)=1 then add (k,l) to the LSP and output the sign of $C_{k,l}$;
If Sn(k,l)=0 then add (k,l) to the end of the LIP ;
}
If L(i,j) ≠ ø,move(i,j)to the end of LIS as type B,and goto b2;
If L(i,j) = ø,remove (i,j) from LIS;
}

b2) If the entry is of type B then
Output Sn(L(i,j));
If Sn(L(i,j))=1 then
{
Add each (k,l)∈O(i,j) to the end of LIS as an entry of type A;
Remove (i,j) from the LIS.
}

iii. **Refinement pass:**
For each entry (i,j) in the LSP, except those included in the last sorting pass (i.e. with same n), output the n-th most significant bit of $|C_{i,j}|$;
iv. Set n=n-1, if n>=0 go to ii, else exit.

4 Reconstructive Error Analysis

In the practice, pre-defined tolerance may be given and a simple version of the original should be produced by a generalization procedure. When it comes to compression, we should guarantee the reconstruction subject to the pre-defined tolerance. It's well-know that the compressive code-stream produced by SPHIT is organized by the significance. In other words, any truncation point almost locates on the rate-distortion curve. According to the similarity between the proposed and SPHIT, we just need to truncate a full code-stream at a proper truncation point to get the final code-stream, which can be used to reconstruct an approximation constrained by the pre-given tolerance. In this section, an exact reconstructive error analysis will be presented first. And then how to get the proper truncation point will be illustrated.

It's well-known, orthogonal wavelet has the property of preserving 2-norm. This property simplifies the analysis of the mean squared error (MSE) of reconstruction signals. However, the MSE can't quantify the local error between the original signal (or curve) and the reconstruction. In fact, to quantify each sample (or point) error, the absolute difference (AD) of each sample should be calculated. Due to the time-frequency principle of wavelet transform, each wavelet coefficient is related to several successive time domain samples of signals. As a result, it's difficult to calculate the AD of each sample.

Fortunately, there exists equivalence between discrete wavelet transform and sub-band decomposition. And polyphase form of filterbank provides an efficient implementation schema and makes the reconstruction error analysis easy.

4.1 Error Analysis in Polyphase Form for Reconstruction

Fig.3 presents two level synthesis procedures in the form of polyphase. The low-resolution approximative signal $f_i(n)$ and the high-frequency coefficients $d_i(n)$ are assembled to generate the high-resolution approximative signal $f_{i+1}(n)$. And then, $f_{i+1}(n)$ *and* $d_{i+1}(n)$ are together used to generate the higher-resolution approximation

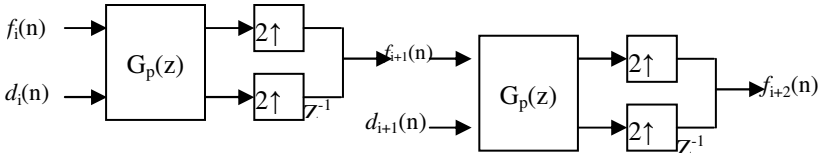

Fig. 3. Polyphase form for reconstruction

$f_{i+2}(n)$. The $G_p(z)$ represents the polyphase matrix in Z-domain corresponding to the synthesis filterbank. The synthesis procedure can be formulated as follow:

$$\hat{F}_{i+1}(z)=\begin{bmatrix}1 & z^{-1}\end{bmatrix}\begin{bmatrix}G_{0,even}(z^2) & G_{1,even}(z^2)\\ G_{0,odd}(z^2) & G_{1,odd}(z^2)\end{bmatrix}\begin{bmatrix}\hat{F}_i(z^2)\\ \hat{D}_i(z^2)\end{bmatrix} \tag{4}$$

where $\hat{F}_i(z)$ is the representation of $f_i(n)$ in Z-domain and $\hat{D}_i(z)$ is the representation of $d_i(n)$.

To descript synthesis procedure clearly, the time domain form can be presented:

$$f_{i+1}(n)=\begin{cases}\sum_{k=0}^{\left\lfloor\frac{M-1}{2}\right\rfloor} g_0(2k)*f_i(\frac{n}{2}-k)+\sum_{k=0}^{\left\lfloor\frac{N-1}{2}\right\rfloor} g_1(2k)*d_i(\frac{n}{2}-k), & n\ is\ even\\ \sum_{k=0}^{\left\lfloor\frac{M}{2}\right\rfloor-1} g_0(2k+1)*f_i(\left\lfloor\frac{n}{2}\right\rfloor-k)+\sum_{k=0}^{\left\lfloor\frac{N}{2}\right\rfloor-1} g_1(2k+1)*d_i(\left\lfloor\frac{n}{2}\right\rfloor-k), & n\ is\ odd\end{cases} \tag{5}$$

where M, N represent the length of the synthesis filters G_0 and G_1 respectively. Based on the linear relation between f_{i+1} and f_i, the AD of each sample at level i+1 can be derived:

$$e_{f_{i+1}}(n)=\tilde{f}_{i+1}(n)-f_{i+1}(n)=\begin{cases}\sum_{k=0}^{\left\lfloor\frac{M-1}{2}\right\rfloor} g_0(2k)*e_{f_i}(\frac{n}{2}-k)+\sum_{k=0}^{\left\lfloor\frac{N-1}{2}\right\rfloor} g_1(2k)*e_{d_i}(\frac{n}{2}-k), & n\ is\ even\\ \sum_{k=0}^{\left\lfloor\frac{M}{2}\right\rfloor-1} g_0(2k+1)*e_{f_i}(\left\lfloor\frac{n}{2}\right\rfloor-k)+\sum_{k=0}^{\left\lfloor\frac{N}{2}\right\rfloor-1} g_1(2k+1)*e_{d_i}(\left\lfloor\frac{n}{2}\right\rfloor-k), & n\ is\ odd\end{cases} \tag{6}$$

where e_{d_i} represents the error introduced into high-frequency sub-band coefficients, $d_i-\tilde{d}_i$. It's clear that the error of sub-band coefficients is transformed to the final reconstruction $\tilde{f}_N$ (or $\tilde{f}$). The AD of $\tilde{f}$, $|\tilde{f}(n)-f(n)|$, is what we are interested in and can be derived by the equation (6) .

Because sub-band coefficients are encoded from MSB to LSB, we can think that the same error depending on the encoded (or decoded) bit-planes is introduced into all sub-band coefficients to simplify the error analysis. As a result, the AD can be derived by

$$\varepsilon_{f_{i+1}} = \left| \tilde{f}_{i+1}(n) - f_{i+1}(n) \right|$$

$$= \begin{cases} \left| \sum_{k=0}^{\lfloor \frac{M-1}{2} \rfloor} g_0(2k) * e_{f_i}(\frac{n}{2} - k) + \sum_{k=0}^{\lfloor \frac{N-1}{2} \rfloor} g_1(2k) * e_{d_i}(\frac{n}{2} - k) \right|, & n \ even \\ \left| \sum_{k=0}^{\lfloor \frac{M}{2} \rfloor - 1} g_0(2k+1) * e_{f_i}(\lfloor \frac{n}{2} \rfloor - k) + \sum_{k=0}^{\lfloor \frac{N}{2} \rfloor - 1} g_1(2k+1) * e_{d_i}(\lfloor \frac{n}{2} \rfloor - k) \right|, & n \ odd \end{cases} \quad (7)$$

$$\leq \begin{cases} \max(\varepsilon_{f_i}) * \sum_{k=0}^{\lfloor \frac{M-1}{2} \rfloor} |g_0(2k)| + \max(\varepsilon_d) * \sum_{k=0}^{\lfloor \frac{N-1}{2} \rfloor} |g_1(2k)|, & n \ even \\ \max(\varepsilon_{f_i}) * \sum_{k=0}^{\lfloor \frac{M}{2} \rfloor - 1} |g_0(2k+1)| + \max(\varepsilon_d) * \sum_{k=0}^{\lfloor \frac{N}{2} \rfloor - 1} |g_1(2k+1)|, & n \ odd \end{cases}$$

$$\varepsilon_{f_1} = \left| \tilde{f}_1(n) - f_1(n) \right|$$

$$\leq \begin{cases} \max(\varepsilon_{f_0}) * \sum_{k=0}^{\lfloor \frac{M-1}{2} \rfloor} |g_0(2k)| + \max(\varepsilon_d) * \sum_{k=0}^{\lfloor \frac{N-1}{2} \rfloor} |g_1(2k)|, & n \ even \\ \max(\varepsilon_{f_0}) * \sum_{k=0}^{\lfloor \frac{M}{2} \rfloor - 1} |g_0(2k+1)| + \max(\varepsilon_d) * \sum_{k=0}^{\lfloor \frac{N}{2} \rfloor - 1} |g_1(2k+1)|, & n \ odd \end{cases}$$

$$= \begin{cases} \varepsilon * \left(\sum_{k=0}^{\lfloor \frac{M-1}{2} \rfloor} |g_0(2k)| + \sum_{k=0}^{\lfloor \frac{N-1}{2} \rfloor} |g_1(2k)| \right), & n \ even \\ \varepsilon * \left(\sum_{k=0}^{\lfloor \frac{M}{2} \rfloor - 1} |g_0(2k+1)| + \sum_{k=0}^{\lfloor \frac{N}{2} \rfloor - 1} |g_1(2k+1)| \right), & n \ odd \end{cases} \quad . (8)$$

As mentioned above, $\max(\varepsilon_{d_i})$ is equal to $\max(\varepsilon_{f_0})$. And we notate $\max(\varepsilon_{d_i})$ as ε, which can be derived by the extensive used mid-point reconstruction rule of sub-band coefficients [8]. Conversely, given the tolerance (or max AD), we can estimate the number of bit-planes that should be encoded.

4.2 An Example: 5/3 Wavelet

In this subsection, we will use the classic 5/3 wavelet to demonstrate the error analysis. The 5/3 wavelet has been extensively used in image compression. Especially, integer 5/3 wavelet has been adopted by JPEG2000 [10]. Because it has one vanishing moment and short filter length, it's suitable for the compression of

piecewise smooth curves. And the polyphase matrix of its synthesis filterbank is shown as follow:

$$G_{p,5/3}(z)=\begin{bmatrix} \frac{1}{2}+\frac{1}{2}z^{-1} & \frac{1}{8}-\frac{3}{4}z^{-1}+\frac{1}{8}z^{-2} \\ 1 & \frac{1}{4}+\frac{1}{4}z^{-1} \end{bmatrix}. \tag{9}$$

By the equation (5), we can give the specific synthesis formulation as

$$f_{i+1}(n)=\begin{cases} f_i(\frac{n}{2}-k)+\frac{1}{4}\left(d_i(\frac{n}{2})+d_i(\frac{n}{2}-1)\right), & n\ is\ even \\ \frac{1}{2}\left(f_i(\left\lfloor\frac{n}{2}\right\rfloor)+f_i(\left\lfloor\frac{n}{2}\right\rfloor-1)\right)+\frac{1}{8}d_i(\left\lfloor\frac{n}{2}\right\rfloor)-\frac{3}{4}d_i(\left\lfloor\frac{n}{2}\right\rfloor-1)+\frac{1}{8}d_i(\left\lfloor\frac{n}{2}\right\rfloor-2), & n\ is\ odd \end{cases}. \tag{10}$$

Accordingly, the formulation (7) and (8) can be respectively specified as follow:

$$\varepsilon_{f_i}(n)\le\begin{cases} \max(\varepsilon_{f_{i-1}}(\frac{n}{2}))+0.5\varepsilon, & n\ is\ even \\ \frac{1}{2}\left(\varepsilon_{f_{i-1}}(\left\lfloor\frac{n}{2}\right\rfloor)+\varepsilon_{f_{i-1}}(\left\lfloor\frac{n}{2}\right\rfloor-1)\right)+\varepsilon, & n\ is\ odd \end{cases} \tag{11}$$

$$\varepsilon_{f_1}(n)\le\begin{cases} 1.5\varepsilon, & n\ is\ even \\ 2\varepsilon, & n\ is\ odd \end{cases}. \tag{12}$$

We use the upper-bound of $\varepsilon_{f_{i-1}}$ and derive the AD of 6th level reconstruction ε_{f_6} as follows:

$$\varepsilon_{f_6}(n)\le\begin{cases} 5.78125\varepsilon, & n\ is\ even \\ 6.11\varepsilon, & n\ is\ odd \end{cases}. \tag{13}$$

Now the number of bit-planes for the reconstruction constrained by predefined tolerance can be estimated. At first, we notate sub-band coefficients as a fixed-point number $x_{N-1}...x_1x_0\bullet x_{-1}...x_{-i}...$, where x_{N-1} is the MSB and $x_i\in\{0,1\}$. According to the mid-point reconstruction rule, if the bit-planes from N-1 to i are decoded, we can estimate $\varepsilon\le 2^{i-1}$. If 6-time wavelet transform are used, according to (13), we can have the relations as table 1.

Table 1. The relations between tolerance and the last bit

Given tolerance	$\mathcal{E}$ (should $\leq$)	Last bit-plane (i)
0.1	0.01637	-5
0.01	0.001637	-9
0.001	0.0001637	-12
0.0001	0.00001637	-15

5 Experiments and Results

In the experiments of this section, we extract a series of polygon objects from a standard shape file which describes the world map. Each vertex contains coordinate information about longitude and latitude. And the value of longitude and latitude can correct to six decimal places. As a result, we multiple the coordinate value by one million to get integer value (often called microdegree).

Considering of the feature of polygon objects, we use 5/3 wavelet as transform kernel to decompose the vector data. To make a good compression result, we perform wavelet decomposition six times. In order to get a lossless compression for those vector data, integer 5/3 wavelet transform is used. In addition, a context-based adaptive binary arithmetic coding procedure [11] is used to get a better compression result.

Firstly, we have tested lossless compression performance of the proposed algorithm. And then lossy compression is tested.

5.1 Lossless Compression Experiments

Table 2 gives the compression performance of sketch curves of some countries (or districts). Because we need a 32-bit integer memory variant to store a coordinate value (in microdegree), it'll cost two 32-bit integers to represent a vertex. As a result, the compression ratio (CR) is calculated by the following formulation.

$$CR = \frac{8 * Number\ of\ vertexes}{Length\ of\ Codestream} \tag{14}$$

Because of the high entropy of curves, the CR may be low. From Table 2, we can see the CR ranges from 1.45 to 1.64 and the average CR is about 1.57.

Table 2. Lossless compression performance

Polygon Objects	**Number of vertexes**	**Compression ratio**
Chinese Mainland	1099	1.57
Kazakhstan	448	1.45
Greenland	2898	1.57
India	557	1.52
Australia	1874	1.64
Russia	4860	1.56
Average		**1.57**

5.2 Lossy Compression Experiments

Table 3 presents the lossy compression performance about the curves data of 'Chinese Mainland', 'India' and 'Australia'. From Table 3, we can see that although the max AD is less than the tolerance, the relation between the last bit-plane and the max AD accords with the estimation in Table 1.

Table 3. Lossy compression performance

Polygon Objects	Last bit-plane (i)	Compression ratio	Max AD
Chinese Mainland	-5	6.98	0.0608
	-9	3.66	0.0028
	-12	2.90	0.0006
	-15	2.12	0.000045
India	-5	5.81	0.0614
	-9	3.26	0.0034
	-12	2.70	0.0005
	-15	2.01	0.000051
Australia	-5	8.26	0.0501
	-9	3.84	0.0019
	-12	3.08	0.0004
	-15	2.22	0.000038

6 Conclusions and Future Work

In order to get an efficient representation for graphics data, this paper proposes a wavelet domain coding algorithm based on a set of hierarchical bi-trees similar with the SPIHT algorithm. Due to the application of zero-tree organization, this code algorithm exhibits good performance for graphics. In addition, we also present a method for the estimation of reconstruction error to bring the coding algorithm to practices.

In the future, we will further apply the proposed algorithm to the generalization and compression of spatial data such as maps and contours. Furthermore, the studies of wavelet transform on curves and better coding method will be our future work.

References

1. Douglas, D., Peucker, T.: Algorithms for the reduction of the number of points required to represent a digitized line or its caricature. The Canadian Cartographer 10(2), 112–122 (1973)

2. Shapiro, J.M.: Embedded image coding using zerotrees of wavelets coefficients. EEE Trans. Signal Processing 41, 3445–3462 (1993)
3. Said, A., Pearlman, W.A.: A New Fast and Efficient Image Codec Based on Set Partitioning in Hierarchical Trees. IEEE Transactions on Circuits and Systems for Video Technology 6, 243–250 (1996)
4. Mallat, S.: A Theory for Multiresolution Signal Decomposition: The Wavelet Representation. IEEE Transactions on Pattern Analysis and Machine Intelligence 11, 674–693 (1989)
5. Cohen, A., Dahmen, W.: Tree Approximation and Optimal Encoding. Appl. Comp. Harm. Anal. 11, 192–226 (2001)
6. Jitao, W., Qiao, W.: A Study on Automatic Cartographic Generalization Using Wavelet Analysis in GIS. Acta Geodaetica et Cartographica Sinica 29, 71–75 (2000) (in Chinese)
7. Yuefeng, H., Zhong Ershun, T.: Real-time Compression of Curve in Mobile Computing. Journal of Computer-Aided Design&Computer Graphics 21(1), 88–93 (2009)
8. David, S., Taubman, T.: JPEG 2000 Image Compression Fundamentals, Standards and Practice, pp. 377–378. Kluwer Academic Publishers (2001)
9. Mallat, S.: A Wavelet Tour of Signal Processing, pp. 220–273. Academic Press (2003)
10. ISO/IEC JTC1/SC29/WG1 N1646R JPEG, Part I Final Committee Draft Version 1.0. ISO (2000)
11. Amir Said, S.: Introduction to Arithmetic Coding - Theory and Practice. Technical report, http://www.hpl.hp.com/techreports/2004/HPL-2004-76.pdf
12. Li, S., Yang, R., Qianqing Qin, C.: Dual Bi-tree Set-Based Coding Algorithm of Vector Graphics Data. In: International Conference on Computational Intelligence and Software Engineering, pp. 1–4. IEEE Press, New York (2009)

Spatial Prediction of Soil Organic Matter Using Bayesian Maximum Entropy with Histogram Soft Data

Chutian Zhang and Yong Yang*

College of Resources and Environment, Huazhong Agricultural University,
430070 Wuhan, China
Key Laboratory of Arable Land Conservation
(Middle and Lower Reaches of Yangtse River), Ministry of Agriculture,
430070 Wuhan, China
yangyong@mail.hzau.edu.cn

Abstract. In consideration of the correlation of soil properties and the surrounding environment, this paper proposed a method to compute histogram soft data based on soil-landscape model with soil attribute values of the sample sites and environmental factors data. The soft data was used in Bayesian Maximum Entropy (BME) to predict the spatial distribution of soil organic matter in Shayang County, Hubei Province, center China. The method of prediction was compared with the ordinary Kriging (OK) by mean error (ME) and mean squared error (MSE). Results showed that the BME predictions were more accurate and successfully estimates the degree of fluctuation in the observations. In this situation the method proposed by this paper to get soft data is applicative and the BME is an effective approach to improve the spatial distribution of soil properties prediction accuracy.

Keywords: Bayesian maximum entropy, Ordinary Kriging, Histogram soft data, Soil-landscape model, Soil organic matter.

1 Introduction

The spatial distributions of soil properties(e.g., organic matter, content of heavy metals) are basis of soil quality evaluation and comprehensive assessment of regional environment. Currently, classical Geostatistics[1,2] and quantitative soil-landscape model[3,4] are two main methods for spatial prediction of soil properties.

The classical Geostatistics methods include kinds of Kriging interpolation and stochastic simulation, ordinary Kriging (OK) is a representative one and has many very successful applications in the field of earth science. But there are still some deficiencies about it, such as the lack of effective utilization of environmental information[5,6], the smoothing effect of predicted result[7,8] and difficult to meet the assumption of single point to multipoint Gauss distribution[9].

* Corresponding author.

F. Bian et al. (Eds.): GRMSE 2013, Part I, CCIS 398, pp. 674–683, 2013.
© Springer-Verlag Berlin Heidelberg 2013

In recent 20 years, quantitative soil-landscape model has become a very active research field in soil science[10-12]. This method is based on Pedogenetic theory, includes some technical means such as digital terrain analysis, GIS and computational methods such as fuzzy clustering algorithm, it makes use of kinds of landscape elements such as topography, vegetation coverage and other soil environmental information[13,14], but it ignores the spatial correlation among sampling points.

To solve the problem above, scholars have put forward various prediction methods based on sampling sites and other auxiliary information, such as co-kriging[15],geographically weighted regression(GWR)[16],regression Kriging[17], stratified Kriging[18,19] and so on. These methods can improve the prediction accuracy[20,21] but still are insufficient in comprehenseive utilization of different environmental information expressed by different data types. For example, stratified Kriging just take the environmental information as a basis of classification.

A new method called the Bayesian maximum entropy (BME), was introduced by Christakos[22,23]. It is the most well-known component of modern spatiotemporal geostatistics. BME provides a general framework for space-time interpolation, it allows the user to incoporate kinds of data under a rigorous and efficient theoretical framework. These data sources may come in various froms, like intervals of values, probability density functions(pdf) or even physical laws[24].

This study has two main objectives: (i) try to propose a method to get histogram soft data based on the theory of soil-landscape model and use this soft data in BME method and (ii) to compare the prediction performance of BME with histogram soft data and OK.

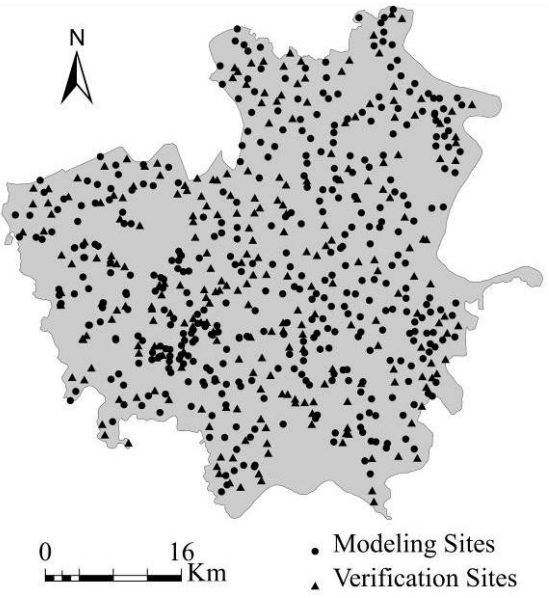

Fig. 1. Soil sampling sites in Shayang County, Hubei Province

2 Materials

2.1 Study Site Description

In this paper, we selected Shayang county as the experimental area. It is located in the central part of Hubei Province China (30°23′~ 55′ N, 111°51′~ 112°42′ E), convering an area of 2044 square kilometers. In ths area, soil samples(0~20cm) were collected at 658 locations in the autumn of 2007, of which 400 will be used for modeling and analysis, 258 for accuracy verification. In this study, we selected soil organic matter(SOM) as the investigated subject.The locations of the sampling sites are shown in Fig.1.

2.2 Environmental Data Description

In this papter, we extracted four terrain factors from 100m resolution DEM in GIS software platform to reflect the terrain characteristics of the study area, including soil texture,relative elevation (*Hr*), rate of gradient (*SOS*), river dynamic index (Ω). We compute the Normalized difference vegetation index (*NDVI*) with Landsat ETM+ image of July 25, 2011 to reflect the state of vegetation cover.

2.3 Validation and Comparison Criteria

In order to validate the prediction accuracy of this method, we set aside a number of sampling points(258) as the validation group, which were not involved in any calculation. Three quantitative criteria were computed from 258 pairs of estimated-observed values, including the Pearson correlation coefficient (r), the mean error or bias (ME) and the mean squared error (MSE). The r measures the strength of the linear relation between the estimated and the observed soil property values and should be close to one for an accurate prediction. The ME should be close to zero and the MSE should be as small as possible.

The mean error (ME) or bias is defined as:

$$ME = \frac{1}{n}\sum_{i=1}^{n}(x_i - y_i) = \bar{x} - \bar{y} \tag{1}$$

The mean squared error (MSE) is:

$$MSE = \frac{1}{n}\sum_{i=1}^{n}(x_i - y_i)^2 = (\bar{x} - \bar{y})^2 + \frac{1}{n}\sum_{i=1}^{n}\left[(x_i - \bar{x}) - (y_i - \bar{y})\right]^2 \tag{2}$$

The first term on the right is the square of the bias (*SB*):

$$SB = (\bar{x} - \bar{y})^2 = ME^2 \tag{3}$$

The second term is the mean squared difference between the estimated and the observed values with respect to the deviation from means, called the mean squared variation (*MSV*). It represents the proportion of the MSE that is not due to the bias. The lager the *MSV* is,the poorer the precision of the predicted values is, because that the means the model do not estimate the variablity of the observed values around their mean adequately. So, Eq.(3) can be rewritten as[25]:

$$MSE = SB + MSV \tag{4}$$

3 Methods

3.1 Bayesian Maximum Entropy

The BME approach provides a rigorous and flexible framework to incorporate various kinds of data into analysis. The information we may get can usually be divided into two categories[26]: General knowledge (G) and the specific knowledge (S). General knowledge is generally applicable and describes the overall characteristics of spatial random fields, including the general laws of nature, mathematical expectation , covariance and so on. Specific knowledge include hard data and soft data. Hard data is the accurate or the measurement error of which can be ignored, soft data is the one with fuzzy nature, like the Nutrient content range extracted from the soil map.

The BME analysis consist of three main stages[23,27]:

(1) Structural or prior stage: The goal of this stage is to get the maximum information entropy using G to ensure the most abundant information is considered in the estimation process.

(2) Meta-prior stage: In this stage, hard data and soft data are expressed with appropriate forms. In our study, values of the soil properties on the sampling sites are the hard data and soft data is represented with the form of histogram.The computation of the soft data will be explained in section 3.2.

(3) Integration or posterior stage: The prior pdf obtained in the prior stage and specific knowledge (S) acquired in the meta-prior stage are integrated in this stage.

3.2 Approach to Get Soft Data

The range of the predicted soil continuous property (*CP*) is represented as [C_{min}, C_{max}], then *CP* is divided by *n* categories based on precision demand in this range, and the range of the k-th group *CP* (denoted as CP_k) is

$$CP_k = [C_{min} + \frac{C_{max} - C_{min}}{n} \times (k-1), C_{min} + \frac{C_{max} - C_{min}}{n} \times k) \tag{5}$$

The mid-value of CP_k (denoted as $\overline{CP_k}$) is

$$\overline{CP_k} = C_{\min} + \frac{C_{\max} - C_{\min}}{n} \times (k - 0.5) \tag{6}$$

With the partition of *CP*, soil samples are divided into *n* groups. For each group, using properties values of soil samples and environmental factor (denoted as *EA*) data on the corresponding position, the quantitative relationship between *CP* and a single *EA* can be calculated, so we can get quantitative relationships. Specifically, the range of *EA* is divided into *NE* categories (EA_1, EA_2, …EA_{NE}), traverse each *CP* group's sampling points, recording the category of *EA* on every position of sampling points. So the quantitative relationship between *CP* with a single *EA* (denoted as $R_{(CP,EA)}$) can be represented by

$$R_{(CP,EA)} = \left((\frac{Count(1)_k}{Count_k}, EA_1), \cdots (\frac{Count(N_E)_k}{Count_k}, EA_{NE}) \right) \tag{7}$$

Where $Count(1)_k$ is the count of *k*-th group's sampling points, $Count(1)_k$ is the count of sampling points belonging to CP_k and EA_1 simultaneously.

Then we can calculate the determination coefficien between every *EA* and *CP* using values of *EA* and *CP* of sampling points, all determination coefficients will be normalized so the sum of them equals to 1.

For every grid in the study area, based on the data of *EA* and $R_{(CP,EA)}$, we can calculate *m* membership degree values based on single *EA*:

$$O_{ij,e}^{k} = R_{(CA_K,\, EA)}(EA = EA_{ij}), (1 \le k \le n) \tag{8}$$

Where EA_{ij} is the value of *EA* in position (*i,j*). In the calculation of similarity, considering the different correlation between *EA* and *CP*, the determination coefficients are introduced as weight. So the similarity between soil porperty in position (*i, j*) and CP_k can be represented as

$$S_{ij}^{k} = \sum_{e=1}^{m} (O_{ij,v}^{k} \times R_v^2) \tag{9}$$

Using this method, we can get similarity list $\left(S_{ij}^{1}, S_{ij}^{2}, \ldots\ldots S_{ij}^{n}\right)$ in poisiton (*i,j*). After normalized, we can use the formula below to express the fuzzy distribution of this soil property in grid (*i, j*) based on environmental factors, which will be used as the source of soft data, Fig.2 illstrates a sample of probability distribution of soft data in position (*i,j*):

$$f_{soft}(z_{ij}) = \left((CP_1, S_{ij}^{1}), (CP_2, S_{ij}^{2}), \ldots\ldots (CP_n, S_{ij}^{n}) \right) \tag{10}$$

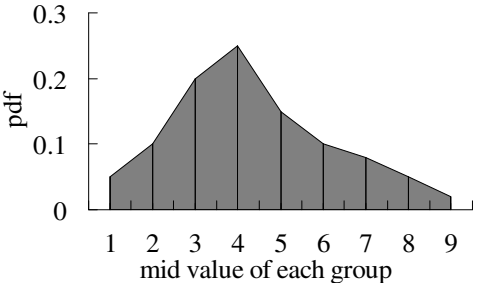

Fig. 2. A sample of probability distribution of soft data

4 Results and Discussion

4.1 Descriptive Statistics

Table 1 gives the summary statistics of SOM in sampling sites.The CV is 23.048% and 21.694% for modeling data and verification data respectively, suggesting the presence of moderate variability.The value of SOM have a large range shown by the maximum and the minimum, and the skewness and kurtosis are close to 0, which means the data is close to the standard normal distribution.

Table 1. Summary statistics for the SOM(g kg-1) of the sampling sites

Group	*N*	Maximum	Minimum	Mean	SD	CV(%)	Skewness	Kurtosis
Modeling	400	34.56	7.51	22.981	5.297	23.048	-0.604	-0.247
Verification	255	34.66	7.78	23.562	5.111	21.694	-0.723	0.174

Notation: *N* is the number of sampling sites, SD is the standard deviation and CV is the coefficient of variation.

4.2 Correlation Analysis

We analyzed the correlation betweent environmental factors and SOM on the modeling sites in SPSS 19.0, the result showed *texture* and *SOS* were significantly positive related with SOM, while *Hr* and *NDVI* were significantly negative related with SOM, which means the content of SOM is higher in region with higher altitude, more complex terrain and higher vegetation coverage.Correlation coefficient of *texture* is 0.321, ranked first among the five environmental factors, this result is coincident with previous studies[28,29]. So we finally selected *texture*, *SOS*, *Hr* and *NDVI* as the auxiliary information. The result of correlation analysis is shown in Table 2.

Table 2. Result of correlation analysis

texture	*Hr*	*SOS*	*NDVI*	*Ω*
0.321**	-0.268**	0.194**	-0.140**	0.093

Notation: ** means the environmental factor is significantly related with SOM at the 0.01 level (bilateral)

4.3 Comparison of Results

The cross-validation criteria r, ME and MSE are given in Table 3 and Fig.3 gives the distributions of the errors.The OK has a larger MSE than that of the BME methods. Fig.3 shows that OK has a more broad error distribution, more of the errors are on the negative side of the curve, which implies that this method is likely to produce larger errors than the BME. The errors for BME have a higher mode and a narrower distribution compared with OK, this is confirmed by its having a smaller MSE values.

Though the ME of this two approaches are both not significantly different from zero, OK results has a smaller bias (ME) compared to the BME approaches, thus giving less biased estimates than BME. The estimates are strongly correlated with the observations for the two techniques and correlation of BME is better than HK.

Table 3. Quantitative criteria for the comparison of the two approaches

Criterion	OK	BME
r	0.615	0.649
ME (dS m^{-1})	-0.118	-0.452
MSE (dS m^{-1})^2	16.509	15.782

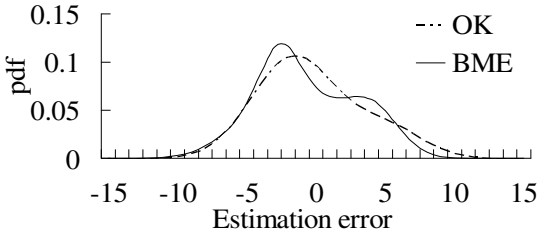

Fig. 3. Distributions of estimation error

The components of MSE can provide more information about the difference between the estimated and the observed values. They are given in absolute values Table 4 and shown as proportions in Fig.4 The OK has a larger MSE than BME, which suggests that BME provides more accurate predictions. In addition, the contribution of the bias to the MSE is almost zero(0.084%) for OK and much smaller than BME(1.292%). This confirms that OK estimates are more unbiased.

The LCS contributs the most to the MSE of the two interpolation methods for both time periods. In particular, it contributs the most to the MSE of the OK estimates with 88.23%, whereas its contribution to BME is 58.98%. This suggests that OK fails to estimate the degree of fluctuation in the observed SOM content even if its SB is smaller than that of BME. However, the SDSD contributed more to the MSE of BME

(39.72%) than to that of OK (11.69%), which indicates that BME failed to estimate the magnitude of fluctuation in the measured SOM content. The MSE of BME is smaller, indicating that it performs better than the OK techniques.

Table 4. The components of MSE as absolute values

Criterion	OK	BME
SB	0.014	0.204
SDSD	1.929	6.270
LCS	14.566	9.309
MSE	16.509	15.782

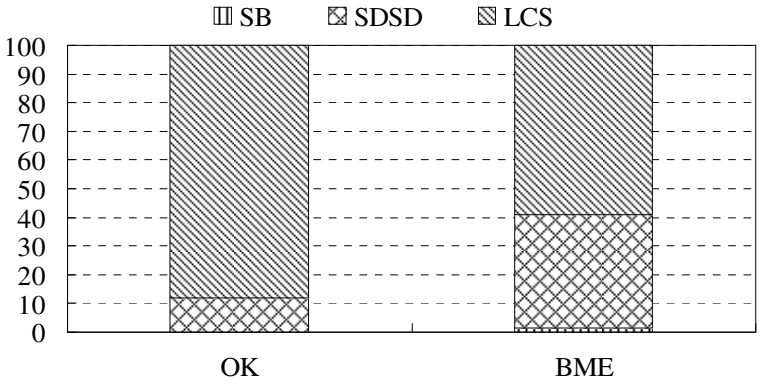

Fig. 4. Contribution of the components of MSE to its total

5 Conclusions

In this paper, we compare the performance of two prediction techniques: BME which can incorporates histogram soft data and the ordinary Kriging(OK) using only hard data in the sampling sites. They were evaluated by crossvalidation with three criteria: Pearson correlation coefficient (r), the mean error or bias (ME) and the mean squared error (MSE). Based on the r and MSE, we can conclude that the predictions from BME are more accurate than those from the OK. The results showed that BME improved considerably the accuracy of the predictions compared to OK by taking into account histogram soft data. By dividing the MSE into three components, we found that BME gave more biased estimates (larger SB) and failed to reproduce the true magnitude of fluctuation among the observations but its LCS is remarkably smaller than that of OK, so it successfully estimates the degree of fluctuation in the observations. In contrast, by integrating soft data into the prediction process, BME produce more accurate predictions

With the development of 3S techniques and other relevant technology, more precise and high quality auxiliary data like DEM and remote sensing image becomes cheaper and readily available. When used efficiently, these kind of information can effectively make up the thorny problem of insufficient measurements or poor accuracy of the soil property sampling. This work proved that BME could incorporate and process various kinds of data as soft data rigorously, leading to more accurate predictions.

Acknowledgments. This study was supported by the National Natural Science Foundation of China under Grant No. 41101193 and the New Teacher Fund for Doctor Station, the Ministry of Education under Grant No. 20100146120018. We also thank the reviewers and the editor for their constructive suggestions.

References

1. Heuvelink, G.B.M., Bierkens, M.F.P.: Combining soil maps with interpolations from point observations to predict quantitative soil properties. Geoderma 55(1-2), 1–15 (1992)
2. Utset, A., López, T., Díaz, M.N.: A comparison of soil maps, kriging and a combined method for spatially predicting bulk density and field capacity of ferralsols in the Havana–Matanzas Plain. Geoderma 96(3), 199–213 (2000)
3. O'Geen, A., Pettygrove, S., Southard, R., Minoshima, H., Verdegaal, P.: Soil-landscape model helps predict potassium supply in vineyards. California Agriculture 62(4), 195–201 (2008)
4. Sun, X.L., Zhao, Y.G., Qin, C.Z., Li, D.C., Zhao, L., Zhang, G.L.: Effects of dem resolution on multi-factor linear soil-landscape models and their application in predictive soil mapping. Acta Pedologica Sinica 05, 971–977 (2008) (in Chinese)
5. Orton, T., Lark, R.: Accounting for the uncertainty in the local mean in spatial prediction by Bayesian Maximum Entropy. Stochastic Environmental Research and Risk Assessment 21(6), 773–784 (2007)
6. Lee, S.-J., Balling, R., Gober, P.: Bayesian Maximum Entropy Mapping and the Soft Data Problem in Urban Climate Research. Annals of the Association of American Geographers 98(2), 309–322 (2008)
7. Goovaerts, P.: Geostatistics for natural resources evaluation. Oxford university Press, New York (1997)
8. Wang, G., Gertner, G., Parysow, P., Anderson, A.: Spatial prediction and uncertainty analysis of topographic factors for the revised universal soil loss equation (RUSLE). Journal of Soil and Water Conservation 55(3), 374–384 (2000)
9. Phillips, S.J., Anderson, R.P., Schapire, R.E.: Maximum entropy modeling of species geographic distributions. Ecological Modelling 190(3-4), 231–259 (2006)
10. Gessler, P.E., Moore, I.D., McKenzie, N.J., Ryan, P.J.: Soil-landscape modelling and spatial prediction of soil attributes. International Journal of Geographical Information Systems 9(4), 421–432 (1995)
11. McKenzie, N.J., Ryan, P.J.: Spatial prediction of soil properties using environmental correlation. Geoderma 89(1-2), 67–94 (1999)
12. Gessler, P., Chadwick, O., Chamran, F., Althous, L., Holmes, K.: Modeling soil-landscape and ecosystem properties using terrain attributes. Soil Science Society of American Journal 64, 2045–2056 (2000)
13. McBratney, A., Mendonca, M., Minasny, B.: On digital soil mapping. Geoderma 117, 3–52 (2003)
14. Zhang, H., Zhang, G.L., Gong, Z.T.: The progress of quantitative soil-landscape modeling-A review. Chinese Journal of Soil Science 3, 339–346 (2004) (in Chinese)
15. Chaplot, V., Walter, C., Curmi, P.: Improving soil hydromorphy prediction according to DEM resolution and available pedological data. Geoderma 97(3-4), 405–422 (2000)
16. Guo, L., Zhang, H.T., Chen, J.Y., Li, R.J., Qin, C.: Comparison between Co-Kriging and Geographically Weighted Regression Model in Spatial Prediction of Soil Attributes. Acta Pedologica Sinica 5, 1037–1042 (2012) (in Chinese)

17. Hengl, T., Heuvelink, G.B.M., Stein, A.: A generic framework for spatial prediction of soil variables based on regression-kriging. Geoderma 120(1-2), 75–93 (2004) (in Chinese)
18. Van Boucneau, M., Thas, H.: Integrating properties of soil map delineations into ordinary kriging. European Journal of Soil Science 49(2), 213–229 (1998)
19. Liu, T.-L., Juang, K.-W., Lee, D.-Y.: Interpolating Soil Properties Using Kriging Combined with Categorical Information of Soil Maps. Soil Sci. Soc. Am. J. 70(4), 1200–1209 (2006)
20. Zhu, Q., Lin, H.S.: Comparing Ordinary Kriging and Regression Kriging for Soil Properties in Contrasting Landscapes. Pedosphere 20(5), 594–606 (2010)
21. Li, Y.: Can the spatial prediction of soil organic matter contents at various sampling scales be improved by using regression kriging with auxiliary information? Geoderma 159(1-2), 63–75 (2010)
22. Christakos, G.: A Bayesian/maximum-entropy view to the spatial estimation problem. Mathematical Geology 22(7), 763–777 (1990)
23. Christakos, G.: Modern Spatiotemporal Geostatistics. Oxford University Press, New York (2000)
24. Bogaert, P., D'Or, D.: Estimating Soil Properties from Thematic Soil Maps. Soil Sci. Soc. Am. J. 66(5), 1492–1500 (2002)
25. Douaik, A., Van, M.M., Tóth, T.: Soil salinity mapping using spatio-temporal kriging and Bayesian maximum entropy with interval soft data. Geoderma 128(3-4), 234–248 (2005)
26. Zhang, B., Li, W.D., Yang, Y., et al.: The Bayesian maximum entropy geostatistical approach and its application in soil and environmental sciences. Acta Pedologica Sinica 48(4), 831–839 (2011) (in Chinese)
27. Christakos, G.: Spatiotemporal information systems in soil and environmental sciences. Geoderma 85(2-3), 141–179 (1998)
28. Galantini, J.A., Senesi, N., Brunetti, G., Rosell, R.: Influence of texture on organic matter distribution and quality and nitrogen and sulphur status in semiarid Pampean grassland soils of Argentina. Geoderma 123(1-2), 143–152 (2004)
29. Kong, X., Dao, T.H., Qin, J., Qin, H., Li, C., Zhang, F.: Effects of soil texture and land use interactions on organic carbon in soils in North China cities' urban fringe. Geoderma 154(1-2), 86–92 (2009)

Remote Sensing Image Mosaic by Incorporating Segmentation and the Shortest Path

Yindi Zhao, Tianqing Han, Shuna Feng, and Congcong Miao

School of Environment Science and Spatial Informatics,
China University of Mining and Technology, Xuzhou, Jiangsu 221116, China
{zhaoyd,hantq,fsn2012,miaocc}@cumt.edu.cn

Abstract. Combining segmentation and shortest path searching, a novel seamline extraction method for remote sensing imagery is presented. It detects an optimal seamline along the boundaries of land cover objects so as to reduce the effect of the discontinuity on the seamline of the mosaic image. First, the valid overlaps of the reference image and the registered image was determined, as well as the starting point and the ending point. Second, watershed segmentation was applied to sketch out the boundaries of salient objects in the overlaps of the reference image. Third, after a difference image between the reference image and the registered image was obtained, those segmentation paths which pass through segments with an enormous difference were removed. Finally, an undirected weighted graph was built according to the remaining segmentation paths, and the seamline defined by the shortest path from the starting point to the ending point was found via the Dijkstra algorithm. Experimental results on Landsat-7 ETM+ images suggested that the presented method was capable of generating a seamless mosaic image.

Keywords: image mosaic, seamline extraction, watershed segmentation, shortest path, Dijkstra algorithm.

1 Introduction

In the field of remote sensing, image mosaic is often used to make a larger image covering the entire region of interest [1]. As a result, there has been significant attention paid to develop automatic techniques for generating seamless remote sensing mosaic images. Generally, image mosaic consists of two main processes. The first process is to register the neighboring images into a unified geographic coordinate system, and the following one is to stitch the registered images into an entire image. Simply superimposing registered images tends to cause visible seams [2]. Thus many approaches have been proposed in order to generate a seamless mosaic image, which can be categorized into two groups: boundary transition smoothing and optimal seamline searching.

Boundary transition smoothing is a rather straightforward way to reduce visible differences between neighboring images. It is commonly referred to as feathering or blending. Multiresolution blending is an effective way to leverage bi-image

F. Bian et al. (Eds.): GRMSE 2013, Part I, CCIS 398, pp. 684–691, 2013.
© Springer-Verlag Berlin Heidelberg 2013

differences of geometric and radiometric properties, which has been successfully used in 2-D panoramas [3] and 3-D models [4]. However, losing clarity of ground object textures is inevitable due to the blurring and ghosting in the overlap. Therefore, the seamline-based mosaic method is an alternative solution. Seamline optimization found in literatures can be mainly classified into two categories: pixel-based methods [5-8] and object-based methods [9-12].

Pixel-based seamline optimization methods do a pixel-by-pixel search by means of path planning techniques. Uyttendaele et al. [5] observed that, for well-registered images, changes in image objects produce the most noticeable artifacts. To overcome this problem, the moving objects were recognized by smoothing the difference image with morphological erode and dilate, and ghost effects caused by moving objects were removed by the weighted vertex cover algorithm whilst positioning the seamline at locations with consistent states. Davis [6] described an image blending method that computed the relative photometric difference of bi-images and searched for the dividing boundary along the low intensity of the difference image using the Dijkstra algorithm, but the computation cost is considerably high for remote sensing image mosaic involving megapixels. Pan and Wang [7] combined image gradients and image difference to avoid seamline crossing edge features. Yang et al. [8] presented a bisector seamline algorithm, in which overlaps between image pairs was approximated by a quadrangle, and a bisecting polyline was detected as the seamline. These pixel-based methods placed seamline without taking the image contents into consideration. As a result, some salient objects might not be circumvented by the seamline, which leads to significant artifacts.

To solve this problem, object-based methods were presented. Zuo et al. [9] distinguished ground area and non-ground area according to the high precision digital surface model (DSM), and used the greedy snake algorithm to detect the optimal seamline circumventing buildings. But the effectiveness of this method is limited to images covering building groups. Wan et al. [10] presented a vector-based seamline determination approach, in which a weighted graph was built by overlapping the existing vector roads with the extracted skeleton, and the lowest cost path referring to the optimal seamline was found by the Floyd–Warshall algorithm. Soille [11] proposed a image compositing procedure based on mathematical morphology and its marker-controlled segmentation paradigm to diminish the visibility of seams in the output mosaic. Gracias et al. [12] divided the overlaps into sets of disjoint segments by watershed segmentation and then searched the seamline using graph cut. Refs. [11, 12] suggest that object boundaries as natural transitions are desirable for image mosaic and thus the seamline along these boundaries is less perceptible in the mosaic image.

In this paper, an automatic image mosaic method by the combination of watershed segmentation and the Dijkstra shortest path search algorithm was developed to make seams invisible while still preserving image texture and details. The paper is organized as follows. Section 2 detailly describes the proposed mosaic scheme by incorporating segmentation and shortest path. The experimental results are given in Section 3. The paper concludes in Section 4.

2 Method

Fig. 1 is the illustration of the proposed image mosaic method, in which image segmentation and the shortest path search are incorporated to extract an optimal seamline. Seamline extraction consists of four steps. Firstly, the valid overlaps between the reference image and the registered one is identified to narrow the subsequent search after registering the neighboring images using the method presented in [13]. The rough seamline as well as its starting point P_s and ending point P_e are then obtained. Secondly, the overlap region of the reference image is segmented by the watershed segmentation algorithm, and then the boundaries of land cover objects are determined. Thirdly, the reversed difference image within the overlaps and the corresponding binary difference image are calculated. The segmentation result is overlaid with the binary image to build an undirected weighted graph, and the shortest path from P_s to P_e is found by the Dijkstra algorithm. Finally, taking the shortest path as the optimal seamline, seamline-based image mosaic is done. In this paper, we focused on seamline search, without considering the issue of color balance.

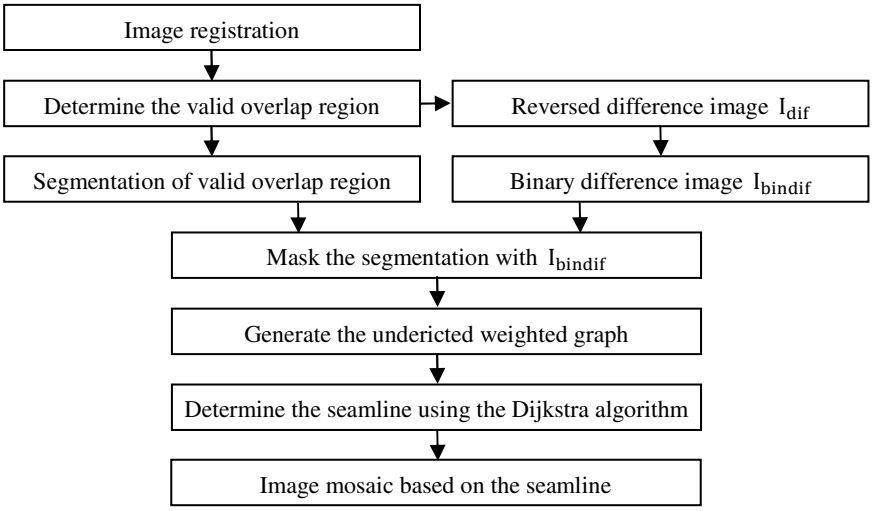

Fig. 1. Flow chart of the proposed method

2.1 Determination of the Valid Overlaps

Valid regions of registered images are quadrangles rather than rectangles and their invalid regions are filled with black pixels. That the seamlines may fall in invalid regions would lead to holes in the output mosaic, unless valid overlaps are determined.

In order to determine the valid overlaps, two simulation images need to be generated in advance. As shown in Fig. 2, A is the same size simulation of the reference image, and B is the same size simulation of the warp image. All of the pixel values in A were initialized to 2. The geometric transformation of B was done by the same way with that of the warp image. The valid region in B was initialized to 1, and the remaining invalid regions were initialized to 0. Fig. 2(c) is the sum of A and B, in which the brighter region with the value 3 corresponds to the valid overlaps. The brighter region is commonly a quadrangle with four vertices. The two vertices that do not match the corners of the input images are defined as the two ends of the seamline, thus the rough seamline can be determined. Note that the initial pixel values of A and B are used to distinguish the valid overlaps which is defined as the region with the maximum pixel value in the sum of A and B, and thus can be set to arbitrary values except 0.

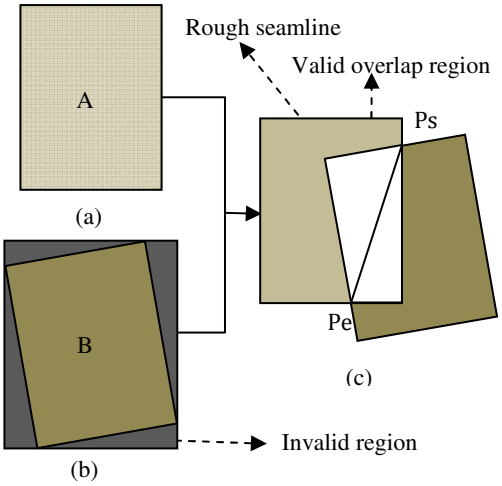

Fig. 2. An illumination of the valid overlaps and rough seamline. (a) is the simulation of reference image. (b) is the simulation of registered warp image. (c) is the determined valid overlaps (denoted by the white box) and the rough seamline (denoted by the solid black line within the white box).

2.2 Watershed Segmentation of the Overlaps

In this part, watershed segmentation is applied to sketch out the boundaries of land cover objects in the valid overlaps of the reference image. These object boundaries will be treated as candidate positions to locate the seamline in the following shortest path search.

Watershed transformation is a popular segmentation approach inspired by topographic relief flooded by water. Existing literatures provide a large number of application examples of watershed segmentation. See Ref. [15] for a review of several existing definitions of the watershed transform and associated algorithms.

In order to avoid over-segmentation caused by noises and surface extrema, the reference image is smoothed using morphological techniques called "opening-by-reconstruction" (erosion followed by morphological reconstruction) and "closing-by-reconstruction" (dilation followed by morphological reconstruction) before watershed segmentation. For the images used in this paper, good smoothing result was achieved using a disk structuring element with a size of 5.

Moreover, segmentation results of reference image are generally not completely consistent with object boundaries in registered image due to the presence of changing objects. As a result, the seamline may pass through those objects. This problem can be improved by determining regions of difference (RODs) between images. First, the difference image of overlaps was calculated and then smoothed using a Gaussian low pass filter. Then, gradation reversal and binarization were applied to the smoothed difference image to determine the RODs. After that, the segmentation paths passing through the RODs were removed to avoid seamline being located in these regions.

2.3 Extraction of Optimal Seamline Using Dijkstra Algorithm

After segmentation, the seamline extraction problem can be formulated as a shortest path searching problem. Here we used the Dijkstra algorithm [14] to solve this problem. An undirected weighted graph $G(V, E)$ needs to be generated before shortest path search.

Suppose each pixel of the segmentation paths as a vertex, and edges exist only between adjacent pixels. Let $V = \{v_1, v_2, v_3, \dots, v_n\}$ denote the set of vertices and $E = \{e_1, e_2, e_3, \dots, e_n\}$ edges in the graph and $W = \{w_1, w_2, w_3, \dots, w_m\}$ weights corresponding to the edges. The weight of the edge linking the two adjacent vertices v_i and v_j is caluclated by

$$w_k = \left(d_i + d_j\right)/2 \quad i, j \in [1, n], k \in [1, m] \ . \tag{1}$$

where d_i is the perpendicular distance from the vertex d_i to the rough seamline, and d_j is the perpendicular distance from the vertex v_j to the rough seamline. That is to say, the weight of each edge is the average distance from the two vertices it joints to the rough seamline. Note that $G(V, E)$ is normally stored as an adjacency matrix in which the number of vertices and edges is often very large due to the large number of pixels in the overlaps. Fortunately, edges exist only between adjacent pixels on the segmentation paths, a vast majority elements in the adjacency matrix are zero. Therefore, it is very beneficial for reducing memory consumption to store the adjacency matrix in a sparse form.

After building the undirected weighted graph, to find the optimal path from the starting point $\mathrm{P_s}$ to the ending point $\mathrm{P_e}$, the Dijkstra algorithm was applied to minimize the cost function defined by formula (2):

$$Cost = \sum_{i=1}^{m} w_i \ . \tag{2}$$

where m is the amount of edges in the path, and w_i is the weight of the i-th edge. The path corresponding to the minimum $Cost$ is defined as the optimal seamline.

3 Experimental Results

To evaluate the performance of the proposed method, a pair of Landsat-7 ETM+ scenes with the same row and the neighboring path were used. The data was provided by the Institute of Remote Sensing and Digital Earth, Chinese Academy of Sciences (http://ids.ceode.ac.cn/index.aspx).The image of path/row 121/036 captured on September 29, 2002 was treated as the reference, and the image of path/row 122/036 on October 6, 2002 the warp. For this series of experimental data, overlapping acquisitions covering XuzhouCity, Jiangsu Province, China occurred across the same row. Two sub-images with the size of 600×600 were cropped from the overlapping regions of the pair of scenes respectively [see Fig. 3(a) and (b)].

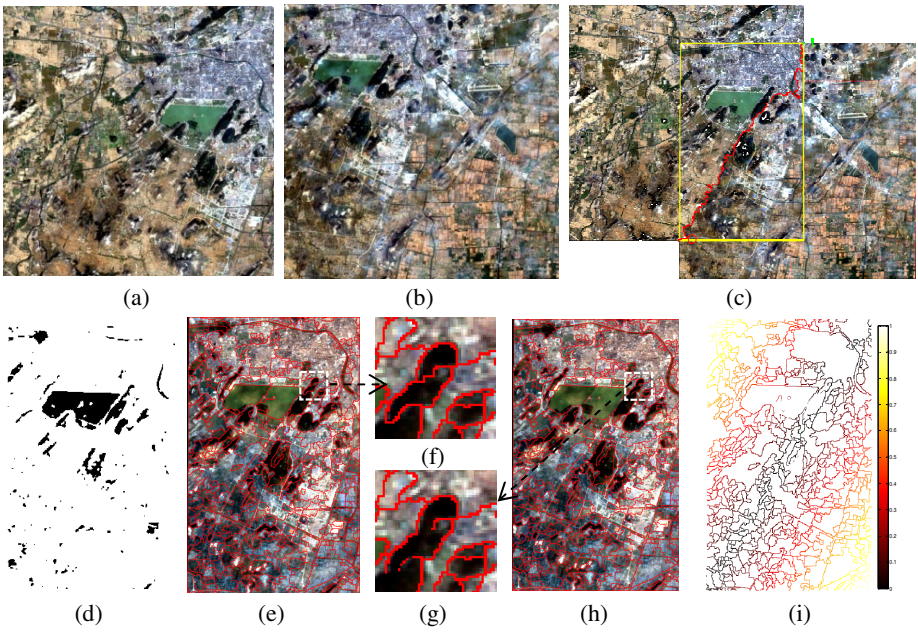

Fig. 3. Seamline extraction of the experimental images. (a) and (b) are the used images, with (a) being the reference image. (c) is the seamline extraction result, in which the valid overlaps is indicated with the yellow box and the seamline is indicated with the red line. (d) is the RODs (black regions) of the overlaps. (e) is the watershed segmentation result superimposed on the overlaps. (h) is the result of masking (e) with (d). (f) and (g) are enlarged views of the white dotted boxes in (e) and (h), (i) illumination of weight of edges in the overlaps.

The watershed segmentation was done after smoothing the reference image as presented as Section 2.2 using a disk structuring element with a size of 5. A threshold of 0.7 was used to determine the RODs after smoothing the difference image using a Gaussian low pass filter with a standard deviation of 1.4 pixels and a 9×9 Gaussian kernel. A computer with an AMD Turion (tm) Ⅱ Dual-Core Mobile M520 2.3GHz

processor, 2GB internal memory was used for data processing, and the all the experiment was simulated with MATLAB.

Fig. 3 shows the mosaic results of the experiment images. As described in Section 2.1, the warp image in Fig. 3(b) was registered with the reference in Fig. 3(a) beforehand. Fig. 3(e) is the valid overlaps overlaid by object boundaries sketched by watershed segmentation. However, the problem of over-segmentation was not completely avoided. Fig. 3(f) is the enlarged view of the white dotted box in Fig. 3(e), in which several segmentation paths passing through the Yunlong Mountain are apparent. The located seamline would not circumvent the mountain if these paths were all involved in the process of seamline optimization. As presented in Section 2.2, the RODs of overlaps shown as black regions in Fig. 3(d) were used to solve this problem. Comparing Fig. 3(d) and the overlaps represented by the yellow box in Fig. 3(c), we can find that most of the black regions in Fig. 3(d) are mountains and waters. This phenomenon is caused by the great relief displacement of mountains in the bi-images and the illumination sensitivity of waters. After gradation reversal and binarization, the mountains and waters were marked as RODs. As shown in Fig.3(f) and Fig.3(g), the segmentation paths passing through the mountains were cuted off so as to make the seamline bypass the mountains. Fig. 3(i) is the weight map of edges. As discussed in Section 2.1, in order to ensure the extracted seamline not be too far from the rough seamline, the edges closer to the rough seamline were given smaller weights. As a result, those edges would be more likely to be a part of the final seamline. Fig. 3(c) is the result of seamline optimization. The optimal seamline was positioned along salient structures, successfully bypassing the mountains and nearing to the rough seamline.

4 Conclusions

This paper presented an automatic image mosaic method via the combination of watershed segmentation and the shortest path search. Different from pixel-based seamline optimization algorithms, the proposed method positions seamlines along boundaries of image objects. RODs are pre-defined after the reversed difference image is binarized. The land cover object boundaries are sketched out using the watershed segmentation algorithm. And then they are refined by removing the segmentation paths passing through the RODs. In the next step, the shortest path as the optimal seamline are extracted by the Dijkstra algorithm when the refined object boundaries are candidate paths. Finally, mosaic is performed based on the extracted seamline. The experimental results on Landsat-7 satellite images suggested that the proposed method was capable of determining an optimal seamline following salient structures and achieving a desirable composited image.

Nevertheless, the study of this paper emphatically discussed the issue of seamline optimization without considering exposure compensation. Color balance should be involved in our further work.

Acknowledgments. The authors would like to acknowledge financial support from the Fundamental Research Funds for the Central Universities (2013QNB11). We would also like to thank the Institute of Remote Sensing and Digital Earth, Chinese Academy of Sciences for providing Landset-7 ETM+ images.

References

1. Goshtasby, A.A.: 2-D and 3-D Image Registration: for Medical, Remote Sensing, and Industrial Applications. John Wiley & Sons Inc., United States (2005)
2. Szeliski, R.: Computer Vision: Algorithms and Applications. Springer (2010)
3. Brown, M., Lowe, D.G.: Recognising Panoramas. In: ICCV 2003: 9th International Conference on Computer Vision, pp. 1218–1225. IEEE Comput. Soc., Los Alamitos (2003)
4. Baumberg, A.: Blending Images for Texturing 3D Models. In: BMVC 2002: British Machine Vision Conference 2002, pp. 613–622. British Machine Vision Assoc., Manchester (2002)
5. Uyttendaele, M., Eden, A., Skeliski, R.: Eliminating Ghosting and Exposure Artifacts in Image Mosaics. In: Proceedings of the 2001 IEEE Computer Society Conference on Computer Vision and Pattern Recognition, CVPR 2001, pp. 509–516. IEEE Comput. Soc., Los Alamitos (2001)
6. Davis, J.: Mosaics of Scenes with Moving Objects. In: Proceedings of the 1998 IEEE Computer Society Conference on Computer Vision and Pattern Recognition, pp. 354–360. IEEE Comput. Soc., Los Alamitos (1998)
7. Pan, J., Wang, M.: A Seam-line Optimized Method Based on Difference Image and Gradient Image. In: 2011 19th International Conference on Geoinformatics. IEEE, Piscataway (2011)
8. Yang, Y., Gao, Y., Li, H., Han, Y.: An Algorithm for Remote Sensing Image Mosaic Based on Valid Area. In: 2011 International Symposium on Image and Data Fusion (ISIDF 2011). IEEE, Piscataway (2011)
9. Zou, Z., Zhang, Z., Zhang, J., Cao, H.: Seamlines Intelligent Detection in Large Scale Urban Orthoimage Mosaicking. Acta Geodaetica et Cartographica Sinica 40, 84–89 (2011)
10. Wan, Y., Wang, D., Xiao, J., Lai, X., Xu, J.: Automatic Determination of Seamlines for Aerial Image Mosaicking Based on Vector Roads Alone. ISPRS Journal of Photogrammetry and Remote Sensing 76, 1–10 (2013)
11. Soille, P.: Morphological Image Compositing. IEEE Transactions on Pattern Analysis and Machine Intelligence 28, 673–683 (2006)
12. Gracias, N., Mahoor, M., Negahdaripour, S., Gleason, A.: Fast Image Blending Using Watersheds and Graph Cuts. Image and Vision Computing 27, 597–607 (2009)
13. Han, T., Zhao, Y., Liu, S., Bai, Y.: Spatially Constrained SURF Feature Point Matching for UAV Images. Journal of Image and Graphics 18, 669–676 (2013)
14. Dijkstra, E.W.: A Note on Two Problems in Connexion with Graphs. Numerische Mathematik 1, 269–271 (1959)
15. Roerdink, J.B.T.M., Meijster, A.: The Watershed Transform: Definitions, Algorithms and Parallelization Strategies. Fundamenta Informaticae 41, 187–228 (2000)

Analysis and Trend Prediction of Water Utilization Structure in Haihe River Basin

Haoyang Sun, Sufen Wang*, Xinmei Hao, Xin Liu, and Jian Kang

Center for Agricultural Water Research in China, China Agricultural University, Beijing, 100083, China
shy74536@sina.com, haox@cau.edu.cn
wwwsf71@163.com

Abstract. Due to the human activities and climate change, the scarcity of water resources and the deterioration of water environment has been a serious problem in Haihe river basin. It is important to study water withdrawal and water utilization structure for sustainable use of water resources in this area. We analyzed the present water utilization structure of Haihe river basin by using the information entropy theory. Results show that water structure entropy value of Beijing and Tianjin is higher than other provinces in the basin and the whole basin, which matches the fact that the agricultural, industrial, domestic, and ecological water use are relatively balanced in Beijing and Tianjin while the proportion of agricultural water use is extremely large in other provinces of the basin. GM (1, 1) model and grey Markov model have been developed for simulation and predicting the evolution of water utilization structure in Haihe river basin. According to the results, the accuracy of grey Markov model was higher, which predicated the reduction of agricultural and industrial water consumption, and the increase of domestic and ecological water consumption in the future. Specifically, the model predicted that the proportion of water utilization structure in terms of ratio of agricultural, industrial, domestic, and ecological water use would change from 64.7:14.9:17.0:3.4 in 2011 to 63.4:12.2:20.2:4.2 in 2020, and the total water consumption will be reduced to 2.9 billion m³.

Keywords: Haihe river basin, water utilization structure, information entropy, grey Markov, prediction model.

1 Introduction

The proportion of water utilized in different economic sectors can reflect the degree of economy and civilization of a country or region from one side, and it is also a reflection of science and technology level. Large industrial water ratio shows high degree of industrialization, while large domestic water ratio means that the civilization degree is higher. Meanwhile the large agricultural water ratio reflects that not only its dominating industry is agriculture, but also the agricultural science and technology

* Corresponding author.

F. Bian et al. (Eds.): GRMSE 2013, Part I, CCIS 398, pp. 692–703, 2013.
© Springer-Verlag Berlin Heidelberg 2013

level is relatively lower [1]. Water utilization structure refers that water consumption of a certain water system in the various departments (mainly refers to agricultural, industrial, domestic and ecological water) accounts for the proportion of the total water consumption in a period of time. Water utilization structure in long-term evolution has its phase characteristics, and is closely related to social and economic development. In the first stage, the use of agricultural water resources accounted for the largest part and the economy is relatively backward. In the second stage, the consumption of industrial water resources increased rapidly and the consumption of agricultural water resources decreased gradually because of the accelerated industrialization. In the third stage, agricultural, industrial and domestic water tended to be equilibrium, and ecological water consumption is small but kept on increasing year by year. The increasing population and the more convenient conditions for residential water use led to the growth of domestic water consumption. With the public and government emphasizing on environmental problems in recent years ,ecological water consumption has a increasing tendency. Information entropy model is established and bring the process of water utilization structure evolution into the model, based on the information entropy calculation year by year and contrast analysis, to reflect the changes in the proportion of water among different water consumption departments. Thus it will make the evolution process more intuitively [2].

In recent years, domestic and international experts and scholars have carried on many quantitative and qualitative researches to the water utilization structure on this subject, mainly concentrated on the water prediction and the analysis of the water use structure evolution. As for the study object, Ke found that the total water consumption was stable with a slight decline, the changing water use structure for domestic water proportion increase, industrial and agricultural water ratio decreased based on analysis on our country's economy [3]. Jenerette made a prediction for the total water demand in 2015, based on population, economic and climate data from 1950 to 2000 in 524 cities around the world [4]. Arouna and Dabbert analyzed determinants of domestic water use in rural areas, which is mainly on households without access to private improved water resources [5]. Jiao et al. built a niche in the utilization of water resources and its entropy model, analyzed the relationship between the ecological niche in the utilization of water resources and ecological environment, and took Anyang city of Henan Province as an example to study [6]. It had been proposed that the better models and methods were needed to analyze the interaction between human and the complex ecosystem comprehensively [7]. In terms of research method, Chang et al. combined the gray connectedness and entropy to establish the discriminant model on the direction of water resources system evolution based on grey relation entropy, which provided a new method for the analysis of water resources system [8]. Fang and Bao constructed the water - ecology - economy coordinated development coupled model for water prediction in Heihe river basin, based on the present situation and possible development trend of water utilization structure by using the principle of System Dynamic Model and coupled the ecological, social and economic factors [9]. Based on the principle of Lorenz Curve and the computational methods of Gini coefficient, Liu and Jin drew the space matching curve of water resource, calculated the matching degree, and evaluated the matching degree according to the

criteria of Gini coefficient which is classified by the United Nations[10]. Huang proposed evaluation index system on water use, which based on three index categories of water use performance, water use quota, water use efficiency and gave a comprehensive evaluation on water use of industry, agriculture, living in three cities of Hunan Province by using Multi-layer grey relational comprehensive evaluation [11]. Chi et al. proposed to combine the artificial neural network and grey prediction method into parallel type grey neural network prediction method to predict the irrigation water consumption, and solved the weighting coefficient of combination model by using the effectiveness of predicting methods as the optimization index [12].

In this paper, firstly, the present situation of water utilization structure in Haihe river basin was analyzed by using the information entropy theory. Secondly, the GM (1, 1) model and the grey Markov model were established, which were used to forecast the future water consumption of different departments in this area. At last, a comparison was made between the results of the two models, and the one with better performance was used for further analysis.

2 Materials and Methods

2.1 Study Area

The Haihe River Basin which covers 0.32 million km^2 valley area, is one of the 7 biggest river basins in China. The population of this area is around 0.13 billion, making up 10 percent of the total population of China. The cultivated area is 0.16 billion acres, making up 11 percent of the total cultivated area of the nation. The average annual precipitation, land surface evaporation and water surface evaporation is 539mm, 470mm and 1100mm, respectively. It can be noticed that the water resource of Haihe River Basin is facing severe issues in terms of water scarcity and failing to match the distributions of local population, cultivated land and productive forces [13]. Among the 7 biggest national river basins, Haihe River Basin has the lowest water resource per capita and per acre. With the increase of population and the development of regional economy, there will have a further increase of water demand, and the current situation of the gap between water supply and demand will be larger. Thus, the water utilization structure and changing trend of this area has attracted much attention.

2.2 Methods

2.2.1 The Information Entropy Theory

Entropy is a kind of state function, referring to the system randomness, which is put forward and first applied in thermodynamics by Rudolf Clausius. After years of development, entropy theory is widely used in control theory, probability theory, number theory, astrophysics, life science, etc. all. The information entropy was introduced by Shannon in the information theory in 1908, whose mathematical expression was also presented. For an uncertain system, discrete random variable X

values for $X = (x_1, x_2, \ldots x_n)$ with the corresponding probability $P = (p_1, p_2, \ldots p_n)$, and $\sum Pi = 1$, so the information entropy of the system is

$$H(x) = -\sum_{i=1}^{m} P_i \ln P_i \quad . \tag{1}$$

$H(x)$ can describe any degree of chaos and disorder of a material or system.

In the expression of the water utilization structure information entropy, suppose that the water consumption of each department is X and the proportion of water use of each department is P. Information entropy value is bigger, which indicates that the more the water allocation of each sector is in a state of equilibrium.

2.2.2 GM (1, 1) Model

The choice of models is crucial for predicting the water utilization structure of the basin. The established model should follow standard practices in terms of theoretical consistency, high fitting degree and strong predictability, and the parameter selection should observe the scientific principle, system principle, operative principle and principle of simplicity and flexibility [14].

The principle of grey model is mainly to deal with the primitive sequence and to weaken the volatility of the original data, so as to further predict the subsequent values of the generated sequences. Then the predictive value of the original sequence will be obtained after inverse accumulating the follow-up sequence [15, 16]. The (1, 1) in the GM (1, 1) model refers to the first order differential and a variable. The model is often used in the prediction of time series, as described below.

First, the original sequence (formula 2) should be accumulated to get new sequence (formula 3), to which first order differential equation will be established (formula 4).

$$X^{(0)} = (x^{(0)}(1), x^{(0)}(2), \ldots, x^{(0)}(n)) \quad . \tag{2}$$

$$X^{(1)} = (x^{(1)}(1), x^{(1)}(2), \ldots, x^{(1)}(n)) \quad . \tag{3}$$

$$\frac{dx^{(1)}}{dt} + ax^{(1)} = u \quad . \tag{4}$$

The predictive series are discrete with regard to time, so it is

$$\frac{\Delta x}{\Delta t} = \frac{x^{(1)}(k+1) - x^{(1)}(k)}{k+1-k} = x^{(1)}(k+1) - x^{(1)}(k) = x^{(0)}(k+1) \quad . \tag{5}$$

$$x^{(0)}(k) + a\frac{1}{2}\left(x^{(1)}(k) + x^{(1)}(k-1)\right) = u; k = 2,3,\ldots,n \quad . \tag{6}$$

The two estimated parameters will be expressed as vector, $\hat{a} = [a, u]^T$. Formula 7 will be obtained by solving the above equations with the least square method.

$$\hat{a} = (B^T B)^{-1} B^T Y \quad . \tag{7}$$

$$Y = \begin{bmatrix} x^{(0)}(2) \\ x^{(0)}(3) \\ \cdots \\ x^{(0)}(n) \end{bmatrix}, \quad B = \begin{bmatrix} -0.5\left(x^{(1)}(2) + x^{(1)}(1)\right) & 1 \\ -0.5\left(x^{(1)}(3) + x^{(1)}(2)\right) & 1 \\ \cdots & \cdots \\ -0.5\left(x^{(1)}(n) + x^{(1)}(n-1)\right) & 1 \end{bmatrix}$$

The model parameters will then be solved, which should be put into the formula 4 to get the answer.

$$x^{(1)}(t) = \left[x^{(1)}(0) - \frac{u}{a} \right] e^{-a(t-1)} + \frac{u}{a} \quad . \tag{8}$$

Then, the prediction formula of GM (1, 1) model will be obtained after restoring the above formula.

$$x^{(0)}(k+1) = (1 - e^a)\left(x^{(0)}(1) - \frac{u}{a} \right) e^{-ak}; k = 1,2,...,n \quad . \tag{9}$$

2.2.3 Grey Markov Model

The Markov model is a model which can reflect the impact of random factors and predict future change tendency of the system based on the shifts and changes within different states, and it is suitable for predicting the stochastic volatility problems [17]. The grey Markov model divides the predictions into state categories and predicts the future outcomes by using the determined state transfer matrix on the basis of those predicted outcomes of the grey system model.

Suppose that there is a set of raw data $x^{(0)}(n)$, a new predicting sequence $y^{(0)}(n)$ can be output by GM (1, 1) model, which will be divided into m condition intervals randomly.

$$\otimes_i = [\otimes_{1i}, \otimes_{2i}]$$

$$\otimes_{1i} = y^{(0)}(n) + \alpha_i \bar{x}^{(0)}(n) \tag{10}$$

$$\otimes_{2i} = y^{(0)}(n) + \beta_i \bar{x}^{(0)}(n); i = 1,2,...,m \quad .$$

The eventual predictive value is the midpoint of this interval.

$$y^{(1)}(n) = \frac{1}{2}(\otimes_{1i} + \otimes_{2i}) \quad . \tag{11}$$

State-transition matrix is the most important part for the Markov prediction model. The k-orders state-transition matrix of Markov chain can be obtained by using P_{ij} to indicate the transfer probability value from stage i to stage j.

$$P^k{}_{ij} = \begin{bmatrix} P^k{}_{11} & P^k{}_{12} & \cdots & P^k{}_{1n} \\ P^k{}_{21} & P^k{}_{22} & \cdots & P^k{}_{2n} \\ \cdots & \cdots & \cdots & \cdots \\ P^k{}_{m1} & P^k{}_{m2} & \cdots & P^k{}_{mn} \end{bmatrix} . \tag{12}$$

First-order state transition matrix will be used in this paper. State transition matrix at time $t+1$ is determined by that of time t.

$$P_{t+1} = P_t P^1{}_{ij} \quad . \tag{13}$$

2.2.4 Two-Norm

Two-Norm, which is also called Euclidean Norm, represents the Euclidean length of the vector x in the n dimensional vector space and can reflect the size of the vector, writing for $\|\cdot\|_2$, whose calculation formula is

$$\|x\|_2 = \left(\sum_{i=1}^{n} |x_i|^2 \right)^{\frac{1}{2}} . \tag{14}$$

If the error values of each set of predicted values are regarded as a vector, the error magnitude of each set of data can be compared by calculating the 2-Norm of the error vector.

2.3 Data Collection

The data of water consumption in Haihe river basin is from *Official Reports on Water Resources of Haihe river basin* (*2003-2011*). The water-consuming system of Haihe River Basin is divided into four departments in this study, namely agricultural water, industrial water, domestic water and ecological water. Agricultural water is comprised by irrigation water and the water used by forest, herd and fishing; Industrial water only stands for the new water used by those enterprises while the recycle water is excluded from this category; domestic water include urban residential water, public water in cities and towns, rural residential water and livestock water; ecological water covers the water used for urban environment and the artificial filling water used by certain rivers, lakes and wetlands [18]. It can be pointed out that a rational analysis and scientific prediction of the water utilization structure of Haihe River Basic is not only a solid foundation of the reasonable distribution of water resources, but also a significant premise for balancing the social and economic development within the basin area [19].

In the Haihe River Basin, the variation trends of total water consumption and agricultural water consumption are most similar while the total water consumption of

industrial and domestic water do not appear to be much different, which means agricultural water occupies the biggest proportion (over 60%) of the total water resources and the variation of agricultural water consumption dominants the variation of total water consumption. Even if the trend of the agricultural water consumption percentage has been dropping noticeably, the number still remains high at the moment. On one hand, it shows that the control of agricultural water consumption of Haihe River Basin has obtained some achievements. On the other hand, it means that developing water-saving and efficient agriculture is the necessary choice of this region. Furthermore, with the rapid development of modern economy, it is difficult to maintain balanced industrial and domestic water consumption. This means that this area has put a great effort to save water. Further, it can be seen that the percentage of ecological water increases year by year and this trend has a direct connection with the increasing awareness of environmental protection by the government and members of the public. The variation trends of the water consumption departments of Haihe River Basin are illustrated in Fig. 1, the proportion of water consumption are showed in Table 1.

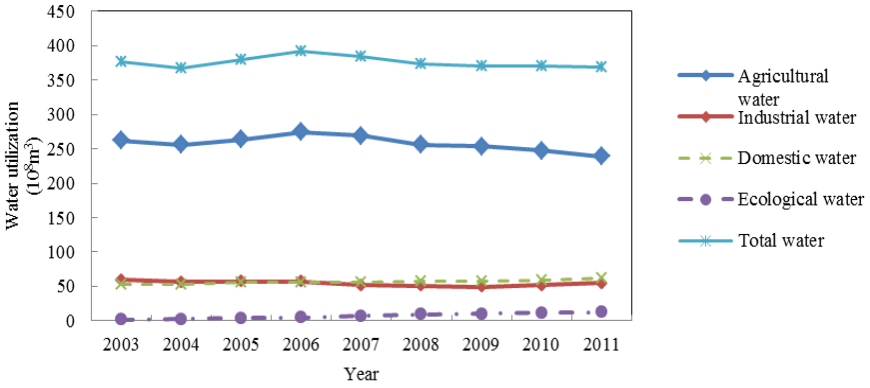

Fig. 1. Change of water utilization in different sectors in the Haihe River Basin

Table 1. Contrast of water utilization structure of the Haihe River Basin in 2003-2011

Year	Agricultural water (%)	Industrial water (%)	Domestic water (%)	Ecological water (%)
2003	69.5	15.8	14.2	0.5
2004	69.6	15.4	14.3	0.7
2005	69.4	14.9	14.6	1.0
2006	70.0	14.5	14.4	1.2
2007	70.1	13.5	14.7	1.7
2008	68.5	13.7	15.3	2.5
2009	68.5	13.3	15.6	2.6
2010	66.9	14.0	15.9	3.1
2011	64.7	14.9	17.0	3.4

3 Results and Discussion

3.1 Analysis of the Information Entropy Values of Different Water Utilization Sectors

According to formula (1), the water utilization structure information entropy's time series of this area can be calculated. The variation of the water utilization structure information entropy can be seen in Fig. 2 (Since the water consumption of different provinces was not published in <*The Official Reports on Water Resources of Haihe River Basin*> (2004), this chart did not list the data from year 2004). Based on Fig. 2, it can be noticed that the water utilization structure entropies of Beijing and Tianjin are higher than those in other provinces and the whole basin area. This result is consistent with the fact that the water consumption structure which includes agricultural, industrial, domestic and ecological water consumption is relatively balanced in Beijing and Tianjin, while the other provinces have an over-large proportion of agricultural water use. Among those provinces, Hebei Province and Shandong Province are the most typical districts since the agricultural water consumption far surpasses other departments. Further, the water utilization structure entropy of Liaoning Province and Inner Mongolia Province fluctuates greatly, but these two provinces are unrepresentative since the areas of these two regions are relatively small and the total water consumption is not considered big.

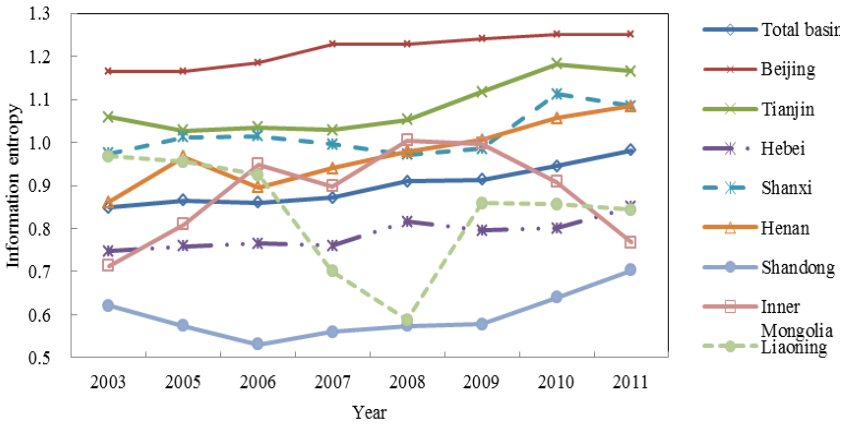

Fig. 2. Information entropy of water utilization structure in the Haihe River Basin

There are close links between the water utilization structure information entropy and the level of regional social and economic development. It can be pointed out that Beijing and Tianjin have better socio-economic conditions than other provinces, but the economy of Haihe River Basin is comprised by the sum of all these districts.

Thus, the GDP per capita is lower than that of Beijing and Tianjin but higher than that of the average among other provinces. According to Fig. 2, the information entropy of Beijing and Tianjin is relatively big; the information entropy of Shandong province is the smallest; and the information entropy of the whole Haihe River Basin is in the middle. During the past 3 years, the information entropy of all the provinces within Haihe River Basin has increased, which means the adjustments of water utilization structure within the basin have had an effect, and the water consumption of different departments and different regions tend to be more balanced. The water utilization structure information entropy of Haihe River Basin shows a high degree of consistency with the local socio-economic level. This fully shows that reasonably adjusting water consumption structure could help promote economic development of this region. Meanwhile, the balance of water consumption structure would provide safeguards for the sustainable development of this area.

3.2 Comparison of Results and Errors of Different Prediction Models

The amount of domestic water from 2003 to 2008 in Haihe river basin was used as the basic data for simulation and prediction, and the practical use of water resources from 2009 to 2011 was used for verifying the accuracy of the model based on the grey Markov model. The results showed that the simulation values of domestic water in Haihe river basin is $58.27\times10^8m^3$, $59.43\times10^8m^3$ and $60.61\times10^8m^3$ in 2009, 2010 and 2011, respectively. The practical value is $57.84\times10^8m^3$, $59.00\times10^8m^3$ and $62.67\times10^8m^3$ in the three years, and total value of the relative error is 0.049. Thus, the accuracy degree of the model is high and can be applied in Haihe river basin for the prediction of domestic water resources.

As the use of ecological water is relative low, so the simulation value is relative high. In order to resolve the problems, the ecological water resources can be obtained by using the total use of water resource subtracting other kinds of water resources rather than predicting the ecological water resource. The predicted value is more reasonable.

Two models for estimating water consumption trend are consistent with the actual situation. The GM (1, 1) model is a linear model, and its modeling method determines whether the output is monotonically increasing or decreasing, producing the larger output error. However, the Grey Markov model, optimizing the GM (1, 1) model, is regarded as sufficient consideration for the relationship between the expected value and actual value. Through the adjustment of model parameters, the difference between the output value and the actual value is minimum, which improves the calculating precision and generates the higher fitting degree with the original sequence, so as to achieve the best estimation results. Therefore, the Grey Markov model is used to predict the future water consumption in Haihe river basin. The model output results and error calculation are listed in table 2, 3, 4, 5.

Table 2. Comparison of results and errors of agricultural water utilization of different prediction models

Year	Actual value (10^8 m^3)	GM (1, 1) (10^8 m^3)	Error (1)	Grey Markov (10^8 m^3)	Error (2)
2003	261.92	272.31	10.39	263.28	1.36
2004	256.14	268.92	12.78	259.89	3.75
2005	263.68	265.57	1.89	262.99	0.69
2006	274.72	262.26	12.46	268.71	6.01
2007	269.37	258.99	10.38	265.44	3.93
2008	255.84	255.76	0.08	262.21	6.37
2009	253.30	252.58	0.72	259.03	5.73
2010	247.61	249.43	1.82	246.85	0.76
2011	239.15	246.32	7.17	237.29	1.86
2-Norm			24.35		12.06

Table 3. Comparison of results and errors of industrial water utilization of different prediction models

Year	Actual value (10^8 m^3)	GM (1, 1) (10^8 m^3)	Error (1)	Grey Markov (10^8 m^3)	Error (2)
2003	59.66	57.0098	2.65	60.27	0.61
2004	56.58	56.2484	0.33	57.34	0.76
2005	56.73	55.4971	1.23	56.58	0.15
2006	56.84	54.7559	2.08	55.84	1.00
2007	52.06	54.0246	1.96	52.12	0.06
2008	51.30	53.3031	2.00	51.40	0.10
2009	49.21	52.5912	3.38	50.69	1.48
2010	51.72	51.8888	0.17	49.99	1.73
2011	55.08	51.1957	3.88	54.46	0.62
2-Norm			6.89		2.75

Table 4. Comparison of results and errors of residential water utilization of different prediction models

Year	Actual value (10^8 m^3)	GM (1, 1) (10^8 m^3)	Error (1)	Grey Markov (10^8 m^3)	Error (2)
2003	53.53	52.3405	1.19	53.17	0.36
2004	52.51	53.3691	0.86	52.82	0.31
2005	55.53	54.4178	1.11	55.25	0.28
2006	56.55	55.4872	1.06	56.32	0.23
2007	56.33	56.5776	0.25	56.03	0.30
2008	57.09	57.6894	0.60	57.14	0.05
2009	57.84	58.823	0.98	58.27	0.43
2010	59.00	59.979	0.98	59.43	0.43
2011	62.67	61.1576	1.51	60.61	2.06
2-Norm			3.03		2.25

Table 5. Comparison of results and errors of water utilization of different prediction models

Year	Actual value (10^8 m^3)	GM (1, 1) (10^8 m^3)	Error (1)	Grey Markov (10^8 m^3)	Error (2)
2003	377.00	382.2231	5.22	372.82	4.18
2004	367.98	380.8241	12.84	371.42	3.44
2005	379.79	379.4303	0.36	386.95	7.16
2006	392.69	378.0415	14.65	385.56	7.13
2007	384.48	376.6578	7.82	384.18	0.30
2008	373.39	375.2792	1.89	373.40	0.01
2009	370.02	373.9056	3.89	364.50	5.52
2010	369.93	372.537	2.61	370.66	0.73
2011	369.59	371.1735	1.58	369.29	0.30
2-Norm			22.27		12.75

4 Conclusions

According to the analysis of information entropy theory for water utilization structure, Haihe River is developing in balance for different water utilization sectors and the increase of entropy year by year closely relates to the rapid development in economy over the entire basin.

Grey Markov model predicts that Haihe river basin water will change smoothly in water utilization for different sectors and the proportion of water utilization structure will change from 64.7:14.9:17.0:3.4 in 2011 to 63.4: 12.2: 20.2: 4.2 in 2020, indicating that the total water consumption will reduce by 29 billion m^3. The proportion of agricultural and industrial water consumption show a downward trend, while the percentage of domestic and ecological water consumption would increase correspondingly from 2011 to 2020. Thus, research on the analysis and projection of water resources structure plays a significant role in the distribution of water resources.

Acknowledgements. This work was financially supported by Special Fund for Agro-scientific Research in the Public Interest (201203077), the National High Technology Research and Development Program of China (863 Program, 2011AA100502) and the International Science & Technology Cooperation Program of China (2013DFG70990).

References

1. Wu, P.T., Feng, H., Niu, W.Q., Gao, J.E., Jiang, D.S., Wang, Y.K., Fan, X.K., Qi, P.: Analysis of Developmental Tendency of Water Distribution and Water-saving Strategies. Transactions of the Chinese Society of Agricultural Engineering 19(1) (2003)

2. Ma, L.H., Kang, S.Z., Su, X.L.: Study on Evolution and Its Driving Forces of Water Utilization Structure of Shiyang River Basin in Northwest arid Areas. Agricultural Research in the Arid Areas 26(1), 125–130 (2008)
3. Ke, L.D.: An Analysis on Trends in Water Utilization in China in 1949-2000. Science and Technology Review 9, 14–18 (2002)
4. Jenerette, G.D.: A Global Perspective on Changing Sustainable Urban Water Supplies. Global and Planetary Change 50(3), 202–211 (2006)
5. Arouna, A., Dabbert, S.: Determinants of DomesticWater Use by Rural Households Without Access to Private Improved Water Sources in Benin: A Seemingly Unrelated Tobit Approach. Water Resources Management 24, 1381–1398 (2010)
6. Jiao, S.X., Wang, L.C., Li, J., Yang, S.X., Li, Y.D., Zhao, R.Q., Yin, Y.X.: Water Consumption Structure Based on the Niche and Its Entropy Model: A Case Study of Anyang City, Henan Province. Resources Science 33(12), 2248–2254 (2011)
7. Committee on Grand Challenges in Environmental Sciences. Grand Challenges in Environmental Sciences. National Academy Press, Washington, D.C. (2001)
8. Chang, J.X., Huang, Q., Wang, Y.M., Xue, X.J.: Water Resources Evolution Direction Distinguishing Model Based on Dissipative Structure Theory and Gray Relational Entropy. Journal of Hydraulic Engineering (11), 107–112 (2002)
9. Fang, C.L., Bao, C.: The Coupling Model of Water-Ecology-Economy Coordinated Development and Its Application in Heihe River Basin. ACTA Geographica Sinica 59(5), 782–790 (2004)
10. Liu, Y., Jin, F.J.: Analysis of Spatial Match of Regional Water Resource. Journal of Liaoning Technical University 24(5), 658–660 (2005)
11. Huang, T.Z., Huang, J.Y.: Water Usage Level Evaluation and Industry Structure Adjusting Policy in Zishui Basin. Advances in Water Resources and Hydraulic Engineering, 20–23 (2008)
12. Chi, D.C., Tang, Y.F., Gu, T., Yu, M., Li, Z., Ma, Z.Z.: Prediction of Irrigation Water Use Using Parallel Gray Neural Network. Transactions of the Chinese Society of Agricultural Engineering 25(5), 26–29 (2009)
13. Kang, S.Z., Yang, J.Z., Pei, Y.S.: Farmland Water Cycle Process and Agriculture Efficient Water Use in Haihe River Basin, pp. v–vi. Science Press, Beijing (2013)
14. Gujarati, D.N.: Econometrics. China Renmin University Press, Beijing (2000)
15. Feng, L.H.: Discussion of the Problem of Grey Forecast Model. Systems Engineering Theory and Practice (12), 125–129 (1997)
16. Zhao, Y.N., Zhang, Q., Ma, Y.L.: The Application of the Gray-BP Network Combination Forecast Model in the Small Sample Problem. Statistics and Decision (231), 14–15 (2007)
17. Blue Menthal, R.M., Getoor, R.K.: Markov Process and Pontential Theory. Academy Press, New York (1986)
18. The Commission of Haihe River Basin. The Official Reports on Water Resources of Haihe River Basin (2003-2011)
19. Liu, B.Q., Yao, Z.J., Gao, Y.C.: Trend and Driving Forces of Water Consumed Structure Changes in Beijing. Resources Science 25(2), 38–43 (2003)

An Automated 3D Approach for Buildings Reconstruction from Airborne Laser Scanning Data

Chunxiao Wang[1,2], Xingshu Hu[2], Min Ji[1], and Ting Li[1]

[1] Geomatics College, Shandong University of Science and Technology, Qingdao, Shandong, 266590, China
[2] The 7th Institute of Topographic Surveying, National Administration of Surveying, Mapping and Geoinformation, HaiKou, HaiNan, 570203, China
{cx8989,huxingshu}@163.com, {jamesjimin,liting_sdust}@126.com

Abstract. 3D city models support many government agencies for development planning as well as climate, fire propagation, and public safety studies. Commercial building modeling software tools require a high degree of interpersonal communication, which is always time-consuming. However, a reliable and highly accurate city model approach is still a challenging task that requires several processing steps of the workflow. This research proposes an automated approach for building reconstruction from airborne laser scanning data. We use a reliable segmentation algorithm to separate roads, trees and meadows from buildings. The parameters for segmentation are of crucial importance for the outline detection and the 3D modeling approach. We describe the theoretical background, the segmentation algorithm, the outline detection, the modeling approach and methods to determine the parameters. We validate the approach by a sub dataset of point cloud data captured by airborne LiDAR system.

Keywords: building modeling, airborne laser, segmentation, outline detection, parameters determination.

1 Introduction

Realistic 3D city models are required for many purposes such as urban planning and safety analysis. Urban areas are usually rapidly changing mainly due to human activities in construction, destruction or extension of topographic elements such as buildings and roads, this leads to requesting a fast data acquisition technique and automatic method for detecting and extracting 3D topographic objects from the data[1].A large amount of work has been done in the field of laser scanning data understanding focused on the development of efficient and robust algorithms to segment, extract and modeling typical man-made objects, such as buildings and roads. Modeling systems vary with respect to data acquisition methods which strongly influences models' characteristics and usefulness. The data acquisition methods could be clustered into those based on photo grammetry (Terrestrial images, Panoramic images, Aerial images),active sensors (Ground laser scanner[2,3], Airborne Lidar [4],), and hybrid sensor systems(Hybrid imagery and laser range sensors, Hybrid DSM or

F. Bian et al. (Eds.): GRMSE 2013, Part I, CCIS 398, pp. 704–712, 2013.
© Springer-Verlag Berlin Heidelberg 2013

aerial image and 2D GIS) [5]. The method proposed in this paper uses 7D data (x, y, z, intensity, red, green, blue)for the segmentation. Based on the segmentation result we try to find the edge or boundary of the point cloud and then construct models.

2 Methodology

The generation of reliable and accurate building models from laser scanning data requires a number of processes. These are point cloud segmentation, building roof detection, outline extraction, roof shape reconstruction, model generation, and finally, model quality analysis.

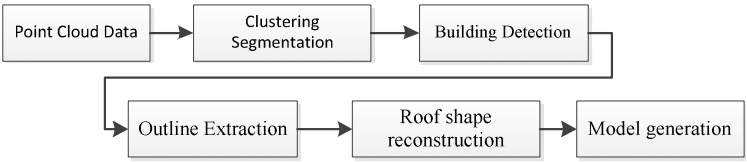

Fig. 1. Buildings reconstruction workflow

Point cloud segmentation, such as spatial clustering and region growing[6-8], try to classify points that are close to each other into a cluster. The cluster algorithms, such as, K-means[9],density-based clustering,[10] fuzzy clustering,[11] self-organizing maps(SOM)[7]wavelet analysis[12], principal component analysis[13] have been applied for the extraction of buildings, trees and other objects from laser scanning data. Meanwhile, they mainly use the 3D data for the extraction. The method proposed in this letter uses 7D data (x, y, z, intensity, red, green, blue) for the segmentation.

In practice, the points of an object in the laser scanning data are close or similar to each other in spatial position, echo intensity and color information. Based on the similarity, cluster analysis algorithms can be applied for the segmentation of the point cloud data. To be more accurate and distinguish objects which are close to each other in spatial space, we use 7 dimension data, spatial position, echo intensity and color information for the segmentation of buildings, roads and trees. Because the 7 dimension have different unit, we standardize the matrix first, then we define the distance between points and develop an efficient searching algorithm. Finally, we use the DBSCAN(Density-Based Spatial Clustering of Applications with Noise)[14]clustering method which needs the neighbor radius r and the minimum number of a cluster *minPts*. Therefore, we propose the scheme demonstrated inFig.2 to address the workflow of the segmentation of point cloud with seven dimension data.

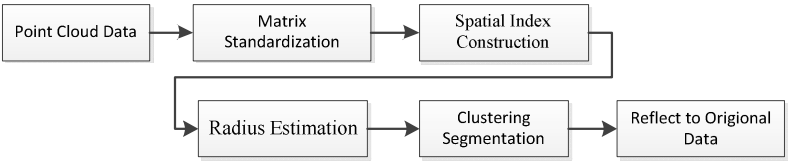

Fig. 2. Segmentation workflow

2.1 Matrix Standardization

The data could be considered as a matrix of points with spatial position, echo intensity and color information as shown below.

$$\begin{bmatrix} x_{11} & x_{12} & \cdots & x_{1m} \\ x_{21} & x_{22} & \cdots & x_{2m} \\ \vdots & \vdots & \vdots & \vdots \\ x_{n1} & x_{n2} & \cdots & x_{nm} \end{bmatrix}$$

Where *n* is the number of points and 1 to m are for x, y, z, red, green, blue, intensity separately. The domain of coordinates is much larger then the domain of color and echo intensity. Therefore, the contribution of the x, y and z variable values to this calculation is huge. It can be said that the distance is practically just the absolute difference in the x, y and z values with only tiny additional contributions from color and echo intensity. The variables are on completely different scales of measurement and the x, y and z coordinate will dominate in the calculation of Euclidean distances. Some form of standardization is necessary to balance out the contributions, and the conventional way to do this is to transform the variables so they all have the same variance of 1. At the same time we center the variables at their means. It is no necessary of calculating distance during this centering, but it makes the variables all have mean zero and easier to compare. The transformation commonly is called standardization according to:

$$Z_{ij} = \frac{\mathrm{x_{ij}} - \mathrm{x_i}}{\delta_{\mathrm{i}}}$$
$$\mathrm{i} = 1,2,\ldots,\ \mathrm{n};\ \ \mathrm{j} = 1,2,\ldots\ \mathrm{m}\ ; \tag{1}$$

Where, $\delta = \sqrt{\frac{1}{m-1}\sum_{j=1}^{m}\left(x_{ij} - x_i\right)^2}$ is the variance, $x_i = \frac{1}{m}\sum_{j=1}^{m} x_{ij}$ is the mean.

Based above on, we define the distance d_{ij} between *Zi* and *Zj* as the following formula

$$d_{ij} = \sqrt{\sum_{l=1}^{m}\left(\mathrm{Z}_{il} - Z_{jl}\right)^2} \tag{2}$$

In order to avoid square root operation, we use the squared distance d_{ij}^2 for the distance comparison between points.

2.2 Spatial Index Construction

We use a k-d tree for spatial searching to find the K nearest neighbors and points located within the given radius of a specific point or location. Generally most tools dealing with point clouds are in three dimensions, for our purpose we extend the

spatial index to seven dimensions(7D) which also consider red, green, blue and intensity. So our k-d trees are 7D k-d trees which have seven levels that splits all children on a specific dimension. The main purpose of the k-d tree is to find the closest points and distances at a given point and radius in the clustering process.

2.3 Radius Estimation

Since the DBSCAN clustering method is sensitive to the given neighborhood size, the determine of radius is important to the clustering results. An initial value for the radius can be determined by a k-distance graph. The k-distance is the distance of the object A to the kth nearest neighbor. The mean k-distance of every point in the standardized data can be calculated by statistic method. As a rule of thumb, k can be derived from the number of dimensions d in the data set, as k>=d+1.With the estimated radius, most major object could be segmented. If the segmentation results are not detailed enough, for example, roads and trees are classified to one cluster, then decrease the radius, otherwise increase it. After a few tests, a proper searching radius can be determined for that point cloud data segmentation. It is an efficient way for the determination of the radius.

2.4 Clustering Segmentation

The cluster definition of DBSCAN is based on the notion of density reachability. Basically, a point P is directly density-reachable from a point Q if it is not farther away than a given distance D (i.e., is a part of its neighborhood), and if P is surrounded by sufficient points, then P and Q are belong to the same cluster. A cluster, which is a subset of the points of the database, satisfies two properties:

1) All points within the cluster are mutually density-connected.
2) If a point is density-connected to any point of the cluster, it is part of the cluster as well.

We add the MaxPts parameter to avoid all points fall into one cluster. The pseudocode is as follows:

```
DBSCAN(D, Radius, MinPts, MaxPts){
   C = 0
   for each unvisited point P in dataset D{
      mark P as visited
      NeighborPts = regionQuery(P, Radius)
      if sizeof(NeighborPts) < MinPts
         mark P as NOISE
      else{
         C = next cluster
         expandCluster(P, NeighborPts, C, Radius, MinPts,
MaxPts)
      }
}
}
```

```
expandCluster(P, NeighborPts, C, Radius, MinPts, MaxPts){
   add P to cluster C
   if sizeof(C) >=MaxPts
      return
   for each point P' in NeighborPts
      if P' is not visited{
         mark P' as visited
         NeighborPts' = regionQuery(P', Radius)
         if sizeof(NeighborPts') >= MinPts
            NeighborPts = NeighborPts joined with
NeighborPts'
      }
      if P' is not yet member of any cluster{
         add P' to cluster C
         if sizeof(C) >=MaxPts
            return
      }
}
regionQuery(P, Radius){
   return all points within P's Radius –neighborhood
}
```

2.5 Reflect to Original Data

Since the clustering segmentation is carried out on the standardized data, the result has to be reflect to the original data. The results record the point indices that fall into the same cluster and we use the indices to classify the original data into clusters.

2.6 Building Detection

After the segmentation, the point cloud data is segmented into many classes. The classes with the most number of points are always roads and trees. Besides these two classes, the rest are almost buildings and roofs. So, we select these classes as buildings.

2.7 Outline Extraction

We project the data to 2D to detect the borders. Computing the convex hull means that a non-ambiguous and efficient representation of the required convex shape is constructed. In a plane, consider the general case when the input to the algorithm is a finite unordered set of points on a Cartesian plane. An important special case in which the points are given in the order of traversal of a simple polygon's boundary is described later in a separate subsection.

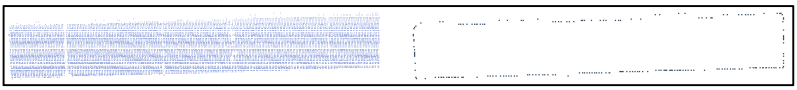

Fig. 3. The outline extraction

2.8 Model Generation

Building roof lines can be generated from the outline points, and the lines can be used to generate the roof polygon. With the height value, rough 3D building models can be generated.

3 Experimental Results

Experiments were carried out in the following section in a Microsoft Visual C++ 2010 environment to validate the proposed approach using airborne and mobile LAS data. The geographical location of airborne dataset is at the City of Baltimore, Maryland, US(NOAA Coastal Services Center, http://www.csc.noaa.gov/lidar). The data was acquired by a Leica Airborne Laser Scanner Model ALS 50 which was used in a Sanborn Aero Commander 500B to acquire the data. The point cloud data have spatial position, echo intensity and color information. Although the DBSCAN algorithm can deal with noisy data, we still had the data filtered in order to have a more accurate statistic results.

3.1 Segmentation

The test point cloud data shown in Fig.5(a) is rendered with color information. This simple scene comprises a baseball field, some tall and low buildings, roads and treeswith3388214 points.. The dataset have been standardized and the result is shown in Fig.5 (b), which is rendered with z value. In order to get the radius properly set, we statistic the k-distance of each standardized point and the statistical result is shown in Fig.4. We tested with radius from 0.06 to 0.16 and found the best result was with the

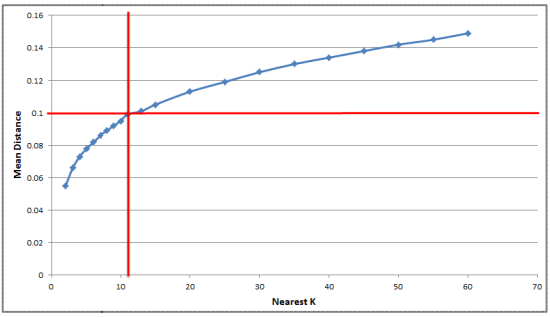

Fig. 4. The mean distance of KNN(k nearest neighbors): the best radius and k is indicated in red line(k=11, d=0.1)

radius setting to 0.1 which is shown by the red line in Fig.4 . The standardized data segmentation result is shown in Fig.5 (c). The final step is reflecting the standardized data segmentation result to the original data which is shown in Fig.5 (d). The result has 87 clusters with the min number of points setting to 2000 and the max setting to 1000000. In the result, the roofs, roads and trees are segmented. In the baseball field, even chairs and the outline of the field are segmented clearly which could be hard to segment only by spatial position.

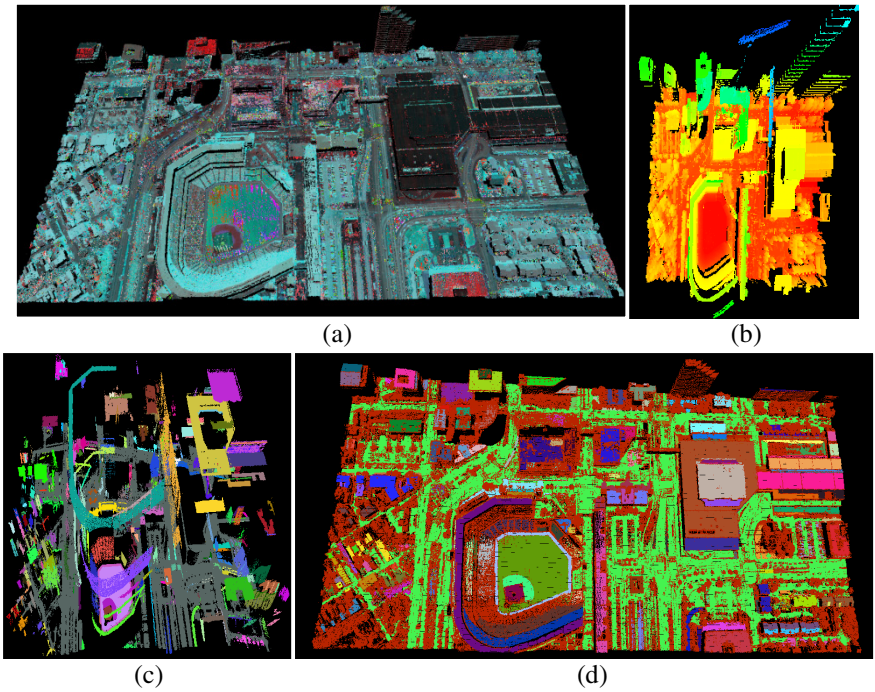

Fig. 5. Airborne scanning data segmentation: (a) original ALS50 data, (b) standardized data, (c) segmentation result of standardized data (radius 0.1), (d)final segmentation result

The computation time consumption depends on the number of points, the radius and the max points of k-d tree leaf. In the two experiments, we set the max points per leaf to 15. The nearer k is to 15, the faster in the segmentation process. In the first experiments, the K is 13 according to the best radius and the computation time is about 2 minutes with 3 million points. Meanwhile in the second experiment, the K is 8 and the computation time is about 3 minutes with only 1 million points. The further K to the max points per leaf, the more time it will take for the segmentation. All experiments has been done on a laptop PC equipped with an Intel Core i7 M 640 Duo 2.80 GHz processor and 8GB RAM.

3.2 Building Detection and Outline Extraction

After the segmentation, the point cloud data is segmented into many classes. The classes with the most number of points are always roads and trees. Besides these two classes, the rest are almost buildings and roofs as shown in Fig.6(a). So, we select these classes as buildings. Then the outline of roofs are extracted as shown in Fig.6(b). Building roof lines can be generated from the outline points, and the lines can be used to generate the roof polygon. With the height value, rough 3D building models can be generated which is shown in Fig.6(c).

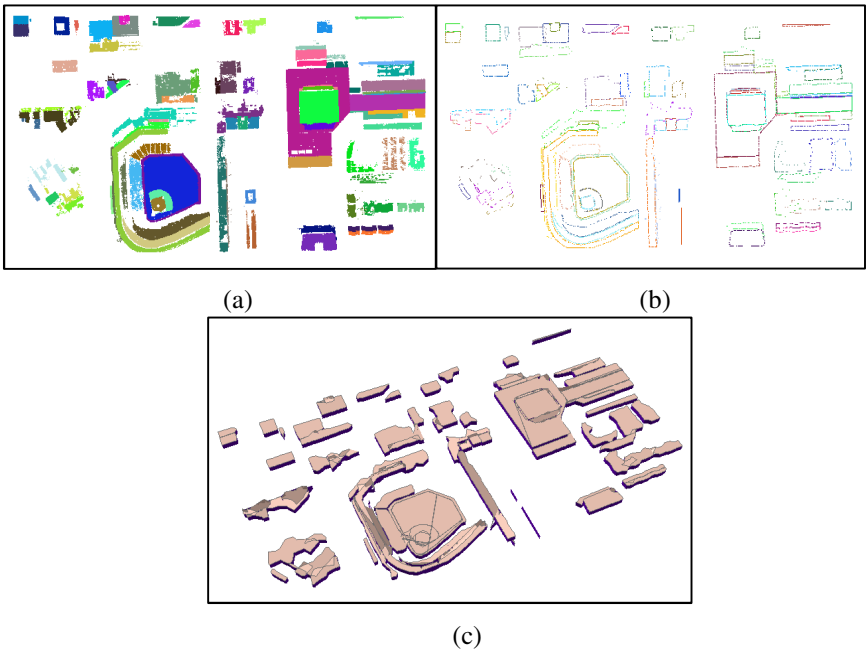

Fig. 6. Building detection and model construction: (a) the building segmentation results, (b) the outline of building roof, (c) the rough 3d model of buildings

4 Conclusion and Future Work

In this paper, we present a simple but efficient and robust approach for the laser scanning data segmentation. The experimental results confirm the validity of the proposed approach. This segmentation technique has several advantages. Firstly, it combines the spatial position with color information and echo intensity which makes the segmentation results more accurate. Secondly, it uses the k-distance method to find the best radius for the DBSCAN clustering algorithm. Based on the segmentation results, building are detected and the roof outlines are extracted Finally, rough 3D building model are automatically generated.

Future research work will focused on the refinement of building detection and outline extraction, and dealing with more roof shapes. We consider that this step may be improved by several segmentation processes and extraction method in the future.

Acknowledgements. Supported By the Key Laboratory of Surveying and Mapping Technology on Island and Reef, National Administration of Surveying, Mapping and Geoinformation (2011A04). The authors are grateful to their colleagues for their constructive comments and suggestions in writing this article.

References

1. Morgan, M., Tempfli, K.: Automatic building extraction from airborne laser scanning data. International Archives of Photogrammetry and Remote Sensing 33(B3/2; pt. 3), 616–623 (2000)
2. Pu, S., Vosselman, G.: Automatic extraction of building features from terrestrial laser scanning. International Archives of Photogrammetry, Remote Sensing and Spatial Information Sciences 36(5), 25–27 (2006)
3. Rutzinger, M., et al.: Automatic extraction of vertical walls from mobile and airborne laser scanning data. The International Archives of Photogrammetry, Remote Sensing and Spatial Information Sciences 38(pt. 3), W8 (2009)
4. Dorninger, P., Pfeifer, N.: A comprehensive automated 3D approach for building extraction, reconstruction, and regularization from airborne laser scanning point clouds. Sensors 8(11), 7323–7343 (2008)
5. Hu, J., You, S., Neumann, U.: Approaches to large-scale urban modeling. IEEE Computer Graphics and Applications 23(6), 62–69 (2003)
6. Filin, S.: Surface clustering from airborne laser scanning data. International Archives of Photogrammetry Remote Sensing and Spatial Information Sciences 34(3/A), 119–124 (2002)
7. Jiang, B.: Extraction of Spatial Objects from Laser-Scanning data using a clustering technique (2004)
8. Roggero, M.: Airborne laser scanning-clustering in raw data. International Archives of Photogrammetry Remote Sensing and Spatial Information Sciences 34(3/W4), 227–232 (2001)
9. Morsdorf, F., et al.: Clustering in airborne laser scanning raw data for segmentation of single trees. International Archives of the Photogrammetry, Remote Sensing and Spatial Information Sciences 34(pt. 3), W13 (2003)
10. Martin Ester, H.-P.K., Jörg, S.: A density-based algorithm for discovering clusters in large spatial databases with noise (1996)
11. Biosca, J.M., Lerma, J.L.: Unsupervised robust planar segmentation of terrestrial laser scanner point clouds based on fuzzy clustering methods. ISPRS Journal of Photogrammetry and Remote Sensing 63(1), 84–98 (2008)
12. Tokunaga, M., Vu, T.T.: Clustering method to extract buildings from airborne laser data. IEEE (2007)
13. Roggero, M.: Object segmentation with region growing and principal component analysis. International Archives of Photogrammetry Remote Sensing and Spatial Information Sciences 34(3/A), 289–294 (2002)
14. Ester, M., et al.: A density-based algorithm for discovering clusters in large spatial databases with noise. In: Proceedings of the 2nd International Conference on Knowledge Discovery and Data Mining. AAAI Press (1996)

The Applications of Spatial and Emerging Information Technologies in Resource and Environmental Auditing

Biao Zhong[1,2,*], Xinyi Xia[1], Kunlei Hou[3], and Yigong Shi[4]

[1] Nanjing Audit University, School of International Auditing, JiangSu Nanjing 211815
bongreat@gmail.com
[2] National Audit Office of P.R. China, Wuhan Branch, Environmental and Financial Section, HuBei Wuhan 430071
[3] Agricultural Bank of China. HanZhong Branch, ShanXi HanZhong 610700
[4] Deloitte Touche Tohmatsu CPA Ltd. Suzhou Branch, JiangSu SuZhou 215000

Abstract. Environmental problems in China are urgent so that resource and environmental auditing is becoming more and more important. The objectives of this study are to introduce spatial and emerging information technologies and its applications in resource and environmental auditing. We synthesized characteristics and advantages of GIS applications and auditing application cases, implemented by National Audit Office of P. R. China, Nanjing Branch and Wuhan Branch, from the practice perspective. In the future, spatial information technology combining with emerging information technologies, including Big Data, Internet of Things, Cloud Computing, Augmented Reality (AR) Technique, large distributed and mobile network will improve the reliability of audit evidences and enhance the auditing conclusions and functions, especially resource and environmental auditing.

Keywords: Spatial information technology, Environmental audit, Geographic information system, National Audit Office of P.R. China.

1 Introduction

Environmental auditing is supervision, assessment, and appraisal of environmental management system and environmental problems, duties in the economic activities of government and enterprises in accordance with the law by audit institutions, internal audit institutions and nongovernmental audit organizations [1]. Compared with natural disasters, this definition theoretically emphasizes environment auditing, and enhances the environmental management of government departments and enterprises. The emphasis of civil audit demonstrates that environment auditing will be a brand-new and

* Corresponding author.
No.86 West Yushan Road, Pukou District,
Nanjing, Jiangsu, 211815 P.R. China, and
Shuiguo Lake, Chagang Xiaoqu, Wuchang District,
Wuhan, Hubei, 430071 P.R. China

F. Bian et al. (Eds.): GRMSE 2013, Part I, CCIS 398, pp. 713–722, 2013.
© Springer-Verlag Berlin Heidelberg 2013

booming direction for future nongovernmental audit. It warns enterprises that it is highly possible to suffer the consequences in the near future if they have not paid enough attention to external impacts to the environment caused by business activities.

Spatial and emerging information technologies combines geographic information system (GIS), global positioning system (GPS), remote sensing (RS), Big Data, Internet of Things, Cloud Computing, Augmented Reality (AR) Technique, communication and network technology. It is also an information technology system that can make all these functions into one, including data observation acquisition from space, data processing, data analysis, and data application. People realize the space of world is stereo, in 3D, so information observed from space is different in nature, as territorial, multidimensional structure and dynamic changes. Compared to traditional two-dimensional data picture, there will be a lot of multi-dimensional spatial data can be used, so more and more people begin to study the spatial information visualization system. The success of two dimensional data model and data structure theory, the progressive development of database theory and technology, graphics theory and other related computer technology, provided the atmosphere for the development of the 3D spatial information technology.

2 Overview and Development Direction of Spatial Information Technology

Nowadays, the information technology has developed continuously. As one of massive information source and state-of-the-art technology, geographic information becomes more and more important. Geographic Information System (GIS) is a system used to collect, store, check, operate, analyze, and display geographic data. It is also a collection of tools used to collect, store, query, transform, and display spatial data. Currently, GIS has been successfully applied to fields of national defense, transportation, environment, etc. It also demonstrates the broad prospects in the area of practice, and gradually becomes one of high-tech hot points.

In recent years, with the development of advantages of GIS, its application tends to be diversified, and gets a lot of attention and rapid development. At the same time, the rapid development of computer science and other sciences also offer GIS advanced research tools and analysis methods. A number of high-tech have been applied to GIS, including remote sensing, infrared and radar technology, three-dimensional technology, artificial intelligence technology and Geographic Position System, which greatly promoted the development of GIS and other related technology.

2.1 Remote Sensing

Remote Sensing is an integrated technology based on principles of transmission and reflection of electromagnetic wave, such as visible light and infrared. Collect and process electromagnetic waves information of target radiation by reusing sensor or other receiving instrument in order to detect and identify all the objects on the ground and image [3]. After decades of research and development, Remote Sensing has been

applied to many fields including general investigation of earth resources, land planning, ocean research, environmental monitoring, pollution analysis, aerial photography, etc. Among them, the application to the fields of earth resources, ocean, pollution and environmental monitoring has become the base of GIS. Remote Sensing is the base and important data source of modern GIS.

2.2 Infrared and Radar Technology

The so-called infrared, refers to electromagnetic waves that all objects can radiate but human eyes are unable to distinguish and identify in nature. Because of its universality, images can be displayed according to objects to be tested and the infrared difference radiated by its background. This image is called heat map. In addition, infrared imaging has been applied to more and more fields with advantages of long operation distance, good anti-interference and penetration ability, and all day work ability, etc[4]. GIS is one of these fields. Because of the maturity of infrared technology, the gradual decline of the cost and all the advantages above, infrared technology has become an essential part of today's GIS. Radar is a typical representative of the application of infrared technology. Modern radar is based on the time difference of infrared emission and acceptance, with attitude data collected by the scanner and other equipment to get the 3D data of the target detected, and then combined the echoed signal returned by monitoring objectives, in order to achieve the effect of precise imaging.

2.3 3D Technology

Three-dimensions space refers to 3 coordinate axes which are two mutually perpendicular, respectively saying left and right space, upper and lower space and front and rear space, and this enables human vision a three-dimension effect. After years of rapid development and wide application, 3D technology has been increasingly popular and mature. There is a growing tendency for 3D that 3D replaces 2D, solids substitute for flat surface and virtual simulation of reality. GIS is no exception for it keeps up with the pace of the times and absorbs the essence of 3D technology for its own. 3D GIS enable it to be more intuitive and visual based on the face to face technology. For example, the GOOGLE EARTH software (http://www.google.com/earth/index.html) has completely adopted 3D technology and it can simulate a 3D earth fully and really. Obviously, 3D technology helps GIS better meet the requirements of users. Imagine an environment auditing with 3D GIS, is remote audit no longer a dream?

2.4 Artificial Intelligence Technology

Artificial Intelligence Technology is the technology of theory, method, technology and application system that uses computer technology to simulate and expound human intelligence. It understands the essence of human intelligence, and then let the computer simulate and respond to external information by the way of human intelligence. The main research areas of Artificial Intelligence Technology are

intelligent robots, voice and image recognition, etc [5, 6]. Image recognition technology is applied to GIS and other areas. Combined with GIS, it obviously enhances the ability of GIS in independent problem-solving, reasoning and decision-making, knowledge representation and application. In term of environmental protection, Artificial Intelligence Technology not only enables GIS intelligently process, analyzes and researches massive geographic data, but also makes GIS solve some complicated practical problems intelligently.

2.5 Geographic Position System

Geographic Position System (GPS) is the technology that comprehensively uses satellite to research, analyze and solve problems. The basic principle is to measure the distance between target and satellite, and work out the specific location of target by comprehensively analyzing the data of distances between several satellites and target. With the advantages of all weather, high precision, high efficiency and automation, GPS, as advanced measurement tools and new productivity, has been applied to multiple high-tech fields including GIS. With the end of the Cold War, the U.S. government gradually canceled SA policy, and GPS has been widely used. The position of ordinary commercial has increased within 1 m. This highly precise, highly developed GPS also makes GIS more mature and perfect [7].

In short, GIS can be combined with a number of high technology and need the co-existence with various sub-technologies. Currently, it has achieved successful application in many important areas related to national economy, such as national defense, planning, transportation, and monitoring. Nowadays, with the increasingly strengthening of people's awareness of environmental protection, environment auditing has risen to a more and more position, and all the advantages of geographic information technology will greatly promote the progress and development.

3 Characteristics and Advantages of GIS Applications in Resource and Environmental Auditing

3.1 Strong Spatial Data Management Ability

Prosperous application of GIS makes collect and process massive geographic information more efficiently, fast and timely. Though analysis and processing, these geographic information can get further geographic data, spatial data, attribute data and other information. Massive geographic information is needed in current environmental auditing, so it requires collection, statistics, processing, analysis and output to a huge number and various geographic information data. In this situation, traditional technology appears to lack the sense of space, and may even hinder the management, query, and analysis of geographic information to some extent. However, GIS reflects the advantages in these aspects as efficiency and timeliness. For instance, GIS can effectively monitor air quality, water quality, and soil quality, but also it can make a more in-depth statistical and analysis to the collected geographic information and

environmental information. In addition, by comparing the change in time and space distribution of geographic information, analyzing different geographic data, GIS realizes the interactive management of geographic information and other information. According to the specific requirements of users, data are output by the forms of charts or other visual forms, which make a large number of original abstract and boring data, become more intuitive and easy to understand. GIS has been already quite mature in data processing and management [8].

3.2 Visualization and Digitalization

The digitized GIS has a variety of features. Firstly, the traditional ordinary paper map only has the information of fixed positions, such as traffic map and administrative map. However, GIS can convert the information into a digital format, and complete the reading and processing of digitalization and geographic information with the software and other tools. Secondly, another important function of GIS is making and displaying 3D digital images, which are produced by various advanced technology. An advanced complete GIS like a digital system, and almost all the shift of images can be done automatically. Finally, in order to enrich data diversity, GIS has lots of data input systems to allow other important data source to provide information, such as image acquisition devices of other databases, scanners and digital cameras, as well as directly from the paper materials (such as map or aerial camera) into geographic information in GIS[9].

The visualization of GIS is mainly in the aspect of cartographic display system, which is a simulated production system aimed at geographic environment. Based on needs of users, it selects appropriate data and material from database, such as spatial characteristics, spatial attributes and other spatial and geographic data. Then quickly generate images on the screen or other output devices according to the information, or use some other devices for image files in order to eventually reach the visual and intuitive results, for instance, electrostatic plotters, pen plotters and printers, etc.

3.3 GIS Database Systems and Spatial Analysis Functions

GIS is a database system with high comprehensiveness and better management ability. In order to make geographic information easier to manage, analyze and develop, GIS will stratify data when creating database. GIS classifies different geographic information according to the nature; the same nature merges together to form a data layer, and all the data layers finally combines into a complete database. This form makes the use of data flexible and convenient. For instance, search for the associated data layer according to user's requirements, and then extract the required data quickly and efficiently. In addition, the analysis results are expressed by the new image based on original data after spatial function change, and the spatial orientation is still consistent with the original data, which can only be realized based on the database system.

The space function transform has a lot of advantages in practical applications; it can be used for overlay analysis, buffer analysis, topological space query, empty set analysis and other complex analysis. In terms of environmental protection, for

example, it can be used to analyze the destruction of soil resource caused by soil erosion, as well as in the so-called regional environmental quality evaluation, to improve the comprehensiveness and reflect the condition of regional pollution as well as the spatial distribution state [10]. The new Earthquake Protection and Disaster Reduction System in Japan after earthquake is a good example. It is a digital map database based on the geographic information including topography, geology and faults, then overlay analyze the geographic information for useful information about earthquake emergency. This system also uses ARCGIS to evaluate the influence of post-earthquake, so as to take timely and effective measures after disaster, and reduce the number of casualties and losses as much as possible. All these are benefits of GIS database; therefore, only a database system can keep up with the trend of the times.

3.4 Advantages of GIS in Environmental Protection and Environmental Auditing

GIS applications in the area of environment include environmental management, environmental impact assessment, pollution analysis, environmental monitoring and auditing, etc.

3.4.1 Environmental Management

With the rapid development of economy, environmental protection has become increasingly important, and it also draws more and more attention, so the environmental protection department has to take heavy task. In order to get rid of the increasingly heavy work of labor statistics and handmade charts, more advanced technology is needed. In this trend, the powerful data management ability of GIS makes it the best choice. GIS can manage the essential data and professional chart scientifically and effectively, which serves the following statistics, analysis and cartography. Combined with the current highly developed computer technology, referring to environment, an environmental management system of practicality, targeted, flexibility, autonomy is formed. Turk [11] proposed several years ago that environmental management is a complex task that should be highly normative, scientific and procedural. GIS is such a spatial decision support system that the operation and results are usually visual, and it enables the environmental management task easier. At the same time, Cinderby [12] also pointed out that the use of GIS combined with traditional geographic data can improve researcher's insight and understanding of the environment, and further improve the effect of the environmental management. All these researches and cases prove that GIS has become an indispensable part of environmental management.

3.4.2 Environmental Impact Assessment

Environmental Impact Assessment is to evaluate the damage and impact on surroundings of some development plans as well as the construction. Surrounding environment includes not only the natural environment, but also the broad social environment; covers not only the impact on the environment, but also the assessment of the impact on the production, dissemination, diffusion and the degree of harm. This cannot be achieved by traditional technology. As a database, GIS, it can process

massive data and information; therefore, it is suitable for current requirement and can assist the government to do the work of Environmental Impact Assessment.

When dealing with the case of Environmental Impact Assessment in Israel, Haklay et al. [13] adopted the method of GIS. They focused on the research of identifying the environmental impact by using GIS, and analyzed the necessity of GIS in the Environmental Impact Assessment, which gradually promoted GIS to become the basic tools of Environmental Impact Assessment.

3.4.3 Pollution Analysis

The main research of Pollution Analysis is non-point-source pollution, the focus and hotspot of current environmental research, which refers to a type of pollution that covers a large range and complex causes. Two years ago, serious consequences of the oil spill in the Gulf of Mexico of the United States have been a serious threat to the ecological environment of the Gulf of Mexico. That even had an impact across the Atlantic, and endangered the survival of birds, fish and other animals. U.S. Environmental Protection Agency urgently made the "National Emergency Plans on Oil and Toxic Substances". Lsserre[14] and others from the Poitiers University in Germany researched and developed a model of nitrate in groundwater movement and migration in the GIS environment. Although the model is relatively simple, only considering the convection migration of the nitrate, by comparing with a more complete model of groundwater---MT3D-MODFLOW, the similarity of the result sufficiently proved the accuracy of the model in GIS environment, and it also showed that GIS will have a bright prospect in the application of pollution analysis.

3.4.4 Environmental Monitoring and Auditing

With the help of GIS, the government can collect, store and analyze environmental information real-time, which enhances the efficiency and effectiveness of government in environmental monitoring. The information is also the important material and original evidence in the following environmental auditing. In addition, in other areas, such as air quality monitoring and auditing, GIS also plays a very important role. Last century, researchers in Chinese Geosciences University entered a mass of air quality data. On this base, efficient and practical information query and air quality assessment function were achieved, which solved the main problems of air quality assessment and auditing, and they put forward a new method based on GIS air quality assessment.

In the cases of 2009 and 2013, Nanjing Branch Office and Wuhan Branch Office of National Audit Office of P. R. China chose ArcGIS as the main tool after comprehensively considering the actual situation and audit plans. In the case of land resource audit at Quzhou and Lishui of Zhejiang province, China in 2009, auditors of National Audit Office of P. R. China, Nanjing Branch Office analyzed information demands according to audit targets, and combined with the available database, previous materials of the Second National Land Survey, so as to find out the direction of audit with GIS. National Audit Office of P. R. China, Wuhan Branch Office utilized GIS to assistant land resource auditing at HuBei Province in 2013. We used ArcGIS and Google Earth to locate specific ore coordinates and verified values of ore and other resources at HuBei Province, China.

4 Trends and Outlook of Emerging New Technologies

In the future, Augmented Reality (AR) Technique, large distributed network and mobile information technology will develop rapidly. New spatial information products will follow the development of three-dimension. Three-dimensional data acquisition and detectable mass data in the dynamic visualization will have good prospects.

Based on the development of BIG Data, Internet of Things, Cloud Computing, and communications technology, combining with the advantages of satellite, aerospace, ground sensing, we can build a three-dimensional monitoring system with fully functional set of remote sensing, communications, navigation and positioning, which has become a modern spatial information technology development trend. Such a comprehensive multi-faceted monitoring system can acquire macro, precision remote sensing information to achieve a variety of topics and update the database quickly.

4.1 Big Data, Internet of Things, and Auditing

Before the concepts of Big Data, personal data is usually ignored by people. Corporate data gets more attention. With the development of Internet and social network, data come from personal computer users has a booming trend, including network logs, traffic and telephone records, medical records, sensors and monitoring cameras. By digging into these data, people will produce a great intrinsic value.

In Chinese market, from the "Twelfth Five-Year Plan", government promote the information processing technology as a key technical innovation projects, which include mass data storage, data mining, intelligent analysis of video images, all of these are playing an important role of the big data. And the other three key technological innovation projects, including information sensing technology, information transmission technology, information security technology, are closely associated with Big Data and Internet of Things.

Therefore, Chinese audit should establish large data utilization system. Fully analyzing the mass data storage, mining potential functions, simplifying the workload and improving audit efficiency.

4.2 Cloud Computing and Augmented Reality Technology's Impact on Auditing

Cloud computing is a combination of network and traditional method of calculation. It will change the basis of entire network calculating and optimize resources. Augmented reality technology is a technology which overlay the real world with scientific simulated taste and sound which is hard to feel by human sensory. By using GPS, orientation sensors, we can insert map into reality landscape directly and monitor the real environment. These techniques are changing the shape of information, definitions of information and methods of information dissemination, and even the structure of information. Cloud computing optimized information function, augmented reality technology also provided a method for utilizing complex information. In the future,

information technology will continue to develop, and spatial information technology is one of the integral parts of it. It is the development of spatial information technology and scientific research applications that provides other cutting-edge technology with three-dimensional structure information.

5 Conclusions

In order to maintain the superiority authority and oversight of the audit, auditing should combines with emerging new information technology, and make spatial information technology better serve our audit services. It will help auditing expand its working range and improve the efficiency. Spatial information technology will merge with more subjects and industries quickly. It will play a landmark leap. It will improve the reliability of audit evidences and enhance the auditing conclusions and functions, especially resource and environmental auditing.

Acknowledgements. This research was supported by Basic Research Program (Natural Science Foundation) Funded Project of JiangSu Province, China (Contract No.: BK2012473), a Project Funded by the Priority Academic Program Development of JiangSu Higher Education Institutions (Audit Science and Technology Preliminary Research Project (Contract No.: YSXKKT27)), National Science Foundation of China (Contract No.: 71273127) and National Social Science Foundation of China (Contract No.: 11BGL062).

References

1. Li, X., Yang, Z.H.: Rerecognition of the definition of environment auditing. Journal of Nanjing Audit University 1, 62–66 (2001) (in Chinese)
2. Wu, X.C.: Basic technology and development of GIS. Geosciences: Journal of China University of Geosciences 4, 329–333 (1998) (in Chinese)
3. Li, D.R.: Digital earth and "3S" technology. China Surveying and Mapping 2, 28–31 (2003) (in Chinese)
4. Wang, Y.Y., Zhang, Y.S., Hua, Y.W.: Analysis of infrared target detecting methods. Infrared Technology 3, 133–136 (2011) (in Chinese)
5. Chen, X.: Researches on artificial intelligence technology in GIS applications. Journal of Graduate Students of Sun Yat-sen University 1, 77–86 (2007)
6. Ren, J., Peng, W.: Analysis of artificial intelligence technology. Education Science & Culture 2, 83–84 (2010) (in Chinese)
7. Hong, Z.J.: GPS (Geographic Position System) applications in ocean surveying. Ocean and Fishery 8, 25–26 (2008) (in Chinese)
8. Liu, Y., Jing, W.T.: GIS and its applications in environmental science. Environment Science 18(2), 62–65 (1997) (in Chinese)
9. Li, J.B.: GIS applications in hospital management. Southwest National Defense Medical 5, 539–540 (2005) (in Chinese)
10. Cao, Y., Hu, G.D.: GIS application status at home and abroad. China Surveying and Mapping 2, 32–33 (in Chinese)

11. Turk, A. Visualization in environmental management: Beyond the buzz word. Landscape and Urban Planning (4), 253–255 (1992)
12. Cinderby, S.: GIS for participation: The future of environmental GIS. International Journal of Environment and Pollution (3), 304–315 (1999)
13. Haklay, M., Feitelson, E., Doytsher, Y.: The potential of a GIS - based scoping system: An israeli proposal and case study. Environmental Impact Assessment Review (9), 439–459 (1998)
14. Lasserre, F., Razack, M., Banton, O.: GIS - linked model for the assessment of nitrate contamination in groundwater. Journal of Hydrology (3), 81–90 (1999); (4), 164–180

A Heterogeneous Web Service Integration Method Based on Middleware

Jie He[1,*], Nengcheng Chen[2], and Wenbao Mi[1]

[1] School of Resource and Environment, Ningxia University,
489 Helanshan West Road, Yinchuan 750021, China
whuhejie@yahoo.com.cn
[2] State Key Laboratory of Information Engineering in Surveying, Mapping and Remote Sensing,
Wuhan University, 129 Luoyu Road, Wuhan 430079, China
cnc@whu.edu.cn

Abstract. Due to directly access and interoperate between different types of web services can't be achieved currently, different versions of the same type of web services through a consultation mechanism to access in an integrated way cause the problem of version inconsistency and the problem of poor reliability. In order to integrate heterogeneous web service efficiently, in this paper, we designed a service middleware to integrate heterogeneous web service trough the used of dynamical schema matching and automatic information retrieval and intelligent data fusion. Firstly, a semantic schema matching method is applied on heterogeneous web service schemas to get the exactly mappings between those schemas, then the matching results is used to design information retrieval and document transformation rules, for different type of services, different data fusion operations is designed. Finally, experiments is done on the integration of multi-version Web Feature Service (WFS) , the integration of multi-version Web Coverage Service (WCS) . And the integration on different type web services is also done between WFS and SOS. Experimental results show that the method is feasible.

Keywords: version negotiation, semantic schema matching, information retrieval, data fusion.

1 Introduction

In order to achieve the spatial information sharing and interoperability, there are many international organizations such as the OGC, ISO/TC211, FGDC are working to develop a series of standards and norms, such as Web Service-based technology, OGC proposes seamless online geographic information processing services and location-based services framework (OWS), which provides a series of abstract specifications and implementation specifications, such as the Web Feature Service (WFS) [1], Web Coverage Service (WCS) [2], Sensor Observation Service

* Corresponding author.

F. Bian et al. (Eds.): GRMSE 2013, Part I, CCIS 398, pp. 723–736, 2013.
© Springer-Verlag Berlin Heidelberg 2013

specification (SOS) [3], and for different types of web services sharing and interoperability in technology to a certain extent. Many international organizations and institutions have also begun the geospatial information interoperability substantive research. Project funded by the European Union (ECDG- Ⅲ) GIPSIE (GIS Interoperability Project Stimulating the Industry in Europe) [4], presided over by the United States National Geographic Information and Analysis Center (NCGIA), the National Science Foundation-funded Varenius project [5], and the DISGIS project completed by the Norwegian Bureau of Surveying and Mapping units [6]. And there are a lot of organizations have developed a variety of web services products, such as the GeoTools[1], Deegree[2], GeoServer[3] and GeoSurf[4] software, etc. Different products realize web service capabilities differ, not all type of web service, every version of a type of web service can achieve. So far, the interoperability between heterogeneous web services (i.e, homogeneous and heterogeneous web services) is still a problem for further study, such as different types of web services (heterogeneous network services) can't be achieved directly interoperable. Access to different versions of the same types of services (homogeneous web service) only by a version negotiation mechanism to achieve a mutually acceptable version of the service, but this mechanism has two major drawbacks: 1. can't meet the user accurate version of the service request; 2. Poor reliability, there is a potential risk of negotiation failure. According to the problems exist currently in integrate heterogeneous web services, resulting in a number of different solutions, such as literature [7, 8] proposed a general geographic data integration framework to access and extract heterogeneous geographic data sources, through the use of dynamic synthesis operation to integrate geographic data. An ontology-driven geographic information systems is proposed in [9], through the ontology to reduce the heterogeneity between the heterogeneous web services or data. A geographic ontology integration method proposed in the literature [10], while the design of geographic ontology matcher named G-Match to match the integrated geographic ontologies. Due to the definition of ontology elements concept in different granularity, the weighting factor calculated dependent on the input ontology itself. SWING (Semantic Web-Service Interoperability for Geospatial Decision Making) [11] provides an open, easy-to-use semantic network services framework for ontology and reasoning tools to annotation, discovery, composition and invocation of web services. Thus ,current web service integration method rely on ontology matching, and the ontology is usually domain-oriented, lack of generic efficient ontology matching methods. Unfortunately, so far, the web service matching problem has not been solved by OAEI (OntologyAlignment Evaluation Initiative).

Based on the above background, this paper presents a heterogeneous web service integration method based on dynamic semantic schema matching and automatic information retrieval and fusion. The central idea including: 1) the exact schema matching [11, 12, 13, 14, 15]. Using a semantic schema matching method based on

[1] http://www.geotools.org/
[2] http://www.deegree.org/
[3] http://www.geoserver.org/
[4] http://www.lmars.whu.edu.cn/prof_web/zhuxinyan/my/geosurf.htm

node similarity [16] to achieve an exact match for heterogeneous web services schema; 2) automatic information retrieval and data fusion. Semantic schema matching results-based for ① homogeneous web services: schema matching mapping relationship (one-to-one) transformed into a different document information retrieval rules using XSLT and other technologies to achieve efficient conversion between different documents; ② heterogeneous web services: according to the mapping relationship between heterogeneous web service schema elements (one-to-one, one-to-many), to design heterogeneous web service fusion model, realize data been copied, composed, decomposed, converted between heterogeneous web services instance data. Eventually achieve the correct uniform access to heterogeneous web services and efficient integration of them.

This paper mainly discuss the building system how to realize the integration of heterogeneous web services. The architecture, the main components of the system is described in section 2. System implementation is discussed in section 3. Section 4 discusses the experiments and discussion. Finally, section 5 summarizes the conclusions.

2 System Architecture

Fig.1 is the system architecture. The system includes three core components, respectively, is the mapping generator, the document transformer and data fuser. Mapping generator is designed to achieve exact match for heterogeneous web services model; document transformer is to achieve automatic conversion and integration of the different versions of homogeneity web service instance; data fuser is designed to realize the integration of heterogeneous web service instance data. For the same version of the same types of service requests can be directly dispatched to the server to implement a service request, the integrated access to the services of the different versions of the same type service including two steps, the one is schema matching between different versions of service schemas, and the other is information extraction and conversion between different documents. In the first step, a semantic schema matching method is applied to generate the element alignments (mappings) between two schemas (instance). In the second step, these mappings are generated into a series of information extraction rules, which used to retrieve data from the source schema and fill to the destination schema. And at last, an evaluation is done to check whether the mapping algorithm is considering the destination schema constraint condition in order to ensure the generate data will not violate the integrity of the destination schema, and to ensure the precision of information retrieval. For the heterogeneous web services, name is, the different types of services, such SOS and WCS, in addition to the schema translation request, before the service conversion would also like to fuse different information models, such as fusion between O&M result model and GML WCS profile or GML features summary table, and a real-time observation metadata generated from SOS registered in the CSW server into a “objectType”. If the observed results are coverage, the metadata “WCSCoverage” generated; if the observation results are features, “WFSLayer” metadata generated. “WCSCoverage” contains the name of the

data set, the geographic range of data, formats, spatial reference, and resolution. "WFSLayer" contains the data set name, feature type, geographic range, spatial reference. Different types of data fusion operations are designed to integrate heterogeneous service instances intelligently as well.

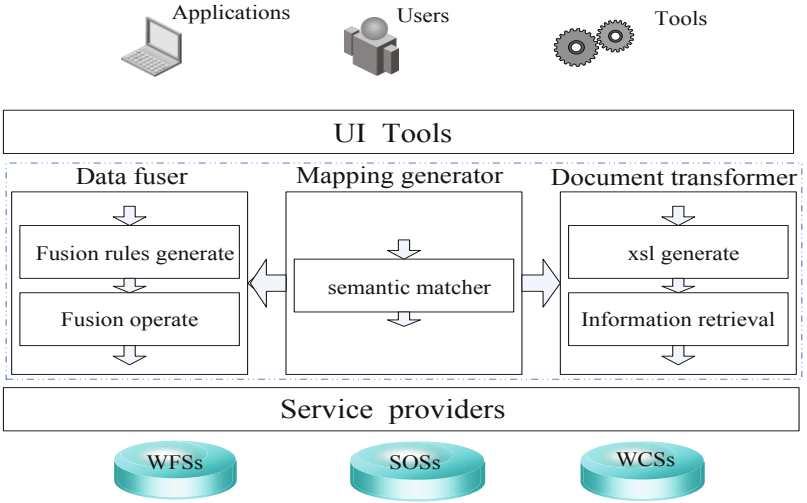

Fig. 1. Architecture of the integration of heterogeneous web services

3 System Implementation

3.1 Schema Matching

Heterogeneous web services schemas are based on different information model which led many semantic heterogeneity problems, such as the same name with different means. If use a syntax-based matching methods are often unable to find these potential semantic mapping relationships, such as elements of "abstract" and "description", semantically corresponding, but can not match in syntax. Therefore, this paper applies a semantic schema matching method proposed in the literature [16]. Fig.2 is the flowchart of semantic schema matching, composed of five steps, they are schema preprocess,comments similarity computation, node concept similarity computation,similarity selection and mappings generation respectively. Due to the differences between the heterogeneous web service schemas led to mapping differences between different service schemas, this difference include: partial match between the two schemas (only some of the elements in the two schemas are correspondent) and the overall match (all the elements in two schemas are associated). For the partial match, a large number of invalid elements involved, not only time consuming, but also increases the chance for errors. In order to maximize the performance of schema matching and to improve match quality, before the matching execution, the matching schemas are divided into fragments and to identify all the

similar fragments and do a fragments match lastly. In this paper, we design a schema segmentation algorithm based on schema tree divide[17]. The process of schema tree segmentation consists of schema tree divide, candidate similar fragments identification and similar fragments output three steps. Firstly , the source schema tree is divided into schema fragements according to the structural of source schema tree, and for each fragment in source schema fragements, we search its similar fragments in the target schema tree, if can not find its correspondent fragments, we apply the same algorithm to divide the target tree, then search similar fragments in target schema fragments, until all source schema fragments have found similar ones in the target schema fragments . The similar schema fragment (subtree) identification is mainly according to whether the root nodes of the two fragments are similar and whether the overall structure of the two fragments are similar [18].

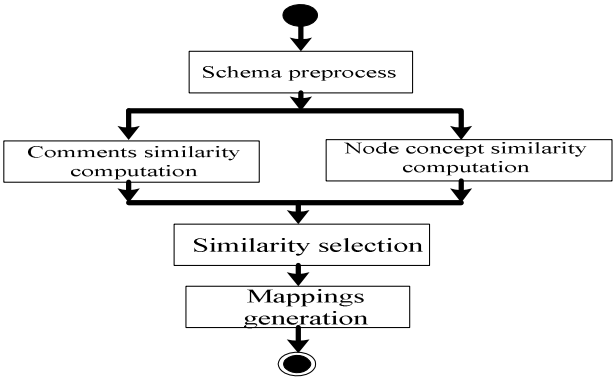

Fig. 2. Process of semantic schema matching

3.2 Automated Information Extraction

The cardinality of correspondence between multi-version homogeneous web services are generally one-to-one relationship, so the integration of homogeneous web services through the use of information extraction and conversion between different versions of web services. Web service instances are XML documents, so take advantage of the existing XML information extraction methods, such as the expansion of full-text information extraction system, or representatives XML standard XPath, XSL, XQuery to handle XML expression and realize information extraction. However, due to the full-text information extraction method does not support index mechanism and can't retrieve more specific elements in the document, so this paper take advantage of schema matching results to generate information extraction rules and form a style sheet file (XSL file). According to information extraction rules (xsl file), apply XSLT Technology we can realize the information retrieval and XML documents transformation. Information extraction rules generation process include: ① mapping path parse and element identification. Separating out the source XML document information extraction path according to the mapping information, separating out the target document node name, node element type, to judge whether the element is

property element or ordinary element; ② style sheet rule tree construction. The build process include: to determine the root of the tree; determine the depth of the tree, and that the maximum number of elements in the mapping path; determine the sub-nodes or sub-trees of each intermediate node; leaf node is the last node element in the path. ③ Format rule tree. Build the rule tree according to the nodes in target path , and get the value path of the text node in terms of the source path.

3.3 Intelligent Data Fusion

Mapping relationships between heterogeneous web services schemas are more complex than the homogeneous web services, in addition to one-to-one relationship, as well as many-to-many or many-to-one relationship, to this end, we transform the complex mapping relationships into data fusion rules between heterogeneous web service instance, and then using the fusion rules generate different fusion operations to realise heterogeneous web service instance information automatic extraction and intelligent integration. The process include：

1. Mapping classification and its nature determination. Firstly, to determine the cardinality of all mappings ; second, for each mapping relationship, determine its property, to know whether they are : ①object attributes, namely description of an object, such as ProviderName ↔ ProviderName in Fig.3; ② geometric properties, relate to the geometric characteristics of elements, such as srsName ↔ srsName; ③ geometric relationships, that is some kind of spatial relationships between geometric elements, shown in Fig.3 surface ↔ values.

2. Fusion operations design. After determine the cardinality and property of the mappings, we can design fusion operations according to mappings. Fig.3 shows the integration between the SOS and WFS service instance. Data fuser through four different operations to achieve the data fusion, include: ① “concat” operation (Concat) , i.e. two or more attribute elements with n: 1 relationship are jointed into a new attribute element; ② “copy” operation(Copy), that is, two attribute elements with 1:1 relationship to achieve data inter-filling and exchange by copying; ③ decomposition operation (Split). For two attributes with 1: n relationship, through a decomposition operation to realize a general attribute be split into several ones and fill in several corresponding sub attribute; ④ transform operation (Transform). Transform operation occurs in a heterogeneous web service instance data has a certain n: 1 relationship in the geometric space, such as to get WFS features’ geometric information from the observation results of SOS, or integrate features in WFS service instance into the SOS observations. The transformation operation realization process include:

① Determining the time and space of the transformed data. Observational data with time and space characteristics, before the transformation we must determine the time and spatial extent of the transformation data first.

② Determining the starting position for data withdrawal and insertion. When the local service instance data extracted from the global service instance data, data

extraction starting position must be determined, when fusing the local service instance data into the global service instance data, the data insertion position must be determined.

③Determining the transform data spatial reference, and realize data transformation in different coordinate systems.

④Determining the transform data format and realize data conversion between different formats, such as convertion between vector data and raster data, convertion between different vector data, convertion between different raster data.

⑤Other data conversion the user demands.

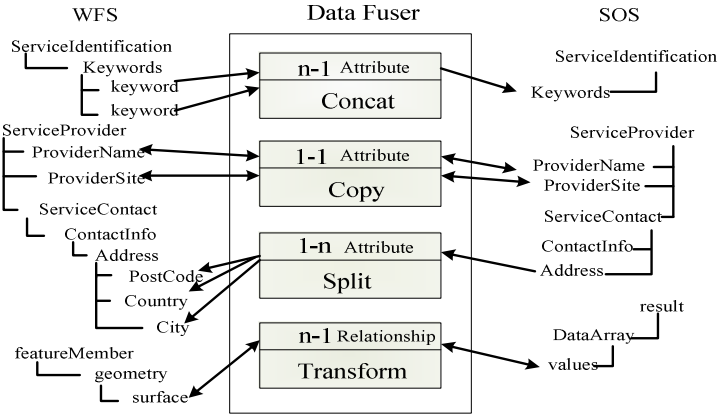

Fig. 3. Data fusion operation

4 Experiments and Discussion

The integration of homogenous web services mainly solve the information model difference caused by different versions service, and through the information retrieval rules generated by XSL generator according to schema matching results, and apply the XSLT document conversion technology to realize documents information automatically extraction and conversion . A multi-version service instance information extraction

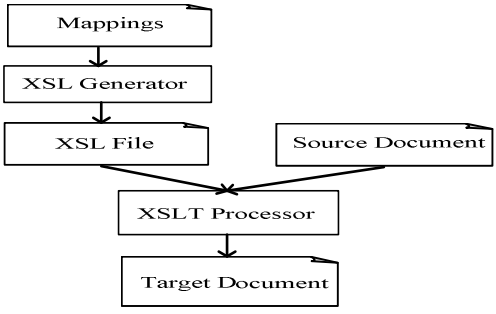

Fig. 4. Process of document information retrieval and transformation

and conversion diagram shows in Fig.4, which mappings are from the results of schema matching components, then mappings are transformed into information extraction rule files generated by the style sheet generator - style sheets. Finally, XSLT processor use style sheets to achieve the conversion from the source document to the target document.

4.1 WFS Multi-version Web Service Instance Information Retrieval and Transformation

The process of XML document transformation by XSLT is divided into two stages: the first stage is the structural transformation, the XSL processor first reads the XML tags and data through parser (DOM or SAX). When the browser read the XML tree structure and data via XML DOM object, the XML tree structure is rearranged and generate a temporary tree, this tree is called the result tree. The second stage is formation. XSL processor to convert the data (formatted) to another well formatted XML document, in

Fig. 5. Transformation between WFS_getFeature service instances

this stage the new structure output in according with the required format. Usually the used XML markup vocabulary is different from the source document. In this paper, WFS server provides is WFS1.0.0 version service, and all other versions of web services will be automatically converted to WFS1.0.0 service instance. The upper half of Fig.5 is parts of WFS_getFeature1.1.0 source XML document, and the lower half of Fig.5 shows parts of the WFS_getFeature1.0.0 target XML document from the information retrieval and transformation over WFS_getFeature1.1.0 document.

4.2 Wcs Multi-version Web Service Instance Information Retrieval and Transformation

In this paper, WCS server serves WCS1.0.0 version service, other versions of WCS instance will be converted into WCS1.0.0 version service through the automatic information retrieval and transformation components. The upper half of Fig.6 is parts of getCoverage1.1.0 source XML document, and the lower half of Fig.6 shows parts of getCoverage1.0.0 target XML document from the integrated conversion over getCoverage1.1.0.

Fig. 6. Transformation between getCoverage service instances

4.3 Experiments on Integration of WCS,WFS and SOS

The WFS web service implementation specification provides operations such as "GetCapabilities", "DescribeFeatureType" and "GetFeature". "GetCapabilities" operation is used to describe a web feature service's capabilities while the "DescribeFeatueType" operation to describe the structure of any feature type a web feature service can service, and the "GetFeature" operation services a request to retrieve feature instance. For SOS, "GetCapabilities" operation provides the ways to access SOS service metadata while the "DescribeSensor" operation to retrieve detailed information about sensors and processes generating those measurements, and the "GetObservation" operation provides access to observations and measurement data via a spatio-temporal query. In this paper, we experiment using WFS "GetCapabilities" operation to get a web feature service capabilities information from the SOS "GetCapabilities" response capability document, and use the "GetFeature" operation to get features of interest from the observational data returned from the response of SOS "GetObservation" operation query requests.

1) SOS "GetCapabilities"->WFS "GetCapabilities"

SOS capability information mainly includes: "ServiceIdentification", "ServiceProvider", "OperationMetadata", "ObservationOfferingList" etc.. "ObservationOfferingList" is composed of multiple "ObservationOffering", and each "ObservationOffering" include: "description", "name", "srsName", "bounderBy", "time", "procedure" and "observedProperty". WFS capability information includes: "ServiceIdentification", "ServiceProvider", "OperationMetadata", "FeatureTypeList", "ServesGMLObjectTypeList", "SupportsGMLObjectTypeList", "Fileter_Capabilities" etc.. "FeatureTypeList" is composed by many "FeatureType", and each "FeatureType" includes: "Name", "Title", "Abstract", "keywords", "DefaultSRS", "OtherSRS", "OutputFormats", "WGS84BoundingBox" etc.. it is not difficult to find, the WFS "ServiceIdentification" and "ServiceProvider" can be mapped up with SOS "ServiceIdentification" and "ServiceProvider", while sub-elements of "FeatureType" are related to those of "ObservationOffering". In this paper, the mapping relationships between SOS "GetCapabilities" and WFS "GetCapabilities" is generated by the semantic matching on the web service schemas of SOS "GetCapabilities" and WFS "GetCapabilities". Fig. 7 shows the semantic matching results.

With matching results, we can extract WFS capability information from SOS capability documents according to the extraction rules generated by the information extract algorithms proposed in second parts. Fig.8 shows the generated extraction rule file. Fig.9 shows parts of WFS capability information document generated from an information extraction and transformation operation on the response XML document of SOS GetCapabilities request. From the WFS capability document , we can see that the related information of "ServiceIdentification", "ServiceProvider" in SOS capability document are extracted and filled to the corresponding element node of WFS capability document, for those sub-elements' instance data of "ObservationOffering" in SOS capability document are extracted and filled into sub-elements , such as "Abstract", "Name", "DefaultSRS", "WGS84BoundingBox" of FeatureType in WFS capability document respectlively. And we can use "GetFeature" operation to extract the elements of interest in according with the information defined in WFS "FeatureType".

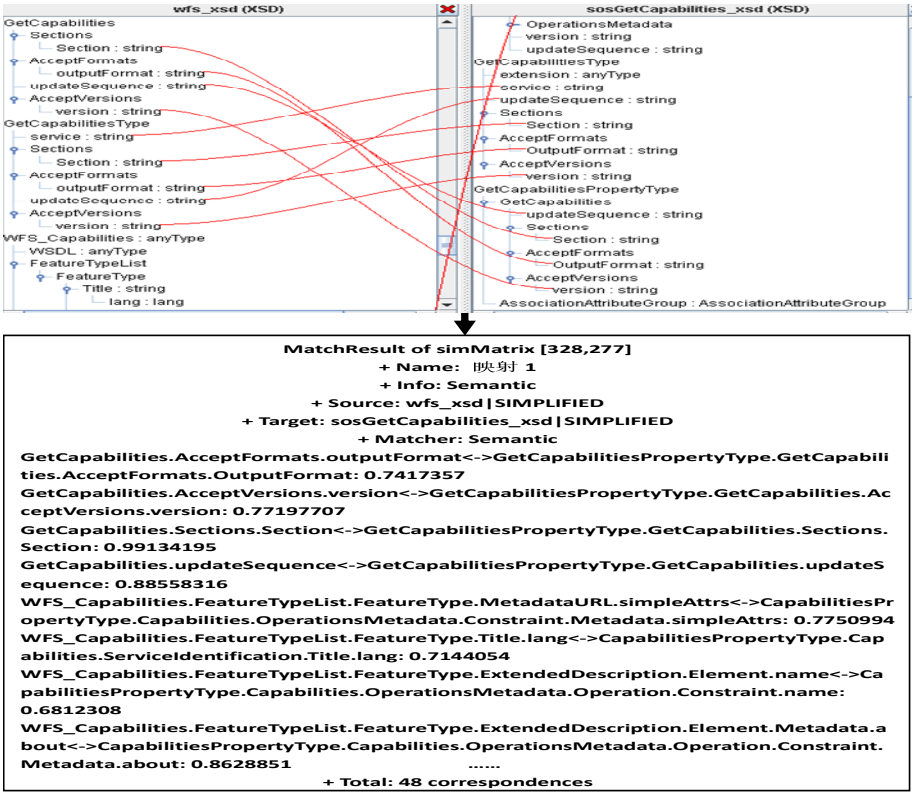

Fig. 7. Mappings between wfsGetCapabilities_xsd and sosGetCapabilities_xsd schema

```
<?xml version="1.0" encoding="UTF8"?>
<xsl:stylesheet version="1.0"mlns:xsl="http:/ /www.w3.org/1999/XSL/Transform"
  <xsl:output method="xml" version="1.0" indent="yes"/>
<xsl:template match="/">
  <xsl:element name="wfs:WFS_Capabilities">
    <xsl:element name="ows:ServiceIdentification">
     <xsl:element name="ows:Title"><xsl:value of
    select="Capabilities/ows:ServiceIdentification/ows:Title"/></xsl:element>
     <xsl:element name="ows:Abstract"><xsl:valueof
    select="Capabilities/ows:ServiceIdentification/ows:Abstract"/></xsl:element>
     <xsl:element name="ows:Keywords"><xsl:valueof
    select="Capabilities/ows:ServiceIdentification/ows:Keywords"/></xsl:element>
     <xsl:element name="ows:Fees"><xsl:valueof
    select="Capabilities/ows:ServiceIdentification/ows:Fees"/></xsl:element>
      <xsl:element name="AccessConstraints"><xsl:value of
select="Capabilities/ows:ServiceIdentification/ows:AccessConstraints"/></xsl:element>
</xsl:element>……</xsl:element></xsl:template></xsl:stylesheet>
```

Fig. 8. The generation xsl file

Fig. 9. The transformation between sosGetCapabilities and wfsGetCapabilities

2) SOS "GetObservation"->WFS "GetFeature"

With the WFS capability information document of the above, we can extract the interested features from the observations. In general, we can use a specific feature name (TYPENAME) or ID (FEATUREID) to retrieve features, and similarly, for SOS, we can get the interested obsercation features by "sosGetFeatureInterest" operation with a given feature ID (FeatureOfInterestId). Therefore, through the feature ID number we can transform WFS "GetFeature" request into "sosGetFeatureInterest" request, and get the interested features from SOS observations.

5 Conclusion and Outlook

Interoperability is a hot and difficult problem of the current research on web services. In this paper, we design a heterogeneous web services integration middleware, through precise matching on web service schema, automatic information extraction and intelligent fusion on web service instance data, to achieve integrated access to different versions of different types of web services. The system has the following advantages:

• Through schema matching and XSL transformation technology to overcome the defects of version negotiation mechanism, achieves to access the exact version of web service.

•·Apply a data fuser component to realize heterogeneous web service transformation and integration.

•·Using service-oriented architecture, design a plug-and-play middleware to improve system scalability and flexibility.

The efficiency and performance of the proposed method do not evaluate in this paper, more experiments will be designed to evaluate the approach in next step, and at the same time, the integration between WCS, WFS and SOS, such as, studies on how to use WCS getCoverage operations to get the demanded coverages from the Observations data of SOS.

Acknowledgements. This work was financially supported by the China Nature Science Foundation (41201393) and Ningxia Nature Science Foundation (NZ12110). The authors thank the anonymous reviewers for their valuable comments and insightful ideas.

References

1. Vretanos, P.A. (ed.): OGC™ web feature service implementation specification (Version 1.0.0). In: Open Geospatial Consortium (OGC), Document Number: 02-058, Wayland, MA, USA, 105 (2002)
2. Whiteside, A., Evans, J.D. (eds.): OGCTM Web Coverage Service Implementation Standard (Version 1.1.2). Open Geospatial Consortium, http://www.opengeospatial.org/standards/wcs (accessed September 1, 2012)
3. Na, A., Priest, M. (eds.): OpenGIS® sensor observation service implementation specification (Version 0.1.5). In: Open Geospatial Consortium, OGC, Document Number: 06-009r1, Wayland, MA, USA, 187 (2006)
4. Kuhn: Open GIS in Europe: The GIPSIE Project. In: GEObit 1998 (1998)
5. Goodchild, M.F., Egenhofer, M.J., Fegeas, R.: Interoperability GISs. Report of a specialist meeting held under the auspices of the Varenius project, Santa Barbara, California (1997)
6. http://www.statk art. no/disgis
7. Chen, C.C., Shahabi, C., Knoblock, C.A.: Utilizing road network data for automatic identification of road intersections from high resolution color orthoimagery. In: Proceedings of the 2nd Workshop on Spatio-Temporal Database Management (STDBM 2004), Toronto, Canada, pp. 1477–1480 (2004)
8. Michalowski, M., Knoblock, C.A.: A constraint satisfaction approach to geospatial reasoning. In: Proceedingsof the 17th Conference on Innovative Applications of Articial Intelligence (IAAA), Pittsburgh, PA, pp. 423–429 (2005)
9. Fonseca, F., Hofer, M.E., Agouris, P., Camara, G.: Using ontologies for integrated geographic information systems. Transactions in GIS 6(3), 231–257 (2002)
10. Hess, G.N., Iochpe, C., Castano, S.: An algorithm and implementation for geoontologies integration. In: Proceedings of the 8th Symposium on GeoInformatics, Campos do Jordão (SP), Brazil, pp. 151–164 (2006)

11. Shvaiko, P., Euzenat, J.: A survey of schema-based matching approaches. Journal on Data Semantics IV, 146–171 (2005)
12. Giunchiglia, F., Shvaiko, P.: Semantic matching. KER Journal 18(3), 265–280 (2003)
13. Giunchiglia, F., Shvaiko, P., Yatskevich, M.: S-Match: An Algorithm and an Implementation of Semantic Matching. In: Bussler, C.J., Davies, J., Fensel, D., Studer, R. (eds.) ESWS 2004. ESWS, vol. 3053, pp. 61–75. Springer, Heidelberg (2004)
14. Giunchiglia, F., Yatskevich, M., Giunchiglia, E.: Efficient semantic matching. In: Gómez-Pérez, A., Euzenat, J. (eds.) ESWC 2005. LNCS, vol. 3532, pp. 272–289. Springer, Heidelberg (2005)
15. Wang, Y., Chen, J.: An Instance-Based Approach for Schema Matching Between GIS Database. Geomatics and Information Science of Wuhan University 33(1), 46–50 (2008)
16. He, J., Chen, N., Zheng, Z., Wang, W.: A Semantic Approach for Multi-Version Web Coverage Service Schema Match. Geomatics and Information Science of Wuhan University 37(2), 210–214 (2012)
17. Chen, N., He, J., Wang, W., Chen, Z.: Extended FRAG-BASE Schema Matching for Multi-version Open GIS Services Retrieval. International Journal of Geographical Information Science 25(7), 1045–1068 (2011)
18. Rahm, E., Do, H.H., Massmann, S.: Matching Large XML Schemas. SIGMOD Record 33(4), 26–31 (2004)

Microwave Staring Correlated Imaging and Resolution Analysis

Yuanpeng Ma, Xuezhi He, Qingquan Meng, Bo Liu, and Dongjin Wang

Department of Electronic Engineering and Information Science
University of Science and Technology of China Hefei, Anhui, P.R. China
myp@mail.ustc.edu.cn

Abstract. Microwave staring imaging system has the capability of reconstructing unknown targets without the requirement for the relative motion between the radar platform and the targets. However, the targets within the 3dB of the radiation beam can not be resolved and consequently its imaging performance is strictly limited by the nominal resolution of the system. Therefore, we propose the novel microwave staring correlated imaging system based on the temporal-spatial stochastic radiation fields, to obtain more detailed information of the targets. Moreover, different from the traditional microwave staring imaging systems, the blurry performance is shared by all the scatters in the scene of interest. Therefore, a new resolution concept named the global resolution is proposed to describe the global resolving performance of the system. The numerical simulations prove that the proposed system has the capability of breaking the resolution limitation to realize super-resolution imaging performance.

Keywords: Microwave staring imaging, temporal-spatial stochastic radiation fields, correlated imaging, super-resolution, global resolution.

1 Introduction

In traditional radar systems such as the synthetic aperture radar (SAR) and the inverse synthetic aperture radar (ISAR), the high azimuthal resolution is achieved by utilizing the relative motion between the radar platform and the target [1]. Therefore, their applications are restricted in practical scenarios where there are hardly any relative motion to be exploited. In such cases, the microwave staring imaging radar systems [2-5] seem to be more appropriate and meaningful.

Further, the phased array imaging systems [3][4] and the focal plane imaging systems [5] are the two most classical categories of the microwave staring imaging radar systems. And they have been widely applied in military surveillance and civil measurements.

Actually, in radar imaging systems, the most significant criterion of evaluating the performance is the imaging resolution. Therefore, the resolution is always a hot topic in the radar imaging fields. However, in literature, the concept of resolution is interpreted in different manners for diversified applications and thus lacks a unified

F. Bian et al. (Eds.): GRMSE 2013, Part I, CCIS 398, pp. 737–747, 2013.
© Springer-Verlag Berlin Heidelberg 2013

definition, as summarized by A. J. den Dekker and A. van den Bos [6]. And among these manners, the definition of two-point resolution based on Rayleigh criterion is most commonly used, which is defined as the capability of resolving two points with equal intensity, and the resolving criterion is the distance between the two points if the central maximum of the point spread function (PSF) for one point coincides with the first zero for the other. This concept is widely used in traditional radar imaging areas because their PSFs are of quasi-sinc shape [7]. Furthermore, this concept can be described in another way as the nominal resolution, which refers to the 3dB main lobe width for the PSF of the dominant scatter in the scene of interest.

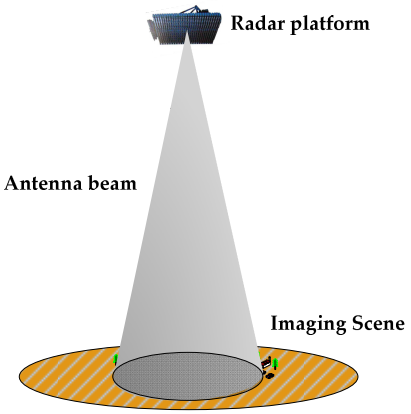

Fig. 1. Traditional microwave staring imaging system

According to the definition of the nominal resolution, the resolution of the traditional microwave staring imaging systems are directly determined by the sizes of the corresponding array apertures. As shown in Fig. 1, in the typical scenario of microwave staring imaging, the 3dB main lobe width of the impulse response is mainly decided by the radar beam. That is to say, any two targets within the beam can not be distinguished in traditional systems. In literature, there are many research about super-resolution radar imaging [8][9]. However, most of them mainly focus on the super-resolution imaging methods instead of the system itself.

Therefore, to realize super-resolution imaging by resolving two closely-located targets within the beam, here we propose a novel system named the microwave staring correlated imaging based on the temporal-spatial stochastic radiation fields. And the key technique lies in the design of the temporal-spatial stochastic radiation fields similar to [10]. Based on the temporal-spatial stochastic characteristics, the orthogonality of the radiation fields at arbitrary different moments can be guaranteed and thus the obtained information of the target at different moments are independent, which makes it possible for the targets within the beam to be distinguished.

Furthermore, for the microwave staring correlated imaging, the resolving capability of different spatial positions can be realized by the global correlated processing. And with the increasing samples of the radiation fields, the global blurry of the imaging result gradually decreases. In fact, different from the traditional

microwave staring imaging, the nominal resolution is not complete enough to describe the imaging performance of our system. Because the blurry is shared by each spatial position and the apportionment ratio is decided by the corresponding temporal-spatial random characteristics of the stochastic radiation fields. Therefore, we propose a new resolution concept as the global resolution, to better adapt to the proposed new system and represent the imaging capability.

The rest of our paper is organized as follows. In Section 2, we introduce the novel microwave staring correlated imaging system in detail and further describe the limitation of the traditional microwave staring imaging. In Section 3, the concept of the global resolution is proposed as compared to the classical nominal resolution. In Section 3, numerical simulations are presented to verify the effectiveness of the proposed system and its related analysis.

2 The Microwave Staring Correlated Imaging System

The microwave staring correlated imaging system based on the temporal-spatial radiation fields is a novel scheme that has the potential of realizing super-resolution performance (Here, the super-resolution refers to breaking the resolving limitation within the beam width). And we will analyze its super-resolution principle in detail as follows.

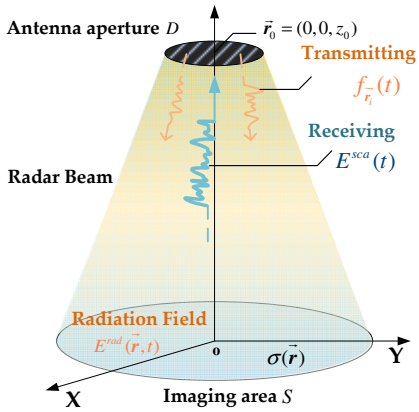

Fig. 2. Microwave Staring Correlated Imaging system

As shown in Fig. 2, the microwave staring correlated imaging system consists of the stationary radar platform and the stationary targets in the scene of interest. And we use a radar platform with aperture size D to measure a fixed area S, and the transmitting radar platform can be constituted by either a single antenna or an antenna array while the receiving radar is placed at the center of the platform. The coordinate system is established in the imaging area with the center of the radar beam as the origin. And the distance between the radar aperture and the imaging scene is z_0, i.e. the coordinate of the radar aperture center is $\mathbf{r}_0 = (0, 0, z_0)$.

According to the electromagnetic propagation theory, each echo contains all the scattering information within the radar beam. Defining the scattering coefficients of

the imaging scene as $\sigma(\mathbf{r})$, the relationship between the scattering field and the scattering coefficients can be represented as

$$E^{sca}(t)=\int_S \frac{1}{4\pi|\boldsymbol{r}-\boldsymbol{r}_0|}E^{rad}\left(t-\frac{|\boldsymbol{r}-\boldsymbol{r}_0|}{\mathrm{c}},\boldsymbol{r}\right)\sigma(\boldsymbol{r})\,d\boldsymbol{r} \tag{1}$$

where $E^{sca}(t)$ and $E^{rad}(t,\mathbf{r})$ denote the received scattering field and the modified radiation field, respectively. And according to the time-domain electromagnetic equation, $E^{rad}(t,\mathbf{r})$ can be expressed as:

$$E^{rad}(t,\boldsymbol{r})=\int_D \frac{1}{4\pi|\boldsymbol{r}-\boldsymbol{r}_i|}f_{r_i}\left(t-\frac{|\boldsymbol{r}-\boldsymbol{r}_i|}{\mathrm{c}}\right)d\boldsymbol{r}_i \tag{2}$$

where $\mathbf{r}_i$ denotes the coordinate of the area within the radar aperture. Further replacing $E^{rad}(t,\mathbf{r})$ in (1) with (2), we have

$$\begin{aligned}E^{sca}(t)&=\int_S E^{rad}\left(t-\frac{|\boldsymbol{r}-\boldsymbol{r}_0|}{\mathrm{c}},\boldsymbol{r}\right)\sigma(\boldsymbol{r})\,d\boldsymbol{r}\\&\approx\frac{1}{16\pi^2 z_0^2}\int_S\int_D f_{r_i}\left(t-\frac{|\boldsymbol{r}-\boldsymbol{r}_0|+|\boldsymbol{r}-\boldsymbol{r}_i|}{\mathrm{c}}\right)d\boldsymbol{r}_i\cdot\sigma(\boldsymbol{r})\,d\boldsymbol{r}\end{aligned} \tag{3}$$

Rewriting (3) in its discrete form, we have the following equation as

$$\boldsymbol{E}^{sca}=\boldsymbol{E}^{rad}\cdot\boldsymbol{\sigma}$$

$$\begin{bmatrix}E^{sca}(t_1)\\E^{sca}(t_2)\\\vdots\\E^{sca}(t_M)\end{bmatrix}\overset{N\to\infty}{=}\begin{bmatrix}E^{rad}(t_1,\boldsymbol{r}_1)&E^{rad}(t_1,\boldsymbol{r}_2)&\cdots&E^{rad}(t_1,\boldsymbol{r}_N)\\E^{rad}(t_2,\boldsymbol{r}_1)&E^{rad}(t_2,\boldsymbol{r}_2)&&E^{rad}(t_2,\boldsymbol{r}_N)\\&\cdots&&\cdots\\E^{rad}(t_M,\boldsymbol{r}_1)&E^{rad}(t_M,\boldsymbol{r}_2)&\cdots&E^{rad}(t_M,\boldsymbol{r}_N)\end{bmatrix}\cdot\begin{bmatrix}\sigma_1\\\sigma_2\\\vdots\\\sigma_N\end{bmatrix} \tag{4}$$

where M and N denote the number of the echo samples and the discretized grids in the imaging scene, respectively.

As analyzed above, in traditional microwave staring imaging systems (as shown in Fig. 1), it is impossible to distinguish any two targets within the radiation beam coverage, without enlarging the antenna aperture or increasing the transmission frequency. Obviously, such limitation directly leads to its rare applications in practical remote sensing scenarios. And the inherent reason for such resolution limitation can be described according to (4). In traditional microwave staring imaging systems, the radiation fields are of direct sinusoidal forms or coherently synthetized by the radiation array. Thus, the radiation samples for arbitrary position r at different moments satisfy a linearly-correlated relationship as

$$\begin{aligned}&\left[E^{rad}(t_i,\boldsymbol{r}_1),E^{rad}(t_i,\boldsymbol{r}_2),...,E^{rad}(t_i,\boldsymbol{r}_N)\right]\\&\propto\left[E^{rad}(t_j,\boldsymbol{r}_1),E^{rad}(t_j,\boldsymbol{r}_2),...,E^{rad}(t_j,\boldsymbol{r}_N)\right],\forall i\neq j\end{aligned} \tag{5}$$

Therefore, the equation sets in (4) are degraded to a single independent equation as

$$\left[E^{sca}\left(t_1\right)\right]^{N\to\infty}=\left[E^{rad}\left(t_1,\boldsymbol{r}_1\right)\quad E^{rad}\left(t_1,\boldsymbol{r}_2\right)\quad\cdots\quad E^{rad}\left(t_1,\boldsymbol{r}_N\right)\right]\cdot\begin{bmatrix}\sigma_1\\ \sigma_2\\ \vdots\\ \sigma_N\end{bmatrix} \tag{6}$$

Obviously, more than one scattering coefficients can not be solved from the single equation (6), and no new scattering information can be extracted with the increase of the observation time of the entire imaging process.

In comparison, since the radiation fields in our microwave staring correlated imaging system are temporal-spatial stochastic, multiple equations can be expected in (4) by properly designing the transmitted signals, and consequently the limitation-breaking resolution can be achieved.

If each two radiation field samples at different moments $E^{rad}(t_i,\mathbf{r})$, $E^{rad}(t_j,\mathbf{r})$ satisfy the following relationship

$$\begin{aligned}\left\langle E_i^{rad},E_j^{rad}\right\rangle^{N\to\infty}&=\sum_{n=1}^{N}E^{rad}\left(t_i,\boldsymbol{r}_n\right)\cdot\left(E^{rad}\left(t_j,\boldsymbol{r}_n\right)\right)^*\\&=\int_S E^{rad}\left(t_i,\boldsymbol{r}\right)\left(E^{rad}\left(t_j,\boldsymbol{r}\right)\right)^*d\boldsymbol{r}=\delta\left(t_i-t_j\right)\end{aligned} \tag{7}$$

Then, the radiation field samples at different moments are orthogonal. Thus, more effective samples with the increase of the observation time can be obtained and in this way more independent equations can be constructed in (4).

Noting that (7) is an ideal condition and can be hardly satisfied in practical scenarios, we propose the realizable temporal-spatial stochastic radiation fields to approximate the relationship in (7). And through orthogonal processing, the obtained multiple equations in (4) can be transformed as

$$\tilde{\boldsymbol{E}}^{sca}=\tilde{\boldsymbol{E}}^{rad}\cdot\boldsymbol{\sigma}$$

$$\begin{bmatrix}\tilde{E}^{sca}\left(t_1\right)\\ \tilde{E}^{sca}\left(t_2\right)\\ \vdots\\ \tilde{E}^{sca}\left(t_M\right)\end{bmatrix}^{N\to\infty}=\begin{bmatrix}\tilde{E}^{rad}\left(t_1,\boldsymbol{r}_1\right) & \tilde{E}^{rad}\left(t_1,\boldsymbol{r}_2\right) & \cdots & \tilde{E}^{rad}\left(t_1,\boldsymbol{r}_N\right)\\ \tilde{E}^{rad}\left(t_2,\boldsymbol{r}_1\right) & \tilde{E}^{rad}\left(t_2,\boldsymbol{r}_2\right) & & \tilde{E}^{rad}\left(t_2,\boldsymbol{r}_N\right)\\ & \cdots & & \cdots\\ \tilde{E}^{rad}\left(t_M,\boldsymbol{r}_1\right) & \tilde{E}^{rad}\left(t_M,\boldsymbol{r}_2\right) & \cdots & \tilde{E}^{rad}\left(t_M,\boldsymbol{r}_N\right)\end{bmatrix}\cdot\begin{bmatrix}\sigma_1\\ \sigma_2\\ \vdots\\ \sigma_N\end{bmatrix} \tag{8}$$

where $\tilde{E}^{sca},\tilde{E}^{rad}$ represent the new scattering field and the radiation field after the orthogonality processing. And to solve the multiple equations in (8), we further propose the correlated imaging method for this novel system.

Based on the discussions above, we propose the processing diagram for the microwave staring correlated imaging based on the temporal-spatial stochastic radiation fields, as shown in Fig. 3.

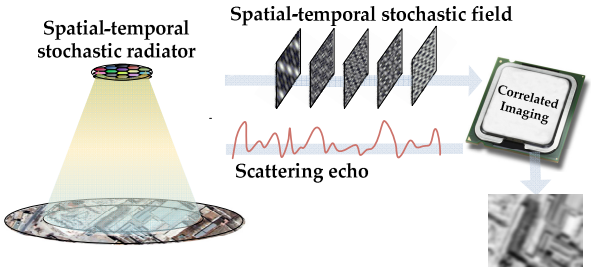

Fig. 3. Detailed processing diagram for the Microwave Staring Correlated Imaging system

Different from the traditional staring imaging, with temporal-spatial stochastic radiation fields, the scattering coefficients of the imaging scene are variously modulated by the radiation field samples at different moments. And the correlated imaging methods are proposed to fully extract the diversely-modulated information of the targets. After solving for the multiple equations in (8), the targets within the same radiation beam can be distinguished to realize super-resolution performance.

3 Resolution Definition for Microwave Staring Correlated Imaging

Resolution, as the most significant performance-evaluating criterion, has been widely studied in radar imaging systems. Taking the nominal resolution into consideration, the imaging results of the traditional microwave staring imaging system and the microwave staring correlated imaging system are presented in Fig. 4(a) and Fig. 4(b), respectively. And there are two main differences about the corresponding imaging results and PSFs of the two systems.

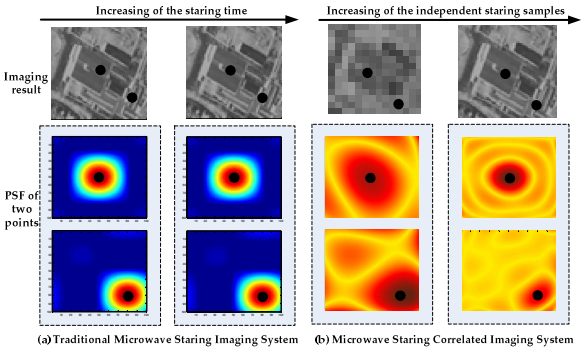

Fig. 4. Imaging result & PSF of the two imaging systems

Firstly, in Fig. 4(a), for any two targets in the imaging scene, the closer they are, the harder can they be distinguished. And the PSF in traditional staring imaging stays invariant while the observation time of the entire imaging process increases. But for

the microwave staring correlated imaging, we can get an increasing orthogonal radiation samples with more observation time, so the PSF and the imaging result varies accordingly (as shown in Fig. 4(b)).

Secondly, for the traditional microwave staring imaging, its PSF is generally of specific circular or rectangular shape, as shown in Fig. 4(a). But for microwave staring correlated imaging, its equivalent PSF of any point (in Fig. 4(b)) may be of arbitrary shape and can be totally different from those of the others.

Therefore, the nominal resolution can effectively describe the resolving capability of the traditional microwave staring imaging systems. However, for the microwave staring correlated imaging, the irregularity of the equivalent PSF invalidates the rule that the closer the two targets, the harder can they be resolved". So the concept of the nominal resolution is no longer appropriate enough to describe the resolving capability of this novel imaging system, and we have to resort to a new concept to fully consider the entire PSF. According to the related discussions in [11], we propose a novel resolution concept that incorporates both of the main lobe and the side lobe of the PSF, instead of only considering the main lobe as in nominal resolution. And the global resolution of the point $\mathbf{r}_c$ is defined as

$$\rho(\boldsymbol{r}_c)=\frac{\int_S\left[\sum_{i=1}^{M}\tilde{E}^{rad}(t_i,\boldsymbol{r}_c)\left(\tilde{E}^{rad}(t_i,\boldsymbol{r})\right)^*\right]^2 d\boldsymbol{r}}{\left[\sum_{i=1}^{M}\tilde{E}^{rad}(t_i,\boldsymbol{r}_c)\left(\tilde{E}^{rad}(t_i,\boldsymbol{r}_c)\right)^*\right]^2} \tag{9}$$

4 Simulation and Analysis

In the simulations, the imaging scene is set as 40m×40m and is discretized into 80×80 bins, so the size of each bin is 0.5m×0.5m. And the global resolution of $\mathbf{r}_c$ is

$$\rho(\boldsymbol{r}_c)=\frac{\sum_{p=1}^{80}\sum_{q=1}^{80}\left[\sum_{i=1}^{M}\tilde{E}^{rad}(t_i,\boldsymbol{r}_c)\left(\tilde{E}^{rad}(t_i,\boldsymbol{r}_{p,q})\right)^*\right]^2}{\left[\sum_{i=1}^{M}E^{rad}(t_i,\boldsymbol{r}_c)\left(\tilde{E}^{rad}(t_i,\boldsymbol{r}_c)\right)^*\right]^2}\times 0.25 \tag{10}$$

Thus we can derive the minimum resolution for the simulation is 0.25m^2 when

$$\sum_{p=1}^{80}\sum_{q=1}^{80}\tilde{E}^{rad}(t_i,\boldsymbol{r}_c)\left(\tilde{E}^{rad}(t_i,\boldsymbol{r}_{p,q})\right)^*=\delta(\boldsymbol{r}_c-\boldsymbol{r}_{p,q}) \tag{11}$$

4.1 Simulation I

1) Under the first simulation condition, the signal of each radiation source is stochastic linear frequency modulated (LFM) signal modulated by Gold sequence. Detailed main

system parameters are shown in Table 1. And four radiation sources are distributed in the configuration shown in Fig. 5.

Table 1. Simulation Parameters

No.	Parameter	Value
1	Array aperture size D	0.6 m
2	Array element spacing	0.15m
3	Number of radiation sources	4
3	Imaging distance z_0	200m
4	Grid spacing ΔS	0.2m
5	Carrier frequency f_c	10GHz
6	Signal bandwidth B	<1GHz
7	Gold Code rate f_s	200 Mbps
8	Linear FM rate	200 Mbps
9	FM index K	2×10^{14}Hz/s
8	Sampling rate f_p	500MHz

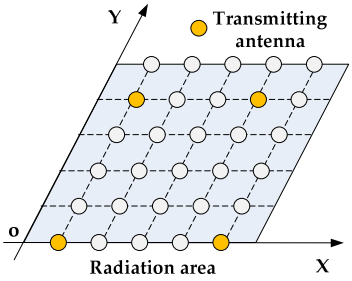

Fig. 5. The configuration of the radiation sources

For this sparse array scenario, we can calculate the equivalent PSF (as in Fig. 6(a)) of the center point of the imaging scene according to the equation (8), and Fig. 6(b) represents the PSF of the traditional staring imaging under the same condition.

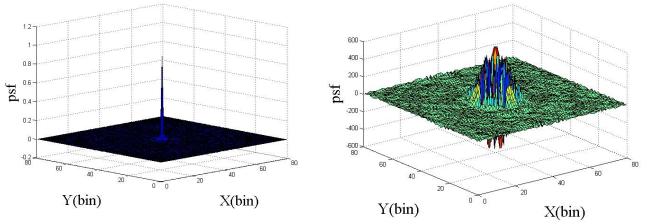

(a) PSF for the new system (b) PSF for the traditional system

Fig. 6. PSF for the two systems (Simulation I (1))

From Fig. 6, we calculate the global resolutions for the two systems as $\rho_{new}(0)=4m^2$, $\rho_{tra}(0)=18.67m^2$ according to equation (10). From the comparison, we get to know that the design of the temporal-spatial radiation fields at different

moments improves the resolving capability when compared with the traditional staring imaging, and the 2-D super-resolution ratio is approximately 4.67 from the viewpoint of the global resolution.

2) In the second simulation condition, we change the configuration of the four radiation sources to be random changing within the 5×5 array shown in Fig. 5. And the corresponding PSF of the two systems are presented in Fig. 7, from which we can calculate the global resolutions as $\rho_{new}(0)=0.28m^2$, $\rho_{tra}(0)=18.67m^2$.

Obviously, the random moving of the configuration can largely improves the PSF performance because more stochastic radiation fields can be obtained. However, for the traditional staring imaging, its resolving capability is manly decided by the aperture size, thus the variation of the configuration does not bring any conspicuous benefit. This phenomenon is well characterized by the concept of global resolution and the 2-D super-resolution ratio is approximately 65.86.

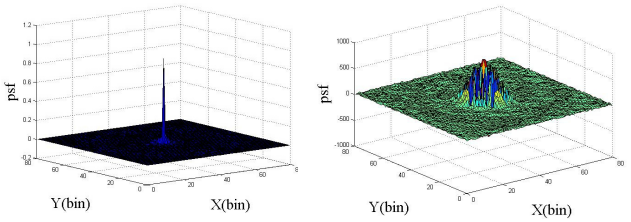

(a) PSF for the new system (b) PSF for the traditional system

Fig. 7. PSF for the two systems (Simulation I (2))

4.2 Simulation II

To fully consider the influence of the system variables, we utilize another set of the simulation parameters, as shown in Table 2.

Table 2. Simulation Parameters

No.	Parameter	Value
1	Array aperture size D	1.2 m
2	Array element spacing	0.3m
3	Number of radiation sources	25
3	Imaging distance z_0	200m
4	Grid spacing ΔS	0.2m
5	Carrier frequency f_c	10GHz
6	Signal bandwidth B	<1GHz
7	Gold Code rate f_s	200 Mbps
8	Linear FM rate	200 Mbps
9	FM index K	2×10^{14} Hz/s
8	Sampling rate f_p	500MHz

1) Here, the full array in Fig. 5 is utilized and the equivalent PSF and its comparison are shown in Fig. 8. From Fig. 8(a), we get to know there is a second peak in the PSF of the new system, which shows the advantage of our proposed global resolution over

the nominal resolution by incorporating the impact of the other peaks and side lobes. And the global resolutions for these two systems can be calculated as $\rho_{new}(0)=0.63m^2$, $\rho_{tra}(0)=8.11m^2$.

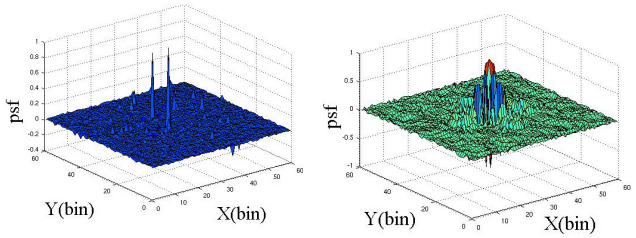

(a) PSF for the new system (b) PSF for the traditional system

Fig. 8. PSF for the two systems (Simulation II (1))

Then, we use only 5 radiation sources, which randomly change their spatial positions within the 5×5 array. And the PSF are shown in Fig. 9, where their corresponding global resolutions are $\rho_{new}(0)=0.65m^2$, $\rho_{tra}(0)=8.00m^2$. Comparing Fig. 8(a) and Fig. 9(a), we get to know that by randomly changing the radiation sources, the imaging performance of a sparse array can be closely approximate to that of the full array.

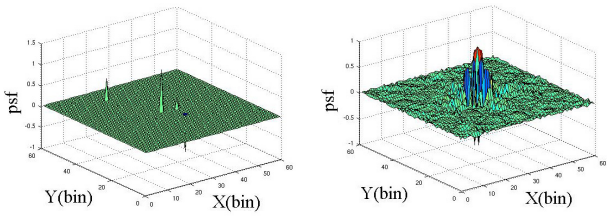

(a) PSF for the new system (b) PSF for the traditional system

Fig. 9. PSF for the two systems (Simulation II (2))

5 Conclusion and Acknowledgement

Further, after analyzing the PSF characteristics of the new system, we get to know that the traditional nominal resolution is not complete enough to describe the complex PSF form of the new system. Therefore, we propose the concept of the global resolution by incorporating both the main lobe and the side lobe information of the PSF. Further, the properties of the global resolution can give a guide for the design of temporal-spatial stochastic radiation fields to better realize super-resolution within the traditional radar beam. In fact, the design of temporal-spatial stochastic radiation fields is still and will be a rather challenging work, and there is a lot of research work worthy to study in the future.

This work is supported by the High-tech Research and Development Program of China under Grant Project No.2011AA120103.

References

1. Bao, Z., Xing, M., Wang, T.: Radar Imaging Technology. Publishing House of Electronics Industry, Beijing (2005)
2. Chaudhuri, S., Rajagopalan, A.N.: Depth from defocus: a real aperture imaging approach. Springer-Verlag New York Incorporated (1999)
3. Scudder, R.M., Sheppard, W.H.: An/spy-1 phased-array antenna. Microwave Journal 17, 51–55 (1974)
4. Kinghorn, A., et al.: Phased array antenna. U.S. Patent No. 8,138,973 (2012)
5. Svedin, J., Huss, L.-G., Karlen, D., Enoksson, P., Rusu, C.: A micromachined 94 Ghz dielectric resonator antenna for focal plane array applications. In: IEEE/MTT-S International on Microwave Symposium, pp. 1375–1378. IEEE (2007)
6. Den Dekker, A.J., Van den Bos, A.: Resolution: a survey. Optical Society of America 14(3), 547–557 (1997)
7. Rodriguez, J.A., Fernandez-Delgado, M., Bregains, J., et al.: A comparison among several techniques for finding defective elements in antenna arrays, 614–614 (2007)
8. Emmanuel, D., Fernandez-Granda, C.: Towards a mathematical theory of super-resolution. arXiv preprint arXiv:1203.5871 (2012)
9. Wong, A.M.H., Eleftheriades, G.V.: Superoscillatory Radar Imaging: Improving Radar Range Resolution Beyond Fundamental Bandwidth Limitations. IEEE Microwave and Wireless Components Letters 22(3), 147–149 (2012)
10. Ahmad, F., Amin, M.G.: Stochastic Model Based Radar Waveform Design for Weapon Detection 48(2), 1815–1826 (2012)
11. Woodward, P.M., Davies, I.L.: A theory of radar information. Philosophical Magazine 41(321), 1001–1017 (1950)

Remote Sensing Image Classification Based on SVM and Object Semantic

Xicheng Tan[1], Yang Song[2], and Wenting Xiang[3]

[1] International School of Software, Wuhan University,
37 Luoyu Rode, Wuhan, China 430079
Xichengtan@gmail.com
[2] Guangzhou Urban Planning & Design Survey Institute
Jianshe road 23, Yuexiu District, Guangzhou, Guangdong Province
sy728540@sohu.com
[3] China Construction Bank
No.25, Finance Street, Xicheng District, Beijing, China, 100033
xiangwenting10@gmail.com

Abstract. Multispectral remote sensing images have been regarded as dataset which contains incredible semantic information. And classifying multispectral remote sensing images could, in a sense, be achieved by analyzing a variety of complex semantic information and distilling skeletonzed information which facilitates the generalization, calculation and decision-making of human beings. However, conventional interpretation of remote sensing images is mostly limited within the extent of feature extraction and selection of merely spectral features of terrestrial objects. This paper present a Remote sensing Image Classification method based on SVM and Object Semantic, and it can obtain better performance of image classification.

Keywords: SVM, Semantic, Ontology, Classification.

1 Introduction

Hyperspectral and High Resolution have been indicated as developing trend of remote sensing technology. However, new image features have provided new challenges for the interpretation. First, the development of images from multispectral to hyperspectral has largely increased the resolution of spectrum and the dimensions of relevant features, which leads to the so-called the Curse of Dimensionality[3]. However, conventional solutions such as Dimension Reduction and Feature Selection, would unquestionably cause the loss of image information, thus bring negative effect upon the accuracy of classification. Second, as the image-space resolution increases, the spatial features of those images multiply, and as a result, the information about their shape, location, size, texture etc. would be highly enriched. The topic of how to extract that information adequately and optimize the result of classification has become increasingly hot.

F. Bian et al. (Eds.): GRMSE 2013, Part I, CCIS 398, pp. 748–755, 2013.
© Springer-Verlag Berlin Heidelberg 2013

Aimed at the features of multispectral images, this paper suggests using Support Vector Machine (SVM) to solve problems provoked by the Curse of Dimensionality. Further research discusses the selection of sorter, the choice of kernel function and other classification algorithms when using SVM to classify multispectral remote sensing images. Meanwhile, this paper uses ontology to build semantic rule descriptions of spatial attributes and it reveals that with semantic rule the results of classification are largely improved. All these methods applied in this paper have showed better extendability and versatility and obviously superior accuracy compared with conventional classification methods.

2 The Drawback of Statistical Classification Method and the Solutions of Svm

Since the idea of SVM was first introduced by Vapnik in 1995, it has experienced a rapid development [1,2]. And over the years, SVM has been widely recommended for its substantial basement of statistical theoretical support, it's plain geometric interpretation and perfect mathematical form. Conventional methods are based on statistical classification, however, the flaws existed in the Minimization of Empirical Risk could lead to problems such as the failure of Expectation Calculation.To solve this problem[4-5], Vanpnik proposed transforming small sample training set to VC Dimensions and exploring the Structural Risk Minimization(SRM) in VC dimensions[6-9].

Assume h is the VC Dimension of F. If the sample number l is bigger than h and if

$$h(\ln\frac{2l}{h}+1)+\ln\frac{4}{\delta}\geq\frac{1}{4}\ldots\ldots\ldots \qquad \ldots\ldots\ldots\ldots\ldots\ldots(1)$$

Then for any probability distribution P(x,y), any $\delta\in(0,1]$ and the function f of any F, the inequality

$$R(f)\leq R_{emp}[f]+\sqrt{\frac{8}{l}\left(h\left(\ln\frac{2l}{h}+1\right)\right)+\ln\frac{4}{\delta}} \ldots\ldots\ldots\ldots\ldots (2)$$

would be true at a probability of $1-\delta$.

The first part of inequality (2) is empiric risk, the second part is called confidence interval and the sum of the two parts is called the structural risk.

From the theorem 1 it could be seen that the empiric risk is the upper bound of the structural risk. Thus, to ensure that the empiric risk is least, both the empiric risk and the confidence interval should be carefully considered. The principle of the minimization of the structural risk is to select a decision function $F(t)$ which relies on the parameter t. This function would grow with the growth of t, and for each t, a function f^t which would ensure that the empiric risk is least could be found in $F(t)$. A value of the structural risk would be obtained correspondingly, and the principle of

the minimization of the structural risk is exactly selecting the t' which ensure the minimization of the structural risk and making the corresponding $f^{t'}$ the decision function[10].

In conventional classification based on statistics, the insufficiency of samples would cause errors in risk calculation, and thus influence the accuracy of classification. However, SVM methods would successfully overcome these disadvantages.

3 Use the Shape and Relationship Semantics to Optimize the Classification

3.1 The Definition of Target Semantic Ontology Library

The definition of the target semantic ontology library needs to correspond with the real problems. In the following picture, there are six terrestrial objects. They are: house, lake, river, vegetation, nudation and road [11,12]. Moreover, water area could be divided into river, natural lake and artificial water area. However, it could also be divided into clean water area and contaminated water area according to the quality of water. The framework of this ontology description is illustrated as Fig.1.

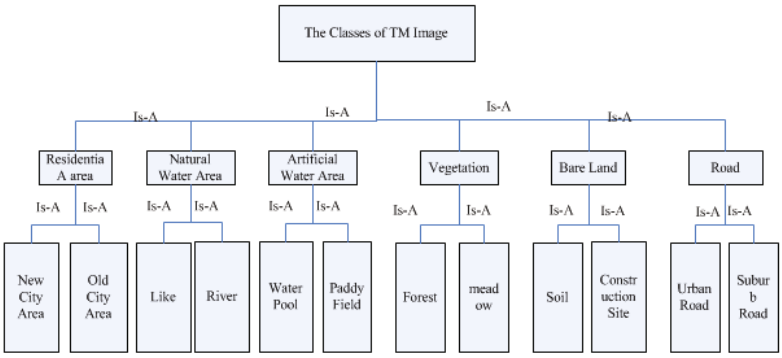

Fig. 1. Classification Ontology Framework of TM Image

Six features of this ontology library is explored in this paper, including two semantic features--Type-Feature and Related Type-Feature.

Type-Features belong to semantic features of lower lever, and could all be solved by feature extraction or selection upon original spectral data, while Related Type-Features acquire further speculations based on classification instead of directly extraction from original spectral data[13].

The semantic feature of TM image is listed as follows:

（1） the information of texture is relatively rich, but the influence on TM images is not obvious.

（2） the information on the shape of relevant categories is rather rich, eg: road, the Long River, and lake.

（3） the Topology Relationship of relevant categories is relatively strong, eg: most of the small lakes are far away from the Long River .

From the analysis of the semantic structure of target objects, the semantic description of target objects could be obtained while integrating and transforming along could not. Therefore, in this paper, the semantic features of target objects are divided into two kinds, one is for the method of feature-extraction of original spectral data, the other is for the method of speculation.

3.2 Semantic Feature of Shape

In real life, different terrestrial objects own different shape features, for example, the Long River is like a strip, lakes are like big surface forms, farmlands are more regular and are always cluster together, roads are like lines. All these are semantic features of the structure of terrestrial elements. The classification of TM images of terrestrial objects is rather difficult. Take road for instance. Due to the fact that the spectral features of road are always close to those of the residential area and open ground. it's quite easy to confuse them. The roads of downtown and suburbs and the roads of the country and mountain areas differ significantly in the aspect of spectral features. The roads of downtown and those of residential area are always mixed, and it's almost impossible to distinguish them by simply investigating spectral features. Moreover, the roads of new downtown has the feature of highlight. However, as the residential areas also have this feature, the roads and the areas could, to a certain degree, mix. Again, the existence of vegetation in mountain areas could lead to the mix of roads and vegetation. However, whether it's downtown, suburbs or mountain areas, they all have boundary lines. Moreover, different water areas may also share similar spectral features. For instance, a clear river may share similar spectral features with lakes, and it's always difficult to tell between natural lakes and artificial lakes also due to their simialr spectral features. But we could find the differences of all kinds of terrestrial objects from their shapes[14]. A collection of the typical features of terrestrial objects is as follows.

(1) river: strip
(2) Lake: surface
(3) artificial water area: almost regular, of small areas and always cluster
(4) road: threadlike
(5) farmland: almost regular and always cluster together
(6) open land: always mix up with roads for their similar spectral features, but roads are streadlike
(7) vegetation: easy to mix up with houses

4 Experiment Results

4.1 Data

The the following TM multispectral images of Wuhan District in 2002 are illustrated as examples.

(a) TM True Color Image

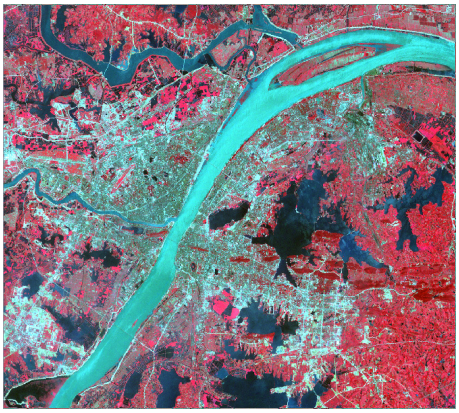

(b) TM432 Fasle Color Image

Fig. 2. TM Image of Wuhan in 2002

TM images have 7 wave bands. TM1(0.45~0.52 μ m) is Blue-Green Band. TM2(0.52~0.60 μ m) as the Blue Band could be used to recognize vegetation. TM3(0.63~0.69 μ m) as the Red Band is located on the red area which is also the absorption area of chlorophyll. This area, however, is most important for the detection of the soil border and geological border in visible lights, and because in this band area, the surface features always show great contrasts, the influence of fog is largely reduced compared with other wave bands and the resolution is better. TM4(0.76~0.90 μ m) is near-infrared band and corresponds to the peak value of vegetation, thus shows great significance when identifying and evaluating vegetation. The ratio of TM2 to TM4 is sensitive to the amount of green livings and their water content. TM5(1.55~1.75m) is middle-infrared band and its reflection is largely relied on the moisture content of the surface soil. This wave band has better capacity of penetrating atmosphere and fogs, and could be used to distinguish road, exposed soil and water area. Moreover, the moisture content of soil could be discerned with this band. TM6(10.4~12.5m) is thermal infrared band and could sense the target of thermal radiation. TM7(2.08~2.35m) is middle-infrared band and could be distinguished by rocks and minerals and could be used to discern the growth of the plants.

The extraction of spectral semantic features could be started by analyzing the features of the image data from all those wave bands, and then the selection of features. Or, it could be done with the computation of the image data or the the transformation of features. Common methods include the computatation of NDVI index, tasseled cap transformation and K-L transformation and so on.

In this paper, five wave bands, TM2~5,7, are selected as the feature vector.

4.2 Result Analysis

The left picture is the result of Mahadistance classification, and the right picture is the result of SVM and Semantic classification. In the result image of Mahaistance , there a lot of pixels in the lake was classified into forest. Some pixels in the river are classified into lake. But in the result image of the SVM and Semantic method, there are fewer pixels that are classified wrong. There are almost no pixels of the lake are classified into forest, and no pixels of river are classified into lake. For the semantic relations are used in the method, the mistakes are eliminated by the semantic constrains.

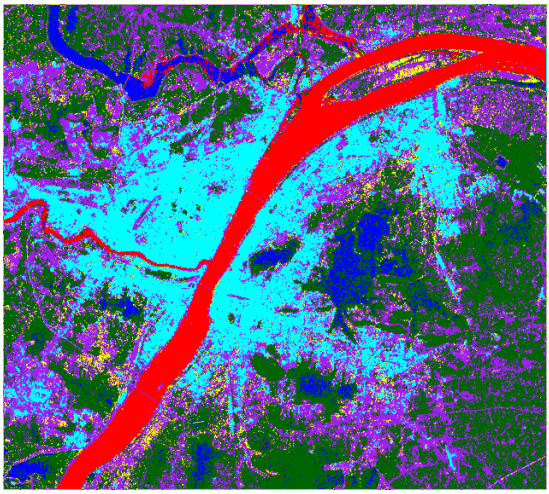

Result of Mahadistance

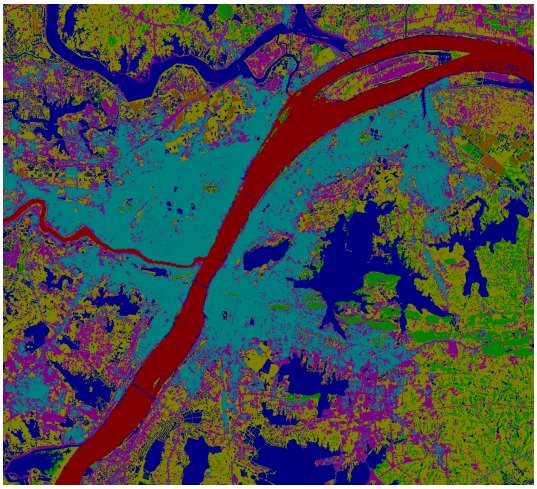

Result of the Method of this research

Acknowledgements. This work was supported by grants from the Guangzhou Science and Technology Plan Projects (2012Y2-00 035; 2013Y2-00031) and the National Natural Science Foundation of China (Grant No. 51277167).

References

[1] Furey, T.S., Cristianini, N., Duffy, N., Bednarski, D.W., Schummer, M., Haussler, D.: Support vector machine classification and validation of cancer tissue samples using microarray expression data. Bioinformatics 16(10), 906–914 (2000)

[2] He, L.M., Kong, F.S., Sheng, Z.Q.: Multiclass SVM based land cover classification with multisource data. In: Proceedings of the Fourth International Conference on Machine Learning and Cybernetics, Guangzhou, China, pp. 3541–3545 (2005)
[3] Huang, X., Zhang, L., Li, P.: Classification of High Spatial Resolution Remotely Sensed Imagery Based Upon Fusion of Multiscale Features and SVM. Journal of Remote Sensing 11(1), 48–54 (2007)
[4] Hammer, B., Gersmann, K.: A note on the universal approximation capability of support vector machines. Neural Process Lett. 17(1), 43–45 (2003)
[5] Kanellopoulos, I., Wilkinson, G.G.: Strategies and best p ractice for neural network image classification. International Journal of Remote Sensing 18(4), 711–725 (1997)
[6] Cristianini, N., Shawe-Taylor, J.: An introduction to support vector machines: and other kernel-based learning methods. Cambridge Press, Cambridge (2000)
[7] Kaya, G.T., Ersoy, O.K., Kamasak, M.E.: Hybrid SVM and SVSA method for classification of remote sensing images. In: IGARSS 2010 (2010)
[8] Kaya, G.T., Ersoy, O.K., Kamasak, M.E.: Hybrid SVM and SVSA Method for Classification of Remote Sensing Images. In: International Geoscience and Remote Sensing Symposium (IGARSS), pp. 2828–2831 (2010)
[9] Yue, S., Li, P., Hao, P.: Svm classification:its contents and challenges. Appl. Math. Chin. Univ. 18(3), 332–342 (2003)
[10] Melgani, F., Bruzzone, L.: Classification of hyperspectral remote sensing images with support vector machines. IEEE Transactions on Geoscience and Remote Sensing 42(8), 1778–1790 (2004)
[11] Tan, X., Bian, F.: Heterogeneous Spatial Information Interoperability Based on Cooperative Ontologies. Geomatics and Information Science of Wuhan University 30(2), 178–181 (2005)
[12] Tan, X., Bian, F.: Heterogeneous Spatial Information System Semantic Interoperability Based on Bayes Data Classification and Ontology. Geomatics and Information Science of Wuhan University 31(8), 724–727 (2006)
[13] Yi, R., Xu, F., Deng, M., Liu, Q.: An Approach for Hierarchical Semantic Classification of IslandBased on Formal Concept Analysis. Geomatics and Information Science of Wuhan University 37(8), 897–901 (2012)
[14] Li, X.-M., Li, G.: The Meaning of Keywords GCMD in the Design of Geosciece Ontology. Remote Sensing Information (5), 92–95 (2008)

The Remote Sensing Identification of Marine Oil Spill Based on Oil Fingerprinting

Wei Pei[1], YongYing Zhu[2], Lin Zeng[1], ShuXia Liu[3], XiangJie Wang[1], and ZiJie An[1]

[1] Environmental Science and Engineering College, Dalian Maritime University, Dalian, China
[2] Ocean and Civil Engineering department, Dalian Ocean University, Dalian, China
[3] Criminal Technology Department, Liaoning Police Academy, Dalian, China
peiweidl@gmail.com, zhuyy@dlou.edu.cn,
pwzwd@163.com, maillsx@163.com, wangxj@dlmu.edu.cn,
zijiedl@dlmu.edu.cn

Abstract. Marine oil spill which is referred to super killer of marine ecological environment is one of the frequent important environmental disaster in offshore area. With the continuous development of Chinese economy, all kinds of oil pollution incident is on the rise, the frequency and risk is also increasing, it brought significant losses of the marine ecological environment, ecological resources and the people. Therefore, this paper combines ocean remote sensing and fingerprint technology to present marine oil spill identification method, and uses the case of an oil spill accident in Dalian to verify the feasibility and effectiveness of this method. The oil type in this incident is identified as crude oil and the amount of oil spill is estimated 30000 to 160000 tons. These Experimental results are consistent with the actual situation and show that this identification method can provide technical support to determine the varieties and amount of oil spill quickly, repair the damaged marine ecological environment and develop the theoretical system of the marine emergency research, and also provided a scientific basis for marine disaster prevention and mitigation and safeguard of national maritime rights and interests.

Keywords: Marine Oil Spill, Remote Sensing, Oil Fingerprinting, Pattern Recognition.

1 Introduction

With the increasing development of globalization, offshore oil transportation volume is also increasing, at the same time, a series of oil spill accidents has occurred more frequently. According to statistics, the annual volume of oil spilled into the sea up to 2~10 million tons [1], which damaged the marine environment and threatens human health greatly. Therefore, after 30 years of exploration and development, many developed countries, especially the coastal states, have established modern analysis system of oil spill based on oil fingerprint technology. They mainly focus on chemical oil fingerprinting methods such as the methods of gas chromatography, high performance liquid chromatography and gas chromatography/mass spectrometry.

F. Bian et al. (Eds.): GRMSE 2013, Part I, CCIS 398, pp. 756–765, 2013.
© Springer-Verlag Berlin Heidelberg 2013

These methods can analyze the composition and structure of oil samples accurately, have outstanding advantages in determining the oil spill varieties and tracking the spill source. However there are some problems such as the low identification efficiency, high cost, complex operation and unable to determine the scope of the oil spill, which limit its popularization and application. The application of oil fingerprint technology also needs the support of oil fingerprint database [2], however the current databases have a lot of problems, such as the less oil samples and lack of oil information with the environmental changes [3]. As it rises in recent decades, ocean remote sensing technology is unable to identify the types of oil spill accurately, however it provides the prerequisites to determine the variety and range of oil spill quickly. Ocean remote sensing is began in the 1970s at the United States, our country starts later, began in the 1980s. However after nearly 30 years of development, especially in May 2002 and April 2007, launched HY-1A and HY-1B satellite successfully, which have our own independent intellectual property rights. It mark that China entered a new era in the aspect of remote sensing satellite monitoring of the ocean [4].

In view of the above, combining the advantage of ocean remote sensing and oil fingerprint technology, this paper present a marine oil spill identification method. First of all, ocean remote sensing technology is used to identify rough range of oil spill, and the spectral information of spilled oil extracted from remote sensing with the spectral information of oil sample in oil fingerprint database is compared, and the amount of oil spill is identified quickly. The rest of the paper is organized as follows. Section 2 introduces the range of oil spill identification with ocean remote sensing technology. In section 3, the fingerprint identification method used for oil spill spectral analysis is presented to determine the varieties and amount of oil spill. Error analysis are shown in Section 4. Finally, section 5 concludes this paper and looks to the future.

2 Identification of the Range of Oil Spill Based on Ocean Remote Sensing

This paper takes Dalian Xingang 716 oil spill accident as an example for oil spill identification. The range of oil spill identification is mainly achieved with ocean remote sensing technology. China Environmental Mitigation satellites (HJ-1A/1B Stars) which can survey China every two days [5] is selected as the satellite remote sensing data source, and Landsat-5 TM images is used for geometric rectification.

2.1 Satellite Image Processing

From July 17, 2010 to the beginning of August is the most stressful and busy period to deal with the oil spill, and also the key time to identify the oil spill with remote

sensing satellites data and method. By comparison, this paper selects the data on July 27th, as shown in Fig. 1. Because that day the weather is sunny and less cloud cover, and satellite images are low noise, high definition. It is more conducive to classification.

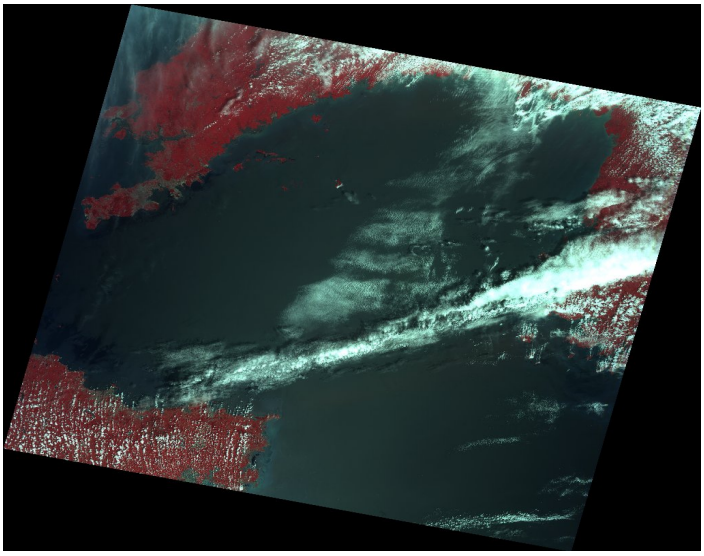

Fig. 1. HJ1A- CCD1 raw data image (level 2) On July 27, 2010

The satellite image processing is divided into two steps. The first step is data preprocessing and the second step is to use supervised classification for terrain classification, so as to extract the interested region which is the area of oil spill. The processing flow chart is shown in Fig. 2.

From the image shown in Fig. 1, different terrain types such as oil spill, sea and land area can be identified clearly, and the darkest parts is oil spill area. The image classification result is shown in Fig. 3, oil spill area, water area, buildings, mountains, cloud and the other are represented with red, blue, yellow, green, blue-green and white.

2.2 Area Statistics

After the classification, the areas of different terrain types will be counted out. The spatial resolution of CCD camera in Environment satellite is 30 meters and each pixel corresponds to a $30 \times 30 = 900$ m² area. Therefore, the area for each terrain type can be got while the pixel points are counted out. The area statistics are shown in Table 1.

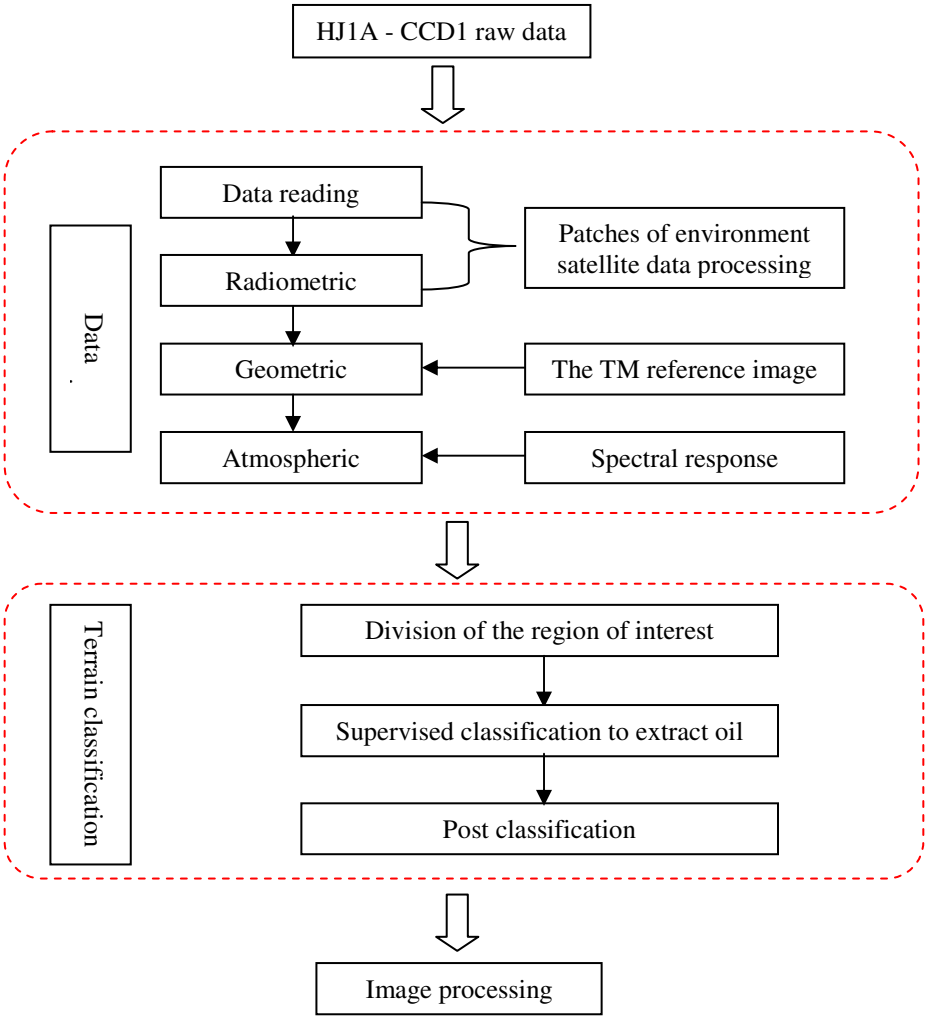

Fig. 2. Image processing flow chart

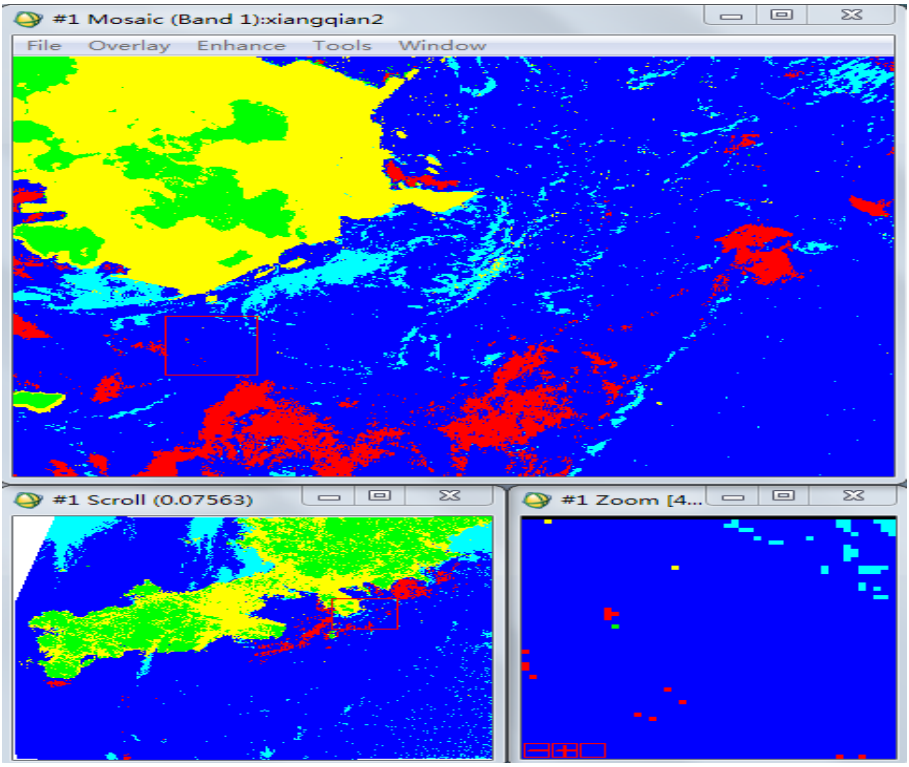

Fig. 3. Classification result

Table 1. Area Statistics

Sequence number	Terrain types	Pixel points	Area (km^2)	Percentage (%)
1	Oil Spillage	149284	134.3556	1.4407
2	seawater	6888995	6200.0955	66.4824
3	buildings	1070148	963.1332	10.3275
4	mountains	1435952	1292.3568	13.8577
5	clouds	606913	546.2217	5.8570
6	else	210837	189.7533	2.0347
7	summation	10362129	9325.9161	100.0000

3 Identification of Oil Spill Based on Oil Fingerprinting

The classification can only determine the scope and area of spilled oil, however not sure what is the type of oil spill. In this section, the spectral information of oil spill area are extracted from the remote sensing image, and compared with the spectral information of oil sample in oil fingerprint database to identify the type of the spilled oil.

3.1 Extraction of Oil Spill Spectrum from Remote Sensing

To make the comparison more convincing, the spectrum extraction is divided into three levels. They are thin oil area, thick oil area and the average thickness area spectrum. The reflectivity of the oil spill area is lower than the seawater area, the representation of the color in remote sensing image is darker than the seawater. The so-called thin oil area is the area which gray value between seawater and oil spill area. The thick oil area is the darkest part of the oil spill area. The average thickness area spectrum is the average spectrum of all the oil spill area. Thin oil, thick oil and average thickness area spectrum information are shown in Table 2 (a), (b) and (c).

Table 2(a). Spectrum information of thin oil area

Wavelength (nm)	Average DN
475	650.736527
560	480.553892
660	296.830838
830	250.002994

Table 2(b). Spectrum information of thick oil area

Wavelength (nm)	Average DN
475	586.71261
560	410.991202
660	292.372434
830	301.167155

Table 2(c). Spectrum information of average thickness area

Wavelength (nm)	Average DN
475	577.868635
560	409.336049
660	296.966395
830	301.209776

3.2 Quantification of Oil Spill Based on Oil Fingerprinting

The reflectivity of different kinds of oil on the surface is different. When oil is same type but with different thickness, it's reflectivity of the surface is also different. The paper takes crude oil as example and obtains different crude oil spectral information on the surface of the sea of different thickness (10 microns to 2000 microns), namely oil fingerprint of crude oil. The spectrum information of crude oil from the experiments are DN values of different thickness in visible light. In order to be more easily compared with extracting spectrum information of remote sensing, the paper extracted four DN values of the band corresponding to the remote sensing images.

In addition, in order to facilitate horizontal comparison, this paper uses 10 microns thickness lubricating oil, kerosene, light diesel oil fingerprint and spectrum extracted from remote sensing data to compare. The same with data processing of crude oil, the spectrum information of these species corresponding to remote sensing data are extracted respectively.

There are thin oil, thick oil, average thickness spectrum information extracted from remote sensing satellites and experimental spectrum information of various kinds of oil products. They will be compared and determine the type of oil spill. This paper will get the oil type which has the biggest correlation coefficient to oil spill (the most close to 1) through calculating the similarities of oil spill area DN and spectrum values of various oil fingerprinting. The similarities are sorted in descending order, and the oil product type corresponding to the maximum similarity be see visually. The similarities of thin oil, thick oil and average thickness oil area are shown in Table 3 (a), (b) and (c).

Table 3(a). Similarity between the thin oil spill area DN and oil fingerprinting (in descending order)

Oil type and thickness (μm)	Similarity
crude oil(1500)	0.863289581
crude oil(500)	0.857083602
crude oil(300)	0.852776792
crude oil(1000)	0.833909378
crude oil(2000)	0.821261867
crude oil(50)	0.820041652
lubricating oil(10)	0.813558721
crude oil(100)	0.807714612
light diesel oil(10)	0.789159910
Kerosene(10)	0.786645742
crude oil(10)	0.780574223

Table 3(b). Similarity between the thick oil spill area DN and oil fingerprinting (in descending order)

Oil type and thickness (μm)	Similarity
crude oil(1500)	0.743266633
crude oil(500)	0.733587386
crude oil(300)	0.729190766
crude oil(1000)	0.708084619
crude oil(50)	0.695781986
lubricating oil(10)	0.689937192
crude oil(2000)	0.687367811
crude oil(100)	0.672876508
light diesel oil(10)	0.662506513
Kerosene(10)	0.658284916
crude oil(10)	0.646774539

Table 3(c). Similarity between the average thickness oil spill area DN and oil fingerprinting (in descending order)

Oil type and thickness (μm)	Similarity
crude oil(1500)	0.748581247
crude oil(500)	0.739468616
crude oil(300)	0.734682852
crude oil(1000)	0.713024409
crude oil(50)	0.699979645
lubricating oil(10)	0.693863564
crude oil(2000)	0.693576452
crude oil(100)	0.678444759
light diesel oil(10)	0.666213219
Kerosene(10)	0.662147527
crude oil(10)	0.651221245

From the three tables, it can be saw clearly that the top three of the similarities which are 1500μm, 500μm and 300μm crude oil are the same. Moreover, two key information can be got here. One is that the type of the oil spill is closest to crude oil. The other is that the average thickness of the oil spill is the closest to 1500μm.

The remote sensing satellite images in this paper are got on July 27, 2010, the oil spill accident has been in the past 10 days. Based on the above, the conclusion can be obtained that the type of oil spill should be crude oil, ten days after the oil spill accident happened, the diffusion area covers 134.3556 km^2. When the density and thickness of the crude oil are 0.81t/m^3 and 1500μm, the amount of oil spill is 163242.054 tons. When the thickness of the oil spill is 300μm, the amount of oil spill is 32648.4108 tons. Thus the oil spill can be estimated in an amount ranging between 32648.4108 and 163242.054 tons. It has a deviation with actual situation and the error analysis will be discussed in section 4.

4 Error Analysis

With the combination between ocean remote sensing and oil fingerprint technology, the amount of oil spill in this paper is acceptable, and the main error sources will be introduced in the identification.

(1) The processing error of remote sensing image. Due to the influence of solar radiation, surface radiation, geometric distortion, aerosols, clouds, etc, the information which are collected with remote sensing satellite sensor can be polluted and lead to all kinds of error. Although in the image preprocessing, radiation calibration, geometric and atmospheric rectification have been performed and reduce the influence to the area of oil spill. However the precise geometric rectification of remote sensing images to the topographic maps and the rigorous atmosphere rectification cannot be performed because the more precise topographic maps and detail weather information on that day could not be got. Therefore, the image preprocessing are rough calibrations. The low accuracy of remote sensing image leads to the error of the collected spectral information.

(2) The data processing error. Various oil spectrum information in oil fingerprinting database is very detailed, their wavelength range from 350 nm to 2500 nm with each wavelength corresponding to a DN. However, the environmental small satellite used in this paper has only four sensors/bands, the center wavelength of each band are 475 nm, 560 nm, 660 nm, 830 nm. In order to be compared with satellite remote sensing data, the four oil fingerprints corresponding to those four center wavelengths must be resampled from the whole oil fingerprint, which makes the oil fingerprint information give a great discount and leads that the general change trend of the curves can be only compared. The lack of information results the inaccurate comparison and a large error.

(3) Weathering, volatilization, seawater dilution effects on spectral information of oil spill. Because the remote sensing image data used in this paper is obtained 10 days after the oil spill accident, the oil spill has already diffused, must have got the weathering on the surface, water dilute, and there will be a part of the spilled oil volatilized. These lead to some deviations occurred in oil spill spectral information extracted from remote sensing images. In addition, the oil fingerprint in database didn't consider the influence of weathering, volatilization and seawater dilution, etc. Both of which can result error.

5 Conclusion

Based on the oil fingerprint technology and ocean remote sensing, we present the identification method of marine oil spill, and uses the case of an oil spill accident in Dalian to analyze. Experimental results show that the oil spill is crude oil and the diffusion area of oil spill 10 days after the accident is 134.3556 km2, moreover the oil spill is estimated in an amount ranging between 32648.4108 and 163242.054 tons. The type of oil spill is consistent with the actual type, and the spilled oil diffusion area and amount are slightly larger. Under the support of the existing oil fingerprint

database, the results obtained with the identification method are all in the range of allowable error, which show that the method is feasibility and effectiveness, and opens up a new idea of identification for marine oil spill, moreover provides an effective technical support to solve the oil spill dissension and protect the marine ecological environment.

Acknowledgments. The work is supported by the National Natural Science Foundation of China under grant no 61001158, Specialized Research Fund for the Doctoral Program of Higher Education (SRFDP no 200801511027), Fundamental Research Funds for the Central Universities and Key Research Program of Ministry of public security of China (Grant No. 2011ZDYJNNGZ026).

References

1. Liu, H.J., Zhang, H.S.: Marine Petroleum Pollution and Treatment Measures. Guangzhou Environmental Science 27(4), 35–38 (2012)
2. Malmquist, L.M., Olsen, R.R., Hansen, A.B., Andersen, O., Christensen, J.H.: Assessment of oil weathering by gas chromatography-mass spectrometry, time warping and principal component analysis. Journal of Chromatography A 1164(1-2), 262–270 (2007)
3. Sun, P.Y., Bao, M.T., Wang, X.P., Zhao, B., Gao, Z.H., Wang, X.L.: Existing state of spilled oil identification and oil fingerprint database construction at home and abroad. Journal of Xi'an Shiyou University (Natural Science Edition) 21(5), 72–78 (2006)
4. Pan, D.L., Gong, F.: Progress in Application Technology of satellite Ocean Remote Sensing in China. Journal of HangZhou Normal University (Natural Science Edition) 10(1), 1–10 (2011)
5. Lan, G.X., Ma, L., Chen, G.W.: Applications of HJ Satellites in Monitoring. Dalian Xingang Oil Spill Incident. Navigation of China 34(4), 89–93 (2011)

The Research on Comprehensive Protection Technology of Highway Environment

Yanhua Wang and Zhulong Li

CCCC First Highway Consultants Co., LTD Xi'an, China
yhwang930@foxmail.com

Abstract. The construction of ecological civilization and sustainable development is an important task for implementing the scientific concept of development, in this paper, According to the highway environment comprehensive protection technology, summarizing the development status of the highway environment protection, comparing the study of the development with the foreign relation subjects, Analysising the existing problems and shortage of the highway environment comprehensive protection technology in our country, and putting forward the future development trend, countermeasures and suggestions.

Keywords: highway environment, comprehensive protection, highway architecture, the design of Highway.

1 Introduction

Inevitably, the construction of highway have a certain impact on the ecological environment nearby, Such as the destruction of vegetation, soil and water loss, the division of land, water, air and noise pollution. How to minimize these effects, reasonably using natural resources based on protecting environment, coordinate the development of highway construction and ecological environment protection, which is a new subject of highway construction facing, nowadays. In recent years, a lot of work on the highway environment protection has been done in China, actively absorbing domestic and foreign advanced experience of the highway design, combining the real problem closely, therefore, it has research value In theory and far-reaching practical significance.

2 Comprehensive Protection and Development Status of the Highway Environment

2.1 The Theory of Highway Architecture

The highway architecture is a comprehensive scientific to research highway construction group, it relates to the content of the highway strip buildings, engineering technology, construction economics, building arts, and the environment

F. Bian et al. (Eds.): GRMSE 2013, Part I, CCIS 398, pp. 766–771, 2013.
© Springer-Verlag Berlin Heidelberg 2013

and landscape. Simply speaking:It leads architecture to the highway industry,research highway by the method of architecture. Basing on this definition,it is not difficult to seethat ecological road, green road, culture road, environmental road and so on Is the field of contemporary architecture, ecological building, green buildings, cultural buildings, sustainable building diversification theory mapping the highway.

The purpose of proposing the highway architecture is based on that make the highway engineering structures or structures as a ribbon of buildings plan and design, use scientific research methods and integrate into highway construction,in case emphasising on a certain technical indicators in the highway construction,neglecting of the highway as a basic public buildings taken into account other indicators, Such as safety performance, environmental coordination, aesthetic, art, light, color and landscape elements, in order to achieve the construction of Highway Engineering Science and harmonious design.Therefore, the road architecture research should include the following aspects:

The basic functional requirements of highway includes not only safe, comfortable and smooth involved in highway engineering disciplines, but also include the demand as public buildings aesthetics, environmental protection, etc..

The highway structure and its technical indicators, including coordination between the internal structure of the road, and local and global coordination, the specific technical parameters is a highway engineering focus of the study or isn't a focus of the highway architectureis, but we should give full consideration to the coordination of technical indicators on the road architecture.

The environmental coordination of highway construction group including road construction group space, color, external environment and the landscape and art coordination. "The research of Chuanzhusi to Jiuzhaigou highway environmental protection and landscape design key technology" establish a new concept based on highway construction "fully respect for nature and the protection of nature" and the synchronization with environmental protection to achieved new innovations and exceed. The achievements have been awarded the 2007 China Institute of Highway Science and Technology Award.

2.2 Route Design Technology

Natural and social environment of the areas along the route is fully taken into account in the design, terrain is used rationally, technical standards are used correctly, linear equalizer is ensured balance.Topographic mapping uses the aerial photogrammetry and the digital mapping technology, control measure uses GPS technology, generating three-dimensional terrain of new technologies and computer-aided design with DTM data, improves continuously the engineering rationality and environmental friendliness of the road longitudinal line selection,"Environmental Engineering technology research and demonstration of Shennongjia Muyuping to Xingshan Zhaojunqiao Highway",the object researched to solved the outstanding environmental problems in Shenyi Highway renovation and expansion, realizes the coordination and optimization of the internal and external route landscape, reduce the impact of road construction on the natural environment, enhances the quality along

the highway landscape, conservation of resources, capital and materials, resolves outstanding resource use and landscape greening.The achievement is awarded for 2009 Highway Institute of Science and Technology.

2.3 Roadbed Design Technology

The highway of the domestic plain area exits a widespread problem that the roadbed construction height is too high. According to statistics, the average embankment height plain area is 3-5 meter in China.The high embankment occupied intensive existing land resources, increased the size and cost of the project, and produced a lot of malpractice in the process of engineering operations. Therefore, judging from the environmental protection and sustainable development, The low embankment design technology received more and more concern, it is also an important measures on the conservation of land resources, reducing ecological damage, and weakening road network cutting.At the same time,The special subgrade construction technology such high liquid limit soil improved road technology and low embankments soft-processing technology achieved a series of international advanced level of scientific research, provided important technical support for the use of road waste soil resources.

2.4 Pavement Design Technology

It carries out systematicly researches such as pavement design specifications and standards, semi-rigid asphalt pavement crack the road fatigue damage and axle load conversion method, the road of large-scale construction technology and equipment development.In the field of the pavement design, it formed a relatively complete performance-based heavy traffic asphalt pavement design method. Using rubber as a paving material, which can not only solve the social problems brought about by the waste tire, is a social welfare obvious environmental project, save a lot of construction investment for the highway construction, find a reasonable way to solve the current some highway problems, provide road users with a durable, smooth, comfortable and quiet environmental quality of the road surface.

2.5 Bridge Engineering and Technology

Taking into account the safety of the bridge and the affect when bridge is finished, it brings out geological, environmental protection, cost, the selection of the bridge foundation is optimized. When the function of bridges use is satisfied, we pursuit the effect of beautiful appearance, reasonable structure, safe and reasonable layout.

2.6 Tunnel Engineering and Technology

Highway tunnel survey and design has improved continuously, we have adopted generally a seismic wave reflection method, acoustic wave reflection method,

infra-red Water Law and geological radar in the work of the initial test in geological exploration and construction phases geological prediction. The various geological survey method is integrated so that the reliability of geological information has been greatly improved, the damage of water and rock through mountain is reduced effectively, environmental impact is reduced. Secondly, in the design concept, environmental awareness has been strengthened, pre-design of construction and the information feedback dynamic design principles of construction phase has been popularized.

3 Comparative Study with the Development of Foreign Subjects

3.1 The Research of Road Network Has Attached Great Importance to the Regional Environmental Impact

The foreign countries pay more attention to the cutting action of the road network to the regional environment, for example, Harvard University Professor Forman believes that: the impact of the road network on the ecological environment is over a broad area, and it has the long-term and cumulative characteristics. The huge network of highways may lead to ecological fragmentation and affect ecological patterns. He pointed out that the influence of United States road network on the ecological environment is large, about 20% of the land area of the United States. However, the study on highway environmental protection in our country mostly concentrated in the ecological and environmental protection and impact assessment of the highway construction, the environmental impact effect is often reduced or weakened.

3.2 Focus on Long-Term Follow-Up Study

According to foreign study found that most ecosystems is in the event of habitat fragmentation, causes the ecological impact of animal populations with a certain time lag effect, therefore, them should not be directly detected. Foreign research has pay attention particularly on basic research and long-term observations. For example, Funded in the transport sector, the western United States Institute of Transportation has carried out more than 10 years of continuous observation to the fatal collision of wild animals and animal Channel validity through the Banff National Park in Canada TCH highway. In contrast, China is generally focused on applied research, for lack of the study of highway construction and operation of long-term effects on the environment, and for lack of the research of tracking assessment on the implementation of environmental protection measures (such as animal channel).

3.3 The Deepening of the Operation Period of the Highway on the Environmental Impact Research

Europe and the United States and other developed countries has completed basically the road network, highway environmental protection research concentrates on the

operation of highway impact on the environment and its protection. For example, the United States pay great importance to for road vegetation management. The management objective is from a single grass to flowers and the attractive and diverse species. They proposed to a series of technical measures: " reducing herbicide use, the protection of groundwater, encouraging the planting of beautiful native plants, preventing weeds, providing wildlife habitat ". Our country is at this stage of the transport infrastructure construction and development recently, we pay more attention to the environmental protection work in the construction process, The research of the highway operations impact on the environment is less.

3.4 Focusing on Non-renewable Environmental Resources Compensation

Highway projects inevitably cause some loss of environmental resources. The foreign take some effective compensation measures, for example, When wetlands are occupied in the highway construction, the same size wetlands are Compensated so that the wetlands are affected Less or not. China is lack of the awareness and exploration, we usually use the financial compensation to resolve, leading to irreversible environmental damage after road construction.

4 Situation Analysis and Policy Recommendations

4.1 Consider the Development of Interdisciplinary

We ought to focus on the absorption and adoption of environmental protection technology about the route selection of highway, environmental design is not just environmental protection design. We should adhere to the sustainable development strategies and the coordinated development of transport construction and environmental protection in the guiding ideology. Combining the highway traffic environmental protection planning and environmental management system, minimizing the impact on the environment, making transport development serve for the prevention and control of environmental pollution, maintaining ecological balance, protecting human good living environment.Using rationally standards and technical specifications, providing the most comprehensive transportation services to society at the smallest environmental cost.

4.2 Strengthen the Landscape Environment Co-ordination Technology of the Planning and Design Stage

Highway construction and environment harmony is an important issue for the highway development in China. Firstly, economic development is more urgent for highway traffic, the highway construction task is heavy, secondly, social progress and the improvement of people's material and cultural level that make the highway function undergo a change in perceptions. It not only require the highway to be safe and fast, but also pay more attention to the highway comfort, beauty and highway

harmony with the surrounding environment, making users feel pleasing. The Highway Landscape Construction is an extremely important aspect of highway construction and should be run through the whole process of road planning and design, creating a linear, smooth, rhythmic sense of rhythm highway, constructing a beautiful image whether the inside or outside of the highway.

References

1. Comprehensive Planning Department of the Ministry of Transport.2010 Highway and Waterway Transport Industry Development Statistical Bulletin. Comprehensive Planning Department of the Ministry of Transport, Beijing (2011)
2. Zhong, D., Liu, K., Wu, K.: 3D Modeling and Visualization of Highway Tunnels. Journal of Engineering Graphics 26(4), 81–87 (2005)
3. Zhang, G., Zhang, P., Jiang, C., et al.: Research on the Application of GIS in Highway Tunnel Information Management System. China Transport Information Industry (10), 104–106 (2007)
4. Zhang, J., Zhu, H., Zhu, Y., et al.: Digital Strata Modeling and Its Application to Xiang'an Subsea Tunnel in Xiamen. Chinese Journal of Rock Mechanics and Engineering 26(6), 1237–1242 (2007)
5. Chuai, J., Jiang, W.: Modeling of Highway Tunnel Scene Simulation. Journal of Chang'an University: Nature Science Edition 26(1), 63–66 (2006)
6. Jie, F., Zhu, H., Li, X., et al.: Temporal GIS Model and Its Application in Tunneling. Chinese Journal of Underground Space and Engineering 5(3), 546–552 (2009)
7. Cheng, P., Li, D., Shi, W., et al.: Bridge Structural Health Monitoring and Management System Based on GPS and GIS Techniques. Journal of Highway and Transportation Research and Development 21(2), 48–52 (2004)
8. Hammons: Development of an Analysis System for Discontinuities in Rigid Airfield Pavement. Louisiana State University, Baton Rouge (1997)
9. Fernando, E.: Analysis Procedure for Load-zoning Pavement. Trasportation Research Record 1860, 117–125 (2003)

Erratum: The Discrimination of Cloud Using the Data of Calipso Based on SVM Method

Jingbo Wang and Xiaoyi Li

International School of Software, Wuhan University, Wuhan, China
Jingbowang.whu@gmail.com, 2496282640@qq.com

F. Bian et al. (Eds.): GRMSE 2013, Part I, CCIS 398, pp. 393–402, 2013.
© Springer-Verlag Berlin Heidelberg 2013

DOI 10.1007/978-3-642-45025-9_76

The paper "The Discrimination of Cloud Using the Data of Calipso Based on SVM Method" authored by Jingbo Wang and Xiaoyi Li, DOI 10.1007/978-3-642-45025-9_39, appearing on pages 393–402 of this publication has been retracted due to plagiarism. The authors used experiment data from a master dissertation without informing the original author.

The original online version for this chapter can be found at
http://dx.doi.org/10.1007/978-3-642-45025-9_39

Erratum: Analysis of Transmission Line's Scattering Characteristics in High Resolution Radar Satelite Image

Jingbo Wang, Qi Chen, and Shuaishuai Deng

International School of Software, Wuhan University, Wuhan, China
Jingbowang.whu@gmail.com, {731996261, 1518254262}@qq.com

F. Bian et al. (Eds.): GRMSE 2013, Part I, CCIS 398, pp. 403–417, 2013.
© Springer-Verlag Berlin Heidelberg 2013

DOI 10.1007/978-3-642-45025-9_77

The paper "Analysis of Transmission Line`s Scattering Characteristics in High Resolution Radar Satelite Image" authored by Jingbo Wang, Qi Chen, Shuaishuai Deng, DOI 10.1007/978-3-642-45025-9_40, appearing on pages 403–417 of this publication has been retracted due to plagiarism. The authors used experiment data from a master dissertation without informing the original author.

The original online version for this chapter can be found at
http://dx.doi.org/10.1007/978-3-642-45025-9_40

Author Index